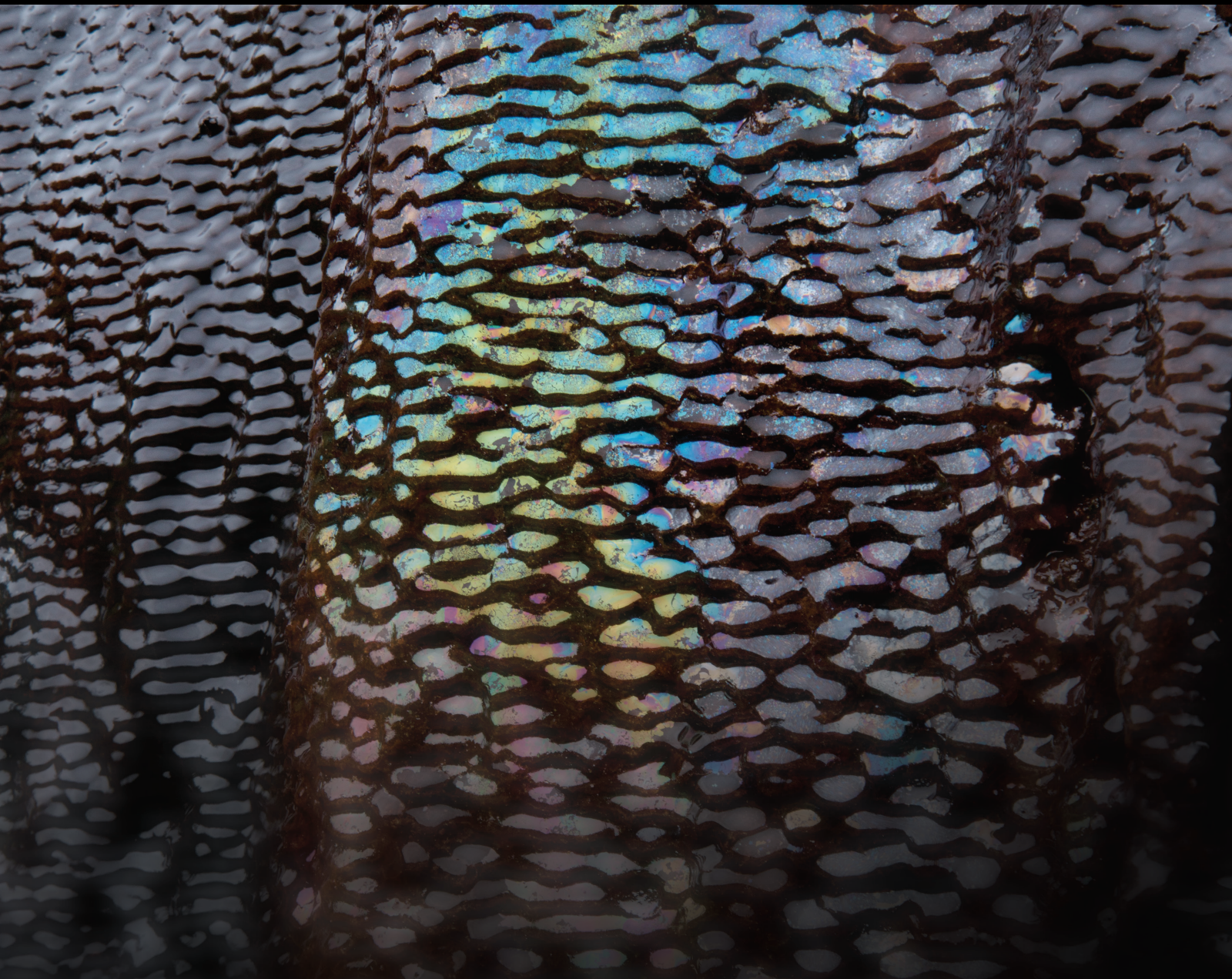


# Multiscale and Multiphysics Approaches to Fluids Flow in Unconventional Reservoirs 2021

Lead Guest Editor: Jianchao Cai

Guest Editors: Stefan Iglauer, Steffen Berg, and Chenhao Sun





---

**Multiscale and Multiphysics Approaches to  
Fluids Flow in Unconventional Reservoirs 2021**

Geofluids

---

**Multiscale and Multiphysics Approaches  
to Fluids Flow in Unconventional  
Reservoirs 2021**

Lead Guest Editor: Jianchao Cai

Guest Editors: Stefan Iglauer, Steffen Berg, and  
Chenhao Sun



---





Copyright © 2022 Hindawi Limited. All rights reserved.

This is a special issue published in "Geofluids." All articles are open access articles distributed under the Creative Commons Attribution License, which permits unrestricted use, distribution, and reproduction in any medium, provided the original work is properly cited.



























# Chief Editor

































Umberta Tinivella, Italy

## Associate Editors

Paolo Fulignati , Italy  
Huazhou Li , Canada  
Stefano Lo Russo , Italy  
Julie K. Pearce , Australia

## Academic Editors

Basim Abu-Jdayil , United Arab Emirates  
Hasan Alsaedi , USA  
Carmine Apollaro , Italy  
Baojun Bai, USA  
Marino Domenico Barberio , Italy  
Andrea Brogi , Italy  
Shengnan Nancy Chen , Canada  
Tao Chen , Germany  
Jianwei Cheng , China  
Paola Cianfarra , Italy  
Daniele Cinti , Italy  
Timothy S. Collett , USA  
Nicoló Colombani , Italy  
Mercè Corbella , Spain  
David Cruset, Spain  
Jun Dong , China  
Henrik Drake , Sweden  
Farhad Ehya , Iran  
Lionel Esteban , Australia  
Zhiqiang Fan , China  
Francesco Frondini, Italy  
Ilaria Fuoco, Italy  
Paola Gattinoni , Italy  
Amin Gholami , Iran  
Michela Giustiniani, Italy  
Naser Golsanami, China  
Fausto Grassa , Italy  
Jianyong Han , China  
Chris Harris , South Africa  
Liang He , China  
Sampath Hewage , Sri Lanka  
Jian Hou, China  
Guozhong Hu , China  
Lanxiao Hu , China  
Francesco Italiano , Italy  
Azizollah Khormali , Iran  
Hailing Kong, China

Karsten Kroeger, New Zealand  
Cornelius Langenbruch, USA  
Peter Leary , USA  
Guangquan Li , China  
Qingchao Li , China  
Qibin Lin , China  
Marcello Liotta , Italy  
Shuyang Liu , China  
Yong Liu, China  
Yueliang Liu , China  
Constantinos Loupasakis , Greece  
Shouqing Lu, China  
Tian-Shou Ma, China  
Judit Mádl-Szonyi, Hungary  
Paolo Madonia , Italy  
Fabien Magri , Germany  
Micòl Mastroicco , Italy  
Agnes Mazot , New Zealand  
Yuan Mei , Australia  
Evgeniy M. Myshakin , USA  
Muhammad Tayyab Naseer, Pakistan  
Michele Paternoster , Italy  
Mandadige S. A. Perera, Australia  
Marco Petitta , Italy  
Chao-Zhong Qin, China  
Qingdong Qu, Australia  
Reza Rezaee , Australia  
Eliahu Rosenthal , Israel  
Gernot Rother, USA  
Edgar Santoyo , Mexico  
Mohammad Sarmadivaleh, Australia  
Venkatramanan Senapathi , India  
Amin Shokrollahi, Australia  
Rosa Sinisi , Italy  
Zhao-Jie Song , China  
Ondra Sracek , Czech Republic  
Andri Stefansson , Iceland  
Bailu Teng , China  
Tivadar M. Tóth , Hungary  
Orlando Vaselli , Italy  
Benfeng Wang , China  
Hetang Wang , China  
Wensong Wang , China  
Zhiyuan Wang , China  
Ruud Weijermars , Saudi Arabia







Bisheng Wu , China  
Da-yang Xuan , China  
Yi Xue , China  
HE YONGLIANG, China  
Fan Yang , China  
Zhenyuan Yin , China  
Sohrab Zendehboudi, Canada  
Zhixiong Zeng , Hong Kong  
Yuanyuan Zha , China  
Keni Zhang, China  
Mingjie Zhang , China  
Rongqing Zhang, China  
Xianwei Zhang , China  
Ye Zhang , USA  
Zetian Zhang , China  
Ling-Li Zhou , Ireland  
Yingfang Zhou , United Kingdom  
Daoyi Zhu , China  
Quanle Zou, China  
Martina Zucchi, Italy

# Contents



## **Study on the Deformation and Stability of Proppant Column in High-Conductivity Channel Fracturing**

Ming Wang , Feng Zhang, and Hanxiang Wang  
Research Article (26 pages), Article ID 3744053, Volume 2022 (2022)



## **Methane Flux Effect on Hydrate Formation and Its Acoustic Responses in Natural Sands**

Qingtao Bu , Tongju Xing , Gaowei Hu , Changling Liu , Chengfeng Li , Jinhuan Zhao ,  
Zihao Wang , Wengao Zhao , and Jiale Kang   
Research Article (12 pages), Article ID 7746386, Volume 2022 (2022)

## **Quantitative Evaluation of Well Performance Affected by Fracture Density and Fracture Connectivity in Fractured Tight Reservoirs**

Wenchao Fang , Xuejie Qin, Chuanxi Liu, Ruyue Wang , Jun Pu, Hanqiao Jiang, and Weiling He  
Research Article (14 pages), Article ID 2805348, Volume 2022 (2022)



## **Analysis of Microstructure and Low Permeability with 3D Digital Rock Modeling**

Jinsui Wu , Min Xing , Shangxian Yin, Ciyuan Zhang, Xuexi Chen, Sihai Yi, Huiqing Lian, and Dongyu Xie  
Research Article (13 pages), Article ID 2462652, Volume 2022 (2022)


## **A New Projection-Based Integrally Embedded Discrete Fracture Model and Its Application in Coupled Flow and Geomechanical Simulation for Fractured Reservoirs**

Dawei Wu , Yuan Di , and Yu-Shu Wu  
Research Article (22 pages), Article ID 7531948, Volume 2022 (2022)



## **Characteristics of Pore-Throat in Tight Sandstones of the Jurassic Ahe Formation in the Northern Tarim Basin**

Tong Lin, Cong Tan , Xing Zhang, Lei Zhao, Hongxing Wei, Lan Wang, Xin Nie , and Xu Zeng  
Research Article (18 pages), Article ID 1139232, Volume 2022 (2022)




## **Study on Downhole Throttling Characteristics of High Water Content Gas**

Jie Zheng, Zhenzhen Li , Yihua Dou, Yarong Zhang, Cheng Bi, Xu Yang, and Jiahui Li  
Research Article (14 pages), Article ID 5257771, Volume 2022 (2022)



## **Evaluation of the Accumulation Conditions and Favorable Areas of Shale Gas in the Upper Palaeozoic Marine-Continental Transitional Facies in the Daning-Jixian Area, Ordos Basin**

Xu Zeng , Wei Wang, Qian Cao, Shangwen Zhou , Guodong Dong, Aiming Wang, Zhixin Chen, and Hua Mei  
Research Article (16 pages), Article ID 2414506, Volume 2022 (2022)

## **A New Method for Calculating the Cementation Exponent of Triple-Porosity Media Reservoirs**



Dahai Wang , Jinbu Li , Lili Liu, Ji Zhang, Zhanhai Yu, and Jun Peng   
Research Article (9 pages), Article ID 4336067, Volume 2022 (2022)

**NMR Analysis Method of Gas Flow Pattern in the Process of Shale Gas Depletion Development**

Rui Shen , Zhiming Hu, Xianggang Duan , Wei Sun, Wei Xiong, and Hekun Guo


Research Article (7 pages), Article ID 3021326, Volume 2022 (2022)

**Paleoenvironment, Geochemistry, and Pore Characteristics of the Postmature to Overmature Organic-Rich Devonian Shales in Guizhong Depression, Southwestern China**

Yanqi Zhang , Li Liu, Changxi Geng, Zhuang Cheng, and Xinxin Fang 

Research Article (18 pages), Article ID 7947116, Volume 2021 (2021)

**A Novel Mathematical Model for Fracturing Effect Evaluation Based on Early Flowback Data in Shale Oil Reservoirs**

Yuhan Wang, Zhengdong Lei, Zhenhua Xu, Jie Liu, Xiaokun Zhang, Erhui Luo, Yuqi Liu, and Pengcheng Liu 


Research Article (14 pages), Article ID 1780937, Volume 2021 (2021)

**Pore Structure and Connectivity of Mixed Siliciclastic-Carbonate Tight Reservoirs in the Palaeogene from Qaidam Basin, NW China**

Xin Wang, Jianhui Zeng , Kunyu Wu, Xiangcheng Gao, Yibo Qiu, Tongzhi Lu, Kunkun Jia, Chen Zhang, Juncheng Qiao, Zixin Xue, Qianyou Wang , and Xiangye Kong 


Research Article (20 pages), Article ID 8348773, Volume 2021 (2021)

**Numerical Study of the Effect of Magnetic Field on Nanofluid Heat Transfer in Metal Foam Environment**

Hamid Shafiee , Elaheh NikzadehAbbasi, and Majid Soltani



Research Article (14 pages), Article ID 3209855, Volume 2021 (2021)

**Transient Pressure Behavior of Complex Fracture Networks in Unconventional Reservoirs**

Gou Feifei, Liu Chuanxi, Ren Zongxiao , Qu Zhan, Wang Sukai, Qin Xuejie, Fang Wenchao, Wang Ping, and Wang Xinzhu




Research Article (11 pages), Article ID 6273822, Volume 2021 (2021)

**Chemical Potential-Based Modeling of Shale Gas Transport**

Jisheng Kou , Lingyun Chen, Amgad Salama, and Jianchao Cai 


Research Article (16 pages), Article ID 2535284, Volume 2021 (2021)

**Dust Concentration Changing Regularities and Dust Reduction Technology by Spray Negative Pressure in Fully Mechanized Mining Face**

Lirong Wu , Hongxuan Chen , Jiamin Li , Shican Fu, and Yuyan Zhuang

Research Article (16 pages), Article ID 1391673, Volume 2021 (2021)

**Accumulation and Distribution of Natural Gas Reservoir in Volcanic Active Area: A Case Study of the Cretaceous Yingcheng Formation in the Dehui Fault Depression, Songliao Basin, NE China**

Fancheng Zeng, Bo Liu , Changmin Zhang, Guoyi Zhang, Jin Gao, Junjie Liu, and Mehdi Ostadhassan



Research Article (17 pages), Article ID 2900224, Volume 2021 (2021)



## Contents


---

### **Fracability Evaluation Method and Influencing Factors of the Tight Sandstone Reservoir**

Jiageng Liu, Lisha Qu, Ziyi Song, Jing Li , Chen Liu, Yongcun Feng , and Haihang Sun



Research Article (15 pages), Article ID 7092143, Volume 2021 (2021)

### **Numerical Study of the Effect of Perforation Friction and Engineering Parameters on Multicluster Fracturing in Horizontal Wells**

Zixi Jiao, Anlin Zhang, Longhuan Du , Yang Yang, and Hua Fan







Research Article (18 pages), Article ID 9969112, Volume 2021 (2021)

### **Nanopore Confinement Effect on the Phase Behavior of CO<sub>2</sub>/Hydrocarbons in Tight Oil Reservoirs considering Capillary Pressure, Fluid-Wall Interaction, and Molecule Adsorption**

Zhixue Zheng , Yuan Di , and Yu-Shu Wu



Research Article (18 pages), Article ID 2435930, Volume 2021 (2021)

### **High-Precision Numerical Simulation on the Cyclic High-Pressure Water Slug Injection in a Low-Permeability Reservoir**

Jie Zhan , Chao Fan , Xianlin Ma , Zigang Zheng , Zezhong Su , and Zhihao Niu 


Research Article (10 pages), Article ID 3507426, Volume 2021 (2021)

### **Study on the Water Invasion and Its Effect on the Production from Multilayer Unconsolidated Sandstone Gas Reservoirs**

Yong Hu, Xizhe Li , Weijun Shen , Changmin Guo, Chunyan Jiao, Xuan Xu, and Yuze Jia

Research Article (9 pages), Article ID 5135159, Volume 2021 (2021)

### **Expansion Velocity Model of Steam-Assisted Gravity Drainage considering Thermal Convection**

Dian-Fa Du, Yao-Zu Zhang , Li-Na Zhang, Meng-Ran Xu, and Xin Liu

Research Article (12 pages), Article ID 9925410, Volume 2021 (2021)

### **Geochemical Characteristics and Oil Source Correlation of Minfeng Area, Dongying Depression, China**

Dongmei Bo, Lin Jiang , Wen Zhao , Youlu Jiang, Hua Liu, and Haowen Ou

Research Article (11 pages), Article ID 9928294, Volume 2021 (2021)

## Research Article

# Study on the Deformation and Stability of Proppant Column in High-Conductivity Channel Fracturing

Ming Wang <sup>1</sup>, Feng Zhang,<sup>2,3</sup> and Hanxiang Wang<sup>2</sup>

<sup>1</sup>Shandong Institute of Petrochemical Technology, Dongying, Shandong 257001, China

<sup>2</sup>China University of Petroleum (East China), Qingdao, Shandong 266580, China

<sup>3</sup>Shengli Oil Field Petroleum Engineering Technology Research Institute, Sinopec, Dongying, Shandong 257000, China

Correspondence should be addressed to Ming Wang; wang\_ming\_001@163.com

Received 5 July 2021; Revised 21 January 2022; Accepted 13 April 2022; Published 14 July 2022

Academic Editor: Hetang Wang

Copyright © 2022 Ming Wang et al. This is an open access article distributed under the Creative Commons Attribution License, which permits unrestricted use, distribution, and reproduction in any medium, provided the original work is properly cited.

The nonlinear constitutive model of the proppant column was established through laboratory experiments on the stability of the proppant column. Based on reservoir geomechanics and the finite element method, a fracture-proppant column interaction model was established for high-conductivity channel fracturing. The effects of in situ stress, reservoir rock elastic parameters, and spatial distribution characteristics of the proppant column on the closure deformation of the high-conductivity fracture channel and the stability of the proppant column were studied. The higher the in situ stress, the higher the contact stress on the rock plate; the lower the height and the larger the diameter of the proppant column, the more prone to deformation and breakage, while the more the effective support decreases with the increase of the in situ stress. Under the condition of constant in situ stress, with the increase of the reservoir elastic modulus, the relative axial displacement of the two slabs decreases gradually, the effective propping ratio of fractures increases, and the reservoir elastic modulus has little effect on the stability of the proppant column. The effective propping ratio decreases with the increase of the proppant column diameter, increases with the increase of the proppant column height, and increases with the increase of the ratio of the reservoir elastic modulus to in situ stress. When the proppant column diameter (proppant column spacing) is less than 3 m, the effective propped fracture ratio increases significantly. Through the above research, the optimal proppant cluster diameter was finally optimized.

## 1. Introduction

Channel fracturing was first proposed by Gillard et al. [1] in 2010, and its process mainly consists of three parts: multi-cluster perforation process, fracturing fluid-blending fiber process, and pulse-pumping process. The sand carrier fluid and the displacement fluid were injected into the formation alternately at a certain time ratio, so that there was no proppant between the adjacent two stages. After the fracturing fluid was gouged and flowed back, the proppant cluster formed an unevenly laid proppant column to support the fracture and formed a high-conductivity channel between the adjacent two proppant columns. In channel fracturing, fibers are added to the fracturing fluid to alter proppant rheology, preventing slug dispersion during migration and settlement, and reducing proppant settlement rates, enabling the formation of an ideal proppant cluster in the fracture.

As a new type of hydraulic fracturing stimulation technology, high diversion channel-fracturing technology has achieved remarkable results in field application, which not only reduces the cost of fracturing operation but also greatly increases the production. Abroad, for example, the Talinskoe field in Siberia has seen a 51% increase in well production after channel fracturing [2–9]. After channel fracturing in the Burgos Basin in Mexico, initial gas well production increased by 32%, and half-year cumulative gas production increased by 19% [10]. Early production in the Qarun field in the Western Desert of Egypt was increased by 89% after channel fracturing [11]. At present, this technology has been widely used in the Shengli oilfield, Sichuan Basin tight gas reservoirs, and Ordos Basin tight oil and gas reservoirs and achieved good results. For example, after channel fracturing in tight oil and gas reservoirs in the Ordos Basin, China, oil well production is 2.4 times that of

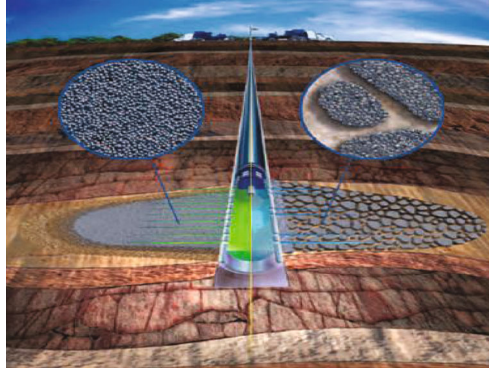


FIGURE 1: Schematic diagram of proppant placement for conventional hydraulic fracturing (left) and high-speed channel fracturing (right) [1].

TABLE 1: Value table of experimental factors.

Factors	Values						
Height of proppant columns (mm)	6	8	10	—	—	—	—
Number of proppant columns	5	7	9	—	—	—	—
Closure pressure (MPa)	0.9	6.9	13.8	20.7	27.6	34.5	41.4

conventional fracturing, and gas well production is 4-5 times that of conventional fracturing [12–18]. Therefore, channel-fracturing technology has a broad application prospect in unconventional oil and gas development.

Fractures are supported by dispersed proppant clumps (or columns) that form low-drag flow paths for fluid flow. Compared to conventional fracturing techniques, high-conductivity channel fracturing overcomes the limitations of fluid flow confined to a porous medium, breaks the design philosophy of evenly distributed proppant, and provides higher fracture conductivity (as shown in Figure 1).

The mechanics characteristic of the proppant column is a major factor affecting the law of channel-fracturing fracture closure, the current characteristics of the channel-fracturing proppant column fracture mechanics study is less, the scholars did not delve into the constitutive relation of the fracturing proppant fracture column, most of the proppant elastomer column was regarded as a line, and this is the blank area of the channel-fracturing study.

Many scholars have conducted a large number of laboratory experiments and theoretical studies on the mechanical characteristics and fracture conductivity of the proppant column in channel fracturing. Nguyen et al. [19] conducted fracture conductivity tests for channel fracturing by placing several small cylindrical proppant columns on rock plates based on the APIRP61 fracture conductivity testing standards. The results showed that when the proppant particles were well consolidated, the effective fracture permeability of channel fracturing increased by 1.5 to 2.5 orders of magnitude in comparison with that of conventional fracturing. In 2016, Yan et al. [20, 21] assumed the proppant column as a cylindrical linear elastomer and established a fracture width model considering the deformation and embedding of the proppant column when deducing the channel compression fracture width model. In 2016, Hou et al. [22] also

TABLE 2: Experimental groups.

Experimental groups	Height (mm)	Number of columns
1	10	9
2	10	7
3	10	5
4	8	9
5	8	7
6	8	5
7	6	9
8	6	7
9	6	5



FIGURE 2: Fracture conductivity testing and analysis system.

considered the deformation of the proppant column when deducing the fracture width model and calculated the deformation amount of the proppant column through the deformation theory of the proppant. Xu et al. [23], Qu et al. [24], and Wen et al. [25] used the FCS-100 flowmeter to simulate the conductivity of the channel fracture under different sand concentrations, fiber mass fractions, and

TABLE 3: Experimental groups.

Mineral type	Quartz	Feldspar	Sodium feldspar	Calcite	Silicon carbide	Hematite
Content (%)	92	5	1	2	—	—

proppant column diameters (10~32.8 mm), but they did not study the deformation and failure rule of the proppant column. Zhang [26] took into account the influence of proppant embedding, the axial deformation of the proppant column, and its arrangement and derived an analytical model for the fracture width and conductivity of channel fracturing. Zhang and Hou [27] took the axial deformation of the proppant column into consideration and regarded the proppant clusters formed in the high-speed channel-fracturing fractures as the seepage zone. Based on the Darcy-Brinkman equation, a mathematical model of high conductivity of the high-speed channel-fracturing fractures was established. Zheng et al. [28] obtained the expression of the fracture width based on the Hertz contact theory and proppant embedding theory and then obtained the final conductivity calculation formula. Moghadasi et al. [29] suggested that the utilization of nanosilica particles during hydraulic fracturing could reduce the fines migration and improve the production performance. Guo and Liu [30], based on the interaction between a single proppant particle and rock, and considering the viscoelastic creep effect of rock, established models of long-term conductivity of the conventional fracture and short-term conductivity of the channel fracture. These fracture conductivity models all assume that the proppant column is an elastomer with a certain elastic modulus, ignoring the nonlinear stress-strain characteristics of the proppant column and the nonuniform variation of the fracture width at the open channel. Meyer et al. [31] regarded the deformation of the fracture wall as elastic deformation. Considering the different structural forms of the proppant column in the fracture, an analytical fracture width model was established based on the Hertz contact theory in elastic half space, and the expression of fracture permeability was derived by using Darcy's law and equivalent seepage resistance principle. Hou et al. [32] used Meyer's method for reference to establish the variation model of the proppant column fracture width in channel fracturing. These two models take into account the elastic deformation characteristics of the fracture wall, but the proppant column is still treated as a rigid body.

In this work, the influences of in situ stress, reservoir rock elastic parameters, and proppant column spatial distribution characteristics on the closure deformation of the high-conductivity fracturing channel and the stability of the support column are studied.

## 2. Deformation Test of Proppant Column in High-Conductivity Channel Fracturing

*2.1. Experimental Scheme.* Our target is to explore the effects of the proppant column height, arrangement spacing (proppant column number), and closure stress on the deformation of the proppant column. Using the experiments, we measure the destruction of the proppant column shape, axial displacement,

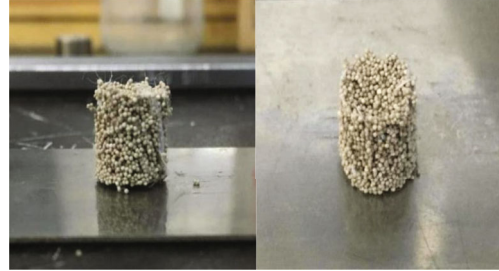


FIGURE 3: Visual observation of proppant shape.



FIGURE 4: Test platform installation.



FIGURE 5: Proppant column after experiment.

radial displacement, and stress-strain characteristics of the proppant column at the stage of compaction and loading pressure. During high-conductivity channel fracturing, the

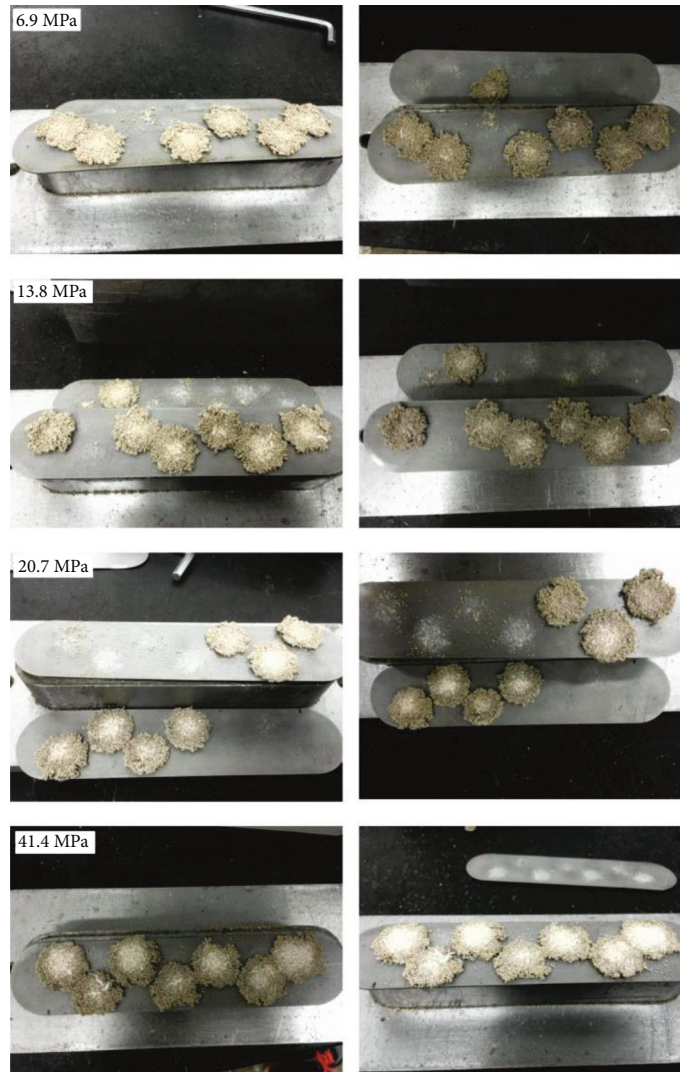


FIGURE 6: Deformation shape of proppant column.

support columns form a cylindrical shape in the cracks one by one, and the height of the support columns describes the width of the cracks. The closing stress of the cracks is applied to the support columns along the axial direction to describe the deformation behavior of the support columns accurately. The values of each factor are shown in Table 1.

The three proppant column heights and the three proppant column numbers in Table 1 were combined to design a total of nine sets of experiments, and seven closure pressures were arranged for each set of experiments. The specific experimental groups are shown in Table 2.

## 2.2. Experimental Equipment and Sample Preparation

**2.2.1. Experimental Equipment and Sample Preparation.** In this experiment, the API standard fracture conductivity test and analysis system was used to conduct simulation experiments. The maximum closure pressure that the equipment could bear was 120 MPa, which could meet the requirements of the experimental design (as shown in Figure 2).

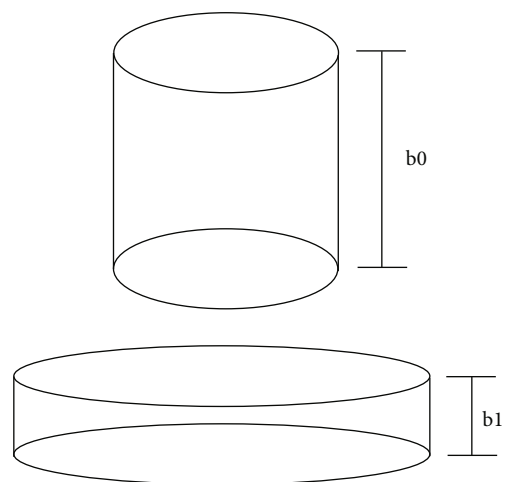


FIGURE 7: Schematic diagram of proppant stress pattern.

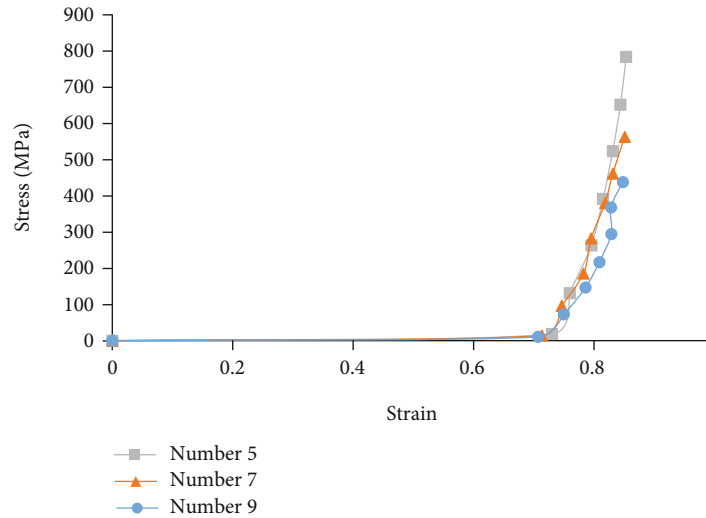


FIGURE 8: Stress-strain curve of proppant column height (initial proppant column height: 10 mm).

**2.2.2. Sample Preparation.** The proppant column material used in this experiment is the 40/70-mesh CARBO proppant. Before the experiment, XRD was used to test the mineral composition of the proppant. The specific results are shown in Table 3.

The proppant column produced in this experiment should be approximately cylindrical, the appearance of each proppant column should be basically the same, and it is not easy to collapse and loose and can effectively gather proppant particles. The specific production steps are as follows:

- (1) First, weigh 33 g of the selected CARBO proppant material, then weigh the fibers according to the ratio of 4‰ and put them into the beaker
- (2) Before adding glue, use hands or a glass rod to break up the fibers in the beaker as much as possible and thoroughly mix them in the proppant particles to prevent the fibers from agglomerating when the glue is added later
- (3) Slowly add glue to the beaker while stirring continuously with a glass rod until the proppant particles, fibers, and glue in the beaker are thoroughly mixed and solidified to form a viscous proppant group
- (4) Put the proppant cluster into a particular metal model (inner diameter 10 mm, height 1 cm) and fill the model with the proppant cluster through mechanical compaction
- (5) Take out the formed proppant column. Put the proppant column into a heating furnace, heat it at 60°C for one hour, and then place it at room temperature for half an hour to obtain a consolidated proppant column (Figure 3).

**2.3. Experimental Steps.** In this experiment, after the guide chamber is assembled as required, the guide chamber is installed on the test platform to ensure the level of the plat-

form. The guide chamber is correctly placed in the center of the platform, and the pressure testing machine is manually rotated to make the upper part of the test machine just contact the guide chamber (as shown in Figure 4).

- (1) *Preparation:* two displacement meters are installed on the diversion chamber.
- (2) *Experimental stage:* the pressure pump is used to pressurize the diversion chamber, and the pressure is set for 1 min under the specified pressure to reach a stable state.
- (3) *Measurement phase:* write down the values of the two displacement meters, calculate the average value as the total axial displacement, and calculate the converted displacement of the proppant column according to the elastic modulus of the diversion chamber and rock sample. The variation of the crack width is recorded during the experiment using the device's axial displacement sensor. It is expected that the deformation of the instrument is negligible.

As can be seen from Figure 5, under the action of axial pressure, the proppant column spreads evenly along the radial circumference, forming an approximately circular wafer-shaped column. The deformation shapes of the proppant column under different closing pressure are shown in Figure 6. Note that during the experiment, we assume the proppant particle-fiber mixture is well cemented and ignore the effect of drag and carrying on the outermost particles of the support column during the flowback of the fracturing fluid. The stability of the support column during the actual fracturing process may be worse than that during the experiment. The accurate study accounting for these effects is the subject of future studies.

**2.4. Nonlinear Constitutive Model of Proppant Column.** In this experiment, the proppant deformation is described as shown in Figure 7.

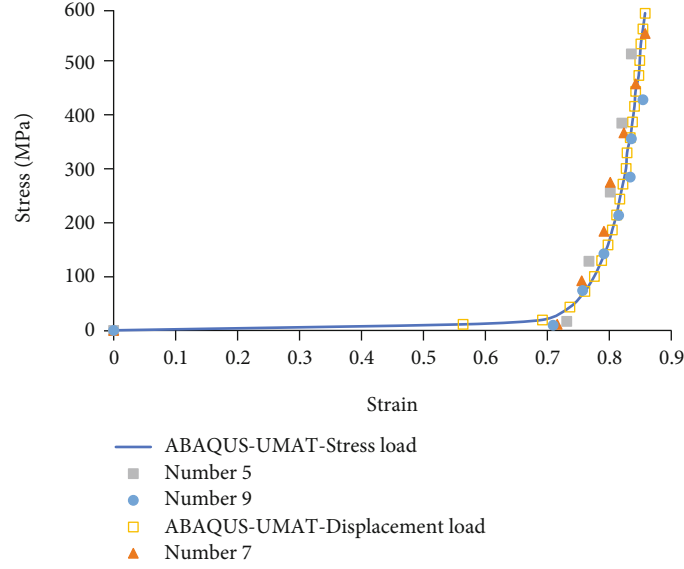


FIGURE 9: Results of numerical verification (initial height of proppant column: 10 mm).

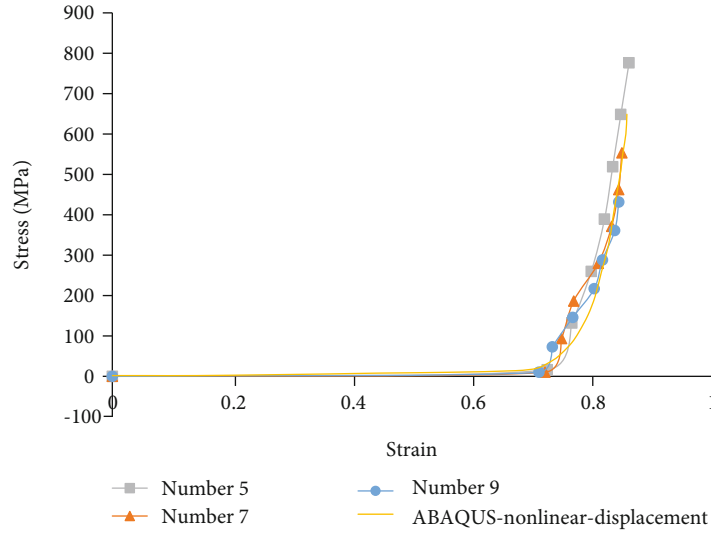


FIGURE 10: Results of numerical verification (initial height of proppant column: 8 mm).

When the initial height is 10 mm and the number of proppant columns is different, the experimental results are shown in Figure 8.

A nonlinear constitutive model is proposed to describe the experimental results. The form of the constitutive model is as follows:

$$\sigma = E\varepsilon + (K\varepsilon)^n, \quad (1)$$

where  $E$  is the equivalent modulus of elasticity,  $K$  is the Hardening coefficient, and  $n$  is the Sclerosing index.

Nonlinear fitting was used to determine the constants of each material. Figure 9 exhibits the results of numerical verification. The  $y$ -axis of this figure is the contact stress caused by the stress concentration. When the initial height of the

proppant column was 10 mm, the results of numerical simulation are in good agreement with the experimental results. Therefore, this constitutive model was further used to calculate the numerical results of a proppant column with an initial height of 8 mm. By comparison with the experimental results, the results that are shown in Figure 10 can be obtained. Our model works well for the proppant columns having different heights.

### 3. Establishment of the Model of Fracturing Crack-Proppant Column Interaction in High-Conductivity Channel

#### 3.1. Model of Fracturing Crack-Proppant Column Interaction in High-Conductivity Channel

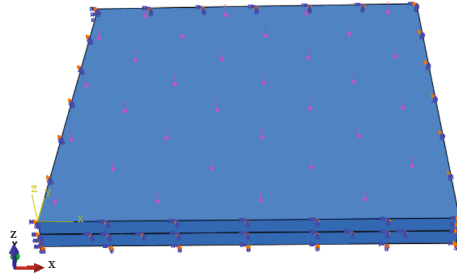


FIGURE 11: Finite element model of fracturing crack-proppant column interaction in high-conductivity channel.

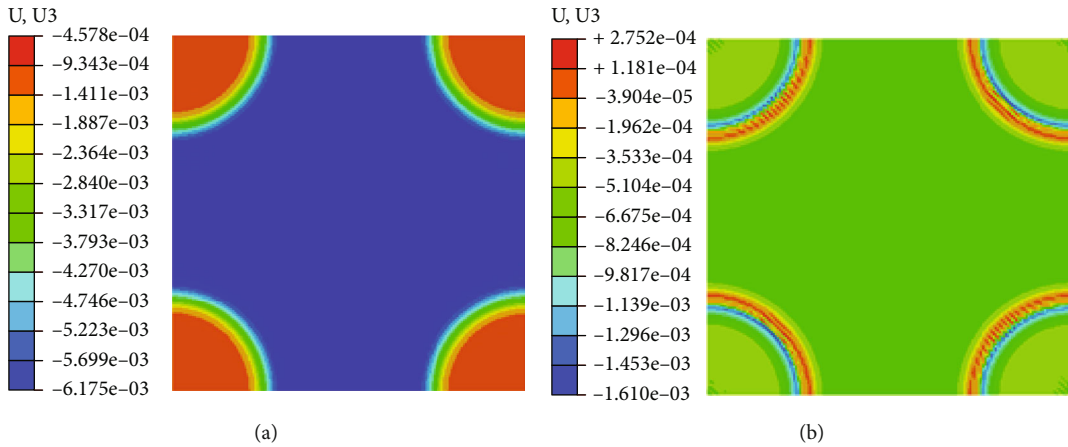


FIGURE 12: Displacement cloud images of Z direction of the upper slab (a) and lower slab (b).

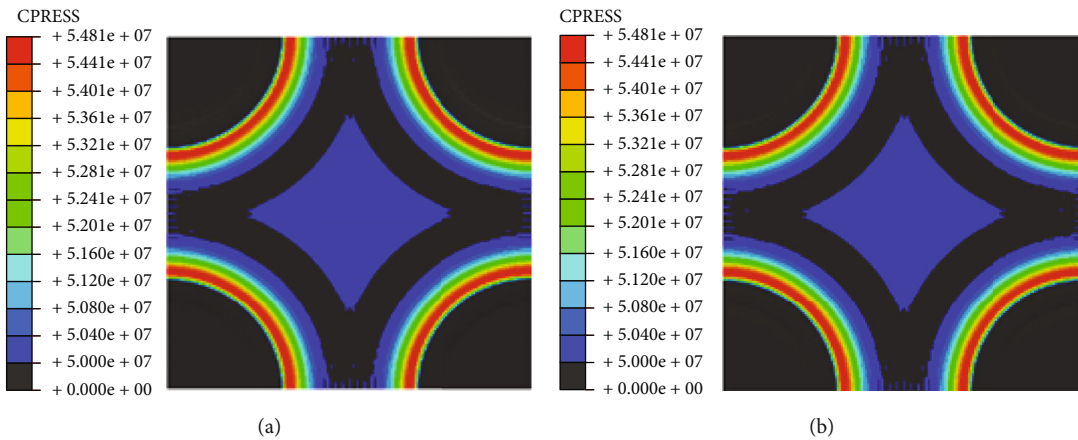


FIGURE 13: Contact stress cloud images of upper slab (a) and lower slab (b).

**3.1.1. Physical Model of Fracturing Crack-Proppant Column Interaction in High-Conductivity Channel.** In this section, based on the parameters of Well A20, a physical model of the fracturing crack-proppant column interaction in the high-conductivity channel was established. The effective fracture length of the well was approximately 150 m, and the total time of pumping priming was about 75 min. It can be calculated from this that the length of pumping priming was 2 m/min, the time of the sand-carrying fluid stage was 2 min, the diameter of the proppant support column was approxi-

mately 5 mm, and the height of fracture was approximately 5 mm. The minimum horizontal principal stress of the reservoir was 50 MPa, the elasticity modulus was 30 GPa, and Poisson's ratio was 0.28. Taking the height of the proppant column as 5 mm, the diameter as 5 m, and the distance as 5 m for the calculation, the parameters required for numerical simulation can be obtained. This article assumes that the support column is tightly bonded together by fibers and ignores the shedding of proppant particles outside the support column during the fracturing process.



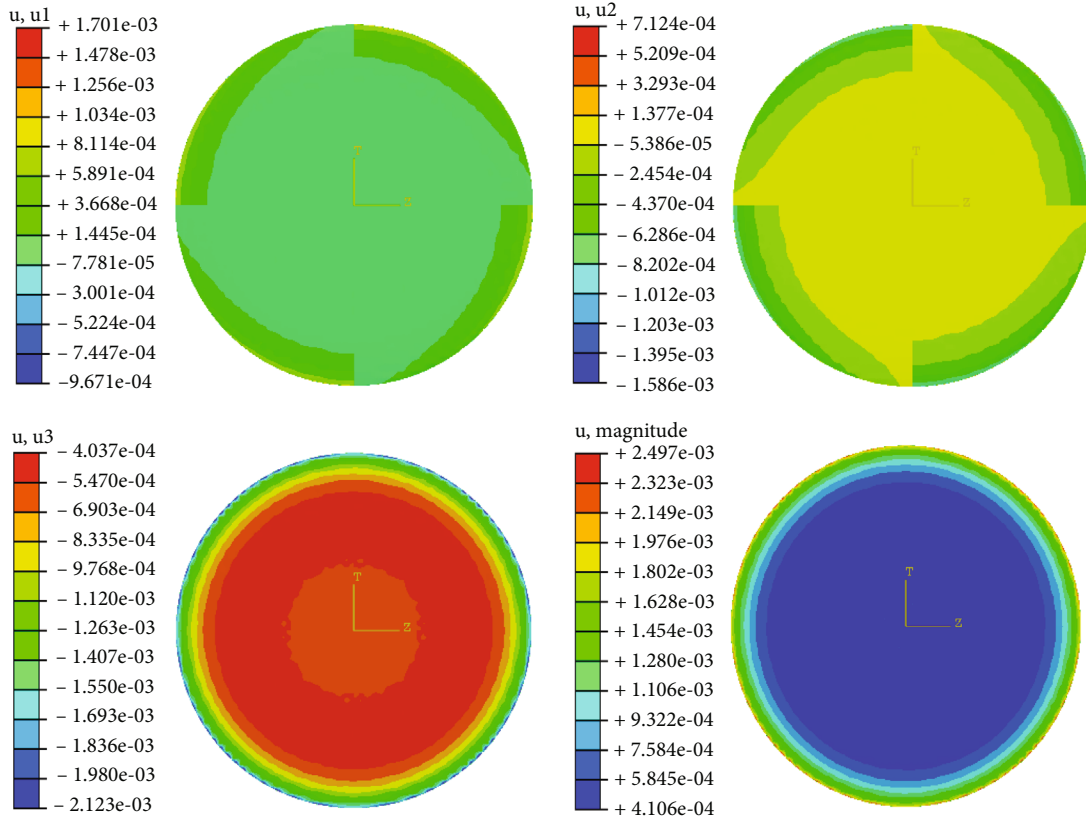


FIGURE 14: Displacement cloud images of proppant column.

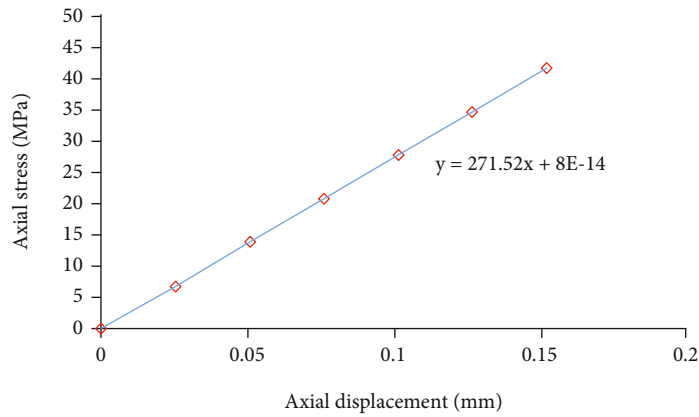


FIGURE 15: Halliburton laboratory experimental data [1].

3.1.2. *Finite Element Model of Fracturing Crack-Proppant Column Interaction in High-Conductivity Channel.* The global size of our finite element model was set at 0.1 m (Figure 11). With partitioning technology of swept mesh entities, the proppant column used hexahedron elements and a global size of 0.025 m. The top and bottom rock plates were subjected to the same closure stress, which were 40 MPa, 50 MPa, and 60 MPa one after another. The upper and lower rock slabs were set as surface-to-surface contact, ignoring the friction generated when the upper and lower rock plates are in contact; the normal direction was set as hard contact, and the scaling factor of hardness is set as 1.

Although in the actual postcompression conditions the proppant particles may be broken under high closing pressure, we have not taken into account this effect in our simulations. The reason is that this study is conducted for tight oil reservoirs in the Shengli oilfields, China, and the fracture closure pressure ranges from 40 to 60 MPa whereas the selected proppant breakage pressure is 70 MPa. Thus, it is expected that proppant breakage may not occur.

3.2. *Analysis of the Simulation Results of Fracturing Crack-Proppant Column Interaction in High-Conductivity Channel.* Based on the finite element model of fracturing

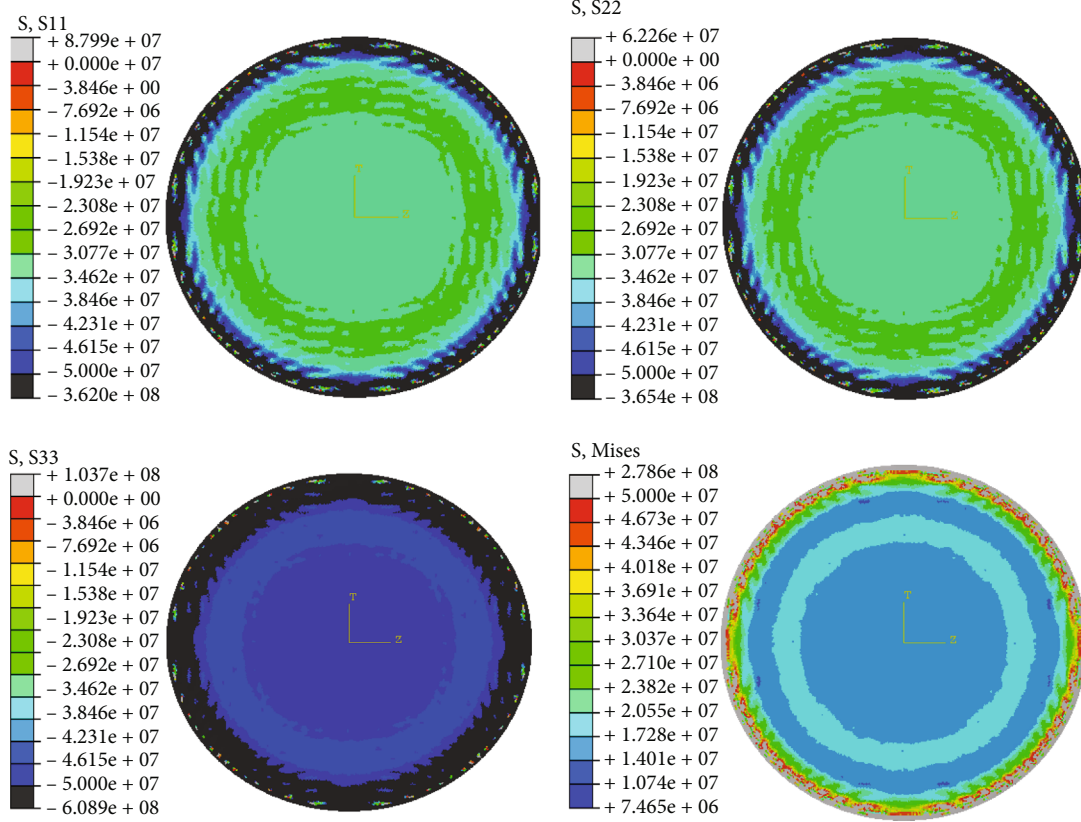


FIGURE 16: Displacement stress cloud images of proppant column.

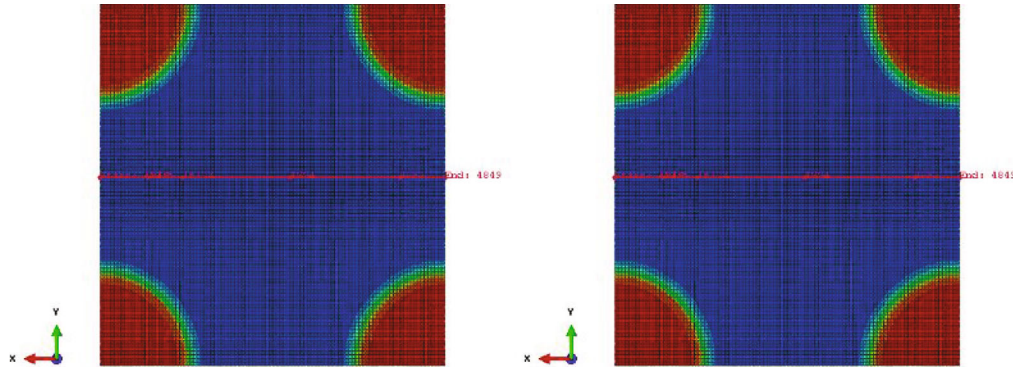


FIGURE 17: Schematic diagram of path.

crack-proppant column established in the previous section, this section simulated the interaction process and obtained the characteristics of the displacement and contact stress of the upper and lower rock plates and the displacement and stress of the proppant column.

As can be seen from Figure 12, the displacement of the center position of the upper slab in the negative direction along the Z direction is 6.175 mm, and the displacement of the center position of the lower slab in the negative direction along the Z direction is 0.6675 mm, so the relative displacement of the upper and lower slabs is 5.5075 mm. Since the total height of the proppant column is 5 mm, the upper

and lower slabs have been in contact, and the proppant column cannot effectively support the fracture.

As can be seen from Figure 13, the contact stress on the outside of the proppant column and the center of the plate is greater than 50 MPa, while the contact stress on the other parts is slightly less than 50 MPa. This indicates that although the fracture is closed, the contact stress in some areas of the fracture is still less than the closure stress of the reservoir. According to the conventional conductivity experiment and theoretical study in the continuous sanding chamber, it is known that the decrease of the fracture closure stress can significantly improve the conductivity of the

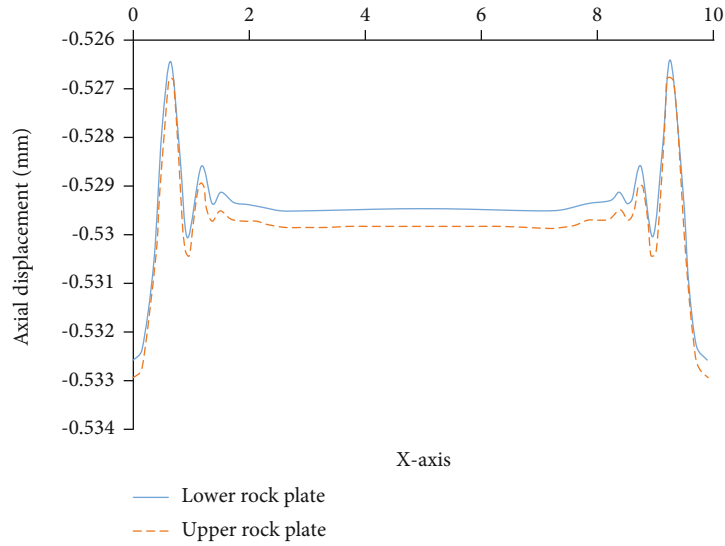


FIGURE 18: Axial displacement curve of upper and lower slabs.

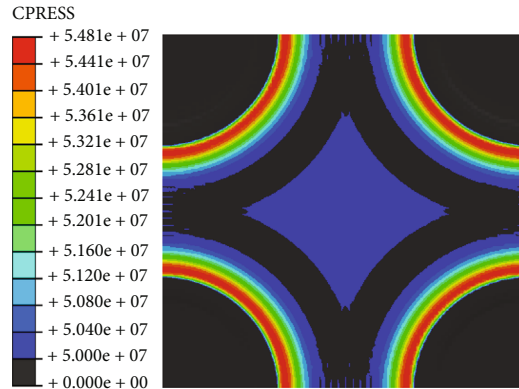


FIGURE 19: Contact stress nephogram of rock plate.

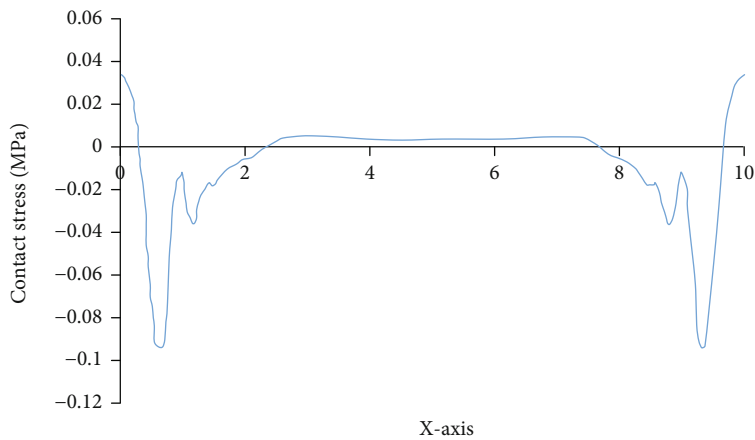


FIGURE 20: Contact stress curve of rock plate.

fracture, and the proppant column can still play a certain role in improving the conductivity of the fracture.

As shown in Figure 14, under the action of a closing stress of 50 MPa, the axial displacement of the proppant col-

umn is 0.21 mm, and the radial displacement in the X and Y directions is 1.7 mm and 1.58 mm, respectively. According to the results of the laboratory slab compression experiment of the proppant column (as shown in Figure 15), the axial

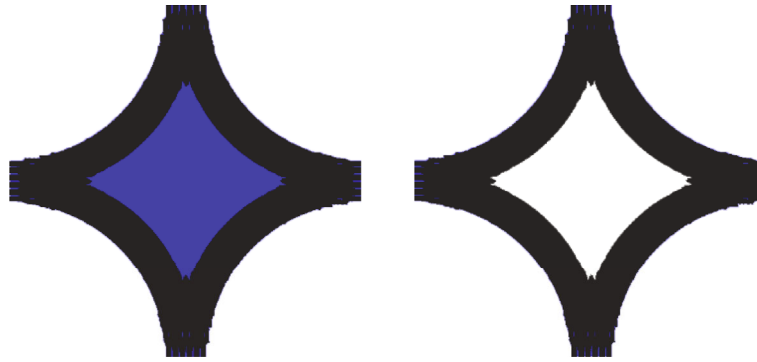


FIGURE 21: Total fracture area and effectively propped fracture zone.

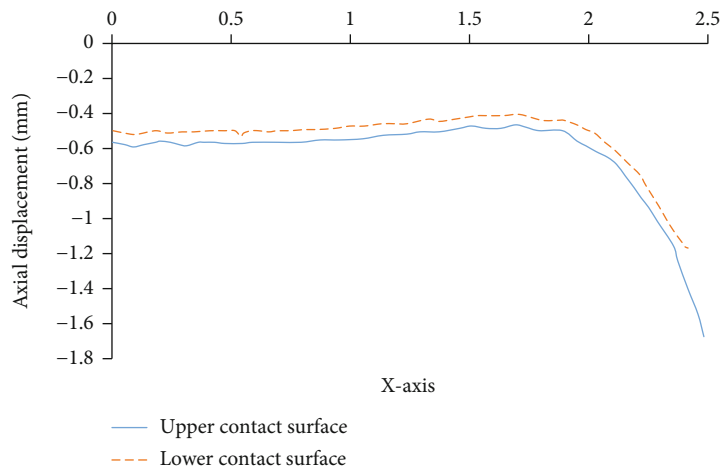


FIGURE 22: Axial displacement of proppant contact surfaces.

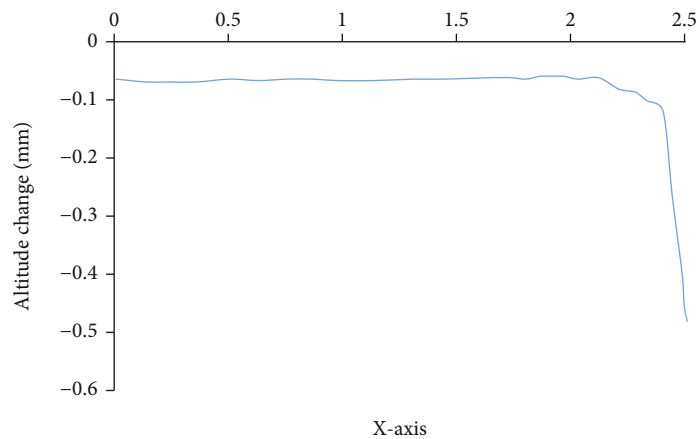


FIGURE 23: Height variation of proppant column.

displacement of the proppant column is about 0.18 mm under the condition of a closing stress of 50 MPa. The numerical simulation results are in good agreement with the experimental results, which indicates that the numerical simulation results have good reliability.

As can be seen from Figure 16, due to its large displacement and large normal stress, the outer ledge of the proppant column is prone to compressive stress failure under

the action of the 50 MPa closing stress. Meanwhile, the local edge is also accompanied by the tensile stress failure, so the proppant column is prone to edge peeling and peripheral diffusion during compression.

*3.2.1. Propping Characteristics of High-Conductivity Channel-Fracturing Fracture.* In order to study whether the fractures in the middle of the proppant column are closed after

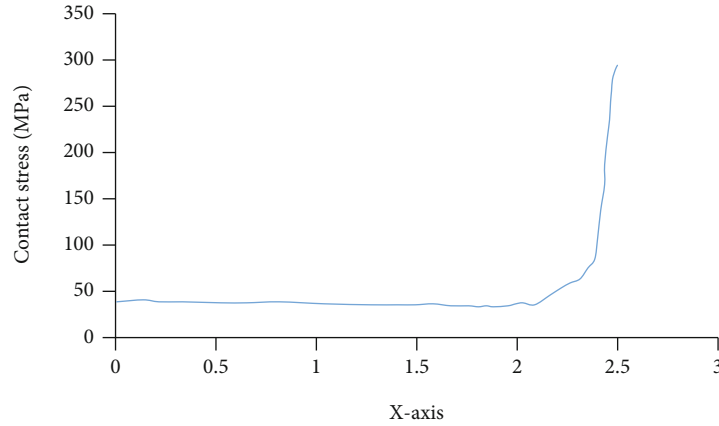


FIGURE 24: Contact stress of proppant interface.

TABLE 4: Detailed parameters of numerical simulation calculation of high-conductivity channel fracturing.

Factors	Value			
Diameter of proppant column (m)	1	3	5	—
Height of proppant column (mm)	2	5	8	—
Crustal stress (MPa)	40	50	60	—
Elastic modulus of the formation (GPa)	25	30	35	40

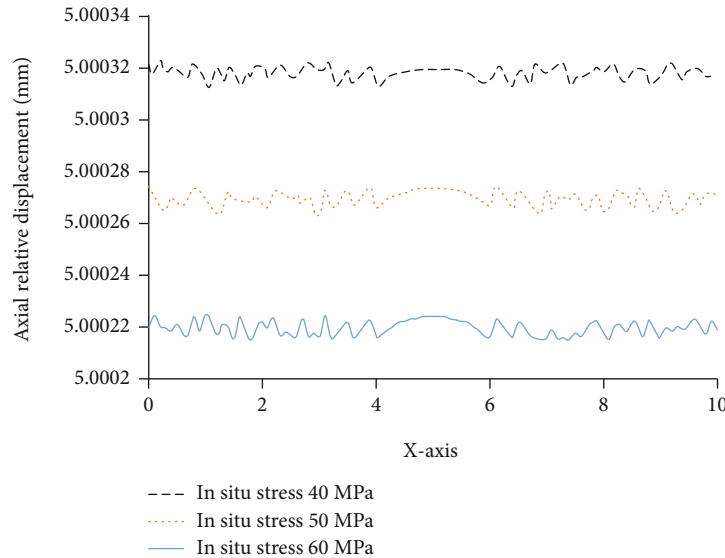


FIGURE 25: Relative axial displacement diagram of two rock slabs under different crustal stresses (elastic modulus 40 GPa).

fracturing fluid flowback in the high-conductivity channel fracturing and the value of the contact stress after closure, a path is set in the middle of the model along the  $X$  and  $Y$  directions (as shown in Figure 17), so as to plot the mutual displacement and contact stress of the left and right fracture walls.

Since the model has the same proppant column size and spacing, only the  $X$  direction calculation results are analyzed according to the symmetry principle.

In the axial displacement curve, the contact surface of the lower rock plate is set as the  $X$ -axis. Under the action

of closure stress, the axial displacements of the two rock plates are both negative. Subtracting the absolute value of the axial displacement of the upper rock plate by 5 mm is to form the comparison diagram as shown in Figure 18. Therefore, the distance between the upper and lower rock plates can be obtained by subtracting the axial displacement of the upper rock plate from the axial displacement of the lower rock plate. As can be seen from the figure, the distance between the two plates is negative, which indicates that the crack has been closed. The larger the negative value is, the

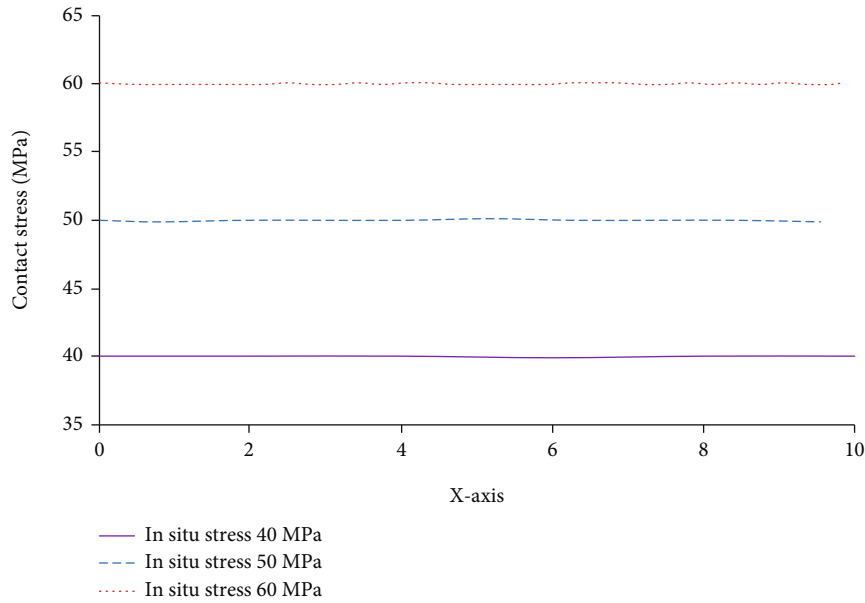


FIGURE 26: Comparison diagram of rock slab contact stress under different crustal stresses (elastic modulus 40 GPa).

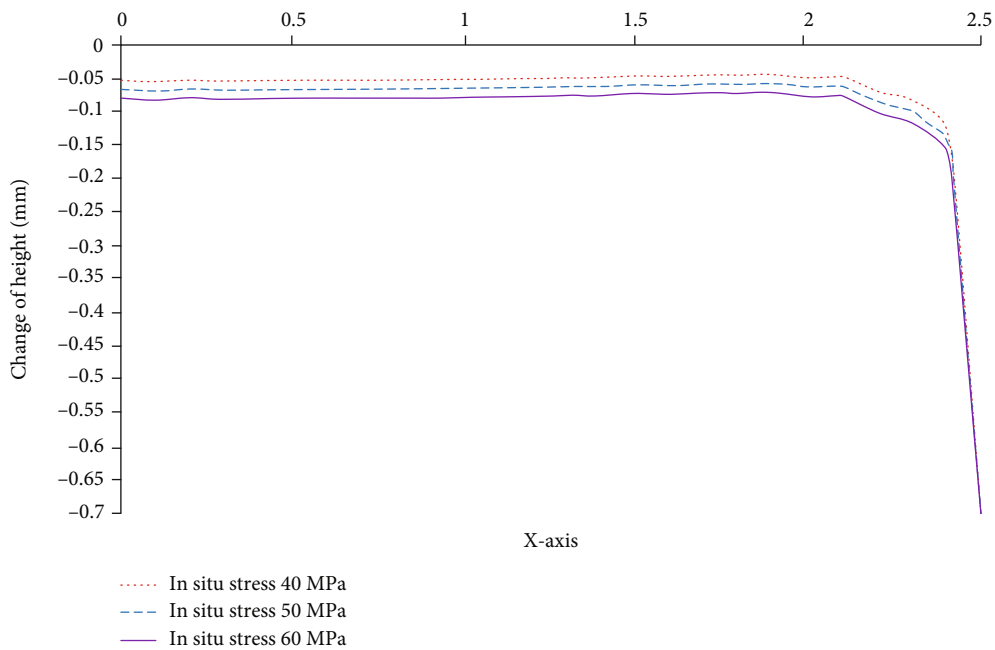


FIGURE 27: The change value of proppant height under different in situ stresses (elastic modulus 40 GPa).

more serious the compaction of the two plates will be. Compared with the two sides of the slab, the compaction degree in the middle part of the slab is more serious.

Figures 19 and 20 are the contact stress nephogram of the rock plate and the contact stress curve of the rock plate, respectively. In Figure 20, 50 MPa has been subtracted from the vertical coordinates, so the X-axis corresponds to the contact stress of 50 MPa. As can be seen from Figure 20, the contact stress at the center of the rock plate is greater than 50 MPa, while the contact stress at some parts of both

ends is less than 50 MPa. The initial crustal stress is 50 MPa, which means that although the fracture is closed after that the proppant column is added, the closure stress in some areas of the fracture decreases, which significantly improves the conductivity of the fracture.

In the contact stress of the rock plate, the proppant column was partially removed to obtain the area shown in Figure 21(a). In the total fracture area, the black part is the area where the closure stress is less than 50 MPa, which is called the effective propping fracture area, as

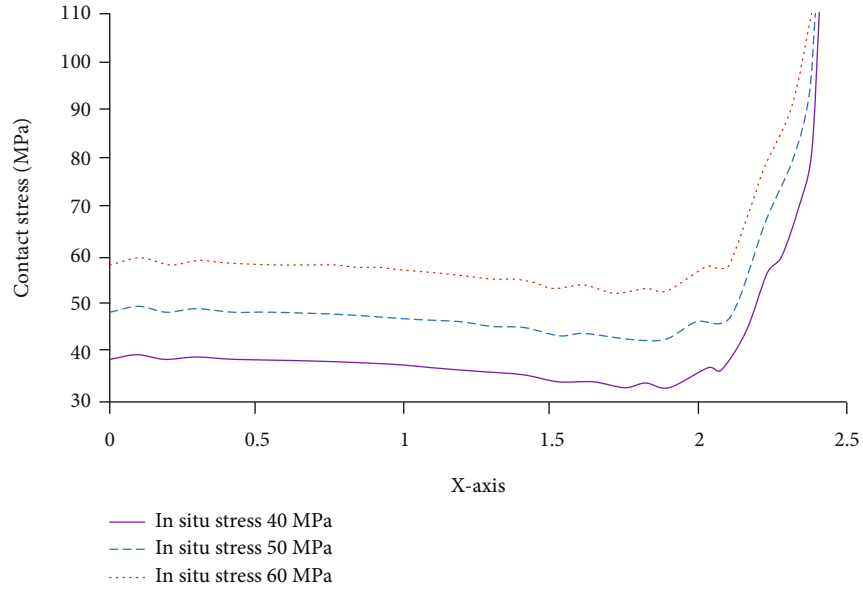


FIGURE 28: Comparison of contact stress of proppant under different in situ stresses (elastic modulus 40GPa).

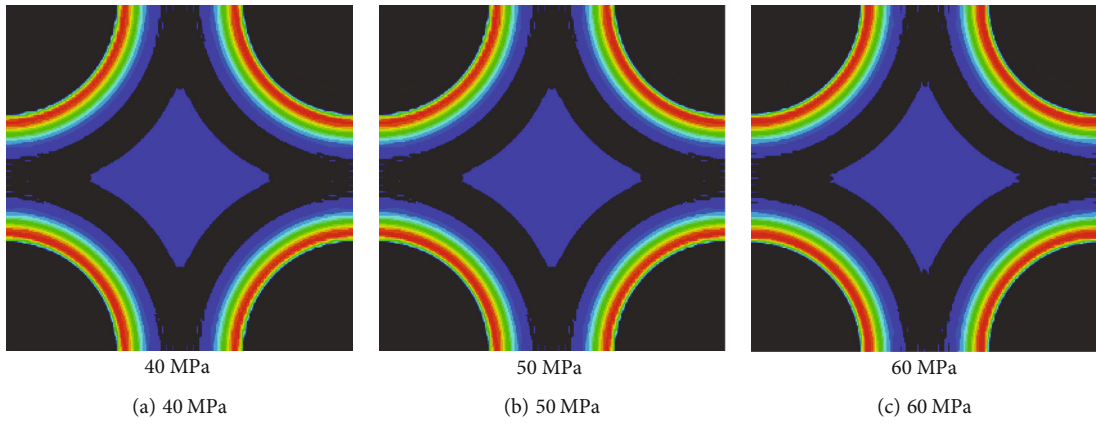


FIGURE 29: Contact stress cloud diagram of rock slab under different in situ stresses.

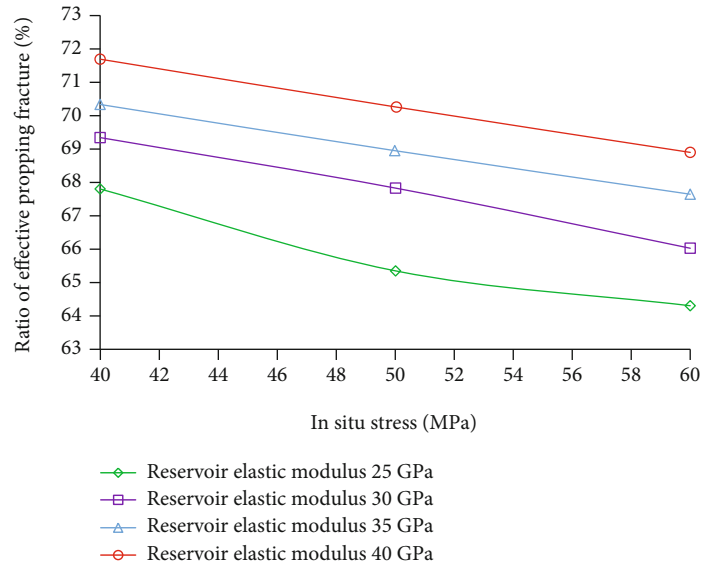


FIGURE 30: The influence of in situ stress on effective supporting cracks.

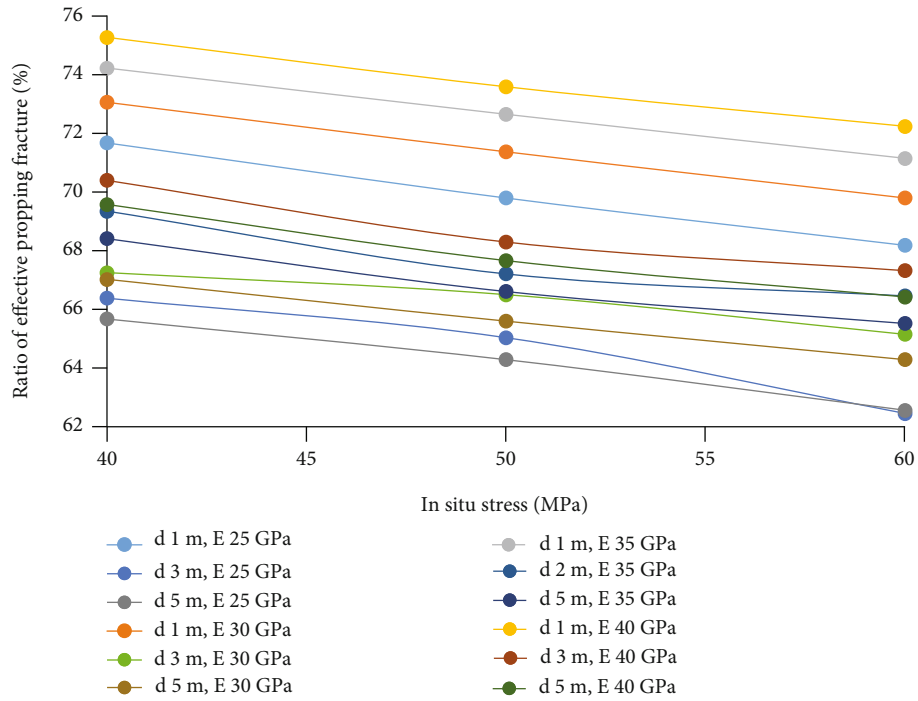


FIGURE 31: The proppant height is 3 mm, and the influence of in situ stress under different diameters on the ratio of effective supporting fractures.

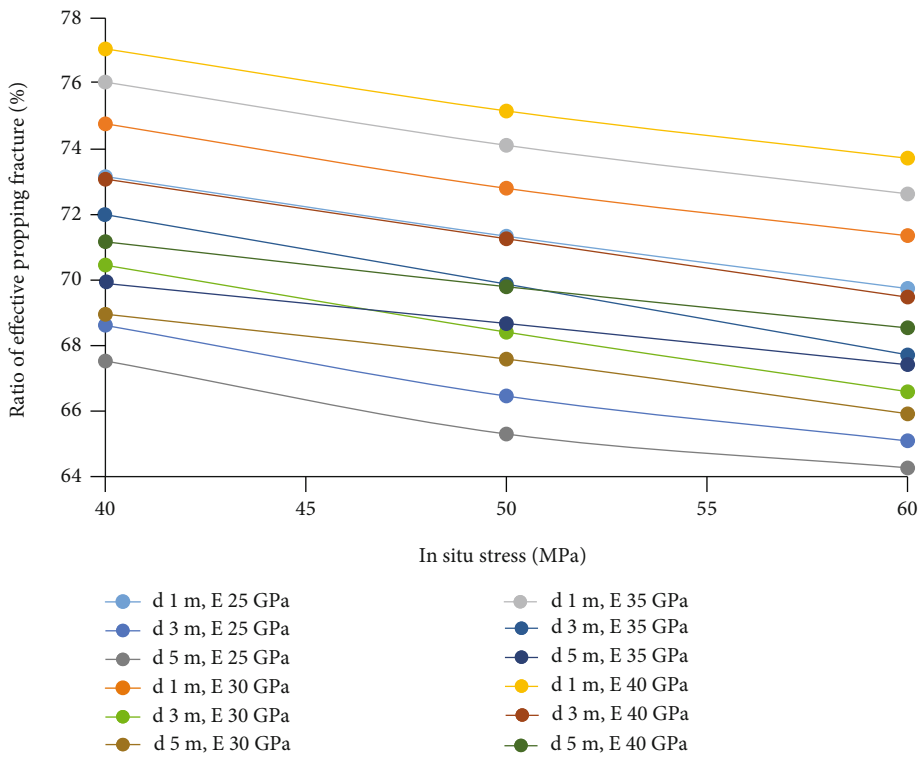


FIGURE 32: The proppant height is 5 mm, and the influence of in situ stress under different diameters on the ratio of effective supporting fractures.



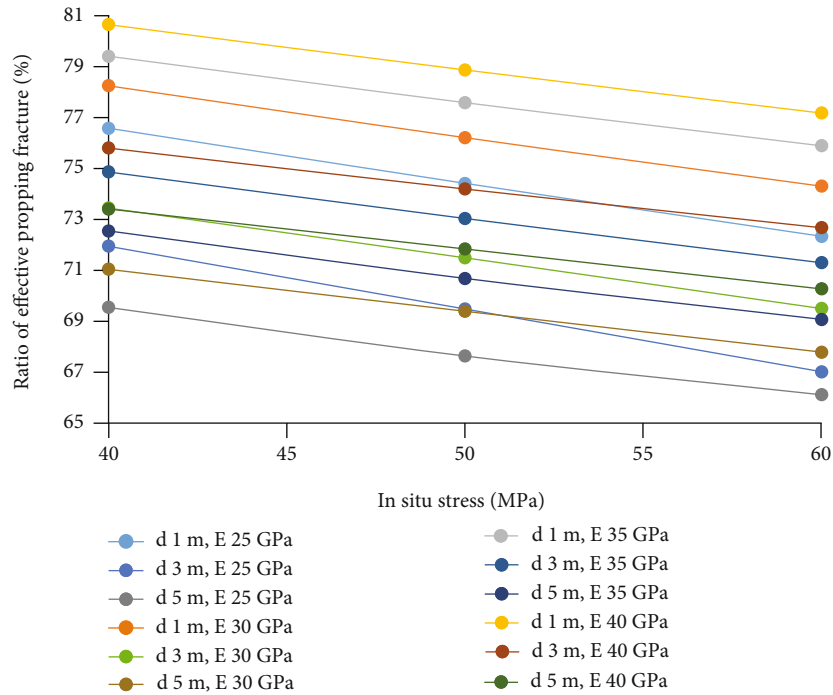


FIGURE 33: The proppant height is 8 mm, and the influence of in situ stress under different diameters on the ratio of effective supporting fractures.

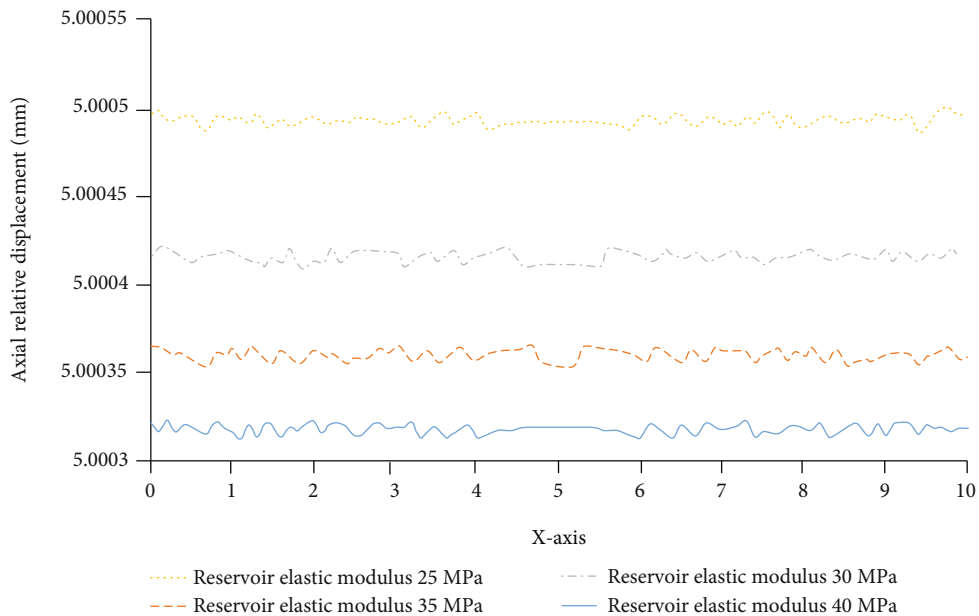


FIGURE 34: Axial relative displacement of two rock slabs under different reservoir elastic moduli (60 MPa in situ stress).

shown in Figure 21(b). Set the total fracture area as  $A$  and the area of the effectively supported fracture area calculated by the graphic analysis software as  $B$ . Assuming that the total fracture area is  $A$ , the area of the effective propping fracture area calculated by the graphic analysis software is  $B$ . After calculation,  $B/A = 0.678$ , indicating that the proportion of the effective propped fractures is 67.8%.

On this basis, the displacement and deformation characteristics of the proppant column are further analyzed to explain the stress-strain form of the proppant column.

As can be seen from Figure 22, the axial displacement of the central part of the proppant column is relatively small, while the axial displacement of the edge of the proppant column is larger. The absolute value of the axial displacement

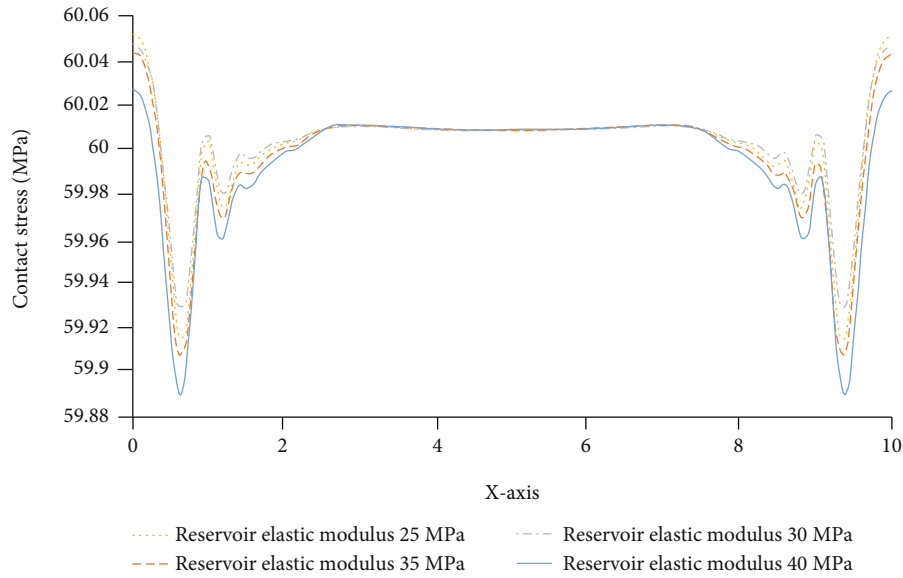


FIGURE 35: Comparison of contact stress of rock slab under different elastic moduli (in situ stress 60 MPa).

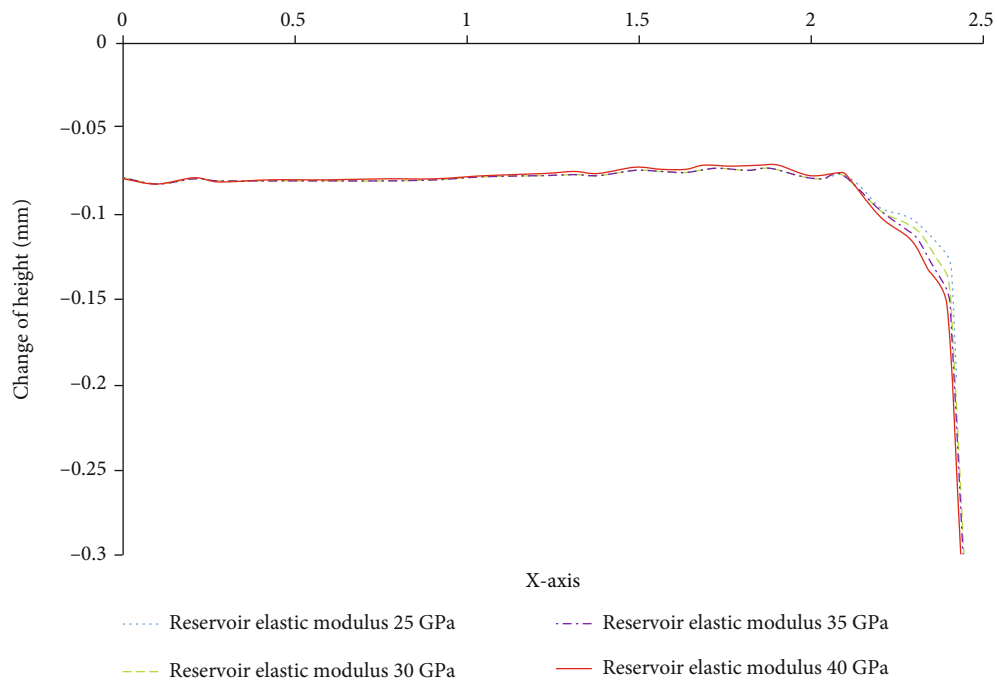


FIGURE 36: The height change of proppant under different elastic moduli (in situ stress 60 MPa).

of the upper contact surface is greater than that of the lower contact surface, so the height of the proppant column decreases. Figure 23 shows the compression of different parts of the proppant column. What is seen from the figure is that the height of the edge part of the proppant column decreases significantly.

The force distribution between the two contact surfaces of the proppant column is basically the same. As we can see from Figure 24, the contact stress is the largest at the edge of the proppant column, so compressive stress failure is more likely to occur and the proppant column is more

prone to edge peeling and peripheral diffusion during compression.

#### 4. Closure Deformation and Stability of Highly Conductive Fracture Channels and Proppant Columns

The crustal stress of the reservoir in the B oilfield is 40~60 MPa, the elastic modulus is 25~40 GPa, and Poisson's ratio is 0.27~0.28, which are in line with the geological

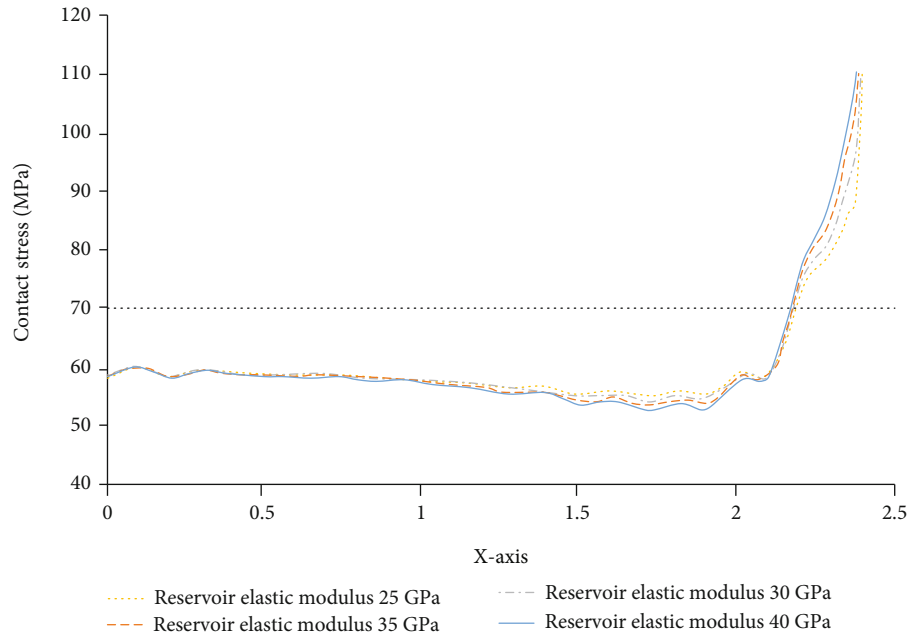


FIGURE 37: Contact stress of proppant under different elastic moduli (in situ stress 60 MPa).

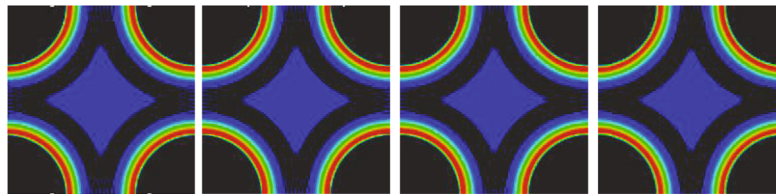


FIGURE 38: Contact stress cloud diagram of rock slab under different reservoir elastic moduli (25 GPa, 30 GPa, 35 GPa, and 40 GPa).

conditions of high-conductivity channel fracturing. The heights of the proppant columns were 3 mm, 5 mm, and 8 mm. The diameters of the proppant columns were 1 m, 3 m, and 5 m, respectively. This means that the model sizes were 2 m, 6 m, and 10 m, respectively.

Now, the elastic modulus of the formation is set as 25 GPa, 30 GPa, 35 GPa, and 40 GPa, and Poisson's ratio is 0.28. The minimum horizontal principal stresses are 40 MPa, 50 MPa, and 60 MPa; the elastic modulus of the proppant column is 1.7 GPa and Poisson's ratio is 0.41. The heights of the proppant column are 3 mm, 5 mm, and 8 mm; the diameters of the proppant columns are 1 m, 3 m, and 5 m, respectively. This means that the sizes of the models are 10 m, 6 m, and 2 m, respectively. Under the above parameter setting conditions, a total of 108 sets of numerical simulation calculations are required, some parameters of which are shown in Table 4.

**4.1. Influence of Crustal Stress on Fracture Closure Deformation and Stability.** In the case of the elastic modulus of 40 GPa, a proppant column with the height of 5 mm and the diameter of 5 m was taken as an example to discuss the effect of crustal stress on fracture closure deformation and stability.

#### 4.1.1. Influence of Crustal Stress on Fracture Closure Deformation

(1) *Displacement Correlation of Two Fracture Planes.* As can be seen from Figure 25, with the increase of crustal stress, the relative axial displacement of the two rock slabs also increases, and the two rock slabs are compressed more closely. The relative axial displacements of the two rock plates under each pressure are greater than 5 mm, which indicates that the fracture has been closed.

(2) *Contact Stress Correlation of Two Fracture Planes.* The upper and lower slabs are in contact with each other, so the contact stresses on the upper and lower surfaces are the same. It can be seen from Figure 26 that, with the increase of the crustal stress, the contact stress on the rock plate gradually increases, making it more prone to deformation and breakage.

**4.1.2. The Influence of In Situ Stress on the Stability of Fracture-Proppant.** It can be seen from Figure 27 that the height change value of the proppant also increases with the increase of the in situ stress. From the contact stress shown in Figure 28, it can be seen that the contact stress of the proppant increases with the increase of the in situ stress.

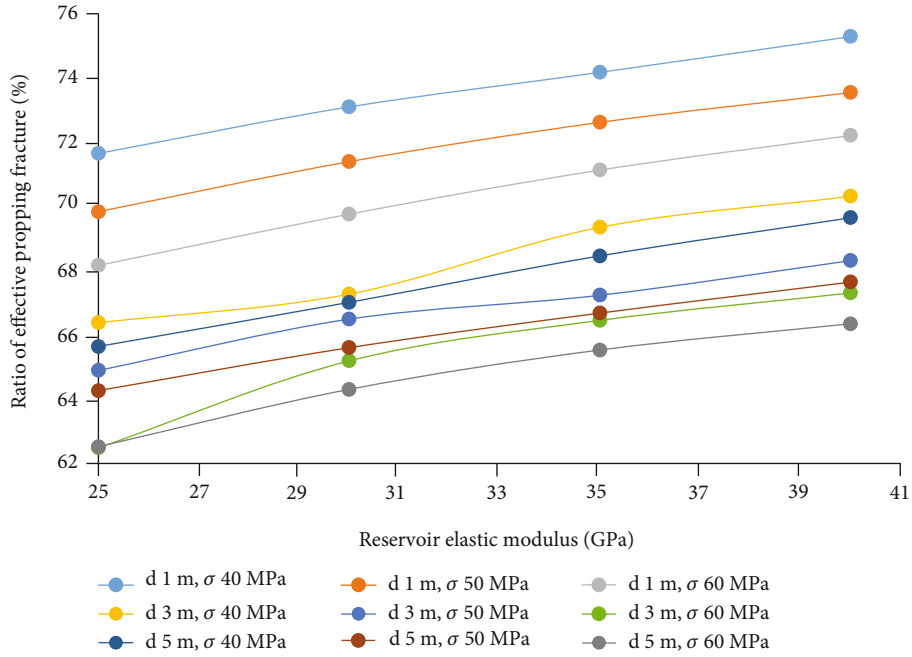


FIGURE 39: The influence of reservoir elastic modulus at 3 mm height and different diameters on the ratio of effective supporting fractures.

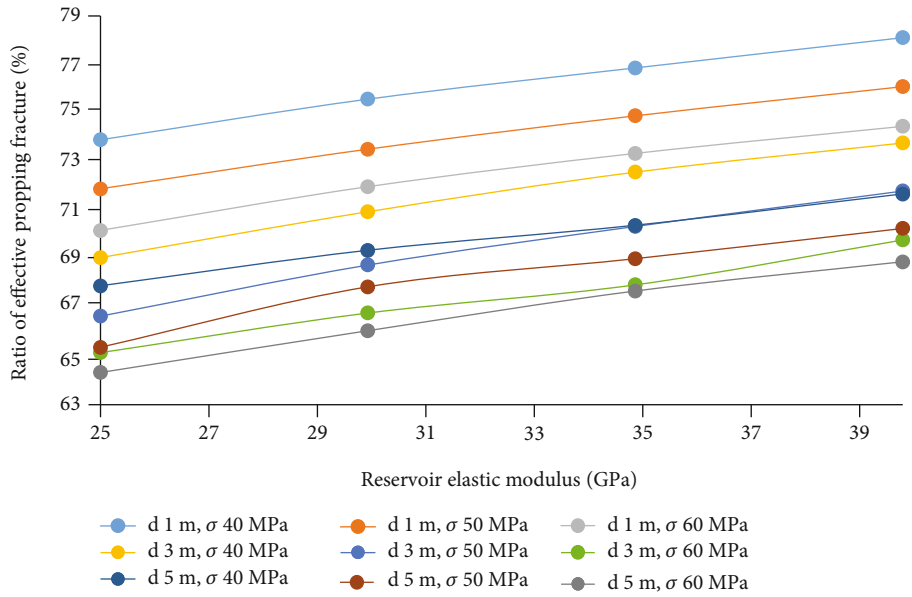


FIGURE 40: The influence of reservoir elastic modulus at 5 mm height and different diameters on the ratio of effective supporting fractures.

The greater the in situ stress, the larger the change of the proppant height, diameter, and contact stress.

4.1.3. The Influence of Reservoir Elastic Modulus on the Stability of Fracture-Proppant

(1) Proportion of Effective Supporting Cracks (Taking a Proppant with a Height of 5 mm and a Diameter of 5 m as an Example). As shown in Figure 29, from left to right, the contact stress cloud diagrams of rock slabs under in situ stress of 40 MPa, 50 MPa, and 60 MPa (elastic modulus 40 GPa) are

shown. Using graphic analysis software, it is possible to calculate the proportion of effective supporting cracks under various stresses: 40 MPa is 71.69%, 50 MPa is 70.26%, and 60 MPa is 68.9%. Figure 30 shows that when the elastic modulus of the reservoir remains unchanged, as the in situ stress increases, the effective support ratio of the fracture decreases.

(2) The Influence of In Situ Stress on Effective Supporting Cracks under Different Height-to-Diameter Ratios. According to Figures 31–33, the simulation results show that when the elastic modulus is constant, the effective support ratio decreases with

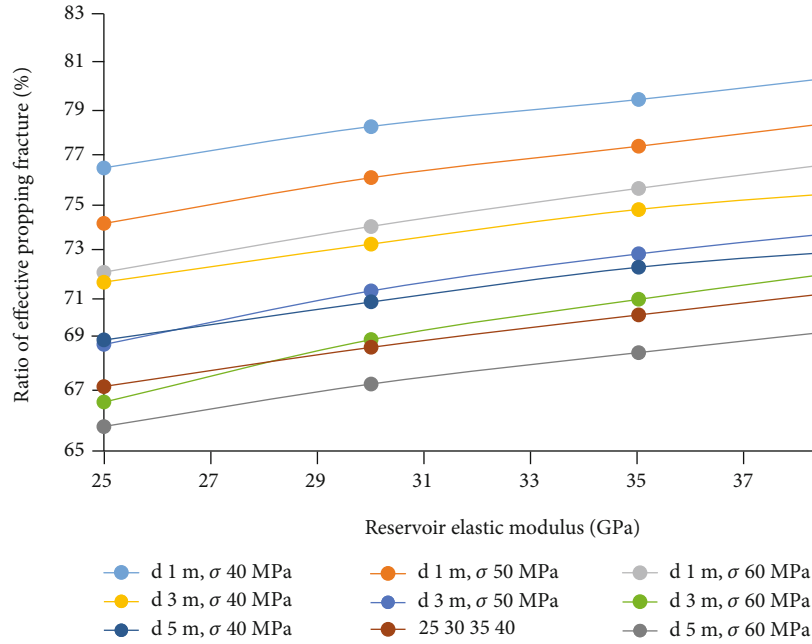
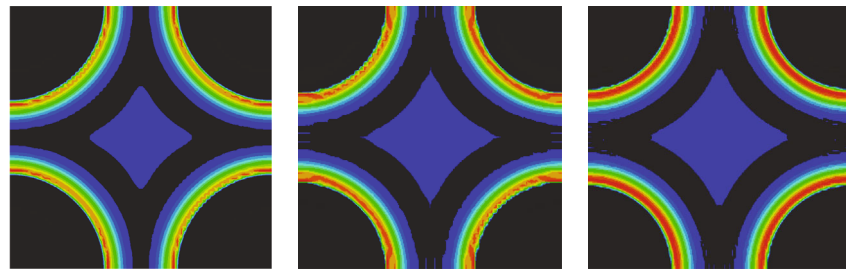


FIGURE 41: The influence of reservoir elastic modulus at 8 mm height and different diameters on the ratio of effective supporting fractures.



(a) Diameter of proppant 1 m (b) Diameter of proppant 3 m (c) Diameter of proppant 5 m

FIGURE 42: Contact stress cloud diagram of rock slab under different proppant diameters.

the increase of the in situ stress, and the reservoir elastic modulus has a greater influence on the effective support ratio.

**4.2. Influence of Reservoir Elastic Modulus on Fracture Closure Deformation and Stability.** When the in situ stress is 60 MPa, a proppant with a height of 5 mm and a diameter of 5 m is taken as an example to explore the influence of the reservoir elastic modulus on fracture closure deformation and stability.

#### 4.2.1. Influence of Reservoir Elastic Modulus on Fracture Closure Deformation

(1) *The Relationship between the Displacements of the Upper and Lower Fracture Surfaces.* It can be seen from Figure 34 that under the condition of constant in situ stress, as the elastic modulus of the reservoir increases, the relative axial displacement of the upper and lower rock slabs gradually decreases.

(2) *The Relationship between the Contact Stresses of the Upper and Lower Cracks.* It can be seen from Figure 35 that under the

condition of a constant in situ stress, as the elastic modulus of the reservoir increases, the contact stress on the part of the rock slab with a contact stress of less than 60 MPa gradually decreases, and the central parts of the rock slab are basically the same, but the slabs change irregularly on both sides.

**4.2.2. The Influence of Reservoir Elastic Modulus on the Stability of Fracture-Proppant.** It can be seen from Figure 36 that under the condition of a constant in situ stress, the decrease in the height of the edge of the proppant increases as the elastic modulus of the reservoir increases, while the remaining part decreases.

It can be seen from Figure 37 that under the condition of a constant in situ stress, the contact stress at the edge of the proppant increases as the elastic modulus of the reservoir increases, while the remaining part decreases.

Under the condition of the constant in situ stress, after the elastic modulus of the reservoir changes, no matter the height or contact stress, the change is very small. Therefore,

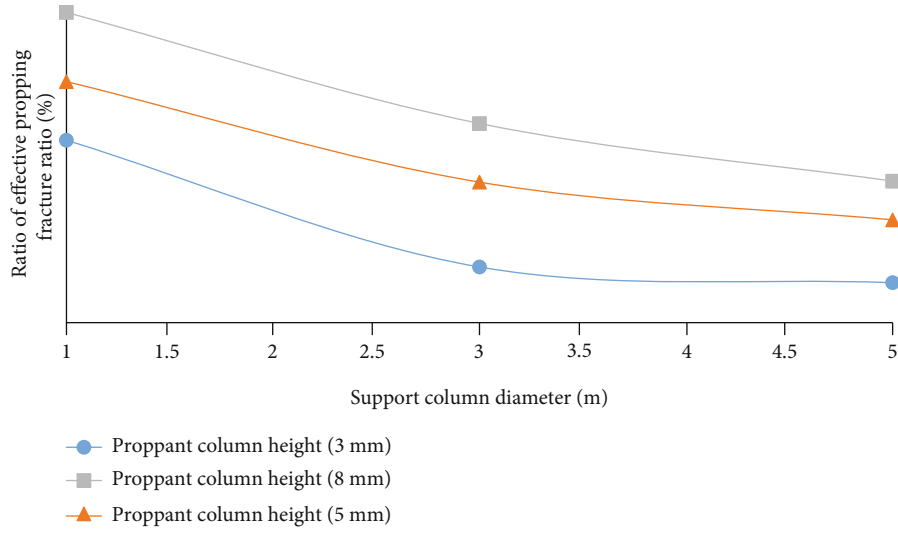


FIGURE 43: The effect of proppant diameter on effective supporting fractures.

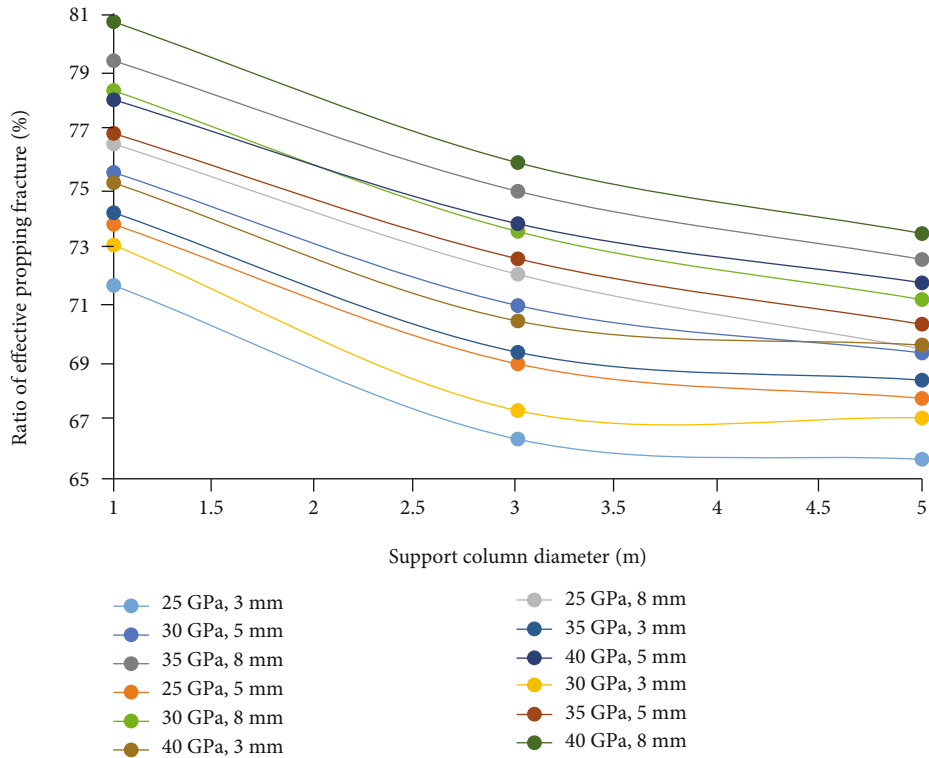


FIGURE 44: The effect of proppant diameter on the ratio of effective supporting fractures (in situ stress 40 MPa).

it can be concluded that the elastic modulus of the reservoir has little effect on the stability of the proppant.

As shown in Figure 38, from left to right, the contact stress cloud diagrams of the rock slab under the in situ stress of 25 GPa, 30 GPa, 35 GPa, and 40 GPa (elastic modulus 60 MPa) are shown. Using graphic analysis software, the proportion of effective supporting fractures under each reservoir elastic modulus can be calculated: 25 GPa is 64.32%, 30 GPa is 66.05%, 35 GPa is 67.64%, and 40 GPa is 68.90%.

This shows that under the condition of a constant in situ stress, as the elastic modulus of the reservoir increases, the effective support ratio of fractures increases.

(1) Influence of Reservoir Elastic Modulus on Effective Supporting Fractures with Different Height-to-Diameter Ratios. According to Figures 39–41, the simulation results show that the ratio of effective supporting fractures increases with the increase of the elastic modulus of the reservoir,

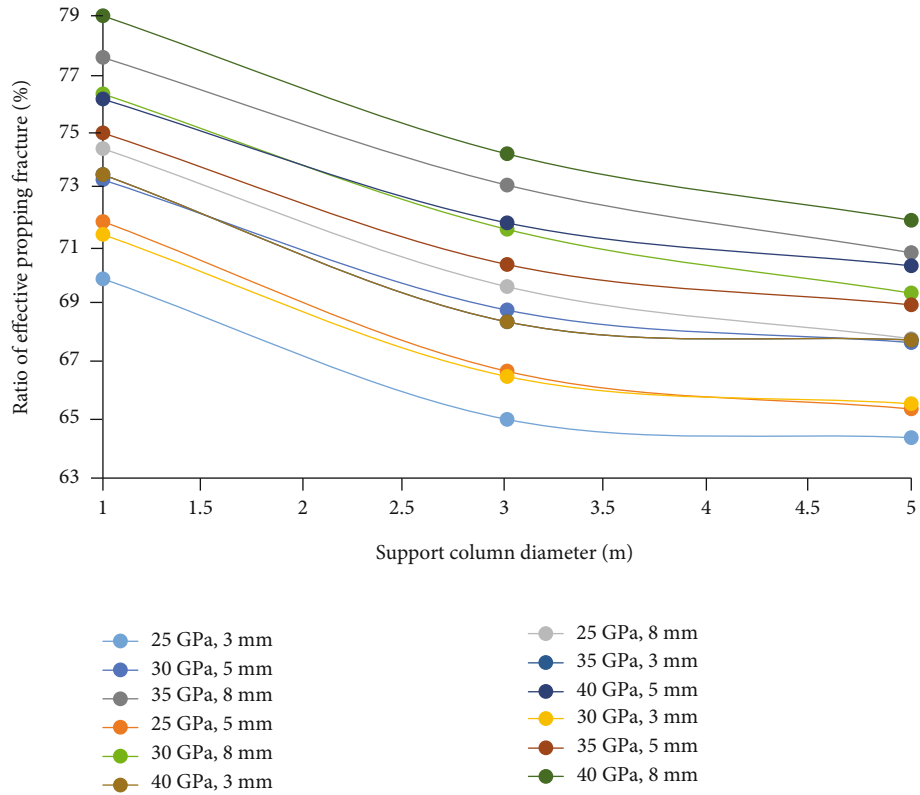


FIGURE 45: The effect of proppant diameter on the ratio of effective supporting fractures (in situ stress 50 MPa).

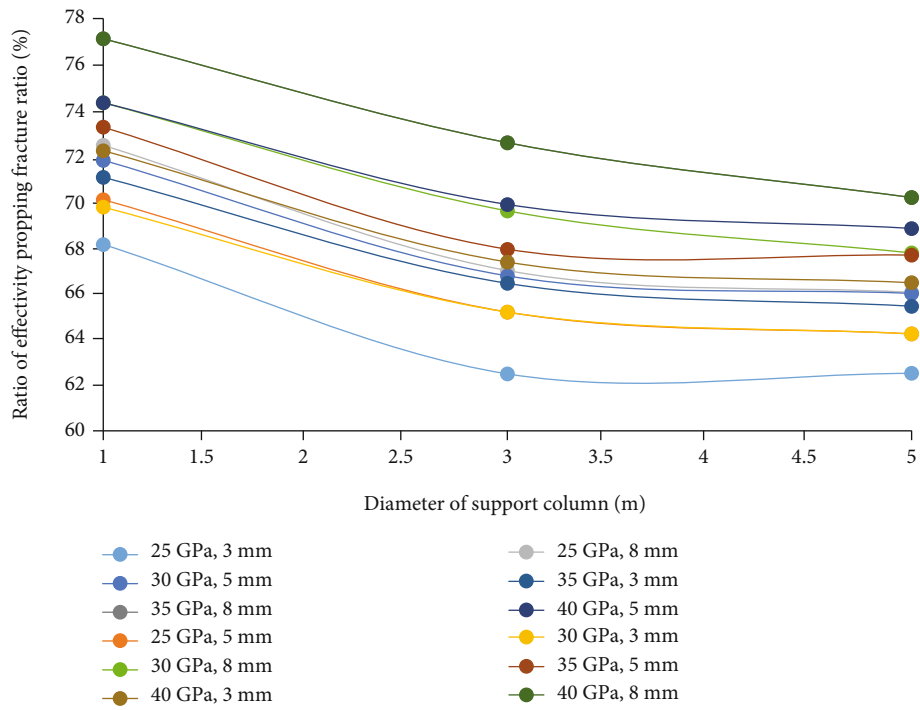


FIGURE 46: The influence of proppant diameter on the ratio of effective supporting fractures (in situ stress 60 MPa).

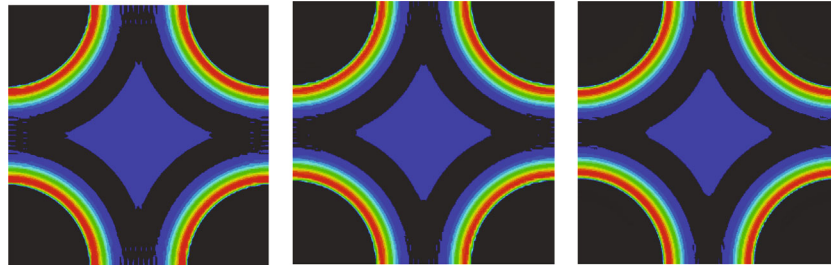


FIGURE 47: Contact stress cloud diagram of rock slab under different proppant heights (3 mm, 5 mm, and 8 mm).

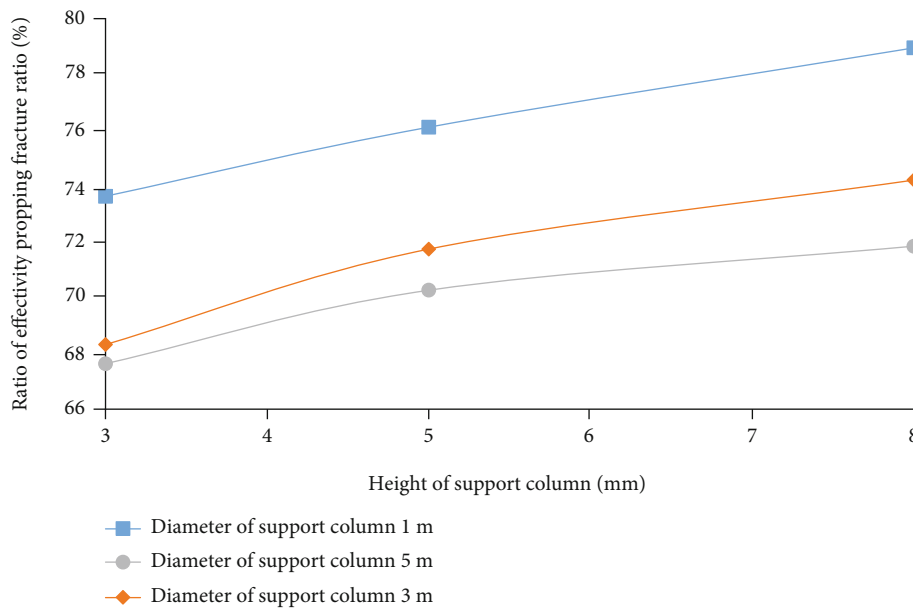


FIGURE 48: The effect of proppant height on effective supporting fractures.

and this increasing trend is not affected by the in situ stress.

4.3. *The Influence of Proppant Diameter (Spacing) on Fracture Closure Deformation and Stability.* When the height of the proppant is 5 mm, the in situ stress is set to 50 MPa and the elastic modulus of the reservoir is 40 GPa. The effect of the proppant diameter on fracture closure deformation and stability is explored.

4.3.1. *Ratio of Effective Supporting Cracks.* As shown in Figure 42, from left to right, the contact stress cloud diagrams of the rock slab when the proppant diameter is 1 m, 3 m, and 5 m (the height of the proppant is 5 mm) are shown. Using graphic analysis software, the proportion of effective supporting fractures under each proppant diameter can be calculated: 1 m is 76.02%, 3 m is 71.76%, and 5 m is 70.26%. Figure 43 shows that when the proppant height remains the same, as the diameter of the proppant increases, the effective support ratio of the fracture decreases.

4.3.2. *The Effect of Proppant Diameter on Effective Supporting Fractures under Different In Situ Stresses and*

*Elastic Moduli.* When the in situ stress is 40 MPa, 50 MPa, and 60 MPa, and the elastic modulus is 25 GPa, 30 GPa, 35 GPa, and 40 GPa, the influence of the proppant diameter under the elastic modulus on the effective support fracture is shown in Figures 44–46.

According to the above simulation results, it can be seen that the ratio of effective proppant fractures decreases with the increase of the proppant diameter, and this decreasing trend is not affected by the height of the proppant. When the diameter of the proppant is 5 m, the in situ stress is set to 50 MPa, and the elastic modulus of the reservoir is 40 GPa. The effect of the proppant height on fracture closure deformation and stability is explored.

(1) *Ratio of Effective Supporting Cracks.* As shown in Figure 47, from left to right, the contact stress cloud diagrams of the rock slab when the proppant height is 3 mm, 5 mm, and 8 mm (proppant diameter 5 m) are shown. Using graphic analysis software, the proportion of effective supporting cracks under each proppant column height can be calculated: 3 mm is 67.68%, 5 mm is 70.26%, and 8 mm is 71.86%. Figure 48 shows that when the diameter of the



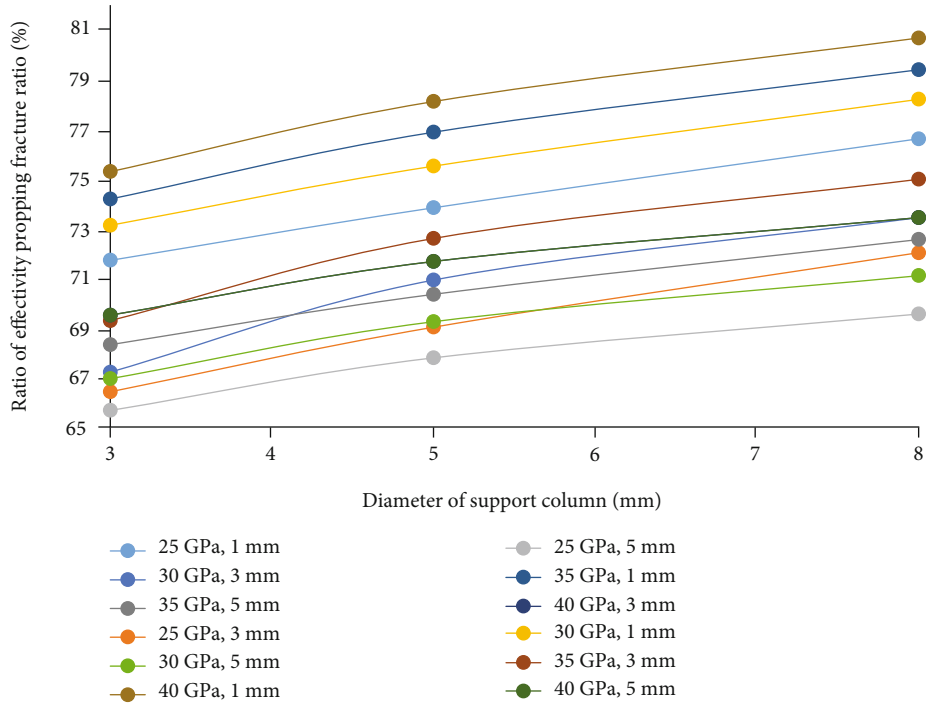


FIGURE 49: The effect of proppant height on the ratio of effective propped fractures under 40 MPa in situ stress and different elastic moduli.

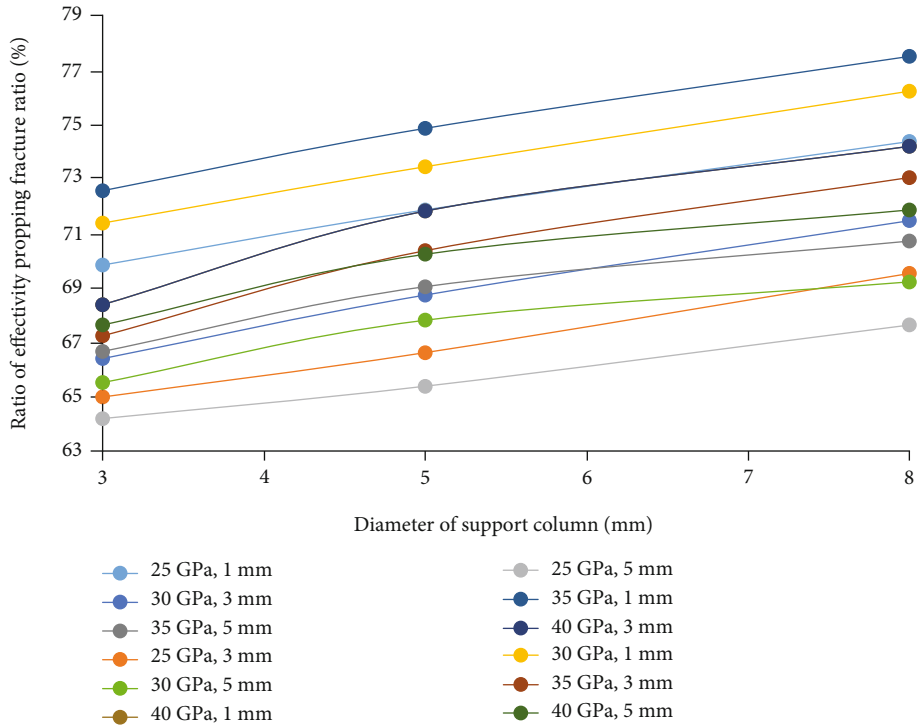


FIGURE 50: The effect of proppant height on the ratio of effective propped fractures under 50 MPa in situ stress and different elastic moduli.

proppant remains unchanged, as the height of the proppant increases, the effective support ratio of the fracture increases.

(2) The Effect of Proppant Height on Effective Supporting Fractures under Different In Situ Stresses and Elastic Moduli.

According to the above simulation results (Figures 49–51), it can be seen that the ratio of effective supporting fractures increases with the height of the proppant column, and this increasing trend is not affected by the diameter of the proppant column.

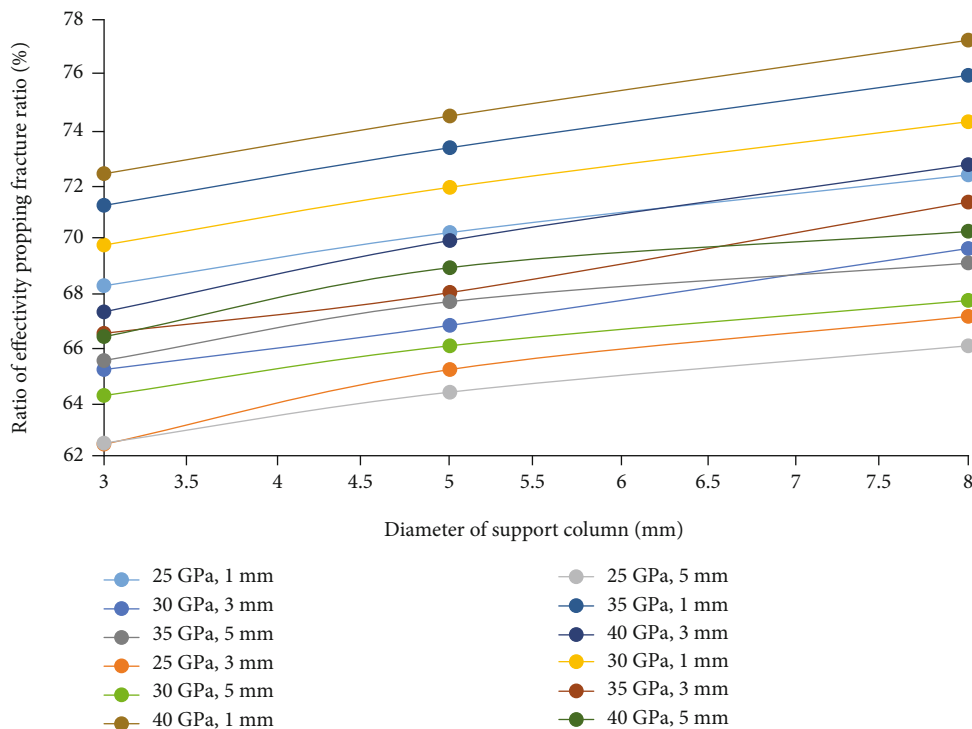


FIGURE 51: The effect of proppant height on the ratio of effective propped fractures under 60 MPa in situ stress and different elastic moduli.

### 5. Conclusion

This paper studies the influence of in situ stress, reservoir rock elastic parameters, and spatial distribution characteristics of proppant on the closed deformation of high-conductivity fracturing channels and the stability of the proppant. The main conclusions are as follows:

- (1) The proppant particles have a large pore space in the low pressure section. As the pressure increases, the particles are compressed and tightly arranged. The axial and radial deformations of the proppant increase rapidly at the beginning of loading, and the strain changes slowly under high stress
- (2) The greater the in situ stress, the greater the contact stress on the rock slab, the lower the height of the proppant, the larger the diameter, and the easier for the proppant to deform and break, while the effective support ratio decreases as the in situ stress increases
- (3) Under the condition of constant in situ stress, as the elastic modulus of the reservoir increases, the relative axial displacement of the two rock slabs gradually decreases, and as the effective support ratio of the fracture increases, the impact of reservoir elastic modulus on the stability of proppant decreases
- (4) The effective support ratio of fractures decreases with the increase of the proppant diameter, increases with the increase of the proppant height, and increases with the ratio of reservoir elastic modulus

to in situ stress. When the proppant diameter (proppant spacing) is less than or equal to 3 m, the ratio of effective supporting fractures increases significantly

### Data Availability

Data will be made available on request.

### Conflicts of Interest

The authors declare that they have no conflicts of interest.

### References

- [1] M. Gillard, O. Medvedev, A. Peña, A. Medvedev, F. Peñacorada, and E. d’Huteau, “A new approach to generating fracture conductivity,” in *SPE Annual Technical Conference and Exhibition*, Florence, Italy, September 2010.
- [2] R. Kayumov, A. Klyubin, A. Yudin et al., “First channel fracturing applied in mature wells increases production from Talinskoe oilfield in Western Siberia,” in *SPE Russian Oil and Gas Exploration and Production Technical Conference and Exhibition*, Moscow, Russia, October 2012.
- [3] S. Wang, X. Wang, L. Bao, Q. Feng, X. Wang, and S. Xu, “Characterization of hydraulic fracture propagation in tight formations: a fractal perspective,” *Journal of Petroleum Science and Engineering*, vol. 195, article 107871, 2020.
- [4] L. Yang, C. Chen, Y. Liu, and Y. Zheng, “A comparative study of ion diffusion during water imbibition in shale, sandstone and volcanic rock,” *Capillarity*, vol. 3, no. 2, pp. 16–27, 2020.
- [5] S. Xu, Q. Feng, S. Wang, F. Javadpour, and Y. Li, “Optimization of multistage fractured horizontal well in tight oil based

- on embedded discrete fracture model,” *Computers & Chemical Engineering*, vol. 117, pp. 291–308, 2018.
- [6] S. Wang, C. Qin, Q. Feng, F. Javadpour, and Z. Rui, “A framework for predicting the production performance of unconventional resources using deep learning,” *Applied Energy*, vol. 295, article 117016, 2021.
  - [7] T. Guo, S. Wang, S. Liu, J. Xu, N. Qi, and Z. Rui, “Physical simulation of hydraulic fracturing of large-sized tight sandstone outcrops,” *SPE Journal*, vol. 26, no. 1, pp. 372–393, 2021.
  - [8] Q. Feng, S. Xu, X. Xing, W. Zhang, and S. Wang, “Advances and challenges in shale oil development: a critical review,” *Advances in Geo-Energy Research*, vol. 4, no. 4, pp. 406–418, 2020.
  - [9] Z. Rui, T. Guo, Q. Feng, Z. Qu, N. Qi, and F. Gong, “Influence of gravel on the propagation pattern of hydraulic fracture in the glutenite reservoir,” *Journal of Petroleum Science and Engineering*, vol. 165, pp. 627–639, 2018.
  - [10] A. Valenzuela, J. Guzmán, S. Chávez et al., “Field development study: channel fracturing increases gas production and improves polymer recovery in Burgos Basin, Mexico North,” in *SPE Hydraulic Fracturing Technology Conference*, The Woodlands, Texas, USA, February 2012.
  - [11] A. A. Gawad, J. Long, T. El-Khalek et al., “Novel combination of channel fracturing with rod-shaped proppant increases production in the Egyptian Western Desert,” in *SPE European Formation Damage Conference & Exhibition*, Noordwijk, The Netherlands, June 2013.
  - [12] A. Q. Li, L. J. Mu, X. W. Li, Y. Haihua, T. Judd, and L. Yaolan, “The channel fracturing technique improves tight reservoir potential in the Ordos Basin,” in *SPE/IATMI Asia Pacific Oil & Gas Conference and Exhibition*, Nusa Dua, Bali, Indonesia, October 2015.
  - [13] M. Meng, Z. Chen, X. Liao, J. Wang, and L. Shi, “A well-testing method for parameter evaluation of multiple fractured horizontal wells with non-uniform fractures in shale oil reservoirs,” *Advances in Geo-Energy Research*, vol. 4, no. 2, pp. 187–198, 2020.
  - [14] Y. He, S. Cheng, Z. Sun, Z. Chai, and Z. Rui, “Improving oil recovery through fracture injection and production of multiple fractured horizontal wells,” *Journal of Energy Resources Technology*, vol. 142, no. 5, article 053002, 2020.
  - [15] Z. Rui, K. Cui, X. Wang et al., “A quantitative framework for evaluating unconventional well development,” *Journal of Petroleum Science and Engineering*, vol. 166, pp. 900–905, 2018.
  - [16] C. Li, H. Singh, and J. Cai, “Spontaneous imbibition in shale: a review of recent advances,” *Capillarity*, vol. 2, no. 2, pp. 17–32, 2019.
  - [17] F. Guo, S. Wang, Q. Feng, X. Yao, Q. Xue, and X. Li, “Adsorption and absorption of supercritical methane within shale kerogen slit,” *Journal of Molecular Liquids*, vol. 320, article 114364, 2020.
  - [18] Y. Heider, “A review on phase-field modeling of hydraulic fracturing,” *Engineering Fracture Mechanics*, vol. 253, article 107881, 2021.
  - [19] P. D. Nguyen, L. K. Vo, C. Parton, J. Heeter, R. Gashimov, and P. O’Connell, “Evaluation of low-quality sand for proppant-free channel fracturing method,” in *International Petroleum Technology Conference*, Malaysia, 2014.
  - [20] X. Yan, Z. Huang, X. Yan, J. Yao, Y. Li, and L. Gong, “Theoretical analysis of high flow conductivity of a fracture induced in HiWay fracturing,” *Acta Physica Sinica*, vol. 64, no. 13, article 134703, 2015.
  - [21] X. Yan, Z. Huang, J. Yao, W. Song, Y. Li, and L. Gong, “Theoretical analysis of fracture conductivity created by the channel fracturing technique,” *Journal of Natural Gas Science & Engineering*, vol. 31, pp. 320–330, 2016.
  - [22] T. Hou, S. Zhang, B. Yu et al., “Theoretical analysis and experimental research of channel fracturing in unconventional reservoir,” in *SPE Europec Featured at Eage Conference and Exhibition*, Vienna, Austria, May 2016.
  - [23] G. Xu, S. Zhang, L. Wang, and J. Han, “Influence factors analysis of proppant fracture in channel fracturing,” *Fault-Block Oil & Gas Field*, vol. 22, no. 4, pp. 534–537, 2015.
  - [24] Z. Qu, L. Zhou, G. Qu, D. Huang, Y. Yang, and H. Xu, “Experimental evaluation on influencing factors of flow conductivity for channel fracturing proppant,” *Petroleum Geology and Recovery Efficiency*, vol. 22, no. 1, pp. 122–126, 2015.
  - [25] Q. Wen, Y. Yang, F. Wang, X. Duan, L. Yang, and Z. Jin, “Experimental study on an innovative proppant placement method for channel fracturing technique,” *Journal of China University of Petroleum*, vol. 40, no. 5, pp. 112–117, 2016.
  - [26] J. C. Zhang, “Theoretical conductivity analysis of surface modification agent treated proppant,” *Fuel*, vol. 134, pp. 166–170, 2014.
  - [27] J. C. Zhang and J. R. Hou, “Theoretical conductivity analysis of surface modification agent treated proppant II - channel fracturing application,” *Fuel*, vol. 165, pp. 28–32, 2016.
  - [28] X. J. Zheng, M. Chen, B. Hou et al., “Effect of proppant distribution pattern on fracture conductivity and permeability in channel fracturing,” *Journal of Petroleum Science and Engineering*, vol. 149, pp. 98–106, 2017.
  - [29] R. Moghadasi, A. Rostami, and A. Hemmati-Sarapardeh, “Application of nanofluids for treating fines migration during hydraulic fracturing: experimental study and mechanistic understanding,” *Advances in Geo-Energy Research*, vol. 3, no. 2, pp. 198–206, 2019.
  - [30] J. C. Guo and Y. X. Liu, “Modeling of proppant embedment: elastic deformation and creep deformation,” in *SPE International Production and Operations Conference & Exhibition*, Doha, Qatar, May 2012.
  - [31] B. R. Meyer, L. W. Bazan, D. E. Walls, and B. C. Brinzer, “Theoretical foundation and design formulae for channel and pillar type propped fractures – a method to increase fracture conductivity,” in *SPE Annual Technical Conference and Exhibition*, Amsterdam, The Netherlands, October 2014.
  - [32] B. Hou, X. J. Zheng, M. Chen, Z. Ye, and D. Chen, “Parameter simulation and optimization in channel fracturing,” *Journal of Natural Gas Science and Engineering*, vol. 35, pp. 122–130, 2016.

## Research Article

# Methane Flux Effect on Hydrate Formation and Its Acoustic Responses in Natural Sands

Qingtao Bu <sup>1,2</sup>, Tongju Xing <sup>3,4</sup>, Gaowei Hu <sup>1,2</sup>, Changling Liu <sup>1,2</sup>, Chengfeng Li <sup>1,2</sup>,  
Jinhuan Zhao <sup>1,2</sup>, Zihao Wang <sup>1</sup>, Wengao Zhao <sup>1</sup>, and Jiale Kang <sup>1</sup>

<sup>1</sup>Key Laboratory of Gas Hydrate, Ministry of Natural Resources, Qingdao Institute of Marine Geology, Qingdao 266237, China

<sup>2</sup>Laboratory for Marine Mineral Resources, Qingdao National Laboratory for Marine Science and Technology, Qingdao 266237, China

<sup>3</sup>Qingdao Geo-Engineering Surveying Institute (Qingdao Geological Exploration and Development Bureau), Qingdao 266100, China

<sup>4</sup>Key Laboratory of Geological Safety of Coastal Urban Underground Space, Ministry of Natural Resources, Qingdao 266100, China

Correspondence should be addressed to Qingtao Bu; [bqt881110@163.com](mailto:bqt881110@163.com) and Gaowei Hu; [hgw-623@163.com](mailto:hgw-623@163.com)

Received 7 October 2021; Accepted 4 May 2022; Published 30 May 2022

Academic Editor: Mohammed Fattah

Copyright © 2022 Qingtao Bu et al. This is an open access article distributed under the Creative Commons Attribution License, which permits unrestricted use, distribution, and reproduction in any medium, provided the original work is properly cited.

The acoustic properties of hydrate deposits are important parameters for hydrate geophysical exploration, and the gas leakage model plays a very important role in hydrate accumulation systems. In order to reflect the gas supply environment during hydrate formation, a high-pressure device with a simulated leakage system was designed to achieve different methane flux supplies. The effects of different methane fluxes on the hydrate formation rate and the maximum hydrate saturation were obtained. The results in this study indicate that similar hydrate formation rates occur in systems with different methane fluxes. However, when the methane flux is large, it takes longer to reach the maximum hydrate saturation, and the larger the methane flux, the larger the hydrate saturation formed. In each methane flux system, the elastic velocity increased slowly with increasing hydrate saturation at the beginning of hydrate formation, but velocity increased quickly when the hydrate saturation reached 50–60%. In order to take into account the effect of the gas, the calculated values of the elastic velocity model were compared with the experimental data, which indicated that the BGTL theory and the EMT model are more adaptable and can be used to deduce hydrate morphology. In the large methane flux system, the hydrate mainly forms at grain contacts when the hydrate saturation is 10–60%. As the hydrate saturation reaches 60–70%, hydrate forms first in the pore fluid, and then the hydrates contact sediment particles.

## 1. Introduction

Natural gas hydrates are considered to be very promising potential clean energy sources in the future [1, 2]. Geophysical exploration methods remain the primary means of exploring for marine gas hydrates [3]. Hydrate-bearing sediments exhibit higher acoustic velocities compared to background sediments [4, 5], and the presence of hydrates will affect the physical properties of the reservoir [6–9]. When the temperature and pressure conditions exceed the phase equilibrium conditions, hydrates are difficult to preserve. Therefore, it is not very clear how wave velocities vary with the saturation of hydrate. Simulation experiment in the laboratory is an effective way to obtain data to understand the link between the velocity and saturation.

In recent years, a variety of detection methods have found that methane flux is an important controlling factor for hydrate formation. The methane leakage system plays an important role in the formation of hydrate. Mahabadi et al. [10] simulated the migration and capture of bubbles using pore network models extracted from 3D images of in situ sediments. The results show that the distribution of bubble size becomes wider with bubble transport as the bubbles are coalescing. Methane release from temperature-induced hydrate decomposition in the West Svalbard continental margin was studied by Thatcher et al. [11]. Wang et al. [12] used magnetic resonance imaging (MRI) to observe the formation and decomposition of hydrates in dynamic conditions. It was found that the optimal gas migration rate

resulted in the maximum hydrate saturation in porous media and the gas upward migration system ratio. The downward gas transport system can change the spatial structure of porous media more. The scale of methane flux is one of the most important factors influencing the hydrate formation process. Different seepage fluxes will influence the rate of hydrate formation, the amount of hydrocarbon accumulation, and the occurrence of hydrate deposits. It is helpful to further understand the formation characteristics of leakage hydrates by simulating the formation of hydrate in different methane fluxes.

Currently, most experimental studies on the acoustic characteristics of hydrate reservoirs have been conducted in static experimental systems. Priest et al. [13, 14] focused on how hydrate affects wave velocity under different gas-to-water ratios. Winters et al. [15] investigated how hydrate affects wave velocity in different sediments. Hu [16–19] investigated the formation and decomposition of hydrate in consolidated and unconsolidated sediments, and Hu et al. [4] and Bu et al. [5] also studied hydrate dissociation characteristics in sediments from the South China Sea. Andhumoudine et al. [20] also studied the elastic properties of coal based on digital core technology and finite element method. It is not easy to conduct experiments on formation of hydrate in a dynamic gas leakage system. Few experimental studies of gas leakage systems have been performed, and hydrate generation experiments are difficult for different methane flux modes. Most prior experiments were conducted using a single methane flux, and only a small number of experiments studied the acoustic properties. Gao et al. [21] studied the kinetic process of methane hydrate formation under confining pressures, they developed a novel triaxial horizon fixed bed reactor, and obtained the influence of several key factors (i.e., water-gas ratio, pressure, temperature and the presence of NaCl) on the kinetic behavior of methane hydrate formation. The evolution of gas and water profiles and triaxial pressure in the process of hydrate dissociation have also been studied [22]. They also conducted a multi-stage depressurization to adjust the fluid production behavior of hydrate sediments and obtained good results [23]. An experimental setup was developed to simulate a real depositional system [24], with a water inflow at the top and a gas inflow at the bottom, and the experimental setup is capable of acoustic velocity detection. Kwon and Cho [25] did CO<sub>2</sub> hydrate generation experiments by fluid injection and obtained acoustic parameters during the experiments. Liu et al. [26] conducted hydrate generation experiments and tested acoustic velocities in a CH<sub>4</sub>-CO<sub>2</sub> replacement reaction apparatus, which was a gas dynamic transport system. Guan et al. [27] simulated the formation process of gas hydrate in a gas leakage system, and tested the relevant physical parameters. A special high-pressure device was designed by Bu et al. [28] to study the effect of gas on hydrate saturation and velocities during vertical gas migration conditions. However, they did not quantify the methane flux during the experiment process. Most of the above studies were carried out in closed reaction vessels, therefore it is not possible to characterize the migration of gas in the sediment during hydrate formation.

In order to reflect the formation of hydrate under gas leakage conditions, a simulator was designed to realize hydrate formation in sediments under various methane flux conditions, using an additional gas flow control system to control the methane supply. The waveform data and water content were obtained by combining ultrasonic techniques with time domain reflection (TDR). The data were then used to study the variations in hydrate saturation and the correlation between velocity and saturation as a function of methane flux.

## 2. Experiment

*2.1. Experimental Facilities and Materials.* The hydrate simulation experimental setup consists of five parts: high-pressure reactor and gas distribution section, pressure control section, refrigeration section, gas flow rate control section, and test section (Figure 1). For a detailed description of the specifics of the experimental setup refer to reference [29]. Figure S5 in the Supplementary Materials exhibits the inner of the apparatus, especially for the microporous sintered plate.

In a previous study, several methods were used to simulate the formation of hydrate in a gas migration system [23]. Based on this gas migration system, a BROOKS mass flow controller was applied to the gas path to achieve gas flow control in the reaction system. Experiments were then carried out under different methane flux supply modes, and the influence of different methane fluxes on the hydrate saturation and its acoustic response characteristics were studied by a series of experiments.

As the BROOKS mass flow controller needs a constant gas pressure for the measurement, a TESCOM manual pressure-reduction valve and a manual back-pressure valve were used in the flow measurement set-up before and after the installation, and the gas pressure was maintained at 29 MPa (which is the maximum pressure of the mass flow controller). Under this condition, the flow measurement and control meter can achieve the expected measurement and control accuracy. In order to automatically switch the mass flow controller between different flows, a pneumatic ball valve was installed on the gas piping between the controller outlet and the back-pressure valve inlet. The control system automatically selects the appropriate flow meter, and opens or cuts off the gas line, depending on the flow rate. The ball valve was placed in the controller outlet in order to protect the controller from the impact of pressure and the impact of the direction pressure. After the gas moves across the pressure-reducing valve, the mass flow controller, the gas-control ball valve, and the back-pressure valve, the gas pressure is maintained at the preset pressure (less than 20 MPa) and introduced into the experimental system by a TESCOM pneumatic control valve.

For the experiment, the sand particle size is 0.15–0.30 mm [30], the solution used for the experiments was a 0.03% concentration of sodium dodecyl sulfate solution. The gas used in the experiments was pure CH<sub>4</sub> gas, the concentration of CH<sub>4</sub> gas was 99.9%.

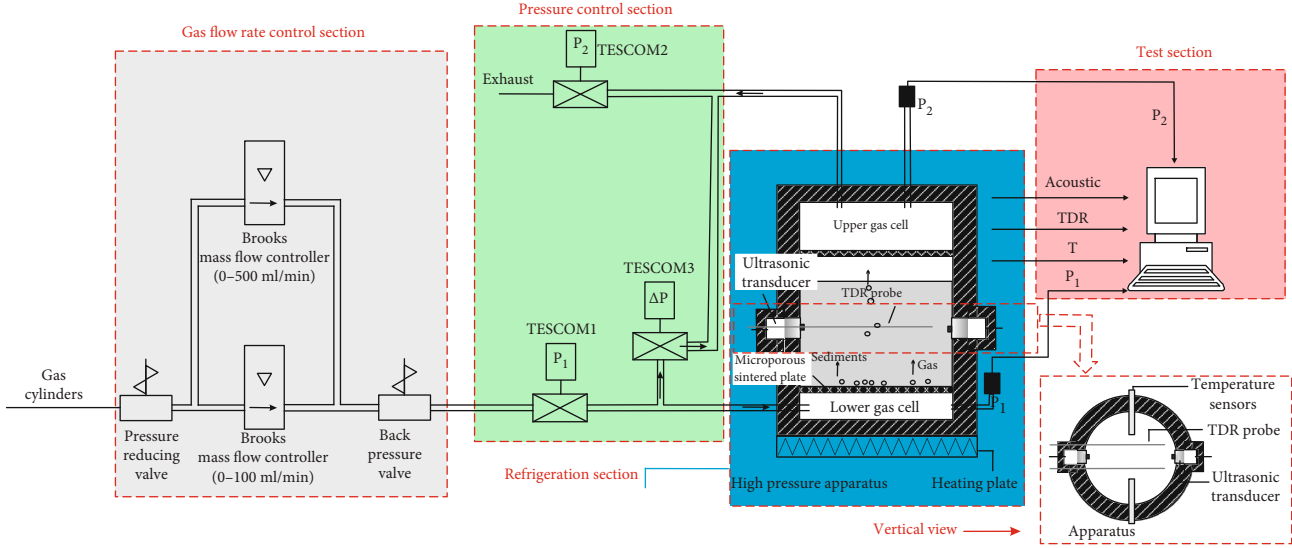


FIGURE 1: An experimental device for gas hydrate formation and acoustic velocity detection with different methane flux (Modified from [29]).

2.2. *Experimental Method and Procedure.* In this experiment, we still use ultrasonic detection and TDR detection to obtain acoustic wave travel time and water content [5, 18]. The detailed measuring method of the acoustic data and hydrate saturation are described in Text S1 and S2 in the Supplementary Materials.

The P-wave velocity and S-wave velocity are determined by equations (1) and (2):

$$V_p = \frac{L}{t_p - t_{0p}} \quad (1)$$

$$V_s = \frac{L}{t_s - t_{0s}} \quad (2)$$

Here,  $L$  represents the detection length between the sensors,  $t_{0p}$  and  $t_{0s}$  represent the Intrinsic propagation time of the sensors, and  $t_p$  and  $t_s$  represent the times of the P- and S- waves. Figure S1–S3 and Table S1–S2 in the Supplementary Materials exhibit the Calibration of the ultrasonic transducers.

For hydrate deposits, the main application is the model of Wright et al. [31]:

$$\theta_v = -11.9677 + 4.506072566K - 0.14615K^2 + 0.0021399K^3 \quad (3)$$

Here,  $\theta_v$  represents the water content, and  $K$  represents the dielectric constant, Figure S4 and Table S3 in the Supplementary Materials exhibit the calibration of the TDR probes. And we can calculate the hydrate saturation according to the water content ( $\theta_v$ ) and porosity ( $\phi$ ) of the samples:

$$S_h = (\phi - \theta)/\phi \times 100\% \quad (4)$$

In this study, we use X-rays to transmit through the test sample. The X-ray CT images were obtained using the different absorption of the rays by the substances. The different densities and thicknesses of the components, allowed us to obtain information on the distribution of each component in the CT images [5].

The experiment steps for gas hydrate formation with different methane fluxes were:

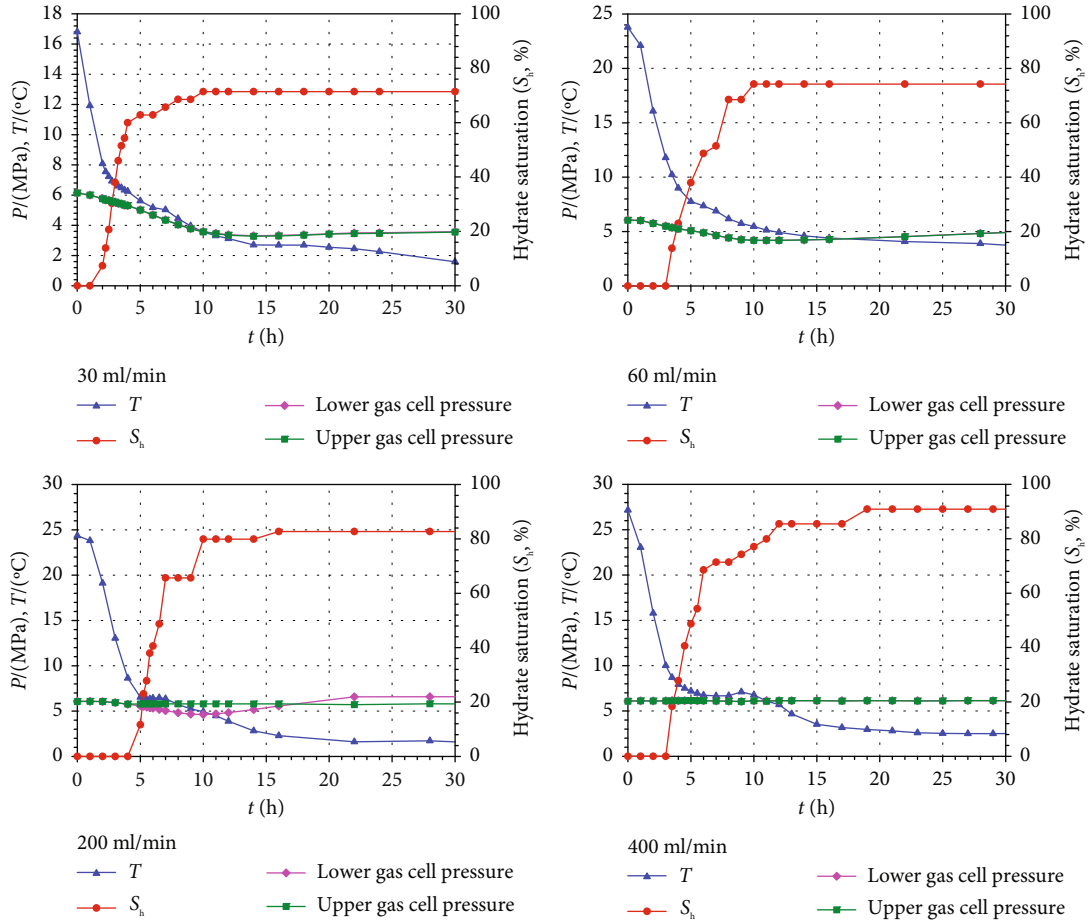
- (1) Firstly, the different sensors are positioned in the reactor in the right place
- (2) Methane gas was introduced into the reactor and pressurized to 6 MPa. Set a pressure difference of 0.3-0.5 MPa in the reactor
- (3) Depending on the requirements of different experimental cases, the mass flow controller was set in the range of 0-500 ml/min to achieve the required control of methane flow
- (4) After the reactor was installed, turn on the temperature control system and control the temperature of the whole experimental system to 2°C
- (5) When the pressure in the reactor remained constant for a long time, it was considered that the hydrate was no longer generated, and the cooling system was shut down, and then increasing the temperature so that the hydrate began to dissociate

The CT scanning experiment procedure during hydrate formation stage with methane flux was as follows.

- (1) The sand and 3.5 wt.% NaCl solution are loaded into the reaction chamber for CT scanning, the sample chamber is connected to the gas migration system, the gas enters from the lower part of the sample chamber and flows out from the upper part

TABLE 1: Effect of methane flux on hydrate formation.

Run no.	Gas flux mode/(ml/min)	$T/^\circ\text{C}$	Upper gas cell pressure/MPa	Lower gas cell pressure/MPa	Maximum hydrate saturation/%	$V_s$ (m/s)	$V_p$ (m/s)
1	30	2.25	3.46	3.51	71.4	1291	2670
2	30	3.06	3.77	3.78	71.4	1287	2674
3	30	2.09	3.22	3.26	71.4	1285	2668
4	60	4.07	4.52	4.54	74.2	1328	2722
5	60	3.90	4.82	4.84	74.2	1327	2721
6	60	3.58	5.53	5.54	74.2	1332	2735
7	200	1.61	5.70	6.57	82.7	1531	3150
8	200	1.95	5.18	6.11	82.7	1535	3167
9	200	1.55	6.09	6.38	82.7	1533	3153
10	400	2.52	6.11	6.12	90.9	1638	3298
11	400	3.02	6.15	6.31	90.9	1618	3287
12	400	2.72	6.05	6.11	90.9	1635	3293

FIGURE 2: Variation in temperature, pressure and hydrate saturation ( $S_h$ ) during gas hydrate formation in different methane fluxes (Data for Figure 2 are in Table S4 in the Supplementary Materials). (Methane flow rate: 30 ml/min、60 ml/min、200 ml/min、400 ml/min).

- (2) Inject methane gas into the reactor, control the upper and lower gas pressure difference at 0.3 MPa, realize the gas migration from the bottom to the upper part, and control the pressure of the reactor at 6.5 MPa
- (3) Turn on the cooling system and begin to form hydrates. In the different stages of hydrate formation process, when X-CT scanning is required, the gas inlet and outlet of the reaction chamber are closed,

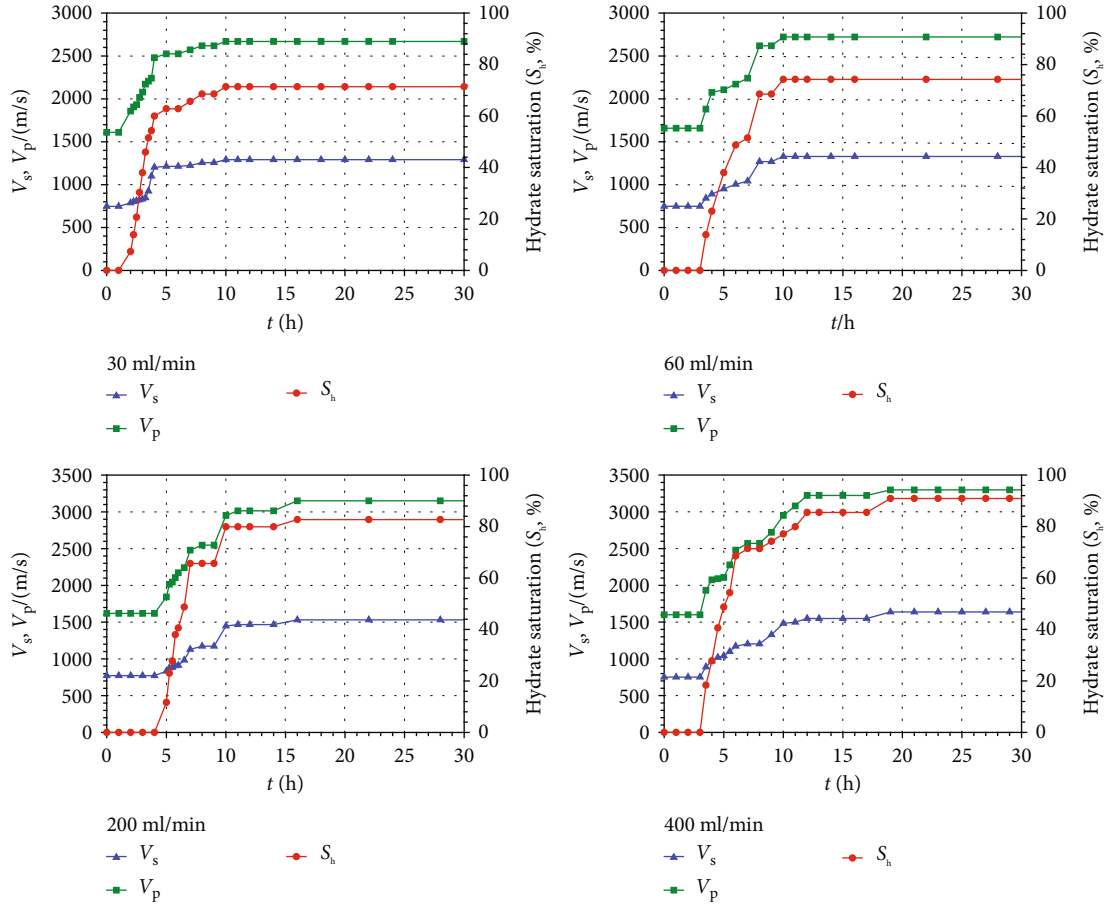


FIGURE 3: Variation in hydrate saturation and wave velocity during hydrate formation (30 ml/min \(\cdot\) 60 ml/min \(\cdot\) 200 ml/min \(\cdot\) 400 ml/min), (Data for Figure 3 are in Table S5 in the Supplementary Materials).

and the reaction kettle is transferred to the CT laboratory instrument for scanning

- (4) The variation of distribution and pore morphology of each component with methane flux was observed. For more information about the steps of CT analysis, please refer to reference [32, 33].

In this study, acoustic experiments on hydrate-bearing sediments under different methane flux conditions and X-CT scanning cannot be performed simultaneously, so when performing X-CT scanning observations, we only performed scanning observations under different pressure conditions to help analysis.

### 3. Results

**3.1. Hydrate Formation Process.** Due to the limitations of laboratory simulation scales, it is not possible to simulate a large range of methane fluxes as in the field. Methane flow rates of 30 ml/min, 60 ml/min, 200 ml/min, and 400 ml/min were carried out in a multi-cycle simulation experiment under different methane flux supply modes. 12 experiment runs were conducted (Table 1) and one run of experimental data from each flux mode was selected for analysis. The

observed variations in pressure, temperature, and hydrate saturation during the experiment process are shown in Figure 2.

As the experiment was conducting, the pressure of the apparatus was decreased before the maximum saturation of the hydrate was reached in the 30 ml/min and 60 ml/min modes. This indicates that for the 30 ml/min and 60 ml/min methane supply modes, the methane consumption rate was higher than the methane supply rate. With the onset of hydrate formation, methane consumption was gradually reduced. When the maximum hydrate saturation was reached and the saturation no longer increased, the internal pressure in the chamber gradually increased. When the methane supply was controlled at 200 ml/min, there were only small fluctuations in the lower gas chamber of the reactor, indicating that the 200 ml/min supply rate was comparable to the methane consumption rate during hydrate formation. When the methane supply was controlled at 400 ml/min, the pressure did not change substantially, indicating that the gas supply rate equaled the methane consumption during hydrate formation and maintained the pressure. From Figure 2, an abnormal temperature point can be observed during the formation of hydrate. Although hydrate formation generally occurs as temperature decreases, when the hydrate first formed in the experiment,



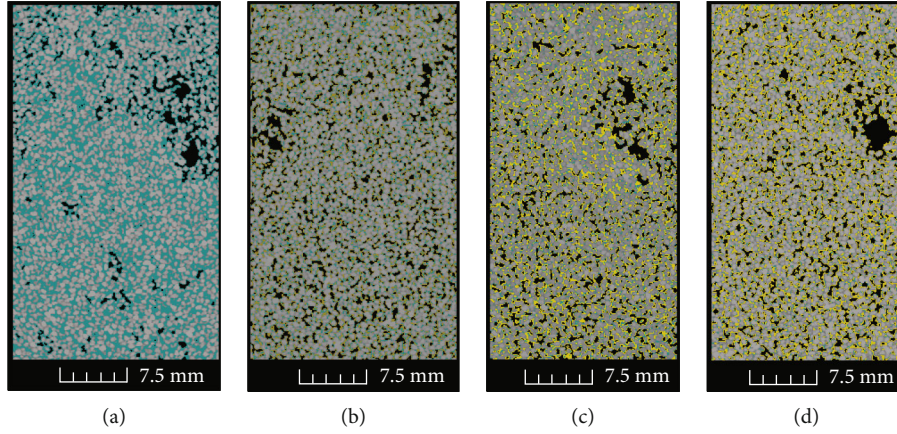


FIGURE 4: Micro-distribution of gas hydrate during hydrate formation process under methane flux conditions. (a) Hydrate saturation =0%, (b) Hydrate saturation =22.13%, (c) Hydrate saturation =47.33%, (d) Hydrate saturation =59.87%. The yellow is methane hydrate. The blue is NaCl solution. The light gray is sands. The black is methane gas.

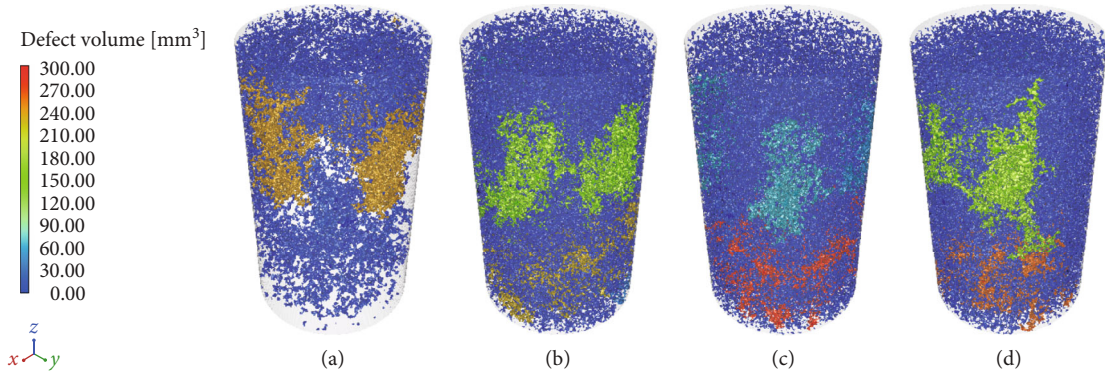


FIGURE 5: Extracted gas distribution during hydrate formation process under methane flux conditions. (a) Gas ratio =5.35%, (b) Gas ratio =11.65%, (c) Gas ratio =11.99%, (d) Gas ratio =11.35%. Different colors represent the size of the gas volume.

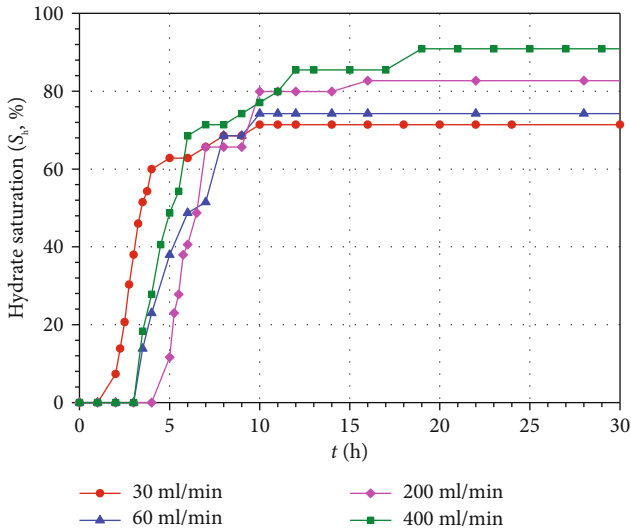


FIGURE 6: Effect of methane flux on hydrate formation (Data for Figure 6 are in Table S6 in the Supplementary Materials).

the temperature was unusually elevated due to the exothermic process. Such temperature anomalies are present in the four different methane flux modes, but vary little

TABLE 2: Effect of methane flux on hydrate formation rate and hydrate saturation.

Gas flux	Time	Maximum hydrate saturation
30 ml/min	10 h	71.4%
60 ml/min	10 h	74.2%
200 ml/min	16 h	82.7%
400 ml/min	19 h	90.9%

between the 30 ml/min and 60 ml/min flow rate modes with slight fluctuations. Very obvious temperature anomalies can be seen from the 200 ml/min and 400 ml/min flow rate modes. This may be because more hydrate forms in the larger methane flux mode than in the smaller methane flux mode, resulting in a large temperature fluctuation during the temperature drop.

*3.2. Variation of Wave Velocity under Different Methane Flux Conditions.* For the different methane flux modes, 12 experiment runs were conducted. The results show that each experiment has good repeatability, indicating that the equipment is stable and reliable. Here, we illustrate the results with an example. When gas hydrate formed in the system,

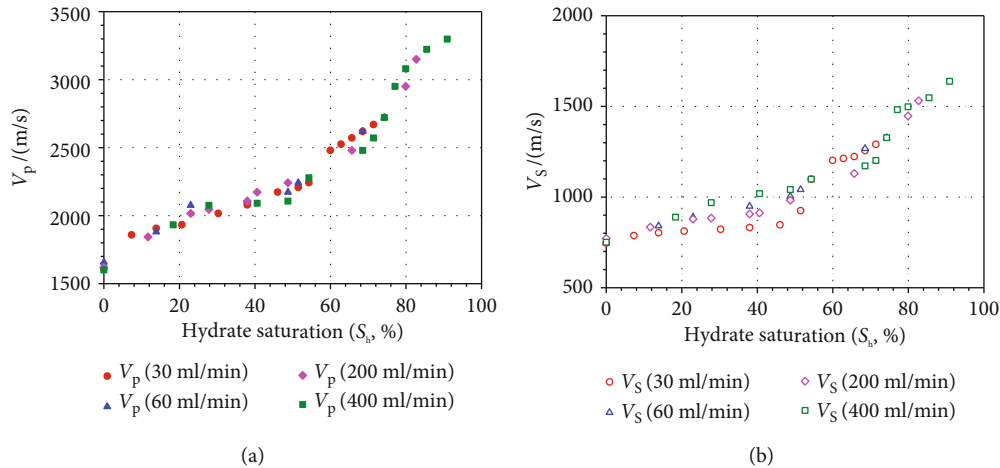


FIGURE 7: Variation in wave velocities with hydrate saturation in different methane flux. (a) Variation of P-wave velocity. (b) Variation of S-wave velocity (Data for Figure 7 are in Table S7 in the Supplementary Materials).

the detected wave velocities increased as hydrate saturation increasing, and the trend is basically the same (Figure 3). In the non-hydrate sediments, the P-wave velocities were 1601–1657 m/s and the S-wave velocities were 746–771 m/s. Due to the different amounts of hydrate formation at different methane fluxes, larger saturation of the hydrate results in larger wave velocities. Under the condition of 30 ml/min methane supply, the hydrate saturation reached 71% and the P-wave velocity reached 2669 m/s and the S-wave velocity was 1291 m/s. When the methane flux was 400 ml/min, the hydrate saturation reached 90.9%, the P-wave velocity was 3298 m/s and the S-wave velocity reached 1638 m/s.

**3.3. The Morphology of Hydrate and Gas during Hydrate Formation Process under Methane Flux Conditions.** The diameter of the experimental sample is 25 mm and the height is 50 mm. This study mainly considers the influence of gas flux, so we intercept almost the entire sample size for analysis. The hydrate saturation data is obtained by analyzing the reconstructed three-dimensional image through X-CT technology, and calculating the proportion of hydrate in the selected area [5]. The micro-distribution of the samples was observed at different moments during the formation of hydrate (Figure 4), the hydrate saturation is 0%, 22.13%, 47.33%, and 59.87%, respectively. Under the condition of gas flux, it can be clearly observed from Figure 4 that the spatial distribution of gas in the sediment varies during the different formation stages of hydrate, and the methane gas is not constant in one position. In order to better observe the gas distribution in different stages of hydrate formation, we extracted the gas in different stages separately and obtained the statistical gas volume size. Before the formation of hydrate, the proportion of gas was 5.35% (Figure 5(a)), and gas clusters were distributed on the upper part of the sediment. With the formation of hydrate, the proportion of gas in the entire system gradually stabilized, and it can be clearly observed that the volume of a single gas is getting larger, and a channel of methane gas is formed from bottom to top in the sediment (Figure 5).

## 4. Discussion

**4.1. Effect of Methane Flux on Hydrate Formation Rate and Hydrate Saturation.** The effects of different methane fluxes on hydrate formation rates and maximum hydrate saturation were obtained from the experiments (Figure 6, Table 2). Under different methane flux conditions, where the saturation of the hydrate changes with time, the slope of each curve is similar, which indicates that the hydrate formation rates are similar under different conditions. At low methane flow rates (30 ml/min and 60 ml/min gas flow rate), the maximum saturation was reached at 10 h, and at 16 h at a flow rate of 200 ml/min, while at 400 ml/min gas flow rate, 19 h was needed to reach the maximum hydrate saturation. It is shown that the smaller the methane flux was, the less time was required to generate the maximum hydrate saturation under the experimental conditions, and the larger the methane flux was, the longer the time required to reach the maximum hydrate saturation. The hydrate saturation reached 71.4% at a gas flow rate of 30 ml/min. When the inlet flow rate was increased to 400 ml/min, the hydrate saturation was 90.9%. Thus, the larger the methane flux, the easier it is to form high-saturation hydrate.

**4.2. Hydrate Saturation Changes with Wave Velocities and Velocity Model Verification.** Using the obtained experimental data, correlation of hydrate saturation and acoustic velocity at different methane flow rates was established (Figure 7). It is showed that the wave velocities increase gradually as hydrate saturation increasing. The different methane flux patterns show a more consistent trend. When the hydrate began to form, the wave velocity exhibits a relatively rapid growth. In the hydrate formation stage, the wave velocities show a relatively gentle growth trend. At a hydrate saturation of 50–60%, the rate of increase in the wave velocities is significantly larger.

Comparing the calculated values of the velocity model with the experimental values in the BGTL theory (Figure 8), the parameters used in the model are shown in

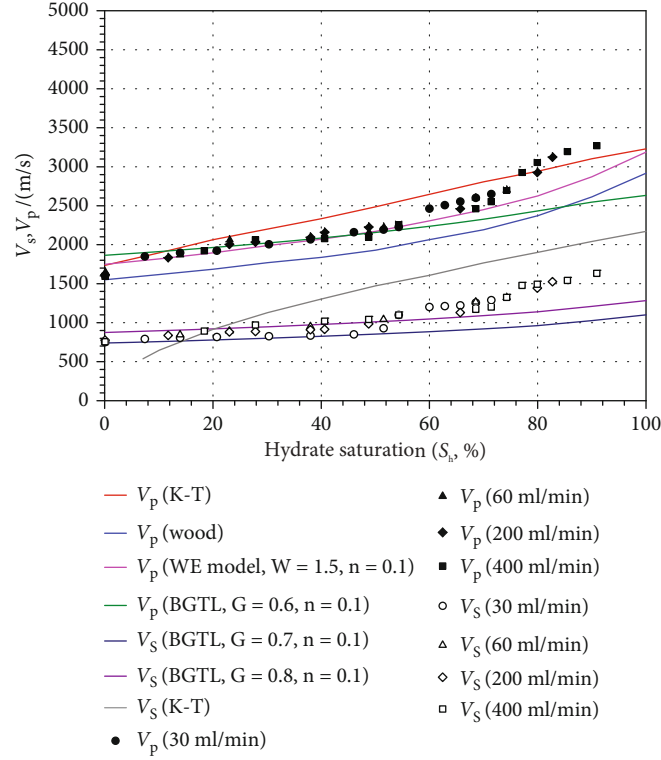


FIGURE 8: Variation of measured and model-calculated  $V_p$  and  $V_s$  with hydrate saturation (Data for Figure 8 are in Table S8 in the Supplementary Materials).

TABLE 3: Mineral composition and physical parameters of the experimental sediments [34–36].

Mineral	Content(%)	$\rho(\text{g/cm}^3)$	K(Gpa)	G(Gpa)
Magnetite	1.94	5.21	161	91.4
Amphibole	1.10	3.12	87	43
Epidote	0.55	3.4	106.2	61.2
Quartz	38.95	2.65	36.6	45
Feldspar	57.46	2.62	76	26
Water		1.032	2.5	0
Pure hydrate		0.9	5.6	2.4
Gas		0.235	0.1	0

Table 3. When  $G=0.6$  and  $n=0.1$ , and the hydrate saturation is 0–50%, the predicted P-wave velocity is similar to the measured value. When  $G=0.7$ ,  $n=0.1$  and  $G=0.8$ , and  $n=0.1$ , the S-wave velocity predicted by BGTL is close to the experimental value when the hydrate saturation is 0–50%. In the weight equation, when  $W=1.5$  and  $n=0.1$ , the predicted P-wave velocity tends to be similar to the experimental value, but there is a certain difference between the calculated value and the actual value. The results of the Wood equation and the K-T equation are different from those of the experimental value, and are not suitable for estimating the velocity in this system.

In addition to the above models, there is a more important equivalent theoretical model for the study of the velocity model of hydrate reservoirs. The effective medium theory

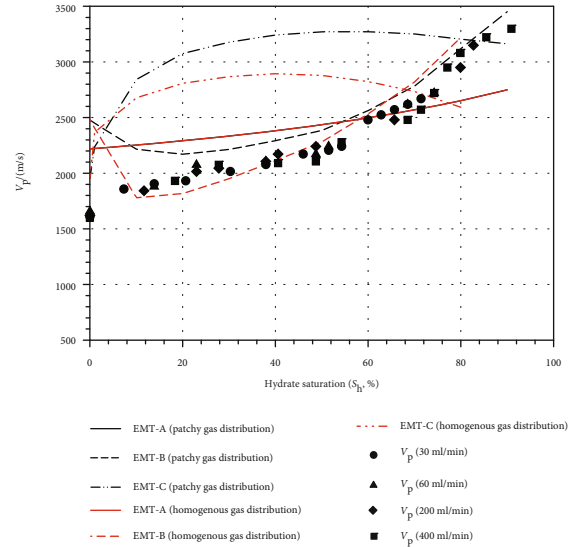


FIGURE 9: Variation of measured  $V_p$  and the calculated  $V_p$  from the EMT model with hydrate saturation (Data for Figure 9 are in Table S9 in the Supplementary Materials).

(EMT) [34, 35] is suitable in this study. In previous research, we considered the influence of gas on the wave velocity of hydrate sediments and verified the relevant models [29].

The microscopic distribution pattern of hydrate will affect the flow characteristics and acoustic properties of the reservoir [5, 37]. For example, to explain the effects of creep microstructure and axial strain on the permeability of

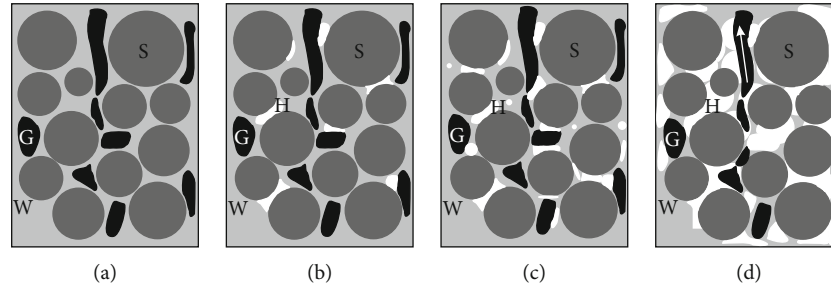


FIGURE 10: Hydrate morphology in a high methane leakage system. (a) No hydrate. (b) Hydrates first form on the surface of gas bubble and at grain contacts. (c) Hydrates form across the entire sample (mainly formed in the grain contact, a small amount is formed in the pore fluid). (d) The end of hydrate formation (with a methane leakage channel). S represents the sand grain. W represents water. H represents gas hydrate. G represents methane gas.

hydrate reservoirs, Cai et al. [38] proposed a very good fractal model based on fractal geometry theory. In this study, we performed calculations using the adjusted model and compared the measured results with the calculated results (Figure 9). In the methane flux system with the formation of hydrates, the distribution of gas and water in the deposition system should occur in different modes. Figure 9 shows the results for the homogeneous gas distribution (H) and the patchy gas distribution (P) when the new model is applied. When the hydrate saturation is 10-30%, the experimental data fall in the region between EMT-B (P) and EMT-B (H), and the test value of P-wave velocity is similar to mode EMT-B (H). At hydrate saturation of 30-60%, the test values are close to EMT-B (H), indicating that hydrate is formed along the grain contact surface and the gas in the system is uniformly distributed. At 60-70% saturation, the test values are close to the EMT-A model. After the hydrate saturation reaches more than 80%, the test values are close to mode EMT-B.

In the different micro-distribution modes, the hydrate will have different elastic effects on the hydrate-bearing sediments. It is also important to explore the distribution pattern of hydrate in sediments by using the link between the measured velocity and saturation, combined with the rock physics model. Based on the obtained experimental results and the comparative analysis with the theoretical model, the mechanism of hydrate formation in methane flux mode can be examined. From Figure 9, when the hydrate saturation is 10-60%, the hydrate mainly formed along grain contacts, which is an important stage of hydrate formation. Generally, when the free gas reaches suitable hydrate formation conditions, hydrate directly forms at the gas-water interface [39]. However, in this reaction system, it is difficult for hydrates to stably develop in pore spaces due to the presence of larger gases and fluid fluxes. Sediment particles, as a stable deposition medium, can provide a relatively stable environment for the formation of hydrates, thus exhibiting hydrate formation at this stage in the form of particle contact. When the hydrate saturation gradually increases, about 60-70%, the pore space is relatively small, and the hydrate gradually forms in the pore-filling mode. As hydrate continues to be generated, once the pore space has produced a large amount of hydrate, the hydrate generation pattern gradually develops toward the contact mode. In the case of

a high methane flux leakage system, where the gas has a large influence on the elastic wave velocity of the hydrate-bearing sediments, the gas factor needs to be taken into account in the theoretical calculation. It is necessary to adjust the equivalent theoretical model to consider the influence of gas. The effective medium theory (EMT), which considers the gas factor, can not only estimate the hydrate saturation, but also help to predict the micro-distribution pattern of hydrate.

**4.3. Hydrate Morphology in Methane Flux Mode.** In the methane flux mode, the gas flow rate is set and the gas flows through the system at a set flow rate throughout the reactor. From the results of the previous investigation, it can be seen that the field methane flux is quite different from the methane flux used in experimental conditions. Laboratory conditions represent a high methane leakage system. Under such conditions, larger gas and fluid fluxes will make it more difficult for hydrates to be stably generated in pore fluids. The obtained experimental data and theoretical model calculation results show that hydrate is mainly formed along grain contacts at 10-60% saturation. And, the results are similar to mode EMT-A at 60-70% hydrate saturation. After 80% or more hydrate saturation, the calculated values are close to mode EMT-B.

Therefore, it is inferred that in the high methane flux leakage system, hydrates are first mainly formed by the grain contact mode (Figure 10), and then hydrates formed in the pore-filling mode. As the hydrate saturation increases, the hydrates in the fluid contact the sediment particles and the hydrates formed in the grain contact mode.

In the methane flux mode, high methane fluxes will form more hydrates around the gas bubbles. When the hydrate saturation is 10-60%, under the same hydrate saturation conditions, the higher the methane flux, the higher the shear modulus, and the greater the hydrate contribution to the sediment skeleton. (Figure 11). From the results calculated by the BGTL theoretical model, it can also be seen that the change of the parameter  $n$  can suitably reflect the changes in hydrate deposits. The parameter  $n$  is mainly related to the partial pressure and the consolidation degree of the sample. The smaller the value of  $n$ , the better the consolidation of the sample. It is clear that the larger the methane flux, the smaller the value of  $n$ , which indicates that the hydrate lends greater support to the sediment frame strength.

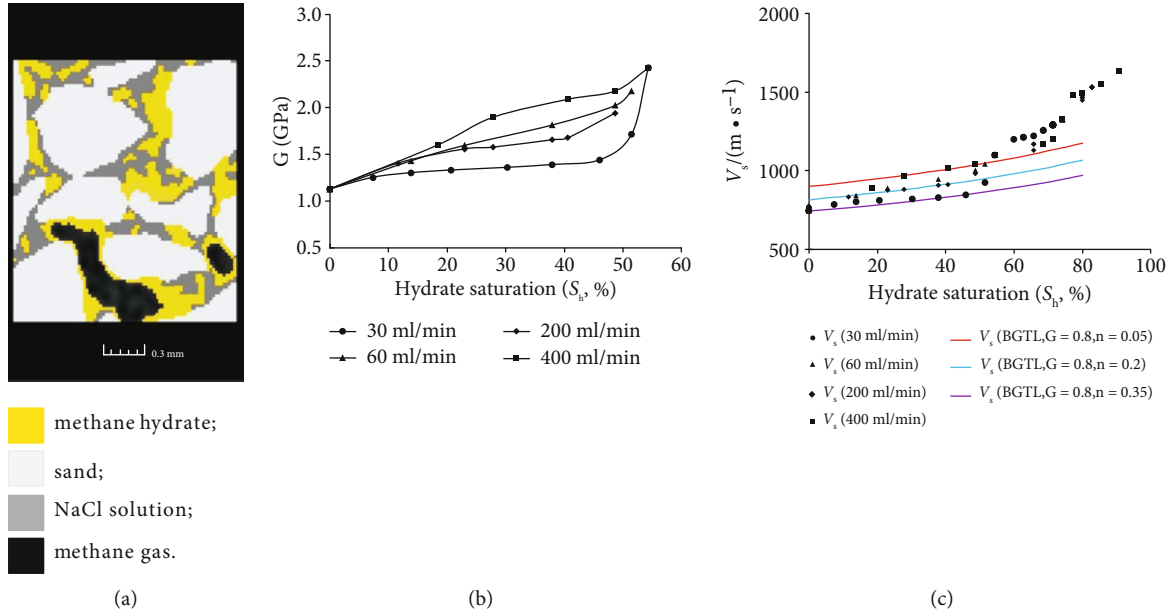


FIGURE 11: Hydrate distribution with changes in shear modulus and shear wave velocity. (a) Pore scale distribution of gas hydrates in sediments by X-CT (modified from [19]), (b) Variation in shear modulus with hydrate saturation in different methane flux, (c) Variation in S-wave velocities with hydrate saturation and analysis of the value of BGTL theory (Data for Figure 11 are in Table S10 in the Supplementary Materials).

## 5. Conclusions

The hydrate simulation experiments were conducted in different methane flux supply modes. The temperature, pressure, saturation, and wave velocities of the hydrate-bearing sediments were measured and the methane flux at the inlet side was controlled. The experimental data were analyzed and the model was verified. The main findings are:

- (1) Smaller methane flux supplies result in less time required to generate the maximum hydrate, and the higher the methane flux, the more time is required to reach the maximum hydrate saturation. The hydrate formation rates are similar at different methane supply fluxes. The hydrate saturation reached 71.4% at a gas flow rate of 30 ml/min, and hydrate saturation reached 90.9% at an inlet flow rate of 400 ml/min. The larger the methane flux, the easier it is to form a high-saturation hydrate
- (2) Model relationship between hydrate saturation and acoustic velocity in different methane flux models was established from the obtained experimental data. When hydrate first formed, the velocity increased slowly with hydrate saturation, while velocity increased quickly as the saturation reached 50–60%. The results are verified using different petrophysical equations, effective medium theory, and the BGTL theoretical model. The results show that the BGTL theory has good adaptability to the experimental results and can provide suggestions for the selection of model parameters. The effective medium theory is modified and adjusted, and the effective

medium theory is used in gas-bearing conditions. The experimental values are more consistent with the theoretical results of EMT-B (homogenous gas distribution) at 10–60% hydrate saturation, and can provide some guidance regarding the morphology of the hydrate

- (3) The hydrate morphology during this experiment was investigated. In the methane flux supply mode, the hydrate was mainly produced by particle contact mode in the gas flow supply mode, and hydrate mainly formed in grain contact mode when the hydrate saturation was 10–60%. As the hydrate saturation reached 60–70%, hydrate formed in the pore-filling mode, then the hydrate in the fluid gets contact with sediments, and finally the hydrate form at the grain contact. In the methane flux mode, the higher the methane flux, the higher the shear modulus, and the greater the hydrate contribution to the sediment skeleton

## Data Availability

The data used in the article are in the supplementary materials. Data are available on request.

## Conflicts of Interest

The authors declare that they have no conflicts of interest.

## Acknowledgments

This research was supported financially by the National Natural Science Foundation of China (No. 41906067), the

Shandong Provincial Natural Science Foundation (No. ZR2019BD051), the Shandong Special Fund of Pilot National Laboratory for Marine Science and Technology (Qingdao) (No.2021QNLM020002), the China Postdoctoral Science Foundation (Grant No. 2018 M632634), the Shandong Province Postdoctoral Innovation Project (201902050), and also by the Marine Geological Survey Program (DD20221704).

## Supplementary Materials

The Supplementary Materials contain text S1 and S2, Figure S1–S5, Table S1, S2 and S3. Text S1 and S2 introduce the measuring method of the acoustic data and hydrate saturation, separately. Figure S1–S3 exhibit the Calibration of the ultrasonic transducers. Figure S4 exhibits the Calibration of the TDR probes. Figure S5 exhibits the inner of the apparatus, especially for the microporous sintered plate. Table S1, S2 and S3 are the detail data of the calibration. And also the supporting information contains Table S4, S5, S6, S7, S8, S9 and S10. They are the detailed data of Figures 2, 3, 4–9, 11. (*Supplementary Materials*)

## References

- [1] Z. R. Chong, S. H. B. Yang, P. Babu, P. Linga, and X.-S. Li, “Review of natural gas hydrates as an energy resource: prospects and challenges,” *Applied Energy*, vol. 162, pp. 1633–1652, 2016.
- [2] Y. Li, C. He, N. Wu et al., “Laboratory Study on Hydrate Production Using a Slow, Multistage Depressurization Strategy,” *Geofluids*, vol. 2021, Article ID 4352910, 13 pages, 2021.
- [3] Y. Li, L. Liu, Y. Jin, and N. Wu, “Characterization and development of marine natural gas hydrate reservoirs in clayey-silt sediments: a review and discussion,” *Advances in Geo-Energy Research*, vol. 5, no. 1, pp. 75–86, 2021.
- [4] G. Hu, Y. Ye, J. Zhang, C. Liu, and Q. Li, “Acoustic response of gas hydrate formation in sediments from South China Sea,” *Marine & Petroleum Geology*, vol. 52, no. 2, pp. 1–8, 2014.
- [5] Q. Bu, G. Hu, C. Liu, T. Xing, C. Li, and Q. Meng, “Acoustic characteristics and micro-distribution prediction during hydrate dissociation in sediments from the South China Sea,” *Journal of Natural Gas Science and Engineering*, vol. 65, pp. 135–144, 2019.
- [6] J. Cai, W. Wei, X. Hu, and D. A. Wood, “Electrical conductivity models in saturated porous media: A review,” *Earth-Science Reviews*, vol. 171, pp. 419–433, 2017.
- [7] J. Cai, Z. Zhang, W. Wei, D. Guo, S. Li, and P. Zhao, “The critical factors for permeability-formation factor relation in reservoir rocks: Pore-throat ratio, tortuosity and connectivity,” *Energy*, vol. 188, p. 116051, 2019.
- [8] L. Liu, N. Wu, C. Liu et al., “Maximum Sizes of Fluid-Occupied Pores within Hydrate-Bearing Porous Media Composed of Different Host Particles,” *Geofluids*, vol. 2020, Article ID 8880286, 14 pages, 2020.
- [9] L. Liu, Z. Zhang, C. Li et al., “Hydrate growth in quartzitic sands and implication of pore fractal characteristics to hydraulic, mechanical, and electrical properties of hydrate-bearing sediments,” *Journal of Natural Gas Science and Engineering*, vol. 75, p. 103109, 2020.
- [10] N. Mahabadi, X. Zheng, T. S. Yun, L. Van Paassen, and J. Jang, “Gas bubble migration and trapping in porous media: Pore-scale simulation,” *Journal of Geophysical Research: Solid Earth*, vol. 123, no. 2, pp. 1060–1071, 2018.
- [11] K. E. Thatcher, G. K. Westbrook, S. Sarkar, and T. A. Minshull, “Methane release from warming-induced hydrate dissociation in the west svalbard continental margin: timing, rates, and geological controls,” *Journal of Geophysical Research: Solid Earth*, vol. 118, no. 1, pp. 22–38, 2013.
- [12] P. Wang, S. Wang, Y. Song, and M. Yang, “Methane Hydrate Formation and Decomposition Properties During Gas Migration in Porous Medium,” *Energy Procedia*, vol. 105, pp. 4668–4673, 2017.
- [13] J. A. Priest, A. I. Best, and C. R. I. Clayton, “A laboratory investigation into the seismic velocities of methane gas hydrate-bearing sand,” *Journal of Geophysical Research: Solid Earth*, vol. 110, no. B4, 2005.
- [14] J. A. Priest, E. V. L. Rees, and C. R. I. Clayton, “Influence of gas hydrate morphology on the seismic velocities of sands,” *Journal of Geophysical Research: Solid Earth*, vol. 114, no. 11, 2009.
- [15] W. J. Winters, W. F. Waite, D. H. Mason, L. Y. Gilbert, and I. A. Pecher, “Methane gas hydrate effect on sediment acoustic and strength properties,” *Journal of Petroleum Science & Engineering*, vol. 56, no. 1-3, pp. 127–135, 2007.
- [16] G. Hu, *Experimental Study on Acoustic Response of Gas Hydrates to Sediments from South China Sea [Ph. D. Thesis]*, Faculty of Earth Sciences, China University of Geosciences, Wuhan, China, 2010.
- [17] G. Hu, Y. Ye, J. Zhang, C. Liu, S. Diao, and J. Wang, “Acoustic properties of gas hydrate-bearing consolidated sediments and experimental testing of elastic velocity models,” *Journal of Geophysical Research: Solid Earth*, vol. 115, no. B2, 2010.
- [18] G. Hu, Y. Ye, J. Zhang, S. Diao, and C. Liu, “Acoustic properties of hydrate-bearing unconsolidated sediments measured by the bender element technique,” *Chinese Journal of Geophysics*, vol. 55, no. 6, pp. 635–647, 2012.
- [19] G. Hu, C. Li, Y. Ye, C. Liu, J. Zhang, and S. Diao, “Observation of gas hydrate distribution in sediment pore space,” *Chinese Journal of Geophysics*, vol. 57, no. 5, pp. 1675–1682, 2014.
- [20] A. Andhumoudine, X. Nie, Q. Zhou et al., “Investigation of coal elastic properties based on digital core technology and finite element method,” *Advances in Geo-Energy Research*, vol. 5, no. 1, pp. 53–63, 2021.
- [21] Q. Gao, J. Zhao, Z. Yin, D. Yang, and C. Zhang, “Experimental study on methane hydrate formation in quartz sand under triaxial condition,” *Journal of Natural Gas Science and Engineering*, vol. 85, p. 103707, 2020.
- [22] Q. Gao, J. Zhao, Z. Yin, D. Yang, and C. Zhang, “Experimental study on fluid production from methane hydrate sediments under the marine triaxial condition,” *Energy & Fuels*, vol. 35, no. 5, pp. 3915–3924, 2021.
- [23] Q. Gao, Z. Yin, J. Zhao, D. Yang, and P. Linga, “Tuning the fluid production behaviour of hydrate-bearing sediments by multi-stage depressurization,” *Chemical Engineering Journal*, vol. 406, p. 127174, 2020.
- [24] M. Eaton, D. Mahajan, and R. Flood, “A novel high-pressure apparatus to study hydrate-sediment interactions,” *Journal of Petroleum Science & Engineering*, vol. 56, no. 1-3, pp. 101–107, 2007.

- [25] T. Kwon and G. Cho, "Evolution of compressional wave velocity during CO<sub>2</sub>Hydrate formation in sediments," *Energy & Fuels*, vol. 23, no. 11, pp. 5731–5736, 2009.
- [26] B. Liu, H. Pan, X. Wang, F. Li, C. Sun, and G. Chen, "Evaluation of different CH<sub>4</sub>-CO<sub>2</sub> replacement processes in hydrate-bearing sediments by measuring p-wave velocity," *Energies*, vol. 6, no. 12, pp. 6242–6254, 2013.
- [27] J. Guan, D. Li, H. Zhou, D. Liang, and L. Wan, "A experimental system simulate formation and dissociation of the leak gas hydrate," *Nature Gas Industry*, vol. 32, no. 5, pp. 1–4, 2012.
- [28] Q. Bu, G. Hu, Y. Ye et al., "The elastic wave velocity response of methane gas hydrate formation in vertical gas migration systems," *Journal of Geophysics and Engineering*, vol. 14, no. 3, pp. 555–569, 2017.
- [29] Q. Bu, G. Hu, C. Liu et al., "Effect of methane gas on acoustic characteristics of hydrate-bearing sediment-model analysis and experimental verification," *Journal of Ocean University of China*, vol. 20, no. 1, pp. 75–86, 2021.
- [30] C. Liu, Y. Ye, S. Sun, Q. Chen, Q. Meng, and G. Hu, "Experimental studies on the P-T stability conditions and influencing factors of gas hydrate in different systems," *Science China Earth Sciences*, vol. 56, no. 4, pp. 594–600, 2013.
- [31] J. Wright, F. Nixon, S. Dallimore, and O. Matsubayashi, *A method for direct measurement of gas hydrate amounts based on the bulk dielectric properties of laboratory test media paper presented at 4th International Conference on Gas Hydrates*, Tokyo Institute of Technology, Yokohama, Japan, 2002.
- [32] C. Li, G. Hu, W. Zhang et al., "Influence of foraminifera on formation and occurrence characteristics of natural gas hydrates in fine-grained sediments from Shenhu area, South China Sea," *Science China Earth Sciences*, vol. 59, no. 11, pp. 2223–2230, 2016.
- [33] C. Li, C. Liu, G. Hu et al., "Investigation on the multiparameter of hydrate-bearing sands using nano-focus X-ray computed tomography," *Journal of Geophysical Research: Solid Earth*, vol. 124, no. 3, pp. 2286–2296, 2019.
- [34] J. Dvorkin, M. Prasad, A. Sakai, and D. Lavoie, "Elasticity of marine sediments: rock physics modeling," *Geophysical Research Letters*, vol. 26, no. 12, pp. 1781–1784, 1999.
- [35] M. B. Helgerud, J. Dvorkin, A. Nur, A. Sakai, and T. Collett, "Elastic-wave velocity in marine sediments with gas hydrates: effective medium modeling," *Geophysical Research Letters*, vol. 26, no. 13, pp. 2021–2024, 1999.
- [36] T. Ahrens, *Mineral Physics & Crystallography: a handbook of physical constants*, Published by American Geophysical union, 1995.
- [37] J. Cai, Y. Xia, S. Xu, and H. Tian, "Advances in multiphase seepage characteristics of natural gas hydrate sediments," *Chinese Journal of Theoretical and Applied Mechanics*, vol. 52, no. 1, pp. 208–223, 2019.
- [38] J. Cai, Y. Xia, C. Lu, H. Bian, and S. Zou, "Creeping microstructure and fractal permeability model of natural gas hydrate reservoir," *Marine and Petroleum Geology*, vol. 115, p. 104282, 2020.
- [39] E. Spangenberg, M. Priegnitz, K. Heeschen, and J. M. Schicks, "Are laboratory-formed hydrate-bearing systems analogous to those in nature?," *Journal of Chemical & Engineering Data*, vol. 60, no. 2, pp. 258–268, 2015.

## Research Article

# Quantitative Evaluation of Well Performance Affected by Fracture Density and Fracture Connectivity in Fractured Tight Reservoirs

Wenchao Fang<sup>1</sup>,<sup>ORCID</sup> Xuejie Qin,<sup>1</sup> Chuanxi Liu,<sup>1</sup> Ruyue Wang<sup>1</sup>,<sup>ORCID</sup> Jun Pu,<sup>1</sup> Hanqiao Jiang,<sup>2</sup> and Weiling He<sup>1</sup>

<sup>1</sup>SINOPEC Petroleum Exploration and Production Research Institute, Beijing 100083, China

<sup>2</sup>Department of Petroleum Engineering, China University of Petroleum (Beijing), Beijing 102249, China

Correspondence should be addressed to Wenchao Fang; [wenchaoxf2011@outlook.com](mailto:wenchaoxf2011@outlook.com) and Ruyue Wang; [wry1990@vip.qq.com](mailto:wry1990@vip.qq.com)

Received 24 August 2021; Revised 21 February 2022; Accepted 4 March 2022; Published 5 April 2022

Academic Editor: Bailu Teng

Copyright © 2022 Wenchao Fang et al. This is an open access article distributed under the Creative Commons Attribution License, which permits unrestricted use, distribution, and reproduction in any medium, provided the original work is properly cited.

Understanding the relationship between petroleum recovery and characteristics of hydraulic fracture network is a key component of economic development of tight reservoirs. Owing to the limitations inherent in current reservoir simulators, optimization of fracture network has been simply focused on the parameters of fracture conductivity, fracture number, aperture, and so on. Deeper insight into the effect of decisive parameters, such as fracture density and fracture connectivity on the well production in tight reservoirs, is now required to maximize the petroleum recovery. In this work, a newly developed discrete fracture simulator is applied to comprehensively study the effect of fracture density and fracture connectivity in tight reservoirs. Conceptual models with different fracture densities and different fracture connectivity are firstly designed and simulated to explore how these two parameters affect the reservoir behavior and establish the equations for effect measurement. Then, we simulate models with different well placement strategies and a fixed set of natural fractures to determine the optimal strategy. Finally, simulations are performed on a field-scale reservoir with three long fractured horizontal wells. Results demonstrate that increases in either fracture density or fracture connectivity can significantly improve well production. However, an optimal value exists considering the economic profit. Compared to the fracture density, fracture connectivity plays a more important role in affecting the well production. In a tight reservoir with abundant natural fractures, making the horizontal well parallel to the direction of natural fractures is determined to be the optimal well placement strategy. The heterogeneous distribution of remaining oil in real tight oil reservoirs is mainly caused by the heterogeneous distribution of fracture density and fracture connectivity.

## 1. Introduction

Nowadays, tight reservoir provides a significant fraction of petroleum production around the world [1–3]. Extraction of fluids from tight reservoirs mainly relies on the large-scale hydraulic fracturing which creates complex fracture network in the reservoir. This fracture network provides significant conduits for fluids to flow at economic rates while bringing great challenges to the reservoir simulation [4, 5]. Since reservoir simulation is an important tool of optimizing stimulation design, completion practice, and development

strategy, determination of the simulation-based solution for optimal development of tight reservoir also faces a great challenge. Fracture network optimization is the primary issue of improving recovery of tight reservoir. Understanding the relationship between fracture network parameters and petroleum recovery will greatly benefit the economic development of tight reservoir [6]. Long and Witherspoon were among the first to investigate the significant effect of fracture network parameter on reservoir performance [7]. In their study, through utilizing a numerical code [8] developed to determine permeability of a fractured system, they



demonstrated that as degree of fracture interconnection increases, the permeability of the fractured system increases. In current commercial reservoir simulators, a dual-continuum model, known as the sugar-cube model, is widely used to perform optimization for fractured reservoir. In this model, the fractured rock is generally idealized as an equivalent continuum medium through assuming that the matrix is partitioned by an orthogonal fracture network [9–11]. Except for the recognized shortcomings that are inherent in a dual-continuum model, namely, inadequacy of modeling reservoir with a limited number of flow-dominant fractures [4, 12] and having difficulty in correctly evaluating the exchange terms between the matrix and the fractures [13, 14], the dual-continuum model also cannot be used to optimize some specific fracture parameters, such as fracture density and fracture connectivity because of the fixed configuration of fracture network in the models. Hence, in the past decades, optimization of the fracture network was limited to simple parameters such as fracture conductivity, fracture number and fracture aperture. In 2006, Mayerhofer et al. performed a parametric study using a commercial simulator to show how fracture network size and density, fracture conductivity, matrix permeability, and gaps in the network affect well productivity [15]. Warpinski et al. conducted similar studies, and simulation results demonstrated that shale reservoir with ultralow permeability requires an interconnected fracture network of moderate conductivity with a relatively small spacing between fractures to obtain reasonable recovery factor [16]. Through performing simulations with CMG-IMEX, the economic optimal fracture conductivity and well number for the cases with and without geomechanics in Bakken tight reservoir were determined by Yu and Sepehrnoori [17]. In the study of Saputelli et al., simulation results obtained by Nexus revealed that an optimal number of fractures should be determined in tight reservoir since increasing number of fractures will not always improve the short-term economics [18]. Optimization of these fracture network parameters is critical because of the high cost of drilling and fracturing treatment. However, deeper insights into the relationships between more fracture network parameters and the reservoir performances are required for the best understanding of the tight reservoir development.

Recently, a discrete fracture model (DFM) in which the fractures are represented explicitly and individually rather than idealized as continuous media was developed. The DFM makes it possible for reservoir engineers to optimize complex fracture parameters. However, development of DFMs is still at its early stage. Currently, there are two typical categories of DFM: embedded discrete fracture model (EDFM) and unstructured discrete fracture model (UDFM). In the EDFM, a conventional structured mesh is used to represent the matrix while the fractures are discretely embedded in the matrix [19, 20]. And in the UDFM, fractures are represented by discretely distributed entities and the matrix is partitioned in an unstructured manner conforming to the geometry of fracture network [13, 21, 22]. The EDFM is currently not efficient enough when handling large-scale complex fracture network owing to the boundary element approach used to evaluate the effective matrix permeability

associated with the small fractures. The evaluation process becomes expensive while the number of fractures increases [23]. The UDFM currently can only simulate incompressible fluid flow problems, which means energy supplement strategy, such as water or gas injection, must be applied in the simulations. However, energy supplement is currently not practical in tight reservoirs since the matrix in these reservoirs is extremely tight and the fractures can bypass oil in the matrix, leading to a very low efficiency of the energy supplement strategy [24]. Oil extraction from the tight reservoirs is currently mainly relied on the natural formation energy and the mechanisms of rock and fluid expansion [25–27]. Hence, rock and fluid compressibility are critical factors that need to be taken account in the simulators developed for tight reservoirs.

Owing to the limitations of current commercial reservoir simulators and DFM, a comprehensive study of the optimizations of fracture density and fracture connectivity in the large-scale complex fractured network based on reservoir simulation has not been reported in the literature so far. In this study, equations characterizing the fracture density and fracture connectivity are firstly established. Then, a newly developed in-house discrete fracture simulator (SC-CFR) which is capable of modeling compressible rock and fluid and handling large-scale complex fracture networks is used to perform reservoir simulations to quantitatively study the effect of fracture density and fracture connectivity on the reservoir behavior [28]. Some novel physical models including conceptual models and large-scale complex fractured models analogous to the real tight reservoirs are designed for the optimizations of fracture density and fracture connectivity. Through analyzing simulation results of these models, we demonstrate the crucial or even decisive effect of fracture density and fracture connectivity on the tight reservoir behavior. Functions for effect measurement are also proposed. Results presented in this work can help reservoir engineers gain an insight into the optimization of fracture network, which will greatly contribute to the improvement of future horizontal well completion and fracturing strategy and the resultant maximization of economic benefit of tight reservoir development.

## 2. Description of the Simulator

The framework of the SC-CFR is shown in Figure 1. The SC-CFR is mainly composed of five independent but interrelated modules. The edge-constrained Delaunay Triangulation scheme in which fractures are represented individually and explicitly with a lower dimension than the matrix is utilized to grid the physical domain [29, 30]. A transmissibility list that includes connections of matrix-matrix, matrix-fracture and fracture-fracture is evaluated by a two-point flux-approximation (TPFA) method [21]. Spatial discretization of the mathematical model is greatly simplified by three discrete operators that are defined to represent the expressions of divergence, gradient, and average as their original forms and, thus, enable rapid prototyping of the numerical model. The nonlinear discretized equation system is solved by modified Newton's method in which the Jacobian matrix

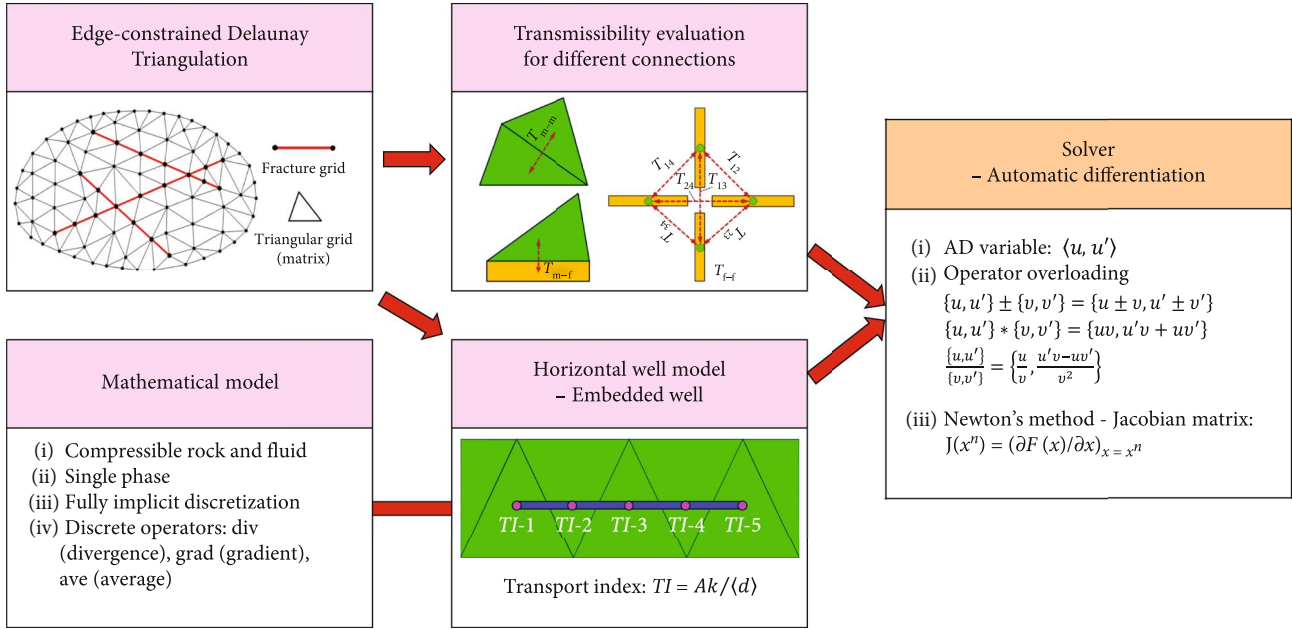


FIGURE 1: Framework and technical details of the SC-CFR.

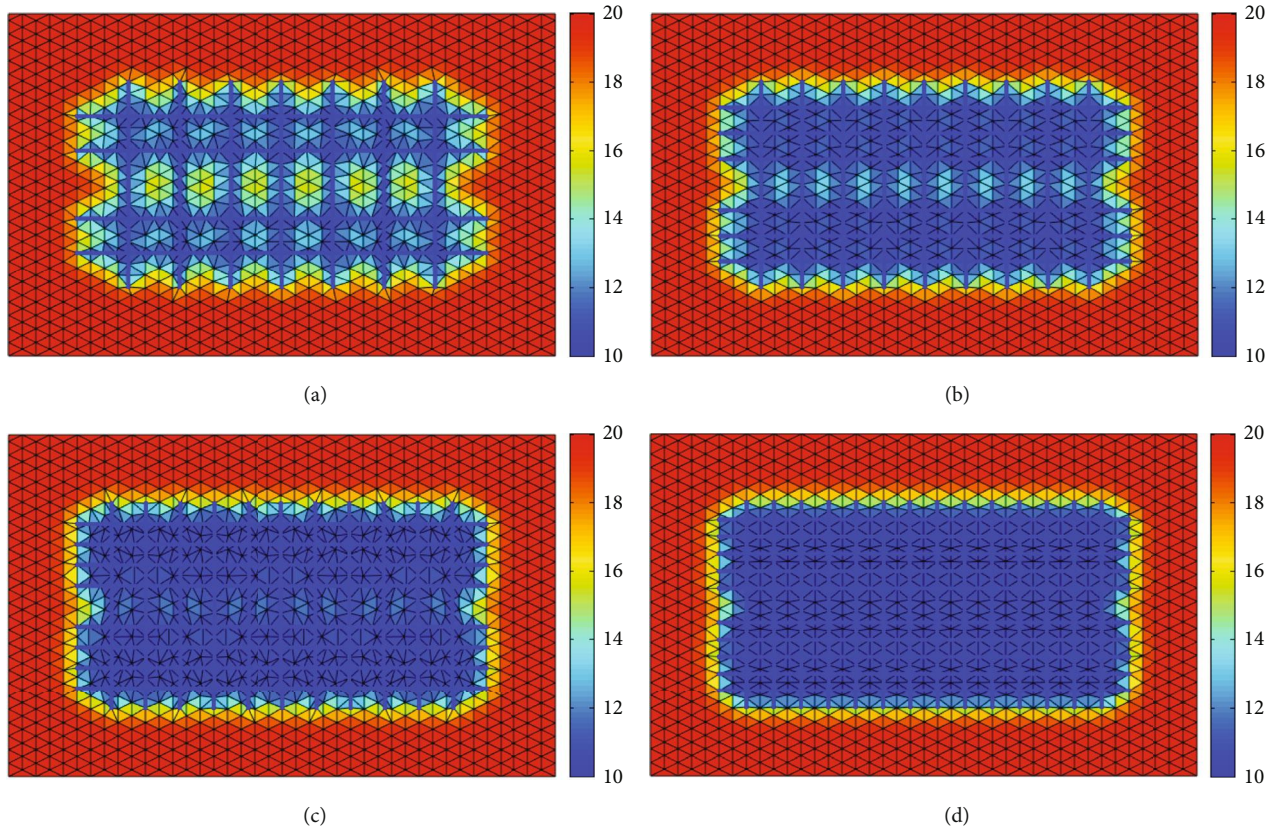


FIGURE 2: Reservoir pressure profiles at  $t = 50$  days: (a)  $FD = 0.05$ ; (b)  $FD = 0.07$ ; (c)  $FD = 0.09$ ; (d)  $FD = 0.11$ .

is computed by the automatic differentiation (AD) technique. Application of the AD can greatly enhance the efficiency and accuracy of simulation models, especially for the models with complex grid systems [31–33].

The concept of embedded well which is inspired by the embedded discrete fracture model is defined in our simulator to establish the well model (Figure 2 in [19]). In this model, a horizontal well is treated as a fracture, which is

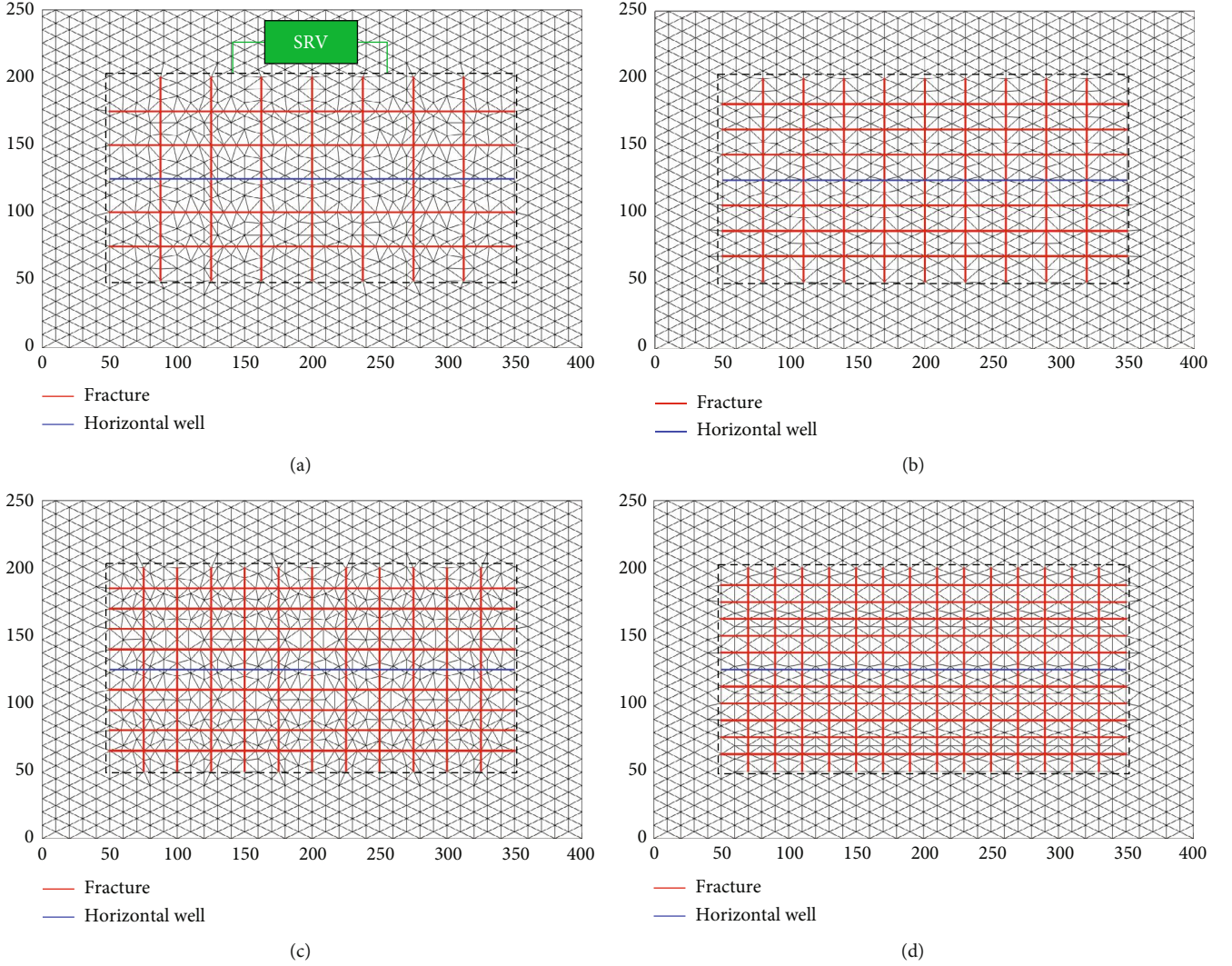


FIGURE 3: Grids with different fracture densities: (a) FD = 0.05; (b) FD = 0.07; (c) FD = 0.09; (d) FD = 0.11.

embedded in the background grid. The flux between grid and the well is determined by the transport index (TI) [19, 20]. The geometry of the well can be very flexible in the embedded well model since the well lines do not need to conform to the grid edges.

### 3. Effect of Fracture Density

As shown in Figure 3, four physical models with different fracture densities of the fracture networks are established. Sizes of the models are 400 m × 250 m. To minimize the influence of fracture connectivity, fracture networks are created in the same pattern; namely, fractures are only distributed either in  $x$ -direction or  $y$ -direction, and fractures in each direction are equally spaced. Sizes of the SRV in the four models are set to be the same. We define the fracture density herein as

$$FD = \frac{SL_f}{A_{SRV}}, \quad (1)$$

TABLE 1: Simulation parameters for the four models with different fracture densities.

Parameter	Value
Initial reservoir pressure (MPa)	20
Matrix permeability (mD)	0.01
Matrix porosity (%)	8
Fracture permeability (mD)	50000
Fracture porosity (%)	60
Fracture aperture (m)	0.0025
Rock compressibility factor (MPa <sup>-1</sup> )	$1 \times 10^{-5}$
Oil compressibility factor (MPa <sup>-1</sup> )	$1 \times 10^{-3}$
Oil viscosity (mPa·s)	5
Reservoir oil density (kg/m <sup>3</sup> )	850
Volume factor	1.13
Well bottom-hole pressure (MPa)	10
Simulation time (days)	200

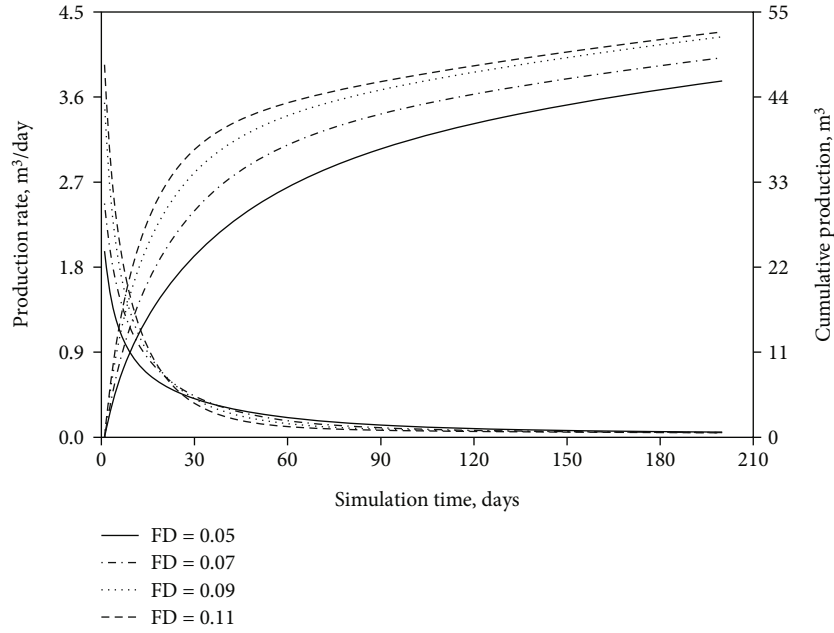


FIGURE 4: Comparison of well performances of the four models with different fracture densities.

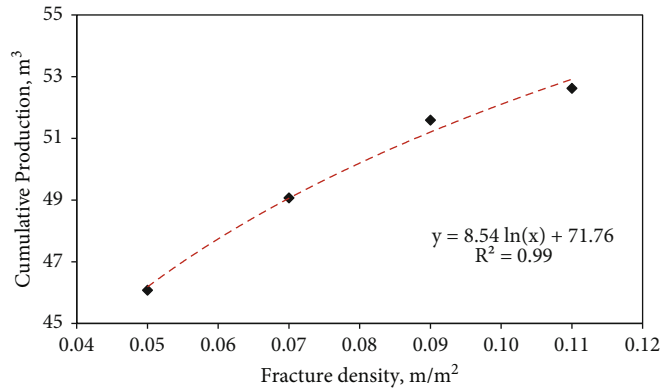


FIGURE 5: Relation equation between fracture density and 200-day cumulative production.

where FD is fracture density of fracture network ( $m/m^2$ );  $SL_f$  is sum of lengths of all fractures in the SRV (m);  $A_{SRV}$  is area of the SRV ( $m^2$ ).

Simulation parameters for the four models are the same and are listed in Table 1. The matrix permeability and matrix porosity are set to be as low as 0.01 mD and 8%, respectively, in order to capture the characteristics of the in tight reservoirs [34].

We simulate the four models by using SC-CFR. Figure 4 shows the comparison result of well performances of the four models. In tight reservoirs, fractures are the main channels for fluids to flow from the reservoirs to the wells. Therefore, it can be observed in Figure 4 that the well productivity increases significantly with the increasing fracture density. Increasing FD from 0.05 to 0.07 leads to 6.5% growth in 200-day cumulative production. However, Figure 4 also depicts that after the fracture density exceeds 0.09, the increase of production become much slighter. Increasing

FD from 0.09 to 0.11 only leads to 1.2% growth in 200-day cumulative production. This is mainly because the reserve in the SRV is limited, and the fluids in the area beyond SRV cannot flow into the SRV owing to the extremely tight matrix (Figure 2). Considering that the fracture network with bigger fracture density requires bigger cost of hydraulic fracturing, the optimization of fracture density is suggested.

In addition, the production rate curves in Figure 4 illustrates that the significant influence of fracture density on the well production only occurs in the early period (<60 days) of reservoir development. After that time, the well production is mainly provided by the matrix in the SRV; hence, the fracture density has little effect on the well production and the well produces in a low rate for a long period.

To validate the interpretations above and directly depict the reservoir behaviors of models with different fracture densities, reservoir pressure profiles at a certain simulation time (50 days) for the four models are obtained and shown

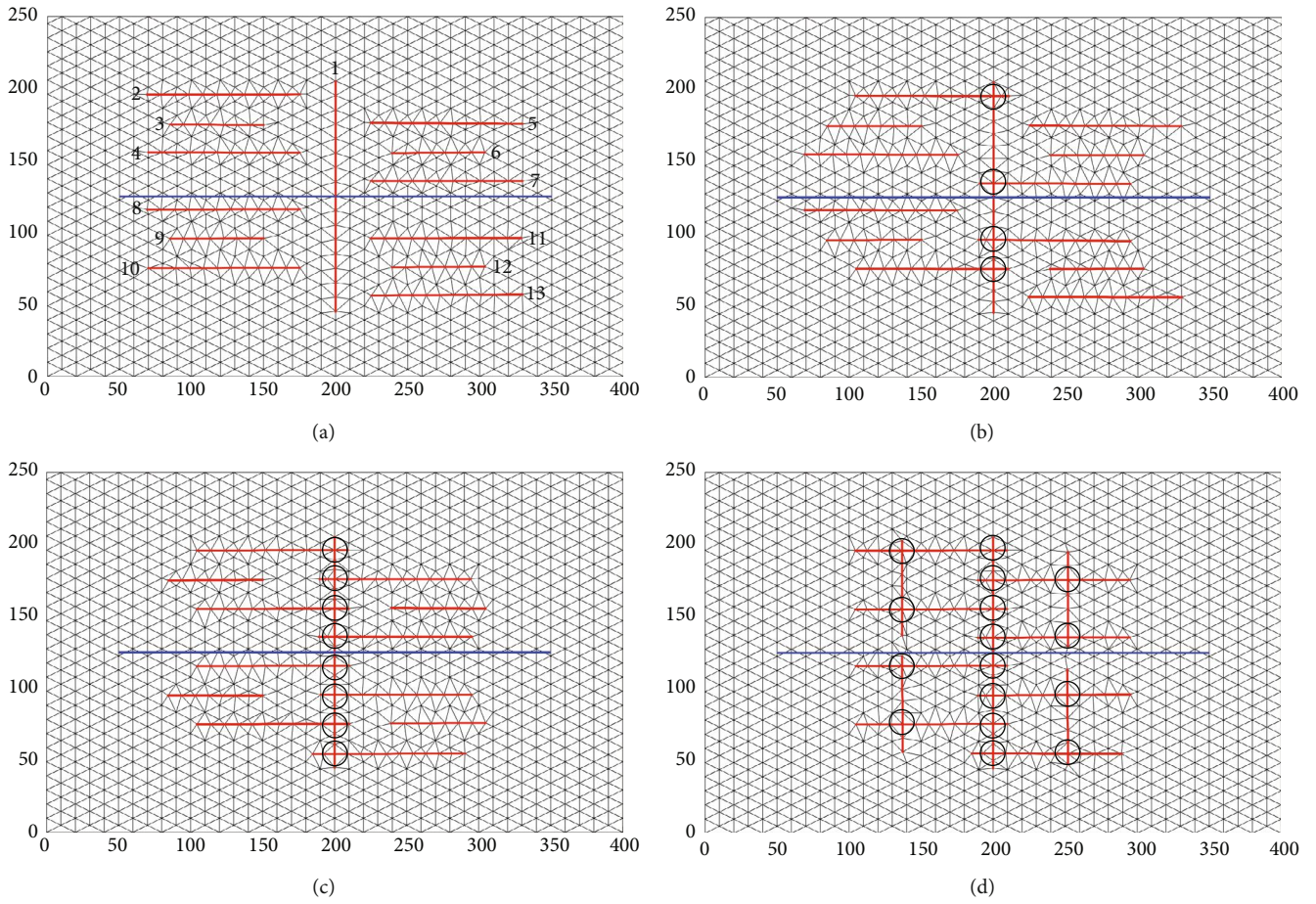


FIGURE 6: Grids with different fracture connectivity: (a) FC = 0; (b) FC = 0.15; (c) FC = 0.31; (d) FC = 0.62.

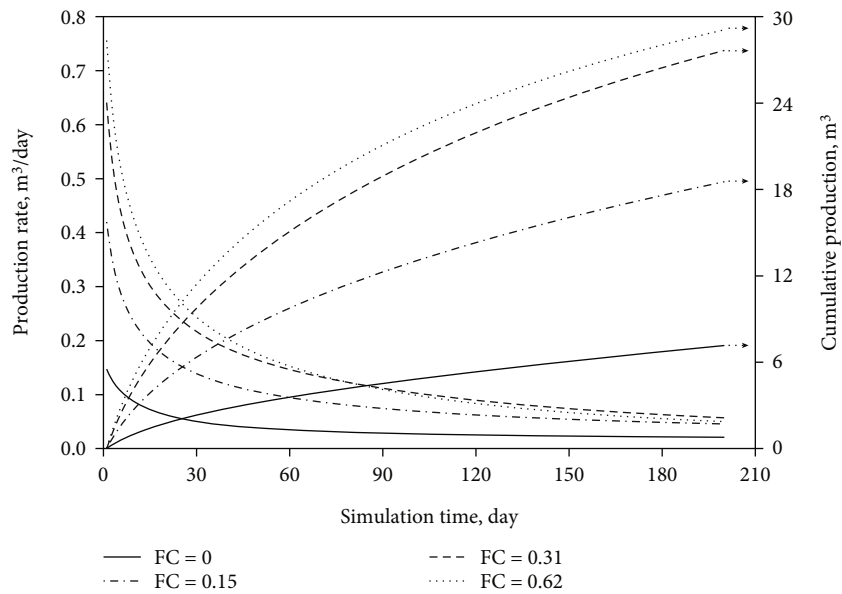


FIGURE 7: Comparison of well performances of the four models with different fracture connectivity.

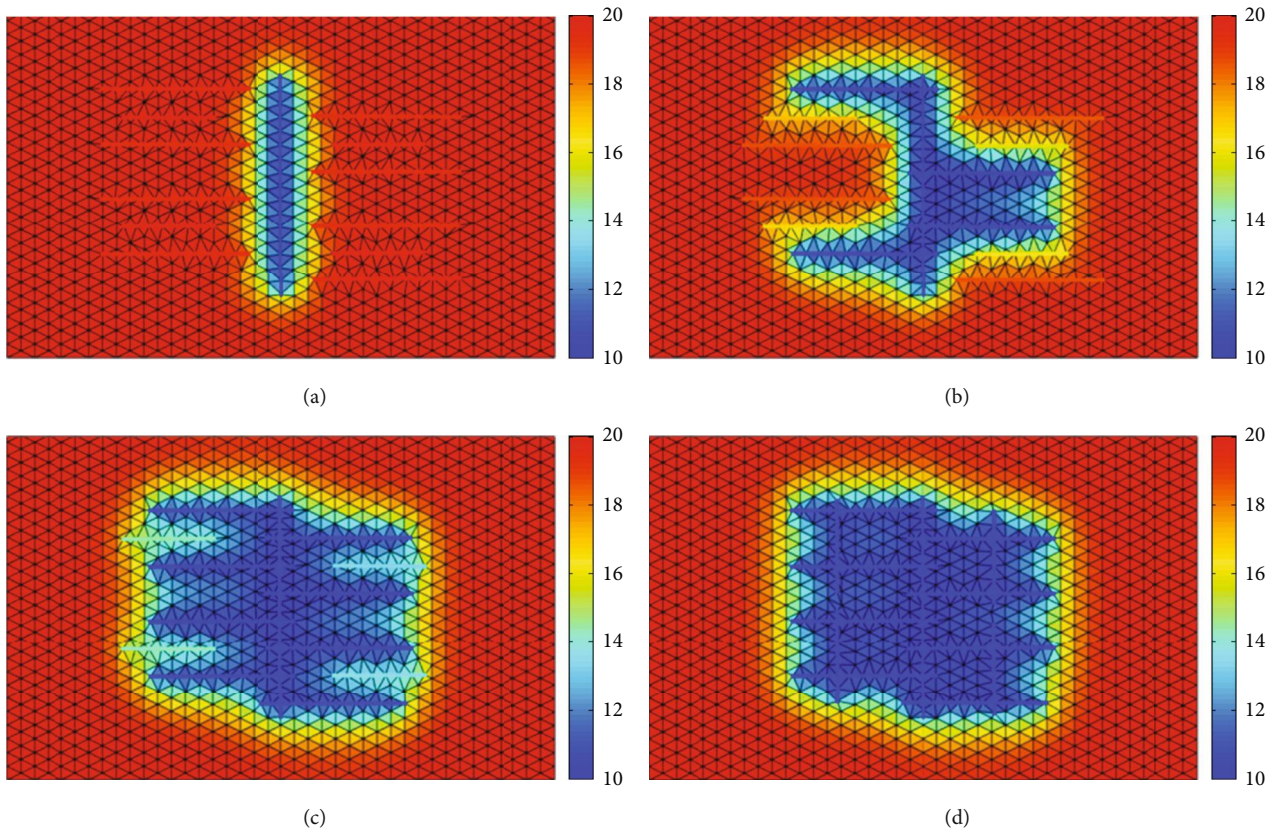


FIGURE 8: Reservoir pressure profiles at  $t = 200$  days: (a)  $FD = 0.05$ ; (b)  $FD = 0.07$ ; (c)  $FD = 0.09$ ; (d)  $FD = 0.11$ .

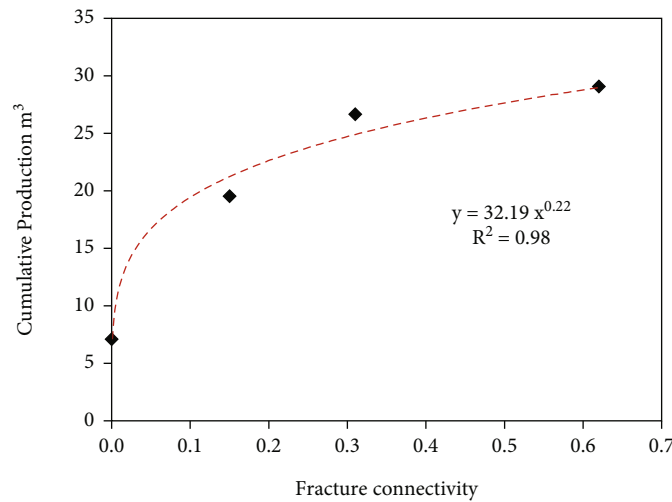


FIGURE 9: Relation equation between fracture connectivity and 200-day cumulative production.

in Figure 2. As can be seen, in cases of  $FD = 0.05$ ,  $0.07$ , and  $0.09$ , the extent of pressure drawdown in the SRV increases dramatically with the increasing fracture density. However, the pressure in the SRV of  $FD = 0.09$  is almost already at its lowest value and widest extend, which means increasing fracture density will not make a big difference. Therefore, when  $FD$  increases from  $0.09$  to  $0.11$ , the change in pressure profile is less noticeable. In all the four models, pressures of the areas beyond SRV keep at their initial values.

The relation equation for the effect measurement of fracture density is obtained by curve fitting, as shown in Figure 5. As can be seen, the cumulative production over fracture density shows the law of logarithmic equation:

$$Q = 8.54 \ln (FD) + 71.76, \quad (2)$$

where  $Q$  is cumulative production ( $m^3$ ).

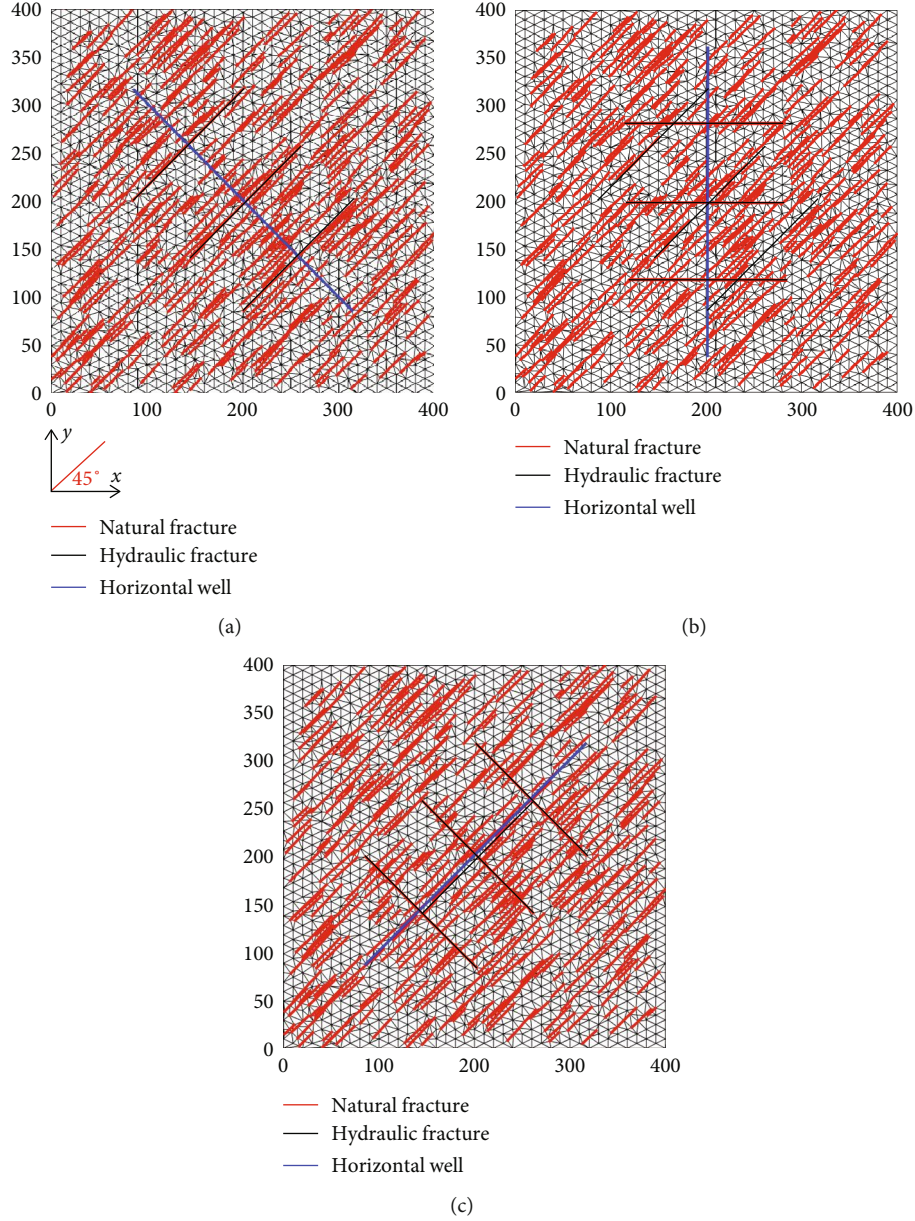


FIGURE 10: Densely fractured models with different strategies of well placement: (a)  $\theta = 90^\circ$ ; (b)  $\theta = 45^\circ$ ; (c)  $\theta = 0^\circ$ .

#### 4. Effect of Fracture Connectivity

In this section, we first investigate how the fracture connectivity impacts the reservoir behavior through simulating four conceptual models. Then, we take the well placement optimization as an example to show the important role that fracture connectivity plays in field development. The fracture connectivity is defined as

$$FC = \frac{N_{\text{inter}}}{N_{\text{end}}}, \quad (3)$$

where  $N_{\text{inter}}$  is number of nodes at fracture intersections and  $N_{\text{end}}$  is the number of fracture endpoints.

*4.1. Conceptual Models.* The four physical models for simulation of fracture connectivity are shown in Figure 6. Each model contains 13 fractures, and fracture No. 1 (F1) can be treated as a dominant fracture which is created by hydraulic fracturing of the well, and other fractures can be treated as nature fractures. From model (a) to model (d), more and more natural fractures intersect with F1. And in model (d), some nature fractures intersect with each other. Simulation parameters herein are the same with parameters listed in Table 1.

The obtained well productions of the four models are compared in Figure 7, from which we can observe that the bigger the fracture connectivity, the higher the well production (158.9% and 49.2% increase in 200-day cumulative production when increasing FC from 0 to 0.15 and from 0.15 to

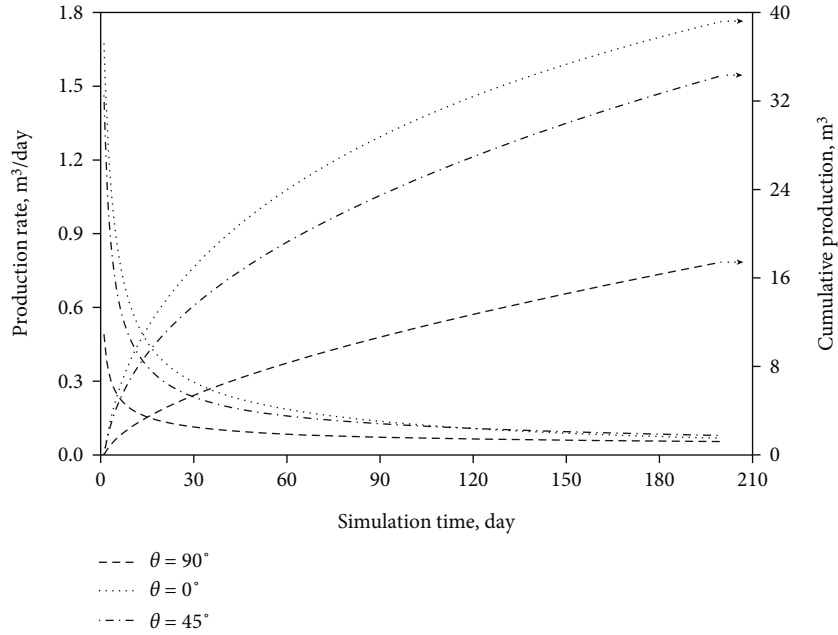


FIGURE 11: Comparison of well performances of the three models with different well placement strategies.

0.31, respectively). However, when increasing FC from 0.31 to 0.62, the increase in cumulative production (5.1%) significantly decreases. This is also because of the limited reserves in the SRV.

Through comparing Figure 4 with Figure 7, we can find that the fracture connectivity plays a more important role in impacting the well production than the fracture density does. Even though the fracture densities in model (a) and model (d) are almost the same, well production dramatically differs from each other because of the different fracture connectivities.

Figure 8 shows the reservoir pressure profiles of the four models obtained at the last step of the simulation. The regions of pressure drawdown in these profiles differ dramatically from each other although sizes of SRV and numbers of fracture in SRV are almost the same. In model (a), none of the natural fractures contributes to improving the well production since they disconnect with F1. We characterize the fracture that has no interconnections with other fractures as dead fracture (DF) in this study. As can be seen from Figure 8, with the decreasing number of DFs, the region of pressure drawdown becomes larger and larger; namely, more and more fluid is produced from the SRV.

It can be concluded from the interpretations above that the fracture connectivity almost plays a decisive role in the development of fractured tight reservoirs. Hence, in real reservoir development, optimization of fracture connectivity in the SRV should be paid much attention to.

The relation equation for the effect measurement of fracture connectivity is obtained by curve fitting, as shown in Figure 9. As can be seen, the cumulative production over fracture connectivity shows the law of power equation:

$$Q = 32.19 * FC^{0.22}. \quad (4)$$

*4.2. Well Placement Optimization considering Fracture Connectivity.* In real reservoirs, natural fractures are pre-existing fractures, which means their orientations cannot be adjusted as what we did in Figure 6. Hence, the optimization of fracture connectivity should be focused on optimizing parameters of hydraulic fractures and well placement. In this section, we consider the hydraulic fractures as multistage fractures that are perpendicular to the horizontal well, and numbers and lengths of the hydraulic fractures are considered constants. Under these assumptions, optimization of the well placement becomes our main focus.

To capture the densely distributed natural fractures in tight reservoirs, three physical models with the same set of nature fracture which is composed of 400 fractures (randomly distributed at different positions) are established. Typically, in the real reservoirs, fractures of a same fracture set propagate in the same direction owing to the fixed directions of principal stresses [35, 36]. Therefore, all natural fractures in our models are placed at a 45-degree angle from the  $x$ -direction. The three physical models are shown in Figure 10. Horizontal wells in the models are placed at different directions. Suppose the angle between the horizontal well and the natural fractures is  $\theta$ , then in models (a), (b), and (c),  $\theta = 90^\circ$ ,  $45^\circ$ , and  $0^\circ$ , respectively. Simulation parameters are also the same with the parameters listed in Table 1.

Well performances of the three models differ significantly from each other, which can be observed in Figure 11. With the decreasing  $\theta$ , well production increases dramatically. The reason can be interpreted by Figure 10, in which the natural fracture network is simplified as equally spaced lines. As can be seen, in scenario (a), none of the natural fractures intersect with the hydraulic fracture; hence, fluid can be only produced from a very small region around the hydraulic fracture, resulting in a low production. In scenario (b), each hydraulic fracture intersects with three



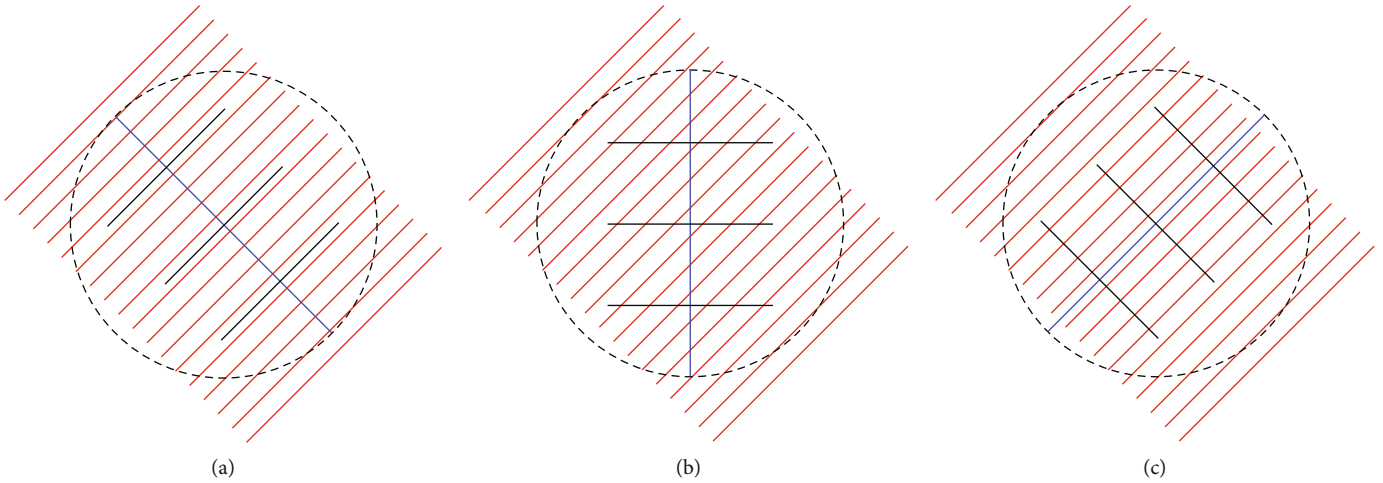


FIGURE 12: Simplified models considering different well placement strategies: (a)  $FC = 0$ ; (b)  $FC = 0.5$ ; (c)  $FC = 0.67$ .

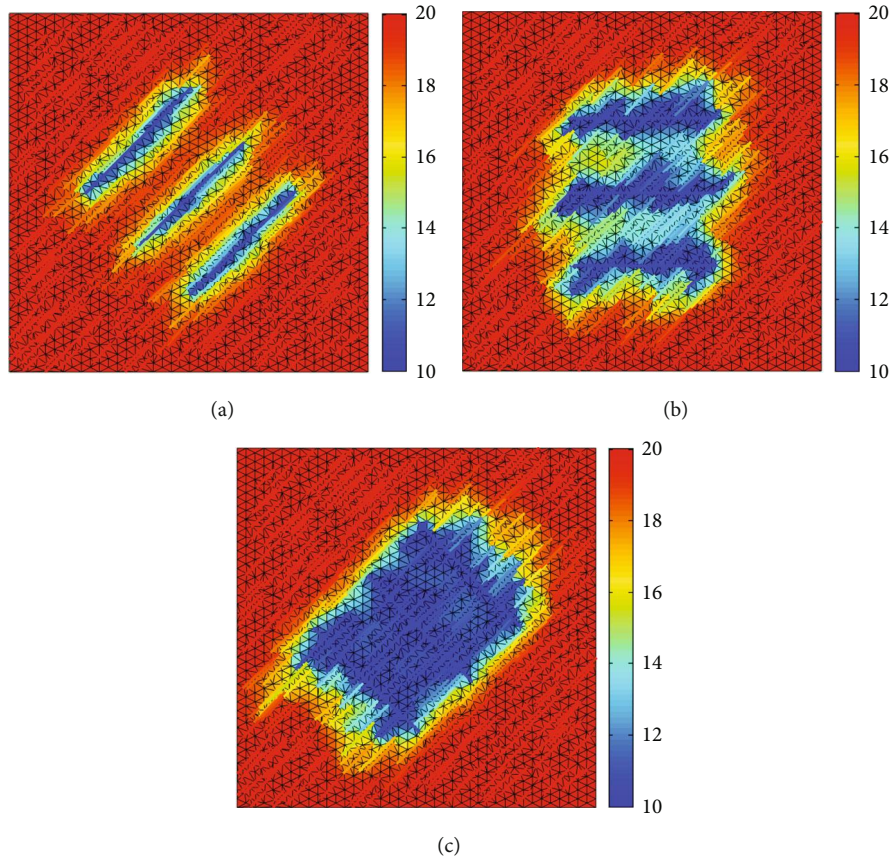


FIGURE 13: Reservoir pressure profiles at  $t = 200$  days: (a)  $\theta = 90^\circ$ ; (b)  $\theta = 45^\circ$ ; (c)  $\theta = 0^\circ$ .

natural fractures, resulting in a much higher well production. And in scenario (c), each hydraulic fracture intersects with four natural fractures, resulting in the highest production. The FC values obtained by Equation (2) are 0, 0.5, and 0.67 for scenarios (a), (b), and (c), respectively (Figure 12).

The reservoir pressure profiles of the three models obtained at the last step of simulation are shown in

Figure 13, which fully validates the interpretations above. With the decreasing  $\theta$ , the size of region of pressure draw-down increases significantly, resulting in the increase in well production.

According to the above simulation results and considering that, in Figure 12, no matter what direction the horizontal well is placed, each hydraulic fracture can at most intersect with four natural fractures, we conclude that for

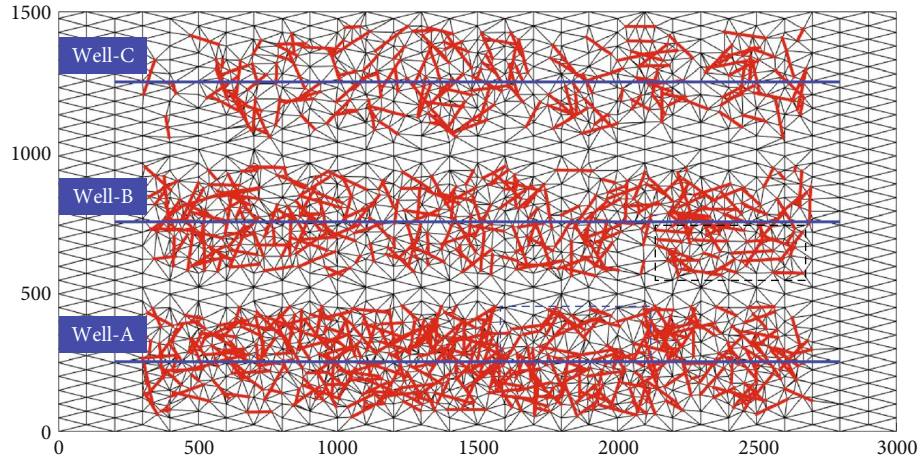


FIGURE 14: A large-scale densely fractured model containing three long horizontal wells.

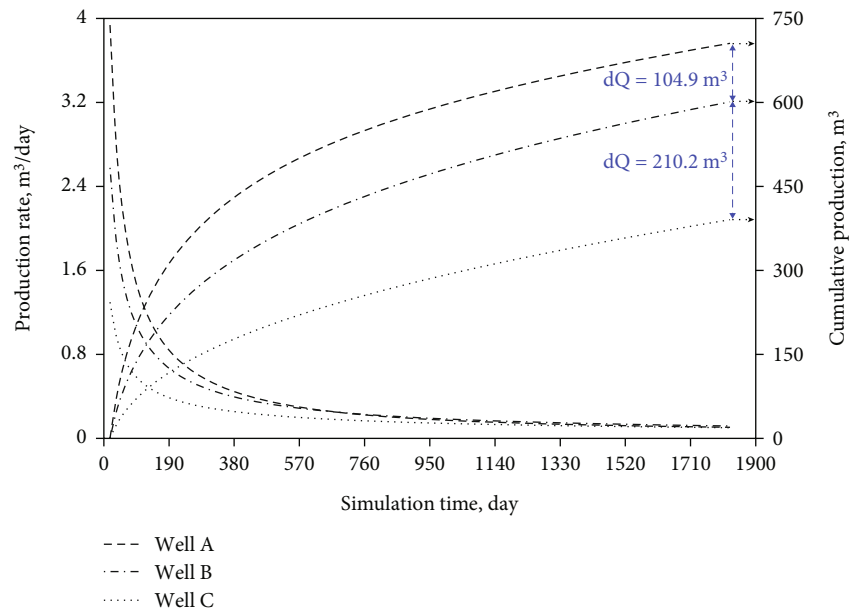


FIGURE 15: Comparison of well performances of the three long horizontal wells.

densely fractured tight reservoirs, the optimal direction of the horizontal well is being parallel to the direction of natural fractures.

### 5. Simulation of Large-Scale Densely Fractured Model

In this section, a field-scale model containing three long horizontal wells is established. Each well is stimulated by large-scale hydraulic fracturing that creates complex fracture network around the well. The fracture densities of the fracture networks are set to be different from each other. Through performing simulation on this model, we aim to illustrate how the fracture density and fracture connectivity significantly impact the development of real tight reservoirs.

Figure 14 shows the grid of our model. The size of the model is 3000 m × 1500 m. The length of each horizontal well

is 2600 m. The number of fractures around Well-A, Well-B, and Well-C is 350, 250, and 150, respectively. The fractures are randomly distributed around the wells. The SRV of the three fracture networks is the same, namely, 2400 m × 400 m. The fracture density and fracture connectivity around the three wells are calculated by using equations (1) and (3). The density of fractures around Well-A, Well-B, and Well-C is 0.035 m/m<sup>2</sup>, 0.025 m/m<sup>2</sup>, and 0.016 m/m<sup>2</sup>, respectively. The connectivity of fractures around Well-A, Well-B, and Well-C is 0.573, 0.424, and 0.223, respectively. Simulation time herein is 5 × 365 days. Other simulation parameters are the same with the parameters listed in Table 1.

The obtained well productions are compared in Figure 15. As can be seen, the trend of production variation with the increasing fracture density is similar with the trend depicted in Figure 4. Increasing the number of fractures from 150 (FD = 0.016, FC = 0.223) to 250 (FD = 0.025, FC = 0.424)

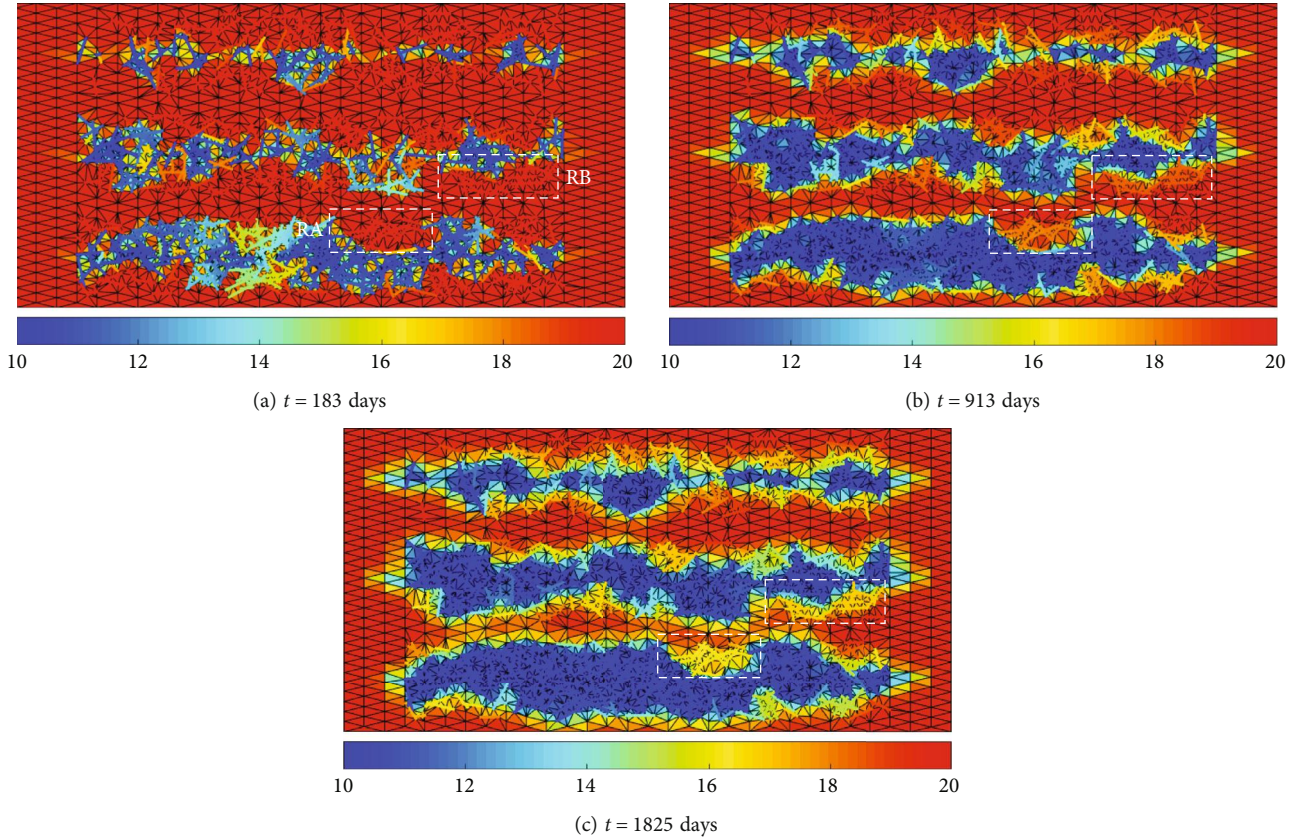


FIGURE 16: Time evolution of reservoir pressure profile in the multi-well densely fractured model.

leads to a production increase of  $210.2\text{ m}^3$ , which is much greater than the production increase resulting from the increase of fracture number from 250 to 350 ( $FD = 0.035$ ,  $FC = 0.573$ ). Figure 16 shows the time evolution of reservoir pressure profile. As can be seen, the region of pressure drawdown around each well extends little with time and does not contact with each other, indicating the negligible impact of interwell interference on well production. This phenomenon is attributed to the extremely tight matrix in tight reservoirs.

It can also be observed in Figure 16 that pressure distribution in the SRV of every well is highly heterogeneous. In the traditional sand reservoirs, the main reason will be directed to the reservoir heterogeneity which is caused by the heterogeneous distribution of rock permeability. However, in the densely fractured tight reservoirs, this phenomenon is attributed to the heterogeneous distribution of fracture density and fracture connectivity. Take the region (RA) highlighted by blue dotted line around Well-A (Figure 14) and the region (RB) highlighted by black dotted line around Well-B for example; in RA, fracture density is considerably smaller than that of any other regions around Well-A, resulting in the much smaller pressure drawdown of this region. In RB, although the fracture density is as big as that of other regions around Well-B, the pressure drawdown of this region is still smaller than that of any other regions. This is because most fractures in RB are laid in the same direction ( $x$ -direction), resulting in an unfavorable fracture connectivity. Since RA and RB are bypassed zones and typically, it is very difficult

to extract the remaining fluids from the bypassed zones through conventional technics; it is suggested that the fracturing treatments should be optimized to make the distribution of fracture density and fracture connectivity in the SRV as uniform as possible.

## 6. Conclusions

A new workflow based on reservoir simulation is designed to quantitatively study the effect of fracture density and fracture connectivity on the well performance in tight reservoir. The simulations are performed using an in-house discrete fracture simulator which is capable of modeling compressible rock and fluid and handling complex fracture networks. The results indicate that fracture density and fracture connectivity are two factors that can dramatically affect reservoir behaviors of densely fractured tight reservoirs. Equations for effect measurement are proposed. Optimizations of these two parameters should be taken into account in the stimulation design. For the optimization of fracture density, larger scale of hydraulic fracturing does not always lead to greater economic benefit. An optimal fracture density needs to be determined when considering the high cost of hydraulic fracturing. The primary issue of optimizing fracture connectivity is to identify the propagation direction of natural fracture since the optimal direction of the horizontal well is being parallel to the direction of natural fractures. In tight reservoirs, we reveal that the heterogeneous distribution of remaining oil is

mainly caused by the heterogeneous distributions of fracture density and fracture connectivity. Hence, we suggest that the fracturing treatments should be optimized to make the distribution of fracture density and fracture connectivity in the SRV as uniform as possible.

## Data Availability

All data included in this study are available upon request by contact with the corresponding author.

## Conflicts of Interest

The authors declare that they have no conflicts of interest.

## Acknowledgments

This research is supported by the NSFC Basic Research Program on Deep Petroleum Resource Accumulation and Key Engineering Technologies (U19B6003) and Sinopec Research Project (P19031-2).

## References

- [1] Y. S. Wu and P. Fakcharoenphol, "A unified mathematical model for unconventional reservoir simulation," in *SPE EUR-OPEC/EAGE Annual Conference and Exhibition*, OnePetro, May 2011.
- [2] D. M. Jarvie, "Shale resource systems for oil and gas: Part 2-Shale-oil resource systems," *AAPG Memoir*, vol. 97, pp. 89–119, 2012.
- [3] Q. Feng, S. Xu, X. Xing, W. Zhang, and S. Wang, "Advances and challenges in shale oil development: a critical review," *Advances in Geo-Energy Research*, vol. 4, no. 4, pp. 406–418, 2020.
- [4] A. Moinfar, W. Narr, M. H. Hui, B. T. Mallison, and S. H. Lee, "Comparison of discrete-fracture and dual-permeability models for multiphase flow in naturally fractured reservoirs," in *SPE Reservoir Simulation Symposium*, OnePetro, 2011.
- [5] R. C. Liu, Y. J. Jiang, N. Huang, and S. Sugimoto, "Hydraulic properties of 3D crossed rock fractures by considering anisotropic aperture distributions," *Advances in Geo-Energy Research*, vol. 2, no. 2, pp. 113–121, 2018.
- [6] C. L. Cipolla, "Modeling production and evaluating fracture performance in unconventional gas reservoirs," *Journal of Petroleum Technology*, vol. 61, no. 9, pp. 84–90, 2009.
- [7] J. C. S. Long and P. A. Witherspoon, "The relationship of the degree of interconnection to permeability in fracture networks," *Journal of Geophysical Research - Solid Earth*, vol. 90, no. B4, pp. 3087–3098, 1985.
- [8] J. C. S. Long, *Investigation of Equivalent Porous Medium Permeability in Networks of Discontinuous Fractures*, University of California, 1983, Ph.D. thesis.
- [9] J. E. Warren and P. J. Root, "The behavior of naturally fractured reservoirs," *SPE Journal*, vol. 3, no. 3, pp. 245–255, 1963.
- [10] L. Mei, H. Zhang, L. Wang, Q. Zhang, and J. C. Cai, "Fractal analysis of shape factor for matrix-fracture transfer function in fractured reservoirs," *Oil & Gas Science and Technology - Revue d'IFP Energies nouvelles*, vol. 75, p. 47, 2020.
- [11] J. C. Cai, W. Wei, X. Y. Hu, R. C. Liu, and J. J. Wang, "Fractal characterization of dynamic fracture network extension in porous media," *Fractals*, vol. 25, no. 2, p. 1750023, 2017.
- [12] H. Hoteit and A. Firoozabadi, "Compositional modeling of discrete-fractured media without transfer functions by the discontinuous Galerkin and mixed methods," *SPE Journal*, vol. 11, no. 3, pp. 341–352, 2006.
- [13] T. H. Sandve, I. Berre, and J. M. Nordbotten, "An efficient multi-point flux approximation method for discrete fracture-matrix simulations," *Journal of Computational Physics*, vol. 231, no. 9, pp. 3784–3800, 2012.
- [14] M. Karimi-Fard and A. Firoozabadi, "Numerical simulation of water injection in fractured media using the discrete-fracture model and the Galerkin method," *SPE Reservoir Evaluation and Engineering*, vol. 6, no. 2, pp. 117–126, 2003.
- [15] M. J. Mayerhofer, E. P. Lolon, J. E. Youngblood, and J. R. Heinze, "Integration of microseismic-fracture-mapping results with numerical fracture network production modeling in the Barnett shale," in *SPE Annual Technical Conference and Exhibition*, OnePetro, September 2006.
- [16] N. R. Warpinski, M. J. Mayerhofer, M. C. Vincent, C. L. Cipolla, and E. P. Lolon, "Stimulating unconventional reservoirs: maximizing network growth while optimizing fracture conductivity," *Journal of Canadian Petroleum Technology*, vol. 48, no. 10, pp. 39–51, 2009.
- [17] W. Yu and K. Sepehrnoori, "Optimization of well spacing for Bakken tight oil reservoirs," in *SPE/AAPG/SEG Unconventional Resources Technology Conference*, OnePetro, August 2014.
- [18] L. Saputelli, C. Lopez, A. Chacon, and M. Soliman, "Design optimization of horizontal wells with multiple hydraulic fractures in the Bakken shale," in *SPE/EAGE European Unconventional Resources Conference and Exhibition*, OnePetro, February 2014.
- [19] L. Li and S. H. Lee, "Efficient field-scale simulation of black oil in a naturally fractured reservoir through discrete fracture networks and homogenized media," *SPE Reservoir Evaluation & Engineering*, vol. 11, no. 4, pp. 750–758, 2008.
- [20] A. Moinfar, A. Varavei, K. Sepehrnoori, and R. T. Johns, "Development of an efficient embedded discrete fracture model for 3D compositional reservoir simulation in fractured reservoirs," *SPE Journal*, vol. 19, no. 2, pp. 289–303, 2014.
- [21] M. Karimi-Fard, L. J. Durlofsky, and K. Aziz, "An efficient discrete-fracture model applicable for general-purpose reservoir simulators," *SPE Journal*, vol. 9, no. 2, pp. 227–236, 2004.
- [22] M. G. Edwards, "Unstructured, control-volume distributed, full-tensor finite-volume schemes with flow based grids," *Computational Geosciences*, vol. 6, no. 3/4, pp. 433–452, 2002.
- [23] V. Lenti and C. Fidelibus, "A BEM solution of steady-state flow problems in discrete fracture networks with minimization of core storage," *Computational Geosciences*, vol. 29, no. 9, pp. 1183–1190, 2003.
- [24] A. Moinfar, A. Varavei, K. Sepehrnoori, and R. T. Johns, "Development of a novel and computationally-efficient discrete-fracture model to study IOR processes in naturally fractured reservoirs," in *SPE Improved Oil Recovery Symposium*, OnePetro, 2012.
- [25] A. Orangi, N. R. Nagarajan, M. M. Honarpour, and J. J. Rosenzweig, "Unconventional shale oil and gas-condensate reservoir production, Impact of rock, fluid, and hydraulic fractures," in *SPE Hydraulic Fracturing Technology Conference*, OnePetro, 2011.

- [26] P. Lemonnier and B. Bourbiaux, "Simulation of naturally fractured reservoirs. State of the art," *Oil & Gas Science and Technology*, vol. 65, no. 2, pp. 263–286, 2010.
- [27] J. Cai, H. Hajibeygi, J. Yao, and S. M. Hassanizadeh, "Advances in porous media science and engineering from InterPore2020 perspective," *Advances in Geo-Energy Research*, vol. 4, no. 4, pp. 352–355, 2020.
- [28] W. Fang, C. Liu, J. Li et al., "A discrete modeling framework for reservoirs with complex fractured media: theory, validation and case studies," *Journal of Petroleum Science and Engineering*, vol. 170, pp. 945–957, 2018.
- [29] C. Johnson, *Numerical solution of partial differential equations by the finite element method*, Courier Corporation, 2012.
- [30] H. Mustapha, "A Gabriel-Delaunay triangulation of 2D complex fractured media for multiphase flow simulations," *Computational Geosciences*, vol. 18, no. 6, pp. 989–1008, 2014.
- [31] V. O. E. Kjelseth, *Efficient Calculation of Derivatives Using Automatic Differentiation*, University of Oslo, 2014, Master's thesis.
- [32] C. H. Bischof, H. M. Bücker, P. Hovland, U. Naumann, and J. Utke, *Advances in Automatic Differentiation*, Springer, Berlin Heidelberg, 2008.
- [33] J. G. Kim and S. Finsterle, *Application of Automatic Differentiation in TOUGH2*, Lawrence Berkeley National Laboratory, 2003.
- [34] C. L. Cipolla, N. R. Warpinski, M. J. Mayerhofer, E. Lolon, and M. C. Vincent, "The relationship between fracture complexity, reservoir properties, and fracture treatment design," *SPE Production & Operations*, vol. 25, no. 4, pp. 438–452, 2010.
- [35] J. F. Gale, R. M. Reed, and J. Holder, "Natural fractures in the Barnett shale and their importance for hydraulic fracture treatments," *AAPG Bulletin*, vol. 91, no. 4, pp. 603–622, 2007.
- [36] D. M. Reeves, D. A. Benson, and M. M. Meerschaert, "Transport of conservative solutes in simulated fracture networks: 1. Synthetic data generation," *Water Resources Research*, vol. 44, no. 5, p. 5404, 2008.

## Research Article

# Analysis of Microstructure and Low Permeability with 3D Digital Rock Modeling

Jinsui Wu <sup>1,2</sup>, Min Xing <sup>2</sup>, Shangxian Yin,<sup>2</sup> Ciyuan Zhang,<sup>2</sup> Xuexi Chen,<sup>2</sup> Sihai Yi,<sup>2</sup> Huiqing Lian,<sup>2</sup> and Dongyu Xie<sup>2</sup>

<sup>1</sup>State Key Laboratory of Oil and Gas Reservoir Geology and Exploitation, Southwest Petroleum University, Chengdu 610500, China

<sup>2</sup>Department of Safety Engineering, North China Institute of Science and Technology, Beijing 101601, China

Correspondence should be addressed to Jinsui Wu; 200700797wjs@ncist.edu.cn and Min Xing; 1765898497@qq.com

Received 8 October 2021; Revised 21 December 2021; Accepted 1 February 2022; Published 3 March 2022

Academic Editor: Steffen Berg

Copyright © 2022 Jinsui Wu et al. This is an open access article distributed under the Creative Commons Attribution License, which permits unrestricted use, distribution, and reproduction in any medium, provided the original work is properly cited.

The sandstone microstructure and permeability are important parameters for quantitative evaluation of groundwater/oil/gas resources and prediction of flow rates of water/oil/gas. In this study, we applied seven low-permeability sandstone samples obtained from North China to research the microstructure and permeability based on digital core technology. Rock images were collected by X-ray microcomputed tomography ( $\mu$ CT), and then software (Avizo) was applied to analyze the microstructure and calculate the parameters such as porosity, connected porosity, average equivalent diameter, tortuosity, and shape factor. By introducing the shape factor into the Kozeny–Carman equation, we modified the Kozeny–Carman equation and found that the modified equation is a function of porosity, diameter of particles, tortuosity, and particle shape factor.

## 1. Introduction

The characteristics of low-permeability reservoirs are widely used to improve the water injection effect of low-permeability oilfields or exploit oil and gas resources. The research of low permeability is essential to studying the reservoir characteristics. Reasonable characterization and quantitative analysis of the complex pore structures inside rock were the basis for solving many underground reservoir characteristics [1]. The research on the microstructure of the digital core was mainly based on the study of the 3D digital core. Knackstedt et al. [2] controlled the finite size effect, discretion error, and statistical fluctuations to obtain high-precision results by using X-micron CT scanners; Tian and Han [3] used X-ray CT to examine the evolution of concrete internal damage. Wang et al. [4] combined CT and the pore network model to analyze the influence of particle size on permeability in hydrate-containing porous media. Wang et al. [5] used fractal theory and X-ray CT imaging to carry out three-dimensional modeling and analysis of the coal pore structure. Cao et al. [6] used computed

tomography data to analyze the capillary pressure of the dense sandstone based on a digital rock model. Qin et al. [7] used the fractal and multifractal methods such as box dimension and moment method combined with X-CT imaging techniques to analyze the structure of the volcanic vesicle. Yang et al. [8] used X-ray tomography to determine the distribution of residual oil in sandstone with different permeability.

Permeability was the key relationship between microstructure and macroscopic physical properties of porous media [9], and it was not only affected by the geometry or shape of the pore space but also by the topological structure [10]. The pore space connectivity of porous media was an important factor affecting the flow characteristics of tight sandstone [11]. The tortuosity of the pore structure has an important effect on macroscopic transport properties. Nakashima found that the diffusion rate and permeability decreased with the increase of tortuosity [12]. The pore size and mean coordination number also affected the overall permeability, and the permeability increased with the increase of the pore size distribution width [13, 14]. Sueyoshi

et al. also found that permeability mainly depends on the porosity and pore size of the flow path [15].

Various methods have been attempted to calculate permeability; Hu and Blunt used an improved maximum ball algorithm to study the overall network pore structure and calculate permeability [16]. A support vector regression (SVR) model was developed to evaluate the low porosity and permeability of sandstone reservoirs by Feng et al. [17]. Wei et al. [18] used the relevant parameters of the porous media to figure out the KC constant of the Kozeny–Carman equation, which thus contributes to the further study and analysis of the permeability. Kozeny–Carman (KC) equation expressed the relationship of permeability and porosity of porous media micropore structure [19–21]:

$$k = \frac{\varphi^3}{c(1-\varphi)^2 S^2} = \frac{\varphi^3}{36c\tau^2(1-\varphi)^2} d^2, \quad (1)$$

where  $k$  is the permeability;  $\varphi$  is the porosity;  $d$  is the average particle radius;  $\tau$  is the tortuosity; and  $c$  is the empirical constant.

However, the traditional Kozeny–Carman equation was an empirical formula. For a heterogeneous system, the calculated permeability was large, 10 or more times than the actual [22]. Many modified equations were presented. Pape et al. [23] proposed an equation for sand and gravel:

$$k = \frac{\varphi r^2}{8\tau^2} \left( \frac{2\varphi}{3\tau^2(1-\varphi)} \right)^{2(D_f-1)}, \quad (2)$$

where  $r$  is the particle radius and  $D_f$  is the fractal dimension of the medium.

Civan [24] proposed an equation for general porous media:

$$\sqrt{\frac{k}{\varphi}} = \gamma \left( \frac{\varphi}{1-\varphi} \right)^\beta. \quad (3)$$

Costa [25] proposed an expression suitable for porous rocks:

$$k = C \frac{\varphi^n}{1-\varphi}. \quad (4)$$

Based on the fractal theory, Yu [26] derived the permeability expression through a curved capillary model.

$$k = \frac{\pi}{128} \frac{L_0^{1-D_T}}{A} \frac{P_m}{\Delta P} \frac{D_f \lambda_{\max}^{3+D_T}}{3+D_T-D_f}, \quad (5)$$

where  $D_T$  is the tortuosity fractal dimension,  $L_0$  is the characteristic length, and  $\lambda_{\max}^{3+D_T}$  is the maximum pore diameter.

Xu and Yu [27] also established a modified K-C equation based on the fractal theory:

$$k = C_f \left( \frac{\varphi}{1-\varphi} \right)^{(1+D_T)/2} \lambda_{\max}^2. \quad (6)$$

Among them,  $C_f$  is as follows:

$$C_f = \frac{(\pi D_f)^{(1-D_T)/2} [4(2-D_f)]^{(1-D_T)/2}}{128(3+D_T-D_f)}. \quad (7)$$

Karacan [28] used the fractal method to calculate the porosity and permeability of mining, and the permeability expression was as follows:

$$k = \frac{\pi}{16A_T} \frac{L_0^{1-D_T}}{\alpha} \frac{D_p}{2.531+D_T-D_p} \cdot \eta_{\max}^{2.531+D_T} \left[ 1 - \left( \frac{\eta_{\min}}{\eta_{\max}} \right)^{2.531+D_T-D_p} \right], \quad (8)$$

where  $A_T$  is the total area;  $\eta_{\max}$  is the maximum diameter of the pore;  $\eta_{\min}$  is the minimum diameter of the pore; and  $D_p$  is the fractal dimension of the pore.

Xia et al. [29] used twelve three-dimensional digital cores of sandstone reservoir rocks to evaluate permeability in terms of fractal dimension, lacunarity, and succolarity. The permeability was rewritten as follows:

$$k = 0.0239e^{23.98SU}, \quad (9)$$

where  $SU$  is the succolarity, indicating the ability of the fluid to move in the porous medium.

Shen et al. [30] proposed the equivalent Kozeny–Carman equation to establish a permeability prediction model:

$$k = \frac{\varphi^3}{180(1-\varphi)^2} d^N. \quad (10)$$

In the formula,  $N=2.44$ , and the unit of  $k$  is the same with the unit of  $d^{2.44}$ , i.e.,  $m^{2.44}$ . This is different with the unit in the KC equation.

To sum up, digital rock cores (X-ray (CT) scanning) were used to obtain the structure of the rock cores, and some permeability prediction models have been proposed. The research was mainly on higher permeability, and few low-permeability prediction models had been established. The low-permeability model generally contained empirical constants or modified permeability units.

This paper used X-ray CT scanning technology and Avizo software to study and calculate pore and particle structure parameters of low-permeability sandstones. Finally, the pore and particle structure parameters were used to predict permeability. In addition, the shape factor was introduced to modify the KC equation.

## 2. The Porosity and Permeability Obtained by Experiments

In this work, 7 natural sandstone samples were collected at depths of 430 m–735 m below the sea level of North China. These 7 natural sandstone samples were abbreviated as GQ1, GQ2, GQ3, LA1, LA2, TL1, and TL2. Samples GQ1, GQ2, and GQ3 were from Gequan Mine, samples LA1 and LA2 were from Lu'an Mine, and TL1 and TL2 were from Tunlan Mine. The permeability and porosity were tested using the core company's high- and low-permeability meter CAT112

and a helium porosity meter from American Coretest company Phi220; the experiment results are shown in Table 1.

Based on the measured data, the map of sandstone porosity and permeability is shown in Figures 1 and 2.

As can be seen from Figure 1, the porosity of sandstone in Gequan Mine is high, while the porosity of the Lu'an samples is relatively low. The highest porosity of Tunlan Mine (TL1) is 5.66%, and the lowest porosity of Lu'an Mine (LA1) is 0.38%.

Figure 2 shows the experiment permeability, and the permeability of Tunlan Mine (TL2) is the highest. Comparing Figures 1 and 2, it can be found that high porosity does not lead to high permeability; for example, the porosity of the samples GQ1, GQ2, GQ3, and TL1 is higher than that of other three samples (LA1, LA2, and TL2); however, the permeability values of the samples GQ1, GQ2, GQ3, TL1, LA1, and LA2 are relatively close, the porosity of Tunlan Mine (TL2) is 1.14%, but the permeability is 0.0870 mD; this is higher than other samples.

### 3. X-Ray Micro-CT Experiments and Calculations

**3.1. The Pore and Particle Diameters.** This paper used a desktop micrometer CT scanner (NanoVoxel-3000) to measure samples of approximately 1 cm. As an example, Figure 3 shows the sample GQ1 reconstructed images of three directions.

Avizo software was used to analyze the reconstructed 3D digital core. In order to better adjust the threshold so that the connected porosity is close to the measured porosity, a 3D digital core of  $200 \times 200 \times 200$  was selected as the target study area which was larger than REV, and the voxel edge length was  $18.05 \mu\text{m}$ . In addition,  $200 \times 200 \times 200$  is also the study region in Figures 4–6.

Median filtering and interactive threshold segmentation were performed to obtain the three-dimensional pore structure of the core. Figure 4 shows the three-dimensional pore extraction process.

The pores of rock samples were divided into connected pores and isolated pores, i.e., total pores = connected pores + isolated pores, as shown in Figure 5, the green parts are isolated pores, and the purple parts are connected pores. The GQ1 total porosity is 7.85%, where the isolated porosity is 3.34% and the connected porosity is 4.51%. It can be seen that the connected pore is about the experimentally measured data size. The porosity distribution of all rock samples is as follows (see Table 2).

To understand the distribution of pores with different pore sizes, the total pores were screened according to the pore size through the pore segmentation module of Avizo, and the pore size of the sample was obtained (as shown in Figure 6). The overall pore size distribution is shown in Figure 7.

Figure 7 shows that the  $40\text{--}80 \mu\text{m}$  diameters of the pore's aperture are the most widely distributed about 40%. The

proportion of large pores is relatively small, and the pores larger than  $400 \mu\text{m}$  are mainly connected pores. This was mainly due to the close connection of multiple pores, which resulted in the threshold segmentation as a whole. Finally, we obtained the sample GQ1's average pore diameter as  $68 \mu\text{m}$ .

The particle part was obtained after removing the pores in the sample (see Figure 8). Through the analysis of diameters, we can see that the particles with a diameter of  $0\text{--}25 \mu\text{m}$  account for the largest proportion. The final analysis shows that the average particle diameter of the sample GQ1 is  $35 \mu\text{m}$ . The diameter distributions of pores and particles for all rock samples are as follows (see Table 3).

**3.2. Shape Factor Analysis of Rock Samples.** In reality, not all the pores/capillaries are spherical, and the shape of the particles has an effect on the permeability [31, 32]. Nemeck and Levec researched shape factor of trilobe and quadralobe particles and the effect on the permeability [33]. Safari et al. developed a porosity-permeability relationship for ellipsoidal grains [34].

We used the Label Analysis module of Avizo software (see Figure 9) to analyze the pores' shape factor. The calculation of the shape factor was based on the ideal sphere model. The calculation equation is

$$\sigma = \frac{A^3}{36 \times \pi \times V^2}, \quad (11)$$

where  $s$  is the shape factor,  $A$  is the area, and  $V$  is the volume of the pore.

Because of the presence of partially elongated pores, the surface area of the pore becomes larger, resulting in a shape factor greater than 1. According to the demarcation point of the shape factor, the pores' shape factor was divided; GQ1's image as a sample is shown in Figure 10. The shape factors of the pores and particles of the average sample GQ1 are 2.03 and 1.24, respectively.

Figure 11 shows the statistic of the GQ1's pores and particles' shape factor distribution in each section.

Table 4 shows the average shape factor distribution of pores and particles for all rock samples.

**3.3. Tortuosity Analysis of Rock Samples.** The ball-and-stick model can intuitively show the connection among the pores. The GQ1's ball-and-stick model was established as shown in Figure 12.

The ball-and-stick model showed the connection between the internally connected pores in the rock sample. For this reason, the tortuosity can be analyzed by the ball-and-stick model. Tortuosity = path length/straight-line distance between two points.

$$\tau = \frac{L_t}{L_0}. \quad (12)$$

The tortuosity of the pore for all samples can be shown as follows (see Table 5).



TABLE 1: Experiment results of porosity and permeability.

Serial number	Sample number	Length (mm)	Diameter (mm)	Quality (g)	Confining pressure (psi)	Pore pressure (psi)	Porosity (%)	Permeability (mD)
1	GQ1	35.70	25.73	45.44	560	200	4.42	0.0144
2	GQ2	28.63	25.45	36.19	560	200	3.88	0.0102
3	GQ3	25.47	25.62	32.46	560	200	4.58	0.0084
4	TL1	37.94	25.67	48.18	560	200	5.66	0.0073
5	TL2	38.22	25.50	52.48	560	200	1.14	0.0870
6	LA1	37.88	25.69	53.39	560	200	0.38	0.0069
7	LA2	36.65	25.53	49.44	560	200	0.74	0.016

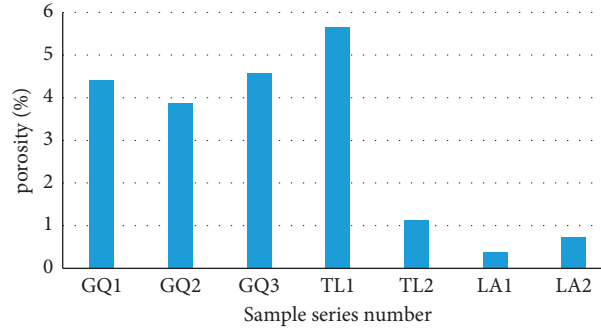


FIGURE 1: Sandstone sample porosity distribution.

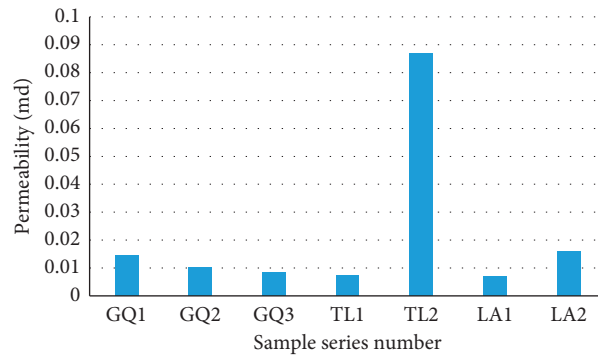


FIGURE 2: Sandstone sample permeability distribution.

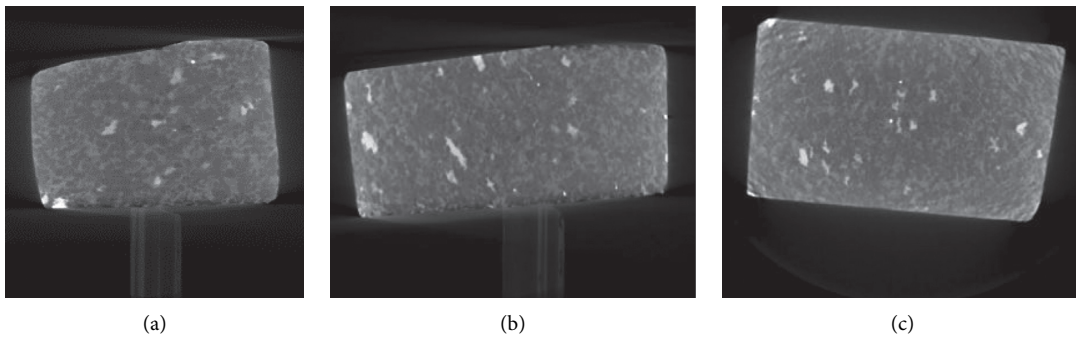


FIGURE 3: GQ1 reconstructed images of three directions. (a) X-axis direction. (b) Y-axis direction. (c) Z-axis direction.

## 4. Permeability Prediction Model

4.1. *Kozeny–Carman Equation.* The Kozeny–Carman equation, which was first proposed by Kozeny [19] in 1927

and revised by Carman [20, 21], was abbreviated as the KC equation. It was widely used in many fields to estimate and predict hydraulic conductivity, such as underground seepage, oil and gas field exploitation, chemical engineering,

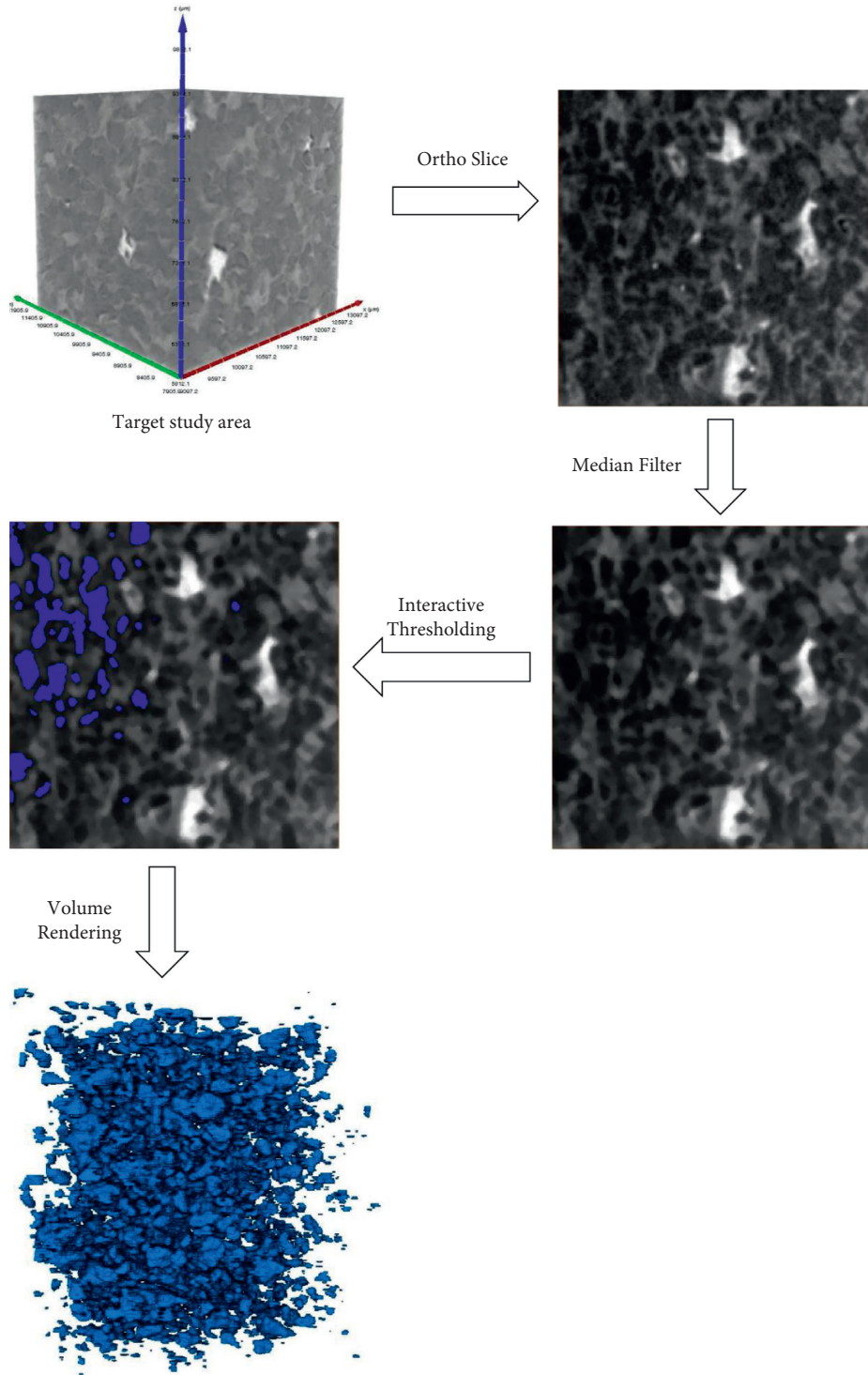


FIGURE 4: Three-dimensional pore extraction process.

biochemistry, and electrochemistry. According to the KC equation, the permeability  $k$  and porosity  $\phi$  of the porous medium can be expressed as

$$k = \frac{\phi^3}{c(1 - \phi)^2 S^2} = \frac{\phi^3}{36c(1 - \phi)^2 d^2}. \quad (13)$$

In the above formula,  $c$  and  $S$  are the Kozeny constant and the specific surface area of the solid phase, respectively. Considering the tortuosity effect (tortuosity  $\tau$ ), the KC equation can be further expressed as [35, 36]

$$k = \frac{\phi^3}{36c(1 - \phi)^2 \tau^2 d^2}. \quad (14)$$

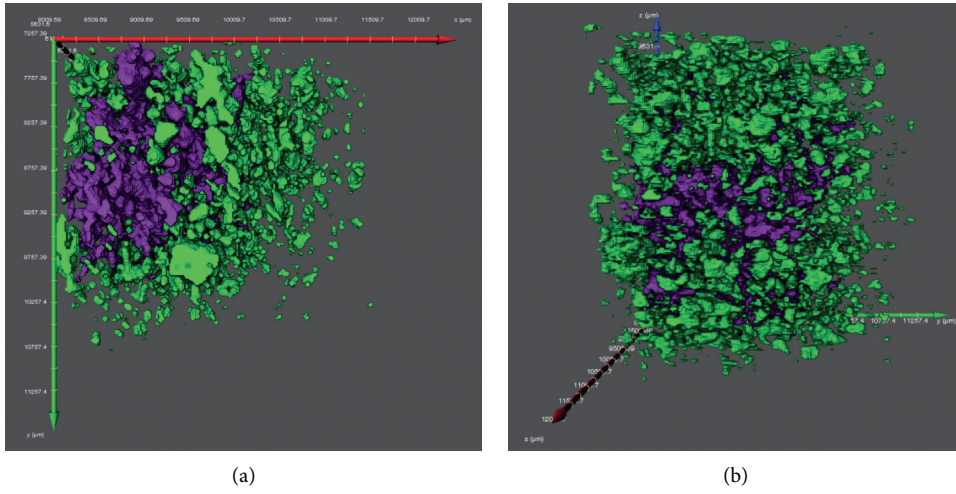


FIGURE 5: The perspective of total pores in the study area. (a) Total pores' perspective 1. (b) Total pores' perspective 2.

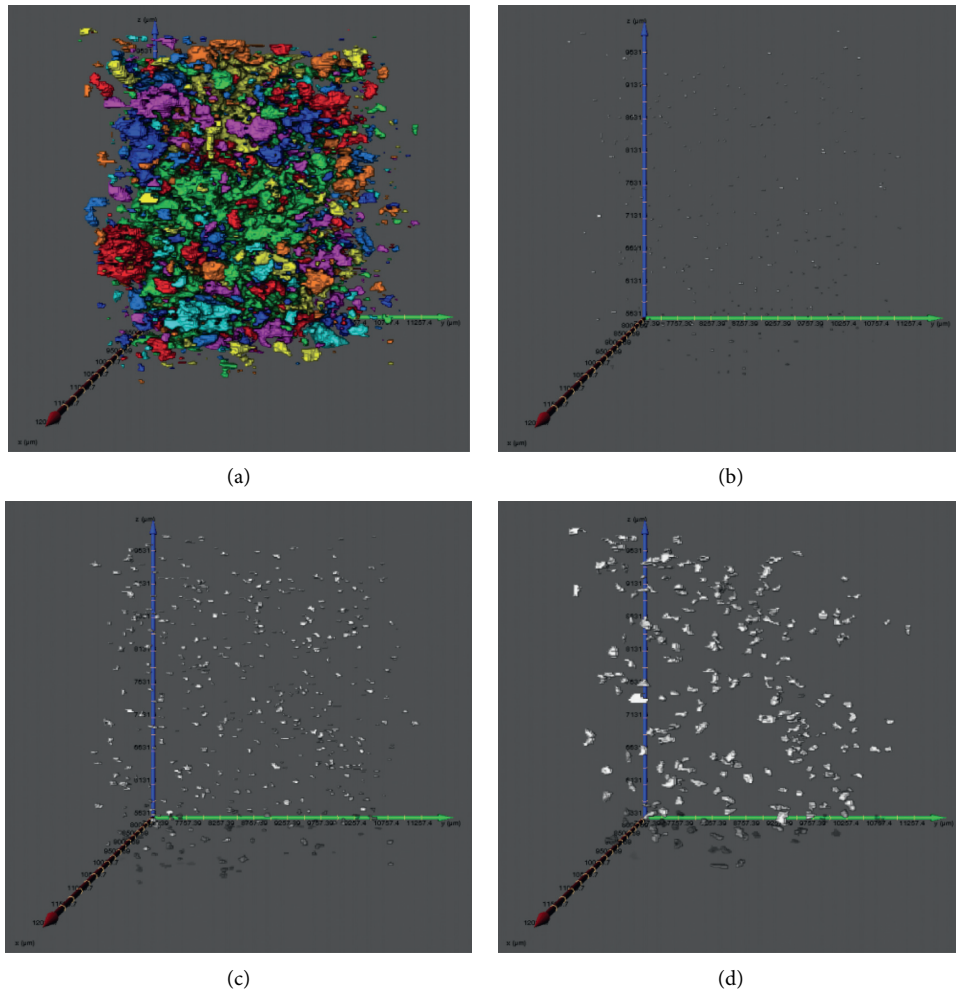


FIGURE 6: Continued.

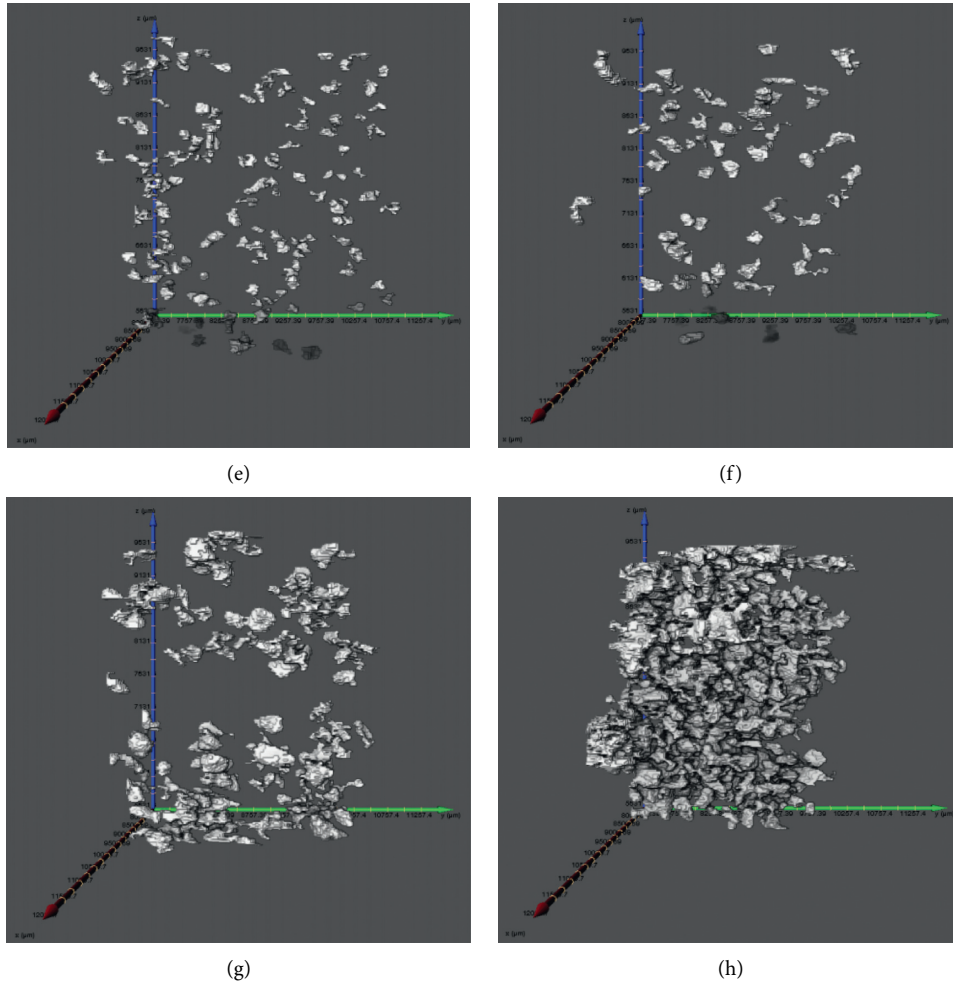


FIGURE 6: Aperture distribution diagram of total pores. (a) Total pores divided by equivalent diameter. (b) 0–40  $\mu\text{m}$  aperture. (c) 40–80  $\mu\text{m}$  aperture. (d) 80–120  $\mu\text{m}$  aperture. (e) 120–160  $\mu\text{m}$  aperture. (f) 160–200  $\mu\text{m}$  aperture. (g) 200–400  $\mu\text{m}$  aperture. (h) Aperture greater than 400  $\mu\text{m}$ .

TABLE 2: Pore type and porosity.

Rock sample	Total porosity (%)	Isolated porosity (%)	Connected porosity (%)	The overall proportion of isolated pores (%)	The overall proportion of connected pores (%)
GQ1	7.85	3.34	4.51	42.55	57.45
GQ2	4.81	0.93	3.88	19.33	80.67
GQ3	6.55	1.97	4.58	30.08	69.92
TL1	6.54	0.94	5.6	14.37	85.63
TL2	2.35	1.21	1.14	51.49	48.51
LA1	2.51	2.13	0.38	84.86	15.14
LA2	1.62	0.88	0.74	54.32	45.68

Kaviany [36] believed that if the value of  $t$  was approximately  $21/2$ , then for spherical particles,  $c$  was 2.5. Although the KC equation was widely used, people have noticed its limitations. The value of  $c$  varied widely in different scenarios. Therefore, we did not consider  $c$  as a key factor when establishing the permeability model.

*4.2. Modification of the Kozeny–Carman (KC) Equation.* Introducing a shape factor into the Kozeny–Carman equation and based on the traditional KC permeability prediction model, a permeability prediction model with shape factor as an influencing factor is established:

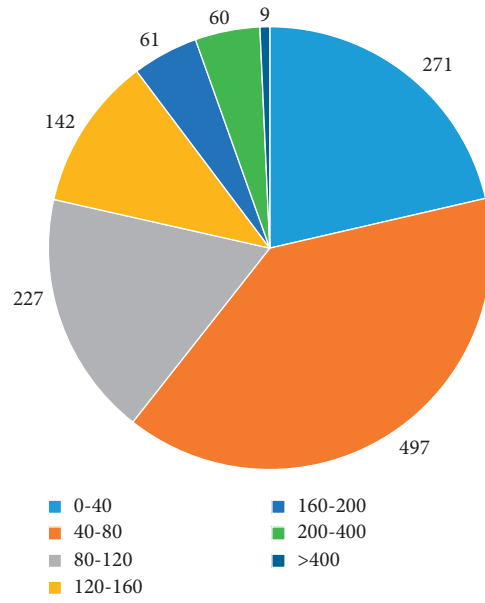


FIGURE 7: Distribution diagram of pores' size.

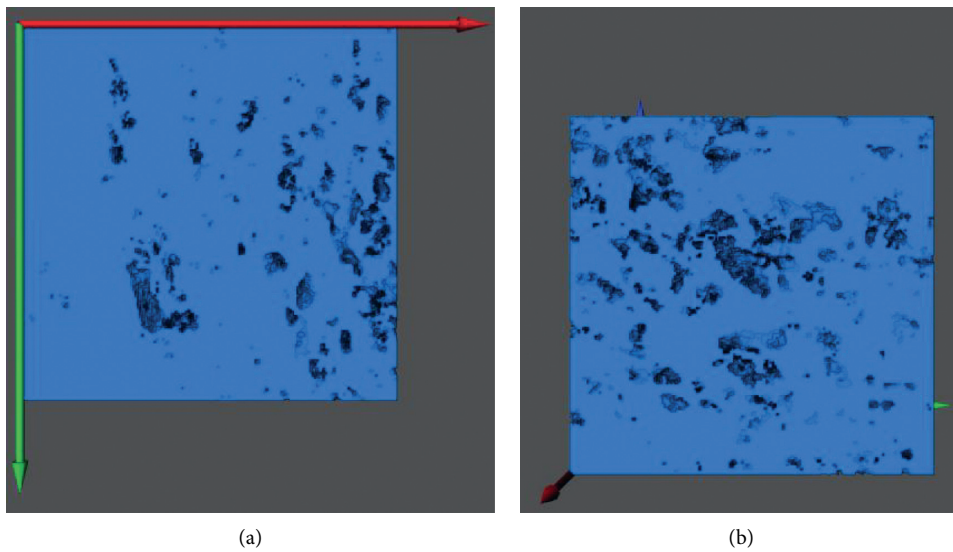


FIGURE 8: Continued.

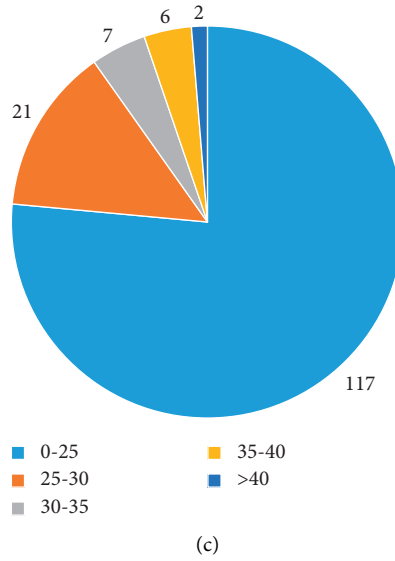


FIGURE 8: The particles in the study area. (a) Particles’ perspective 1. (b) Particles’ perspective 2. (c) Diameter of particles.

TABLE 3: The diameter of pores and particles.

Name of the rock sample	Average diameter of the connected pore (μm)	Average diameter of the particle (μm)
GQ1	68.10	35.00
GQ2	45.00	43.00
GQ3	52.53	26.00
TL1	63.30	49.77
TL2	29.00	40.00
LA1	34.30	28.50
LA2	39.21	53.48

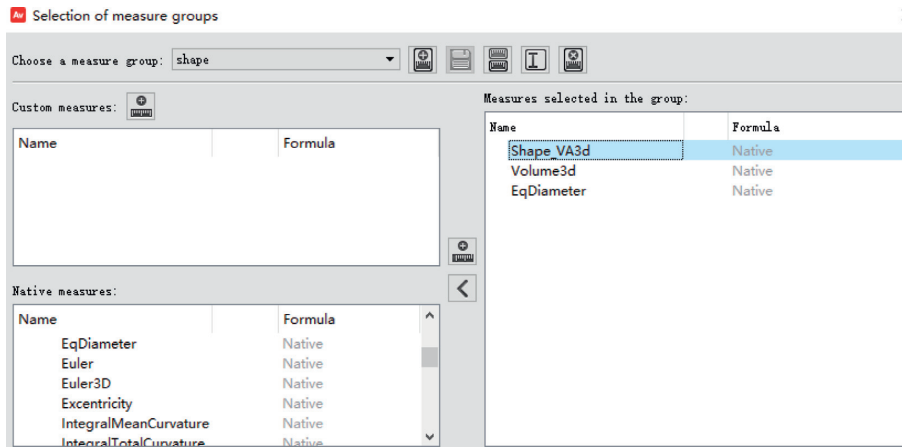


FIGURE 9: Shape factor module.

$$k = \frac{\varphi^3}{36\tau^2(1-\varphi)^2\sigma^n}d^2, \quad (15)$$

where  $s$  is the pore shape factor and  $n$  is the constant.

After analyzing and discussing the cores with different shape factors, it can be found that the exponent of the shape factor was  $\pm 15.8$ . When the exponent of the shape factor was 15.8 for samples GQ2, GQ3, and LA2 and the exponent was

$-15.8$  for samples GQ1, TL1, TL2, and LA1, the errors of calculated permeability and experiment permeability were small. The obtained permeability prediction model is as follows:

$$k = \frac{\varphi^3}{36\tau^2(1-\varphi)^2\sigma^{\pm 15.8}}d^2. \quad (16)$$

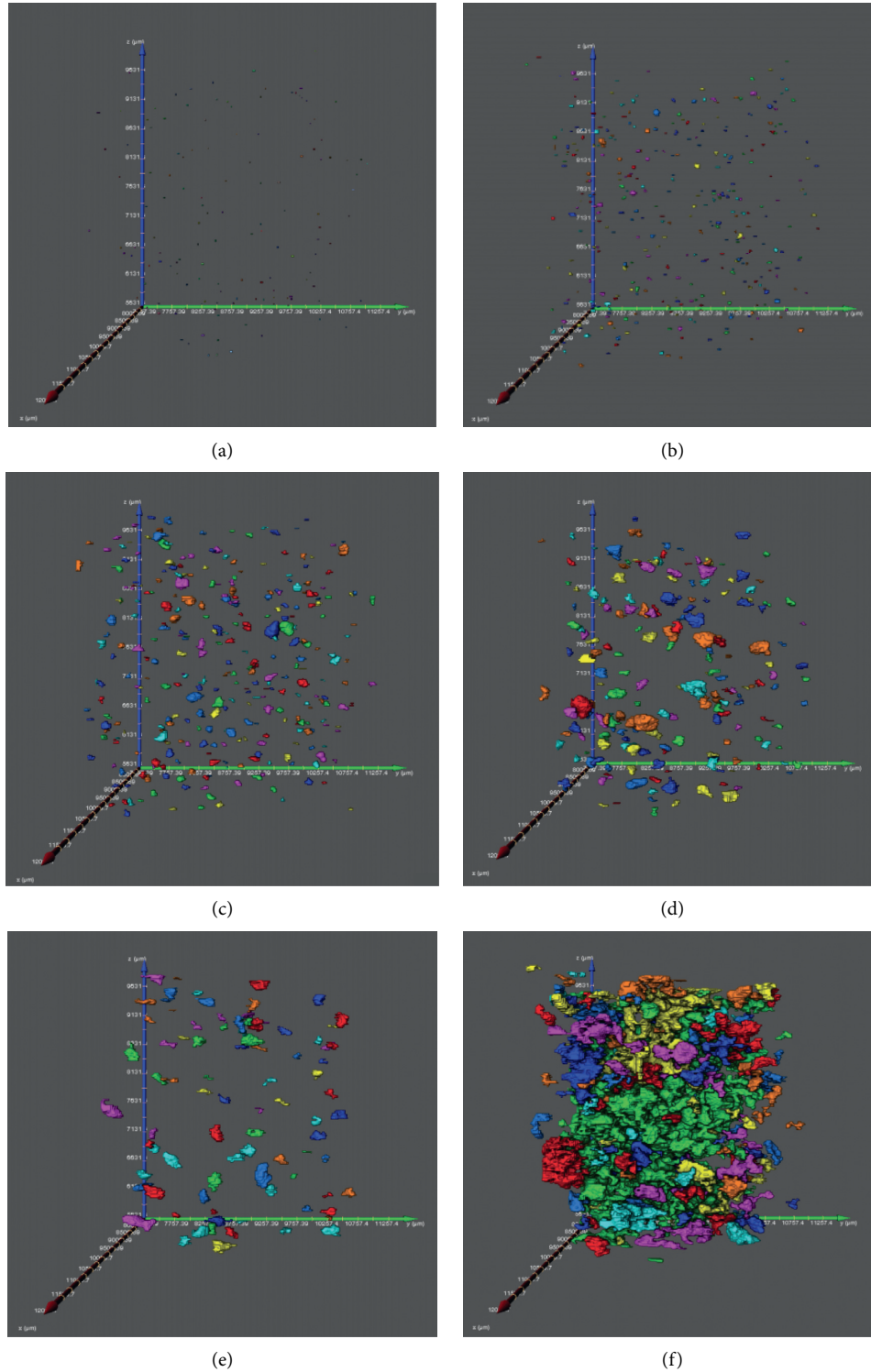


FIGURE 10: Distribution of GQ1's pore shape factor. (a) 0–0.5 shape factor section. (b) 0.5–1 shape factor section. (c) 1–1.5 shape factor section. (d) 1.5–2 shape factor section. (e) 2–2.5 shape factor section. (f) The section of shape factor greater than 2.5.

Using formula (16), the theoretical permeability and relative error are calculated when  $n$  is  $\pm 15.8$  (as shown in Table 6).

The calculated permeability errors of the samples are within 15.6%, and these errors are acceptable in engineering

applications. Table 6 shows that shape factors have an effect on the permeability; however, since only seven samples were used, the data were small. This exponent may be different from the test samples, so the exponent values of  $\pm 15.8$  require further investigation.

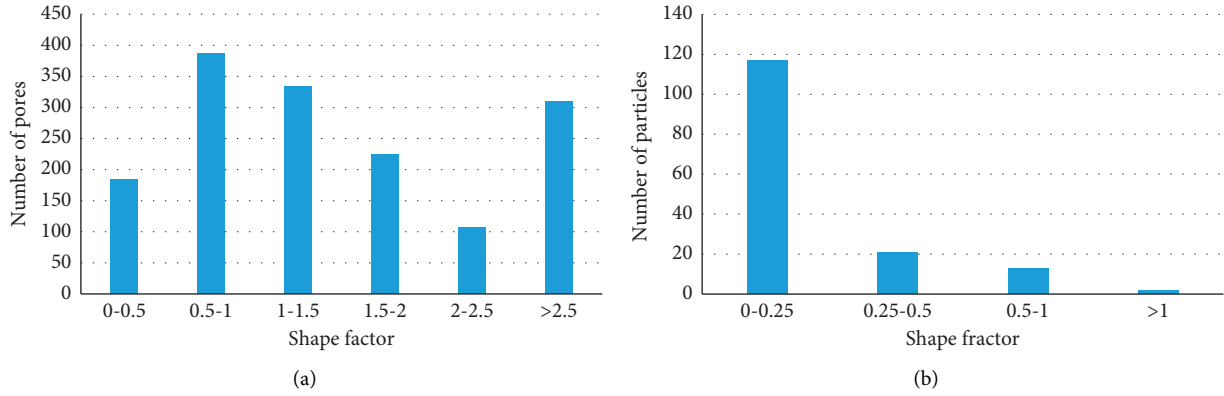


FIGURE 11: Statistics of GQ1's pore and particle shape factor. (a) Shape factor of pores. (b) Shape factor of particles.

TABLE 4: The shape factor of pores and particles.

Name of the rock sample	Particles' shape factor	Pores' shape factor
GQ1	1.24	2.03
GQ2	0.80	1.69
GQ3	0.82	2.01
TL1	1.40	2.42
TL2	0.83	0.59
LA1	0.75	0.52
LA2	1.20	0.59

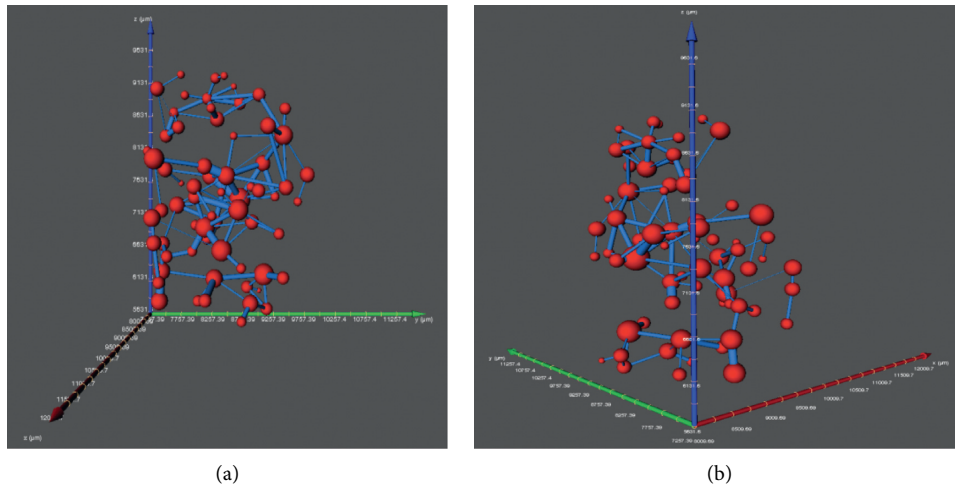


FIGURE 12: GQ1's ball-and-stick model. (a) Angle of view one of the ball-and-stick model. (b) Angle of view two of the ball-and-stick model.

TABLE 5: The tortuosity of pores.

Name of the rock sample	Pore tortuosity
GQ1	2.93
GQ2	3.17
GQ3	3.22
TL1	3.22
TL2	5.50
LA1	4.52
LA2	6.02



TABLE 6: Core permeability and relative error.

Name of the rock sample	Actual permeability (mD)	Theoretical permeability (mD)	Relative error (%)
GQ1	0.0144	0.0138	4.3
GQ2	0.0102	0.0096	5.6
GQ3	0.0084	0.0084	0.3
TL1	0.0052	0.0067	7.9
TL2	0.0870	0.0869	0.2
LA1	0.0069	0.0058	15.6
LA2	0.0160	0.0163	1.8

## 5. Conclusion

This paper used X-ray CT scanning technology and Avizo software to study and calculate pore and particle structure parameters of low-permeability sandstones. Finally, the pore and particle structure parameters were used to predict permeability. In addition, the shape factor was introduced to modify the KC equation.

In this study, seven sandstone samples were collected from the Lu'an, Gequan, and Tunlan coal mines, China. The pore and particle geometric parameters of the samples were analyzed by CT experiments and Avizo software. The permeability and porosity were tested using the core company's high- and low-permeability meter CAT112 and a helium porosity meter from American Coretest company Phi220. The three-dimensional digital cores were analyzed by Avizo software, and a permeability prediction model was established. From these studies, the following conclusions may be drawn:

- (1) The microstructures of the pore and particle can be well captured using CT experiments on sandstones and rock cores, and the structures of samples can be effectively obtained using Avizo software.
- (2) Through experiments, it was found that the degree of correlation between porosity and permeability was not very high, and there were the cases of low porosity and high permeability.
- (3) The parameters such as porosity, connected porosity, average equivalent diameter, tortuosity, and shape factor can be calculated by Avizo software from the extracted volume.
- (4) It can be concluded that the shape factors have an effect on the permeability. By introducing the shape factor into the Kozeny–Carman equation, we modified the Kozeny–Carman equation.

## Data Availability

The data used to support the findings of this study are included within the article.

## Conflicts of Interest

The authors declare that they have no conflicts of interest.

## Acknowledgments

This paper was partially supported by the Open Fund (PSLN1410) of State Key Laboratory of Oil and Gas

Reservoir Geology and Exploitation (Southwest Petroleum University) and supported by the National Science Foundation of China (51974126, 52174181, and 51204069) and Funding Projects for Basic Scientific Research Business Fees in Central Universities (3142015092 and 3142015093).

## References

- [1] Q. Xu, X. Liu, Z. Yang, and J. Wang, "The model and algorithm of a new numerical simulation software for low permeability reservoirs," *Journal of Petroleum Science and Engineering*, vol. 78, no. 2, pp. 239–242, 2011.
- [2] M. A. Knackstedt, C. H. Arns, M. Saadatfar et al., "Elastic and transport properties of cellular solids derived from three-dimensional tomographic images," *Proceedings of The Royal Society A*, vol. 462, no. 2073, pp. 2833–2862, 2006.
- [3] W. Tian and N. Han, "Pore characteristics (>0.1 mm) of non-air entrained concrete destroyed by freeze-thaw cycles based on CT scanning and 3D printing," *Cold Regions Science and Technology*, vol. 151, pp. 314–322, 2018.
- [4] J. Wang, J. Zhao, Y. Zhang, D. Wang, Y. Li, and Y. Song, "Analysis of the effect of particle size on permeability in hydrate-bearing porous media using pore network models combined with CT," *Fuel*, vol. 163, pp. 34–40, 2016.
- [5] G. Wang, J. Shen, S. Liu, C. Jiang, and X. Qin, "Three-dimensional modeling and analysis of macro-pore structure of coal using combined X-ray CT imaging and fractal theory," *International Journal of Rock Mechanics and Mining Sciences*, vol. 123, Article ID 104082, 2019.
- [6] Y. Cao, M. Tang, Q. Zhang, J. Tang, and S. Lu, "Dynamic capillary pressure analysis of tight sandstone based on digital rock model," *Capillarity*, vol. 3, no. 2, pp. 28–35, 2020.
- [7] M. Qin, S. Xie, J. Zhang et al., "Petrophysical texture heterogeneity of vesicles in andesite reservoir on micro-scales," *Journal of Earth Science*, vol. 32, no. 4, pp. 799–808, 2021.
- [8] Y. Yang, H. Yang, L. Tao et al., "Microscopic determination of remaining oil distribution in sandstones with different permeability scales using computed tomography scanning," *Journal of Energy Resources Technology*, vol. 141, Article ID 092903, 2019.
- [9] H. Bian, Y. Xia, C. Lu, X. Qin, Q. Meng, and H. Lu, "Pore structure fractal characterization and permeability simulation of natural gas hydrate reservoir based on CT images," *Geofluids*, vol. 2020, Article ID 6934691, 9 pages, 2020.
- [10] J. T. Fredrich, A. A. DiGiovanni, and D. R. Noble, "Predicting macroscopic transport properties using microscopic image data," *Journal of Geophysical Research:Solid Earth*, vol. 111, Article ID B03201, 2006.
- [11] M. A. Mousavi and S. L. Bryant, "Connectivity of pore space as a control on two-phase flow properties of tight-gas sandstones," *Transport in Porous Media*, vol. 94, no. 2, pp. 537–554, 2012.

- [12] Y. Nakashima and S. Kamiya, "Mathematica programs for the analysis of three-dimensional pore connectivity and anisotropic tortuosity of porous rocks using X-ray computed tomography image data," *Journal of Nuclear Science and Technology*, vol. 44, no. 9, pp. 1233–1247, 2007.
- [13] S. Tian, W. Ren, G. Li, R. Yang, and T. Wang, "A theoretical analysis of pore size distribution effects on shale apparent permeability," *Geofluids*, vol. 2017, Article ID 7492328, 26 pages, 2017.
- [14] Y. Yang, Y. Li, J. Yao et al., "Formation damage evaluation of a sandstone reservoir via pore-scale X-ray computed tomography analysis," *Journal of Petroleum Science and Engineering*, vol. 183, Article ID 106356, 2019.
- [15] K. Sueyoshi, T. Yokoyama, and I. Katayama, "Experimental measurement of the transport flow path aperture in thermally cracked granite and the relationship between pore structure and permeability," *Geofluids*, vol. 2020, Article ID 8818293, 10 pages, 2020.
- [16] D. Hu and M. J. Blunt, "Pore-network extraction from micro-computerized-tomography images," *Physical Review E*, vol. 80, Article ID 036307, 2009.
- [17] F. Feng, P. Wang, Z. Wei et al., "A new method for predicting the permeability of sandstone in deep reservoirs," *Geofluids*, vol. 2020, Article ID 8844464, 16 pages, 2020.
- [18] W. Wei, J. Cai, J. Xiao, Q. Meng, B. Xiao, and Q. Han, "Kozeny-Carman constant of porous media: insights from fractal-capillary imbibition theory," *Fuel*, vol. 234, pp. 1373–1379, 2018.
- [19] J. Kozeny, "Ueber kapillare Leitung des Wassers im Boden. Stizungsber," *Akad Wiss Wiss Wien*, vol. 136, pp. 1271–1306, 1927.
- [20] P. C. Carman, "Fluid flow through granular beds," *Transactions of the Institution of Chemical Engineers*, vol. 15, pp. 150–167, 1937.
- [21] P. C. Carman, *Flow of Gases through Porous Media*, Butterworths, London, UK, 1956.
- [22] P. Mostaghimi, M. J. Blunt, and B. Bijeljic, "Computations of absolute permeability on micro-CT images," *Mathematical Geosciences*, vol. 45, no. 1, pp. 103–125, 2013.
- [23] H. Pape, C. Clauser, and J. Iffland, "Variation of permeability with porosity in sandstone diagenesis interpreted with a fractal pore space model," *Pure and Applied Geophysics*, vol. 157, no. 4, pp. 603–619, 2000.
- [24] F. Civan, "Scale effect on porosity and permeability: kinetics, model, and correlation," *AIChE Journal*, vol. 47, no. 2, pp. 271–287, 2001.
- [25] A. Costa, "Permeability-porosity relationship: a reexamination of the Kozeny-Carman equation based on a fractal pore-space geometry assumption," *Geophysical Research Letters*, vol. 33, no. 2, Article ID L02318, 2006.
- [26] B. Yu, "Analysis of flow in fractal porous media," *Applied Mechanics Reviews*, vol. 61, no. 5, pp. 1239–1249, 2008.
- [27] P. Xu and B. Yu, "Developing a new form of permeability and Kozeny-Carman constant for homogeneous porous media by means of fractal geometry," *Advances in Water Resources*, vol. 31, no. 1, pp. 74–81, 2007.
- [28] C. Ö. Karacan, "Prediction of porosity and permeability of caved zone in longwall gobs," *Transport in Porous Media*, vol. 82, no. 2, pp. 413–439, 2010.
- [29] Y. Xia, J. Cai, E. Perfect, W. Wei, Q. Zhang, and Q. Meng, "Fractal dimension, lacunarity and succolarity analyses on CT images of reservoir rocks for permeability prediction," *Journal of Hydrology*, vol. 579, Article ID 124198, 2019.
- [30] P.-F. Shen, X.-S. Li, and G. Li, "Gas permeability and shape factor of natural sediments in the South China Sea," *Journal of Natural Gas Science and Engineering*, vol. 83, Article ID 103626, 2020.
- [31] D. Metha and M. C. Hawley, "Wall effect in packed columns," *Industrial and Engineering Chemistry Process Design and Development*, vol. 8, pp. 280–286, 1969.
- [32] J. Wu and B. Yu, "A fractal resistance model for flow through porous media," *International Journal of Heat and Mass Transfer*, vol. 50, no. 19–20, pp. 3925–3932, 2007.
- [33] D. Nemeč and J. Levec, "Flow through packed bed reactors: 1. Single-phase flow," *Chemical Engineering Science*, vol. 60, no. 24, pp. 6947–6957, 2005.
- [34] M. Safari, R. Gholami, M. Jami, M. A. Ananthan, A. Rahimi, and W. S. Khur, "Developing a porosity-permeability relationship for ellipsoidal grains: a correction shape factor for Kozeny-Carman's equation," *Journal of Petroleum Science and Engineering*, vol. 205, Article ID 108896, 2021.
- [35] J. Bear, *Dynamics of Fluid in Porous Media*, Elsevier, New York, NY, USA, 1972.
- [36] M. Kaviany, *Principles of Heat Transfer in Porous Media*, Springer-Verlag, New York, NY, USA, 2nd edition, 1995.

## Research Article

# A New Projection-Based Integrally Embedded Discrete Fracture Model and Its Application in Coupled Flow and Geomechanical Simulation for Fractured Reservoirs

Dawei Wu <sup>1,2</sup>, Yuan Di <sup>1,2</sup> and Yu-Shu Wu<sup>3</sup>

<sup>1</sup>College of Engineering, Peking University, Beijing 100871, China

<sup>2</sup>Institute of Energy, Peking University, Beijing 100871, China

<sup>3</sup>Petroleum Engineering Department, Colorado School of Mines, Golden CO 80401, USA

Correspondence should be addressed to Yuan Di; diyuan@mech.pku.edu.cn

Received 8 July 2021; Revised 16 November 2021; Accepted 18 January 2022; Published 23 February 2022

Academic Editor: Stefan Iglauer

Copyright © 2022 Dawei Wu et al. This is an open access article distributed under the Creative Commons Attribution License, which permits unrestricted use, distribution, and reproduction in any medium, provided the original work is properly cited.

The embedded discrete fracture model (EDFM) has been popular for the modeling of fractured reservoirs due to its flexibility and efficiency while maintaining the complex geometry of fracture networks. Though the EDFM has been validated for single-phase flow simulations, some recent cases show that the EDFM might result in apparent errors in multiphase flow situations. The projection-based embedded discrete fracture model (pEDFM) and the integrally embedded discrete fracture model (IEDFM) are two recently developed methods, which intend to improve the accuracy of the EDFM. In this study, a projection-based integrally embedded discrete fracture model (pIEDFM) is proposed, which combines the advantages of the pEDFM and the IEDFM. Similar to the pEDFM, the pIEDFM uses a kind of additional connections between fracture and nonneighboring matrix cells to obtain more physically authentic velocity fields. As a significant improvement, a semi-analytical cone-shaped pressure distribution that follows the IEDFM is adopted in the pIEDFM to capture the sharp pressure change near the fracture surfaces. Comparisons with benchmark results and explicit-fracture fine grid simulation results show that the pIEDFM provides accurate solutions using a moderate amount of grids. The proposed pIEDFM is also applied to coupled flow and geomechanical simulation for fractured reservoirs. Comparison of our coupled simulation results with that of the EDFM shows that the pIEDFM is applicable for the coupled simulation, and the different methods for matrix-fracture transmissibility between the pIEDFM and the EDFM may lead to deviations in stress fields predicted by geomechanical modeling, which eventually affects the oil production, water cut, and oil saturation profiles.

## 1. Introduction

Numerical simulation approaches for fractured reservoirs have drawn great attention in past decades. Due to the significant permeability difference between the less permeable rock matrix and the highly conductive fractures, modeling multiphase flow in fractured media has become challenging. Barenblatt et al. [1] first proposed a concept of dual porosity to describe the seepage process in fractured rocks. Warren and Root [2] extended the concept of dual porosity and developed the dual-porosity model. Kazemi et al. [3, 4] introduced the dual-porosity model into petroleum engineering and applied the method in the

modeling of fractured reservoirs. Later, a series of numerical approaches were developed as extensions of the dual-porosity model, including the dual-porosity dual-permeability model [5, 6], the triple-porosity dual-permeability model [7], and the multiple interacting continuum model [8]. All these models can be classified as dual-continuum models. Dual-continuum models provide an efficient way of simulating fractured reservoirs. However, the geometries of the fractures are lost in the assumption of dual-porosity models, and the real fracture network cannot be represented in dual-continuum models [9]. Panfili et al. [10] showed that the homogenization used in dual-continuum models could introduce unphysical fracture flows between disconnected

areas. Moinfar et al. [11] investigated the examples of reservoirs with complex fracture networks where dual-continuum models cannot provide precise solutions.

A discrete fracture model (DFM) [12–15] was developed to solve the limitations of dual-continuum models. In the discrete fracture model, every fracture is treated explicitly and individually, providing a more physical and realistic representation of fractures, especially with complex geometries [16, 17]. However, to adapt to the complex fracture networks, unstructured matrix grids are commonly used in the DFM, which causes difficulties in gridding. In fracture networks composed of microscale fractures, the generated unstructured grids are usually in large numbers, which causes high computational cost, making the DFM impractical in actual field studies [18].

The embedded discrete fracture model (EDFM) was proposed by Li and Lee [19] as an alternative to the DFM and dual-continuum models. In the EDFM, the Cartesian grids are used in matrix discretization to keep the efficiency of the method. The fractures are discretized explicitly as control volumes, also known as fracture elements. The fracture elements are embedded into their parent matrix grids through matrix-fracture connections. The EDFM has been successfully implemented in vertical fracture cases [19], nonvertical fracture cases [18], and nonplanar fracture cases [20, 21]. Some authors [22, 23] combined the EDFM with dual-continuum methods to model reservoirs with multiscale fractures. Moinfar et al. [24] applied the EDFM in coupled flow and geomechanical simulations of fractured reservoirs.

Though the EDFM has been validated in various studies of its accuracy for single-phase flow simulations, it may result in apparent errors in some cases for multiphase simulations. Figure 1 shows a matrix block  $M$  intersected by a fracture. The two matrix fractions of  $M$  separated by the fracture are marked as A and B. As illustrated in Figure 1(a), in the realistic situation, an incoming water flow that moves towards a fracture in the water flooding process first enters fraction B and then is split into two parts that move along ( $F_1$ ) and across ( $F_2$ ) the fracture, respectively. However, in the EDFM, the two fractions A and B are combined as an intact matrix block instead of being considered as two individual grids. Thus, the water flow across the fracture from fraction A to fraction B cannot be exhibited. Instead, the averaged flow between the fracture and the matrix block  $M$  is evaluated ( $F_{m-f}$ ), as shown in Figure 1(b). The water from fractions A and B can flow towards the fracture simultaneously, which increases the water flux that moves along the fracture and results in an “unphysical flux split” in the EDFM. Therefore, the water flux along the fracture is overestimated, and the water flux across the fracture is underestimated [25].

To solve this problem, a projection-based embedded discrete fracture model (pEDFM) is proposed by Tene and others. [26]. Jiang and Younis proved [25] that a more physical flux split could be achieved in the pEDFM, thus fixing the erroneous water displacement process predicted by the EDFM. Olorode et al. [27] extended the pEDFM to three-dimensional cases and investigated 3D compositional

modeling with the pEDFM. Rao et al. [28] modified the original pEDFM and developed a micro-translation algorithm to help select projection-face combinations.

Another limitation of the EDFM is the oversimplified assumption for pressure distribution in the matrix domain adjacent to fracture. In the EDFM, an approximate linear pressure distribution assumption is used around the fractures. However, a cone-shaped distribution of pressure is usually generated due to the large difference in permeability between matrix and fracture, as shown in Figure 2. The oversimplified assumption in the EDFM may lead to errors in calculating the transmissibilities of matrix-fracture connections [29]. An integrally embedded discrete fracture model (IEDFM) [30] has been proposed to improve the transmissibility calculation of the EDFM. In the IEDFM, the transmissibilities of matrix-fracture connections are derived semi-analytically, which obtains the more realistic pressure distribution near the fracture surfaces and improves the accuracy of modeling flow in fractured reservoirs. The IEDFM is later extended to the modeling of anisotropic fractured reservoirs [31].

A projection-based integrally embedded discrete fracture model (pIEDFM) is proposed in this study, which combines the advantages of the pEDFM and the IEDFM. Similar to the pEDFM, additional matrix-fracture connections are added in the pIEDFM between a fracture element and the nonneighboring matrix elements along the fracture projection directions. The transmissibilities of neighboring and nonneighboring matrix-fracture connections in the pIEDFM are derived semi-analytically using the methods in the IEDFM. The accuracy of the pIEDFM is validated by benchmark results and fine grid simulation results. The proposed pIEDFM is then applied in coupled flow and geomechanical simulation for fractured reservoirs. The applicability of the proposed numerical method is examined.

## 2. Governing Equations for Fractured Reservoir Simulation

**2.1. Mass Conservation Equations.** The mass conservation equations in fractured media are given as follows:

$$\frac{\partial}{\partial t}(\phi S_{\beta} \rho_{\beta}) + \nabla \cdot (\rho_{\beta} \mathbf{v}_{\beta}) = q_{\beta}^w + q_{\beta}^{fm}, \quad (1)$$

where  $\beta$  represents fluid phases,  $\phi$  is the porosity,  $S_{\beta}$  is the saturation of phase  $\beta$ ,  $\rho_{\beta}$  is the density of phase  $\beta$ ,  $\mathbf{v}_{\beta}$  is the velocity of phase  $\beta$ ,  $q_{\beta}^w$  is the flux term of phase  $\beta$  from wells, and  $q_{\beta}^{fm}$  is the flux term of phase  $\beta$  between matrix and fracture elements.

The velocity of phase  $\beta$  is defined by Darcy’s law:

$$\mathbf{v}_{\beta} = -\frac{k k_{r\beta}}{\mu_{\beta}} (\nabla P_{\beta} - \rho_{\beta} g \nabla Z) = -\frac{k k_{r\beta}}{\mu_{\beta}} \nabla \Psi_{\beta}, \quad (2)$$

where  $k$  is the absolute permeability,  $k_{r\beta}$  is the relative permeability of phase  $\beta$ ,  $\mu_{\beta}$  is the viscosity of phase  $\beta$ ,  $P_{\beta}$  is the pressure of phase  $\beta$ ,  $g$  is the gravitational acceleration,  $Z$  is the depth, and  $\Psi_{\beta}$  is the flow potential of phase  $\beta$ .

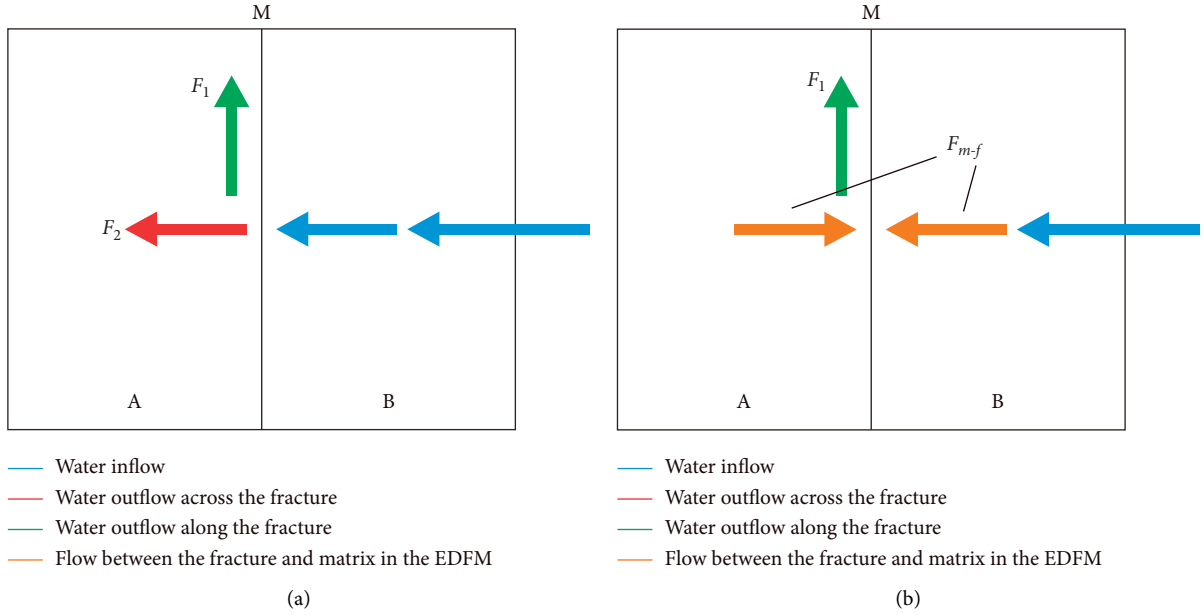


FIGURE 1: Flow process for water displacement across a fracture in (a) realistic scenario and (b) EDFM.

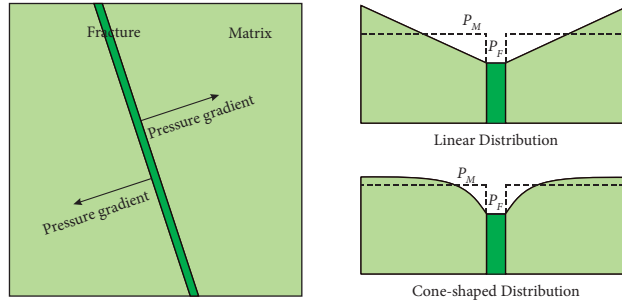


FIGURE 2: Illustration of linear and cone-shaped pressure distributions in fractured media.

Equation (1) is discretized using the control-volume finite difference scheme in space and first-order scheme in time, which gives the following:

$$\begin{aligned} & \left[ (\phi S_{\beta} \rho_{\beta})_i^{n+1} - (\phi S_{\beta} \rho_{\beta})_i^n \right] \frac{V_i}{\Delta t} \\ & = \sum_j F_{\beta,ij}^{n+1} + \sum_k F_{\beta,ik}^{fm,n+1} + Q_{\beta,i}^{W,n+1}, \end{aligned} \quad (3)$$

where subscript  $i$  denotes the values of element  $i$ , superscript  $n + 1$  represents the current time level, superscript  $n$  represents the previous time level,  $F_{\beta,ij}$  is the flow term for phase  $\beta$  between element  $i$  and element  $j$  where  $i$  and  $j$  are the same type of element (matrix or fracture),  $F_{\beta,ik}^{fm}$  is the flow term for phase  $\beta$  through the matrix-fracture

connection of element  $i$  and element  $k$ , and  $Q_{\beta,i}^W$  is the flux term of phase  $\beta$  from wells.

The flow terms  $F_{\beta,ij}$  and  $F_{\beta,ik}^{fm}$  are expressed as follows:

$$\begin{aligned} F_{\beta,ij} &= T_{ij} \left( \frac{\rho_{\beta} k_{r\beta}}{\mu_{\beta}} \right)_{ij+1/2} (\Psi_{\beta,j} - \Psi_{\beta,i}), \\ F_{\beta,ik}^{fm} &= T_{ik} \left( \frac{\rho_{\beta} k_{r\beta}}{\mu_{\beta}} \right)_{ik+1/2} (\Psi_{\beta,k} - \Psi_{\beta,i}), \end{aligned} \quad (4)$$

where subscripts  $ij + 1/2$  and  $ik + 1/2$  denote proper averages of properties at the interface, and  $T_{ij}$  and  $T_{ik}$  are the transmissibilities of the connections.

The transmissibility of a connection is the harmonic average of two half-transmissibilities:

$$\begin{aligned}
T_{12} &= \frac{T_1 T_2}{T_1 + T_2}, \\
T_1 &= \frac{A_{12} k_1}{d_1}, \\
T_2 &= \frac{A_{12} k_2}{d_2}.
\end{aligned} \tag{5}$$

where  $T_1$  and  $T_2$  are the half-transmissibilities of element 1 and element 2,  $k_1$  and  $k_2$  are the absolute permeabilities, and  $d_1$  and  $d_2$  are the distances from the centers of elements to the interface.

**2.2. EDFM.** The reservoir matrix is discretized using the Cartesian grids, and additional fracture elements are added to represent the fracture control volumes. Thus, there are three kinds of connections between elements in the EDFM: matrix-matrix, fracture-fracture, and matrix-fracture connections. For matrix-matrix and fracture-fracture connections, the transmissibilities can be derived geometrically from the two-point flux approximation (TPFA) using (5).

For matrix-fracture connection in 2D reservoir cases, the half-transmissibilities of matrix and fracture can be derived as follows:

$$\begin{aligned}
T_m &= \frac{2A_f k_m}{d_{fm}}, \\
T_f &= \frac{2A_f k_f}{d_f},
\end{aligned} \tag{6}$$

where  $A_f$  is the fracture surface area,  $k_m$  is the matrix permeability,  $k_f$  is the fracture permeability,  $d_f$  is the fracture center distance from the interface, which equals half of the fracture aperture, and  $d_{fm}$  is the equivalent distance between matrix and fracture elements.

Using the approximation of linear pressure distribution around fractures, the equivalent distance can be given as follows:

$$d_{fm} = \frac{\int r_{if} dV}{V}, \tag{7}$$

where  $r_{if}$  is the distance from fracture and  $V$  is the volume of the matrix.

### 3. Projection-Based Integrally Embedded Discrete Fracture Model

In the proposed pIEDFM, the connection relationship establishment follows the rules of the pEDFM, where additional connections are introduced between the fracture element and the nonneighboring matrix element along the fracture projection directions. As shown in Figure 3, the fracture element  $f$  has two projections on the boundary of matrix element  $i$ , which have the area of  $A_{mX}^P$  and  $A_{mY}^P$ , respectively. The fracture element  $f$  is connected to its

neighboring matrix element  $i$  and two nonneighboring matrix elements  $j$  and  $k$ . The criterion of selecting the matrix faces of fracture projections follows the work of Jiang and Younis [25]. The matrix faces that are closer to the fracture center are selected as the projected faces in each dimension.

For matrix-matrix connections, the projected areas of fractures are eliminated from the interface area. The modified interface area between matrix  $i$  and matrix  $j$  is given as follows:

$$\bar{A}_{ij} = A_{ij} - A_{mX}^P, \tag{8}$$

where  $A_{ij}$  is the original interface area between matrix  $i$  and matrix  $j$ , and  $A_{mX}^P$  is the fracture projection area along the  $x$ -direction. When a fracture cuts through the matrix elements, the matrix-matrix connection will be removed.

Figure 4 shows an example of the connection establishment in the pIEDFM and the EDFM. There are four matrix elements marked as M1, M2, M3, and M4. The two fractures are discretized into several fracture segment elements by the matrix block boundaries. The fracture segment elements represented by blue lines with red dots are marked as F1, F2, F3, F4, F5, and F6. In the EDFM, there are 4 matrix-matrix connections, 5 fracture-fracture connections, and 6 matrix-fracture connections. However, in the pIEDFM, 3 matrix-matrix connections, 5 fracture-fracture connections, and 14 matrix-fracture connections are included. The number of matrix-fracture connections increases in the pIEDFM due to the additional connections between the fracture segments and the nonneighboring matrix elements.

In the pIEDFM, the matrix-matrix and fracture-fracture connection transmissibilities can be directly derived using (5). The calculation formulations of matrix-fracture connection transmissibilities are derived on the basis of the IEDFM, where the fractures are considered as series of point sinks and the transmissibilities are solved semi-analytically. The pressure distribution inside a matrix can be derived from the point sinks that form the fracture, thus reproducing the cone-shaped distribution of pressure to improve the simulation accuracy of fluid exchange between matrix and fracture. In the pIEDFM, the transmissibility between the fracture and the neighboring matrixes and the transmissibility between the fracture and the nonneighboring matrixes are calculated separately.

Figure 5 presents a schematic for the calculation of matrix-fracture transmissibilities in the pIEDFM. In the vicinity of a fracture, the pressure of point  $X$  can be derived as the superposition of all the pressure drops caused by point sinks:

$$P_X(x, y) = \sum_{i=1}^{N_s} \frac{q_{S_i} \mu}{2\pi h k_m} \ln r_{iX} + C_p, \tag{9}$$

where  $h$  is the height of the strata,  $N_s$  is the number of point sinks,  $q_{S_i}$  is the flow rate of sink  $S_i$ ,  $r_{iX}$  is the distance between point  $X$  and sink  $S_i$ , and  $C_p$  is a constant related to the fracture pressure.

When fractures are assumed to be equipotential, selecting several reference points  $F_j$  on the fracture surface forms a linear equation system:

$$P_F = \sum_{i=1}^{N_S} \frac{q_{S_i} \mu}{2\pi h k_m} \ln r_{ij} + C_P \quad (j = 1, \dots, N_S), \quad (10)$$

where  $r_{ij}$  is the distance between reference point  $F_j$  and sink  $S_i$ .

The linear equation system can be rewritten as follows:

$$\sum_{i=1}^{N_S} \frac{\xi_i}{2\pi h} \ln r_{ij} = 1 \quad (j = 1, \dots, N_S), \quad (11)$$

where  $\xi_i$  is defined as follows:

$$\xi_i = \frac{\mu q_{S_i}}{k_m (P_F - C_P)}. \quad (12)$$

Solving the linear equation system gives the exact expression of pressure at point  $X$ :

$$P_X(x, y) = \sum_{i=1}^{N_S} \frac{\xi_i \ln r_{iX}}{2\pi h} (P_F - C_P) + C_P. \quad (13)$$

The transmissibility between the fracture element  $f$  and the neighboring matrix element  $m$  can be derived as follows:

$$T_{fm} = \frac{k_m}{\lambda - 1} \sum \xi_i \quad (14)$$

$$\lambda = \frac{1}{V_m} \iint \frac{\sum_{i=1}^{N_S} \xi_i \ln r_{iX}}{2\pi h} dV_X,$$

where  $V_m$  is the volume of matrix  $m$ .

Similarly, the transmissibility between the fracture element  $f$  and the nonneighboring matrix element  $m_p$  can be given as follows:

$$T_{fm_p} = \frac{k_m A_m^P}{(\lambda_p - 1)A} \sum \xi_i \quad (15)$$

$$\lambda_p = \frac{1}{V_{m_p}} \iint \frac{\sum_{i=1}^{N_S} \xi_i \ln r_{iX_p}}{2\pi h} dV_{X_p},$$

where  $V_{m_p}$  is the volume of matrix  $m_p$ ,  $A$  is the area of the interface, and  $A_m^P$  is the area of the fracture projection on the interface.

## 4. Modeling of Geomechanics

**4.1. Deformation of Fractures.** The deformation behavior of fracture is strongly stress-dependent and nonlinear. An empirical model based on experimental laboratory data is used to calculate the fracture moduli [32]. For a fracture under normal stress, Young's modulus is as follows:

$$E_F = \frac{k_{ni} w_0}{(1 - \sigma_n / \Delta u_{\max} k_{ni} + \sigma_n)^2}, \quad (16)$$

$$k_{ni} = -7.15 + 1.75 \text{JRC} + 0.02 \frac{\text{JCS}}{w_0}, \quad (17)$$

$$\Delta u_{\max} = -0.1032 - 0.0074 \text{JRC} + 0.02 \left( \frac{\text{JCS}}{w_0} \right)^{-0.251},$$

where  $k_{ni}$  is the initial fracture normal stiffness,  $w_0$  is the zero-stress fracture aperture,  $\sigma_n$  is the effective normal stress,  $\Delta u_{\max}$  is the maximum normal closure of fracture, JRC is the joint roughness coefficient, and JCS is the joint compressive strength.

The fracture aperture change under normal stress is given as follows:

$$\Delta w = \frac{\sigma_n}{k_{ni} + \sigma_n / \Delta u_{\max}}. \quad (18)$$

For a fracture under shear stress, the shear modulus is as follows:

$$G_F = K_j (\sigma_n)^{n_j} \left( 1 - \frac{\tau R_f}{\tau_{\text{peak}}} \right)^2, \quad (19)$$

$$K_j = -17.19 + 3.86 \text{JRC}$$

$$\tau_{\text{peak}} = \sigma_n \tan \left[ \text{JRC} \log_{10} \left( \frac{\text{JCS}}{\sigma_n} \right) + \varphi_r \right], \quad (20)$$

where  $K_j$  is the stiffness number,  $n_j$  is the stiffness exponent,  $\tau$  is the shear stress,  $\tau_{\text{peak}}$  is the peak shear stress,  $R_f$  is the failure ratio, and  $\varphi_r$  is the residue friction angle.

Deformation of a fracture under shear stress is the combination of horizontal shear displacement and vertical shear displacement, also known as fracture dilation. The horizontal shear displacement of a fracture is given as follows:

$$\delta_h = \frac{\tau L}{G_F}, \quad (21)$$

where  $L$  is the characteristic length of the fracture.

The vertical shear displacement (dilation) uses an empirical model given as follows [33]:

$$\delta_v = \begin{cases} \frac{1}{3} \tan\left(\text{JRClog}\left(\frac{\text{JCS}}{\sigma_n}\right)\right) \delta_h \left(2 \frac{\delta_h}{\delta_{h,\text{peak}}} - 1\right) \\ (\delta_h < \delta_{h,\text{peak}}), \\ \int_{\delta_{h,\text{peak}}}^{\delta_h} \tan\left(\text{JRClog}\left(\frac{\text{JCS}}{\sigma_n}\right)\right) \left(\frac{\delta_{h,\text{peak}}}{\delta_h}\right)^{0.381} d\delta_h \\ + \delta_{v,\text{peak}} (\delta_h \geq \delta_{h,\text{peak}}), \end{cases}$$

$$\delta_{h,\text{peak}} = 0.0077L^{0.45} \left(\frac{\sigma_n}{\text{JCS}}\right)^{0.34} \cos\left(\text{JRClog}\left(\frac{\text{JCS}}{\sigma_n}\right)\right),$$

$$\delta_{v,\text{peak}} = \delta_{h,\text{peak}} \tan\left(\frac{1}{3M_D} \text{JRClog}\left(\frac{\text{JCS}}{\sigma_n}\right)\right), \quad (22)$$

where  $\delta_{h,\text{peak}}$  is the peak horizontal shear displacement,  $\delta_{v,\text{peak}}$  is the peak vertical shear displacement, and  $M_D$  is a damage coefficient.

For a fracture under normal and shear stress, both normal aperture change and fracture dilation contribute to the overall fracture aperture change. Thus, the fracture aperture under stress is given as follows:

$$w_m = w_0 - \Delta w + \delta_v. \quad (23)$$

The fracture aperture in (23) is the average point-to-point distance between two fracture surfaces, which is defined as the ‘‘mechanical’’ aperture. However, actual fractures have rough walls and variable aperture, and the mechanical aperture is not appropriate in calculating the hydraulic conductivity of the fracture. The ‘‘hydraulic’’ aperture is determined by flow analysis and is better for describing the fracture conducting capacity. An empirical relationship between hydraulic aperture and mechanical aperture can be given as follows [34]:

$$w_h = \begin{cases} \frac{w_m^2}{\text{JRC}^{2.5}}, & (\delta_h \leq 0.75\delta_{h,\text{peak}}), \\ w_m^{0.5} \text{JRC}_{\text{mob}}, & (\delta_h \geq \delta_{h,\text{peak}}), \end{cases} \quad (24)$$

$$\text{JRC}_{\text{mob}} = \frac{\arctan(\tau/\sigma_n) - \varphi_r}{\log(\text{JCS}/\sigma_n)},$$

where  $\text{JRC}_{\text{mob}}$  is the mobilized joint roughness coefficient.

Generally, the hydraulic aperture of a fracture is smaller than the mechanical aperture due to the roughness and tortuosity of fracture walls.

**4.2. Mechanical Equilibrium Equation.** The governing equation of geomechanics, also known as the mechanical

equilibrium equation, is obtained from the momentum conservation law:

$$\rho \frac{d^2 \mathbf{u}^s}{dt^2} = \frac{\partial \boldsymbol{\sigma}}{\partial \mathbf{x}} + \rho \mathbf{f}, \quad (25)$$

where  $\rho = (1 - \phi)\rho_s + \phi \sum \rho_\beta S_\beta$  is the density of the fluid-solid mixture,  $\rho_s$  is the density of rock skeleton,  $\mathbf{u}^s$  is the displacement vector of rock skeleton,  $\boldsymbol{\sigma}$  is the total stress tensor, and  $\mathbf{f}$  is the body force, which is gravity in this work. In static analysis, the dynamic term in the left-hand side of (25) can be omitted.

In a fractured porous media, matrix and fracture are considered as two separate porous spaces that contain fluid, and the dual-porosity effective stress law is given as follows [35]:

$$\boldsymbol{\sigma}' = \boldsymbol{\sigma} + \alpha_M P_M \mathbf{I} + \alpha_F P_F \mathbf{I}, \quad (26)$$

where  $\boldsymbol{\sigma}'$  is the effective stress tensor,  $P_M$  is the average pressure of matrix blocks,  $P_F$  is the average pressure of fractures,  $\alpha_M$  is the Biot coefficient of matrix,  $\alpha_F$  is the Biot coefficient of fracture, and  $\mathbf{I}$  is the identity matrix.

Equation (25) is discretized using finite element method (FEM), which gives the following:

$$\mathbf{K} \Delta \mathbf{u}_N - \alpha_M \mathbf{K}_v \Delta P_M - \alpha_F \mathbf{K}_v \Delta P_F = \Delta \mathbf{F}, \quad (27)$$

where  $\mathbf{K} = \int_V \mathbf{B}^T \mathbf{D} \mathbf{B} dV$  is the nodal stiffness matrix,  $\mathbf{B}$  is the strain-nodal displacement matrix,  $\mathbf{D}$  is the elastic stiffness matrix,  $\Delta \mathbf{u}_N$  is the nodal displacement increment vector,  $\mathbf{K}_v$  is the volumetric stiffness vector,  $\Delta P_M$  and  $\Delta P_F$  are the average pressure increment in matrix and fractures, and  $\Delta \mathbf{F}$  is the external loading increment vector.

The establishment of the elastic stiffness matrix  $\mathbf{D}$  of a fractured porous media uses the equivalent continuum approach. In the local coordinate system of fracture, the compliance matrix can be written as follows:

$$\mathbf{C} = \gamma \mathbf{P} \mathbf{C}_M \mathbf{P} + (1 - \gamma) \mathbf{C}_F, \quad (28)$$

where  $\mathbf{C}$  is the compliance matrix of the equivalent jointed rock mass,  $\mathbf{C}_M$  and  $\mathbf{C}_F$  are the compliance matrixes for the rock matrix and fracture,  $\mathbf{P}$  is a coefficient matrix, and  $\gamma$  is the volume fraction of the rock matrix.

The compliance matrix in the global coordinate system  $\mathbf{C}_{\text{global}}$  can be obtained from coordinate transformation:

$$\mathbf{C}_{\text{global}} = \mathbf{T}^T \mathbf{C} \mathbf{T}, \quad (29)$$

where  $\mathbf{T}$  is the coordinate transformation matrix related to fracture orientation.

The elastic stiffness matrix  $\mathbf{D}$  is the inversion of the compliance matrix  $\mathbf{C}_{\text{global}}$ :

$$\mathbf{D} = \mathbf{C}_{\text{global}}^{-1}. \quad (30)$$

**4.3. Coupling Strategy.** An iterative coupling strategy is employed. The flow and geomechanical modules are invoked sequentially in every iterative loop. In each iteration, the flow simulation is first performed. The pressure and saturation



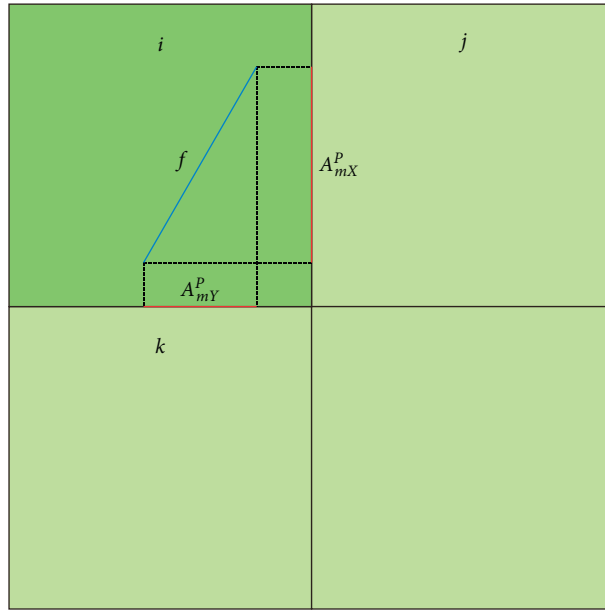


FIGURE 3: Illustration of connections in the pEDFM.

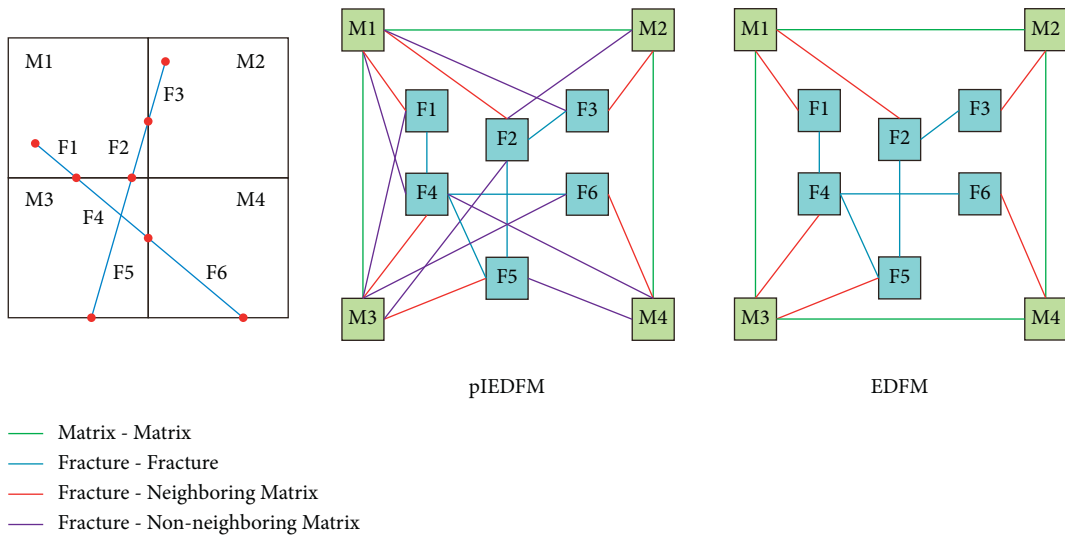


FIGURE 4: Schematic for connections in the pIEDFM and the EDFM.

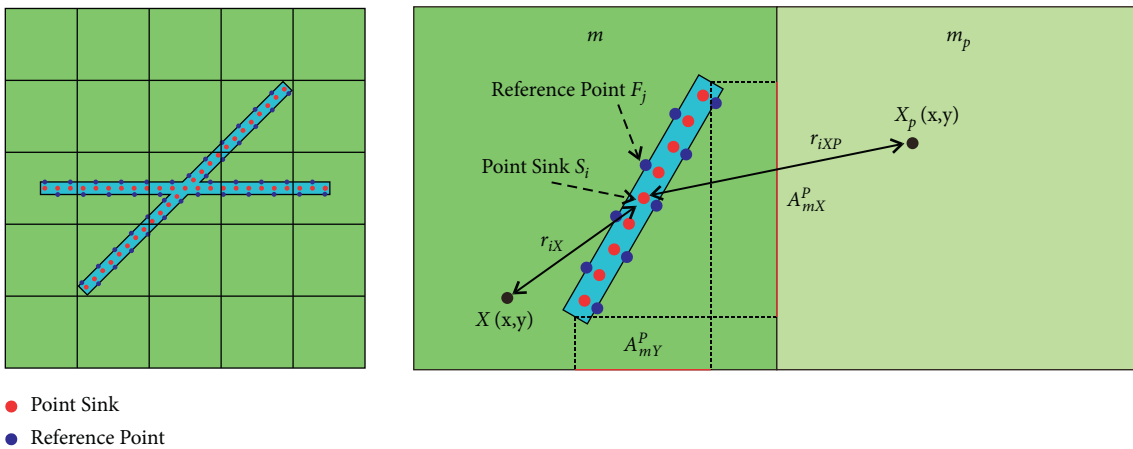


FIGURE 5: Schematic for the calculation of matrix-fracture transmissibility.

information from flow simulation results are then be passed to the geomechanical module to calculate the stress, strain, and displacement results. The changes in hydraulic properties, such as porosity and permeability, are updated before the flow simulation of the next iterative step. The update for hydraulic properties of the matrix and fractures is performed separately. For matrix, empirical relationships are used [36]:

$$\begin{aligned}\phi &= \phi_r + (\phi_0 - \phi_r)e^{-a\sigma_m'} \\ k &= k_0 e^{c(\phi/\phi_0 - 1)},\end{aligned}\quad (31)$$

where  $\phi_r$  is the residual porosity,  $\phi_0$  is the zero-stress porosity,  $\sigma_m'$  is the mean effective stress,  $k_0$  is the zero-stress permeability, and  $a$  and  $c$  are the update parameters.

In addition to the porosity and permeability updating functions, the capillary pressure in rock matrix is updated by the Leverett function:

$$P_c = P_{c0} \frac{\sqrt{k_0/\phi_0}}{\sqrt{k/\phi}}. \quad (32)$$

For fracture, the porosity and permeability are updated from the aperture change:

$$\phi_F = \frac{w}{w_0} \phi_{F0}. \quad (33)$$

$$k_F = k_{F0} \left( \frac{w}{w_0} \right)^2, \quad (34)$$

where  $\phi_{F0}$  is the zero-stress fracture porosity and  $k_{F0}$  is the zero-stress fracture permeability.

The fracture stiffness is also updated using (16) and (19) before the next iteration loop. The iteration process stops when the convergence criteria of both flow and geomechanical modules are reached. Then, the simulation process of the next time step starts.

## 5. Validation of the pIEDFM

**5.1. Validation with Benchmark Results.** The simulation results of the pIEDFM are compared with the benchmark results presented in the work of Karimi-Fard et al. [37]. As shown in Figure 6, a simple fractured reservoir with horizontal and vertical fractures is considered.

The porosity of the matrix is 0.20, and the permeability is 1 mD. The fracture aperture is 0.1 mm. The block is initially saturated with oil. Water is injected from the bottom left corner. The mixture of oil and water is produced from the top right corner. The viscosities of oil and water are 0.45 cP and 1.0 cP. The relative permeability curves in both rock matrix and fractures are linear. Capillary pressure is neglected in both matrix and fractures. The simulation is performed until 2 PV of water is injected.

Figure 7 shows a good agreement of the cumulative oil produced between the pIEDFM results and the fine grid results from the work of Karimi-Fard et al. Figure 8 shows the water saturation profiles across the reservoir after 0.1 PV, 0.3 PV, and 0.5 PV of water injection. For

comparison, the results from the EDFM simulations are presented as well. It is indicated that a better agreement is reached between the pIEDFM results and the benchmark results. The water flow across the fracture is underestimated in the EDFM, while the pIEDFM precisely recreates the water saturation profile with minor differences.

**5.2. Validation with Fine Grid Simulation.** The proposed pIEDFM is further validated by a reservoir case with one fracture, and the performances of the pIEDFM and the traditional EDFM are compared. The reservoir is 0.15 m  $\times$  0.15 m  $\times$  1.0 m in size and discretized by 30  $\times$  30 Cartesian grids in the pIEDFM and EDFM, as shown in Figure 9. The porosity of the matrix is 0.20. The permeability of the matrix is 1 mD. The fracture aperture is 0.5 mm. The initial stress of the reservoir is 10.0 MPa in the x-direction and y-direction and 25.0 MPa in the z-direction.

The reservoir is initially saturated with oil with the density of 800.0 kg/m<sup>3</sup> and the viscosity of 0.45 cP. Water with the density of 1000.0 kg/m<sup>3</sup> and the viscosity of 1.0 cP is injected from the bottom left corner. The injection rate is 0.1 m<sup>3</sup>/day. The mixture of oil and water is produced from the top right corner with fixed bottom hole pressure of 10.0 MPa. Linear relative permeability curves are used in both matrix and fractures, and capillary pressure is neglected. The initial pressure in the reservoir is 10.0 MPa. The simulation is run for 1800 seconds.

The pIEDFM and EDFM simulation results are compared to the fine grid explicit-fracture results, which are assumed to be exact. In the fine grid explicit-fracture simulation, the reservoir is discretized by 300  $\times$  300 Cartesian grids. The grid size equals the aperture of the fracture, and the fracture is treated explicitly as a series of highly permeable grids. The oil saturation profile after 1800 seconds of injection is shown in Figure 10 and used as the reference results in the following discussions.

In Figure 11, the oil saturation profiles of the pIEDFM and EDFM after 1800 seconds of injection are compared with the fine grid oil saturation profile. To support the discussion, an upscaling is performed on the fine grid oil saturation profile. It can be found that the oil saturation profile of the pEDFM shows better agreement with the fine grid results than the EDFM. Figure 12 presents the profiles of absolute oil saturation error of the pIEDFM and EDFM simulation results against the fine grid result, which also indicates that the pIEDFM outperforms the EDFM in recreating the realistic oil saturation distribution. In the EDFM results, the oil saturation around the center of the fracture is higher than the fine grid results, which shows that the water displacement across the fracture is underestimated. Besides, the oil saturation around the upper edge of the fracture is lower than the fine grid results, which shows that the water displacement along the fracture is overestimated.

The simulation scenarios are repeated using finer mesh grids (60  $\times$  60). Figure 13 and Figure 14 show the oil saturation profiles and oil saturation error profiles of the

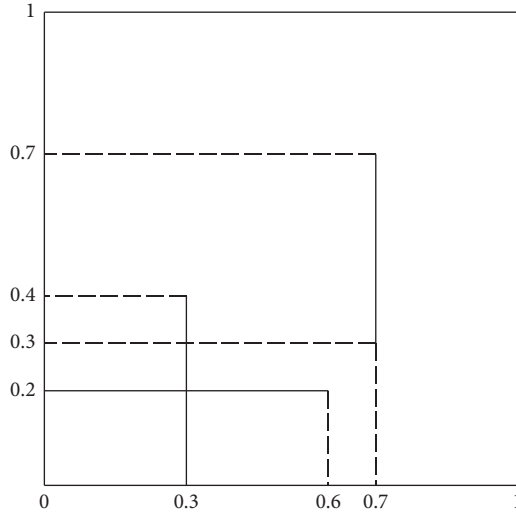


FIGURE 6: Configuration of the reservoir.

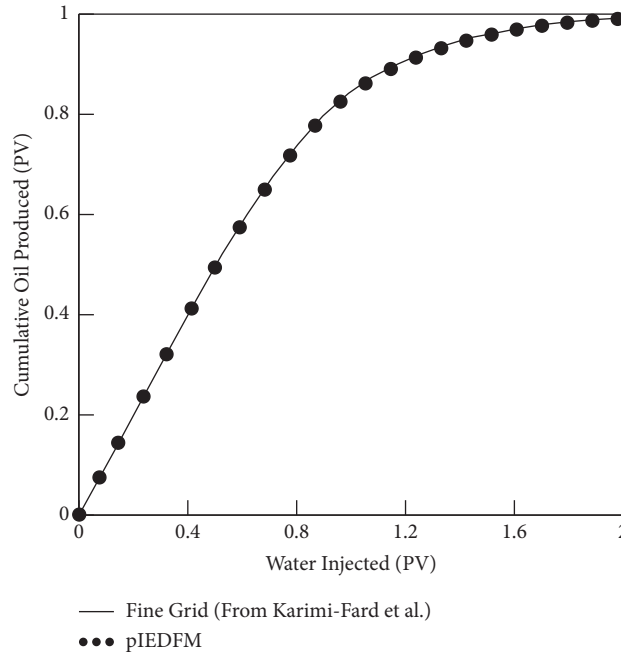


FIGURE 7: Comparison of cumulative oil produced.

pIEDFM and EDFM simulations after 1800 seconds of injection. After mesh refinement, the pIEDFM saturation profile shows a much better match with the fine grid results. However, the improvement of the EDFM results is limited, which indicates that mesh refinements cannot effectively reduce the errors caused by the unphysical flux split in the EDFM. By adding additional connections between the fractures and the nonneighboring matrix cells, the pIEDFM successfully captures the realistic flux split and reduces the errors in predicting oil saturation distributions. Figure 15 shows the flow fields of the oil phase in the fine grid, pIEDFM, and EDFM results, which demonstrates that the pIEDFM can obtain more realistic velocity fields than the EDFM around the fracture surfaces.

A mesh sensitivity analysis is performed to examine the performance of the pIEDFM at different grid densities. The  $L_2$  norm is introduced to represent the overall error of oil saturation:

$$L_2 = \sqrt{\frac{\sum_{i=1}^N (S_o^i - S_o^{i, \text{fine-grid}})^2}{N}}, \quad (35)$$

where  $N$  is the number of sample points and  $S_o^{i, \text{fine-grid}}$  is the upscaled fine grid oil saturation. Figure 16 compares the  $L_2$  norm of the pIEDFM and the EDFM at different grid sizes. The results show that the error of pIEDFM decreases with the refinement of matrix grids, which demonstrates the convergence of the method. The pIEDFM has better

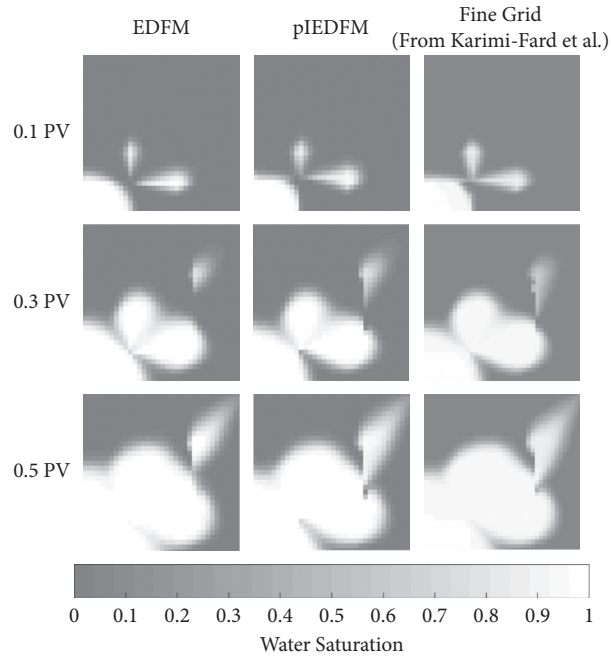


FIGURE 8: Water saturation profiles after 0.1 PV, 0.3 PV, and 0.5 PV of water injection.

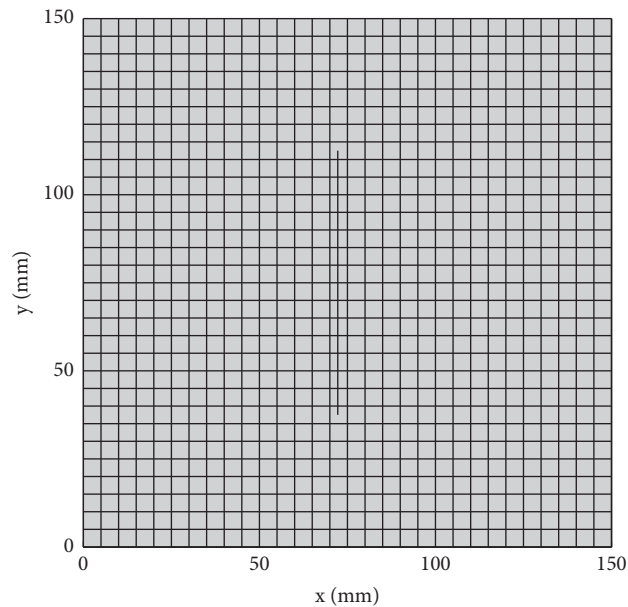


FIGURE 9: Mesh of the reservoir with one fracture.

agreement with the fine grid results than the EDFM at all grid sizes, showing the superiority of the proposed method.

To demonstrate the improvement of the pIEDFM in capturing the realistic pressure fields, pressure distributions in three slices of the reservoir that pass through the lower edge of the fracture, the center of the fracture, and the upper edge of the fracture, respectively, are investigated, as shown in Figure 17. Figure 18 shows the pressure distributions of the fine grid results in the three slices, which are obviously nonlinear.

Figure 19 shows the distributions of errors in the oil pressure of the pIEDFM and EDFM results compared with the fine grid results. It can be found that the pIEDFM has significant advantages in predicting the pressure distribution than the EDFM. In the EDFM, the nonlinear pressure changes near fractures cannot be considered, which results in apparent errors near the fracture surface, while the pIEDFM better captures the sharp pressure change in the vicinity of fractures.

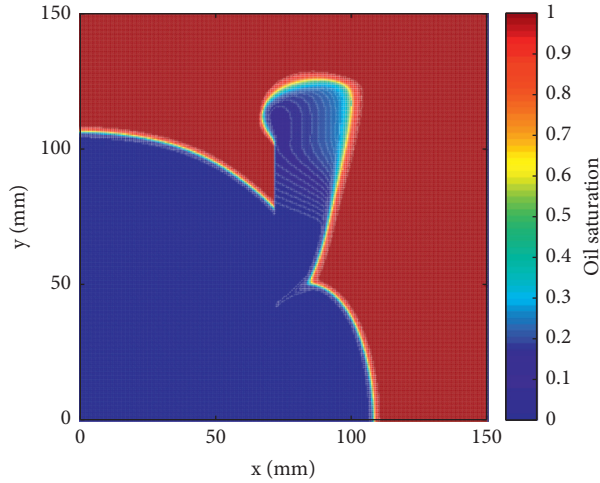


FIGURE 10: Oil saturation profile for the fine grid simulation after 1800 seconds of injection.

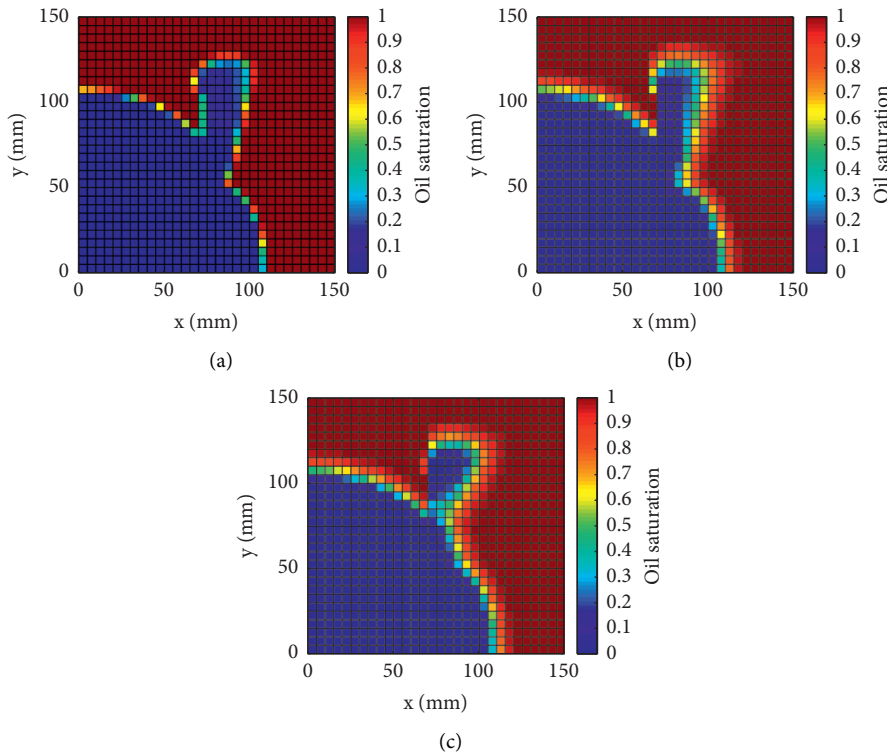


FIGURE 11: Oil saturation profiles for (a) upscaled fine grid simulation, (b) pIEDFM, and (c) EDFM after 1800 seconds of injection.

### 6. Applications of pIEDFM in Coupled Flow and Geomechanical Simulations

The proposed pIEDFM is applied in coupled flow and geomechanical reservoir simulations. The simulation scenarios are repeated using the original EDFM for comparisons of the reservoir geomechanical behaviors predicted by the pIEDFM and the EDFM.

A 2D reservoir with natural fractures that penetrate the entire depth of the reservoir is investigated, and the configuration of which is shown in Figure 20. The principle stress

directions of the reservoir are assumed to align with the axis directions, and zero internal friction angle is considered. Thus, the average strike angle of the fractures is  $\pm 45^\circ$  from the axis directions. The average length of the fractures is 10m. The reservoir is discretized by  $30 \times 30$  Cartesian grids. The porosity of the matrix is 0.15. The zero-stress permeability of the matrix is 5 mD. The zero-stress fracture aperture is 0.3 mm. The initial stress is 6.0 MPa in the x-direction and y-direction and 18.0 MPa in the z-direction. Under the initial stress condition, the initial matrix permeability is 2.023 mD, and the initial fracture aperture is 0.222 mm.

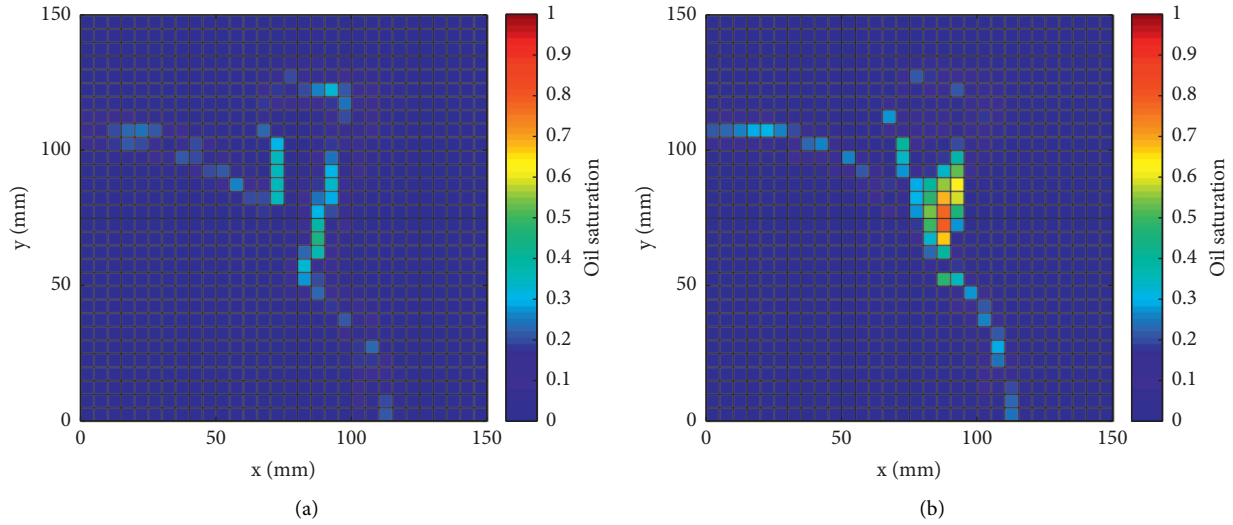


FIGURE 12: Oil saturation error profiles for (a) pIEDFM and (b) EDFM after 1800 seconds of injection.

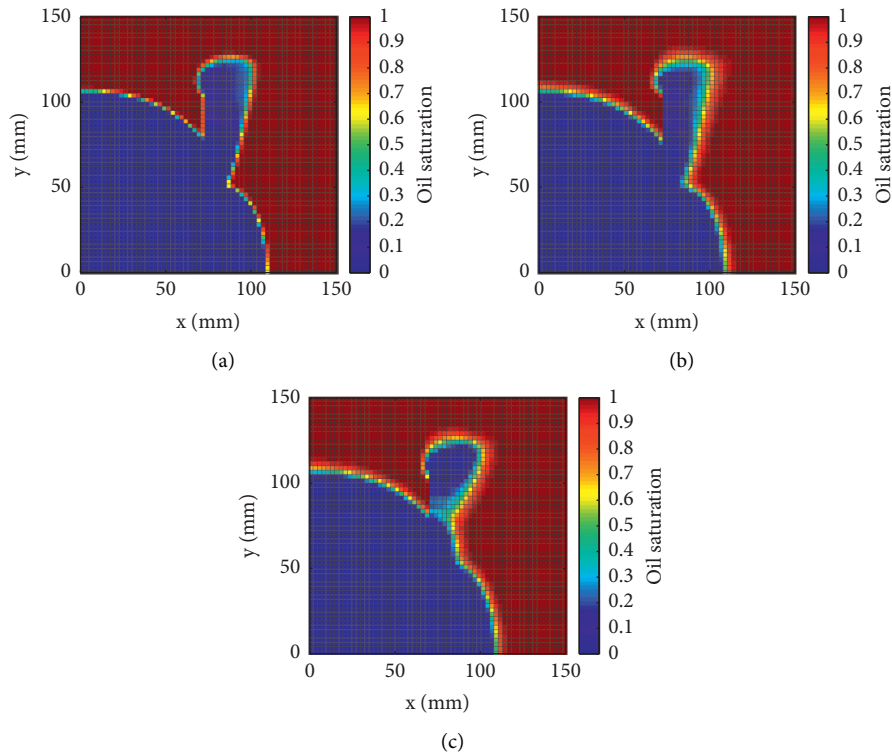


FIGURE 13: Oil saturation profiles after mesh refinement for (a) upscaled fine grid simulation, (b) pIEDFM, and (c) EDFM after 1800 seconds of injection.

The reservoir is initially saturated with oil with the density of  $800.0 \text{ kg/m}^3$  and the viscosity of  $5.0 \text{ cP}$ . Water is injected from an injection well located at the bottom left corner at the constant bottom hole pressure of  $20.0 \text{ MPa}$ . The water density is  $1000.0 \text{ kg/m}^3$ , and the water viscosity is  $0.9 \text{ cP}$ . The mixture of oil and water is produced from the top right corner with fixed bottom hole pressure of  $5.0 \text{ MPa}$ . The relative permeability for fracture is assumed to be linear, and the Brooks–Corey model is used for the relative permeability

of the matrix, as shown in Figure 21. The capillary pressure curve of the rock matrix is presented in Figure 22, while capillary pressure in the fractures is neglected. The initial pressure in the reservoir is  $20.0 \text{ MPa}$ . The mechanical parameters are listed in Table 1. The simulations are run for 20000 days of production.

Figure 23 compares the oil saturation profiles for the pIEDFM and EDFM simulations after 5000, 10000, and 20000 days of production. The oil saturation profiles

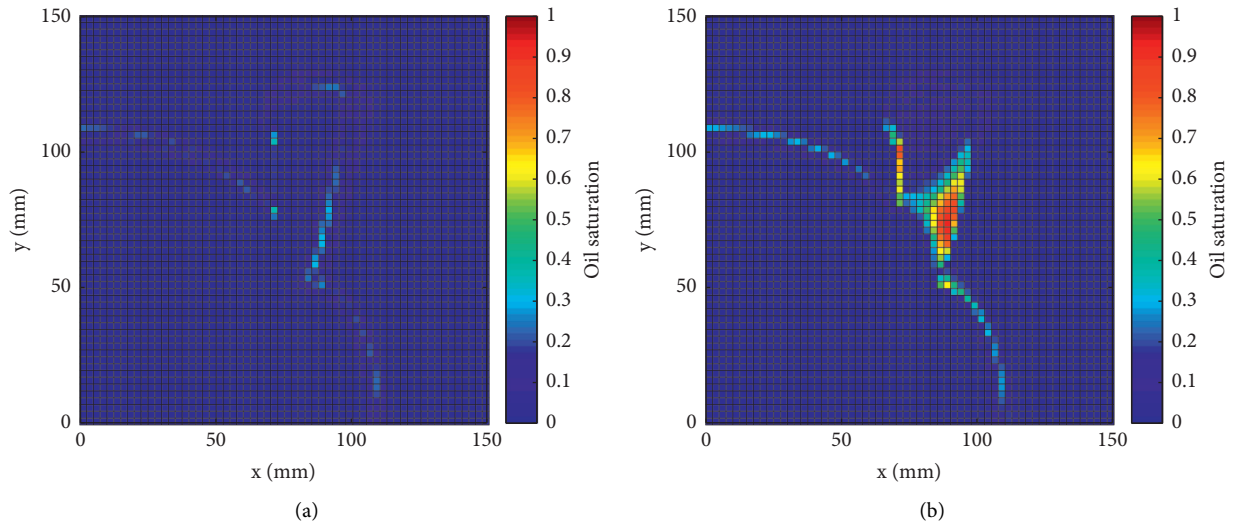


FIGURE 14: Oil saturation error profiles after mesh refinement for (a) pIEDFM and (b) EDFM after 1800 seconds of injection.

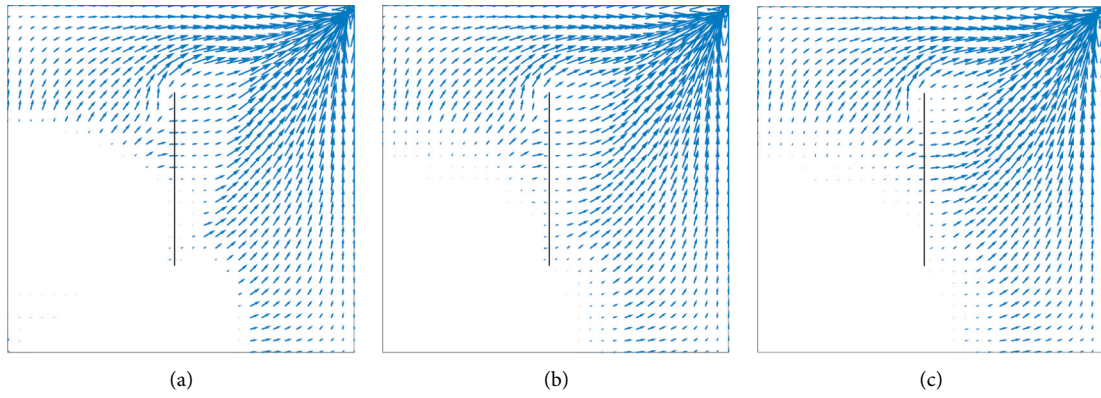


FIGURE 15: Oil phase flow fields for (a) upscaled fine grid simulation, (b) pIEDFM, and (c) EDFM after 1800 seconds of injection.

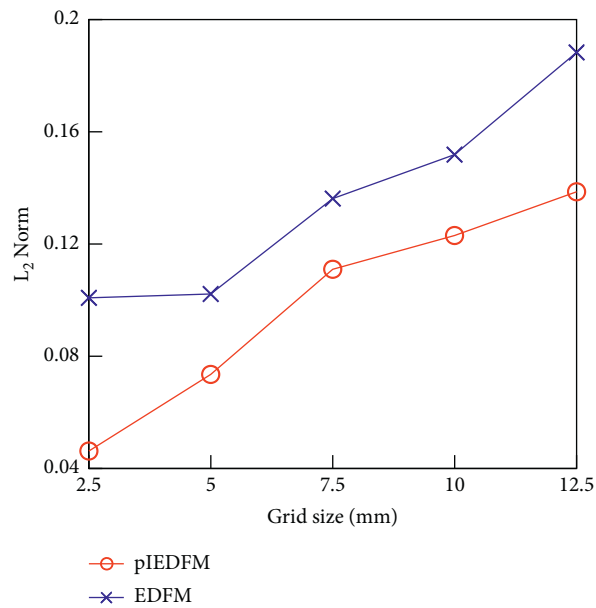


FIGURE 16:  $L_2$  norm against grid size.

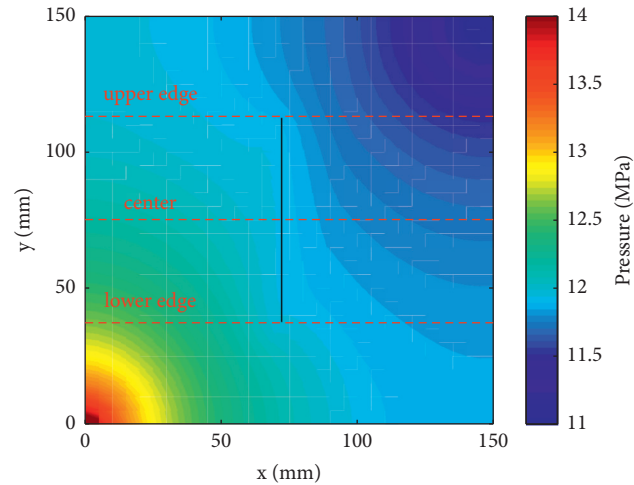


FIGURE 17: Oil pressure distribution of the fine grid simulation after 1800 seconds of injection.

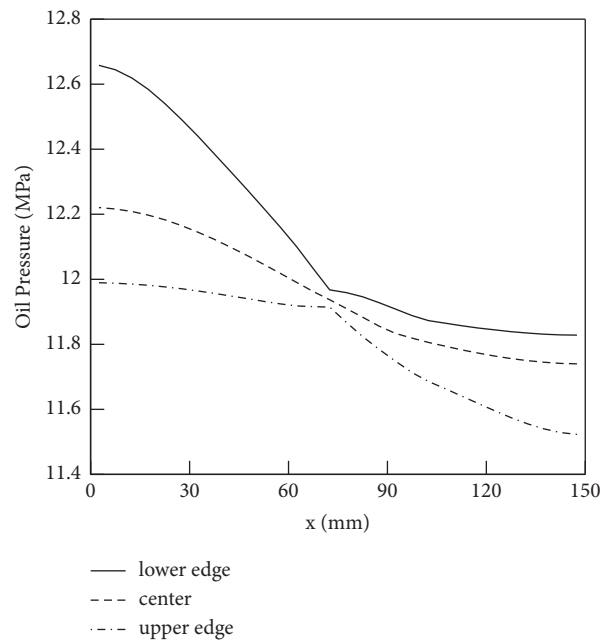


FIGURE 18: Oil pressure distributions in the slices of the fine grid pressure profile.

demonstrate that the water flow across the fractures is more prominent in the pIEDFM results. Due to the limitation in capturing the proper flux split through a fracture, the EDFM is incapable of representing the accurate multiphase displacements across a fracture.

Figure 24 shows the producing rate histories of oil and water from the production well. In both coupled and uncoupled simulations, the water producing rate predicted by the pIEDFM is larger than the EDFM, which can be attributed to the underestimation of water displacement process across fractures by the EDFM predictions. Due to the more prominent water flow across the fractures in the pIEDFM simulations, more oil is displaced from the reservoir, resulting in the higher steady-state oil rate. Figure 25 presents the cumulative oil and water production histories,

showing that the difference in the water displacement process between the pIEDFM and the EDFM affects not only the results of flow simulation but also the geomechanical performance of the reservoir. At 15000 days of production, the ratio of cumulative oil production in the coupled case to the uncoupled case is 92.7% for the pIEDFM simulation and 93.9% for the EDFM simulation, and the ratio of cumulative water production is 20.8% for the pIEDFM simulation and 19.0% for the EDFM simulation.

Figure 26 compares the water cut histories of pIEDFM and EDFM simulations. In uncoupled simulations, the water breakthrough time is day 6112 for the pIEDFM and day 5904 for the EDFM. The primary reason for the earlier water breakthrough in the EDFM simulations can be attributed to the overestimation of flow along the fractures since more



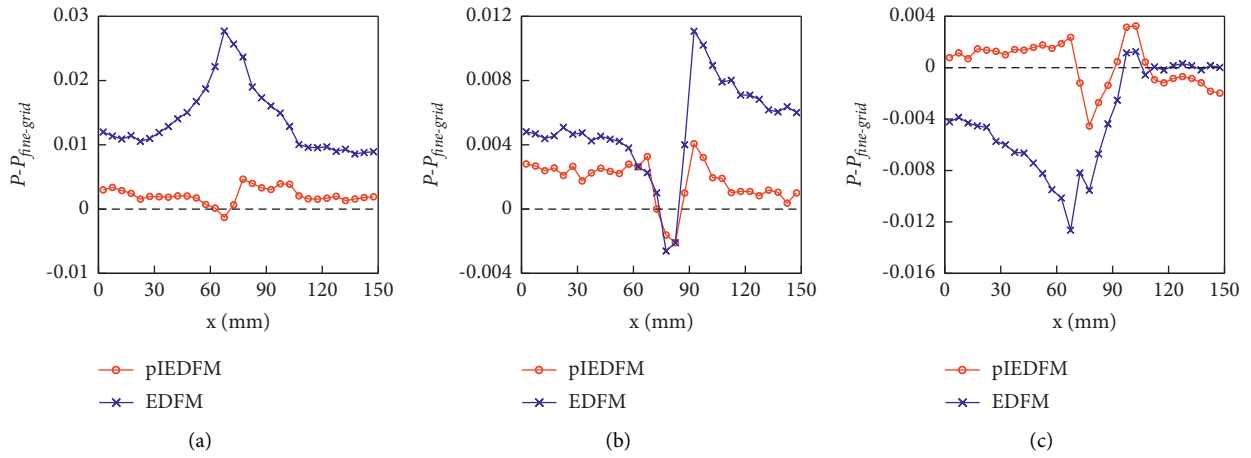


FIGURE 19: Oil pressure errors in the (a) lower edge, (b) center, and (c) upper edge slices.

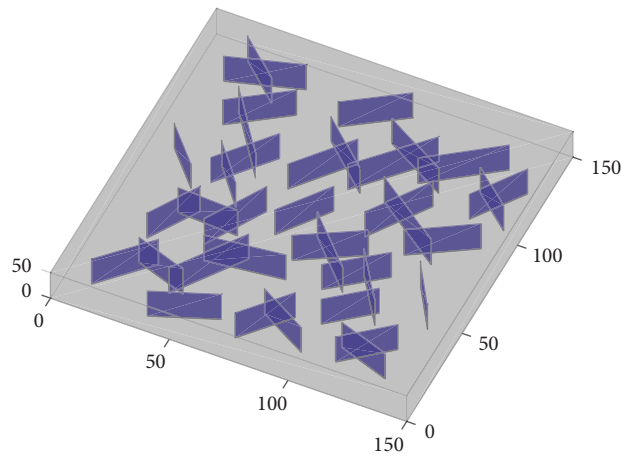


FIGURE 20: Structure of the fractured reservoir.

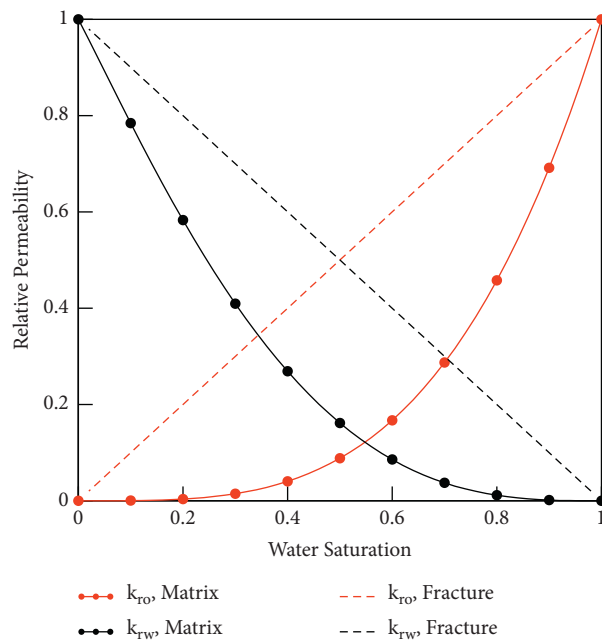


FIGURE 21: Relative permeability curves of the rock matrix and fracture.

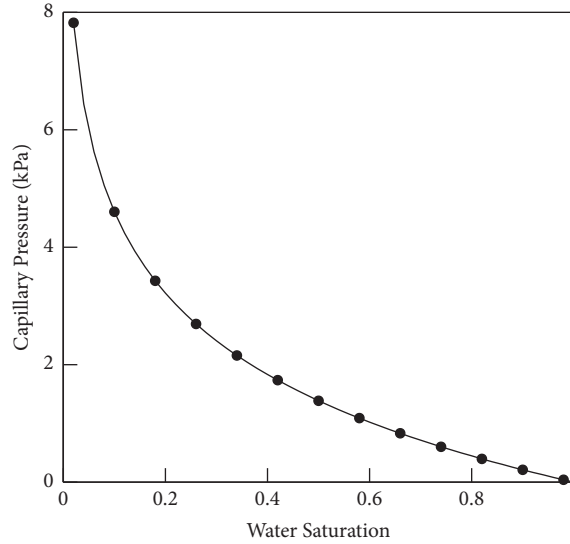


FIGURE 22: Capillary pressure of the rock matrix.

TABLE 1: Mechanical parameters.

Parameter	Value
Matrix Young's modulus, $E$	15.0 GPa
Matrix Poisson ratio, $\nu$	0.25
Joint roughness coefficient, JRC	12.0
Joint compressive strength, JCS	65.0 MPa
Failure ratio, $R_f$	1.0
Stiffness exponent, $n_j$	0.8
Fracture residue angle, $\varphi_r$	30.0
Matrix residue porosity, $\phi_r$	0.18
Matrix porosity update parameter, $a$	0.05 MPa <sup>-1</sup>
Matrix permeability update parameter, $c$	23.0
Biot coefficient of matrix, $\alpha_M$	0.875
Biot coefficient of fracture, $\alpha_F$	0.025

than half of the fractures orient towards the production well. When geomechanics is considered, the water breakthrough time will be delayed due to the permeability reduction in the rock matrix and the closure of fractures. In coupled simulations, the water breakthrough time is day 10926 for the pIEDFM and day 11157 for the EDFM. In contrast, the predicted water breakthrough time is earlier in the pIEDFM simulation, which indicates that the EDFM simulation is more affected by the coupling effect of geomechanics.

The mean effective stress profiles of the pIEDFM and the EDFM simulations after 20000 days of production are compared in Figure 27. The mean effective stress profiles show that the reservoir is more consolidated during the

depletion in the EDFM simulations, which is also supported by the contour map presented in Figure 28.

In coupled simulations, the error in the effective stress field leads to differences in permeability distribution between the pIEDFM and EDFM results. Figure 29 presents the permeability profiles for the pIEDFM and EDFM simulations at 20000 days of production, which indicates that the reservoir is more prone to the permeability reduction in the EDFM simulations. Figure 30 shows the distribution of differences in the permeability field between the pIEDFM and EDFM results, and the contour maps are compared in Figure 31. In most areas across the reservoir, the permeability of the pIEDFM results is higher than the EDFM

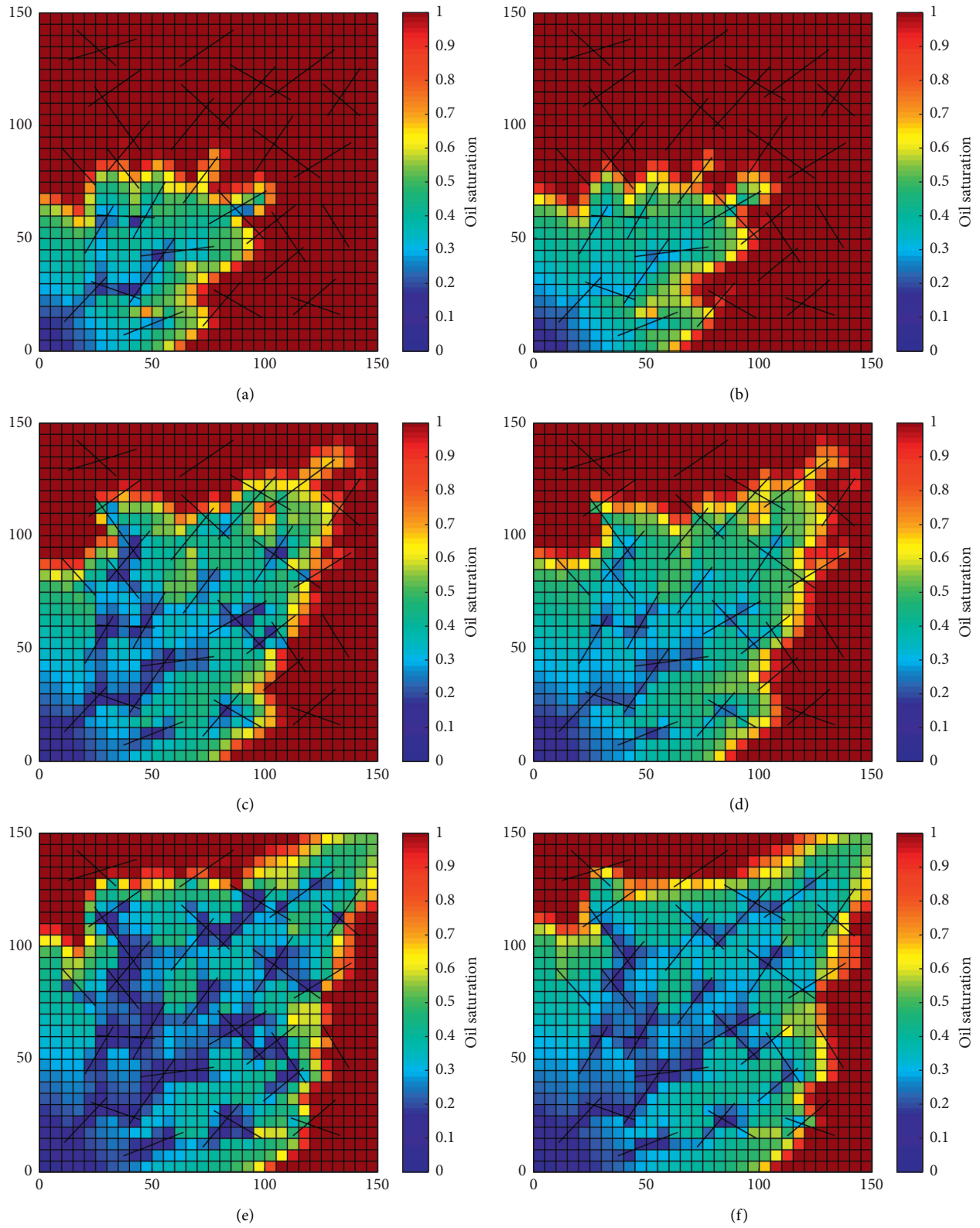


FIGURE 23: Oil saturation profiles for the pIEDFM simulation after (a) 5000 days, (c) 10000 days, and (e) 20000 days of production and the EDFM simulation after (b) 5000 days, (d) 10000 days, and (f) 20000 days of production.

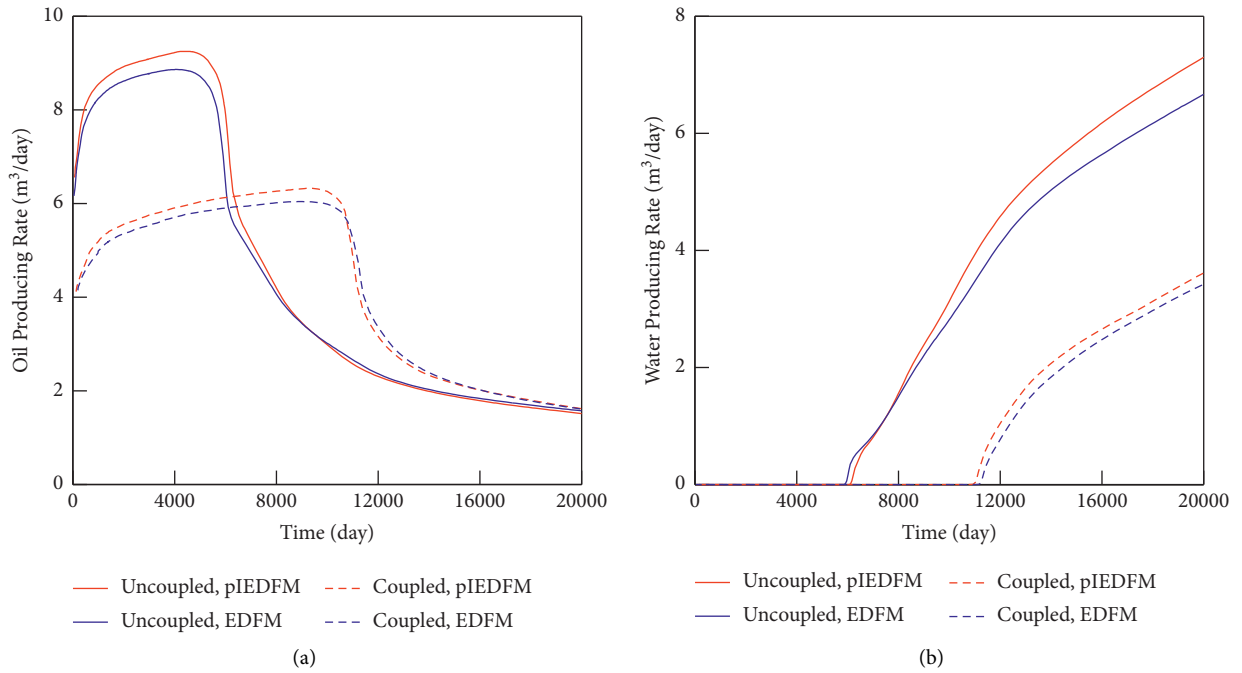


FIGURE 24: (a) Oil and (b) water producing rate histories.

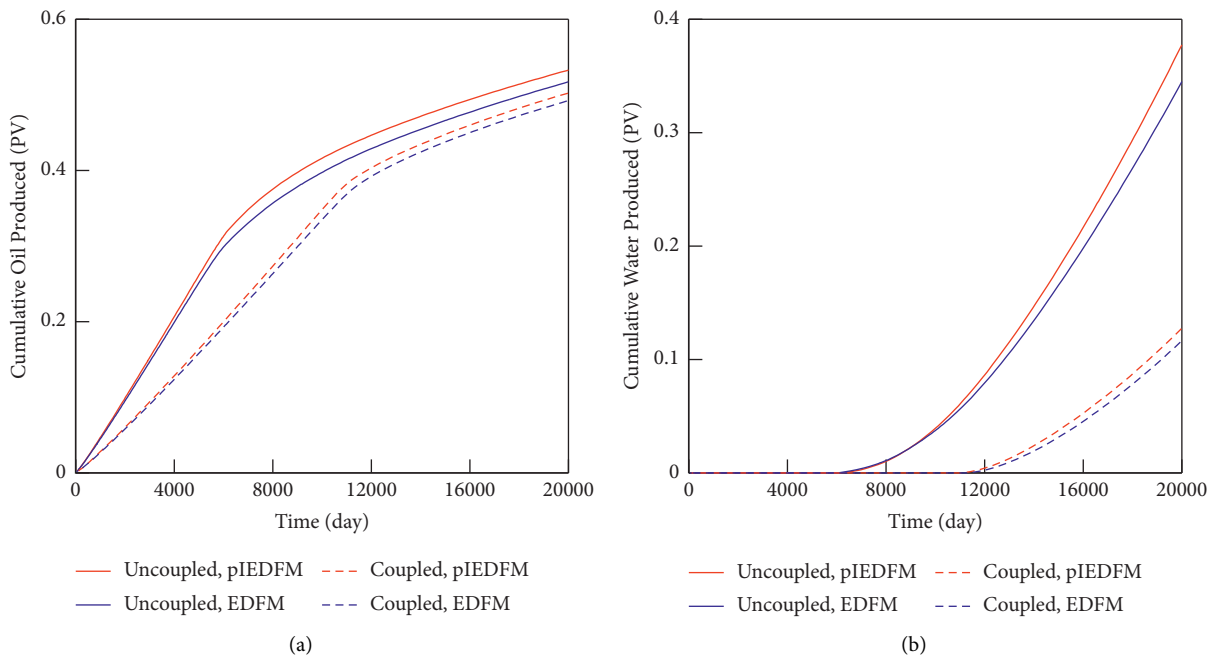


FIGURE 25: Cumulative (a) oil and (b) water production histories.

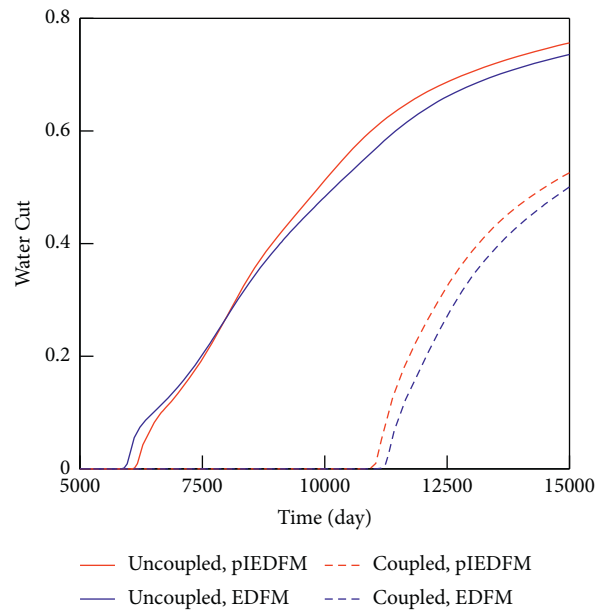


FIGURE 26: Water cut histories.

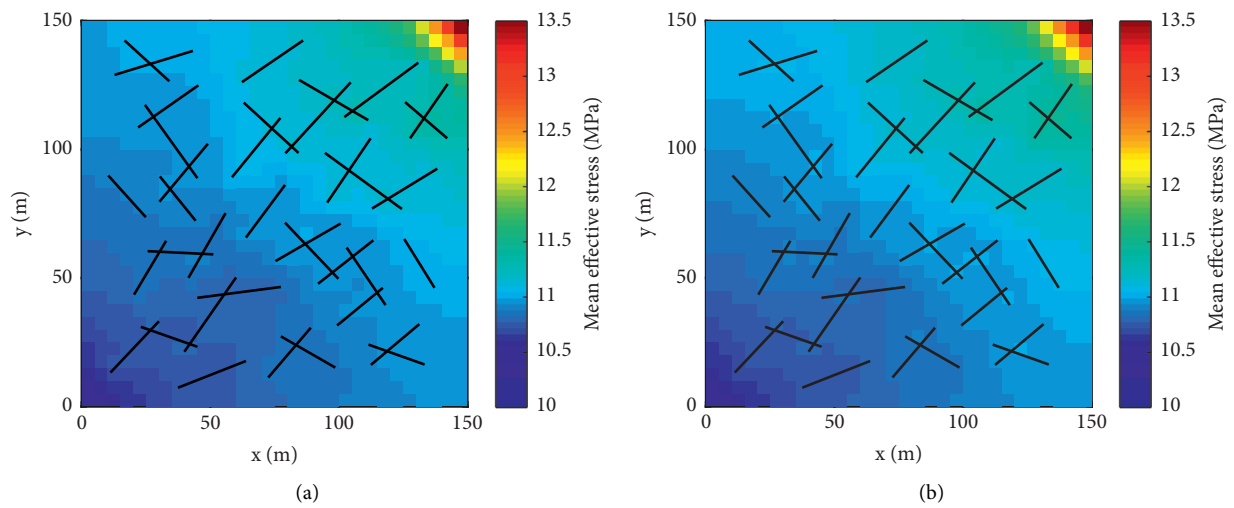


FIGURE 27: Mean effective stress profiles for (a) pIEDFM and (b) EDFM after 20000 days of production.

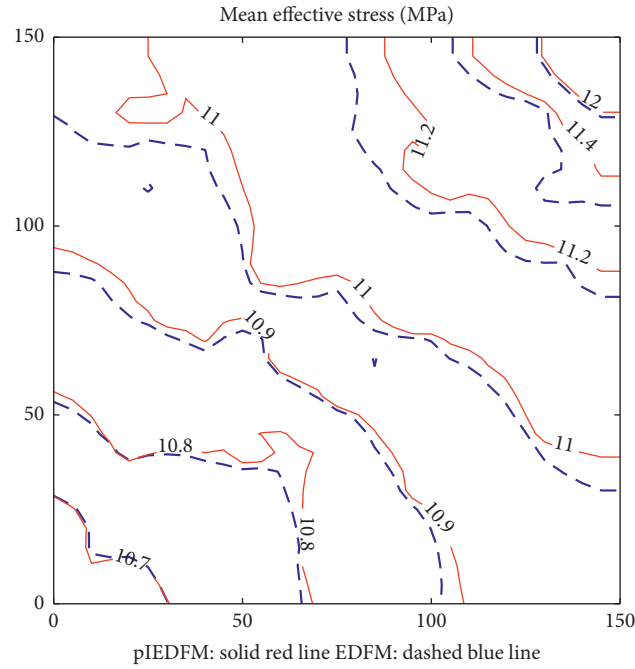


FIGURE 28: Contour map of mean effective stress field after 20000 days of production.

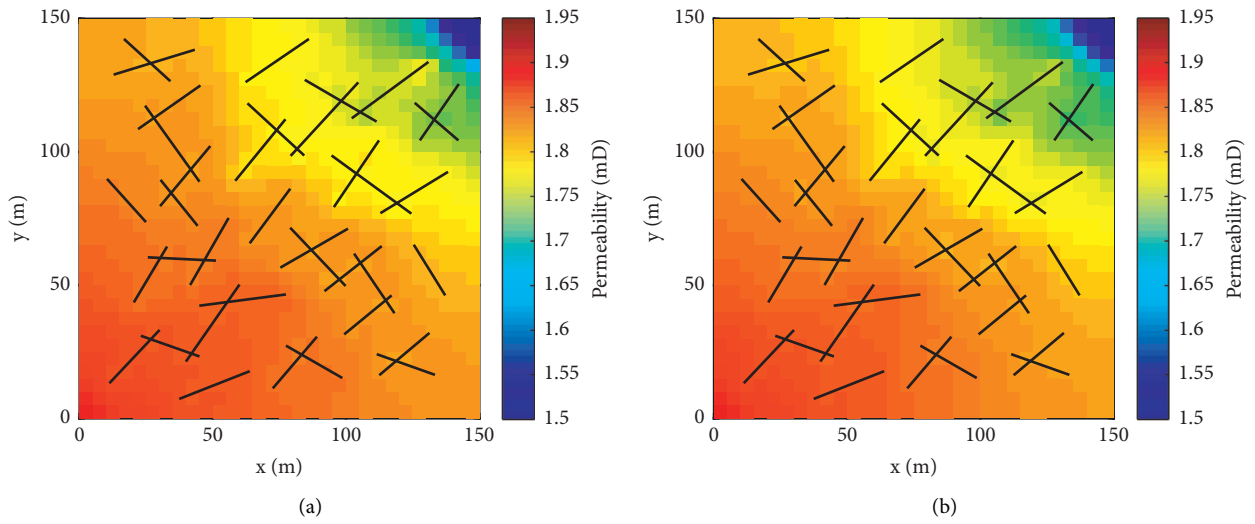


FIGURE 29: Permeability profiles for (a) pIEDFM and (b) EDFM after 20000 days of production.

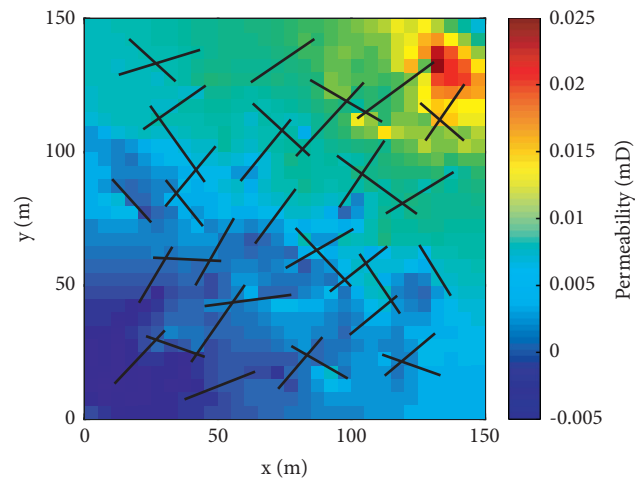


FIGURE 30: Permeability difference between the pIEDFM and EDFM results.

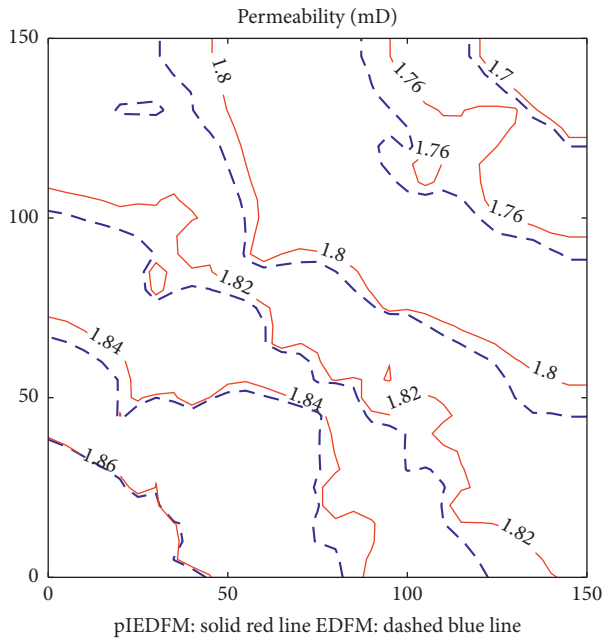


FIGURE 31: Contour map of permeability distribution after 20000 days of production.

results, and the main differences in permeability appear near the production well.

The apparent delay in water breakthrough time, the differences in effective stress, and permeability distributions demonstrate that the EDFM might lead to deviations in the results of coupled flow and geomechanical simulations, and the pIEDFM could effectively reduce these deviations.

## 7. Conclusions

A projection-based integrally embedded discrete fracture model is proposed. In the pIEDFM, additional connections are added between fracture elements and the non-neighboring matrix elements to provide a more realistic representation of the flux split process of water inflow across a fracture. The transmissibility of connections between the fracture element and the neighboring matrix element and the transmissibility of connections between the fracture element and the additional nonneighboring matrix element are calculated separately using a semi-analytical cone-shaped pressure distribution around the fracture surfaces. The accuracy of the pIEDFM is validated by the benchmark results and the explicit-fracture fine grid results. The performances of the pIEDFM and the EDFM are compared and discussed through a single fracture water flooding case. The pIEDFM is applied in coupled flow and geomechanical simulations, and the results are compared with that of the EDFM. The conclusions are as follows:

- (1) Good agreements in the saturation profiles are reached between the pIEDFM simulations and the benchmark results, which addresses the accuracy of the pIEDFM in modeling the multiphase flow process in fractured media.

- (2) Comparison of the EDFM and the pIEDFM results with the explicit-fracture fine grid simulation results shows that the pIEDFM can obtain a more physically authentic velocity field and better predict the multiphase flow process in fractured reservoirs. The oil saturation of the pIEDFM shows good agreement with the fine grid results using a moderate amount of meshes.
- (3) The pIEDFM has significant advantages in predicting the pressure distribution than the EDFM. Compared with the EDFM results, the pressure errors around the fracture surfaces are obviously reduced in the pIEDFM, showing that the nonlinear pressure change in the vicinity of the fracture can be captured.
- (4) Application of the pIEDFM in coupled flow and geomechanical simulations shows that the differences in predicting the water displacement process between the pIEDFM and the EDFM affect not only the results of production and saturation profiles but also the geomechanical performance of the reservoir. The biased water displacement process in the EDFM leads to deviations in the predictions of the water breakthrough time, the effective stress field, and the stress-dependent permeability distribution. Thus, it is promising to incorporate the pIEDFM in coupled flow and geomechanical simulations for fractured reservoirs.

## Data Availability

All data used can be found in our manuscript.

## Conflicts of Interest

The authors declare that there are no conflicts of interest regarding the publication of this study.

## Acknowledgments

This project was funded by the Joint Fund for Enterprise Innovation and Development of NSFC (Grant no. U19B6003-02-06) and the National Natural Science Foundation of China (Grant no. 51674010).

## References

- [1] G. I. Barenblatt, I. P. Zheltov, and I. N. Kochina, "Basic concepts in the theory of seepage of homogeneous liquids in fissured rocks [strata]," *Journal of Applied Mathematics and Mechanics*, vol. 24, no. 5, pp. 1286–1303, 1960.
- [2] J. E. Warren and P. J. Root, "The behavior of naturally fractured reservoirs," *Society of Petroleum Engineers Journal*, vol. 3, no. 3, pp. 245–255, 1963.
- [3] H. Kazemi, "Pressure transient analysis of naturally fractured reservoirs with uniform fracture distribution," *Society of Petroleum Engineers Journal*, vol. 9, no. 4, pp. 451–462, 1969.
- [4] H. Kazemi H, L. S. Merrill, and K. L. Porterfield, "Numerical simulation of water-oil flow in naturally fractured," *Society of Petroleum Engineers Journal*, vol. 16, no. 6, pp. 317–326, 1976.

- [5] J. R. Gilman, "An efficient finite-difference method for simulating phase segregation in the matrix blocks in double-porosity reservoirs," *SPE Reservoir Engineering*, vol. 1, no. 4, pp. 403–413, 1986.
- [6] J. R. Gilman and H. Kazemi, "Improved calculations for viscous and gravity displacement in matrix blocks in dual-porosity simulators," *Journal of Petroleum Technology*, vol. 40, no. 1, pp. 60–70, 1988.
- [7] Y.-S. Wu, Y. Di, Z. Kang, and P. Fakcharoenphol, "A multiple-continuum model for simulating single-phase and multiphase flow in naturally fractured vuggy reservoirs," *Journal of Petroleum Science and Engineering*, vol. 78, no. 1, pp. 13–22, 2011.
- [8] Y. S. Wu and K. Pruess, "A multiple-porosity method for simulation of naturally fractured petroleum reservoirs," *SPE Reservoir Engineering*, vol. 3, no. 1, pp. 327–336, 1988.
- [9] S. Geiger-Boschung, S. Matthai, and J. Niessner, "Black-oil simulations for three-component, three-phase flow in fractured porous media," *SPE Journal*, vol. 14, no. 2, pp. 338–354, 2007.
- [10] P. Panfili, A. Cominelli, and R. Colin, "Efficient and effective field scale simulation of hydraulic fractured wells: methodology and application," in *SPE Reservoir Characterisation and Simulation Conference and Exhibition UAE, Abu Dhabi*, 2015.
- [11] A. Moinfar, W. Narr, and M. H. Hui, "Comparison of discrete-fracture and dual-permeability models for multiphase flow in naturally fractured reservoirs," in *SPE Reservoir Simulation Symposium* Woodlands, Texas, USA, 2011.
- [12] J. Noorishad and M. Mehran, "An upstream finite element method for solution of transient transport equation in fractured porous media," *Water Resources Research*, vol. 18, no. 3, pp. 588–596, 1982.
- [13] M. Karimi-Fard and A. Firoozabadi, "Numerical simulation of water injection in fractured media using the discrete-fracture model and the Galerkin method," *SPE Reservoir Evaluation and Engineering*, vol. 6, no. 2, pp. 117–126, 2003.
- [14] T. H. Sandve, I. Berre, and J. M. Nordbotten, "An efficient multi-point flux approximation method for discrete fracture-matrix simulations," *Journal of Computational Physics*, vol. 231, no. 9, pp. 3784–3800, 2012.
- [15] S. K. Matthai, A. Mezentsev, and M. Belayneh, "Finite element-node-centered finite-volume two-phase-flow experiments with fractured rock represented by unstructured hybrid-element meshes," *SPE Reservoir Evaluation and Engineering*, vol. 10, no. 4, pp. 740–756, 2007.
- [16] O. M. Olorode, C. M. Freeman, and G. J. Moridis, "High-resolution numerical modeling of complex and irregular fracture patterns in shale gas and tight gas reservoirs," *SPE Reservoir Evaluation and Engineering*, vol. 16, no. 4, pp. 443–455, 2013.
- [17] O. Al-Hinai, G. Singh, and G. Pencheva, "Modeling multiphase flow with nonplanar fractures," in *SPE Reservoir Simulation Symposium* Woodlands, Texas, USA, 2013.
- [18] A. Moinfar, A. Varavei, and K. Sepehrnoori, "Development of an efficient embedded discrete fracture model for 3D compositional reservoir simulation in fractured reservoirs," *SPE Journal*, vol. 19, no. 2, pp. 289–303, 2014.
- [19] L. Li and S. H. Lee, "Efficient field-scale simulation of black oil in a naturally fractured reservoir through discrete fracture networks and homogenized media," *SPE Reservoir Evaluation and Engineering*, vol. 11, no. 4, pp. 750–758, 2008.
- [20] Y. Xu, J. S. Cavalcante Filho, and W. Yu, "Discrete-fracture modeling of complex hydraulic-fracture geometries in reservoir simulators," *SPE Reservoir Evaluation and Engineering*, vol. 20, no. 2, pp. 403–422, 2017.
- [21] W. Yu, Y. Xu, M. Liu, K. Wu, and K. Sepehrnoori, "Simulation of shale gas transport and production with complex fractures using embedded discrete fracture model," *AIChE Journal*, vol. 64, no. 6, pp. 2251–2264, 2018.
- [22] A. Moinfar, A. Varavei, and K. Sepehrnoori, "Development of a coupled dual continuum and discrete fracture model for the simulation of unconventional reservoirs," in *SPE Reservoir Simulation Symposium* Woodlands, Texas, USA, 2013.
- [23] W. Li, Z. Dong, and G. Lei, "Integrating embedded discrete fracture and dual-porosity, dual-permeability methods to simulate fluid flow in shale oil reservoirs," *Energies*, vol. 10, no. 10, p. 1471, 2017.
- [24] A. Moinfar, K. Sepehrnoori, and R. T. Johns, "Coupled geomechanics and flow simulation for an embedded discrete fracture model," in *SPE Reservoir Simulation Symposium* Woodlands, Texas, USA, 2013.
- [25] J. Jiang and R. M. Younis, "An improved projection-based embedded discrete fracture model (pEDFM) for multiphase flow in fractured reservoirs," *Advances in Water Resources*, vol. 109, pp. 267–289, 2017.
- [26] M. Tene, S. B. M. Bosma, and M. S. Al Kobaisi, "Projection-based embedded discrete fracture model (pEDFM)," *Advances in Water Resources*, vol. 105, pp. 205–216, 2017.
- [27] O. Olorode, B. Wang, and H. U. Rashid, "Three-dimensional projection-based embedded discrete-fracture model for compositional simulation of fractured reservoirs," *SPE Journal*, vol. 25, no. 4, pp. 2143–2161, 2020.
- [28] X. Rao, L. Cheng, R. Cao, P. Jia, H. Liu, and X. Du, "A modified projection-based embedded discrete fracture model (pEDFM) for practical and accurate numerical simulation of fractured reservoir," *Journal of Petroleum Science and Engineering*, vol. 187, Article ID 106852, 2020.
- [29] B. Yan, L. Mi, Z. Chai, Y. Wang, and J. E. Killough, "An enhanced discrete fracture network model for multiphase flow in fractured reservoirs," *Journal of Petroleum Science and Engineering*, vol. 161, pp. 667–682, 2018.
- [30] R. Shao and Y. Di, "An integrally embedded discrete fracture model with a semi-analytic transmissibility calculation method," *Energies*, vol. 11, no. 12, p. 3491, 2018.
- [31] R. Shao, Y. Di, D. Wu, and Y.-S. Wu, "An integrally embedded discrete fracture model for flow simulation in anisotropic formations," *Energies*, vol. 13, no. 12, p. 3070, 2020.
- [32] S. C. Bandis, A. C. Lumsden, and N. R. Barton, "Fundamentals of rock joint deformation," *International Journal of Rock Mechanics and Mining Sciences & Geomechanics Abstracts*, vol. 20, no. 6, pp. 249–268, 1983.
- [33] P. Asadollahi and F. Tonon, "Constitutive model for rock fractures: revisiting Barton's empirical model," *Engineering Geology*, vol. 113, no. 1–4, pp. 11–32, 2010.
- [34] R. Olsson and N. Barton, "An improved model for hydro-mechanical coupling during shearing of rock joints," *International Journal of Rock Mechanics and Mining Sciences*, vol. 38, no. 3, pp. 317–329, 2001.
- [35] M. Bai, "On equivalence of dual-porosity poroelastic parameters," *Journal of Geophysical Research: Solid Earth*, vol. 104, no. B5, pp. 10461–10466, 1999.
- [36] J. Rutqvist, Y.-S. Wu, C.-F. Tsang, and G. Bodvarsson, "A modeling approach for analysis of coupled multiphase fluid flow, heat transfer, and deformation in fractured porous rock," *International Journal of Rock Mechanics and Mining Sciences*, vol. 39, no. 4, pp. 429–442, 2002.
- [37] M. Karimi-Fard, L. J. Durlofsky, and K. Aziz, "An efficient discrete-fracture model applicable for general-purpose reservoir simulators," *SPE Journal*, vol. 9, no. 2, pp. 227–236, 2004.



## Research Article

# Characteristics of Pore-Throat in Tight Sandstones of the Jurassic Ahe Formation in the Northern Tarim Basin

Tong Lin,<sup>1</sup> Cong Tan ,<sup>1</sup> Xing Zhang,<sup>2</sup> Lei Zhao,<sup>3</sup> Hongxing Wei,<sup>2</sup> Lan Wang,<sup>1</sup> Xin Nie ,<sup>4</sup> and Xu Zeng<sup>1</sup>

<sup>1</sup>Research Institute of Petroleum Exploration & Development, PetroChina, Beijing 100083, China

<sup>2</sup>Research Institute of Exploration and Development, Tarim Oilfield Company, PetroChina, Korla, Xinjiang 834000, China

<sup>3</sup>Qingdao Geo-Engineering Surveying Institute (Qingdao Geological Exploration and Development Bureau), Qingdao 266000, China

<sup>4</sup>Key Laboratory of Exploration Technologies for Oil and Gas Resources, Yangtze University, Wuhan, Hubei 430100, China

Correspondence should be addressed to Cong Tan; 340330888@qq.com

Received 30 August 2021; Revised 30 November 2021; Accepted 16 December 2021; Published 28 January 2022

Academic Editor: Chenhao Sun

Copyright © 2022 Tong Lin et al. This is an open access article distributed under the Creative Commons Attribution License, which permits unrestricted use, distribution, and reproduction in any medium, provided the original work is properly cited.

In order to clarify the characteristics of pore-throat in tight sandstone reservoirs in the Dibei area of the Kuqa Depression in the Tarim Basin (Northwest China) and to make clear its impact on reservoir quality and productivity, microscopic observation and quantitative analysis of 310 tight sandstones in the Kuqa Depression are carried out by using various methods. Microscopic observation shows that the shapes of the pores are flat, oval, and long-narrow. A great number of throats connect the nanoscale pores in the form of a network. Quantitative analyses including RCMP (rate-controlled mercury penetration), HPMI (high-pressure mercury injection), NA (nitrogen adsorption), and routine and stress-dependent core analysis show that the peak of pores radius ranges from 125  $\mu\text{m}$  to 150  $\mu\text{m}$ , and the throat radius is in the range of 1  $\mu\text{m}$ -4  $\mu\text{m}$ . The throat space accounts for about 2/3 of the total space of the tight sandstones, which is the major storage space for natural gas. The space shape has a great influence on the reservoir seepage capacity, particularly under the condition of overburden pressure. The pores with throat radius greater than 300 nm have free fluid, and they contribute more than 98% of the reservoir permeability. The pore spaces with throat radius among 300 nm-52 nm can release fluids by reservoir stimulation. The pore-throats with radius < 52 nm cannot release the irreducible hydrocarbon fluids. In addition, formation pressure is easy to destroy tight sandstone reservoir. The research results will provide insights into the efficient recovery of natural gas in tight sandstones.

## 1. Introduction

Porosity and permeability are two major parameters for evaluating reservoir quality, and there is usually a good linear correlation between them [1–4]. However, in unconventional reservoirs (such as tight sandstone reservoir, shale reservoir, tight limestone, and volcanic reservoir), the correlation between porosity and permeability is not as close as that in conventional reservoirs [5–7]. More and more researchers have realized that the throat in the reservoir is the key factor to affect the seepage capacity of the reservoir, and it also determines the oil and gas production capacity of the reservoir [8–12]. Nelson [13] has introduced the distribution of throat sizes in different types of rocks. Based on his measured data, it is believed that changes in throat size have the most

significant impact on reservoir permeability. If the throat size changes by one order of magnitude, the permeability value will change by more than two orders of magnitude, so that throat is a critical parameter to evaluate reservoir quality. Pittman established a method to evaluate the quality of low-permeability reservoir by throat size as early as 1989 and achieved good results [14]. Reservoir quality evaluation with throat as a parameter, especially the evaluation of tight sandstone reservoirs, is relatively scientific and effective, and a lot of achievements have been made in related research ([14]; Lu et al., 1997; [15]; Wen et al., 2005; [16]; Li et al., 2007; [17, 18]; Li et al., 2012; [19]).

For the tight sandstone reservoirs, the size, distribution, and morphology of pore-throat are closely related to reservoir quality [20–22]. When Deng et al. [23] carried out

sandstone reservoir classification, they clearly pointed out that the long and narrow fractures between grains and quartz secondary enlarged edges have obvious control effect on reservoir quality and oil and gas production, and this type of fracture is very sensitive to stress.

The tight sandstone gas-bearing area of the Jurassic Ahe Formation in the eastern Kuqa Depression, Tarim Basin, located close to the source of China's "West to East Gas Transmission", is an important succession field of natural gas supply in the future. However, the understanding of tight sandstone gas reservoir in the Ahe Formation is still very limited, so that many wells have damaged the reservoir in the process of drilling or reservoir stimulation, which has seriously affected the tight gas productivity in this area. Therefore, it is necessary to study the microscopic characteristics of tight reservoirs in the Ahe Formation.

The main purpose of this study is to characterize the pore-throat of the tight sandstone reservoirs in the Dibei area of the Kuqa Depression in the Tarim Basin (Northwest China) and decipher the relationship between reserves and productivity with throat based on multiproxy of quantitative measurement. It is hoped to provide some enlightenment for the effective exploitation of natural gas in tight sandstone.

## 2. Geological Setting

**2.1. Tectonic Setting.** The Kuqa Depression is situated at the north edge of the Tarim Basin (Figure 1) [24]. It is a foreland depression which was formed in the subduction and collision of the Tarim plate to the Tianshan Mountain in the Triassic [25–28]. Influenced by the shallow layers of the South Tianshan orogenic belt thrusting southward, a series of E-W direction thrust faults are developed in the Kuqa foreland, thrusting towards the basin [29]. The Dibei area is located in the middle section of the Yiqikelike fault belt, the north margin of the Yangxia sag in the east of Kuqa Depression, with the characteristics of linear anticlines, faulted anticlines, and faulted nose structures (Figure 2) [24]. The fault belts began to thrust at the Late Miocene and continued until now. The tectonic movements in the Jurassic and Early Cretaceous led to a transformation from fault propagation folds to large-scale fault-bend anticlines in the Dibei area [30]. Compressional uplift and erosion during the Late Cretaceous resulted in the formation of current structural and sedimentary features in the study area [31–33].

**2.2. Features of Tight Sandstone Gas Reservoir.** More than ten wells have drilled the tight sandstone reservoir in the Ahe Formation ( $J_1a$ ) of the Lower Jurassic in the study area. Among them, Well Yn2 has obtained high-yield industrial gas flow, Well Yn5 is a low-yield gas well, and other wells have different levels of oil and gas, indicating that Dibei is an important area for oil and gas accumulation.

The reservoir of the Ahe Formation is buried in the depth between 4500 and 5000 m and consists of channel sandstone of the braided river delta plain. Laterally, the sandstones are continually distributed with an average thickness of 180–230 m. Vertically, the Ahe Formation can be divided into several fining-upward sedimentary cycles. From

bottom to top, conglomeratic sandstones of braided river channel in flood plain facies are gradually transformed to siltstones and mudstones of flood plain facies. Due to the erosion of the lateral migration of the channel sandstone in the floodplain facies, the top silt is generally absent, and the lower part of the channel is retained, forming several sets of incomplete cycles. The physical properties of the reservoir are positively correlated with the sedimentary cycle; the porosity and permeability of the coarse sandstone at the cycle bottom are apparently better than those of the fine sandstone at the top.

The sandstones of the Ahe Formation deposited under the control of the provenance and sedimentary facies belts of the southern Tianshan Mountains in the north [37–39]. The lithology is feldspar lithic sandstone or lithic sandstone, with moderate particle sorting properties, and mainly composed of the coarse sandstone, conglomeratic sandstone, and medium sandstone. The sandstone is compact and has almost no macroscopic dissolved pores in cores, but dissolved fractures and tectonic fractures are observed in several wells.

## 3. Samples and Methods

56 samples of 7 wells were collected from the tight sandstone of the Ahe Formation in the study area (Figure 1). All the samples are from the depth of 4000–5000 m except for the samples from Well Mn1 in the eastern part of the study area are at the depth of 965–1150 m. The length of the cylindrical core samples is 5–12 cm, and the cross-sectional diameter is 2.5 cm. Series of matching analyses were carried out for the 56 samples (Table 1), including thin section (CTS), scanning electron microscope (SEM), confocal laser scanning microscope (CLSM), rate-controlled mercury penetration (RCMP), high-pressure mercury injection (HPMI), nitrogen adsorption (NA), porosity and permeability analysis under normal pressures (PPNP), and overburden pressures (PPOP).

Before grinding thin sections, the samples were injected with epoxy resin of the mixture of ferrocyanide and alizarin red under vacuum pressure, so that the pore space of sandstone reservoir can be clearly observed under the single polarized light microscope, and the characteristics and content of calcite cement can be easily identified. Similarly, when grinding laser confocal thin sections, a special enhanced fluorescent agent was injected into the samples; therefore, the subtle cracks which cannot be observed in casting sections can be identified by the intense fluorescence under laser excitation.

**3.1. RCMP.** RCMP (rate-controlled mercury penetration) experiment was conducted on the ASPE-730 model equipment from American Coretest Systems Company. Before analysis, the plunger samples were washed and dried, and the porosity and permeability were measured. Then, the samples were immersed in mercury solution after vacuum, the interfacial tension and contact angle were kept unchanged, and mercury was injected into the core at a very low constant speed (0.00005 ml/min). When the pressure reached at 900 psi (about 6.2 MPa), the experiment ended. During the experiment, real-time monitoring and automatic

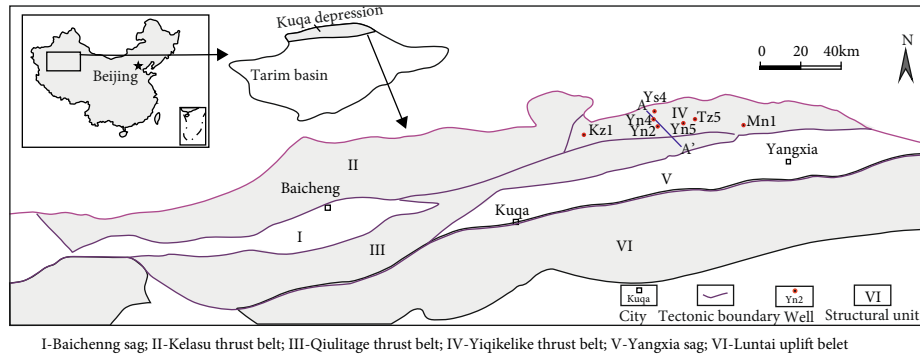


FIGURE 1: Regional, geological, and structural map of Dibe area in Kuqa Depression, Tarim Basin, Northwestern China (modified from [34–36]).

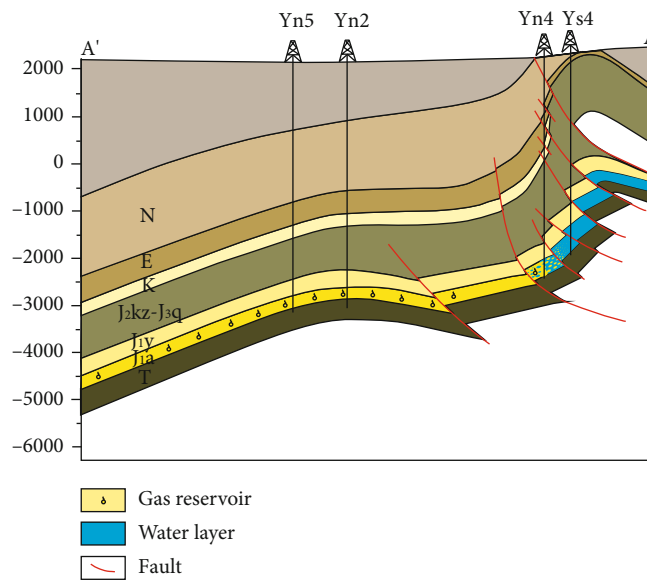


FIGURE 2: Structural section map of east Kuqa Depression.

TABLE 1: Analysis items and number of sandstone samples in the study area.

Well no.	Analysis items						PPNP and PPOP
	CTS	SEM	CLSM	RCMP	HPMI	NA	
Yn5	16	16	16	3	16	16	16
Yn2	10	10	10			10	10
Yn4	13	13	13		11	13	11
Ys4	8	8	8			8	
Kz1	2	2	2		2	2	2
Tz2	3	3	3		3	3	3
Mn1	4	4	4	1	4	4	4

data acquisition and output were carried out by the computer system. The pore structure information was obtained according to the rise and fall of mercury pressure.

3.2. *HPMI*. The HPMI (high-pressure mercury injection) experiment was carried out on the full automatic AutoPore

IV9520 mercury injection apparatus. The pore diameter is 3 nm-1000  $\mu\text{m}$ , and the volumetric accuracy of mercury injection and ejection is less than 0.1  $\mu\text{l}$ ; the highest injection pressure can be 414 MPa. All the samples were made into core columns and dried for 24h before conducting this experiment.

3.3. *NA*. The NA (nitrogen adsorption) experiment was carried out by using the QUADRASORB SI specific surface area and porosity analyzer made by American Quanta Chrome Company. The pore diameter measuring range of the instrument is 0.35-400 nm. Before the experiment, the samples were vacuum pretreated at 150°C for 24 hours, and then, the high-purity nitrogen (with purity higher than 99.999%) was used as adsorbate to measure nitrogen adsorption capacity under different pressures at -195.8°C. Taking the relative pressure as X-axis and adsorption capacity of unit sample weight as Y-axis, nitrogen adsorption-desorption isothermal lines were drafted. According to the two BET constant formulas, the BET straight line graph with relative pressures between 0.05 and 0.35 was drawn to obtain the

specific surface area of the samples. The BJH (Barrett-Joyner-Halenda) method was applied to calculate the desorption branch of the nitrogen adsorption isothermal line to obtain the pore size distribution.

The variation law of the porosity and permeability along with the overburden pressures can be found out by the porosity and permeability analysis under net overburden pressures; therefore, the true value in formation conditions can be simulated. It is very important for tight sandstone gas reservoir with strong stress sensibility. The pressure of the reservoir in the study area is 82 MPa, and the simulated test pressure scope of the instrument is among 2.1~67.6 MPa. Affected by the instrument performance, the maximum net overburden pressure is 55 MPa. The experiment process was recorded by measuring the porosity and permeability at one point every 5 MPa. We can infer the characteristics of porosity and permeability from the variation of porosity and permeability with pressure.

## 4. Results

### 4.1. Micro-Observation Characters of Reservoir Spaces

**4.1.1. Microscope.** It is found that the shape and distribution of pores are obviously influenced by the microfractures. The dissolved pores are mainly developed along the microfractures (Figures 3(a) and 3(b)). The pore profiles are elongated elliptic, and their long axis directions are coincident with the extension directions of the microfractures (Figure 3(b)). Some dissolved pores can form macropores with the long axis perpendicular to the fracture due to dissolution expansion (Figure 3(a)). Another manifestation of pores affected by microfractures is “clustering development of micropores”, that is, the dissolved micropores “clustered” to form a dissolution band (Figure 3(c)). Under the microscope, the micropores near the center of the band develop intensively, while the number of micropores far away from the center of the band decreases and gradually becomes isolated. However, some microfractures do not play a role in the dissolution of pores. These fractures are characterized by clean and free of impurities, parallel distribution of several fractures, large opening width of fractures (0.15~0.5 mm), and concave convex confrontation on both sides of fractures (Figure 3(d)).

The pore morphology of the Ahe Formation can be classified into three types: (1) short-axis pores: the pores are nearly round with smaller length/width ratio (Figure 3(a)); (2) long-axis pores: the pores are in apparently flat oval shape (Figure 3(b)), and the length of the long axis is 3 to 10 times of the short axis; (3) lamellar pores: the pores are in long-narrow lamellar shape (Figure 3(d)). The major pore shapes in the study area are long-axis pores and lamellar pores.

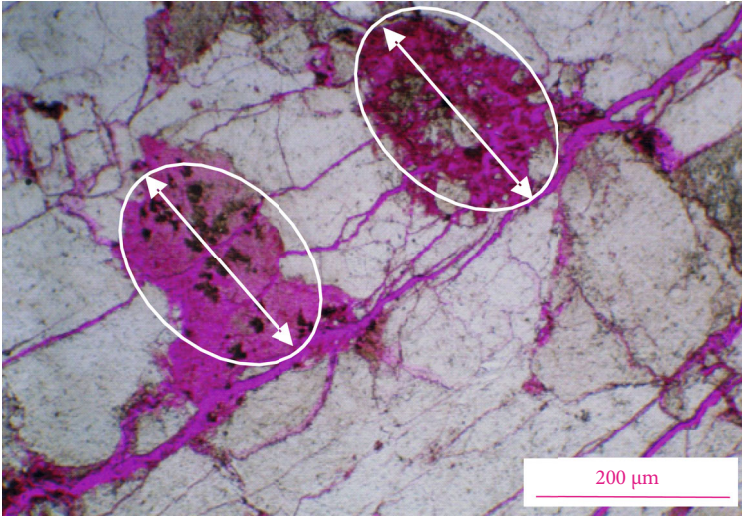
The results of cast thin section show that the primary pores of tight sandstone reservoir in Ahe Formation ( $J_{1a}$ ) are not developed, and the secondary dissolution pores are scattered and isolated, with small pore radius (50  $\mu\text{m}$ –150  $\mu\text{m}$ ) and poor connectivity between pores. The intergranular muddy dissolution micropores are well developed,

followed by intergranular dissolution pores. Microfractures occupy the main pore space in some samples, and they are also one of the important types of reservoir space in the study area.

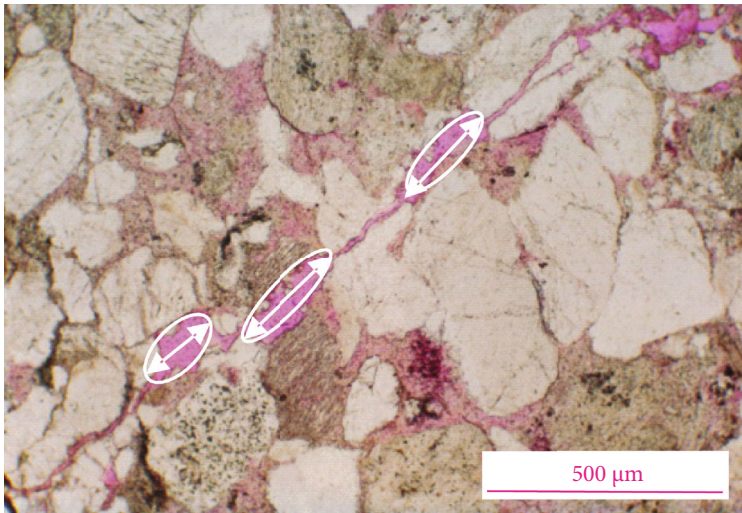
**4.1.2. SEM.** It can be clearly seen under SEM that the particles are filled with clay minerals of different shapes; among them, the hair and needle-like illite are the most developed (Figure 4(a)), which is symbiotically filled with the page-like kaolinite and filled between or within the particles (Figures 4(a) and 4(b)). Three types of pore-throat features can be identified: (1) pore-throats between particles and clay minerals, with a long-narrow shape (Figures 4(c) and 4(d)), and the width is between 2  $\mu\text{m}$  and 5  $\mu\text{m}$ . This kind of pore-throat is very common here. (2) Intercrystalline pores, mainly formed by secondary quartz overgrowth (Figure 4(e)) or developed in kaolinite (Figure 4(f), with pore diameter of about 10  $\mu\text{m}$ ). (3) Dissolved fractures in feldspar: the fractures are flat and discontinuous distributed along the joint surfaces of feldspar (Figures 4(g) and 4(h)). SEM observation results show that the areas displayed by dyeing agent in casting thin sections are not entirely pores; most of them are the adsorption color after being filled by clay minerals. The actual gas storage space is the intergranular pores of the clay minerals, so a more precise definition of the pore should belong to the throat. It is precisely because these clay minerals filled in the grain adsorb the dye, which is mistakenly regarded as the pore space (casting color) under the microscope, resulting in the face ratio value under the casting thin section generally larger; thus, the reservoir space of the rock is mistakenly estimated. It can be seen from Figure 4(f) that almost 90% of the pore space is filled by kaolinite and illite. Most of the reservoir spaces in Dibe gas reservoir are micropore-throats.

**4.1.3. CLSM.** Confocal laser scanning microscope (CLSM) can make up for the shortcomings of traditional polarizing microscope and scanning electron microscope to obtain high-definition and high-resolution images. What is more, it can clearly display and quantitatively count the micropore-throat by adding special fluorescent agent to the thin section [11, 40, 41]. Thus, CLSM has obvious advantages in the study of tight reservoir. In this study, the fractures and pores (especially the tiny throats) that are hardly observed in traditional casting thin sections are readily identified by using CLSM (Figure 5). The results show that the main reservoir spaces are microdissolution pores, and a small amount of intergranular macropores are developed. The throats are important reservoir spaces that should not be ignored and there is a close connection between pores and throats in the reservoir. The throat is distributed in network and communicated with nanopores, thus forming a tight reservoir oil and gas storage and transportation system.

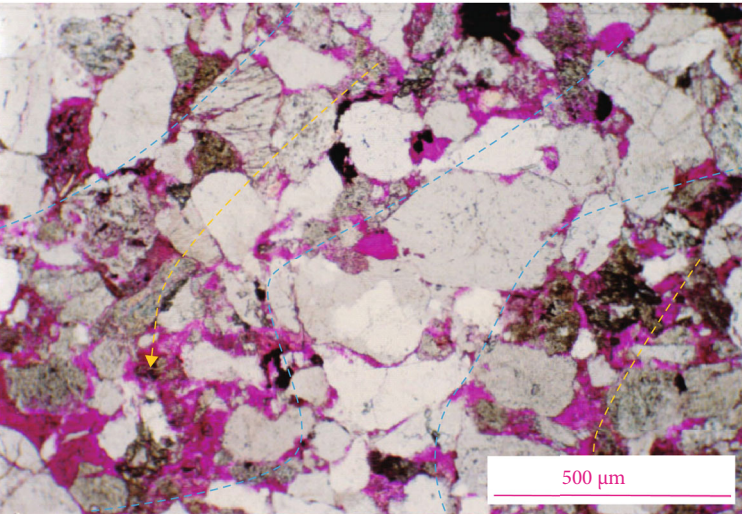
**4.2. Quantitative Measurements of Reservoir Space.** The throat diameters of sandstone, tight sandstone, and shale are very different [13]. Therefore, different techniques are needed for further research.



(a)

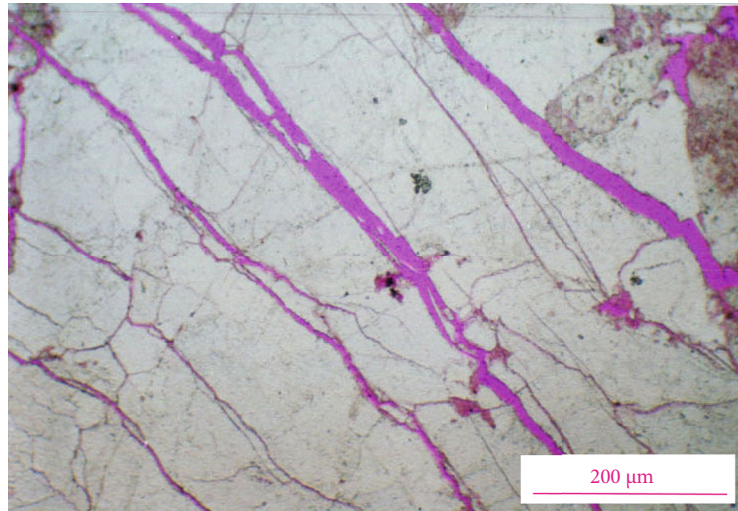


(b)



(c)

FIGURE 3: Continued.



(d)

FIGURE 3: Thin sections of photomicrographs showing microscopic features of Dibeitight sandstone reservoirs in Ahe Formation. (a) Well Yn5, J<sub>1</sub>a, brachy pores: the pores are intersected by fractures and are nearly in rounded shape. (b) Well Yn2, J<sub>1</sub>a: the pores are developed in flat and long-axis shape. (c) Well Yn4, J<sub>1</sub>a: the secondary dissolved micropores are developed in clustering and banding form. (d) Well Yn5, J<sub>1</sub>a: the microfissures are nearly parallel with bigger openness, without impurity between fissures.

**4.2.1. Rate-Controlled Mercury Penetration.** The RCMP has an obvious advantage in evaluating pores and throats, especially for tight sandstone reservoir, which can effectively reflect the number, size, and distribution characteristics of pores and throats [42, 43]. Compared with conventional mercury penetration technique, the RCMP can inject mercury into rock pores at very low and constant rate (generally 0.00005 ml/min). By detecting the pressure fluctuation during the mercury penetration, the RCMP can separate pores and throats in rocks; thus, the detection results can provide the capillary pressure curves of pores and throats and obtain the rock microstructure characteristic parameters such as pore radius distribution, throat radius distribution, and radius ratio of pore-throat distribution.

The throat saturation values of the tight sandstone samples (except for sample Yn5-3) in the Ahe Formation are obviously higher than the pore saturation values (Table 2), which is quite different from the analysis results of conventional sandstone reservoirs. The saturation values of pores of conventional sandstone reservoirs are higher than those of throats, which may be caused by the development of microfractures. Figure 6 shows the distribution feature of the throats and pores in sample Yn5-2 with RCMP. It can be seen that the main peak value of the throat radius is 1  $\mu\text{m}$ , and the main peak value of the pore radius is among 125–150  $\mu\text{m}$ .

**4.2.2. High-Pressure Mercury Injection.** In conventional mercury penetration analysis, the mercury injection pressure is generally less than 50 MPa, and the minimum throat radius that mercury can enter is about 0.01  $\mu\text{m}$ . However, the throat radius value in tight sandstones is widely distributed, with a minimum of 10 nm [13]. Hence, the conventional mercury penetration data cannot truly reflect the distribution feature of throats in reservoirs. The maximum injection pressure of HPMI can reach as high as 400 MPa; therefore, it

can be used to approximately reflect the whole distribution scope of the throats.

In view of the fact that there are many fractures in the sandstone samples, the high pressure can easily damage the samples during the injection process. Therefore, 200 MPa of the mercury injection pressure was selected in this study. The minimum throat radius under 200 MPa pressure is 3.7 nm, which is basically close to the size of the oil and gas molecules. The data of 27 samples shows that the average mercury injection saturation is 67.2%, and the maximum mercury injection saturation is 87% (Figure 7). Though they are apparently higher than that reflected by conventional mercury penetration data, it is still unable to achieve 100% mercury injection saturation. The main reason is that there are invalid pores in the sample, and the throats which connected by these pores are much smaller, or these pores are isolated from the throats and fail to communicate with the pore-throat network. However, these invalid pores still occupy part of the pore volume, so that the pores cannot be fully filled by mercury penetration. Such deficiency can be overcome by the combination of HPMI and nitrogen adsorption techniques to comprehensively obtain the unavailable pore space volumes in samples.

**4.2.3. Nitrogen Adsorption Isotherm Analysis.** The NA test method can make up for the shortage of other analysis and test on the observation of micropore and can focus on the distribution characteristics of throat radius below 100 nm; thus, it has a good effect on identifying the micropore and throat features in tight reservoirs [44, 45].

The results of nitrogen adsorption and desorption isotherms (Figure 8) show that the distribution status and shape of the pores and throats can be qualitatively evaluated by the shape of the adsorption isotherm. According to the classification of International Union of Pure and Applied

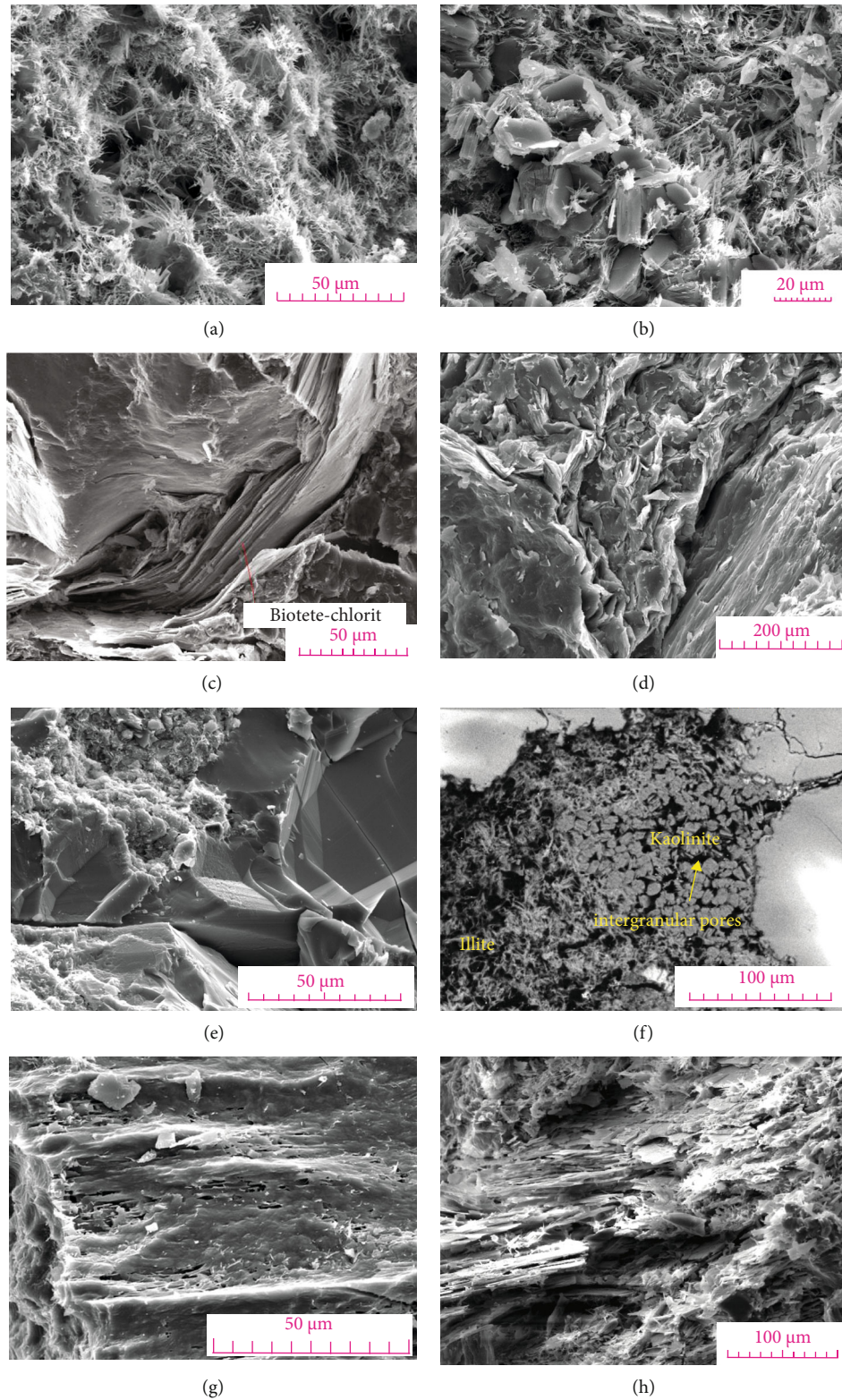


FIGURE 4: Scanning electron microscope photomicrographs showing pore space and morphology of minerals filled in space in the Ahe Formation of Dibe area. (a) Yn2, J<sub>1y</sub>, 4538.31 m: intergranular fibrous illite and smectite mixed layers. (b) Yn5, J<sub>1y</sub>, 4562.8 m: kaolinite in book-like form and illite in hair-like form. (c) Yn5, J<sub>1y</sub>, 4562.8 m: pores and fissures between lamella biotite and chlorite minerals. (d) Yn5, J<sub>1y</sub>, 4562.8 m: long-narrow fissures between grains. (e) Yn, J<sub>1a</sub>, 4851.8 m: intercrystalline pores between secondary quartz crystals. (f) Ys4, J<sub>1a</sub>, 3981.6 m: kaolinite and illite filling between grains in thin sections under SEM. (g) Yn5, J<sub>1a</sub>, 5007.1 m: the dissolved micropores in feldspar are developed along joint seams. (h) Yn5, J<sub>1a</sub>, 4775.23 m: flat fissures are formed by corrosion along joint seams in feldspar.

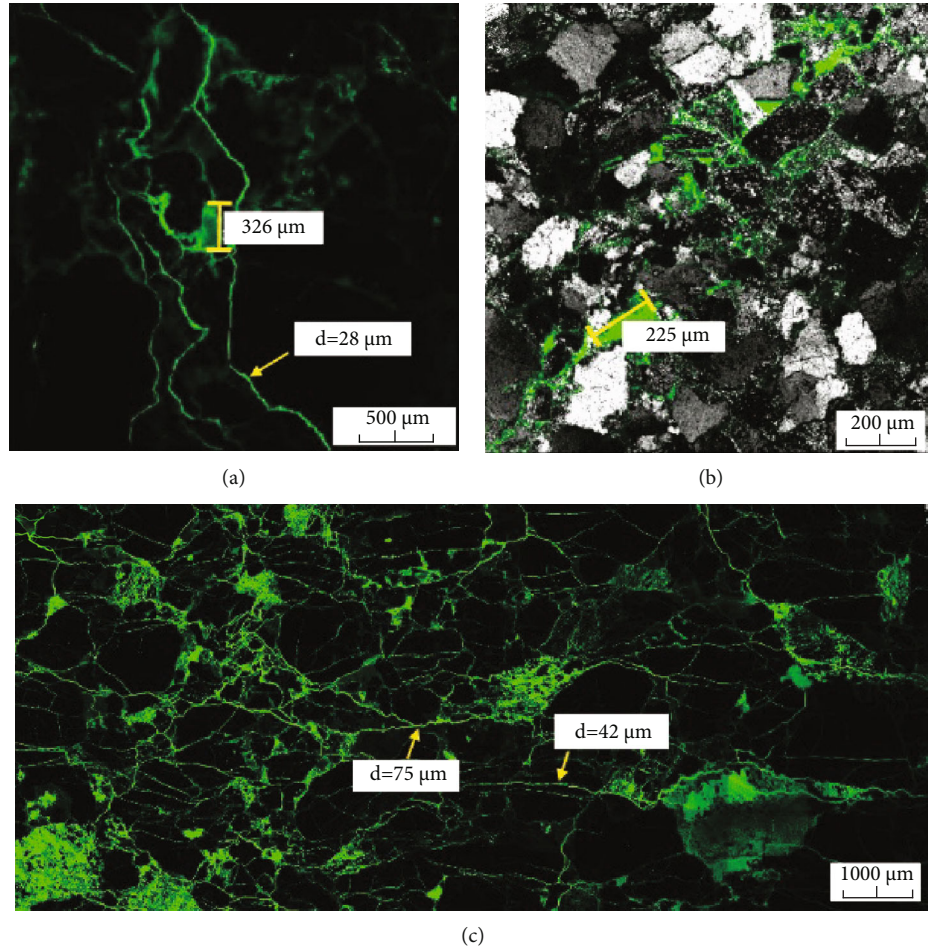


FIGURE 5: Scanning laser confocal microscope photomicrographs showing slot pore characteristics in the Ahe Formation of Dibe area. (a) Well Yn2: clear structural fractures. (b) Well Yn2, J<sub>1a</sub>: corroded bands with clustering tiny corrosion pores. Tiny pores are clear. (c) Well Yn5, J<sub>1a</sub>: a thin section image of scanning laser confocal microscope, showing connected throats and corroded pores in network style.

TABLE 2: Result of rate-controlled mercury penetration in the study area.

No.	Yn5-1	Yn5-2	Yn5-3	mn1-1
Gasometry porosity (%)	9.30	6.96	8.18	19.65
Gasometry permeability ( $10^{-3} \mu\text{m}^2$ )	1.06	0.293	11.030	14.360
Apparent rock density ( $\text{g}/\text{cm}^3$ )	2.42	2.49	2.44	2.12
Bulk volume of rock sample VB ( $\text{cm}^3$ )	1.77	3.41	4.48	1.88
Pore volume of rock sample VP ( $\text{cm}^3$ )	0.16	0.24	0.37	0.37
Penetrated mercury saturation in throat (%)	26.70	25.44	28.29	41.02
Penetrated mercury saturation in pore (%)	10.08	10.89	29.48	23.18
Total penetrated mercury saturation (%)	36.78	36.33	57.77	64.20

Chemistry (IUPAC), the form of the adsorption isotherm of the Dibe reservoirs is type IV. The adsorption isotherm is different from the desorption isotherm, and the hysteresis loop can be seen. A platform can be observed in the area with high  $P/P_0$  value (greater than 0.4), and it ends up with the isotherm upward. This type of isotherm indicates that the samples in this area are chiefly medium pores (the diameters of the medium pores are between 2 and 50 nm, according to the classification of IUPAC). The pores in this order cannot be observed in other analytical methods.

**4.2.4. Routine and Stress-Dependent Core Analysis.** It is very important to evaluate the influence of pore-throat morphology on tight gas reservoir quality under formation pressure, because low-permeability reservoirs are very sensitive to the confining pressure [23, 46]. The permeability values measured under normal pressures cannot truly reflect the reservoir seepage capacity under formation pressure [16]. Related statistics show that the permeability under overburden pressures is only 1/10 of that under normal pressure. The sandstone samples of the gas reservoir in Dibe area also show



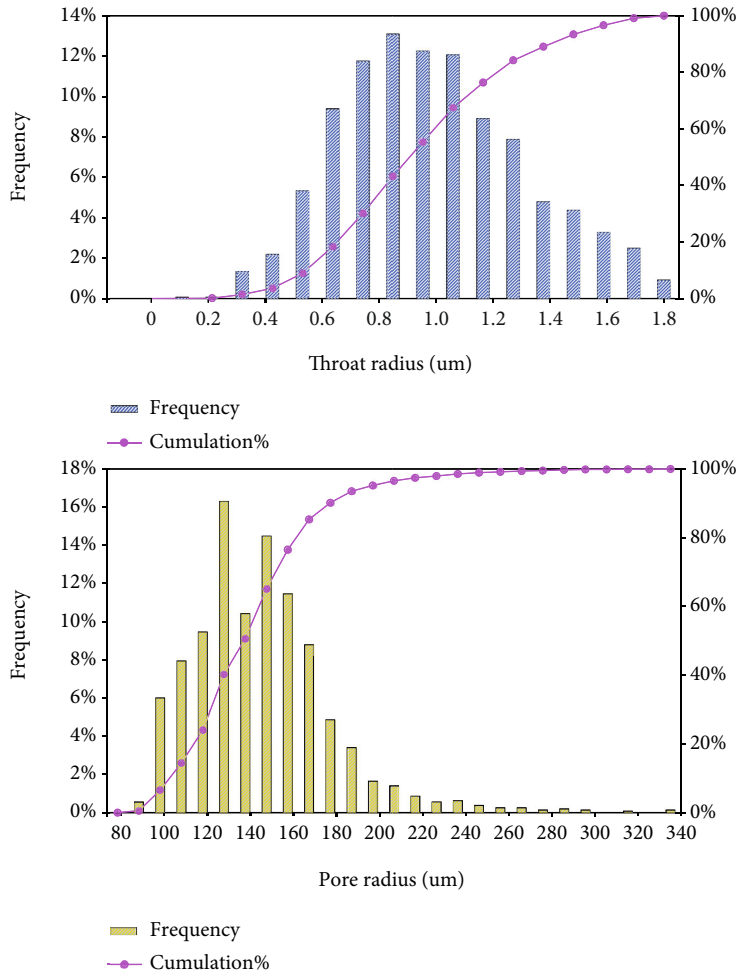


FIGURE 6: Distribution feature of throats and pores in reservoirs of Yn5-2 samples.

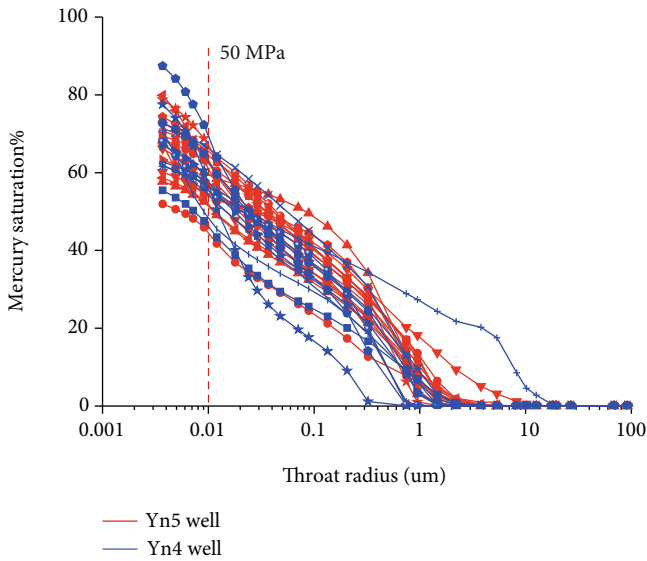


FIGURE 7: HPMI curve feature of tight sandstone reservoirs in Dibeai area.

that the permeability value under overburden pressure is much smaller than that under normal pressures. However, there is a great difference in the variation trend of permeability of different samples under the overburden pressure.

Figure 9 shows that the permeability values of the samples in type II and III under overburden pressure (50 MPa) are almost less than 0.1 mD, which is 1-2 orders of magnitude lower than that under normal pressures, while the permeability values of the loose samples in type I did not change. On the contrary, the porosity value of the loose samples in type I decreases obviously under overburden pressure, while that of the samples in type II and III has no obvious change. Dibeai tight gas reservoir is dominated by type II reservoir, followed by type III reservoir.

**4.3. Pore-Throat Morphology of Tight Sandstone Reservoirs.** Primary pores in the tight sandstone of the Ahe Formation are not well developed under the microscope. The dissolved pores are generally distributed in isolation, with the pore radius of 50 to 150 μm, and the connectivity of intercrystalline pores is poor. The main dissolution pores are the intergranular dissolution pores, followed by the intragranular dissolution pores, which are developed in feldspar grains and volcanic debris grains. Microfractures occupy the main

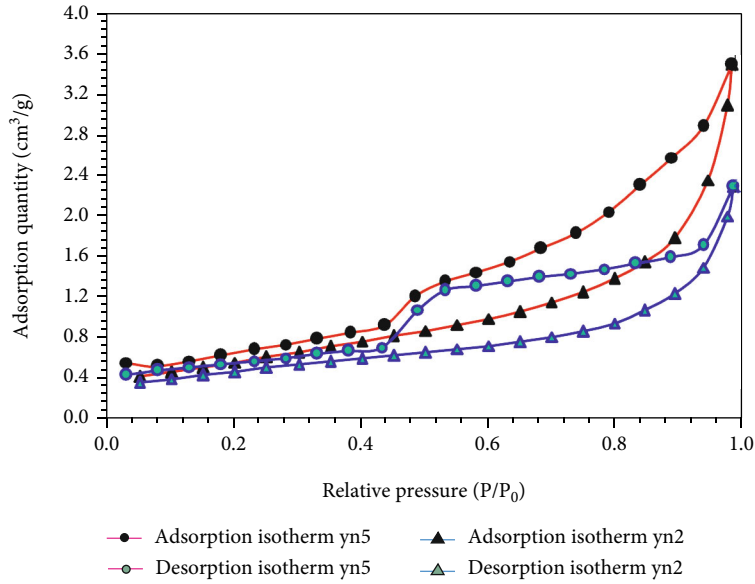


FIGURE 8: Low-temperature nitrogen adsorption and desorption isotherm for tight sandstone in the study area.

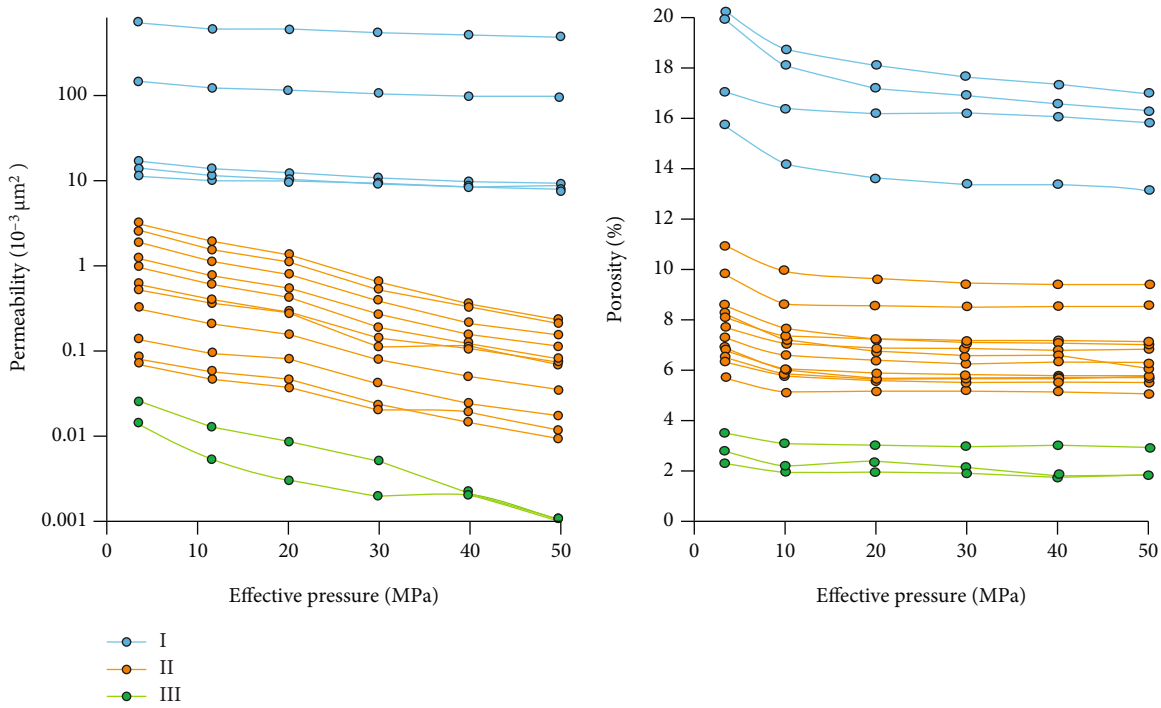


FIGURE 9: Correlation between porosity and permeability under overburden pressure of tight sandstone samples in the Dibe area.

pore space of some samples and are also one of the main reservoir space types in this area.

The hysteresis loop of nitrogen adsorption test (Figure 8) can reflect the features of sample pore-throats. It can be divided into four types, and different types reflect different morphological features of the pore-throat. According to the hysteresis loop (desorption curve), there are two major types of pore morphology in the samples. (1) inkbottle-shaped pores with small caliber and wide body, and the big pore-throat is unfavorable for gas seepage and (2) pores in

plate and flat shape; this type of sample is generally composed of flake particles, such as clay or clustered micropores. This conclusion is consistent with the morphological features previously observed intuitively, indicating that the tight reservoirs in the study area are mainly composed of micropore in intergranular clay minerals, followed by the long-narrow and flat throats.

4.4. Pore-Throat Sizes and Distribution in Tight Sandstones. Rate-controlled mercury penetration (RCMP) and high-

pressure mercury injection (HPMI) are effective methods for analyzing pore-throat radius from different perspectives. It can be concluded from the result of RCMP that the throat radius in tight sandstones is mainly distributed in the range of 0.4–2  $\mu\text{m}$  (the main peak is at around 1  $\mu\text{m}$ ), and the pore radius is distributed in a wider scope of 75–350  $\mu\text{m}$  (the main peak is among 125–150  $\mu\text{m}$ ) (Figure 6). The peak value of the pore-throat ratio ranged from 40 to 150  $\mu\text{m}$ . They are generally represented as the shape of small caliber with wide body.

The average pore-throat radius distribution reflected by the HPMI testing (Figure 10) shows that the peak of the pore-throat radius is around 0.324  $\mu\text{m}$ , and most pore-throats radii are smaller than 2  $\mu\text{m}$ . To carry out HPMI and NA tests for the same sample, taking the data of two methods in the same coordinate system for mapping, it can well reflect the widest range of the pore-throat radius distribution in the tight sandstone samples. Figure 11 shows the average pore-throat radius distribution graph by matching the data of HPMI and NA of 27 samples. The NA testing results show that abundant micropores with radius smaller than 50 nm are still developed and their total pore volume accounts for more than 15% of the total pore volume.

## 5. Discussion

*5.1. Throats Are the Major Storage Spaces for Tight Sandstone Gas Reservoir.* RCMP data of four samples shows that the throat radius of the reservoirs in Dibe area ranges from 1  $\mu\text{m}$  to 4  $\mu\text{m}$  (Figure 11(a)), and the peak ratios of pore-throat radius range from 40 to 150 (Figure 11(b)). The average mercury injection saturation of gas reservoirs is 48.77%, in which the average mercury injection saturations of pores and throats are 18.4% and 30.37%, respectively. Thus, throats contribute more than 60% of the total gas spaces. The throats not only play the role of connecting the pores and throats but also are the major reservoir spaces in tight gas reservoirs. It is obviously different from the cognition that pores are the major reservoir spaces in conventional reservoirs.

According to the pore radius calculation formula (BJH), the pore radius distribution scope and pore volumes of the samples in nitrogen adsorption test are obtained (Figure 11). The volumes of the pores with 2–50 nm account for more than 14.3% of the total pore volume. Under the HPMI condition, 40% of the pore-throat volume cannot be measured. Even if it is assumed that the adsorption test can identify the total connected throat volume, nearly 30% of the pores still cannot be identified by existing technology, which is considered as the isolated and invalid pores in samples. According to the NA test results of 56 samples, the throat volumes below 50 nm account for about 45% of the total porosity, micropores (<2 nm), and mesopores (2–50 nm), and ineffective pores occupy 64% of the pore space [47].

*5.2. The Effect of Throat Morphology on Reservoir Seepage Capacity.* Pore-throat morphology is an important parameter for reservoir evaluation. Some researchers have attempted to study the characteristics of complex pore struc-

ture by fractal geometry theory [48, 49]. In fact, pore-throat morphology is random and disordered, and accurately, descriptions remain uncertain. In this study, pore-throat morphology can be distinguished by the curves of the adsorption and desorption in nitrogen adsorption test, which is a comprehensive reflection of all pore-throat morphology (Figure 8). The radius ratio of the connecting pore-throat and the length/width ratio of pores (or throats) are used to simply characterize the pore-throat morphology (Figure 11(b)). Figure 11(a) shows the percentage of the throats with different radius in the samples. It does not display the shape of the pore-throat, but only the size of the throat. The wider the curve is, the larger the throat exists in the sample. Figure 11(b) shows the distribution range and frequency of the ratio of pore radius to throat radius, which represents the shape of the pore-throat. The larger the ratio is, the more asymmetric the pore-throat is, such as the inkbottle-shaped pore-throat (with small caliber and wide body). The smaller the ratio is, the more regular the shape of pore-throat is, such as oval and round shape. When the ratio is about 100, the pore-throat is flat and slender strip.

The peak of the pore-throat ratio in sample mn1-1 with permeability value of 14.36 mD is located in the horizontal coordinates of 40. With the decrease of permeability, the pore-throat ratio corresponding to the peak increases gradually. It can be seen that the primary peak is 150 when the permeability is 0.29 mD (sample Yn5-2). Therefore, the primary peak position of the pore-throat ratios is closely related to the permeability value, indicating that the permeability is not only affected by pore-throat size, but also by pore-throat morphology, although it can be seen from Figure 11(a) that the permeability value has a certain correlation with the throat size of the reservoir; for example, the larger the permeability value of the sample, the larger the proportion of the large throat. The morphology of pore-throat reflected by the ratio of pore-throat is the indicator of reservoir seepage ability. The effect of the throat on the seepage capacity is only shown as the slippage effect of gas when the throat radius is small, resulting in smaller permeability value [50]. However, it is the ratio of pore-throat, that is, the shape of pore-throat, that really reflects the seepage capacity of reservoir.

By comparing the pore-throat shapes of type I, II, and III samples, it is considered that the main reason for the differences of porosity and permeability under overburden pressure is the closure effect of the long-narrow and flat throats, followed by the blockage effect of clay minerals on the throats. The porosity of the samples in type I under normal pressure is bigger than 15%, mainly developing big-radius pores (their diameters are generally among 0.2–0.5 mm), with smaller length/width ratios (about 1). The relationship between grains is point contact or line contact, and the grains in some samples are suspended. Due to the development of pore space, the change of grain framework under overburden pressure results in the decrease of pore space and porosity. However, there is still plenty of seepage space among the grains, and the decrease of seepage capacity of fluid is much limited. For the type II samples of tight

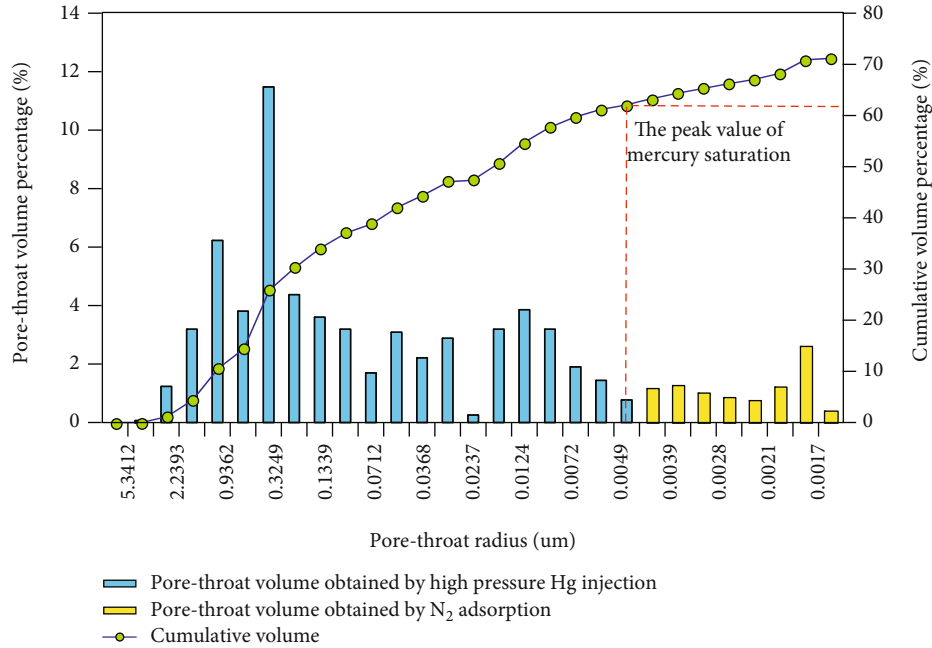


FIGURE 10: Pore-throat radius distribution features in high-pressure mercury penetration and nitrogen adsorption.

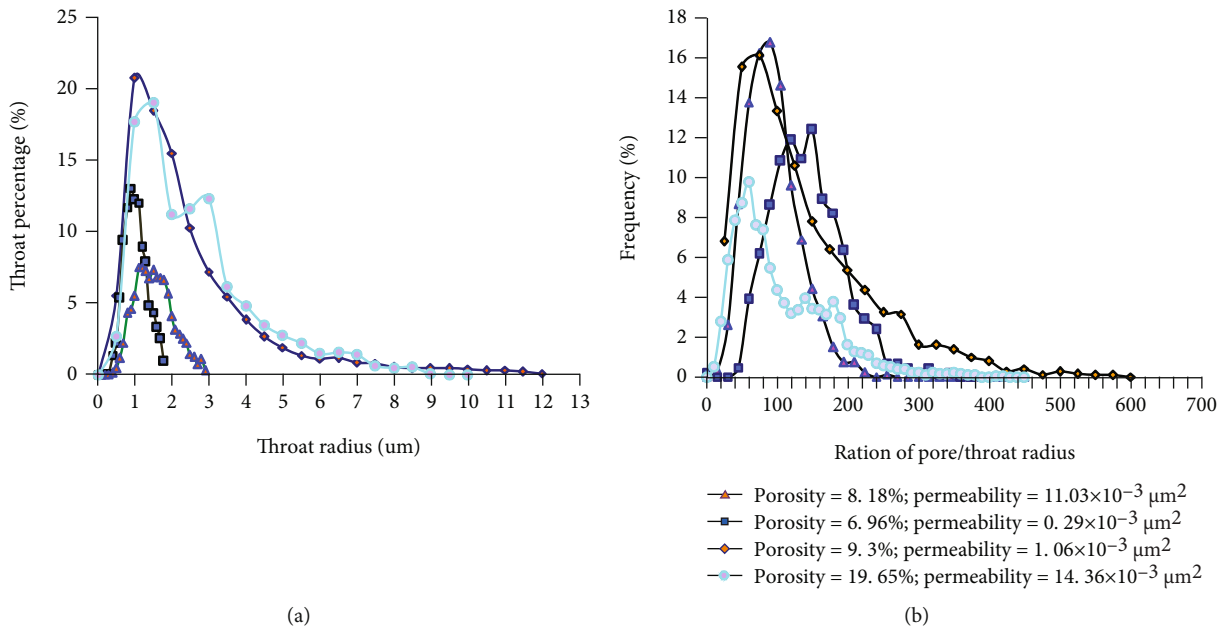


FIGURE 11: Distribution of throat radius and ratio of pore-throat radius for tight sandstones of different porosity-permeability properties.

sandstone, the decrease of pore spaces in reservoirs under overburden pressure is mainly reflected in the closure effect of the long-narrow and flat micropore-throats or compression into narrower pore-throat. For the total pore-throat space, the decreased volume may be smaller, but for the seepage capacity of pore-throats, the decrease of the space can directly result in the closure of the throat and the increase of the fluid slippage effect, which seriously affects the fluid seepage capacity. Therefore, the long-narrow space

with large pore-throat ratios in reservoirs has apparent influence on reservoir quality.

In tight sandstones, the reservoir quality is relatively sensitive to clay minerals and the existence of clay minerals can seriously block the microthroats. For the reservoir of this long-narrow pore-throat type in this area, the clay minerals aggravate the plugging of pore-throat and seriously hinder the flow of fluid. There are lots of muddy matrices in type III samples. The matrix is mainly primary clay minerals.

The pseudo matrix phenomenon occurred during the process of compaction can seriously reduce the pore spaces. Improper modification measures in the drilling may aggravate the blockage of the throats. Due to the strong acid sensitivity of the reservoir in this area, the later acid fracturing process is easy to cause reservoir pollution, thus missing the discovery of the gas layers. At present, the nitrogen drilling technology can effectively protect the reservoirs in the Dibe area, so that the discovery rate and drilling success rate of gas layers during later period are significantly improved.

**5.3. Determination of Cutoff Value of Throat Radius.** Throat radius is the key factor for controlling gas seepage capacity in reservoirs. The fluids in different throat radius intervals have great differences of flow modes and seepage capacity. The results of HPMI experiments show that the pore spaces with the throat radius  $> 0.3 \mu\text{m}$  in tight sandstone samples contribute more than 98% of the fluid permeability. If 98% of the fluid flow capacity is taken as the free flow space of reservoir throats [51], then  $0.3 \mu\text{m}$  throat radius is the minimum value of free fluid pore space. When the throat radius in reservoirs is greater than  $0.3 \mu\text{m}$ , the fluids in the space can be naturally produced without external force, and this part of gas corresponds to the natural gas production during the exploitation of tight sandstone reservoirs.

As the space with radius larger than  $0.3 \mu\text{m}$  is in a small proportion, the porosity and permeability of the tight gas reservoirs are low, and the gas productivity under natural condition is very limited. Therefore, it is necessary to stimulate the reservoirs, such as fracturing, to improve the productivity of single well. In the process of stimulation, the reservoir throats are actually widened, so that the gas bounded in the smaller throat in the early stage can be released to form productivity. Further detailed studies are still needed to determine whether the throats with radius smaller than  $0.3 \mu\text{m}$  can be entirely stimulated into actual production capacity. In this study, the minimum movable fluid pore radius (i.e., the lower limit of throat radius for reservoir stimulation) in reservoirs can be determined by a nuclear magnetic centrifuged laboratory experiment.

Centrifuged experiment for the brine-saturated samples can be used to calibrate the  $T_2$  cutoff value of the movable fluid in tight sandstones [52]. In this paper, the magnetic resonance experiments under various centrifugal conditions were carried out, and it found that with a gradual increase of centrifugal force, the movable water in water-saturated samples was gradually expelled. When the centrifugal force reached 2.75 MPa, there is almost no difference (or very small difference) between the  $T_2$  spectrogram curve and the spectrogram curve at 2.42 MPa. Thus, it can be concluded that 2.75 MPa is the limited value of the movable water that can be expelled from tight sandstones by centrifugal force. This means that the throat radius corresponding to 2.75 MPa is the minimum throat radius for the movable fluid in samples (Figure 12). As there is capillary force balance between porous medium and water when the water is subjected to centrifugal force, it is necessary to convert the interaction between water and capillary into that between

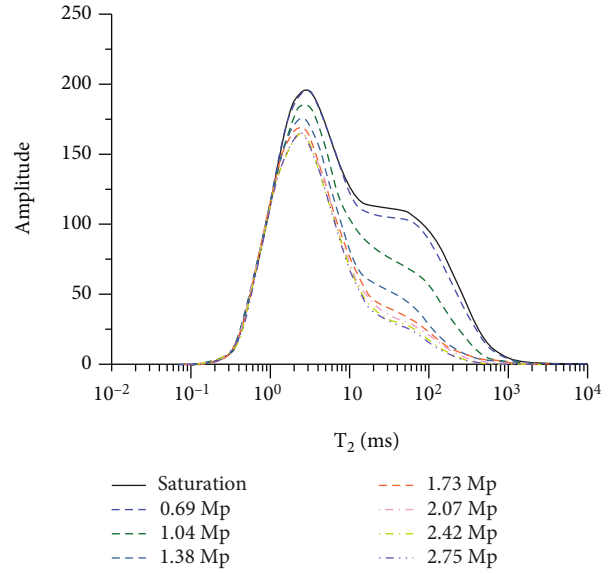


FIGURE 12:  $T_2$  spectrogram curve in various pressures for tight sandstones in study area.

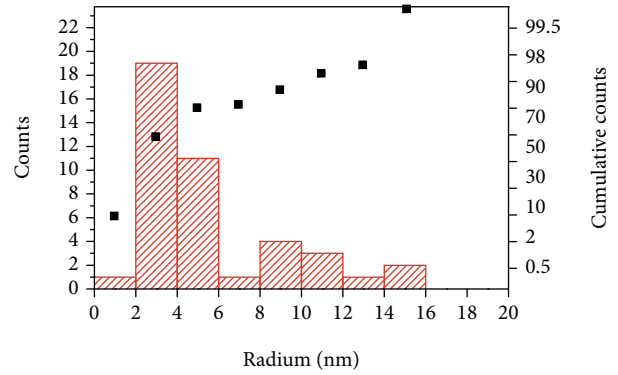


FIGURE 13: Distribution graph of immobile water film thickness in cores of tight sandstone in Dibe area.

gas and capillary. The capillary force formula in porous medium is as follows:

$$P_c = \frac{2\rho \cos \theta}{r}, \quad (1)$$

where  $P_c$  is the capillary force in porous medium (MPa).  $\rho$  is the interfacial tension between gas and water, which is 72 N/m under normal condition.  $\theta$  is the wetting angle, being  $0^\circ$  for gas-water centrifuge.  $r$  is the pore-throat radius (mm).

According to Equation (1), the corresponding throat radius is  $0.052 \mu\text{m}$  under the centrifugal condition of 2.75 MPa. Thus, it can be considered that the pore space with throat radius among  $0.3\text{-}0.052 \mu\text{m}$  in tight sandstone reservoirs can be converted to be movable fluid after reconstruction, and  $0.052 \mu\text{m}$  is the cutoff value of working movable fluid.

Theoretically, as long as the throat radius in reservoirs is larger than that of the gas, it can be used as the gas storage space. In fact, due to the existence of bound water in the

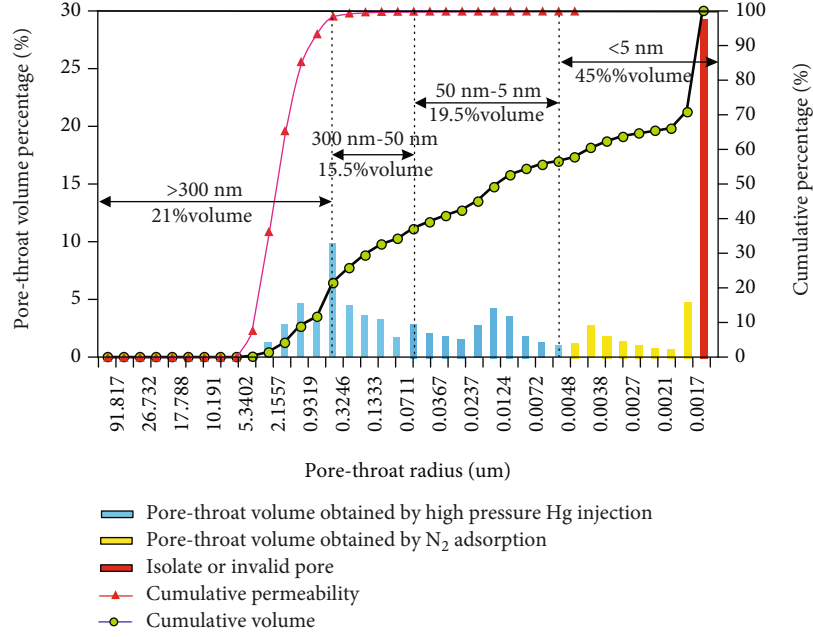


FIGURE 14: Distribution of pore-throat radius, cut off values, and their percentages in total pore spaces in tight sandstone reservoirs of Ahe Formation in Dibe area.

TABLE 3: Calculation parameters and results of tight sandstone gas reserves in Dibe area.

Gas-bearing area (km <sup>2</sup> )	Net thickness (m)	Net porosity (%)	Gas saturation (%)	Volume factor	Geologic gas reserves (10 <sup>8</sup> m <sup>3</sup> )	Recoverable gas reserves (10 <sup>8</sup> m <sup>3</sup> )
35.2	102.1	6.7	63	0.00267	568.2	284.1

reservoir, the water film of the irreducible water can block the pore-throats and prevent the invasion of the gas.

When the pore-throats are blocked by the bound water, the throat radius which is equal to the thickness of the bound water film on the two walls is the low limit of the throat radius for natural gas injection, so the thickness of the bound water film can be used as the low limit of the pore-throat radius for natural gas injection [53]. The formula for the thickness of bound water film is as follows:

$$d_i = 7142\Phi * \frac{S_{wi}}{A_i * \rho}, \quad (2)$$

where  $d_i$  is the bound water film thickness (0.1 nm).  $\varphi$  is the core porosity (%).  $S_{wi}$  is the bound water saturation (%).  $A$  is the specific surface area of core (m<sup>2</sup>/g).  $\rho$  is the core density (g/cm<sup>3</sup>).

Figure 13 is the distribution graph of bound water film thickness calculated by Equation (2) of 42 cores in this area. The major bound water film thickness in pore-throats is about 5 nm. Thus, 5 nm can act as the lower limit for gas charging in tight reservoirs.

Figure 14 shows the distribution range of throat radius and the percentage of pore volume occupied by different throat radius in tight sandstone reservoirs. The free fluid pore volume with throat radius that exceeds 300 nm accounts for 21% of total pore volume. The storage space

with throat radius among 300-50 nm that can be reconstructed to obtain movable fluid accounts for 15% of total pore space. The reservoir space of irreducible fluid with low-limit throat radius among 50-5 nm for gas charging accounts for 19% of total pore space. The isolated and invalid pore space accounts for 45%.

5.4. Calculation of Geological Reserves and Recoverable Reserves. The calculation of tight gas reserves is based on the following formula:

$$G_c = 0.01 \times A_g \times h \times \Phi \times S_{gi} \times \frac{1}{B_{gi}}, \quad (3)$$

where  $G_c$  is the total geological reserves of condensate gas (10<sup>8</sup> m<sup>3</sup>).  $A_g$  is the gas-bearing area (km<sup>2</sup>).  $h$  is the average effective thickness (m).  $\Phi$  is the average porosity (%).  $S_{gi}$  is the initial gas saturation (%).  $B_{gi}$  is the original gas volume factor.

The calculation parameters of reserves in the study area are shown in Table 3. According to Equation (3), the geological reserves of natural gas in this area can be calculated to be 568.2 × 10<sup>8</sup> m<sup>3</sup>. The recoverable reserves are 284.1 × 10<sup>8</sup> m<sup>3</sup> by the classification method and 50% of other gas parameters of the basin.

Table 4 shows the geological reserves and recoverable reserves of natural gas calculated by using the gas-bearing

TABLE 4: Calculation parameters and results of tight sandstone gas reserves by throat method.

Area	Gas-bearing area (km <sup>2</sup> )	Net thickness (m)	Net porosity (%)	Net pore space (%)	Movable fluid pore space (without stimulation) (%)	Movable fluid pore space (after stimulation) (%)	Volume factor	Geologic gas reserves (10 <sup>8</sup> m <sup>3</sup> )	Natural recoverable gas reserves (10 <sup>8</sup> m <sup>3</sup> )	Recoverable gas reserves after stimulation (10 <sup>8</sup> m <sup>3</sup> )
Dibei	35.2	102.1	6.7	55	21	36.5	0.00267	496.01	189.39	329.17

interval of throat in Figure 14. Compared with Table 2, the geological reserves of natural gas decreased by 12.7% to  $496.01 \times 10^8 \text{ m}^3$ , but the recoverable reserves increased by 15.87% to  $329.17 \times 10^8 \text{ m}^3$ , of which the natural gas produced without transformation was  $189.39 \times 10^8 \text{ m}^3$ , and the production increased by  $139.79 \times 10^8 \text{ m}^3$  after transformation. Therefore, for tight sandstone gas reservoir, fracturing is very necessary.

## 6. Conclusions

Various methods are used to characterize the pore-throat of the tight sandstones in the Kuqa Depression, and the relationship between reserves and productivity with throat is discussed. The main conclusions drawn from this thesis are as follows:

- (1) The sandstone gas reservoirs in the Dibe area are tight, with high matrix content and abundant clay minerals. The major reservoir spaces are long-narrow and flat pore-throats and the clay mineral intergranular micropores
- (2) The throat radius in reservoirs is mainly distributed between 1 and  $4 \mu\text{m}$ , and the throats account for nearly 2/3 of spaces of the tight sandstones. The shape of the pore-throat directly affects the production capacity of the reservoir
- (3) The pores with throat radius greater than 300 nm have free fluid, and they contribute more than 98% of the reservoir permeability. The pore spaces with throat radius between 300 nm and 52 nm can expel fluids by stimulation. The pore-throats with radius  $< 52 \text{ nm}$  cannot release the irreducible hydrocarbon fluids even if they have been charged with hydrocarbons, and they are inefficient pore-throats. Such pore-throats account for 65% of the tight sandstone reservoirs in the Dibe area
- (4) Under the formation pressure, the tight sandstone reservoir with long-flat pore-throat is easy to have the closure of the throat and the compression circulation space, which makes the seepage capacity decrease sharply. In addition, the clay minerals in pore-throats can lead to more serious blocking effect, which hinders the fluid seepage
- (5) According to the pore-throat distribution characteristics of tight sandstone reservoir, the calculation of tight gas geological reserves and recoverable reserves is carried out. There are some differences between this calculation result and the conventional calculation result, which is reflected in the reduction of geological reserves by 12.7% and the increase of recoverable reserves by 15.87%

## Data Availability

Analysis of diagenetic system and pore evolution of clastic reservoir (ID: 2021DJ0402) is available upon reasonable request from the corresponding author.

## Conflicts of Interest

The authors declare that they have no conflicts of interest.

## References

- [1] D. J. Hartmann and E. A. Beaumont, "Predicting reservoir system quality and performance," in *Exploring for Oil and Gas Traps: AAPG Treatise of Petroleum Geology: Handbook of Petroleum Geology*, E. A. Beaumont and N. H. Foster, Eds., pp. 9–154, AAPG Special, 1999.
- [2] W. Yang, Z. Y. Xie, and H. Jin, "Reservoir evaluation and pooling mechanism of the Xujiache Formation in the Sichuan Basin," *Natural Gas Industry*, vol. 30, no. 12, pp. 10–15, 2010.
- [3] Y. F. Yang, K. Wang, Q. F. Lv et al., "Flow simulation considering adsorption boundary layer based on digital rock and finite element method," *Petroleum Science*, vol. 18, no. 1, pp. 183–194, 2021.
- [4] L. Zheng, Z. J. Jin, and S. N. Zhang, "Features and evaluation of the Paleozoic tight sandstone reservoirs of the Rub Al Khali Basin in the Middle East," *Oil and Gas Geology*, vol. 34, pp. 475–482, 2013.
- [5] C. Cheng, K. F. Lu, and X. K. He, "Based on the R35 of mercury injection data to quantitative classification, evaluation and reservoir characteristics—a case study of E15 layer in X field," *Journal of Oil and Gas Technology*, vol. 36, pp. 16–20, 2014.
- [6] M. Y. Feng, T. Liu, T. Lin, X. H. Liu, N. X. Li, and A. H. Xi, "Fracture fillings and implication of fluid activities in volcanic rocks: Dixi Area in Kelameili Gas Field, Junggar Basin, North-western China," *Minerals*, vol. 9, no. 3, p. 154, 2019.
- [7] J. J. Sun, H. K. Guo, and W. Liu, "Characteristics of micro pore-throat in low permeability volcanic gas reservoir," *Fault-Block Oil & Gas Field*, vol. 17, pp. 548–552, 2010.
- [8] D. S. Guang, *China's Unconventional Oil and Gas Geology*, Petroleum Industry Press, Beijing, 1995.
- [9] J. J. Li, Y. Liu, Y. J. Gao, B. Y. Cheng, and H. Q. Jiang, "Pore-scale study of the pressure-sensitive effect of sandstone and its influence on multiphase flows," *Petroleum Science*, vol. 16, no. 2, pp. 382–395, 2019.
- [10] Z. Li, Y. Duan, Q. Fang, and M. Wei, "A study of relative permeability for transient two-phase flow in a low permeability fractal porous medium," *Advances in Geo-Energy Research*, vol. 2, no. 4, pp. 369–379, 2018.
- [11] T. Lin, S. W. Yi, M. L. Ye, Q. G. Ran, H. X. Wei, and W. H. Liu, "Characteristic of tight sandstone gas reservoir and the enrichment regularity in eastern Kuqa Depression," *Geological Science and Technology Information*, vol. 33, pp. 116–122, 2014.
- [12] R. M. Slatt and N. R. O'Brien, "Pore types in the Barnett and Woodford gas shales: contribution to understanding gas storage and migration pathways in fine-grained rocks," *AAPG Bulletin*, vol. 95, no. 12, pp. 2017–2030, 2011.
- [13] P. H. Nelson, "Pore-throat sizes in sandstones, tight sandstones, and shales," *AAPG Bulletin*, vol. 93, pp. 329–340, 2009.
- [14] E. D. Pittman, "Relationship of porosity and permeability to various parameters derived from mercury injection-capillary pressure curves for sandstone1," *AAPG Bulletin*, vol. 76, pp. 191–198, 1992.
- [15] R. Aguilera, "Incorporating capillary pressure, pore aperture radius, height above free water table, and Winland  $r_{35}$  values on picket plots," *AAPG Bulletin*, vol. 86, pp. 605–624, 2002.



- [16] M. Y. Hu, S. X. Li, and G. Q. Wei, "Reservoir appraisal of tight sandstones of upper Triassic Xujiahe formation in the western Sichuan foreland basin," *Natural Gas Geosciences*, vol. 17, pp. 456–462, 2006.
- [17] M. Nobakht and C. R. Clarkson, "Analysis of production data in shale gas reservoirs: rigorous corrections for fluid and flow properties," in *SPE Eastern Regional Meeting*, pp. 85–98, Columbus, Ohio, USA, 2011.
- [18] R. Christopher, J. L. Clarkson, P. K. Jensen, and M. F. Pederesen, "Innovative methods for flow-unit and pore-structure analyses in a tight siltstone and shale gas reservoir," *AAPG Bulletin*, vol. 96, no. 2, pp. 355–374, 2012.
- [19] Z. Y. Gao, Y. P. Fan, Q. X. Xuan, and G. W. Zheng, "A review of shale pore structure evolution characteristics with increasing thermal maturities," *Advances in Geo-Energy Research*, vol. 4, no. 3, pp. 247–259, 2020.
- [20] Y. Li, X. Gao, S. Meng, P. Wu, and D. Elsworth, "Diagenetic sequences of continuously deposited tight sandstones in various environments: a case study from Upper Paleozoic sandstones in the Linxing area, eastern Ordos basin, China," *AAPG Bulletin*, vol. 103, no. 11, pp. 2757–2783, 2019.
- [21] Y. Li, J. Yang, Z. Pan, S. Meng, K. Wang, and X. Niu, "Unconventional natural gas accumulations in stacked deposits: a discussion of Upper Paleozoic coal-bearing strata in the east margin of the Ordos basin, China," *Bulletin of the Geological Society of China*, vol. 93, no. 1, pp. 111–129, 2019.
- [22] Y. Li, W. Xu, P. Wu, and S. Meng, "Dissolution versus cementation and its role in determining tight sandstone quality: a case study from the Upper Paleozoic in northeastern Ordos basin, China," *Journal of Natural Gas Science and Engineering*, vol. 78, 2020.
- [23] H. Deng, R. Leguizamon, and R. Aguilera, "Petrophysics of triple porosity tight gas reservoirs with a link to gas productivity," *SPE Reservoir Evaluation & Engineering*, vol. 14, no. 5, pp. 566–577, 2011.
- [24] J. Lai, G. Wang, Z. Fan et al., "Fracture detection in oil-based drilling mud using a combination of borehole image and sonic logs," *Marine and Petroleum Geology*, vol. 84, pp. 195–214, 2017.
- [25] S. P. Chen, L. J. Tang, Z. J. Jin, C. Z. Jia, and X. J. Pi, "Thrust and fold tectonics and the role of evaporites in deformation in the Western Kuqa Foreland of Tarim Basin, Northwest China," *Marine and Petroleum Geology*, vol. 21, no. 8, pp. 1027–1042, 2004.
- [26] X. F. Fu, Y. Song, Y. F. Lü, and Y. H. Sun, "Rock mechanic characteristic of gypsum cover and conservation function to gas in the Kuche Depression, the Tarim Basin," *Petroleum Geology & Experiment*, vol. 28, pp. 25–29, 2006.
- [27] P. L. Li, *Tectonic Sedimentary and Accumulation in Tarim Basin*, Geological Publishing House, Beijing, 2010.
- [28] S. Q. Li, L. Feng, P. C. Tang, G. Rao, and Y. Bao, "Calculation of depth to detachment and its significance in the Kuqa Depression: a discussion," *Petroleum Science*, vol. 6, no. 1, pp. 17–20, 2009.
- [29] J. Lai, G. Wang, S. Wang et al., "A review on the applications of image logs in structural analysis and sedimentary characterization," *Marine and Petroleum Geology*, vol. 95, pp. 139–166, 2018.
- [30] J. Lai, D. Li, G. Wang et al., "Earth stress and reservoir quality evaluation in high and steep structure: the Lower Cretaceous in the Kuqa Depression, Tarim Basin, China," *Marine and Petroleum Geology*, vol. 101, pp. 43–54, 2019.
- [31] D. F. He, X. Y. Zhou, H. J. Yang, G. L. Lei, and Y. J. Ma, "Geological structure and its controls on giant oil and gas fields in Kuqa Depression, Tarim Basin: a clue from new shot seismic data," *Geotectonica et Metallogenia*, vol. 33, pp. 19–32, 2009.
- [32] C. Z. Jia, H. L. Chen, S. F. Yang, H. F. Lu, and Y. Z. Zhou, "Late Cretaceous uplifting process and its geological response in Kuqa Depression," *Acta Petroleum Sinica*, vol. 24, pp. 1–5, 2003.
- [33] X. Wang, C. Z. Jia, and S. F. Yang, "Geometry and kinematics of the Kuqa fold-and-thrust belt in the southern Tianshan," *Chinese Journal of Geology*, vol. 37, pp. 372–384, 2002.
- [34] J. Lai, G. Wang, Y. Chai et al., "Deep burial diagenesis and reservoir quality evolution of high-temperature, high-pressure sandstones: examples from Lower Cretaceous Bashijiqike Formation in Keshen area, Kuqa Depression, Tarim Basin of China," *AAPG Bulletin*, vol. 101, no. 6, pp. 829–862, 2017.
- [35] T. Nian, G. Wang, C. Xiao, L. Zhou, L. Deng, and R. Li, "The in situ stress determination from borehole image logs in the Kuqa Depression," *Journal of Natural Gas Science and Engineering*, vol. 34, pp. 1077–1084, 2016.
- [36] T. Nian, Z. Jiang, G. Wang et al., "Characterization of braided river-delta facies in the Tarim Basin Lower Cretaceous: application of borehole image logs with comparative outcrops and cores," *Marine and Petroleum Geology*, vol. 97, pp. 1–23, 2018.
- [37] Z. Gao, H. Guo, R. Zhu, L. Zhang, and Y. Sun, "Sedimentary response of different fan types to the Paleogene–Neogene Basin transformation in the Kuqa Depression, Tarim Basin, Xinjiang Province," *Acta Geologica Sinica*, vol. 83, no. 2, pp. 411–424, 2009.
- [38] Z. Li, D. X. Wang, and W. Lin, "Mesozoic–Cenozoic elastic composition in Kuqa Depression, northwest China: implication for provenance types and tectonic attributes," *Acta Petrologica Sinica*, vol. 20, pp. 655–661, 2004.
- [39] C. S. Lin, J. Y. Liu, Y. M. Zhang, J. Xiao, J. Chen, and Y. Ji, "Depositional architecture of the Tertiary tectonic sequences and their response to foreland tectonism in the Kuqa Depression, the Tarim Basin," *Science*, vol. 45, no. 3, pp. 250–258, 2002.
- [40] Y. Q. Jiang, L. Chen, C. Jiang et al., "Characterization techniques and trends of the pore structure of tight reservoirs," *Geological Science and Technology Information*, vol. 33, pp. 63–70, 2014.
- [41] X. D. Sun, L. M. Suo, M. Z. Zhang, and P. J. Wang, "New progress of reservoir research by the technology of laser confocal scanning microscope analysis in the Daqing exploration area," *Acta Petrologica Sinica*, vol. 21, pp. 1479–1488, 2005.
- [42] H. Gao, W. Xie, and J. P. Yang, "Pore throat characteristics of extra-ultra low permeability sandstone reservoir based on constant-rate mercury penetration technique," *Petroleum Geology & Experiment*, vol. 33, pp. 206–214, 2011.
- [43] Y. L. Gao and Z. G. Zhang, "Valuation on difference of pore throat structure of low permeability sandstone by constant mercury penetration technique," *Geological Science and Technology Information*, vol. 30, pp. 73–76, 2011.
- [44] G. R. L. Chalmers and R. Marc Bustin, "On the effects of petrographic composition on coalbed methane sorption," *International Journal of Coal Geology*, vol. 69, no. 4, pp. 288–304, 2007.

- [45] D. Prinz and R. Littke, "Development of the micro- and ultra-microporous structure of coals with rank as deduced from the accessibility to water," *Fuel*, vol. 84, pp. 1645–1652, 2005.
- [46] N. H. Kilmer, N. R. Morrow, and J. K. Pitman, "Pressure sensitivity of low permeability sandstones," *Journal of Petroleum Science and Engineering*, vol. 1, no. 1, pp. 65–81, 1987.
- [47] R. G. Loucks, R. M. Reed, S. C. Ruppel, and D. M. Jarvie, "Morphology, genesis, and distribution of nanometer-scale pores in siliceous mudstones of the Mississippian Barnett shale," *Journal of Sedimentary Research*, vol. 79, no. 12, pp. 848–861, 2009.
- [48] L. M. Ma, C. Y. Lin, and M. W. Fan, "Quantitative classification and evaluation of reservoir based on fractal features of micro-pore structures," *Journal of Oil and Gas Technology*, vol. 34, pp. 15–19, 2012.
- [49] T. Zhang, S. Y. Xu, and K. Yang, "Application of fractal dimension of micro pore structure," *Journal of Daqing Petroleum Institute*, vol. 34, pp. 44–47, 2010.
- [50] G. S. He, *Reservoir Physics*, Petroleum Industry Press, Beijing, 1993.
- [51] A. Salah, "The impact of pore geometry aspects on porosity-permeability relationship-a critical review to evaluate NMR estimated permeability," in *Paper presented at the North Africa Technical Conference and Exhibition*, Cairo, Egypt, 2012.
- [52] X. C. Wang, Y. R. Fan, S. G. Deng, K. Z. Li, Z. Q. Li, and J. L. Jiang, "Irreducible water saturation determination based on centrifugal test data," *Journal of China University of Petroleum*, vol. 33, pp. 76–79, 2009.
- [53] Y. Xiang, D. Xiang, and Y. C. Yang, "Study of gas recovery and water film thickness in water drive for tight sandstone gas reservoir," *Journal of Chengdu University of Technology Science and Technology Edition*, vol. 26, pp. 389–391, 1999.

## Research Article

# Study on Downhole Throttling Characteristics of High Water Content Gas

Jie Zheng,<sup>1,2,3,4</sup> Zhenzhen Li<sup>id</sup>,<sup>1,2</sup> Yihua Dou,<sup>1,2</sup> Yarong Zhang,<sup>5</sup> Cheng Bi,<sup>3</sup> Xu Yang,<sup>3</sup> and Jiahui Li<sup>1,2</sup>

<sup>1</sup>School of Mechanical Engineering, Xi'an Shiyou University, Xi'an, Shaanxi 710065, China

<sup>2</sup>Xi'an Key Laboratory of Wellbore Integrity Evaluation, Xi'an, Shaanxi 710055, China

<sup>3</sup>Xi'an Special Equipment Inspection Institute, Xi'an, Shaanxi 710065, China

<sup>4</sup>School of Power and Energy, Northwestern Polytechnical University, Xi'an, Shaanxi 710072, China

<sup>5</sup>School of Science, Xi'an University of Architecture and Technology, Xi'an, Shaanxi 710055, China

Correspondence should be addressed to Zhenzhen Li; [lizhenzhen1997@126.com](mailto:lizhenzhen1997@126.com)

Received 7 October 2021; Revised 6 December 2021; Accepted 22 December 2021; Published 24 January 2022

Academic Editor: Steffen Berg

Copyright © 2022 Jie Zheng et al. This is an open access article distributed under the Creative Commons Attribution License, which permits unrestricted use, distribution, and reproduction in any medium, provided the original work is properly cited.

In order not to hinder gas production, we usually hope that the bottom hole effusion can be discharged to the surface with high-pressure natural gas. For the production data of high water content gas wells, the problems of insufficient water content and liquid-carrying capacity affecting gas well production should be considered. Based on the wellbore gas-liquid two-phase pipe flow theory and heat transfer theory, the temperature and pressure coupling prediction model of a high water-bearing gas well is established. Combined with the downhole throttling mechanism and gas-liquid two-phase homogeneous flow theory, the temperature and pressure field distribution model is established. The results show that compared with the Ramey model and Hassan and Kabir model, the temperature and pressure coupling prediction model of high water-bearing gas wells established in this study has the smallest coefficient of variation in the four groups of data tests. Based on this, the effects of different working conditions and choke diameter on downhole throttling characteristics of high water-bearing gas wells are analyzed. The findings of this study are helpful to better predict the wellbore temperature and pressure coupling of high water-bearing gas wells and provide more effective help for the smooth production of gas wells.

## 1. Research Status of Gas-Liquid Two-Phase Well

The prediction of wellbore temperature and pressure field has always been a major problem of common concern to scientists [1] because it is related to the accurate construction of oil production technology [2, 3], the safety of pipe string [4–6], the normal use of various downhole tools [7], the reliability of production process [8], and the wax and scale prevention of oil and gas wells affected by temperature and pressure [9–12]. Nowadays, in the daily production process of gas wells, the phase change of natural gas in the wellbore is becoming more and more common [13, 14]. For example, affected by the formation and other environmental factors, formation water or other free water

often appears in the wellbore of producing gas wells, and a large amount of accumulation will lead to fluid accumulation in the wellbore. The site often hopes that the water infiltrating from the formation to the bottom of the well can be carried to the ground by high-pressure natural gas fluid in time. In order to solve this engineering problem, many scholars have proposed new calculation methods to calculate and obtain the relevant data of gas well temperature, pressure field, and liquid carrying.

Abdelhafiz et al. [15] proposed a model for predicting the temperature distribution of vertical wellbore systems under circulation and shut-in conditions. The model can simulate the transient temperature disturbance of drilling fluid, drill string, casing string, cement behind the casing, and surrounding rock formation. However, the coupling

effect of temperature and pressure is not considered in the model. Turner first considered the wellbore flow process and established the droplet model. Among them, the calculation formula of critical gas velocity and the droplet parameters carried by gas flow are obtained based on the droplet geometric size and force model [16]. However, the model has requirements for the gas-liquid ratio. When the gas-liquid ratio reaches a specific value ( $GLR > 1400 \text{ m}^3/\text{m}^3$ ), the model can be applied to the gas well with annular fog flow. Based on Turner's model, Gray considered the influence of temperature gradient, gas composition, fluid acceleration, and other factors during liquid carrying in gas wells and obtained the wellbore pressure drop of gas-liquid two-phase pipe flow by using an empirical model [17]. However, the Gray model has no different flow patterns, which is only applicable to stable wellbore flow and not applicable to production wells with effusion. In 2006, Ghalambor and Xu proposed a new liquid-carrying model for gas wells [18]. In view of the difficulty in calculating the pressure of multiphase flow gas wells, a simplified process is adopted. It is considered that the kinetic energy of the gas is only slightly higher than that required for liquid carrying in order to bring droplets from the bottom of the well to the surface. A method to predict critical flow is used to solve the defects of the Turner model, which cannot effectively calculate the pressure of multiphase flow gas wells, but the model only explains the droplet being brought out of the wellhead from the macro perspective, without considering the effects of droplet morphology and wellbore environment. Based on the formation process of droplets in gas wells, Li et al. proposed an ellipsoidal droplet model considering factors such as pressure and environment [19]. The calculation method of liquid-carrying critical flow is obtained. Compared with the Turner model, the calculated value is about 38% of its result, which is more accurate than the Turner model, but the model does not take into account the influence of wellbore pressure and temperature environment on liquid-carrying capacity. In 2010, Chaoyang adopted a new ellipsoid model [20], considered the influence of droplet physical model and size on stress mode, analyzed the liquid-carrying process of gas wells with liquid in the wellbore, and obtained a new ellipsoid calculation model. However, the application is limited by the field well conditions.

In 2012, Zhibin and Yingchuan considered the influence of droplet parameters, stress model, and other factors on the liquid-carrying capacity and gave a reasonable explanation for the difference in the calculation results of liquid-carrying capacity of each gas field [21], but the model ignored the change of fluid flow pattern in the wellbore. In 2012, Zhi et al. established the critical liquid-carrying model in the throttling process. It is qualitatively analyzed that downhole throttling can improve the liquid-carrying capacity of gas wells [22], but the model fails to solve the quantitative relationship between liquid-carrying flow and gas production. In 2014, Gang simplified the calculation of droplet surface tension, ignored the influence of surface tension on the critical flow of liquid carrying, and replaced it with quantitative constant. It is considered that the surface tension will change with different temperatures and pressure

[23], but the quantitative relationship between surface tension and temperature and pressure is not described. In 2018, aiming at the problem of insufficient liquid-carrying capacity of low-pressure and low-yield gas wells, Yang calculated the changes of critical liquid-carrying flow at different depths [24] and obtained that high-pressure gas wells mostly occurred at the wellhead and low-pressure and low-yield gas wells mostly occurred at the bottom of the well. However, he did not establish an appropriate critical liquid-carrying flow prediction model but made a qualitative judgment. In 2020, Jinbao established the prediction model of critical liquid-carrying velocity of inclined gas wells based on the characteristics of gas-liquid two-phase flow [25] and carried out multiparameter sensitivity analysis. The prediction effect of the model based on an annular fog flow pattern is better.

Through the above data investigation, it is concluded that considering the throttling process, there is little research on the change of critical liquid carrying the flow of gas well, and the research on the change of flow pattern in wellbore on the change of critical liquid carrying the flow of gas well is rarely involved. Therefore, it is necessary to study the simulation of two-phase throttling temperature and pressure field in high water-bearing gas wells. In addition, the above methods do not mention the prediction of wellbore temperature and pressure of high water cut natural gas under high temperature and high pressure. Therefore, taking the gas wells in the Daning Jixian block as the research object, this paper not only considers the wellbore heat transfer but also considers the influence of formation temperature and wellbore pressure on the phase state of natural gas, establishing the wellbore pressure coupling model of water-bearing gas wells, and discusses the tubing diameter, gas production, and the relationship between gas water ratio and wellbore temperature field and pressure field. The technical process of this study is shown in Figure 1.

Firstly, the gas-liquid two-phase pipe flow model of a high water-bearing gas well is given. Secondly, the gas well temperature and pressure are calculated according to the model, and the relative errors are compared with the Ramey model, Hassan and Kabir model, and field measured data. Then, the downhole throttling model of high water content gas well is introduced to calculate the throttling pressure and temperature drop of high water content gas well, and an example of gas well throttling pressure and temperature drop is analyzed. Finally, the numerical simulation of downhole throttling is carried out.

## 2. Temperature Pressure Coupling Calculation of High Water-Bearing Gas Well

Based on the wellbore heat transfer mechanism, considering the gas thermophysical parameters and Joule Thomson coefficient, a wellbore pressure-temperature coupling prediction model for high water-bearing gas wells is established. The relationship between the prediction model and Hassan and Kabir model, Ramey model, and field measured data is explored by using the coefficient of variation method, the accuracy of the model is verified, the sensitivity of wellbore temperature and pressure field is analyzed, and the

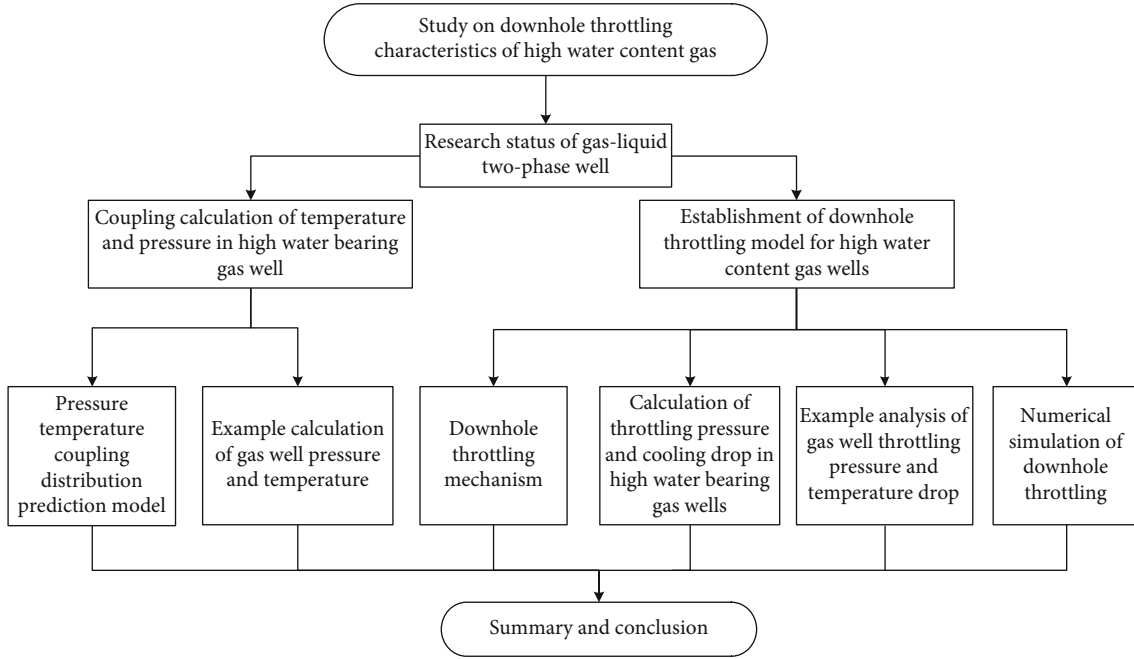


FIGURE 1: Technical flowchart.

relationship between tubing inner diameter, gas production, and gas water ratio and wellbore temperature and pressure field of high water cut gas wells is explored. The wellbore temperature and pressure coupling model of single-phase gas well and the temperature and pressure calculation model of high water-bearing gas well are established, respectively. The models are verified by Daji 14-1 and Daji 4-5 gas wells.

**2.1. Prediction Model of Wellbore Pressure Temperature Coupling Distribution in High Water-Bearing Gas Wells.** Gas wells with low liquid content are generally treated as single-phase pure gas wells, but for gas wells with high water content, the pressure and temperature prediction model of single-phase gas wells cannot meet the accuracy requirements, so it is necessary to reestablish the pressure and temperature prediction model on the basis of considering water content.

In the daily production and management of natural gas wells, the gas phase plays a dominant role, and there is only a small amount of liquid. However, with the continuous extension of production time, the liquid content in the wellbore will also increase so that the flow characteristics in the whole wellbore are completely different from the flow of pure gas, reflecting the characteristics of two-phase flow. In addition, due to the continuous attenuation of temperature and pressure in the wellbore from the bottom to the ground, mass exchange between gas and liquid occurs, and the physical parameters of gas and liquid change at the same time. Therefore, it is necessary to establish a gas-liquid two-phase pipe flow model in high water-bearing gas wells to describe the dynamic model of gas and liquid wellbore flow.

The fluid flow in the wellbore is regarded as one-dimensional flow, that is, the flow parameters and physical parameters of gas and liquid phases on any section of the

pipeline are uniform, which is the average value of the section. The homogeneous flow model in the two-phase flow research method is used for analysis.

**2.1.1. Continuity Equation.** Take the one-dimensional micro element section  $dz$  to study; its diameter is  $d$  and the pipe cross-sectional area is  $A$ , as shown in Figure 2. Establish the flow model along the flow direction, and the continuity equation can be expressed as

$$\rho_g u_g a + \rho_l u_l (1 - a) = \frac{Q}{A} = G. \quad (1)$$

Known

$$\rho_m = a\rho_g + (1 - a)\rho_l. \quad (2)$$

In the homogeneous flow model, the sliding velocity ratio is 1, that is, it is considered that there is no sliding between gas and liquid phases, and the volumetric void fraction is equal to the mass void fraction, so the following can be obtained:

$$\rho_m = \beta\rho_g + (1 - \beta)\rho_l. \quad (3)$$

**2.1.2. Momentum Equation.** Similar to single-phase flow, the momentum equation of homogeneous flow can be expressed in the form of three pressure drop gradients, which can be expressed as

$$-\frac{dp}{dz} = \left(\frac{dp_g}{dz}\right) + \left(\frac{dp_f}{dz}\right) + \left(\frac{dp_a}{dz}\right). \quad (4)$$

The pressure gradient generated by the gravity of

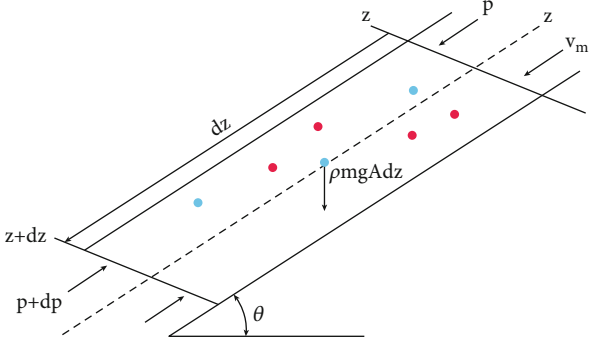


FIGURE 2: Micro element diagram of one-dimensional gas-liquid two-phase flow.

homogeneous flow is

$$\left(\frac{dp_g}{dz}\right) = \rho_m \sin \theta. \quad (5)$$

The friction gradient can be expressed as

$$\left(\frac{dp_f}{dz}\right) = \frac{\tau \pi d}{A}. \quad (6)$$

Sorting:

$$\left(\frac{dp_f}{dz}\right) = 2\rho_m g \cdot f \frac{1}{d} \frac{v^2}{g}. \quad (7)$$

The acceleration pressure gradient can be expressed as

$$\left(\frac{dp_a}{dz}\right) = G^2 \frac{dv_m}{dz}. \quad (8)$$

Sorting:

$$-\frac{dp}{dz} = \rho_m \sin \theta + 2\rho_m g \cdot f \frac{1}{d} \frac{v^2}{g} + G^2 + \frac{dv_m}{dz}. \quad (9)$$

**2.1.3. Energy Equation.** In the homogeneous flow model, according to the principle of energy conservation, the energy conservation equation of micro element is

$$\begin{aligned} & \text{Flow work} + \text{Internal energy} + \text{Kinetic energy} \\ & + \text{Potential energy} \\ & = \text{Add heat energy} - \text{External work of the system.} \end{aligned} \quad (10)$$

It can be expressed as

$$d(pv) + dU + d\left(\frac{1}{2}u^2\right) + g \sin \theta dz = dq - dw. \quad (11)$$

Substitute the basic parameters of two-phase flow:

$$\begin{aligned} d[apu_g + (1-a)pu_l] + dq - pd[au_g + (1-a)u_l] \\ + d\left[\frac{1}{2}au_g^2 + \frac{1}{2}(1-a)u_l^2\right] \\ + \rho q \sin \theta dz = dq - dw. \end{aligned} \quad (12)$$

Because there is no external work during gas-liquid two-phase flow in the wellbore, therefore

$$\begin{aligned} d[apu_g + (1-a)pu_l] + dq - pd[au_g + (1-a)u_l] \\ + d\left[\frac{1}{2}au_g^2 + \frac{1}{2}(1-a)u_l^2\right] \\ + \rho q \sin \theta dz = dq. \end{aligned} \quad (13)$$

By introducing the specific enthalpy and taking the micro element section with the length of  $dz$  on the oil pipe, the energy conservation equation can be obtained as follows:

$$\frac{dh}{dz} = -\frac{V_m dV_m}{dz} - g \sin \theta - \frac{q}{Q}. \quad (14)$$

The specific enthalpy is a function of temperature and pressure, namely,

$$dh = \left[\frac{\partial h}{\partial T}\right]_p dT + \left[\frac{\partial h}{\partial p}\right]_T dp = C_p dT - C_J C_p dp. \quad (15)$$

The heat transferred radially to the contact surface between the cement sheath and the formation is expressed as

$$Q_1 = -2\pi r_{to} U_{to} (T_f - T_s) dz. \quad (16)$$

The radial heat transfer from the cement layer to the surrounding stratum is

$$Q_2 = -\frac{2\pi k_e (T_s - T_{ei}) dz}{f(t)}. \quad (17)$$

The heat transferred to the second contact surface is equal to the heat given to the surrounding formation by the second contact surface. The outlet temperature of each section can be obtained simultaneously:

$$\begin{aligned} T_{f\text{out}} = e^{\lambda(z_{\text{out}} - z_{\text{in}})} \left( T_{f\text{in}} - \frac{g \sin \theta}{\lambda C_p} + \frac{\eta}{\lambda} - T_{\text{ein}} + \frac{g_l}{\lambda} \right) \\ + \frac{g \sin \theta}{\lambda C_p} - \frac{\eta}{\lambda} + T_{\text{eout}} + \frac{g_l}{\lambda}, \\ \eta = C_J \frac{dp}{dz} - \frac{v}{C_p} \frac{dv}{dz}, \lambda = \frac{2\pi r_{to} U_{to} k_e}{C_p w (k_e + f(t) r_{to} U_{to})}. \end{aligned} \quad (18)$$

TABLE 1: Structural parameters of well Daji 14-1 and Daji 4-5.

	Daji 14-1 well	Daji 4-5 well	Gas water ratio (m <sup>3</sup> /m <sup>3</sup> )	800
Artificial bottom hole (m)	2448.3	2472.3	Tubing wall thickness (mm)	6.45
Outer diameter of surface casing (mm)	244.5	244.5	Formation thermal conductivity (W/(m·K))	1.72
Wall thickness of surface casing (mm)	8.94	8.94	Thermal conductivity of oil pipe (W/(m·K))	50.5
Outer diameter of gas reservoir casing (mm)	139.7	139.7	Thermal conductivity of casing (W/(m·K))	50.5
Gas reservoir casing wall thickness (mm)	9.17	9.17	Thermal conductivity of cement sheath (W/(m·K))	0.95
Gas production (m <sup>3</sup> /d)	30715	51220	Annular thermal convection coefficient (W/(m <sup>2</sup> ·K))	0.86
Outer diameter of oil pipe (mm)	88.9	88.9	Fluid convection heat transfer coefficient (W/(m <sup>2</sup> ·K))	0.82

The Joule Thomson coefficient can be expressed as [26]

$$C_J = \frac{1}{C_p} \left[ \left( \frac{W_g T}{Z_g \rho_g} \right) \left( \frac{\partial Z_g}{\partial Z} \right)_p - \frac{(1 - W_g)(1 - \beta T)}{\rho_l} \right], \quad (19)$$

where  $\beta = (1/\nu)(\partial V/\partial T)_p = (-1/\rho)(\partial \rho/\partial T)_p$ .

The wellbore pressure-temperature coupling model of the high water-bearing gas well needs to be solved by an iterative method. The wellbore is divided into  $n$  sections. Assuming that the thermophysical parameters in each section are equal, the bottom hole temperature and pressure parameters are set as the boundary conditions, and the relevant physical parameters of the next section are calculated according to the temperature and pressure until the complete wellbore is calculated.

**2.2. Example Calculation of Gas Well Pressure and Temperature.** Based on the established temperature and pressure coupling model of the high water-bearing gas well, the above model is verified in combination with the field actual wellbore data, and the relative errors between the Ramey model [27], Hassan and Kabir model, temperature-pressure coupling model of high water-bearing gas well, and field measured data are compared. The temperature and pressure distribution of wellbore temperature-pressure field with the change of tubing size, gas production, and gas water ratio is analyzed.

**2.2.1. Comparison of Wellbore Temperature and Pressure Field Models.** Table 1 shows the wellbore structure parameters of Daji 14-1 and Daji 4-5 in a block.

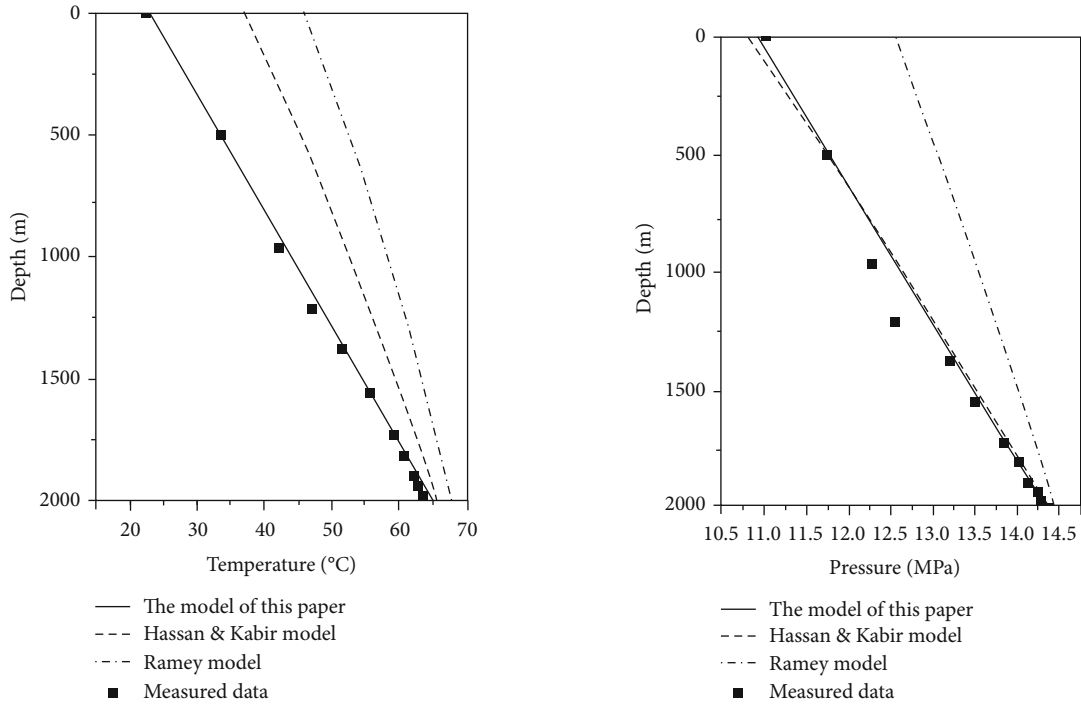
For the above Daji 14-1 well, the surface casing running depth is 554.91 m, the gas reservoir casing running depth is 2471.75 m, the surface casing running depth of Daji 4-5 well is 554.64 m, and the gas reservoir casing running depth is 2486.47 m. As the overall GWR of the two wells is less than 2000, they cannot be treated as single-phase gas wells. Using the temperature pressure coupling theoretical model of high water-bearing gas wells, write the measured basic parameters of gas wells into the program (such as bottom-hole temperature, bottom hole pressure, well depth, and fluid density in the well) as the initial conditions and replace them into the temperature pressure coupling theoretical model of high water-bearing gas wells set above. The well is divided into micro element segments

for an iterative solution. Because the fourth-order Runge Kutta method is more accurate to solve the differential equation, the fourth-order Runge Kutta method is used to solve the differential equation. To sum up, the calculation results through MATLAB programming are shown in Figure 3.

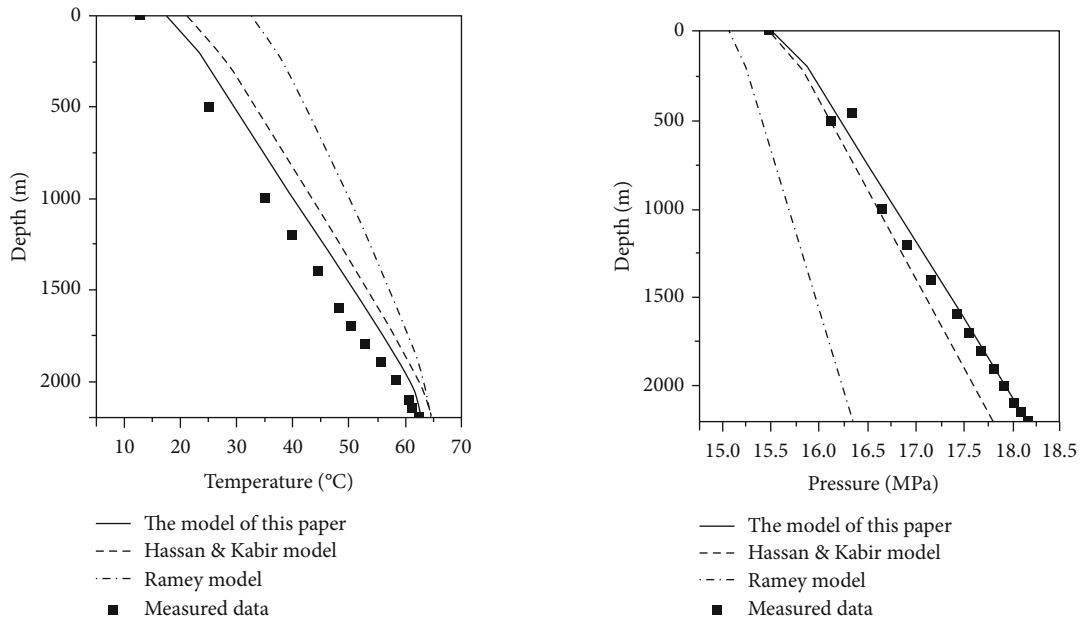
As shown in Figure 3, the wellbore temperature and pressure coupling prediction model of high water-bearing gas well established in this paper has higher accuracy and is closer to the field measured data than the Hassan and Kabir model and Ramey model. It can be seen from the figure that the Ramey model cannot correctly judge the wellbore temperature and pressure field of the high water-bearing gas well; the Hassan and Kabir model is more accurate than the Ramey model because it has the theoretical basis of a two-phase pipe flow model. However, when calculating the wellbore temperature and pressure field, it adopts the method of first calculating the pressure drop and independently considers the relationship between pressure change and temperature change, which has a large deviation from the field reality. For Daji 14-1 well model, the temperature prediction is more accurate and the pressure prediction error is large. There are two reasons for this phenomenon: (1) the model is caused by the discontinuity of formation pressure gradient in pressure calculation; (2) the actual measurement error of the measured pressure data will also lead to the deviation from the theoretical calculation value. For Daji 4-5 well, wellbore pressure prediction is more accurate and temperature error is relatively large. This may be due to the approximate continuous change of geothermal gradient in the calculation of formation temperature. The theoretical model can be applied to engineering practice.

**2.2.2. Model Error Analysis.** Since the dimensions and well conditions of the four groups of data in Figure 3 are different from each other, a unified error cannot be used for comparative analysis. The coefficient of variation is introduced to describe the deviation between the models relative to the field measured data. The coefficient of variation can be expressed as

$$C_v = \frac{\sigma}{\mu}. \quad (20)$$



(a) Comparison of wellbore temperature distribution of Daji 14-1 well (b) Comparison of wellbore pressure distribution of Daji 14-1 well



(c) Comparison of wellbore temperature distribution of Daji 4-5 well (d) Comparison of wellbore pressure distribution of Daji 4-5 well

FIGURE 3: Wellbore temperature and pressure distribution.

Through the coefficient of variation analysis of the four groups of data, the results are shown in Table 2.

The data discrete points in Table 2 are represented in two-dimensional coordinates, as shown in Figure 4.

As shown in Figure 4, the temperature-pressure coupling prediction model of high water-bearing gas well established in this paper has the smallest coefficient of variation in the four groups of data tests, indicating that the dispersion degree with the field measured data is the smallest and has the highest accuracy.

### 3. Establishment of Downhole Throttling Model for High Water-Bearing Gas Wells

This paper introduces the pressure and temperature changes of natural gas fluid in the gas wellbore through the choke and puts forward the solution model of downhole throttling pressure and temperature. Mainly for single-phase gas wells and high water content gas wells in downhole throttling operation, combined with downhole throttling mechanism, the downhole throttling pressure and temperature drop



TABLE 2: Coefficient of variation of each model.

Coefficient of variation CV	Paper model	Hassan and Kabir model	Ramey model
Wellbore temperature of Daji 14-1 well	0.114	0.162	0.284
Wellbore pressure of Daji 14-1 well	0.041	0.080	0.083
Wellbore temperature of Daji 4-5 well	0.169	0.256	0.293
Wellbore pressure of Daji 4-5 well	0.022	0.037	0.042

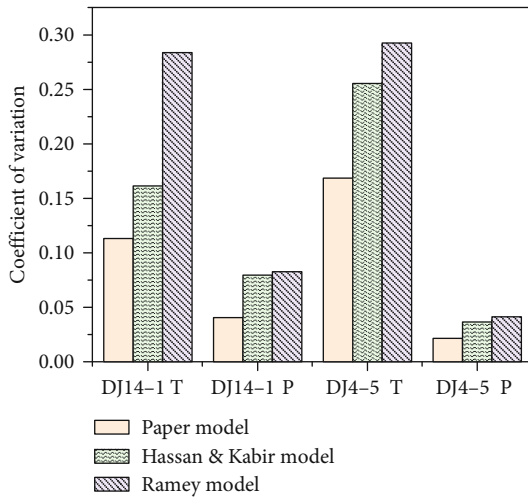


FIGURE 4: Comparison of coefficient of variation of each model.

model is established to predict the fluid flow parameters before and after throttling. Combined with the wellbore pressure and temperature prediction model, the whole wellbore pressure and temperature distribution under throttling conditions is obtained. Finally, the accuracy of the model is verified by comparing field data.

**3.1. Downhole Throttling Mechanism.** For conventional gas well testing, a fixed nozzle or variable nozzle is usually used for throttling and depressurization. It is of great theoretical value and practical significance to study the variation of pressure and temperature with flow and orifice diameter before and after throttling [28].

**3.1.1. Thermodynamic Analysis of Downhole Throttling.** The process of downhole high-pressure fluid passing through the choke belongs to isentropic expansion, accompanied by the conversion of pressure energy and kinetic energy. Natural gas does not exchange heat with the outside world during throttling, which is called adiabatic throttling [29]. Enthalpy is a function of pressure and temperature. Due to the isenthalpy process, the pressure drop after throttling is caused by the change of temperature. Adiabatic throttling effect is

usually expressed by the Joule Thomson coefficient.

$$\alpha_H = \left( \frac{\partial T}{\partial p} \right)_H. \quad (21)$$

The throttling coefficient is a physical parameter related to the specific state of gas, which can be calculated by looking up the diagram method and calculation formula. The average throttling coefficient can be calculated by means of the enthalpy pressure diagram and isenthalpy calculation formula of natural gas, and the gas temperature after throttling can be obtained. If the temperature drop after throttling is too large and the gas temperature is too low, resulting in condensation or frost, it is advisable to reduce the gas adiabatic throttling coefficient, and measures can be taken to reduce the throttling pressure drop and increase the gas temperature before throttling.

**3.1.2. Downhole Throttling Critical Flow Conditions.** When natural gas flows through the choke in the well, the flow process obeys the nozzle flow equation, that is, there are critical and subcritical areas, as shown in Figure 5.

When  $(p_2/p_1) \leq (2/(k+1))^{k/(k-1)}$ , the natural gas flow reaches the critical flow state, and the pressure wave generated before throttling will not be transmitted to after throttling.

When  $(p_2/p_1) > (2/(k+1))^{k/(k-1)}$ , the natural gas flow is subcritical, and the pressure wave generated before throttling will be transmitted to after throttling, resulting in wellhead pressure fluctuation [30].

Therefore, the fluid is generally required to be in a critical flow state for downhole throttling design.

**3.2. Calculation of Throttling Pressure and Cooling Drop in High Water-Bearing Gas Wells**

**3.2.1. Calculation of Throttling Pressure Drop in High Water-Bearing Gas Wells.** According to the theorem of momentum, there are

$$G_{g2}v_{g2} + G_{l2}v_{l2} - G_{g1}v_{g1} - G_{l1}v_{l1} = (p_1 - p_2)A_2. \quad (22)$$

It is assumed that there is no mass exchange between gas and liquid phases and their respective densities do not change significantly. Continuity equations are available:

$$\begin{aligned} G_{g1} &= G_{g2} = Gx, \\ G_{l1} &= G_{l2} = G(1-x), \end{aligned} \quad (23)$$

$$\begin{aligned} v_{g1} &= \frac{G_{g1}}{\rho_g A_{g1}} = \frac{Gx}{\rho_g A_1 \alpha}, \\ v_{g2} &= \frac{G_{g2}}{\rho_g A_{g2}} = \frac{Gx}{\rho_g A_2 \alpha}, \end{aligned} \quad (24)$$

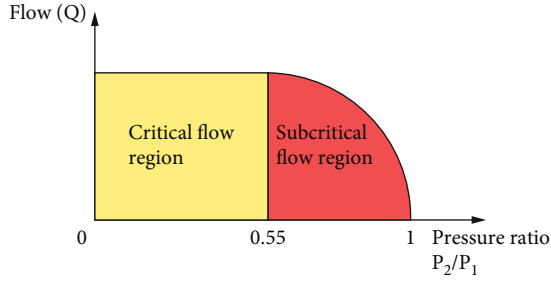


FIGURE 5: Flow characteristics of downhole choke.

$$\begin{aligned} v_{11} &= \frac{G_{11}}{\rho_l A_{11}} = \frac{G(1-x)}{\rho_l A_1(1-\alpha)}, \\ v_{12} &= \frac{G_{12}}{\rho_l A_{12}} = \frac{G(1-x)}{\rho_l A_2(1-\alpha)}, \end{aligned} \quad (25)$$

where  $\alpha_H$  is the change rate of temperature with pressure during natural gas throttling, if  $\alpha_H > 0$ . After throttling, the temperature will be consistent with the change of pressure.  $\alpha_H$  is not only a function of pressure but also a function of temperature. Therefore,  $\Delta T$  can only be solved approximately.

Approximate calculation

$$\Delta T = \sum_{p_1}^{p_2} \overline{\alpha_H} \Delta p, \quad (26)$$

where  $\overline{\alpha_H}$  is the average value of  $\alpha_H$  in the range of  $\Delta p$ . The calculation method is

$$\overline{\alpha_H} = \sum_{p_2}^{p_1} y_i \alpha_H. \quad (27)$$

Substituting equations (22), (23), and (24) into equation (27) can obtain

$$p_2 - p_1 = \frac{G^2}{A_1^2 \rho_l A_2} \left( 1 - \frac{A_1}{A_2} \right) \left[ \frac{(1-x)^2}{1-\alpha} + \frac{\rho_l x^2}{\rho_g \alpha} \right]. \quad (28)$$

For homogeneous flow, the section void fraction is equal to the mass void fraction, and the above formula can be simplified as

$$\Delta p = \frac{G^2}{A_1^2 \rho_l A_2} \left( 1 - \frac{A_1}{A_2} \right) \left[ 1 + x \left( \frac{\rho_l}{\rho_g} - 1 \right) \right]. \quad (29)$$

Obviously, through the above formula, on the premise of knowing the mass flow and fluid parameters, the gas-liquid two-phase throttling pressure drop can be calculated by formula (29).

**3.2.2. Calculation of Throttling Temperature Drop in High Water-Bearing Gas Wells.** In the process of gas-liquid communication through the choke, because the specific heat

capacity of the liquid is much larger than that of the gas, the temperature reduction rate of the liquid is much slower than that of the gas, so the energy transfer direction is from the liquid with higher temperature to the free gas with lower temperature. In addition, because the gas-liquid two-phase flow velocity in the throat of the choke is very fast, which is generally close to or exceeds the Mach number, the heat and mass balance of the gas-liquid two-phase cannot be established again in a very short time and can only be reestablished from the throttle outlet to the pressure recovery section. The basic equation satisfied by the heat exchange capacity is

$$Q_{\text{吸气}} = Q_{\text{放液}} \quad (30)$$

Obviously, equation (30) expresses that the heat absorbed by the gas phase is equal to the heat released by the liquid phase when the gas and liquid are connected through the choke. Ignoring the changes of mass fraction and specific heat capacity with pressure and temperature conditions, equation (30) can be expressed as

$$(1-M_g)C_{Vl}(T_1 - T_2) = M_g C_{Vg}(T_2 - T_g). \quad (31)$$

The left end of equation (31) fully exchanges heat to obtain heat balance due to the high temperature of the liquid phase and the heat released by the liquid; the right end represents the heat absorbed by the gas due to the low temperature of the gas phase.

Generally, the enthalpy difference is used to calculate the energy change of material in the process. The enthalpy of material is the sum of ideal gas enthalpy  $H_0$  and isothermal enthalpy difference  $H - H_0$  at this temperature. The thermodynamic equation of isothermal enthalpy difference is

$$H - H_0 = \int_0^V \left[ T \left( \frac{\partial p}{\partial T} \right)_V - p \right] dV + RT(Z - 1). \quad (32)$$

The equation of state of natural gas can be transformed into pressure in the form of

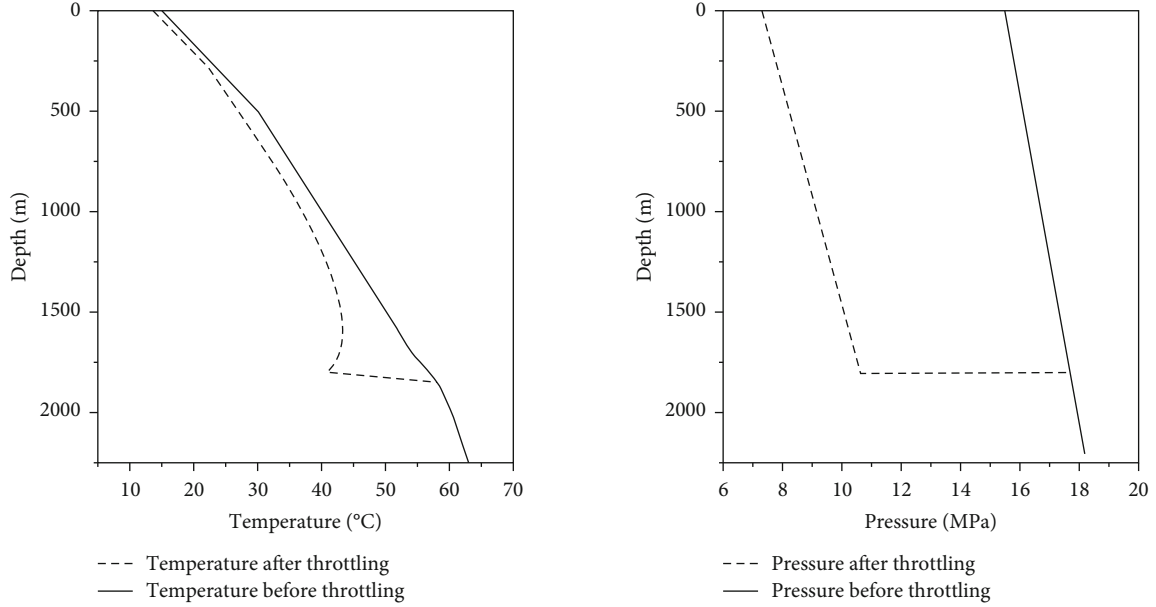
$$\left( \frac{\partial p}{\partial T} \right)_V = \frac{R}{V-b} - \frac{\partial \alpha / \partial T}{V(V+b) + b(V-b)}. \quad (33)$$

Substituting (32) into (31), the isothermal enthalpy difference formula can be obtained:

$$\frac{H - H_0}{RT} = \frac{T(\partial \alpha / \partial T) - \alpha(T)}{RT2\sqrt{2b}} \ln \frac{Z + 2.414B}{Z - 0.414B} + (Z - 1), \quad (34)$$

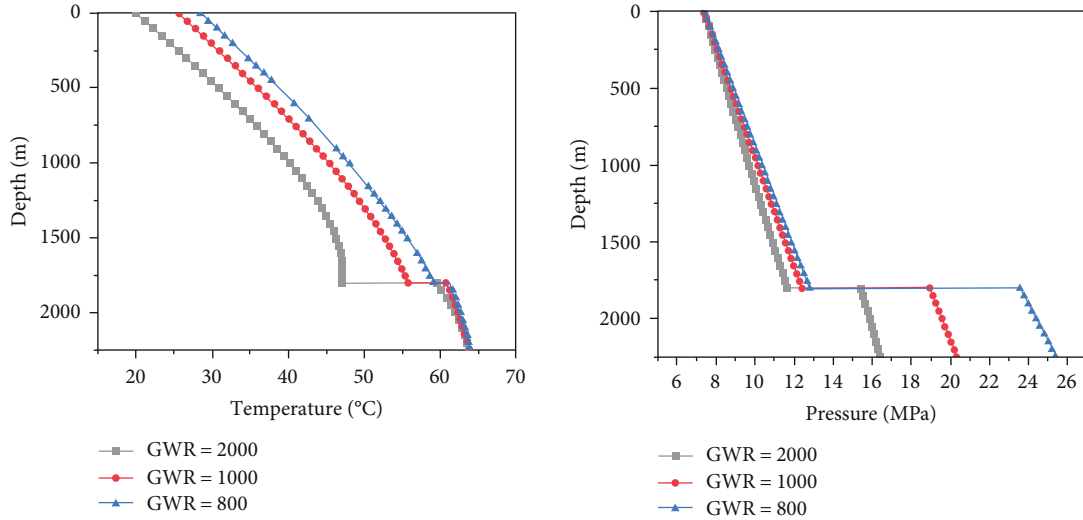
$$T \frac{\partial \alpha}{\partial T} = - \sum_{i=1}^n \sum_{j=1}^n x_i x_j m_j (\alpha_i \alpha_j T_{rj})^{0.5} (1 - k_{ij}), \quad (35)$$

$$B = \frac{bp}{RT}. \quad (36)$$



(a) Temperature comparison of Daji 4-5 well before and after throttling (b) Pressure comparison of Daji 4-5 well before and after throttling

FIGURE 6: Choke temperature and pressure distribution of Daji 4-5 well.



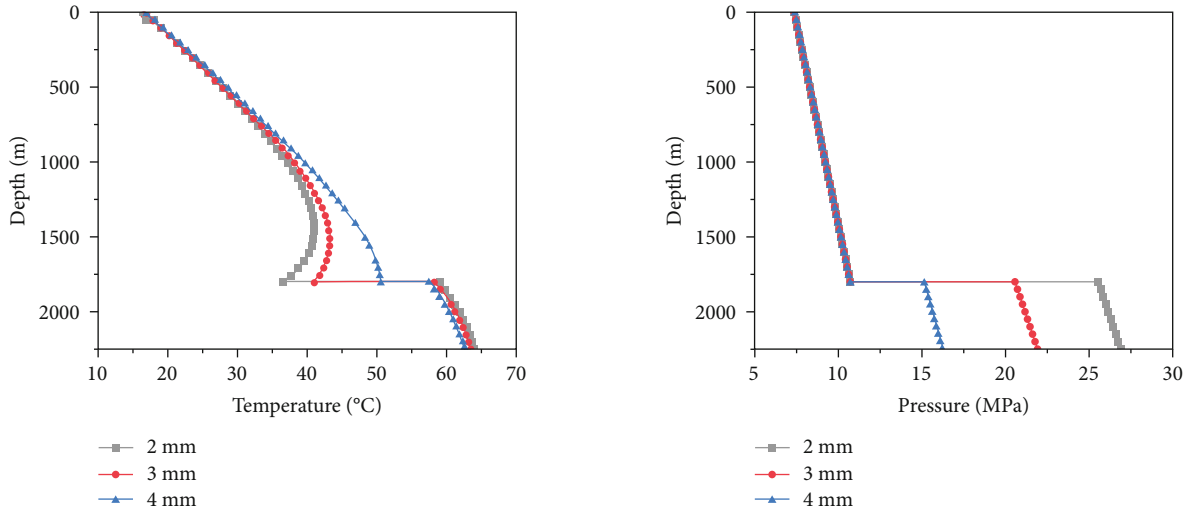
(a) Effect of gas water ratio on throttle temperature distribution (b) Effect of gas water ratio on throttle pressure distribution

FIGURE 7: Effect of gas water ratio on throttle temperature and pressure distribution.

3.3. Example Analysis of Gas Well Throttling Pressure and Temperature Drop. After obtaining the throttling pressure drop and temperature drop models of single-phase gas wells and high water content gas wells, combined with the wellbore temperature and pressure model, the wellbore temperature and pressure field under throttling condition can be analyzed. Taking Daji 4-5 gas well as an example, the wellbore temperature and pressure field under throttling conditions are analyzed and its sensitivity is also analyzed. The effects of water content, choke diameter, and gas production on the temperature-pressure field under throttling conditions are mainly considered. Combined with field data, the depth of the downhole choke is verified and analyzed.

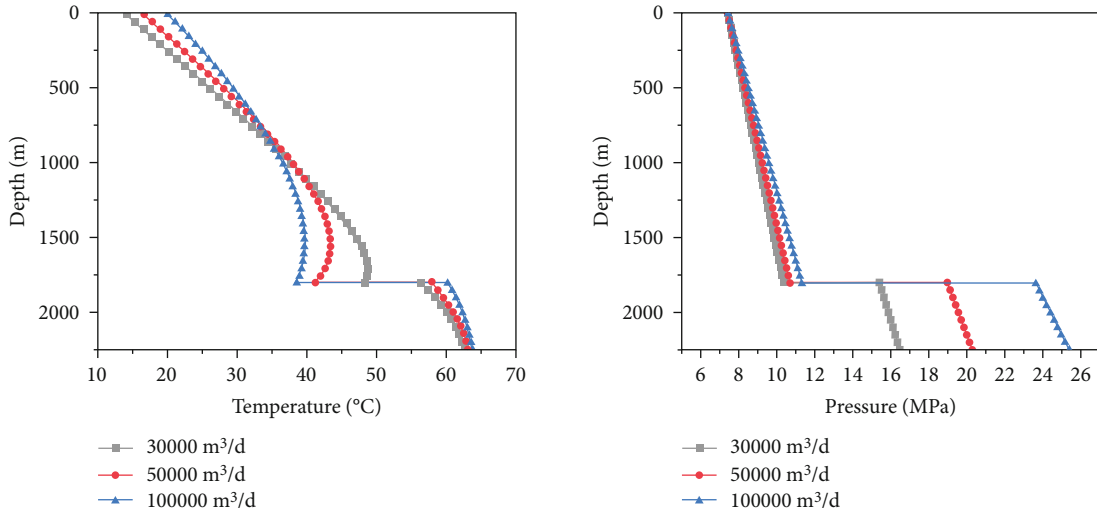
Combined with the hydrate distribution curve of well Daji 4-5,  $T_h = 14.5^\circ\text{C}$  and surface temperature  $T_d = 12.96^\circ\text{C}$  can be obtained. Combined with the field data, the ground temperature gradient of well Daji 4-5 is  $2.4^\circ\text{C}/100\text{m}$ , and  $M_0 = 41\text{ m}^\circ\text{C}$  can be obtained after conversion. Take  $B_K = 0.5$  and  $k = 1.3$ , and iteratively obtain  $Z_1 = 0.85$  at the corresponding temperature through the deviation coefficient of wellbore natural gas. Select 4 mm choke diameter and substitute formula (35) as follows:

$$L_{\min} \geq 41 \times \left[ (14.5 + 273) \times 0.5^{-0.85 \times (1.3-1)/1.3} - (12.96 + 273) \right]. \quad (37)$$



(a) Influence of choke nozzle diameter on throttle temperature distribution (b) Influence of choke nozzle diameter on throttle pressure distribution

FIGURE 8: Effect of throttle nozzle diameter on throttle temperature and pressure distribution.



(a) Effect of gas production on throttling temperature distribution (b) Effect of gas production on throttling pressure distribution

FIGURE 9: Effect of gas production on throttling temperature and pressure distribution.

By solving equation (37), the minimum running depth of well Daji 4-5 choke is 1800 m. The node analysis method is used to obtain the wellbore temperature and pressure distribution under throttling conditions. The steps are as follows: (1) the temperature and pressure distribution from the bottom of the well to the inlet of the choke is solved by the wellbore temperature and pressure program. (2) The temperature and pressure distribution in the throttling section is solved by using the throttling temperature and pressure drop model. (3) Taking the throttled temperature and pressure as the new initial value and substituting it into the temperature and pressure calculation program, the temperature and pressure distribution from the choke outlet to the wellhead is solved. The calculated results are shown in Figures 2 and 3.

It can be seen from Figure 6 that the wellbore temperature and pressure distribution change strongly after throttling. When the downhole choke is lowered at the position of 1800 m in the wellbore, the temperature and pressure have a sudden change at this position, and the temperature and pressure have decreased significantly. Due to the heating of the fluid in the wellbore by the ground temperature gradient, the temperature of the fluid in the wellbore will recover after throttling and then gradually decrease until the wellhead. The wellhead temperature after throttling is slightly lower than that before throttling, but the overall difference is small. After throttling, the pressure decreases greatly, making the wellhead in a low-pressure state compared with that before throttling, to achieve the purpose of preventing hydrate formation.

In the actual downhole throttling process, there are many factors affecting the wellbore temperature and pressure distribution after throttling, such as gas water ratio, choke diameter, and gas production. Through the field data, combined with the established throttling model, the sensitivity of the throttled wellbore is analyzed. The results are shown in Figures 7–9.

Combined with the throttling temperature and pressure distribution model of single-phase gas well and the throttling temperature and pressure distribution model of high water-bearing gas well, the throttling sensitivity of the Daji 4-5 gas well is analyzed. Figure 7 shows that (1) with the decrease of gas water ratio, the fluid water content in the wellbore increases and the throttling temperature decreases more; (2) on the premise of keeping the wellhead flow pressure unchanged, change the gas-water ratio to obtain the pressure change after throttling. With the decrease of gas-water ratio, the pressure before throttling becomes higher and higher, and the throttling pressure drop becomes larger and larger. Figure 8 shows that (1) with the increase of nozzle diameter, the throttling temperature drop becomes smaller and smaller. This is because the increase of nozzle diameter increases the amount of fluid passing through the nozzle at the unit interface, resulting in the weakening of the throttling effect, resulting in a smaller throttling temperature drop; (2) with the increase of orifice diameter, the throttling pressure drop decreases gradually. Figure 9 shows that (1) with the increase of gas production, the temperature before throttling gradually increases, and the throttling temperature drops gradually increases. The higher the production, the higher the wellhead temperature after throttling. (2) With the increase of gas production, the pressure before throttling increases gradually, and the pressure drop increases gradually.

**3.4. Numerical Simulation of Downhole Throttling.** In order to obtain the variation of internal parameters of the throttling flow field, CFD simulation can be used. The gas-water mixing choke can be regarded as a steady and compressible flow problem of fluid through sudden contraction and sudden expansion pipeline. The purpose of the solution is to simulate the velocity field and temperature field of the downhole choke through Fluent. The working medium is gas-water two-phase fluid. Usually, the fluid flow state will change after passing through this pipeline. With reference to the actual parameters of the well example, the outer diameter is selected as  $\Phi 73$  mm tubing movable downhole choke with an inner diameter of  $\Phi 62$  mm, choke diameter  $d = 3.8$  m, length  $l = 20$  mm, inlet section  $L_1 = 100$  mm, and outlet section  $L_2 = 300$  mm. The structural model is shown in Figure 10.

The structural grid in this paper is mainly generated by ICEM CFD 2020 R2, and the boundary layer at the throttle valve is encrypted. At the same time, in order to reduce the number of grids, a coarser grid is used in the part where the inlet and outlet are far away from the throttle valve. The grid diagram is shown in Figure 11. Through the grid independence analysis, the number of grids greater than 200,000 has no effect on the calculation results. Finally, about

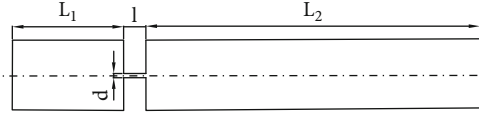


FIGURE 10: Geometric model of restrictor.

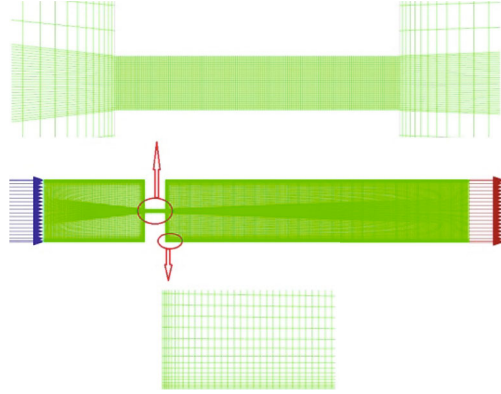


FIGURE 11: Schematic diagram of mesh.

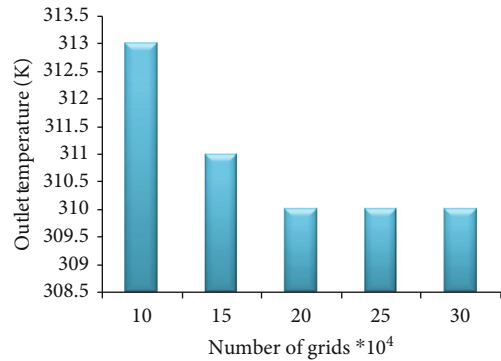


FIGURE 12: Mesh independence.

200,000 grids are selected for calculation, as shown in Figure 12.

We use Fluent to run the model. First, open multiphase model, energy model, and viscous model, respectively. Then, in the multiphase flow model, phase 1 is defined as the main phase as methane, and phase 2 is defined as the dispersed phase as water-liquid. Throttle inlet pressure  $p_1 = 17.5$  MPa,  $T_1 = 340$  K. Throttle outlet pressure  $p_2 = 6$  MPa,  $T_2 = 300$  K. The flow of natural gas in the restrictor is considered as a steady state.

Using energy equation and standard  $k - \omega$  model, the natural gas flow in the restrictor is regarded as a compressible fluid. The mixture homogenization model based on pressure is used to simulate the changes of pressure, velocity, and temperature in the internal flow field of the restrictor.

The general change trend of pressure is that the gas pressure before throttling does not change significantly. The cross-sectional area at the throttling inlet decreases sharply and the flow rate increases abruptly (as shown in Figure 13), resulting in the instantaneous reduction of the

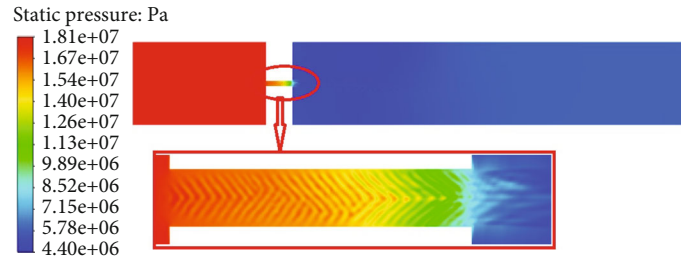


FIGURE 13: Pressure nephogram and curve of flow field in restrictor.

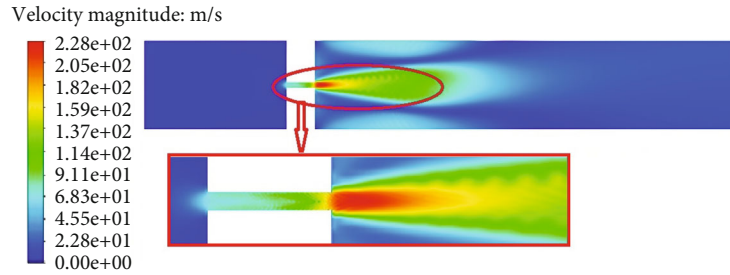


FIGURE 14: Cloud diagram and curve of flow field velocity in restrictor.

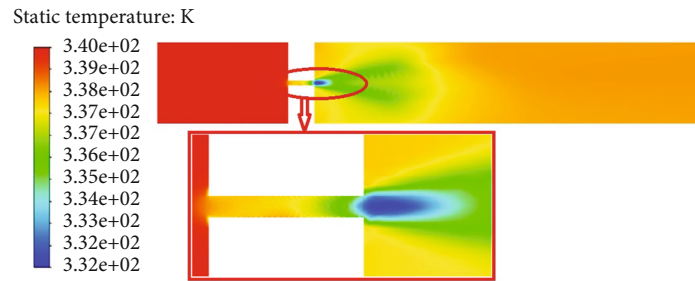


FIGURE 15: Cloud diagram and curve of total temperature of flow field in restrictor.

internal flow field from high pressure to low pressure (as shown in Figure 14). Throttling converts the pressure energy into kinetic energy. Near the throttling outlet, the flow rate of high-speed gas begins to decrease with the mixing with the surrounding gas. The pressure rises to a certain extent and then tends to be stable. It can be seen from the temperature distribution curve in Figure 15 that there is a large temperature drop process at the throttling position. The temperature of the fluid reaches the lowest value after passing through the throttling nozzle, and then, the low-temperature gas and the surrounding gas fuse and rise gradually under the action of the ground temperature gradient.

#### 4. Summary and Conclusions

Compared with the Ramey model and Hassan and Kabir model, the wellbore temperature and pressure coupling prediction model of the high water content gas well in this paper is closer to the field measured data.

- (1) With the decrease of gas water ratio, the fluid water content in the wellbore increases and the throttling temperature decreases more
- (2) On the premise of keeping the wellhead flow pressure unchanged, change the gas-water ratio to obtain the pressure change after throttling. With the decrease of gas-water ratio, the pressure before throttling becomes higher and higher, and the throttling pressure drop becomes larger and larger. With the increase of the orifice diameter, the throttling temperature drop becomes smaller and smaller. This is because the increase of the orifice diameter increases the amount of fluid passing through the orifice at the unit interface, resulting in the weakening of the throttling effect, resulting in the smaller throttling temperature drop
- (3) With the increase of orifice diameter, the throttling pressure drop decreases gradually. With the increase of gas production, the temperature before throttling increases gradually, and the throttling temperature drop increases gradually. The higher the production, the higher the wellhead temperature after throttling
- (4) With the increase of gas production, the pressure before throttling increases gradually, and the pressure drop increases gradually. There is a large

temperature drop process at the throttling position. When the fluid passes through the throttling nozzle, the temperature reaches the lowest value, and then, the low-temperature gas merges with the surrounding gas and rises gradually under the action of the ground temperature gradient

In conclusion, through comparison, the model established in this paper has more accurate prediction data, but this research model is only applicable to the prediction and calculation of temperature and pressure field of high water cut two-phase flow gas wells.

## Nomenclature

$\rho_g$ and $\rho_l$ :	Gas density and liquid density ( $\text{kg/m}^3$ )
$u_g$ and $u_l$ :	Gas flow rate and liquid flow rate (m/s)
$a$ :	Section air content
$Q$ :	Mass flow (kg/s)
$G$ :	Mass flow rate ( $\text{kg}/(\text{m}^2 \cdot \text{s})$ )
$\beta$ :	Volumetric gas content
$\tau$ :	Shear stress between fluid and pipe wall ( $\text{N}/\text{m}^2$ ), $\tau = (A/\pi d)\rho_m g \cdot 4f(1/d)(v^2/2g)$
$f$ :	The frictional resistance coefficient of two-phase flow
$G$ :	Mass flow rate ( $\text{kg}/(\text{m}^2 \cdot \text{s})$ )
$v_m$ :	The specific volume of two-phase flow ( $\text{kg}/\text{m}^3$ )
$h$ :	Specific enthalpy (J/kg)
$V_m$ :	Flow rate of mixture (m/s)
$q$ :	Heat of unit control body (J/m·s)
$Q$ :	Mass flow of wellbore fluid (kg/s)
$C_p$ :	Specific heat capacity of fluid at constant pressure (J/(kg·K))
$C_J$ :	Joule Thomson coefficient of gas-liquid two-phase fluid
$r_{to}$ :	Outer diameter of oil pipe (m)
$U_{to}$ :	Total heat transfer coefficient ( $\text{J}/(\text{m} \cdot \text{s} \cdot \text{K})$ )
$T_f$ :	Wellbore fluid temperature (K)
$T_s$ :	Temperature of the second contact surface (K)
$k_e$ :	Formation thermal conductivity ( $\text{J}/(\text{m} \cdot \text{s} \cdot \text{K})$ )
$T_{ei}$ :	Formation temperature at any depth (K)
$f(t)$ :	Dimensionless time function
$T_{f\text{out}}$ :	Fluid temperature at the outlet of each section (K)
$z_{\text{out}}$ :	Outlet of each section (m)
$z_{\text{in}}$ :	Entrance of each section (m)
$T_{f\text{in}}$ :	Fluid temperature at the inlet of each section (K)
$T_{e\text{out}}$ :	Formation temperature at the outlet of each section (K)
$T_{e\text{in}}$ :	Formation temperature at the inlet of each section (K)
$w$ :	Mass flow of wellbore fluid (kg/s)
$W_g$ :	Gas mass flow (kg/s)
$Z_g$ :	Deviation coefficient of natural gas
$\rho_g$ :	Gas density ( $\text{kg}/\text{m}^3$ )
$\rho_l$ :	Liquid density ( $\text{kg}/\text{m}^3$ )
$C_v$ :	Coefficient of variation
$\sigma$ :	Standard deviation

$\mu$ :	Average value
$G$ :	Mass flow (kg/s)
$v$ :	Flow rate (m/s)
$A_2$ :	Throat sectional area ( $\text{m}^2$ ); $g$ and $l$ , respectively, represent gas phase and liquid phase, and 1 and 2 represent throttle inlet and throttle throat, respectively
$x$ :	Mass air content
$\alpha$ :	Section void content
$y_i$ :	Mole fraction of component $i$ in the gas phase
$\Delta T$ :	Temperature change before and after throttling (K)
$\Delta p$ :	Pressure change before and after throttling (MPa)
$p_1$ and $p_2$ :	Pressure value before and after throttling (MPa)
$M_g$ :	Gas phase mass fraction
$C_{vl}$ :	Specific heat capacity of liquid phase at constant volume (kJ/(kg·K))
$C_{vg}$ :	Specific heat capacity of gas phase at constant volume (kJ/(kg·K))
$T_2$ :	Temperature before throttling (K)
$T_2$ :	Gas-liquid two-phase heat balance temperature after throttling (K)
$T_g$ :	Temperature under downstream pressure of isoenthalpy process (K)
$k_{ij}$ :	Adiabatic index of natural gas with different components
$T_{rj}$ :	Comparison temperature of component $j$ (K)
$R$ :	Gas constant (8314 kJ/(kmol·K)).

## Data Availability

The manuscript is a data self-contained article, whose results were obtained from the laboratory analysis, and the entire data are presented within the article.

## Conflicts of Interest

The authors declare that there is no conflict of interest regarding the publication of this paper.

## Acknowledgments

This project was supported by the National Natural Science Foundation of China (52004215, 12101482, and 51674199) and Graduate Innovation and Practical Ability Training Program of Xi'an Shiyou University (YCS211053).

## References

- [1] B. Moradi, M. Ayoub, M. Bataee, and E. Mohammadian, "Calculation of temperature profile in injection wells," *Journal of Petroleum Exploration and Production Technology*, vol. 10, no. 2, pp. 687–697, 2020.
- [2] X. Li, J. Zhang, X. Tang, G. Mao, and P. Wang, "Study on wellbore temperature of riserless mud recovery system by CFD approach and numerical calculation," *Petroleum*, vol. 6, no. 2, pp. 163–169, 2020.

- [3] H. Jung, D. N. Espinoza, and S. A. Hosseini, "Wellbore injectivity response to step-rate CO<sub>2</sub> injection: coupled thermo-poro-elastic analysis in a vertically heterogeneous formation," *International Journal of Greenhouse Gas Control*, vol. 102, article 103156, 2020.
- [4] Z. Guo, H. Wang, and M. Jiang, "A simple analytical model of wellbore stability considering methane hydrate saturation-dependent elastoplastic mechanical properties," *Journal of Petroleum Science and Engineering*, vol. 207, article 109104, 2021.
- [5] Y. Li, Y. Cheng, C. Yan et al., "Mechanical study on the wellbore stability of horizontal wells in natural gas hydrate reservoirs [J]," *Journal of Petroleum Science and Engineering*, vol. 207, article 109104, 2021.
- [6] Z. Wang, M. Yang, and Y. Chen, "Numerical modeling and analysis of induced thermal stress for a non-isothermal wellbore strengthening process," *Journal of Petroleum Science and Engineering*, vol. 175, pp. 173–183, 2019.
- [7] W. Sifan, Z. Ankang, and H. Dongfeng, "Research and Field Tests of Coiled Tubing Fishing Technology for Sand-Buried Throttles [J]," *Petroleum Drilling Techniques*, vol. 49, no. 5, pp. 108–113, 2021.
- [8] H. N. Wang, X. P. Chen, M. J. Jiang, and Z. Y. Guo, "Analytical investigation of wellbore stability during drilling in marine methane hydrate-bearing sediments," *Journal of Natural Gas Science and Engineering*, vol. 68, article 102885, 2019.
- [9] L. Zhang, S. Qu, C. Wang, and B. Guan, "Prediction temperature field and wax deposition based on heat-fluid coupling method," *Journal of Petroleum Exploration and Production Technology*, vol. 9, no. 1, pp. 639–644, 2019.
- [10] M. Mansourpoor, R. Azin, S. Osfouri, and A. A. Izadpanah, "Study of wax disappearance temperature using multi-solid thermodynamic model," *Journal of Petroleum Exploration and Production Technology*, vol. 9, no. 1, pp. 437–448, 2019.
- [11] J. Yang, Y. Feng, B. Zhang, Y. Tang, and Z. Jiang, "A blockage removal technology for natural gas hydrates in the wellbore of an ultra-high pressure sour gas well," *Natural Gas Industry B*, vol. 8, no. 2, pp. 188–194, 2021.
- [12] H. Wang, "A non-isothermal wellbore model for high pressure high temperature natural gas reservoirs and its application in mitigating wax deposition," *Journal of Natural Gas Science and Engineering*, vol. 72, article 103016, 2019.
- [13] Y. Gholamzadeh, M. Sharifi, A. Karkevandi-Talkhoonchah, and M. K. Moraveji, "A new physical modeling for two-phase wellbore storage due to phase redistribution," *Journal of Petroleum Science and Engineering*, vol. 195, article 107706, 2020.
- [14] N. Wei, J. Zhao, W. Sun et al., "Non-equilibrium multiphase wellbore flow characteristics in solid fluidization exploitation of marine gas hydrate reservoirs," *Natural Gas Industry B*, vol. 6, no. 3, pp. 282–292, 2019.
- [15] M. M. Abdelhafiz, L. A. Hegele, and J. F. Oppelt, "Temperature modeling for wellbore circulation and shut-in with application in vertical geothermal wells," *Journal of Petroleum Science and Engineering*, vol. 204, article 108660, 2021.
- [16] R. G. Turner, M. G. Hubbard, and A. E. Dukler, "Analysis and prediction of minimum flow rate for the continuous removal of liquids from gas wells," *Journal of Petroleum Technology*, vol. 21, no. 11, pp. 1475–1482, 1969.
- [17] H. E. Gray, *Vertical Flow Correlation in Gas Wells [J]*. *User Manual for API14B, Subsurface Controlled Safety Valve Sizing Computer Program*, 1974.
- [18] B. Guo, A. Ghalambor, and C. Xu, "A systematic approach to predicting liquid loading in gas wells," *SPE Production & Operations*, vol. 21, no. 1, pp. 81–88, 2006.
- [19] M. Li, S. L. Li, and L. T. Sun, "New view on continuous-removal liquids from gas wells," *SPE Production & Facilities*, vol. 17, no. 1, pp. 42–46, 2002.
- [20] P. Chaoyang, "Study on critical liquid carrying flow of gas wells [J]," *Journal of Petroleum*, vol. 12, no. 1, pp. 72–74, 2010.
- [21] W. Zhibin and L. Yingchuan, "Continuous liquid carrying mechanism of gas wells [J]," *Journal of Petroleum*, vol. 33, no. 4, pp. 681–686, 2012.
- [22] Y. Zhi, M. Jixiang, and H. Pan, "Study on downhole throttling and its influence on liquid carrying capacity [J]," *Inner Mongolia petrochemical industry*, vol. 12, no. 7, pp. 6–9, 2012.
- [23] L. Gang, "A new method for critical flow of liquid carrying in gas wells [J]," *Fault block oil and gas reservoir*, vol. 21, no. 3, pp. 339–343, 2014.
- [24] Z. Yang, "Analysis of wellbore effusion in low production and low pressure gas wells [J]," *Neijiang science and technology*, vol. 39, no. 5, pp. 74–75, 2018.
- [25] D. Jinbao, *Study on Gas-Liquid Two-Phase Flow Characteristics and Critical Liquid Carrying Model in Gas Well Bore [D]*, Xi'an University of petroleum, 2020.
- [26] M. Wei and L. Zheng, "Coupling analysis of gas well wellbore pressure and temperature [J]," *Natural Gas Industry*, vol. 19, no. 6, pp. 66–68, 1999.
- [27] H. Ramey Jr., "Wellbore heat transmission," *Journal of Petroleum Technology*, vol. 14, no. 4, pp. 427–435, 1962.
- [28] Y. Yu, W. Wang, Y. Peng, H. Tan, Z. Dong, and W. Zhou, "Application and design method of downhole throttling technology for ultra-high pressure gas wells [J]," *Natural gas and oil*, vol. 38, no. 6, pp. 80–85, 2020.
- [29] Z. Youwei, S. Haiguang, Z. Yuhao, J. Zhichen, S. Yufa, and G. Yonghai, *Hydrate prevention analysis of downhole throttling technology for deep-water high-pressure gas wells [C] // Proceedings of the 31st national hydrodynamic Symposium (Volume II)*, pp. 253–260, 2020.
- [30] Q. Caiting, *Analysis of Downhole Choke Point System of Water Producing Gas Well [D]*, Northeast Petroleum University, 2018.



## Research Article

# Evaluation of the Accumulation Conditions and Favorable Areas of Shale Gas in the Upper Palaeozoic Marine-Continental Transitional Facies in the Daning-Jixian Area, Ordos Basin

Xu Zeng <sup>1</sup>, Wei Wang,<sup>2</sup> Qian Cao,<sup>1</sup> Shangwen Zhou <sup>1</sup>, Guodong Dong,<sup>3</sup> Aiming Wang,<sup>4</sup> Zhixin Chen,<sup>2</sup> and Hua Mei<sup>4</sup>

<sup>1</sup>Research Institute of Petroleum Exploration and Development of PetroChina, Beijing 10083, China

<sup>2</sup>Hebei Gas Storage Branch Company of China Petroleum Huabei Oilfield Company, Langfang 065007, China

<sup>3</sup>Exploration and Development Research Institute of China Petroleum Changqing Oilfield Company, Xi'an 710000, China

<sup>4</sup>Exploration and Development Research Institute of China Petroleum Qinghai Oilfield Company, Dunhuang 732001, China

Correspondence should be addressed to Xu Zeng; [zengxu20212021@163.com](mailto:zengxu20212021@163.com)

Received 18 August 2021; Revised 3 December 2021; Accepted 17 December 2021; Published 17 January 2022

Academic Editor: Afshin Davarpanah

Copyright © 2022 Xu Zeng et al. This is an open access article distributed under the Creative Commons Attribution License, which permits unrestricted use, distribution, and reproduction in any medium, provided the original work is properly cited.

This study focuses on the organic-rich mud shale in the Upper Palaeozoic transitional facies in the southeastern margin of the Ordos Basin. It systematically analyzes the shale gas accumulation conditions of the organic-rich mud shale in the Lower Permian Shanxi-Taiyuan Formation, including the thickness, distribution, organic matter type and content, thermal maturity, reservoir space, gas-bearing property, and rock brittleness. The results show that the thick dark mud shale contains a high organic matter content, is a suitable kerogen type for gas generation, and exhibits moderate thermal evolution, providing excellent conditions for hydrocarbon accumulation. Residual primary pores formed by shale compaction, secondary pores formed by organic matter hydrocarbon generation, clay mineral transformation and dissolution, and fractures provide suitable reservoir spaces for shale gas. The shale in the study area has a higher gas content than the shale strata in the marine basins of the United States. In addition, the content of brittle minerals such as quartz is higher, and Poisson's ratio is lower, facilitating the subsequent transformation. The accumulation conditions indicate the high potential of the study area for shale gas exploration and development. The geological analogy method is used to compare the study area with five major shale gas basins in the United States. The results indicate that the shale gas resources of the Shanxi-Taiyuan Formation in the study area are in the range of  $2800\text{--}3200 \times 10^8 \text{ m}^3$ . The primary controlling factors affecting shale gas reservoirs in this area are the abundance of organic matter, thermal maturity, shale thickness, and quartz content. Favorable areas are predicted based on these factors.

## 1. Introduction

Shale gas is an unconventional natural gas [1–3]. Due to the increasing difficulty of the exploration of China's conventional oil and gas resources and the success of the shale gas revolution in the United States, China's shale gas production has reached 20 billion cubic meters, accounting for 28% of the growth of total natural gas production [4]. Shale gas production has become an essential part of China's natural gas production. Shale gas in the United States is dominated by marine facies [5]. In contrast, China's shale gas resources

are predominantly marine-continental transitional facies, with a volume of about  $19.8 \times 10^{12} \text{ m}^3$ , accounting for 25% of China's total shale gas resources [6], representing an important aspect of shale gas exploration. China's marine-continental transitional organic-rich shale is widely distributed in the Ordos and Sichuan Basins. These areas have good shale gas resources and the potential for exploration and development [7–9]. The Ordos Basin in China is a large onshore petroliferous basin with natural gas resources of  $29.2 \times 10^{12} \text{ m}^3$ . A preliminary breakthrough in shale gas exploration in the marine-continental transitional facies

has been achieved at the eastern margin of the basin [10]. However, few studies have been conducted on shale gas in marine-continental transitional facies in China. Some scholars have investigated the sedimentary environment, shale gas-bearing characteristics, and storage space of the shale gas resources in the marine-continental transitional facies in the Upper Palaeozoic of the Ordos Basin. However, these studies were based on regional data of the entire basin. It is also necessary to select representative blocks in the basin to conduct in-depth research on the exploration potential of the entire basin. Some scholars focused on the evaluation and optimization of favorable shale gas exploration areas in this region. Yan et al. [11] and Zhai et al. [12] carried out an evaluation of favorable areas for shale gas exploration in the Upper Palaeozoic transitional facies of the Ordos Basin and investigated the shale gas deposition environment, source rock characteristics, and gas-bearing properties. Dazhong et al. [13] analyzed the shale development environment and single well production conditions to evaluate the prospects of marine-continental transitional shale gas exploration in the Ordos Basin. An evaluation of favorable areas for gas exploration requires a comprehensive analysis with a focus on the generation, storage, and sealing characteristics of shale gas. An analysis of the accumulation conditions based on a single factor is insufficient to support the subsequent oil and gas exploration [14]. This study focuses on the Daning-Jixian area at the southeastern margin of the Ordos Basin. Many exploratory wells have been drilled in the study area, and some have shown significant oil and gas potential in the shale section of the Shanxi-Taiyuan Formation of the Permian strata in the Upper Palaeozoic facies. Therefore, this study systematically investigates the characteristics of the organic matter, petrology, storage space, and mechanical properties of the shale section in the block. Other accumulation features, such as formation brittleness and roof and floor conditions, which are closely related to shale gas exploration and development, are evaluated. The study area is scientifically and comprehensively evaluated by comparing its shale gas zones with those of the United States, and favorable regions are predicted based on geological conditions. This study provides a foundation for evaluating the exploration potential of the Upper Palaeozoic shale gas region in the entire Ordos Basin.

## 2. Geological Background

**2.1. Structure.** The study area is located at the southeastern margin of the Ordos Basin on the western flank of the Lvliang Mountain anticline and the west side of the Zijingshan fault zone. As shown in Figure 1, the study area is characterized by a northwest-inclined monoclinic structure. The strata strike northeast or north-northeast and dip gently to the west or northwest, with dip angles of  $5^{\circ}$ – $10^{\circ}$ . The entire structure is nearly rectangular and has a north-south orientation (Figure 1). Few geological structures are found in the study area, such as small folds and faults. For example, the Guyi-Yaoqu anticline and Xueguan-Yukou flexure spreading in the northeast-southwest direction are parallel, juxtaposed, and run through the entire area. The Guyi-Yaoqu anticline is the main structure in the study area. Its overall trend is  $30^{\circ}$ , the length is 40 km, and it has a steep eastern

flank and gentle western flank. In conjunction with the Guyi-Yaoqu anticline, the Xueguan-Yukou flexure developed at a distance of 3 km–3.5 km from the southeastern side of the anticline and parallel to it, with a total length of nearly 40 km. Its flexural strength is strong at both ends and weak in the middle [15]. In addition, small-scale anticlines have developed locally, such as the Hougetai anticline, Shanggoukou syncline, Fengjialing anticline, and Huangjiazhuang syncline. The primary fault structure in the study area is the Zijingshan fault zone on the eastern side, whose attitude is moderately steep near the flexure zone. There are relatively few faults in the study area; most are small faults, with no large faults in the central and deep areas.

**2.2. Stratigraphy.** The basement of the basin in the study area is composed of Cambrian, Ordovician, Carboniferous, Permian, Triassic, Neogene, and Quaternary strata. The Upper Palaeozoic includes the Carboniferous and Permian strata. The lower Permian consists of marine-continental transitional to continental delta deposits, forming thick layers of dark mud shale. The upper Shihezi Formation and Shiqianfeng Formation have developed sand-shale interbedded deposits. The regional geological conditions indicate that the Permian Taiyuan and Shanxi Formations are potential areas to develop marine-continental transitional facies shale gas reservoirs. Therefore, these two formations are the target horizons of this study (Figure 2).

**2.2.1. Carboniferous Strata (C).** Only the Benxi Formation of the Upper Carboniferous strata has been developed, with layers of coal-bearing rock deposited in a marine and alternative continental environment. This formation has parallel unconformity contact with the underlying Fengfeng Formation of the Middle Ordovician. It is mainly characterized by yellow-green bauxitic mudstone with thin coal seams and limestone strata.

**2.2.2. Permian Strata (P).** The Permian strata are widely distributed in the study area, mainly including marine-continental transitional coal-bearing strata, continental clastic coal-bearing strata, and clastic non-coal-bearing strata. The Taiyuan Formation, Shanxi Formation, Shihezi Formation, and Shiqianfeng Formation are found from bottom to top. Relatively complete Permian strata have been exposed in Taitou Town, Shanxi Province, and the section has been measured and investigated. As shown in Figure 2, the Taiyuan Formation is mainly composed of dark mud shale, limestone, and sandstone. The limestone is abundant and rich in biological fossils. The Shanxi Formation is primarily composed of continental clastic rocks with many coal seams in the lower part. Based on the regional data, it has been concluded that the Shihezi Formation is in direct contact with the underlying Shanxi Formation and the overlying Shiqianfeng Formation. There are multiple sand and mudstone assemblages with interbeds of unequal thickness. A massive thick layer of grayish-yellow, grayish-green, medium-thick, medium coarse-grained sandstone has developed at the bottom of the Lower Shihezi Formation, marking the bottom of the Shihezi Formation.

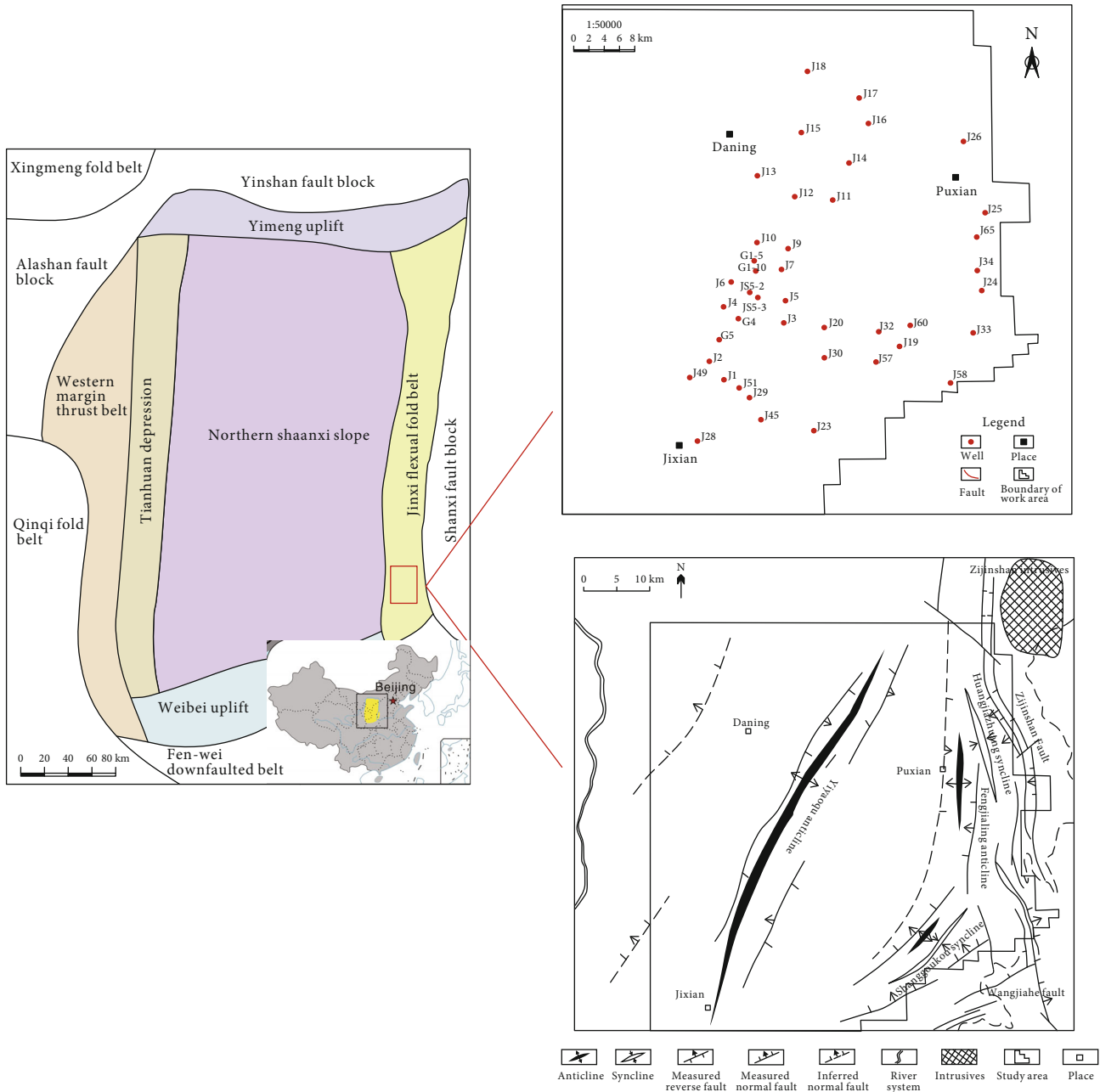


FIGURE 1: The location of the study area.

### 3. Samples and Methods

Total organic carbon (TOC) is an essential indicator for evaluating the abundance of organic matter. A total of 383 core samples were analyzed for organic carbon, including 280 samples from the Shanxi Formation and 103 samples from the Taiyuan Formation.

The petrological characteristics of the shale gas reservoir were quantitatively characterized by X-ray diffraction (XRD) analysis, a method to determine the internal spatial distribution of materials consisting of crystals [16]. Random-powder XRD (Bruker D2 PHASER X-ray diffractometer) was used to analyze

the mineral components. The shale powder (<300 mesh) was placed in a sample plate and scanned from 4.5° to 50° with a step length 0.02°. Core samples from more than 20 exploration wells in the area were analyzed using whole-rock XRD.

Imaging techniques and quantitative measurement were used to analyze the micropore structure of the shale. A field emission scanning electron microscope (FE-SEM) was used to analyze 15 samples from 6 exploration wells (J6, J51, J5, J57, and J45). The dried samples were pressed into cubes (1 cm × 1 cm × 1 cm), which were polished by argon ions. The samples were analyzed by the SEM to obtain the backscattered electron (BSE) image of the sample. A pore permeability

Stratigraphic unit				Thickness (m)	Lithology	Lithology features	Sedimentary subfacies	Sedimentary facies
Member	Period	Series	Group					
Paleozoic	Permian	Lower Permian	Upper Permian			Medium thick bedded grey sandstone	Delta plan	Delta
			Shanxi formation	40	Gray black and gray green mud shale mixed with gray sandstone with coal seams	Delta front		
				153.5		Prodelta		
			Taiyuan formation		Gray thick limestone, gray sandstone and gray black shale are developed in the main body, with thin coal seams	Shallow lacustrine	Lacustrine	
				449		Delta front	Delta	
105	Front water shelf	Continental						
Carboniferous	Upper Carboniferous	Beixi formation		The main sedimentary feature is yellow green aluminous mudstone with thin limestone and coal seams	Shallow sea shelf	Continental		

FIGURE 2: The C-P measured section column of the Taitou profile in Shanxi Province.

test was conducted on samples obtained from 20 exploration wells in the Shanxi Formation and Taiyuan Formation to determine the overburden pressure.

### 3.1. Source Rock Characteristics

**3.1.1. Organic Matter Characteristics.** A large dark mud shale area exists in the study area, representing favorable conditions for the development of source rocks. The abundance of organic matter determines the hydrocarbon generation capacity of shale and its adsorption capacity for shale gas.

As shown in Figure 3, the highest value of TOC in the samples of the Shanxi Formation is 29.25%, and the lowest value is 0.07%; 67.86% of the samples have a TOC of 0%–2%, and 32.14% have a TOC higher than 2%. The highest value of the samples from the Taiyuan Formation is 22.52%, and the lowest value is 0.011%; 43.69% of the samples have a TOC of 0%–2%, 40.78% of the samples have a TOC of 2%–4%, and 56.31% of the sample have a TOC higher than 2%. The TOC content of the five major shale gas basins in North America is 0%–25% [17], and the lower limit is generally

2.0% [18]. Based on previous studies, 2.0% was used as the lower limit of TOC to evaluate the organic matter abundance in the study area. As shown in Figure 4, areas in the Shanxi Formation with a TOC higher than 2% are mainly located in the central and eastern areas of the study area (wells G1-10, J7, J1, G5, G4, J3, J20, J45, J19, J24, J34, and J25), with the highest value of 19.57%. Areas with a TOC higher than 2% in the Taiyuan Formation are located in a region with northeast to southwest orientation. The northeast to southwest direction represented by Wells J16-J9-G5 is a high-value area with a TOC of more than 6%. Wells J25-J19-J23 in the east represent a high-value area of organic carbon content, with values exceeding 5%. The area between the wells with the two high values has a relatively low organic carbon content, but the organic carbon content in wells J20 and J29 is relatively high (more than 4%). In summary, the organic carbon content of more than 32.14% (56.31%) of the samples in the Shanxi group (Taiyuan group) is higher than 2%. The study area is rich in organic matter. The primary type of organic matter in the Shanxi Formation and Taiyuan Formation in the study area is type II2, which is rich in humic kerogen and can

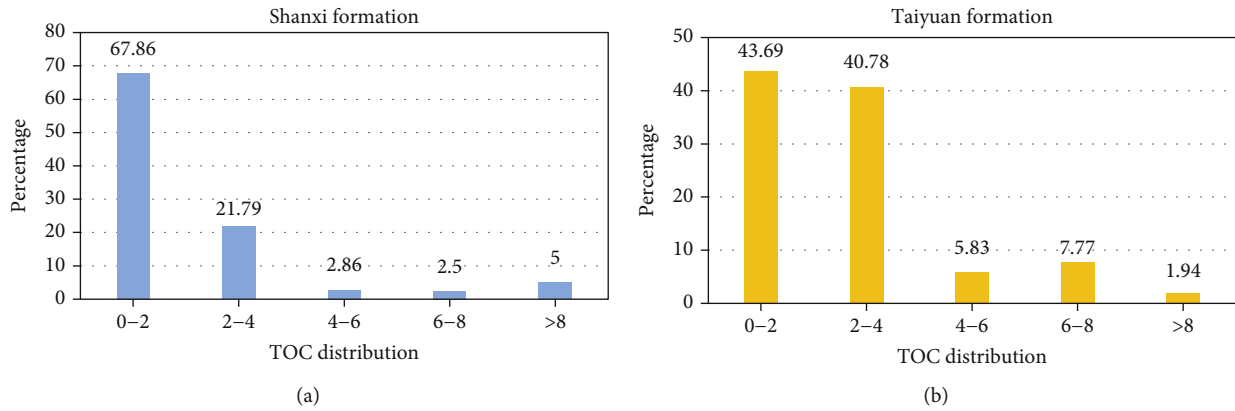


FIGURE 3: The total organic carbon content of the mud (shale) stone reservoirs in the study area.

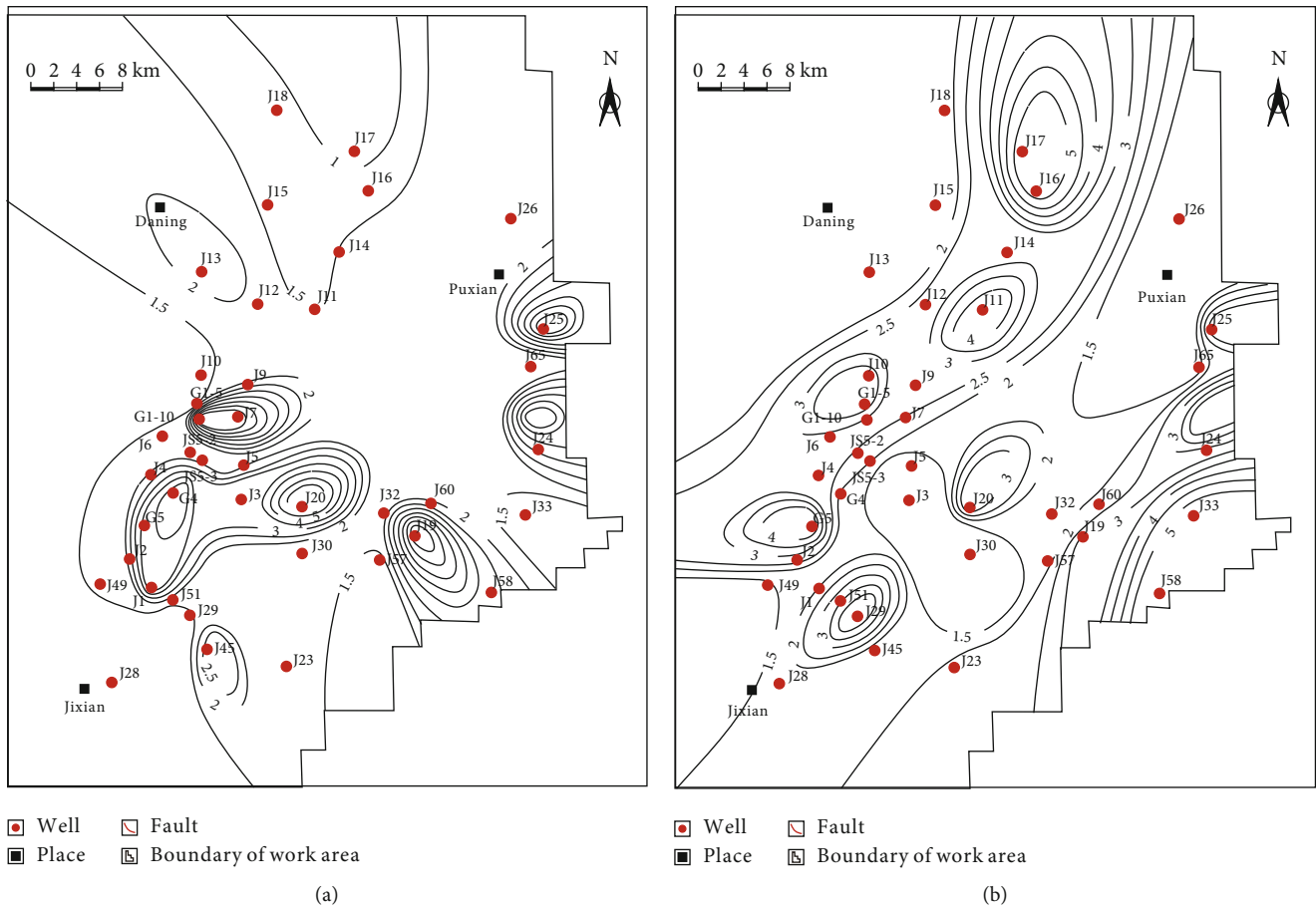


FIGURE 4: The contour map of the TOC of mud (shale) reservoirs in the study area. (a) Shanxi Formation; (b) Taiyuan Formation.

generate large amounts of natural gas [19]. Therefore, these two areas show excellent potential for shale gas formation.

**3.1.2. Shale Thickness.** The burial depth of the Shanxi Formation in the study area is 571 m–1447.5 m, and the shale thickness is 23.18 m–99.84 m, with an average of 54.18 m. The shale is thicker in the northeast, with a maximum thickness of more than 90 m. Only a few well areas in the central, western, and

eastern parts of the study area show high shale thickness values. The burial depth of the Taiyuan Formation is 620.5 m–1503 m, and the thickness of the shale ranges from 17.22 m to 66.94 m, with an average of 30.72 m, thinner than the shale of the Shanxi Formation. Wells J11 and J13 in the northwest, east, and south of the study area have larger shale thicknesses (Figure 5). In summary, the shale in the study area is relatively thick and has adequate conditions for shale gas

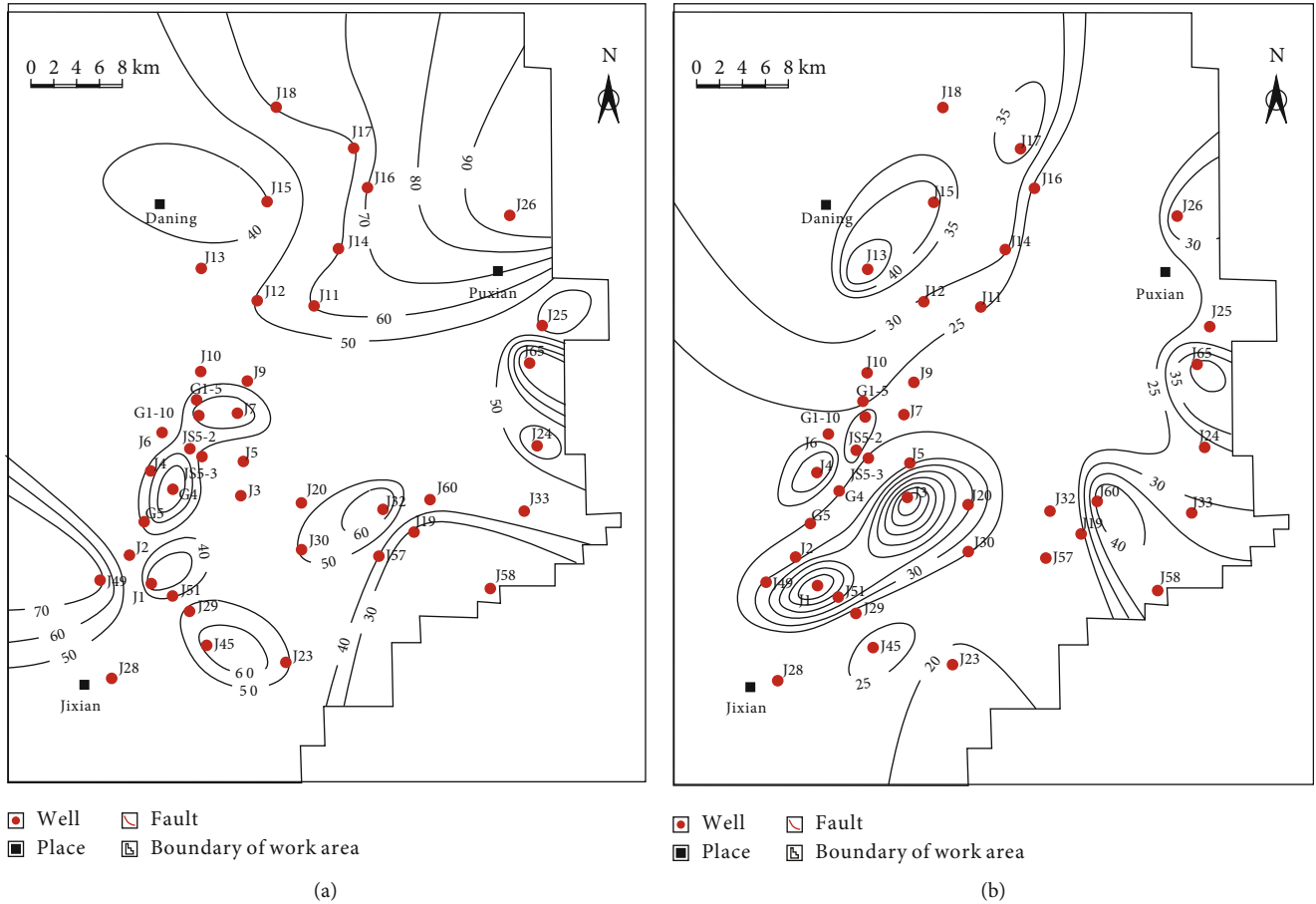


FIGURE 5: The contour map of the thickness of the mud (shale) reservoirs in the study area. (a) Shanxi Formation; (b) Taiyuan Formation.

hydrocarbon accumulation. The area experienced deep burial historically and subsequent uplift, resulting in a relatively shallow burial depth [20].

**3.1.3. Types of Organic Matter.** Under normal circumstances, the four components in kerogen can be observed under the microscope (vitrinite, inertinite, exinite, and sapropelite). Different types of kerogen are formed by different combinations of these four microscopic components. The hydrogen-rich sapropelite and chitinous formations have better hydrocarbon generation potential [20]. Vitrinite generally has only gas generation potential. Fluoro vitrinite has the potential to generate oil, while inertite cannot generate oil or gas.

The analysis results show that the main type of organic matter in the Shanxi Formation in the study area is type II<sub>2</sub>, with some occurrences of type III. The Taiyuan Formation is dominated by type II<sub>2</sub>, with some occurrences of type III. Therefore, the main type of organic matter in the Shanxi Formation and Taiyuan Formation in the study area is type II<sub>2</sub>.

**3.1.4. Thermal Maturity.** The statistics of the samples show that the vitrinite reflectance values of the shale in the study area are in the range of 1.0%–3.0%, and more than 80% are in the range of 1.0%–2.0%, which is favorable for shale gas formation.

As shown in Figure 6, the vitrinite reflectance of the Shanxi Formation is relatively low in the north and high in the south, with the highest value of over 2.2% in Well J45 in the south. The vitrinite reflectance characteristics are similar in the Taiyuan Formation. The highest values are found in Wells J45 and J23 (>2.1%), and most of the values in the north are lower than 1.4%. In summary, the vitrinite reflectance values are high in the south and low in the north; thus, the south of the study area is more favorable for shale gas generation than the north (Figure 6).

### 3.2. Reservoir Characteristics

**3.2.1. Mineral Composition.** The results show that clay minerals are the dominant minerals in the shale member of the study area, followed by quartz and plagioclase. The plagioclase content is low, but the areas of plagioclase are well developed. The average mineral composition of the shale members of the Shanxi Formation is as follows: clay (51.04%), quartz (40.74%), potassium feldspar (1.00%), plagioclase (2.56%), calcite (1.00%), dolomite (4.00%), pyrite (3.00%), and siderite (7.10%). The average mineral composition of the shale member of Taiyuan Formation is as follows: clay (48.35%), quartz (40.91%), potassium feldspar (1.56%), plagioclase (1.68%), calcite (24.00%), dolomite (2.67%), pyrite (4.23%), and siderite

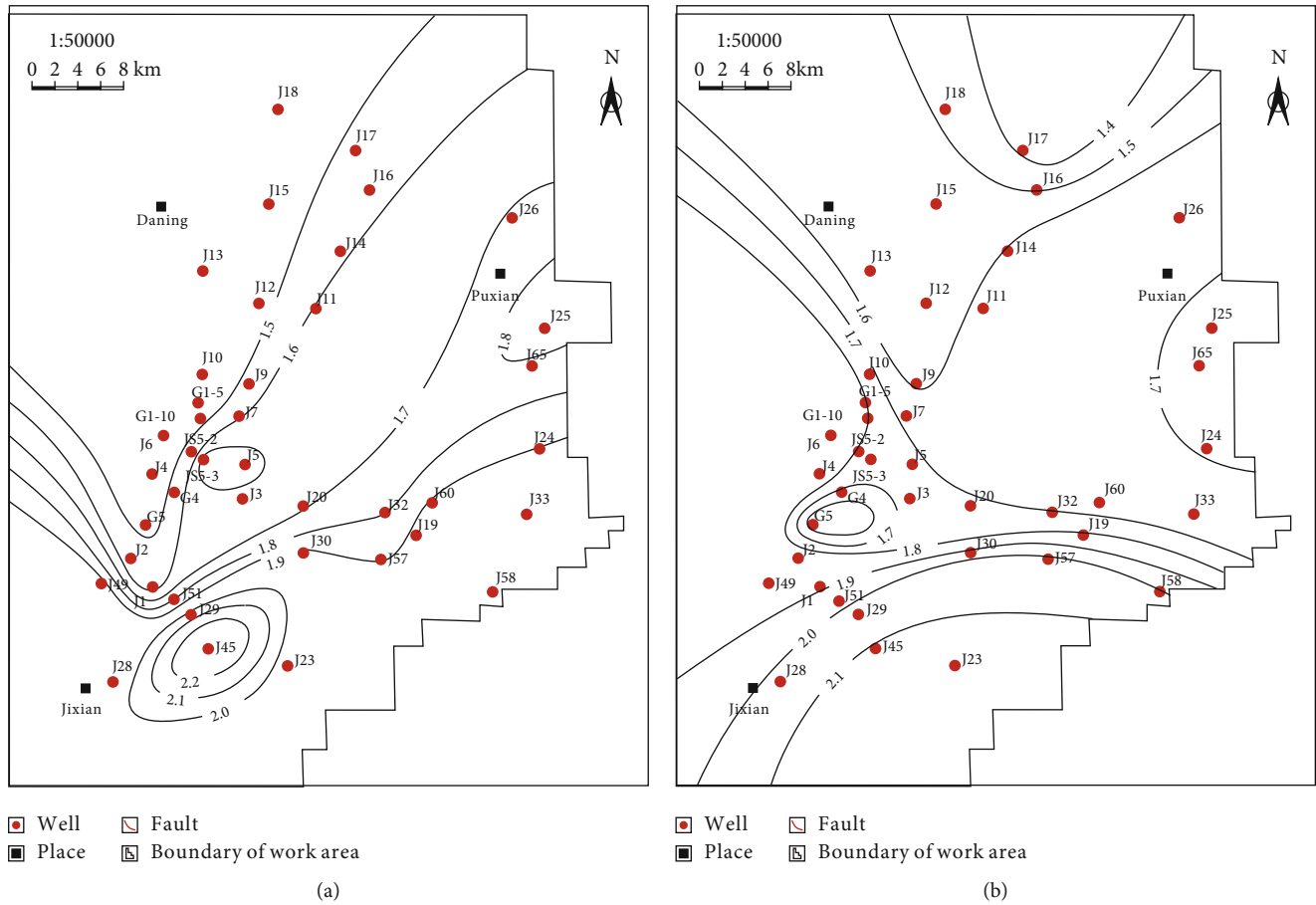


FIGURE 6: The contour map of vitrinite reflectance (Ro) of the mud (shale) stone reservoirs in the study area. (a) Shanxi Formation; (b) Taiyuan Formation.

(4.04%) (Figure 7). The quartz content of the Shanxi Formation is higher than 35%, and the quartz areas are located in the northwest, central-east, and southwest of the study area. Wells J13, J15, and J32 have the highest quartz content (>50%).

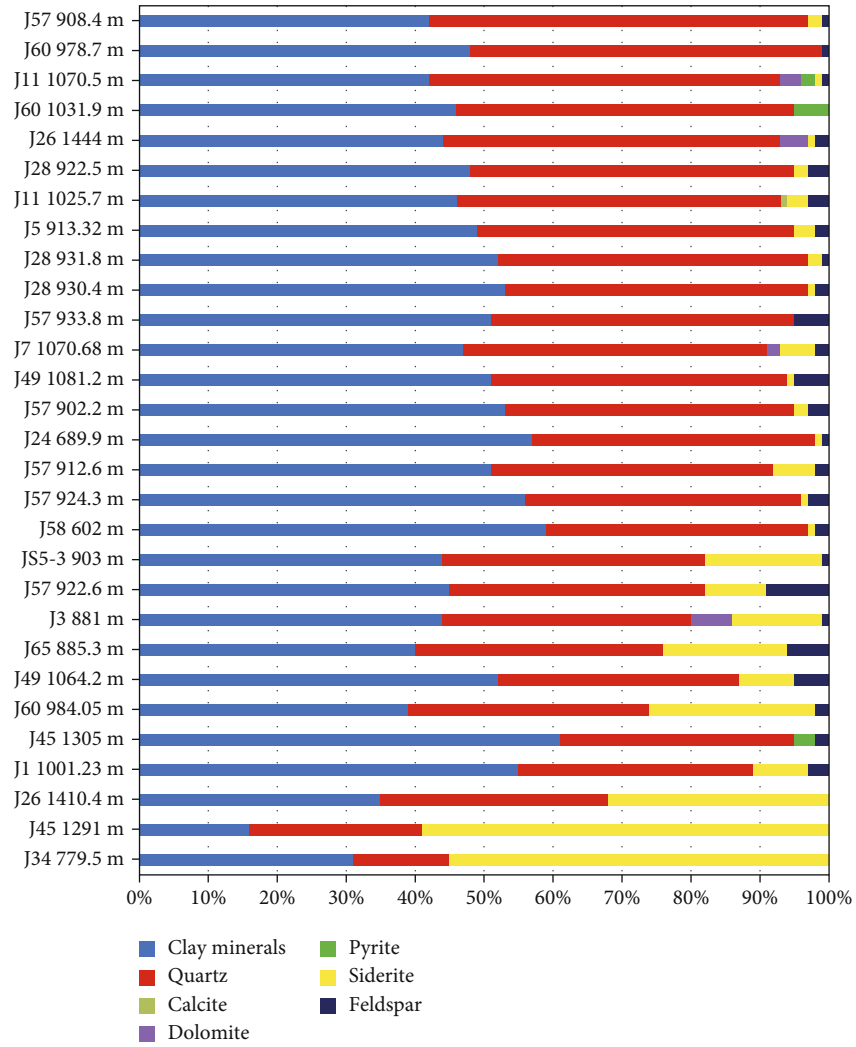
The quartz content in the Taiyuan Formation is relatively high (>30%) in many areas, and the highest value exceeds 60%. Quartz is found in wells J17, J25, J65, and J58; only G1-5, G1-10, J29, and J49 have a quartz content of less than 20%. Regarding clay minerals, the average illite content of the Shanxi Formation is 25.97%, and the high-value area is located near Well J7, with a quartz content of more than 45%. The areas near Well J15 in the north, J3, J6, and J7 in the middle, and J28, J30, and J24 in the south have relatively higher illite contents (>25%). In the Taiyuan Formation, the average illite content is 21.29%, and that of Well J15 is higher than 35%. The relatively high-value areas in the region are found in the northwest and southeast of the study area, with contents exceeding 20%. The average content of clay minerals in the ironite-montmorillonite mixed layers in the Shanxi Formation is 36.50%. The contents are generally low in the center and high around the periphery. The high-value areas of ironite-montmorillonite mixed layers are in the vicinity of Wells J12 in the northwest, J26 in the northeast, G4 in the west, and J60 and J65 in the southeast of the study area, with

contents exceeding 35%. The average content of the ironite-montmorillonite mixed layer in the Taiyuan Formation is 26.60%. Wells J16, J9, J4, and J28 in the northwest and southwest of the study area and Wells J20, J19, and J34 in the southeast are relatively high-value development areas with a content of more than 25%.

**3.2.2. Storage Space.** The porosity of the shale formation in the study area is generally less than 3%, and the permeability is less than 0.1 md. The porosity of the Shanxi formation ranges from 0.72% to 1.33%. Relatively high-value areas are located in the north, central, and western regions of the study area. The porosity of the Taiyuan formation ranges from 0.76% to 2.61%. Relatively high-value areas are found in a few well areas in the north, west, and southeast of the study area.

The reservoir space of mud shale in the study area includes matrix pores and fractures, especially pores related to organic matter, clay minerals, and dissolution. The pores include primary pores, secondary pores, intergranular pores, and dissolution pores. Fractures include structural fractures and diagenetic fractures (Figure 8).

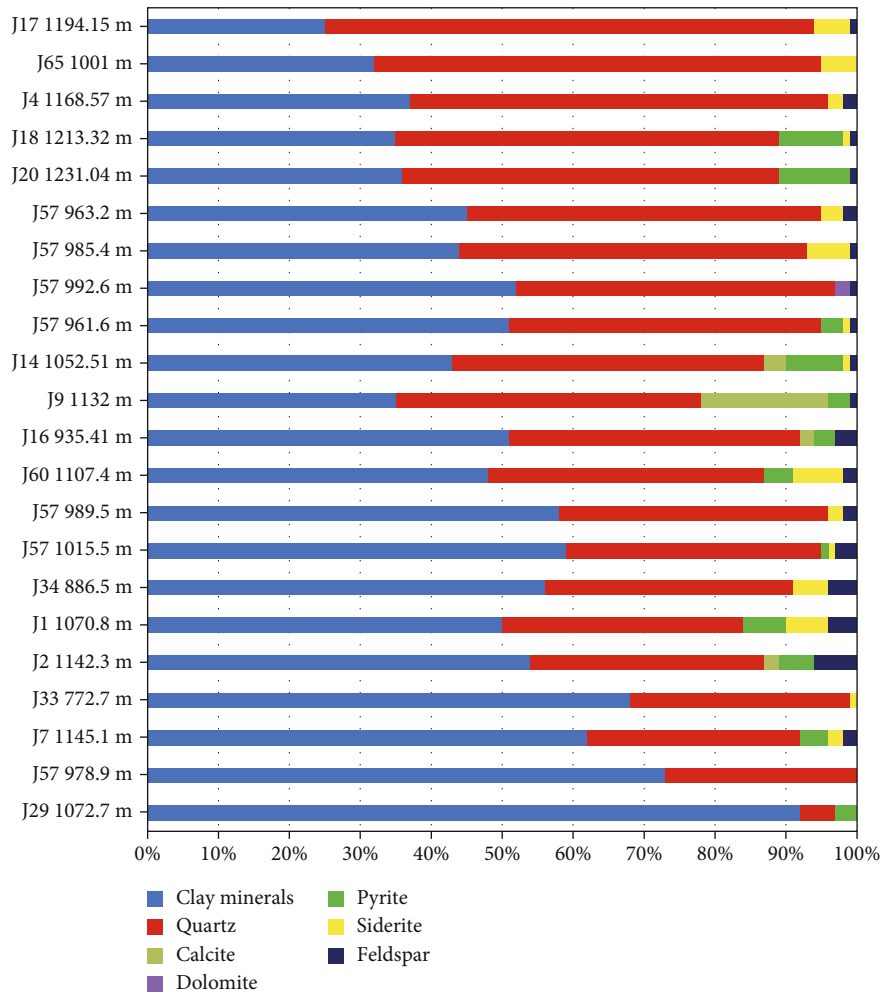
- (1) Residual primary pores: these are scattered among the silty intergranular pores of the clay flakes. The



(a)

FIGURE 7: Continued.





(b)

FIGURE 7: The detrital components of the mud (shale) stone reservoirs in the study area. (a) Shanxi Formation; (b) Taiyuan Formation.

samples from the Shanxi Formation mostly exhibit point-line contacts between particles, whereas those from the Taiyuan Formation primarily show line-concave-convex contacts and some point-line contacts. The compaction increases, and the number of residual primary pores decreases substantially with the burial depth.

- (2) Organic matter pores: these are pores formed in the organic matter in the shale by large amounts of hydrocarbon generation, including micropores inside organic matter, pores between organic matter and other detritus, and pores formed by dissolution of organic matter clumps. Most pores have a honeycomb or irregular shape, and the pore size is about 5–30  $\mu\text{m}$ .
- (3) Micropores formed by clay mineral transformation: the montmorillonite in the ironite/montmorillonite mixed-layer clay minerals is transformed into illite, and micropores are generated due to volume reduction. Secondary dissolution pores are produced by

the strong dissolution of feldspar and rock debris along the joints. Most of the pores are arranged in long strips, and the pore size ranges from 5  $\mu\text{m}$  to 20  $\mu\text{m}$ .

- (4) Fractures: the study area is located at the margin of the basin. Fractures have developed in the shale segment. Most have high angles, and a few have low angles, and most are filled with calcite.

**3.2.3. Brittleness and Mechanical Properties of the Reservoir.** The brittleness of rock depends primarily on its petrological characteristics [21]. The higher the content of brittle components (such as silica), the stronger the brittleness of the rock is [22, 23]. The average quartz content and clay content in the target strata in the study area are 40% and 49%, respectively. The silica content is relatively high, which is favorable for the fracturing of shale gas reservoirs [24, 25]. Poisson’s ratio ( $\mu$ ) of the rock is an indispensable rock mechanics parameter for fracturing, drilling, and engineering. It is the ratio of the relative transverse compression to the relative

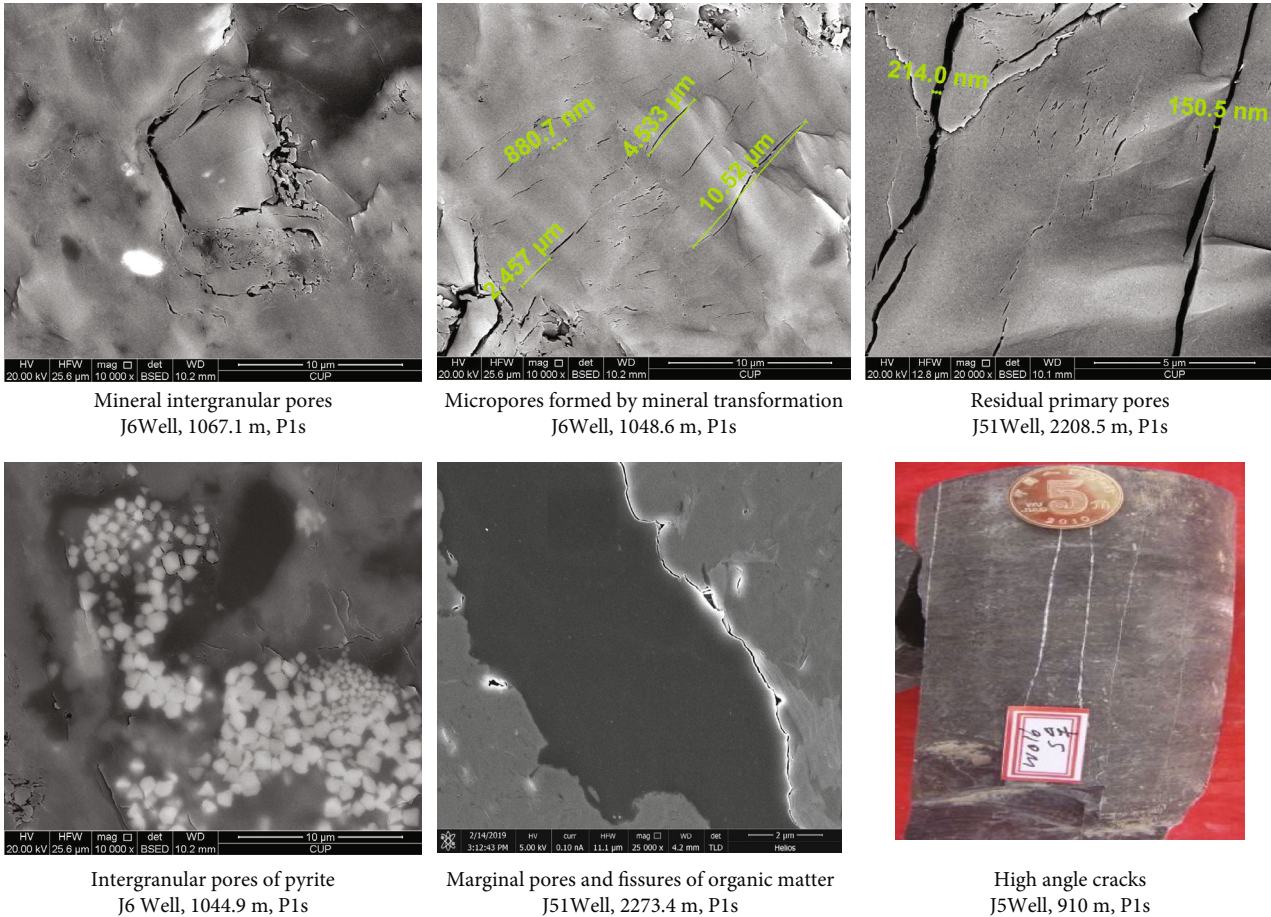


FIGURE 8: Scanning electron microscopy images of the shale.

longitudinal elongation of an elastomer; it is typically calculated using the density and the time difference between the P-wave and S-wave.

The shear wave velocity was calculated using the empirical formula and acoustic time difference and density data, and Poisson's ratio and Young's modulus were calculated. Figure 9 shows the results for Well Ji 5. Poisson's ratio is below 0.35, with an average of 0.32, and Young's modulus is generally above 20.00 MPa, which is similar to the shale brittleness of the Monterey formation in the San Joaquin Basin of the United States. According to well logging data, Poisson's ratio of the Shanxi Formation is 0.29–0.45, with an average of 0.31. Poisson's ratio of the Taiyuan Formation is 0.28–0.42, with an average of 0.31. At present, it is generally believed that Poisson's ratio of shale is relatively high ( $>0.4$ ) and the plasticity is high, whereas sandstone has a relatively low Poisson's ratio ( $<0.3$ ) and high brittleness. Therefore, the lower the Poisson's ratio of rock, the higher its brittleness is. Poisson's ratios of the shale reservoirs in the study area are generally less than 0.35. Therefore, they contain components with high brittleness, which results in good mechanical properties of shale gas reservoirs after fracturing. Only Well J18 in the north has a high Poisson's ratio, and the mudstone has high plasticity, which is not conducive to fracturing and shale gas reservoir development.

**3.3. Gas Content Analysis.** The total gas content of the Barnett shale in the Fort Worth Basin is  $8.49\text{--}9.91\text{ m}^3/\text{t}$ , with an adsorbed gas content of 40%–60%, ranking first among all shale gas scales. The gas content of the Antrim shale in the Michigan Basin is  $1.415\text{--}2.83\text{ m}^3/\text{t}$ , indicating a positive correlation with the organic carbon content. This shale gas formation has a high proportion of adsorbed gas (more than 70%). The total gas content of the Ohio shale source rocks in the Appalachian Basin ranges from  $1.70\text{ to }2.83\text{ m}^3/\text{t}$ , and the adsorbed gas content is about 50%. The total gas content of the New Albany Shale in the Illinois Basin is relatively low, ranging from  $1.13\text{ to }2.26\text{ m}^3/\text{t}$ , and that of the Lewis shale in the San Juan Basin ranges from  $0.42\text{ to }1.27\text{ m}^3/\text{t}$ , with 60% to 88% adsorbed gas content. The gas contents of the Gordondale shale ( $0.7\text{--}3.0\text{ m}^3/\text{t}$ ) in northeastern British Columbia, Canada, and the Qiongzusi shale ( $0.27\text{--}1.03\text{ m}^3/\text{t}$ ) are significantly lower than that of the Barnett shale ( $8\text{--}9\text{ m}^3/\text{t}$ ). The measured gas content of the shale core of Well Daji 51 in the study area is  $0.5\text{--}3.7\text{ m}^3/\text{t}$ , indicating an upper-medium level.

**3.4. Calculation of Resource Quantity.** The resource quantity of the Shanxi Formation and Taiyuan Formation in the study area was calculated. Although the shale gas reservoirs are discontinuous, they have strong heterogeneity. Therefore, the resource quantity of shale gas reservoirs should be calculated

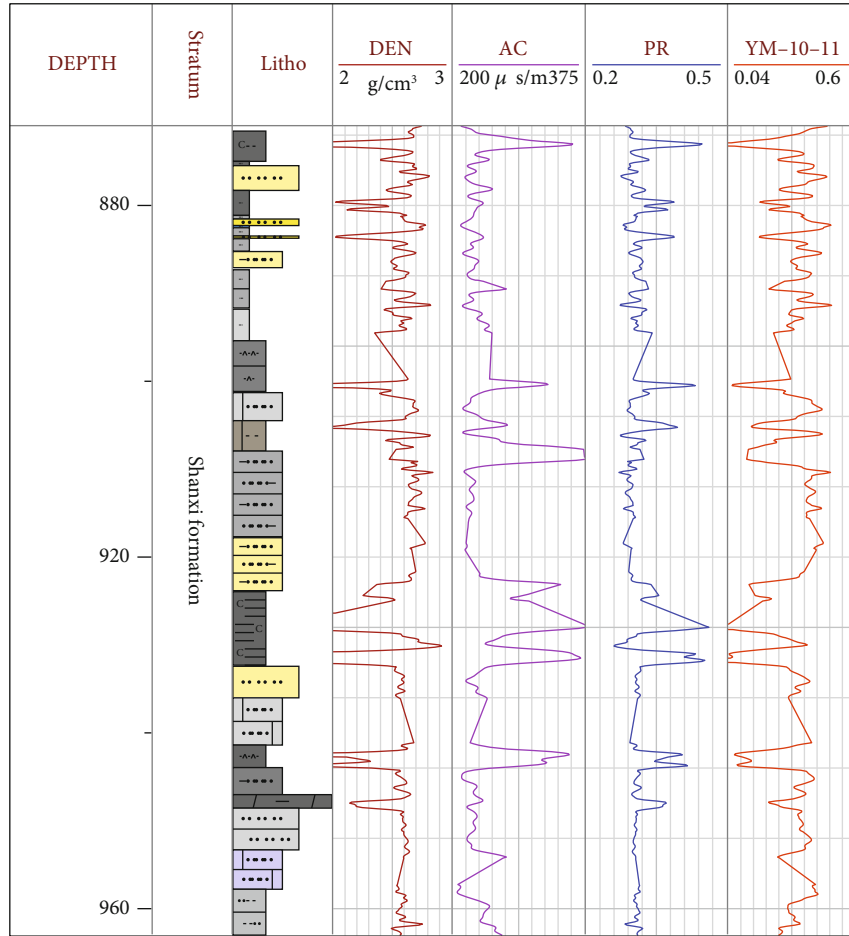


FIGURE 9: Calculation results of rock mechanics parameters of Well J5.

by integrating geological factors, technical factors, and economic factors. At present, evaluation methods of shale gas resources in foreign countries include the analogy method, material balance method, trend curves, and numerical simulations. Since the study area is currently in the early stage of shale gas exploration, there are insufficient geological data. Thus, we used existing data, regional geological survey data, the geological characteristics of mature shale gas reservoirs in the province, and resource evaluation to determine the resource quantity in the Shanxi Formation and Taiyuan Formation by analogy. One of the key parameters in the analogy method is the selection of the calibration area. The study area was compared with five major shale gas basins in North America using six evaluation parameters: organic carbon content, maturity, brittle mineral content, porosity, thickness, and burial depth. We created a comprehensive score for all shale gas basins and used the basin with the closest score as the calibration area.

As shown in Table 1, Barnett shale has the highest score, followed by the New Albany Shale and the Ohio Shale. The Shanxi Formation in the study area has a score of 72.98, which is lower than the score of the five largest shale gas basins in North America. It is most similar to the Antrim Basin shale. Therefore, the Antrim Basin shale is selected

as the calibration area. Equation (1) is used for an analogy calculation of the shale gas resources in the study area and the calibration area to obtain the shale gas resources in the study area. The calculation results are listed in Table 2.

$$R_i = \left(\frac{S}{A_i}\right) \cdot (\lambda/\lambda_i) \cdot Q_i, \quad (1)$$

where  $R_i$  is the number of analogous resources in the study area ( $\times 10^{12} \text{ m}^3$ );  $S$  is the area of the study site ( $\times 10^4 \text{ km}^2$ );  $A_i$  is the calibration area ( $\times 10^4 \text{ km}^2$ );  $\lambda/\lambda_i$  is the study area and calibration area score ratio; and  $Q_i$  is the resource amount in the calibration area ( $\times 10^{12} \text{ m}^3$ ).

As shown in Table 2, the Shanxi Formation and Taiyuan Formation have similar geological conditions, areas, and shale gas resources. Compared with the shale in the Antrim Basin, the resources of the Shanxi Formation and Taiyuan Formation are  $1500 \times 10^8 \text{ m}^3$  and  $1300 \times 10^8 \text{ m}^3$ , respectively. The average analogous resources of the Shanxi Formation and Taiyuan Formation are  $1680 \times 10^8 \text{ m}^3$  and  $1560 \times 10^8 \text{ m}^3$ , respectively, and the total amount of resources in this area is  $2,800\text{--}3,200 \times 10^8 \text{ m}^3$ .

TABLE 1: Comparison of five shale gas basins in the United States and two in the southeastern Ordos Basin.

Parameters	Weight coefficient	Barnett		Antrim		Ohio		New Albany		Lewis		Shanxi formation		Taiyuan formation	
		Features	Score	Features	Score	Features	Score	Features	Score	Features	Score	Features	Score	Features	Score
TOC (%)	0.25	4.5	80	0.3-24	92	0-4.7	66	1-25	86	0.45-2.5	45	0.51-29.15	46.2	0.011-22.52	50.6
Ro (%)	0.15	1.0-1.3	78	0.4-0.6	34	0.4-1.3	56	0.4-1.0	32	1.6-1.88	100	1.45-2.341	94.8	1.25-2.165	94
Brittle minerals (%)	0.15	35-50	96	20-41	74	45-60	100	50	100	50-75	100	28-58	84	27-69	81
Porosity (%)	0.10	4-5	80	9	100	4.7	80	10-14	100	3-5.5	72	0.5-3.1	32.5	0.9-4.9	34.5
Thickness (m)	0.20	61-91	100	49	80	91-305	100	30-122	92	152-579	100	23.18-99.84	81.8	17.22-66.94	56
Buried depth (m)	0.15	1981-2591	79	183-732	90	610-1524	98	183-1494	96	914-1829	92	571-1447.5	100	620.5-1503	99.5
Score			86		78.7		82.6		84.1		82.3		72.98		68.475

TABLE 2: Comparison of the shale gas resources in the United States and the Lower Permian formation in the southeastern Ordos Basin after calibration.

Shale name	Area $\times 10^4$ km <sup>2</sup>	Resources $\times 10^{12}$ m <sup>3</sup>	Resources of the Shanxi Formation $\times 10^{12}$ m <sup>3</sup>	Resources of the Taiyuan Formation $\times 10^{12}$ m <sup>3</sup>
Barnett	3.81	5.66	0.37	0.35
Antrim	3.16	0.99-2.15	0.15	0.13
Ohio	25.01	6.37-7.02	0.07	0.07
New Albany	9.08	2.44-4.53	0.10	0.09
Lewis	3.0909	1.74	0.15	0.14

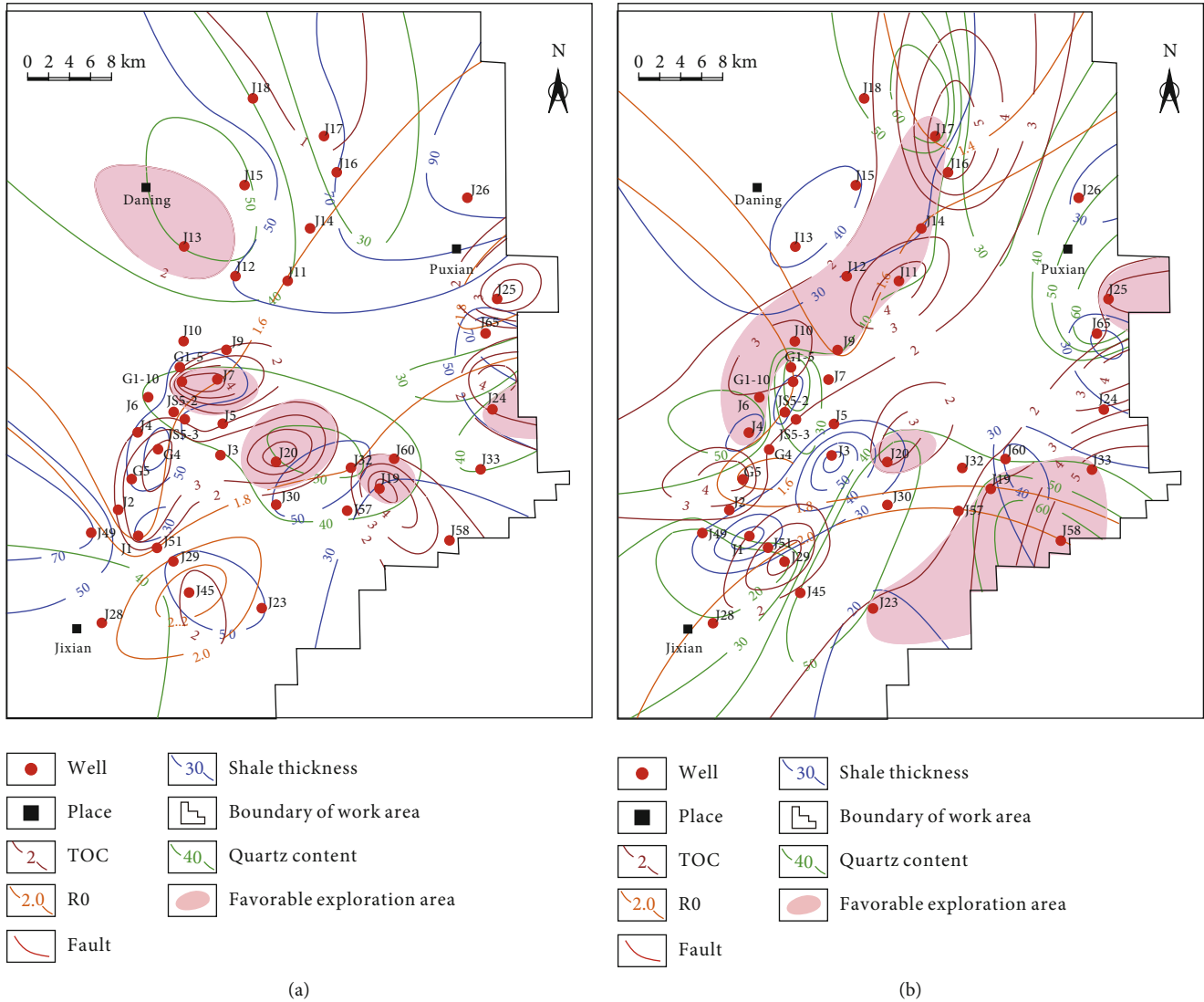


FIGURE 10: Prediction results of favorable areas for shale gas exploration in the lower Permian strata in the southeastern Ordos Basin. (a) Shanxi Formation; (b) Taiyuan Formation.

### 4. Discussion

4.1. Comparison of Shale Gas Characteristics in the Daning-Jixian Block and in the United States. The commercially developed shale gas in the United States has a higher organic matter content (above 5% on average) than the domestic shale gas. However, its maturity is generally lower than 2% before the main gas generation stage, resulting in insufficient hydrocarbon generation (shale gas) and limited resource potential. China’s main shale gas areas include the Qiongzhusi shale and Longmaxi shale in the Sichuan Basin, the Shanxi-Taiyuan formation in the Ordos Basin, and the Cambrian-Ordovician shales in the Tarim Basin. Their high maturity of organic matter means that they are in the high maturity and overmaturity stages beyond the main gas generation stage [8]. The degree of transformation from organic matter to hydrocarbon is relatively high, and the resource amount is massive. Shale gas reservoirs in the United States are mainly carbonate rocks in shale layers and generally have

a thickness of less than 50 m [26], limiting the abundance of shale gas. Meanwhile, shale gas reservoirs in the United States are brittle, form structural fractures easily, and have poor roof and floor conditions [27]. However, domestic shale is generally thicker. For example, the thickness of the shale in the study area of the Edong gas field exceeds 100 m in some areas. The roof and floor conditions are superior, providing good source rock and preservation conditions for the generation and preservation of shale gas. These conditions are favorable to the development and preservation of shale gas reservoirs. Furthermore, the three major shale gas areas in China are located in several large basins, such as the Ordos Basin. The widely distributed shales are superimposed in the same basin with a relatively high concentration and strong comparability, which is conducive to large-scale exploration and development.

4.2. Prediction of Favorable Shale Gas Zones. Based on previous studies [27–31] and the geological characteristics of the

study area, the following factors should be considered to predict favorable shale gas zones. (1) When the abundance of organic matter is high and has reached a certain level of thermal maturity, the hydrocarbon gas can be stored in the form of adsorbed gas on the surface of the clay and organic matter [32, 33]. Therefore, the abundance and thermal maturity of organic matter are crucial geological factors for determining shale gas accumulation. (2) The porosity and permeability of the mud-shale formation are low, and there is no significant difference between the regions in the study area. (3) The shale formation depends on the brittleness degree of the formation, which is related to the mineral type. Usually, a high silica content results in better mechanical properties of the shale gas reservoir. Therefore, the main factors affecting the economic value of shale gas reservoirs are the abundance of organic matter, thermal maturity, thickness, and quartz content. Thus, the favorable areas for shale gas exploration were predicted using these factors.

Figure 10 shows the prediction results of the favorable areas for shale gas exploration. The favorable areas in the Shanxi Formation are located in the central and eastern parts of the study area and in the north near Daning area. The organic carbon content of the favorable area in the middle is 2%–8%, the vitrinite reflectance ranges from 1.5% to 2.0%, the thickness ranges from 20 m to 70 m, and the quartz content is 40%–52%. In the favorable eastern area, the organic carbon content is 2%–4%, the vitrinite reflectance exceeds 1.8%, the thickness is larger than 60 m, and the quartz content is greater than 40%. In the favorable northern area near Daning, the organic carbon content is greater than 2, the vitrinite reflectance is higher than 1.3%, the thickness is larger than 40 m, and the quartz content exceeds 50%.

The favorable areas in the Taiyuan Formation are located in the northwest, southeast, east, and middle of the study area. The favorable area in the northwest contains 2%–7% organic carbon, the vitrinite reflectance is 1.3%–1.9%, the thickness is 20 m–40 m, and the quartz content is 40%–70% quartz. In the southeast, the organic carbon content is 2%–9%, the vitrinite reflectance is 1.6%–2.2%, the thickness is 17 m–40 m, and the quartz content is 40%–70%. In the eastern part, the organic carbon content is 2%–4%, the vitrinite reflectance is greater than 1.7%, the thickness is larger than 25 m, and the quartz content exceeds 60%. The central area has a TOC of 2%–3.5%, vitrinite reflectance of more than 1.6%, and a thickness greater than 35 m, and the quartz content exceeds 55%.

## 5. Conclusions

The Shanxi-Benxi Formation in the study area is a transitional marine-continental shale system with good reservoir-forming conditions. The organic matter in the study area is abundant, the kerogen type is predominantly of type II 2, and the area has high maturity. These conditions are favorable for gas generation.

The Shanxi-Benxi Formation has diverse reservoir spaces and contains mainly residual primary pores formed by compaction, secondary pores formed by organic matter hydrocarbon generation and clay mineral transformation, secondary dissolution pores, and fractures. The average content of clay

minerals is about 50%, the quartz content near the provenance is relatively high, and Poisson's ratio is 0.31. The rock is brittle and fractures easily.

The shale gas reservoir characteristics in the study area and five major shale gas basins in the United States were compared using the analogy method based on geological conditions. The Antrim Basin was selected as the calibration area. The cumulative resources of the Shanxi and Taiyuan Formations in the study area were calculated as  $2,800\text{--}3,200 \times 10^8 \text{ m}^3$ .

The organic matter abundance, thermal maturity, thickness, and quartz content are the main controlling factors affecting the development of shale gas in the study area. The favorable areas of shale gas are predicted using these factors. The most favorable areas of the Shanxi Formation are located in the middle, east, and north of the study area, and those of the Taiyuan Formation are located in the northwest, southeast, and east, with a small area in the middle.

## Data Availability

Data is not available for confidential reasons.

## Conflicts of Interest

The authors declare that they have no conflicts of interest.

## Acknowledgments

This research was funded by the Key Exploration Technologies and Target Evaluation of Large Natural Gas Fields (No. 2019b-0603), a major science and technology project of the PetroChina Company. We appreciate the guidance provided by the China University of Petroleum (Beijing) and the support for the experiments and tests by the State Key Laboratory of Petroleum Resources and Prospecting, Beijing. Some of the data were provided by the National Energy Shale Gas R&D (Experiment) Center.

## References

- [1] J. B. Curtis, "Fractured shale-gas systems," *AAPG Bulletin*, vol. 86, no. 11, pp. 1921–1938, 2002.
- [2] Q. Gou and S. Xu, "Quantitative evaluation of free gas and adsorbed gas content of Wufeng-Longmaxi shales in the Jiaoshiha area, Sichuan Basin, China," *Advances in Geo-Energy Research*, vol. 3, no. 3, pp. 258–267, 2019.
- [3] X. Nie, Y. Wan, D. Gao, C. Zhang, and Z. Zhang, "Evaluation of the in-place adsorbed gas content of organic-rich shales using wireline logging data: a new method and its application," *Frontiers of Earth Science*, vol. 15, no. 2, pp. 301–309, 2021.
- [4] Z. Qiu and C. Zou, "Controlling factors on the formation and distribution of "sweet-spot areas" of marine gas shales in South China and a preliminary discussion on unconventional petroleum sedimentology," *Journal of Asian Earth Sciences*, vol. 194, p. 103989, 2020.
- [5] D. M. Jarvie, R. J. Hill, T. E. Ruble, and R. M. Pollastro, "Unconventional shale-gas systems: the Mississippian Barnett shale of north-central Texas as one model for thermogenic shale-gas assessment," *AAPG Bulletin*, vol. 91, no. 4, pp. 475–499, 2007.

- [6] D. Dong, Y. Wang, X. Li et al., "Breakthrough and prospect of shale gas exploration and development in China," *Natural Gas Industry B*, vol. 3, no. 1, pp. 12–26, 2016.
- [7] Q. Cao, Z. Chen, J. Zhao, J. Dang, J. Song, and B. Chen, "Numerical simulation study of pore-throat evolution of upper paleozoic in Ordos Basin, China," *Geofluids*, vol. 2021, Article ID 5517494, 11 pages, 2021.
- [8] Y. Shu, S. Sang, Y. Lin, and H. Zheng, "Natural gas accumulation characteristics in the linxing area, Ordos basin, NW China: revealed from the integrated study of fluid inclusions and basin modeling," *Geofluids*, vol. 2020, Article ID 8695497, 28 pages, 2020.
- [9] C. ZOU, G. ZHAI, G. ZHANG et al., "Formation, distribution, potential and prediction of global conventional and unconventional hydrocarbon resources," *Petroleum Exploration and Development*, vol. 42, no. 1, pp. 14–28, 2015.
- [10] T. Xuan, Z. H. Jin-Chuan, D. I. Wen-Long et al., "The reservoir property of the upper Palaeozoic marine-continental transitional shale and its gas-bearing capacity in the southeastern Ordos Basin," *Earth Science Frontiers*, vol. 23, no. 2, p. 147, 2016.
- [11] D. Yan, W. Huang, and X. Lu, "Contrast of reservoir forming conditions of marine-continental transitional shale gas in different sedimentary environments in the lower Yangtze area of China," *China Coal Society*, vol. 417, pp. 1778–1787, 2016.
- [12] G. Zhai, Y. Wang, G. Liu, Z. Zhou, C. Zhang, and X. Liu, "Enrichment and accumulation characteristics and prospect analysis of the Permian marine continental multiphase shale gas in China," *Sedimentary Geology and Tethyan Geology*, vol. 40, pp. 102–117, 2020.
- [13] D. Dazhong, Q. Zhen, Z. Leifu et al., "Progress on sedimentology of transitional facies shales and new discoveries of shale gas," *Acta Sedimentologica Sinica*, vol. 39, no. 1, pp. 29–45, 2021.
- [14] K. Li, G. Chen, W. Li, X. Wu, J. Tan, and J. Qu, "Characterization of marine-terrigenous transitional Taiyuan formation shale reservoirs in Hedong coal field, China," *Advances in Geo-Energy Research*, vol. 2, no. 1, pp. 72–85, 2018.
- [15] L. Tracy, C. Chen, S. Park, M. L. Davisson, and R. C. Ewing, "Measurement of UO<sub>2</sub> surface oxidation using grazing-incidence x-ray diffraction: Implications for nuclear forensics," *Journal of Nuclear Materials*, vol. 502, pp. 68–75, 2018.
- [16] J. Teng, X. Ma, X. Dong, H. Yang, and P. H. Song, "An analysis of the accumulation and potential of oil and gas resources in the second deep space (5000~10000m)," *Chinese Journal of Geophysics*, vol. 60, no. 8, pp. 3191–3214, 2017.
- [17] S. Lu, W. Huang, F. Chen et al., "Classification and evaluation criteria of shale oil and gas resources: discussion and application," *Petroleum Exploration and Development*, vol. 39, no. 2, pp. 268–276, 2012.
- [18] J. G. Speight, *Deep shale oil and gas*, Gulf Professional Publishing, 2016.
- [19] S. Guo, Z. Wang, and X. Ma, "Exploration prospect of shale gas with Permian transitional facies of some key areas in China," *Petroleum Geology & Experiment*, vol. 43, no. 3, pp. 377–385, 2021.
- [20] W. Ding, D. Zhu, J. Cai, M. Gong, and F. Chen, "Analysis of the developmental characteristics and major regulating factors of fractures in marine-continental transitional shale-gas reservoirs: a case study of the Carboniferous-Permian strata in the southeastern Ordos Basin, central china," *Marine and Petroleum Geology*, vol. 45, pp. 121–133, 2013.
- [21] R. F. LaFollette and W. D. Holcomb, "Practical data mining: lessons learned from the Barnett shale of North Texas," in *Paper presented at the SPE Hydraulic Fracturing Technology Conference*, The Woodlands, Texas, USA, 2011.
- [22] C. Liang, Z. Jiang, C. Zhang, L. Guo, Y. Yang, and J. Li, "The shale characteristics and shale gas exploration prospects of the lower Silurian Longmaxi shale, Sichuan basin, South China," *Journal of Natural Gas Science and Engineering*, vol. 21, pp. 636–648, 2014.
- [23] X. Li, S. Hu, and K. Cheng, "Suggestions from the development of fractured shale gas in North America," *Petroleum Exploration and Development*, vol. 34, no. 4, p. 392, 2007.
- [24] R. Wang, Z. Hu, L. Dong et al., "Advancement and trends of shale gas reservoir characterization and evaluation," *Oil & Gas Geology*, vol. 42, no. 1, pp. 54–65, 2021.
- [25] H. Nie, X. Tang, and R. Bian, "Controlling factors for shale gas accumulation and prediction of potential development area in shale gas reservoir of south China," *Acta Petrolei Sinica*, vol. 4, 2009.
- [26] C. Zou, Q. Zhao, D. Dong et al., "Geological characteristics, main challenges and future prospect of shale gas," *Journal of Natural Gas Geoscience*, vol. 2, no. 5-6, pp. 273–288, 2017.
- [27] A. Bechtel, J. Jia, S. A. Strobl et al., "Palaeoenvironmental conditions during deposition of the upper cretaceous oil shale sequences in the Songliao Basin (NE China): implications from geochemical analysis," *Organic Geochemistry*, vol. 46, pp. 76–95, 2012.
- [28] K. M. Bohacs, A. R. Carroll, J. E. Neal et al., "Lake-basin type, source potential, and hydrocarbon character," *Lake basins through space and time: AAPG Studies in Geology*, vol. 46, pp. 3–34, 2000.
- [29] C. Jia, "Breakthrough and significance of unconventional oil and gas to classical petroleum geology theory," *Petroleum Exploration and Development*, vol. 44, no. 1, pp. 1–10, 2017.
- [30] Y. MA, X. CAI, P. ZHAO et al., "China's shale gas exploration and development: understanding and practice," *Petroleum Exploration and Development*, vol. 45, no. 4, pp. 589–603, 2018.
- [31] T. Zhang, Y. Li, and S. Sun, "Phase equilibrium calculations in shale gas reservoirs," *Capillarity*, vol. 2, no. 1, pp. 8–16, 2019.
- [32] W. A. Ruyue, N. I. Haikuan, and H. U. Zongquan, "Controlling effect of pressure evolution on shale gas reservoirs: a case study of the Wufeng-Longmaxi Formation in the Sichuan Basin," *Natural Gas Industry*, vol. 40, no. 10, pp. 1–11, 2020.
- [33] A. B. Andhumoudine, X. Nie, Q. Zhou et al., "Investigation of coal elastic properties based on digital core technology and finite element method," *Advances in Geo-Energy Research*, vol. 5, no. 1, pp. 53–63, 2021.



## Research Article

# A New Method for Calculating the Cementation Exponent of Triple-Porosity Media Reservoirs

Dahai Wang <sup>1</sup>, Jinbu Li <sup>1</sup>, Lili Liu,<sup>1</sup> Ji Zhang,<sup>1</sup> Zhanhai Yu,<sup>1</sup> and Jun Peng <sup>2</sup>

<sup>1</sup>Exploration and Development Research Institute of PetroChina Changqing Oilfield Company, Xi'an 710018, China

<sup>2</sup>College of Earth Science and Technology, Southwest Petroleum University, 610599, China

Correspondence should be addressed to Jun Peng; pengjun@swpu.edu.cn

Received 18 July 2021; Revised 1 November 2021; Accepted 9 November 2021; Published 7 January 2022

Academic Editor: Jianchao Cai

Copyright © 2022 Dahai Wang et al. This is an open access article distributed under the Creative Commons Attribution License, which permits unrestricted use, distribution, and reproduction in any medium, provided the original work is properly cited.

The value of a cementation exponent, usually obtained by rock and electricity experiments, significantly affects the calculation of water saturation, thickness of the hydrocarbon reservoir, and recovery rate. The determination of the cementation exponent for porous-media reservoirs has been a challenge because of the limited core sampling. A new method was proposed to determine the value of cementation exponent for complex triple-porosity media reservoirs in the work. Firstly, the work discussed the effects of fractures and nonconnected vugs on the cementation exponent of the reservoir as well as the calculation method of the cementation exponent of the dual-porosity media reservoir. Then, a new model for calculating the cementation exponent of triple-porosity media reservoirs was derived by combining the Maxwell-Garnett theory and series-parallel theory, which matched with the real physical-experiment data of rocks. The results showed that the fractures decreased the cementation exponent of the reservoir but the vugs increased. The mixture of matrix pores, fractures, and vugs made the value of the cementation exponent of the triple-porosity media reservoir vary around 2.0. The conductivity of the triple-porosity media reservoir was the external macroscopic expression of the microscopic conductive network. The new calculation model of the cementation exponent proposed in the work could reasonably predict the cementation exponent of the strongly inhomogeneous triple-porosity media reservoir.

## 1. Introduction

With the development of the world's oil and gas exploration, the oil and gas reserves and output obtained in fractured-vuggy reservoirs have become larger and larger. In the past decades, the petrophysical analysis of the triple-porosity media reservoirs with fractures and vugs has been a hot spot in the oil and gas industry. For the reservoir with serious heterogeneity and complex pore structure [1], the application of Archie's equation is limited due to the significant difference in porosity indices for different reservoirs. The complexity of the pore structure dramatically enlarges the range of the pore structure exponent in the Archie equation and affects the solution of water saturation. People have been exploring the calculation methods and value of cementation exponent (porosity index)  $m$  of the triple-porosity reservoirs adapted to the complex pore structure to improve the application of Archie's equation.

$m$  is the cementation index of the reservoir, also known as the porosity index, reflecting the cementation of the reservoir, pore-throat tortuosity, and fracture opening, especially for the connectivity of pores. Its physical significance is to characterize the influence of the pore structure (microscopic characteristics of the reservoir space) on the conductivity of the rock.  $m$  is the slope of the relationship between formation-resistivity factor  $F$  and porosity  $\Phi$  in the logarithmic coordinate system. The changes in  $F$  of sandstone reservoirs with porosity are relatively consistent, but the influence of the changes in permeability on  $F$  is not apparent, especially in the case of low permeability [2]. In a triple-porosity media reservoir, the distribution and variation of cementation exponent  $m$  of the reservoir is a geometric parameter, which is mainly controlled by three different pore types (matrix pores, fractures, and vugs) and their coupling relationship.

Towle [3] noticed the variation of pore index  $m$  in Archie's equation. For reservoirs with vugs, the  $m$  value is between 2.67 and 7.3, while for the reservoirs with fractures, that is less than 2, and the matrix porosity is 0 in the Towle model. Aguilera [4] introduced a dual-porosity model that can handle matrix and fracture pores, considering three different Archie cementation indices: matrix ( $m_b$ ), fracture ( $m_f = 1$ ), and the combined index of the two ( $m$ ). The dual-porosity model proposed by Rasmus [5] considers the change of fracture curvature, but this model causes  $m$  to be greater than  $m_b$ , with the increased total porosity. Rasmus [6] used the Maxwell-Garnett theoretical model to establish the relationship between formation resistivity factor  $F$  and porosity  $\Phi$  of a two-porous system with vugs and fractures and intergranular pores as the matrix. Karst caves increase the cementation index of the reservoir, while fractures reduce the cementation index of the reservoir.

Serra [7] established a model suitable for fractures and unconnected vugs to plot the relationship between porosity exponent  $m$  and the total porosity. Aguilera [8] improved the Serra model, showing that a more suitable equation should include matrix porosity  $\Phi_b$  related to the total volume of the matrix system. According to the series-parallel connection method, an equation for calculating the  $m$  value is derived [8], which is suitable for the dual pore system of the matrix and fractures or the matrix and unconnected vugs. Aguilera [9] proposed a triple-porosity model suitable for the matrix, combining fractures and unconnected vugs. Berg [10] developed a new  $m$ -value calculation method of the triple-porosity model using effective medium theory to derive the dual-porosity equation.

Olusola et al. [11] developed a unified equation for electromagnetic mixing rules, which is used to calculate the  $m$  value of dual-porosity or triple-porosity reservoirs (systems). Besides, Berg's new three-porosity model method is used. C. Aguilera and R. Aguilera [12] considered the influence of fracture dip on porosity exponent  $m$ . Al-Ghamdi et al. [13] improved Aguilera's triple-porosity model by strictly treating the scales associated with each matrix, fracture, and vug. Piedrahita and Aguilera [14] established a dual-porosity analysis model to quantitatively calculate secondary mineralization (cementation) and tortuosity in natural fractures. If the influences of matrix, fractures, and vugs are not taken into consideration, it may lead to errors in selecting the  $m$  value. Then, significant errors occur in calculating water saturation, the thickness of oil and gas reservoir, and recovery factor.

The previous petrophysical experiments and theoretical models are beneficial, but they are not practical enough to obtain the  $m$  value of a triple-porosity medium reservoir with serious heterogeneity. The work focused on determining the value of cementation exponent  $m$  of the triple-porosity media reservoirs (such as carbonate) with pores, fractures, and vugs.

## 2. Materials and Methods

The intense chemical and biological actions of carbonate rocks cause the uneven salinity distribution of formation water, the tortuous and bifurcated conductive path, and

the apparent nonlinear characteristics [15]. Many factors influence  $m$ , such as porosity, pore-throat size, type of rock particles, type and distribution of clay content, degree of cementation, and overburden pressure [16, 17]. All these are controlled by sedimentation, tectonics, and diagenesis. The storage space (pore structure) of the reservoir is the primary manifestation of the three control effects.

Lucia [18] adopted an improved version of Dunham's classification, dividing the fabrics into grain-based and argillaceous-based so that the geological classification is compatible with petrophysical classification. Pores are divided into intergranular pores and vuggy porosity. Intergranular porosity is commonly mentioned as matrix porosity by reservoir engineers. Vuggy porosity is divided into independent vugs (referred to as nonconnected vugs) and contacted vugs (referred to as connected vugs). In the three-porosity model of carbonate reservoir, Pores are divided into matrix pores, fractures, and nonconnected vugs. The traditional Archie equation and understanding are based on the sandstone reservoir with homogeneity and single pore structures. It is a regular fitting of experimental data of core resistivity [19]. Since the carbonate reservoir is seriously heterogeneous and anisotropic, the pore structure is no longer single but a complex triple-porosity medium with intergranular pores, natural fractures, and cave storage spaces. Therefore, the conductive path is also highly complicated. In the petrophysical experiments, it is difficult to obtain a complete core in fractures and vugs, which causes errors between the laboratory-measured value and the actual  $m$  value of the triple-porosity media reservoirs (see Figure 1).

For serious heterogeneous triple-porosity media reservoirs such as carbonate rocks, traditional petrophysics experiments are limited in understanding due to the artificial selection of core samples. As a result, the electrical characteristics of reservoir rock cannot be fully understood [20]. Especially in low-porosity formations, the relationship between electrical conductivity and porosity is more complicated, and pore-throat ratio, tortuosity, and connectivity are three important influencing factors [21]. The combination of the theoretical model and simulation can provide insights into how the microscopic petrophysical properties affect the macroscopic conductivity of porous media [22]. It is especially true for triple-porosity medium carbonate reservoirs with simultaneous development of vugs and fractures (see Figure 1). Therefore, the work discussed the  $m$ -value calculation method of dual-porosity media reservoirs and the influence of fractures and caves on the  $m$  value of the reservoir and then proposed the new calculation method of the  $m$  value of triple-porosity media reservoirs with pores, fractures, and vugs of reservoir space.

*2.1. Calculation of the Value of Cementation Exponent  $m$  of Dual-Porosity Media Reservoirs with Matrix Pores and Nonconnected Vugs.* Sen et al. [23] used a Maxwell-Garnett mathematical relationship to simulate the current performance of mixtures of rock particles and water. Kenyon and Rasmus [24] used these expressions to simulate the low-frequency conductivity and high-frequency dielectric measurement of oolitic limestone (with large spherical



FIGURE 1: Core sampling of the petrophysical experiment: (a) reservoir with matrix pores, (b) reservoir with matrix pores and fractures, (c) reservoir with matrix pores and vugs, and (d) reservoir with matrix pores, fractures, and vugs.

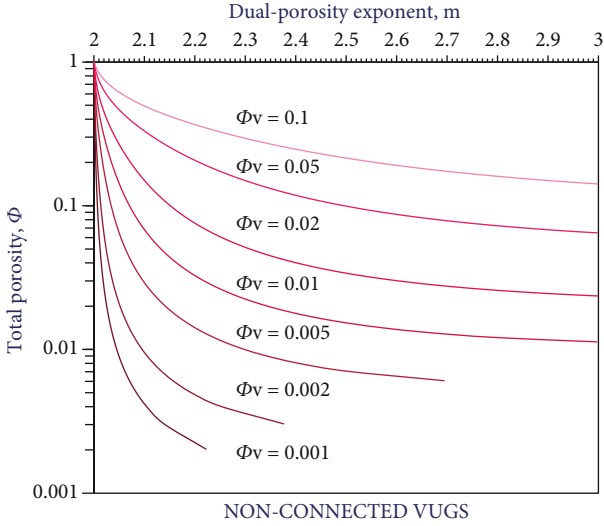


FIGURE 2:  $m$  determined as a function of dual-porosity media reservoirs with only matrix pores and nonconnected vugs ( $m_b = 2$ ) [6].

secondary pores and intergranular pores). Besides, they presented the low-frequency conductivity response (inductive or lateral) of a mixture of water-filled spherical pores embedded in a host material (matrix). Rasmus [6] simulated the influence of karst caves on formation resistivity factor  $F$  according to the Maxwell-Garnett mathematical relationship and plotted the relationship between  $F$  and total porosity (the fraction of intergranular pore volume and secondary pore volume). The larger spherical secondary pores in the oolitic limestone can be regarded as vugs because they are much larger than the intergranular pores. The mathematical form proves that cementation exponent  $m$  of the reservoir with the dual-porosity system (intergranular pores and vugs) will become larger because of vugs.

The low-frequency conductivity response (the reciprocal of resistivity) deduced by Rasmus, the Maxwell-Garnett equation, and the Archie equation are used to derive the equation of the  $m$  value of the dual-porosity-system reservoir composed of the matrix with intergranular pores and nonconnected vugs [6] (see Equation (1)).

$$m = \frac{\lg \left\{ \phi_b^{mb} \left[ \left( 1 + 2\phi_v - 2\phi_b^{mb}(\phi_v - 1) \right) / \left( \phi_b^{mb}(2 + \phi_v) + 1 - \phi_v \right) \right] \right\}}{\lg \phi} \quad (1)$$

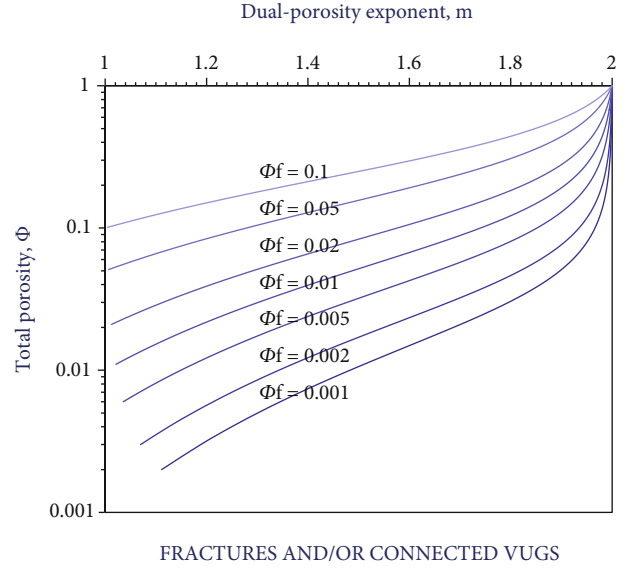


FIGURE 3:  $m$  determined as a function of dual-porosity media reservoirs with only matrix pores and fractures (or connected vugs) ( $m_b = 2$ ) [8].

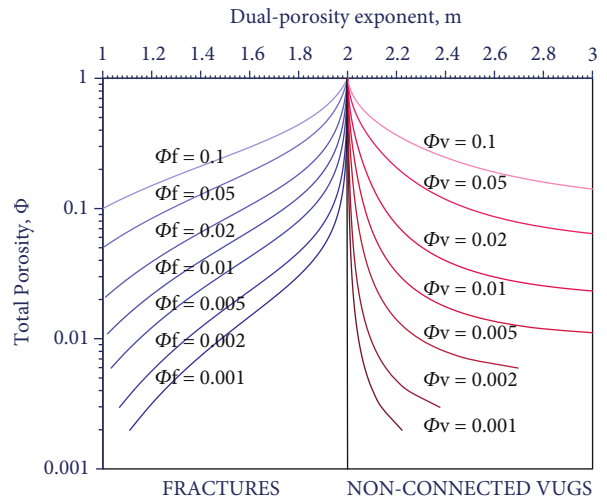


FIGURE 4: Influences of fractures [8] and nonconnected vugs [6] on the  $m$  value of the reservoir.

According to Equation (1), the relationship between the total porosity and cementation exponent  $m$  of the dual-porosity media system of matrix pores and nonconnected

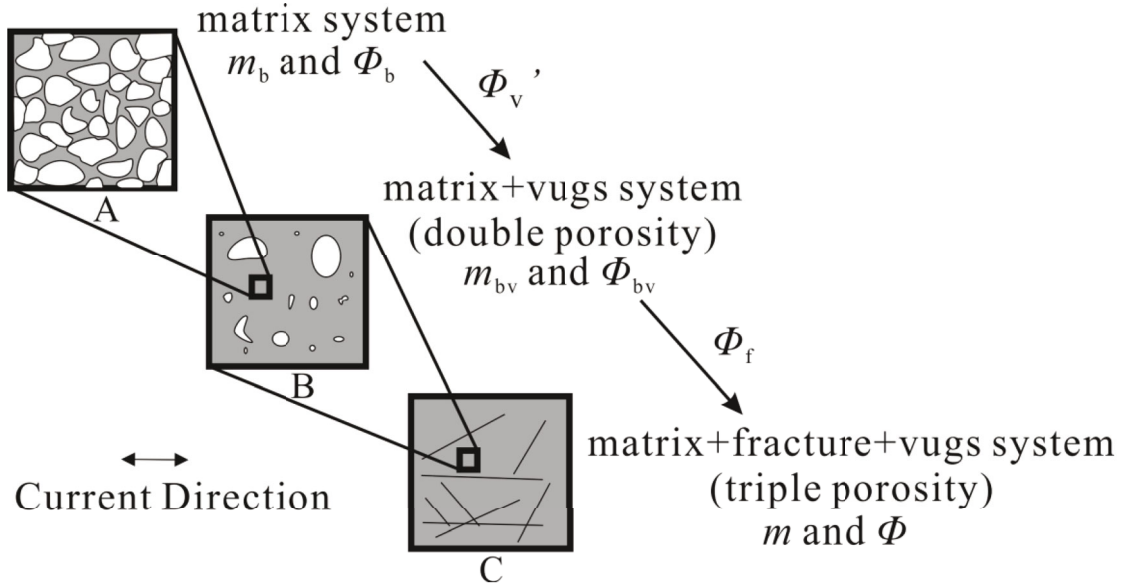


FIGURE 5: Calculation model and process of the  $m$  value of the triple-porosity composite system modified according to the Berg [10] calculation model.

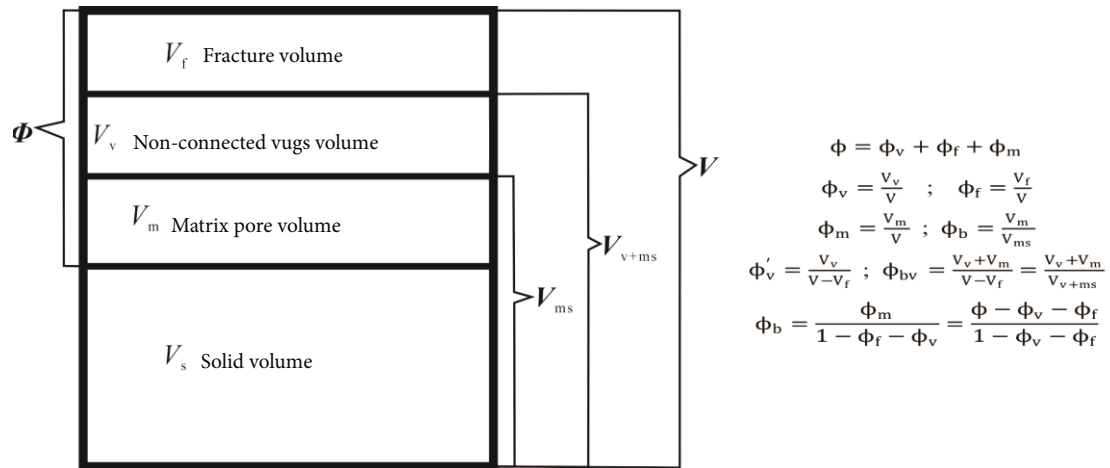


FIGURE 6: Petrophysical volume model of the triple-porosity medium composite system [20].

vugs is presented (see Figure 2), showing that the cementation exponent of the dual-porosity media system is greater than 2 because of vug porosity [6]. As the vug porosity increases, the  $m$  value of the dual-porosity system increases.

**2.2. Calculation of the Value of Cementation Exponent  $m$  of Dual-Porosity Media Reservoirs with Matrix Pores and Fractures (or Connected Vugs).** Aguilera [8] modeled a reservoir with matrix porosity and fracture porosity (or a reservoir with matrix porosity and connected vugs) as a parallel resistance network. The  $\Phi_b$  value corresponds to the matrix porosity, equaling to the pore space in the matrix divided by the volume of the matrix system [8]. It modifies the misconception that the matrix porosity  $\Phi_b$  in the  $m$ -value calculation model of Serra [7] is attached to the

volume of the composite system.  $\Phi$  represents the total porosity (matrix+fractures or matrix+connected vugs) of the reservoir, and a calculation model for the  $m$  value of a dual-porosity reservoir composed of the matrix and fractures is obtained.

Rasmus [5] placed the fracture volume in parallel with a limestone volume containing matrix pores and the resistivity-responding model of the limestone containing intergranular porosity with fractures embedded within. Besides, the equation to calculate the  $m$  value is derived based on the parallel connection of the fractures and matrix. The equation includes the parameter of fracture curvature. This model is advantageous, but the parameter of fracture curvature should be smaller when the total porosity increases. Otherwise, it will cause the problem of  $m > m_b$ . Rasmus simulated the influence of fractures on the formation resistivity

factor  $F$  and plotted it as a function of total porosity (matrix porosity and fracture porosity).  $m$  decreases as fracture porosity increases, following the conclusion of Aguilera [8]. Equation (2) shows the  $m$  value in a dual-porosity system with intergranular pores and fractures, developed by Aguilera [8].

$$m = \frac{\lg [\phi_f + \phi_b^{mb}(1 - \phi_f)]}{\lg \phi} \quad (2)$$

Equation (2) [8] is used to plot the relationship between the total porosity and cementation exponent  $m$  of the matrix and fracture dual-porosity system (see Figure 3). The cementation indices of the dual-porosity system are less than two due to fracture porosity. As fracture porosity increases, the  $m$  value of the dual-porosity system decreases.

**2.3. Calculation of the Value of Cementation Exponent  $m$  of Triple-Porosity Media Reservoirs (Matrix Pores-Fractures-Vugs).** Developed fractures in a three-porosity medium reservoir reduce the  $m$  value of the reservoir, and the developed vugs increase the  $m$  value of the reservoir. It shows the influence of fractures and nonconnected vugs on the  $m$  value of the reservoir (see Figure 4). However, triple-porosity medium reservoirs such as carbonate reservoirs often develop matrix pores, fractures, and vugs. The combination of the three types of storage spaces is complex and diverse. The rock matrix and the three types of storage spaces exist like the network. Current often flows along the path of minimum conductance, and the actual conductive path is more complex than that of the theoretical model.

The conductivity mechanism of the macroscale triple-porosity media reservoir is the coexistence and interaction of several equivalent conductivity models. The resistivity of the triple-porosity media reservoir is the macroscopic distribution of the micro series-parallel network system. Aguilera [9] deduced the equation for calculating the  $m$  value of carbonate reservoir with three porosity media combinations of matrix pores, fractures, and vugs. Matrix pores are used to connect with fractures in parallel, and then, the combination of matrix pores and fractures is utilized to connect in series with nonconnected vugs.

For triple-porosity media reservoirs with pores, fractures, and vugs, the calculation method of the  $m$  value for triple-porosity media reservoirs developed in the work is to follow the calculation method of Berg's triple-porosity model [10]. After obtaining total porosity  $\Phi_{bv}$  of the dual-

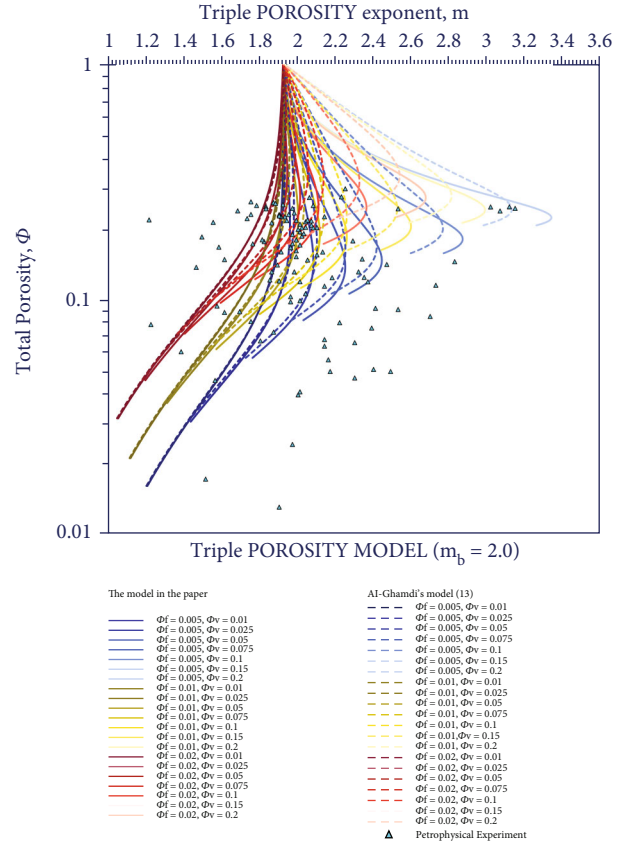


FIGURE 7:  $m$  determined as a function of triple-porosity media reservoirs with matrix pores, fractures, and vugs ( $m_b = 2.0$ ). The experimental data comes from Ragland [17].

porosity system of matrix and vugs in the triple-porosity system,  $\Phi_{bv}$  and  $\Phi_v'$  are introduced into the Maxwell-Garnett theoretical relationship to calculate the cementation exponent of the dual-porosity media system with the matrix and vugs [6] in triple-porosity media composite system  $m_{bv}$ . Then, block cementation exponent  $m_b$  and block pores  $\Phi_b$  in the dual-porosity media system with the matrix and fractures are replaced with cementation exponent  $m_{bv}$  and total porosity  $\Phi_{bv}$  of the dual-porosity system with the matrix and vugs. Finally, the Aguilera equation [8] was used to calculate the cementation exponent of the dual-porosity media system with the matrix and fractures and was simplified to obtain Equation (3) for calculating the  $m$  value of triple-porosity media reservoirs.

$$m = \frac{\lg \left\{ \phi_f + (1 - \phi_f) \left[ (\phi_v + \phi_b(1 - \phi_v - \phi_f)) / (1 - \phi_f) \right] \right\}}{\lg \phi} \frac{\lg \left\{ \phi_b^{mb} \left( (1 + 2\phi_v - \phi_f + 2\phi_b^{mb}(1 - \phi_v - \phi_f)) / (\phi_b^{mb}(2 - 2\phi_v + \phi_v) + 1 - \phi_v - \phi_f) \right) \right\}}{\lg \left\{ (\phi_v + \phi_b(1 - \phi_v - \phi_f)) / (1 - \phi_f) \right\}} \quad (3)$$

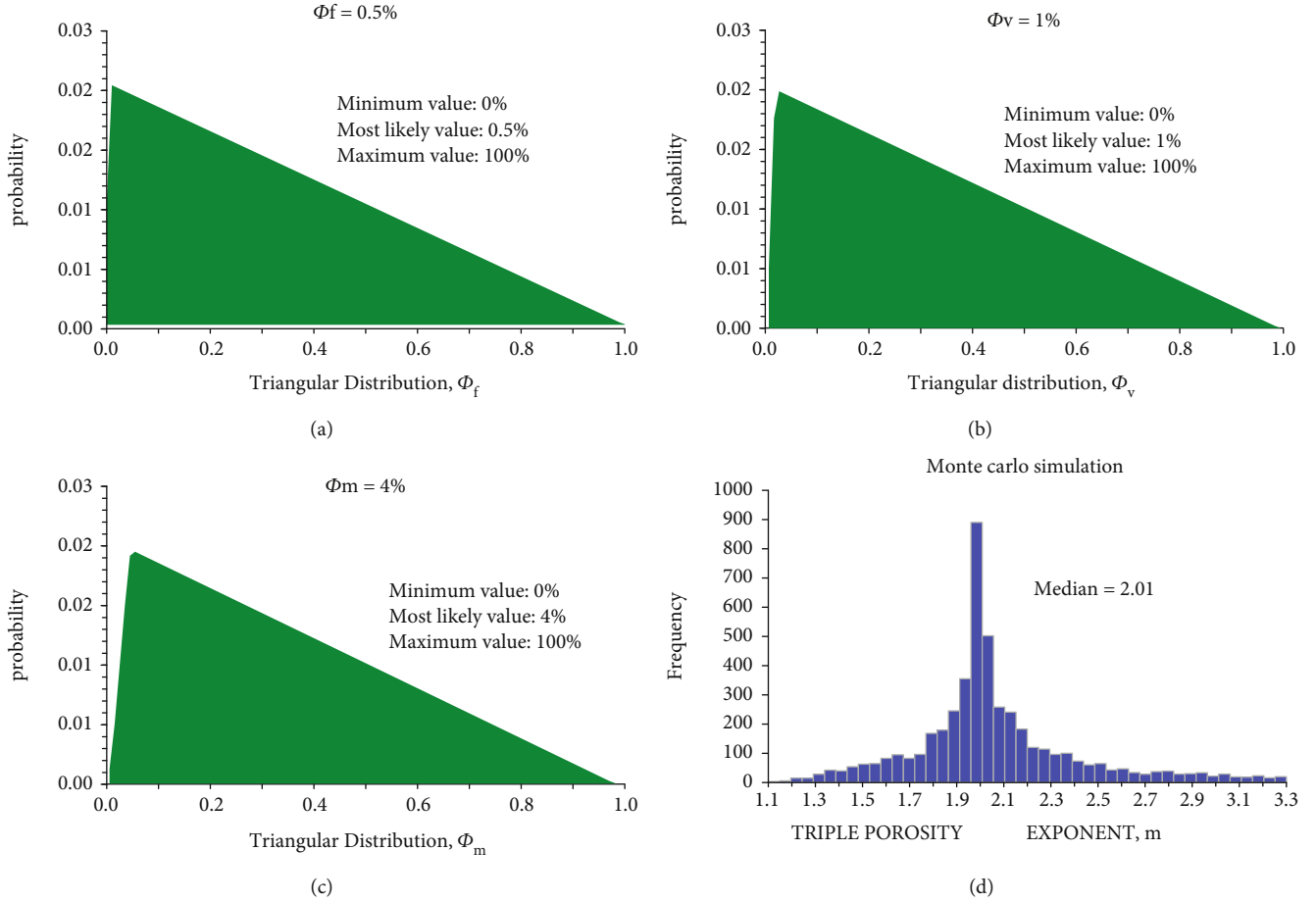


FIGURE 8:  $m$  value of low-porosity triple-pore medium reservoir (low-porosity carbonate rock) predicted by Monte Carlo simulation [20].

The calculation process is presented in the Appendix and Figure 5 shows the model-development process. Figure 6 shows the volume model of the triple-porosity value of a triple-porosity media reservoir.

A, B, and C are the schematic diagrams showing the physical models of each step. A represents the water-soaked intergranular pores, B the system with the matrix and vugs (the vugs are filled with water), and C the composite system (intergranular pores, vugs, and fractures). The total porosity and cementation exponent ( $\Phi_{bv}$  and  $m_{bv}$ ) of the dual-porosity system with the matrix and vugs in the triple-porosity composite system are calculated by  $m_v$  and  $\Phi_v$ , using Equation (1) of the dual-porous system with the matrix and vugs.  $\Phi_{bv}$  and  $m_{bv}$  are taken as matrix block porosity  $\Phi_b$  and corresponding cementation exponent  $m_b$  in Equation (2) of the dual-porosity system with the matrix and fractures combining  $\Phi_f$ .

The volume of the composite system is composed of the volumes of fractures, nonconnected vugs, matrix volume, and solid matrix.  $V_{ms}$  is the volume of the matrix block of the composite system,  $V_{v+ms}$  is the volume of the double-hole system with the matrix and vugs in the composite system, and  $V$  is the total volume of the composite system.

### 3. Results and Discussion

According to the triple-porosity model developed in the work (see Equation (3)), we obtained the relationship between the total porosity and cementation exponent  $m$  of the triple-porosity medium composite system with different combinations of fractures and nonconnected vug porosity (see Figure 7). The  $m$  value of the triple-porosity medium composite system (such as carbonate reservoir) varied from 1 to 3.6, mainly distributed in the range of 1.8 to 2.2 and converged at 2. The complex and long geological evolution process has led to serious heterogeneity of the triple-porosity media reservoir, making the irregular combination of matrix pores, fractures, and vugs in the reservoir and uncertain distribution characteristics. The decreased  $m$  value caused by fractures (or connected vugs) and the increased  $m$  value caused by nonconnected vugs offset each other, so the  $m$  value of the triple-porosity media reservoirs changed around 2.

The triple-porosity model developed in the work is more convergent than Al-Ghamdi et al.'s model [13], so the former is reliable. The rock petrophysics experiment data of carbonate rock were sampled by Ragland [17] in the Middle East. Most of the data points fell within the results calculated by substituting several hypothetical fracture-vug-

TABLE 1:  $m$  values of the triple-porosity media reservoir at various combinations of matrix porosity, fracture porosity, and nonconnected vug porosity.

$\Phi_f$ (v/v)	Assumptions		Results $m$	Sensitivity		
	$\Phi_v$ (v/v)	$\Phi_m$ (v/v)		$\Phi_f$	$\Phi_v$	$\Phi_m$
0.005	0.005	0.05	2.00	-16.6%	79.7%	-3.7%
0.005	0.01	0.05	2.01	-16.3%	79.4%	-4.3%
0.005	0.025	0.05	2.01	-15.9%	78.8%	-5.3%
0.005	0.05	0.05	2.02	-16.5%	75.0%	-8.5%
0.005	0.075	0.05	2.03	-17.1%	75.6%	-7.3%
0.005	0.1	0.05	2.04	-16.5%	71.1%	-12.4%
0.005	0.15	0.05	2.07	-12.7%	67.5%	-19.8%
0.005	0.2	0.05	2.08	-13.2%	61.4%	-25.4%
0.005	0.05	0.05	2.02	-15.2%	76.3%	-8.6%
0.01	0.05	0.05	2.02	-15.9%	77.2%	-7.0%
0.025	0.05	0.05	2.02	-13.7%	79.7%	-6.6%
0.05	0.05	0.05	2.01	-13.1%	81.4%	-5.4%
0.075	0.05	0.05	2.01	-12.4%	81.2%	-6.4%
0.1	0.05	0.05	2.01	-10.2%	84.1%	-5.7%
0.15	0.05	0.05	2.00	-9.4%	85.8%	-4.8%
0.2	0.05	0.05	2.00	-8.1%	87.4%	-4.5%
0.005	0.01	0.005	2.02	-13.3%	82.2%	-4.5%
0.005	0.01	0.01	2.01	-14.6%	80.4%	-5.0%
0.005	0.01	0.025	2.01	-16.0%	79.9%	-4.1%
0.005	0.01	0.05	2.01	-15.6%	80.8%	-3.6%
0.005	0.01	0.075	2.01	-18.4%	77.5%	-4.2%
0.005	0.01	0.1	2.01	-20.1%	75.7%	-4.2%
0.005	0.01	0.15	2.01	-20.9%	75.1%	-4.1%
0.005	0.01	0.2	2.00	-20.1%	75.3%	-4.6%

type combinations into Equation (3) (see Figure 7). It also corroborated the accuracy of the triple-porosity model developed in the work. In the upper left corner of Figure 7, there are a small number of rock-electricity experimental data points that do not fall within the results calculated by substituting several hypothetical fracture-vug-type combinations into Equation (3). These rock samples have many fractures and few or even no holes, which do not belong to the combination of several fracture-vug-type ratios assumed in Figure 7. Three-porosity media reservoirs also have dual-porosity media reservoirs of the local matrix-porosity fracture type and matrix-porosity vug type, and the heterogeneity and anisotropy of triple-porosity media reservoirs are very common. The changes in time and space scales of many influencing factors such as structure, sedimentation, and diagenesis have led to limitations in man-made assumptions due to the evolution of the earth's complex systems.

Wang and Peng [20] used the Monte Carlo method to simulate the random distribution of fractures and vugs in carbonate reservoirs. The method was used as a supplement to the model in the work to make the predicted results more accurate. For the triple-porosity reservoir with unknown severe heterogeneity, the porosity of different reservoir spaces in the reservoir is first incorporated into Equation

(3) for cementation index  $m$ . Then, the  $m$  value of the triple-porosity media reservoir can be predicted by simulation. As an example, Monte Carlo simulation [20] predicts that the  $m$  value of the triple-porosity media reservoir with  $\Phi_f = 0.5\%$ ,  $\Phi_v = 1\%$ , and  $\Phi_m = 4\%$  (low-porosity carbonate rock) is equal to 2.01, using the triple-porosity model developed in the work for 10,000 experiments (see Figure 8). Since the dual-porosity medium reservoir is a particular case of the triple-porosity one, this method can be used to obtain the  $m$  value.

Table 1 lists the  $m$  value of the triple-porosity media reservoir by Monte Carlo simulation based on the new triple-porosity models (see Equation (3)), setting the different ratios of matrix porosity, fracture porosity, and nonconnected vug porosity. The results show that the  $m$  value of the triple-porosity media reservoir converges at 2, and fractures decreased the  $m$  value but with increased vugs. The sensitivity of nonconnected vug porosity is more significant than that of fracture porosity and matrix porosity.

#### 4. Conclusions

The conductivity of the triple-porosity media reservoir was the external macroscopic expression of the microscopic conductive network. In the triple-porosity media reservoirs with

severe heterogeneity, such as carbonate rock, the carefully selected small-scale core plugs without vugs and/or microfractures could not represent the large-scale rock detected by the resistivity meter. Parameter  $m$  obtained by the laboratory analysis of the core plug should be used with caution.

In the triple-porosity medium reservoir, fractures decreased the  $m$  value, but vugs increased. The mixing of intergranular pores, vugs, and fractures made the  $m$  value of the triple-porosity media reservoir vary around 2.

The work proposed a new model for calculating the cementation exponent of the triple-porosity medium reservoir. It could predict the  $m$  value of an unknown triple-porosity medium reservoir with severe heterogeneity.

## Appendix

The vug porosity of the dual-porosity system with the matrix and vugs in the triple-porosity composite system is expressed as

$$\phi'_v = \frac{\phi_v}{1 - \phi_f}. \quad (\text{A.1})$$

$$m_{bv} = \frac{\lg \left\{ \phi_b^{\text{mb}} \left( \left( 1 - \phi_f + 2\phi_v + 2\phi_b^{\text{mb}}(1 - \phi_v - \phi_f) \right) / \left( 1 - \phi_f - \phi_v + \phi_b^{\text{mb}}(2 - 2\phi_f + \phi_v) \right) \right) \right\}}{\lg \{ (\phi_v + \phi_b(1 - \phi_v - \phi_f)) / (1 - \phi_f) \}}. \quad (\text{A.5})$$

An equation for calculating the  $m$  value of the dual-porosity system with the matrix and fractures [8] is expressed as

$$m = \frac{\lg \left[ \phi_f + \phi_b^{\text{mb}}(1 - \phi_f) \right]}{\lg \phi}. \quad (\text{A.6})$$

$$m = \frac{\lg \left\{ \phi_f + (1 - \phi_f) \left[ (\phi_v + \phi_b(1 - \phi_v - \phi_f)) / (1 - \phi_f) \right] \right\} \lg \left\{ \phi_b^{\text{mb}} \left( \left( 1 + 2\phi_v - \phi_f + 2\phi_b^{\text{mb}}(1 - \phi_v - \phi_f) \right) / \left( \phi_b^{\text{mb}}(2 - 2\phi_f + \phi_v) + 1 - \phi_v - \phi_f \right) \right) \right\}}{\lg \phi}. \quad (\text{A.7})$$

The total porosity of the dual-porosity system with the matrix and vugs in the triple-porosity composite system is expressed as

$$\phi_{bv} = \phi'_v + \phi_b(1 - \phi'_v). \quad (\text{A.2})$$

After simplifying,

$$\phi_{bv} = \frac{\phi_v + \phi_m}{1 - \phi_f} = \frac{\phi_v + \phi_b(1 - \phi_v - \phi_f)}{1 - \phi_f}. \quad (\text{A.3})$$

An equation for calculating the  $m$  value of the dual-porosity system with the matrix and vugs [6] is denoted as

$$m = \frac{\lg \left\{ \phi_b^{\text{mb}} \left[ \left( 1 + 2\phi_v - 2\phi_b^{\text{mb}}(\phi_v - 1) \right) / \left( \phi_b^{\text{mb}}(2 + \phi_v) + 1 - \phi_v \right) \right] \right\}}{\lg \phi}. \quad (\text{A.4})$$

After substituting  $\Phi_v$  and  $\Phi_{bv}$  into Equation (A.4), we obtain

Cementation exponent  $m$  of the triple-porosity composite system is calculated by substituting total porosity  $\Phi_{bv}$  (see Equation (A.3)) and corresponding cementation index  $m_{bv}$  (see Equation (A.5)) of the dual-porosity system with matrix and vugs as the  $\Phi_b$  and  $m_b$  of the dual-porosity system with matrix and fractures into Equation (A.6). Then, Equation (A.7), i.e., Equation (3) in the main text, is obtained.

## Nomenclature

- $\Phi$ : The total porosity of the composite system (the triple-porosity system with intergranular pores, fractures, and vugs)  
 $\Phi_f$ : The porosity of natural fractures, attached to the overall volume of the composite system  
 $\Phi_v$ : The porosity of nonconnected vugs, attached to the overall volume of the composite system

- $\Phi_m$ : The porosity of the matrix block attached to the overall volume of the composite system  
 $\Phi_b$ : The porosity of the matrix block attached to the whole volume of the matrix system, equivalent to the porosity of a nonfracture core plug  
 $\Phi'_v$ : The proportion of the vug volume in the composite system to the remaining volume of the composite system without fractures (the dual-porosity system with the matrix and vugs in the composite system)



- $\Phi_{bv}$ : The proportion of the volume of the vugs and the matrix pore volume in the composite system to the remaining volume of the composite system without fractures (the total porosity of the dual-porosity system with matrix and vugs in the composite system)
- $m$ : The porosity exponent (cementation exponent) of the composite system
- $m_b$ : The porosity exponent of the matrix block in the composite system (the porosity exponent of  $\Phi_b$ )
- $m_{bv}$ : The porosity exponent of the dual-porosity system with the matrix and vugs in the composite system (the porosity exponent of  $\Phi_{bv}$ ).

## Data Availability

The data used to support the findings of this study are available from the corresponding author upon request.

## Conflicts of Interest

The authors declare that there is no conflict of interest.

## Acknowledgments

The work was supported by the National Science and Technology Major Project (Grant No. 2016ZX05050) and the National Natural Science Foundation of China (Grant No. 41872166).

## References

- [1] M. A. Knackstedt, "Probing pore systems in carbonates: correlations to petrophysical properties," in *SPWLA 49th Annual Logging Symposium Edinburgh*, Society of Petrophysicists and Well-Log Analysts, Edinburgh Scotland, 2008.
- [2] G. E. Archie, "Classification of carbonate reservoir rocks and petrophysical considerations," *AAPG Bulletin*, vol. 36, no. 2, pp. 278–298, 1952.
- [3] G. Towle, "An analysis of the formation resistivity factor-porosity relationship of some assumed pore geometries," in *SPWLA 3rd annual logging symposium*, Society of Petrophysicists and Well-Log Analysts, Houston, Texas, 1962.
- [4] R. Aguilera, "Analysis of naturally fractured reservoirs from conventional well logs (includes associated papers 6420 and 6421)," *Journal of Petroleum Technology*, vol. 28, no. 7, pp. 764–772, 1976.
- [5] J. C. Rasmus, "A variable cementation exponent,  $m$ , for fractured carbonates," *The Log Analyst*, vol. 24, no. 6, pp. 13–23, 1983.
- [6] J. C. Rasmus, "A summary of the effects of various pore geometries and their wettabilities on measured and in-situ values of cementation and saturation exponents," in *SPWLA 27th Annual Logging Symposium*, Society of Petrophysicists and Well-Log Analysts, 1986.
- [7] O. Serra, *Formation microscanner image interpretation*, Schlumberger Educational Services, 1989.
- [8] M. S. A. R. Aguilera, "Improved models for petrophysical analysis of dual porosity reservoirs," *Petrophysics*, vol. 44, no. 1, pp. 21–25, 2003.
- [9] R. F. Aguilera, "A triple porosity model for petrophysical analysis of naturally fractured reservoirs," *Petrophysics*, vol. 45, no. 2, pp. 157–166, 2004.
- [10] C. R. Berg, "Dual porosity equations from effective medium theory," in *SPE Annual Technical Conference and Exhibition*, Society of Petroleum Engineers, San Antonio, Texas, 2006.
- [11] B. K. Olusola, G. Yu, and R. Aguilera, "The use of electromagnetic mixing rules for petrophysical evaluation of dual- and triple-porosity reservoirs," *SPE Reservoir Evaluation & Engineering*, vol. 16, no. 4, pp. 378–389, 2013.
- [12] C. G. Aguilera and R. Aguilera, "Effect of fracture dip on petrophysical evaluation of naturally fractured reservoirs," *Journal of Canadian Petroleum Technology*, vol. 48, no. 7, pp. 25–29, 2009.
- [13] A. Al-Ghamdi, B. Chen, H. Behmanesh, F. Qanbari, and R. Aguilera, "An improved triple porosity model for evaluation of naturally fractured reservoirs," in *Trinidad and Tobago Energy Resources Conference*, Society of Petroleum Engineers, Port of Spain, Trinidad, 2010.
- [14] J. Piedrahita and R. Aguilera, "A petrophysical dual porosity model for evaluation of secondary mineralization and tortuosity in naturally fractured reservoirs," in *Spe Low Perm Symposium*, Society of Petroleum Engineers, Denver, Colorado, 2016.
- [15] D. Ahmadi, "Dual pore network model of electrical resistivity for carbonate rocks," in *Society of Core Analysts*, Society of Petrophysicists and Well-Log Analysts, Avignon, France, 2014.
- [16] B. S. Nabawy, "Impacts of the pore- and petro-fabrics on porosity exponent and lithology factor of Archie's equation for carbonate rocks," *Journal of African Earth Sciences*, vol. 108, pp. 101–114, 2015.
- [17] D. A. Ragland, "Trends in cementation exponents ( $m$ ) for carbonate pore systems," *Petrophysics*, vol. 43, no. 5, pp. 434–446, 2002.
- [18] F. J. Lucia, "Rock-fabric/petrophysical classification of carbonate pore space for reservoir characterization," *AAPG Bulletin*, vol. 79, no. 9, pp. 1275–1300, 1995.
- [19] G. E. Archie, "The electrical resistivity log as an aid in determining some reservoir characteristics," *Transactions of AIME*, vol. 146, no. 1, pp. 54–62, 1942.
- [20] D. Wang and J. Peng, "Determination of the appropriate value of  $m$  for evaluation of carbonate reservoirs with vugs and fractures at the well-log scale," *Petrophysics*, vol. 60, no. 3, pp. 429–437, 2019.
- [21] W. Wei, J. Cai, X. Hu, and Q. Han, "An electrical conductivity model for fractal porous media," *Geophysical Research Letters*, vol. 42, no. 12, pp. 4833–4840, 2015.
- [22] J. Cai, W. Wei, X. Hu, and D. A. Wood, "Electrical conductivity models in saturated porous media: a review," *Earth-Science Reviews*, vol. 171, pp. 419–433, 2017.
- [23] P. N. Sen, C. Scala, and M. H. Cohen, "A self-similar model for sedimentary rocks with application to the dielectric constant of fused glass beads," *Geophysics*, vol. 46, no. 5, pp. 781–795, 1981.
- [24] J. C. Rasmus and W. E. Kenyon, "An improved petrophysical evaluation of oomoldic Lansing-Kansas city formations utilizing conductivity and dielectric log measurements," in *SPWLA 26th Annual Logging Symposium*, Society of Petrophysicists and Well-Log Analysts, Dallas, Texas, 1985.

## Research Article

# NMR Analysis Method of Gas Flow Pattern in the Process of Shale Gas Depletion Development

Rui Shen , Zhiming Hu, Xianggang Duan , Wei Sun, Wei Xiong, and Hekun Guo

Research Institute of Petroleum Exploration & Development, PetroChina Company Limited, 20 Xueyuan Road, Haidian District, Beijing 100083, China

Correspondence should be addressed to Rui Shen; shenrui523@126.com

Received 6 July 2021; Accepted 16 December 2021; Published 10 January 2022

Academic Editor: Chenhao Sun

Copyright © 2022 Rui Shen et al. This is an open access article distributed under the Creative Commons Attribution License, which permits unrestricted use, distribution, and reproduction in any medium, provided the original work is properly cited.

Shale gas reservoirs have pores of various sizes, in which gas flows in different patterns. The coexistence of multiple gas flow patterns is common. In order to quantitatively characterize the flow pattern in the process of shale gas depletion development, a physical simulation experiment of shale gas depletion development was designed, and a high-pressure on-line NMR analysis method of gas flow pattern in this process was proposed. The signal amplitudes of methane in pores of various sizes at different pressure levels were calculated according to the conversion relationship between the NMR  $T_2$  relaxation time and pore radius, and then, the flow patterns of methane in pores of various sizes under different pore pressure conditions were analyzed as per the flow pattern determination criteria. It is found that there are three flow patterns in the process of shale gas depletion development, i.e., continuous medium flow, slip flow, and transitional flow, which account for 73.5%, 25.8%, and 0.7% of total gas flow, respectively. When the pore pressure is high, the continuous medium flow is dominant. With the gas production in shale reservoir, the pore pressure decreases, the Knudsen number increases, and the pore size range of slip flow zone and transitional flow zone expands. When the reservoir pressure is higher than the critical desorption pressure, the adsorbed gas is not desorbed intensively, and the produced gas is mainly free gas. When the reservoir pressure is lower than the critical desorption pressure, the adsorbed gas is gradually desorbed, and the proportion of desorbed gas in the produced gas gradually increases.

## 1. Introduction

Deep shale gas in China is abundant and owning an immense potential for exploitation, which is becoming a key area for shale gas production in future [1, 2]. The shale gas reservoir is a kind of unconventional gas reservoir, with ultralow porosity and ultralow permeability, being complex in pore structure [3]. A large number of pores with diameter smaller than 50 nanometers are well developed in shale gas reservoir [4–6]. In addition, microfractures and micron-sized pores also exist, with a storage space system of multi-scale. The gas in shale reservoirs is in a free or adsorbed state, with a complicated shale gas flow mechanism. According to the concentration of the gas, with Knudsen number ( $K_n$ ), the gas flow can be divided into four types, including continuous flow, slip flow, transitional flow, and free molecular flow [7, 8]. The  $K_n$  is the ratio of the average molecular

free path to the characteristic scale. The scale of pores in shale gas reservoirs varies significantly, resulting in different gas flowing patterns in different scale pores. However, there is a lack of the experimental method for quantitatively characterizing the pattern of shale gas flow in shale reservoirs.

NMR core analyzing method has been widely used in the field of oil and gas seepage mechanics, including the NMR porosity testing [9, 10], movable fluid saturation testing [11], water-driving-oil NMR analysis [12–17], gas-driving-oil NMR analysis [18], and NMR pore structure characterization [19–22]. When the study objects change from conventional reservoirs to unconventional reservoirs such as tight oil and shale oil reservoirs, the pore sizes are getting smaller and smaller, and the pore structures are becoming more and more complex. Particularly, large errors might occur when conducting the water-driving-oil and gas-driving-oil experiments on tight oil or shale oil cores with

conventional sampling method due to the very small flow rate. In contrast, with the online NMR method under high-temperature and high-pressure, the variation of fluid relaxation in the core can be monitored in real-time, allowing a more accurate measurement of the variation of oil and water in the core. Therefore, the application of NMR core analysis technology will be further expanded when studying the seepage mechanics for unconventional oil and gas reservoirs [23].

During shale gas depletion development experiment, combined with high-temperature and high-pressure online NMR analysis technology, the occurrence and recovering regulation of adsorbed and free gas can be analyzed. Some key parameters can be calculated from the experiment, such as the critical desorption pressure and the recovering proportion of adsorbed gas [24]. The above experiments have all suggested that the gas production from shale gas reservoirs decreased rapidly at the initial stage and became slow at the middle and late stages, which is consistent with the gas production in the actual production process of shale gas wells [25]. The critical desorption pressure of the shale gas from the Longmaxi Formation in the Sichuan Basin is 12–15 MPa. When the reservoir pressure is lower than this critical desorption pressure, the recoverable degree of adsorbed gas increases significantly. When the produced shale gas is mainly free gas, the recoverable degree of adsorbed gas is low.

The low magnetic field NMR  $T_2$  spectrum distribution is directly related to the pore structure and can reflect the pore distribution of the sample to a certain extent [26, 27]. The key to study the pore size distribution with NMR test is to determine the surface relaxation rate and the shape of the pores. Generally, the surface relaxation rate is calculated by comparison with the capillary force curve obtained from the mercury intrusion capillary pressure experiment. By selecting an appropriate conversion coefficient ( $C$ ), the capillary pressure curve can be coincided with the pseudo capillary pressure curve. The derivation process of an equation for the conversion of the NMR transverse relaxation time  $T_2$  value to the throat radius was proposed. On an assumption that a linear relationship exists between  $T_2$  and the pore size distribution, the conversion coefficients of the NMR pore size distribution  $T_2$  spectrum and the pore radius were calculated. Then, the NMR  $T_2$  distribution was converted to the NMR capillary force curve, during which the value of the conversion coefficient ( $C_0$ ) ranges from 33.3 to 250 [28–30]. As for the double-peak  $T_2$  spectrum, two capillary pressure curves were separately constructed on both micropore and macropore segments by using two different power functions, and the linear method and power function method were used to construct the capillary pressure curve separately [31]. Li et al. proposed that under the condition of pore diameters less than  $5\ \mu\text{m}$ , the  $T_2$ -pore diameter relationship curves of the brine saturated sample and the oil-saturated sample are almost overlapped, indicating that the  $T_2$  distribution is irrelevant with the fluid volume, but only associated with the pore size. In this case, no matter what fluid is saturated in the pores, the  $T_2$  distribution is linearly related to the pore size distribution [32]. Hürlimann et al. deter-

mined the surface relaxation rate of sandstone and  $S/V$  value through diffusion experiment [33].

This paper presents an on-line NMR analysis method of flow pattern in the experimental process of shale gas depletion development. Specifically, the relative amplitude of methane in pores of various sizes under different pressure conditions is calculated according to the conversion relationship between  $T_2$  spectrum and pore radius, and then, the flow patterns of methane in pores of various sizes under different pore pressure conditions are analyzed as per the flow pattern determination criteria. Application of this method is exemplified in the first submember of the first member of the Silurian Longmaxi Formation (L11) in Well Ning 203.

## 2. Materials and Methods

**2.1. Experimental Methods.** The shale core sample was collected from the Long11 submember of the Silurian Longmaxi Formation in Well Ning 203 in the Changning area of the Sichuan Basin. The core sample, with a length of 73.62 millimeters and a diameter of 25.72 millimeters, was taken from depth interval ranging from 2384.69 m to 2384.86 m. The porosity of the core sample is 6.07%, and the Klinkenberg permeability is 1.02 mD. To truly reveal the seepage characteristics of natural gas in the reservoir, methane gas with a purity of 99.99% was used during the experimental process. A high-temperature and high-pressure online NMR core analyzer (ReCore-2515), which is independently developed by the Seepage Fluid Mechanics research laboratory of Research Institute of Petroleum Exploration and Development, PetroChina, was used in this experiment. The experimental setup is shown in Figure 1.

The experiment includes four main steps. Firstly, dry the core sample at  $105^\circ\text{C}$  for 48 hours, cool it to room temperature in a drying dish, and put it into the holder. Secondly, test the air tightness of the system, open the inlet valve of the holder and close the outlet valve, evacuate the core until it reaches the vacuum requirements, and then close the vacuum pump valve. Thirdly, the methane gas is injected into the core, pressurized to 20 MPa, and fully saturated for 24 days to simulate the original occurrence state of adsorbed methane gas. The change of methane gas signal in the rock core is detected in real time during the saturation process. And the final equilibrium pressure is set at 18.26 MPa. When the inlet and outlet pressures no longer change after 96 hours, the core is considered to return to its original state. Due to the tightness and adsorption characteristics of the shale reservoir, this process might last up to tens of days. Finally, open the outlet, start the depletion development experiment, and record the NMR  $T_2$  spectrum, the pressure at each measuring point, and gas production data at the outlet valve in real-time.

The experiment includes four main steps. (1) The core was dried at  $105^\circ\text{C}$  for 48 h and then cooled to  $25^\circ\text{C}$  in a drying dish before being put into a holder. (2) Check the tightness of the system. Open the inlet valve of the holder and close the outlet valve to vacuum the core. Close the inlet valve after reaching the vacuum requirement. (3) Methane gas is injected into the core in a constant pressure mode to

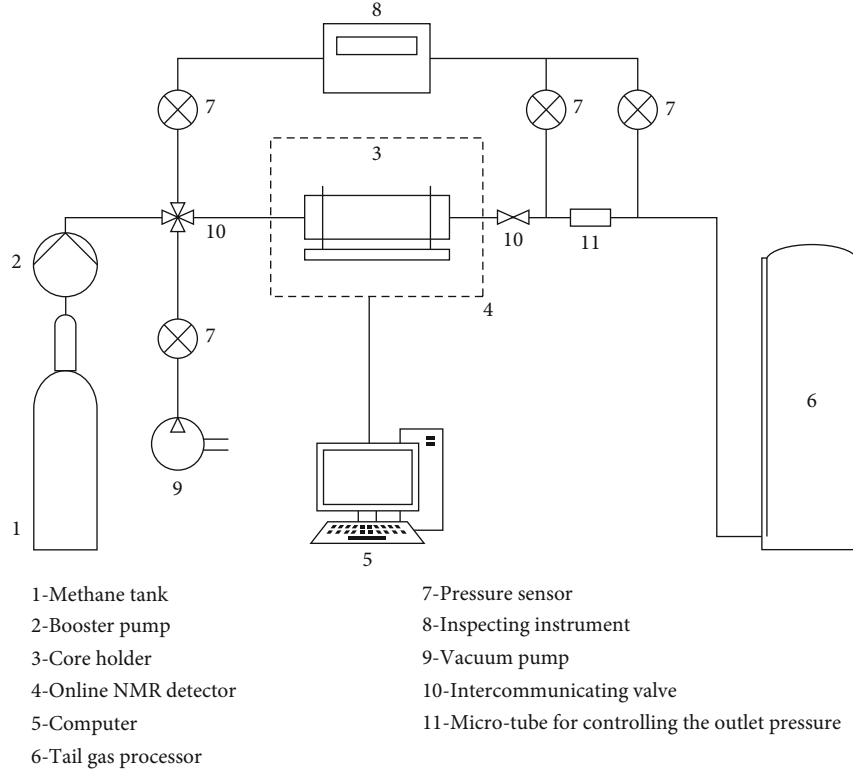


FIGURE 1: Flow diagram of the NMR experiment for analyzing shale gas depletion development.

restore the original reservoir occurrence. Record the pressure at both ends of the core and close the gas source after saturation to 18.26 MPa at the inlet and outlet of the core. When the inlet and outlet pressures do not change during 96h, the core is restored to the original occurrence state. Due to the density and adsorption properties of shale reservoirs, this process can last for tens of days. (4) Open the outlet valve, start the depletion development experiment. The data of  $T_2$  spectrum, pressure at each measuring point, and gas production at outlet were recorded during the experiment.

**2.2. NMR Pore Size Distribution.** Low-magnetic-field NMR test results can provide abundant information on the fluid in porous media. In general, the relaxation time of fluid in porous media includes bulk relaxation, surface relaxation, and diffusion relaxation. In this study, the Carr-Purcell-Meiboom-Gill test sequence has been used, and only the surface relaxation needs to be considered [34, 35]. The relationship between the information of fluid in pores and relaxation time of the NMR test is shown in Equation (1):

$$\frac{1}{T_2} = \frac{1}{\rho_2} \frac{S}{V}, \quad (1)$$

where  $T_2$  is the relaxation time, ms;  $\rho_2$  is the surface relaxation rate,  $\mu\text{m}\cdot\text{ms}^{-1}$ ; and  $S/V$  is the ratio of specific surface area to pore volume,  $\mu\text{m}^{-1}$ .

According to Equation (1), small pores have larger  $S/V$  values. Therefore, small pores have shorter relaxation times than large pores. The relationship between the  $T_2$  spectrum and the pore radius can be expressed by:

$$\frac{S}{V} = \frac{F_s}{d/2}, \quad (2)$$

where  $F_s$  is the shape factor of pores (3 for spherical pores and 2 for columnar pores), dimensionless, and  $d$  is the pore diameter,  $\mu\text{m}$ . According to Equation (1) and Equation (2), the relationship between the pore diameter ( $d$ ) and the relaxation time ( $T_2$ ) can be obtained:

$$d = CT_2, \quad (3)$$

where  $C$  is conversion coefficient set as  $33 \mu\text{m}\cdot\text{ms}^{-1}$  according to data range proposed in the literature [16].

**2.3. Determination of the Flowing Pattern.** Gas molecules frequently collide with each other during the movement process. The gas transportation process comes from the thermal motion of molecules. The collision causes the molecules to change continuously the direction and rate of movement, making the molecular movement path very tortuous. The collision also allows molecules to exchange continuously the energy and momentum, being the necessary prerequisites for the balance of the system. The path that the actual gas molecules travel between two collisions is called the free path. For gas molecules, the average distance between two

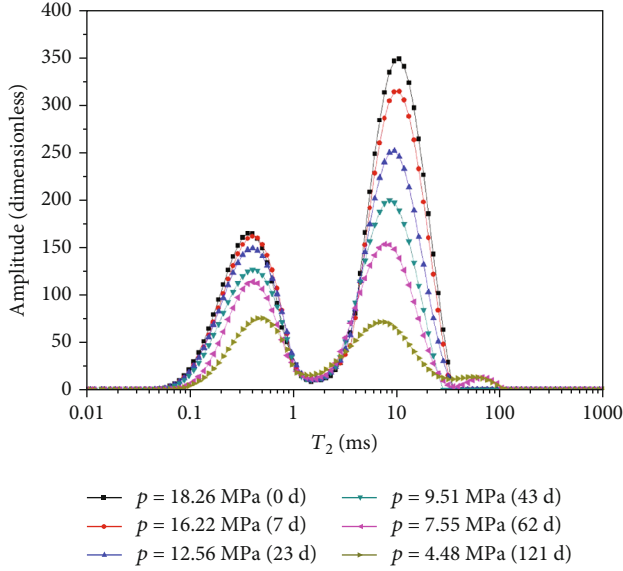


FIGURE 2: The  $T_2$  spectrum distribution at different stages.

adjacent collisions, known as the average free path of the molecule, is a physical quantity of only statistical significance, as shown in Equation (4) [36, 37]:

$$\lambda = \frac{k_B T}{\sqrt{2\pi} d_g^2 p}, \quad (4)$$

where  $d_g$  is the effective diameter of the molecule,  $\mu\text{m}$ ;  $p$  is the gas pressure, MPa;  $k_B$  is the Boltzmann's constant, J/K; and  $T$  is the temperature, K.

Knudsen number ( $K_n$ ) represents the ratio of the average free path of molecules ( $\lambda$ ) to the characteristic length ( $L$ ) of the object in the flow field.

### 3. Results and Discussion

**3.1. Experimental Results.** Figure 2 illustrates the  $T_2$  spectrum distribution at six stages during the experiment, including at the beginning and when the experiment was carried out for 7, 23, 43, 62, and 121 days, respectively. At the beginning of the experiment, there are two peaks in the  $T_2$  spectrum, and the signal amplitude of the right peak is about 1 times higher than that of the left peak, indicating that there are relatively many macropores in the shale core sample. The first 23 days of the experiment is equivalent to the initial stage of the experiment. As the average pore pressure of the core decreased, the signal amplitude corresponding to the right peak also decreased, but the signal amplitude corresponding to the left peak was almost unchanged, indicating that the gas recovered at the initial stage was mainly free gas in macropores, and the free gas and adsorbed gas in the mesopores and macropores were less recovered. This gas production law is in good accordance with the actual gas well production performance. When the experiment entered the middle and late stages, that is, 23 days after the experiment, the signal amplitude of the right peak and the

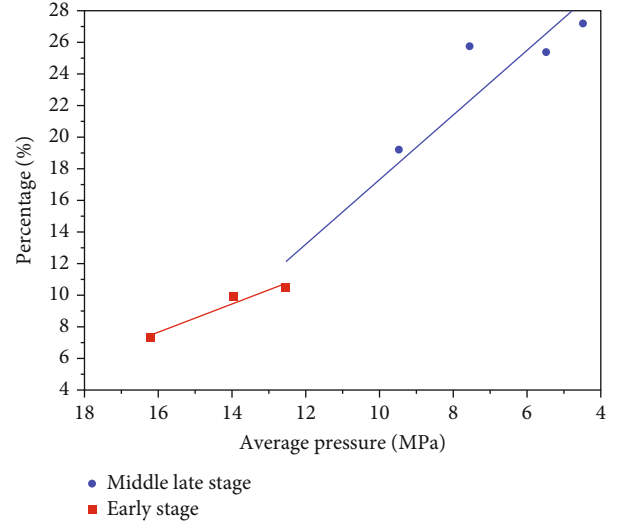


FIGURE 3: The proportion of adsorbed gas in the total produced gas at different average pore pressures.

left peak began to decrease simultaneously, indicating that the gas in the pores of all scales has been recovered. At present, it is generally believed that the adsorbed gas mainly exists in pores of nanoscale (i.e., pores with a pore size of smaller than 100 nanometers) [36]. According to Figure 2, the signal of the left peak varies slightly as the average pore pressure is higher than 12.6 MPa, indicating that the adsorbed gas has not been widely desorbed. When the average pore pressure is less than 12.6 MPa, the signal amplitude of the left peak begins to gradually decrease with the decrease of the average pore pressure, indicating that the critical desorption pressure is around 12.6 MPa, and the large-scale desorption of adsorbed gas only occurs when the pore pressure is lower than the critical desorption pressure. When the average pore pressure is greater than 12.6 MPa, the proportion of adsorbed gas in the total produced gas is less than 10%. With the production of methane from shale, the proportion of adsorbed gas in the total produced gas gradually increases, and it reaches 27.2% when the average pressure is 4.48 MPa, as shown in Figure 3.

**3.2. Discussion of the Flowing Pattern of Shale Gas during the Depletion Development.** According to Equation (3), the relaxation time at the horizontal axis in Figure 4 was converted into pore diameter. The average pressure of pores in the shale gas depletion development experiment dropped from 18.26 MPa to 4.48 MPa, and the NMR  $T_2$  spectrum corresponding to the two pressure states is shown in the following figure. According to Equation (3), the molecular free paths were, respectively, calculated as  $\lambda_{p=18.26\text{ MPa}}$  and  $\lambda_{p=4.48\text{ MPa}}$ . The Knudsen number  $K_n$  is obtained by the ratio of molecular free path to characteristic scale. The flow state can be divided by the interval of  $K_n$ . That is, according to the degree of gas concentration, the flow can be divided into four regions based on  $K_n$ . This comprises continuous flow ( $K_n < 0.01$ ), slip flow ( $0.01 \leq K_n < 0.1$ ), transitional flow ( $0.1 \leq K_n < 10$ ), and free molecular flow ( $K_n \geq 10$ ) [8, 9].

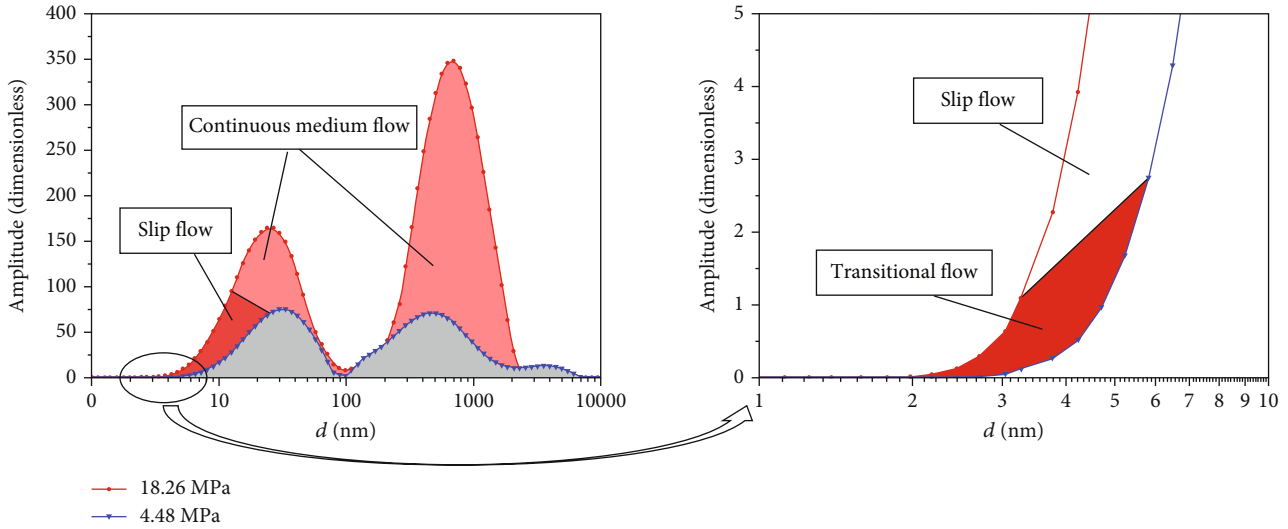


FIGURE 4: The amplitude distribution of the NMR signal corresponding to the pores of each scale under two pressure states at the beginning and end of the experiment (a) Full scale pore diameter distribution. (b) A magnified view of pore diameter 1-10 nm.

The nuclear magnetic resonance  $T_2$  spectrum of methane saturated shale has obvious bimodal characteristics. Methane is mainly adsorbed on the surface of nanopores in shale. The adsorption is mainly controlled by surface relaxation. The relaxation time is short between 0.1 and 1.0 ms, and the main peak is 0.4 ms, corresponding to the left peak on the  $T_2$  spectrum of NMR. Free methane exists in larger shale pores, which is not bound by pore wall, and has a long relaxation time which corresponds to the right peak on  $T_2$  spectrum. The relaxation time is between 1 and 100 ms, and the main peak is 10 ms. Thus, the signal quantity of adsorbed/free state of methane gas in shale can be determined by  $T_2$  spectrum. However, it is generally believed that the adsorbed gas mainly exists in pores of nanoscale (i.e., pores with a pore size less than 100 nanometers) [34]. Therefore, by calculating the ratio of the amplitude of the left peak to the total amplitude in the  $T_2$  spectrum at the pressure of 18.26 MPa, the proportion of the adsorbed gas in the total gas in the initial state can be determined as 33.3%.

The free path of the gas molecule was calculated according to equation (3), and then, the  $K_n$  number was obtained by dividing it through the pore diameter. Figure 5 shows how the  $K_n$  number varies with the pore size at average pore pressure conditions of 18.26 MPa and 4.48 MPa, respectively. According to the criterion for determining flowing pattern, there are three flowing patterns, which include continuous flow, slip flow, and transitional flow during the shale gas depletion development experiment. When the average pore pressure of cores is 18.26 MPa, the pore size is less than 1.39 nm for transitional flow, 1.39–12.47 nm for slip flow, and more than 12.47 nm for continuous medium flow. When the average pore pressure is 4.48 MPa, the pore size is less than 5.81 nm for transitional flow, 5.81–57.1 nm for slip flow, and more than 57.1 nm for continuous medium flow. In Figure 4, the ratio of the area enveloped by the signal amplitude line for each flow pattern under each average pore

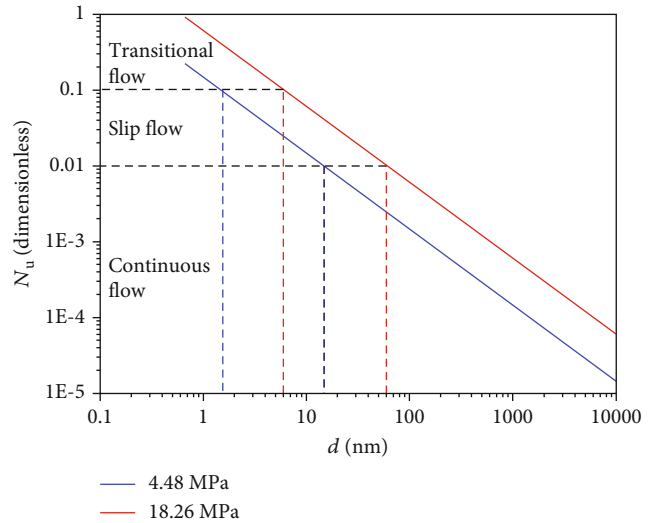


FIGURE 5: The distribution of  $K_n$  number under the pressure conditions at the beginning and end of the experiment.

pressure and the X-axis to the area enveloped by the whole signal amplitude line, and the X-axis is the proportion of the flow pattern under the average pore pressure.

Between Figures 4 and 5, it can be inferred that (1) when the pressure is 18.26 MPa, the flow pattern is mainly slip flow and continuous medium flow, with the former observed in pores with diameter of 1.39–12.47 nm, accounting for 6.1% of the total flow, and the latter in pores with diameter > 12.47 nm, that is, the Darcy flow, accounting for 93.9% of the total flow; and (2) when the pressure is 4.48 MPa, transitional flow occurs in the pores with diameter < 5.81 nm, accounting for 0.3% of the total flow; slip flow occurs in pores with diameter of 5.81–57.1 nm, accounting for 41.5% of the total flow; and continuous medium flow occurs in pores with diameter > 57.1 nm, accounting for 58.2% of the total flow.

Continuous medium flow is dominant at high pore pressure. However, it is important to note that continuous production in the shale reservoir results in a decrease in pore pressure, increase in Knudsen number, and an expansion of the pore size range of the slip flow zone and transitional zone, with both zones also being characterized by an increase in the proportion of diffusion flux to total flux. In the slip flow zone, there is a thin gas layer near the wall, that is, the Knudsen diffusion layer, and the flow in this zone needs to be simulated by the slip boundary conditions near the wall. In the transitional flow zone, the Knudsen diffusion layer is wider to trap most of the fluids, and the flow in this zone needs to be described by rarefied gas dynamics. The gas flow patterns obtained by NMR analysis are consistent with the findings in previous studies [36, 38], proving that the propose method is scientific and practical.

At present, there is little research on shale gas flow pattern analysis. For shale, a porous medium with large pore space scale span, usually only static flow pattern analysis under a certain pressure, is carried out. However, this is limited to flow pattern analysis under several characteristic scales. This study provides a dynamic analysis method of flow pattern in the process of depletion development. It is expected to be applied to the flow pattern analysis of depletion development of deep shale gas reservoirs under high reservoir pressure.

#### 4. Conclusions

The on-line NMR analysis method of gas flow pattern can quantitatively analyze the gas flow patterns occurred under different pressure and pore size conditions in the process of shale gas depletion development and clarify the contribution of each flow pattern to the total flux in such process.

The shale gas depletion development experiment reveals three flow patterns: continuous medium flow, slip flow, and transitional flow. When the pore pressure is high, the continuous medium flow is dominant. With the decrease of pore pressure, the Knudsen number increases, and the pore size range of slip flow zone and transitional flow zone expands.

In the process of shale gas depletion development, there is a critical desorption pressure. When the reservoir pressure is higher than the critical desorption pressure, the adsorbed gas is not desorbed intensively, and the produced gas is mainly free gas. When the reservoir pressure is lower than the critical desorption pressure, the adsorbed gas is gradually desorbed, and the proportion of desorbed gas in the produced gas gradually increases.

#### Data Availability

Data available on request.

#### Conflicts of Interest

The authors declare no competing interests.

#### Acknowledgments

This paper is supported by the National Major Research Program for Science and Technology of China (2017ZX05037-001) and the Research Fund for Basic Research and Strategic Reserve Technology of Institutes Directly under CNPC (2018D-500806).

#### References

- [1] W. Shen, X. Li, T. Ma, J. Cai, X. Lu, and S. Zhou, "High-pressure methane adsorption behavior on deep shales: experiments and modeling," *Physics of Fluids*, vol. 33, no. 6, article 063103, 2021.
- [2] X. Guo, D. Hu, Y. Li et al., "Theoretical progress and key technologies of onshore ultra-deep oil/gas exploration," *Engineering*, vol. 5, no. 3, pp. 458–470, 2019.
- [3] X. Ma, J. Xie, and R. Yong, "Geological characteristics and high production control factors of shale gas reservoirs in Silurian Longmaxi Formation, southern Sichuan Basin, SW China," *Petroleum Exploration and Development*, vol. 47, no. 5, pp. 901–915, 2020.
- [4] Y. Wang, H. Wang, C. Zhang, X. Li, and D. Dong, "Fracture pore evaluation of the Upper Ordovician Wufeng to Lower Silurian Longmaxi Formations in southern Sichuan Basin, SW China," *Petroleum Exploration and Development*, vol. 44, no. 4, pp. 563–572, 2017.
- [5] Y. Li, X. Liu, S. Gao et al., "A generalized model for gas flow prediction in shale matrix with deduced coupling coefficients and its macroscopic form based on real shale pore size distribution experiments," *Journal of Petroleum Science and Engineering*, vol. 187, article 106712, 2020.
- [6] Y. Zhao, L. Peng, S. Liu, B. Cao, Y. Sun, and B. Hou, "Pore structure characterization of shales using synchrotron SAXS and NMR cryoporometry," *Marine and Petroleum Geology*, vol. 102, pp. 116–125, 2019.
- [7] Y. Liu, Y. Yao, D. Liu, S. Zheng, G. Sun, and Y. Chang, "Shale pore size classification: an NMR fluid typing method," *Marine and Petroleum Geology*, vol. 96, pp. 591–601, 2018.
- [8] M. Knudsen, "Die Gesetze der Molekularströmung und der inneren Reibungsströmung der Gase durch Röhren," *Annalen der Physik*, vol. 333, no. 1, pp. 75–130, 1909.
- [9] Y. Wu, K. Pruess, and P. Persoff, "Gas flow in porous media with Klinkenberg effects," *Transport in Porous Media*, vol. 32, no. 1, pp. 117–137, 1998.
- [10] X. Li, Y. Kang, and M. Haghghi, "Investigation of pore size distributions of coals with different structures by nuclear magnetic resonance (NMR) and mercury intrusion porosimetry (MIP)," *Measurement*, vol. 116, pp. 122–128, 2018.
- [11] J. Li, S. Lu, G. Chen, M. Wang, S. Tian, and Z. Guo, "A new method for measuring shale porosity with low-field nuclear magnetic resonance considering non-fluid signals," *Marine and Petroleum Geology*, vol. 102, pp. 535–543, 2019.
- [12] M. Appel, "Nuclear magnetic resonance and formation porosity," *Petrophysics*, vol. 45, no. 3, pp. 296–307, 2004.
- [13] Y. Song and R. Kausik, "NMR application in unconventional shale reservoirs - a new porous media research frontier," *Progress in Nuclear Magnetic Resonance Spectroscopy*, vol. 112–113, pp. 17–33, 2019.

- [14] Z. Liu, D. Liu, Y. Cai, Y. Yao, Z. Pan, and Y. Zhou, "Application of nuclear magnetic resonance (NMR) in coalbed methane and shale reservoirs: a review," *International Journal of Coal Geology*, vol. 218, article 103261, 2020.
- [15] J. Liu and J. Sheng, "Experimental investigation of surfactant enhanced spontaneous imbibition in Chinese shale oil reservoirs using NMR tests," *Journal of Industrial and Engineering Chemistry*, vol. 72, pp. 414–422, 2019.
- [16] C. Dai, R. Cheng, X. Sun et al., "Oil migration in nanometer to micrometer sized pores of tight oil sandstone during dynamic surfactant imbibition with online NMR," *Fuel*, vol. 245, pp. 544–553, 2019.
- [17] P. Zhang, S. Lu, J. Li, C. Chen, H. Xue, and J. Zhang, "Petrophysical characterization of oil-bearing shales by low-field nuclear magnetic resonance (NMR)," *Marine and Petroleum Geology*, vol. 89, pp. 775–785, 2018.
- [18] I. Gupta, C. Rai, and C. Sondergeld, "Study impact of sample treatment and insitu fluids on shale wettability measurement using NMR," *Journal of Petroleum Science and Engineering*, vol. 176, pp. 352–361, 2019.
- [19] S. Su, Z. Jiang, X. Shan et al., "The wettability of shale by NMR measurements and its controlling factors," *Journal of Petroleum Science and Engineering*, vol. 169, pp. 309–316, 2018.
- [20] Y. Yuan and R. Rezaee, "Fractal analysis of the pore structure for clay bound water and potential gas storage in shales based on NMR and  $N_2$  gas adsorption," *Journal of Petroleum Science and Engineering*, vol. 177, pp. 756–765, 2019.
- [21] Y. Volokitin, W. Looyestijn, W. Slijkerman, J. Hofman, X. Jing, and L. Riepe, "A practical approach to obtain primary drainage capillary pressure curves from NMR core and log data," *Petrophysics*, vol. 42, no. 4, pp. 334–343, 2001.
- [22] W. Sun, Y. Zuo, Z. Wu et al., "Fractal analysis of pores and the pore structure of the lower Cambrian Niutitang shale in northern Guizhou province: investigations using NMR, SEM and image analyses," *Marine and Petroleum Geology*, vol. 99, pp. 416–428, 2019.
- [23] E. Silletta, M. Franzoni, G. Monti, and R. Acosta, "Influence of exchange in NMR pore size/relaxation correlation experiments," *Microporous and Mesoporous Materials*, vol. 269, pp. 17–20, 2018.
- [24] S. Zhang, J. Yan, Q. Hu et al., "Integrated NMR and FE-SEM methods for pore structure characterization of Shahejie shale from the Dongying Depression, Bohai Bay Basin," *Marine and Petroleum Geology*, vol. 100, pp. 85–94, 2019.
- [25] X. Ma, S. Guo, D. Shi, Z. Zhou, and G. Liu, "Investigation of pore structure and fractal characteristics of marine-continental transitional shales from Longtan Formation using MICP, gas adsorption, and NMR (Guizhou, China)," *Marine and Petroleum Geology*, vol. 107, pp. 555–571, 2019.
- [26] Y. Yao, J. Liu, D. Liu, J. Chen, and Z. Pan, "A new application of NMR in characterization of multiphase methane and adsorption capacity of shale," *International Journal of Coal Geology*, vol. 201, pp. 76–85, 2019.
- [27] M. Testamanti and R. Rezaee, "Considerations for the acquisition and inversion of NMR  $T_2$  data in shales," *Journal of Petroleum Science and Engineering*, vol. 174, pp. 177–188, 2019.
- [28] M. Tan, K. Mao, X. Song, X. Yang, and J. Xu, "NMR petrophysical interpretation method of gas shale based on core NMR experiment," *Journal of Petroleum Science and Engineering*, vol. 136, pp. 100–111, 2015.
- [29] M. Fleury and M. Romero-Sarmiento, "Characterization of shales using  $T_1$ - $T_2$  NMR maps," *Journal of Petroleum Science and Engineering*, vol. 137, pp. 55–62, 2016.
- [30] P. Zhao, L. Wang, C. Xu et al., "Nuclear magnetic resonance surface relaxivity and its advanced application in calculating pore size distributions," *Marine and Petroleum Geology*, vol. 111, pp. 66–74, 2020.
- [31] S. Zheng, Y. Yao, D. Liu, Y. Cai, and Y. Liu, "Nuclear magnetic resonance surface relaxivity of coals," *International Journal of Coal Geology*, vol. 205, pp. 1–13, 2019.
- [32] J. Li, W. Jin, L. Wang, Q. Wu, and J. Lu, "Quantitative relationship between NMR  $T_2$  and pore size of shale gas reservoir from core experiment," *Well Logging Technology*, vol. 40, no. 4, pp. 460–464, 2016.
- [33] M. Hürlimann, L. Latour, and C. Sotak, "Diffusion measurement in sandstone core: NMR determination of surface-to-volume ratio and surface relaxivity," *Magnetic Resonance Imaging*, vol. 12, no. 2, pp. 325–327, 1994.
- [34] J. Lai, S. Wang, C. Zhang et al., "Spectrum of pore types and networks in the deep Cambrian to Lower Ordovician dolostones in Tarim Basin, China," *Marine and Petroleum Geology*, vol. 112, article 104081, 2020.
- [35] J. Lai, G. Wang, Z. Wang et al., "A review on pore structure characterization in tight sandstones," *Earth-Science Reviews*, vol. 177, pp. 436–457, 2018.
- [36] F. Javadpour, D. Fisher, and M. Unsworth, "Nanoscale gas flow in shale gas sediments," *Journal of Canada Petroleum Technology*, vol. 46, no. 10, pp. 55–61, 2007.
- [37] W. Shen, F. Song, X. Hu, G. Zhu, and W. Zhu, "Experimental study on flow characteristics of gas transport in micro- and nanoscale pores," *Scientific Reports*, vol. 9, no. 1, p. 10196, 2019.
- [38] S. Muncaci, I. Ardelean, and S. Boboia, "The effect of diffusion in internal gradients on nuclear magnetic resonance transverse relaxation measurements," *AIP Conference Proceedings*, vol. 1565, pp. 133–136, 2013.



## Research Article

# Paleoenvironment, Geochemistry, and Pore Characteristics of the Postmature to Overmature Organic-Rich Devonian Shales in Guizhong Depression, Southwestern China

Yanqi Zhang<sup>1,2</sup>, Li Liu<sup>1</sup>, Changxi Geng<sup>1,2</sup>, Zhuang Cheng<sup>3</sup>, and Xinxin Fang<sup>4,5</sup>

<sup>1</sup>School of Geosciences, Jilin University, Changchun 130061, China

<sup>2</sup>Daqing Drilling Engineering Company, Daqing Oilfield Co. Ltd., Daqing 163458, China

<sup>3</sup>Daqing Drilling & Geological Logging No. 1 Company, Daqing 163458, China

<sup>4</sup>Institute of Geomechanics, Chinese Academy of Geological Sciences, Beijing 100081, China

<sup>5</sup>Key Laboratory of Paleomagnetism and Tectonic Reconstruction, Ministry of Natural Resources, Beijing 100081, China

Correspondence should be addressed to Yanqi Zhang; 183268205@qq.com and Xinxin Fang; 8530324@qq.com

Received 11 August 2021; Accepted 12 November 2021; Published 30 December 2021

Academic Editor: Steffen Berg

Copyright © 2021 Yanqi Zhang et al. This is an open access article distributed under the Creative Commons Attribution License, which permits unrestricted use, distribution, and reproduction in any medium, provided the original work is properly cited.

Investigating shale pore characteristics has deepened our understanding of shale reservoir, while that of postmature-overmature shales is yet to be revealed, which is especially critical for shale gas evaluation in southern China. Ten Middle-Upper Devonian organic-rich shale samples were collected from well GY-1 in the Guizhong Depression, and the paleoenvironment, geochemistry, and pore system were analyzed with a series of experiments, including trace element analysis, X-ray diffraction (XRD), field emission scanning electron microscopy (FESEM), low-pressure N<sub>2</sub> adsorption, and source rock geochemistry. Results show that the Middle-Upper Devonian shales in the Guizhong Depression are organic-rich mudstones with TOC ranging from 0.14% to 6.21%, which is highest in the Nabiao Formation (*D<sub>2</sub>n*) and Lower Luofu Formation (*D<sub>2</sub>l*) that were deposited in the anoxic and weak hydrodynamic deep-water shelf. They are thermally postmature to overmature with equivalent vitrinite reflectance (EqVR<sub>o</sub>) of 3.40%~3.76% and type I kerogen. The lithofacies in *D<sub>2</sub>n* and *D<sub>2</sub>l* are primarily siliceous/argillaceous mixed shale as well as a few siliceous argillaceous shales and argillaceous siliceous shales as well. Organic matter- (OM-) hosted pores within bitumen are primary storage volume, rather than inorganic pores (interparticle and intraparticle) which are rare. The total helium porosity of samples varies between 1.20% and 4.49%, while total surface area and pore volume are 2.39-14.22 m<sup>2</sup>/g and 0.0036-0.0171 ml/g, respectively. Porosity, pore surface area, and pore volume are in accordance with increasing TOC, R<sub>o</sub>, and siliceous mineral contents. Considerable OM-macropores are found in shales with R<sub>o</sub> > 3.6% in our study which demonstrates that the porosity at postmature to overmature stage (R<sub>o</sub> = 3.5–4.0%) does not change fundamentally. The high level of maturity is not considered the main controlling factor that affects shale gas content, and more attention should be paid to preservation conditions in this area.

## 1. Introduction

Shales have attracted significant attention in the past few years because of their emergence as unconventional hydrocarbon reservoirs [1–3]. Identifying and producing reserves from shales in south China have gained considerable exploration interest and activity, which have made significant progress [4, 5]. Unlike conventional sandstone and carbonate reservoirs with microscale pores, shales are typically domi-

nated by nanoscale pores [6]. The pore structure characterization using various techniques has gained a high research priority as they are essential in a potential shale reservoir evaluation. The direct imaging methods, e.g., CT scan, field emission scanning electron microscopy (FESEM), focused ion beam-scanning electron microscopy (FIB-SEM), and transmission electron microscopy (TEM) [7–11], provide information on pore size, pore morphology, and connectivity of the pore networks. The indirect methods, e.g., mercury

injection porosimetry (MIP), low-pressure gas adsorption ( $\text{CO}_2$  and  $\text{N}_2$ ), and small-angle and ultra-small-angle neutron scattering (SANS and USANS), can be employed to investigate porosity, specific surface area, and pore size distribution [10, 12, 13]. Organic matter-hosted pores have been identified as an important pore system in gas shales [9, 14–18]. Thermal maturity has been considered by previous studies as one of the critical controllers of organic pore growth [1, 13, 19–23]. Researchers have tried to restore the hydrocarbon generation process and associated organic pore growth through pyrolysis, which can cover the weakness of measurements mentioned above in pore system characterization and prediction [24–29]. However, pyrolysis differs remarkably with geological conditions in temperature, pressure, medium, heating model, etc. Many investigations reported that nanoscale pores were generated due to kerogen degradation with increasing thermal maturity, but commonly shrank as a result of high temperature and pressure and no available oil cracking into gas in deep basin [9, 13, 14, 30]. The conversation among micropore, mesopore, and macropore was found, and an evolution model of porosity with thermal maturity was established [13, 21, 31]. However, the pyrolysis results typically require the constraint from high- to over-high-mature natural shale samples. Therefore, characterizing the pore system of such high-mature Devonian shales in the Guizhong Depression can provide insight into the shale gas resource assessment in China.

Dian-Qian-Gui Basin is an important petroliferous basin in south China with high petroleum exploration potential [32]. The Devonian marine deposits in the Guizhong Depression are characterized by good hydrocarbon accumulation conditions and considerable petroleum resource potential [33–36]. GY-1 well was drilled at the northwest of the Guizhong Depression to investigate the occurrence of the Devonian shale, understand its geochemical characteristics and storage capacity, and evaluate shale gas resource potential. It is the first well drilling all shales in the Devonian with a completion depth of 1205.5 m (Lower Devonian Lianhuashan Formation). Coring for the whole well section provides considerable evidence for us to analyze hydrocarbon generation potential and reservoir quality. In this study, we will (1) investigate geochemistry and pore system of Devonian shales in the Guizhong Depression that can be further compared with organic-rich shales from other basins in South China and other countries and (2) discuss the organic matter-hosted pores in postmature to overmature stage and the contributors to their development.

## 2. Geological Settings

The Dian-Qian-Gui Basin is situated in southwest China in the provinces of Yunnan (Dian), Guizhou (Qian), and Guangxi (Gui) (Figure 1). It lies in the northern Nanpanjiang orogenic fold zone along the southwest margin of the Yangtze (South China) Precambrian craton [37, 38] at the join of the Tethyan Himalayan and Pacific Ocean tectonic plates [39, 40].

Guizhong Depression in the north-central Guangxi is a secondary structural unit in the northeastern Dian-Qian-

Gui Basin with an area of  $4.6 \times 10^4 \text{ km}^2$ . Structurally, it is located at the joint of the southwest margin of Yangtze block and South China Caledonian fold belt, which is sandwiched between the Pacific tectonism and the Tethys tectonism [41].

The Guizhong Depression is adjacent to the Xuefengshan Uplift in the north, Qiannan Depression in the northwest, Guilin Depression and Dayaoshan Uplift in the east, and Nanpanjiang Depression and Luodian Fault Depression in the west. It is bounded by the Longsheng-Yongfu Fault, the Nandan-Duan Fault in the west, and the Dayaoshan Fault in the east. The depression can be divided into several sags and salients (Figure 1).

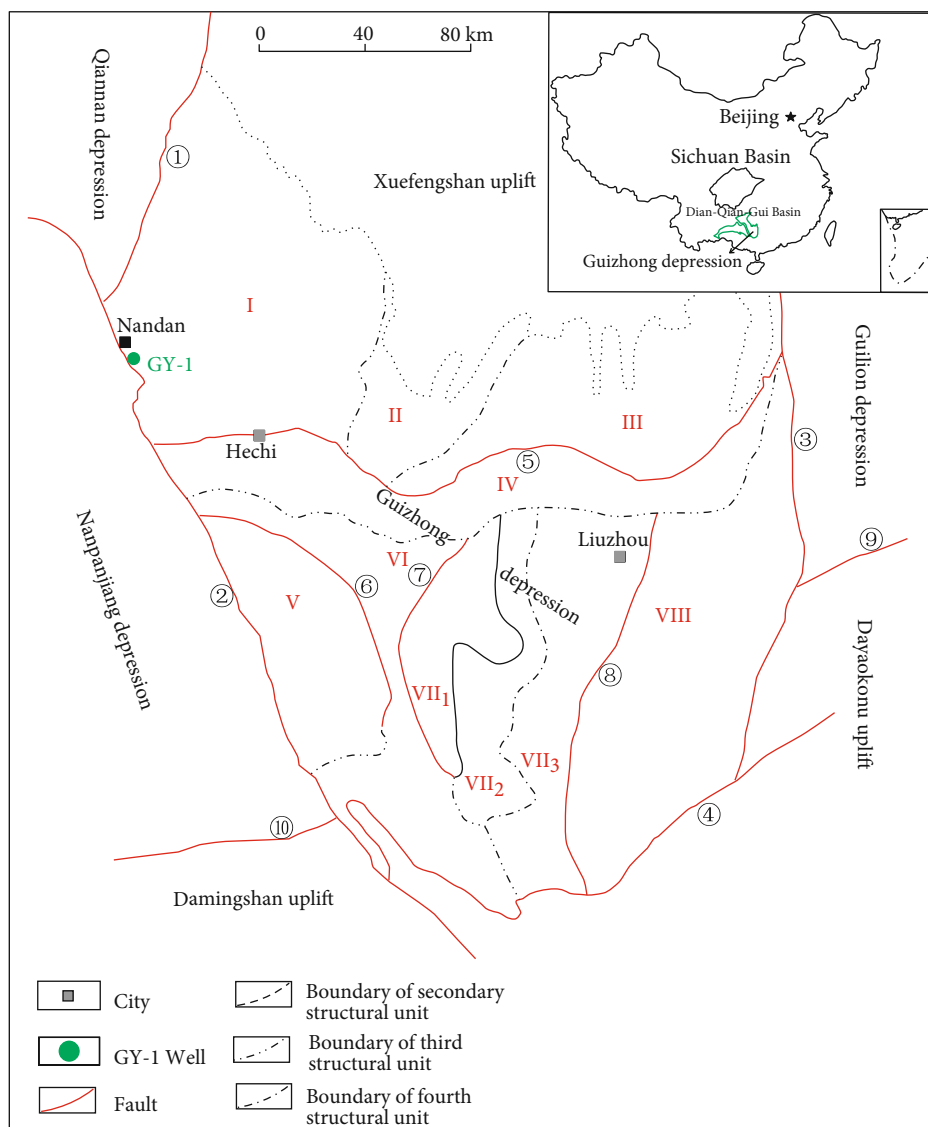
Guizhong Depression was a large marine deposition center during Late Paleozoic due to the Caledonian movement, which is currently a residual basin filled by the Upper Paleozoic and Triassic [41]. During the Lianhuashan and Nagaoling period, terrigenous clastic sandstone with silty mudstone was deposited in the Guizhong Depression. The paleo-Tethyan extensional rift during the late Devonian resulted in regional tension with deposition as well as the growth of NW-trending and NNE-NE-trending faults. Meanwhile, the transgression extended from south to north, forming the platform-basin sedimentary framework, e.g., the basin facies mainly occurred at the western depression, depositing Yilan and Tangding siltstone, limestone, and black marl. The increasing rifting during the Middle Devonian gave rise to the growth of NW-trending and nearly NS-trending faults and high relative sea level, enlarging platform and basin and forming alternation of platform and basin. Consequently, Nabiao and Luofu black carbonaceous shale, siliceous shale, and marl were deposited in semideep water to deep water [41].

The Upper Devonian Liujiang Formation in the GY-1 well is mainly limestone and siliceous rocks in the upper section and calcareous mudstone interbedded with thin argillaceous limestone in the lower section. The Middle Devonian Luofuyang Formation is calcareous mudstone and thin gray marl, while the Nabiao Formation is characterized by calcareous mudstone with decreasing calcareous content from the top to the bottom with considerable tentaculites. The Tangding Formation is dominated by gray-light gray silty mudstone with marl lenses and framboidal pyrite at the top. The Lower Devonian is typically light gray fine sandstone and dark grey silty mudstone. The thickness of the Lower Liujiang Formation, Luofu Formation, Nabiao Formation, and the Upper Tangding Formation in the GY-1 well is over 600 m, which is dominated by carbonaceous shale and marl depositing in deep-water shelf and shallow-water shelf (Figure 2).

## 3. Samples and Methods

Ten core samples from the GY-1 well were collected to perform trace elements analysis, X-ray diffraction (XRD), field emission scanning electron microscopy (FESEM), low-pressure  $\text{N}_2$  adsorption, and source rock geochemistry (total organic carbon (TOC), kerogen microscopic examination, and bitumen reflectance).

*3.1. Trace Element Analysis.* Samples were cleaned in an ultrasound bath and then were oven-dried. After that, they



Structural unit: I-Huanjiang sag II-Luocheng salient III-Liucheng slope IV-Yishanfault-sag V-Mashanfault-salient VI-Hongdu sag VII-Liujiang Salient VII<sub>1</sub>=Datang anticline belt VII<sub>2</sub>-Heshan syncline belt VII<sub>3</sub>-Liuzhou anticline belt VII-Xiangzhou Sag  
 Fault: ① Sandu fault ② Nandan-Kunlun guan fault ③ Longshegn-Yongfu fault ④ Pingxiang-Dali fault ⑤ Hechi-Liucheng fault ⑥ Jiagui-Gupeng fault ⑦ Limiao-Qiaoxian fault ⑧ Liuzhou-Laibin fault ⑨ Lipu fault ⑩ Xialei-Lingma fault

FIGURE 1: Location and structural units of the Guizhong Depression.

were disaggregated into grains (<200 meshes) by physical crushing with an agate mortar. The measurement was conducted using the acid dissolution method in the State Key Laboratory of Isotope Geochemistry, Guangzhou Institute of Geochemistry, Chinese Academy of Sciences. Dried powders were burned in the oven at 700°C for 3 hours to remove organic compounds. 0.37-0.45 mg of remaining was dissolved using HNO<sub>3</sub>, HF, and HClO<sub>4</sub> in the PTFE sampling bottom. The analysis was performed using a PEELan6000 ICP-MS.

3.2. X-Ray Diffraction (XRD) Analysis. The XRD experiment was performed using a ZJ207 Bruker D8 advance X-ray diffractometer following the oil and gas industry standards

(SY/T5463-2010). The shale samples were crushed smaller than 300 mesh sizing and hand-mixed with ethanol in a mortar and pestle and then smear-mounted on glass slides for XRD analysis. The X-ray diffractometer with Cu X-ray tube operated at 40 kV and 30 mA and scanned from 2° to 70° at a step of 0.02°, and the data was semiquantified using Jade® 6.0 software.

3.3. Geochemistry of Source Rocks. Kerogen microscopic examination, TOC, and bitumen reflectance measurements were carried out in the Experimental Research Center of Wuxi Research Institute of Petroleum Geology, SINOPEC. Kerogen maceral in the sediments was identified using

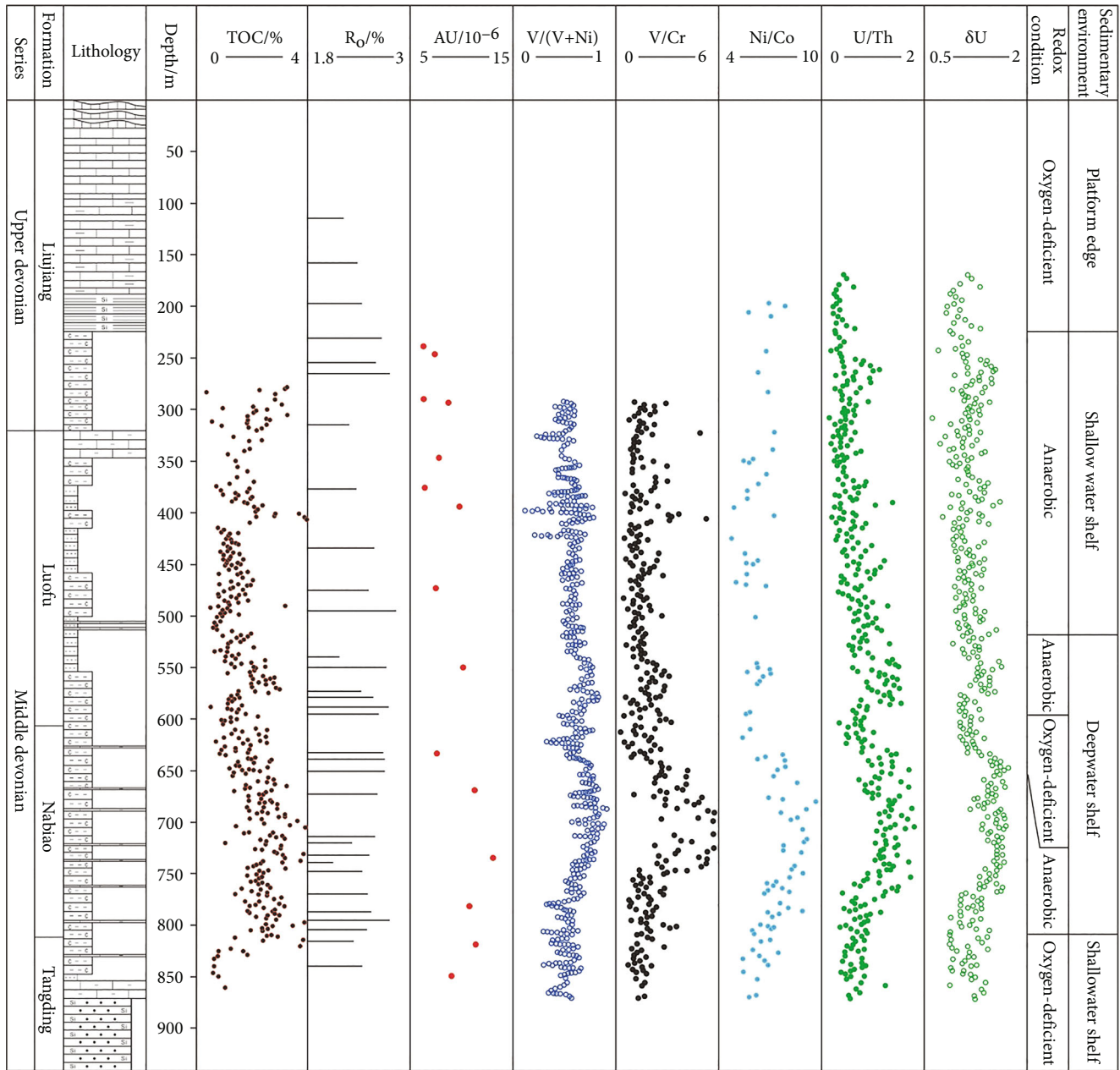


FIGURE 2: Stratigraphic column of the GY-1 well. The trace element data and the paleoenvironment are explained.

LEICA DMRX Polarization microscope DM4500P, while the kerogen type was determined using the percentage compositions of individual maceral and corresponding weighting coefficients following the Chinese National Standards SY/T 5125-2014. For TOC analysis, each sample (0.10 g) was prepared with 12.5% HCl to remove carbonates in a sterilized crucible and was washed in distilled water every half an hour for three days and then were oven-dried. TOC analysis was conducted in a LECO CS-230 carbon analyzer following the Chinese National Standards GB/T19145-2003. With no vitrinite in the samples, the optical feature and bitumen reflectance was determined through observing polished sur-

faces of samples using MSP 200 microphotometer following the Chinese National Standards SY/T5124-2012.

### 3.4. Field Emission Scanning Electron Microscopy (FESEM).

The FESEM observation was carried out at China University of Petroleum, Beijing. Shale samples were cut into about one-centimeter square, which was polished to produce flat surfaces using dry emery paper. After that, they were milled by sputtering away shale material via momentum transfer with a focused 30 kV beam of argon ions in a focused ion beam (FIB) system. Representative samples were coated with carbon to produce a conductive surface, which was inspected

TABLE 1: Major element content and element ratios of Devonian shale of GY-1 well.

Depth	Sr × 10 <sup>-6</sup>	Rb × 10 <sup>-6</sup>	Th × 10 <sup>-6</sup>	Pb × 10 <sup>-6</sup>	As × 10 <sup>-6</sup>	Zn × 10 <sup>-6</sup>	Ni × 10 <sup>-6</sup>	Mn × 10 <sup>-6</sup>	Cr × 10 <sup>-6</sup>	V × 10 <sup>-6</sup>	Ti × 10 <sup>-6</sup>	S × 10 <sup>-6</sup>	Ba × 10 <sup>-6</sup>	Nb × 10 <sup>-6</sup>	Bi × 10 <sup>-6</sup>	δU	V/(V+Ni)	Ni/Co	U/Th	Au × 10 <sup>-6</sup>	Sr/Ba	
300.70 m	91.16	69.79	11.01	17.49	9.27	40.64	144.93	207.42	99.38	166.97	2735.54	22489.38	827.12	7.29	8.69	1.3	0.54	1.68	5.88	0.45	10.81	0.3
350.10 m	93.43	72.54	8.94	15.23	5.01	31.86	119.88	178.04	79.43	175.22	2730.23	10514.21	768.42	8.65	8.13	0.87	0.51	2.21	5.47	0.26	11.42	0.22
399.70 m	124.73	136.84	14.87	43.16	18.82	31.99	138.24	386.86	165.02	135.58	4063.01	21241.92	734.01	12.94	13.64	1.3	0.59	0.82	7.23	0.44	9.85	0.19
451.30 m	145.89	151.77	68.97	14.7	9.51	74.33	128.48	333.27	159.78	157.48	4373.91	6268.96	803.56	12.69	13.66	1.22	0.55	0.99	5.01	0.71	7.56	0.19
499.50 m	112.81	92.88	6.39	10.64	0.001	53.14	133.7	286.59	71.72	190.87	3464.37	3513.37	936.34	8.82	7.91	1.45	0.59	2.66	6.17	0.9	8.2	0.19
550.70 m	110.17	89.57	11.58	20.19	20.62	99.26	170.06	268.02	101.64	231.84	3718.66	19320.6	913.31	11.61	2.03	1.29	0.63	2.28	5.19	0.6	10.2	0.33
599.90 m	114.31	80.92	6.6	40.08	39.61	119.05	193.03	222.82	99.69	288.39	3620.85	24523.35	877.75	9.59	8.41	1.34	0.67	2.89	5.59	0.67	9.11	0.25
649.50 m	87.5	79.42	17.86	34.28	19.6	165.57	150.07	274.15	89.57	373.79	2523.86	7612.05	1211.87	9.12	18.34	1.42	0.71	4.17	6.93	1.3	7.63	0.28
700.30 m	31.04	294.81	5.45	13.58	8.7	81.84	97.68	348.11	0.001	132.09	531.95	2881.06	1341.49	6.01	9.44	1.43	0.87	5.67	7.12	0.84	6.32	0.43
750.20 m	86.64	81.85	9.54	59.83	25.87	255.47	173.8	216.88	134.4	381.8	2502.73	28648.95	1113.62	9.15	10.01	1.55	0.69	2.84	7.85	1.13	7.13	0.09
799.40 m	66.76	58.97	12.75	25.21	43.28	96.88	183.84	337.36	83.93	232.4	2182.99	15541.45	1428.57	8.75	10.64	1.04	0.68	2.77	8.32	0.47	9.89	0.33
848.30 m	33.21	26.63	6.04	13.29	7.77	93.99	128.95	3481.92	0.001	110.67	619	3735.33	807.5	6.23	9.01	0.92	0.46	1.75	6.26	0.55	11.49	0.56
901.80 m	151.6	84.64	14.5	48.94	8.29	48.16	101.39	148.73	120.8	178.74	5550.84	2847.54	511.3	16.74	10.66	0.89	0.42	1.48	4.93	0.64	8.73	0.03
951.20 m	95.12	125.06	22.98	6.54	8.72	19.58	76.69	249	120.38	217.8	4583.87	3012.26	762.31	14.06	20.54	1.16	0.51	1.81	5.76	0.46	10.03	0.04

TABLE 2: Kerogen microscopic composition and determined kerogen type index.

Depth (m)	Formation	Sapropelinite (%)		Exinite (%)	Vitrinite (%)	Inertinite (%)	TI	Type
		Amorphous solid	Alginite	Benthic algae				
231	$D_3l$	56	18	26	-	-	87	I
255	$D_3l$	58	17	25	-	-	87.5	I
475	$D_2l$	63	15	22	-	-	89	I
495	$D_2l$	64	18	18	-	-	91	I
579	$D_2l$	65	14	21	-	-	89.5	I
595	$D_2l$	62	14	24	-	-	88	I
639	$D_2n$	67	15	18	-	-	91	I
651	$D_2n$	62	13	25	-	-	87.5	I
739	$D_2n$	65	15	20	-	-	90	I
795	$D_2n$	70	14	16	-	-	92	I

Note:  $TI = 100 \times a + 100 \times b1 + 50 \times b2 + 10 \times c1 + (-75) \times c2 + (-100) \times d$ , where TI is the kerogen type index,  $a$  is the sapropelinite (%),  $b1$  is the resinite (%),  $b2$  is the cutinite, suberinite, sporinite, amorphous solid, and benthic algae (%),  $c1$  is the perhydrated vitrinite (%),  $c2$  is the normal vitrinite (%), and  $d$  is the fusinite (%).

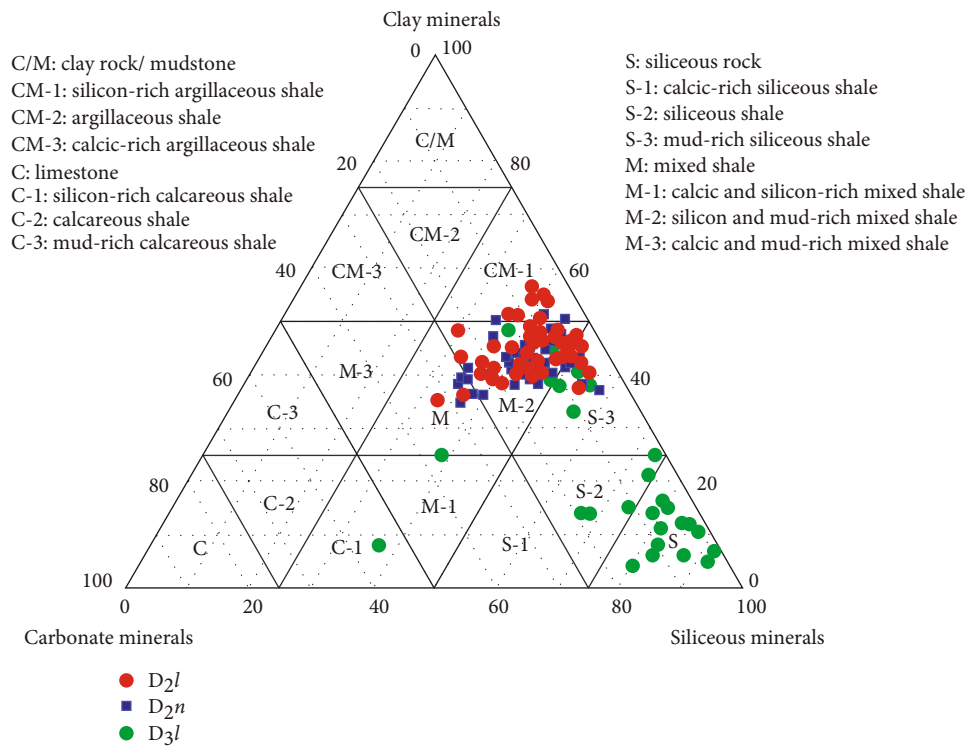


FIGURE 3: Mineral composition of the Upper-Middle Devonian samples of GY-1 well determined by XRD.

using an FEI Helios NanoLab™ 650 FESEM with a resolution of 2.5 nm under accelerating voltage of 2 kV and a working distance of 4 mm.

**3.5. Ultra-Low-Pressure  $N_2$  Adsorption.** Ultra-low-pressure  $N_2$  adsorption analyses were carried out at  $-196^\circ\text{C}$  and relative pressure of  $10^{-7}$ -0.995 using a Quantachrome® Autosorb-iQ2-MP apparatus at China University of Petroleum, Beijing. Detailed information can refer to [42]. Pri-

mary parameters in this measurement are surface area, pore volume, average pore diameter, etc. The surface area was calculated using the BET (Brunauer-Emmett-Teller) equation. The pore volume and pore size distribution were determined using the Barrett, Joyner, and Halenda (BJH) method with relative pressure of 0.06-0.99. The average pore diameters were calculated using the ratio of the total adsorbed nitrogen amount to the available surface area with the assumption of cylindrical pore geometry [43].

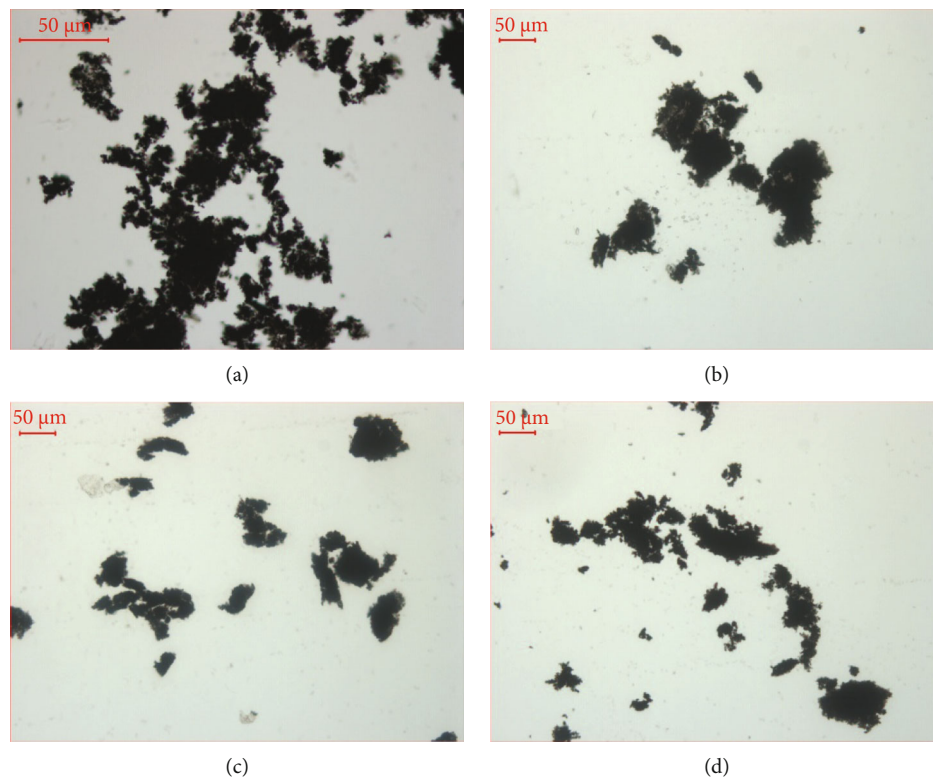


FIGURE 4: The amorphous and algal bodies of sapropelite from kerogen microscopic examination: (a)  $D_{3l}$  (231 m), (b)  $D_{2l}$  (579 m), (c)  $D_{2n}$  (639 m), and (d)  $D_{2n}$  (795 m).

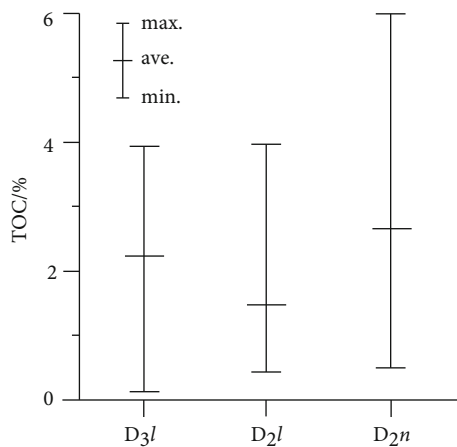


FIGURE 5: TOC statistical results of the  $D_{3l}$ ,  $D_{2l}$ , and  $D_{2n}$  source rocks.

## 4. Results

**4.1. Paleoenvironment and Petrology.** Basin paleoenvironment generally determines its initial productivity and redox conditions, which can be recorded by sedimentary geochemistry [44, 45]. Main and trace elements of shale have been employed to rebuild the paleoenvironment [46], e.g., redox-sensitive elements including V, Co, Cr, Ni, Mo, and U, which can be used to infer redox conditions [46, 47], because these elements are typically insoluble in reducing

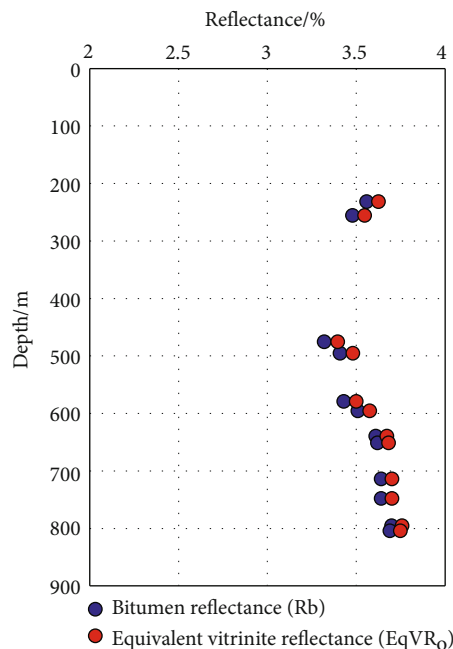


FIGURE 6: The bitumen reflectances and the determined equivalent vitrinite reflectance of GY-1 well.

environment and consequently accumulate in the anaerobic environment but loss in the oxygen-rich environment. Parameters, e.g., Ni/Co, V/Cr, and U/Th, are widely used to identify redox conditions [48]. The measurement shows

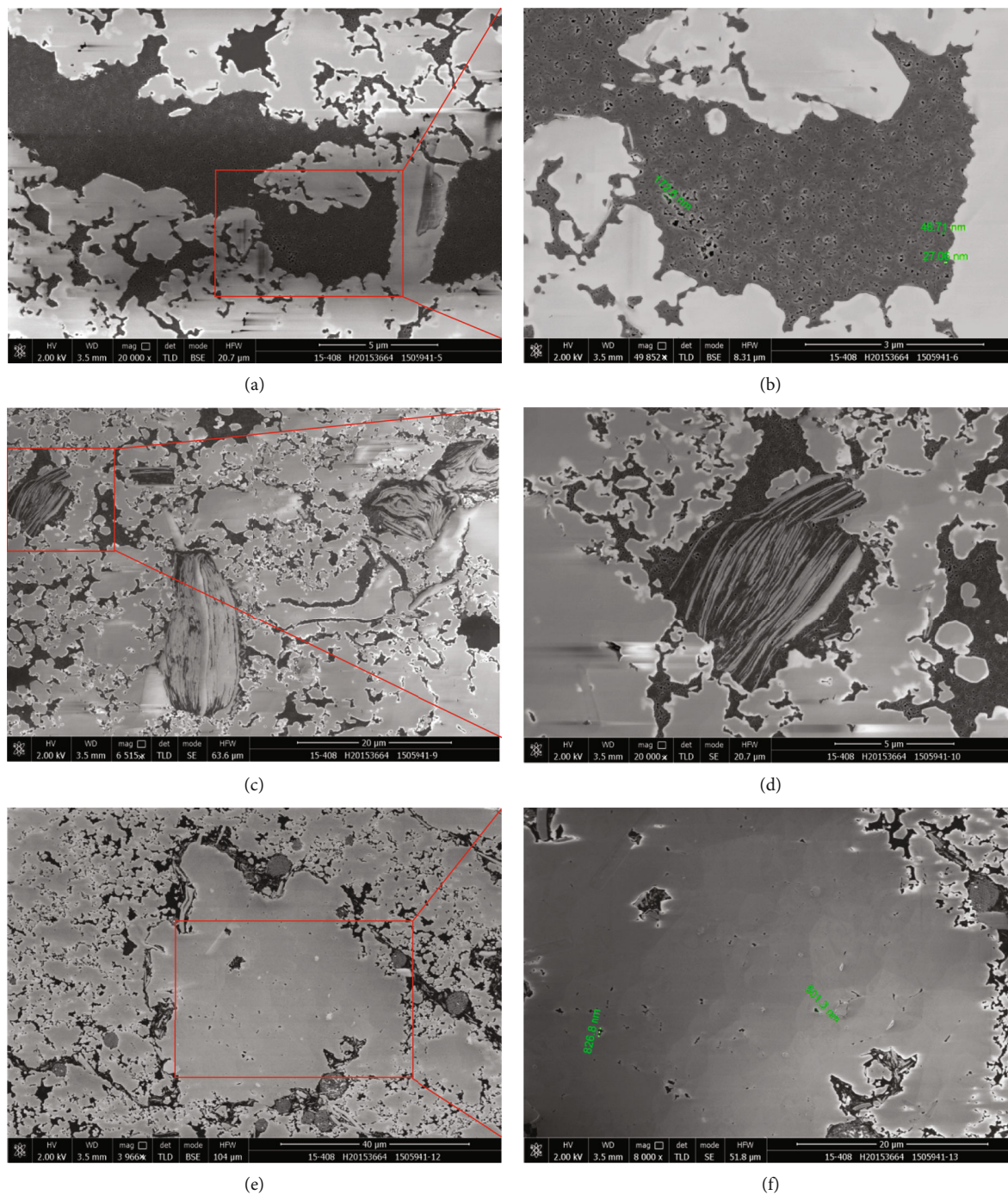


FIGURE 7: Continued.



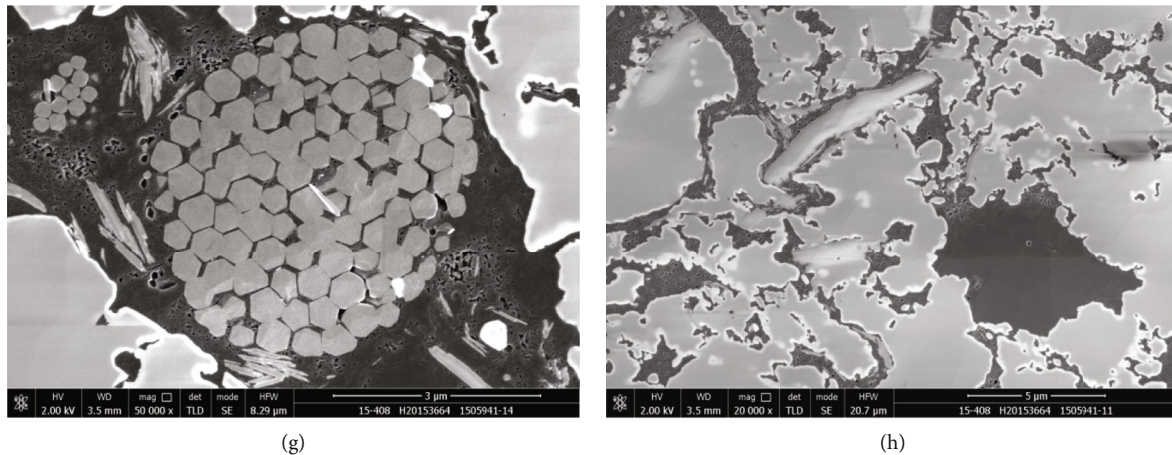


FIGURE 7: SEM images of microscopic pores from the siliceous shale (255 m of well GY-1, S-2 in Figure 3): (a, b) OM-pores, (c, d) OM-clay mineral complexes, (e, f) micropores in the quartz particles, (g) residual pores between pyrite crystals are filled with organic matter, and micropores are developed within it or/and at the edge, and (h) no OM-pores developed in some organic matter.

that the  $V/(V+Ni)$  is in a range of 0.31–0.90 with a high value in the Upper-Middle Nabiao carbonaceous shale (636.00 m–771.7 m) and Lower Luofu Formation (536.20–592.83 m).  $Ni/Co$  generally ranges from 4.74 to 9.69 with a high value in the Middle-Lower Nabiao Formation (648.35 m–790.60 m).  $U/Th$  varies between 0.09 and 2.03, while the value is higher in the Nabiao Formation (684.10 m–807.50 m) and Lower Luofu Formation (523.74 m–598.20 m) and decrease toward the Upper Luofu Formation and Tangding Formation. Uranium isotope is relatively high in the Nabiao Formation and Lower Luofu Formation.  $Au$  ( $\times 10^{-6}$ ) varies in a similar trend with other elements, which is high in the Nabiao carbonaceous shale (Figure 2 and Table 1). These trace elements suggest that the Nabiao Formation and the Lower Luofu Formation were deposited in an anaerobic and reducing environment, while Luofu Formation and Tangding Formation were in the high-energy and well-circled environments. Also, TOC and indicators of redox environment, e.g.,  $V/Cr$ ,  $Ni/Co$ , and  $U/Th$ , follow a similar trend (Figure 2). Furthermore, tentaculites were found in both Devonian outcrop and Luofu and Nabiao core samples. These thin-wall tentaculites are typically zooplankton in deep water, indicating a deep-water deposition environment. In addition, the occurrence of considerable framboidal pyrite is a good indicator of a reductive deep-water environment. Thus, the Tangding Formation was deposited in oxygen-poor and shallow water with low TOC. Nabiao black shale was developed in an anoxic and deep-water environment with weak hydrodynamic, which contributes to the development and preservation of abundant organic matter. Different from that, the Luofu Formation was deposited in a weakly toxic environment with low organic matter abundance.

X-ray diffraction measurement indicates that such shale gas reservoir is mineralogically composed of quartz, calcite, clay minerals, dolomite, plagioclase, siderite, and pyrite (Table 2). Liujiang Formation is characterized by the highest quartz content with a value over 90%, which is primarily siliceous rock with siliceous shale, mud-rich siliceous shale, and

silicon-/mud-rich shale of secondary importance.  $D_2n$  and  $D_2l$  are primarily siliceous/argillaceous mixed shale as well as a small proportion of siliceous argillaceous shale and argillaceous siliceous shale (Figure 3). Researchers have reported that the storage space of shales varies with lithofacies, which have a significant impact on organic matter enrichment, gas adsorption, and storage capacity [31, 49–51].

## 4.2. Geochemical Analysis

**4.2.1. Kerogen Types.** Kerogen's microscopic examination suggests that the Upper-Middle Devonian in the GY-1 well is dominated by the sapropelic group, with a small amount of exinite, but no vitrinite and inertinite. The sapropelic group consists mainly of amorphous bodies and algae bodies (Figure 4), while the exinite is mainly amorphous benthic algae. The determined kerogen type index indicates that the Upper-Middle Devonian is dominated by type I kerogen (Table 2).

**4.2.2. TOC.** TOC is highest in the  $D_2n$  shales, ranging from 0.53% to 6.0% with an average value of 2.65% (Figure 5), and is lower in the  $D_3l$  shales, ranging from 0.14% to 3.94% with an average value of 2.23%. The TOC of the  $D_2l$  shales are relatively low (0.43%–3.96%, averaging 1.52%). However, the lower  $D_2l$  have relatively high TOC values (Figure 2). In general, measured TOC values indicate high hydrocarbon generation potential in these shales, and the  $D_2n$  and the lower  $D_2l$  are high quality that were deposited in the anoxic and weak hydrodynamic deep-water shelf.

**4.2.3. Thermal Maturity.** As mentioned above, the kerogen of the Devonian source rocks in the GY-1 well is dominated by amorphous solid with no vitrinite. Thus, bitumen reflectances ( $R_b$ ) were measured using organic maceral analysis. The equivalent vitrinite reflectance was determined using an empirical formula from [52]:  $EqVR_o = (R_b + 0.2443)/1.0495$ . The results show that samples are thermally

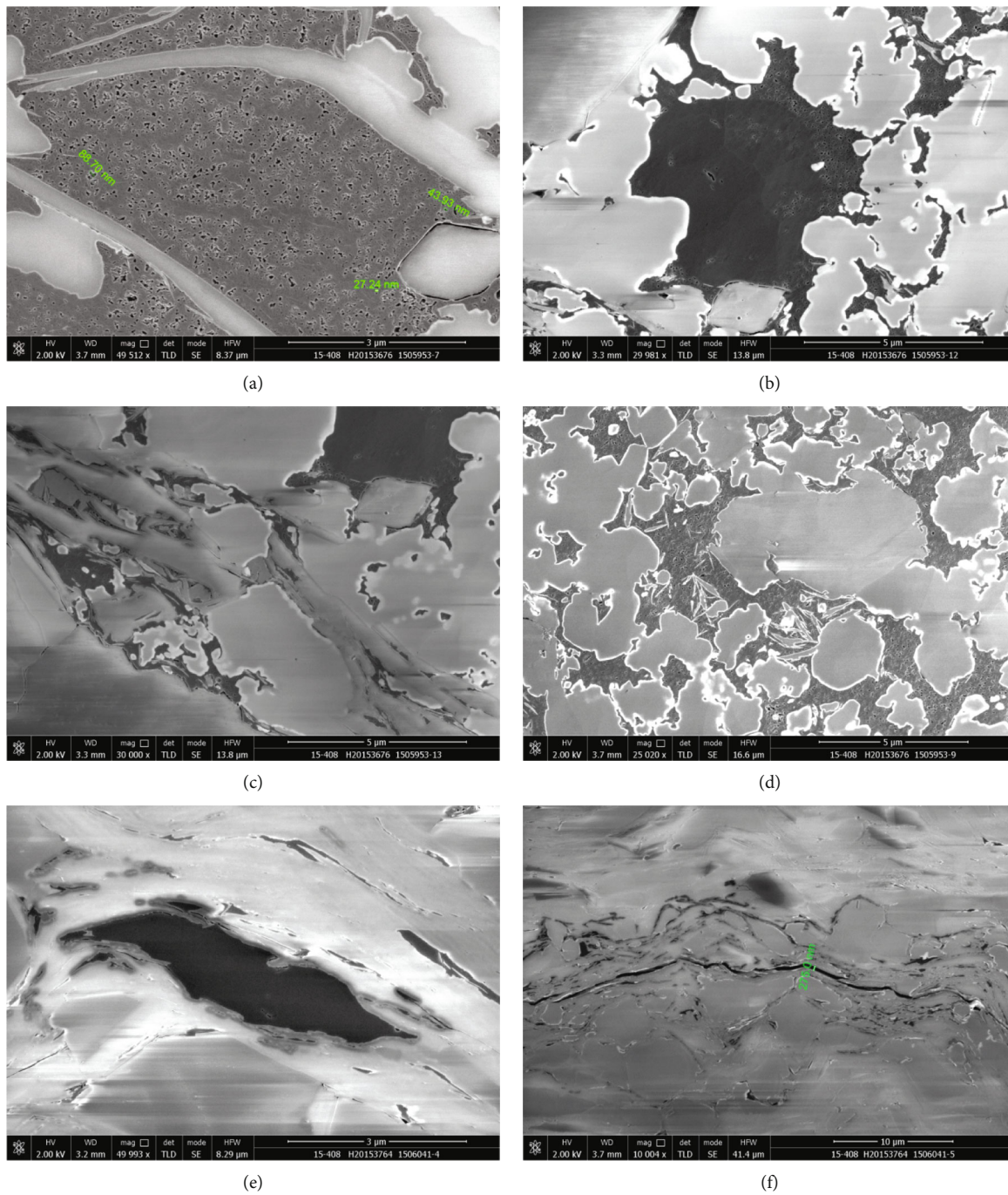


FIGURE 8: Continued.

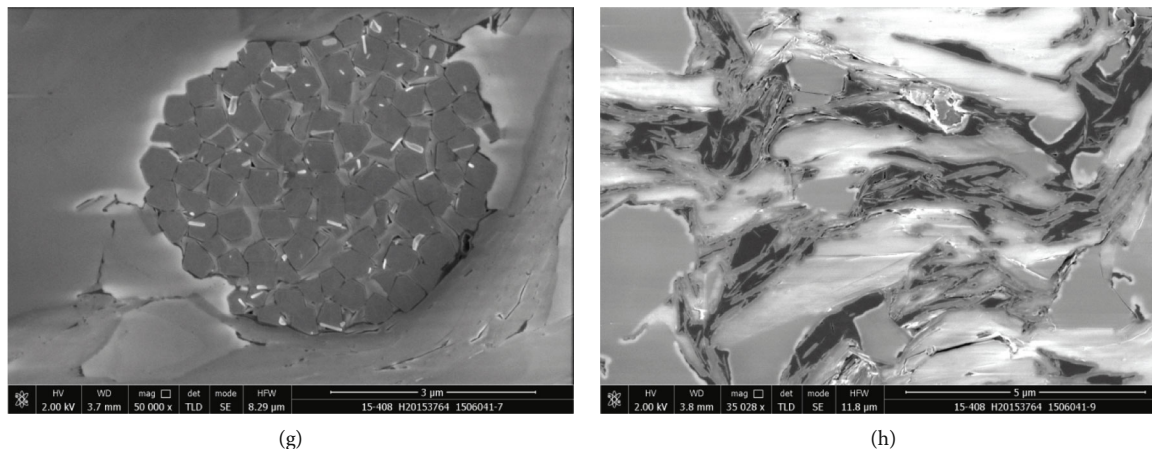


FIGURE 8: SEM images of microscopic pores from the siliceous lime shale (231 m of well GY-1, C-1 in Figure 3): (a) OM-pores, (b) differentially developed OM-pores, (c, e) shrunken microfractures between organic matter and minerals, (d) OM-pores and clay minerals, (f) microfractures along with minerals, (g) residual pores between pyrite crystals and a little organic matter, and (h) shrunken microfractures.

postmature to overmature with equivalent vitrinite reflectance ( $EqVR_o$ ) of 3.40–3.76% (Figure 6).

**4.3. Pore Types.** Significant effort has been devoted to identifying and describing the complex pore systems within fine-grained reservoirs [6–8, 16, 20, 31, 42]. Pores in shale can be classified as (a) organic-matter-hosted pores, (b) interparticle pores (pores between grains and crystals), (c) intraparticle pores (pores within grains, crystals, and clay aggregates), and microfractures [7, 31]. FESEM analysis was carried out on samples from GY-1 well to observe pore types. Various types of pores with different sizes were observed in these samples, including residual primary pores in the broken particles with infill of organic matter, isolated dissolution pores in particles, interlayer pores of clay mineral supported by rigid particles, micropores within biological residues (pores in preserved tentaculite fragments), microfractures between mineral grains, intercrystalline pore of pyrite, and organic matter-hosted pores (Figures 7–9). Organic matter-hosted pores are the most common and abundant pores with various shapes and sizes, while inorganic pores are uncommon in these samples, which may be attributed to the intensive compaction and high thermal maturity. Specifically, organic pores are generally bubble-like, honeycomb-like, and crescent-like as well as an ellipse in shape; they are generally connected by tubular throats, forming a micropore system in the organic matter. According to the International Union of Pure and Applied Chemistry (IUPAC) classification, organic pores here are primarily mesopores with a pore diameter of 2–50 nm and macropores with pore diameter higher than 50 nm. The occurrences of organic pores are heterogeneous, since they cannot be found in some organic matters, but are abundant in migrated organic matters, namely, solid bitumen.

## 5. Discussion

**5.1. Contributors to Pore Development.** Researchers have concluded that the pore structure of organic-rich shale is

generally governed by diagenesis, organic matter, mineral components, thermal maturity, kerogen type, etc., depending on specific geological conditions [14, 23, 53–57]. Shale lithofacies have important controls on porosity and pore structure due to different sedimentary environments and mineralogical variations [19, 51, 58–61]. The same scenario can also be observed in our study. In the organic-rich siliceous shale, there are many micropores in the quartz grains, and the microcracks at the edges of the grains are well developed. The pores between mineral grains are generally filled with organic matter, and the OM pores are very developed. In siliceous lime shale, there are a few microcracks in the calcite grains. The pores between mineral grains are generally filled with organic matter and the OM pores are well developed. Siliceous dolomitic shale has a small number of microcracks developed along the edges of the grains. The pores between the clay mineral grains are filled with a small amount of finely dispersed organic matter with few pores developed. In carbonaceous shale, a small amount of organic matter is filled in the pores between mineral particles, and the organic matter is small and dispersed. The internal micropores of the organic matter are well developed, and the internal micropores of a small amount of massive organic matter are not developed.

In the FESEM images (Figures 7–9), considerable pores are concentrated in organic matter. Furthermore, the positive correlations between the porosity, the SSA, and the TPV and TOC confirm that organic matter contributes significantly to pore development (Figure 10, Table 3). Previous studies suggested that organic pores are not well developed in all organic matter [18, 62]. The FESEM images show that some organic matter does not develop pores (Figure 9(c)), and/or pore development is significantly different among adjacent organic matters (Figure 8(b)). Identifying OM types and deciphering their controls on OM pore developments is one of our next priorities.

Quartz of the Devonian shales in the Guizhong Depression is primarily biogenic in origin, as inferred from the positive correlation between the quartz content and TOC

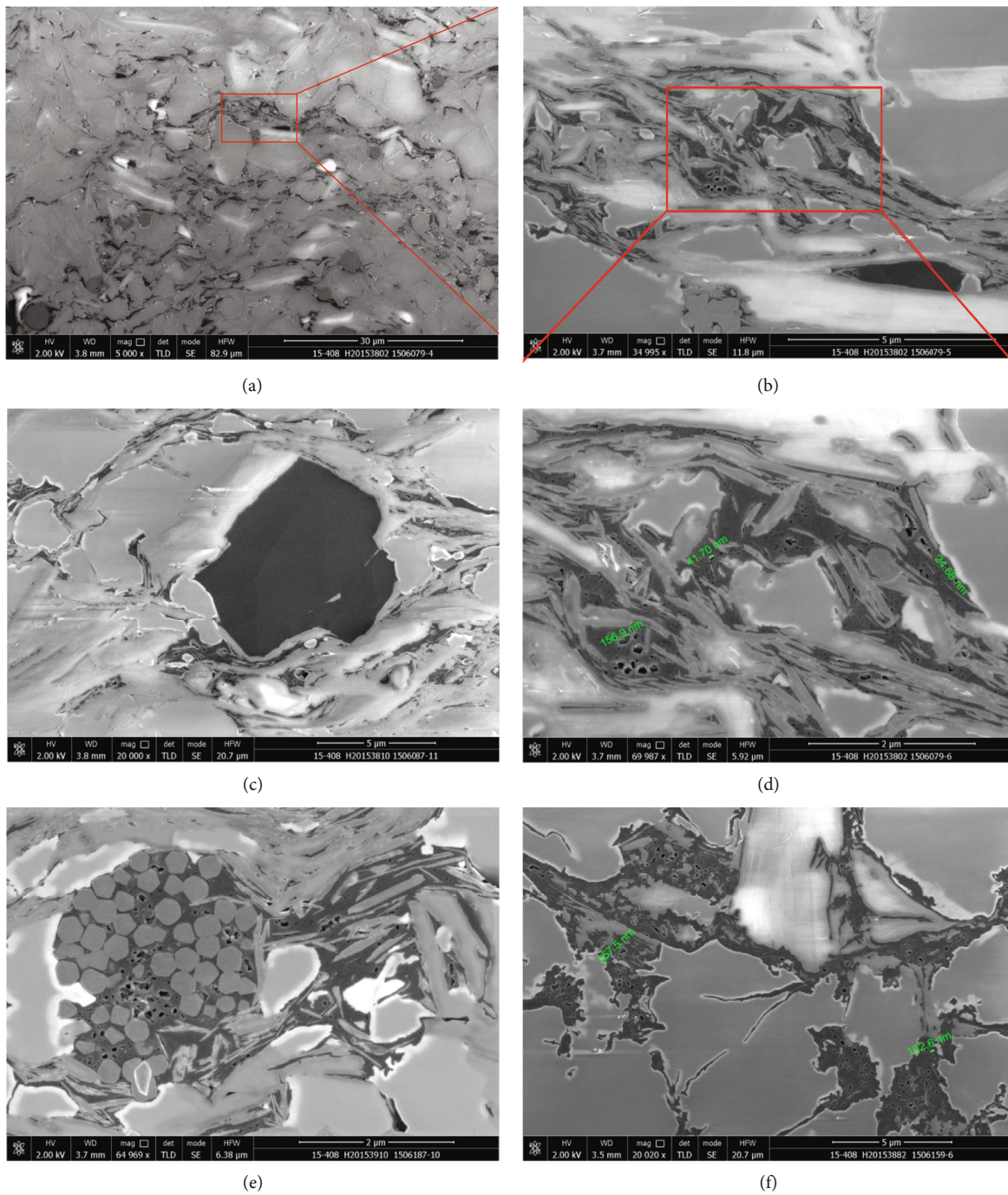


FIGURE 9: Continued.

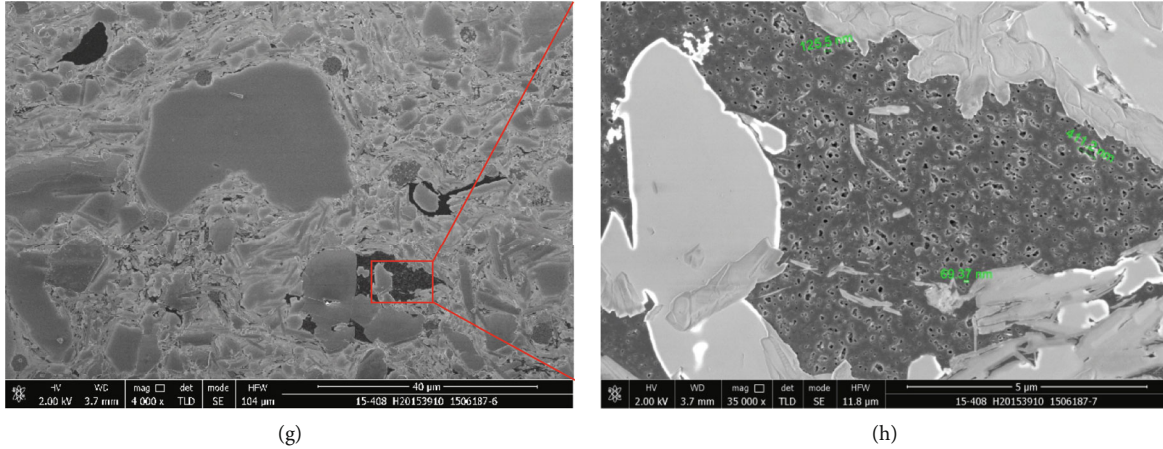


FIGURE 9: SEM images of microscopic pores from the siliceous carbonaceous shale (475 m of well GY-1, M-2 in Figure 3): (a, b, d, f, and h) OM-pores, (c) no OM-pores developed in the organic matter, (e) residual pores between pyrite crystals are filled with organic matter, and micropores are developed within it, and (g) different types of organic matter.

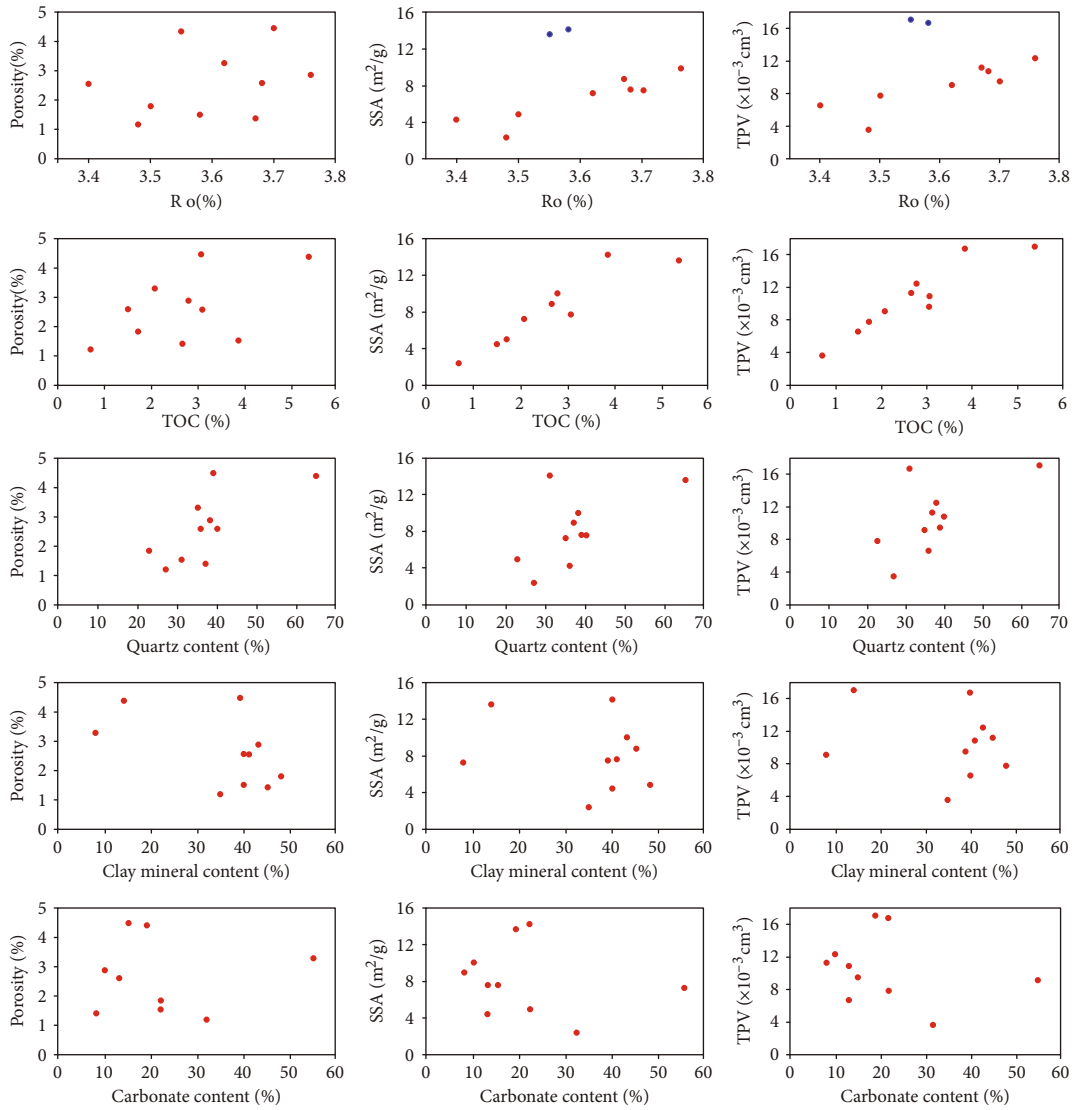


FIGURE 10: Variation of pore structure parameters (porosity, specific surface areas (SSA), and total pore volumes (TPV)) with  $R_o$ , TOC, and mineral content.

TABLE 3: TOC,  $R_o$ , mineral composition, and pore structure parameters of the studied samples from GY-1 well.

Formation	Depth (m)	TOC (%)	$R_o$ (%)	Porosity (%)	Clay (%)	Quartz (%)	Potash feldspar (%)	Total rock XRD							BET surface area(m <sup>2</sup> /g)	BJH pore volume(ml/g)
								Plagioclase (%)	Calcite (%)	Dolomite (%)	Siderite (%)	Anhydrite (%)	Pyrite (%)			
$D_3l$	231	2.07	3.62	3.29	8	35			55						7.245	0.009
$D_3l$	255	5.37	3.55	4.4	14	65			16	3					13.640	0.017
$D_2l$	475	1.49	3.4	2.59	40	36	1		2	11	2	2			4.376	0.0066
$D_2l$	495	0.7	3.48	1.2	35	27			2	30	2	1			2.385	0.0036
$D_2l$	579	1.72	3.5	1.81	48	23			4	18	2	1			4.949	0.0078
$D_2l$	595	3.85	3.58	1.52	40	31			17	5	2	1			14.215	0.0168
$D_2n$	639	2.67	3.67	1.41	45	37	1		1	7	2	1			8.880	0.01129
$D_2n$	651	3.07	3.68	2.59	41	40			8	5	1	1			7.615	0.011
$D_2n$	739	3.05	3.7	4.49	39	39			3	12		1			7.580	0.0096
$D_2n$	795	2.78	3.76	2.88	43	38	1		9	1	1	1			10.030	0.0124

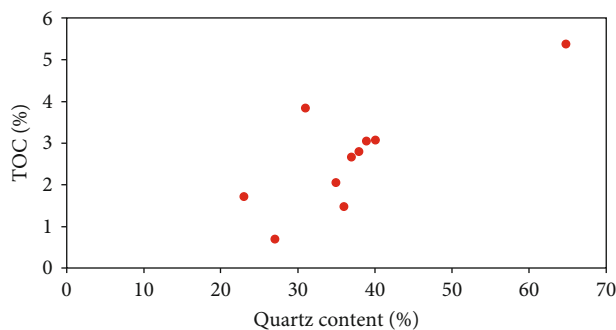


FIGURE 11: The positive correlation between the quartz content and TOC.

(Figure 11). The quartz-rich samples generally have higher porosities, SSAs, and TPVs. In addition, the brittle quartz cements provide a rigid framework that prevents pores from collapsing. Furthermore, the dissolution of quartz particles was observed (Figure 7(f)). Although pores associated with the framework of clay flakes and dissolution of carbonates can be observed, the porosity, SSA, and TPV have no clear relationship with clay or carbonate content (Figure 10). The pore volume of the shale matrix is made up of the volume provided by organic matter, clay minerals, and framework minerals [56]. Thus, this may mean that these two types of pores contribute little to the total pores of shale, compared to the pores provided by organic matter.

**5.2. Organic Matter-Hosted Pores in a Postmature to Overmature Stage.** Thermal maturation has been considered an important contributor to pore growth in shales due to the kerogen degradation into liquid hydrocarbon and gas [1, 13]. However, increasing burial depth and temperature enables kerogen in the shales to generate volatile hydrocarbon with increasing hydrogen and decreasing molecular mass, chemically converting the kerogen into residual carbon with low hydrogen, which is defined as carbonization of organic matter [31, 63]. During carbonization, OM-hosted pores are destroyed, merged, and collapsed [14, 64]. Specifically, previous studies show that the degradation of kerogen and dissoluble bitumen as well as methanation generally ceased with a minor increase in micropore and macropore volume at  $R_o > 2.6\%$  [65]. Organic carbonification in shale commonly occurs at  $R_o$  of 3.2% when organic pore volume begins to decrease due to the compaction and mineral infill [65]. Organic pores in marine shale are typically poor at  $R_o > 3.0\%$ , with most of the pore diameter  $< 100$  nm [66]. However, organic pores in this study are well grown at  $R_o$  of 3.5%, and surface areas and pore volume of nanoscale pores typically increase with thermal maturity despite a similar thermal maturity range ( $R_o$  3.40%–3.76%) (Figure 9). Considerable macropores were found in samples with  $R_o > 3.6\%$ . Supplementally, Cheng and Xiao [67] found that both the specific surface area and nanopore volume of organic-rich shales increased with maturity, which allowed them to keep certain porosities even in very high maturities ( $R_o$  3.5%–4.0). Thus, we are more confident than some scholars about the shale pore volume in postmature to over-

mature stage [13, 28, 70] and consolidate, to a certain extent, the pore evolution diagram with increasing thermal maturity proposed by [31].

We do agree with some studies in suggesting that the macroporous in the shales are transformed into mesopores and micropores, and the organic nanopores decrease, causing nanopore volume to be displayed a decreasing trend under the condition of extremely high thermal maturity [21, 22, 55]. Of course, it cannot be denied that the evolution of organic porosity with increasing maturity is influenced by several factors [30]. Our study, however, demonstrates also that porosity at postmature to overmature stage ( $R_o = 3.5 - 4.0\%$ ) does not change fundamentally. In other words, the porosity under the high level of maturity is satisfying for shale gas storage. Consequently, the level of maturity may not be the main controlling factor that affects shale gas content, and more attention should be paid to preservation conditions.

## 6. Conclusion

- (1) Nabiao shale ( $D_{2n}$ ) and Lower Luofu shale ( $D_{2l}$ ) were deposited in anoxic and weak hydrodynamic deep-water shelf, which contributes to the development and preservation of organic matter. The Upper Luofu Formation ( $D_{2l}$ ) and Liujiang Formation ( $D_{3l}$ ) were deposited in an oxygen-poor shallow-water shelf. X-ray diffraction indicates that the lithofacies in  $D_{2n}$  and  $D_{2l}$  are primarily siliceous/argillaceous mixed shales as well as minor siliceous argillaceous shales and argillaceous siliceous shales
- (2) The Middle-Upper Devonian shales in Guizhong Depression are organic-rich with TOCs of 0.14–6.21%. TOC is highest in the Nabiao Formation ( $D_{2n}$ ) and Lower Luofu Formation ( $D_{2l}$ ), which are thermally postmature to overmature with EqVR<sub>o</sub> ranging from 3.40% to 3.76% and type I kerogen
- (3) OM-pores are dominant pore types. Porosity, surface areas, and pore volumes exhibit positive correlations with TOC,  $R_o$ , and siliceous mineral contents. Considerable macropores were found in shales with  $R_o > 3.6\%$  in our study which demonstrates that porosity at postmature to overmature stage ( $R_o = 3.5 - 4.0\%$ ) does not change fundamentally

## Data Availability

All data included in this study are available upon request by contact with the corresponding authors.

## Conflicts of Interest

The authors declare that they have no conflicts of interest.

## Acknowledgments

This study is supported by the Daqing Oilfield Research Project (110017333001036).

## References

- [1] D. M. Jarvie, R. J. Hill, T. E. Ruble, and R. M. Pollastro, "Unconventional shale-gas systems: the Mississippian Barnett shale of north-central Texas as one model for thermogenic shale-gas assessment," *AAPG Bulletin*, vol. 91, no. 4, pp. 475–499, 2007.
- [2] K. E. Williams, "Source rock reservoirs are a unique petroleum system," in *Adapted from a poster presentation given at the AAPG 2013 Annual Convention and Exhibition*, Pittsburgh, Pennsylvania, USA, 2013.
- [3] C. N. Zou, R. Zhu, Z. Q. Chen et al., "Organic-matter-rich shales of China," *Earth-Science Reviews*, vol. 189, pp. 51–78, 2019.
- [4] X. N. Xie, F. Hao, Y. C. Lu et al., "Differential enrichment mechanism and key technology of shale gas in complex areas of South China," *Earth Science*, vol. 42, no. 7, pp. 1045–1056, 2017.
- [5] C. X. Sun, H. K. Nie, W. Dang et al., "Shale gas exploration and development in China: current status," *Geological Challenges, and Future Directions*, vol. 35, no. 45, pp. 6359–6379, 2021.
- [6] P. H. Nelson, "Pore-throat sizes in sandstones, tight sandstones, and shales," *AAPG Bulletin*, vol. 93, no. 3, pp. 329–340, 2009.
- [7] R. G. Loucks, R. M. Reed, S. C. Ruppel, and D. M. Jarvie, "Morphology, genesis, and distribution of nanometer-scale pores in siliceous mudstones of the Mississippian Barnett shale," *Journal of Sedimentary Research*, vol. 79, no. 12, pp. 848–861, 2009.
- [8] T. Dong, N. B. Harris, K. Ayranci, C. E. Twemlow, and B. R. Nassichuk, "Porosity characteristics of the Devonian Horn River shale, Canada: insights from lithofacies classification and shale composition," *International Journal of Coal Geology*, vol. 141–142, pp. 74–90, 2015.
- [9] M. Pommer and K. Milliken, "Pore types and pore-size distributions across thermal maturity," *Eagle Ford Formation, Southern Texas, AAPG Bulletin*, vol. 99, pp. 1713–1744, 2015.
- [10] J. Wu, Y. Yuan, S. Niu, X. Wei, and J. Yang, "Multiscale characterization of pore structure and connectivity of Wufeng-Longmaxi shale in Sichuan Basin, China," *Marine and Petroleum Geology*, vol. 120, 2020.
- [11] M. Garum, P. Glover, P. Lorinczi, R. Drummond-Brydson, and A. Hassanpour, "Micro- and nano-scale pore structure in gas shale using X $\mu$ -CT and FIB-SEM techniques," *Energy & Fuels*, vol. 34, no. 10, pp. 12340–12353, 2020.
- [12] C. R. Clarkson, N. Solano, R. M. Bustin et al., "Pore structure characterization of North American shale gas reservoirs using USANS/SANS, gas adsorption, and mercury intrusion," *Fuel*, vol. 103, no. 45, pp. 606–616, 2013.
- [13] M. Mastalerz, A. Schimmelmann, A. Drobniak, and Y. Chen, "Porosity of Devonian and Mississippian New Albany shale across a maturation gradient: insights from organic petrology, gas adsorption, and mercury intrusion," *AAPG Bulletin*, vol. 97, no. 10, pp. 1621–1643, 2013.
- [14] M. E. Curtis, B. J. Cardott, C. H. Sondergeld, and C. S. Rai, "Development of organic porosity in the Woodford shale with increasing thermal maturity," *International Journal of Coal Geology*, vol. 103, pp. 26–31, 2012.
- [15] C. J. Modica and S. G. Lapierre, "Estimation of kerogen porosity in source rocks as a function of thermal transformation: example from the Mowry shale in the Powder River Basin of Wyoming," *AAPG Bulletin*, vol. 96, no. 1, pp. 87–108, 2012.
- [16] K. L. Milliken, M. Rudnicki, D. N. Awwiller, and T. W. Zhang, "Organic matter-hosted pore system, Marcellus Formation (Devonian), Pennsylvania," *Bulletin*, vol. 97, no. 2, pp. 177–200, 2013.
- [17] C. Yang, Y. Xiong, and J. Zhang, "Comprehensive understanding of OM-hosted pores in transitional shale: a case study of Permian Longtan shale in South China based on organic petrographic analysis," *Gas Adsorption, and Xray Diffraction Measurements, Energy & Fuels*, vol. 33, no. 9, pp. 8055–8064, 2019.
- [18] H. Nie, Z. Jin, C. Sun, Z. He, G. Liu, and Q. Liu, "Organic matter types of the Wufeng and Longmaxi Formations in the Sichuan Basin, South China: implications for the formation of organic matter pores," *Energy & Fuels*, vol. 33, no. 9, pp. 8076–8100, 2019.
- [19] L. Zhang, S. Lu, S. Jiang et al., "Effect of shale lithofacies on pore structure of the Wufeng-Longmaxi shale in Southeast Chongqing, China," *Energy & Fuels*, vol. 32, no. 6, pp. 6603–6618, 2018.
- [20] H. Bodhisatwa, D. A. Wood, and V. Vikram, "Pore characteristics of distinct thermally mature shales: influence of particle size on low-pressure CO<sub>2</sub> and N<sub>2</sub> adsorption," *Energy & Fuels*, vol. 32, pp. 8175–8186, 2018.
- [21] W. M. Ji, F. Hao, H. Schulz, Y. Song, and J. Q. Tian, "The architecture of organic matter and its pores in highly mature gas shales of the Lower Silurian Longmaxi Formation in the Upper Yangtze platform, South China," *AAPG Bulletin*, vol. 103, no. 12, pp. 2909–2942, 2019.
- [22] L. Song and T. R. Carr, "The pore structural evolution of the Marcellus and Mahantango shales," *Appalachian Basin, Marine and Petroleum Geology*, vol. 114, 2020.
- [23] C. Xue, J. Wu, L. Qiu, Q. Y. Liu, and J. Zhong, "Effect of thermal maturity on pore type and size in transitional shale reservoirs: an example from the Upper Paleozoic Shanxi Formation, Ordos Basin, China," *Energy Fuels*, vol. 34, no. 12, pp. 15736–15751, 2020.
- [24] H. Y. Hu, "Porosity evolution of the organic-rich shale with thermal maturity increasing," *Acta Petrolei Sinica*, vol. 34, no. 5, pp. 820–825, 2013.
- [25] J. Chen and X. Xiao, "Evolution of nanoporosity in organic-rich shales during thermal maturation," *Fuel*, vol. 129, pp. 173–181, 2014.
- [26] L. H. Xue, W. Yang, J. Zhong, Y. Xu, and G. J. Chen, "Porosity evolution of the organic-rich shale from simulated experiment with geological constrains, samples from Yanchang Formation in Ordos Basin," *Acta Geologica Sinica*, vol. 89, no. 5, pp. 970–978, 2015.
- [27] Z. L. Ma, L. J. Zheng, X. H. Xu, F. Bao, and X. L. Yu, "Thermal simulation exploration on the formation and evolution of organic pores in organic-rich shale," *Acta Petrolei Sinica*, vol. 38, no. 1, pp. 23–30, 2017.
- [28] X. Wang, Z. Jiang, S. Jiang et al., "Pore evolution and formation mechanism of organic-rich shales in the whole process of hydrocarbon generation: study of artificial and natural shale samples," *Energy & Fuels*, vol. 34, no. 1, pp. 332–347, 2020.
- [29] Y. Wang, L. Liu, Q. Hu, L. Hao, X. Wang, and Y. Sheng, "Nanoscale pore network evolution of Xiamaling marine shale during organic matter maturation by hydrous pyrolysis," *Energy & Fuels*, vol. 34, no. 2, pp. 1548–1563, 2020.
- [30] J. Klaver, G. Desbois, R. Littke, and J. L. Urai, "BIB-SEM characterization of pore space morphology and distribution in



- postmature to overmature samples from the Haynesville and Bossier shales,” *Marine and Petroleum Geology*, vol. 59, pp. 451–466, 2015.
- [31] L. T. Ko, R. G. Loucks, T. Zhang, S. C. Ruppel, and D. Shao, “Pore and pore network evolution of Upper Cretaceous Boquillas (eagle ford-equivalent) mudrocks: results from gold tube pyrolysis experiments,” *AAPG Bulletin*, vol. 100, no. 11, pp. 1693–1722, 2016.
- [32] J. H. Meng, R. F. Pan, H. Chen, and X. L. Tang, “Shale gas accumulation condition and resource potential analysis of Devonian in Dian-Qian-Gui Basin,” *Geoscience*, vol. 30, no. 1, pp. 181–191, 2016.
- [33] X. Y. He, G. S. Yao, X. S. He, Z. L. Chen, and P. W. Wang, “An evaluation of depositional environment and potential of Devonian source rocks in Guizhong Depression,” *Acta Petrolei Sinica*, vol. 32, no. 2, pp. 273–279, 2011.
- [34] K. M. Wang, “Shale gas accumulation conditions of Devonian strata in Guizhong Depression,” *Geology in China*, vol. 40, no. 2, pp. 430–438, 2013.
- [35] P. W. Wang, Z. L. Chen, X. Y. He et al., “Shale gas accumulation conditions and play evaluation of the Devonian in Guizhong Depression,” *Oil & Gas Geology*, vol. 33, no. 3, pp. 353–363, 2012.
- [36] Y. Zhou, D. Y. Zhou, Q. Q. Meng, D. W. Zhang, and Y. J. Wu, “Geological conditions and exploration potential of shale gas in Central Guangxi basin, China,” *Journal of Chengdu University of Technology*, vol. 41, no. 5, pp. 529–537, 2014.
- [37] I. Metcalfe, “Pre-cretaceous evolution of SE Asian terranes,” *Geological Society, London, Special Publications*, vol. 106, no. 1, pp. 97–122, 1996.
- [38] J. X. Cai and K. J. Zhang, “A new model for the Indochina and South China collision during the Late Permian to the Middle Triassic,” *Tectonophysics*, vol. 467, no. 1–4, pp. 35–43, 2009.
- [39] A. Yin and S. Nie, “A Phanerozoic palinspastic reconstruction of China and its neighboring regions,” in *The Tectonic Evolution of Asia*, A. Yin and T. M. Harrison, Eds., pp. 442–485, Cambridge University Press, New York, NY, USA, 1996.
- [40] Z. M. Zheng, J. G. Liou, and R. G. Coleman, “An outline of the plate tectonics of China,” *Geological Society of America Bulletin*, vol. 95, no. 3, pp. 295–312, 1984.
- [41] B. J. Liu and X. S. Xu, *Lithofacies Palaeogeography Atlas of Southern China*, Geology Press, Beijing, 1994.
- [42] G. Wang and Y. Ju, “Organic shale micropore and mesopore structure characterization by ultra-low pressure N<sub>2</sub> physisorption: experimental procedure and interpretation model,” *Journal of Natural Gas Science and Engineering*, vol. 27, pp. 452–465, 2015.
- [43] M. M. Labani, R. Rezaee, A. Saeedi, and A. Hinai, “Evaluation of pore size spectrum of gas shale reservoirs using low pressure nitrogen adsorption, gas expansion and mercury porosimetry: a case study from the Perth and Canning basins, Western Australia,” *Journal of Petroleum Science and Engineering*, vol. 112, pp. 7–16, 2013.
- [44] S. J. Li, K. H. Xiao, Y. J. Wu, S. X. Long, and L. G. Cai, “Developmental controlling factors of Upper Ordovician Lower Silurian high quality source rocks in marine sequence, South China,” *Acta Sedimentologica Sinica*, vol. 26, no. 5, pp. 872–880, 2008.
- [45] H. J. Chang, X. L. Chu, L. J. Feng, J. Huang, and Q. R. Zhang, “Redox sensitive trace elements as paleoenvironments proxies,” *Geological Review*, vol. 55, no. 1, pp. 91–99, 2009.
- [46] N. Tribouillard, T. J. Algeo, T. Lyons, and A. Riboulleau, “Trace metals as paleoredox and paleoproductivity proxies: an update,” *Chemical Geology*, vol. 232, no. 1–2, pp. 12–32, 2006.
- [47] S. M. Rimmer, “Geochemical paleoredox indicators in Devonian-Mississippian black shales, Central Appalachian Basin (USA),” *Chemical Geology*, vol. 206, no. 3–4, pp. 373–391, 2004.
- [48] B. Jones and D. A. C. Manning, “Comparison of geochemical indices used for the interpretation of palaeoredox conditions in ancient mudstones,” *Chemical Geology*, vol. 111, no. 1–4, pp. 111–129, 1994.
- [49] G. Wang and T. R. Carr, “Organic-rich Marcellus shale lithofacies modeling and distribution pattern analysis in the Appalachian Basin,” *AAPG Bulletin*, vol. 97, no. 12, pp. 2173–2205, 2013.
- [50] C. Han, Z. Jiang, M. Han, M. Wu, and W. Lin, “The lithofacies and reservoir characteristics of the Upper Ordovician and Lower Silurian black shale in the southern Sichuan Basin and its periphery, China,” *Marine and Petroleum Geology*, vol. 75, pp. 181–191, 2016.
- [51] W. Yang, R. S. Zuo, Z. X. Jiang et al., “Effect of lithofacies on pore structure and new insights into pore-preserving mechanisms of the over-mature Qiongzhusi marine shales in Lower Cambrian of the southern Sichuan Basin, China,” *Marine and Petroleum Geology*, vol. 98, pp. 746–762, 2018.
- [52] J. Schoenherr, R. Littke, and J. L. Urai, “Polyphase thermal evolution in the infra-Cambrian Ara Group (South Oman Salt Basin) as deduced, by maturity of solid reservoir bitumen,” *Organic Geochemistry*, vol. 38, no. 8, pp. 1293–1318, 2017.
- [53] S. Henares, L. Caracciolo, G. Cultrone, J. Fernández, and C. Viseras, “The role of diagenesis and depositional facies on pore system evolution in a Triassic outcrop analogue (SE Spain),” *Marine and Petroleum Geology*, vol. 51, no. 2, pp. 136–151, 2014.
- [54] L. M. Anovitz and D. R. Cole, “Characterization and analysis of porosity and pore structures,” *Reviews in Mineralogy and Geochemistry*, vol. 80, no. 1, pp. 61–164, 2015.
- [55] X. Tang, Z. Jiang, and S. Jiang, “Effect of organic matter and maturity on pore size distribution and gas storage capacity in high-mature to post-mature shales,” *Energy & Fuels*, vol. 30, no. 11, pp. 8985–8996, 2017.
- [56] F. Yang, Z. Ning, Q. Wang, R. Zhang, and B. M. Krooss, “Pore structure characteristics of Lower Silurian shales in the southern Sichuan basin, China: insights to pore development and gas storage mechanism,” *International Journal of Coal Geology*, vol. 156, pp. 12–24, 2016.
- [57] O. Iqbal, E. Padmanabhan, A. Mandal, and J. Dvorkin, “Characterization of geochemical properties and factors controlling the pore structure development of shale gas reservoirs,” *Journal of Petroleum Science and Engineering*, vol. 206, 2021.
- [58] S. Xu, Q. Gou, F. Hao et al., “Shale pore structure characteristics of the high and low productivity wells, Jiaoshiba shale gas field, Sichuan Basin, China: dominated by lithofacies or preservation condition?,” *Marine and Petroleum Geology*, vol. 114, p. 104211, 2020.
- [59] Q. Y. Gou, S. Xu, F. Hao, Z. G. Shu, S. He, and Z. R. Wu, “Differences in the nanopore structure of organic-rich shales with distinct sedimentary environments and mineral compositions,” *Energy & Fuels*, vol. 35, no. 20, pp. 16562–16577, 2021.

- [60] M. A. Iqbal, R. Rezaee, G. Smith, and J. M. Ekundayo, "Shale lithofacies controls on porosity and pore structure: an example from Ordovician Goldwyer Formation, Canning basin, Western Australia," *Journal of Natural Gas Science and Engineering*, vol. 89, 2021.
- [61] F. Yang, S. Xu, F. Hao et al., "Petrophysical characteristics of shales with different lithofacies in Jiaoshiba area, Sichuan basin, China: implications for shale gas accumulation mechanism," *Marine and Petroleum Geology*, vol. 109, pp. 394–407, 2019.
- [62] P. Luo and N. N. Zhong, "The role of residual bitumen on the pore structure of organic-rich shales from low to over mature: insight from shale and coal samples after the hydrous pyrolysis," *International Journal of Coal Geology*, vol. 226, 2020.
- [63] Y. M. Wang, D. Z. Dong, X. Z. Cheng, J. Huang, S. Wang, and S. Wang, "Electric property evidences of carbonification of organic matters in marine shales and its geologic significance: a case study of the Lower Cambrian Qiongzhusi shale in the southern Sichuan Basin," *Natural Gas Industry*, vol. 1, no. 2, pp. 129–136, 2014.
- [64] S. F. Wang, Z. Y. Zhang, D. Z. Dong et al., "Microscopic pore structure and reasons making reservoir property weaker of Lower Cambrian Qiongzhusi shale, Sichuan Basin, China," *Natural Gas Geoscience*, vol. 27, no. 9, pp. 1619–1628, 2016.
- [65] D. W. Waples, "The kinetics of in-reservoir oil destruction and gas formation: constraints from experimental and empirical data, and from thermodynamics," *Organic Geochemistry*, vol. 31, no. 6, pp. 553–575, 2000.
- [66] F. Wang, J. Guan, W. Feng, and L. Bao, "Evolution of overmature marine shale porosity and implication to the free gas volume," *Petroleum Exploration and Development*, vol. 40, no. 6, pp. 819–824, 2013.
- [67] P. Cheng and X. M. Xiao, "Gas content of organic-rich shales with very high maturities," *Journal of China Coal Society*, vol. 38, no. 45, pp. 737–741, 2013.

## Research Article

# A Novel Mathematical Model for Fracturing Effect Evaluation Based on Early Flowback Data in Shale Oil Reservoirs

Yuhan Wang,<sup>1,2</sup> Zhengdong Lei,<sup>2</sup> Zhenhua Xu,<sup>1,2</sup> Jie Liu,<sup>1,2</sup> Xiaokun Zhang,<sup>1</sup> Erhui Luo,<sup>2</sup> Yuqi Liu,<sup>2</sup> and Pengcheng Liu<sup>1</sup> 

<sup>1</sup>School of Energy Resources, China University of Geosciences, Beijing 100083, China

<sup>2</sup>Research Institute of Petroleum Exploration and Development, PetroChina, Beijing 100083, China

Correspondence should be addressed to Pengcheng Liu; liupengcheng8883@sohu.com

Received 7 October 2021; Accepted 3 December 2021; Published 16 December 2021

Academic Editor: Chenhao Sun

Copyright © 2021 Yuhan Wang et al. This is an open access article distributed under the Creative Commons Attribution License, which permits unrestricted use, distribution, and reproduction in any medium, provided the original work is properly cited.

For shale oil reservoirs, the horizontal well multistage fracturing technique is mostly used to reform the reservoir in order to achieve economic and effective development. The size of the reservoir reconstruction volume and the quantitative characterization of the fracture system are of great significance to accurately predict the productivity of shale oil wells. There are few flowback models for shale oil reservoirs. To solve this problem, first, a physical model of the simultaneous production of oil, gas, and water in the early flowback stage of shale oil development is established using the material balance equation for a fracture system. Second, the physical model of the underground fracture system is simplified, which is approximately regarded as a thin cylindrical body with a circular section. The flow of the fluid in the fracture system is approximately regarded as radial flow. In this model, the expansion of the fluid and the closure of the fracture are defined as integrated storage coefficients to characterize the storage capacity of the fracture system. Then, the curves illustrating the relationships between the oil-water ratio and the cumulative oil production and between the gas-water ratio and the cumulative gas production are drawn, and the curves are used to divide the flowback stage into an early stage and a late stage because the flowback process of shale oil wells exhibits obvious stage characteristics. Finally, the reservoir reconstruction volume and the related hydraulic fracture parameters are estimated based on the material balance method, and the rationality of the model is verified via numerical simulation. The interpretation results of this novel model are more accurate, making it an effective way to evaluate the hydraulic fracture parameters and transformation effect, and it has guiding significance for the evaluation of the hydraulic fracturing effect in the field.

## 1. Introduction

In recent years, the exploration and development of unconventional oil and gas resources, such as shale oil, have increased, and unconventional oil and gas resources with rich reserves have been discovered all over the world. The broad prospects of the development of unconventional oil and gas resources have been demonstrated [1–5]. The properties of unconventional oil and gas reservoirs are significantly different from those of conventional oil and gas reservoirs. Unconventional reservoirs are generally characterized by low porosity and low permeability and the development of micro- and nanopores, and most of them do not have natural production capacity [6–8]. Currently, we

mainly rely on multistage hydraulic fracturing of horizontal wells to form a complex fracture network in the reservoir and increase the effective drainage area in order to obtain industrial oil flow. Multistage fractured horizontal wells (MFHWs) have resulted in significant improvements in reservoir permeability and conductivity through horizontal well drilling and volumetric fracturing. During volumetric fracturing, hydraulically fractured fractures are formed perpendicular to the horizontal wellbore, and a complex fracture network is formed through the connection of the natural fractures inside the reservoir with the hydraulically fractured fractures [9–13]. The stimulated reservoir volume (SRV) is an important index used to evaluate the production capacity of MFHWs. Developing a method of effectively and correctly

understanding the fracture network after volume fracturing has become a common hot topic of interest among scholars. Microseismic monitoring and postpressure evaluation techniques are currently used to interpret the parameters of MFHW fracturing modifications. However, the application of the above techniques is limited by cost factors and data interpretation techniques [14–18], and there has been a large gap between the actual application results and the awareness and needs of miners.

The drainage and production data in the initial stage of well opening after fracturing is the first-hand data that can best reflect the effect of fracturing. In recent years, these data have been deeply studied to evaluate the fracturing effect of MFHWs [19–25]. The fracture network formed by fracturing is initially filled with fracturing fluid. Therefore, analysis of the production data during early flowback should reveal the reservoir capacity and conductivity of the fractures. In the past, MFHWs were mostly used for the development of tight sandstone reservoirs. For tight sandstone reservoirs, there would be an obvious single-phase water flow stage during the initial flowback. It was found that by obtaining the flowback rate and flow pressure during the initial stage of flowback, combined with tracer data, the relevant information about the hydraulic fractures could be obtained from rate transient analysis of the flowback data. Abbasi et al. [26] proposed a single-phase rate transient analysis (RTA) model to analyze the water production data for hydraulic fractures and established a corresponding analytical mathematical model. Clarkson et al. [27, 28] divided the flowback stage of tight oil wells into preinvasion and postinvasion stages and established an analytical model to extract the fracture half-length and permeability from these two stages (permeability and fracture half-length).

Unlike tight sandstone reservoirs, shale gas wells are usually in the stage of rapid gas-water two-phase coproduction in the early stage of flowback. Postpressure shale gas wells are usually in a rapid gas and water production phase. Adefidipe et al. [29–32] divided the postpressure drainage of shale gas wells into an early gas production stage (EGP) and a late gas production stage (LGP) based on the turning point of the gas-to-liquid ratio curve. A volumetric analysis of the water and gas production data was performed by dividing the shale gas well production data phases, and a method of estimating the effective fracture volume by modeling the fracture system based on the two-phase material balance equation was proposed. The effective compression coefficient term and the linear dynamic relative permeability function were introduced to extend the existing single-phase analysis and two-phase simulation models to the analysis of shale gas reservoir flowback data. For shale oil reservoirs, Chen et al. [33–39] proposed a flowback model for complex fracture network shale oil reservoirs. During the numerical solution and inversion processes, it was necessary to use numerical solutions and semianalytical solutions to describe the flow of two-phase water and oil in a fracture and matrix system. In order to facilitate practical applications, in recent years, many researchers have used empirical decline curves to analyze multiflowback data. Jones and Blasingame [40, 41] applied hyperbolic and modified hyper-

bolic models to predict multiphase flow during reverse discharge. Fu et al. [42, 43] and Fu et al. [44] observed the harmonic decline behavior of the water return discharge and estimated the initial fracture volume versus final water production via decreasing curve analysis.

The goal of this study was to continue to develop an analytical model for the quantitative analysis of hydraulic fracturing flowback data. However, unlike in previous studies, the development of the mathematical model considers the transition from single-phase flow to multiphase flow when the formation fluid breaks through the fracture (three phases of oil, gas, and water). The expansion of the free gas in the fracture network, the expansion of the remaining fracturing fluid, and the closure effect of the fractures are considered in the model. These factors are considered as a comprehensive storage coefficient. Based on the single-phase diffusion equation, a complete mathematical model of shale oil flowback was established. Finally, the mathematical model was used to calculate the parameters related to the cracks in combination with the actual production data. The results obtained from the model were compared with the commercial software (Fracman) results, and the results were found to be relatively close. The calculated fracture data were also used for historical fitting of this field (using the commercial tNavigator software). The fitting results are good, which further demonstrates that the results of the model are reasonable. It is of great guiding significance for field production.

## 2. Mathematical Model

*2.1. Mathematical Model of Material Balance.* In order to relate the flow and pressure at the beginning of the flowback operation to the fracture and reservoir properties, in this study, a simple conceptual model was constructed for shale oil drainage return analysis (Figure 1). First, we described the conceptual model by constructing the material balance equation using the analytical equation. Next, we described the flow pattern of the fluid in the fractures at the beginning of the flowback by analyzing the production dynamic data. This led to obtaining the corresponding analytical solution by combining the continuity equation and the diffusion equation. Finally, the linear relationship between rate normalized pressure (RNP) and the matter equilibrium time (MBT) was established.

We made the following assumptions about this conceptual model. (1) The initial production during flowback occurs only in the fracture. (2) All of the fluid flows obey Darcy's law. The effects of gravity and capillary pressure are negligible. (3) The contribution of the early production fluid from the matrix is negligible. (4) The fracture system contains an initial water (fracturing fluid) saturation of  $S_{wi}$ ; the initial free gas saturation is  $S_{gi}$ ; and the initial oil content saturation is  $S_{oi}$ . (5) The production from the horizontal wells is driven by fluid expansion within the fractures and closure of the fractures.

As can be seen from Figure 1, we approximate the entire crack system as a closed system. The equation describing the material balance in the crack obeys the law of conservation of mass. The fracture section is the SRV area formed by the hydraulic fracturing fractures, the secondary fractures generated by fracturing, and the natural fractures

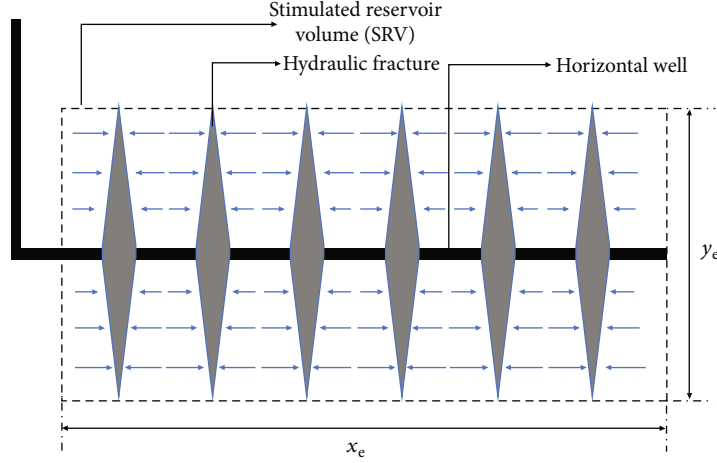


FIGURE 1: Schematic diagram of a multistage fractured horizontal well.

communicated after fracturing. The matrix section is a shale matrix connected to the fracture section. The wellbore section consists of a horizontal section and a vertical section. In this study, we defined a comprehensive compressibility factor, which takes into account gas expansion, oil expansion, fracturing fluid expansion, and fracture closure. The material balance equation is as follows:

Mass of inflow – mass of outflow = mass of increase, i.e.,

$$\begin{aligned} & q_m \rho_m B_m - q_g \rho_g B_g - q_o \rho_o B_o \\ &= \frac{\partial}{\partial t} [V_g(t) \rho_g + V_o(t) \rho_o] \\ &+ \frac{\partial}{\partial t} [V_{wbg}(t) \rho_g + V_{wbo}(t) \rho_o] c, \end{aligned} \quad (1)$$

where  $B$  is the volume factor, which is the ratio of the reservoir fluid volume under formation conditions to the fluid volume under surface conditions.  $V_g$  is the volume of the gas phase in the fracture at any time when the fracture is filled with the oil, gas, and water phases. Similarly,  $V_o$  is the volume of the oil phase in the fracture at any given time when the interior of the fracture is filled with the oil, gas, and water phases. This model assumes that the fluid flowing from the matrix into the fracture is negligible for a short period of time during the initial stage of the flowback. The variation in the fluid volume with time and the fluid density in the fractures and wellbore are described by the following equation:

$$V_f(t) = V_o(t) + V_g(t) + V_w(t). \quad (2)$$

For  $q_m = 0$ , solving Equations (1) and (2) simultaneously gives

$$\begin{aligned} -q_g \rho_g B_g - q_o \rho_o B_o &= \frac{\partial}{\partial t} [(V_f - V_o - V_w) \rho_g + (V_f - V_g - V_w) \rho_o] \\ &+ V_{wbg} \frac{\partial \rho_{wbg}}{\partial t} + V_{wbo} \frac{\partial \rho_{wbo}}{\partial t}. \end{aligned} \quad (3)$$

For the convenience of calculation, Equation (3) is split into two parts:

$$-q_o \rho_o B_o = \frac{\partial}{\partial t} [(V_f - V_g - V_w) \rho_o] + V_{wbo} \frac{\partial \rho_{wbo}}{\partial t}, \quad (4)$$

$$-q_g \rho_g B_g = \frac{\partial}{\partial t} [(V_f - V_o - V_w) \rho_g] + V_{wbg} \frac{\partial \rho_{wbg}}{\partial t}. \quad (5)$$

According to the isothermal compressibility of the fluid,

$$c = -\frac{1}{V} \frac{\partial V}{\partial p} = \frac{1}{\rho} \frac{\partial \rho}{\partial p} = \frac{1}{\rho} \frac{\partial \rho}{\partial t} \frac{\partial t}{\partial p}. \quad (6)$$

Then, we can obtain the following formulas:

$$\begin{aligned} \frac{\partial \rho_o}{\partial t} &= \rho_o c_o \frac{\partial p_f}{\partial t}, \\ \frac{\partial \rho_g}{\partial t} &= \rho_g c_g \frac{\partial p_f}{\partial t}, \\ \frac{\partial \rho_w}{\partial t} &= \rho_w c_w \frac{\partial p_f}{\partial t}. \end{aligned} \quad (7)$$

Substituting Equation (7) into Equations (4) and (5) and simplifying gives

$$-q_o B_o = \frac{\partial}{\partial t} (V_f - V_g - V_w) + c_o V_o \frac{\partial p_f}{\partial t} + V_{wbo} c_o \frac{\partial p_{wb}}{\partial t}, \quad (8)$$

$$-q_g B_g = \frac{\partial}{\partial t} (V_f - V_o - V_w) + c_g V_g \frac{\partial p_f}{\partial t} + V_{wbg} c_g \frac{\partial p_{wb}}{\partial t}. \quad (9)$$

Due to the fact that  $V_f$ ,  $V_g$ , and  $V_w$  are all functions of time  $t$ , Equations (8) and (9) can be treated as follows:

$$-q_o B_o = \frac{\partial V_f}{\partial t} - \frac{\partial V_g}{\partial t} - \frac{\partial V_w}{\partial t} + c_o V_o \frac{\partial p_f}{\partial t} + V_{wbo} c_o \frac{\partial p_{wb}}{\partial t}, \quad (10)$$

$$-q_g B_g = \frac{\partial V_f}{\partial t} - \frac{\partial V_o}{\partial t} - \frac{\partial V_w}{\partial t} + c_g V_g \frac{\partial p_f}{\partial t} + V_{wbg} c_g \frac{\partial p_{wb}}{\partial t}. \quad (11)$$

Among them,  $V_o$ ,  $V_g$ , and  $V_w$  are considered to be functions of the cumulative oil production, cumulative gas production, and cumulative water production over time, respectively.  $O_{fi}$ ,  $G_{fi}$ , and  $W_{fi}$  are defined as the original oil volume, original gas volume, and original water volume in the fracture, respectively.  $O_p$ ,  $G_p$ , and  $W_p$  are the oil, gas, and water outputs after blowout production, respectively.

$$V_o(t) = (O_{fi} - O_p) B_o, \quad (12)$$

$$V_g(t) = (G_{fi} - G_p) B_g, \quad (13)$$

$$V_w(t) = (W_{fi} - W_p) B_w. \quad (14)$$

Equations (12), (13), and (14) can be substituted into Equations (10) and (11) to obtain

$$-q_o B_o = \frac{\partial V_f}{\partial t} - \frac{\partial (G_{fi} - G_p) B_g}{\partial t} - \frac{\partial (W_{fi} - W_p) B_w}{\partial t} + c_o B_o (O_{fi} - O_p) \frac{\partial p_f}{\partial t} + V_{wbo} c_o \frac{\partial p_{wb}}{\partial t}, \quad (15)$$

$$-q_g B_g = \frac{\partial V_f}{\partial t} - \frac{\partial (O_{fi} - O_p) B_g}{\partial t} - \frac{\partial (W_{fi} - W_p) B_w}{\partial t} + c_g B_g (G_{fi} - G_p) \frac{\partial p_f}{\partial t} + V_{wbg} c_g \frac{\partial p_{wb}}{\partial t}. \quad (16)$$

Based on the equation for the compression coefficient of the fluid and using the chain derivation rule, we can rewrite Equations (15) and (16) as

$$\begin{aligned} & -\left(q_o B_o + q_g B_g + q_w B_w\right) \\ & = \left[ \frac{\partial V_f}{\partial p_f} + (O_{fi} - O_p) B_o c_o + (G_{fi} - G_p) B_g c_g \right. \\ & \quad \left. + (W_{fi} - W_p) B_w c_w \right] \frac{\partial p_f}{\partial t} + V_{wbo} c_o \frac{\partial p_{wb}}{\partial t}, \end{aligned} \quad (17)$$

$$\begin{aligned} & -\left(q_o B_o + q_g B_g + q_w B_w\right) \\ & = \left[ \frac{\partial V_f}{\partial p_f} + (O_{fi} - O_p) B_o c_o + (G_{fi} - G_p) B_g c_g \right. \\ & \quad \left. + (W_{fi} - W_p) B_w c_w \right] \frac{\partial p_f}{\partial t} + V_{wbg} c_g \frac{\partial p_{wb}}{\partial t}. \end{aligned} \quad (18)$$

By combining Equations (17), (18), (15), and (16), we obtain

$$\begin{aligned} & -\left(q_o B_o + q_g B_g + q_w B_w\right) \\ & = \left[ \frac{\partial V_f}{\partial p_f} + (O_{fi} - O_p) B_o c_o + (G_{fi} - G_p) B_g c_g \right. \\ & \quad \left. + (W_{fi} - W_p) B_w c_w \right] \frac{\partial p_f}{\partial t} \\ & \quad + \frac{1}{2} V_{wbg} c_g \frac{\partial p_{wb}}{\partial t} + \frac{1}{2} V_{wbo} c_o \frac{\partial p_{wb}}{\partial t}. \end{aligned} \quad (19)$$

The rate of change of the pressure in the wellbore with respect to time can be assumed to be approximately the same as the rate of change of the pressure in the fracture with respect to time during the early stage of flowback, and the volume of the fracture after fracturing is much larger than the volume of the wellbore. Therefore,  $V_{wb}$  can be neglected.

We can simplify Equation (19) to

$$\begin{aligned} & -\left(q_o B_o + q_g B_g + q_w B_w\right) \\ & = \left[ \frac{\partial V_f}{\partial p_f} + (O_{fi} - O_p) B_o c_o + (G_{fi} - G_p) B_g c_g \right. \\ & \quad \left. + (W_{fi} - W_p) B_w c_w \right] \frac{\partial p_f}{\partial t}. \end{aligned} \quad (20)$$

The expression of the initial fracture volume is defined, which is a function of the initial oil saturation, initial gas saturation, and initial water saturation.

$$V_{fi} = \frac{O_{fi} B_{oi}}{S_{oi}} = \frac{G_{fi} B_{gi}}{S_{gi}} = \frac{W_{fi} B_{wi}}{S_{wi}}. \quad (21)$$

Both sides of the equation are normalized using Equation (21).

$$\begin{aligned} & -\frac{\left(q_o B_o + q_g B_g + q_w B_w\right)}{V_{fi}} \\ & = \left[ \frac{1}{V_{fi}} \frac{\partial V_f}{\partial p_f} + \frac{(O_{fi} - O_p) B_o c_o}{O_{fi} B_{oi} S_{oi}} + \frac{(G_{fi} - G_p) B_g c_g}{G_{fi} B_{gi} S_{gi}} \right. \\ & \quad \left. + \frac{(W_{fi} - W_p) B_w c_w}{W_{fi} B_{wi} S_{wi}} \right] \frac{\partial p_f}{\partial t}. \end{aligned} \quad (22)$$

During the production process, the volume coefficient of the water hardly changes. By sorting out Equation (22), we can obtain

$$\begin{aligned} & -\frac{\left(q_o B_o + q_g B_g + q_w B_w\right)}{V_{fi}} \\ & = \left[ \frac{1}{V_{fi}} \frac{\partial V_f}{\partial p_f} + \left(1 - \frac{O_p}{O_{fi}}\right) \frac{B_o}{B_{oi}} S_{oi} c_o + \left(1 - \frac{G_p}{G_{fi}}\right) \right. \\ & \quad \left. \frac{B_g}{B_{gi}} S_{gi} c_g + \left(1 - \frac{W_p}{W_{fi}}\right) S_{wi} c_w \right] \frac{\partial p_f}{\partial t}. \end{aligned} \quad (23)$$

The total fluid produced in the initial stage of flowback is defined as  $q_t$ . In addition, a comprehensive storage coefficient function  $C_a$  is defined. Using these two newly defined functions, Equation (23) can be simplified as follows:

$$\frac{\partial p_f}{\partial t} = -\frac{q_t}{C_a V_{fi}}, \quad (24)$$

$$C_a = \frac{1}{V_{fi}} \frac{\partial V_f}{\partial p_f} + \left(1 - \frac{O_p}{O_{fi}}\right) \frac{B_o}{B_{oi}} S_{oi} c_o + \left(1 - \frac{G_p}{G_{fi}}\right) \frac{B_g}{B_{gi}} S_{gi} c_g + \left(1 - \frac{W_p}{W_{fi}}\right) S_{wi} c_w, \quad (25)$$

$$q_t = q_o B_o + q_g B_g + q_w B_w. \quad (26)$$

Each item in  $C_a$  describes a different driving mechanism within the fracture system during the initial stage of flowback. It includes the effects caused by the fluid expansion and the crack closure with time.

**2.2. Model of Fracturing Fluid Flow in Fracture.** Based on the material balance equation and diffusion equation, the mathematical model of the initial stage of flowback was established. There are many fracture forms after fracturing. When the crack height remains constant and the crack length increases, the longitudinal section of the crack is elliptical, and the crack shape is closer to the Perkins-Kern-Nordgren (PKN) model. In this study, we approximated the fracture surface sheet as a thin layer of cylinders, and the longitudinal section was approximately regarded as a circle. The flow of the underground fluid from the fracture space into the horizontal wellbore can be simplified as radial flow (Figure 2).

In this model, we considered the temperature and viscosity to be fixed values, ignored the influence of gravity, and simplified the fluid flow as single-phase radial flow of a slightly compressible fluid.

As is shown in the figure, the diffusion coefficient equation of the fluid flowing radially to the horizontal wells through the hydraulic fractures in the initial stage of flowback is

$$\frac{1}{r} \frac{\partial}{\partial r} \left( r \frac{\partial p_f}{\partial r} \right) = -\frac{\phi_f C_t \mu}{k_f} \frac{\partial p_f}{\partial t}. \quad (27)$$

Substituting Equation (24) into Equation (27) gives

$$\frac{1}{r} \frac{\partial}{\partial r} \left( r \frac{\partial p_f}{\partial r} \right) = \frac{\phi_f C_t \mu}{k_f} \frac{q_t}{C_a V_{fi}}. \quad (28)$$

By integrating  $r$  on both sides of Equation (26) at the same time, we obtain

$$r \frac{\partial p_f}{\partial r} = \frac{1}{2} r^2 \frac{\phi_f C_t \mu}{k_f} \frac{q_t}{C_a V_{fi}} + C_1. \quad (29)$$

When  $r = r_e$  and  $\partial p_f / \partial r = 0$ , then  $C_1$  is

$$C_1 = -\frac{1}{2} r_e^2 \frac{\phi_f C_t \mu}{k_f} \frac{q_t}{C_a V_{fi}}. \quad (30)$$

Equation (29) can be written as

$$r \frac{\partial p_f}{\partial r} = \frac{1}{2} (r^2 - r_e^2) \frac{\phi_f C_t \mu}{k_f} \frac{q_t}{C_a V_{fi}}. \quad (31)$$

Integrating both the left and right ends of Equation (31) with respect to  $r$  gives

$$p_f(r, t) = \left( \frac{1}{4} r^2 - \frac{1}{2} r_e^2 \ln r \right) \frac{\phi_f C_t \mu}{k_f} \frac{q_t}{C_a V_{fi}} + C_2. \quad (32)$$

When  $r = r_w$ ,  $p = p_{wf}$ , and we assume that  $r_w^2 / r_e^2 \approx 0$ ,  $C_2$  can be calculated at this time as follows:

$$C_2 = p_{wf} + \frac{\phi_f C_t \mu}{k_f} \frac{q_t r_e^2}{2 C_a V_{fi}} \ln r_w. \quad (33)$$

Thus, Equation (32) can be written as

$$p_f(r, t) = p_{wf} + \frac{\phi_f C_t \mu}{k_f} \frac{q_t r_e^2}{2 C_a V_{fi}} \left( \ln \frac{r_w}{r} + \frac{r^2}{2 r_e^2} \right). \quad (34)$$

Here, we use Equation (35) to combine the average reservoir pressure with the pressure in the fracture and the bottom hole flow pressure:

$$\bar{p}(t) = \frac{\left( \int_{r_w}^{r_e} p_f dV_f \right)}{\left( \int_{r_w}^{r_e} dV_f \right)}, \quad (35)$$

where the volume of the cylinder can be represented by

$$dV_f = 2\pi r h_f \phi_f dr. \quad (36)$$

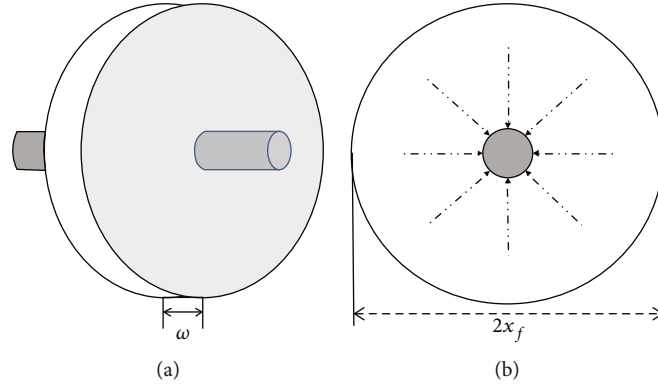


FIGURE 2: Model of fracturing fluid flow in fracture. (a)  $\omega$  is the width of the fracture. (b)  $x_f$  is the half-length of the fracture.

Substituting Equation (36) into Equation (35) gives

$$\bar{p}(t) = \frac{\left( \int_{r_w}^{r_e} p_f r dr \right)}{\left( \int_{r_w}^{r_e} r dr \right)}. \quad (37)$$

Substituting Equation (34) into Equation (37) gives

$$\bar{p}(t) = \frac{\left\{ \int_{r_w}^{r_e} \left[ p_{wf} + \left( \phi_f C_t \mu / k_f \right) (q_t r_e^2 / 2 C_a V_{fi}) (\ln(r_w/r) + (r^2/2r_e^2)) \right] r dr \right\}}{\left( (r_e^2 - r_w^2) / 2 \right)}. \quad (38)$$

According to the partial integral, the solution of Equation (38) can be obtained as follows:

$$\bar{p}(t) = p_{wf} + \frac{\left( \phi_f C_t \mu / k_f \right) (q_t r_e^2 / 2 C_a V_{fi}) \left( (r_e^2 / 2) \ln(r_w/r_e) + ((r_e^2 - r_w^2) / 4) + ((r_e^4 - r_w^4) / 8 r_e^2) \right)}{\left( (r_e^2 - r_w^2) / 2 \right)}. \quad (39)$$

Equation (39) is sorted to obtain the following formula:

$$\bar{p}(t) = p_{wf} + \frac{\phi_f C_t \mu}{k_f} \frac{q_t r_e^2}{2 C_a V_{fi}} \left( \ln \frac{r_w}{r_e} + \frac{3}{4} \right), \quad (40)$$

where order  $r_e^2/(r_e^2 - r_w^2) \approx 1$  and  $(r_e^2 + r_w^2)/r_e^2 \approx 1$ .

In the early stage of flowback, fluid expansion and fracture closure are the main factors affecting the fluid flow. According to the law of conservation of matter and the comprehensive storage coefficient,

$$N_o B_o + N_g B_g + N_w B_w = -C_a V_{fi} (\bar{p} - p_i). \quad (41)$$

By substituting the form of Equation (41) into Equation (40) and dividing both sides of the equation by  $q_t$ , we obtain the rate normalization equation:

$$\frac{p_i - p_{wf}}{q_t} = \frac{N_o B_o + N_g B_g + N_w B_w}{q_t C_a V_{fi}} + \frac{\phi_f C_t \mu}{k_f} \frac{r_e^2}{2 C_a V_{fi}} \left( \ln \frac{r_w}{r_e} + \frac{3}{4} \right), \quad (42)$$

where  $(p_i - p_{wf})/q_t$  is the rate normalized pressure (RNP), and  $(N_o B_o + N_g B_g + N_w B_w)/q_t$  is regarded as the material

balance time (MBT). Thus, we can rewrite Equation (42) as

$$\text{RNP} = \frac{1}{C_a V_{fi}} \text{MBT} + \frac{\phi_f C_t \mu}{k_f} \frac{r_e^2}{2 C_a V_{fi}} \left( \ln \frac{r_w}{r_e} + \frac{3}{4} \right). \quad (43)$$

$V_{fi}$  can be calculated as follows:

$$V_{fi} = O_{fi} B_{oi} + G_{fi} B_{gi} + W_{fi} B_{wi} + \Delta V_f. \quad (44)$$

In the early stage of flowback, assuming that the fracture stiffness  $S_f$  is a constant value, the closed volume of the fracture can be expressed as

$$\Delta V_f = A_f \Delta \omega_f = A_f \frac{\Delta p_f}{S_f}. \quad (45)$$

Substituting Equation (45) into Equation (44) and sorting it gives

$$\begin{aligned} & O_p B_o + G_p B_g + W_p B_w \\ &= O_{fi} \left( \frac{B_o}{B_{oi}} - 1 \right) + G_{fi} \left( \frac{B_g}{B_{gi}} - 1 \right) \\ &+ W_{fi} B_{wi} C_w \Delta p + A_f \frac{\Delta p}{S_f}. \end{aligned} \quad (46)$$



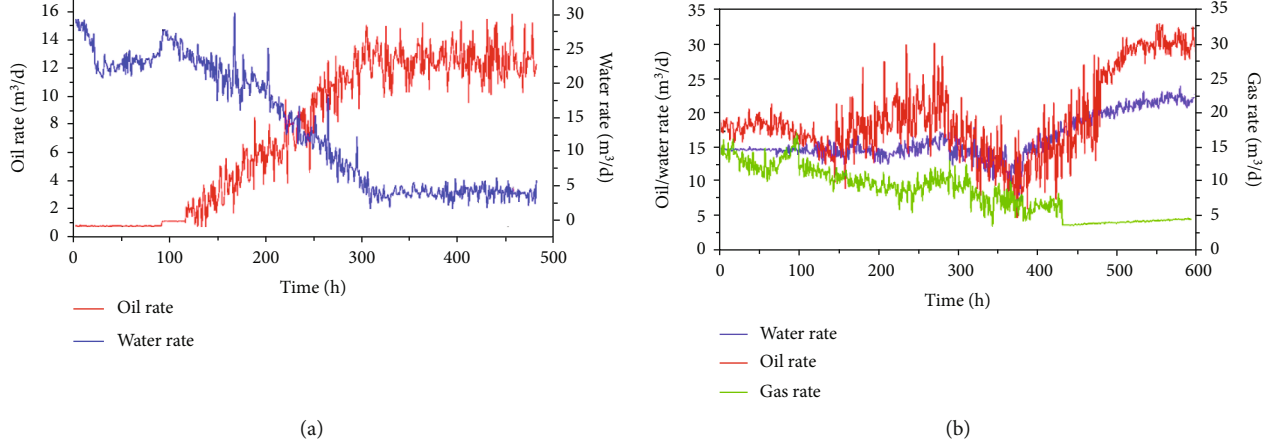


FIGURE 3: Diagnostic charts of the oil, gas, and water rates versus time for (a) well A and (b) well B.

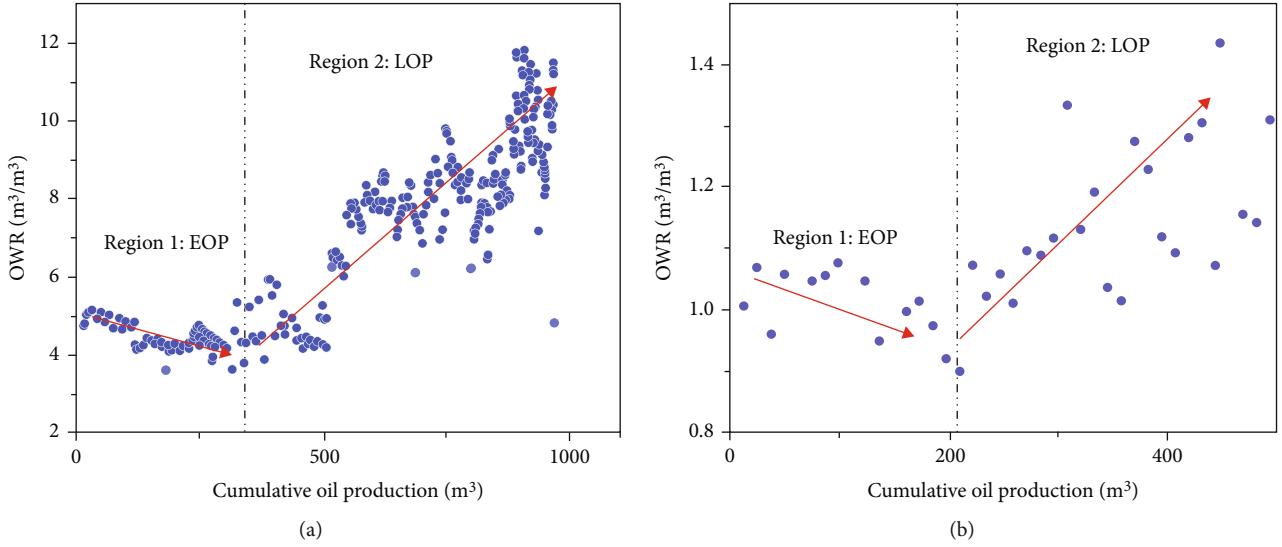


FIGURE 4: Diagnostic chart of the OWR versus cumulative oil production for (a) well A; (b) well B.

Before the well is opened for production, the initial water volume in the fracture system and the total initial fracture volume obey the following relationship:

$$\begin{aligned} W_{fi}B_{wi} &= V_{fi}S_{wi} = \frac{O_{fi}B_{oi}}{S_{oi}}S_{wi} = \frac{G_{fi}B_{gi}}{S_{gi}}S_{wi} \\ &= \frac{1 - S_{oi} - S_{gi}}{S_{oi}}O_{fi}B_{oi} = \frac{1 - S_{oi} - S_{gi}}{S_{gi}}G_{fi}B_{gi}. \end{aligned} \quad (47)$$

Based on Equation (21), the material balance equation for calculating the volume of the fracture system in the fracturing reconstruction can be obtained:

$$\begin{aligned} O_p B_o + G_p B_g + W_p B_w &= O_{fi} \left( \frac{B_o}{B_{oi}} - 1 \right) + G_{fi} \left( \frac{B_g}{B_{gi}} - 1 \right) \\ &+ \left( \frac{1 - S_{oi} - S_{gi}}{S_{oi}} O_{fi} B_{oi} C_w + \frac{A_f}{S_f} \right) \Delta p. \end{aligned} \quad (48)$$

Due to the small compression coefficient of the water phase, the contribution of the water phase expansion in the fracture is negligible compared to the repulsion energy provided by the fracture closure. Therefore, Equation (48) can be further simplified to obtain the curve of the relationship between the total recovery volume and the pressure drop. We conducted linear regression of this curve to obtain the slope and intercept of the line. According to the obtained linear intercept, we can calculate the initial volume of the reconstructed fracture system:

$$\begin{aligned} V_{fi} &= \frac{O_{fi}B_{oi}}{S_{oi}} = \frac{a - G_{fi}B_{gi}[(B_g/B_{gi}) - 1]}{[(B_o/B_{oi}) - 1]S_{oi}} \\ &= \frac{G_{fi}B_{gi}}{S_{gi}} = \frac{a - O_{fi}B_{oi}[(B_o/B_{oi}) - 1]}{[(B_g/B_{gi}) - 1]S_{gi}}. \end{aligned} \quad (49)$$

The total surface area of the fracture system of the fracture modification can be obtained from the slope of the

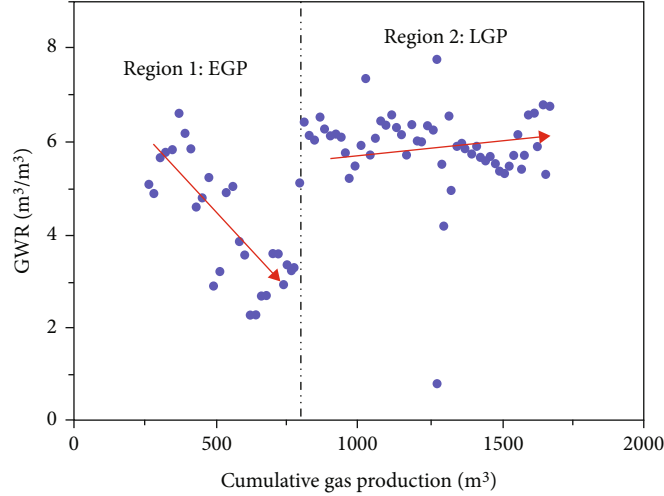


FIGURE 5: Diagnostic chart of the GWR versus cumulative gas production for well B.

regression line, and the fracture stiffness  $S_f$  of the shale can be obtained experimentally.

$$A_f = bS_f. \quad (50)$$

Equation (43) combines the material balance equation and diffusion equation, ignores the factors with relatively small influences, and finds a linear equation that is easy to apply to the actual production on site. By describing the linear relationship between the RNP and MBT, the calculations can be performed based on the production data measured in the early stages of reworking. We regard Equation (43) as a univariate linear equation, where  $1/C_a \cdot V_{fi}$  can be regarded as the slope of the curve. We can calculate the total storage coefficient of the fluid by calculating the slope of the curve. The intercept can be calculated to characterize the crack half-length of the radial flow under the PKN model.

### 3. Results and Discussion

**3.1. Flowback Data Extraction.** In order to establish a suitable mathematical model of early flowback in shale oil wells, in this study, the flowback data of fractured horizontal wells in the shale oil reservoir in block X in the Changqing Oilfield were analyzed, and the diagnostic curves of the changes in the oil, gas, and water productions with time and the changes in the oil-water ratio and gas-water ratio with cumulative gas production were drawn. The production data for this block were screened and sorted out, and several representative wells were selected for data analysis. By analyzing the flowback data, we obtained the oil production per hour, water production per hour, gas production per hour, total liquid production in different time periods, and bottom hole flow pressure in different time periods. Using the above data and formulas, we analyzed two typical wells and obtained the relevant parameters of the fracturing transformation.

In 2012, Abbasi et al. [26] drew related diagnostic charts by analyzing the flowback data for the tight oil and gas wells in Cardium. These diagnostic charts describe the relationships between the gas and water productions with time, as well as the relationship between the gas-water flow ratio and the cumulative gas produced. In this study, we used these diagnostic diagrams to describe the relationship between the oil-water ratio and the cumulative oil production and the relationship between the gas-water ratio and the cumulative gas production. According to the production data for the selected wells, a diagnostic map was drawn to determine the initial flowback time.

We selected the production data for two wells for analysis. Figures 3(a) and 4(a) show the oil production rate, water production rate, and oil-water ratio (OWR) of well A; and Figures 3(b), 4(b), and 5 show the oil production rate, gas production rate, water production rate, gas-water ratio (GWR), and OWR of well B. In the early stage of flowback, as well A was opened for flowback, oil was produced simultaneously with the fracturing fluid, and when well B was opened for flowback, oil, gas, and fracturing fluid were produced simultaneously. Therefore, it is necessary to consider multiphase simultaneous production in the flowback model. However, we can divide the flowback data for the shale oil into different regions according to the relationships shown in Figures 4 and 5, including early water production (EOP), early gas production (EGP), late oil production (LOP), and late gas production (LGP).

As the diagnostic rate diagram shows the instantaneous oil production, it can be inferred that the two phases (oil-water) or three phases (oil-gas-water) coexisted in the fracture network in the reconstruction area after hydraulic fracturing. When the fracture has just formed, it can be considered that the fracture is completely occupied by fracturing fluid, or there is a small amount of oil and gas only in the part connecting to the natural fracture. The fracturing construction period is long, and well blocking measures are usually taken after fracturing. During shut-in, under the

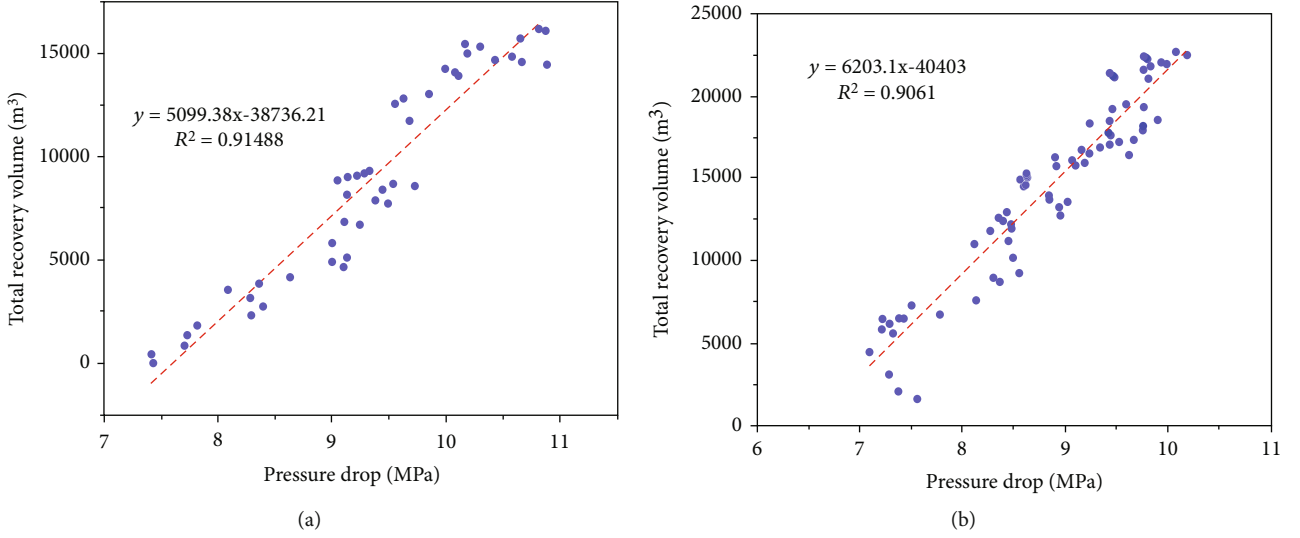


FIGURE 6: Plot of the total recovery volume versus pressure drop for (a) well A and (b) well B.

action of gravitational differentiation and imbibition, the fluid in the matrix flows into the fracture network, leading to the coexistence of two phases (oil-water) or three phases (oil-gas-water). In the EOP and EGP regions, the trend line of the scattered points exhibits a negative slope, indicating that the initial oil saturation and gas saturation in the fracture network decreased as the production and development progressed. In the LOP and LGP areas, after part of the injected fracturing fluid flowed back, the water production gradually decreased. At this time, the oil or gas in the matrix flowed into the fractures, and the oil and gas production were supplemented. The slope of the trend line of the scatter plot of the oil-water ratio versus the gas-water ratio becomes positive and passes through the early flowback stage.

**3.2. Flowback Data Analysis.** The early flowback data for well A and well B were analyzed, and the relationship between the total production volume and the pressure drop was drawn. It can be seen from Figures 6(a) and 6(b) that there is a strong linear correlation between the total recovery volume and the pressure drop. The initial crack system volume can be calculated using Equation (49). It is generally accepted that the volume of the hydraulic fractures formed during the hydraulic fracturing does not exceed the Total Injected Volume (TIV). The minimum value of the initial oil saturation in the hydraulic fractures can be inferred from Equation (49). The initial volume of the fracture system (including the hydraulic fractures and fracture modification zones that communicate with the natural fractures, which can be approximated as the SRV) is calculated by substituting the derived minimum initial oil saturation into Equation (48) and based on the total recovery volume versus pressure drop curve. Since the initial gas production from well B was small, the relevant parameters for well A can be used to estimate the initial volume of the oil phase in the SRV. Through the final calculation, it can be estimated that based on the data presented in Table 1, the SRV of well A was  $4.673 \times$

TABLE 1: Fracturing simulation construction parameters.

	Well A	Well B
$C_t$ (MPa <sup>-1</sup> )	$2.43 \times 10^{-5}$	$1.89 \times 10^{-5}$
$\mu$ (mPa·s)	1.21	1.15
$k_f$ ( $\mu\text{m}^2$ )	2036	3623
$S_{oi}$ (%)	46	38
$S_{gi}$ (%)	0	14
$\Phi_f$		1
$B_o$ (m <sup>3</sup> /m <sup>3</sup> )		1.08
$B_{oi}$ (m <sup>3</sup> /m <sup>3</sup> )		1.27
$B_g$ (m <sup>3</sup> /m <sup>3</sup> )		0.00411
$B_{gi}$ (m <sup>3</sup> /m <sup>3</sup> )		0.00437
$S_f$ (MPa/m)		$4.421 \times 10^5$

$10^6$  m<sup>3</sup>, and the area of the reformed fracture system was  $2.254 \times 10^9$  m<sup>2</sup>, while the SRV of well B was  $4.851 \times 10^6$  m<sup>3</sup>, and the area of the reformed fracture system was  $2.742 \times 10^9$  m<sup>2</sup>.

The linear relationship between the RNP and MBT was found by combining the EOP and EGP phases of the two completed MHFWs in Figure 7. The relationship between the fracture permeability, porosity, and fracture half-length was calculated using Equation (48), and the corresponding fracture half-length was obtained by estimating the fracture permeability [45]. It was calculated using the data given in Table 1. The hydraulic fracture half-length of well A was about 151 m, and the hydraulic fracture half-length of well B was 172 m.

**3.3. Numerical Simulation and Example Application.** In order to verify the effectiveness of the calculation method

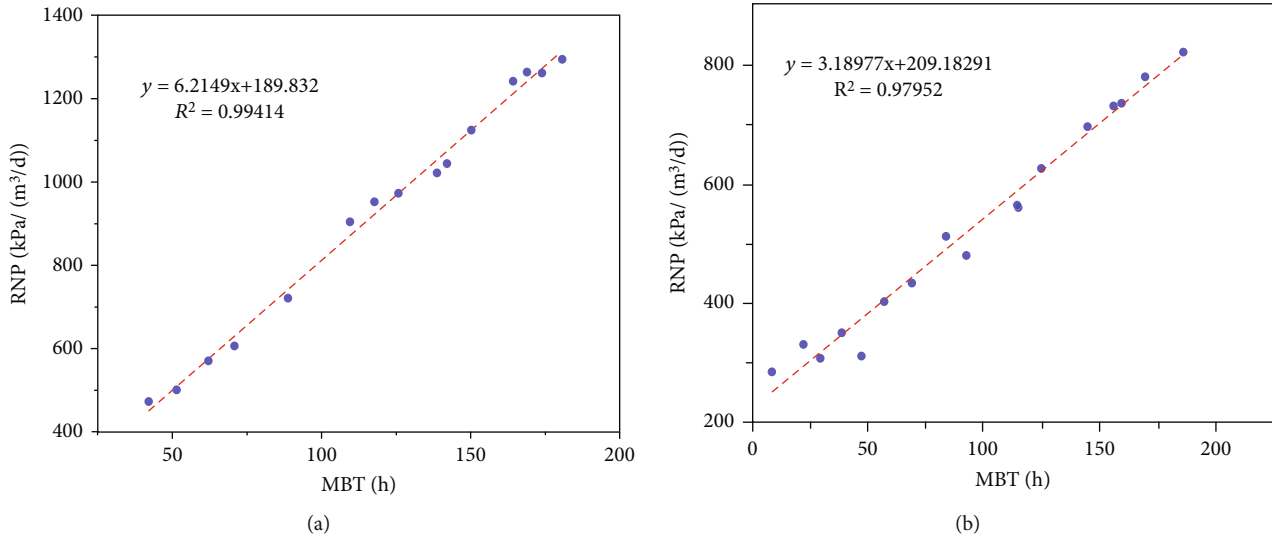


FIGURE 7: Plot of RNP versus MBT for (a) well A and (b) well B.

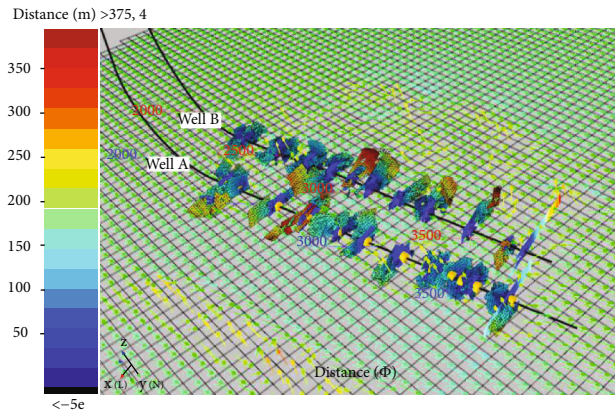


FIGURE 8: Schematic diagram of the half-length in the fracture simulation.

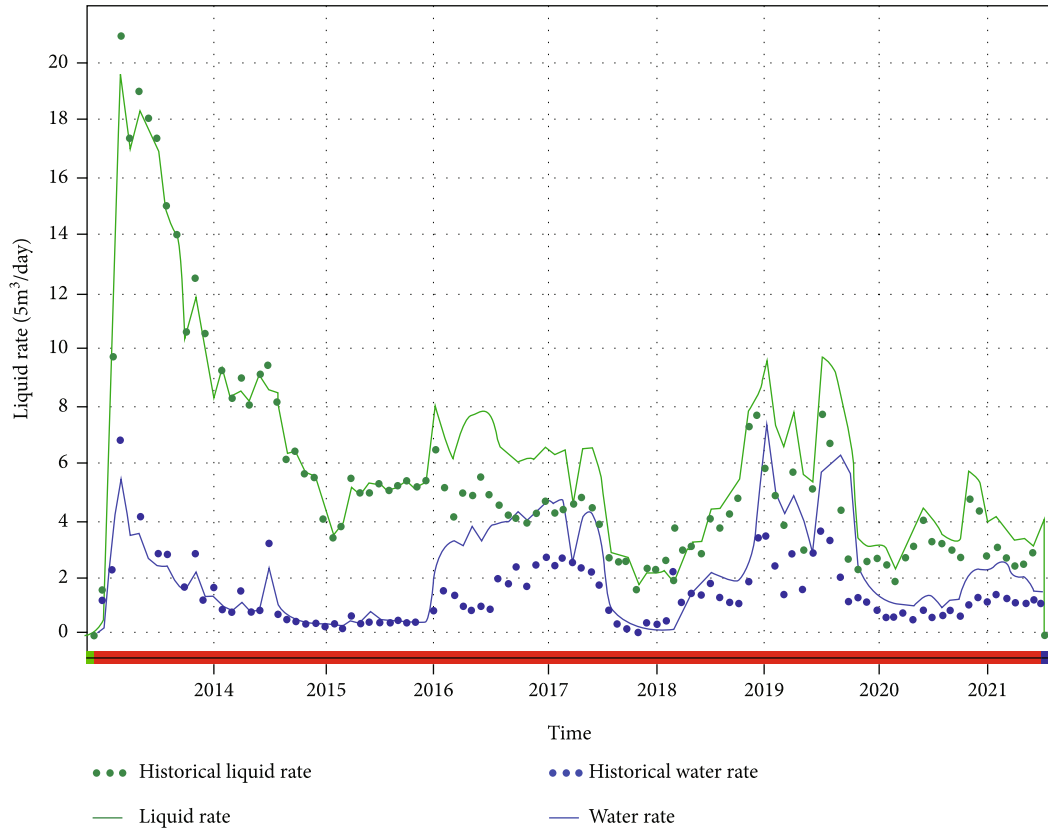
TABLE 2: Fracturing simulation construction parameters.

Well	Number of fracturing sections	Average displacement (m <sup>3</sup> /min)	Total fracturing liquid volume (m <sup>3</sup> )	Length of horizontal well section (m)	Sand content (%)
A	13	3.5	7473	1284.78	2.5
B	11	3.0	6553.5	1369.78	2.5

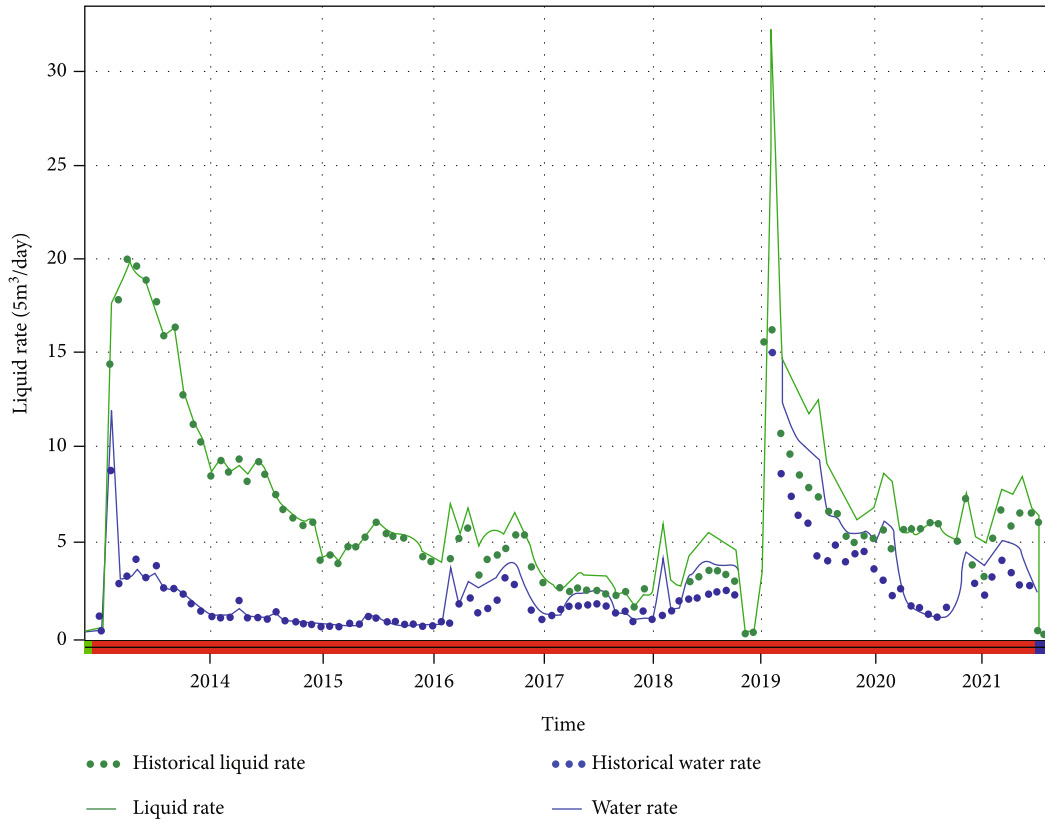
developed in this study, hydraulic fracturing simulations and historical fitting of production performance data were carried out using the actual geological model, fracturing construction parameters, and production performance data for wells A and B. Figure 8 shows the half-length results of the fracturing simulation of the fractures in the two wells. Using the actual geological model and in situ stress parameters provided on site, an in situ stress model was established using the FracMan software, and the actual fracturing construction parameters were used for the fracturing simulation. Table 2 presents the fracturing simulation parameters of the two wells. The average half crack length of the simulated crack in well A is 162.3 m. The average half crack

length of the simulated crack in well B is 189.6 m. These values are close to the calculation results.

Using the tNavigator reservoir numerical simulation software, the actual model of the well area was established. The relevant parameters of the fracture half-length and reconstruction area were calculated using this method, the dataset for the model, and the historical fitting. The production time of the two wells was from April 2013 to May 2021. As shown in Figure 9, the fitting results of the daily liquid production and daily water production of the two wells are good, which further demonstrates that the fracture parameters calculated using this method can reflect the actual transformation degree of the reservoir fracturing fractures better and have application value.



(a)



(b)

FIGURE 9: Historical fitting results of the daily liquid production and daily water production: (a) well A and (b) well B.

## 4. Conclusions

- (1) The material balance equation for the fracture system was used to establish a physical model for the simultaneous production of oil, gas, and water in the early flowback stage of a shale oil development. The physical model of the underground fracture was simplified and was approximately regarded as a thin-layer cylindrical body with a circular section, and the fluid flow was regarded as radial flow. Then, the novel mathematical model of multiphase flow flowback in the early stage of shale oil development was obtained by comprehensively considering the expansion of the fluid and the closure of the fractures in the model
- (2) The flowback stage of the shale oil exhibited obvious phase characteristics. According to the OWR and GWR, the flowback stage can be divided into an early stage and a late stage. Based on the early flowback stage, the SRV material balance model was established, and the size of the SRV was calculated based on the curve of the relationship between the total recovery volume and the pressure drop. Then, based on the mathematical model of the multiphase flowback in the early stage of shale oil development, the equation for the correlation between the RNP and MBT was obtained, and the relationship between the fracture permeability and the fracture half-length was calculated from it
- (3) The novel mathematical model was compared with commercial software results, and the resulting errors were found to be small. The obtained data were applied to a field example of historical fitting, and the fitting accuracy was high. The proposed model provides a novel and convenient calculation method for understanding the characteristics of hydraulic fracture parameters in production sites, and it has guiding significance for the development of unconventional reservoirs

## Nomenclature

$q$ :	Rate ( $\text{m}^3/\text{d}$ )
$\rho$ :	Density ( $\text{kg}\cdot\text{m}^{-3}$ )
$V$ :	Volume ( $\text{m}^3$ )
$V_{wb}$ :	Volume of fluid in wellbore ( $\text{m}^3$ )
$V_{wbo}$ :	Volume of oil in wellbore ( $\text{m}^3$ )
$V_{wbg}$ :	Volume of gas in wellbore ( $\text{m}^3$ )
$t$ :	Time (d)
$\mu$ :	Fluid viscosity (mPa·s)
$B$ :	Volume compressibility ( $\text{m}^3/\text{m}^3$ )
$c$ :	Compressibility (1/MPa)
$C_t$ :	Total compressibility (1/MPa)
$C_a$ :	Total storage coefficient
$O_{fi}$ :	Initial free oil volume ( $\text{m}^3$ )
$G_{fi}$ :	Initial free gas volume ( $\text{m}^3$ )
$W_{fi}$ :	Initial free water volume ( $\text{m}^3$ )

$r_e$ :	Drainage radius (m)
$r_w$ :	Wellbore radius (m)
$p_{wf}$ :	Flowing bottom hole pressure (MPa)
$p_{wb}$ :	Pressure of fluid in wellbore (MPa)
$\bar{p}$ :	Average reservoir pressure (MPa)
$p_i$ :	Initial reservoir pressure (MPa)
$N$ :	Production of fracturing fluid ( $\text{m}^3$ )
$X_e$ :	Horizontal well length (m)
$Y_e$ :	Fracture length (m)
$\phi_f$ :	Fracture bulk porosity (%)
$A_f$ :	Total surface area of modified crack system ( $\text{m}^2$ )
$S_f$ :	Fracture stiffness of shale (MPa/m)
$\omega$ :	Crack width ( $\mu\text{m}$ ).

## Subscripts

$w$ :	Water
$g$ :	Gas
$f$ :	Fracture
$m$ :	Matrix.

## Data Availability

The data used to support the findings of this study are inter-section within the article.

## Conflicts of Interest

The authors declare that there is no conflict of interests regarding the publication of this paper.

## Acknowledgments

This work was supported by the Chinese National Natural Science Foundation (No. 51774256 and No. 51974356).

## References

- [1] X. Zhao, L. H. Zhou, X. G. Pu et al., "Exploration breakthroughs and geological characteristics of continental shale oil: a case study of the Kongdian Formation in the Cangdong Sag, China," *Marine and Petroleum Geology*, vol. 102, pp. 544–556, 2019.
- [2] L. Y. Zhang, J. Y. Li, and Z. Li, "Continental basin in the key geological problems of shale oil exploration and development – a case study of Dongying sag," in *The Oil Shale Resources and Exploration and Development Technology International Symposium*, Wuxi, China, 2012.
- [3] L. J. Fan, L. J. J. Durlofsky, and H. A. A. Tchelepi, "Numerical simulation of the in-situ upgrading of oil shale," *SPE Journal*, vol. 15, no. 2, pp. 368–381, 2010.
- [4] W. Zhou, S. Gupta, R. Banerjee, B. Poe, J. Spath, and M. Thambynayagam, "Production forecasting and analysis for unconventional resources," in *International Petroleum Technology Conference*, Beijing, China, 2013.
- [5] C. Yang and J. Liu, "Petroleum rock mechanics: an area worthy of focus in geo-energy research," *Advances in Geo-Energy Research*, vol. 5, no. 4, pp. 351–352, 2021.




- [6] R. Heller, J. Vermynen, and M. Zoback, "Experimental investigation of matrix permeability of gas shales," *AAPG Bulletin*, vol. 98, no. 5, pp. 975–995, 2014.
- [7] K. Liu and M. Ostadhassan, "The impact of pore size distribution data presentation format on pore structure interpretation of shales," *Advances in Geo-Energy Research*, vol. 3, no. 2, pp. 187–197, 2019.
- [8] F. Javadpour, "Nanopores and apparent permeability of gas flow in mudrocks (shales and siltstone)," *Journal of Canadian Petroleum Technology*, vol. 48, no. 8, pp. 16–21, 2009.
- [9] P. A. Goode and F. J. Kuchuk, "Inflow performance of horizontal wells," *SPE Reservoir Engineering*, vol. 6, no. 3, pp. 319–323, 1991.
- [10] S. Al Rbeawi and D. Tiab, "Productivity index and inflow performance of hydraulically fractured formations," in *SPE Annual Technical Conference and Exhibition*, San Antonio, Texas, USA, October 2012.
- [11] Y.-L. Zhao, B.-C. Shan, L.-H. Zhang, and Q.-G. Liu, "Seepage flow behaviors of multi-stage fractured horizontal wells in arbitrary shaped shale gas reservoirs," *Journal of Geophysics and Engineering*, vol. 13, no. 5, pp. 674–689, 2016.
- [12] H. Tang, Z. Chai, B. Yan, and J. Killough, "Application of multi-segment well modeling to simulate well interference," in *SPE/AAPG/SEG Unconventional Resources Technology Conference*, Austin, Texas, USA, July 2017.
- [13] Z. Rui, J. Lu, Z. Zhang et al., "A quantitative oil and gas reservoir evaluation system for development," *Journal of Natural Gas Science and Engineering*, vol. 42, pp. 31–39, 2017.
- [14] C. Xiao, Y. Dai, L. Tian et al., "A semianalytical methodology for pressure-transient analysis of multiwell-pad-production scheme in shale gas reservoirs, part 1: new insights into flow regimes and multiwell interference," *SPE Journal*, vol. 23, no. 3, pp. 885–0905, 2018.
- [15] L. Jia, S. H. Cheng, S. Huang et al., "A comprehensive model combining Laplace-transform finite-difference and boundary-element method for the flow behavior of a two-zone system with discrete fracture network," *Journal of Hydrology*, vol. 551, pp. 453–469, 2017.
- [16] Y.-L. Zhao, L.-H. Zhang, J.-X. Luo, and B.-N. Zhang, "Performance of fractured horizontal well with stimulated reservoir volume in unconventional gas reservoir," *Journal of Hydrology*, vol. 512, pp. 447–456, 2014.
- [17] C. R. Clarkson, "Production data analysis of unconventional gas wells: review of theory and best practices," *International Journal of Coal Geology*, vol. 109–110, pp. 101–146, 2013.
- [18] B. Suliman, R. Meek, R. Hull, H. Bello, D. Portis, and P. Richmond, "Variable stimulated reservoir volume (SRV) simulation: eagle ford shale case study," in *SPE Unconventional Resources Conference-USA, Society of Petroleum Engineers*, The Woodlands, Tex, USA, 2013.
- [19] Z. Chen, X. Liao, X. Zhao, W. Yu, and K. Sepehrnoori, "A workflow based on a semianalytical model to estimate the properties of stimulated reservoir volume of tight-oil wells," *Journal of Petroleum Science and Engineering*, vol. 178, pp. 892–903, 2019.
- [20] D. Ilk, D. M. Anderson, G. W. J. Stotts, L. Mattar, and T. A. Blasingame, "Production-data analysis—challenges, pitfalls, diagnostics," *SPE Reservoir Evaluation & Engineering*, vol. 13, no. 3, pp. 538–552, 2010.
- [21] M. A. Abbasi, D. O. Ezulike, H. Dehghanpour, and R. V. Hawkes, "A comparative study of flowback rate and pressure transient behavior in multifractured horizontal wells completed in tight gas and oil reservoirs," *Journal of Natural Gas Science and Engineering*, vol. 17, no. 2, pp. 82–93, 2014.
- [22] J. W. Crafton, "Modeling flowback behavior or flowback equals "Slowback"," in *SPE Shale Gas Production Conference*, Fort Worth, Texas, USA, November 2008.
- [23] Y. Shen, H. Ge, X. Zhang, L. Chang, D. Liu, and J. Liu, "Impact of fracturing liquid absorption on the production and water-block unlocking for shale gas reservoir," *Advances in Geo-Energy Research*, vol. 2, no. 2, pp. 163–172, 2018.
- [24] O. D. Ezulike and H. Dehghanpour, "Modelling flowback as a transient two-phase depletion process," *Journal of Natural Gas Science and Engineering*, vol. 19, pp. 258–278, 2014.
- [25] T. Liang, L. Shao, E. Yao et al., "Study on fluid-rock interaction and reuse of flowback fluid for gel fracturing in desert area," *Geofluids*, vol. 2018, Article ID 8948961, 9 pages, 2018.
- [26] M. A. Abbasi, H. Dehghanpour, and R. V. Hawkes, "Flowback analysis for fracture characterization," in *SPE Canadian Unconventional Resources Conference*, Calgary, Alberta, Canada, October 2012.
- [27] C. R. Clarkson, F. Qanbari, J. D. Williams-Kovacs et al., "Fracture propagation, leakoff and flowback modeling for tight oil wells using the dynamic drainage area concept," in *SPE Western Regional Meeting*, Bakersfield, California, April 2017.
- [28] Y. Wu, L. Cheng, L. Ma et al., "A transient two-phase flow model for production prediction of tight gas wells with fracturing fluid-induced formation damage," *Journal of Petroleum Science and Engineering*, vol. 199, article 108351, 2021.
- [29] O. A. Adefidipe, H. Dehghanpour, and C. J. Virues, "Immediate gas production from shale gas wells: a two-phase flowback model," in *SPE Unconventional Resources Conference*, The Woodlands, Texas, USA, 2014.
- [30] Q. Chen, S. Wang, D. Zhu, G. Ren, Y. Zhang, and J. Hu, "A comprehensive model for estimating stimulated reservoir volume based on flowback data in shale gas reservoirs," *Geofluids*, vol. 2020, Article ID 8886988, 14 pages, 2020.
- [31] Y. Xu, O. Adefidipe, and H. Dehghanpour, "A flowing material balance equation for two-phase flowback analysis," *Journal of Petroleum Science and Engineering*, vol. 142, pp. 170–185, 2016.
- [32] Y. Xu, O. A. Adefidipe, and H. Dehghanpour, "Estimating fracture volume using flowback data from the Horn River Basin: a material balance approach," *Journal of Natural Gas Science and Engineering*, vol. 25, pp. 253–270, 2015.
- [33] Z. Chen, X. Liao, W. Yu, and X. Zhao, "Transient flow analysis in flowback period for shale reservoirs with complex fracture networks," *Journal of Petroleum Science and Engineering*, vol. 170, pp. 721–737, 2018.
- [34] F. Zhang and H. Emami-Meybodi, "Flowback fracture closure of multi-fractured horizontal wells in shale gas reservoirs," in *SPE/AAPG Eastern Regional Meeting*, Pittsburgh, Pennsylvania, USA, October 2018.
- [35] F. Zhang and H. Emami-Meybodi, "A semianalytical method for two-phase flowback rate-transient analysis in shale gas reservoirs," *SPE Journal*, vol. 25, no. 4, pp. 1599–1622, 2020.
- [36] C. R. Clarkson and J. D. Williams-Kovacs, "A new method for modeling multi-phase flowback of multi-fractures horizontal tight oil wells to determine hydraulic fracture properties," in *SPE Annual Technical Conference and Exhibition*, New Orleans, Louisiana, USA, October 2013.
- [37] C. R. Clarkson, F. Qanbari, and J. D. Williams-Kovacs, "Innovative use of rate-transient analysis methods to obtain

- hydraulic-fracture properties for low-permeability reservoirs exhibiting multiphase flow,” *Leading Edge*, vol. 33, no. 10, pp. 1108–1122, 2014.
- [38] Y. Xu, O. A. Adefidipe, and H. Dehghanpour, “Volumetric analysis of two-phase flowback data for fracture characterization,” in *SPE Western Regional Meeting*, Garden Grove, California, USA, April 2015.
- [39] P. Jia, L. Cheng, C. R. Clarkson, S. Huang, Y. Wu, and J. D. Williams-Kovacs, “A novel method for interpreting water data during flowback and early-time production of multi-fractured horizontal wells in shale reservoirs,” *International Journal of Coal Geology*, vol. 200, pp. 186–198, 2018.
- [40] D. O. Ezulike, H. Dehghanpour, and R. V. Hawkes, “Understanding flowback as a transient two-phase displacement process: an extension of the linear dual-porosity model,” in *SPE Unconventional Resources Conference*, Calgary, Alberta, Canada, November 2013.
- [41] M. R. Jones and T. A. Blasingame, “A direct method for short-term forecasting of multi-phase production rates using flowback data,” in *SPE/AAPG/SEG Unconventional Resources Technology Conference*, Denver, Colorado, USA, 2019.
- [42] M. Brown, E. Ozkan, R. Raghavan, and H. Kazemi, “Practical solutions for pressure-transient responses of fractured horizontal wells in unconventional shale reservoirs,” *SPE Reservoir Evaluation and Engineering*, vol. 14, no. 6, pp. 663–676, 2011.
- [43] Y. Fu, H. Dehghanpour, D. O. Ezulike, and R. S. Jones Jr., “Estimating effective fracture pore volume from flowback data and evaluating its relationship to design parameters of multistage-fracture completion,” *SPE Production & Operations*, vol. 32, no. 4, pp. 423–439, 2017.
- [44] Y. Fu, H. Dehghanpour, S. Motealleh, C. M. Lopez, and R. Hawkes, “Evaluating fracture volume loss during flowback and its relationship to choke size: fastback vs. slowback,” *SPE Production & Operations*, vol. 34, no. 3, pp. 615–624, 2019.
- [45] Y. Cho, O. G. Apaydin, and E. Ozkan, “Pressure-dependent natural-fracture permeability in shale and its effect on shale-gas well production,” *SPE Reservoir Evaluation & Engineering*, vol. 16, no. 2, pp. 216–228, 2013.



## Research Article

# Pore Structure and Connectivity of Mixed Siliciclastic-Carbonate Tight Reservoirs in the Palaeogene from Qaidam Basin, NW China

Xin Wang,<sup>1,2</sup> Jianhui Zeng<sup>1,2</sup>,, Kunyu Wu,<sup>3</sup> Xiangcheng Gao,<sup>4</sup> Yibo Qiu,<sup>4</sup> Tongzhi Lu,<sup>1,2</sup> Kunkun Jia,<sup>1,2</sup> Chen Zhang,<sup>1,2</sup> Juncheng Qiao,<sup>1,2</sup> Zixin Xue,<sup>1,2</sup> Qianyou Wang<sup>1,2</sup>,,  
and Xiangye Kong<sup>1,2</sup>,

<sup>1</sup>College of Geosciences, China University of Petroleum, Beijing 102249, China

<sup>2</sup>State Key Laboratory of Petroleum Resources and Prospecting, China University of Petroleum, Beijing 102249, China

<sup>3</sup>Qinghai Oil Field Company, CNPC, Dunhuang, Gansu 736202, China

<sup>4</sup>Exploration and Development Institute, Shengli Oilfield Company, SINOPEC, Dongying, Shandong 257015, China

<sup>5</sup>Department of Earth, Ocean, and Ecological Sciences, University of Liverpool, Liverpool L69 3GP, UK

Correspondence should be addressed to Jianhui Zeng; [zengjh@cup.edu.cn](mailto:zengjh@cup.edu.cn)

Received 8 July 2021; Revised 12 October 2021; Accepted 16 October 2021; Published 16 November 2021

Academic Editor: Afshin Davarpanah

Copyright © 2021 Xin Wang et al. This is an open access article distributed under the Creative Commons Attribution License, which permits unrestricted use, distribution, and reproduction in any medium, provided the original work is properly cited.

The pore structure and connectivity in petroleum reservoirs are controlled in part by their petrological properties. Mixed siliciclastic-carbonate rocks have complex compositions and heterogeneous spatial distributions of the various minerals. As a result, the study of the pore structure and connectivity of mixed siliciclastic-carbonate tight reservoirs has been limited. In this study, methods such as thin section microscopy, X-ray diffraction, X-ray computed tomography, low pressure N<sub>2</sub> adsorption, and spontaneous imbibition were adopted to comprehensively analyze the petrological properties, pore structure, and connectivity of the mixed siliciclastic-carbonate tight reservoirs in the upper member of the Xiaganchaigou Formation in the Yingxi Area, Qaidam Basin. The results showed that micrometer-sized pores in mixed siliciclastic-carbonate tight reservoirs are mainly dissolution pores, and that the spatial distribution of the pores is highly heterogeneous. The average pore radius range, average throat radius range, and average coordination number range of micronmeter-sized pores are 2.09~3.42 μm, 1.32~2.19 μm, and 0.48~1.49, respectively. Restricted by the concentrated distribution of local anhydrite, the connectivity of micronmeter-sized pores develops well only in the anhydrite, showing negligible contribution to the overall reservoir connectivity. In contrast, nanometer-sized pores in the mixed siliciclastic-carbonate tight reservoirs are mainly intercrystalline pores in dolomite. The range of nanometer-sized pores diameters is mainly distributed in 1.73-31.47 nm. The pores have a smooth surface, simple structure, and relatively homogeneous spatial distribution. The dissolution of dolomite intercrystalline pores by acidic fluids increases the connectivity of the nanometer-sized pores. This paper presents genetic models for microscopic pore structures and connectivity of mixed siliciclastic-carbonate rocks, making possible the evaluation on the quality of the mixed siliciclastic-carbonate tight reservoirs.

## 1. Introduction

Mixed siliciclastic-carbonate deposits are defined as sediments consisting of both extrabasinal (e.g., epiclastic or terrigenous) and intrabasinal (autochthonous to parautochthonous) components, and they are an important type of continental sedimentary facies [1-3]. The sedimentary

texture and mineral composition of mixed siliciclastic-carbonate tight reservoirs are by definition more varied than pure sandstones and carbonates [3-5]. There are 1.454 billion tons of recoverable oil in tight reservoirs in China, with more than 40% in mixed siliciclastic-carbonate tight reservoirs [2]. The huge resource potential has result in studies of the classification, depositional setting, and heterogeneity

of the mixed siliciclastic-carbonate rocks [6–13]. So far, many breakthroughs have been made on the classification and depositional setting of mixed siliciclastic-carbonate rocks [5, 9, 10, 12]. However, understanding the pore structure and connectivity of mixed siliciclastic-carbonate tight reservoirs, and the associated key controlling factors, is still lacking [14, 15].

Pore structure and pore connectivity are two important factors influencing the storage and flow capacity of tight reservoirs [16–19]. There have been numerous theoretical research on the micro- and nanometer-sized pore structures of tight sandstone reservoirs [18–22]. Due to effects caused by compaction and diagenesis, tight sandstone reservoirs are frequently featured by broad pore-sized distributions [17, 23], ranging from a few nanometers to tens of micrometer, in addition to complex pore structures and poor pore throat connectivity [23–26]. In contrast, there are few studies of pore structure and connectivity mixed siliciclastic-carbonate tight reservoirs with complicated mineral compositions and diversified sedimentary textures. Determining the pore structures and their connectivity, as well as the intrinsic relationship between both the aspects of mixed siliciclastic-carbonate tight reservoirs, is key to understanding the heterogeneity in reservoirs quality.

The Yingxiongling Tectonic Belt is located in the western part of the Chaixi Depression in the Qaidam Basin. The petroleum resources are estimated to be 1.9 billion tons [27]. The cumulative proven petroleum reserves in the belt are ~500 million tons, accounting for 60% of the total reserves in the Qaidam Basin [27]. Mixed siliciclastic-carbonate tight reservoirs are characterized by complex mineral compositions, heterogeneity, which hampers the efficient development of these reservoirs [27]. In this study, thin section microscopy, X-ray diffraction, X-ray computed tomography, low pressure  $N_2$  adsorption, and spontaneous inhibition were used to study the petrological properties, pore structure, and connectivity in the mixed siliciclastic-carbonate tight reservoirs of the upper member of the Xia-ganchaigou Formation ( $E_3^2$ ) in the Yingxi Area. Finally, a genetic model for the pore structure and connectivity at micrometer and nanometer scales has been established. This study provides a scientific basis for the evaluation of mixed siliciclastic-carbonate reservoirs.

## 2. Geological Settings

The Yingxi area is located in the western part of the Chaixi Depression in the Qaidam Basin (Figure 1(a)). Since the Cenozoic, the basin has been compressed from two directions by the Altun Mountain and the Kunlun Mountain, experiencing three stages of tectonic evolution in the process. This resulted in the formations of well-developed faults in the area and various other complex tectonic styles, such as Shizigou-Huatugou and Youyuanou, giving birth to a diverse tectonic framework altogether (Figure 1(b)) [28, 29]. The sedimentary process has been controlled by the process of regional tectonic evolution [30]. Under the arid paleoclimate, the depositional setting of the  $E_3^2$  member underwent an initial salinization stage, the main salinization

stage, and finally saline lake stage, successively (Figure 1(c)) [31, 32]. At the initial salinization stage, the basin formed a moderate-to-deep water depth lacustrine sedimentary environment. This was the stage where the main source rocks developed. At the intermediate stage, a saline lacustrine sedimentary environment dominated; as a result of a general decrease in sedimentation rates together with increased evaporation, the lake salinity generally increased, while the water depth changed from shallow nearshore to moderate-depth in a high-frequency oscillatory trend, combining into a considerably intensified development period for mixed siliciclastic-carbonate reservoirs. Finally, saline lake development, which featured the least active rate of supply from the sources and increased evaporation, leads to the sedimentary recycling characterized by the evaporation of lake water and drying out of the lake.

## 3. Samples and Methods

**3.1. Samples and Sample Preparation.** Eight samples of the mixed siliciclastic-carbonate rocks were collected from core taken from wells S220 and S41-6-1 in the upper member of Palaeogene Ganchaigou Formation. The sample number and the corresponding depths are shown in Table 1. Standard samples (cylinders with a length of 5 cm and a diameter of 2.5 cm) were drilled in the core. Afterwards, the samples were washed to remove residual oil in the standard samples, after which the samples were dried at 120°C for 24 h. Sample preparation is performed in the State Key Laboratory of China University of Petroleum (Beijing).

**3.2. Thin Section Microscopy.** 2 mm slices were cut from the top of each standard samples and ground into 0.3 mm sized thin section. The thin section was then impregnated under vacuum with blue epoxy to highlight the pore spaces. In addition, half of each thin section was stained with alizarin red S and K-ferricyanide to identify carbonate cementation. The samples were then observed with ZEISS Axioskop 40 optical microscope in the State Key Laboratory of China University of Petroleum (Beijing) under reflected light and transmitted light (polarized light), in order to determine the clastic constituents and structure, as well as the type of cement in the reservoir [17]. The detailed information of samples are list in Table 1.

**3.3. X-Ray Diffraction (XRD).** A chip of about 5 g was taken from each sample and then crushed to particles about 48  $\mu\text{m}$ . At room temperature (25°C), XRD analysis was performed with an Ultima IV automatic XRD analyzer (Rigaku, Tokyo, Japan) in the State Key Laboratory of China University of Petroleum (Beijing). The Joint Committee on Powder Diffraction Standards, International Diffraction Data Center (JCPDS-ICDD) was founded in 1941 to produce a primary reference of X-ray powder diffraction data. During the experiment, the X-ray diffraction spectrum mainly refers to the database from JCPDS-ICDD to identify the mineral components in the mixed siliciclastic-carbonate rocks. The detailed information of samples are list in Table 1.

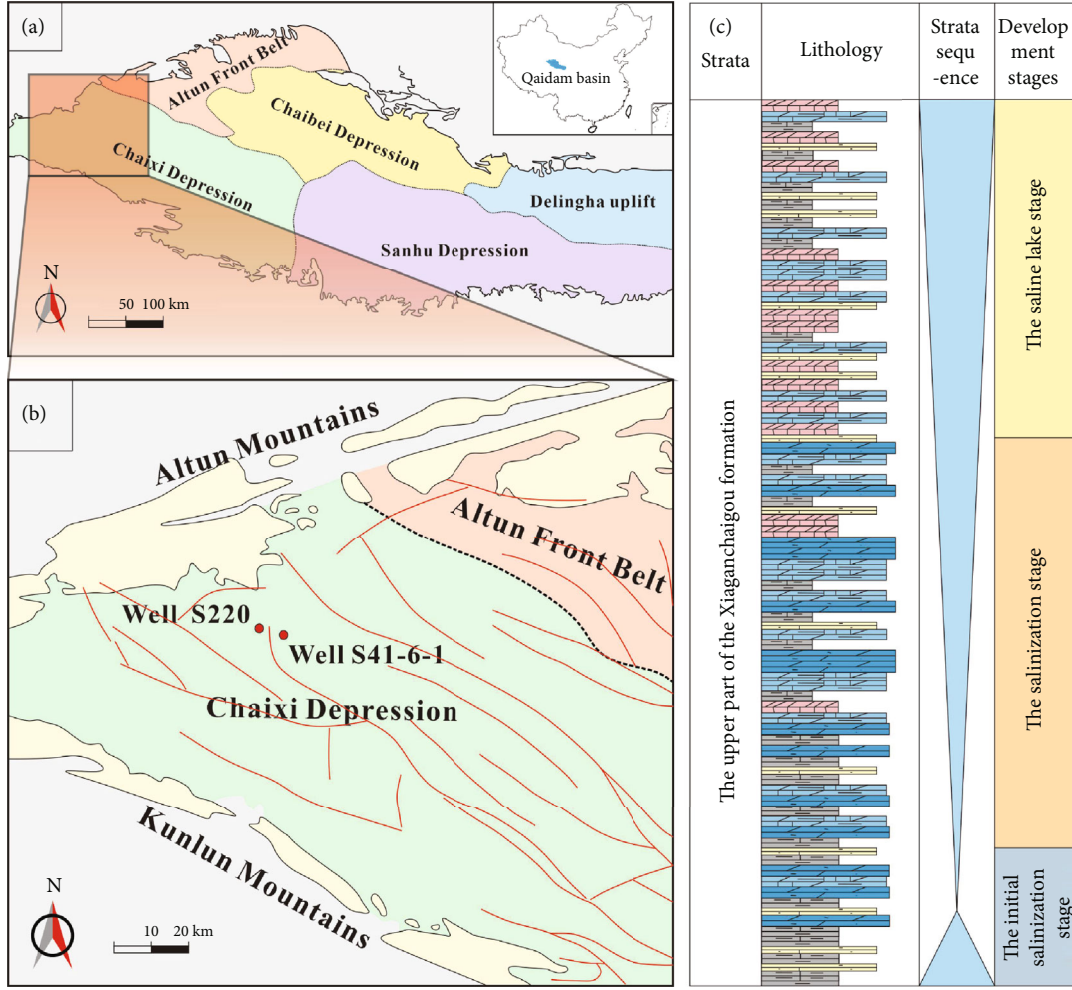


FIGURE 1: (a) Map showing the tectonic subdivisions of the Qaidam Basin in the northwestern China and the location of research area (indicated by the box). (b) Map showing the location and Chaixi Depression and targeted boreholes. (c) Vertical profile of the Upper member of Palaeogene Xiaganchaigou Formation showing lithology and sequences.

TABLE 1: Details of tight reservoir samples collected from the  $E_3^2$  member of Xiaganchaigou Formation, Qaidam Basin.

Sample ID	Well ID	Formation	Reservoir type	Depth (m)
MSCSs-1	S41-6-1	$E_3^2$	LDR	3863.11
MSCSs-2	S41-6-1	$E_3^2$	LDR	3862.22
MSCSs-3	S41-6-1	$E_3^2$	LDR	3863.26
MSCSs-4	S220	$E_3^2$	LDR	4309.97
MSCSs-5	S41-6-1	$E_3^2$	SCR	3864.81
MSCSs-6	S220	$E_3^2$	SCR	3944.24
MSCSs-7	S220	$E_3^2$	MSCR	4317.26
MSCSs-8	S220	$E_3^2$	MSCR	4312.14

LDR: rocks containing more than 50% carbonate minerals; SCR: rocks containing more than 50% siliceous clastic minerals; MSCR: rocks containing less than 50% of any mineral.

3.4. X-Ray Computed Tomography (CT). A cylindrical sample with a diameter of 0.25 cm was drilled from each standard sample. Zeiss Xradia Versa-510 micro-CT in the State Key Laboratory of China University of Petroleum (Beijing)

was used to scan the sample at a scan resolution of  $1 \mu\text{m}$ . The scan voltage and current were set to 120 keV and  $10 \mu\text{A}$ , respectively, to ensure good X-ray penetration. 991 two-dimensional (2D) tomographic images were obtained via CT scan per sample, and these were reconstructed into three-dimensional (3D) gray images using a back projection algorithm [33–35]. The pore network model (PNM) established based on a maximum spherical algorithm was coupled with Avizo Software Kit to perform grayscale segmentation of the reconstructed images [33–35]. The pore system was differentiated from the rock matrix based on the difference in X-ray attenuation observed from the penetration of materials with varying densities [36]. Finally, the number, volume, and radius of pores and throats could be obtained from the recorded statistics [37]. The detailed information of samples are list in Table 1.

3.5. Low Pressure  $N_2$  Adsorption. About 1~2 g of powder sample ( $187.5 \mu\text{m}$ ) was prepared from the standard core. The sample was degassed at  $110^\circ\text{C}$  under a vacuum for about 14 h to remove the adsorbed moisture and volatile substances. A Micromeritics® Tristar II 3020 surface area

analyzer in the State Key Laboratory of China University of Petroleum (Beijing) was used for low pressure ( $<0.127$  MPa)  $N_2$  adsorption analysis. The relative pressure ( $P/P_0$ ) range of  $N_2$  adsorption was set to 0.001 to 0.995. The adsorption isotherm curve was then automatically generated using the built-in device software based on the desired adsorption theories [38–41]. In addition, the surface area, pore volume, and pore size distribution were calculated [17, 42]. The detailed information of samples are list in Table 1.

**3.6. Spontaneous Imbibition (SI).** SI is a capillary force controlled process, in which the nonwetting phase is spontaneously displaced by the wetting phase only via capillary suction. A cube with a side length of 1 cm was prepared from the standard sample. Afterwards, all sides (except for the top and the bottom) were coated with fast curing clear epoxy resin to generate absorption only in a vertical direction. Water and n-decane were used to displace the nonwetting phase air. In order to ensure that a sample was at irreducible water saturation initially, all samples were dried at  $60^\circ\text{C}$  ( $140^\circ\text{F}$ ) for at least 48 h, after which the imbibition experiment was carried out. SI analyzer was used for spontaneous imbibition experiments in the State Key Laboratory of China University of Petroleum (Beijing). The schematic diagram, experimental procedure, and data processing method of the SI experiment were as described in detail by Gao and Hu [43]. The detailed information of samples are list in Table 1.

## 4. Results

### 4.1. Petrologic Properties and Classification of Mixed Siliciclastic-Carbonate Tight Reservoirs

**4.1.1. Petrologic Properties.** The XRD data for the samples (Figure 2) show that the minerals found in the eight samples are mainly siliceous clastic minerals (quartz, potassium feldspar, plagioclase), carbonate minerals (calcite, iron dolomite, dolomite), sulfate minerals (gypsum, glauberite, anhydrite), clay minerals, a small amount of other minerals (pyrite, stone salt, and siderite), etc. The samples can be generally characterized by the presence of significant differences in the contents of various mineral types, as well as the significant discrepancies in the contents of the same mineral in different samples (Figure 2). The distribution of mineral types is also complex, highlighting the characteristic of mixed siliciclastic-carbonate deposition as a whole. Microscopically, anhydrite was cemented severely, but the inner of anhydrite was obviously dissolved (Figures 3(a) and 3(b)). Dolomite minerals were mainly structurally composed of micrite or microcrystals and were mixed with siliceous clastic particles (Figures 3(c) and 3(d)).

**4.1.2. Classification of Mixed Siliciclastic-Carbonate Tight Reservoirs.** Based on the relative minerals contents (clay, carbonate, siliciclastic, and sulfate minerals), the samples are classified into three types (siliceous clastic rocks, lime-dolostone rocks, mixed siliciclastic-carbonate rocks) [5, 44]. Rocks with a relative content of terrestrial clastic minerals greater than 50% are defined as siliceous clastic rocks

(SCR), while those that hold more than 50% of carbonate are called lime-dolostone rocks (LDR). Rocks with minerals relative content of each type below 50% are called mixed siliciclastic-carbonate rocks (MSCR). Reservoir classification is shown in Table 1.

### 4.2. Pore Structure and Connectivity of Mixed Siliciclastic-Carbonate Tight Reservoirs

**4.2.1. Characterization of Connectivity and Pore Structures by CT.** The eight samples were scanned by CT. The images of 3D pore throat spatial distribution and the PNM of the pore system in the mixed siliciclastic-carbonate tight reservoirs obtained from the grayscale segmentation processing are shown in Figure 4. The images of 3D pore throat spatial distribution were then superimposed and marked with colors. The pore sizes and connectivity of each sample can be directly observed (Figure 4). In adjacent regions, the same color means implies connected pores, while different colors indicate isolated or disconnected pores [37]. It is lesser that the volume covered by the pores of the same color (Figures 4(a), 4(c), 4(e), 4(g), 4(i), 4(k), 4(m), and 4(o)). The overall connectivity of the pore system is poorer. However, in areas where pores are locally concentrated, the connectivity of the local pore system is the better (Figures 4(a), 4(c), 4(e), 4(g), 4(i), 4(k), 4(m), and 4(o)). Furthermore, significant differences in the spatial distribution of the pore system were also found in the three types of the mixed siliciclastic-carbonate tight reservoirs. The spatial distribution of pore of lime-dolostone tight reservoirs is relatively homogeneous (Figures 4(a)–4(h)), while the heterogeneities of the spatial distributions of pore in the tight reservoirs of siliceous clastic rocks (Figures 4(i)–4(l)) and mixed siliciclastic-carbonate rocks (Figures 4(m)–4(p)) are high.

The distribution of the pore and throat radius of the eight samples calculated with the PNM [33–35] is shown in Figure 5 and Table 2. The X ray CT method could not characterize the nanometer-sized pores due to resolution limitations. The pore radius values fall between 1 and  $40\ \mu\text{m}$ , while the throat radius values plot in the range of  $1\sim 25\ \mu\text{m}$ . The pore radius in Figure 5(a) shows two overlapping peaks. The first peak is between  $3.5$  and  $5\ \mu\text{m}$ . These pores make up the main micrometer scale pore space in the mixed siliciclastic-carbonate tight reservoirs. The second peak is between  $7.5$  and  $9\ \mu\text{m}$ . The throat radius peaks are concentrated between  $4$  and  $5\ \mu\text{m}$  (Figure 5(b)). Different types of tight reservoirs also present similar pores and throat combination characteristics. The average pore radius range, average throat radius range, and average coordination number range are  $2.09\sim 3.42\ \mu\text{m}$ ,  $1.32\sim 2.19\ \mu\text{m}$ , and  $0.48\sim 1.49$ , respectively (Table 2).

**4.2.2. Characterization of Pore Structure by  $N_2$  Adsorption.** Nanopore that cannot be determined by X-ray micro-CT can be measured by the nitrogen adsorption method [17]. The nanopore size distribution curves of the eight samples are shown in Figure 6. These curves were derived using the BJH model [39, 40]. Significant differences in pore size distributions as a function of lithology can be observed. The

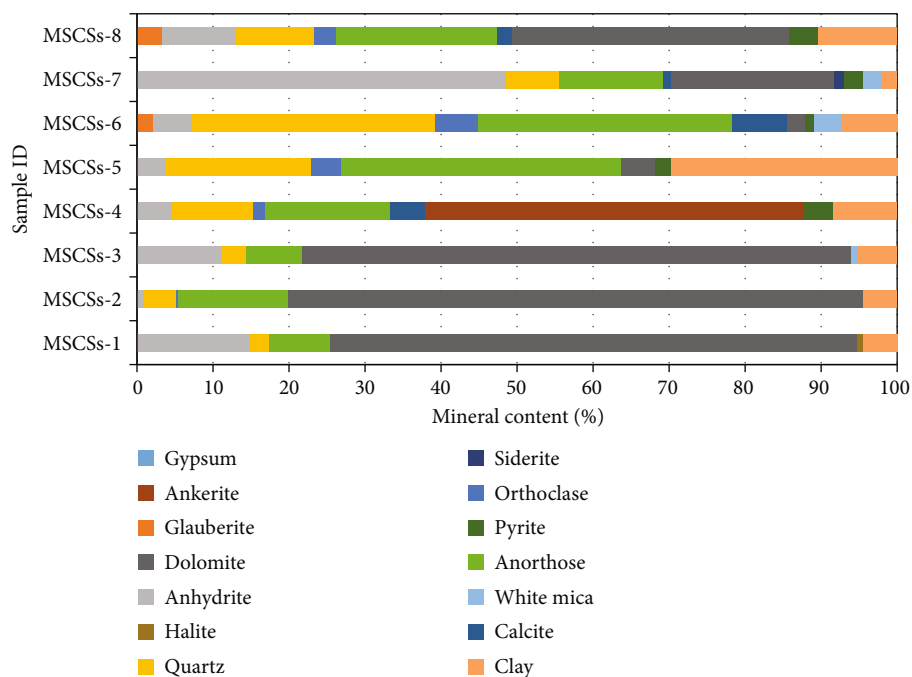


FIGURE 2: Mineral composition of the eight samples collected from the E<sub>3</sub><sup>2</sup> member of the Xiaganchaigou Formation.

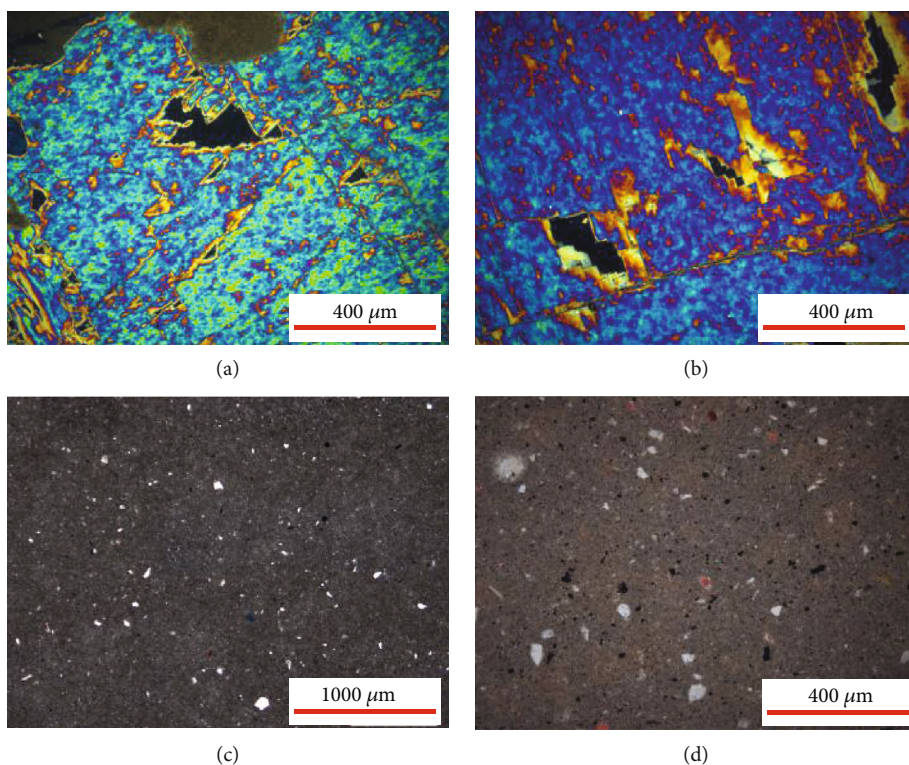


FIGURE 3: Microscopic observation of the Palaeogene Xiaganchaigou Formation samples from Qaidam Basin. Massive development of gypsum cements and remaining of numerous microscale dissolution pores: (a) 4312.14 m and (b) 4317.26 m. Mixed sedimentation of micrite or microcrystal dolomite and siliceous clastic particles: (c) 3864.81 m and (d) 3863.11 m.

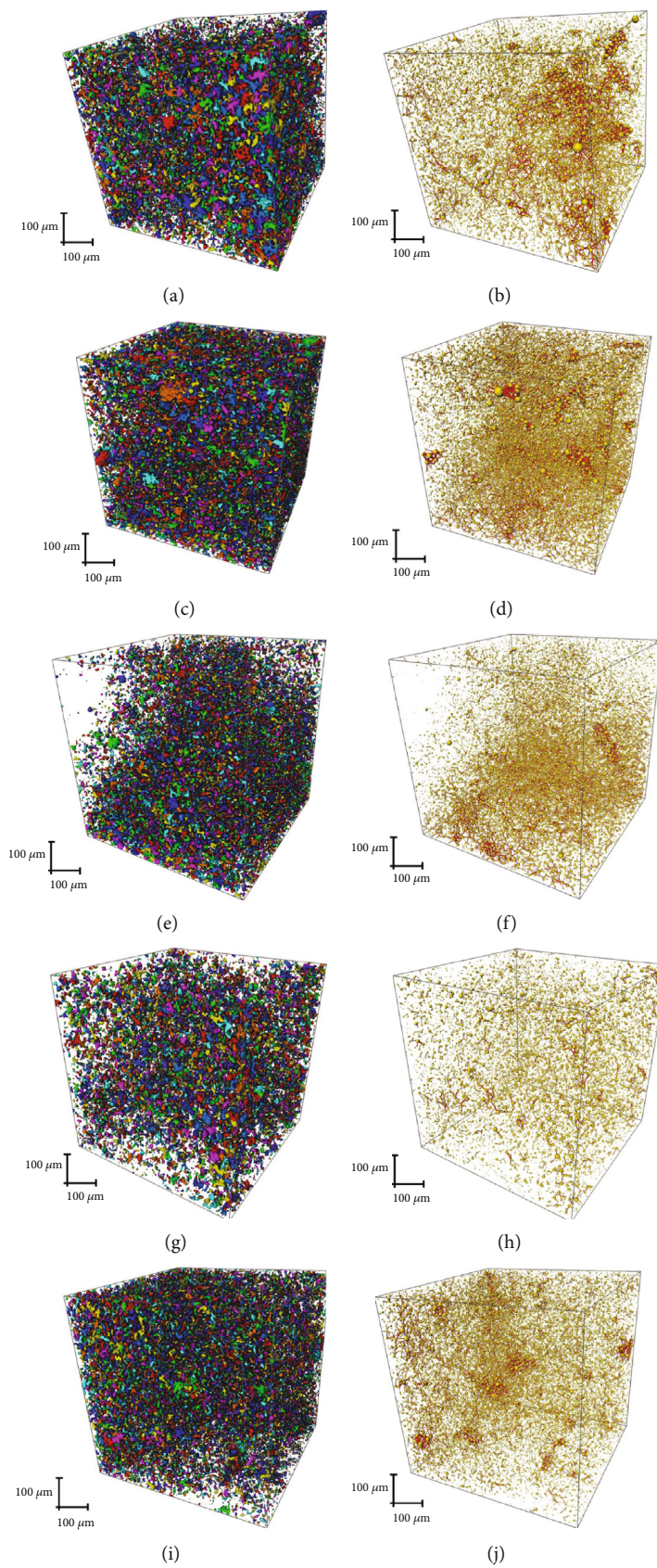


FIGURE 4: Continued.

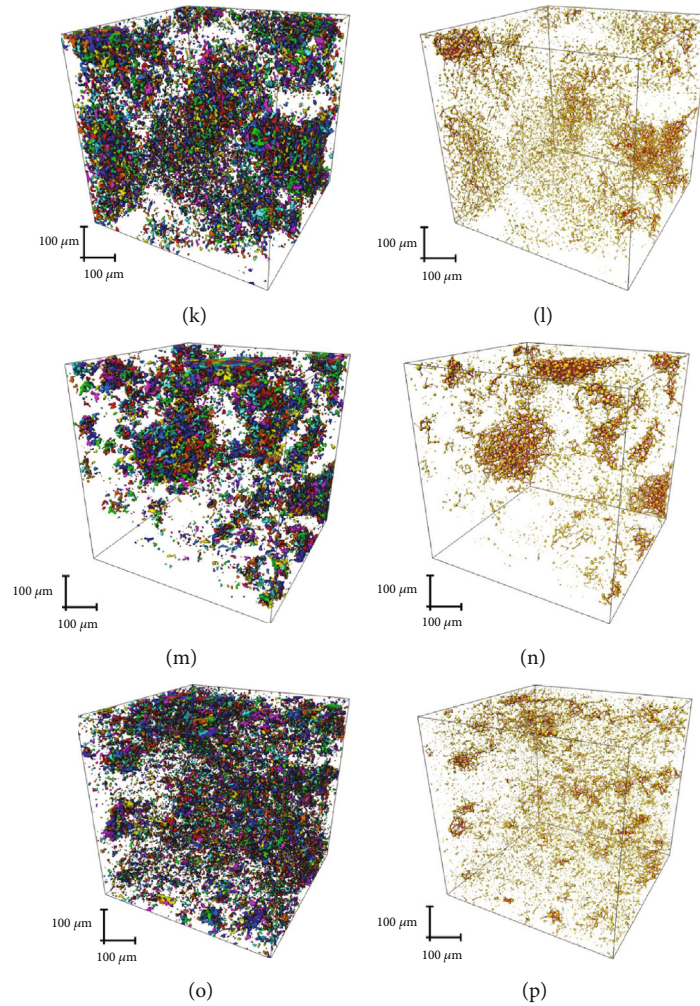


FIGURE 4: 3D micro-CT imaging on the pore throat networks of tight reservoir samples from the Upper member of Palaeogene Xiaganchaigou Formation, Qaidam Basin. (a) MSCSs-1. (b) MSCSs-1. (c) MSCSs-2. (d) MSCSs-2. (e) MSCSs-3. (f) MSCSs-3. (g) MSCSs-4. (g) MSCSs-4. (i) MSCSs-5. (j) MSCSs-5. (k) MSCSs-6. (l) MSCSs-6. (m) MSCSs-7. (n) MSCSs-7. (o) MSCSs-8. (p) MSCSs-8.

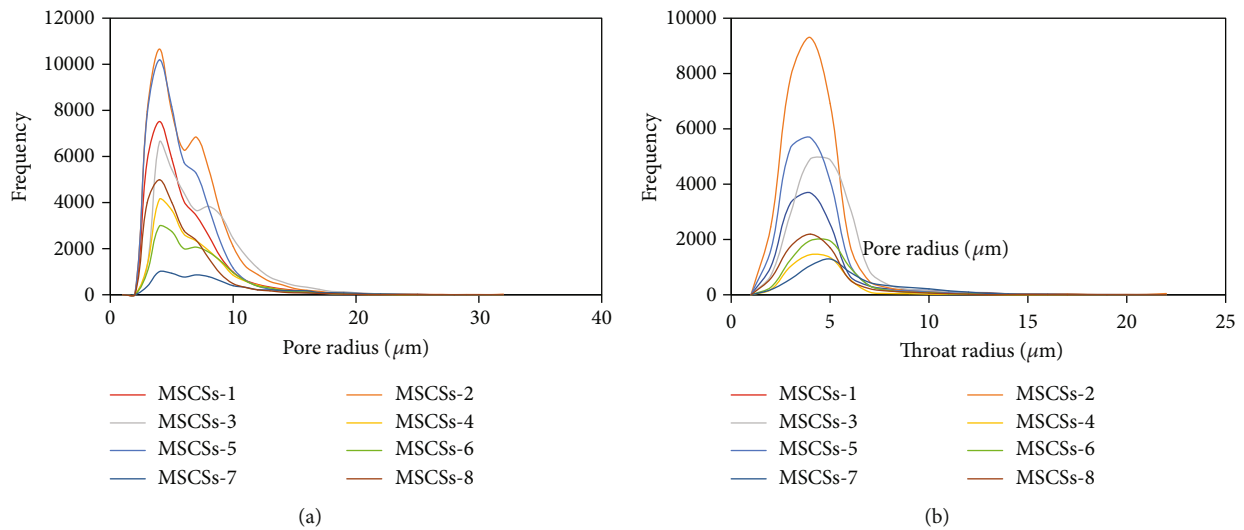


FIGURE 5: Pore throat size distribution of tight reservoir samples from the upper member of Palaeogene Xiaganchaigou Formation, Qaidam Basin.

TABLE 2: Pore structure parameters of the Palaeogene Xiaganchaigou Formation samples measured by 3D micro-CT imaging.

Sample ID	Reservoir type	Average pore radius ( $\mu\text{m}$ )	Average throat radius ( $\mu\text{m}$ )	Average coordination number
MSCSs-1	LDR	2.225	1.522	0.733
MSCSs-2	LDR	2.384	1.367	1.086
MSCSs-3	LDR	2.948	1.651	0.998
MSCSs-4	LDR	2.570	1.486	0.477
MSCSs-5	SCR	2.091	1.320	0.813
MSCSs-6	SCR	2.752	1.629	0.845
MSCSs-7	MSCR	3.420	2.190	1.485
MSCSs-8	MSCR	2.089	1.435	0.663

range of pore diameters is 2-100 nm, while the pore diameter distributions of most samples show a bimodal pattern (Figures 6(a), 6(d), and 6(e)–6(h)). The first peak appears between 1.73 and 3.07 nm and the other between 5.61 and 31.47 nm. The distribution curves of the pore size of the remaining samples show a unimodal pattern (Figures 6(b) and 6(c)), with peaks tending to occur between 2.7027 and 2.8617 nm.

The fractal fitted curves of the eight samples can be divided into two different linear segments, corresponding to relative pressures ( $P/P_0$ ) of 0-0.45 and 0.45-1 (Figure 7). Satisfactory linear correlation between segments indicates that the two segments have different gas adsorption behaviors. Therefore, considering the differences in the gas adsorption behavior, the fractal dimensions should also be separately defined in two parts [42]. At the low pressure segment ( $P/P_0=0-0.45$ ), van der Waals' force is the main force of gas adsorption responsible for the monolayer adsorption. At this point, the fractal dimension can describe the fractal characteristics of pore surface expressed as  $D_1$  [38–40]. As the pressure increases ( $P/P_0=0.45-1$ ), the gas adsorption is transformed into multilayer adsorption mainly via capillary condensation. At this point, the fractal dimension can describe the fractal characteristics of pore structure expressed as  $D_2$  [38–40].

As shown in Table 3, the BJH total pore volume (BJH TPV), BJH average pore diameter (BJH APD), and fractal dimensions ( $D_1$  and  $D_2$ ) have been obtained from the low pressure  $N_2$  adsorption isotherms analysis. LDR samples have relatively higher values of BJH TPV and  $D_1$ . BJH TPV falls within the range of 0.003533~0.020521  $\text{cm}^3/(\text{g}\cdot\text{nm})$ , averaging 0.011569  $\text{cm}^3/(\text{g}\cdot\text{nm})$ , while BJH APD falls between 18.6645 and 21.8562 nm, averaging 20.3105 nm.  $D_1$  is within the range 2.4274~2.5537, averaging 2.5084, while  $D_2$  is within the range

of 2.2331~2.5073, averaging 2.4149. The SCR samples have relatively higher BJH APD and lower BJH TPV values. The MSCR samples have relatively higher value of  $D_2$ .

4.2.3. *Characterization of Connectivity of Micronano Pores by SI.* The SI experiments use water and n-decane and showed that samples were unstable when they settled into the fluid in the first 30 seconds or so, resulting in fluctuations in weight (Figure 8). After the initial stage of instability, the cumulative height of the fluid imbibed was linearly proportional to the time (Figure 8). The gradient of the logarithmic relationship between the cumulative SI height and the time is shown in Table 4, and this represents the connectivity of hydrophilic (from the water experiments) and lipophilic (from the n-decane experiments) pores. According to the Handy equation and imbibition theory [45, 46], if an imbibition slope of 0.5 is obtained, porous media have in theory good pore connectivity for the fluid used, while lower slopes (<0.5) may indicate a low pore connectivity to the fluid [43].

The slope for imbibition of n-decane is always greater than that for water, indicating that the connectivity of oil-wetting pores in the samples is superior to that of hydrophilic pores. For the four LDR samples with relatively higher content of carbonate minerals, the spontaneous imbibition slope of n-decane is greater than the theoretical value 0.5, with a mean of 0.583, indicating that the connectivity of oil-wetting pores is good. For the SCR and MSCR samples with relatively lower content of carbonate minerals, the average value of the slope of n-decane is 0.49 and 0.47, respectively, both of which are close to the theoretical value 0.5. Although the spontaneous imbibition slope is lower than that in LDR samples, it also shows favorable connectivity of oil-wetting pores. The connectivity of hydrophilic pores varies widely among different types of samples for all samples. The connectivity of hydrophilic pores in LDR samples is low, showing range of values from 0.242 to 0.394. There is a great difference in the connectivity of hydrophilic pores in SCR and MSCR samples, with slope values of 0.255 and 0.476 and 0.164 and 0.423, respectively.

## 5. Discussion

5.1. *The Influence of Mineral Composition on the Structure and Connectivity of Micrometer Scale Pores in Mixed Siliciclastic-Carbonate Tight Reservoirs.* At the penecontemporaneous stage, part of the  $E_3^2$  stratum is above water and is affected by the leaching of atmospheric fresh water [47]. Since the Yingxi Area is the  $\text{CaCO}_3$ - $\text{CaSO}_4$ - $\text{H}_2\text{O}$ - $\text{CO}_2$  diagenetic system, the atmospheric fresh water demonstrated higher proclivity to dissolve gypsum cements or crystals to form dissolution pores [47, 48]. At the diagenetic stage, the gypsum gradually dehydrated into anhydrite [47, 49]. Afterwards, the dissolution pores formed at the penecontemporaneous stage were retained in anhydrite minerals (Figures 3(a) and 3(b)). As a result, the higher the anhydrite content, the greater the average pore radius, average throat radius, and coordination number (Figures 9(a), 9(d), and 9(g)). Therefore, the dissolution and dehydration conversion



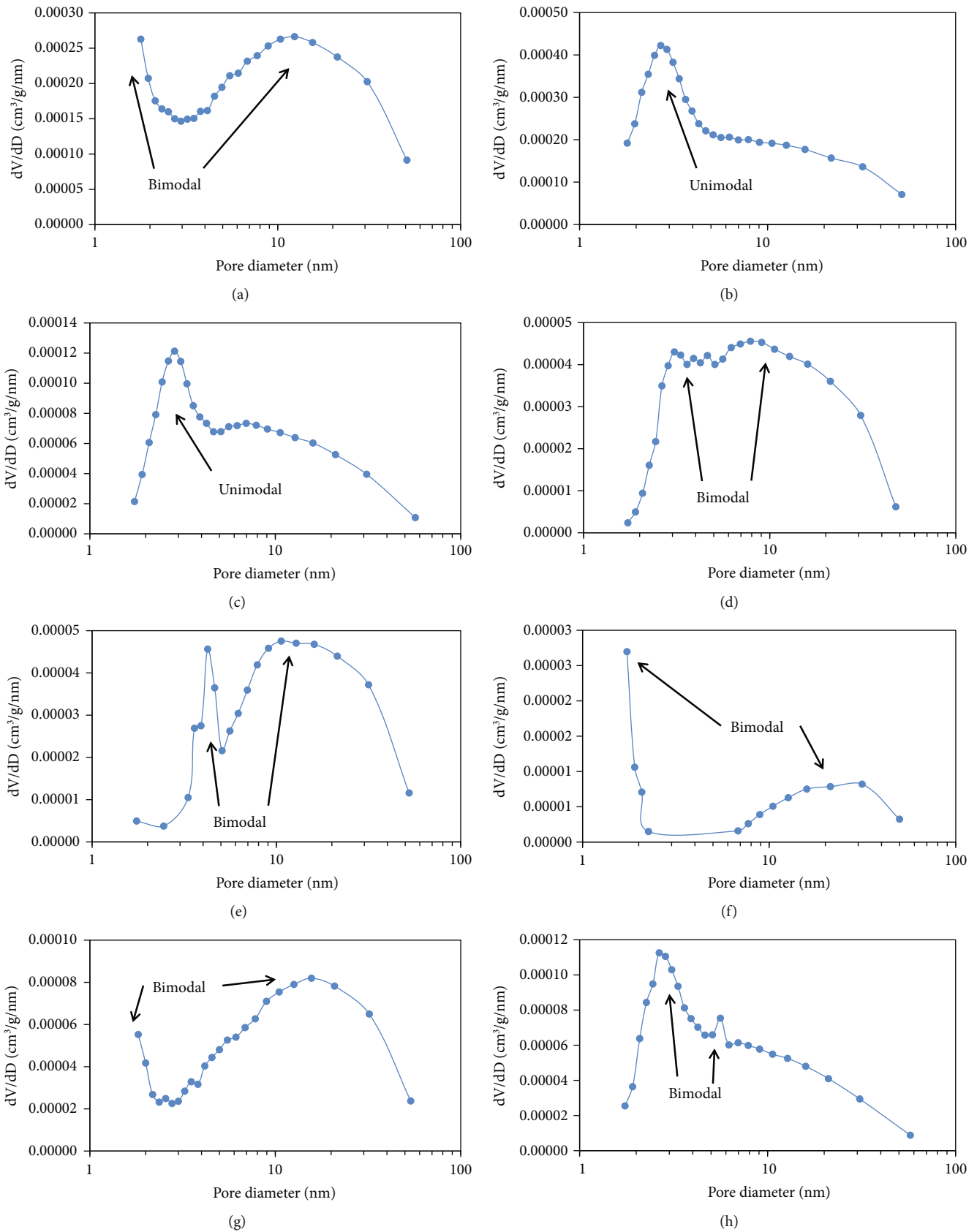


FIGURE 6: Pore-sized distribution of tight reservoir samples from the Palaeogene Xiaganchaigou Formation samples measured by low pressure N<sub>2</sub> adsorption. (a) MSCSs-1. (b) MSCSs-2. (c) MSCSs-3. (d) MSCSs-4. (e) MSCSs-5. (f) MSCSs-6. (g) MSCSs-7. (h) MSCSs-8.

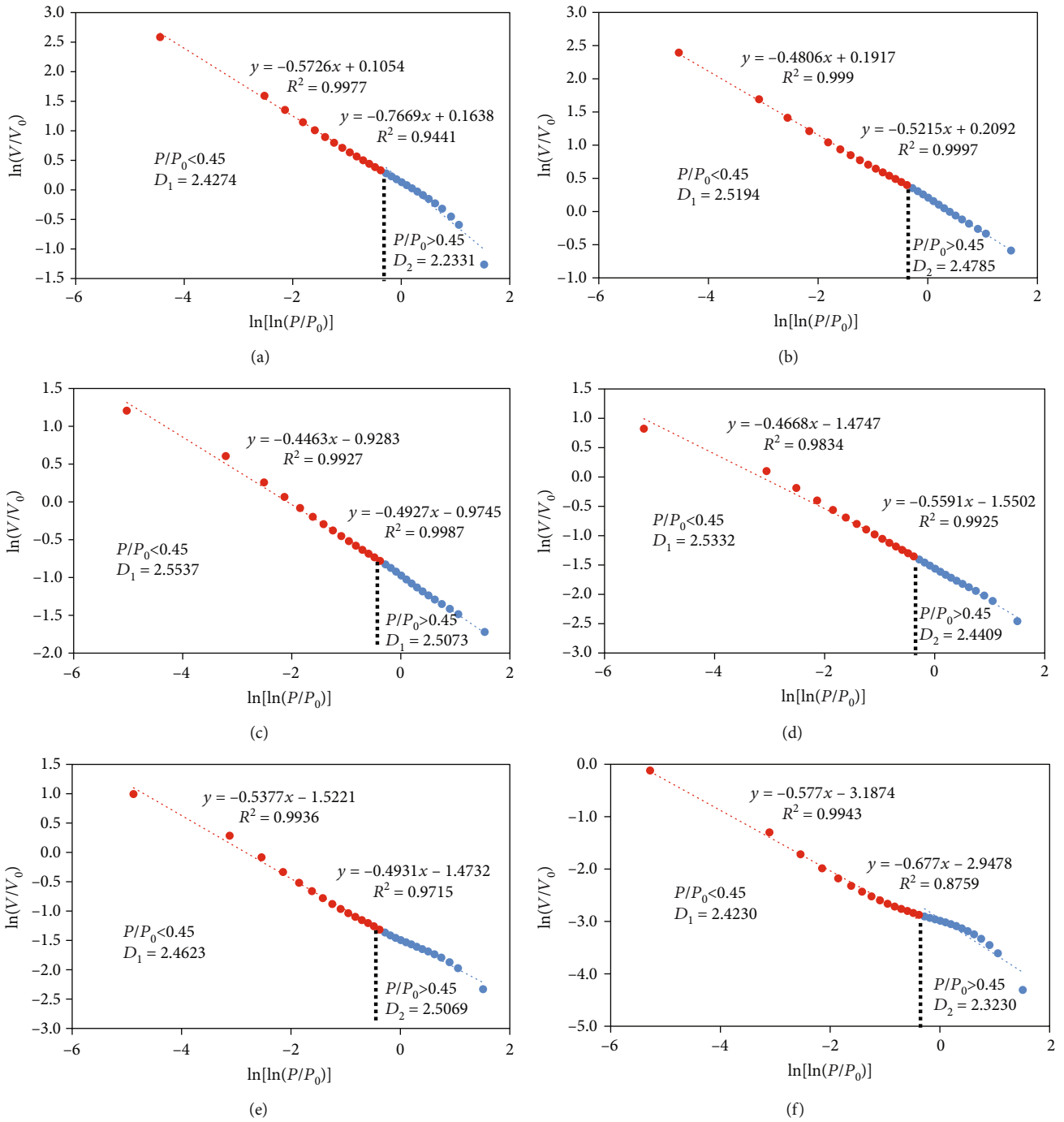


FIGURE 7: Continued.

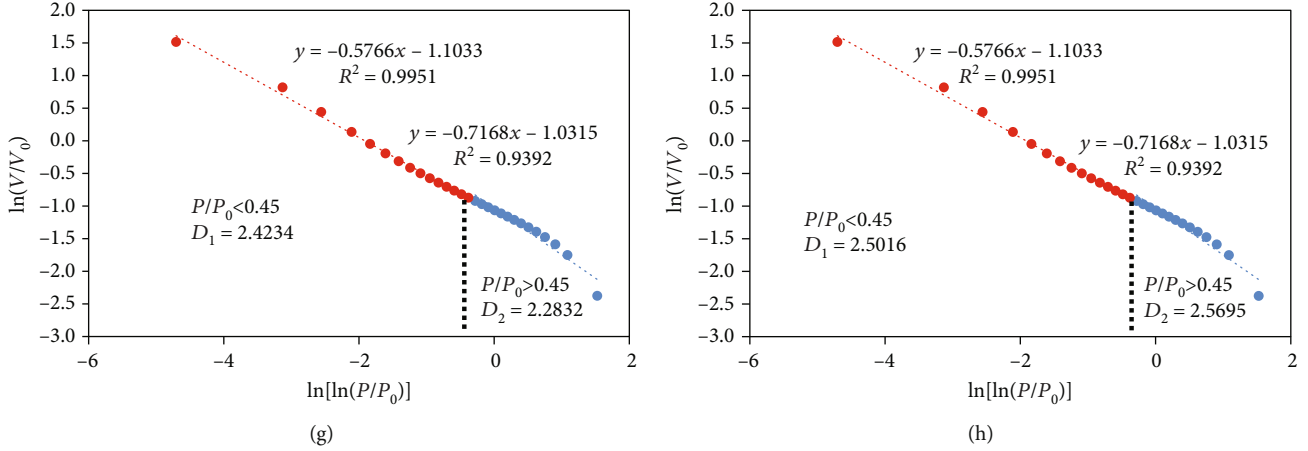


FIGURE 7: Pore fractal characteristics of the eight samples. (a) MSCSs-1. (b) MSCSs-2. (c) MSCSs-3. (d) MSCSs-4. (e) MSCSs-5. (f) MSCSs-6. (g) MSCSs-7. (h) MSCSs-8.

TABLE 3: Pore structure parameters of the eight samples measured by low pressure N<sub>2</sub> adsorption.

Sample ID	Reservoir type	BJH TPV (cm <sup>3</sup> /g)	BJH APD (nm)	D <sub>1</sub>	D <sub>2</sub>
MSCSs-1	LDR	0.020521	21.856200	2.4274	2.2331
MSCSs-2	LDR	0.017060	18.664500	2.5194	2.4785
MSCSs-3	LDR	0.005161	18.894500	2.5537	2.5073
MSCSs-4	LDR	0.003533	21.826900	2.5332	2.4409
MSCSs-5	SCR	0.004156	26.547600	2.4623	2.5069
MSCSs-6	SCR	0.001375	34.995100	2.4230	2.3230
MSCSs-7	MSCR	0.007042	25.639500	2.4234	2.2832
MSCSs-8	MSCR	0.003725	16.384000	2.5016	2.5695

of gypsum are the main contributors of micronmeter-sized pores and throats. Nevertheless, the contribution of the pore and throat system in the anhydrite to the reservoir is extremely limited. On the one hand, as restricted by the spatial distribution of anhydrite, the spatial distribution of pores in mixed siliciclastic-carbonate tight reservoirs with relatively developed anhydrite is highly heterogeneous (Figures 4(m)–4(p)); on the other hand, the cementation of anhydrite at the diagenetic stage blocks the connection between the pore network in anhydrite and the outside world. As a result, numerous developed connected pores in anhydrite minerals fail to improve the overall connectivity in the reservoir. Clay minerals are common cements and interstitial materials in reservoirs and often block reservoir space [50]. Accordingly, the higher the content of clay minerals, the smaller the average pore radius, the average throat

radius, and the coordination number (Figures 9(c), 9(f), and 9(i)). Therefore, clay minerals are the main destroyer of micronmeter-sized pores and throats. Since the duration of the sedimentary and diagenetic processes of dolomite is short, the main structures are either micrite or microcrystal (Figures 3(c) and 3(d)). The intercrystalline pores and their later intercrystal dissolution pores are mainly nanometer scale [51]. Therefore, the dolomite content has no control over the structure and connectivity of micro pores (Figures 9(b), 9(e), and 9(h)).

5.2. *The Influence of Mineral Composition on the Structure of Nanometer Scale Pores in Mixed Siliciclastic-Carbonate Tight Reservoirs.* The nanometer-sized pores in the eight samples are mainly controlled by the dolomite content (Figures 10(b) and 10(e)), while anhydrite content and the content of clay minerals have no obvious control effect on nanometer-sized pores (Figures 10(a), 10(c), 10(d), and 10(f)). The volume of nanometer-sized pores increases with the increase of dolomite content (Figure 10(b)). At the penecontemporaneous stage, with the intense water evaporation, the crystallization and differentiation of sulfate minerals occur [47]. As a result, Mg<sup>2+</sup> is enriched in large quantities. Under gravity, the bittern in which Mg<sup>2+</sup> is enriched permeates below the formation; and metasomatism occurs between bittern and calcite to form dolomite [47, 51, 52]. Numerous developed intercrystalline pores in dolomite minerals are mainly formed by the volume shrinkage caused by the replacement of Mg<sup>2+</sup> with smaller radius to Ga<sup>2+</sup> with larger radius [51–53]. The high mud content in carbonatites results in the small scale of intercrystalline pores in dolomite and the disconnection between pore. Therefore, the more developed the dolomite, the larger proportion of pores with smaller pores and the smaller the average of the pore radius in the reservoir (Figure 10(e)). Meanwhile, the dolomite formed earlier has compaction pressure solubility resistance, inhibiting the damage to the reservoir caused by compaction and pressure dissolution [53]. Intercrystalline pores are generally preserved in this way.

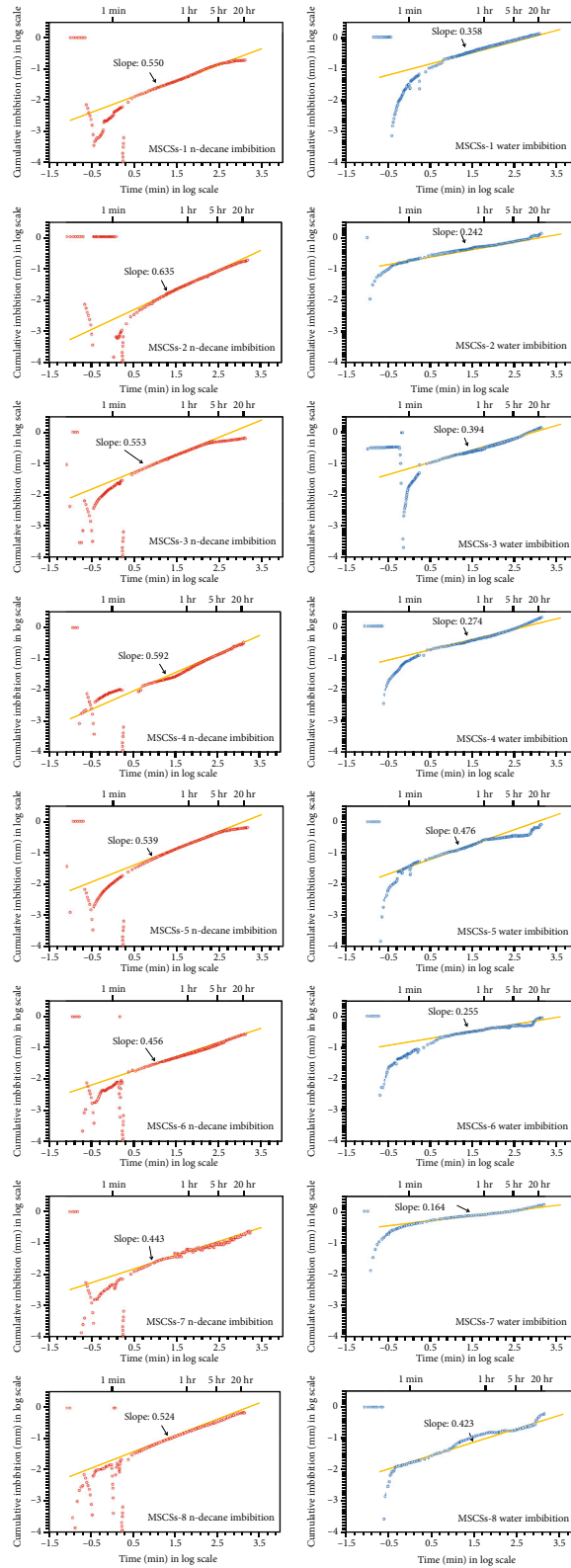


FIGURE 8: Connectivity of oil-wetting pores and water pores measured by spontaneous imbibition.

Meanwhile, the fractal dimension was used to analyze the relation between the mineral composition and pore structure in the mixed siliciclastic-carbonate tight reservoirs. As shown in Figures 10(g) and 10(j), both  $D_1$  and  $D_2$  are

negatively correlated to the anhydrite content, indicating that the increase of the anhydrite content may lead to simpler pore structure and smoother pore surface. This is consistent with previous findings [49, 54]. As shown in

TABLE 4: Pore connectivity parameters of the eight samples measured by spontaneous imbibition.

Sample ID	Reservoir type	Fluid used	Imbibition slope
MSCSs-1	LDR	n-Decane	0.550
		Water	0.358
MSCSs-2	LDR	n-Decane	0.635
		Water	0.242
MSCSs-3	LDR	n-Decane	0.553
		Water	0.394
MSCSs-4	LDR	n-Decane	0.592
		Water	0.274
MSCSs-5	SCR	n-Decane	0.539
		Water	0.476
MSCSs-6	SCR	n-Decane	0.456
		Water	0.255
MSCSs-7	MSCR	n-Decane	0.443
		Water	0.164
MSCSs-8	MSCR	n-Decane	0.524
		Water	0.423

\*The density of water is 1.0 g/cm<sup>3</sup>, and the viscosity of water is 1.002 mPa-sec; the density of n-decane is 0.73 g/cm<sup>3</sup>, and the viscosity of n-decane is 0.84 mPa-sec.

Figures 10(h) and 10(k),  $D_1$  is positively correlated to the dolomite content, while the dolomite content have no obvious control effect on  $D_2$ . In the process of dolomitization, polyhedral pores are transformed into tetrahedral pores [55]. In consequence, intercrystalline pores with a smooth surface appear as dolomite crystals increase. The content of clay minerals partly controls the complexity of the nanopores structure [56]. Compared with other minerals, clay minerals have more complicated chemical structure. Most pores in clay minerals are of a triangular, serrated, or other irregular shape. In consequence, the pore network becomes more complicated.  $D_2$  is positively correlated to clay minerals (Figure 10(l)), indicating that the increase of the content of clay minerals has made the pore structure more complex. Clay minerals have no correlation with  $D_1$  (Figure 10(i)).

*5.3. The Influence of Mineral Composition on Connectivity of Pores in Mixed Siliciclastic-Carbonate Tight Reservoirs.* Unlike conventional reservoirs, the mineral composition of mixed siliciclastic-carbonate tight reservoirs is more complicated [3–5]. Moreover, the wettability of different minerals results in different pore connectivity of the reservoir to different fluids [43]. According to the statistical results, the strong cementation of anhydrite destroys the connectivity of both oil-wetting and hydrophilic pores in the reservoir (Figures 11(a) and 11(d)). Dolomite is a lipophilic mineral and a main contributor to the connectivity of oil-wetting pores in the reservoir (Figure 11(b)). Clay minerals are hydrophilic minerals and are the main contributors to the

connectivity of hydrophilic pores in the reservoir (Figure 11(f)).

The precipitation of sulfate minerals occurred twice in the sediments [47]. The first precipitation occurs at the penecontemporaneous stage. The lake water is gradually salinized with the evaporation and concentration of the water in the lake basin. The sulfate mineral components enter a saturated state, and gypsum begins to precipitate and fill between clastic grains and between clastic grains in carbonates. The second precipitation occurs at the diagenetic stage. The gypsum gradually dehydrates into anhydrite due to the increase of formation temperature and pressure. The anhydrite is cemented in the dissolution pores in gypsum and the intercrystalline pores in dolomite minerals. Therefore, the spontaneous imbibition slope of both n-decane and water decreases with the increase of the anhydrite content (Figures 11(a) and 11(d)), and the connectivity of both oil-wetting and hydrophilic pores is broken.

The dissolution of minerals by organic acids is of great significance for the connectivity of the reservoir [57]. The source rocks in the Yingxi area reached the peak of oil generation in the Pliocene Epoch [58]. The acid fluid produced by the hydrocarbon generation and expulsion from organic matter can make the intercrystalline pores in the dolomite minerals formed at the penecontemporaneous stage transform into intercrystalline dissolution pores [51, 59]. In carbonates, the mud content is high; the intercrystalline scale between minerals is small, and most pores are isolated ones. The large-scale development of intercrystalline dissolution pores causes a slight increase in the pore size and passivation of edges, which improve the connectivity of intercrystalline pores and the reservoir effectiveness [59]. A great number of the intercrystalline dissolution pores formed by the dissolution by organic acids can be preserved for they are formed late and protected by hydrocarbon fluid. Therefore, the spontaneous imbibition slope of n-decane increases with the increase of dolomite content, and the connectivity of oil-wetting pores is improved (Figure 11(b)), but content of clay minerals and the spontaneous imbibition slope of n-decane are not correlated (Figure 11(c)).

The clay minerals in the upper member of Xiaganchai-gou Formation, Oligocene, Yingxi Area, mainly are chlorite, illite, and illite-smectite mixed layer at the B substage of the diagenetic stage [58]. Previous studies have shown that for reservoirs with high illite-smectite mixed-layer content, the water-rock interaction optimizes the connected hydrophilic pore system, resulting in high water absorption capacity [43]. Therefore, the spontaneous imbibition slope of water increases with the increase of the content of clay minerals, and the connectivity of hydrophilic pores is improved (Figure 11(f)), but dolomite content and the spontaneous imbibition slope of water are not correlated (Figure 11(e)).

*5.4. Genetic Model for Pore Structure and Connectivity of Mixed Siliciclastic-Carbonate Tight Reservoirs and Reservoir Evaluation.* A genetic model for the pore structure and connectivity of mixed siliciclastic-carbonate tight reservoirs has been established on the basis of the above discussion of the petrologic, pore structure, and pore connectivity

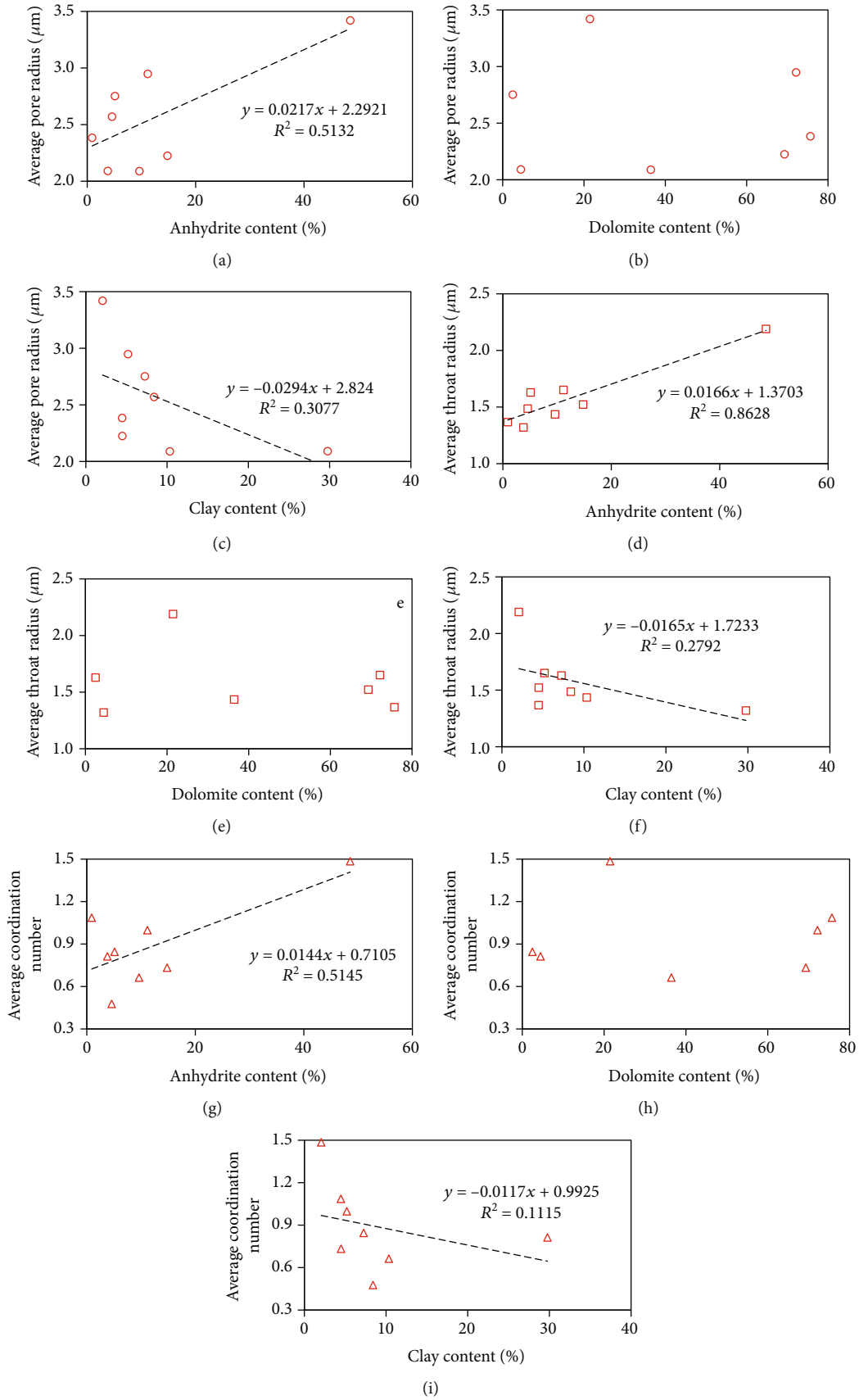


FIGURE 9: Crossplots of 3D CT parameters and mineral compositions of the eight samples.

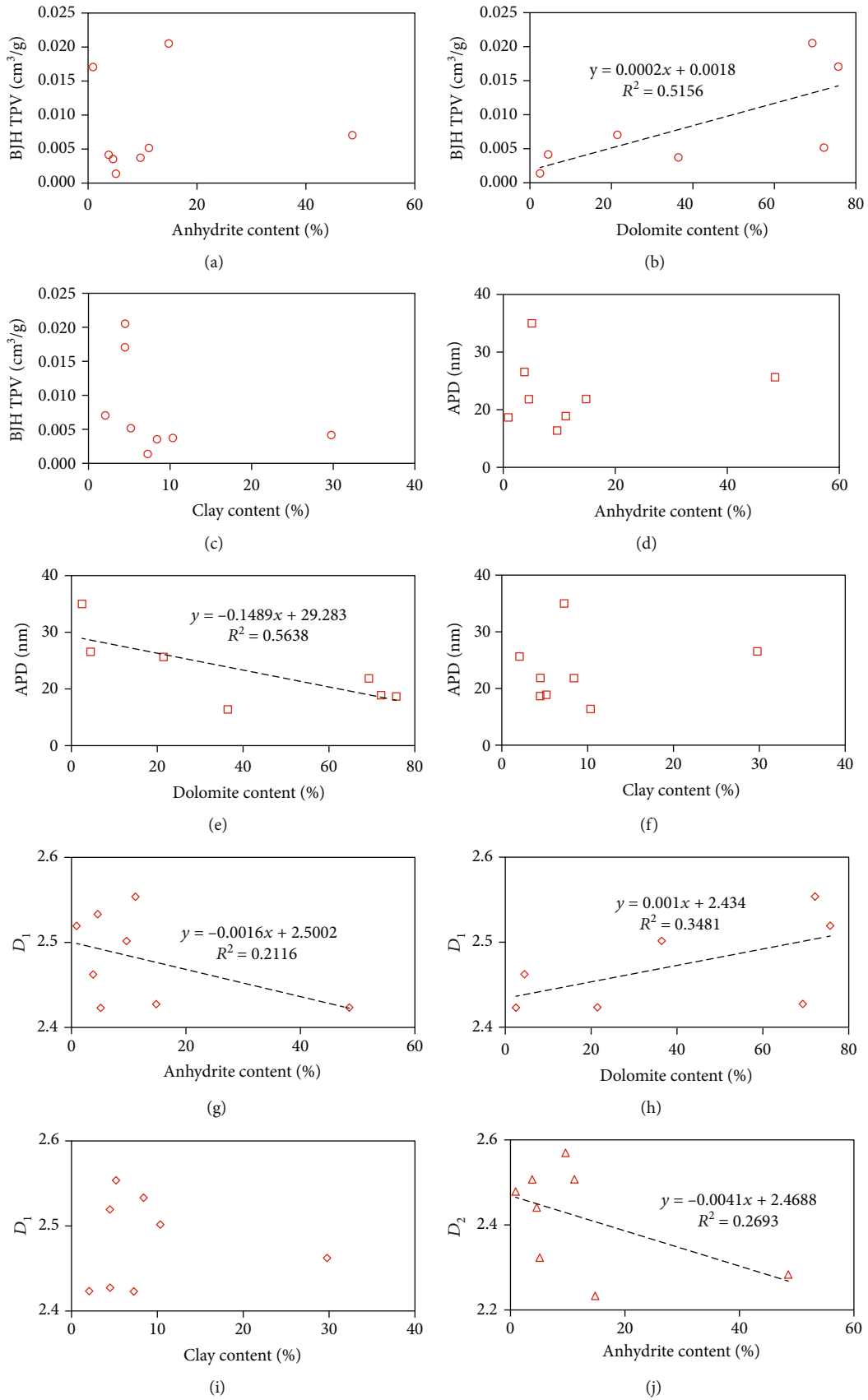


FIGURE 10: Continued.

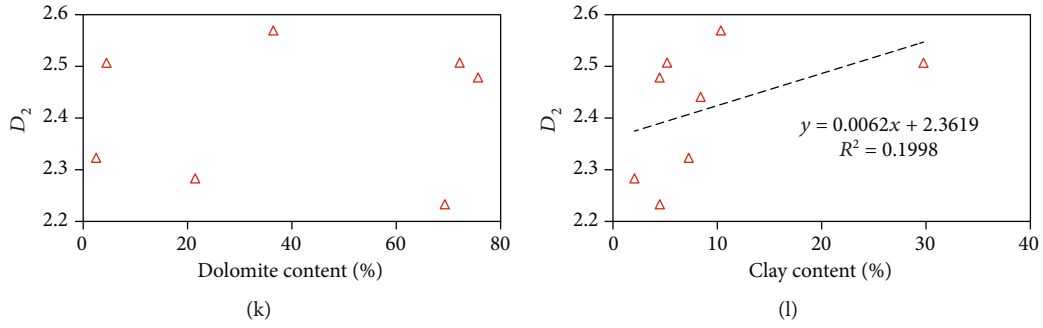


FIGURE 10: Crossplots of  $N_2$  adsorption parameters and mineral compositions of the Palaeogene Xiaganchaigou Formation samples from Qaidam Basin.

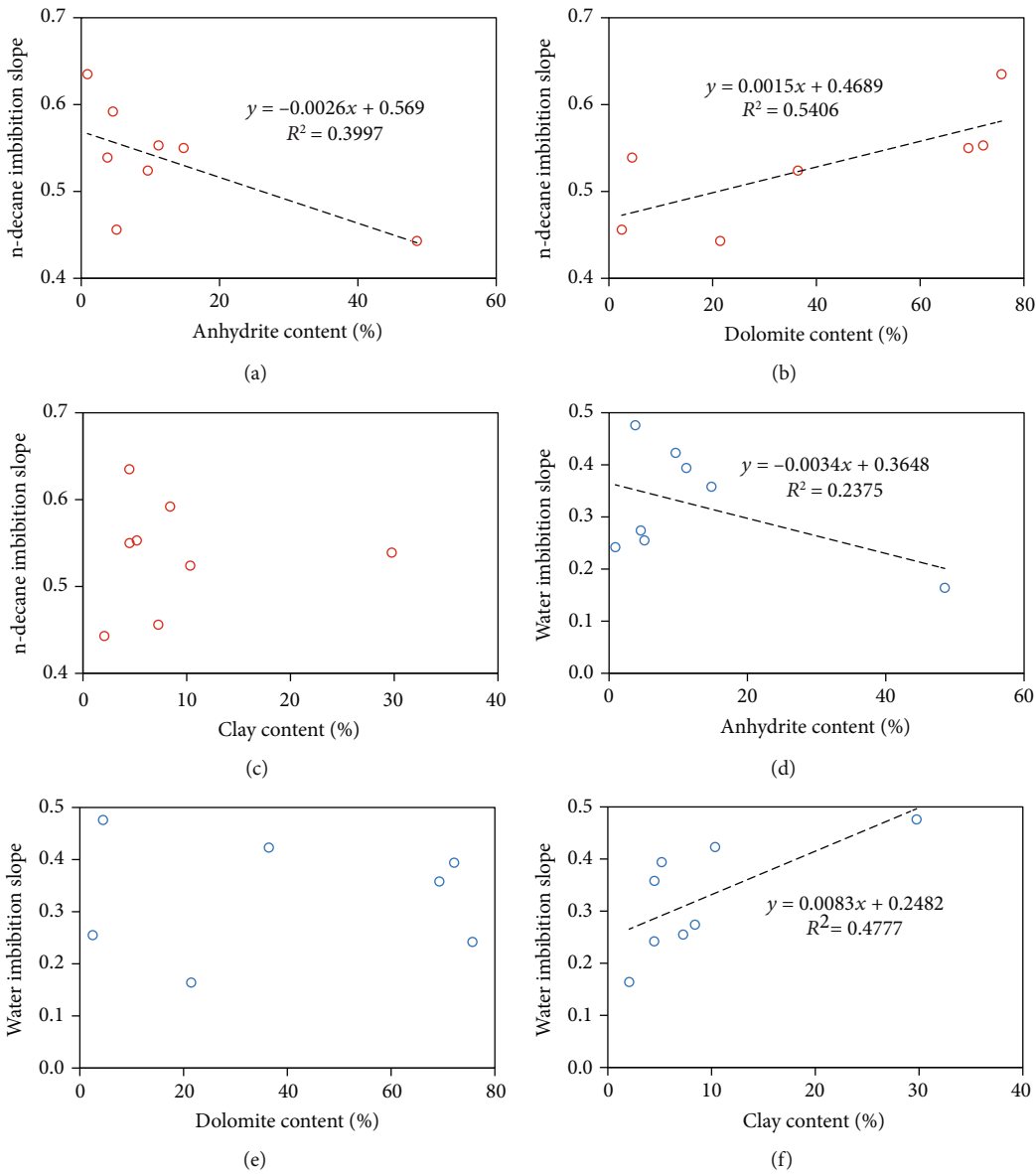


FIGURE 11: Crossplots of spontaneous imbibition parameters and mineral compositions of the Palaeogene Xiaganchaigou Formation samples from Qaidam Basin.



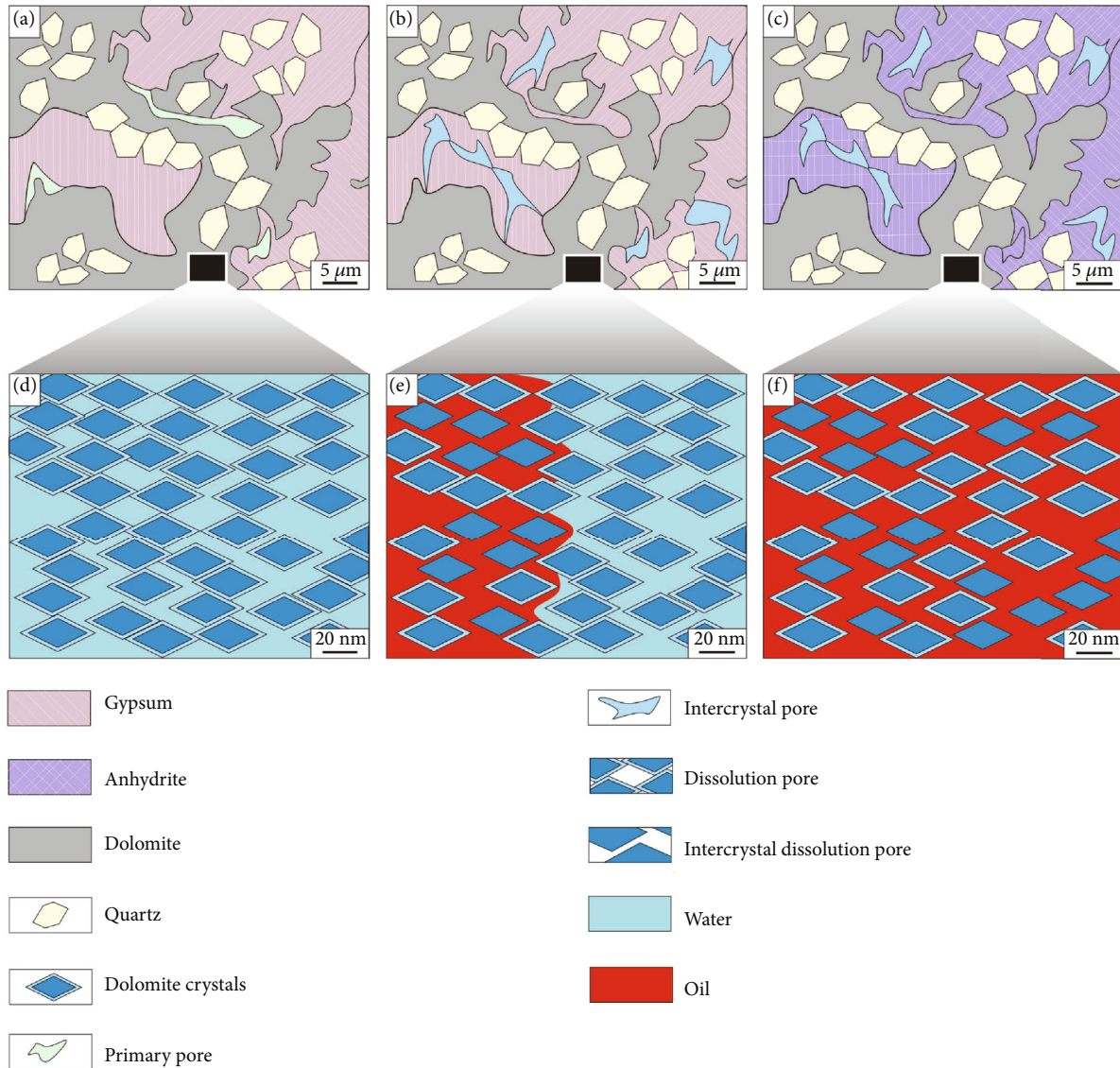


FIGURE 12: A genetic model for pore structure and connectivity of tight the mixed siliciclastic-carbonate sediment reservoirs.

properties of the samples from the upper member of the Xia-ganchaigou Formation in the Yingxi Area and in combination with the depositional setting and diagenetic evolution sequence in this area.

At the early penecontemporaneous stage, the evaporation continuously strengthened as the palaeoclimate gradually became drier [47]. The lake basin water begins to recede and became more saline. The sulfate mineral components enter a saturated state [48]. Gypsum began to precipitate and fill between clastic grains and between clastic grains in carbonates, and the primary pores were filled (Figure 12(a)). The primary pores are destroyed. Meanwhile, the concentration of  $Mg^{2+}$  in water increased as the sulfate minerals precipitate [51–53]. The continuous infiltration of the high-salinity bittern experienced metasomatism of the carbonate sediments, which promoted dolomitization, and resulted in the large-scale development of the intercrystalline pores associated with the dolomitization (Figure 12(d)) [51–53]. The dolomite formed earlier has strong compaction

pressure solubility resistance, inhibiting the damage to the reservoir caused by compaction and pressure dissolution. Intercrystalline pores are generally preserved in this way and provide space for the later migration and accumulation of fluid [53]. At the late penecontemporaneous stage, the level of the lake continued to fall as the water evaporation continued. The rapid and short-term fresh water dissolution occurred in locally exposed topographic highlands [51]. Since the Yingxi Area was a  $CaCO_3$ - $CaSO_4$ - $H_2O$ - $CO_2$  diagenetic system, the atmospheric fresh water preferentially dissolved gypsum to form micrometer-sized dissolution pores (Figure 12(b)) [47, 48]. At the early diagenetic stage, with the increase in burial depth, the temperature and pressure of the formation also increased, and the gypsum was transformed into anhydrite by dehydration [47]. Since the cement of anhydrite is strong, the micrometer-sized dissolution pores in gypsum are sealed in anhydrite (Figure 12(c)). Consequently, micrometer-sized pores are controlled by the spatial distribution of anhydrite minerals. And the spatial

distribution is highly heterogeneous. There are well connected micropores in anhydrite, but their contribution to the overall connectivity of the reservoir is extremely limited. At the mid diagenetic stage (Figure 12(e)), the organic acid fluid from the source rocks is injected into the reservoir for the dissolution of the dolomite minerals already formed [51, 58]. On the basis of nanometer-sized intercrystalline pores, dolomite intercrystalline increased, and pores are formed to connect the relatively isolated intercrystalline dissolution pores (Figure 12(f)). A great number of the intercrystalline dissolution pores can be preserved for they are formed late and protected by hydrocarbon fluid [58]. Since the content of dolomites is high and they are equally distributed, the spatial distribution of nanoscale intercrystalline pores and intercrystalline dissolution pores in dolomite is also homogeneous.

Since the mineral composition of mixed siliciclastic-carbonate tight reservoirs is complex, the spatial distribution is highly heterogeneous. According to the classification of mixed siliciclastic-carbonate tight reservoirs in Section 4.1.2, different types of tight reservoirs provide different reservoir spaces and migration channels for oil and gas. The main reservoir space in LDR is dominated by intercrystalline pores and intercrystalline dissolution pores. The pores are numerous and are equally distributed. Meanwhile, intercrystalline dissolution pores also provide favorable tight oil migration channels for reservoirs. The main reservoir space in reservoirs of SCR and MSCR is dominated by the dissolution pores in anhydrite. The spatial distribution of pores is highly heterogeneous. The pore throat system in the anhydrite is developed, but its contribution to the overall connectivity of the reservoir is extremely limited. Dominant channel cannot be provided for the migration of tight oil. Moreover, the internal dissolution pores cannot act as the reservoir space for tight oil. Therefore, LDR is the high-quality tight oil reservoirs in the upper member of Xiaganchaigou Formation in Yingxi Area.

## 6. Conclusions

The micrometer-sized pores in mixed siliciclastic-carbonate tight reservoirs are dominated by the dissolution pores formed by the gypsum dissolution at the penecontemporaneous stage and are well preserved in anhydrite at the diagenetic stage. The average pore radius range, average throat radius range, and average coordination number range of micronmeter-sized pores are 2.09~3.42  $\mu\text{m}$ , 1.32~2.19  $\mu\text{m}$ , and 0.48~1.49, respectively. Restricted by the concentrated distribution of local clumps in the anhydrite, the spatial distribution of pore structure shows high heterogeneity. The pore connectivity is well developed in anhydrite. Nevertheless, under the strong cementation of anhydrite, the contribution of the throat system in the anhydrite to the reservoir is extremely limited.

The nanometer-sized pores in mixed siliciclastic-carbonate tight reservoirs mainly are the intercrystalline pores formed by the dolomitization at the penecontemporaneous stage. The range of nanometer-sized pores diameters is mainly distributed in 1.73-31.47 nm. The pore has a

smooth surface, simple structure, and relatively homogeneous spatial distribution. At the diagenetic stage, a large number of intercrystalline dissolution pores were formed by the dissolution of carbonates by acidic fluids and connected the isolated intercrystalline pores of dolomite and increased the connectivity of oil-wetting pores in reservoirs.

Relatively developed nanometer-sized pores can be found in LDR. The spatial distribution of these nanometer-sized pores is highly homogeneous, and BJH TPV falls within the range of 0.003533~0.020521  $\text{cm}^3/(\text{g}\cdot\text{nm})$ , providing large reservoir space for the enrichment of tight oil. Meanwhile, the oil-wetting pores in LDR has well-developed connectivity and spontaneous imbibition slope of n-decane within the range of 0.55~0.635, providing advantageous migration channels for the filling of tight oil, making them high-quality tight oil reservoirs in the upper member of Xiaganchaigou Formation in the Yingxi Area.

## Data Availability

The main data used to support the study is available within the article. If readers are interested in the data, you can communicate with corresponding author and obtain these data by email.

## Conflicts of Interest

The authors declare that they have no conflicts of interest.

## Authors' Contributions

Xin Wang and Tongzhi Lu contributed equally to this work.

## Acknowledgments

This work is financially supported by the grants from the National Natural Science Foundation of China (No.41972147 and No. 42002050), the China Postdoctoral Science Foundation Funded Project (No. 2020M680815), the China University of Petroleum (Beijing) Research Startup Fund Project (No. ZX20200054), and the Supported by Science Foundation of China University of Petroleum, Beijing (No. 2462020XKBH009).

## References

- [1] Y. Dong, X. Zhu, S. Hua et al., "Genetic types and evolutionary model of mixed clastic-carbonate deposits in the lower part of the Sha-1 Formation, the Huanghua Depression," *Oil & Gas Geology*, vol. 32, pp. 98–107, 2011.
- [2] R. Zhu, C. Zou, S. Wu et al., "Mechanism for generation and accumulation of continental tight oil in China," *Oil Gas Geology*, vol. 40, pp. 1168–1184, 2019.
- [3] M. Myrow, "Mixed siliciclastic-carbonate deposition in an early cambrian oxygen-stratified basin, chapel island formation, southeastern newfoundland," *Journal of Sedimentary Research*, vol. 62, pp. 455–473, 1992.
- [4] G. Brooks, L. Doyle, B. Suthard, S. Locker, and A. Hine, "Facies architecture of the mixed carbonate/siliciclastic inner continental shelf of west-Central Florida: implications for Holocene

- barrier development,” *Marine Geology*, vol. 200, no. 1-4, pp. 325–349, 2003.
- [5] J. Mount, “Mixed siliciclastic and carbonate sediments: a proposed first-order textural and compositional classification,” *Sedimentology*, vol. 32, no. 3, pp. 435–442, 1985.
- [6] C. Brett and G. Baird, “Carbonate-shale cycles in the Middle Devonian of New York: An evaluation of models for the origin of limestones in terrigenous shelf sequences,” *Geology*, vol. 13, no. 5, pp. 324–327, 1985.
- [7] C. Yang and Q. Sha, “Sedimentary environment of the middle Devonian Qujing Formation, Qujing, Yunnan province: a kind of mixing sedimentation of terrigenous clastics and carbonate,” *Acta Sedimentologica Sinica*, vol. 8, pp. 59–66, 1990.
- [8] J. Martin-Chivelet, “Sequence stratigraphy of mixed carbonate-siliciclastic platforms developed in a tectonically active setting, Upper Cretaceous, Betic continental margin (Spain),” *Journal of Sedimentary Research*, vol. 65B, pp. 235–254, 1995.
- [9] R. Dorsey and S. Kidwell, “Mixed carbonate-siliciclastic sedimentation on a tectonically active margin: example from the Pliocene of Baja California Sur, Mexico,” *Geology*, vol. 27, no. 10, pp. 935–938, 1999.
- [10] A. Campbell, “Shelf-geometry response to changes in relative sea level on a mixed carbonate-siliciclastic shelf in the Guyana Basin,” *Sedimentary Geology*, vol. 175, no. 1-4, pp. 259–275, 2005.
- [11] F. García-Hidalgo, J. Gil, and M. Segura, “Internal anatomy of a mixed siliciclastic-carbonate platform: the Late Cenomanian–Mid Turonian at the southern margin of the Spanish Central System,” *Sedimentology*, vol. 54, no. 6, pp. 1245–1271, 2007.
- [12] E. Gischler, R. Ginsburg, J. Herrle, and S. Prasad, “Mixed carbonates and siliciclastics in the quaternary of southern Belize: Pleistocene turning points in reef development controlled by sea-level change,” *Sedimentology*, vol. 57, no. 4, pp. 1049–1068, 2010.
- [13] T. Komatsu, H. Naruse, Y. Shigeta et al., “Lower Triassic mixed carbonate and siliciclastic setting with Smithian- Spathian anoxic to dysoxic facies, An Chau basin, northeastern Vietnam,” *Sedimentary Geology*, vol. 300, pp. 28–48, 2014.
- [14] S. Zhang, Y. Cao, R. Zhu et al., “Characterization of lacustrine mixed fine-grained sedimentary rocks using coupled chemostratigraphic-petrographic analysis: a case study from a tight oil reservoir in the Jimusar Sag, Junggar Basin,” *Marine and Petroleum Geology*, vol. 99, pp. 453–472, 2019.
- [15] T. Li, Z. Huang, Y. Feng et al., “Reservoir characteristics and evaluation of fluid mobility in organic-rich mixed siliciclastic-carbonate sediments: a case study of the lacustrine Qiketai Formation in Shengbei Sag, Turpan-Hami Basin, Northwest China,” *Journal of Petroleum Science and Engineering*, vol. 185, p. 106667, 2020.
- [16] J. Cai, E. Edmund, C. Cheng, and X. Hu, “Generalized Modeling of Spontaneous Imbibition Based on Hagen–Poiseuille Flow in Tortuous Capillaries with Variably Shaped Apertures,” *Langmuir*, vol. 30, no. 18, pp. 5142–5151, 2014.
- [17] J. Lai, G. Wang, Z. Wang et al., “A review on pore structure characterization in tight sandstones,” *Earth-Science Reviews*, vol. 177, pp. 436–457, 2018.
- [18] L. Anovitz and D. Cole, “Characterization and analysis of porosity and pore structures,” *Reviews in Mineralogy & Geochemistry*, vol. 80, no. 1, pp. 61–164, 2015.
- [19] Z. Diao, S. Li, W. Liu, H. Liu, and Q. Xia, “Numerical study of the effect of tortuosity and mixed wettability on spontaneous imbibition in heterogeneous porous media,” *Capillarity*, vol. 4, no. 3, pp. 50–62, 2021.
- [20] B. Bai, R. Zhu, S. Wu et al., “Multi-scale method of Nano(micro)-CT study on microscopic pore structure of tight sandstone of Yanchang Formation, Ordos Basin,” *Petroleum Exploration Development*, vol. 40, no. 3, pp. 354–358, 2013.
- [21] A. Ghanizadeh, C. Clarkson, S. Aquino, O. Ardakani, and H. Sanei, “Petrophysical and geomechanical characteristics of Canadian tight oil and liquid-rich gas reservoirs: I. Pore network and permeability characterization,” *Fuel*, vol. 153, pp. 664–681, 2015.
- [22] A. Giri, S. Tarafdar, P. Gouze, and T. Dutta, “Fractal pore structure of sedimentary rocks: simulation in 2-d using a relaxed bidisperse ballistic deposition model,” *Journal of Applied Geophysics*, vol. 87, pp. 40–45, 2012.
- [23] G. Desbois, J. Urai, P. Kukla, J. Konstanty, and C. Baerle, “High-resolution 3D fabric and porosity model in a tight gas sandstone reservoir: a new approach to investigate microstructures from mm- to nm-scale combining argon beam cross-sectioning and SEM imaging,” *Journal of Petroleum Science and Engineering*, vol. 78, no. 2, pp. 243–257, 2011.
- [24] L. Jiao, P. Ø. Andersen, J. Zhou, and J. Cai, “Applications of mercury intrusion capillary pressure for pore structures: a review,” *Capillarity*, vol. 3, no. 4, pp. 62–74, 2020.
- [25] J. Cai, Z. Zhang, W. Wei, D. Guo, S. Li, and P. Zhao, “The critical factors for permeability-formation factor relation in reservoir rocks: Pore-throat ratio, tortuosity and connectivity,” *Energy*, vol. 188, article 116051, 2019.
- [26] K. Higgs, H. Zwingmann, A. Reyes, and R. Funnell, “Diagenesis, porosity evolution, and petroleum emplacement in tight gas reservoirs, Taranaki Basin, New Zealand,” *Journal of Sedimentary Research*, vol. 77, no. 12, pp. 1003–1025, 2007.
- [27] K. Wu, C. Liao, X. Li et al., “Geological characteristics of hydrocarbon pool in Yingxiongling Structural Zone, Qaidam Basin,” *Geoscience*, vol. 34, no. 2, pp. 378–389, 2020.
- [28] J. Wang, Y. Wang, Z. Liu, J. Li, and P. Xi, “Cenozoic environmental evolution of the Qaidam Basin and its implications for the uplift of the Tibetan Plateau and the drying of Central Asia,” *Palaeogeography, Palaeoclimatology, Palaeoecology*, vol. 152, no. 1-2, pp. 37–47, 1999.
- [29] Z. An, J. Kutzbach, W. Prell, and S. Porter, “Evolution of Asian monsoons and phased uplift of the Himalaya-Tibetan plateau since Late Miocene times,” *Nature*, vol. 411, no. 6833, pp. 62–66, 2001.
- [30] A. Xiao, L. Wu, H. Li, and L. Wang, “Tectonic processes of the Cenozoic Altyn Tagh Fault and its coupling with the Qaidam Basin, NW China,” *Acta Petrologica Sinica*, vol. 29, pp. 2826–2836, 2013.
- [31] J. Pan, H. Li, Z. Sun, D. Liu, C. Wu, and C. Yu, “Tectonic responses in the Qaidam basin induced by Cenozoic activities of the Altyn Tagh fault,” *Acta Petrologica Sinica*, vol. 31, pp. 3701–3712, 2015.
- [32] C. Wu, C. Yan, H. Li et al., “Cenozoic tectonic evolution of the western Qaidam Basin and its constrain on the growth of the northern Tibetan Plateau,” *Acta Petrologica Sinica*, vol. 29, pp. 2211–2222, 2013.
- [33] F. A. Dullien, *Porous Media: Fluid Transport and Pore Structure*, Academic Press, Cambridge, MA, USA, 2012.

- [34] M. He, Y. Zhou, K. Wu et al., "Pore network modeling of thin water film and its influence on relative permeability curves in tight formations," *Fuel*, vol. 289, p. 119828, 2021.
- [35] Z. Wang, H. Li, X. Lan, K. Wang, Y. Yang, and V. Lisitsa, "Formation damage mechanism of a sandstone reservoir based on micro-computed tomography," *Advances in Geo-Energy Research*, vol. 5, no. 1, pp. 25–38, 2021.
- [36] R. Ketcham, "Computational methods for quantitative analysis of three-dimensional features in geological specimens," *Geosphere*, vol. 1, no. 1, pp. 32–41, 2005.
- [37] N. Alyafei, T. McKay, and T. Solling, "Characterization of petrophysical properties using pore-network and lattice- Boltzmann modelling: choice of method and image sub-volume size," *Journal of Petroleum Science and Engineering*, vol. 145, pp. 256–265, 2016.
- [38] A. Dabrowski, "Adsorption – from theory to practice," *Advances in Colloid and Interface Science*, vol. 93, no. 1-3, pp. 135–224, 2001.
- [39] T. Li, Z. Huang, J. Zhao, X. Xu, and X. Guo, "Pore structure characteristics and their influencing factors: a case study from the middle jurassic mixed siliciclastic carbonate rocks, Turpan-Hami basin, Northwest China," *Journal of Petroleum Science and Engineering*, vol. 203, article 108611, 2021.
- [40] E. Barrett, L. Joyner, and P. Halenda, "The determination of pore volume and area distributions in porous Substances. I. Computations from Nitrogen Isotherms," *Journal of the American Chemical Society*, vol. 73, no. 1, pp. 373–380, 1951.
- [41] L. Chen, Z. Jiang, K. Liu, and F. Gao, "Quantitative characterization of micropore structure for organic-rich lower Silurian shale in the Upper Yangtze Platform, South China: implications for shale gas adsorption capacity," *Advances in Geo-Energy Research*, vol. 1, no. 2, pp. 112–123, 2017.
- [42] Y. Li, Z. Wang, Z. Pan, X. Niu, Y. Yu, and S. Meng, "Pore structure and its fractal dimensions of transitional shale: a cross-section from east margin of the Ordos Basin, China," *Fuel*, vol. 241, pp. 417–431, 2019.
- [43] Z. Gao and Q. Hu, "Initial water saturation and imbibition fluid affect spontaneous imbibition into Barnett shale samples," *Journal of Natural Gas Science and Engineering*, vol. 34, pp. 541–551, 2016.
- [44] X. Zhang, "Classification and origin of mixosedimentite," *Geological Science and Technology Information*, vol. 19, pp. 31–34, 2000.
- [45] L. Handy, "Determination of effective capillary pressures for porous media from imbibition data," *Aime*, vol. 219, no. 1, pp. 75–80, 1960.
- [46] A. Hunt, R. Ewing, and B. Ghanbarian, "Percolation theory for flow in porous media," in *Lecture Notes in Physics 880*, p. 447, Springer, Heidelberg, Germany, 3rd edition, 2014.
- [47] Y. Xiong, X. Tan, K. Wu, Q. Xu, Y. Liu, and Y. Qiao, "Petrogenesis of the Eocene lacustrine evaporites in the western Qaidam Basin: implications for regional tectonic and climate changes," *Sedimentary Geology*, vol. 416, p. 105867, 2021.
- [48] R. Kuechler, K. Noack, and T. Zorn, "Investigation of gypsum dissolution under saturated and unsaturated water conditions," *Ecological Modelling*, vol. 176, no. 1-2, pp. 1–14, 2004.
- [49] D. Loope, J. Mason, H. Bao, R. Kettler, and C. Zanner, "Deformation structures and an alteration zone linked to deposition of volcanogenic sulphate in an ancient playa (Oligocene of Nebraska, USA)," *Sedimentology*, vol. 52, no. 1, pp. 123–139, 2005.
- [50] D. Ren, Z. Zhou, R. Liang, R. Zhou, N. Liu, and J. Nan, "Characteristics of clay minerals and its impacts on reservoir quality of tight sandstone gas reservoir: a case from Sulige Gas Field, Ordos Basin," *Lithologic Reservoirs*, vol. 31, no. 4, pp. 42–53, 2019.
- [51] J. Feng, J. Cao, K. Hu et al., "Dissolution and its impacts on reservoir formation in moderately to deeply buried strata of mixed siliciclastic-carbonate sediments, northwestern Qaidam Basin, northwest China," *Marine & Petroleum Geology*, vol. 39, no. 1, pp. 124–137, 2013.
- [52] C. Huang, J. Yuan, G. Tian, L. Wu, X. Pan, and Y. Hui, "The geochemical characteristics and formation mechanism of the Eocene lacustrine dolomite reservoirs in the western Qaidam," *Earth Science Frontiers*, vol. 23, no. 3, pp. 230–242, 2016.
- [53] C. Huang, Z. Fan, J. Yuan, L. Wu, and G. Chen, "The characteristics of dolomite reservoir in saline lacustrine Basin, Qaidam, China," *Carbonates & Evaporites*, vol. 31, no. 3, pp. 307–317, 2016.
- [54] L. Aylmore, M. Karim, and J. Quirk, "Dissolution of gypsum, monocalcium phosphate, and superphosphate fertilizers in relation to particle size and porous structure," *Australian Journal of Soil Research*, vol. 9, no. 1, pp. 21–32, 1971.
- [55] K. Zhang, X. Pang, Z. Zhao et al., "Pore structure and fractal analysis of lower carboniferous carbonate reservoirs in the Marsel area, Chu-Sarysu basin," *Marine and Petroleum Geology*, vol. 93, pp. 451–467, 2018.
- [56] X. Shao, X. Pang, H. Li, and X. Zhang, "Fractal analysis of pore network in tight gas sandstones using NMR method: a case study from the Ordos basin, China," *Energy & Fuels*, vol. 31, no. 10, pp. 10358–10368, 2017.
- [57] R. Surdam, L. Crossey, E. Hagen, and H. Heasler, "Organic-inorganic interactions and sandstone diagenesis," *AAPG Bulletin*, vol. 73, no. 1, pp. 1–23, 1989.
- [58] W. Zhang, X. Jian, L. Fu, F. Feng, and P. Guan, "Reservoir characterization and hydrocarbon accumulation in late Cenozoic lacustrine mixed carbonate-siliciclastic fine-grained deposits of the northwestern Qaidam basin, NW China," *Marine and Petroleum Geology*, vol. 98, pp. 675–686, 2018.
- [59] X. Fan, G. Wang, Y. Li et al., "Pore structure evaluation of tight reservoirs in the mixed siliciclastic- carbonate sediments using fractal analysis of NMR experiments and logs," *Marine and Petroleum Geology*, vol. 109, pp. 484–493, 2019.

## Research Article

# Numerical Study of the Effect of Magnetic Field on Nanofluid Heat Transfer in Metal Foam Environment

Hamid Shafiee <sup>1</sup>, Elaheh NikzadehAbbasi,<sup>2</sup> and Majid Soltani<sup>3,4,5,6</sup>

<sup>1</sup>Department of Mechanical Engineering, Shahid Bahonar University of Kerman, Kerman, Iran

<sup>2</sup>Department of Chemical Engineering, Shahid Bahonar University of Kerman, Kerman, Iran

<sup>3</sup>Department of Mechanical Engineering, K.N. Toosi University of Technology, Tehran, Iran

<sup>4</sup>School of Optometry and Vision Science, Faculty of Science, Department of Electrical and Computer Engineering, Faculty of Engineering, University of Waterloo, Waterloo, Canada

<sup>5</sup>Waterloo Institute for Sustainable Energy (WISE), University of Waterloo, Waterloo, Ontario, Canada

<sup>6</sup>Advanced Energy Initiative Center, K.N. Toosi University of Technology, Tehran, Iran

Correspondence should be addressed to Hamid Shafiee; [h.shafiee@eng.uk.ac.ir](mailto:h.shafiee@eng.uk.ac.ir)

Received 28 August 2021; Revised 2 October 2021; Accepted 18 October 2021; Published 8 November 2021

Academic Editor: Jianchao Cai

Copyright © 2021 Hamid Shafiee et al. This is an open access article distributed under the Creative Commons Attribution License, which permits unrestricted use, distribution, and reproduction in any medium, provided the original work is properly cited.

The magnetic field can act as a suitable control parameter for heat transfer and fluid flow. It can also be used to maximize thermodynamic efficiency in a variety of fields. Nanofluids and porous media are common methods to increase heat transfer. In addition to improving heat transfer, porous media can increase pressure drop. This research is a computational simulation of the impacts of a magnetic field induced into a cylinder in a porous medium for a volume fraction of 0.2 water/ $\text{Al}_2\text{O}_3$  nanofluid with a diameter of  $10\ \mu\text{m}$  inside the cylinder. For a wide variety of controlling parameters, simulations have been made. The fluid flow in the porous medium is explained using the Darcy-Brinkman-Forchheimer equation, and the nanofluid flow is represented utilizing a two-phase mixed approach as a two-phase flow. In addition, simulations were run in a slow flow state using the finite volume method. The mean Nusselt number and performance evaluation criteria (PEC) were studied for different Darcy and Hartmann numbers. The results show that the amount of heat transfer coefficient increases with increasing the number of Hartmann and Darcy. In addition, the composition of the nanofluid in the base fluid enhanced the PEC in all instances. Furthermore, the PEC has gained its highest value at the conditions relating to the permeable porous medium.

## 1. Introduction

The most important parameters discussed in heating systems and industrial centers are the increase of heat transfer and advanced and optimal cooling [1]. Optimization of heat transfer systems to increase the heat flux in most thermal equipment is possible by increasing the surface and then increasing the volume and size of the equipment [1]. Helps to cool the tool and workpiece (cooling property), reduces wear and friction between the tool and the workpiece (lubrication property), transfers chips outside the cutting area (liquid flow property), prevents heat transfer from the tool and workpiece to Gates (heat absorption property), and separates cutting debris from the part and tools (increasing surface quality) are the advantages of shear fluid [2]. Nano-

fluid technology has attracted the attention of many researchers due to its thermal conductivity and higher heat transfer ability than conventional heat transfer fluids or fluids containing particles in microdimensions [3]. By using nanofluids in industrial equipment, thermal performance can be significantly increased, in which case a large benefit will be given to industrial units both in terms of energy savings and in terms of better equipment performance [4, 5]. Liquids are commonly used in industry for heat transfer and cooling. The growth and development of industry and manufacturing activities have led researchers and manufacturers to take a fresh look at heat transfer and cooling fluid methods [5]. Nanofluids are a new kind of fluids derived from the distribution of nanosized particles in regular fluids. They have many possibilities for industrial uses. Nanofluids

employ particles of sizes ranging from 1 nm to 100 nm. Metal particles like copper (Cu), silver (silver), and metal oxides such as aluminum oxide ( $\text{Al}_2\text{O}_3$ ) and copper oxide (CuO) make up these particles [6, 7]. The thermal conductivity of conventional heat transfer fluids is low. The thermal conductivity of the fluid is improved by distributing nanoparticles in the base fluid, which is one of the key elements in heat transfer, resulting in high conductivity [8].

Heat transfer has always been one of the significant challenges in engineering. Many methods have been proposed to increase or control heat transfer. One of these methods is the use of nanofluids for heat transfer [9]. On the other hand, recognizing nanofluid flow in the presence of external fields and the impact of external fields on the nanofluid heat transfer rate is the subject of much discussion in engineering and medical sciences. Magnetic fields are one of the external fields applied to the fluid, which has been considered in recent decades due to its special properties. Many works have been performed on the impact of such fields on flow characteristics, heat transfer, and other fluid transfer properties. Most research has a theoretical and numerical basis, and considerable experimental work has not been done in alternating magnetism and heat transfer, especially in the field of slow current, which has its application [10]. Cooling devices are among the essential concerns of factories and industries and everywhere that somehow face heat transfer. The usage of modern and optimal cooling technologies is unavoidable in these circumstances. The most common technique to improve current heat transfer devices is to expand their surface area, which always raises their volume and size. Therefore, new and effective coolers are needed to overcome this problem. Nanofluids have been proposed as a new solution in this field. In terms of the effect of a magnetic field on slow flow nanofluid heat transfer, the problem can be studied from two perspectives. First, the magnetic effect is added to the Navier-Stokes equation, which shows the magnetic effect as an external force. The second view is the effect that the magnetic field has on the physical properties of the nanofluid [11].

In recent years, according to laboratory studies on the effect of the magnetic field on the viscosity and specific heat capacity of biphasic fluids such as nanoparticles, the results show that the observed changes may be due to the presence of particles in the fluid or the change in fluid flow behavior applied in the presence of a magnetic field. Also, laboratory and computational studies on the effect of magnetic waves as a targeted drug transfer agent in the body attempted to study various factors affecting motion using experimental and numerical work and heat transfer of nanofluids in the presence of magnetic fields. In this numerical research, new methods to increase the heat transfer coefficient, such as magnetic field application and injection of nanoparticles, are simulated, and their efficiency is determined.

Dukhan and Chen [12] conducted a study examining the heat transfer inside a sample of the commercially available metal foam heat sink, which is given a constant heat flux by an electronic device. They found from the empirical findings that as the distance from the heated surface rises, its temperature decreases rapidly. Calmidi

and Mahajan [13] obtained the effective conduction coefficient of conductivity for aluminum foam in one study. The effective heat transfer coefficient is a property of metal foam that measures the ability of a metal foam to transfer heat through the air and the solid metal part in the state of free flow. In recent years, many research groups have tried to study and apply these porous materials from a practical point of view. Boyd and Hooman [14] designed and studied a model for studying the power of using metal foams in interconnected fuel cells. They found from this study that a heat exchanger made of metal foam with an air-cooled fluid with the same pressure difference could be an excellent alternative to the same sample with a water-cooled fluid. Odabae and Hooman [15] conducted a study to replace heat exchangers with metal foams instead of finned tubes in water-cooled condensers. In this study, they concluded that using these metal foams can have 2 to 6 times better performance in terms of heat transfer (to increase the pressure drop is reasonable and acceptable). Lin et al. [16] also studied heat exchangers. They studied six samples of heat exchangers, 3 of which were made of copper metal foam and the other three samples of nonporous heat exchangers made of copper. In this experiment, they found that copper foam has a higher heat transfer and a lower pressure drop. Several strategies for increasing heat transfer from an item have been presented. Using a fluid with better heat transfer characteristics is one of these techniques. Nanofluids are a new category of fluids with superior thermal properties over conventional fluids. These fluids are made up of a base fluid and nanometer-sized particles. These particles, usually metals, metal oxides, or nanotubes, boost the coolant's conductivity and heat transfer coefficient.

Chen et al. [17] studied the natural convective heat transfer investigation of nanofluids affected by the electrical field. The heat transfer performance of resuspended nanofluid under the electric field is significantly increased compared to the pure base fluid, which increases with the improvement of voltage, concentration, and direction change time. Qi et al. [18] investigated the effects of rotation angle and metal foam on the natural convection of nanofluids in a cavity under an adjustable magnetic field. They showed that the horizontal magnetic field is not essential for increased thermal performance. However, the vertical magnetic field shows an opposite trend and has a positive contribution to thermal performance. The cavity with a rotation angle  $\alpha = 90$  degrees shows the highest thermal performance. Izadi et al. [19] study on impingement cooling of a porous metal CPU cooler saturated with nanofluid under the magnetic field effects. The results show that increasing the Darcy number can increase the heat transfer performance. At the same time, contrasting trends are found for the aspect ratio and the Eckert number. The Rabbani et al. [20] study experimentally investigated the thermal performance and the pressure drop in copper tubes partially filled with open-cell metal foams using MgO nanofluid. It has been observed that the pressure drop and the Nusselt number depend significantly on the Reynolds number. Further results show that nanofluid and porous media inside the

tubes significantly increase the pressure drop and the heat transfer coefficient. Ameri et al. [21] studied the use of a single-phase method modified with a thermal dispersion model that includes a heterogeneous distribution of nanoparticle concentrations to evaluate the thermal performance in a porous foam tube. The results show that the concentration heterogeneity is proportional to the metal foam's mean nanoparticle concentration, Reynolds number, and porosity. The velocity and temperature cross-sectional profiles in the dispersion model are flatter than the samples obtained from the homogeneous model. In addition, it is found that the Nusselt number differs directly from the mean concentration and the Reynolds number. At the same time, the inverse ratio for porosity varies. This reduction is in less deep porosities. Badfar et al. [22] studied the use of drug-coated ferrite nanoparticles to target magnetic drugs to the stenosis area of the conduit. For varied magnetic numbers, the issue was solved. The impact of the wire's position as a magnetic field on the MDT also was investigated. Previous studies have investigated the increase in heat transfer in porous media when nanofluids are used. The magnetic field is activated separately and in combination. Studies have shown that a few previous studies have investigated the forced displacement heat transfer and the nanofluid magnetic field within a cylinder in a porous medium, taking into account Darcy and Hartmann numbers. In this research, simultaneously, the impact of the magnetic field's presence, nanoparticles, and porous medium on heat transfer will be investigated numerically. Aluminum oxide ( $\text{Al}_2\text{O}_3$ ) nanoparticles and metal foam nickel (Ni) are considered. The effect of nanoparticle concentration and the intensity and direction of magnetic field application will be investigated. The results will be analyzed using Nusselt number, pressure drop, average speed, velocity, and outlet temperature.

## 2. Methods and Material

**2.1. Problem Geometry.** Figure 1 schematically shows the forced heat transfer for  $\text{Al}_2\text{O}_3$  nanofluid inside a two-dimensional cylinder (symmetrical axis view) with a magnetic field angle of  $0^\circ < \Psi < 90^\circ$ . This schematic includes a pipe with a length of 0.3 m and a diameter of 0.01 m. Pure water or  $\text{Al}_2\text{O}_3$  nanofluid, which enters the tube in a gentle axial direction with the same entrance velocity and  $U_{\text{in}}$  and  $T_{\text{in}}$  temperatures, is the fluid inside the tube. This paper used water and aluminum nanofluids (water/ $\text{Al}_2\text{O}_3$ ) with a volume fraction of 0.2 nanofluids. Also, the diameter of aluminum nanofluid is equal to 10 micrometers. A uniform magnetic field of magnitude  $B_0$  was also applied to the fluid flow. This research is aimed at comparing the thermal efficiency of the nanofluid in question to that of the base fluid. The impact of variables like Darcy and Hartmann numbers was also investigated. The problem is simulated in several different modes to investigate the magnetic field, the porous medium, and the impact of the nanofluid (water and  $\text{Al}_2\text{O}_3$  nanofluid). Different Darcy numbers (0.1, 0.01, 0.001, and 0.0001) have been investigated to investigate the porous medium.

Also, different Hartmann numbers (10, 20, 30, and 40) and different magnetic field orientations (0, 30, 60, and 90 degrees) have been investigated to investigate the magnetic field. Nickel is also thought to be present in a porous metal foam environment.

**2.2. The Governing Equations.** The equations of mass, momentum, and energy for a 2D steady-state flow are shown here:

$$\begin{aligned} \frac{\partial u}{\partial x} + \frac{\partial v}{\partial y} &= 0, \\ \frac{1}{\varepsilon^2} \left( u \frac{\partial u}{\partial x} + v \frac{\partial u}{\partial y} \right) &= -\frac{1}{\rho_{nf}} \frac{\partial p}{\partial x} + \frac{\vartheta_{nf}}{\varepsilon} \left( \frac{\partial^2 u}{\partial x^2} + \frac{\partial^2 u}{\partial y^2} \right) \\ &\quad + \frac{\sigma_{nf} B_0^2}{\rho_{nf}} (v \sin(\psi) \cos(\psi) - u \sin^2(\psi)) \\ &\quad - \frac{\vartheta_{nf} u}{K} - \frac{\vartheta_{nf} C_d |\vec{u}|}{\sqrt{k}} u, \\ \frac{1}{\varepsilon^2} \left( u \frac{\partial v}{\partial x} + v \frac{\partial v}{\partial y} \right) &= -\frac{1}{\rho_{nf}} \frac{\partial p}{\partial y} + \frac{\vartheta_{nf}}{\varepsilon} \left( \frac{\partial^2 v}{\partial x^2} + \frac{\partial^2 v}{\partial y^2} \right) \\ &\quad + \frac{\sigma_{nf} B_0^2}{\rho_{nf}} (v \sin(\psi) \cos(\psi) - v \cos^2(\psi)) \\ &\quad - \frac{\vartheta_{nf} v}{K} - \frac{\vartheta_{nf} C_d |\vec{v}|}{\sqrt{k}} v, \\ u \frac{\partial T}{\partial x} + v \frac{\partial T}{\partial y} &= \alpha_{nf} \left( \frac{\partial^2 T}{\partial x^2} + \frac{\partial^2 T}{\partial y^2} \right). \end{aligned} \quad (1)$$

Several variables in dimensionless equations are described as follows:

$$\begin{aligned} X &= \frac{x}{D}, \\ Y &= \frac{y}{D}, \\ U &= \frac{u}{U_{\text{in}}}, \\ V &= \frac{v}{U_{\text{in}}}, \\ P &= \frac{P}{\rho U_{\text{in}}^2}, \\ \theta &= k_f \frac{T - T_{\text{in}}}{q' D}, \end{aligned} \quad (2)$$

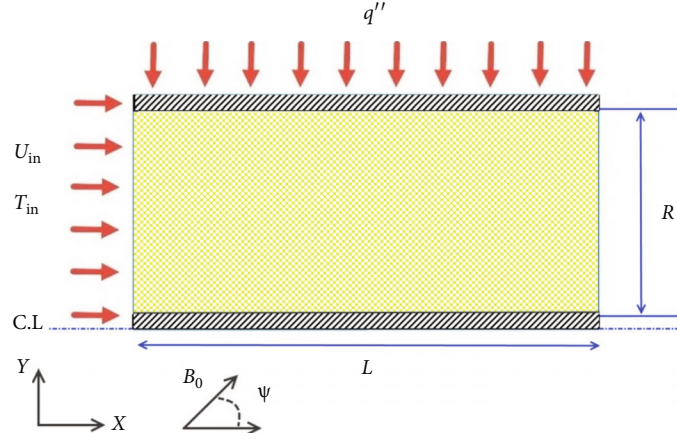


FIGURE 1: Schematic showing the problem that was resolved.

$$\begin{aligned}
 C_d &= \frac{1.75}{\sqrt{150}\epsilon^{3/2}}, \\
 \text{Pr} &= \frac{\vartheta_f}{\alpha_f}, \\
 \text{Re} &= \frac{\rho_f U D}{\mu_f}, \\
 \text{Nu} &= \frac{hD}{k}, \\
 \text{Da} &= \frac{k}{D^2}, \\
 \text{Ha} &= B_0 D \sqrt{\frac{\sigma_f}{\mu_f}}.
 \end{aligned} \tag{3}$$

In Equation (3),  $C_d$ , Pr, Re, Nu, Da, and Ha denote the inertial coefficients of the porous medium, Prantel, Reynolds, Nusselt, Darcy, and Hartmann, respectively. The dimensionless form of the equations may be derived by replacing the dimensionless parameters in

$$\frac{\partial U}{\partial X} + \frac{\partial V}{\partial Y} = 0, \tag{4}$$

$$\begin{aligned}
 \frac{1}{\epsilon^2} \left( U \frac{\partial U}{\partial X} + V \frac{\partial U}{\partial Y} \right) &= -\frac{\rho_f}{\rho_{nf}} \frac{\partial P}{\partial X} + \frac{\vartheta_f}{\vartheta_{nf}} \frac{1}{\text{Re} \cdot \epsilon} \left( \frac{\partial^2 U}{\partial X^2} + \frac{\partial^2 U}{\partial Y^2} \right) \\
 &+ \frac{\rho_f}{\rho_{nf}} \frac{\sigma_{nf}}{\sigma_f} \frac{\text{Ha}^2}{\text{Re}} (V \sin(\psi) \cos(\psi) - U \sin^2(\psi)) \\
 &- \frac{U}{\text{ReDa}} - \frac{\epsilon C_d |\vec{U}|}{\sqrt{\text{Da}}} U,
 \end{aligned} \tag{5}$$

$$\begin{aligned}
 \frac{1}{\epsilon^2} \left( U \frac{\partial V}{\partial X} + V \frac{\partial V}{\partial Y} \right) &= -\frac{\rho_f}{\rho_{nf}} \frac{\partial P}{\partial Y} + \frac{\vartheta_f}{\vartheta_{nf}} \frac{1}{\text{Re} \cdot \epsilon} \left( \frac{\partial^2 V}{\partial X^2} + \frac{\partial^2 V}{\partial Y^2} \right) \\
 &+ \frac{\rho_f}{\rho_{nf}} \frac{\sigma_{nf}}{\sigma_f} \frac{\text{Ha}^2}{\text{Re}} (U \sin(\psi) \cos(\psi) - V \sin^2(\psi)) \\
 &- \frac{V}{\text{ReDa}} - \frac{\epsilon C_d |\vec{V}|}{\sqrt{\text{Da}}} V,
 \end{aligned} \tag{6}$$

$$U \frac{\partial T}{\partial X} + V \frac{\partial T}{\partial Y} = -\frac{k_{nf}}{k_f} \frac{1}{\text{Re} \cdot \text{Pr}} \frac{(\rho c_p)_f}{(\rho c_p)_{nf}} \left( \frac{\partial^2 \theta}{\partial X^2} + \frac{\partial^2 \theta}{\partial Y^2} \right). \tag{7}$$

In recent decades, the physical properties of nanofluids have received more attention. In this study, water was considered the main fluid in which aluminum particles were used as the most common nanoparticles. The following equations have been used to determine the effective coefficients of electrical conductivity, density, volumetric thermal expansion, heat capacity, and thermal penetration of the studied nanofluid:

$$\sigma_{\text{hnf}} = (1 - \phi)\sigma_f + \phi\sigma_{\text{np}}, \tag{8}$$

$$\rho_{\text{hnf}} = (1 - \phi)\rho_f + \phi\rho_{\text{np}}, \tag{9}$$

$$(\rho\beta)_{\text{hnf}} = (1 - \phi)(\rho\beta)_f + \phi(\rho\beta)_{\text{np}}, \tag{10}$$

$$(\rho c_p)_{\text{hnf}} = (1 - \phi)(\rho c_p)_f + \phi(\rho c_p)_{\text{np}}, \tag{11}$$

$$\alpha_{\text{hnf}} = \frac{k_{\text{hnf}}}{(\rho c_p)_{\text{hnf}}}. \tag{12}$$

In Equations (8)–(12), hnf, f, and np represent the properties of composite nanofluids, pure fluids, and nanoparticles, respectively. Maxwell and Brinkmann equations were used to calculate the thermal conductivity and viscosity of the nanofluid:



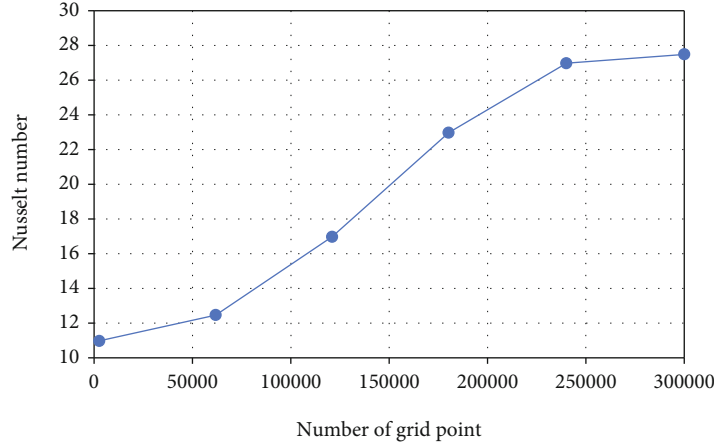


FIGURE 2: Changes in the Nusselt number with different numbers of networks.

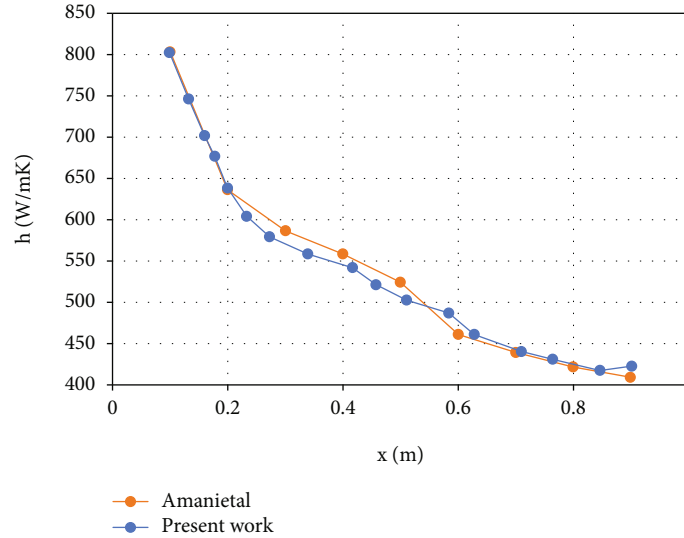


FIGURE 3: Check the validity of the results with Amani et al.

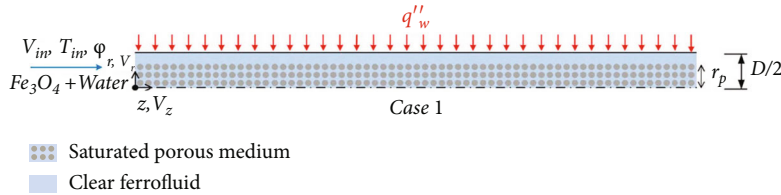


FIGURE 4: Geometrics description of the problem.

$$k_{hnf} = \frac{k_{np} + (n-1)k_f - (n-1)(k_f - k_{np})\phi}{k_{np} + (n-1)k_f + (k_f - k_{np})\phi} k_f, \quad (13)$$

$$\mu_{hnf} = \frac{\mu_f}{(1-\phi)^{2.5}}$$

2.3. *Mesh Independence.* Network generation is a crucial element of the simulation because of the influence of mesh on time, convergence, and solution outcomes. In addition, compared to an irregular network, a regular network has a better effect on the mentioned parameters. Significantly,

networks close to the wall must be small enough to assess the slopes of the sloping physical properties in that area. A regular grid with incremental components throughout the radius was employed since these slopes are perpendicular to the walls. As illustrated in Figure 2, network independence is also demonstrated. In the network span, the comparative difference of Nusselt numbers was  $1500 \times 50$  and  $3000 \times 100$  under 0.5 percent, as shown by Figure 2. In this case, 50 and 1500 networks were evaluated along the Y and X axes, respectively. As mentioned in the boundary condition problem, water enters the canal at 25°C and Reynolds 500.

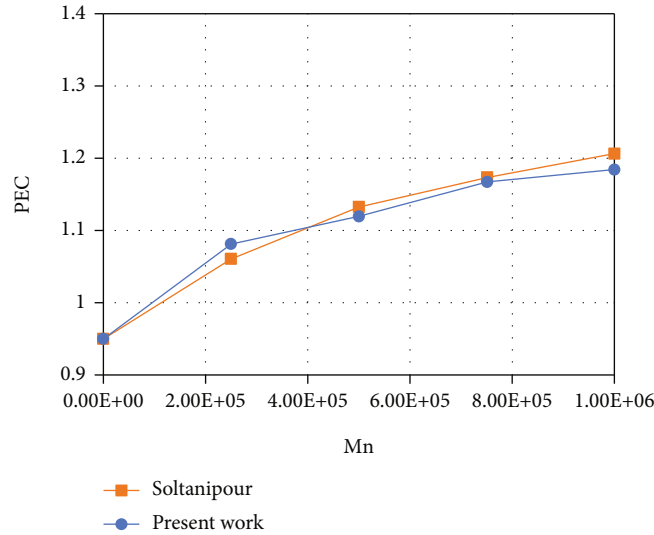


FIGURE 5: Check the validity of the results with Soltanipour and Pourfattah [23].

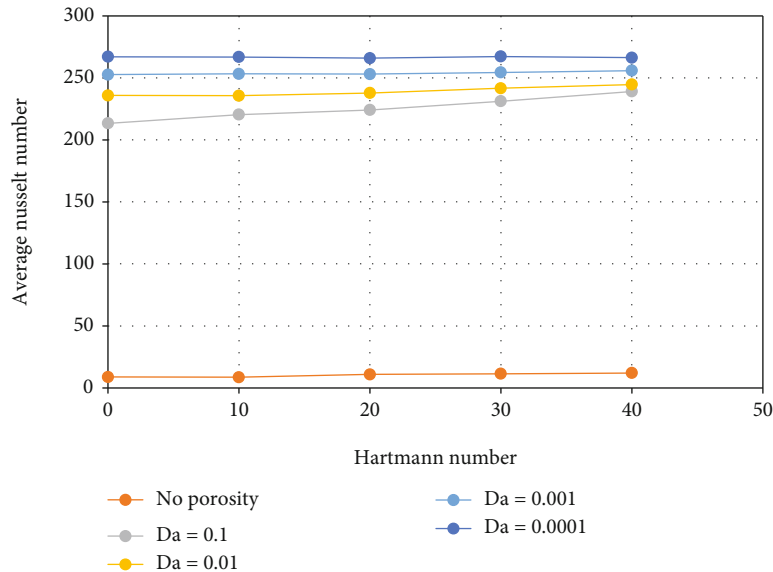


FIGURE 6: Average Nusselt number based on Hartmann number for different numbers of Darcy using water as the base fluid for 0.2 nanofluids.

**2.4. Validation.** Before reviewing the results, it is necessary to confirm the validity of the obtained results. In order to validate the numerical results, the heat transfer coefficient values provided by Amani et al. [23] in the porous metal foam tube under the constant magnetic field have been examined using the heat transfer convection subject  $\text{Fe}_3\text{O}_4$  nanofluid.  $\text{Fe}_3\text{O}_4$  nanofluid with a volume fraction of 0.2 and a diameter of 10 micrometers has been used. A nonuniform two-dimensional network is employed in this numerical research. Smaller networks are utilized in these regions because the temperature and velocity gradients between the pipe's intake and surface are considerable. The volume control approach is used to discretize the collection of equations. For diffusion and convective terms, the basic technique is employed to link velocity and pressure, whereas

the second-order upstream method is utilized. The simulation is run on a  $30 \times 4$  grid. For the equations of continuity, motion, and energy, convergence criteria are set so that residuals are smaller than 5-10. The validity of the findings is examined in Figure 3.

In order to make the validation more accurate, it is necessary to compare this research with Soltanipour and Pourfattah [24]. In this paper, a semiporous pipe has diameter  $D$  and length  $L$ , and the value of  $L/D$  is 15. The  $\text{Fe}_3\text{O}_4$ /water magnetic nanofluid enters the tube at a uniform velocity  $V_{in}$ , temperature  $T_{in}$ , and particle void fraction  $\Phi_{in}$ . The tube wall receives a constant  $q'_w$  flux. In investigated geometry, as shown in Figure 4, a porous layer with radius  $r_p$  is located in the core of the tube.

To check the validity of both velocity and temperature fields, it is necessary to validate the PEC criterion of Soltanipour

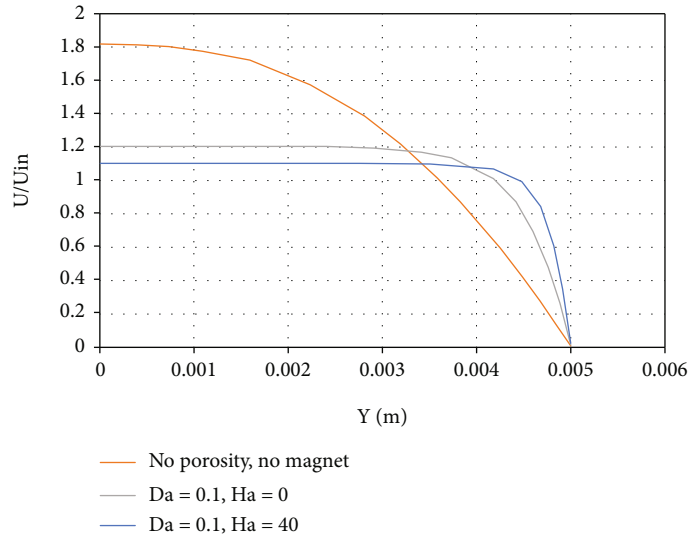


FIGURE 7: Dimensional dimensionless velocity versus radius of the cylinder for different inclination angles using water as base fluid.

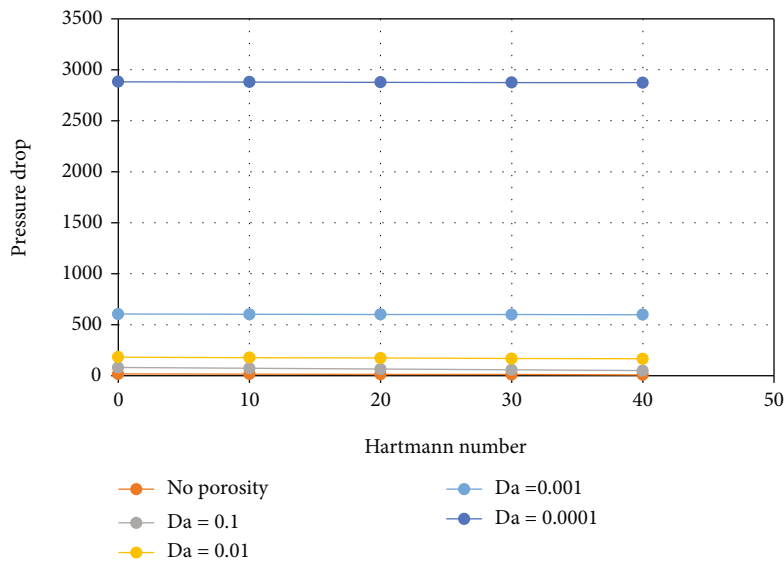


FIGURE 8: The impact of the Hartmann and Darcy numbers on the pressure drop in water and 0.2 nanofluids. The direction of the magnetic field is in the  $y$ -direction ( $\psi = 90$ ).

and Pourfattah [24]. In Figure 5, the value of the PEC parameter in terms of the magnetic field is investigated. In this case, it is assumed that the porous medium occupies half the radius of the pipe.

According to the data obtained from comparing the results of Amani et al. [23] and Soltanipour and Pourfattah [24], the validity of the present study was confirmed.

### 3. Results and Discussion

**3.1. Magnetic Field Effects on Heat Transfer.** Heat transfer and flow behavior are both influenced by the magnetic field. By boosting the magnetic field, the flow can be stabilized and

controlled. Figure 6 shows the difference in the mean of the Nusselt number vs. the Hartmann number in several bags with and without porosity. The direction of the magnetic field is in the  $y$ -direction ( $\psi = 90$ ). The Hartmann number might be regarded as an improvement on the average Nusselt number, indicating an inhibitory effect of Lorentz force ( $\vec{F} = \vec{J} \times \vec{B}$ ). The Hartmann number is the standard Lorentz volumetric force. An increment in it implies that the magnetic field is becoming more intense, furthermore increasing the Nusselt number by reducing the Darcy number from 0.1 to 0.0001 (as a consequence of diminishing the average permeability). In the absence of a porous medium, because nothing stops the flow of fluid and the velocity of the fluid

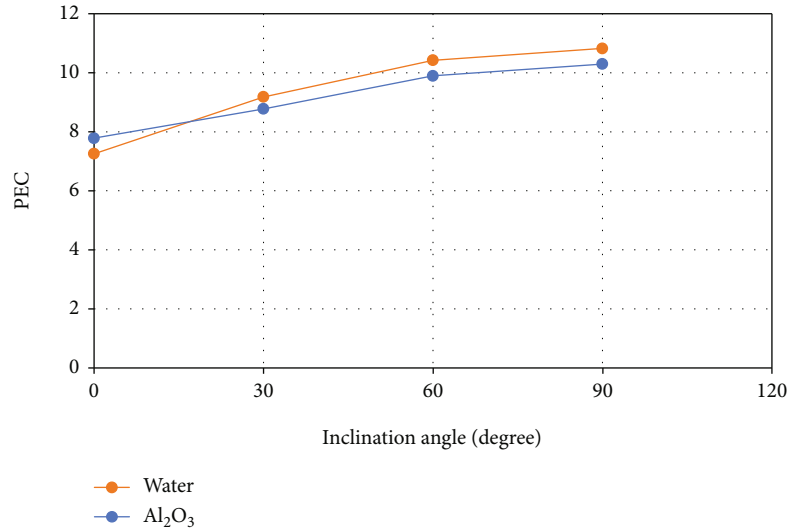


FIGURE 9: PEC for water and nanofluid 0.2 as a function of magnetic field direction ( $Ha = 40$ ,  $Da = 0.1$ ).

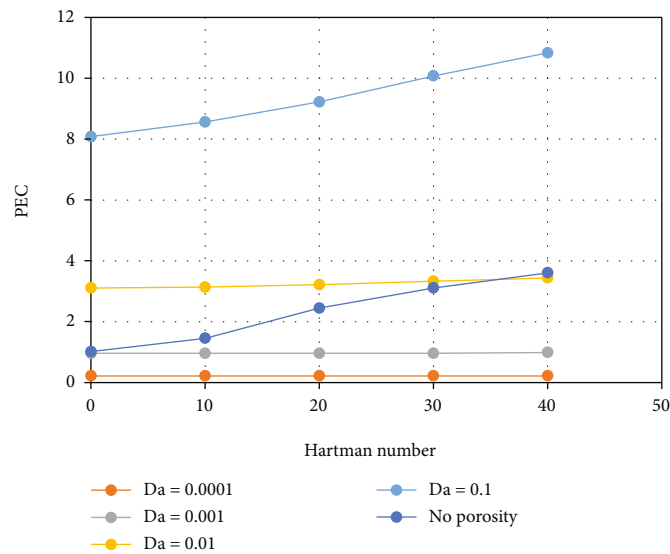


FIGURE 10: PEC changes against the effects of magnetic field and porosity using water as the base fluid for nanofluid 0.2.

along the channel is not reduced, the amount of heat transfer is significantly reduced. As a result, heat transfer can be increased by simultaneously using the porous medium and the magnetic field.

The proportion of the input to the essential configuration speed is referred to as  $U/U_{in}$  dimensionless relevant quantity. Figure 7 shows how the dimensional velocity ratio develops regarding the cylinder radius with water as the base fluid. Figure 7 additionally takes account of the influences of porosity and magnetic field.

It is noteworthy that in Figure 7, the ratio of speed without dimension decreases from 0 to 0.005. Then, as the radius increases, it decreases further and finally reaches zero in the radius of 0.005. Near the wall, high-speed slopes may also be seen (at  $Y = 0.005$ ). The average Nusselt number is increased by more significant velocity gradients in the wall, which

increases the heat transfer rate.  $U/U_{in}$  drops, as shown in Figure 7, using the magnetic field and porosity in the simulation at the beginning of the graph, the slope of the dimensionless velocity curve near the wall rises.

**3.2. The Impacts of the Hartmann Number on Pressure Drop.** Figure 8 depicts the influence of the Hartmann number on pressure drop, with pressure drops diminishing as the Hartmann number increases. This can be attributed to the heat transfer due to the magnetic field. This is due to the intensification of heat transfer due to the presence of a magnetic field. In addition, the pressure drop is shown by increasing the porosity from 0.0001 to 0.1 in the fixed Hartmann number. It has been observed that in the absence of a porous medium, because the medium does not block the fluid and

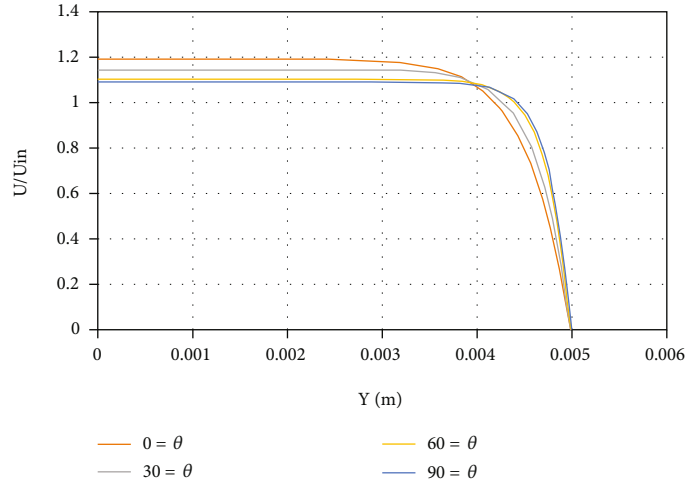


FIGURE 11: Dimensional dimensionless speed versus cylinder radius ratio for different magnetic field angles for  $Al_2O_3$  nanofluid.

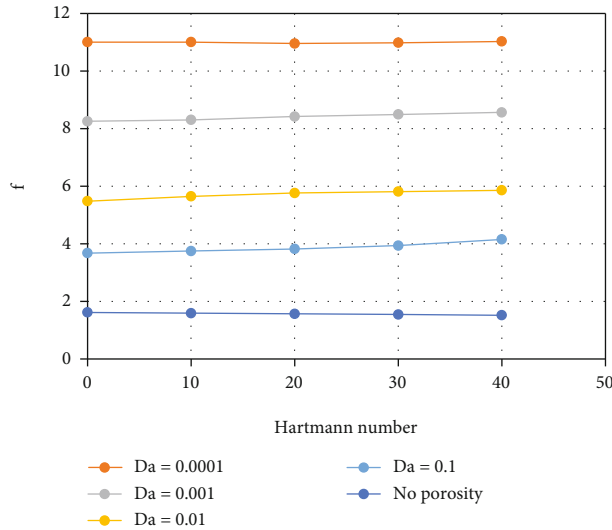


FIGURE 12: Effects of the Hartmann number on the friction factor at different Darcy numbers.

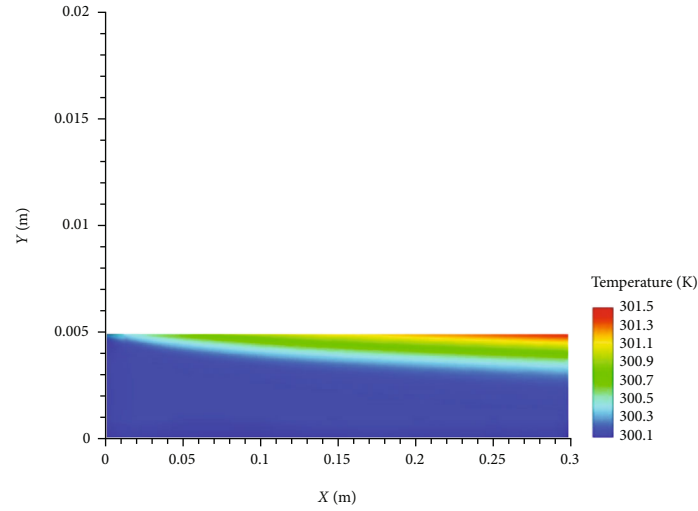
the velocity of the fluid is not decreasing, the amount of pressure is the lowest value compared to the other cases.

**3.3. Magnetic Field Orientation Impacts on Nanofluids.** The effect of the magnetic field orientation on the PEC (performance evaluation criterion) for a fluid comprising nanofluid is shown in Figure 9. The impact of mixing nanoparticles with the base fluid is also depicted. PEC increased somewhat with a shift in the orientation of the magnetic field from 0 to 90 degrees for all fluids, then dropped with an additional modification in orientation. This indicates a crucial orientation of the magnetic field. The magnetic field has the most significant impact on forced nanofluid convection in a chamber. According to the findings, the PEC in the investigated nanofluid was highest when the magnetic field was 90 degrees inclined. The proportion of the Nusselt number in each model of porosity and volume fraction of nanoparticles

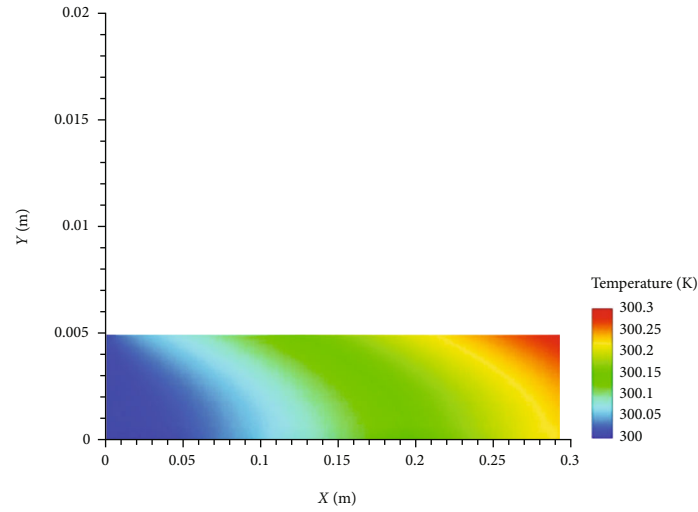
to the Nusselt number in the basic design, in the identical Reynolds number, is referred to as  $Nu/Nu_b$ . The function of the porosity approach or the composition of nanoparticles in improving heat transfer can be better understood using this ratio. Performance evaluation criteria (PEC) can be described as Equation (8) in this context:

$$PEC = \frac{Nu/Nu_b}{(\Delta P/\Delta P_b)^{1/3}} \tag{14}$$

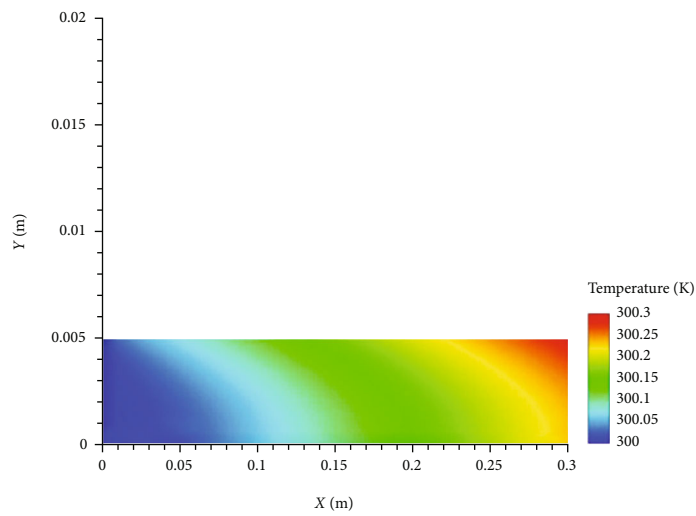
The PEC is applicable in comparing the hydrodynamic and thermal performance of the systems. Figure 10 presents the PEC values calculated for different Darcy numbers as a function of the Hartmann number. According to Figure 10, for a fixed Darcy number, an increment can be observed in the PEC due to Hartmann number enhancement which



(a)



(b)



(c)

FIGURE 13: (a) Temperature contour for different Darcy and Hartmann numbers for water and nanofluid 0.2% ( $Da = 0$ ,  $Ha = 0$ ). (b) Temperature contour for different Darcy and Hartmann numbers for water and nanofluid 0.2% ( $Da = 0.1$ ,  $Ha = 0$ ). (c) Temperature contour for different Darcy and Hartmann numbers for water and nanofluid 0.2% ( $Da = 0.1$ ,  $Ha = 40$ ).

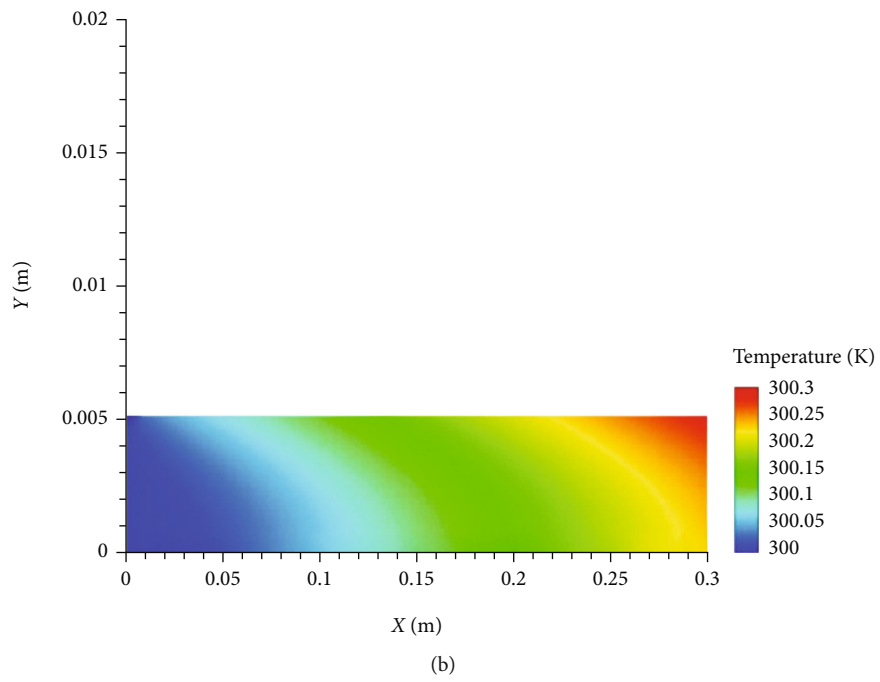
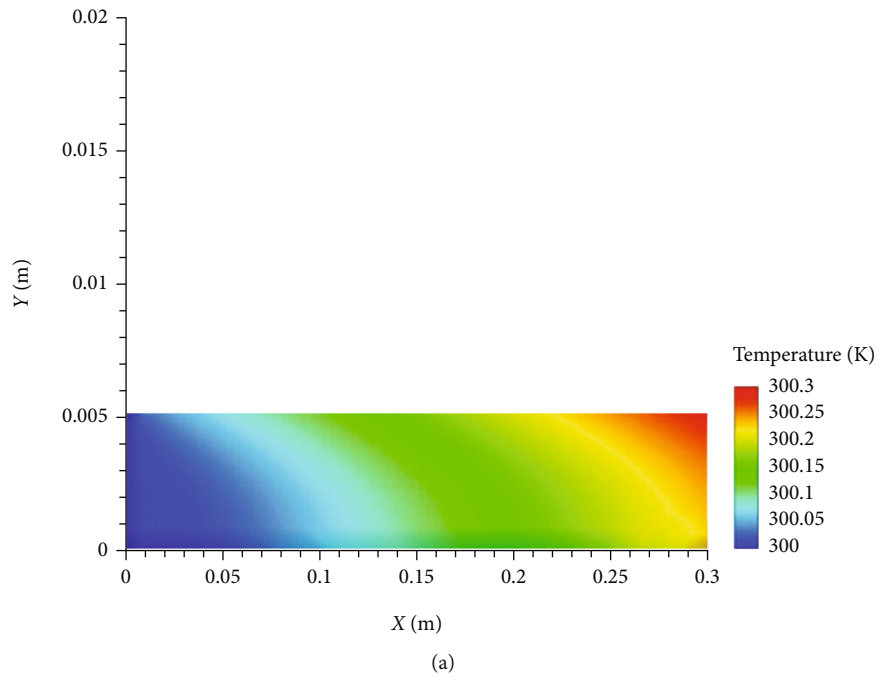


FIGURE 14: Continued.

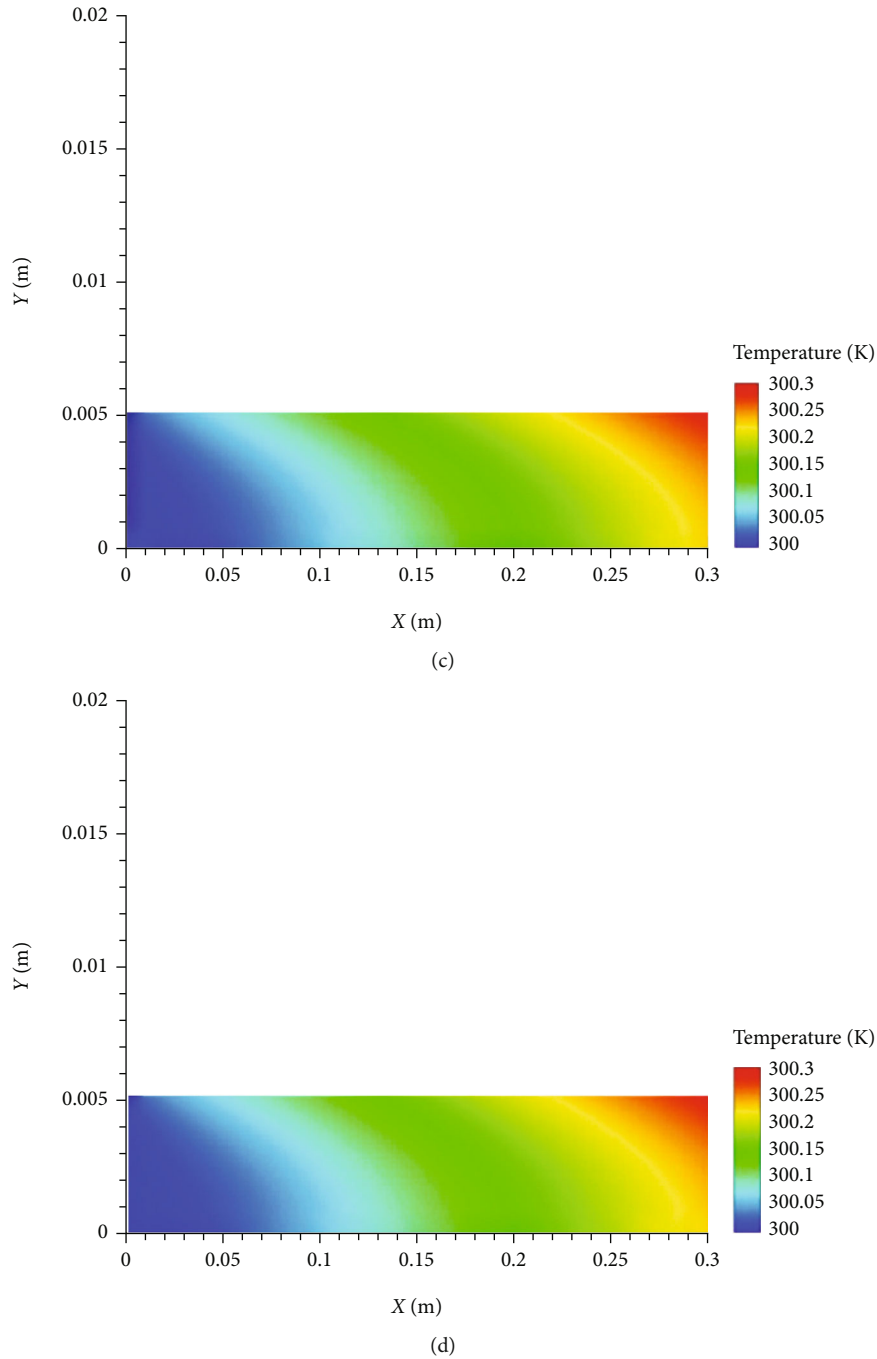


FIGURE 14: (a) Temperature contour for various slope angles for  $\text{Al}_2\text{O}_3$  nanofluid ( $\text{Da} = 0.1$ ,  $\text{Ha} = 40$ ,  $\psi = 0^\circ$ ). (b) Temperature contour for various slope angles for  $\text{Al}_2\text{O}_3$  nanofluid ( $\text{Da} = 0.1$ ,  $\text{Ha} = 40$ ,  $\psi = 30^\circ$ ). (c) Temperature contour for various slope angles for  $\text{Al}_2\text{O}_3$  nanofluid ( $\text{Da} = 0.1$ ,  $\text{Ha} = 40$ ,  $\psi = 60^\circ$ ). (d) Temperature contour for various slope angles for  $\text{Al}_2\text{O}_3$  nanofluid ( $\text{Da} = 0.1$ ,  $\text{Ha} = 40$ ,  $\psi = 90^\circ$ ).

could be assigned to the impact of Lorentz forces on the flow. Maximum PEC (10.81) was recorded at Darcy and Hartmann numbers of 0.1 and 40, respectively. Thus, these values were taken as the default values for PEC calculations and investigation of the impact of magnetic field orientation for various nanofluid compositions.

Figure 11 depicts the dimensional velocity ratio variations for  $\text{Al}_2\text{O}_3$  nanofluid as a function of cylinder radius. In Figure 11, the impact of the slope angle is also studied. The velocity ratio without dimension diminishes from 0 to 0.005,

then lowers again as the radius increases, as seen in Figure 9. Finally, when the radius becomes 0.005, the relative velocity reaches zero. As depicted in Figure 11, increasing the inclination angle from  $0^\circ$  to  $90^\circ$  at the beginning of the curve decreases the dimensionless velocity ratio but increases close the  $U/U_{in}$  slope wall. As shown in Figure 11, the magnetic field affects the Nusselt number in each direction. The magnetic field is more effective when applied vertically ( $90^\circ$ ) than in other directions. In addition, the higher the Nusselt number, the higher the PEC. Therefore, the PEC enhance.



**3.4. The Impact of Hartmann and Darcy Numbers in Friction Factor.** Figure 12 compares the effect of the Hartmann number on the coefficient of friction. The increasing Hartmann number and decreasing Darcy number leads to increasing the coefficient of friction, which is attributed to the high-velocity slope. As a result, the shear stresses of the wall are intensified. For example, by placing a porous medium with  $Da = 10^{-4}$ , the coefficient of friction increases by about 7.2 times. However, the effect of the Hartmann number is negligible compared to the Darcy number. In other words, the application of the Hartmann number has no significant effect on current losses.

**3.5. The Impact of Hartmann and Darcy Numbers in Temperature Counters.** Figure 13(a) shows temperature lines for water as the base fluid in various Darcy and Hartmann values. According to Figure 13(b), the heat transfer rate is improved using the magnetic field and porosity.

In the lack of a magnetic field and a porous nickel media, temperature variations are small and thermal performance is minor, as illustrated in Figure 13(c). As the Darcy and Hartmann values rise, the percentage of convection in the overall heat transfer velocity rises. Furthermore, when Lorentz forces and the permeability of the environment grow, the convection term gets stronger. When a result, as Darcy and Hartmann's numbers rise, the temperature gradient near the wall rises. Better heat transfer performance is achieved with a thin thermal boundary layer close to the wall.

**3.6. Impacts of Magnetic Field Direction on Temperature Contours.** Figures 14(a)–14(d) depict the temperature profile of  $Al_2O_3$  as the nanofluid at the maximum Darcy and Hartmann numbers, 0.1 and 40, respectively.

As shown in Figures 14(a)–14(d), the temperature profile improves when the slope angle changes from  $0^\circ$  to  $90^\circ$ . Also, a maximum temperature gradient is created for the  $90^\circ$  mode. As previously stated, a thin thermal boundary layer near the wall allows for improved heat transfer.

## 4. Conclusion

The effects of mixing a magnetic field and a nanofluid ( $Al_2O_3$ ) into the water in a porous nickel medium on heat transfer were examined in this work. The use of cylindrical geometry, where the walls are subjected to constant and uniform heat flux, was investigated. A two-phase mixed model using a two-phase technique was employed to model the nanofluid flow. The following are some of the study's findings:

- (i) The average Nusselt number rises with decreasing Darcy number and increasing Hartmann number
- (ii) The pressure drop with increasing Hartmann and Darcy numbers shows a downward pattern
- (iii) Improving PEC can be achieved by increasing the Hartmann and Darcy numbers

- (iv) In all cases investigated, adding additional metal nanofluids to the base fluid enhances the mean Nusselt number and PEC
- (v) The PEC achieves its most excellent value for permeable porous medium (for example, media with  $Da = 0.1$  and  $Ha = 40$ )
- (vi) Increasing the orientation of the magnetic field to a certain value ( $90$  degrees) leads to an increase in PEC, and then, increasing the orientation angle reduces the PEC value. The magnetic field near  $90^\circ$  leads to the highest PEC in the nanofluid under study

## Symbols

$B$ :	The intensity of the magnetic field
$C$ :	Specific heat ( $J kg^{-1} K^{-1}$ )
$g$ :	Gravity acceleration ( $m s^{-2}$ )
$J$ :	Electric current density
$K$ :	Permeability of porous medium ( $m^2$ )
$k$ :	Thermal conductivity ( $W m^{-1} K^{-1}$ )
$L$ :	Length (m)
$P$ :	Dimensionless pressure
$p$ :	Pressure (Pa)
$q''$ :	Heat flux ( $W m^{-2}$ )
$R$ :	Radius (m)
$T$ :	Temperature (K)
$U, V$ :	Dimensionless velocity
$u, v$ :	Velocity components ( $m s^{-1}$ )
$X, Y$ :	Dimensionless cylindrical coordinates
$x, y$ :	Cylindrical coordinates (m).

### Greek Symbols

$\alpha$ :	Thermal diffusivity ( $m^2 s^{-1}$ )
$\beta$ :	Thermal expansion coefficient ( $K^{-1}$ )
$\varepsilon$ :	Porosity
$\theta$ :	Dimensionless temperature
$\vartheta$ :	Kinematic viscosity ( $m^2 s^{-1}$ )
$\mu$ :	Dynamic viscosity ( $kg m^{-1} s^{-1}$ )
$\rho$ :	Density ( $kg m^3$ )
$\sigma$ :	Electrical conductivity ( $\Omega^{-1} m^{-1}$ )
$\varphi$ :	Volume fraction
$\psi$ :	Magnetic field angle.

### Abbreviations

Da:	Darcy number
Ha:	Hartmann number
MHD:	Magnetohydrodynamics
Nu:	Nusselt number
Pr:	Prandtl number
Re:	Reynolds number.

## Data Availability

The manuscript is a numerical and mathematical simulation of CFD equations. Therefore, there is not any dataset for the manuscript.

## Conflicts of Interest

We declare no conflict of interest.

## References

- [1] Q. Chen, J.-H. Hao, and T. Zhao, "An alternative energy flow model for analysis and optimization of heat transfer systems," *International Journal of Heat and Mass Transfer*, vol. 108, pp. 712–720, 2017.
- [2] Z. Shah, M. R. Hajizadeh, N. A. Alreshidi, W. Deebani, and M. Shutaywi, "Entropy optimization and heat transfer modeling for Lorentz forces effect on solidification of NEPCM," *International Communications in Heat and Mass Transfer*, vol. 117, article 104715, 2020.
- [3] P. H. Jadhav, G. Trilok, N. Gnanasekaran, and M. Mobedi, "Performance score based multi-objective optimization for thermal design of partially filled high porosity metal foam pipes under forced convection," *International Journal of Heat and Mass Transfer*, vol. 182, article 121911, 2022.
- [4] Y. Menni, A. J. Chamkha, and A. Azzi, "Nanofluid transport in porous media: a review," *Special Topics & Reviews in Porous Media: An International Journal*, vol. 10, no. 1, pp. 49–64, 2019.
- [5] Y. Cui, J. Zhu, S. Zoras, and J. Zhang, "Comprehensive review of the recent advances in PV/T system with loop-pipe configuration and nanofluid," *Renewable and Sustainable Energy Reviews*, vol. 135, p. 110254, 2021.
- [6] M. Sheikholeslami and H. B. Rokni, "Simulation of nanofluid heat transfer in presence of magnetic field: a review," *International Journal of Heat and Mass Transfer*, vol. 115, pp. 1203–1233, 2017.
- [7] S. Yekani Motlagh, A. Sharifi, M. Ahmadi, and H. Badfar, "Presentation of new thermal conductivity expression for  $\text{Al}_2\text{O}_3$ -water and  $\text{CuO}$ -water nanofluids using gene expression programming (GEP)," *Journal of Thermal Analysis & Calorimetry*, vol. 135, no. 1, 2019.
- [8] Y. He, Y. Jin, H. Chen, Y. Ding, D. Cang, and L. Huilin, "Heat transfer and flow behaviour of aqueous suspensions of  $\text{TiO}_2$  nanoparticles (nanofluids) flowing upward through a vertical pipe," *International Journal of Heat and Mass Transfer*, vol. 50, no. 11–12, pp. 2272–2281, 2007.
- [9] M. U. Sajid and H. M. Ali, "Recent advances in application of nanofluids in heat transfer devices: a critical review," *Renewable and Sustainable Energy Reviews*, vol. 103, pp. 556–592, 2019.
- [10] S. Nazari and D. Toghraie, "Numerical simulation of heat transfer and fluid flow of water-CuO nanofluid in a sinusoidal channel with a porous medium," *Physica E: Low-dimensional Systems and Nanostructures*, vol. 87, 2017.
- [11] A. Sharifi, S. Y. Motlagh, and H. Badfar, "Investigation of the effects of two parallel wires' non-uniform magnetic field on heat and biomagnetic fluid flow in an aneurysm," *International Journal of Computational Fluid Dynamics*, vol. 32, no. 4–5, pp. 248–259, 2018.
- [12] N. Dukhan and K.-C. Chen, "Heat transfer measurements in metal foam subjected to constant heat flux," *Experimental Thermal and Fluid Science*, vol. 32, no. 2, pp. 624–631, 2007.
- [13] V. V. Calmidi and R. L. Mahajan, "Forced convection in high porosity metal foams," *Journal of Heat Transfer*, vol. 122, no. 3, pp. 557–565, 2000.
- [14] B. Boyd and K. Hooman, "Air-cooled micro-porous heat exchangers for thermal management of fuel cells," *International Communications in Heat and Mass Transfer*, vol. 39, no. 3, pp. 363–367, 2012.
- [15] M. Odabae and K. Hooman, "Application of metal foams in air-cooled condensers for geothermal power plants: an optimization study," *International Communications in Heat and Mass Transfer*, vol. 38, no. 7, pp. 838–843, 2011.
- [16] Y. R. Lin, J. H. Du, W. Wu, L. C. Chow, and W. Notardonato, "Experimental study on heat transfer and pressure drop of recuperative heat exchangers using carbon foam," *Journal of Heat Transfer*, vol. 132, no. 9, 2010.
- [17] Y. Chen, P. Luo, Q. Tao, X. Liu, and D. He, "Natural convective heat transfer investigation of nanofluids affected by electrical field with periodically changed direction," *International Communications in Heat and Mass Transfer*, vol. 128, p. 105613, 2021.
- [18] C. Qi, J. Tang, Z. Ding, Y. Yan, L. Guo, and Y. Ma, "Effects of rotation angle and metal foam on natural convection of nanofluids in a cavity under an adjustable magnetic field," *International Communications in Heat and Mass Transfer*, vol. 109, p. 104349, 2019.
- [19] A. Izadi, M. Siavashi, H. Rasam, and Q. Xiong, "MHD enhanced nanofluid mediated heat transfer in porous metal for CPU cooling," *Applied Thermal Engineering*, vol. 168, p. 114843, 2020.
- [20] P. Rabbani, A. Hamzhepour, M. Ashjaee, M. Najafi, and E. Houshfar, "Experimental investigation on heat transfer of  $\text{MgO}$  nanofluid in tubes partially filled with metal foam," *Powder Technology*, vol. 354, pp. 734–742, 2019.
- [21] M. Ameri, M. Amani, and P. Amani, "Thermal performance of nanofluids in metal foam tube: thermal dispersion model incorporating heterogeneous distribution of nanoparticles," *Advanced Powder Technology*, vol. 28, no. 10, pp. 2747–2755, 2017.
- [22] H. Badfar, S. Y. Motlagh, and A. Sharifi, "Numerical simulation of magnetic drug targeting to the stenosis vessel using  $\text{Fe}_3\text{O}_4$  magnetic nanoparticles under the effect of magnetic field of wire," *Cardiovascular Engineering and Technology*, vol. 11, no. 2, pp. 162–175, 2020.
- [23] M. Amani, M. Ameri, and A. Kasaeian, "Investigating the convection heat transfer of  $\text{Fe}_3\text{O}_4$  nanofluid in a porous metal foam tube under constant magnetic field," *Experimental Thermal and Fluid Science*, vol. 82, pp. 439–449, 2017.
- [24] H. Soltanipour and F. Pourfattah, "Simultaneous use of non-uniform magnetic field and porous medium for the intensification of convection heat transfer of a magnetic nanofluid inside a tube," *Journal of the Brazilian Society of Mechanical Sciences and Engineering*, vol. 43, no. 10, pp. 1–19, 2021.

## Research Article

# Transient Pressure Behavior of Complex Fracture Networks in Unconventional Reservoirs

Gou Feifei,<sup>1</sup> Liu Chuanxi,<sup>1</sup> Ren Zongxiao ,<sup>2,3</sup> Qu Zhan,<sup>2,3</sup> Wang Sukai,<sup>4</sup> Qin Xuejie,<sup>1</sup> Fang Wenchao,<sup>1</sup> Wang Ping,<sup>2,3</sup> and Wang Xinzhu<sup>2,3</sup>

<sup>1</sup>State Key Laboratory of Shale Oil and Gas Enrichment Mechanisms and Effective Development, China

<sup>2</sup>College of Petroleum Engineering, Xi'an Shiyou University, Xi'an 710065, China

<sup>3</sup>Xi'an Shiyou University Shanxi Key Laboratory of Well Stability and Fluid & Rock Mechanics in Oil and Gas Reservoirs, China

<sup>4</sup>Engineering Technology Research Institute Xibu Drilling Engineering Company, Karamay 834000, China

Correspondence should be addressed to Ren Zongxiao; 765802228@qq.com

Received 15 May 2021; Revised 5 June 2021; Accepted 12 October 2021; Published 3 November 2021

Academic Editor: Jianchao Cai

Copyright © 2021 Gou Feifei et al. This is an open access article distributed under the Creative Commons Attribution License, which permits unrestricted use, distribution, and reproduction in any medium, provided the original work is properly cited.

Unconventional resources have been successfully exploited with technological advancements in horizontal-drilling and multistage hydraulic-fracturing, especially in North America. Due to preexisting natural fractures and the presence of stress isotropy, several complex fracture networks can be generated during fracturing operations in unconventional reservoirs. Using the DVS method, a semianalytical model was created to analyze the transient pressure behavior of a complex fracture network in which hydraulic and natural fractures interconnect with inclined angles. In this model, the complex fracture network can be divided into a proper number of segments. With this approach, we are able to focus on a detailed description of the network properties, such as the complex geometry and varying conductivity of the fracture. The accuracy of the new model was demonstrated by ECLIPSE. Using this method, we defined six flow patterns: linear flow, fracture interference flow, transitional flow, biradial flow, pseudoradial flow, and boundary response flow. A sensitivity analysis was conducted to analyze each of these flow regimes. This work provides a useful tool for reservoir engineers for fracture designing as well as estimating the performance of a complex fracture network.

## 1. Introduction

Technological advances in horizontal-drilling and multistage hydraulic-fracturing have stimulated a boom in unconventional resource generation throughout the world, especially in North America. Because of the presence of stress isotropy and preexisting natural fractures, complicated fracture networks can be created in unconventional reservoirs when conducting stimulation treatments [1, 2] (Fisher et al., 2002; Maxwell et al., 2002). Knowledge of the fluid flow behavior in these complex fracture networks is essential information to evaluate the performance and effectiveness of stimulation.

Several models have been established by scholars to predict the behavior of fracture networks in unconventional reservoirs in the last decade. These models can be divided into three categories. The first category is the analytical method,

based on the well-known dual-porosity model [3, 4] (Warren and Root, 1963; Kazemi, 1969), which is comprised of the fracture network and surrounding matrix. Analytical models [5–9] (Brown et al., 2011; Ozkan et al., 2011; Xu et al., 2013; Leng et al., 2014; Ting et al., 2015) were developed to investigate the transient pressure behavior of multistage fractured horizontal wells on the basis of the dual-porosity hypothesis. These analytic models have helped engineers gain a comprehensive insight into the performance of fracture networks and have provided practical tools to evaluate stimulation effectiveness. However, the fracture network is very complex, and the dual-porosity medium may not rigorously capture the details of the fracture network characteristics, such as the irregular spatial distribution, complex interconnected scenarios, and conductivity heterogeneity of the fractures.

The second category is semianalytical and was developed using the method of source function [10, 11] (Zhao et al., 2014; Pin et al., 2015). In these models, the complex fracture network can be divided into a proper number of segments. This approach allows one to focus on a detailed description of the network properties and overcomes the shortcomings of the analytical method. Yet, these semianalytical models cannot accurately simulate the fluid flow in a reservoir. These semianalytical models assume that the fluid flow in the reservoir is 2D in an infinite plate reservoir, and the source function cannot consider the effects of fracture geometry. We show an approach that can overcome these shortcomings in the model described below.

The third category is numerical simulation, in which the hydraulic and natural fractures are usually represented by high permeability refined grids [12–14] (Palagi and Aziz, 1994; Skoreyko and Peter, 2003; Li et al., 2003). Based on a structured grid system in conventional numerical simulators [15–17], Mayerhofer et al. (2010), Warpinski et al. (2008), and Cipolla (2009) simulated the production of orthogonal networks in shale gas reservoirs. These works qualitatively analyzed how the size and density, fracture conductivity, matrix permeability, and gaps in fracture networks affect the horizontal well productivity. However, the numerical methods are time-consuming and have inherent uncertainties that could cause them to be less accurate.

In view of this, there is still lack of an efficient and rigorous approach to model the flow behavior of complex fracture networks in unconventional reservoirs. The main objective of this paper is to develop a semianalytical model that can evaluate the performance of such networks more rigorously and efficiently compared to the existing methods. This new model is based on the DVS (distributed volume sources) method [18] (Valko et al. 2007), in which the fractures in the network are explicitly represented by discrete segments to concentrate on the details of the network characteristics, such as the complex geometry and varying conductivity. The DVS model can simulate fluid flow in a closed boundary reservoir in 3D. The accuracy of the new model was demonstrated by ECLIPSE. Then, using this method, we defined the flow patterns of the fluid in the reservoir and conducted a sensitivity analysis of the transient pressure behavior.

## 2. Establishment of the Theoretical Model

First, we describe the fracture network used to introduce our approach and then provide the mathematic model for the reservoir and fracture flow.

*2.1. Physical Model.* For convenience, natural fractures were assumed to develop along the main hydraulic fractures orthogonally, as shown in Figure 1. The other assumptions were as follows:

- (1) The reservoir is anisotropic and homogeneous with closed boundaries (shaped like a box)
- (2) The horizontal fractured well produces at a constant rate

- (3) To simplify the flow model of natural fractures, which is in the middle of two main fractures, the bisector of the distance between two hydraulic fractures is a no-flow boundary (labeled in green in Figure 1). The red arrows (in Figure 1) represent the flow directions in natural fractures, which are in the middle of two main fractures. Fluid flows from the natural fractures into the hydraulic fractures, then through the main fractures into wellbore
- (4) The flow model inner fractures are 1D
- (5) The impacts of gravity and capillary forces are neglected
- (6) The orthogonal fracture network is symmetric about the horizontal fractured well.

From Figure 1, we can see that the total number of hydraulic fractures is  $T_H$  and the number of natural fractures is  $T_N$ . The distance of the main fractures is  $\Delta L_H$  and of the natural fractures is  $\Delta L_N$ . The half-length of the hydraulic fracture is  $L_H$  and of the natural fracture is  $L_N$ . The green dashed lines represent no-flow boundaries in accordance with assumption (3). Part of the fracture network is divided in the dashed box and enlarged for clarity. Each main fracture is separated into  $S_H$  segments, and the natural fracture is discretized into  $S_N$  segments. Thus, the total number of segments in the fracture network is  $T_H \times S_H + T_N \times S_N$ . Each of the segments can be considered a little fracture, so that the pressure response caused by the complex fracture network can be calculated by the superposition of the pressure effects (a detailed introduction is provided in Section 2.2.1).

### 2.2. Mathematical Model

*2.2.1. Reservoir Flow.* Different techniques were developed to solve the single-phase slightly compressible flow problems in porous media in which the fluid is removed or injected from the oil well. One of the most widely used methods is the source function presented by Gringarten and Ramey [19]. From then on, the source function approach was successfully applied to accurately evaluate the performance of a vertical well, horizontal well, horizontal well with hydraulic fractures, and so on [20–23] (Cinco-Ley et al., 1981; Guppy et al., 1982; Ozkan, 1988; Chen et al., 1997). The major disadvantage of this method is the inherent singularity of the solution wherever the point source is placed. Valko et al. (2007) established the DVS method to remove this limitation by assuming a source not in the form of a point but in the form of a rectilinear volume extended inside the surrounding rectilinear porous media. The DVS method has the capability to handle complicated well/fracture configurations. However, the major weakness of the DVS method is the difficulty in calculating the behavior of the complex fracture network because the inner “source box” must be parallelized with the reservoir boundaries. In the following, this shortcoming is eliminated by a new DVS function. The new DVS can calculate the pressure response when the

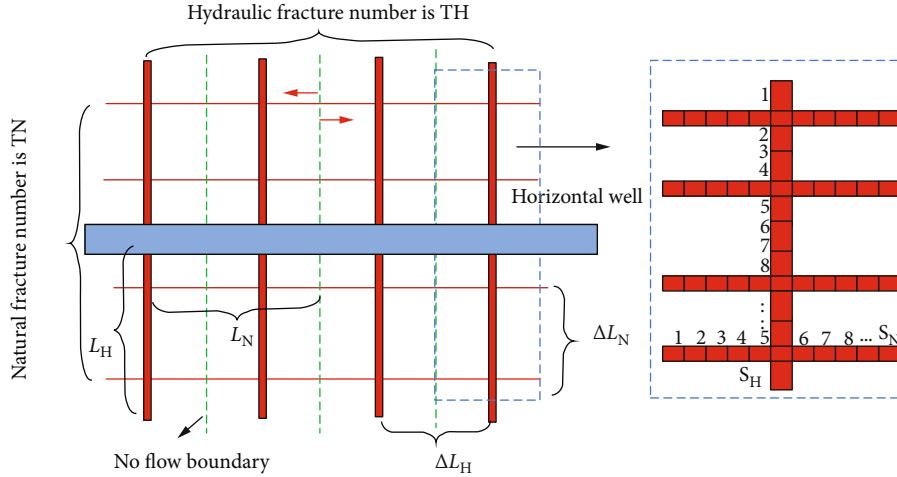


FIGURE 1: Physical model and discretized fracture segments of a complex fracture network.

surfaces of the fracture have inclined angles with the reservoir boundary's directions.

(1) *Valko's (2007) DVS Model*. First, the main principle of Valko's (2007) DVS method will be introduced. A schematic of Valko's (2007) DVS is shown in Figure 2. The reservoir is homogeneous with closed boundaries (box-shaped). The inner "source box" is assumed to be a smaller rectilinear box with surfaces parallel to the reservoir boundaries (for simplicity, the inner "source box" can be considered a little fracture).

As shown in Figure 2, the geometry of this model is described with the following parameters: reservoir dimen-

sions in the  $x$ ,  $y$ , and  $z$  directions ( $x_e$ ,  $y_e$ , and  $z_e$ , respectively); reservoir permeability along the principal axes ( $k_x$ ,  $k_y$ , and  $k_z$ ); coordinates of the center point of the source ( $c_x$ ,  $c_y$ , and  $c_z$ ); and half-lengths of the source in the  $x$ ,  $y$ , and  $z$  directions ( $w_x$ ,  $w_y$ , and  $w_z$ , respectively). The mathematical model for the volume source in closed boundaries was established by Valko et al. (2007) and is shown in Appendix A.

The pressure response of a rectilinear reservoir with closed boundaries for an instantaneous withdrawal from the volume source was given by Valko (2007) and is as follows (the definitions of the dimensionless variables are shown as Appendix B):

$$\begin{aligned}
 P_{\delta D}(x_D, y_D, z_D, t_D) = & \left[ 1 + \sum_{n=1}^{\infty} \frac{\sin n\pi(c_{xD} + w_{xD}) - \sin n\pi(c_{xD} - w_{xD})}{2n\pi w_{xD}} \cos n\pi x_D e^{-n^2\pi^2(k_x/k)(L/x_e)^2 t_D} \right] \\
 & \times \left[ 1 + \sum_{n=1}^{\infty} \frac{\sin n\pi(c_{yD} + w_{yD}) - \sin n\pi(c_{yD} - w_{yD})}{2n\pi w_{yD}} \cos n\pi y_D e^{-n^2\pi^2(k_y/k)(L/y_e)^2 t_D} \right] \\
 & \times \left[ 1 + \sum_{n=1}^{\infty} \frac{\sin n\pi(c_{zD} + w_{zD}) - \sin n\pi(c_{zD} - w_{zD})}{2n\pi w_{zD}} \cos n\pi z_D e^{-n^2\pi^2(k_z/k)(L/z_e)^2 t_D} \right].
 \end{aligned} \tag{1}$$

Using Equation (1), we obtained a 3D solution of the instantaneous pressure response in anisotropic reservoirs where the permeability along the three axes is different from each other ( $k_x$ ,  $k_y$ , and  $k_z$ ). In addition, contrary to Gringarten's source function, Equation (1) can take the dimension of volume source ( $2w_x$ ,  $2w_y$ , and  $2w_z$ ) into account.

(2) *Establishment of the New DVS Model*. The presence of volume source surfaces in the  $x - y$  plane, which are not par-

allel to the reservoir boundaries, is a common occurrence in complex fracture networks. The schematic for this case is shown in Figure 3.

The inclined angle between the volume source and the  $x$ -axis is denoted as  $\theta_x$ . The endpoint coordinates of the inclined source are  $(c_{x1}, c_{y1})$  and  $(c_{x2}, c_{y2})$ . The  $c_x$  coordinate of the center line for a particular volume source (labeled blue dashed line in Figure 3) is a constant when  $\theta_x = 90^\circ$ . At other

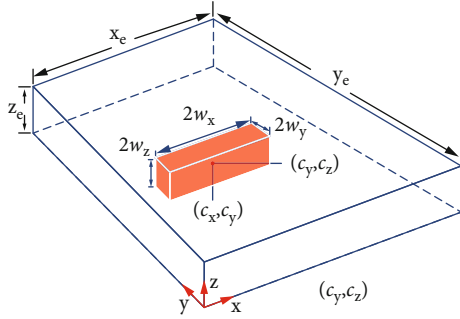


FIGURE 2: Schematic of the volume source in closed boundaries.

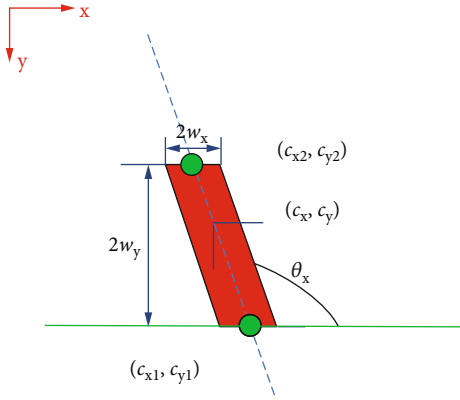


FIGURE 3: The surface of the volume source is not parallel to the reservoir boundaries.

angles, the  $c_x$  coordinate of the center line is a function of  $y$ . As shown in Equation (A.4),  $c_x$  is a term in the Heaviside unit-step function. The role of the Heaviside unit-step function in Equation (A.1) is to limit the position and geometry of the volume source. Therefore, the solution form for the volume source surfaces that are not parallel to reservoir

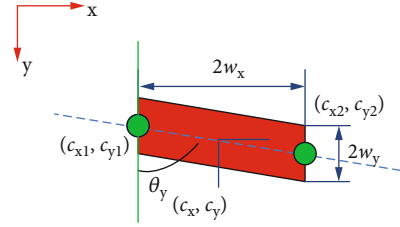


FIGURE 4: The surface of volume source is not parallel to the reservoir boundaries.

boundaries is the same as that in Equation (1), with the addition of a formula to calculate  $c_x$  (shown as Equation (2)).

The geometrical relationship between  $c_x$  and  $y$  is presented as follows.

$$c_x = \begin{cases} c_{x1} + (y - c_{y1})/\tan \theta_x, \theta_x \neq \frac{\pi}{2} \\ c_{x1}, \theta_x = \frac{\pi}{2}. \end{cases} \quad (2)$$

Figure 4 shows the case in which the volume source forms an angle  $\theta_y$  with the  $y$ -axis.

The geometrical relationship between  $c_y$  and  $x$  is similar to Equation (2) and is as follows.

$$c_y = \begin{cases} c_{y1} + (x - c_{x1})/\tan \theta_y, \theta_y \neq \frac{\pi}{2} \\ c_{y1}, \theta_y = \frac{\pi}{2}. \end{cases} \quad (3)$$

Therefore, the pressure response for an instantaneous withdrawal from a volume source, which can have arbitrarily angle (in  $x/y$  or both  $x$  and  $y$  directions), is given as follows:

$$P_{\delta D}(x_D, y_D, z_D, t_D) = \left[ 1 + \sum_{n=1}^{\infty} \frac{\sin n\pi(c_{xD} + w_{xD}) - \sin n\pi(c_{xD} - w_{xD})}{2n\pi w_{xD}} \cos n\pi x_D e^{-n^2\pi^2(k_x/k)(L/x_e)^2 t_D} \right] \\ \times \left[ 1 + \sum_{n=1}^{\infty} \frac{\sin n\pi(c_{yD} + w_{yD}) - \sin n\pi(c_{yD} - w_{yD})}{2n\pi w_{yD}} \cos n\pi y_D e^{-n^2\pi^2(k_y/k)(L/y_e)^2 t_D} \right] \\ \times \left[ 1 + \sum_{n=1}^{\infty} \frac{\sin n\pi(c_{zD} + w_{zD}) - \sin n\pi(c_{zD} - w_{zD})}{2n\pi w_{zD}} \cos n\pi z_D e^{-n^2\pi^2(k_z/k)(L/z_e)^2 t_D} \right], \quad (4)$$

$$c_{xD} = \begin{cases} c_{xD1} + (y_D - c_{yD1})/\tan \theta_x, \theta_x \neq \frac{\pi}{2} \\ c_{xD1}, \theta_x = \frac{\pi}{2}, \end{cases} \quad (5)$$

$$c_{yD} = \begin{cases} c_{yD1} + (x_D - c_{xD1})/\tan \theta_y, \theta_y \neq \frac{\pi}{2} \\ c_{yD1}, \theta_y = \frac{\pi}{2}. \end{cases}$$

From Equations (4) and (5) generalized the forms of Valko's solution, which is specific condition when  $\theta = 90^\circ$  is presented.

To obtain the response of the reservoir for a continuous volume source, we numerically integrate the pressure derivative solution over time:

$$p_D(x_D, y_D, z_D, t_D) = q_D \int_0^{t_D} p_{\delta D}(x_D, y_D, z_D, \tau) d\tau. \quad (6)$$

As for the complex fracture network, shown in Figure 1, each segment can be considered a volume source; therefore, the total number of volume sources is

$$N_T = T_H \times S_H + T_H \times T_N \times S_N. \quad (7)$$

The pressure response at any point in the reservoir (or inside the fracture network) can be calculated by superimposing the source function of the  $N_T$  segments. Thus, the dimensionless pressure of fracture  $i$  can be obtained as follows.

$$p_{Di} = \sum_{j=1}^{n=N_T} q_{Dj} p_{Di,j}. \quad (8)$$

In Equation (8),  $q_{Dj}$  represents the source strength of the segment  $j$ , and  $p_{Di,j}$  represents the dimensionless pressure calculated at the center of segment  $i$  if the source is placed in segment  $j$ .

Applying Equation (8) to all of the fracture segments in the fracture network,  $N_T$  equations are obtained.

**2.2.2. Fracture Flow Model.** Following assumptions (3) and (4), the flow model was established for the fracture network. According to (Gringarten, et al. 1974; Cinco-Ley et al., 1988) [24, 25], the diffusivity equation in the fractures can be described as follows.

$$\frac{k_f}{\mu} \frac{\partial^2 p_f}{\partial x^2} + \frac{q_f}{w_f h} = 0. \quad (9)$$

The initial condition is

$$p_f \Big|_{t=0} = p_i. \quad (10)$$

The inner boundary condition is

$$p_f \Big|_{x=0} = p_w. \quad (11)$$

The outer boundary condition is

$$\frac{\partial p_f}{\partial x} \Big|_{x=L_H} = 0. \quad (12)$$

With the definitions for the dimensionless variables (see Appendix B), the above equations can be adapted as follows:

$$-\frac{\partial^2 p_{fD}}{\partial x_D^2} + \frac{L}{hC_{fD}} q_{fD} = 0, \quad (13)$$

$$p_{fD} \Big|_{t_D=0} = 0, \quad (14)$$

$$p_{fD} \Big|_{x_D=0} = p_{wD}, \quad (15)$$

$$\frac{\partial p_{fD}}{\partial x_D} \Big|_{x_D=L_H} = 0. \quad (16)$$

Solving Equation (13) with the initial condition and boundary conditions, pressure drawdown in the fracture can be obtained as follows:

$$p_{fD}(x_D) - p_{wD} = \frac{L}{hC_{fD}} \int_0^{x_D} \int_0^{\xi} q_{fD}(u) du d\xi - \frac{L}{hC_{fD}} q_{fD} x_D. \quad (17)$$

Discretizing Equation (17) gives the dimensionless pressure drawdown in each fracture segment as follows, for hydraulic fracture segments:

$$p_{fDi}(x_{Di}) - p_{wD} = \frac{L}{hC_{fDj}} \left[ \frac{\Delta x_D}{8} Q_{fDi} + \sum_{j=1}^{i-1} Q_{fDi} \left( \frac{\Delta x_D}{2} + x_{Di} - j\Delta x_D \right) - x_{Di} \sum_{j=1}^{S_H} Q_{fDi} \right]. \quad (18)$$

In Equation (22),  $i = 1, 2, \dots, T_H \times S_H$ ,  $\Delta x_D = L_{FDH}/S_H$ , and  $x_{Di} = (i - 1/2)\Delta x_D$ .

Based on assumption (3), fluid flows from the natural fractures into the hydraulic fractures and then through the main fractures into the wellbore. Therefore, the expression for  $Q_{fDi}$  is shown as follows:

$$Q_{fD} = \begin{cases} q_{fD} + \sum_{k=1}^{SN} \frac{q_{fDk} L_{fDN}}{L_{fDH}}, & \text{for cross segments} \\ q_{fD}, & \text{for independent segments.} \end{cases} \quad (19)$$

In Equation (19),  $q_{fDk}$  represents the flux into the natural fracture segments.

For the natural fracture segments, we have the following:

$$p_{fDi}(x_{Di}) - p_{wD} = \frac{L}{hC_{fDj}} \left[ \frac{\Delta x_D}{8} q_{fDi} + \sum_{j=1}^{i-1} q_{fDi} \left( \frac{\Delta x_D}{2} + x_{Di} - j\Delta x_D \right) - x_{Di} \sum_{j=1}^{SN} q_{fDi} \right]. \quad (20)$$

In Equation (20),  $i = 1, 2, \dots, T_H \times T_N \times S_N$ ,  $\Delta x_D = L_{FDN}/S_N$ , and  $x_{Di} = (i - 1/2)\Delta x_D$ .

Therefore, other  $N_T$  equations are obtained. Considering the continuity condition along with the fracture face, the flux

TABLE 1: Data used for semianalytical and numerical models.

Reservoir length, m	1610	Permeability of hydraulic fractures, D	28
Reservoir width, m	1610	Length of natural fractures, m	200
Reservoir thickness, m	10	Width of natural fractures, m	0.0028
Reservoir compressibility, MPa <sup>-1</sup>	0.00022	Permeability of natural fractures, D	28
Reservoir permeability, mD	0.1	Wellbore radius, m	0.15
Fluid viscosity, pas	0.001	Production rate, m <sup>3</sup> /d	0.5
Length of hydraulic fractures, m	200	Reservoir initial pressure, MPa	14.6
Width of hydraulic fractures, m	0.0028	Reservoir porosity	0.1

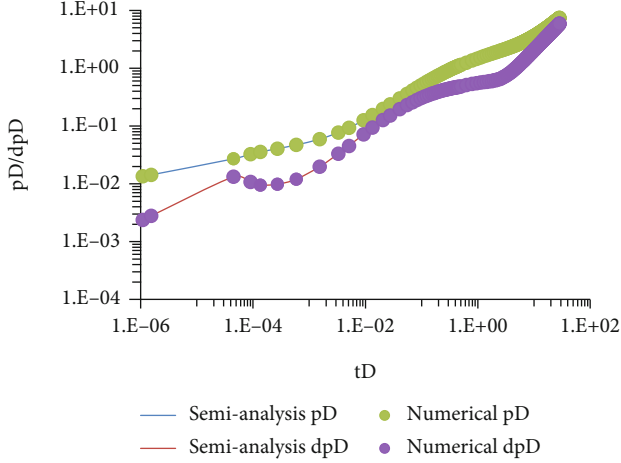


FIGURE 5: Comparison of the semianalytic model and numerical results.

and pressure should satisfy the following condition:

$$\begin{aligned} p_{fDi} &= p_{Di}, \\ q_{fDi} &= q_{Di}. \end{aligned} \quad (21)$$

The assumption of constant production rate requires

$$\sum_{i=1}^{N_T} q_{fDi} = 1. \quad (22)$$

Currently we have obtained  $2N_T + 1$  equations from Equations (8), (18), (20), and (22). Similarly, there are  $2N_T + 1$  unknowns, including  $p_{wD}$ ,  $q_{Di}$ , and  $p_{Di}$ . Using the Gauss-Jordan elimination, the  $p_{wD}$  can be obtained by simultaneously solving the system of equations.

### 3. Results and Discussion

**3.1. Model Validation.** The accuracy of this new model was verified using ECLIPSE (Schlumberger 2010). The orthogonal fracture network for the simulation included four main hydraulic fractures and four natural fractures (similar to Figure 1). The grid scale in the simulation was  $161 \times 161 \times 10$ , and the volume of the reservoir was  $1610 \times 1610 \times 10$  m<sup>3</sup>. Details for the parameters used in the calculations are summarized in Table 1.

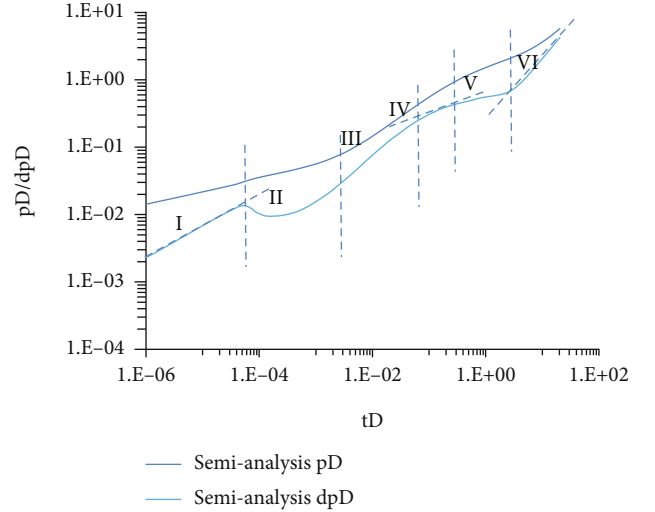


FIGURE 6: Flow regimes of the complex fracture network.

The results of the semianalytical model and ECLIPSE are compared in Figure 5 (where  $dpD$  represents the derivative of the dimensionless pressure  $pD$ ). From the figure, it is observed that there is a good agreement between our model and the ECLIPSE results.

Type curves of the transient pressure behavior for the complex fracture network are shown in Figure 6. From Figure 6, we can see that six main flow regimes can be recognized as follows:

Regime I is linear flow. As is commonly known, the typical feature of this flow behavior is that the slope of the dimensionless derivative pressure is equal to 0.5.

Regime II is a relatively rare occurrence in the literature. Figure 6 shows that a ‘‘cave’’ occurs at the end of linear flow. Few published papers have discussed this phenomenon, although published work shows this ‘‘cave’’ phenomenon (Pin et al., 2015). To further examine the ‘‘cave’’ behavior, we conducted calculations to analyze this phenomenon in Section 2.2.1 (Figure 7). The results showed that this ‘‘cave’’ reflects the effects of interference between hydraulic fractures and natural fractures. Therefore, we denote this process as ‘‘fracture interference flow.’’

Regime III is transitional flow, generally raised at the end of Regime II.

Regime IV is biradial flow, which can be recognized by a one-third slope of the dimensionless derivative pressure.



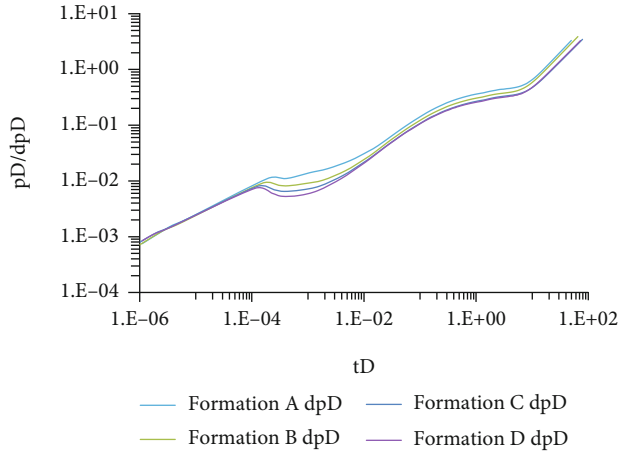


FIGURE 7: Comparison of dimensionless derivative pressure for the four reservoirs.

TABLE 2: The combinations of  $k_{fH}$  and  $k_{fN}$ .

Reservoirs	Permeability of hydraulic fractures, D	Permeability of natural fractures, D
Formation A	28	1.4
Formation B	28	4.4
Formation C	28	8.8
Formation D	28	28

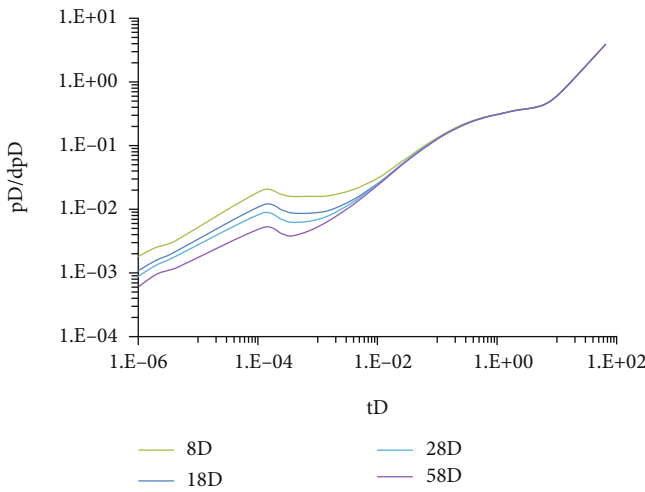


FIGURE 8: Comparison of dimensionless derivative pressure for four cases.

This regime has been observed by several other researchers (Zhao et al.,2013; Luo et al.,2014; Chen et al.,2015) [26–28].

Regime V is pseudoradial flow with the derivative pressure stabilized at a value of 0.5.

Regime VI is reservoir boundary response flow. In this stage, transient pressure has spread to the outer closed boundaries. The dimensionless derivative pressure curve tilted up and converged to a straight line with unit slope.

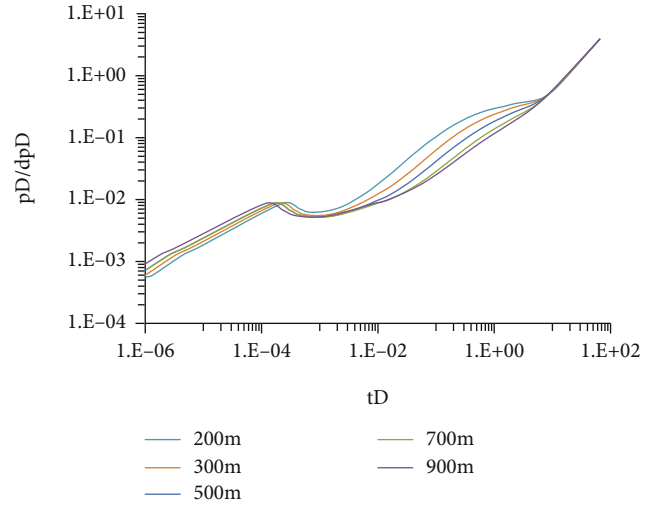


FIGURE 9: Comparison of type curves with different fracture geometry.

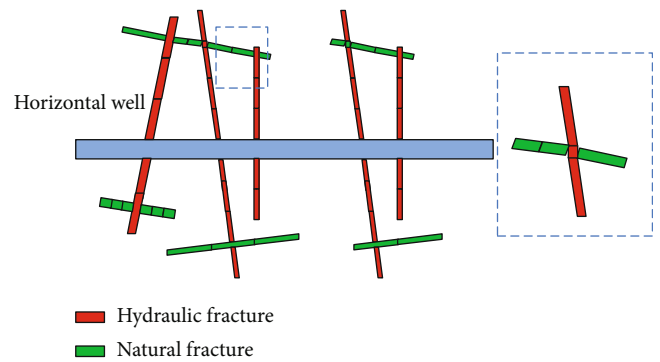


FIGURE 10: Sketch of unorthogonal fracture network.

### 3.2. Effect of Fracture Permeability

3.2.1. *Effect of Varying the Natural Fracture’s Permeability.* Fracture permeability is a key parameter for fractured wells. Here, the effect of fracture permeability on the behavior of transient pressure and fluid flow regimes is evaluated. We considered the permeability of the hydraulic fractures to be constant and varied the natural fracture’s conductivity. The combinations of  $k_{fH}$  and  $k_{fN}$  are shown in Table 2.

The effect of natural fracture permeability on transient pressure response of the four formations is shown in Figure 7 (the following results are based on data from Table 1).

From Figure 7, we can see that natural fracture permeability primarily affects the fracture interference flow. Larger permeability values for the natural fracture corresponded to a deeper “cave” in the typical curve. This is a result of the increasing permeability of natural fractures, causing larger fluid flow into natural fractures, leading to a stronger interference between hydraulic fractures and natural fractures. This flow regime is a typical signature of transient pressure behavior in complex fracture network.

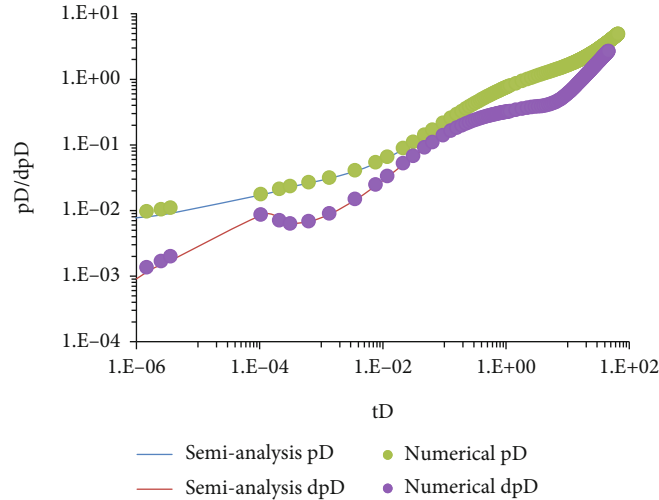


FIGURE 11: Comparison between numerical results and semianalysis results.

**3.2.2. The Permeability of the Complex Fracture Network Is Homogeneous.** Assuming that the proppant is evenly distributed throughout the network, it is suggested that the permeability of the complex network is homogeneous. The data in Table 1 were used in the following calculations. Four cases that were investigated in which permeability of the fracture network were 8D, 18D, 28D, and 58D. Figure 8 shows the effect of fracture permeability on the transient response behavior of the complex network.

From Figure 8, we can see that the permeability of the complex fracture network only influences the pressure response in the early stages of the process.

**3.3. Effect of the Complex Fracture network's Geometry.** The geometry of the fracture network also has an important influence on the pressure response in unconventional reservoirs. For simplicity, it was assumed that all of the fractures have the same length. Five cases were considered in which the fracture lengths were equal to 200 m, 300 m, 500 m, 700 m, and 900 m individually. These values were chosen to investigate the effect of the complex fracture network's geometry on the pressure behavior. The following results are based on the data in Table 1.

The results of Figure 9 indicate that the geometry of the fracture network primarily affects transitional flow, biradial flow, and pseudoradial flow. It had no significant effect on other flow regimes. With the increase of fracture length, the period of transitional flow is also increased, and the biradial flow and pseudoradial flow gradually faded out.

**3.4. Unorthogonal Fracture Network.** In this section, the transient pressure behavior of unorthogonal fracture networks is investigated. Figure 10 shows a sketch of an unorthogonal fracture network used in the following calculation.

Figure 10 shows an unorthogonal complex fracture network that is composed of several fracture segments with arbitrary angles. From the dashed box in Figure 10, we can see that the discretization is not perfect in the connection of two fractures. There are gaps in the connections, because

the surface of the volume source must be a parallelogram. However, we assumed that the flow inside the fracture network was continuous. The permeability of hydraulic fracture was set to 40D, and that of natural fracture was 10D. The total length of the fracture network was 1000 m, and the other pertinent data are listed in Table 1. The semianalytical model results were verified by the results of ECLIPSE (Schlumberger 2010), shown in Figure 11.

The comparison between numerical results and this new model is shown in Figure 11. The difference of the new model compared with ECLIPSE is relatively large in the early period. The reason for this difference may be a result of assumption (3) and the imperfect connections between two fractures in our model, as mentioned above. Except for early time, the semianalytical model matches very well with the numerical results.

## 4. Conclusions

This paper provides a semianalytical model for the transient pressure behavior in unconventional reservoirs that have a complex fracture network. The model is capable of simulating the complex fracture network with varying conductivities and complex geometry. Although most of the results and discussion have been restricted to an orthogonal fracture network, we have demonstrated that the approach can be used for unorthogonal fracture networks in which hydraulic and natural fractures interconnect with arbitrary inclined angles by direct comparison with numerical results. The following conclusions can be drawn:

- (1) We present a more flexible DVS model based on the work by Valko. Then a semianalytical model was established to describe transient pressure behavior of complex fracture networks in unconventional reservoirs with closed boundaries. The accuracy of the new model was demonstrated by comparison with numerical results. In addition, the model used 3D flow to simulate the reservoir flow (in Section 2.2.1)

- (2) The process of fluid flow in unconventional reservoirs with complex network can be divided into six flow regimes: linear flow, fracture interference flow, transitional flow, biradial flow, pseudoradial flow, and boundary response flow. Note that the “fracture interference flow” is a new flow regime that requires additional work to more fully describe it. Through the research in Sections 2.2 and 3.3, we determined that the permeability of the complex fracture networks has a significant influence on the fracture interference flow regime
- (3) The results of a sensitivity analysis show that the permeability of the fractures significantly influences earlier stage fluid flow (linear flow and fracture interference flow). The geometry of the fracture network primarily affects transitional flow, biradial flow, and pseudoradial flow (shown in Figure 9).

As shown in Figure 11, the model deviates slightly from the numerical results in unorthogonal fracture networks. However future work will be focused on the optimization of the model for this case. Even so, the model is a useful tool to investigate the flow behavior of complex fracture networks. With this essential knowledge, we can evaluate well performance and stimulation effectiveness in unconventional reservoirs.

## Appendix

### A. The diffusivity equation for the volume source model is given by Valko et al. (2007) as follows.

$$\eta_x \frac{\partial^2 p}{\partial x^2} + \eta_y \frac{\partial^2 p}{\partial y^2} + \eta_z \frac{\partial^2 p}{\partial z^2} + \frac{1}{\phi c_t} Q(x, y, z, t) = \frac{\partial p}{\partial t}, \quad (\text{A.1})$$

where  $\eta_i = k_i / \phi \mu c_t$ ,  $i = x, y, z$ .

The initial condition is

$$p(x, y, z, 0) = p_i. \quad (\text{A.2})$$

The closed boundary conditions are

$$\begin{aligned} \left. \frac{\partial p}{\partial x} \right|_{x=0} &= \left. \frac{\partial p}{\partial x} \right|_{x=x_e} = 0, \\ \left. \frac{\partial p}{\partial y} \right|_{y=0} &= \left. \frac{\partial p}{\partial y} \right|_{y=y_e} = 0, \\ \left. \frac{\partial p}{\partial z} \right|_{z=0} &= \left. \frac{\partial p}{\partial z} \right|_{z=z_e} = 0. \end{aligned} \quad (\text{A.3})$$

$Q(x, y, z, t)$  in Equation (A.1) is the source function which, for the instantaneous volume source, is written as

$$\begin{aligned} Q(x, y, z, t) &= \frac{qB}{8w_x w_y w_z} \delta(t) [H(x - c_x - w_x) - H(x - c_x + w_x)] \\ &\quad \times [H(y - c_y - w_y) - H(y - c_y + w_y)] \\ &\quad \times [H(z - c_z - w_z) - H(z - c_z + w_z)]. \end{aligned} \quad (\text{A.4})$$

In Equation (A.4),  $\delta(t)$  and  $H(x)$  represent the Dirac delta function and the Heaviside unit-step function, respectively. The Dirac delta function makes the source instantaneous, and the Heaviside unit-step function limits the geometry of the source.

### B. The dimensionless parameters are defined as follows:

$$p_D = \frac{kL}{q\mu B} (p_i - p), \quad (\text{B.1})$$

$$p_{fD} = \frac{kL}{q\mu B} (p_i - p_f), \quad (\text{B.2})$$

$$p_{wD} = \frac{kL}{q\mu B} (p_i - p_w), \quad (\text{B.3})$$

$$q_{fD} = \frac{q_f L}{qB}, \quad (\text{B.4})$$

$$C_{fD} = \frac{k_f w_f}{kL}, \quad (\text{B.5})$$

$$t_D = \frac{k}{\phi \mu c_t L^2} t, \quad (\text{B.6})$$

$$x_D = \frac{x}{L} y_D = \frac{y}{L} z_D = \frac{z}{L}, \quad (\text{B.7})$$

$$c_{xD} = \frac{c_x}{x_e}, \quad (\text{B.8})$$

$$c_{yD} = \frac{c_y}{y_e}, \quad (\text{B.9})$$

$$k = (k_x k_y k_z)^{1/3}, \quad (\text{B.10})$$

$$L = (L_x L_y L_z)^{1/3}. \quad (\text{B.11})$$

### Nomenclature

- $x_e$ : Length of reservoir in  $x$  direction, m
- $y_e$ : Width of reservoir in  $y$  direction, m
- $z_e$ : Height of reservoir in  $z$  direction, m
- $L$ : Length, m
- $w$ : Width, m
- $c$ : Coordinate of midpoint of volume source, m
- $k$ : Permeability,  $\text{m}^2$
- $T_H$ : Total number of hydraulic fractures, integer
- $T_N$ : Total number of natural fractures, integer
- $S_H$ : Total segments of one hydraulic fracture, integer
- $S_N$ : Total segments of one natural fracture, integer

$p_w$ : Wellbore pressure, Pa  
 $p$ : Pressure, Pa  
 $p_\delta$ : Instantaneous pressure, Pa  
 $N_T$ : Total number of fracture segments, integer  
 $\mu$ : Viscosity, MPas  
 $h$ : Height of fracture in  $z$  direction, m  
 $q$ : Flow rate,  $\text{m}^3/\text{d}$   
 $t$ : Time, second.

### Subscripts

D: Dimensionless  
 N: Natural fracture  
 H: Hydraulic fracture  
 f: Fracture  
 $i, j$ : Fracture segments number, integer.

### Data Availability

Data is available when required.

### Conflicts of Interest

The authors declare that they have no conflicts of interest.

### Acknowledgments

This work is funded by the State Key Laboratory of Shale Oil and Gas Enrichment Mechanisms and Effective Development, National Natural Science Foundation of China (Grant No. 51804258, 51974255, and 51874241), Natural Science Basic Research Program of Shaanxi Province (Grant No. 2019JQ-807, 2020JM-544, 2018JM-5054), and the Youth Innovation Team of Shaanxi Universities.

### References

- [1] M. K. Fisher, C. A. Wright, B. M. Davidson et al., *Integrating fracture mapping technologies to optimize stimulations in the Barnett Shale*, Society of Petroleum Engineers, 2002.
- [2] S. C. Maxwell, T. I. Urbancic, N. Steinsberger, and R. Zinno, *Microseismic imaging of hydraulic fracture complexity in the Barnett Shale*, Society of Petroleum Engineers, 2002.
- [3] J. E. Warren and P. J. Root, "The behavior of naturally fractured reservoirs," *Society of Petroleum Engineers Journal*, vol. 3, no. 3, pp. 245–255, 1963.
- [4] H. Kazemi, "Pressure transient analysis of naturally fractured reservoirs with uniform fracture distribution," *Society of Petroleum Engineers Journal*, vol. 9, no. 4, pp. 451–462, 1969.
- [5] M. Brown, E. Ozkan, R. Raghavan, and H. Kazemi, "Practical solutions for pressure transient responses of fractured horizontal wells in unconventional shale reservoirs," *Society of Petroleum Engineers Journal*, vol. 2, no. 3, pp. 235–245, 2011.
- [6] E. Ozkan, M. Brown, R. Raghavan, and H. Kazemi, "Comparison of fractured horizontal well performance in tight sand and shale reservoirs," *SPE Reservoir Evaluation and Engineering*, vol. 14, no. 2, pp. 248–259, 2011.
- [7] B. X. Xu, M. Haghghi, X. F. Li, and D. Cooke, "Development of new type curves for production analysis in naturally fractured shale gas/tight gas reservoirs," *Journal of Petroleum Science and Engineering*, vol. 105, no. 1, pp. 107–115, 2013.
- [8] L. Tian, C. Xiao, M. Liu et al., "Well testing model for multi-fractured horizontal well for shale gas reservoirs with consideration of dual diffusion in matrix," *Journal of Natural Gas Science and Engineering*, vol. 21, pp. 283–295, 2014.
- [9] T. Huang, X. Guo, and F. Chen, "Modeling transient flow behavior of a multiscale triple porosity model for shale gas reservoirs," *Journal of Natural Gas Science and Engineering*, vol. 23, pp. 33–46, 2015.
- [10] Y. L. Zhao, L. H. Zhang, J. X. Luo, and B. N. Zhang, "Performance of fractured horizontal well with stimulated reservoir volume in unconventional gas reservoir," *Journal of Hydrology*, vol. 512, pp. 447–456, 2014.
- [11] P. Jia, L. Cheng, S. Huang, and H. Liu, "Transient behavior of complex fracture networks," *Journal of Petroleum Science and Engineering*, vol. 132, pp. 1–17, 2015.
- [12] C. L. Palagi and K. Aziz, "Use of Voronoi grid in reservoir simulation," *Society of Petroleum Engineers Journal*, vol. 2, no. 2, pp. 69–77, 1994.
- [13] F. Skoreyko and H. Peter, "Use of PEBI grids for complex advanced process simulators," in *Paper SPE 79685-MS Presented at the SPE Reservoir Simulation Symposium*, TX, USA, 2003.
- [14] B. Li, Z. Chen, and G. Huan, "The sequential method for the black-oil reservoir simulation on unstructured grids," *Journal of Computational Physics*, vol. 192, no. 1, pp. 36–72, 2003.
- [15] M. J. Mayerhofer, E. P. Lolon, N. R. Warpinski, C. L. Cipolla, D. Walser, and C. M. Rightmire, "What is stimulated reservoir volume (SRV)?," *SPE Production & Operations*, vol. 25, no. 1, pp. 89–98, 2010.
- [16] N. R. Warpinski, M. J. Mayerhofer, M. C. Vincent, C. L. Cipolla, and E. P. Lolon, "Stimulating unconventional reservoirs: maximizing network growth while optimizing fracture conductivity," *Journal of Canadian Petroleum Technology*, vol. 48, no. 10, pp. 39–51, 2009.
- [17] C. L. Cipolla, "Modeling production and evaluating fracture performance in unconventional gas reservoirs," *Journal of Petroleum Technology*, vol. 61, no. 9, pp. 84–90, 2009.
- [18] P. P. Valko and S. Amini, *The method of distributed volumetric sources for calculating the transient and pseudosteady state productivity of complex well-fracture configurations*, Society of Petroleum Engineers, 2007.
- [19] A. C. Gringarten and H. J. Ramey, "The use of source and Green's functions in solving unsteady-flow problems in reservoirs," *Society of Petroleum Engineers Journal*, vol. 13, no. 5, pp. 285–296, 1973.
- [20] H. Cinco-Ley and V. F. Samaniego, "Transient pressure analysis for fractured wells," *Society of Petroleum Engineers Journal*, vol. 33, no. 9, pp. 1749–1766, 1981.
- [21] K. H. Guppy, H. Cinco-Ley, H. J. Ramey, and V. F. Samaniego, "Non-Darcy flow in wells with finite-conductivity vertical fractures," *Society of Petroleum Engineers Journal*, vol. 22, no. 5, pp. 681–698, 1982.
- [22] E. Ozkan, *Performance of Horizontal Wells*, PhD Dissertation, University of Tulsa, Tulsa, Oklahoma, 1988.
- [23] C.-C. Chen and R. Rajagopal, "A multiply-fractured horizontal well in a rectangular drainage region," *Society of Petroleum Engineers Journal*, vol. 2, no. 4, pp. 455–465, 1997.
- [24] A. C. Gringarten, H. J. Ramey, and R. Raghavan, "Unsteady-state pressure distributions created by a well with a single infinite-conductivity vertical fracture," *Society of Petroleum Engineers Journal*, vol. 14, no. 4, pp. 347–360, 1974.

- [25] H. Cinco-Ley and H.-Z. Meng, *Pressure transient analysis of wells with finite conductivity vertical fractures in double porosity reservoirs*, Society of Petroleum Engineers, 1988.
- [26] Z. Chen, X. Liao, X. Zhao, S. Lv, and L. Zhu, *A Semianalytical Approach for Obtaining Type Curves of Multiple-Fractured Horizontal Wells with Secondary-Fracture Networks*, Society of Petroleum Engineers, 2016.
- [27] Y.-l. Zhao, L.-h. Zhang, J.-z. Zhao, J.-x. Luo, and B.-n. Zhang, ““Triple porosity” modeling of transient well test and rate decline analysis for multi-fractured horizontal well in shale gas reservoirs,” *Journal of Petroleum Science and Engineering*, vol. 110, pp. 253–262, 2013.
- [28] W. Luo, C. Tang, and X. Wang, “Pressure transient analysis of a horizontal well intercepted by multiple non-planar vertical fractures,” *Journal of Petroleum Science and Engineering*, vol. 124, pp. 232–242, 2014.

## Research Article

# Chemical Potential-Based Modeling of Shale Gas Transport

Jisheng Kou <sup>1,2</sup>, Lingyun Chen,<sup>1</sup> Amgad Salama,<sup>3</sup> and Jianchao Cai <sup>4</sup>

<sup>1</sup>School of Mathematics and Statistics, Hubei Engineering University, Xiaogan, 432000 Hubei, China

<sup>2</sup>School of Civil Engineering, Shaoxing University, Shaoxing, 312000 Zhejiang, China

<sup>3</sup>Process System Engineering, Faculty of Engineering and Applied Science, University of Regina, 3737 Wascana Pkwy, Regina, Saskatchewan, Canada S4S 0A2

<sup>4</sup>State Key Laboratory of Petroleum Resources and Prospecting, China University of Petroleum, Beijing 102249, China

Correspondence should be addressed to Jianchao Cai; [caijc@cug.edu.cn](mailto:caijc@cug.edu.cn)

Received 6 August 2021; Accepted 6 September 2021; Published 4 October 2021

Academic Editor: Bailu Teng

Copyright © 2021 Jisheng Kou et al. This is an open access article distributed under the Creative Commons Attribution License, which permits unrestricted use, distribution, and reproduction in any medium, provided the original work is properly cited.

Shale gas plays an increasingly important role in the current energy industry. Modeling of gas flow in shale media has become a crucial and useful tool to estimate shale gas production accurately. The second law of thermodynamics provides a theoretical criterion to justify any promising model, but it has been never fully considered in the existing models of shale gas. In this paper, a new mathematical model of gas flow in shale formations is proposed, which uses gas density instead of pressure as the primary variable. A distinctive feature of the model is to employ chemical potential gradient rather than pressure gradient as the primary driving force. This allows to prove that the proposed model obeys an energy dissipation law, and thus, the second law of thermodynamics is satisfied. Moreover, on the basis of energy factorization approach for the Helmholtz free energy density, an efficient, linear, energy stable semi-implicit numerical scheme is proposed for the proposed model. Numerical experiments are also performed to validate the model and numerical method.

## 1. Introduction

Shale gas has become a significant energy resource over the last decade. Shale gas refers to natural gas composed of primarily methane, which is trapped within the pores of fine-grained sedimentary rocks with rich micropores and relatively low permeability. The shale gas reservoirs differ from conventional natural gas reservoirs that apart from free gas in the pores and fractures, a certain amount of gas is adsorbed onto the solid surfaces, and as a result, it can not only store shale gas but also generate gas [1–4]. Experimental investigations have indicated that adsorbed gas storage capacity is primarily affected by shale reservoir conditions, such as temperature, pressure, and shale matrix pore structures [2, 3, 5, 6]. A number of adsorption models have been developed to describe the methane adsorption in shale gas reservoirs. The Langmuir model [7] and Dubinin-Radushkevich (D-R) model [8] are the most popularly employed models to describe the gas adsorption in

micropore-rich materials. Methane under shale formation conditions usually stays at the supercritical state, and consequently, the classical models that require a saturation pressure cannot be applied to describe the gas adsorption under supercritical conditions [3, 9]. By the use of gas density rather than gas pressure, modified formulations of the Langmuir and D-R models have been developed for supercritical conditions [3, 9]. In this paper, it is shown that the use of gas density will also be beneficial for ensuring thermodynamical consistency of the models.

Modeling of gas flow in shale media plays a crucial role in predicting shale gas production [10–19]. For gas flow in tight porous media, the most remarkable phenomenon is the so-called Klinkenberg effect [20], which results from slip flow of gas molecules through very small pores. This effect leads to the apparent permeability that is generally greater than the absolute permeability of a porous medium [14, 15]. By using the apparent permeability, the shale gas flow equation can be simply formulated as the form of Darcy's

law, which states that gas velocity is proportional to the pressure gradient [12–19, 21].

As general principles, the fundamental laws of thermodynamics play a significant role in modeling of various physical problems [22–24]. Specially, the second law of thermodynamics states that any spontaneous process in an isolated system will always lead to an escalation in the entropy of this system. In terms of the second law of thermodynamics, for an isothermal system, any dynamical process should obey an energy dissipation law [22], and a promising model should preserve this property. Nevertheless, energy dissipation laws for modeling of shale gas transport have been scarcely studied so far. In this paper, a new mathematical model is proposed, which uses gas density instead of pressure as the primary variable and introduces chemical potential gradient instead of pressure gradient as the primary driving force. It is rigorously proved that the proposed model obeys an energy dissipation law, and thus, it is thermodynamically consistent (that is, it obeys the second law of thermodynamics).

Numerical algorithms that preserve the energy dissipation law at the discrete level, the so-called energy stable methods, are preferred as well [25–27]. In general, it is a quite challenging issue to construct such methods since the commonly used explicit or implicit scheme could not inherit a discrete energy dissipation law. The energy factorization (EF) approach for the Helmholtz free energy density [26] is a newly developed approach to design efficient energy stable numerical methods. An appealing feature of this approach is that it leads to linear, easy-to-implement, and energy stable numerical schemes, and this advantage is more notable for numerical simulation of realistic fluids. Due to its excellent features, this approach has been successfully extended to phase-field models [28, 29]. In this work, using the EF approach, an efficient, linear, energy stable semi-implicit numerical scheme is constructed for the proposed model of shale gas transport.

The rest of this paper is organized as follows. In Section 2, a chemical potential-based model of gas flow in shale media is proposed, which is proved to obey an energy dissipation law. An efficient, linear, energy stable semi-implicit numerical method is proposed in Section 3. In Section 4, numerical experiments are performed to validate the proposed model and numerical scheme. Finally, some concluding remarks are provided in Section 5.

## 2. Model Equations

In this section, a chemical potential-based model of shale gas transport is proposed. The chemical potential is defined as the derivative of Helmholtz free energy density. In Appendix A, we elaborate on the Helmholtz free energy density determined by Peng-Robinson equation of state [30].

Molar density ( $\text{mol m}^{-3}$ ) of methane is denoted by  $c$ . For specific temperature  $T(\text{K})$ , the Helmholtz free energy density, denoted by  $f(c)$ , is a function of molar density  $c$  as described in Appendix A. The chemical potential is defined as the derivative of Helmholtz free energy density function  $f(c)$  with respect to molar density

$$\mu(c) = f'(c), \quad (1)$$

where  $\mu$  is the chemical potential ( $\text{Pa}\cdot\text{mol}^{-1}\text{m}^3$ ) and  $f(c)$  is the Helmholtz free energy density (Pa).

For specific temperature and pressure, a cubic equation is solved to obtain molar density of methane, and moreover, the solutions of  $c$  are not unique in general. In contrast, for specific temperature and molar density, the pressure can be uniquely and explicitly calculated from the Peng-Robinson equation of state [30], which is formulated in Appendix B. Consequently, under the constant temperature, molar density is preferred to pressure as the primary variable in numerical simulation.

For specific temperature, the pressure becomes a function of molar density  $c$  only. Moreover, the pressure relates to the Helmholtz free energy density and chemical potential as [22]

$$p = c\mu - f, \quad (2)$$

where  $p$  is the pressure (Pa). The chain rule gives the relationship between the pressure gradient and chemical potential gradient.

$$\nabla p = \nabla(c\mu) - \nabla f = c\nabla\mu + \mu\nabla c - \mu\nabla c = c\nabla\mu. \quad (3)$$

Let  $\phi$  denote the porosity. In tight reservoirs with abundant micropores, the Klinkenberg effect cannot be neglected, and thus, the apparent permeability [14, 15] is expressed as

$$K_{\text{app}} = K_0 \left(1 + \frac{b}{p}\right), \quad (4)$$

where  $b$  is the Klinkenberg slippage factor (Pa) and  $K_0$  is the intrinsic permeability (md). The slippage factor accounts for the slippage effect on permeability of gas in reservoirs. Various formulations for the slippage factor have been developed in the literature, and the following formulation [13] is used in this work:

$$b = \eta\sigma \sqrt{\frac{8\pi RT\phi}{M_w K_0}}, \quad (5)$$

where  $\eta$  is the gas viscosity (Pa·s),  $\sigma$  is the comprehensive coefficient,  $R$  is the universal gas constant ( $\text{m}^3\cdot\text{Pa}\cdot\text{mol}^{-1}\cdot\text{K}^{-1}$ ), and  $M_w$  is the molar weight of gas ( $\text{g}\cdot\text{mol}^{-1}$ ). On the basis of the apparent permeability, the velocity can be described by the form of Darcy's law as

$$u = -\frac{K_{\text{app}}}{\eta} \nabla p, \quad (6)$$

where  $u$  is the Darcy velocity ( $\text{m}\cdot\text{s}^{-1}$ ) and  $K_{\text{app}}$  is the apparent permeability (md). Applying relation (3), the following chemical potential-based velocity formulation is obtained:

$$u = -\frac{K_{\text{app}}}{\eta} c \nabla \mu. \quad (7)$$

In the shale gas reservoir, there is a large amount of gas adsorbed onto micropores in addition to free gas. The adsorbed gas has no mobility unless it converts to free gas, and consequently, it is assumed to have no contribution to the free energy. In the context of shale gas,  $c$  stands for the free gas density, and meanwhile,  $c_{\text{ads}}$  represents the adsorbed gas molar density. In order to describe the adsorption of gas, there have been several models proposed in the literature, which can be classified into two classes according to their primary variables, namely, the pressure-based models and density-based models. One famous pressure-based model is the classical Langmuir isotherm adsorption model [7]. The pressure-based models are not suitable to describe the gas adsorption under supercritical conditions [3, 9]. The density-based models have been developed and extensively applied to characterize the adsorption that occurs in shale media. Two modified adsorption models using molar density as the primary variable are described in Appendix C, which are employed in this paper due to their consistency to the chemical potential-based model. The mass accumulation of both free and adsorbed gas is given by  $c_{\text{tot}} = \phi c + (1 - \phi)c_{\text{ads}}$ , where  $c_{\text{ads}}$  is the adsorbed gas density ( $\text{mol}\cdot\text{m}^{-3}$ ). The mass balance equation can be expressed as

$$\frac{\partial c_{\text{tot}}}{\partial t} + \nabla \cdot (\mathbf{u}c) = 0. \quad (8)$$

Furthermore, a density-dependent function is defined as

$$\varphi(c) = \frac{\partial c_{\text{tot}}}{\partial c} = \phi + (1 - \phi) \frac{\partial c_{\text{ads}}}{\partial c}, \quad (9)$$

and then, (8) can be rewritten as

$$\varphi(c) \frac{\partial c}{\partial t} + \nabla \cdot (\mathbf{u}c) = 0. \quad (10)$$

For an isothermal dynamical system, the second law of thermodynamics leads to a certain energy dissipation law [22]. A distinctive feature of the proposed model is that it obeys an energy dissipation law, and as a consequence, it is thermodynamically consistent. Let  $\Omega$  be a connected and smooth space domain with the boundary  $\partial\Omega$ , and further, let  $\mathbf{n}$  denote the normal unit outward vector to  $\partial\Omega$ . Multiplying (10) by  $\mu(c)$  and then integrating it over the domain, it follows that

$$\int_{\Omega} \mu(c) \varphi(c) \frac{\partial c}{\partial t} d\mathbf{x} + \int_{\Omega} \mu(c) \nabla \cdot (\mathbf{u}c) d\mathbf{x} = 0. \quad (11)$$

TABLE 1: Physical properties of methane.

$P_c$ (bar)	$T_c$ (K)	Acentric factor	$M_w$ (g/mole)
45.99	190.56	0.011	16.04

The definition of chemical potential and integration by parts lead to

$$\int_{\Omega} \varphi(c) \frac{\partial f(c)}{\partial t} d\mathbf{x} + \int_{\partial\Omega} \mu(c) c \mathbf{u} \cdot \mathbf{n} ds - \int_{\Omega} \mathbf{u} \cdot c \nabla \mu(c) d\mathbf{x} = 0. \quad (12)$$

Substituting (7) into (12) yields

$$\int_{\Omega} \varphi(c) \frac{\partial f(c)}{\partial t} d\mathbf{x} + \int_{\partial\Omega} \mu(c) c \mathbf{u} \cdot \mathbf{n} ds = - \int_{\Omega} \frac{K_{\text{app}}}{\eta} c^2 |\nabla \mu|^2 d\mathbf{x}. \quad (13)$$

The right-hand side term of (13) represents the energy-dissipation rate. In order to demonstrate this property clearly, the adsorption effect is disregarded and the no-flow boundary condition is applied on the entire boundary of the domain, i.e.,  $\mathbf{u} \cdot \mathbf{n} = 0$ . In this situation, total free energy within the domain is defined as

$$F(t) = \int_{\Omega} \phi f(c) d\mathbf{x}, \quad (14)$$

and from (13), the following energy dissipation law can be derived:

$$\frac{\partial F(t)}{\partial t} = - \int_{\Omega} \frac{K_{\text{app}}}{\eta} c^2 |\nabla \mu|^2 d\mathbf{x} \leq 0, \quad (15)$$

which implies that total free energy would be dissipated over time until an equilibrium state is reached.

### 3. Numerical Method

In this section, a linear, efficient numerical scheme is proposed, and it is able to ensure the energy dissipation law at the discrete level. Denote by  $\tau$  the time step size and also denote by  $t_n = n\tau$  the time. In the time discrete scheme,  $c^n$  stands for the approximation of molar density  $c$  at time  $t_n$ .

*3.1. Energy Factorization Approach.* The proposed scheme employs the EF approach for the Helmholtz free energy density [26], which leads to the linear discrete chemical potential inheriting the energy dissipation property. The Helmholtz free energy density can be expressed as a sum of three contributions

$$f(c) = f_{\text{ideal}}(c) + f_{\text{repulsion}}(c) + f_{\text{attraction}}(c), \quad (16)$$

where

$$f_{\text{ideal}}(c) = cRT \ln(c), \quad (17)$$



TABLE 2: Parameters of the model used in example 1.

Parameter	Value	Unit	Description
$\phi$	0.05	—	Porosity
$r$	10	nm	Averaged pore diameter
$R$	8.3144621	$\text{m}^3 \cdot \text{Pa} \cdot \text{mol}^{-1} \cdot \text{K}^{-1}$	Ideal gas constant
$T$	300	K	Temperature
$\eta$	$10^{-5}$	Pa·s	Viscosity
$\sigma$	$10^{-3}$	—	Comprehensive coefficient

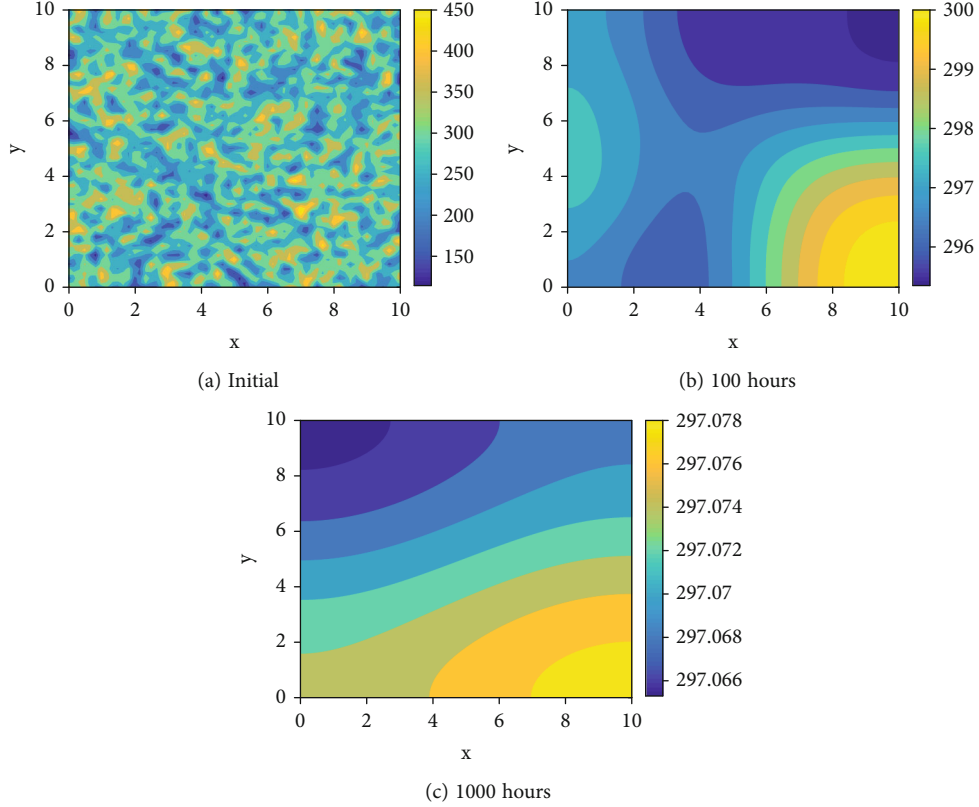


FIGURE 1: Gas density distributions computed by the proposed model in example 1 at different times.

$$f_{\text{repulsion}}(c) = -cRT \ln(1 - \beta c), \quad (18)$$

$$f_{\text{attraction}}(c) = \frac{\alpha(T)c}{2\sqrt{2}\beta} \ln \left( \frac{1 + (1 - \sqrt{2})\beta c}{1 + (1 + \sqrt{2})\beta c} \right). \quad (19)$$

Here,  $R$  is the universal gas constant and the parameters  $\alpha$  and  $\beta$  are described in Appendix A. The energy factorization approach gives the discrete chemical potential as

$$\mu^{n+1} = \mu_{\text{ideal}}^{n+1} + \mu_{\text{repulsion}}^{n+1} + \mu_{\text{attraction}}^n, \quad (20)$$

where

$$\mu_{\text{ideal}}^{n+1} = RT \ln(c^{n+1}) + RT \frac{c^{n+1} - 1}{c^{n+1}}, \quad (21)$$

$$\mu_{\text{repulsion}}^{n+1} = RTG'(c^n) \left( 2G(c^n) + G'(c^n)(c^{n+1} - c^n) \right) - \lambda RT, \quad (22)$$

$$\begin{aligned} \mu_{\text{attraction}}^n = & \frac{\alpha(T)}{2\sqrt{2}\beta} \left( \ln \left( 1 + (1 - \sqrt{2})\beta c^n \right) + \frac{(1 - \sqrt{2})\beta c^n}{1 + (1 - \sqrt{2})\beta c^n} \right) \\ & - \frac{\alpha(T)}{2\sqrt{2}\beta} \left( \ln \left( 1 + (1 + \sqrt{2})\beta c^n \right) + \frac{(1 + \sqrt{2})\beta c^n}{1 + (1 + \sqrt{2})\beta c^n} \right). \end{aligned} \quad (23)$$

In (22),  $G(c)$  is an intermediate energy function, which is defined as

$$G(c) = \sqrt{\lambda c - c \ln(1 - \beta c)}, \quad (24)$$

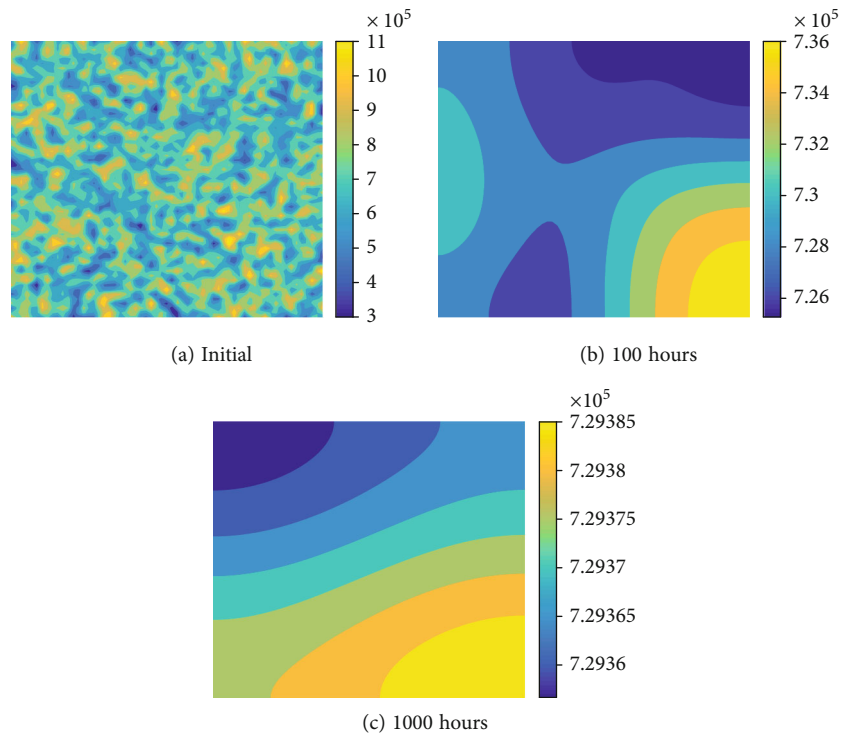


FIGURE 2: Pressure distributions computed by the proposed model in example 1 at different times.

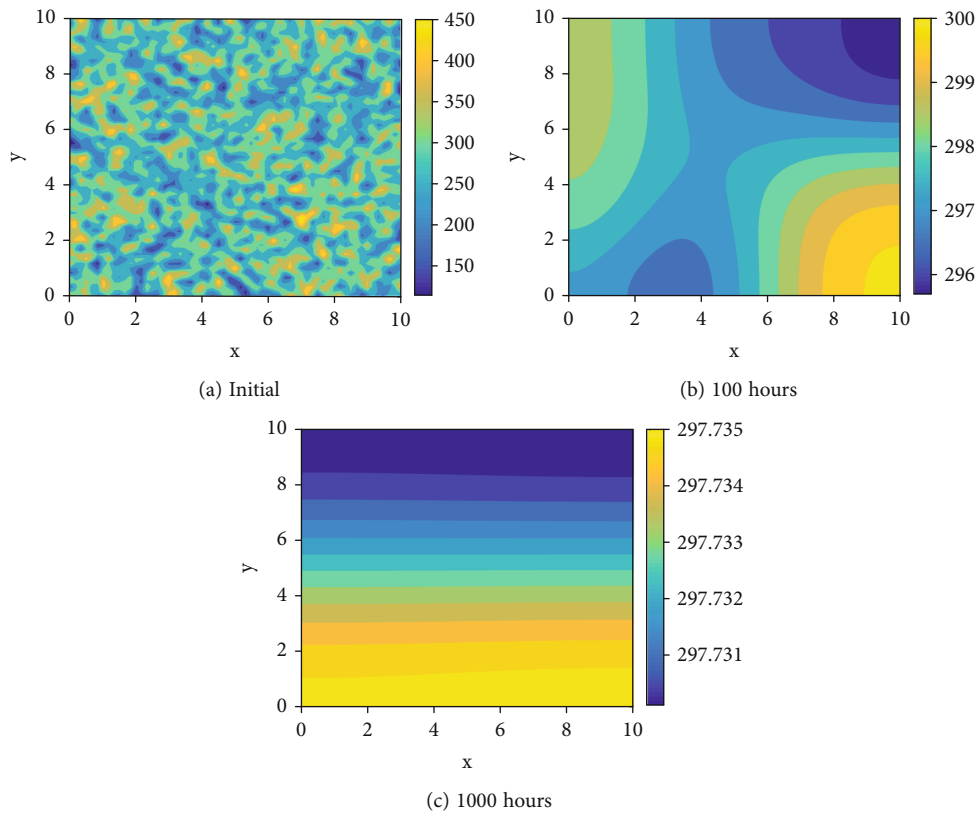


FIGURE 3: Gas density distributions computed by the classical model in example 1 at different times.

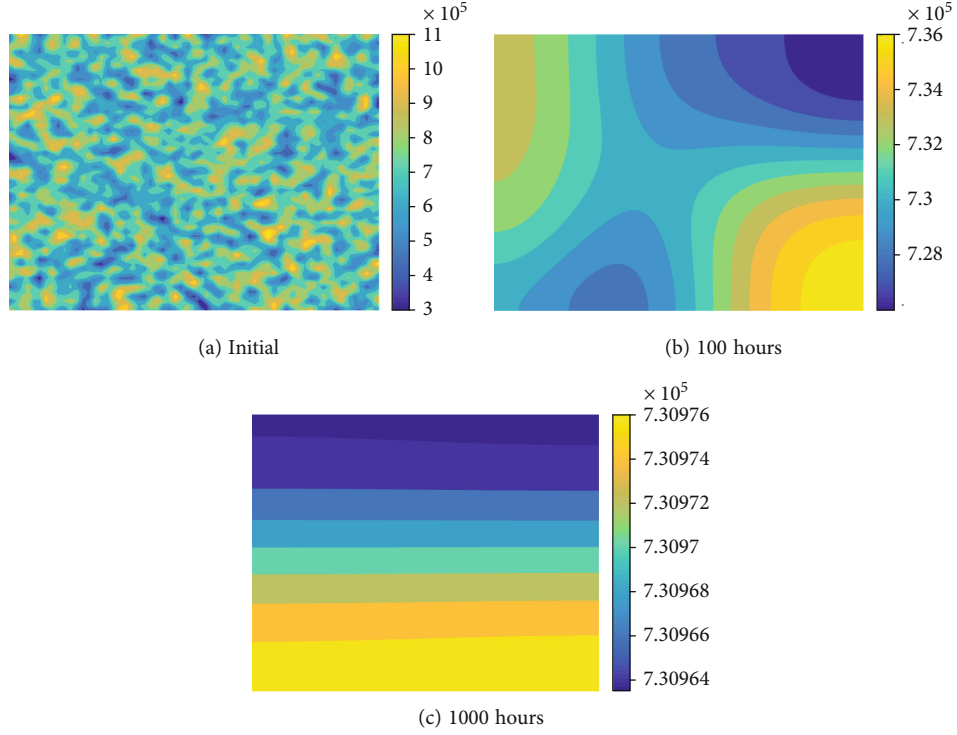


FIGURE 4: Pressure distributions computed by the classical model in example 1 at different times.

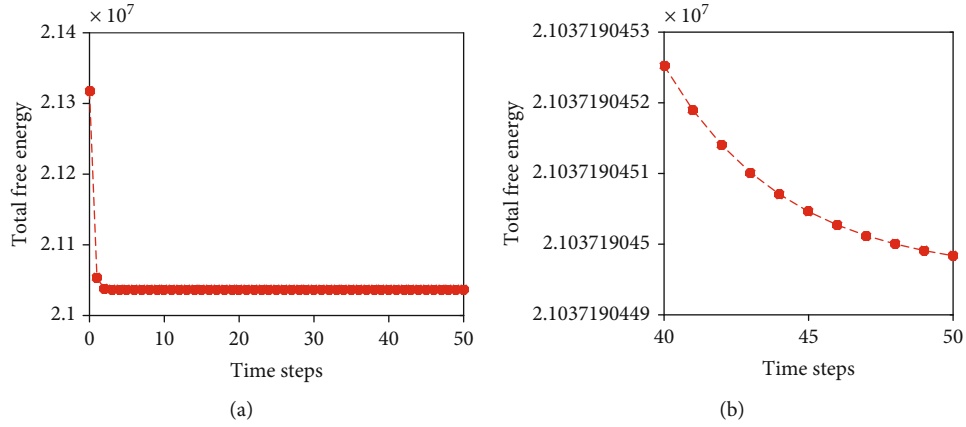


FIGURE 5: Total energy profiles of the proposed model in example 1.

where  $\lambda$  is the dimensionless stabilization constant. Apparently, the discrete chemical potential  $\mu^{n+1}$  is a linear function of  $c^{n+1}$  only. From the physical point of view, the boundedness of molar density  $c$  is assumed as

$$0 < c \leq \rho, \quad \rho\beta < 1, \quad (25)$$

where  $\rho$  is the upper bound of molar density. Let  $\epsilon_0 = \rho\beta$ . If the stabilization constant  $\lambda$  in (24) is chosen such that

$$\lambda \geq \frac{\epsilon_0}{(1 - \epsilon_0)^2} + \left( \frac{\epsilon_0^2}{(1 - \epsilon_0)^4} - 2 \ln(1 - \epsilon_0) \frac{\epsilon_0}{(1 - \epsilon_0)^2} \right)^{1/2}. \quad (26)$$

It has been proved in [26] that the discrete chemical potential (20) satisfies the following energy inequality:

$$f(c^{n+1}) - f(c^n) \leq \mu^{n+1}(c^{n+1} - c^n). \quad (27)$$

**3.2. Discrete Scheme.** On the basis of the discrete chemical potential given in (20)–(23), the proposed semi-implicit time discrete scheme reads as follows:

$$\varphi(c^n) \frac{c^{n+1} - c^n}{\tau} + \nabla \cdot (\mathbf{u}^{n+1} c^n) = 0, \quad (28)$$

$$\mathbf{u}^{n+1} = -\frac{K_{\text{app}}^n}{\eta} c^n \nabla \mu^{n+1}. \quad (29)$$

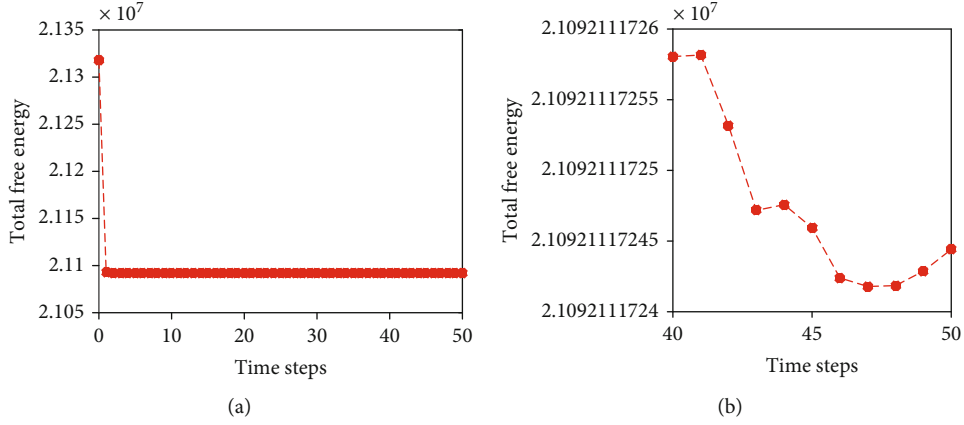


FIGURE 6: Total energy profiles of the classical model in example 1.

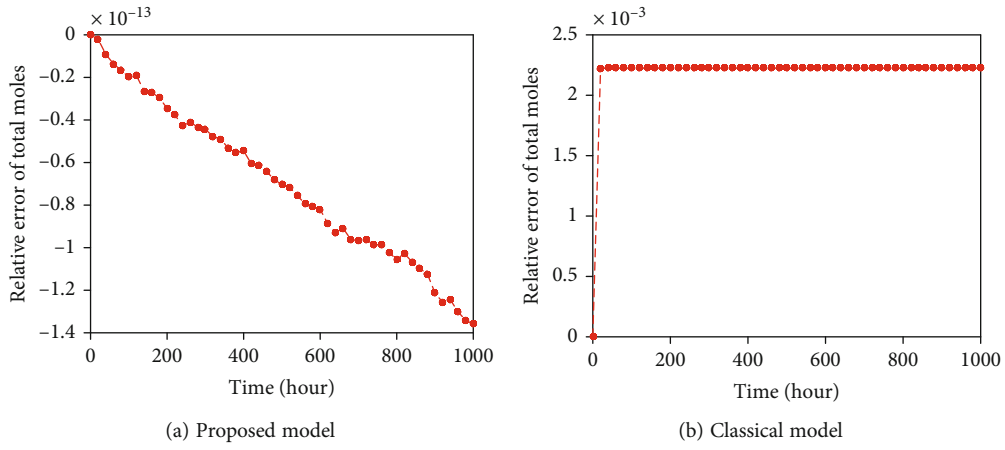


FIGURE 7: Comparison of total moles conservation in example 1.

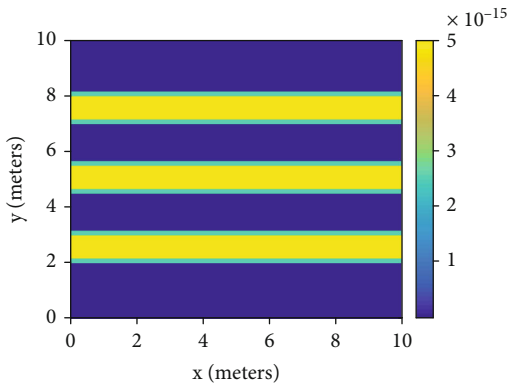


FIGURE 8: Intrinsic permeability in example 2.

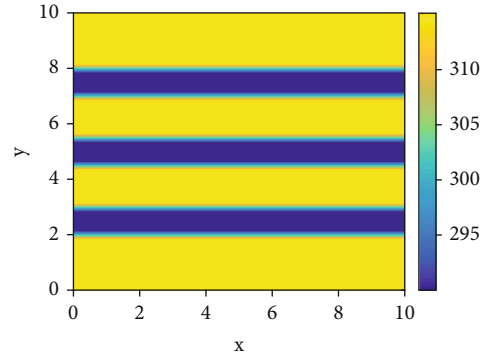


FIGURE 9: Initial adsorption density in example 2.

The apparent permeability is explicitly calculated as

$$K_{app}^n = K_0 \left( 1 + \frac{b}{p(c^n)} \right), \quad (30)$$

where the pressure can be directly obtained by (2) using  $c^n$ .

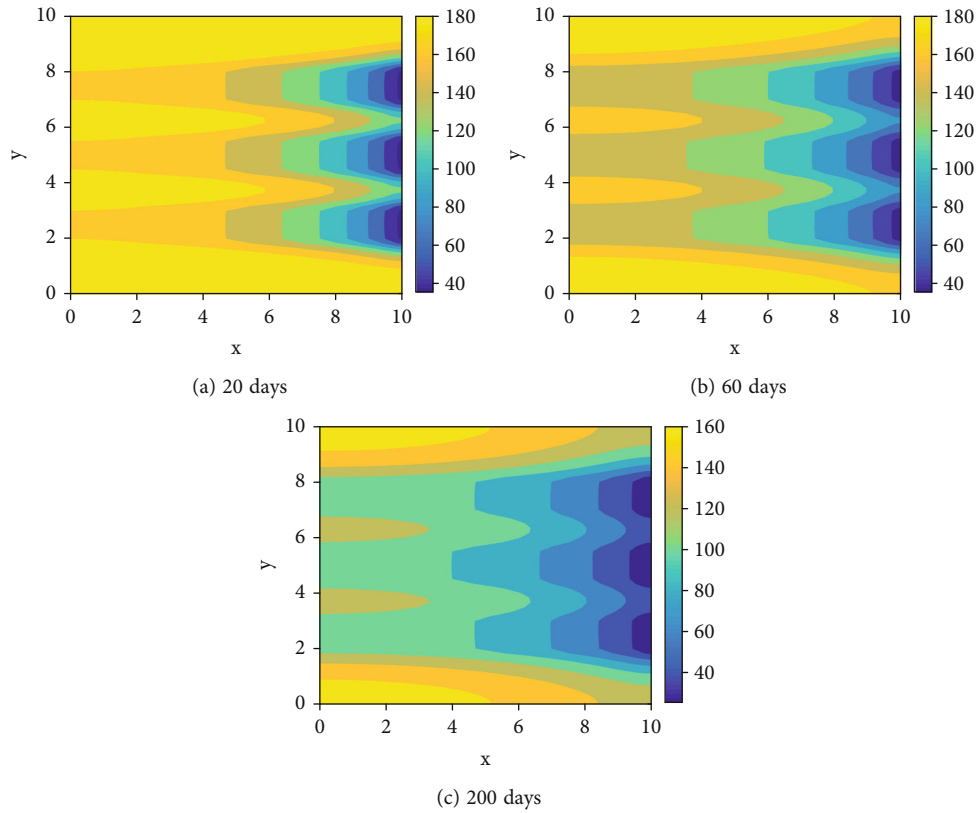
Combining (28) and (29) yields a single linear equation of  $c^{n+1}$  as

$$\varphi(c^n) \frac{c^{n+1} - c^n}{\tau} - \nabla \cdot \frac{K_{app}^n}{\eta} c^{n2} \nabla \mu^{n+1} = 0, \quad (31)$$

which is easy to be solved due to the fact that  $\mu^{n+1}$  is a linear function of  $c^{n+1}$ .

TABLE 3: Parameters of the model used in example 2.

Parameter	Value	Unit	Description
$\phi$	0.02, 0.05	—	Porosity
$r$	10, 200	nm	Averaged pore diameter
$R$	8.3144621	$\text{m}^3 \cdot \text{Pa} \cdot \text{mol}^{-1} \cdot \text{K}^{-1}$	Ideal gas constant
$T$	360	K	Temperature
$\mathcal{D}$	0.1, 0.2	—	Pore structure parameter
$\eta$	$10^{-5}$	Pa·s	Viscosity
$\sigma$	0.82	—	Comprehensive coefficient
$c_a$	322,302	$\text{mol} \cdot \text{m}^{-3}$	Adsorbed gas phase density
$c_M$	322,302	$\text{mol} \cdot \text{m}^{-3}$	Maximum absolute adsorption density

FIGURE 10: Gas density distributions in example 2 with  $c_b = 20 \text{ mol/m}^3$  at different times.

As depicted in Appendix C, it is assumed that  $\varphi(c) > 0$ . It is ready to prove that the proposed numerical scheme preserves a discrete energy dissipation law. Multiplying Equations (28) and (29) by  $\mu^{n+1}$  and  $c^n \nabla \mu^{n+1}$ , respectively, and then integrating them over the domain  $\Omega$ , we obtain

$$\int_{\Omega} \mu^{n+1} \varphi(c^n) \frac{c^{n+1} - c^n}{\tau} d\mathbf{x} + \int_{\Omega} \mu^{n+1} \nabla \cdot (\mathbf{u}^{n+1} c^n) d\mathbf{x} = 0, \quad (32)$$

$$\int_{\Omega} \mathbf{u}^{n+1} \cdot c^n \nabla \mu^{n+1} d\mathbf{x} = - \int_{\Omega} \frac{K_{\text{app}}^n}{\eta} |c^n \nabla \mu^{n+1}|^2 d\mathbf{x}. \quad (33)$$

It follows from (32) and (33) that

$$\begin{aligned} \int_{\Omega} \mu^{n+1} \varphi(c^n) \frac{c^{n+1} - c^n}{\tau} d\mathbf{x} &= - \int_{\Omega} \mu^{n+1} \nabla \cdot (\mathbf{u}^{n+1} c^n) d\mathbf{x} \\ &= \int_{\Omega} \mathbf{u}^{n+1} \cdot c^n \nabla \mu^{n+1} d\mathbf{x} \\ &\quad - \int_{\partial\Omega} \mu^{n+1} c^n \mathbf{u}^{n+1} \cdot \mathbf{n} ds \\ &= - \int_{\Omega} \frac{K_{\text{app}}^n}{\eta} |c^n \nabla \mu^{n+1}|^2 d\mathbf{x} \\ &\quad - \int_{\partial\Omega} \mu^{n+1} c^n \mathbf{u}^{n+1} \cdot \mathbf{n} ds. \end{aligned} \quad (34)$$

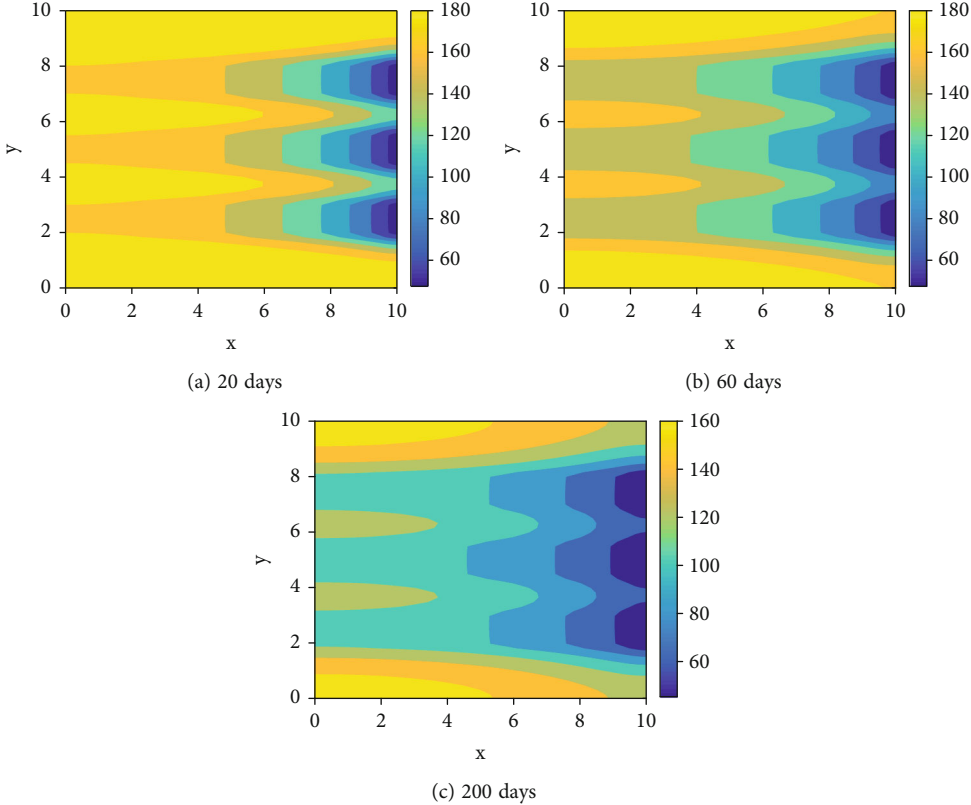


FIGURE 11: Gas density distributions in example 2 with  $c_b = 40 \text{ mol/m}^3$  at different times.

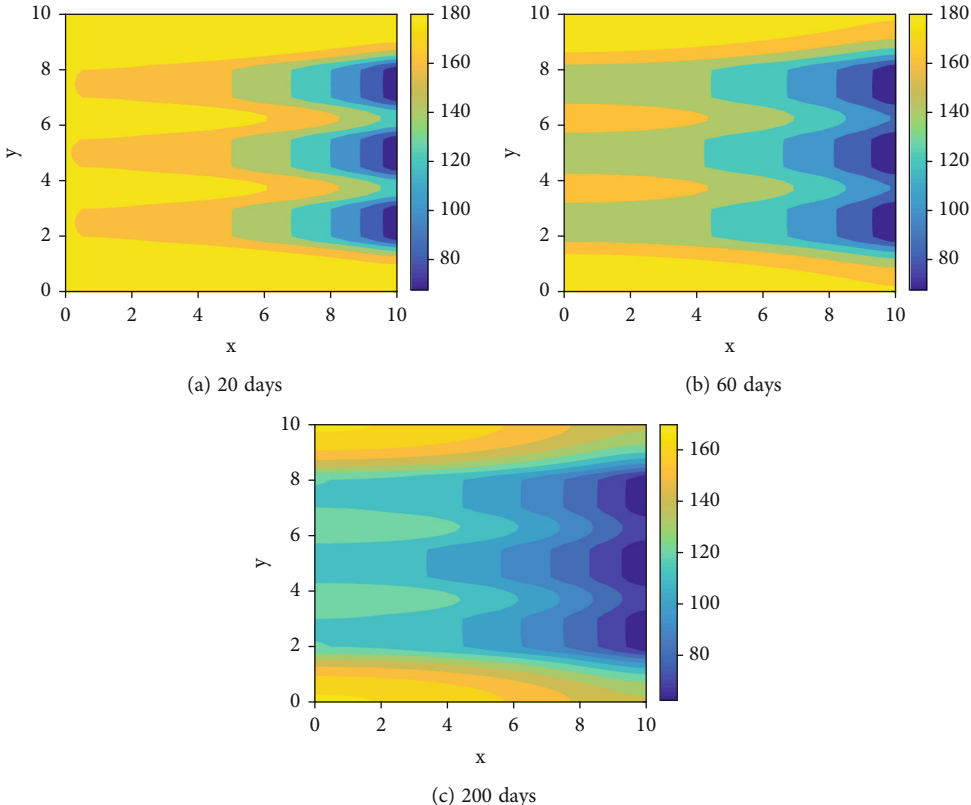


FIGURE 12: Gas density distributions in example 2 with  $c_b = 60 \text{ mol/m}^3$  at different times.

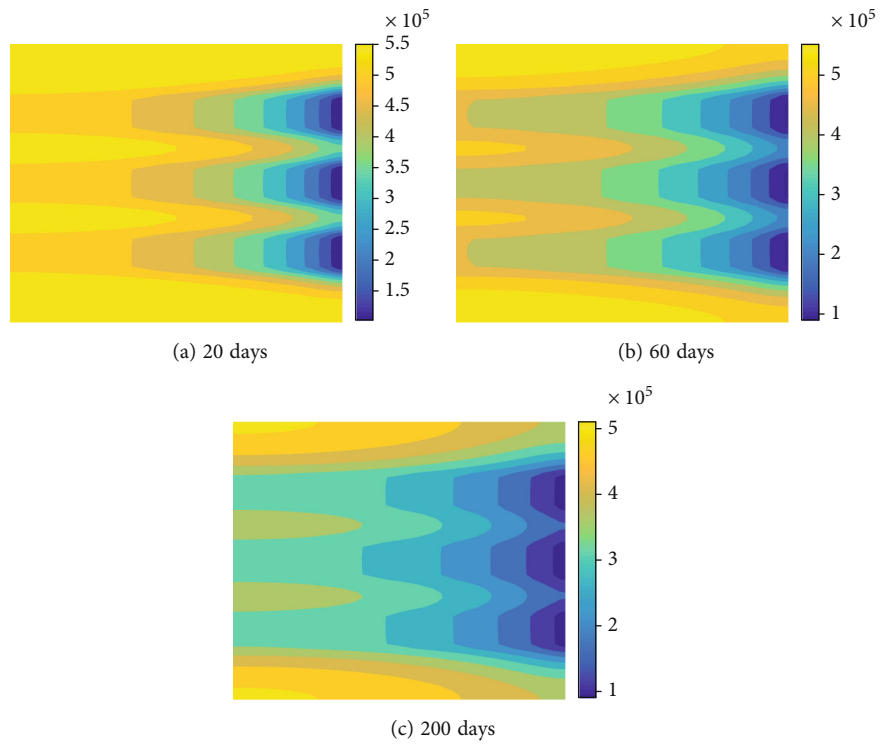


FIGURE 13: Pressure distributions in example 2 with  $c_b = 20 \text{ mol/m}^3$  at different times.

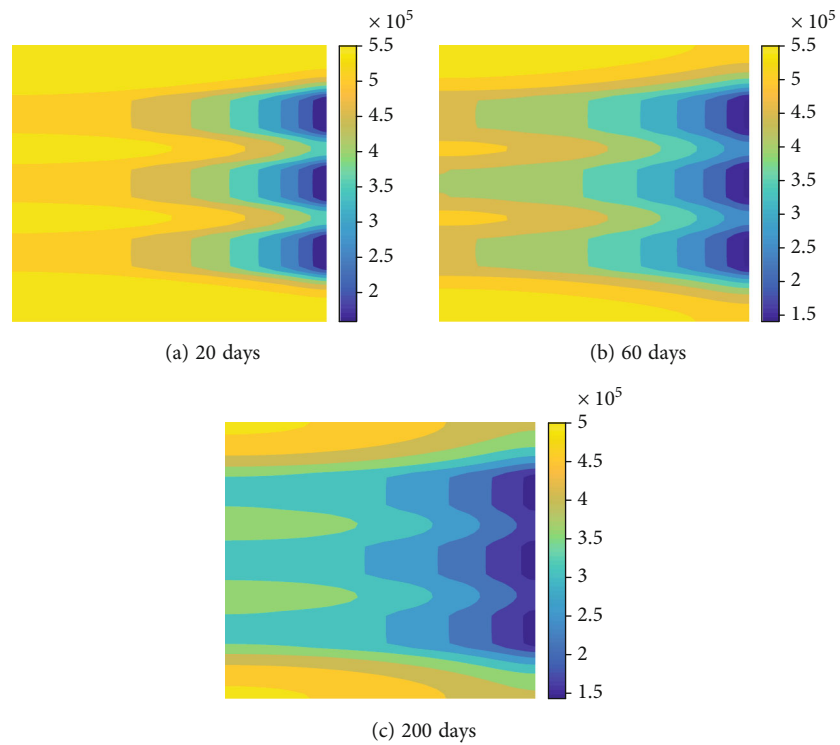


FIGURE 14: Pressure distributions in example 2 with  $c_b = 40 \text{ mol/m}^3$  at different times.

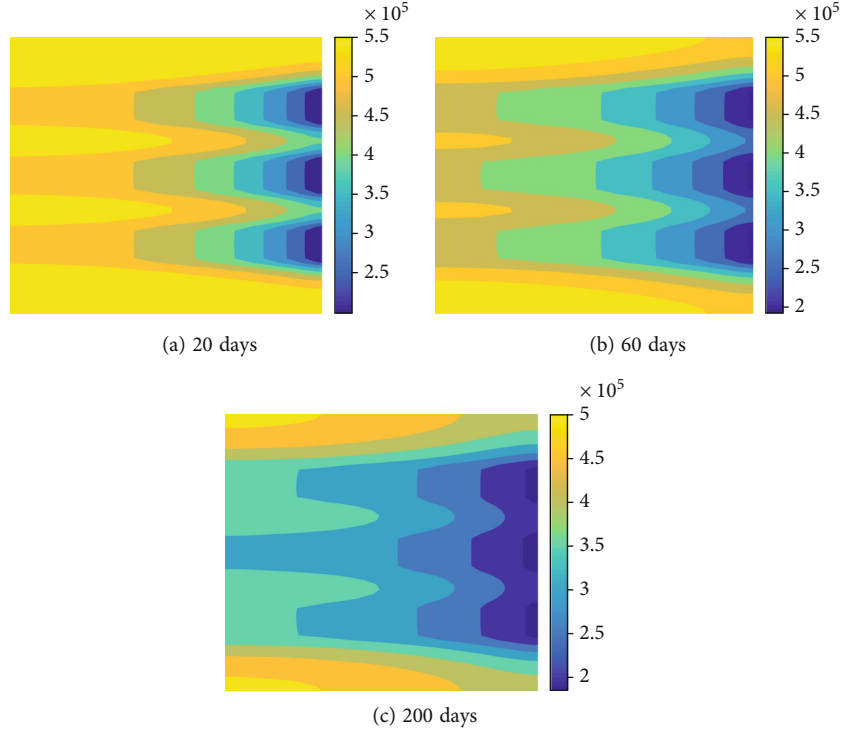


FIGURE 15: Pressure distributions in example 2 with  $c_b = 60 \text{ mol/m}^3$  at different times.

On the other hand, it follows from (17) that

$$\int_{\Omega} \mu^{n+1} \varphi(c^n) (c^{n+1} - c^n) d\mathbf{x} \geq \int_{\Omega} \varphi(c^n) (f(c^{n+1}) - f(c^n)) d\mathbf{x}. \quad (35)$$

As a consequence of (34) and (35), the following discrete energy dissipation law is obtained

$$\begin{aligned} \int_{\Omega} \varphi(c^n) \frac{f(c^{n+1}) - f(c^n)}{\tau} d\mathbf{x} + \int_{\partial\Omega} \mu^{n+1} c^n \mathbf{u}^{n+1} \cdot \mathbf{n} ds \\ \leq - \int_{\Omega} \frac{K_{\text{app}}^n}{\eta} |c^n \nabla \mu^{n+1}|^2 d\mathbf{x}. \end{aligned} \quad (36)$$

Equation (31) can be further spatially discretized using the cell-centered finite difference (CCFD) method, which is a popular discrete method in various fluid flow fields [25, 26].

#### 4. Numerical Examples

In this section, the performance of the proposed model and numerical method is demonstrated through some numerical tests. The spatial domain in all numerical tests is a square domain  $[0, 10] \times [0, 10]$ , and the length unit is meter. A uniform rectangular mesh with 3600 grid cells is used to divide the domain. The gas is methane and its physical properties are listed in Table 1. The modified Dubinin’s adsorption

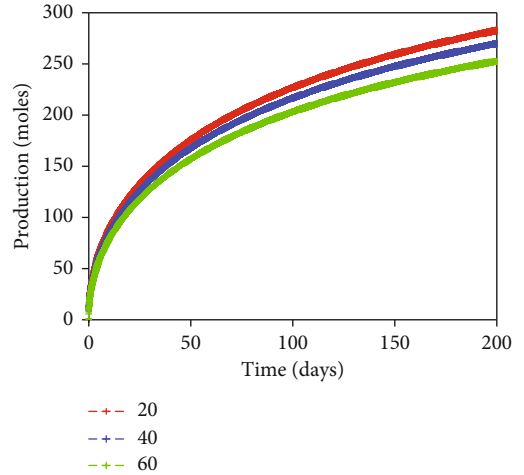


FIGURE 16: The cumulative production under different values of  $c_b$ .

model is used, and the initial velocity is taken to be zero for all tests.

The Hagen-Poiseuille equation is used to calculate the intrinsic permeability of gas flow in cylinders [13].

$$K_0 = \frac{r^2}{8}, \quad (37)$$

where  $r$  refers to the averaged pore diameter (nm).

*4.1. Example 1: Verification of the Energy Dissipation Property.* In this example, the aim is to verify the energy dissipation property of the model and numerical scheme. For



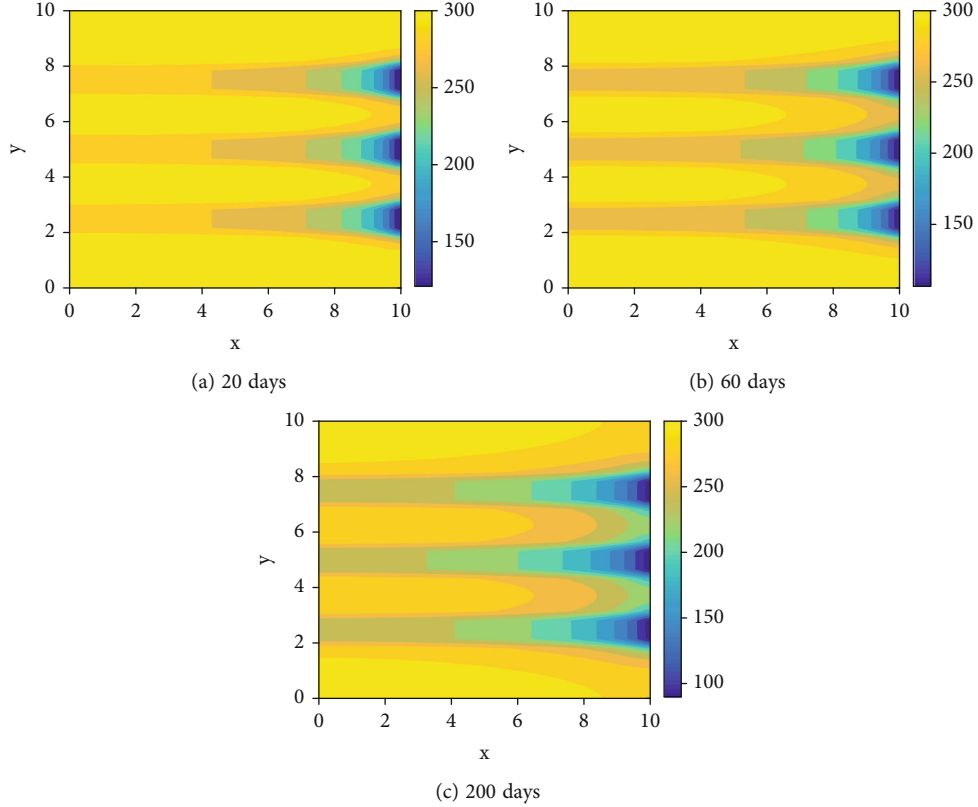


FIGURE 17: Adsorption density distributions in example 2 with  $c_b = 20 \text{ mol/m}^3$  at different times.

this purpose, the adsorption of methane is disregarded and the no-flow boundary condition is applied on the entire boundary of the domain, i.e.,  $\mathbf{u} \cdot \mathbf{n} = 0$ . In this situation, total free energy is expressed as

$$F^n = \int_{\Omega} \phi f(c^n) d\mathbf{x}. \quad (38)$$

From (36), the following energy dissipation law at the discrete level is obtained

$$F^{n+1} - F^n \leq -\tau \int_{\Omega} \frac{K_{\text{app}}^n}{\eta} |c^n \nabla \mu^{n+1}|^2 d\mathbf{x} \leq 0, \quad (39)$$

which implies that total free energy would be decreasing with time steps until an equilibrium state is reached. The physical parameters used in this example are listed in Table 2.

The stabilization constant in (24) is taken as  $\lambda = 0.0375$ . The time step size is chosen as  $\tau = 20$  hours, and 50 time steps are simulated. The initial methane density is generated by a random way.

The proposed model and numerical scheme are employed to simulate this problem. Dynamics of molar density and pressure is illustrated in Figures 1 and 2. For comparison, the classical pressure-based model is also applied to simulate the same problem, and the corresponding molar density and pressure are shown in Figures 3 and

4. The classical model are described in detail in Appendix D. Although two models produce slightly different results, it is clearly observed that due to spatial inhomogeneity of molar density, the fluid system tends to reach an equilibrium state where molar density becomes uniform in space.

Figure 5 depicts total free energy profiles of the proposed model and numerical scheme. Total energy is always decreasing monotonously over time, and thus, theoretical result is validated. For comparison, total free energy computed by the classical model is also plotted in Figure 6. Despite the decrease of total energy occurring in the simulation of the classical model, total energy is obviously oscillating and not monotonously decreasing over time as shown in the zoom-in plot.

The performance of two models in preserving the property of total mole conservation is also compared. The relative error of total moles is defined as

$$\Delta_c^n = \frac{\int_{\Omega} c^n d\mathbf{x} - \int_{\Omega} c^0 d\mathbf{x}}{\int_{\Omega} c^0 d\mathbf{x}}. \quad (40)$$

Figure 7 depicts the relative errors of total moles computed by two models. It can be observed that the proposed model can guarantee this key property very well within the range of roundoff errors, whereas the classical pressure-based model can cause a nonnegligible mass loss even in this simple problem. This means that the use of molar density as

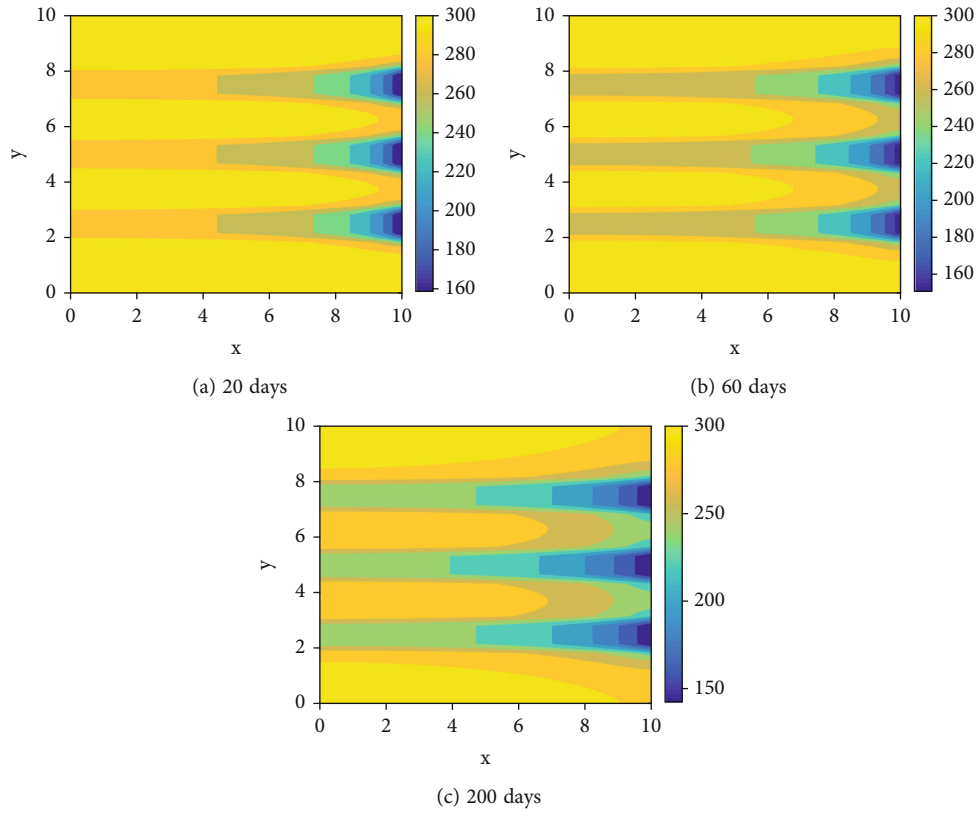


FIGURE 18: Adsorption density distributions in example 2 with  $c_b = 40 \text{ mol/m}^3$  at different times.

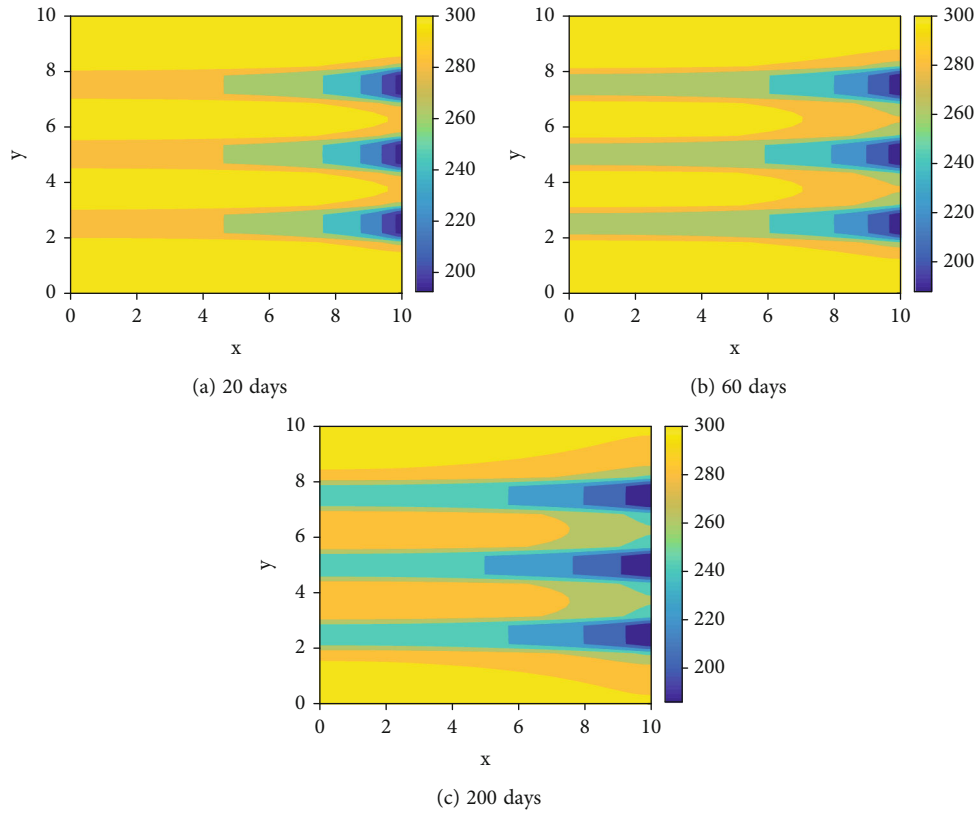


FIGURE 19: Adsorption density distributions in example 2 with  $c_b = 60 \text{ mol/m}^3$  at different times.

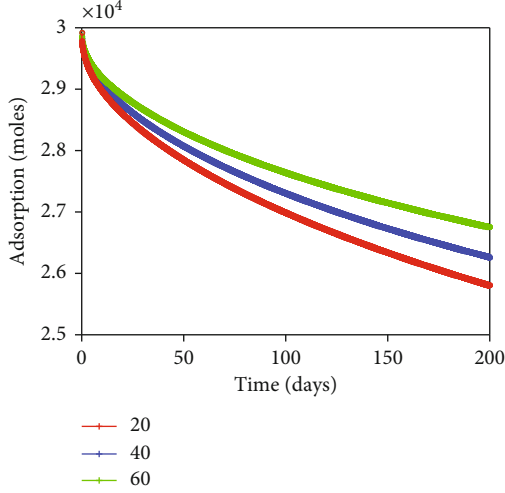


FIGURE 20: Total adsorption curves under different values of  $c_b$ .

the primary variable has a great advantage in guaranteeing mass conservation.

4.2. *Example 2.* A gas reservoir with multiple high-permeable layers is considered in this example. The intrinsic permeability of the reservoir is illustrated in Figure 8. The layers with high permeability are denoted by

$$\Omega_m = \{x = (x, y): x \in [0, L_x], y \in [0.2L_y, 0.3L_y] \cup [0.45L_y, 0.55L_y] \cup [0.7L_y, 0.8L_y]\}, \quad (41)$$

where  $L_x = L_y = 10$  m. The initial gas density is uniform and equal to  $200 \text{ mol/m}^3$ , while the initial adsorption density is illustrated in Figure 9. The gas is flowing out from the production boundary  $\Gamma$ , which locates on the right end of the domain

$$\Gamma = \{x = (x, y): x = L_x, y \in [0.2L_y, 0.3L_y] \cup [0.45L_y, 0.55L_y] \cup [0.7L_y, 0.8L_y]\}. \quad (42)$$

The boundary condition on the production end is specified as

$$c(x, y, t) = c_b, \quad (x, y) \in \Gamma, \quad (43)$$

where  $c_b$  is the gas production density. The rest boundaries are closed, and no mass transfer across these boundaries takes place. The physical parameters used in this example are listed in Table 3. The stabilization constant in (24) is taken as  $\lambda = 0.0148$ , and the time step size is chosen as  $\tau = 0.8$  hour.

Tests with  $c_b = 20, 40, 60 \text{ mol/m}^3$  are performed. The gas density distributions at various times computed with  $c_b = 20, 40, 60 \text{ mol/m}^3$  are illustrated in Figures 10–12, while the corresponding pressure contours are shown in Figures 13–15. The cumulative gas production profiles under different values of  $c_b$  are also plotted in Figure 16. These results indi-

cate that the production density has a great effect on the gas production; in fact, the increase of  $c_b$  can largely reduce the cumulative gas production. The adsorption densities at different times computed with  $c_b = 20, 40, 60 \text{ mol/m}^3$  are shown in Figures 17–19. The total adsorption amounts under different values of the production density are illustrated in Figure 20. It is clearly observed that the remaining total adsorption amounts are against the increase of production density. This means that a large production density may not be preferred for the sake of achieving optimal gas production.

## 5. Conclusions

A new mathematical model of gas flow in shale media has been proposed. Different from the existing models, the proposed model uses gas density instead of pressure as the primary variable, and it employs chemical potential gradient rather than pressure gradient as the primary driving force. This distinctive feature brings up with thermodynamical consistency of the proposed model; that is, the model obeys an energy dissipation law, which implies the satisfaction of the second law of thermodynamics. Physically, energy stable numerical methods that preserve a discrete energy dissipation law are strongly demanded for numerical approximation of the model. For this purpose, on the basis of the energy factorization approach, an efficient, linear, energy stable semi-implicit numerical scheme is proposed for the proposed model, which inherits an energy dissipation law at the discrete level. Numerical experiments are performed, and numerical results show that the model and numerical method can not only ensure energy stability but also provide physically reasonable results.

## Appendix

### A. Helmholtz Free Energy Density

The Helmholtz free energy density determined by Peng-Robinson equation of state [30] is described in detail. Let  $c$  denote molar density of a substance. For specific temperature  $T$ , the Helmholtz free energy density  $f(c)$  is expressed as [22, 26, 31, 32].

$$f(c) = RT \ln(c) - RT \ln(1 - \beta c) + \frac{\alpha(T)c}{2\sqrt{2}\beta} \ln \left( \frac{1 + (1 - \sqrt{2})\beta c}{1 + (1 + \sqrt{2})\beta c} \right), \quad (A.1)$$

where  $R$  is the universal gas constant ( $\text{m}^3 \cdot \text{Pa} \cdot \text{mol}^{-1} \cdot \text{K}^{-1}$ ). The parameters  $\alpha$  and  $\beta$  in (A.1) can be calculated using the critical properties and acentric factor of a specific substance

$$\alpha = 0.45724 \frac{R^2 T_c^2}{P_c} \left[ 1 + m \left( 1 - \sqrt{T_r} \right) \right]^2, \quad \beta = 0.07780 \frac{RT_c}{P_c}, \quad (A.2)$$

where  $T_r = T/T_c$  is the reduced temperature,  $T_c$  is the critical

temperature (K),  $P_c$  is the critical pressure (Pa), and  $m$  is calculated from the acentric factor  $\omega$  as follows:

$$\begin{aligned} m &= 0.37464 + 1.54226\omega - 0.26992\omega^2, \quad \omega \leq 0.49, \\ m &= 0.379642 + 1.485030\omega - 0.164423\omega^2 + 0.016666\omega^3, \quad \omega > 0.49. \end{aligned} \quad (\text{A.3})$$

## B. Peng-Robinson Equation of State

The pressure in terms of the Peng-Robinson equation of state [30] is expressed as

$$p = \frac{cRT}{1 - \beta c} - \frac{\alpha c^2}{1 + 2\beta c - \beta^2 c^2}, \quad (\text{B.1})$$

where the parameters are described as in Appendix A.

## C. Adsorption Models

The original Langmuir isotherm adsorption model [7] uses gas pressure as the primary variable, but it is not suitable to describe the gas adsorption under supercritical conditions [3]. The modified Langmuir isotherm model that uses gas density rather than pressure takes the form [3]

$$c_{\text{ads}} = c_M \frac{\gamma c}{1 + \gamma c}, \quad (\text{C.1})$$

where  $c_M$  is the maximum absolute adsorption density ( $\text{mol} \cdot \text{m}^{-3}$ ) and  $\gamma$  is the Langmuir constant ( $\text{mol}^{-1} \cdot \text{m}^3$ ). Based on the Polanyi adsorption potential theory, Dubinin [8] developed an adsorption model, which is modified using density instead of pressure as [3, 9].

$$c_{\text{ads}} = c_M e^{-\mathcal{D}(\ln(c_a/c))^2}, \quad (\text{C.2})$$

where  $c_M$  still stands for the maximum absolute adsorption density,  $c_a$  is the adsorbed phase density ( $\text{mol} \cdot \text{m}^{-3}$ ), and  $\mathcal{D}$  is the pore structure parameter.

The derivatives of  $c_{\text{ads}}$  defined in (C.1) and (C.2) can be calculated as follows:

$$\begin{aligned} \frac{\partial c_{\text{ads}}}{\partial c} &= \frac{\gamma c_M}{(1 + \gamma c)^2}, \\ \frac{\partial c_{\text{ads}}}{\partial c} &= 2\mathcal{D}c_M e^{-\mathcal{D}(\ln(c_a/c))^2} \cdot (\ln(c_a/c))/c. \end{aligned} \quad (\text{C.3})$$

## D. Pressure-Based Model

The classical pressure-based model of shale gas can be formulated as [12].

$$\varphi(c) \frac{\partial c}{\partial p} \frac{\partial p}{\partial t} - \nabla \cdot c \frac{K_{\text{app}}}{\eta} \nabla p = 0, \quad (\text{D.1})$$

where the relevant variables and parameters are the same to those in Section 2. The linear semi-implicit scheme reads as

$$\varphi(c^n) \frac{\partial c(p^n)}{\partial p} \frac{p^{n+1} - p^n}{\tau} - \nabla \cdot c^n \frac{K_{\text{app}}^n}{\eta} \nabla p^{n+1} = 0. \quad (\text{D.2})$$

## Data Availability

The data that support the findings of this study are available from the corresponding author upon reasonable request.

## Conflicts of Interest

The authors declare that they have no conflicts of interest.

## Authors' Contributions

J. Kou and L. Chen contributed equally to this work.

## Acknowledgments

We thank the reviewers for their constructive suggestions and comments. This work is supported by the National Natural Science Foundation of China (No. 42172159).

## References

- [1] Z. Gao, Y. Fan, Q. Xuan, and G. Zheng, "A review of shale pore structure evolution characteristics with increasing thermal maturities," *Advances in Geo-Energy Research*, vol. 4, no. 3, pp. 247–259, 2020.
- [2] W. Shen, X. Li, T. Ma, J. Cai, X. Lu, and S. Zhou, "High-pressure methane adsorption behavior on deep shales: experiments and modeling," *Physics of Fluids*, vol. 33, no. 6, article 063103, 2021.
- [3] X. Song, X. Lu, Y. Shen, S. Guo, and Y. Guan, "A modified supercritical Dubinin-Radushkevich model for the accurate estimation of high pressure methane adsorption on shales," *International Journal of Coal Geology*, vol. 193, pp. 1–15, 2018.
- [4] P. Whitelaw, C. N. Uguna, L. A. Stevens et al., "Shale gas reserve evaluation by laboratory pyrolysis and gas holding capacity consistent with field data," *Nature Communications*, vol. 10, no. 1, p. 3659, 2019.
- [5] T. F. T. Rexer, M. J. Benham, A. C. Aplin, and K. M. Thomas, "Methane adsorption on shale under simulated geological temperature and pressure conditions," *Energy & Fuels*, vol. 27, no. 6, pp. 3099–3109, 2013.
- [6] D. J. K. Ross and R. M. Bustin, "Characterizing the shale gas resource potential of Devonian-Mississippian strata in the western Canada sedimentary basin: application of an integrated formation evaluation," *AAPG Bulletin*, vol. 92, no. 1, pp. 87–125, 2008.
- [7] I. Langmuir, "The adsorption of gases on plane surfaces of glass, mica and platinum," *Journal of Chemical Physics*, vol. 40, no. 9, pp. 1361–1403, 1918.
- [8] M. M. Dubinin, "Adsorption in micropores," *Journal of Colloid and Interface Science*, vol. 23, no. 4, pp. 487–499, 1967.
- [9] R. Sakurovs, S. Day, S. Weir, and G. Duffy, "Application of a modified Dubinin-Radushkevich equation to adsorption of gases by coals under supercritical conditions," *Energy & Fuels*, vol. 21, no. 2, pp. 992–997, 2007.

- [10] J. Cai, D. Lin, S. Harpreet, W. Wei, and S. Zhou, "Shale gas transport model in 3D fractal porous media with variable pore sizes," *Marine and Petroleum Geology*, vol. 98, pp. 437–447, 2018.
- [11] J. Cai, D. Lin, H. Singh, S. Zhou, Q. Meng, and Q. Zhang, "A simple permeability model for shale gas and key insights on relative importance of various transport mechanisms," *Fuel*, vol. 252, pp. 210–219, 2019.
- [12] M. F. El-Amin, J. Kou, and S. Sun, "Mixed finite element simulation with stability analysis for gas transport in low-permeability reservoirs," *Energies*, vol. 11, p. 208, 2018.
- [13] C. Guo, B. Bai, M. Wei, X. He, and Y.-S. Wu, "Study on gas permeability in nano pores of shale gas reservoirs," in *SPE Unconventional Resources Conference*, Calgary, Alberta, Canada, 2013.
- [14] F. Javadpour, "Nanopores and apparent permeability of gas flow in mudrocks (shales and siltstone)," *Journal of Canadian Petroleum Technology*, vol. 48, no. 8, pp. 16–21, 2009.
- [15] F. Javadpour, D. Fisher, and M. Unsworth, "Nanoscale gas flow in shale gas sediments," *Journal of Canadian Petroleum Technology*, vol. 46, no. 10, 2007.
- [16] E. Mohagheghian, H. Hassanzadeh, and Z. Chen, "Estimation of shale apparent permeability for multimechanistic multi-component gas production using rate transient analysis," *Energy & Fuels*, vol. 33, no. 3, pp. 1990–1997, 2019.
- [17] A. Salama, M. F. El-Amin, K. Kumar, and S. Sun, "Flow and transport in tight and shale formations," *Geofluids*, vol. 2017, Article ID 4251209, 21 pages, 2017.
- [18] J. Zhao, J. Yao, M. Zhang et al., "Study of gas flow characteristics in tight porous media with a microscale lattice Boltzmann model," *Scientific Reports*, vol. 6, p. 32393, 2016.
- [19] J. Yuan, R. Jiang, Y. Cui, J. Xu, Q. Wang, and W. Zhang, "The numerical simulation of thermal recovery considering rock deformation in shale gas reservoir," *International Journal of Heat and Mass Transfer*, vol. 138, pp. 719–728, 2019.
- [20] L. J. Klinkenberg, "The permeability of porous media to liquids and gases," *Production Practice*, 1941.
- [21] G. Sheng, Y. Su, H. Zhao, and J. Liu, "A unified apparent porosity/permeability model of organic porous media: coupling complex pore structure and multi-migration mechanism," *Advances in Geo-Energy Research*, vol. 4, no. 2, pp. 115–125, 2020.
- [22] J. Kou and S. Sun, "Thermodynamically consistent modeling and simulation of multi-component two-phase flow with partial miscibility," *Computer Methods in Applied Mechanics and Engineering*, vol. 331, pp. 623–649, 2018.
- [23] G. Lebon, D. Jou, and J. Casas-Vázquez, *Understanding Non-Equilibrium Thermodynamics*, Springer-Verlag, Berlin Heidelberg, 2008.
- [24] G. Zhu, J. Kou, B. Yao, Y.-s. Wu, J. Yao, and S. Sun, "Thermodynamically consistent modelling of two-phase flows with moving contact line and soluble surfactants," *Journal of Fluid Mechanics*, vol. 879, pp. 327–359, 2019.
- [25] J. Kou, S. Sun, and X. Wang, "Linearly decoupled energy-stable numerical methods for multicomponent two-phase compressible flow," *SIAM Journal on Numerical Analysis*, vol. 56, no. 6, pp. 3219–3248, 2018.
- [26] J. Kou, S. Sun, and X. Wang, "A novel energy factorization approach for the diffuse-interface model with Peng–Robinson equation of state," *SIAM Journal on Scientific Computing*, vol. 42, no. 1, pp. B30–B56, 2020.
- [27] J. Shen, J. Xu, and J. Yang, "The scalar auxiliary variable (SAV) approach for gradient flows," *Journal of Computational Physics*, vol. 353, pp. 407–416, 2018.
- [28] X. Wang, J. Kou, and J. Cai, "Stabilized energy factorization approach for Allen–Cahn equation with logarithmic Flory–Huggins potential," *Journal of Scientific Computing*, vol. 82, no. 2, p. 25, 2020.
- [29] X. Wang, J. Kou, and H. Gao, "Linear energy stable and maximum principle preserving semi-implicit scheme for Allen–Cahn equation with double well potential," *Communications in Nonlinear Science and Numerical Simulation*, vol. 98, article 105766, 2021.
- [30] D. Peng and D. B. Robinson, "A new two-constant equation of state," *Industrial and Engineering Chemistry Fundamentals*, vol. 15, no. 1, pp. 59–64, 1976.
- [31] T. Jindrová and J. Mikyska, "Fast and robust algorithm for calculation of two-phase equilibria at given volume, temperature, and moles," *Fluid Phase Equilibria*, vol. 353, pp. 101–114, 2013.
- [32] T. Jindrová and J. Mikyska, "General algorithm for multiphase equilibria calculation at given volume, temperature, and moles," *Fluid Phase Equilibria*, vol. 393, pp. 7–25, 2015.

## Research Article

# Dust Concentration Changing Regularities and Dust Reduction Technology by Spray Negative Pressure in Fully Mechanized Mining Face

Lirong Wu <sup>1,2</sup> Hongxuan Chen <sup>1</sup> Jiamin Li <sup>1</sup> Shican Fu,<sup>1</sup> and Yuyan Zhuang<sup>1</sup>

<sup>1</sup>College of Safety and Environmental Engineering, Shandong University of Science and Technology, Qingdao 266590, China

<sup>2</sup>State Key Laboratory of Mining Disaster Prevention and Control co-Founded by Shandong Province and the Ministry of Science and Technology, Shandong University of Science and Technology, Qingdao 266590, China

Correspondence should be addressed to Jiamin Li; [lijiamin980328@126.com](mailto:lijiamin980328@126.com)

Received 27 June 2021; Accepted 13 August 2021; Published 1 October 2021

Academic Editor: Chenhao Sun

Copyright © 2021 Lirong Wu et al. This is an open access article distributed under the Creative Commons Attribution License, which permits unrestricted use, distribution, and reproduction in any medium, provided the original work is properly cited.

The dust concentration changing regularities are the basis to take dust depression measures, which is greatly influenced by the airflow. In the software of FLUENT, the value of ventilation velocity is set as a constant, which cannot express the real ventilation. According to the flow characteristics of the sublayer and data from Nicholas' experiment, the ventilation velocity distribution formula of sublayer in the inlet section of fully mechanized caving coal face is deduced. The boundary condition of velocity is given by UDF. Taking the 3<sup>top1110</sup> fully mechanized caving coal face as an example, the dust distribution in the process of coal mining and hydraulic support shifting was studied. According to the dust-spray coupling experiment, three types of nozzle are chosen based on the efficiency of dust suppression. Combining the dust migration rule and the characteristics of nozzles, the negative pressure-secondary dust suppression devices of spray were developed and applied. And the above measures have lowered the dust concentration effectively.

## 1. Introduction

High-concentration dust has been an issue that impedes the safe and efficient coal mining in fully mechanized mining faces. Coal dust is one of the five major disasters in coal mines, which can not only lead to dust and gas explosion accidents but also cause workers' pneumoconiosis. According to the notification by the National Health and Family Planning Commission of PRC, the cumulative number of occupational disease cases in China was as high as 951359 by 2017, of which 853847 were pneumoconiosis cases, accounting for 89.8% of the total occupational disease cases in China. It is predicted that the pneumoconiosis cases in China will keep rising in the coming 10-15 years [1, 2].

In order to control the dust effectively, making clear the coal dust concentration changeable rule is the basis. And much research had been done by numerical simulation. Lai [3] used the finite volume method of computational fluid dynamics to solve the problem and compiled a computer

program to simulate the distribution of wind speed and dust concentration in the three-dimensional space of fully mechanized working face. Nakayama et al. [4], Patankar and Joseph [5], and Yu et al. [6] used a large eddy simulation (LES) method to simulate gas movement, and the Eulerian Lagrangian method was used to simulate dust particle movement. According to the two basic flow field types of plane wake flow and turbulent jet, the spatial distribution characteristics of dust particles with different Stokes (st) numbers were numerically simulated. Housiadas et al. [7] and Wang et al. [8] studied the air flow field and dust concentration distribution law of the extraction type local ventilation mode in the heading face. Liu et al. [9] and Niu et al. [10] carried out numerical simulation on the dust movement law of working flour by using computational fluid dynamics FLUENT software. Zhou et al. [11, 12], Wu [13], and Sun et al. [14] studied the dust movement law of multiple dust sources in a fully mechanized caving face and the influencing factors of dust concentration. Yao et al. [15] studied the influence of

different parameters on the dust flow law of a fully mechanized caving face and the dust generation law of different working procedures in steeply inclined fully mechanized caving face. Ren et al. [16] focused on airflow and coal dust dynamics at the intersection between the fully mechanized caving face and the air intake lane and proposed an optimal layout of air curtain at the entrance of air intake lane and working face based on the results of numerical simulation.

The application of spray technology in fully mechanized coal caving workplace is aimed at reducing the coal dust concentration. Since 1980s, all kinds of dust removal technologies have been developed, and the theory of spray and dust suppression has been continuously improved [17]. At present, most of the coal faces use spray dust control technology to prevent dust, and in most cases, high pressure is taken to improve dust removal efficiency. High-pressure spray dust suppression technology is applied earlier in the United States, the former Soviet Union, Germany, and other countries [18, 19]. The dust reduction efficiency of the shearer driver was 94%. Although high-pressure spray can improve the efficiency of dust fall, high-pressure spray will cause dust disturbance, resulting in secondary dust. Therefore, nozzle installation location, spray pressure, and flow rate need to be adjusted. A large number of experiments and studies have been carried out by the US Mining Bureau, and a new type of external spray cleaning device for Drum Shearers has been developed, which makes the dust laden airflow and fresh air flow run separately and overcomes the eddy current effect produced by the external spray system in adverse wind spray [20]. Liu [21] used LS-2000 split type laser atomization droplet size analyzer to measure the droplet size, distribution, and velocity of different swirl water mist nozzles and obtained the optimal structural parameters of the medium and low-pressure single fluid through swirl atomizing nozzle. Wang et al. [22] used the three-dimensional LDV/APV system to measure the three-dimensional velocity of the spray field of the dust suppression nozzle accurately. The experimental results show that with the increase of the nozzle set fluid pressure, the fog particle size gradually decreases, the radial coverage of the fog field expands, and the volume flux of the dusty air increases gradually. Zhou et al. [23] designed a nozzle atomization experimental system by using Winner313 laser particle size analyzer. The atomizing particle size of the common nozzles in the coal mining face was measured, and it was determined that the spray particle size distribution at 8 MPa had the best effect on the dust reduction in the coal mining face. Peng et al. [24] added a fan to the shearer's spray device to develop an air-assisted PM10 control device, in combination with the airflow-carrying-droplet mechanism. Wang et al. [25, 26] had done the experimental study on dust reduction via spray using a surfactant solution.

In order to control the coal dust concentration in the fully mechanized mining face more effectively, this paper first deduced ventilation velocity distribution formula of base course in inlet section and wrote the inlet velocity programs (UDF), which was interpreted in FLUENT, replacing the constant value set as usual. Then, the ventilation velocity set in the numerical simulation can express the real condi-

tion and does the dust concentration changeable rule. Based on the nozzle jet characteristic experiment and spray dust fall experiment, the preferable nozzles have been selected. Combining the dust production regulation and nozzle characteristics, the negative pressure resecondary dust suppression device is used, which has two effects. First, the proper nozzles have been chosen and set in the dust suppression device. Based on the dust migration rule, the spray direction of nozzles is adjusted. Then, the dust produced in the process of coal mining can be depressed to a great extent. Second, in order to catch the dust, the negative pressure resecondary dust suppression theory is used in the device. Based on the above, the dust can be controlled effectively.

## 2. Methods

*2.1. Theoretical Study of Dust Migration Rule.* In fully mechanized mining faces, the gas flow control equations apply the three dimensional steady incompressible Navier-Stokes equation. The turbulent flow model uses the  $k-\varepsilon$  double equation model. The momentum transfer is considered, and the heat passage is neglected.

Continuous equation:

$$\frac{\partial}{\partial x_i}(\rho u_i) = 0. \quad (1)$$

Equation of motion:

$$\frac{\partial c}{\partial x_i}(\rho u_i u_j) = -\frac{\partial p}{\partial x_i} + \frac{\partial}{\partial x_i} \left[ (\mu + \mu_t) \left( \frac{\partial u_j}{\partial x_i} + \frac{\partial u_i}{\partial x_j} \right) \right] \quad (2)$$

$k$  equation:

$$\frac{\partial}{\partial x_i}(\rho u_i k) = \frac{\partial}{\partial x_i} \left[ \left( \mu + \frac{\mu_t}{\sigma_k} \right) \frac{\partial k}{\partial x_i} \right] + G_k - \rho \varepsilon. \quad (3)$$

$\varepsilon$  equation:

$$\begin{aligned} \frac{\partial}{\partial x_i}(\rho u_i \varepsilon) &= \frac{\partial}{\partial x_i} \left[ \left( \mu + \frac{\mu_t}{\sigma_\varepsilon} \right) \frac{\partial \varepsilon}{\partial x_i} \right] + \frac{C_{\varepsilon 1} \varepsilon}{k} G_k \varepsilon^2 - C_{\varepsilon 2} \rho \frac{\varepsilon^2}{k}, \\ \mu_t &= C_{\mu} \rho \frac{k^2}{\varepsilon}, \\ G_K &= \mu_t \frac{\partial u_j}{\partial x_i} \left( \frac{\partial u_j}{\partial x_i} + \frac{\partial u_i}{\partial x_j} \right), \end{aligned} \quad (4)$$

where  $G_K$  is the turbulent kinetic energy change rate generated by shear force changes;  $k$  is the turbulent kinetic energy,  $m^2/s^2$ ;  $\varepsilon$  is the turbulent dissipation rate,  $m^2/s^3$ ;  $\mu$  is the laminar viscous coefficient, Pa·s;  $\mu_t$  is the turbulent viscosity coefficient, Pa·s;  $p$  is the the turbulence of effective pressure, Pa;  $\rho$  is the gas density,  $kg/m^3$ ;  $x_i$  is the coordinate in the direction of  $x$ ,  $y$ , and  $z$ , m;  $\mu_t$  is the ventilation of fluid

in the direction of  $x$ ,  $y$ , and  $z$ , m/s;  $C_{\varepsilon 1}$ ,  $C_{\varepsilon 2}$ ,  $C_{\mu}$ ,  $\sigma_{\varepsilon}$ , and  $\sigma_k$  are the constant, taking 1.44, 1.92, 0.09, 1.3, and 1.0 successively.

The particle motion equation is solved by the integral operation in discrete time steps. And the movement track is as follows:

$$\frac{dx}{dt} = u_p. \quad (5)$$

**2.2. Theoretical Analysis of Ventilation Velocity Distribution at Entrance Section.** The ventilation velocity distribution in the fully mechanized mining coal face affects the dust migration rule. According to the different Reynolds numbers, the fluid flow can be divided into the laminar flow and turbulent flow.

For the cylindrical space, when the fluid flow state is laminar, the velocity distribution law of the section is a rotating paraboloid. When the fluid flow state is turbulent, as its flow mechanism is different from laminar flow, its velocity distribution is fundamentally different from that of laminar flow. In most areas near the pipe axis, the transverse pulsation of fluid particles makes the momentum exchange between the flow layers more intense, which becomes the turbulent core area. The pulsation of the laminar flow thin layer near the wall disappears due to wall restriction. At the same time, the viscous force between the laminar flow layers makes the velocity drop sharply and the velocity gradient is large. This thin layer is called the viscous bottom layer. According to the Prandtl hypothesis and Nicholas experiment, the velocity distribution function of the viscous bottom layer and turbulent core area in cylindrical space section can be obtained.

The velocity distribution formula of the entrance section of the fully mechanized caving coal face should adopt the noncylindrical space velocity distribution formula. For noncylindrical spaces, in the early 1950s, B-H-Voronin (Soviet Union mine ventilation scientist) published the velocity distribution function on the cross-section of the roadway. In 1977, the ventilation safety department of Northeast Institute of technology revised the formula deduced by B-H Voronin on the basis of experimental research. In 1982, Ji Chaosong (Professor of Beijing Institute of iron and steel) theoretically deduced the distribution function of tunnel wind speed which is different from that derived by B-H Voronin. In 1989, Yu Yuejin analyzed the defects of the formula on the basis of the above research and put forward the L-Prandtl formula of the velocity distribution in the roadway according to the Prandtl hypothesis. The above formula does not distinguish the difference of velocity between the viscous bottom and turbulent core. Based on the above research, the velocity distribution formula of the noncylindrical space viscous bottom is derived in this paper [27].

In the viscous bottom layer, the velocity distribution can be approximately considered a straight line distribution, that is,

$$\frac{dv_x}{dy} = \frac{v_x}{y}. \quad (6)$$

The stress can be approximately expressed as follows:

$$\tau = \mu \frac{v_x}{y}, \quad y \leq \delta, \quad (7)$$

where  $\delta$  is the thickness of the viscous bottom layer. It can be obtained from formula (7):

$$v_x = v_*^2 \frac{y}{\nu}. \quad (8)$$

Let

$$v_* = \sqrt{\frac{\tau}{\rho}}. \quad (9)$$

In formula (9),  $v_*$  is the resistance velocity. According to Bernoulli's equation and Darcy's law, the following formula can be deduced:

$$v_* = \bar{v} \sqrt{\frac{\lambda}{8}} = \bar{v} \frac{\sqrt{\alpha}}{\rho}, \quad (10)$$

where  $\lambda$  is the Darcy coefficient, dimensionless and  $\alpha$  is the friction coefficient,  $\text{kg/m}^3$ .

According to the Nikolaz experiment, the following formula is satisfied in the laminar flow region:

$$\lambda = \frac{64}{Re} = \frac{64\nu}{v_x d}, \quad (11)$$

where  $d$  is the equivalent diameter, m.

Formulas (10) and (11) are substituted into formula (8), and the velocity distribution formula of the viscous bottom zone expressed by  $\bar{v}$ ;  $r/r_0$  is as follows:

$$v_x = \bar{v} \sqrt{2 \left(1 - \frac{r}{r_0}\right)}. \quad (12)$$

L-Prandtl's two hypotheses are as follows:

- (1) The turbulent shear stress is constant along the section and equal to the wall shear stress  $\tau$
- (2) There is a linear relationship between the mixing length  $l$  and the distance  $y$  to the cylinder wall, i.e.,  $l = ky$

For the turbulent region, according to Prandtl's above hypothesis, there is

$$\tau = \rho k^2 y^2 \left(\frac{dv_x}{dy}\right)^2. \quad (13)$$

It can be obtained from formulas (9) and (13):

$$\frac{dv_x}{dy} = \frac{v_*}{ky}. \quad (14)$$



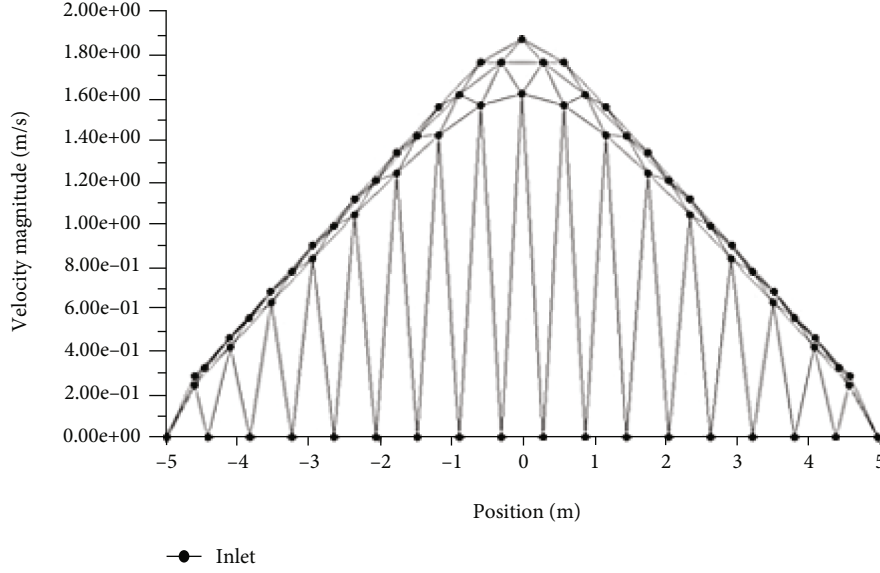


FIGURE 1: The ventilation in the entry section at the  $x$ -axis.

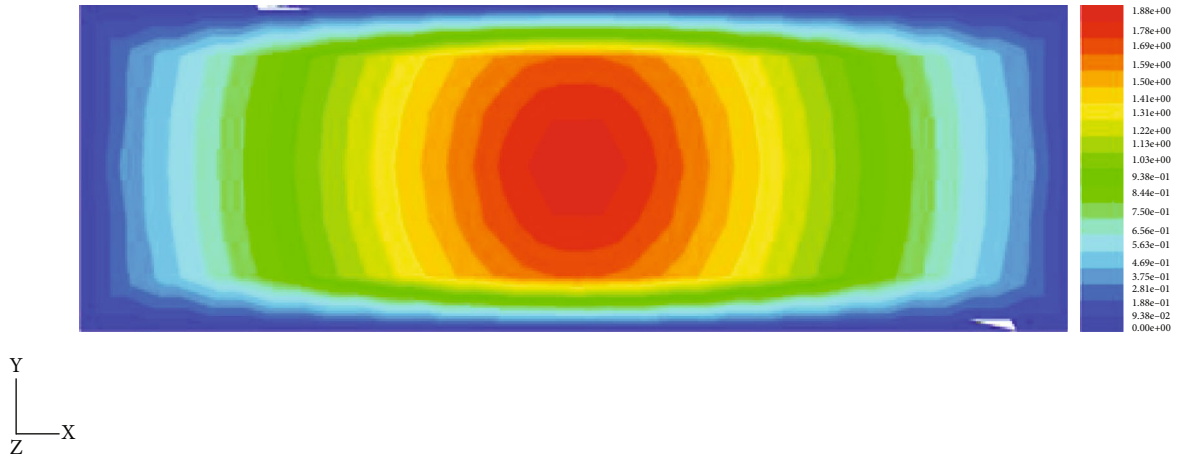


FIGURE 2: The ventilation in the entry section at the  $x$ -axis.

By integrating formula (14), the following can be obtained:

$$v_x = \frac{1}{k} v_* \ln y + C. \quad (15)$$

Assuming that the velocity at the boundary between the viscous bottom and turbulent flow is expressed by  $v_b$ , then, the boundary condition is  $y = \phi \varepsilon$ ,  $v_x = v_b$ . Substituting the boundary condition into formula (15), the following results can be obtained:

$$C = v_b - \frac{1}{k} v_* \ln \phi \varepsilon, \quad (16)$$

where  $\phi$  is the shape coefficient determined by the roughness of the cylinder wall and  $\varepsilon$  is the absolute roughness of the pipe wall.

Substituting formula (16) into (15), then,

$$v_x = \frac{1}{k} v_* \ln \frac{y}{\phi \varepsilon} + v_b. \quad (17)$$

Let  $C_2 = (v_b/v_*) - (1/k) \ln \phi$ , then,

$$\frac{v_x}{v_*} = \frac{1}{k} \ln \frac{y}{\varepsilon} + C_2. \quad (18)$$

According to the Nicholas experiment curve,  $k = 0.40$ , and  $C_2 = 8.48$ , then, the results are as follows:

$$\frac{v_x}{v_*} = 2.5 \ln \frac{y}{\varepsilon} + 8.48. \quad (19)$$

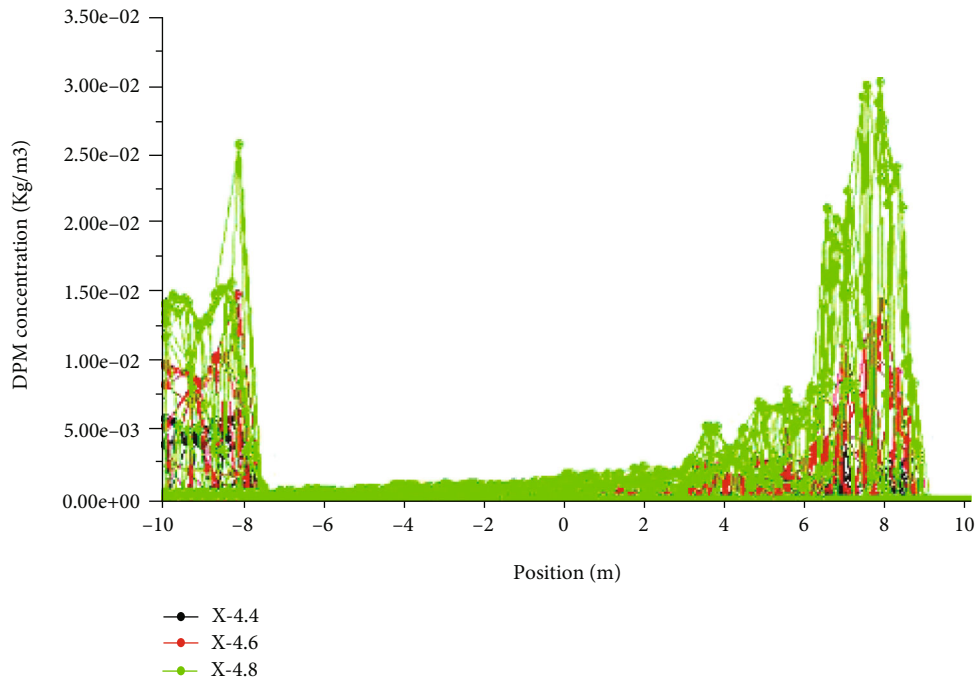


FIGURE 3: Variation chart of dust concentration in different sections of coal mining operation.

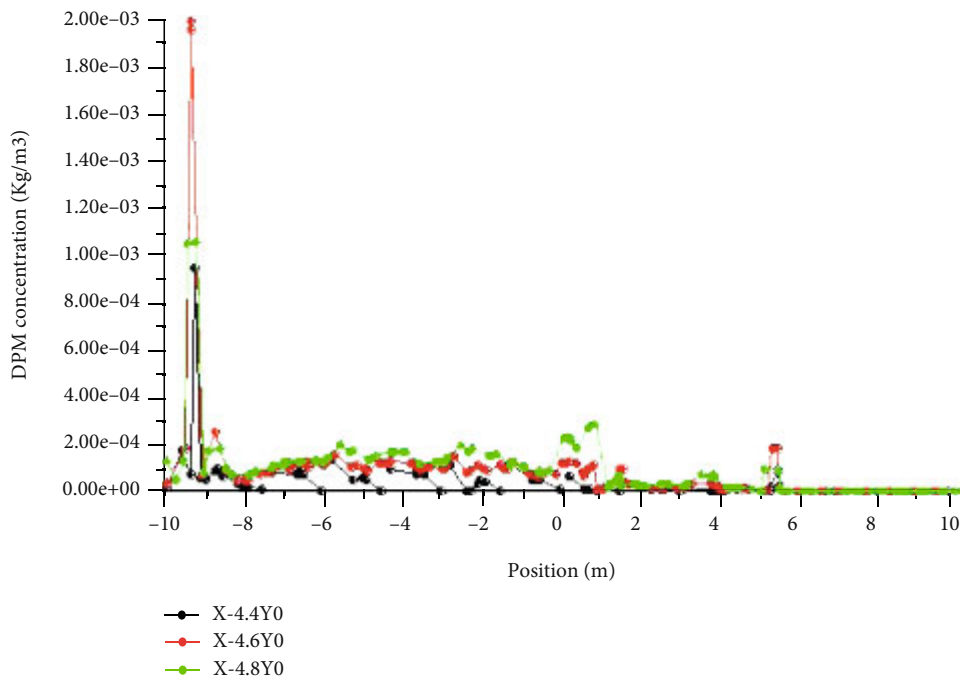


FIGURE 4: Variation chart of dust concentration in coal mining operation.

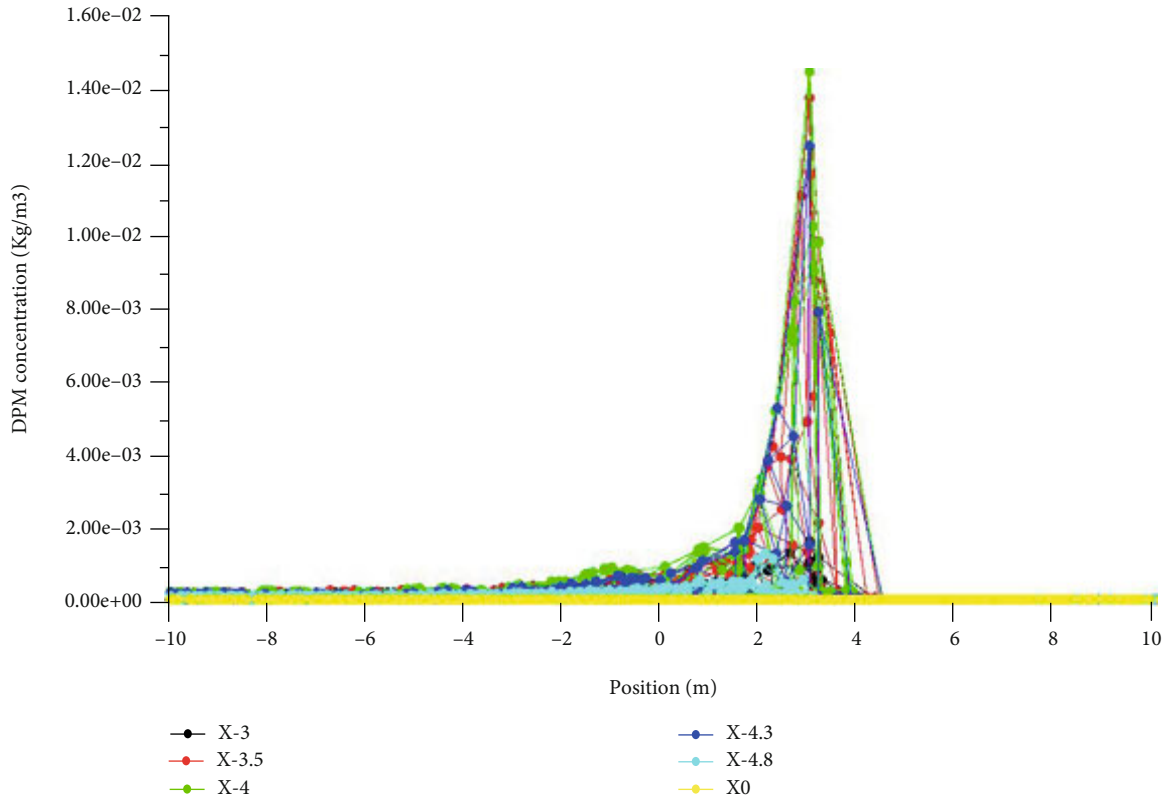


FIGURE 5: Variation chart of dust concentration in support shifting operation.

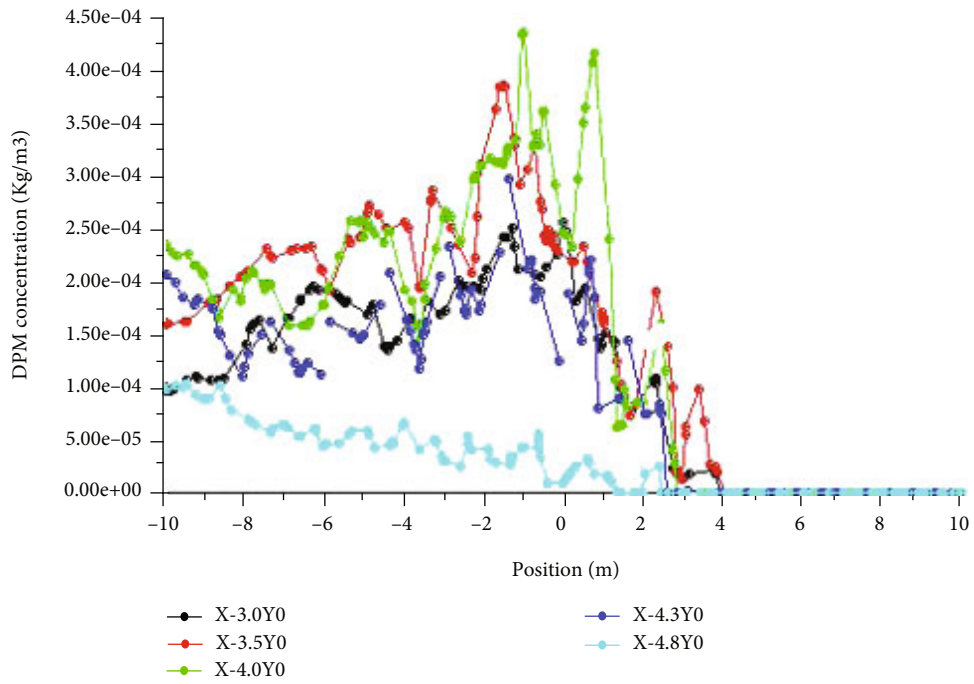







FIGURE 6: Variation chart of dust concentration in support shifting operation.

TABLE 1: Nozzles used in atomization characteristic experiment.

Type	No.	Orifice diameter (mm)	Fog flow shape	Atomization type	Physical picture
A	1#	1.1	Sector	Cone-shaped guide groove direct type	
	2#	1.4			
	3#	1.6			
B	4#	1.6	Solid cone	Mixed type with X-shaped guide core	
	5#	2.0			
	6#	2.4			
C	7#	1.2	Hollow cone	Side guide hole centrifugal	
	8#	1.6			
	9#	2.0			
D	10#	2.4	Square solid cone	Hybrid type with cross opening and X-shaped guide core	
	11#	1.6			
	12#	1.9			
E	13#	2.4	Solid cone	Mixed type with X-shaped guide core	
	14#	2.3			
	15#	2.8			
	16#	3.2			

According to the Nicholas experiment curve, the relationship between  $k - \varepsilon$  and  $\varepsilon$  is as follows:

$$\varepsilon = 7.4r_0 10^{1/-2\sqrt{\lambda}}. \quad (20)$$

By substituting formulas (9) and (20) into (19),  $\rho = 1.2 \text{ kg/m}^3$  is set, and the velocity distribution formula of turbulent area expressed by  $\bar{v}$  and  $\alpha; r/r_0$  is as follows:

$$v_x = \bar{v} \left[ 1 + 3.17\sqrt{\alpha} + 2.28\sqrt{\alpha} \ln \left( 1 - \frac{r}{r_0} \right) \right]. \quad (21)$$

Formulas (12) and (21) are the velocity distribution formulas of the viscous bottom layer and turbulent area of a noncircular pipe, respectively. The section of the fully mechanized caving coal face can be regarded as a kind of noncircular pipe, so formulas (12) and (21) are also applicable to the distribution of wind speed at the entrance section of the fully mechanized coal caving face.

### 3. The Simulation of Dust Concentration in Fully Mechanized Mining Workface

Taking the 3<sup>top1110</sup> work face in the Gao Zhuang Coal Mine as the research object, the dust concentration changing reg-

ularities are simulated by the software of FLUENT. Based on the actual situation of 3<sup>top1110</sup> working face, the rectangular region is made with the length, width, and height of 20.0 m, 10.0 m, and 3.0 m, respectively. The parameters and boundary conditions of numerical simulation are determined, in which the value of the inlet velocity magnitude is set by UDF(velocity\_inlet).

In the standard FLUENT module, the entrance velocity can only be given as a constant value, but in reality, the velocity is a variable on the workface section. User-defined function (UDF) can be used to define the entrance velocity at different positions on the entry face, so as to better calculate the velocity field inside the workface. And the simulation results can better reflect the actual situation of the fully mechanized mining face.

According to the velocity distribution theory at the entrance section of the fully mechanized mining face, the flow state of air flow in workface determines the distribution of velocity. Therefore, the flow state of 3<sup>top1110</sup> workface in the Gao Zhuang Coal Mine should be identified firstly. When the average velocity of workface is 2 m/s, the Reynolds number is calculated as follows:

$$\text{Re} = \frac{vd}{\nu} = \frac{2.4S/C}{\nu} = \frac{2.4 \cdot 30/26}{14.8 \cdot 10^{-6}} = 623700. \quad (22)$$



(a) Simulation tunnel



(b) Doppler laser beam and data acquisition system

FIGURE 7: Closed experiment box.

It can be seen that the flow state of the workface is turbulent.

According to the velocity distribution formula at the entrance section of the fully mechanized mining face and the actual situation  $3^{\text{top1110}}$  workface, the UDF velocity of inlet velocity magnitude (m/s) is compiled by using C language\_Let.

User-defined function UDF velocity inlet is interpreted in FLUENT software and set as the boundary condition of velocity at the entrance section of the fully mechanized mining face. The variation of velocity along the  $x$ -axis direction of the entrance section is shown in Figure 1. The velocity distribution at the entrance section is shown in Figure 2.

From Figures 1 and 2, it can be seen that the velocity of the workface wall is zero, and the velocity increases from the wall to the core. In the core point the velocity reaches the maximum. The distribution curve of velocity along the  $x$ -axis direction of the entrance section approximates a parabola.

When the dust produced by the shearer cutting coal is considered separately, the dust source is the front and rear drums of the shearer. When the average velocity is 2 m/s, the dust concentration on the face 0.2 m, 0.4 m, and 0.6 m away from the coal wall is displayed in Figure 3. The dust concentration on the line 0.2 m, 0.4 m, and 0.6 m away from the coal wall and 1.5 m above the ground is shown in Figure 4.

When the dust produced by hydraulic support moving operation is considered separately, the average wind speed

at the inlet of 2 m/s and the dust source as a line source are set, which is located at the top of the second hydraulic support at the air inlet, close to the edge of the coal outlet ( $-4.3 < x < 0.7, z = 2.9$ ). Assuming that 20 particles are randomly generated at the dust source, the dust concentration distribution at 0.2 m, 0.7 m, 1 m, 1.5 m, 2 m, and 5 m away from the coal wall is shown in Figure 5. The dust concentration distribution along the  $z$ -axis direction at the distance of 0.2 m, 0.7 m, 1 m, 1.5 m, 2 m, and 5 m away from the coal wall and 1.5 m above the ground is shown in Figure 6.

#### 4. Experiment on Characteristics of Nozzles and Spray Dust Fall

*4.1. Experiment on Atomization Characteristics of Nozzle.* In order to optimize the nozzles suitable for spraying and dust fall in the fully mechanized mining face, 5 types of stainless steel nozzles (expressed separately by A–E) including 16 kinds of stainless steel nozzles (1#–16#, respectively) are collected, the traits of which are shown in Table 1. The experiments on atomization characteristics and spray dust fall are completed in the simulation tunnel, which are shown in Figures 7(a) and 7(b). The conventional performance parameters of A–E (1#–16#) nozzles are researched and the conventional performance parameters of A–E (1#–16#) nozzles can be seen in Table 2).

Based on the atomization angle, effective range, and flow of the nozzles, considering the shape and droplet density of the fog flow field observed in the field, 8 kinds of nozzles

TABLE 2: Measurement data of conventional performance parameters of 1#–16# nozzles under different pressures.

Type	No.	Pressure (MPa)	Atomization angle (°)	Effective range (m)	Flow (L/min)	Type	No.	Pressure (MPa)	Atomization angle (°)	Effective range (m)	Flow (L/min)
A	1#	2	111.7	1.0	3.45	C	9#	2	97.8	2.1	3.41
		4	111.2	1.6	4.12			4	90.3	3.3	4.43
		6	110.8	2.4	5.13			6	83.1	3.7	5.49
		8	110.5	3.7	5.86			8	75.7	4.2	6.67
	2#	2	125.1	1.8	3.92		10#	2	96.5	2.5	4.63
		4	123.6	3.2	5.53			4	91.9	3.5	6.13
		6	122.0	3.7	7.13			6	85.3	4.2	7.31
		8	121.9	4.3	7.67			8	76.0	4.3	7.83
	3#	2	99.5	2.0	4.36		11#	2	80.1	2.3	3.67
		4	99.1	2.8	5.98			4	71.6	3.3	4.83
		6	99.0	3.5	7.16			6	71.0	4.1	5.89
		8	98.9	5.2	8.51			8	69.3	4.7	6.83
4#	2	67.7	3.2	4.07	D	12#	2	75.4	3.3	4.42	
	4	65.2	3.9	5.75			4	73.1	3.8	5.60	
	6	62.6	5.0	6.81			6	68.7	4.7	7.29	
	8	59.1	5.1	7.66			8	68.4	5.2	8.72	
B	5#	2	69.8	3.3	4.63	13#	2	71.7	3.3	6.20	
		4	59.3	4.3	6.13		4	66.6	4.3	8.19	
		6	56.2	4.8	7.72		6	65.5	5.1	10.27	
		8	55.5	5.2	9.13		8	61.8	6.1	11.71	
6#	2	72.1	3.5	6.86	14#	2	91.4	2.5	3.77		
	4	61.6	4.5	9.00		4	87.6	3.4	5.14		
	6	59.9	5.2	10.76		6	79.4	4.5	6.28		
	8	59.3	5.7	12.54		8	73.5	5.3	7.05		
7#	2	94.5	1.2	1.29	E	15#	2	80.6	3.8	7.39	
	4	84.5	1.7	1.57			4	67.6	4.6	10.23	
	6	82.9	2.3	2.14			6	65.2	4.9	12.38	
	8	75.8	2.7	2.63			8	62.5	6.5	14.76	
C	8#	2	90.0	1.2	2.29	16#	2	81.4	4.0	10.32	
		4	88.3	1.9	2.85		4	75.5	5.2	13.73	
		6	83.6	2.8	3.43		6	67.0	7.2	16.96	
		8	81.5	3.0	3.94		8	65.9	7.8	19.89	

were selected from 16 kinds of nozzles, including 2# and 3# nozzles in type A, 4# and 5# nozzles in type B, 9# nozzles in type C, 11# and 12# nozzles in type D, and 14# nozzles in type E nozzles. In order to be different from the number of nozzles in conventional parameter measurement, in the atomization characteristic test, according to the order of 8 kinds of nozzles in 16 kinds of nozzles, they are numbered as nozzle 1 to nozzle 8, respectively.

According to the experimental results of the nozzle jet characteristics (atomization characteristic parameter table of the experimental nozzle under different pressures can be seen in Tables 3–6), with the increase of spray pressure, the  $D_{0.1}$ ,  $D_{0.5}$ ,  $D_{0.9}$ ,  $D_{32}$ , and  $D_{43}$  particle sizes of 8 nozzles decreased. The smaller the nozzle droplet diameter, the better the atomizing effect of nozzles, and the stronger

the ability to capture respirable dust. Considering spray equipment can tolerate 8 MPa water pressure, the water pressure of 8 MPa is adopted, under which each nozzle droplet diameter can reach the minimum in experiment. In experiment, nozzle 8 has the best atomization effect. The percentage of respirable dust being captured of 8 nozzles under the water pressure of 8 MPa is shown in Table 7. The routine atomization parameters are summarized in Table 8.

4.2. *Spray Dust Fall Experiment.* To test the dust reduction effectiveness of nozzles, the spray dust fall experiment was done with the water pressure of 8 MPa and fan speed of 300r/min. The coal dust samples with different particle sizes were prepared. In the experiment, the particle size and

TABLE 3: Atomization characteristic parameter table of nozzles under 2 MPa pressure.

No.	$D_{0.1}$ ( $\mu\text{m}$ )	$D_{0.5}$ ( $\mu\text{m}$ )	$D_{0.9}$ ( $\mu\text{m}$ )	$D_{32}$ ( $\mu\text{m}$ )	$D_{43}$ ( $\mu\text{m}$ )
1	28.833	65.546	113.142	53.363	68.985
2	25.716	54.966	86.534	45.485	56.285
3	48.874	86.483	132.942	75.410	89.000
4	51.577	93.528	145.390	80.718	96.097
5	33.047	73.819	127.594	58.829	78.308
6	24.844	53.743	85.320	44.235	55.053
7	26.609	55.939	87.507	46.458	57.278
8	23.917	53.212	84.784	43.759	54.539

TABLE 4: Atomization characteristic parameter table of nozzles under 4 MPa pressure.

No.	$D_{0.1}$ ( $\mu\text{m}$ )	$D_{0.5}$ ( $\mu\text{m}$ )	$D_{0.9}$ ( $\mu\text{m}$ )	$D_{32}$ ( $\mu\text{m}$ )	$D_{43}$ ( $\mu\text{m}$ )
1	23.658	53.669	90.793	43.633	56.344
2	24.066	50.636	82.936	42.703	52.668
3	42.843	77.647	124.600	66.840	80.353
4	51.627	86.723	135.630	72.746	89.276
5	25.109	54.049	87.664	44.546	55.444
6	22.426	49.404	81.704	41.471	51.436
7	24.645	51.669	83.909	43.986	53.651
8	21.902	48.869	81.159	40.957	50.942

TABLE 5: Atomization characteristic parameter table of nozzles under 6 MPa pressure.

No.	$D_{0.1}$ ( $\mu\text{m}$ )	$D_{0.5}$ ( $\mu\text{m}$ )	$D_{0.9}$ ( $\mu\text{m}$ )	$D_{32}$ ( $\mu\text{m}$ )	$D_{43}$ ( $\mu\text{m}$ )
1	21.034	46.394	75.532	37.782	47.737
2	22.108	45.713	74.358	36.810	47.160
3	39.360	69.499	107.095	59.635	72.266
4	41.084	70.803	114.184	62.172	74.025
5	23.118	47.626	81.559	40.272	50.267
6	20.532	44.457	70.674	36.978	45.721
7	21.660	47.451	73.998	37.042	47.054
8	20.015	43.935	70.274	36.656	45.139

TABLE 6: Atomization characteristic parameter table of nozzles under 8 MPa pressure.

No.	$D_{0.1}$ ( $\mu\text{m}$ )	$D_{0.5}$ ( $\mu\text{m}$ )	$D_{0.9}$ ( $\mu\text{m}$ )	$D_{32}$ ( $\mu\text{m}$ )	$D_{43}$ ( $\mu\text{m}$ )
1	19.621	41.353	72.306	34.982	44.372
2	19.672	40.022	65.718	34.770	41.933
3	33.075	63.474	105.248	55.575	71.094
4	35.159	62.507	97.962	54.554	63.796
5	22.597	45.320	75.432	38.846	47.944
6	18.804	39.043	62.833	34.393	41.644
7	20.586	40.581	64.996	35.781	42.892
8	18.342	38.541	62.321	33.951	41.162

distribution of coal dust were analyzed by using Doppler laser interferometer (PDI200MD), and the dust concentration was measured by AKFC-92A dust sampler. And 8 kinds of nozzle spray dust fall efficiency are shown in Table 9.

### 4.3. Research on Spray Dust Fall Devices of Negative Pressure

#### 4.3.1. Theory of Spray Dust Fall with Negative Pressure

(1) *Water Mist Piston Mechanism.* When the nozzle is sprayed outwards, the water mist is formed when the diffusing diameter of the water mist is equal to or larger than the inner diameter of the nozzle. The air inside the nozzle is pushed out by the water mist, and then, the vacuum is formed, thus forming negative pressure. Under the negative pressure, the dust laden airflow can enter the nozzle of the spray device through the suction part.

In the nozzle, the dust in the dusty air flow is repeatedly impacted by the water mist, combined with the water mist, ejected from the pipe, and settles due to the loss of suspension capacity in the air. At the same time, the mixture composed of purified air and water mist continues to be ejected at high speed by the nozzle, forming a negative pressure field at the ejection end, sucking the surrounding dusty air flow into the jet, so that the dust in the air flow can be further washed.

(2) *Entrainment Mechanism of Water Jet.* When the high-speed fog and air flow are ejected, there is a discontinuity with the air flow in the workface. Due to the inevitable interference, the discontinuity loses its stability and generates a vortex. The vortex sucks the surrounding dusty gas into the jet, continuously moves, deforms, and splits to produce turbulence. Its influence gradually develops to the inner and outer sides, forming two free turbulent mixing layers inside and outside. Due to the transverse transmission of momentum, the entrained dusty gas obtains momentum flows forward with the originally emitted fog and air flow, so that the dust in the air flow can collide with the droplets to achieve the purpose of dust reduction. At the same time, the atomized droplets in the jet lose momentum, reduce the velocity, form a certain velocity gradient in the mixing layer, and appear as shear stress. As a result of entrainment and mixing, the jet section expands continuously, while the flow velocity decreases continuously.

4.3.2. *Spray Dust Fall Device of Negative Pressure in Coal Mining Operation.* Combining dust migration rules in coal mining operation and characteristics of nozzles, the spray dust fall device of negative pressures in coal mining operation have been researched, which are shown in Figures 8(a) and 8(b).

The dust control device of negative pressure for coal mining operation is shown in Figure 8(a). It is composed of 4 nozzles and 16 suction ports distributed on the side part. The device is mainly used for reducing the dust generated at the drum and moving along the transverse section of the fully mechanized top coal caving face. The layout of the three spray dust fall devices in coal mining operations is

TABLE 7: The percentage of respirable dust being captured of 8 nozzles under the water pressure of 8 MPa.

Nozzle parameter	1	2	3	4	5	6	7	8
Percentage (%)	84.51	90.73	62.95	62.02	77.11	91.13	86.44	91.36

TABLE 8: The routine atomization parameters of 8 nozzles under the water pressure of 8 MPa.

Nozzle Parameter	1	2	3	4	5	6	7	8
Spray angle (°)	121.8	98.9	59.1	55.5	75.8	69.2	68.3	73.6
Effective range (m)	4.4	5.3	5.2	5.3	4.3	4.7	5.2	5.3
Flow (L/min)	7.66	8.50	7.66	9.12	6.67	6.86	8.75	7.07

TABLE 9: The spray dust removal efficiency with the pressure of 8 MPa and fan rotate speed of 300 r/min.

Nozzle number	Dust removal rate (%)	
	Total dust	Respirable dust
Nozzle 1	42.71	35.87
Nozzle 2	39.21	32.39
Nozzle 3	50.37	46.61
Nozzle 4	47.32	41.71
Nozzle 5	56.30	51.21
Nozzle 6	63.56	59.78
Nozzle 7	60.72	56.17
Nozzle 8	65.82	61.70

shown in Figure 8(b). They are located on the upper, middle, and bottom of the shearer arm.

In order to control the dust concentration effectively, the type of nozzles should be chosen on the basis of the dust migration rule and the characteristics of nozzles. From Figures 3 and 4, in the process of coal mining, under the action of gravity, wind flow, and collision between dusts, it not only exists the transverse diffusion in the workplace but also the longitudinal diffusion to the outlet under the action of wind flow. It is mainly vertical diffusion, and the transverse diffusion range is limited. In the experiments on characteristics of nozzles and spray dust fall, three kinds of nozzles are optimized. Nozzle 5 has a small flow, large atomization angle, and small range. The atomization angles of nozzle 6 and nozzle 8 are less than nozzle 5, and the range and flow are greater than nozzle 5.

The concentration of the dust near the shearer drum is larger, and the granularity is larger. The spray direction of the nozzles located on the upper and bottom of the shearer arm points to the direction of the coal seam. Combining the dust migration rule with the characteristics of nozzles, the nozzle types in the upper dust fall device are nozzle 8, nozzle 8, nozzle 5 and nozzle 5, respectively, and in the bottom part, the nozzle types from left to right are nozzle 5, nozzle 5, nozzle 5 and nozzle 5. The spray direction of the nozzles located on the middle of the shearer arm is adjusted to the direction of the air flow, and the nozzle type is all selected by nozzle 8.

4.3.3. *Spray Dust Fall Device of Negative Pressure in Shifting Operation.* Combining dust migration rules in shifting operation and characteristics of nozzles, the spray dust fall device of negative pressures in shifting operation have been researched, which are shown in Figure 9.

From Figures 5 and 6, in the process of shifting operation, under the action of gravity, air flow, and dust collision, there is not only the transverse diffusion of workplace section but also the longitudinal diffusion to the outlet end under the action of air flow. The trend of diffusion to the rear of the support is greater than that to the coal wall, and respiratory dust accounts for a certain proportion.

The device is mainly composed of two side suction ports (A), one rear suction port (B), and five nozzles (three in the front and one on each side). The three front nozzles (D) are nozzle 5, nozzle 6, and nozzle 5 from top to bottom, and nozzle 6 is selected for side nozzle (C).

After spraying, 3 nozzles at the front and 2 nozzles on the side (1 nozzles on each side) are sprayed to form a fog field, so that the inhaled dust can be fully mixed, coagulated, and settled at the location of the spray port with the fog field. After the nozzle is sprayed, the ejector airflow will be generated, so that the dust will be inhaled from the side suction port and the rear dust collection port. The side dust suction port is rectangular, which is mainly used to inhale the dust generated during frame moving. The rear dust suction port is bell shaped, which can not only absorb the dust generated by the moving frame but also the dust transported to the sidewalk of the hydraulic support.

#### 4.3.4. Application Effect

(1) *Analysis on Dust Reduction Effect of Coal Mining Operation.* The field application effect of the dust fall device with negative pressure in coal mining operation is shown in Figure 10. Dust concentration before and after opening of devices and dust fall rate are shown in Table 10.

(2) *Dust Reduction Effect Analysis of Moving Frame Operation.* The field application effect of the two negative dust fall devices with negative pressure for shifting operation is shown in Figure 11. Dust concentration before and after opening of devices and dust fall rate are shown in Table 11.



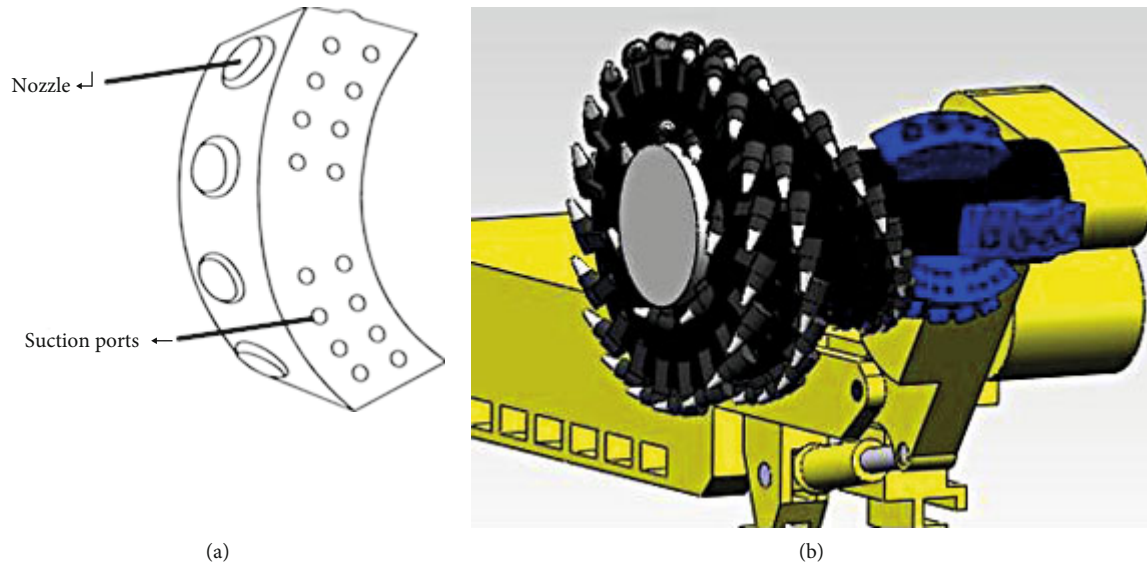
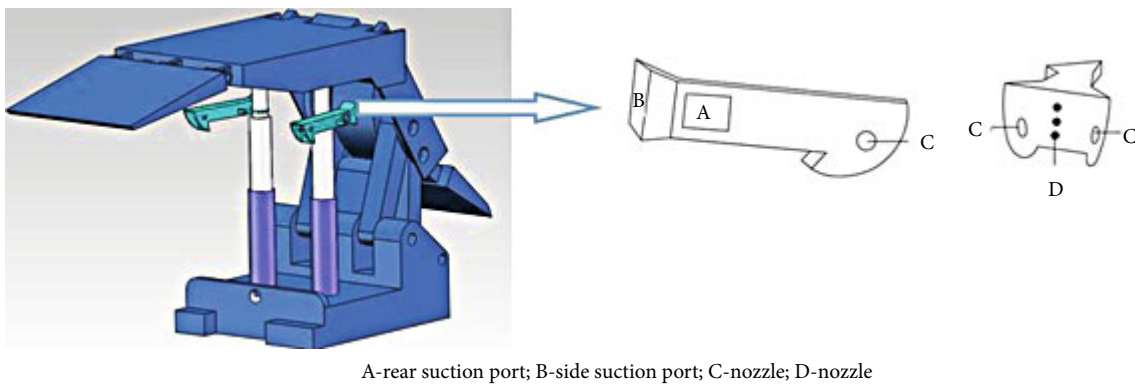


FIGURE 8: Two times dust suppression device for negative pressure in coal mining operation.



A-rear suction port; B-side suction port; C-nozzle; D-nozzle

FIGURE 9: Two times dust suppression device for spraying negative pressure in shifting operation.

## 5. Analysis and Discussion

**5.1. Dust Concentration Changing Regularities in Coal Mining Operation.** It can be seen from Figure 3 that due to the limited trend of dust horizontal diffusion, the maximum dust concentration values on the sections 0.2 m, 0.4 m, and 0.6 m away from the coal wall gradually decrease. Due to the effect of ventilation velocity, the maximum dust concentration at the rear drum is greater than that at the front drum. It can be seen from Figure 4 that the dust concentration in the  $x$ -axis direction starts to increase under the leading role of inertia at the initial moment and then gradually decreases under the action of ventilation. At the height of 1.5 m away from the ground and at the distance of 0.2 m, 0.4 m, and 0.6 m away from the coal wall, the maximum dust concentration value first increases and then decreases, and the dust concentration reaches the maximum at 0.4 m away from the coal wall.

**5.2. Dust Concentration Changing Regularities in Support Shifting Operation.** It can be seen from Figure 5 that the dust

generated by the support shifting in the fully mechanized mining face diffuses from the dust source to both sides of the support along the  $z$ -axis direction, reaches the maximum concentration near the dust source, and decreases greatly along both sides of the support. The maximum dust concentration at 1 m away from the coal wall is the largest, the maximum dust concentration at the distance of 0.7 m, 1.5 m, and 2 m away from the coal wall is reduced, and the dust concentration at 5 m away from the coal wall is very small.

It can be seen from Figure 6 that the maximum dust concentration at the distance of 0.2 m, 0.7 m, 1 m, 1.5 m, and 2 m away from the coal wall and at the height of 1.5 m above the ground is different. The dust concentration is the lowest at 0.2 m away from the coal wall, increases at the position 0.7 m away from the coal wall, reaches the maximum value at 1.0 m away from the coal wall, and gradually decreases at the position 1.5 m and 2.0 m away. It also can be seen from Figure 6 that the dust concentration starts to produce dust at about  $z = 3$ , and then, the variation range of dust concentration along the wind direction is not very large at the distance of 0.7 m, 1.5 m, and 2 m away from the coal wall.



FIGURE 10: Field application diagram of negative dust collecting device in coal mining operation.

TABLE 10: Dust concentration before and after opening of devices and dust fall rate.

No.	Dustiness	Total dust concentration (mg/m <sup>3</sup> )		Exhaled dust concentration (mg/m <sup>3</sup> )		Total dust fall rate	Exhalation rate
		Before opening	After	Before opening	After		
1#	Coal	500	53.1	350	92.7	0.89	0.73
2#	Coal	1100	90.3	500	100.8	0.91	0.79
3#	Coal	1300	113.6	700	140	0.91	0.80
4#	Coal	900	98.7	600	178.2	0.89	0.70
5#	Coal	800	76.2	400	159	0.90	0.60
6#	Coal	400	59.6	200	63.2	0.85	0.68
7#	Coal	220	32.6	100	39.8	0.85	0.60

The dust concentration at 1 m away from the coal wall begins to increase significantly and then changes little. However, the dust concentration at 0.2 m away from the coal wall gradually increases, but the overall concentration is not large. It can be seen that the dust concentration is high near the dust source; the dust not only diffuses to the outlet but also diffuses to the coal wall in the turbulent area.

### 5.3. Experiment on Atomization Characteristics of Nozzles.

From Table 2, it is can be seen that with the increase of spray pressure, the atomization parameters of nozzles decrease, and the atomization effect is improved in different degrees. Because the mist flow shape of nozzle 2 and nozzle 1 is a sector and the area is small, the dust removal effect is relatively poor in the fully mechanized mining face. Therefore in 8 MPa pressure the atomization effect of nozzle 3-nozzle 8 was studied, which is shown in Tables 7 and 8. According to the droplet particle size data such as  $D_{0.1}$ ,  $D_{0.5}$ ,  $D_{0.9}$ ,  $D_{32}$ ,  $D_{43}$ , and best dust collected particle size of respirable dust,

nozzle 3-nozzle 8 are divided into three categories based on the atomization effect. Nozzle 6 and nozzle 8 belong to the first class and have the best atomizing effect. Nozzle 8's atomization quality indexes have the better comprehensive effect, and the percentage of respirable dust being captured was more than 91%. The atomizing angle of nozzle 8 is greater than that of nozzle. The nozzle range is greater, and the flow is slightly larger. Nozzle 5 and nozzle 7 are the second class and have the second atomization effect. The atomizing angle of nozzle 5 is 75.8 degrees and has the maximum atomizing angle in 8 nozzles. Nozzle 5 has the minimum range of 4.3 m and the smallest flow of 6.67 L/min. But, the percentage of respirable dust being captured is 77.11% and is smaller than that of nozzle 6 and nozzle 8. The nozzle 3 and nozzle 4 are the third kinds of nozzles, and the atomizing effect is the worst.

5.4. Spray Dust Fall Experiment. From Table 9 it is can be seen that the ranking of dust removal is: nozzle 8 > nozzle



FIGURE 11: Field application diagram of dust collecting device in support shifting operation.

TABLE 11: Dust concentration and dust fall rate before and after opening of devices.

No.	Dustiness	Total dust concentration (mg/m <sup>3</sup> )		Exhaled dust concentration (mg/m <sup>3</sup> )		Total dust fall rate	Exhalation rate
		Before opening	After	Before opening	After		
1#	Coal	360	22.8	160	35.6	0.93	0.77
2#	Coal	500	30.1	200	60.1	0.93	0.70
3#	Coal	480	32.8	210	51.3	0.93	0.75
4#	Coal	400	38.7	190	44.3	0.90	0.76
5#	Coal	320	20.1	180	36.8	0.93	0.79
6#	Coal	200	19.7	130	26.9	0.90	0.79
7#	Coal	130	12.1	80	17.6	0.91	0.78

6 > nozzle 7 > nozzle 5 nozzle 3 > nozzle 4. The total dust and respirable dust reduction rate of nozzle 8 reached 65.82% and 61.70%, respectively, those of nozzle 6 reached 63.56% and 59.78%, respectively, and those of nozzle 5 reached 56.30% and 51.21%, respectively, which are lower than those of nozzle 6 and nozzle 8. Therefore, considering the comprehensive atomization characteristics and spray dust reduction experimental results, as the flow of nozzle 5 is small and the atomizing angle is big, nozzle 5 is suitable when the range is not big and the respirable dust content is small. When the respirable dust content is larger, nozzle 6 and nozzle 8 can be selected. When the desired range is larger than 5 m, nozzle 8 can be selected; otherwise, nozzle 6 can be selected.

*5.5. Analysis and Discussion of Spray Dust Fall Effect.* From Table 10 and Figure 10, it is known that in 3<sup>top1110</sup> coal mining face, the total dust concentration and exhaled dust concentration reached the highest value of 1300 mg/m<sup>3</sup> and 700 mg/m<sup>3</sup>, respectively, when the negative pressure dust removal device is not opened. The total dust fall rate was 85% to 91%, and the exhaled dust fall rate was 60% to 80% before and after using the negative dust removal device. The dust concentration in the work face decreased significantly.

From Table 11 and Figure 11, it is known that in 3<sup>top1110</sup> coal mining face shifting work the highest value of total dust concentration and exhaled dust concentration reached

500 mg/m<sup>3</sup> and 200 mg/m<sup>3</sup>, respectively, when the negative pressure two times dust removal device is not opened. The total dust fall rate was 90% to 93%, and the exhaled dust fall rate was 70% to 79% before and after using the negative dust removal device. The dust concentration in the work face decreased significantly.

## 6. Conclusions

- (1) The mechanism of dust generation and migration rules in fully mechanized mining face are analyzed. Based on the characteristics of turbulent flow viscous bottom layer and the relevant data of Nicholas experiment, the ventilation velocity distribution formula of the viscous bottom part at the entrance section of fully mechanized mining face is derived:  $v_x = \bar{v} \sqrt{2(1 - r/r_0)}$
- (2) The user-defined function of entrance section velocity of the 3<sup>top1110</sup> fully mechanized coal mining face of Gao Zhuang Coal Mine is compiled by using C language and is set as the boundary condition of entrance speed in FLUENT software. FLUENT software is used to simulate the dust migration law of coal mining and support shifting operations under different conditions
- (3) Based on the experiment of spray and dust fall of nozzles in the 3<sup>top1110</sup> fully mechanized coal mining face of Gao Zhuang Coal Mine, 3 kinds of nozzles with better dust reduction effect were selected. Among them, nozzle 5 had a smaller flow rate and larger atomization angle and had little requirement for range. Nozzle 5 could be selected for the smaller respirable dust content. For the larger respirable dust content, nozzle 6 and nozzle 8 could be selected. When the range requirement was greater than 5 m, choose nozzle 8; otherwise, choose nozzle 6
- (4) According to the law of dust movement in the 3<sup>top1110</sup> fully mechanized mining face and the characteristics of nozzles, two spray dust reduction devices of negative pressure in the fully mechanized mining face of Gao Zhuang Coal Mine were studied. By using the negative pressure dust fall device, in the coal mining operation, the total dust fall rate was 85% to 91% and the exhaled dust fall rate was 60% to 80%. And in the support shifting operation, the total dust fall rate was 90% to 93% and the exhaled dust fall rate was 70% to 79%.

## Data Availability

The raw/processed data required to reproduce these findings cannot be shared at this time as the data also forms part of an ongoing study.

## Conflicts of Interest

The authors declare that they have no conflicts of interest.

## Acknowledgments

The authors thank the help of Professor Gang Zhou and Professor Wen Nie in the experiment of spray dust fall. The research was sponsored by the Key research and development plan of Shandong Province (Project No. 2017GSF220016).

## References

- [1] H. M. Yu, W. M. Cheng, L. R. Wu, H. Wang, and Y. Xie, "Mechanisms of dust diffuse pollution under forced-exhaust ventilation in fully-mechanized excavation faces by CFD-DEM," *Powder Technology*, vol. 317, pp. 31–47, 2017.
- [2] G. B. Zhang, B. Sun, S. Z. Song, H. Wang, and G. Zhou, "CFD comparative analysis on the pollution characteristics of coal dust under turbulent airflow from coal cutting in the fully mechanized mining face," *Process Safety and Environmental Protection*, vol. 146, pp. 515–530, 2021.
- [3] Y. S. Lai, *Study on dust distribution law and computer simulation of fully mechanized working face*, China University of mining and technology, 1995.
- [4] S. Nakayama, K. Uchino, and M. Inoue, "Three dimensional flow measurement at heading face and application of CFD," *Shigen-To-Sozai*, vol. 112, pp. 639–644, 1996.
- [5] N. A. Patankar and D. D. Joseph, "Modeling and numerical simulation of particulate flows by the Eulerian- Lagrangian approach," *International Journal of Multiphase Flow*, vol. 27, no. 10, pp. 1659–1684, 2001.
- [6] M. Z. Yu, H. H. Jin, L. H. Chen, J. H. Fan, and K. F. Cen, "Cen. large eddy simulation study on the movement and diffusion characteristics of dust particles," *Journal of Environmental Science*, vol. 25, pp. 891–895, 2005.
- [7] C. Housiadas, Y. Drossinos, and M. Lazaridis, "Effect of small-scale turbulent fluctuations on rates of particle formation," *Journal of Aerosol Science*, vol. 35, no. 5, pp. 545–559, 2004.
- [8] X. Z. Wang, Z. A. Jiang, S. Wang, and Y. Liu, "Numerical simulation of dust concentration distribution in coal roadway driving process," *Journal of China Coal Society*, vol. 32, pp. 386–390, 2007.
- [9] Y. Liu, Z. A. Jiang, W. Cai, F. Z. Zhou, D. Guo, and B. D. Liu, "Numerical simulation of the dust movement rule in fully-mechanized coal faces," *Journal of University of Science and Technology Beijing*, vol. 29, pp. 351–353, 2007.
- [10] W. Niu, Z. A. Jiang, and Y. Liu, "Numerical simulation on dust movement regularities at fully-mechanized coal faces and its utilization," *Journal of Liaoning Technical University, Natural Science*, vol. 29, pp. 357–360, 2010.
- [11] Z. Gang, *Research of theory about dust prevention by water-cloud and relevant techniques for fully-mechanized caving coal face*, Shandong University of Science and Technology, 2009.
- [12] G. Zhou, W. M. Cheng, L. J. Chen, and W. Nie, "Numerical simulation and application of dust concentration spatial distribution in fully mechanized top coal caving face," *Journal of China Coal Society*, vol. 35, pp. 2094–2099, 2010.
- [13] L. R. Wu, *Study on dust movement rule of fully mechanized top coal caving working face and two times dust suppression device with spray negative pressure*, Beijing University of science and technology, 2014.
- [14] B. Sun, W. M. Cheng, H. Wang, and J. Y. Wang, "Influence of rotary flow wind of drum in fully mechanized mining face on

- lateral dispersion law of coal dust in cutting,” *Journal of China Coal Society*, vol. 8, pp. 2269–2279, 2018.
- [15] X. W. Yao, G. L. Lu, and K. L. Xu, “Numerical simulation of dust generation at different procedures in steeply inclined fully-mechanized caving face,” *Journal of China Coal Society*, vol. 40, pp. 389–396, 2015.
- [16] T. Ren, Z. Wang, and J. Zhang, “Improved dust management at a longwall top coal caving (LTCC) face - A CFD modelling approach,” *Advanced Powder Technology*, vol. 29, no. 10, pp. 2368–2379, 2018.
- [17] C. Hankwon, P. H. Jin, and D. J. Hee, “Flame synthesis of silica nanoparticles by adopting two-fluid nozzle spray,” *Colloids and Surfaces A: Physicochemical and Engineering Aspects*, vol. 1, pp. 140–144, 2008.
- [18] N. I. Jayaraman and R. A. Jankowski, “Atomization of water sprays for quartz dust control,” *Applied Industrial Hygiene*, vol. 3, no. 12, pp. 327–331, 1988.
- [19] L. J. Goldbeck and A. D. Marti, “Dust control at conveyor transfer points: containment, suppression and collection,” *Bulk Solids Handling*, vol. 16, pp. 367–372, 1996.
- [20] W. M. Cheng, W. Nie, G. Zhou, and Q. M. Zuo, “Study on dust reduction performance of high pressure spray atomization particle size in coal mine,” *Journal of China University of Mining and Technology*, vol. 40, pp. 185–189, 2011.
- [21] Z. C. Liu, “Theoretical analysis and experimental study on fire extinguishing of straight through swirl water mist nozzle,” *Sichuan, Southwest Jiaotong University*, 2008.
- [22] X. Q. Wang, J. Qin, and Z. W. Xie, “Application of three dimensional LDV/APV system in measurement of characteristic parameters of dust nozzle,” *Journal of China Coal Society*, vol. 35, pp. 269–272, 2010.
- [23] G. Zhou, W. Nie, and W. M. Cheng, “Analysis of influence of high pressure atomization dust suppression on micro parameters of dust particles in fully mechanized top coal caving face,” *Journal of China Coal Society*, vol. 39, pp. 2053–2059, 2014.
- [24] H. T. Peng, W. Nie, H. M. Yu et al., “Research on mine dust suppression by spraying: development of an air-assisted PM10 control device based on CFD technology,” *Advanced Powder Technology*, vol. 30, no. 11, pp. 2588–2599, 2019.
- [25] P. F. Wang, R. H. Liu, M. Tang, W. Zhang, and Z. Gui, “Experimental study on atomization characteristics and dust suppression efficiency of high-pressure spray in underground coal mine,” *Journal of China Coal Society*, vol. 40, pp. 2124–2130, 2015.
- [26] P. F. Wang, H. Han, C. Tian, R. Liu, and Y. Jiang, “Experimental study on dust reduction via spraying using surfactant solution,” *Atmospheric Pollution Research*, vol. 11, no. 6, pp. 32–42, 2020.
- [27] Y. Yu, “Investigations into roadway air velocity distribution,” *Journal of Huainan Mining Institute*, vol. 1, pp. 17–24, 1989.

## Research Article

# Accumulation and Distribution of Natural Gas Reservoir in Volcanic Active Area: A Case Study of the Cretaceous Yingcheng Formation in the Dehui Fault Depression, Songliao Basin, NE China

Fancheng Zeng,<sup>1,2</sup> Bo Liu ,<sup>1,3</sup> Changmin Zhang,<sup>1</sup> Guoyi Zhang,<sup>2</sup> Jin Gao,<sup>2</sup> Junjie Liu,<sup>3</sup> and Mehdi Ostadhassan<sup>3</sup>

<sup>1</sup>Yangtze University, Wuhan, Hubei Province 434100, China

<sup>2</sup>Company of Jilin Oilfield, Songyuan, Jilin Province 138000, China

<sup>3</sup>Northeast Petroleum University, Daqing, Heilongjiang Province 163318, China

Correspondence should be addressed to Bo Liu; [liubo6869@163.com](mailto:liubo6869@163.com)

Received 16 July 2021; Accepted 4 September 2021; Published 30 September 2021

Academic Editor: Chenhao Sun

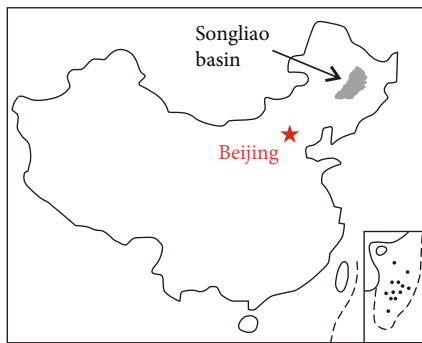
Copyright © 2021 Fancheng Zeng et al. This is an open access article distributed under the Creative Commons Attribution License, which permits unrestricted use, distribution, and reproduction in any medium, provided the original work is properly cited.

Tight gas sandstone and volcanic gas reservoirs have received global attention in the energy arena for further exploration and exploitation attempts. Considering the Yingcheng Formation of Dehui fault depression in the Songliao Basin as an example, this study focused on the accumulation and distribution of natural gas reservoirs in volcanic area in a fault depression basin. Volcanic activities occurred in the Yingcheng Formation, which is distributed centrally in the northwest of the study area. During the sedimentation of the Yingcheng Formation, fan-delta, lacustrine, and nearshore subaqueous fan facies were deposited. The source rocks of the Yingcheng Formation have high abundance of organic matter mainly in type III at high-overmature stages, indicating favorable conditions for gas production. The porosity of volcanic reservoir is 3.0%-14.8%, the permeability is 0.0004 mD-2.52 mD, and the pore types are mainly secondary dissolved pores and fractures. Besides, the porosity of the tight sandstone reservoir is 0.5%-11.2%, and the permeability is 0.0008 mD-3.17 mD. The pore types are mainly interparticle pores, with a small proportion of intraparticle pores and microfractures. The intrusion of late volcanic magma provided sufficient heat for the thermal maturity progression of organic matter in Yingcheng Formation and promoted the generation of natural gas in large quantities. Volcanic rocks formed at the early and middle stages of volcanic activities occupied the sedimentary space and hindered the development of sedimentary sand bodies to a certain extent. However, volcanic rocks can become the seal to promote the formation of tight sandstone gas traps. Comparing tight sandstone reservoirs with volcanic ones, the latter are less affected by compaction; thus, their petrophysical properties do not vary much with depth, showing more homogeneous characteristics. The pyroclastic rocks influenced by volcanic activity and the secondary pores formed by dissolution in the later stages also provide reservoir space for gas accumulation. Ultimately, the tight sandstone and volcanic rocks in the study area form a complex gas reservoir system, which can become a reference for exploration and exploitation of natural gas in other petroliferous fault depressions that are affected by volcanisms.

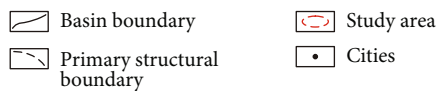
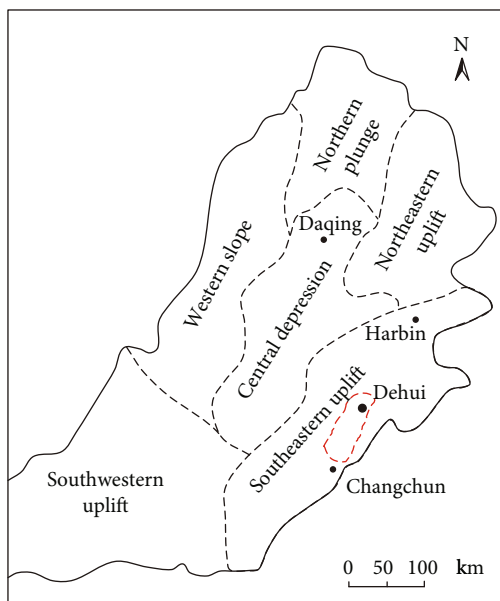
## 1. Introduction

IEA [1] estimates that global tight gas sandstone resources are roughly  $209.6 \times 10^{12} \text{ m}^3$ . Additionally, exploration and development of tight gas sandstone reservoirs has supported the driving force for increasing global natural gas production

in recent years [2]. In China, huge tight sandstone gas reservoirs exist in major oil-bearing basins, including the Tarim, Ordos, and Songliao Basins [3, 4]. As of 2016, gas production from tight sandstone reservoirs has reached  $330 \times 10^8 \text{ m}^3$ , accounting for one-quarter of China's annual natural gas production [3]. In this regard, volcanic gas reservoirs have also

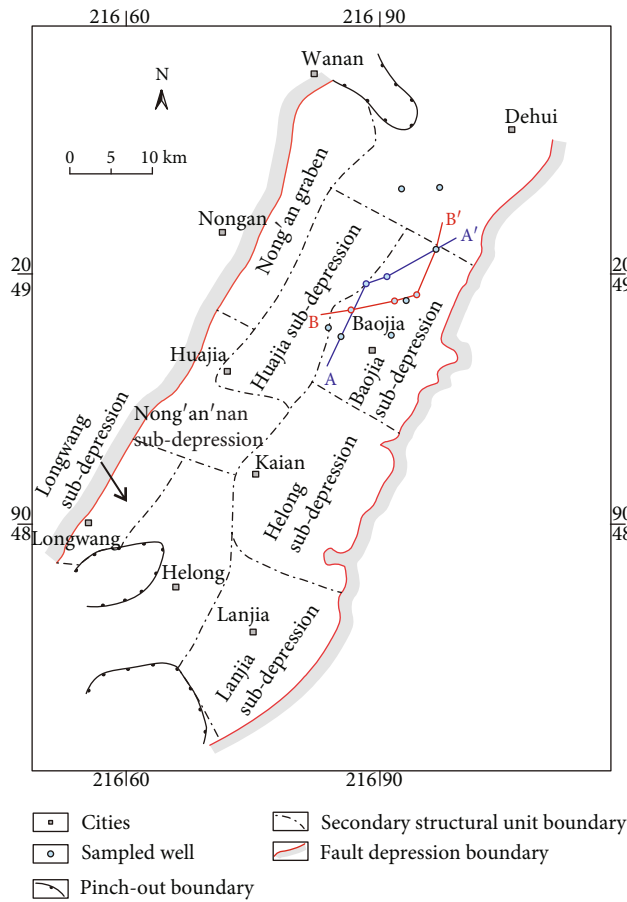


(a)

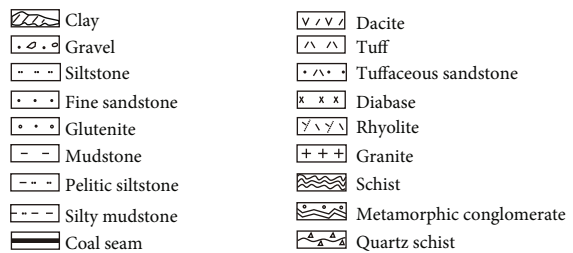
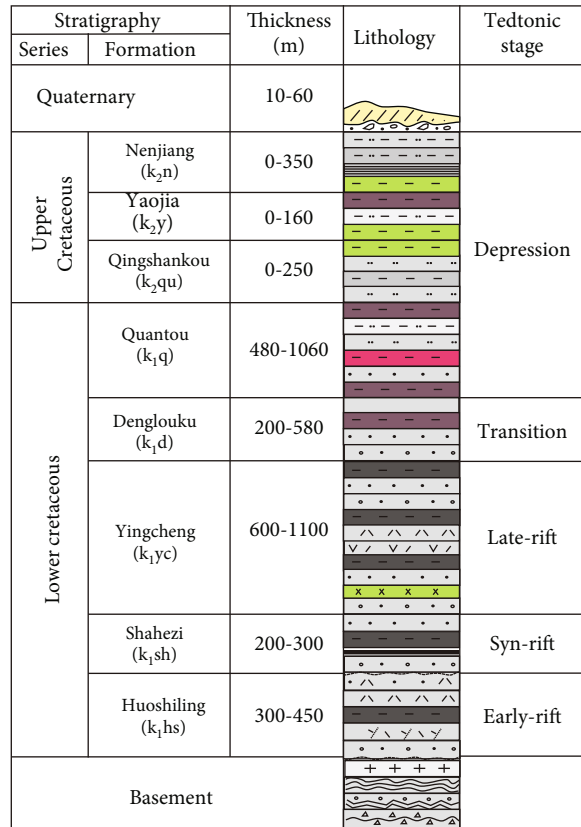


(b)

FIGURE 1: Continued.



(c)



(d)

FIGURE 1: (a) Geographic location of the Songliao Basin. (b) Location of Dehui Depression in the Southern Songliao Basin. (c) Tectonic units of the Dehui Depression. (d) Generalized Mesozoic-Cenozoic stratigraphy of the Dehui depression, showing the formation thickness, lithology, and stage of tectonic evaluation.

been found sporadically where tight sandstone gas reservoirs are abundant, such as the Lower Cretaceous in the Songliao Basin, the Jurassic in the Hailaer Basin, and the Upper Paleozoic of the Ordos Basin. The tight gas sandstone reservoirs and volcanic gas reservoirs in the volcanically active areas together constitute a complex gas accumulation system which requires further investigation [5–8].

In basins located on the eastern China, volcano-sedimentary sequences have been widely developed since the Late Mesozoic [7]. During volcanism, a large number of igneous formations were formed, accompanied by various clastic deposits from igneous materials and volcanic lacustrine deposits during the intercalation period, forming an interactive sedimentary sequence [9]. In addition to the creation of these volcanic reservoirs, volcanic activity also has had an impact on the accumulation of natural gas in tight sandstones regionally [10]. Moreover, the influence of volca-

nisms on the basin sedimentation manifests itself in the following ways: first, volcanic activity can be used as a regional provenance, providing supply for the basin sedimentation [11, 12]. However, such volcanic activities in the island arc belt not only would change the composition of the supply in the sedimentary system but also play a role in blocking the distribution of the sedimentary system, alter topography, promote the formation or migration of the basin depocenter, develop around it, and thus form a new sedimentary system. Secondly, volcanic activity is also an important event that impacts the basin accommodation. Due to rapid accumulation of volcanic eruptions in some areas, the basin is affected by the thermal subsidence, and somehow, this was accelerated regionally, causing the total water volume to decrease. Conversely, in other areas of the depression, the influence of volcanic activities has been weak; therefore, the change of accommodative space is not significant [13]. This means



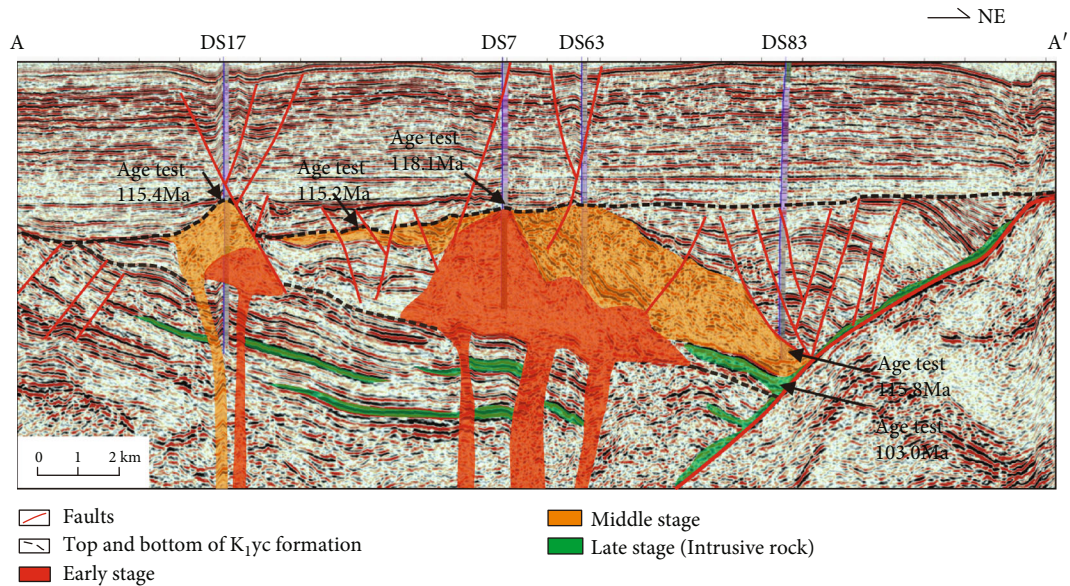


FIGURE 2: The seismic profile shows the volcanic activity of the  $K_{1yc}$  in the Dehui Depression; location of the profile is shown in Figure 1 (modified from [28]).

the overall accommodative space for sediment load varies regionally throughout the basin. In addition, volcanic activities are often accompanied by large-scale hydrothermal events where high temperature as well as high pressure hydrothermal flux upwashes and enters the strata. As a result, this hydrothermal fluid contains rich soluble ions and will have persistent effects of detrital (mineral), which makes its diagenetic intensity to be strong [14]. In addition to the impact of volcanic activities that explained how would influence sedimentation in the basin, syndepositional volcanism controls the development of reservoirs mainly by providing soluble components and promoting the formation of fractures [15]. This has happened via the dissolution of chemically unstable soluble pyroclastic components that were preserved in the adjacent sedimentary sand bodies within the pores during the middle to late burial stages. Furthermore, during the periods of volcanic activity, the influx of a large amount of magma flew into the sedimentary sequence that resulted in the brittle rupture of consolidated sandstone to form microfractures, which increased the reservoir space and permeability of the reservoir [16, 17].

In such events, volcanic ash would be beneficial to the enrichment and preservation of organic matter [18, 19] and promotes the conversion of organic matter to hydrocarbons [20–22]. These were some positive impacts of volcanic activities on various components of the petroleum system; however, its destructive effects on hydrocarbon accumulation cannot be neglected either. For example, volcanic activities can disrupt oil and gas accumulation significantly by creating channels or associated faults to damage the integrity of the trap and creating seepages for the accumulated hydrocarbons to escape the reservoir [17]. In addition, the heat source provided by volcanic activity also causes dehydration of minerals containing crystalline water in the adjacent sediments to recrystallize, which would fill the pores and fractures, reducing connectivity and deteriorating reservoir petrophysical properties.

Songliao Basin is a large petroliferous basin developed on the basement of the Upper Paleozoic metamorphic rock series. During the rift period, there were intense tectonic movements and frequent volcanic activities. However, the combination of volcanism and sedimentation created good conditions for the formation of oil and gas reservoirs [23, 24]. In recent years, several large tight natural gas reservoirs have been discovered in the Songliao Basin [25], while some are associated with the volcanic rocks of the basin [6, 26, 27]. In the Dehui fault depression that is the subject of this study, both major tight sandstone and volcanic gas reservoirs are found in the Cretaceous strata, with great potential for resources and are good exploration prospects.

In this study, tight gas sandstone and volcanic gas reservoir influenced by the volcanic activity of the Yingcheng Formation in the Dehui fault depression of the southern Songliao Basin has been assessed. By systematically sampling the source rocks, volcanic rocks, and tight sandstones in the study area and analyzing and examining them for total organic carbon (TOC) content, vitrinite reflectance ( $R_o$ ), and reservoir physical property (porosity and permeability), the geochemical characteristics of the source rocks and the petrophysical properties of the reservoir rock including the volcanic and tight sandstone are understood. The goal of this study is to analyze the effects of volcanic activity in the area on the accumulation of natural gas. Furthermore, we comprehensively investigated the complexity of the petroleum system that is formed in the volcano-sedimentary sequence, to provide reference for the exploration and prospect evaluation in this petroliferous basin for future developments.

## 2. Geologic Setting

**2.1. Location and Stratigraphy.** The Dehui fault depression is located in the southeast uplift of the Songliao Basin

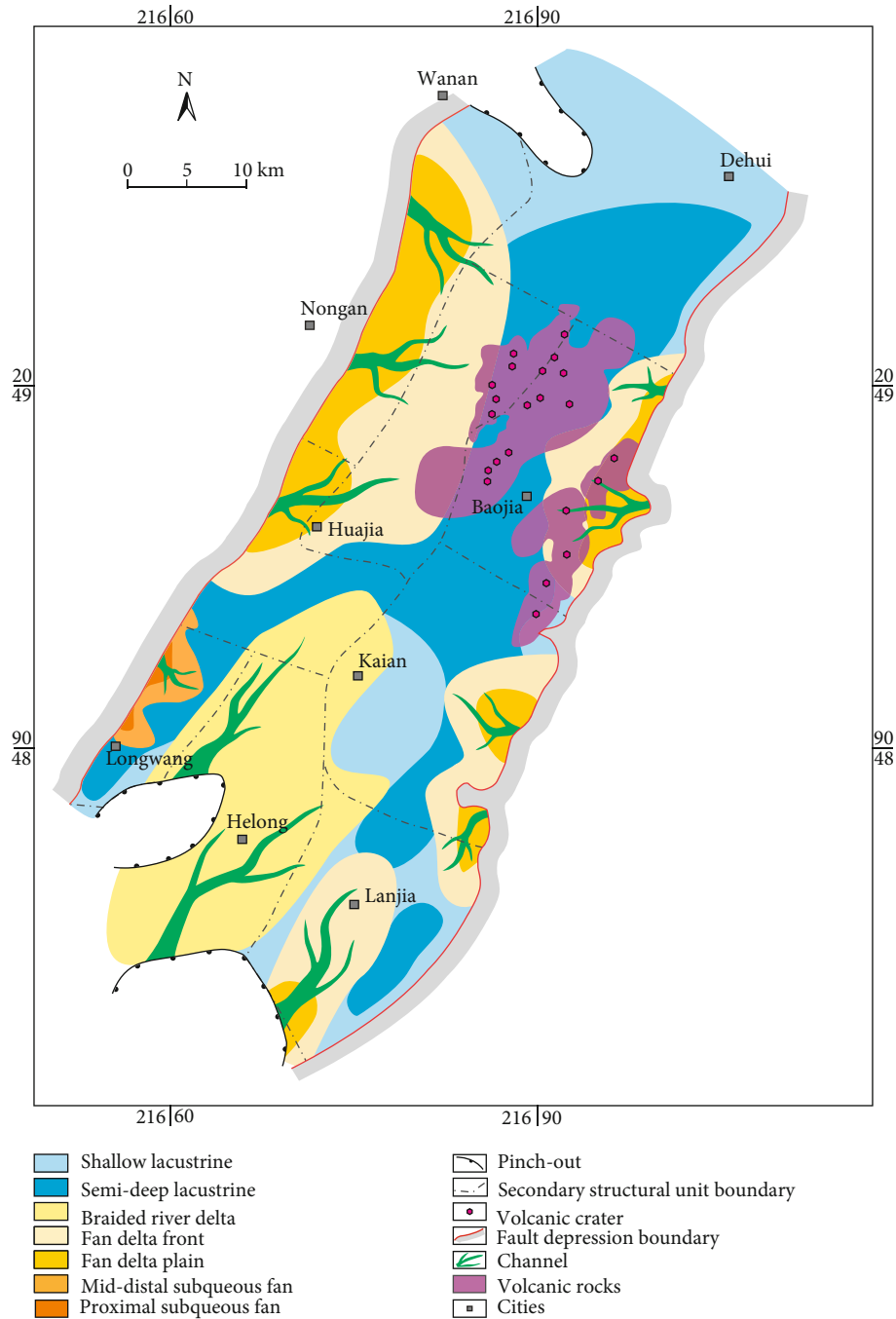


FIGURE 3: The sedimentary facies map of the K<sub>1</sub>yc in the Dehui Depression shows the distribution of volcanic and sedimentary rocks.

(Figure 1(a); [5]). It is a sedimentary fault depression with synrift and thermal subsidence double-layered structure developed on the basement of Upper Paleozoic metamorphic rock series, covering an area of 4053 km<sup>2</sup> (Figure 1(b)). The fault depression generally presents an NNE trending double fault-controlled graben, which is cut by NNE trending faults, forming a structural pattern of horst-graben-steps. It can be further divided into seven secondary structural units, including the Nong'an Graben, Huajia Subdepression, Baojia Subdepression, Nong'an'nan Subdepression, Helong Subdepression, Lanjia Subdepression, and Longwang Subdepression (Figure 1(c)).

Since the Mesozoic, the fault depression has undergone several tectonic activities of subsidence and uplift, and the Mesozoic and Cenozoic strata with a thickness of more than 5000 m have been deposited [23]. The strata developed from bottom to top in this area are the Carboniferous-Permian basement, the lower Cretaceous Huoshiling Formation (K<sub>1</sub>hs), Shahezi Formation (K<sub>1</sub>sh), Yingcheng Formation (K<sub>1</sub>yc), Denglouku Formation (K<sub>1</sub>d), Quantou Formation (K<sub>1</sub>q), the upper Cretaceous Qingshan-kou Formation (K<sub>2</sub>qn), Yaojia Formation (K<sub>2</sub>y), Nenjiang Formation (K<sub>2</sub>n), and Quaternary (Figure 1(d)), among which the Yingcheng Formation is the target layer of this study.

TABLE 1: Results of Rock-Eval pyrolysis.

Depth (m)	TOC (%)	S <sub>1</sub> (mg/g)	S <sub>2</sub> (mg/g)	T <sub>max</sub> (°C)	S <sub>1</sub> + S <sub>2</sub> (mg/g)	HI (mg HC/g TOC)	PI
2856.60	2.28	2.53	1.85	486.00	4.38	81.14	0.58
2856.65	3.24	0.63	1.57	490.00	2.20	48.46	0.29
2857.00	2.67	1.11	1.58	490.00	2.69	59.18	0.41
2857.35	2.02	0.36	1.05	489.00	1.41	51.98	0.26
2857.70	3.19	0.94	1.86	489.00	2.80	58.31	0.34
2858.20	2.43	0.65	1.31	491.00	1.96	53.91	0.33
2858.70	3.03	0.73	1.63	489.00	2.36	53.80	0.31
2859.49	1.96	0.81	2.47	488.00	3.28	126.02	0.25
2859.50	1.69	0.51	0.95	490.00	1.46	56.21	0.35
2860.00	2.06	0.54	1.06	488.00	1.60	51.46	0.34
2860.70	3.33	0.29	0.68	490.00	0.97	20.42	0.30
2861.40	0.22	0.02	0.14	482.00	0.16	63.64	0.13
2861.90	2.18	0.52	1.24	488.00	1.76	56.88	0.30
2862.20	2.12	0.33	0.96	489.00	1.29	45.28	0.26
2862.70	2.12	0.53	1.08	490.00	1.61	50.94	0.33
2863.30	2.12	0.39	1.28	488.00	1.67	60.38	0.23
2863.80	2.17	0.36	1.14	490.00	1.50	52.53	0.24
2864.00	2.13	0.23	1.18	487.00	1.41	55.40	0.16
2864.40	2.39	0.38	1.20	490.00	1.58	50.21	0.24
2864.90	1.40	0.14	0.68	489.00	0.82	48.57	0.17
2865.20	1.59	0.23	0.87	488.00	1.10	54.72	0.21
2865.70	3.10	0.61	1.77	490.00	2.38	57.10	0.26
2866.20	1.97	0.40	1.08	490.00	1.48	54.82	0.27
2866.80	1.95	0.22	1.02	488.00	1.24	52.31	0.18
2867.00	2.19	0.31	1.19	488.00	1.50	54.34	0.21
2867.20	2.00	0.39	1.00	488.00	1.39	50.00	0.28
2867.90	1.40	0.26	0.87	487.00	1.13	62.14	0.23
2868.20	1.80	0.43	0.99	488.00	1.42	55.00	0.30
2868.70	1.77	0.35	0.98	487.00	1.33	55.37	0.26
2869.40	3.18	0.46	1.80	489.00	2.26	56.60	0.20
2869.70	1.26	0.14	0.72	488.00	0.86	57.14	0.16
2870.20	1.16	0.22	0.66	489.00	0.88	56.90	0.25
2870.50	1.30	0.11	0.72	488.00	0.83	55.38	0.13
2885.50	2.74	0.68	1.53	490.00	2.21	55.84	0.31
3053.95	1.69	0.35	1.87	484.00	2.22	110.65	0.16
3056.00	0.78	0.22	0.61	494.00	0.83	78.21	0.27
3056.25	2.08	0.25	1.23	495.00	1.48	59.13	0.17
3057.55	0.85	0.24	1.09	396.00	1.33	128.24	0.18
3057.85	0.58	0.03	0.39	488.00	0.42	67.24	0.07
3059.38	0.22	0.01	0.15	488.00	0.16	68.18	0.06
3060.45	0.38	0.04	1.07	456.00	1.11	281.58	0.04
3063.14	1.13	0.08	1.50	472.00	1.58	132.74	0.05
3063.43	1.73	0.16	2.72	462.00	2.88	157.23	0.06
3065.50	0.76	0.08	1.46	443.00	1.54	192.11	0.05
3377.98	1.40	0.06	0.42	519.00	0.48	30.00	0.13
3395.94	0.61	0.04	0.47	487.00	0.51	77.05	0.08
3396.90	0.62	0.05	0.41	493.00	0.46	66.13	0.11

TABLE 1: Continued.

Depth (m)	TOC (%)	S <sub>1</sub> (mg/g)	S <sub>2</sub> (mg/g)	T <sub>max</sub> (°C)	S <sub>1</sub> + S <sub>2</sub> (mg/g)	HI (mg HC/g TOC)	PI
2306.00	1.51	2.20	1.15	458.00	3.35	76.16	0.66
2307.00	1.83	6.95	1.18	505.00	8.13	64.48	0.85
2316.00	0.34	1.90	0.34	387.00	2.24	100.00	0.85
2326.00	0.34	2.33	0.33	385.00	2.66	97.06	0.88
2820.00	0.51	1.06	0.35	485.00	1.41	68.63	0.75
2850.00	0.51	0.91	0.31	484.00	1.22	60.78	0.75
2890.00	0.43	1.93	0.36	486.00	2.29	83.72	0.84
2910.00	3.84	4.50	2.83	487.00	7.33	73.70	0.61
2920.00	3.33	3.66	2.23	486.00	5.89	66.97	0.62
2930.00	2.72	2.74	1.80	488.00	4.54	66.18	0.60
2940.00	4.24	1.19	2.64	489.00	3.83	62.26	0.31
2960.00	6.82	1.94	6.47	485.00	8.41	94.87	0.23
2980.00	5.94	1.43	5.19	485.00	6.62	87.37	0.22
3005.00	8.33	2.76	8.62	485.00	11.38	103.48	0.24
3020.00	1.64	1.29	1.23	488.00	2.52	75.00	0.51
3035.00	1.56	1.68	1.04	490.00	2.72	66.67	0.62
3217.54	1.60	0.10	0.49	513.00	0.59	30.63	0.17
3677.60	1.28	0.14	0.49	570.00	0.63	38.28	0.22
2665.00	2.50	3.35	2.76	465.00	6.11	110.40	0.55
2680.00	12.90	4.31	17.22	472.00	21.53	133.49	0.20
2685.00	3.53	2.80	3.59	473.00	6.39	101.70	0.44
2690.00	8.42	3.56	9.97	473.00	13.53	118.41	0.26
2710.00	17.78	4.25	24.81	473.00	29.06	139.54	0.15
2725.00	9.65	6.85	16.05	475.00	22.90	166.32	0.30
2880.00	2.06	1.01	1.73	483.00	2.74	83.98	0.37
2898.00	2.32	1.59	1.84	485.00	3.43	79.31	0.46
2940.00	5.51	6.42	4.99	488.00	11.41	90.56	0.56
2970.00	1.84	4.88	1.50	488.00	6.38	81.52	0.76
2990.00	1.93	5.08	1.68	492.00	6.76	87.05	0.75
3010.00	4.82	4.18	4.19	489.00	8.37	86.93	0.50
3015.00	18.85	7.79	16.80	489.00	24.59	89.12	0.32
3020.00	18.71	6.71	14.31	491.00	21.02	76.48	0.32
3060.00	3.93	12.59	3.42	493.00	16.01	87.02	0.79
3078.00	13.46	14.75	13.15	492.00	27.90	97.70	0.53
3215.00	3.82	10.34	2.26	504.00	12.60	59.16	0.82
3420.00	2.00	0.07	0.46	434.00	0.53	23.00	0.13
3830.00	7.08	9.53	8.45	483.00	17.98	119.35	0.53
2785.00	3.18	20.92	3.06	356.00	23.98	96.23	0.87
2795.00	2.88	18.55	2.72	351.00	21.27	94.44	0.87
2805.00	3.22	21.38	3.30	357.00	24.68	102.48	0.87
2815.00	3.20	17.15	3.21	360.00	20.36	100.31	0.84
2825.00	3.39	19.15	3.11	358.00	22.26	91.74	0.86
2835.00	3.56	23.33	3.40	364.00	26.73	95.51	0.87
2845.00	3.30	18.99	3.41	364.00	22.40	103.33	0.85
2855.00	3.15	16.83	3.14	363.00	19.97	99.68	0.84
2865.00	3.16	11.40	2.66	344.00	14.06	84.18	0.81

TABLE 1: Continued.

Depth (m)	TOC (%)	S <sub>1</sub> (mg/g)	S <sub>2</sub> (mg/g)	T <sub>max</sub> (°C)	S <sub>1</sub> + S <sub>2</sub> (mg/g)	HI (mg HC/g TOC)	PI
2870.00	2.78	6.64	1.63	329.00	8.27	58.63	0.80
2878.00	2.59	11.15	2.35	344.00	13.50	90.73	0.83
2885.00	3.97	14.08	3.09	493.00	17.17	77.83	0.82
2890.00	3.34	21.38	2.87	341.00	24.25	85.93	0.88

TOC: total organic carbon content; S<sub>1</sub>: free hydrocarbons present in the rock; S<sub>2</sub>: petroleum generated by pyrolysis; S<sub>1</sub> + S<sub>2</sub>: genetic potential; T<sub>max</sub>: the temperature at peak evolution of S<sub>2</sub> hydrocarbons (°C); HI: hydrogen index, S<sub>2</sub> divided by TOC × 100; PI: production index, S<sub>1</sub>/(S<sub>1</sub> + S<sub>2</sub>).

**2.2. Volcanic Activities.** During the period of the Yingcheng Formation deposition, numerous volcanic activities happened, leading to the creation of faults in Dehui fault depression [28]. By employing the superposition relationship between volcanic rock mass from 3D seismic data and zircon dating, three periods of volcanic activities in this area were recognized, which first increased and then gradually weakened. During the initial stages of volcanic activity, eruptions mainly occurred at the edge of the depression and near the faults which controlled the depression. Large volcanic groups developed, and later, sedimentary strata covered the volcanic rocks [5]. Drilling through these volcanic rocks confirmed mushroom-like structures with obvious volcanic channels dated 118 Ma, which marks the onset of the Yingcheng Formation. The middle stage of the volcanic activity is dominated by eruption of pyroclastic facies and magma flows along the volcanic channels and faults that were formed during the first stage of volcanism forming a large area of pyroclastic shield. This period is dated back to 115 Ma, which represents the middle stage of the creation of the Yingcheng Formation. Finally, in the late period of volcanic activity, volcanic intrusions were formed, and because of its weakened energy, the magma could not reach the surface and only cut through the strata. This took place about 103 Ma, which coincides with the depositional period of the Denglouku Formation (Figure 2; [28]).

**2.3. Sedimentary Facies.** During the deposition of the Yingcheng Formation, the Songliao Basin was tectonically active, and a number of faults were developed. The Yingcheng Formation is divided into two members while the first member is strongly affected by volcanism, and a large set of volcanic formations are developed around the Dehui fault depression [5]. At the margins of the fault depression, a set of fan-delta and lacustrine facies were deposited, and a mixed sequence of volcanic and clastic sedimentary strata was formed. The sedimentary facies in the study area are mainly fan-deltaic, lacustrine, and nearshore subaqueous fan (Figure 3). The fan-delta is widely developed in the eastern and western margins of the depression, while the braided river delta plain is dominant in the south, and the lacustrine facies center is located in the northeast of the depression. During the sedimentation process, the supply of sediment was hindered by the influence of multiple volcanic activities, which limited the range and thickness of sand bodies that were deposited in the northeast.

**2.4. Petroleum System.** Three sets of petroleum source-reservoir-seal systems are identified in the study area [5,

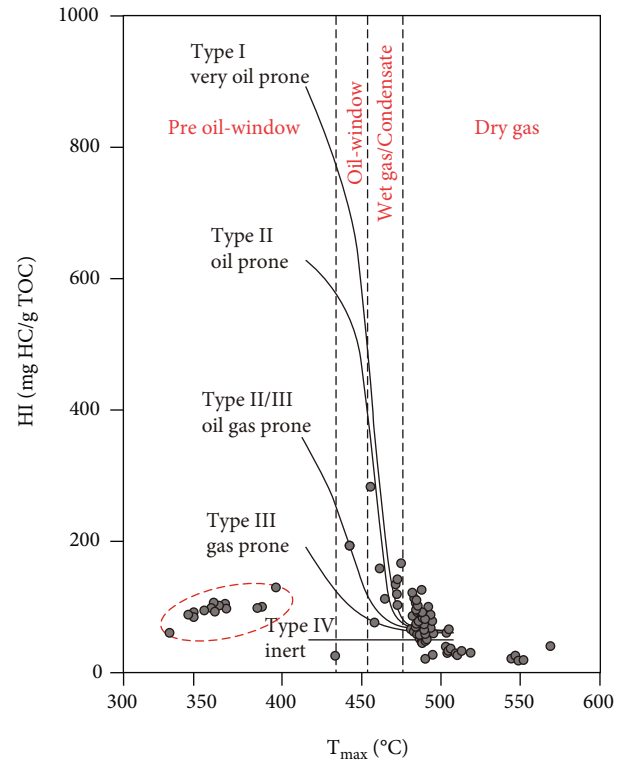


FIGURE 4: Plot of TOC (wt.%) vs. HI (mg HC/g TOC) of the K<sub>1yc</sub> (according to [35]).

25]. In the K<sub>1yc</sub>, K<sub>1sh</sub>, and K<sub>1h</sub>, thick organic-rich mudstones with a high thermal maturity have been proven to be the effective source for the gas. Meanwhile, fine sandstone, siltstone, conglomerate, and volcanic rocks formed during volcanic activity are widely spread in the K<sub>1yc</sub>, K<sub>1sh</sub>, and K<sub>1h</sub> and act as the reservoir for natural gas accumulation. Thick mudstone developed in the K<sub>2d</sub> is almost distributed in the entire southern Songliao Basin and could serve as the regional seal, and mudstone layers in each formation mentioned above can serve as the local caprocks [7].

### 3. Samples and Methods

A total of 235 core samples from the K<sub>1yc</sub> were selected in this study (location of sampling well is shown in Figure 1(c)). From these, 97 mudstone samples were selected for Rock-Eval pyrolysis while 16 were chosen for vitrinite reflectance measurements to characterize the source rock. Moreover, 63 samples from the volcanic and 75 from the

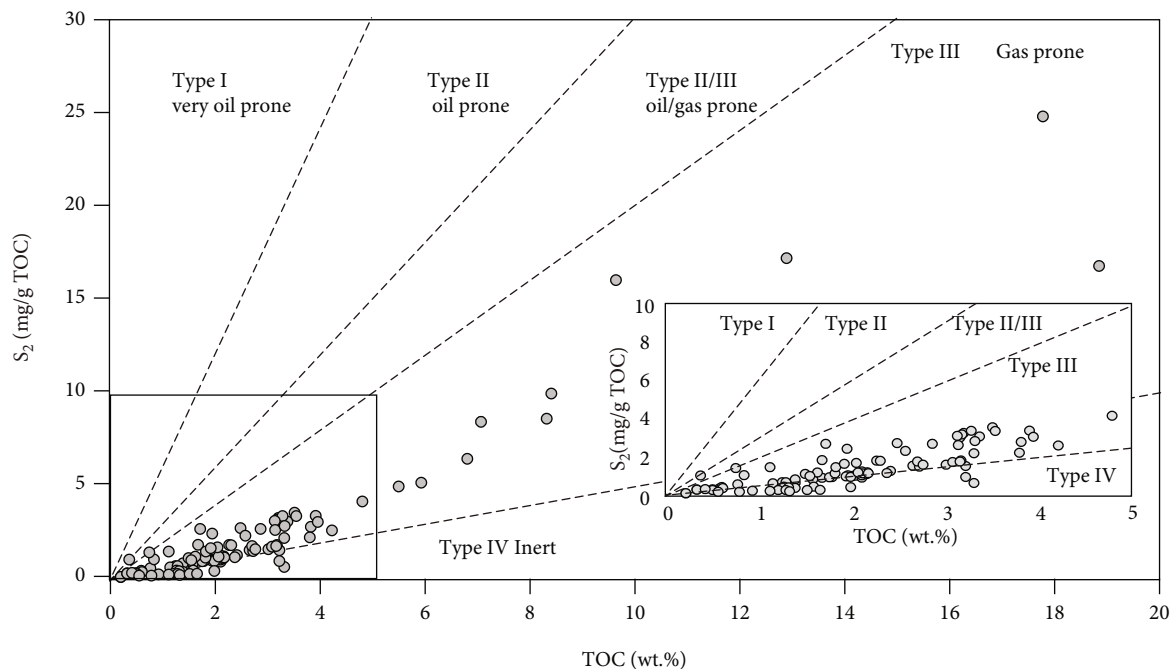


FIGURE 5: The TOC versus  $S_2$  plot for the  $K_{1yc}$  source rock samples (according to [36]).

tight sandstone were tested to characterize petrophysical properties of the reservoir. Thin sections were prepared from all reservoir samples and analyzed by using a petrographic microscope Leica DM2700P to observe pore types.

A total of 97 core samples were pulverized to 100-mesh screen in preparation for geochemical analysis and TOC measurement. The TOC was measured using a LECO CS-230 analyzer, and programmed pyrolysis was performed using a Rock-Eval 6 plus analyzer to obtain  $S_1$  (free hydrocarbons),  $S_2$  (petroleum generated by pyrolysis), and  $T_{max}$  (the temperature at peak evolution) by default method [29, 30].

Vitrinite reflectance ( $R_o$ ) was measured using a microphotometer, and this analysis was performed at the Geochemistry Laboratory of the Northeast Petroleum University. Analysis was performed with an oil immersion objective under normal white light at a wavelength of 546 nm. A mean value was calculated for each sample on the basis of 12-20 measurements on vitrinite [18].

Porosity of core samples (63 volcanic and 75 tight sandstone) was done using core test system AP608 analyzer at Jilin University. The samples were drilled in cylinders with the size of  $1'' \times 4''$ , vacuum-dried at  $180^\circ\text{C}$ , and then analyzed using a minipermeameter for air permeability measurements by nitrogen (air). The experimental temperature and humidity were  $24^\circ\text{C}$  and 35%, respectively [31].

## 4. Results

**4.1. Geochemistry of Source Rock.** Total organic carbon (TOC) in the source rocks of the Yingcheng Formation ranges from 0.22 wt.% to 18.85 wt.%, with an average value of 3.24 wt.%, of which 85.6% is higher than 1.0 wt.%, and 60.8% is higher than 2.0 wt.%, in 97 samples that were tested (Table 1). Pyrolysis data was used to determine the type of

organic matter following geochemical charts. According to Figures 4 and 5, the pyrolysis data of source rocks plotted in the van Krevelen diagram ( $HI$  vs.  $T_{max}$  and  $S_2$  vs. TOC) are pointing to type III, and a small portion of type IV inert organic matter. Therefore, the organic matter type of the source rocks of the Yingcheng Formation is type III, which dominantly generates gas. The samples with abnormal  $T_{max}$  which is demonstrated in Figure 4 have relatively higher PI index, indicating the presence of bitumen remanence in shale samples.

The distribution of potential hydrocarbon generation capacity ( $S_1 + S_2$ ) ranges from 0.16 to 29.06 mg/g, with an average of 6.86 mg/g, among which 35.1% are higher than 6 mg/g, and 14.4% are higher than 20 mg/g. An overview of the samples exhibits that they generally represent a poor to good source rock (Figure 6(a)). The  $HI$  vs. TOC plot explains that most of the samples are located in the regions of very little to questionable gas (Figure 6(b)). Only parts of the samples are demonstrating to be a good source rock and to have fair gas generation potential with lower  $S_2$  at the higher maturations (Figure 6).

**4.2. Maturation of Organic Matter.** The maximum pyrolysis temperature ( $T_{max}$ ) of the source rocks of the Yingcheng Formation was measured between  $329^\circ\text{C}$  and  $570^\circ\text{C}$ , while most values are more than  $470^\circ\text{C}$ , inferring that the source rocks of the Yingcheng Formation are over mature in the gas generation window with the exclusion of the abnormal data under  $400^\circ\text{C}$  (Figure 7(a)). The measured vitrinite reflectance ( $R_o$ ) values of source rocks in the Yingcheng Formation is positively correlated with the burial depth and increases as the formation becomes deeper (Figure 7(b)). Among these 16 samples that were inspected for  $R_o$ , except two that are shallower, the  $R_o$  was found more than 1.4%,

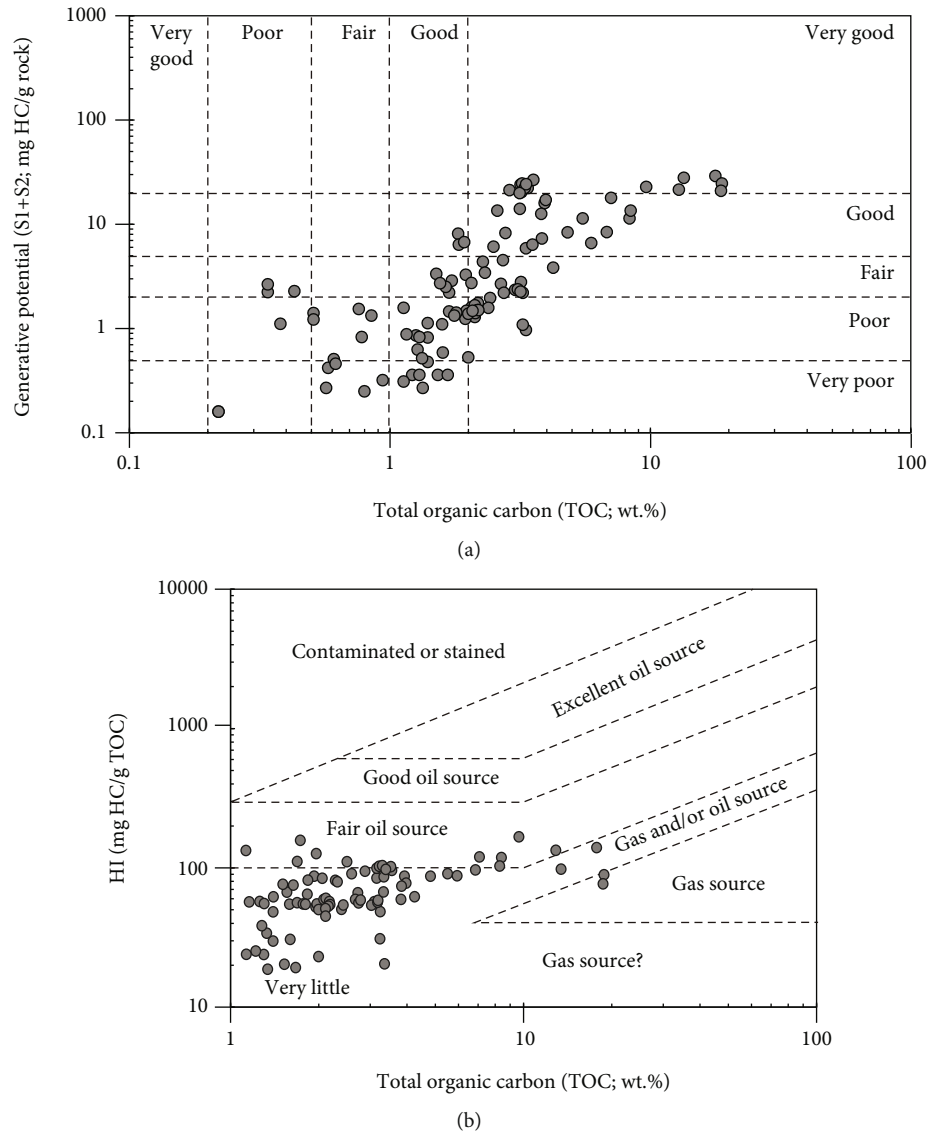


FIGURE 6: (a) Plot of total organic carbon (TOC) vs. generative potential ( $S_1 + S_2$ ) of the  $K_1yc$  (according to [37]). (b) Plot of TOC vs. HI of the  $K_1yc$  in the study area (according to [38]).

while it appears to be more than 2.0% for samples buried deeper than 3000 m (Table 2). Collectively, the organic matter in the source rocks of the Yingcheng Formation in the study area has entered gas generation window and is highly overmatured.

#### 4.3. Petrophysical Properties

**4.3.1. Volcanic Reservoir.** As shown in Figure 2, volcanic rocks are presenting separate seismic reflections attributes compared to other sedimentary layers, making the interpretation of Yingcheng volcanic rocks based on seismic profiles much easier. Volcanic rocks of the Yingcheng Formation are mainly distributed in the northeast of the study area and are controlled by volcanic activities. Their thickness varies from 0 to 400 m and can reach more than 700 m locally (Figure 8). The porosity of the volcanic reservoir rocks of the Yingcheng Formation in the study area is between 3.0% and 14.8%, with

an average value of 7.3%. The porosity distribution is approximately normal, with the main peak around 5%-8%, which also accounts for 74.6% of the entire samples. The permeability of the samples were measured between 0.0004 and 2.52 mD, while the 0.001 to 0.01 mD interval accounts for 43% of the total tested samples.

The pore type of volcanic reservoir rocks is complex and varies but can roughly be divided into three types: (1) primary pores, (2) secondary pores, and (3) fractures based on observations on thin sections. The dominant type is secondary pores, mainly feldspar dissolution pores, which are mostly developed in tuff (Figure 9(a)). Moreover, fractures that are formed by the structural stress are more dominant in dacite in the study area (Figures 9(b) and 9(c)) and occasionally observed in tuff (Figure 9(d)).

**4.3.2. Tight Sandstone Reservoir.** Tight sandstone deposition is controlled by changes in the facies, mainly distributed in

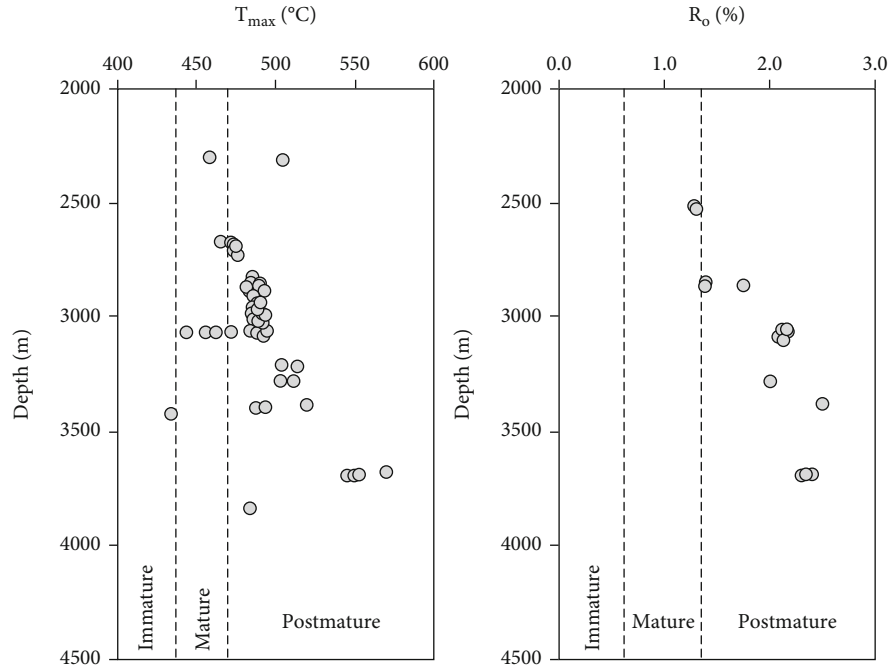


FIGURE 7: (a)  $T_{\max}$  and (b)  $R_o$  versus depth for the  $K_{1yc}$  source rocks samples. Thermal maturity zones are divided according to Peters and Cassa [39].

TABLE 2: Results of vitrinite reflectance experiment.

Well name	Depth (m)	$R_o$ (%)	Num. measu.	SD
DS111	2858.2	1.39	20	0.16
DS111	2859.2	1.76	19	0.04
DS111	2861.9	1.40	20	0.14
DS111	3056.0	2.13	20	0.15
DS111	3063.1	2.15	20	0.11
DS111	3063.4	2.17	20	0.14
DS111	3377.9	2.49	20	0.16
DS17-6	2518.9	1.29	20	0.14
DS17-6	2528.0	1.31	20	0.12
DS81	3085.4	2.12	16	0.06
DS81	3086.0	2.08	12	0.06
DS81	3092.0	2.15	20	0.06
DS83	3280.6	2.01	20	0.13
DS83	3690.2	2.38	20	0.16
DS83	3692.3	2.31	17	0.05
DS83	3692.3	2.40	20	0.17

$R_o$ : vitrinite reflectance; Num. measu.: number of measured points; SD: standard deviation.

the delta front and plain subfacies in the northeast and northwestern areas of the fault depression, with a thickness of 0-400 m (Figure 10). The thickness of sandstone facies in the middle of the fault depression is less than 100 m. Furthermore, the porosity of tight sandstone in the Yingcheng Formation in the study area was measured between 0.5% and 11.2%, with an average value of 5.1%, and its distribu-

tion is also approximately uniform. Comparing their porosity with the volcanic reservoir, the distribution of measured porosity values is relatively dispersed, and 2%-7% of porosity constitutes 69.3% of total collected data. In addition, the permeability of the samples was found to vary between 0.0008 and 3.17 mD, with the peak at 0.001 mD. Considering thin section analysis, the reservoir space in the study area is mainly intergranular pores, with a small amount of intragranular pores and microfractures (Figure 11).

## 5. Discussion

**5.1. Volcanic Effects on Hydrocarbon Generation.** Volcanic intrusions have increased the temperature and pressure of the Yingcheng Formation and promoted the generation and expulsion of hydrocarbon in the source rocks [32]. Bulk geochemical data sets in this study show that deeply buried source rocks of the Yingcheng Formation in the Songliao Basin are widely developed and have good hydrocarbon generation potential. These source rocks are mostly type III kerogen with high TOC content. Additionally, measured  $R_o$  is generally greater than 1.4%, which is overmature, and on the onset of gas generation window. It is speculated that late volcanic intrusions provided sufficient heat source for the transformation of organic matter and caused the generation of natural gas in large quantities. The magmatic thermal field not only improves the geothermal gradient of the basin but also enhances the degree of thermal evolution of the organic matter compensating for the pressure and burial depth. This makes the threshold of gas generation to happen at the shallower depth, enhancing hydrocarbon generation [33]. In the volcanic gas reservoirs, the bitumen is common in micro fractures (Figures 9(b)–9(d)), referring to the



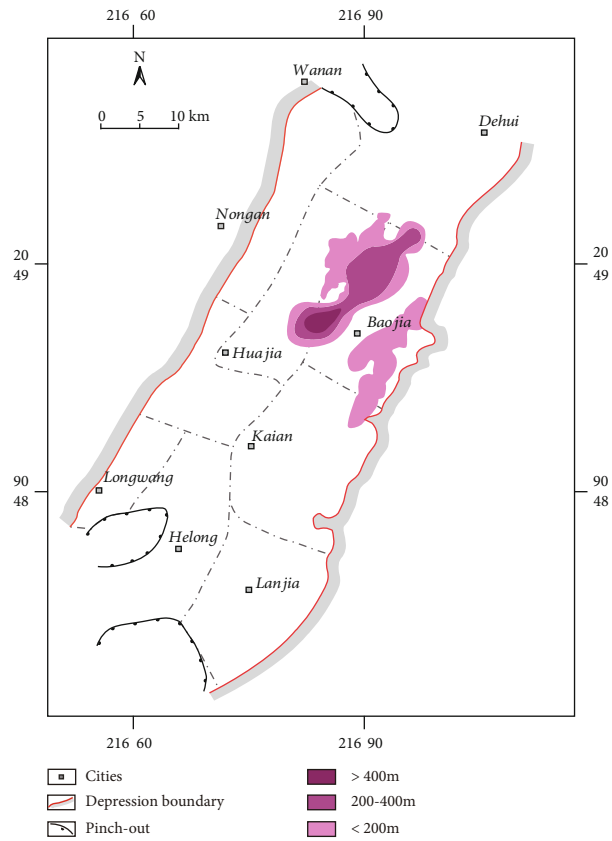


FIGURE 8: Distribution of volcanic rock reservoir of the  $K_{1yc}$ .

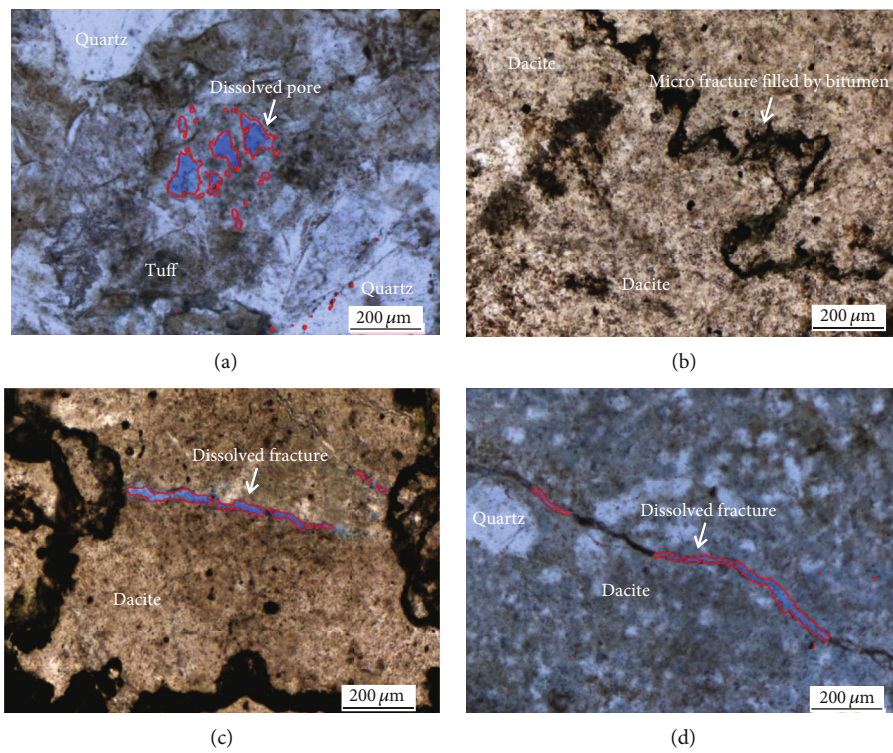


FIGURE 9: Thin section observed by plane-polarized and light perpendicular-polarized light for volcanic reservoir samples for the  $K_{1yc}$ . (a) 2700.0 m, tuff; (b) 2240.0 m, dacite; (c) 2240.9 m, dacite; (d) 2700.0 m, tuff.

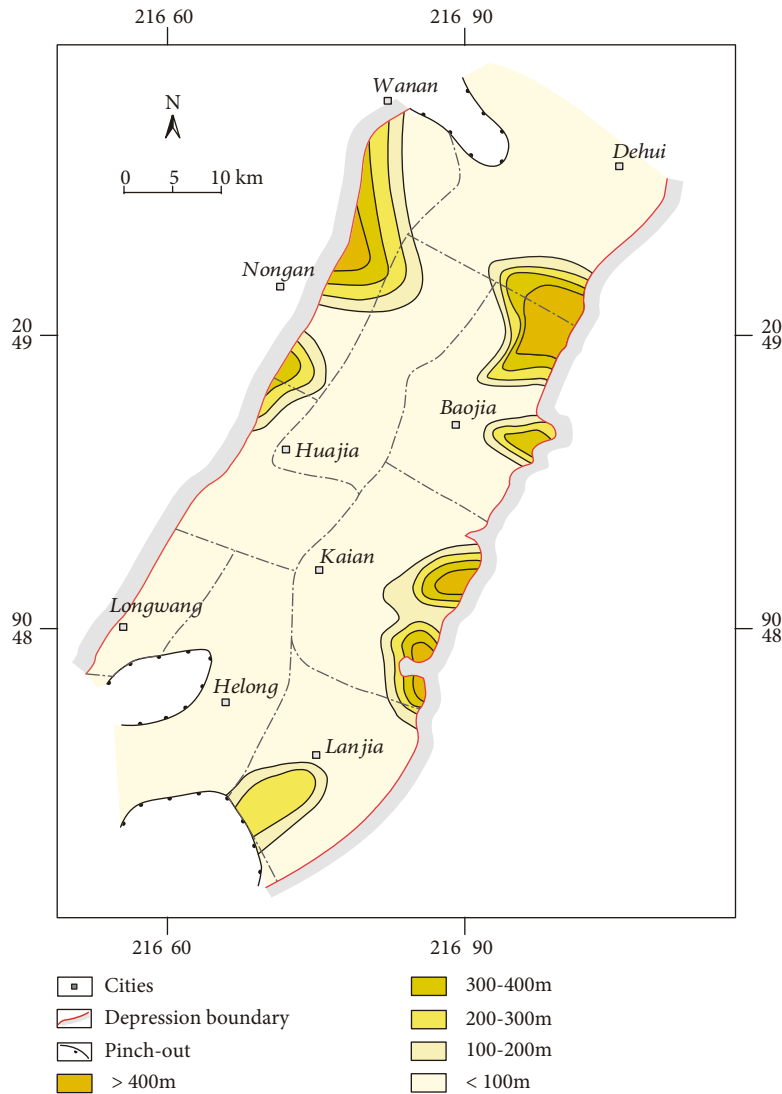


FIGURE 10: Distribution of tight sandstone reservoir of the  $K_{1yc}$ .

abnormal high maturity which is consistent with the high paleo heat flow during the synrift phase [25]. This was caused by the upwelling of mantle plumes and the thinning of the crust, which were accompanied with volcanic activities before the Late Mesozoic-Cenozoic rapid cooling [34].

**5.2. Pore Genesis of Reservoir.** Based on the inspection of thin sections (Figure 9), the volcanic reservoir of the Yingcheng Formation is mainly tuff and dacite, and the pores are mainly from mineral dissolution to create pores and microfractures. As shown in Figure 9, dissolution pores in the volcanic reservoirs such as tuff or dacite are mostly isolated and poorly connected. At the same time, the dissolution microfractures have a short extent, small width and irregularity, and limited in scope and number. Observation of thin sections also revealed the presence of asphaltene filling in the cracks.

Tight sandstone reservoir of the Yingcheng Formation is generally dominated by intragranular dissolution pores, accounting for 89% of the total pores (Figure 11). Among

them, feldspar dissolution pores are the most developed ones, accounting for 35%, followed by lithic dissolution pores with 20%, intergranular dissolution pores 19%, and tuffaceous dissolution pores constituting 15% of the entire measured data. Likewise, a small number of intergranular pores, with 8% of the total pores measured, can also be responsible for a certain number of microfractures, around 3%. The intergranular dissolution pores are filled with autogenous albite, felsic particles, coniferous flake chlorite, and a small amount of illite and other clay minerals. The percentage of total surface porosity observed under the microscope is generally about 3%-10%. This kind of reservoir space is dominated by dissolved pores, nanoscale throat and underdeveloped reservoir characteristics, poor pore connectivity, easy-to-form isolated pores, resulting in “isolated pore space,” and dense characteristics of the reservoir with low permeability overall.

The porosity of tight sandstone is much less than the volcanic rocks at the same depth (Figure 12(a)). The porosity and permeability of sandstones has an obvious decreasing

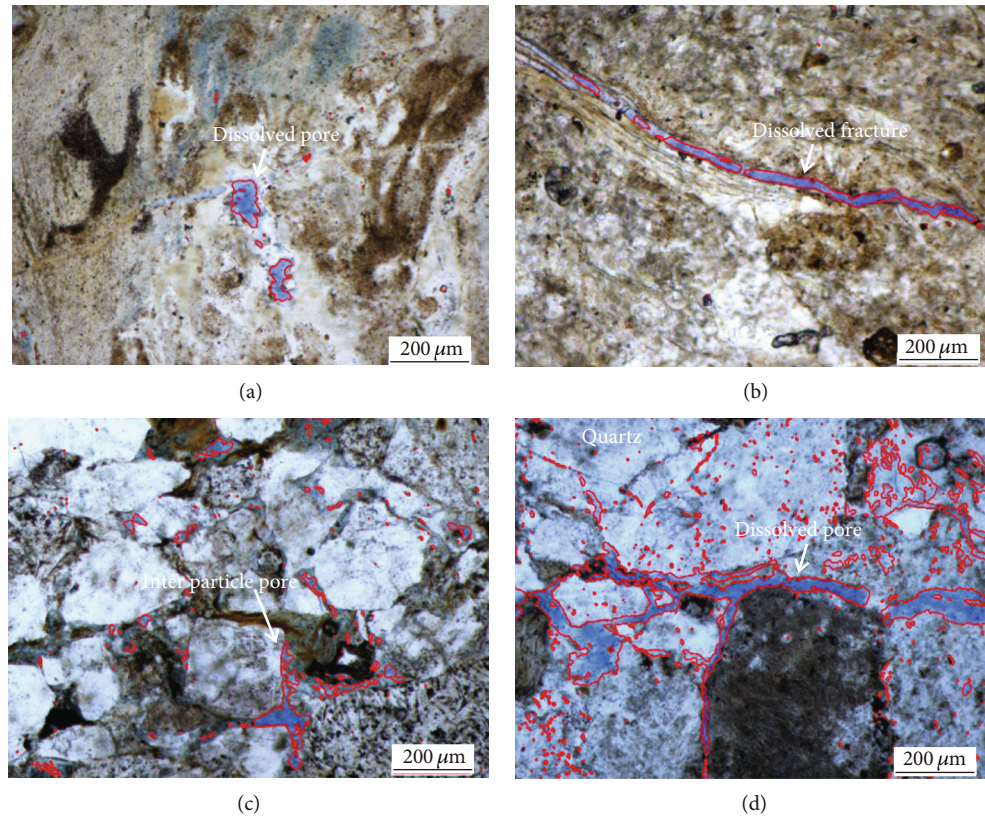


FIGURE 11: Thin section observed by plane-polarized and light perpendicular-polarized light for tight sandstone reservoir samples for the  $K_1y.c.$  (a) 2522 m, tuffaceous sandstone; (b) 2543 m, tuffaceous sandstone; (c) 2803.5 m, tuffaceous sandstone; (d) 2912.5 m, tuffaceous sandstone ((c) and (d) are referenced from [28]).

trend in the range of 2000–4500 m, which is caused by the compaction (Figure 12(b)). However, the porosity and permeability of volcanic reservoirs do not change much with depths, and the values are relatively concentrated, proving that compaction has little influence on the quality of the volcanic reservoir. In comparison with tight sandstone reservoir, the porosity of volcanic rock is relatively similar at shallower depth but generally improves with depth. The permeability of volcanic rocks is less than tight sandstones, but again it enhances with depth. That confirms how the effects of compaction on sandstones and volcanic rocks can be different, causing the sandstone to always have relatively better porosity and permeability at shallower depth, though it is important that one does not overlook the improvement of reservoir properties in the volcanic rock, too, as the formation gets deeper.

**5.3. Gas Accumulation Model in Volcanic Area.** During the formation of the Yingcheng Formation in the study area, the basin was under extension [7]; thus, the controlling depression fault expanded eastward, and the sedimentary area gradually expanded, accompanied by volcanic activities for the entire period. The early subsidence center of the Yingcheng Formation is close to the boundary fault, making the deep extension area small. Moreover, volcanic activity mainly happened in the eastern gentle slope of the basin, which controlled sedimentation in the eastern boundary as well. Likewise, volcanic erosions provided additional sediment supply for the basin. In the middle stages of the

Yingcheng Formation, the depocenter migrated northward to the east, the deep depression area expanded, and the volcanic rocks in the eastern gentle slope area generally eroded. At the end of the deposition of the Yingcheng Formation, the basin shrunk, and the deeper depression area was distributed along the boundary faults. Besides, the stratigraphic distribution range was large with limited thickness, and as the volcanism was strengthened, it affected the entire basin. This caused the strata to get dispersed between the volcanically active areas and the control-depression fault. Therefore, the reservoirs are scattered in the middle and upper parts of the Yingcheng Formation, which made the relationship between the source and the reservoir rocks stronger.

During the earlier phases of volcanic eruption, larger volcanic bodies developed, which controlled the lateral boundaries of the trough of the Yingcheng Formation, to form an updip lateral block due to the tectonic activity that was later followed. The volcanic rocks mainly from tuff in the Yingcheng Formation formed during the middle phases of volcanism have constant thickness (ranging from 80 to 150 m, and more than 200 m locally) and wide lateral distribution, which played the role of the regional caprock [28]. These two volcanic activities promoted the formation of large traps and played a vital role in gas enrichment and preservation. Furthermore, the tuff layer is very dense, is free of fractures, and does not intrude and damage the gas reservoir, sealing the entire tight sandstone reservoir underneath. The early and middle volcanism surrounded the entire Yingcheng

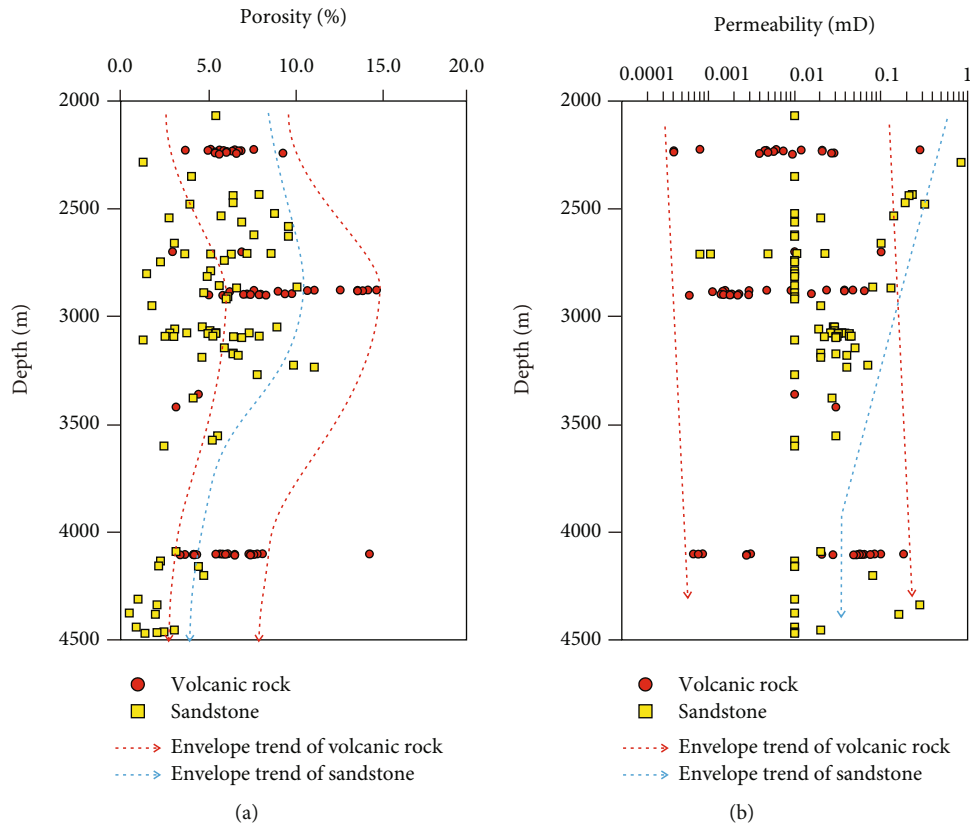


FIGURE 12: (a) Porosity and (b) permeability versus the depth of volcanic rock reservoir and tight sandstone reservoir samples for the  $K_1yc$ .

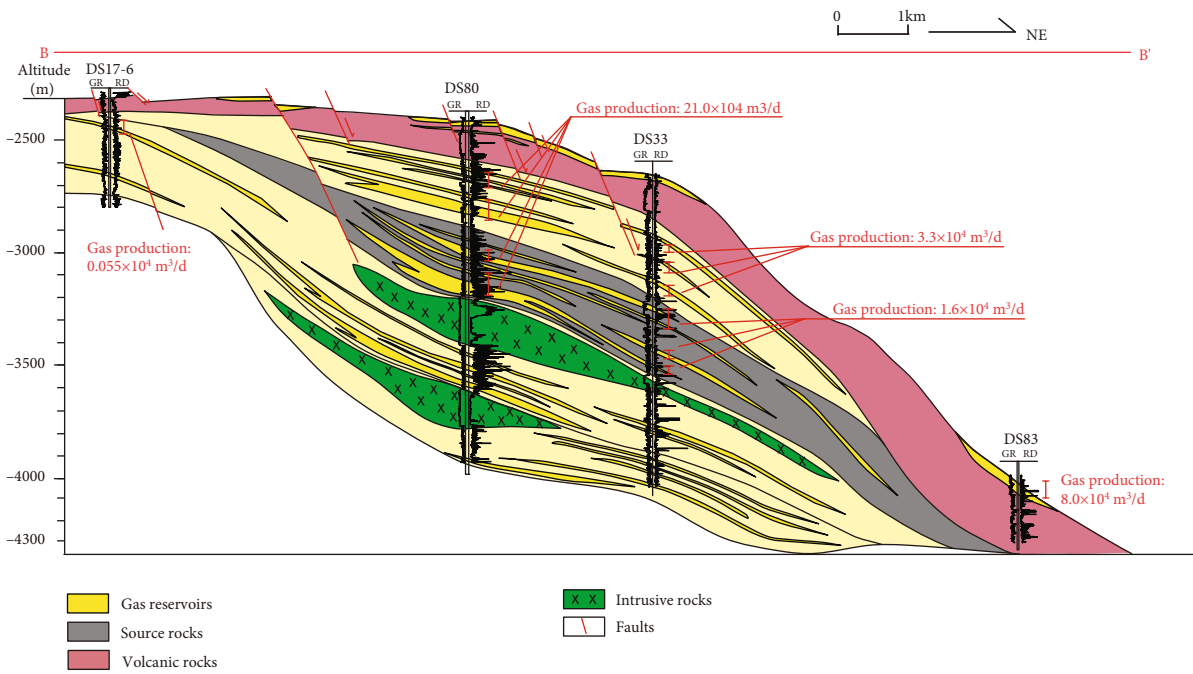


FIGURE 13: Cross-section of gas accumulation in the  $K_1yc$ ; location of the profile is shown in Figure 1. In this section, suitable gas productive zones in the volcanic rock reservoir and tight sandstone reservoir are displayed (modified from [28]).

Formation and supported the formation of tight sandstone gas traps. The above two volcanic activities formed one block and one cap, which provided favorable trap conditions for tight sandstone gas reservoirs (Figure 13).

On the other hand, volcanic rocks in some areas are replaced with sandstone bodies, to become complementary reservoir space. This combination of tight sandstone and volcanic gas reservoirs formed in the same horizon also produced economic quantities of gas. For example, well DS80 showed  $21.0 \times 10^4 \text{ m}^3/\text{d}$  flow rate in the 2650–3200 m interval, well DS33,  $3.3 \times 10^4 \text{ m}^3/\text{d}$  and  $1.6 \times 10^4 \text{ m}^3/\text{d}$  in two separate intervals, and well DS83,  $8.0 \times 10^4 \text{ m}^3/\text{d}$  of high-yielding flow in the upper volcanic zone of the reservoir (Figure 13).

## 6. Conclusion

- (1) The organic carbon content of the source rocks of the Yingcheng Formation in Dehui fault depression varies from 0.22 wt.% to 18.85 wt.%, with an average of 3.05 wt.%. The distribution of potential hydrocarbon generation ( $S_1 + S_2$ ) was found from 0.16 to 29.06 mg/g, with an average of 6.21 mg/g. Additionally, organic matter is mainly type III and at the high-overmaturity, representing favorable conditions for gas generation
- (2) The thickness of volcanic reservoir in the study area is 0–400 m, the porosity is 3.0%–14.8%, the permeability is 0.0004–2.52 mD, and pore types are mainly secondary dissolved pores and fractures. Moreover, the thickness of the tight sandstone reservoir is 0–400 m, the porosity is 0.5%–11.2%, and the permeability is 0.0008–3.17 mD. Pore types are generally intergranular pores, with a small amount of intragranular pores and microfractures
- (3) Late volcanic activity of the Yingcheng Formation in the study area provided sufficient heat source for the organic matter transformation and promoted the generation of natural gas in large quantities
- (4) The petrophysical properties of the tight sandstone reservoir deteriorated significantly with depth and are affected by compaction notably, while the petrophysical properties of volcanic reservoir do not vary much as the formation get deeper representing more homogeneous characteristics. At the same time, secondary pores formed by late dissolution of pyroclasts formed by volcanic activities also provided storage space for gas accumulation
- (5) Volcanic rocks that are formed during the early and middle phases of the Yingcheng Formation development occupied the sedimentary space, which worked against the deposition of sand bodies to some extent. However, volcanic rocks became regional seals as part of the tight sandstone gas trap. Finally, the combination of volcanic rocks and tight sandstones has created a complex petroleum system for the accumulation and preservation of gas in the basin.

## Data Availability

All data sets are included in the manuscript.

## Conflicts of Interest

The authors declare that they have no conflicts of interest.

## Acknowledgments

This study is supported by the Science and Technology Project of Heilongjiang Province (No. 2020ZX05A01) and National Major Project (Nos. 2016ZX05047-005-006 and 2016ZX05027-002-007).

## References

- [1] IEA (International Energy Agency), *World Energy Outlook 2019*, IEA, Washington D C, 2019.
- [2] B. Dudley, *BP Statistical Review of World Energy*, BP Statistical Review, London, UK, 2018.
- [3] C. N. Zou, Z. Yang, D. B. He et al., “Theory, technology and prospects of conventional and unconventional natural gas,” *Petroleum Exploration and Development*, vol. 45, no. 4, pp. 604–618, 2018.
- [4] C. N. Zou, R. Zhu, K. Liu et al., “Tight gas sandstone reservoirs in China: characteristics and recognition criteria,” *Journal of Petroleum Science and Engineering*, vol. 88–89, no. 2, pp. 82–91, 2012.
- [5] H. Jia, H. Ji, L. Wang, D. Yang, P. Meng, and C. Shi, “Tectono-sedimentary and hydrocarbon potential analysis of rift-related successions in the Dehui Depression, Songliao Basin, Northeastern China,” *Marine and Petroleum Geology*, vol. 76, pp. 262–278, 2016.
- [6] F. Jiang, R. H. Cheng, B. T. Ruan, B. Lin, Z. J. Xu, and Z. C. Li, “Formation mechanism of volcanic reservoirs within a volcanostratigraphic framework: the case of the Wangfu fault depression in the Songliao Basin, China,” *Marine and Petroleum Geology*, vol. 84, pp. 160–178, 2017.
- [7] B. Liu, S. He, L. Meng, X. Fu, L. Gong, and H. Wang, “Sealing mechanisms in volcanic faulted reservoirs in Xujiaweizi extension, Northern Songliao Basin, Northeastern China,” *AAPG Bulletin*, vol. 105, no. 8, pp. 1721–1743, 2021.
- [8] B. Liu, Y. Yang, J. Li, Y. Chi, J. Li, and X. Fu, “Stress sensitivity of tight reservoirs and its effect on oil saturation: a case study of Lower Cretaceous tight clastic reservoirs in the Hailar Basin, Northeast China,” *Journal of Petroleum Science and Engineering*, vol. 184, p. 106484, 2020.
- [9] X. Luo, S. Gong, F. J. Sun, Z. H. Wang, and J. S. Qi, “Effect of volcanic activity on hydrocarbon generation: examples in Songliao, Qinsui, and Bohai Bay Basins in China,” *Journal of Natural Gas Science & Engineering*, vol. 38, pp. 218–234, 2017.
- [10] Z. Q. Feng, “Volcanic rocks as prolific gas reservoir: a case study from the Qingshen gas field in the Songliao Basin, NE China,” *Marine and Petroleum Geology*, vol. 25, no. 4–5, pp. 416–432, 2008.
- [11] J. Li, Z. Yang, S. Wu, and S. Pan, “Key issues and development direction of petroleum geology research of source rock strata in China,” *Advances in Geo-Energy Research*, vol. 5, no. 2, pp. 121–126, 2021.

- [12] C. Wang, L. Liu, Y. H. Wang et al., "Recognition and tectonic implications of an extensive Neoproterozoic volcano-sedimentary rift basin along the southwestern margin of the Tarim Craton, northwestern China," *Precambrian Research*, vol. 257, pp. 65–82, 2015.
- [13] E. A. Khalaf, "Variations in eruptive style and depositional processes of Neoproterozoic terrestrial volcano-sedimentary successions in the Hamid area, North Eastern Desert, Egypt," *Journal of African Earth Sciences*, vol. 83, pp. 74–103, 2013.
- [14] M. K. Azer and E. S. Farahat, "Late Neoproterozoic volcano-sedimentary successions of Wadi Rufaiyil, southern Sinai, Egypt: a case of transition from late- to post-collisional magmatism," *Journal of Asian Earth Sciences*, vol. 42, no. 6, pp. 1187–1203, 2011.
- [15] J. N. J. Visser and N. J. Grobler, "Syn depositional volcanism in the Rietgat and arenaceous Bothaville Formations, Ventersdorp Supergroup (late Archaean–early Proterozoic), in South Africa," *Precambrian Research*, vol. 30, no. 2, pp. 153–174, 1985.
- [16] J. Cai, H. Hajibeygi, J. Yao, and S. M. Hassanizadeh, "Advances in porous media science and engineering from InterPore2020 perspective," *Advances in Geo-Energy Research*, vol. 4, no. 4, pp. 352–355, 2020.
- [17] B. Liu, D. Yan, X. Fu, Y. Lü, L. Gong, and S. Wang, "Investigation of geochemical characteristics of hydrocarbon gas and its implications for Late Miocene transpressional strength — a study in the Fangzheng Basin, Northeast China," *Interpretation*, vol. 6, no. 1, pp. T83–T96, 2018.
- [18] B. Liu, A. Bechtel, R. F. Sachsenhofer, D. Gross, R. Gratzler, and X. Chen, "Depositional environment of oil shale within the second member of Permian Lucaogou Formation in the Santanghu Basin, Northwest China," *International Journal of Coal Geology*, vol. 175, pp. 10–25, 2017.
- [19] Y. S. Pan, Z. L. Huang, T. J. Li, X. B. Guo, X. F. Xu, and X. Chen, "Environmental response to volcanic activity and its effect on organic matter enrichment in the Permian Lucaogou Formation of the Malang Sag, Santanghu Basin, Northwest China," *Palaeogeography, Palaeoclimatology, Palaeoecology*, vol. 560, article 110024, 2020.
- [20] S. C. George, "Effect of igneous intrusion on the organic geochemistry of a siltstone and an oil shale horizon in the Midland Valley of Scotland," *Organic Geochemistry*, vol. 18, no. 5, pp. 705–723, 1992.
- [21] B. K. T. Simoneit, S. Bernner, K. E. Peters, and I. R. Kaplan, "Thermal alteration of Cretaceous black shale by diabase intrusions in the Eastern Atlantic–II. Effects on bitumen and kerogen," *Geochimica et Cosmochimica Acta*, vol. 45, no. 9, pp. 1581–1602, 1981.
- [22] Y. G. Sun, J. M. Fu, D. H. Liu, G. Y. Sheng, Z. Y. Chen, and T. S. Wu, "Effects of volcanic activity on organic matter evolution and its significance on petroleum," *Chinese Science Bulletin*, vol. 40, pp. 1019–1022, 1995.
- [23] B. Liu, J. Sun, Y. Zhang et al., "Reservoir space and enrichment model of shale oil in the first member of Cretaceous Qingshan-kou Formation in the Changling sag, southern Songliao Basin, NE China," *Petroleum Exploration and Development*, vol. 48, no. 3, pp. 608–624, 2021.
- [24] P. J. Wang, Y. G. Ren, X. L. Shan, S. B. Sun, C. B. Wan, and W. H. Bian, "The Cretaceous volcanic succession around the Songliao Basin, NE China: relationship between volcanism and sedimentation," *Geological Journal*, vol. 37, no. 2, pp. 97–115, 2002.
- [25] Z. J. Xu, S. Jiang, L. F. Liu et al., "Natural gas accumulation processes of tight sandstone reservoirs in deep formations of Songliao Basin, NE China," *Journal of Natural Gas Science and Engineering*, vol. 83, pp. 103610–103620, 2020.
- [26] H. F. Tang, X. Y. Zhao, X. Liu, C. X. Zhu, W. H. Qu, and W. H. Bian, "Filling characteristics, reservoir features and exploration significance of a volcanostratigraphic sequence in a half-graben basin — a case analysis of the Wangfu Rift Depression in Songliao Basin, NE China," *Marine and Petroleum Geology*, vol. 113, article 104128, 2020.
- [27] H. F. Tang, X. Y. Zhao, M. L. Shao, X. D. Sun, Y. Zhang, and P. Cryton, "Reservoir origin and characterization of gas pools in intrusive rocks of the Yingcheng Formation, Songliao Basin, NE China," *Marine and Petroleum Geology*, vol. 84, pp. 148–159, 2017.
- [28] F. C. Zeng, C. M. Zhang, Z. S. Wei et al., "Main enrichment controlling factors and reservoir characteristics of tight sandstone gas under the influence of volcanic activity," *Acta Geologica Sinica*, vol. 95, no. 3, pp. 895–912, 2021.
- [29] J. Espitalié, F. Marquis, and I. Barsony, "Geochemical logging," in *Analytical Pyrolysis*, K. J. Voorhess, Ed., pp. 53–79, Butterworths, Boston, 1984.
- [30] B. T. Tissot and D. H. Welte, *Petroleum Formation and Occurrences*, Springer Verlag, Berlin, second edition, 1984.
- [31] S. Huang, Y. Wu, X. Meng, L. Liu, and W. Ji, "Recent advances on microscopic pore characteristics of low permeability sandstone reservoirs," *Advances in Geo-Energy Research*, vol. 2, no. 2, pp. 122–134, 2018.
- [32] L. D. Sun, C. H. Yin, C. Liu et al., "Geological characteristics and exploration significance of high-quality source rocks in Yingcheng Formation, Songliao Basin," *Acta Petrologica Sinica*, vol. 40, no. 10, pp. 1172–1179, 2019.
- [33] M. Wang, S. F. Lu, H. T. Xue, J. Wu, and D. W. Liu, "The effects of magmatic intrusions on the maturation of organic matter and its numerical simulation," *Acta Petrologica Sinica*, vol. 26, pp. 177–184, 2010.
- [34] Y. H. Cheng, S. Y. Wang, Y. Li et al., "Late Cretaceous–Cenozoic thermochronology in the southern Songliao Basin, NE China: New insights from apatite and zircon fission track analysis," *Journal of Asian Earth Sciences*, vol. 160, pp. 95–106, 2018.
- [35] K. S. Jackson, P. J. Hawkins, and A. J. R. Bennett, "Regional facies and geochemical, evaluation of southern Denison Trough," *The APEA Journal*, vol. 20, pp. 143–158, 1985.
- [36] F. F. Langford and M. M. Blanc-Valleron, "Interpreting Rock-Eval pyrolysis data using graphs of pyrolyzable hydrocarbons vs. total organic carbon (1)," *American Association of Petroleum Geologists Bulletin*, vol. 74, pp. 799–804, 1990.
- [37] K. E. Peters, "Guidelines for evaluating petroleum source rock using programmed pyrolysis," *AAPG*, vol. 70, pp. 318–329, 1986.
- [38] K. Jackson, P. Hawkins, and A. Bennett, "Regional facies and geochemical evaluation of the southern Denison Trough, Queensland," *The APPEA Journal*, vol. 20, pp. 143–158, 1980.
- [39] K. E. Peters and M. R. Cassa, "Applied source rock geochemistry," in *The Petroleum System—from Source to Trap*, L. B. Magoon and W. G. Dow, Eds., pp. 93–120, AAPG Memoir; American Association of Petroleum Geologists, Tulsa, OK, 1994.

## Research Article

# Fracability Evaluation Method and Influencing Factors of the Tight Sandstone Reservoir

Jiageng Liu,<sup>1</sup> Lisha Qu,<sup>1</sup> Ziyi Song,<sup>2</sup> Jing Li ,<sup>1</sup> Chen Liu,<sup>1</sup> Yongcun Feng ,<sup>3</sup> and Haihang Sun<sup>4</sup>

<sup>1</sup>China University of Petroleum (East China), Qingdao 266580, China

<sup>2</sup>CNOOC Research Institute Co., Ltd., Beijing 100028, China

<sup>3</sup>Research Institute of Exploration and Development, Tarim Oilfield Company, PetroChina, Korla, Xinjiang 84100, China

<sup>4</sup>China University of Petroleum (Beijing), Beijing 201149, China

Correspondence should be addressed to Jing Li; [lijing0681@163.com](mailto:lijing0681@163.com) and Yongcun Feng; [yfeng@cup.edu.cn](mailto:yfeng@cup.edu.cn)

Received 28 June 2021; Accepted 16 August 2021; Published 24 September 2021

Academic Editor: Andrew H. Manning

Copyright © 2021 Jiageng Liu et al. This is an open access article distributed under the Creative Commons Attribution License, which permits unrestricted use, distribution, and reproduction in any medium, provided the original work is properly cited.

Fracability evaluation is the basis of reservoir fracturing and fracturing zone optimization. The tight sandstone reservoir is characterized by low porosity and low permeability, which requires hydraulic fracturing to improve industrial productivity. In this study, a systematic model was proposed for the fracability evaluation of tight sandstone reservoirs. The rock mechanics tests and sonic tests demonstrated that tight sandstone reservoir is characterized by high brittleness, high fracture toughness, and weak development of natural fractures. Numerical simulation was used to analyze the change of reservoir parameters during hydraulic fracturing and the influence of in situ stress on fracture propagation. The results showed that when the horizontal stress anisotropy coefficient is small, natural fractures may lead hydraulic fractures to change direction, and complex fracture networks are easily formed in the reservoir. The horizontal stress anisotropy coefficient ranges from 0.23 to 0.52, and it is easy to produce fracture networks in the reservoir. A new fracability evaluation model was established based on the analytic hierarchy process (AHP). The fracability of tight sandstone reservoir is characterized by the fracability index (FI) and is divided into three levels. Based on the model, this study carried out fracability evaluation and fracturing zone optimization in the study area, and the microseismic monitoring results verified the accuracy of the model.

## 1. Introduction

With the increasing demand for oil and gas resources, the development of unconventional energy has gained more and more attention [1–3]. The unconventional gas reservoir is commonly defined as a reservoir with low permeability (less than 0.1 mD) [4]. Because of its low permeability, hydraulic fracturing is needed [5, 6]. Chong et al. [7] defined the reservoir fracability for the first time; that is, reservoir can be effectively fractured to increase production in the process of hydraulic fracturing. Fracability evaluation is the basis of hydraulic fracturing and fracturing zone optimization.

In fracability evaluation, it is crucial to determine the parameters affecting hydraulic fracturing. Rickman et al. [8] found that rocks with higher brittleness have higher elastic

modulus and lower Poisson's ratio. Some scholars [9, 10] used brittleness index to characterize the fracability of shale reservoir and found that the larger the brittleness index, the better the fracturing effect. However, further research showed that it is not comprehensive to characterize the reservoir fracability only by brittleness index, and there are other factors. Fracture toughness is another important parameter which reflects the energy consumed in the process of rock fracture. Sato and Hashida [11] considered the influence of fracture toughness in hydraulic fracturing and found that the higher the fracture toughness of reservoir, the more difficult it is to be fractured. Huang et al. [12] investigated the effects of rock inherent heterogeneity and grain size on hydraulic fracture initiation and propagation for different propagation regimes through two dimensional discrete element modelings.

Scholars [13, 14] found that fracability is affected by many factors, including not only the characteristics of rock but also the geological characteristics of reservoir. Natural fracture is a weak part of mechanics, which influences the generation and extension of hydraulic fracture [15]. Barani et al. [16] proposed a numerical model which can appropriately simulate two possibilities of the interaction (opening and crossing) of a hydraulic fracture with a natural fracture. Sanchez et al. [17] predicted three main possibilities of fracture interaction (arrest, opening, and crossing) and found that the most important parameters affecting fracture interaction are in situ stresses and the angle of approach between hydraulic fracture and natural fracture. Reservoir rocks and fluids are jointly affected by in situ stress. In situ stress and its anisotropy affect the generation and propagation of hydraulic fractures [18]. Zhu et al. [19] conducted laboratory experiments of hydraulic fracturing and found that as the angle between the direction of wellbore axis and the maximum horizontal stress increases, the fracture roughness, fracture continuity, and the number of secondary fractures increase. Yan et al. [20] found that as the angle between the direction of wellbore axis and the maximum horizontal stress increases, the pressures of fracture initiation and propagation grow. Rabbel et al. [21] found that the fracture opening and propagation mode are related to the magnitude of external stress anisotropy, and strongly anisotropic far-field stresses lead to highly directional connectivity, which may translate to anisotropic fracture permeability. Liu et al. [22] developed a novel fracability evaluation model of hydrate-bearing sediments integrating hydrate saturation, brittleness, stress anisotropy, and mineral composition.

As discussed above, the reservoir fracability is related to many factors, including elastic parameters, brittleness, fracture toughness, natural fractures, and external stress anisotropy. It is difficult to establish a fracability evaluation model considering all factors. On the other hand, in situ stress characteristics have a great influence on hydraulic fracturing, but the fracability study considering external stress anisotropy is very rare. Therefore, this study analyzed the influencing factors of fracability of tight sandstone reservoir based on logging data and laboratory tests and further studied the influence of in situ stress characteristics on hydraulic fracturing through numerical simulation. Finally, we proposed a new systematic model for the fracability evaluation of tight sandstone reservoirs.

## 2. Fracability Parameters

The parameters that affect the fracability were analyzed based on logging data and laboratory tests in this section, which provides the basis for subsequent hydraulic fracturing modeling and fracability evaluation.

**2.1. Geological Settings.** Block 4 of Junggar Basin is located in the Xinjiang Uygur Autonomous Region of China. The strata in this area are well developed and generally gentle, showing the characteristics of thick in the south and thin in the north, thick in the west, and thin in the east. The study area is located in the center of oil source and favorable direc-

tion of oil and gas migration, with high oil and gas abundance. The structure of the study area is shown in Figure 1.

The genesis of tight sandstone reservoir is complex, with low porosity, low permeability, complex pore structure, and secondary pore development. The exploration report shows that the average porosity of tight sandstone in the study area is 4.1%, and the permeability is 0.132~0.839 mD. Although the study area is rich in oil and gas reserves, trial production is not ideal. Conventional exploitation means cannot meet production requirements; so, hydraulic fracturing is needed.

### 2.2. Rock Mechanical Parameters

**2.2.1. Elastic Modulus and Poisson's Ratio.** This work used the sonic logging-based method to calculate the rock mechanical parameters of continuous formation, and the dynamic elastic parameters can be calculated using the transit time of P- and S-waves [23, 24]. Therefore, we carried out triaxial compression tests and sonic tests on 15 rock samples ( $\Phi 25 \times 50$  mm) in the study area. In order to obtain accurate dynamic and static parameter conversion formula, the confining pressure change range is 0-70 MPa. The purpose of the experiment is to measure the acoustic wave velocity corresponding to the elastic parameters of rock under different confining pressure. The comparison of some cores before and after the experiment is shown in Figure 2. It can be seen that the rocks have undergone shear failure. The elastic modulus, Poisson's ratio, and wave velocity under different confining pressures were measured. The results are shown in Table 1, and the stress-strain curves are shown in Figure 3.

It can be seen that with the increase in confining pressure, elastic modulus increases, Poisson's ratio decreases, and wave velocity increases. The dynamic elastic modulus and dynamic Poisson's ratio are calculated using the transit time of P- and S-waves, as shown in Eqs. (1) and (2):

$$E_d = \frac{\rho(3\Delta t_s^2 - 4\Delta t_p^2)}{\Delta t_s^2(\Delta t_s^2 - \Delta t_p^2)} \times 9.299 \times 10^4, \quad (1)$$

$$\mu_d = \frac{0.5\Delta t_s^2 - \Delta t_p^2}{\Delta t_s^2 - \Delta t_p^2}, \quad (2)$$

where  $E_d$  is the dynamic elastic modulus, GPa,  $\mu_d$  is the dynamic Poisson ratio,  $\Delta t_p$  and  $\Delta t_s$  are the P-wave transit time and S-wave transit time,  $\mu\text{s}/\text{ft}$ , and  $\rho$  is the rock density,  $\text{g}/\text{cm}^3$ .

Fit the dynamic and static mechanical parameters and determine the fitting equation:

$$\begin{cases} E_s = 0.680E_d - 5.321, \\ \mu_s = 0.611\mu_d + 0.046, \end{cases} \quad (3)$$

where  $E_s$  is the static elastic modulus, GPa, and  $\mu_s$  is the static Poisson ratio.

Based on sonic logging data (P- and S-wave transit time in Figure 4), Eqs. (1)–(3) can be used to calculate the elastic



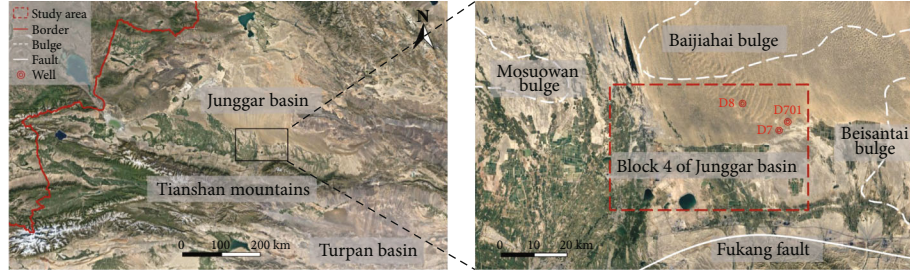


FIGURE 1: Structure of the study area.



FIGURE 2: Tight sandstone cores. (a) Initial state. (b) After failure.

TABLE 1: Results of triaxial compression tests and sonic tests.

Core number	Confining pressure/ MPa	Peak strength/ MPa	Static Poisson's ratio	Static elastic modulus/ GPa	P-wave velocity/ m·s <sup>-1</sup>	S-wave velocity/ m·s <sup>-1</sup>
1	0	54.6	0.258	8.26	3632	1994
2	10	106.9	0.256	11.74	3735	2052
3	10	140.8	0.219	16.28	4122	2400
4	20	136.0	0.185	15.26	3965	2442
5	20	142.9	0.174	14.48	3919	2427
6	30	164.9	0.168	18.90	4180	2630
7	30	172.4	0.188	17.84	4025	2447
8	40	173.4	0.203	16.72	4155	2470
9	40	179.8	0.205	17.33	4054	2428
10	50	194.6	0.217	18.80	4283	2521
11	50	186.3	0.216	17.84	4232	2503
12	60	206.4	0.188	19.84	4225	2547
13	60	210.5	0.198	19.53	4203	2524
14	70	237.3	0.197	22.16	4293	2604
15	70	242.4	0.202	23.53	4322	2634

modulus and Poisson's ratio of continuous formation, as shown in Figure 4.

2.2.2. *Brittleness*. Rock brittleness is an important parameter that affects the reservoir fracability. Obert and Duvall [25] described brittleness as a property of materials that fracture with a little or no plastic flow. In rock mechanics, brittleness is defined as the absence of a plastic deformation before final failure [26]. Brittleness index can be defined by the stress-strain data obtained from uniaxial or triaxial compression tests, that is, the ratio of elastic strain energy to total strain

energy at rock failure [9, 27]. According to the results of the triaxial compression tests, Eq. (4) is used to calculate the brittleness index of 15 cores.

$$B_I = \frac{\int_0^{\epsilon_0} \sigma_s \epsilon_s d\epsilon}{\int_0^{\epsilon_0} \sigma_l \epsilon_l d\epsilon}, \quad (4)$$

where  $B_I$  is the brittleness index,  $\epsilon_0$  is the strain at rock failure,  $\sigma_s$  and  $\epsilon_s$  are the stress and linear elastic strain of linear segment of stress-strain curve, respectively, and

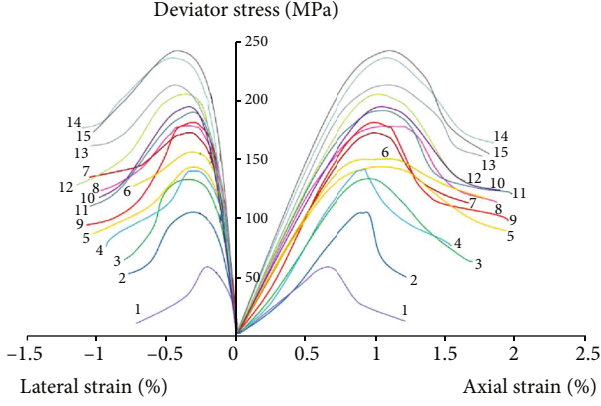


FIGURE 3: Stress-strain curves of 15 cores.

$\sigma_l$  and  $\varepsilon_l$  are the stress and strain before rock completely failure, respectively.

The sonic logging-based method is also used to calculate the brittleness index of continuous formation. The specific process will not be repeated. The results are shown in Figure 4. The brittleness index ranges from 0.50 to 0.83; so, the rock brittleness is high.

**2.2.3. Fracture Toughness.** The failure behavior of reservoir rock is essentially a macroscopic manifestation of energy dissipation and release. Fracture energy, especially postpeak fracture energy, reflects the energy consumed by fracture propagation and is an important factor in determining whether a rock fracture occurs. In this study, a triaxial compression test-based method Wang [28] was used to calculate the postpeak fracture energy and postpeak fracture energy density of 15 cores. The elastic modulus is an important factor affecting the fracture energy. So, we established the fitting formula of elastic modulus and postpeak fracture energy density and found that the fitting result (Figure 5) was good. Therefore, this study used postpeak fracture energy density to characterize the fracture toughness. The fitting equation is shown in Eq. (5).

$$W_{\text{post}} = 0.249E^2 + 3.155E, \quad (5)$$

where  $W_{\text{post}}$  is the postpeak fracture energy density,  $\text{N}\cdot\text{mm}\cdot\text{mm}^{-3}$ , and  $E$  is the elastic modulus, GPa.

Based on the calculation result of elastic modulus in Section 2.2.1, Eqs. (5) can be used to calculate the fracture toughness of continuous formation, as shown in Figure 4. The fracture energy density is mostly between 83.5 and 275.4  $\text{N}\cdot\text{mm}\cdot\text{mm}^{-3}$ ; so, the energy required for fracture propagation is large.

### 2.3. In Situ Stress Characteristics

**2.3.1. In Situ Stress.** The in situ stress was calculated based on logging data and the analysis results above, as shown in Eq. (6).

$$\begin{cases} \sigma_v = \bar{\rho}h_0g + \int_{h_0}^h \rho g dh, \\ \sigma_h = \frac{\mu}{1-\mu}(\sigma_v - \alpha P_p) + \beta_h(\sigma_v - \alpha P_p) + \alpha P_p, \\ \sigma_H = \frac{\mu}{1-\mu}(\sigma_v - \alpha P_p) + \beta_H(\sigma_v - \alpha P_p) + \alpha P_p, \end{cases} \quad (6)$$

where  $\sigma_v$  is the vertical stress, MPa,  $\bar{\rho}$  is the average density of overlying strata,  $\text{g}/\text{cm}^3$ ,  $h_0$  is the initial depth of target layer, m,  $\rho$  is the density of rock layer,  $\text{g}/\text{cm}^3$ ,  $g$  is the gravity acceleration,  $\text{m}/\text{s}^2$ ,  $\sigma_H$  and  $\sigma_h$  are the maximum and minimum horizontal principal stress, MPa, and  $\beta_H$  and  $\beta_h$  are the tectonic stress coefficients in the direction of the maximum and minimum horizontal principal stress. According to the result of field stress test,  $\beta_H$  and  $\beta_h$  are determined as 1.069 and 0.787, respectively;  $\alpha$  is the significant stress coefficient;  $P_p$  is the pore pressure of formation, MPa.

The in situ stress in different depths is shown in Figure 4.

**2.3.2. Horizontal Stress Anisotropy.** The horizontal principal stress anisotropy was characterized by the horizontal stress anisotropy coefficient.

$$K_h = \frac{\sigma_H - \sigma_h}{\sigma_h}. \quad (7)$$

The horizontal stress anisotropy coefficient in different depths is shown in Figure 4.

**2.4. Development Degree of Natural Fracture.** This study used rock rupture criterion to determine the shear fracture rate and tensile fracture rate of different depth strata and calculated the weighted sum of the two to obtain fracture development index, which can quantitatively characterizes the development degree of natural fractures in the study area.

The equation of shear fracture rate is shown in Eq. (8). The larger the shear fracture rate is, the stronger the shear failure degree of reservoir rock is.

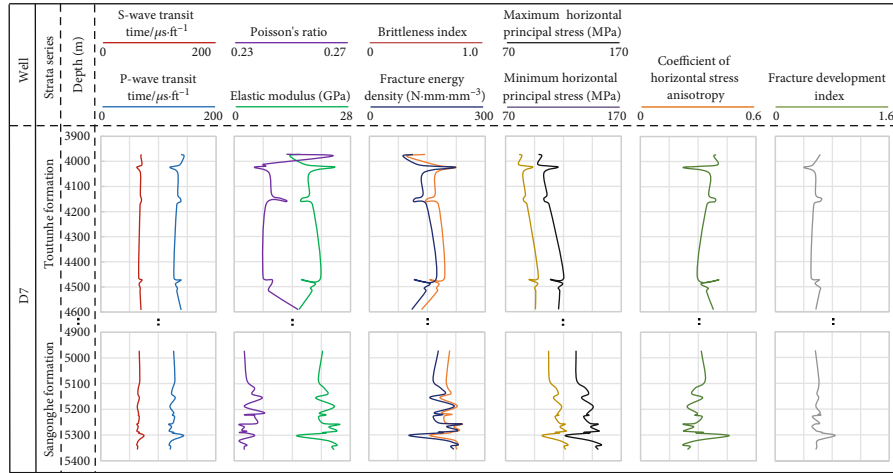
$$I_n = \frac{\tau}{|\tau|} = \frac{(\sigma_H - \sigma_h)}{2|\tau|} \sin 2\alpha, \quad (8)$$

where  $\tau$  is the shear stress on the rock failure surface, MPa,  $|\tau|$  is the shear strength of rock, MPa, and  $\alpha$  is the rock fracture angle,  $^\circ$ .

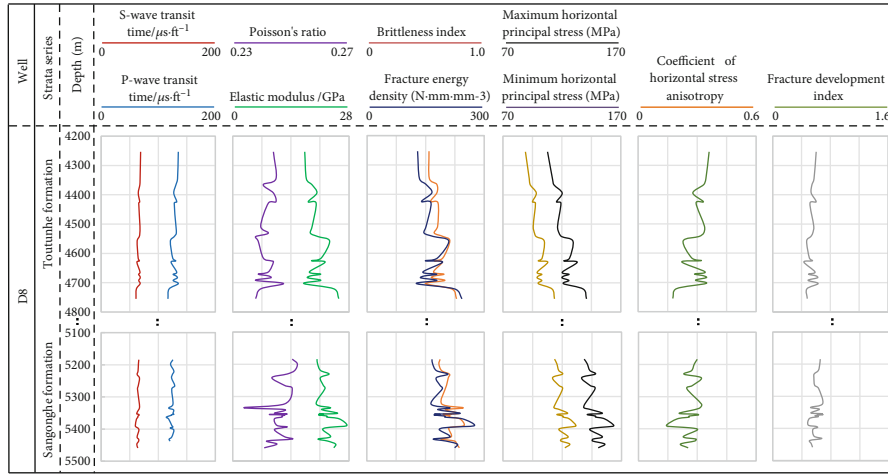
The equation of tensile fracture rate is shown in Eq. (9). The larger the tensile fracture rate is, the stronger the tensile failure degree of reservoir rock is.

$$I_t = \frac{\sigma_t}{|\sigma_t|} = \frac{(\sigma_H - \sigma_h)^2}{8(\sigma_H + \sigma_h)|\sigma_t|}, \quad (9)$$

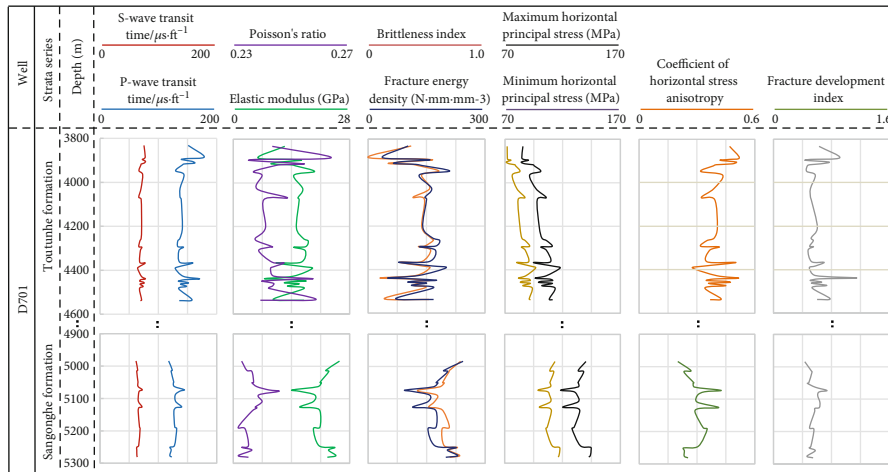
where  $\sigma_t$  is the tensile stress on the rock failure surface, MPa, and  $|\sigma_t|$  is the tensile strength of rock, MPa.



(a)



(b)



(c)

FIGURE 4: Fracability related parameters of three wells in the study area: (a) Well D7, (b) well D8, and (c) well D701.

The equation of fracture development index is shown in Eq. (10).

$$I = aI_n + bI_t, \quad (10)$$

where  $a$  and  $b$  are the proportions of shear fracture and tensile fracture, respectively. According to the statistical results of field data,  $a$  and  $b$  in the study area are 0.7 and 0.3, respectively.

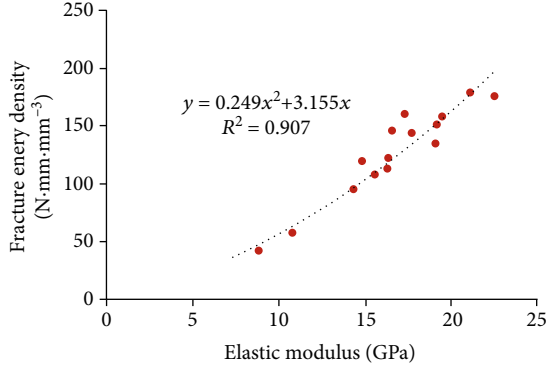


FIGURE 5: Fitting curve of elastic modulus and fracture energy density.

The fracture development index in different depths is shown in Figure 4. The results showed that the fracture development index ranges from 0.4 to 0.8, and most of the study area strata are slightly fracture-developed zones. The fracture development index of a few strata is greater than 0.8, which are fracture-developed zones.

**2.5. Selection and Analysis of Fracability Parameters.** The purpose of hydraulic fracturing is to produce a complex fracture system. The process of producing a fracture system includes the generation and propagation of fractures. These two parts determine the effect of hydraulic fracturing. Rocks with high brittleness are more prone to fracture. In this study, the brittleness index is characterized by the ratio of elastic strain energy to total strain energy at rock failure (Eq. (3)). Fracture toughness affects fracture propagation. In general, the higher the fracture toughness, the more difficult the propagation of fractures. The postpeak fracture energy density is used to characterize the fracture toughness of rock. The brittleness index in the study area ranges from 0.50 to 0.83, and the rock is relatively brittle. The fracture energy density mostly ranges from 83.5 to 275.4 n·mm·mm<sup>-3</sup>, which requires a large amount of energy for fracture propagation.

Natural fracture is a weak part of mechanics. On the one hand, natural fractures can cause stress changes near the wellbore. On the other hand, natural fractures can interact with induced fractures to affect the fracture propagation. The fracture development index mainly ranges from 0.4 to 0.8, and most of the strata are slightly fracture-developed zones.

The in situ stress anisotropy affects the opening and propagation mode of fractures, but the current researches are few and not thorough.

As discussed above, this study considered four factors when establishing the fracability evaluation model, including rock brittleness, fracture toughness, natural fractures, and horizontal stress anisotropy coefficient. Because the influence of horizontal stress anisotropy is uncertain, this study carried out a numerical simulation in Section 3.

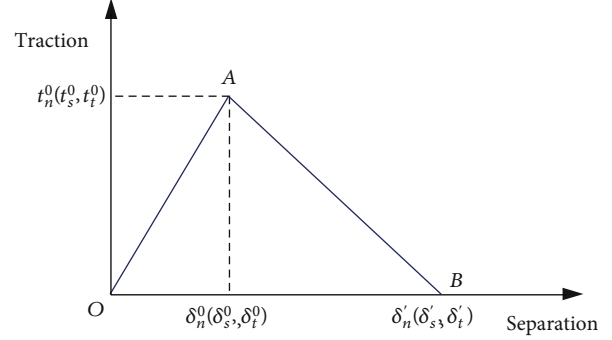


FIGURE 6: Bilinear constitutive model.

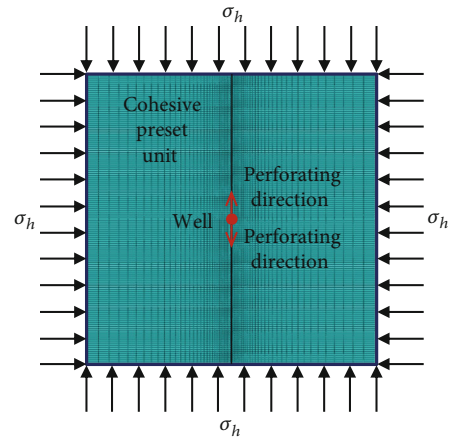


FIGURE 7: Finite element model and grid partition.

### 3. Numerical Simulation of Hydraulic Fracturing

Aiming at the problems analyzed in Section 2, this section carried out numerical simulation to analyze the changes of reservoir parameters during hydraulic fracturing and the influence of in situ stress on fracture propagation.

**3.1. Numerical Model of Hydraulic Fracturing.** Numerical simulation is carried out using the cohesive unit of ABAQUS software. The mechanical behavior of reservoir is described by the traction-separation criterion and bilinear constitutive relationships, and the model is shown in Figure 6.

In Figure 6, the bilinear constitutive model consists of a prepeak linear elastic stage and a postpeak stiffness decrease stage. The damage factor of the model is calculated by Eq. (11).

$$D = \frac{\delta'_n(\delta_n^{\max} - \delta_n^0)}{\delta_n^{\max}(\delta'_n - \delta_n^0)}, \quad (11)$$

where  $\delta_n^{\max}$  is the maximum displacement of the unit, m;  $\delta'_n$  is the displacement at unit failure, m;  $\delta_n^0$  is the displacement at the start of unit damage, m.

TABLE 2: Parameters of numerical simulation.

Parameters	Value	Parameters	Value
Porosity	10%	Permeability	0.1 mD
Elastic modulus	20GPa	Poisson's ratio	0.25
Tensile strength	8 MPa	Shear strength	20 MPa
Vertical stress	60 MPa	Pore pressure	40 MPa
Maximum horizontal principal stress	70 MPa	Minimum horizontal principal stress	50 MPa
Fluid viscosity	0.001 pa·s	Filtration coefficient	$1.0 \times 10^{-14}$ m/pa

In the postpeak stiffness decrease stage, the damage evolution process of material is shown in Eq. (12).

$$\begin{aligned}
 t_n &= \begin{cases} (1-D)\bar{t}_n, & \bar{t}_n \geq 0, \\ \bar{t}_n, & \bar{t}_n < 0, \end{cases} \\
 t_s &= (1-D)\bar{t}_s, \\
 t_t &= (1-D)\bar{t}_t,
 \end{aligned} \quad (12)$$

where  $\bar{t}_n$  is the normal stress, and  $\bar{t}_s$  and  $\bar{t}_t$  are tangential stresses.

The finite element model ( $50 \times 50$  m) is shown in Figure 7. The maximum and minimum horizontal principal stresses are set in the horizontal direction. The perforation position is in the center of the model. The COH24P is selected for cohesive unit.

Combined with the logging data and the experimental analysis in Section 2, the numerical simulation parameters are determined, as shown in Table 2.

**3.2. Whole Process of Hydraulic Fracturing.** Inject water at the perforation position, the injection rate is  $0.001 \text{ m}^2/\text{s}$ . The fracturing lasts for 100 seconds, and then the pump is shut down for 2400 seconds.

The distribution of injection pressure at different times is obtained by numerical simulation, as shown in Figure 8. For the convenience of observation, the deformation scaling factor is set to 100; that is, the crack element is expanded by 100 times. The white arrow represents the flow direction of fluid.

In Figure 8, the fracture is continuously extending along the direction of the maximum horizontal principal stress during water injection. The pressure around the fracture increases rapidly, the two tip areas of fracture are low stress areas, the two sides of fracture are high stress areas, and the closer to propagation area, the higher the stress is. After the pump is stopped, injection pressure gradually decreases, and the low stress areas near fracture tip disappear. When the pump is shut down for 2400 seconds, the regional stress gradually decreases from the fracture edge to the outside. In the whole process, the fluid first flows from the perforation to the low stress areas near fracture tip, and after the pump is shut down, the seepage direction is from the fracture to the surrounding.

The change law of injection pressure and fracture width in the fracturing process is researched, as shown in Figure 9.

In Figure 9, the generation and propagation of fracture during fracturing can be divided into the following four stages:

In the first stage, injection pressure increases rapidly at the moment of injection. At 2.1 seconds, injection pressure reaches the maximum value of 107.4 MPa, the reservoir is damaged, and the fracture width increases rapidly.

In the second stage, from 2.1 to 8.5 seconds, injection pressure gradually decreases to 61.5 MPa. Since the injection pressure is greater than the pressure required for fracture propagation, the fracture width increases, but the increase rate gradually decreases.

In the third stage, from 8.5 to 100.0 seconds, injection pressure is equal to the pressure required for fracture propagation; so, the fracture develops stably.

In the fourth stage, after stopping injection at 100.0 seconds, injection pressure decreases slowly, and the fracture width is stable. At this time, it is necessary to select appropriate proppant to support the fracture.

**3.3. Influence of Horizontal Stress Anisotropy on the Fracturing Effect.** The horizontal stress anisotropy is the most intuitive factor reflecting the characteristics of in situ stress. In this section, the influence of horizontal stress anisotropy on reservoir fracturing with and without considering natural fractures is simulated and analyzed.

**3.3.1. No Natural Fractures.** The model without considering natural fracture is the same as that in 3.1. The minimum horizontal principal stress is 50 MPa, and the maximum horizontal principal stress is 50 MPa, 60 MPa, 70 MPa, and 80 MPa, respectively, which means the coefficient of horizontal stress anisotropy is 0, 0.2, 0.4, and 0.6, respectively. The numerical simulation results at 100 seconds during injection are shown in Figure 10. (when  $\sigma_H = 70$  MPa,  $K_h = 0.4$ , the result is shown in Figure 8(d).)

As shown in Figure 10, with the increase of horizontal stress anisotropy coefficient, the distributions of injection pressure have little change, and the fractures all extend in a single direction. The fracture width of the perforation location is extracted, as shown in Figure 11. There is little difference in fracture width under different horizontal stress anisotropy coefficients.

Therefore, the influence of horizontal stress anisotropy on fracturing effect is minimal when natural fractures are not considered.

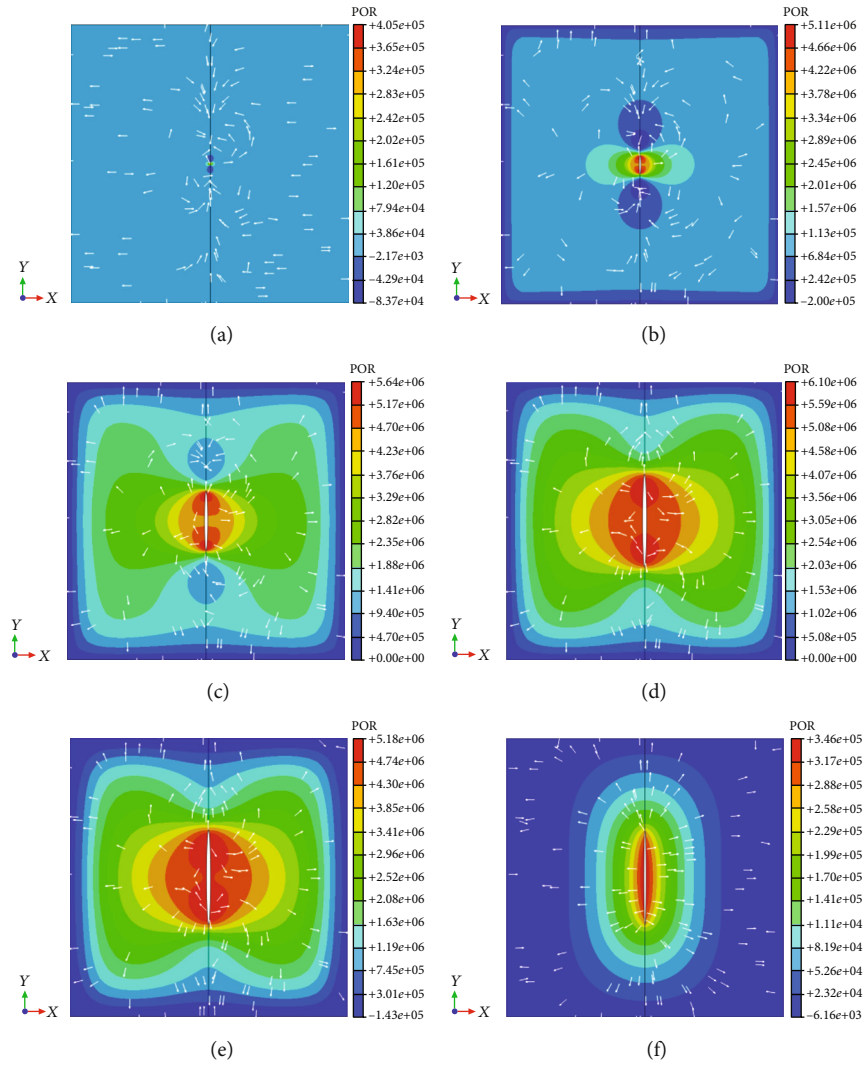


FIGURE 8: Injection pressure nephogram: (a) 0.10 s during injection, (b) 9.70 s during injection, (c) 50.46 s during injection, (d) 100 s during injection, (e) 5.13 s after injection stop, and (f) 2400 s after injection stop.

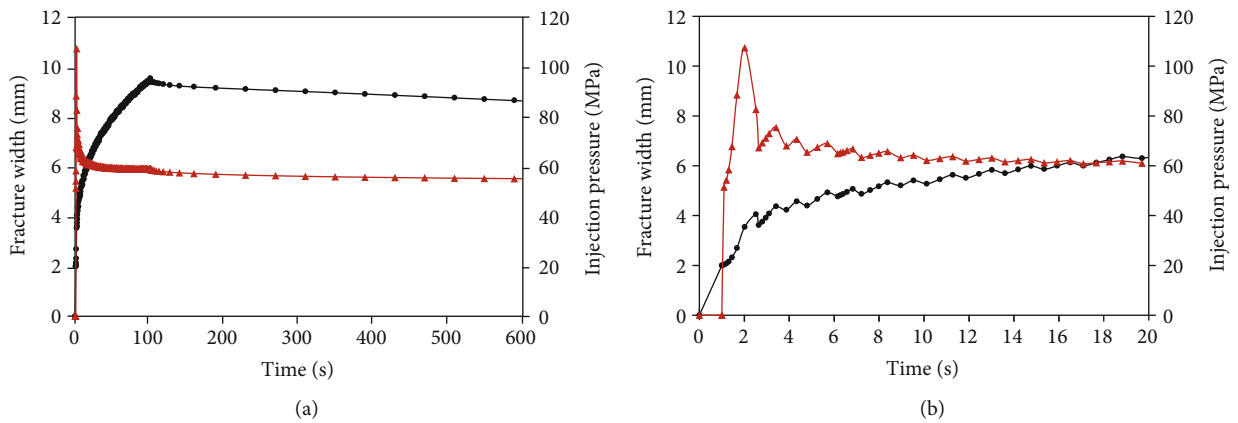


FIGURE 9: Variation curve of injection pressure and fracture width. (a) 0 ~ 600 s. (b) 0 ~ 20s.

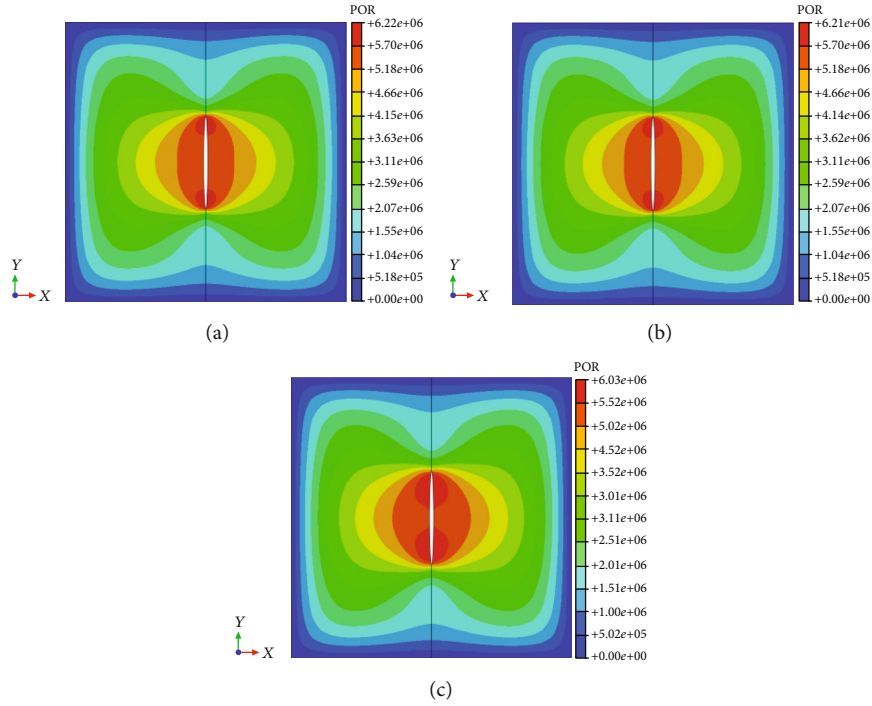


FIGURE 10: Injection pressure nephogram under different in situ stress conditions. (a)  $\sigma_H = 50$  MPa,  $K_h = 0$ . (b)  $\sigma_H = 60$  MPa,  $K_h = 0.2$ . (c)  $\sigma_H = 80$  MPa,  $K_h = 0.6$ .

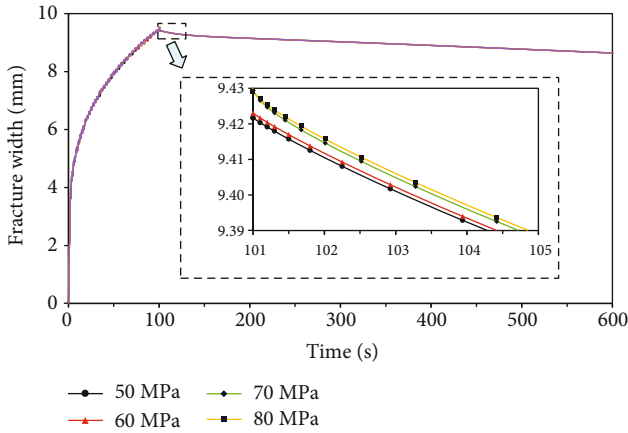


FIGURE 11: Variation curve of fracture width under different horizontal stress anisotropy coefficients.

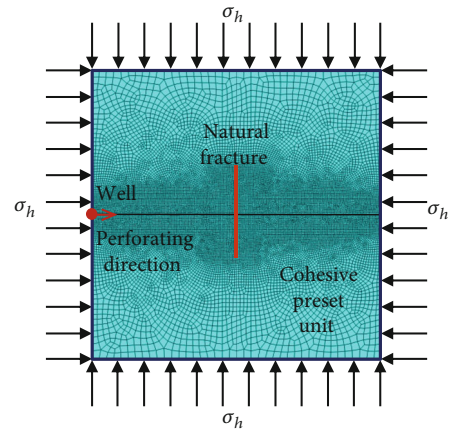


FIGURE 12: Finite element model considering natural fracture.

3.3.2. *Considering Natural Fractures.* The model considering natural fracture is shown in Figure 12. The fracturing time is 150 s, and the deformation scaling factor is 50. Other parameters are the same as the model in 3.1.

- (1) Condition 1: the maximum and minimum horizontal principal stresses are 70 MPa and 50 MPa, respectively, which means the horizontal stress anisotropy coefficient is 0.4. Figure 13 shows the process of fracture propagation. At the beginning of injection, the fracture propagates along the direction of maximum horizontal principal stress, and the distribution of injection pressure is similar to that without

considering natural fractures. At 115.60 seconds, the hydraulic fracture intersects with the natural fracture, and the stress at the intersection increases gradually. Then, the hydraulic fracture passes through the natural fracture and continues to extend along the maximum horizontal principal stress direction. Injection pressure is low at the tip and high on both sides

- (2) Condition 2: the maximum and minimum horizontal principal stresses are both 50 MPa, which means the horizontal stress anisotropy coefficient is 0. Figure 14 shows the process of fracture propagation. At the beginning of injection, the fracture propagates

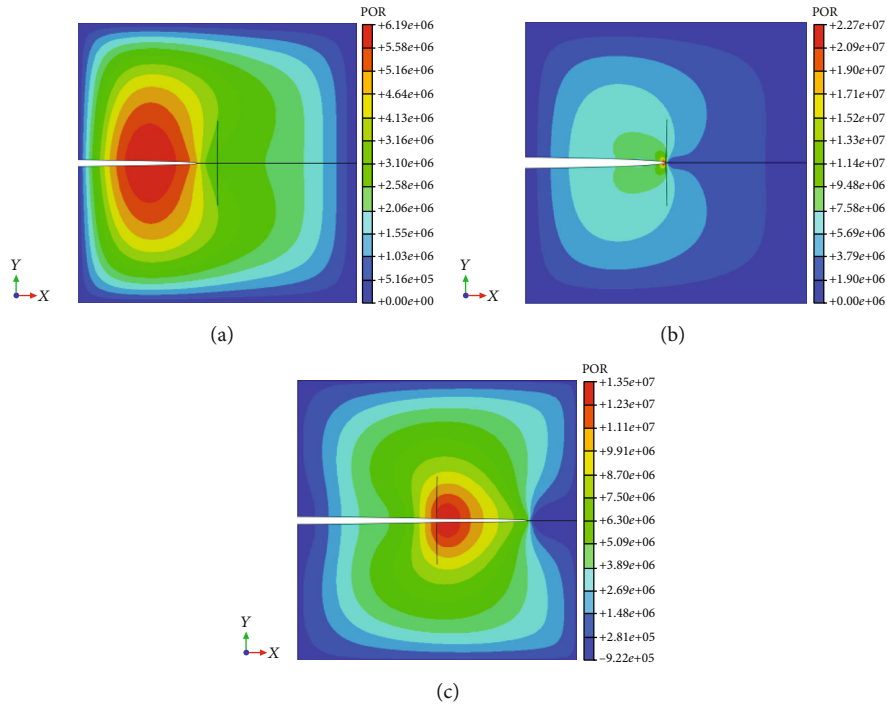


FIGURE 13: Injection pressure and fracture form under condition 1. (a) 60.12 s during injection. (b) 115.60 s during injection. (c) 150.00 s during injection.

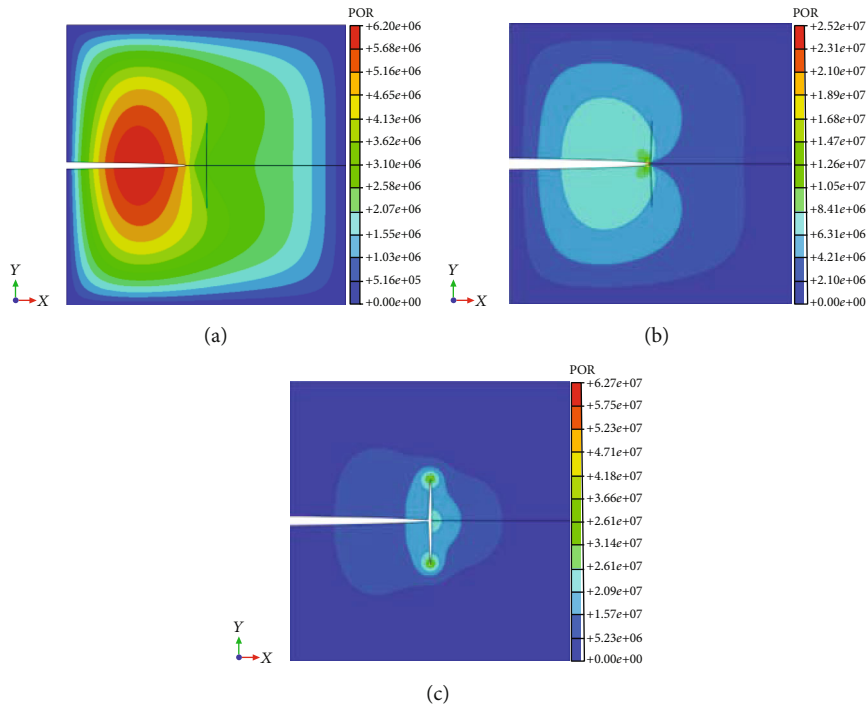


FIGURE 14: Injection pressure and fracture form under condition 2. (a) 60.12 s during injection. (b) 116.70 s during injection. (c) 150.00 s during injection.

along the direction of maximum horizontal principal stress. At 116.70 seconds, the hydraulic fracture intersects with the natural fracture, and the stress at the intersection increases gradually. Then, the nat-

ural fracture opens, and the hydraulic fracture propagates forward along the natural fracture direction. The fracture tip is a high stress area, and the stress in other parts decreases



In conclusion, when considering the influence of natural fractures, different in situ stress conditions have a greater impact on the propagation of hydraulic fracture. When the horizontal stress anisotropy coefficient is large, natural fracture has a little influence on the propagation of hydraulic fracture. Hydraulic fracture is easy to pass through natural fracture and continue to extend along the direction of the maximum horizontal principal stress. When the horizontal stress anisotropy coefficient is small, hydraulic fracture will not extend along the direction of the maximum horizontal principal stress after intersecting with natural fracture, but along the path of natural fracture. In other words, natural fracture is easy to induce the direction of hydraulic fracture to change, thus forming staggered fractures. In practice, there are many natural fractures in the reservoir. Therefore, the smaller the horizontal stress anisotropy coefficient is, the more complex fracture network forms in the reservoir during hydraulic fracturing.

#### 4. Evaluation of Fracability of Tight Sandstone Reservoir

**4.1. Evaluation Model.** This work determines the weight of each influencing factor in fracability evaluation by analytic hierarchy process (AHP) [29] and establishes the fracability evaluation model of tight sandstone reservoir.

**4.1.1. Establishment of the Hierarchical Structure Model.** The problems to be solved are divided into disjoint levels. The factors in the criteria layer are independent of each other, serving the target layer and restricting the index layer, as shown in Figure 15.

**4.1.2. Normalization of Parameters.** Since each parameter has different dimensions, values, and ranges, the parameters are standardized first. The range transformation method is used to normalize the brittleness index, fracture energy density, horizontal stress anisotropy coefficient, and fracture development index.

Brittleness index and fracture development index are positive indexes. The larger the value is, the more advantageous it is for reservoir fracturing. The calculation formula is shown in Eq. (13).

$$S = \frac{X - X_{\min}}{X_{\max} - X_{\min}}, \quad (13)$$

where  $S$  is the normalized parameter value,  $X_{\max}$  and  $X_{\min}$  are the maximum and minimum value of parameters, respectively, and  $X$  is the parameter value of the target interval.

Horizontal stress anisotropy coefficient and fracture energy density are the negative indexes. The larger the value is, the more disadvantageous it is for reservoir fracturing. The calculation formula is shown in Eq. (14).

$$S = \frac{X_{\max} - X}{X_{\max} - X_{\min}}. \quad (14)$$

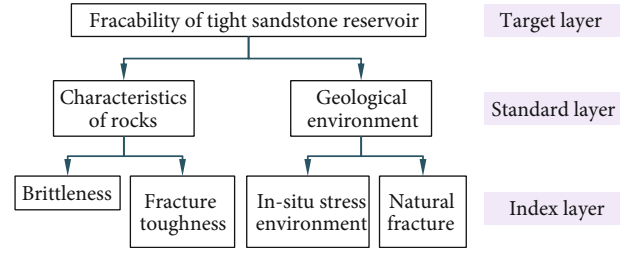


FIGURE 15: Hierarchical structure model.

**4.1.3. Construction of Judgment Matrix.** All the elements that affect the final goal are layered and constrained by the hierarchical model. Assuming that the elements of upper layer are the criteria, a comparison scale  $a_{ij}$  can be used to express the relative importance of factor  $i$  and factor  $j$  in the next level, where  $1 < a_{ij} < 9$ ,  $a_{ij} = 1/a_{ji}$ , and  $a_{ii} = 1$ . The matrix composed of  $a_{ij}$  is called judgment matrix  $A$ .

$$A = \begin{bmatrix} 1 & a_{12} & \cdots & a_{1n} \\ a_{21} & 1 & \cdots & a_{2n} \\ \cdots & \cdots & 1 & \cdots \\ a_{n1} & a_{n2} & \cdots & 1 \end{bmatrix}. \quad (15)$$

Determine the relative importance of each two parameters by establishing a comparison matrix. The judgment matrix is established according to comparison matrix, and the weight of each parameter can be solved. However, this weight has the disadvantage of strong subjectivity. Therefore, the entropy method is used to modify the weights obtained by AHP [30]. The revised judgment matrix is shown in Table 3.

The weight of each parameter is determined according to judgment matrix, as shown in Eqs. (16)-(19).

$$\tilde{A}_{ij} = \left( \frac{a_{ij}}{\sum_{i=1}^n a_{ij}} \right), \quad (16)$$

$$\tilde{W} = \left( \sum_{j=1}^n \frac{a_{1j}}{\sum_{i=1}^n a_{ij}}, \sum_{j=1}^n \frac{a_{2j}}{\sum_{i=1}^n a_{ij}}, \dots, \sum_{j=1}^n \frac{a_{nj}}{\sum_{i=1}^n a_{ij}} \right)^T, \quad (17)$$

$$W = (w_1, w_2, \dots, w_n)^T. \quad (18)$$

The maximum eigenvalue of matrix  $A$  is

$$\lambda_{\max} = \frac{1}{n} \sum_{i=1}^n \frac{(AW)_i}{w_i}. \quad (19)$$

The weights of brittleness index, fracture energy density, horizontal stress anisotropy coefficient, and fracture development index are 0.42, 0.23, 0.23, and 0.12, respectively, and the maximum eigenvalue of judgment matrix is 4.012.

TABLE 3: Judgment matrix of fracability index.

A	Brittleness index	Fracture energy density	Horizontal stress anisotropy coefficient	Fracture development index
Brittleness index	1	2	2	3
Fracture energy density	1/2	1	1	2
Horizontal stress anisotropy coefficient	1/2	1	1	2
Fracture development index	1/3	1/2	1/2	1

TABLE 4: Fracability classification of tight sandstone reservoir.

Reservoir type	Brittleness index	Fracture energy density	Horizontal stress anisotropy coefficient	Fracture development index	Fracability index	Fracability degree
I	0.5 ~ 1	0.7 ~ 1	0.6 ~ 1	0.5 ~ 1	0.569 ~ 1	High
II	0.3 ~ 0.5	0.5 ~ 0.7	0.4 ~ 0.6	0.3 ~ 0.5	0.369 ~ 0.569	Moderate
III	0 ~ 0.3	0 ~ 0.5	0 ~ 0.4	0 ~ 0.3	0 ~ 0.369	Low

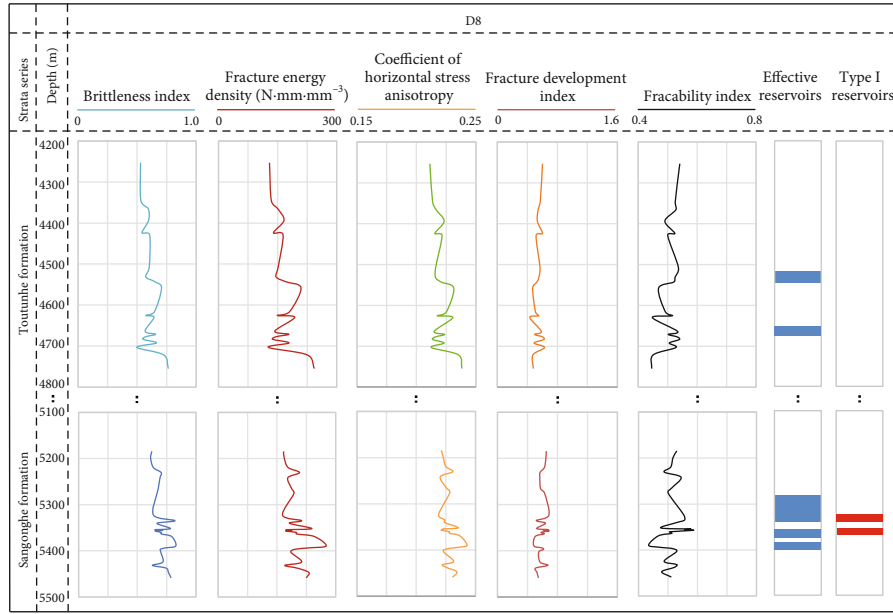


FIGURE 16: Fracability evaluation and fracturing zone optimization of well D8.

4.1.4. *Consistency Check.* To verify the rationality of  $a_{ij}$ , the consistency check of parameter weight is carried out.

$$CI = \frac{\lambda_{\max} - n}{n - 1}, CR = \frac{CI}{RI}, \quad (20)$$

where CI is the consistency index, RI is the average random consistency index, and when  $n = 4$ ,  $RI = 0.89$ ; CR is the consistency proportion, and the smaller the value is, the better the consistency of the parameter weight is, which is generally bounded by 0.1.

The results showed that  $CI = 0.004$  and  $CR = 0.0045 \leq 0.1$ , which met the requirements.

4.1.5. *Characterization and Classification of Fracability.* Fracability index (FI) is used to characterize the fracability of tight sandstone reservoir:

$$FI = 0.42B_{rit} + 0.23W_{post} + 0.23K_h + 0.12I, \quad (21)$$

where  $B_{rit}$  is the brittleness index,  $W_{post}$  is the fracture energy density,  $K_h$  is the horizontal stress anisotropy coefficient, and  $I$  is fracture development index. All of them are normalized values.

This work divides the fracability of tight sandstone reservoir into three grades, as shown in Table 4. The reservoirs with fracability index greater than 0.569 are classified as type I reservoirs, which have high brittleness, poor fracture

TABLE 5: The lower limit of the physical property of the Jurassic in the study area.

Strata series	Method	Cutoff of porosity/%	Cutoff of permeability/mD
Toutunhe Formation	Logging interpretation method	4.22	0.14
	Empirical statistics method	4.30	0.14
	Average	4.26	0.14
Sangonghe Formation	Logging interpretation method	3.71	0.11
	Empirical statistics method	3.57	0.12
	Average	4.64	0.12

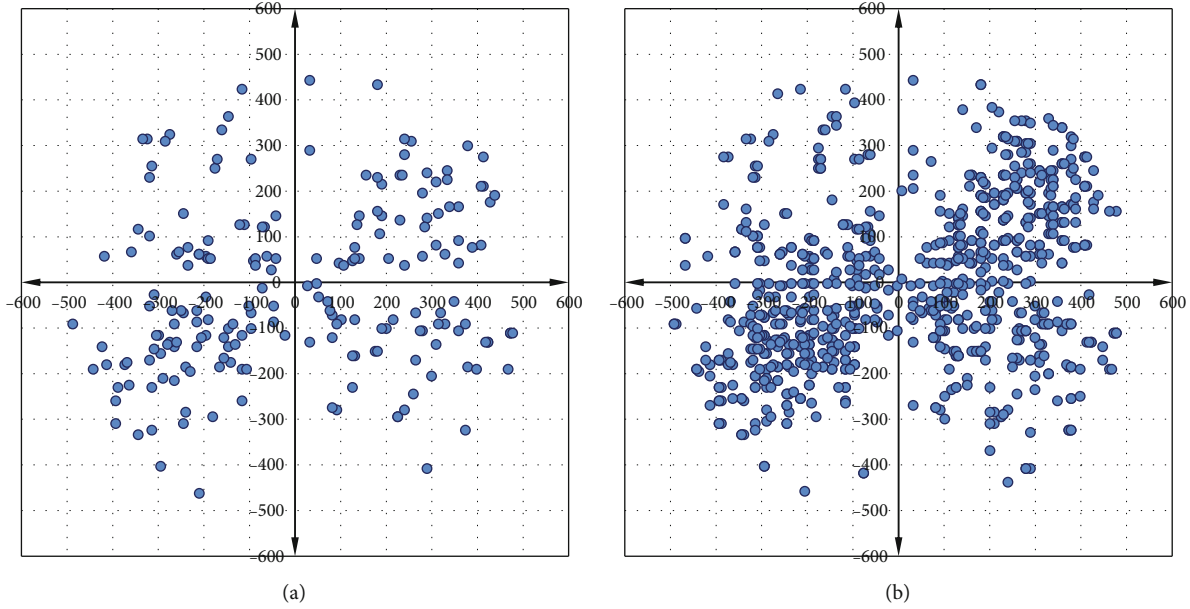


FIGURE 17: The microseismic point map of well D8. (a) Initial stage of hydraulic fracturing. (b) After hydraulic fracturing completed.

toughness, small horizontal stress anisotropy, and relatively developed fractures. The reservoirs with fracability index between 0.369 and 0.569 are classified as type II reservoirs, which should be reformed by increasing pressure or other methods. The reservoirs with fracability index less than 0.369 are classified as type III reservoirs, which are difficult to be fractured.

**4.2. Engineering Application and Model Validation.** Well D8 was taken as an example, and the model established in this paper was used to evaluate the fracability. The result of microseismic monitoring verified the accuracy of the model.

**4.2.1. Fracability Evaluation.** The fracability index in different depths of well D8 is shown in Figure 16. According to the classification of fracability, reservoirs with fracability index greater than 0.569 are type I reservoirs, which are marked in red in Figure 16.

**4.2.2. Selection of the Effective Reservoir.** Effective reservoir refers to the reservoir that can store and percolate fluid (hydrocarbon or formation water) and produce oil and gas with industrial value. The petrophysical cutoff of the effective reservoir in the study area is determined by logging interpretation method and empirical statistics method, as

shown in Table 5. Reservoirs with porosity and permeability greater than the petrophysical cutoff are effective reservoirs, which are marked in blue in Figure 16.

**4.2.3. Optimization of Fracturing Zone.** In Figures 16, 5120-5330 m and 5350-5365 m of well D8 have high fracability and are effective reservoirs, which can be regarded as the preferred fracturing zones.

**4.2.4. Model Validation.** In order to verify the correctness of the fracability evaluation model, we use microseismic monitoring to observe the fracturing effect. Microseismic monitoring is an effective method to study the characteristics of hydraulic fractures. Microseismicity is the occurrence of microearthquakes events caused by the injection of fluid into the borehole [31, 32]. Hydraulic fracturing was carried out in 5350-5365 m interval of well D8. The results of real-time microseismic monitoring before and after fracturing are compared, as shown in Figure 17.

In Figure 17, some northeast trending fractures occurred after hydraulic fracturing. Therefore, the purpose of fracturing is achieved, and the fracturing effect is good, which verifies the accuracy of the fracability evaluation model.

## 5. Conclusions

A new systematic model for fracability evaluation of tight sandstone reservoir has been proposed in this study. It provides technical support for the exploration and development of tight oil and gas.

- (i) Based on the triaxial compression tests and sonic tests, the parameters that affect fracability were analyzed. The brittleness index ranges from 0.50 to 0.83, and the rock is relatively brittle. The fracture energy density mostly ranges from 83.5 to 275.4 n-mm-mm<sup>-3</sup>, which requires a large amount of energy for fracture propagation. The horizontal stress anisotropy coefficient ranges from 0.23 to 0.52, which is easy to form fracture network. The fracture development index mainly ranges from 0.4 to 0.8, and most of the strata are slightly fracture developed zones
- (ii) Numerical simulation was used to analyze the changes of reservoir parameters during hydraulic fracturing and the influence of in situ stress on fracture propagation. When the horizontal stress anisotropy coefficient is large, the hydraulic fracture is easy to pass through the natural fracture and continues to extend along the direction of the maximum horizontal principal stress. When the horizontal stress anisotropy coefficient is small, the natural fracture is easy to induce the hydraulic fracture direction to change, and complex fracture networks are easily formed in the reservoir
- (iii) A new fracability evaluation model of tight sandstone reservoir was established based on the analytic hierarchy process (AHP). The reservoir fracability is characterized by the fracability index (FI) and is divided into three levels. Based on the model, 5120-5330 m and 5350-5365 m of well D8 are selected as fracturing zones. The results of micro-seismic monitoring verify the accuracy of the model

## Data Availability

Data are available upon request.

## Conflicts of Interest

The authors declare that they have no conflicts of interest.

## Acknowledgments

The research described in this paper was financially supported by the National Natural Science Foundation of China (41972138) and the National Great Science Fund of China (ZD2019-183-007 and 2016ZX05002-002).

## References

- [1] Q. Feng, S. Xu, X. Xing, W. Zhang, and S. Wang, "Advances and challenges in shale oil development: a critical review," *Advances in Geo-Energy Research*, vol. 4, no. 4, pp. 406–418, 2020.
- [2] J. D. Hughes, "Energy: a reality check on the shale revolution," *Nature*, vol. 494, pp. 307–308, 2013.
- [3] J. Li, L. Zhang, F. Yang, and L. Sun, "Positive measure and potential implication for heavy oil recovery of dip reservoir using SAGD based on numerical analysis," *Energy*, vol. 193, p. 116582, 2020.
- [4] S. A. Holditch, "Tight gas sands," *Journal of Petroleum Technology*, vol. 58, no. 6, pp. 86–93, 2006.
- [5] L. Britt, "Fracture stimulation fundamentals," *Journal of Natural Gas Science and Engineering*, vol. 8, pp. 34–51, 2012.
- [6] L. Hu, A. Ghassemi, J. Pritchett, and S. Garg, "Characterization of laboratory-scale hydraulic fracturing for EGS," *Geothermics*, vol. 83, p. 101706, 2020.
- [7] K. K. Chong, W. V. Grieser, A. Passman, H. C. Tamayo, N. Modeland, and B. E. Burke, "A completions guide book to shale-play development: a review of successful approaches toward shale-play stimulation in the last two decades," in *Canadian Unconventional Resources and International Petroleum Conference*, Calgary, Canada, 2010.
- [8] R. Rickman, M. J. Mullen, J. E. Petre, W. V. Grieser, and D. Kundert, "A practical use of shale petrophysics for stimulation design optimization: all shale plays are not clones of the Barnett Shale," in *SPE Annual Technical Conference and Exhibition*, Denver, USA, 2008.
- [9] R. Gholami, V. Rasouli, M. Sarmadivaleh, V. Minaeian, and N. Fakhari, "Brittleness of gas shale reservoirs: a case study from the North Perth basin, Australia," *Journal of Natural Gas Science and Engineering*, vol. 33, pp. 1244–1259, 2016.
- [10] I. Rahimzadeh Kivi, M. Zare-Reisabadi, M. Saemi, and Z. Zamani, "An intelligent approach to brittleness index estimation in gas shale reservoirs: a case study from a western Iranian basin," *Journal of Natural Gas Science and Engineering*, vol. 44, pp. 177–190, 2017.
- [11] K. Sato and T. Hashida, "Fracture toughness evaluation based on tension-softening model and its application to hydraulic fracturing," *Pure and Applied Geophysics*, vol. 163, pp. 1073–1089, 2006.
- [12] L. Huang, J. Liu, F. Zhang, E. Dontsov, and B. Damjanac, "Exploring the influence of rock inherent heterogeneity and grain size on hydraulic fracturing using discrete element modeling," *International Journal of Solids and Structures*, vol. 176–177, pp. 207–220, 2019.
- [13] J. Li, X. Li, H. Zhan et al., "Modified method for fracability evaluation of tight sandstones based on interval transit time," *Petroleum Science*, vol. 17, pp. 477–486, 2020.
- [14] A. Suboyin, M. M. Rahman, and M. Haioun, "Hydraulic fracturing design considerations, water management challenges and insights for Middle Eastern shale gas reservoirs," *Energy Reports*, vol. 6, pp. 745–760, 2020.
- [15] F. Zhang, B. Damjanac, and S. Maxwell, "Investigating hydraulic fracturing complexity in naturally fractured rock masses using fully coupled multiscale numerical modeling," *Rock Mechanics and Rock Engineering*, vol. 52, no. 12, pp. 5137–5160, 2019.
- [16] O. R. Barani, N. G. Haghghat, and P. Salmani, "Detailed description of the geomechanical interaction between a cohesive hydraulic fracture and a natural fracture in saturated poroelastic media," *Geotechnical and Geological Engineering*, vol. 38, no. 2, pp. 1689–1705, 2020.

- [17] E. C. M. Sanchez, J. A. R. C. Msc, and D. Roehl, "Numerical simulation of three-dimensional fracture interaction," *Computers and Geotechnics*, vol. 122, p. 103528, 2020.
- [18] S. E. Saberhosseini, R. Keshavarzi, and K. Ahangari, "A new geomechanical approach to investigate the role of in-situ stresses and pore pressure on hydraulic fracture pressure profile in vertical and horizontal oil wells," *Geomechanics and Engineering*, vol. 7, no. 3, pp. 233–246, 2014.
- [19] H. Zhu, J. Deng, S. Liu et al., "Hydraulic fracturing experiments of highly deviated well with oriented perforation technique," *Geomechanics and Engineering*, vol. 6, no. 2, pp. 153–172, 2014.
- [20] C. Yan, X. Ren, Y. Cheng et al., "An experimental study on the hydraulic fracturing of radial horizontal wells," *Geomechanics and Engineering*, vol. 17, no. 6, pp. 535–541, 2019.
- [21] R. Rabbel, K. Mair, O. Galland, C. Grühser, and T. Meier, "Numerical modeling of fracture network evolution in organic - rich shale with rapid internal fluid generation," *JGR Solid Earth*, vol. 125, article e2020JB019445, 2020.
- [22] X. Liu, W. Zhang, Z. Qu et al., "Feasibility evaluation of hydraulic fracturing in hydrate-bearing sediments based on analytic hierarchy process-entropy method (AHP-EM)," *Journal of Natural Gas Science and Engineering*, vol. 81, p. 103434, 2020.
- [23] E. Fjaer, R. M. Holt, P. Hordrud, A. M. Raaen, and R. Risnes, *Petroleum Related Rock Mechanics*, Elsevier, Kidlington, Oxford, UK, 2008.
- [24] R. Gholami, M. Rabiei, V. Rasouli, B. Aadnoy, and N. Fakhari, "Application of quantitative risk assessment in wellbore stability analysis," *Journal of Petroleum Science and Engineering*, vol. 135, pp. 185–200, 2015.
- [25] L. Obert and W. I. Duvall, *Rock Mechanics and the Design of Fractures in Rock*, John Wiley & Sons, New York, NY, USA, 1967.
- [26] J. C. Jaeger, N. G. W. Cook, and R. W. Zimmerman, *Fundamentals of Rock Mechanics*, Blackwell Publ, London, UK, 2007.
- [27] E. Kias, R. Maharidge, and R. Hurt, "Mechanical versus mineralogical brittleness indices across various shale plays," in *SPE Annual Technical Conference and Exhibition Held*, Houston, Texas, USA, 2015.
- [28] X. B. Wang, "Analysis of plastic deformation and fracture energy of rock specimen in uniaxial compression," *Chinese Journal of Rock Mechanics and Engineering*, vol. 24, no. 10, pp. 1735–1739, 2005.
- [29] M. Beynon, "DS/AHP method: a mathematical analysis, including an understanding of uncertainty," *European Journal of Operational Research*, vol. 140, no. 1, pp. 148–164, 2002.
- [30] R. Nagpal, D. Mehrotra, and P. Bhatia, "Usability evaluation of website using combined weighted method: fuzzy AHP and entropy approach," *International Journal of Systems Assurance Engineering and Management*, vol. 7, no. 4, pp. 408–417, 2016.
- [31] S. Shapiro, C. Dinske, and E. Rothert, "Hydraulic-fracturing controlled dynamics of microseismic clouds," *Geophysical Research Letters*, vol. 33, no. 14, article L14312, 2006.
- [32] S. Shi, Z. Liu, J. Feng, G. Feng, and M. Li, "Using 3D seismic exploration to detect ground fissure," *Advances in Geo-Energy Research*, vol. 4, no. 1, pp. 13–19, 2020.

## Research Article

# Numerical Study of the Effect of Perforation Friction and Engineering Parameters on Multicluster Fracturing in Horizontal Wells

Zixi Jiao,<sup>1</sup> Anlin Zhang,<sup>2</sup> Longhuan Du ,<sup>3</sup> Yang Yang,<sup>1</sup> and Hua Fan<sup>4</sup>

<sup>1</sup>Key Laboratory of Deep Underground Science and Engineering, Sichuan University, Ministry of Education, Chengdu 610065, China

<sup>2</sup>College of Water Resource and Hydropower, Sichuan University, Chengdu 610065, China

<sup>3</sup>College of Architecture and Environment, Sichuan University, Chengdu 610065, China

<sup>4</sup>Lingchuang Green House Construction Technology Co., Ltd., Chengdu 610065, China

Correspondence should be addressed to Longhuan Du; [longhuan\\_du@163.com](mailto:longhuan_du@163.com)

Received 8 July 2021; Revised 16 August 2021; Accepted 18 August 2021; Published 1 September 2021

Academic Editor: Steffen Berg

Copyright © 2021 Zixi Jiao et al. This is an open access article distributed under the Creative Commons Attribution License, which permits unrestricted use, distribution, and reproduction in any medium, provided the original work is properly cited.

Simultaneous multiple-fracture treatments in horizontal wellbores have become one of the key methods for economically and efficiently developing oil and gas resources in unconventional reservoirs. However, field data show that some perforation clusters have difficulty propagating fractures due to the internal mechanism of competing initiation and propagation among the fractures. In this paper, the physical mechanisms that influence simultaneous multiple-fracture initiation and propagation are investigated, and the effects of engineering parameters and in situ conditions on the nonuniform development of multiple fractures are discussed. A 3D fracture propagation model was established with ABAQUS to show the influence of the stress shadow effects and dynamic partitioning of the flow rate by simulating the propagation of multiple competing fractures generated in the perforation clusters. Based on the results of these simulations, simultaneous flow in multiple fractures can propagate evenly. Through adjusting the number of perforations in each cluster or the perforation diameter, the effect of the stress shadow can be significantly reduced by increasing the perforation friction, and the factors that affect the development of multiple fractures are changed, from the stress shadow effect to the dynamic partitioning of the flow rate. When the stress shadow effect is dominant, increasing the fracturing fluid viscosity promotes the uniform development of multiple fractures and increases the fracture width. When the dynamic partitioning of the flow rate is dominant, increasing the injection rate greatly affects the uniform development of multiple fractures.

## 1. Introduction

The hydraulic fracturing technique is a widely used well-stimulation technique to effectively and economically develop oil and gas resources in low-permeability unconventional reservoirs [1, 2]. Many field measurements, laboratory tests, and reservoir simulation studies [3–7] have proven that multicluster hydraulic fracturing and horizontal drilling are the key hydraulic fracturing methods. The advantage of multicluster fracturing over conventional hydraulic fracturing is that it allows multiple perforation clusters within a single stage to form several hydraulic fractures simultaneously

through a single pump, resulting in multiple fracture surfaces after fracturing fluid is pumped into the reservoir, thus achieving a larger effective reservoir volume. Bungler [4] believed that when the spacing of perforations was greater than 1.5 h, it was conducive to the uniform development of multiple fractures formed by multicluster fracturing. However, too large of a spacing of perforation clusters made it difficult to form a large effective reservoir volume and improve the ultimate reservoir recovery [8]. At the same time, engineering-analysis results indicated that when perforation cluster spacing was set too closely, multiple fractures had difficulty propagating evenly after initiation

simultaneously. Miller et al. [9] applied the surface tiltmeter fracture mapping method to quantify the fracture volume growth along several horizontal wells and found that the midlateral volume could not achieve the expected value of the perforation cluster design. Spain et al. [10] concluded that close cluster spacing is beneficial for well production, but if the spacing is too close, excessive induced stress causes fracture competition, resulting in the nonuniform development problems of difficult growth of fractures in the midlateral and excessive growth of fractures at both ends. To obtain a reasonable multiple-fracture treatment design and acceptable well production, a deep understanding of the competitive propagation mechanism of fractures during fracturing is urgently needed.

In recent years, increasing attention has been given to the mechanism of simultaneous propagation in multiple fractures in unconventional reservoirs. When multiple fractures propagate simultaneously, individual fracture can be created within each cluster, which is favourable to expand the stimulated reservoir volume. Some laboratory tests have been designed to simulate this process [11, 12]. El Rabaa [11] studied the effect of perforation cluster spacing on hydraulic fracturing through laboratory tests and found that when the main fracture appeared, the remaining fractures were difficult to develop completely. Zhu et al. [12] conducted hydraulic fracturing tests on concrete samples with oriented perforations and found that all fractures initiated from the perforation holes, but not all fractures were fully developed. Compared to tests, numerical simulation methods can better represent the reservoir in situ conditions and the nonlinear dynamic boundary problem, which is influenced by many factors, such as the Young modulus of the target layer, fracturing fluid viscosity, and pump rate [13]. Therefore, the numerical simulation method is suitable for simultaneous multiple-fracture propagation in horizontal wellbores in unconventional reservoirs. For example, based on the displacement discontinuity method, Olson [14] found that when the fracture spacing is small, even if the fluid is evenly distributed between the perforation clusters, middle fractures cannot develop. Cheng [15] demonstrated that when the cluster spacing is reduced to an inadequately small size, production is reduced, and fracture width is limited. With the help of the finite element method, Salimzadeh et al. [16] showed that the interaction between adjacent fractures leads to growth away from each other, which is weakened when the fracture spacing is large. Shin and Sharma [17] built a 3D geomechanical model to explore how various factors control the simultaneous propagation of multiple competing fractures in horizontal wells. Haddad and Sepehrnoori [18] simulated the arbitrary, solution-dependent initiation and propagation path of multiple fractures caused by multicluster hydraulic fracturing and found that different cluster spacings would lead to coalescing, growing parallel, or diverging multiple fractures. From the perspective of the continuum method, Zhao et al. [19] investigated when the spacing between perforations is reduced to a certain extent, the fracturing regions formed by the perforations coalesce after a period of development, and multiple perforations can be considered as a single perforation with a

larger injection rate. In previous studies, scholars found that perforation-cluster spacing, fracture height, target formation thickness, and pumping rate had significant influence on the simultaneous propagation of multiple fractures in a horizontal well [17].

There are two mechanisms of fracture mechanical interaction during the simultaneous propagation of multiple fractures. One is the stress shadow effect, and the other is the dynamic partitioning of the flow rate [20, 21]. Existing models [22–24] have explored the effect of each mechanism on the geometry of multiple fractures. For example, Guo et al. [22] established a 3D seepage-stress-damage coupled multifracture simultaneous propagation model to explore the stress field of multiple fractures with different cluster spaces. Yang et al. [23] built a pseudo-3D model based on the displacement discontinuity method (DDM) and found that perforation friction has an important effect on the dynamic partitioning of the flow rate. The influence of the stress shadow occurs when multiple competing fractures in horizontal wells propagate simultaneously. When fracturing fluid is pumped into multiple fractures, compressive stress that acts on adjacent fracture surfaces can increase the difficulty of multiple fracture propagation and even lead to the closure of the fractures. From the numerical simulation analysis, through a reasonable design, such as the reasonable perforation cluster spacing, the injection rate, and the fracturing fluid viscosity, the adverse effects of the stress shadow can be controlled. Then, the difficult propagation of the fractures along the midlateral and the overdevelopment of fractures at the heel and toe of wellbores can be avoided to a certain extent [25–27]. In addition, the in situ characteristics of the target reservoir, such as in situ stress, Young's modulus, and thickness, can also affect the results of multicluster fracturing with the same design parameters [28–30]. In most numerical studies, the fluid flow rate in each perforation was assumed to be constant, and only the influence of the stress shadow could be considered. However, due to the existence of friction, the flow rate allocated to each fracture affects the geometry of the fractures. Some researchers [31–33] have established a numerical model that can dynamically determine the split of the flow rate in the process of multicluster fracturing. The results showed that the dynamic partitioning of the flow rate has an important influence on the uniform propagation of multiple competing fractures. In actual engineering, to ensure production, it is often necessary to set a small cluster spacing, but the small cluster spacing causes strong stress interference between fractures; thus, it is difficult for some perforation clusters to play a role in stimulation. Therefore, it is necessary to design engineering parameters such as the fracturing fluid viscosity, injection rate, number of perforations in each perforation cluster, and perforation diameter to make multiple fractures propagate evenly. Different fracture designs have different mechanisms that govern the development of multiple fractures. However, few previous studies have comprehensively considered how to combine the effects of different operating parameters on fracture development with the dominant fracture mechanical interaction mechanism to improve the effectiveness of multicluster fracturing.

In this paper, ABAQUS software is used to build a novel 3D multicluster fracturing model that simulates the simultaneous propagation of multiple competing fractures and to investigate the effects of commonly used operating parameters on the uniform propagation of multiple fractures. Importantly, the dynamic partitioning of the flow rate due to the different fluid flow resistances and the stress interaction between the fractures due to the complex in situ conditions is considered in the model. The geometry of each fracture and the fluid flow into each fracture to promote the propagation of multiple fractures are obtained. The influence of fracturing fluid viscosity, injection rate, and perforation friction on the uniform development of multiple fractures is analysed comprehensively by using this model, and some suggestions to promote uniform multiple-fracture growth are proposed.

### 2. Physical Model

After the horizontal well is segmented, multicluster fracturing technology is used. Multicluster fracturing allows multiple perforation clusters in an injection stage of a horizontal well, and then, a fracture is generated in each cluster, increasing the stimulated reservoir volume (SRV) in a single stage after the fracturing fluid is pumped. The simplified physical model of multicluster fracturing within a stage is shown in Figure 1. As it is a complex process for multiple fracture propagation, the following assumptions are introduced:

- (1) The reservoir rock is regarded as an isotropic, poroelastic material
- (2) Each perforation cluster within a stage generates only a main fracture
- (3) Bungler [29] found that when the horizontal stress difference reached 2-3 MPa, the fracture plane bending phenomenon caused by stress shadow effects between adjacent fractures could be effectively suppressed. The fractures are assumed to be planar and vertical
- (4) The fracturing fluid is considered an incompressible Newtonian fluid, and the flow pattern of the fluid in the fractures is consistent with Poiseuille plate flow. In addition, the connection between the pipeline and the formation injection point is filled with fluid

Finally, based on the physical model, the geometry of multiple fractures affected by in situ stress conditions, the operation parameters, and the interaction between multiple competing fractures are discussed.

### 3. Model Geometry

The geometry of the model established in this paper is shown in Figure 2. The model is used to simulate the initiation and propagation of multiple competing fractures within a stage due to multicluster fracturing and consists of reservoirs, upper and lower barriers, a horizontal wellbore, and perforation

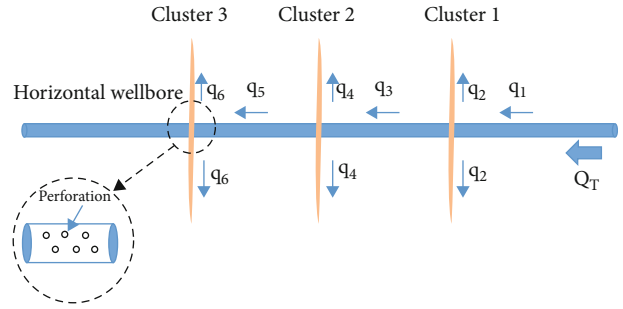


FIGURE 1: Schematic of multicluster fracturing within a stage.

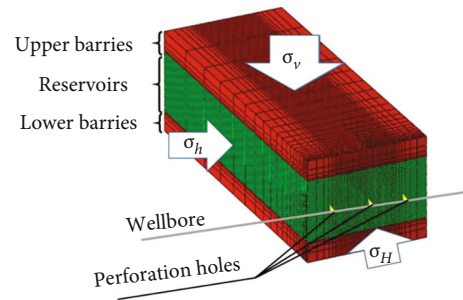


FIGURE 2: Schematic of fracture propagation model.

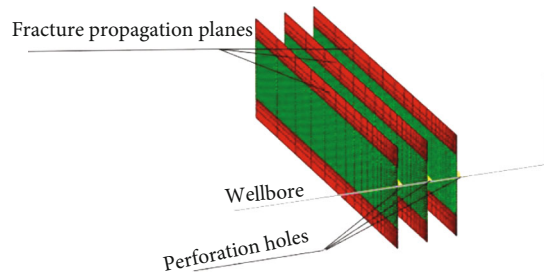


FIGURE 3: A plane of COH3D8P elements was embedded in the C3D8P elements at each perforation cluster to simulate fractures.

holes. Since the initiation and propagation of hydraulic fractures are symmetric on both sides of the wellbore, only one side of the wellbore is taken for modelling. C3D8P elements (8-node brick, trilinear displacement, and trilinear pore pressure) were used to model the reservoir as a porous elastic medium. The cohesive elements (COH3D8P) are embedded at each perforation cluster along the horizontal wellbore to determine the path of the hydraulic fractures to initiate and propagate in a direction perpendicular to the minimum horizontal principal stress, as shown in Figure 3. The FPC3D2 connector element is used to hydraulically connect the perforated clusters to force pressure continuity between the clusters, and pipe flow elements FP3D2 are used in the wellbore to describe the pressure drop due to frictional resistance in the wellbore. Fluid can enter the reservoir only through perforation clusters. The height of the hydraulic fractures is limited by the upper and lower barriers.

### 4. Mathematical Model

#### 4.1. Fluid Flow Model



**4.1.1. Fluid Flow in Fracture and Reservoir.** The flow of fluid within the cohesive elements consists of tangential flow rate and normal flow rate. The tangential flow rate represents fluid flow through the fractures, while the normal flow rate represents the fluid loss to the formation. The tangential flow of fluid within fractures was modelled using Reynold's equation [34, 35].

$$q = -\frac{w^3}{12\mu} \nabla p, \quad (1)$$

where  $q$  is the tangential flow rate,  $m^3/s$ ;  $\nabla p$  is the pressure gradient along the fracture,  $MPa/m$ ;  $w$  is the fracture aperture,  $m$ ; and  $\mu$  is the fracture viscosity,  $cp$ .

The normal flow represents fluid leak-off from the fracture to the formation and can be expressed by setting the fluid leak-off coefficient in the following equation:

$$\begin{cases} q_t = c_t(p_f - p_t), \\ q_b = c_b(p_f - p_b), \end{cases} \quad (2)$$

where  $q_t$  and  $q_b$  are the flow rates into the top and bottom surfaces,  $m^3/s$ , respectively;  $c_t$  and  $c_b$  are the leak-off coefficients of the top and bottom surfaces, respectively;  $p_f$  is the midface pressure,  $Pa$ ; and  $p_t$  and  $p_b$  are the pore pressures on the top and bottom surfaces, respectively.

**4.1.2. Fluid Distribution between Perforation Clusters.** Multi-cluster fracturing within a stage produces multiple competing fractures. When multiple fractures initiate and propagate simultaneously, the fracturing fluid enters each fracture. The dynamic partitioning of the flow rate of each fracture needs to be considered in the model according to the corresponding boundary conditions. When the wellbore storage effect is ignored, it is assumed that the fluid pressure at the inlet of each cluster is equal. In addition, the total injection rate is equal to the sum of the inflow rate of all clusters.

$$Q_{to} = \sum_{i=1}^N Q_i, \quad (3)$$

where  $Q_{to}$  is the sum of all fracture flow rates,  $m^3/s$ ;  $Q_i$  is the flow rate of fracturing fluid distributed in fracture  $I$ ,  $m^3/s$ ; and  $N$  is the number of perforations in each perforation cluster.

By analysing the data from the field experiments and laboratory tests, when the fracturing fluid pumped from the wellbore through the perforation entry to the hydraulic fracture tip, the total pressure dropped, which was due to wellbore friction and perforation-entry friction [36]. Finally, the treating pressure inside the fractures was different from the treating pressure inside the casing. Considering the influence of wellbore friction and perforation-entry friction on fluid flow, according to Kirchhoff's second law [36], the bottomhole treating pressure  $p_w$  is equal to the sum of the pressure  $p_{in}$  at the mouth of the fracture, pressure  $p_b$  caused

by fluid friction in the wellbore, and pressure  $p_f$  caused by fracture-entry friction.

$$p_w = p_{in} + p_b + p_f, \quad (4)$$

where  $p_w$  is the bottomhole treating pressure,  $MPa$ ;  $p_{in}$  is the pressure at the mouth of the fracture,  $MPa$ ;  $p_b$  is the pressure caused by fluid friction in the wellbore,  $MPa$ ; and  $p_f$  is the pressure caused by fracture-entry friction,  $MPa$ .

By using a pipe flow element (FP3D2) in the wellbore, the wellbore frictional pressure drop can be calculated using the Churchill method:

$$\begin{aligned} \Delta P - \rho g \Delta Z &= (C_L + K_i) \frac{\rho v^2}{2}, \\ C_L &= \frac{fL}{D_h}, \\ f &= 8 \left[ \left( \frac{8}{Re} \right)^{12} + \frac{1}{(A+B)^{1.5}} \right]^{1/12} \\ A &= \left[ -2.457 \ln \left( \left( \frac{7}{Re} \right)^{0.9} + 0.27 \left( \frac{K_s}{D_h} \right) \right) \right]^{16}, \\ B &= \left( \frac{37350}{Re} \right)^{16}, \end{aligned} \quad (5)$$

where  $\Delta P$  is the pressure difference at the nodes,  $MPa$ ;  $\Delta Z$  is the elevation difference at the nodes,  $m$ ;  $v$  is the fluid velocity in the pipe,  $m/s$ ;  $\rho$  is the fluid density,  $kg/m^3$ ;  $g$  is the acceleration due to gravity;  $C_L$  is the loss coefficient;  $f$  is the friction of the pipe;  $L$  is the length of the pipe,  $m$ ;  $K_i$  is a directional loss term;  $K_s$  is the roughness of the pipe; and  $D_h$  is the hydraulic diameter.

By using the connector element (FPC3D2), the perforation frictional pressure drop can be calculated according to the formula of Crump [32, 36].

$$p_f = 0.807249 \times \frac{\rho}{n^2 D_p^4 C^2} Q_i^2, \quad (6)$$

where  $n$  is the number of perforations in each perforation cluster;  $D_p$  is the diameter of perforation,  $m$ ; and  $C$  reflects the influence of perforation shape on perforation friction. When the perforation is intact, the value is generally 0.5~0.6, and when the perforation is completely eroded, the value is generally 0.95 [37].

**4.2. CZM Model.** Linear elastic fracture mechanics (LEFM) is one of the common criteria for fracture initiation and propagation. According to LEFM theory, when the stress intensity factor of the rock is greater than the fracture toughness, the fracture initiates and propagates. However, considering only the stress intensity factor makes it difficult to fully characterize the fracture propagation because LEFM does not consider the inelastic region near the crack tip.

The cohesive zone method (CZM) is another method to describe the fracture process zone. When modelling the fracture, the fracture is divided into two parts: one is the real fracture length, and the other is a cohesive zone. Based on the traction-separation criterion, the initiation and propagation behaviours of fractures are simulated. In the early stage, the fracture is subjected to an external load, and the stress increases linearly with the opening/shearing displacement before reaching the threshold value. Once the stress reaches the threshold value, the stress gradually decreases, and at this time, the interface begins to suffer damage.

The quadratic traction-interaction failure criterion [38] is used to simulate fracture initiation and propagation, and the effect of normal stress and tangential stress is considered. A typical cohesive traction-interaction failure criterion is shown in Figure 4. When the crack is initiated, the quadratic interaction function value is 1, and its expression is as follows:

$$\left\langle \frac{t_n}{t_n^0} \right\rangle^2 + \left\langle \frac{t_s}{t_s^0} \right\rangle^2 + \left\langle \frac{t_t}{t_t^0} \right\rangle^2 = 1, \quad (7)$$

where  $t_n$ ,  $t_s$ , and  $t_t$  represent the normal, first, and second shear stress components, Pa, respectively;  $t_n^0$ ,  $t_s^0$ , and  $t_t^0$  represent the peak values of the nominal stress when the deformation is either purely normal to the interface or purely in the first or second shear direction, Pa, respectively; and the symbol  $\langle \rangle$  is the Macaulay bracket used to indicate that a pure compression deformation or stress state does not initiate damage.

After fracture initiation, the damage was evaluated by fracture energy theory. The Benzeggagh and Kenane [39] fracture criterion was introduced to describe the development of fractures after fracture initiation, and the criterion is useful when the critical fracture energies along different tangential directions are the same.

$$G_n^C + (G_s^C - G_n^C) \left\{ \frac{G_s + G_t}{G_n + G_s + G_t} \right\}^\eta = G^C, \quad (8)$$

where  $G_n^C$  represents the critical fracture energy in model I;  $G_s^C$  represents the critical fracture energy in model II;  $G_n$ ,  $G_s$ , and  $G_t$  represent the fracture energy of the normal direction, the first tangential direction, and the second tangential direction, respectively;  $\eta$  is the material parameter.

If the fracture energy reaches or exceeds  $G_C$  ( $G_C = G_n + G_s + G_t$ ), the cohesive element breaks, and the fracture begins to propagate.

## 5. Model Building

In the numerical model, the reservoir is assumed to be homogeneous, and the fracture expands symmetrically on both sides of the wellbore. Therefore, only half of the fractures are established to study the initiation and propagation of multiple fractures. The height of the reservoir model is 30 m, the length is 160 m, and the width is 60 m. The height of the upper and lower layers is set to 10 m, which forces

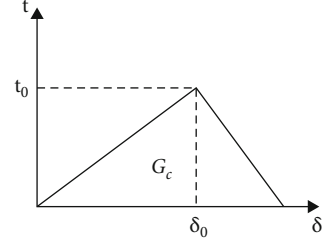


FIGURE 4: Cohesive traction-interaction failure criterion.

fracture propagation to be confined to the target formation. In this model, three perforating clusters are set in a stage, and the cluster spacing is 15 m.

The target formation properties are presented below [3, 21].

The parameters of the upper and lower layers are the same, as follows.

Equation (6) shows that perforation friction changes as the number of perforations or the diameter of perforations changes. When the perforation friction is small, the development of multiple fractures is dominated by the stress shadow effect, intermediate fractures have difficulty developing completely, and the development stops before pumping for 50 s. With the increase in perforating friction, the development of multiple fractures is dominated by the dynamic partitioning of the flow rate, and the three fractures continue to propagate after pumping for 50 s. Different perforation parameters in the fracturing process lead to different pressure drops of perforation clusters and affect the initiation and propagation process of multiple perforation clusters. The hydraulic fracturing design parameters of each working condition are presented below.

## 6. Results and Discussion

In this section, we discuss the simultaneous propagation of multiple fractures formed by multicluster fracturing and the corresponding influencing factors based on the numerical model established in Section 5. For this study, the basic parameters of the reservoir and the upper and lower layers are obtained from Tables 1 and 2, and the engineering parameters used in various working conditions are shown in Table 3.

In the following discussion, fractures 1, 2, and 3 represent the fractures that initiate from the left, middle, and right clusters, respectively, in Figure 3.

**6.1. The Basic Case (Case 1).** In this model, each cluster has 32 perforations, and the perforation diameter is 15 mm. The total injection rate is  $6 \text{ m}^3/\text{min}$ , and the fracturing fluid viscosity is 1 cp. Note that the effect of perforation friction on fracture initiation and propagation is negligible. In this case, the simultaneous initiation and propagation of multiple fractures are mainly affected by stress interference between fractures. The morphologies of three hydraulic fractures after 5 s, 20 s, 30 s, and 50 s of pumping are shown in Figure 5. The colour in the figure represents the width of

TABLE 1: Basic parameters of the target formation.

Minimum horizontal stress (MPa)	30.68
Maximum horizontal stress (MPa)	37.58
Vertical stress (MPa)	55
Young's modulus (GPa)	45
Poisson's ratio	0.2
Reservoir layer thickness (m)	30

TABLE 2: Basic parameters of the upper and lower layers.

Minimum horizontal stress (MPa)	35.68
Maximum horizontal stress (MPa)	39.58
Vertical stress (MPa)	55
Young's modulus (GPa)	90
Poisson's ratio	0.3
Reservoir layer thickness (m)	10

the propagated fracture. The exact value of each colour corresponds to the different opening widths of the fracture in the right panel of the image in meters. The blue areas in the figure represent the fracture propagation planes where the fracture has not yet developed. Other areas represent the fractures. All three fractures started to propagate at the same time when the fracturing fluid was pumped when  $t = 5$  s (see Figure 5). However, as Figure 5 shows, after some time, with the opening of the fractures on both sides, an increased additional compressive stress applied to the middle fracture tends to inhibit the propagation of the middle fracture. Previous studies have proven that when the cluster spacing is small, fractures in the middle position have difficulty propagating due to the inability to allocate enough fracturing fluid, and perforation clusters in the middle position become ineffective. Increasing cluster spacing can weaken the influence of the stress shadow effect, but tight cutting and reasonable distribution of well spacing in horizontal well staging are also the keys to reservoir reconstruction. Therefore, it is an effective way to optimize the multicluster fracturing design within a stage in a horizontal well by adjusting the engineering parameters and setting reasonable perforation parameters to form a sufficient pressure drop so that multiple fractures can form a large effective fracture volume at an appropriate cluster spacing.

*6.2. The Effect of the Injection Rate when the Value of Perforation Friction Is Small (Cases 1 and 2).* The injection rate is an important engineering parameter. Based on the reference model in case 1, different flow rates are considered:  $6 \text{ m}^3/\text{min}$  and  $10 \text{ m}^3/\text{min}$ . Then, the effect of the flow rate on the growth of multiple fractures is studied. The fracture geometry injected with fluid in case 1 is shown in Figure 5, and that injected with fluid in case 2 is shown in Figure 6.

The change curve image of the maximum fracture width along the direction of fracture propagation is shown in Figure 7. Figures 7(a) and 7(b) show that the development of the three fractures has the same trend in the two cases. The width of the fractures increases rapidly with the initia-

tion of the fractures, and then, the width of the middle fracture decreases continuously due to the compressive stress exerted by the propagation of the fractures on both sides until it approaches 0 mm. The fractures on both sides continued to fluctuate, and after a certain period, the widths of the three fractures remained stable with the injection of fluid. Figure 7(a) shows that the maximum fracture widths of fractures 1, 2, and 3 are 1.2 mm, 0.895 mm, and 1.23 mm, respectively. The maximum width of fracture 2 is almost zero after 17 s. It can be seen from Figure 7(b) that the maximum fracture widths of fractures 1, 2, and 3 are 1.406 mm, 0.946 mm, and 1.453 mm, respectively. The maximum width of fracture 2 is almost zero after 14 s. As shown in Figure 6, as the injection rate increases, the lateral fractures propagate for a longer area after pumping the 50 s fracture fluid, and the width of the middle fracture lasts for a shorter period. This means that when the stress shadow effect dominates, higher pump rates cause fluid to enter the middle fracture more difficult and to enter the lateral fracture more quickly, creating more significant compressive stress and resulting in the faster closure of the middle fracture.

The dynamic percentage of the flow rate into each cluster is illustrated in Figure 8. In Figure 8(a), the percentage of flow into fracture 2 is almost 0 after 14 s. The percentage of flow into fracture 1 and fracture 3 is almost identical. The percentage of flow into fracture 1 and fracture 3 is almost the same at first, but as more fracturing fluid is pumped, the flow percentage into fracture 1 is gradually higher than that entering fracture 3, and this trend slowly increases. Figure 8(b) shows that the percentage of flow into fracture 2 is almost zero after 11 s. Combined with Figures 6 and 7, it can be seen that the larger flow volume ratio is the reason why fractures on both sides can propagate a longer area. When fracturing fluid enters the three fractures from the three injection points, the fracturing fluid splits along multiple paths. However, due to the strong stress shadow effect and high injection rate after initiating on both sides of the fracture, the fracturing fluid experiences continuous propagation, and the middle fracture closes after a short time. Fracture 3 at the front of the wellbore contains a larger proportion of fracturing fluid than fracture 1 at the back of the wellbore due to wellbore friction.

After pumping for 20 s and 50 s, the percentage of flow into each cluster is presented in Figure 9. This information is useful for studying the dynamic partitioning of the fluid rate across fractures after fracturing fluid is pumped. The percentage of flow into fracture 2 is the minimum and is much smaller than the percentage of flow into the fractures on either side. The percentage of flow into fracture 3 is more than the percentage of flow into fracture 1 because of the effect of wellbore fluid friction. When the total injection rate ranges from  $6 \text{ m}^3/\text{min}$  to  $10 \text{ m}^3/\text{min}$ , due to the stress shadow effect, fracture 2 still cannot be fully developed, and the flow rate uniformity into both sides of the fracture worsens as the fracturing fluid is pumped, ranging from modest 1.02% and 0.27% at 20 s to 5.63% and 8.198% at 50 s, respectively. Therefore, it is believed that increasing the flow rate is not conducive to the uniform development

TABLE 3: Hydraulic fracturing design parameters in different cases.

Case	Value of the perforation friction	Number of perforations of each cluster	Perforation diameter (mm)	Total injection rate (m <sup>3</sup> /min)	Viscosity (cp)
Case 1	Small	32	15	6	1
Case 2	Small	32	15	10	1
Case 3	Small	32	15	6	100
Case 4	Small	8	15	6	1
Case 5	Large	32	5	6	1
Case 6	Large	32	5	8	1
Case 7	Large	32	5	10	1
Case 8	Large	32	5	6	10
Case 9	Large	32	5	6	100

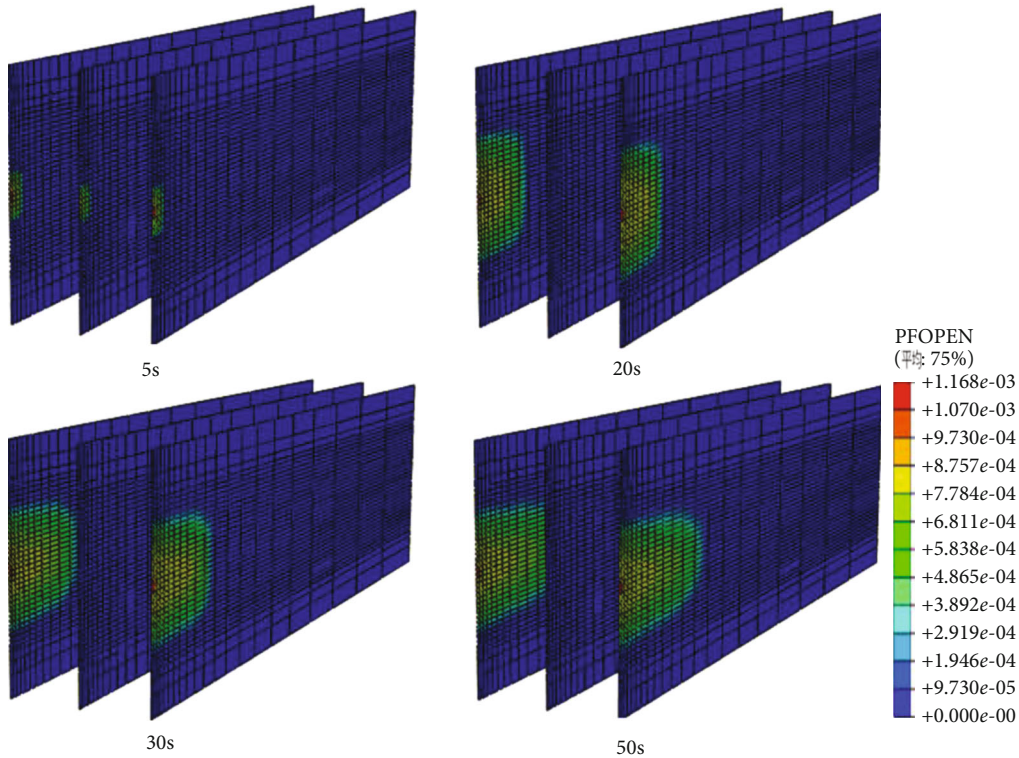


FIGURE 5: Fracture geometry after pumping for 5 s, 20 s, 30 s, and 50 s in case 1.

of fractures when perforation friction is not considered and that the influence of the stress shadow effect is the main factor.

In engineering, when the perforation friction is small, increasing the injection rate is favourable to the development of the fractures on both sides. However, the utilization effect of the middle perforating cluster will be significantly

reduced, which is not conducive to the uniform development of multiple fractures.

6.3. *The Effect of Fracturing Fluid Viscosity when the Value of Perforation Friction Is Small (Case 1 and Case 3).* Fracturing fluid viscosity is an important engineering parameter. Based on the reference model in case 1, different fracturing fluid

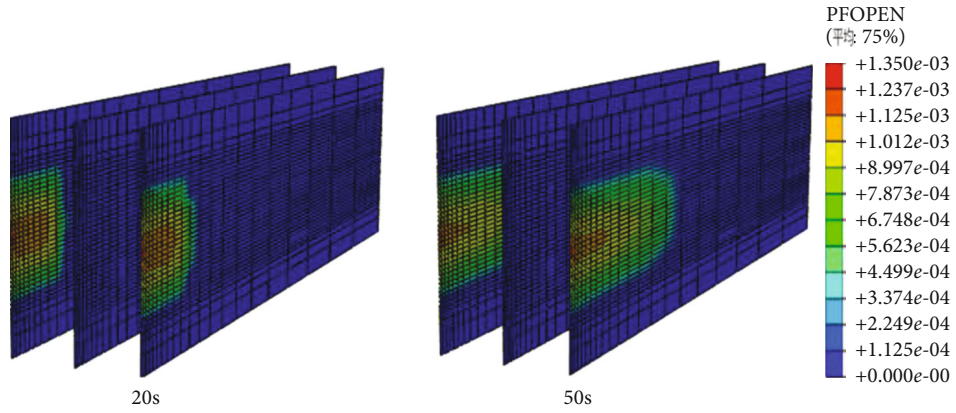


FIGURE 6: Fracture geometry after pumping for 20 s and 50 s in case 2.

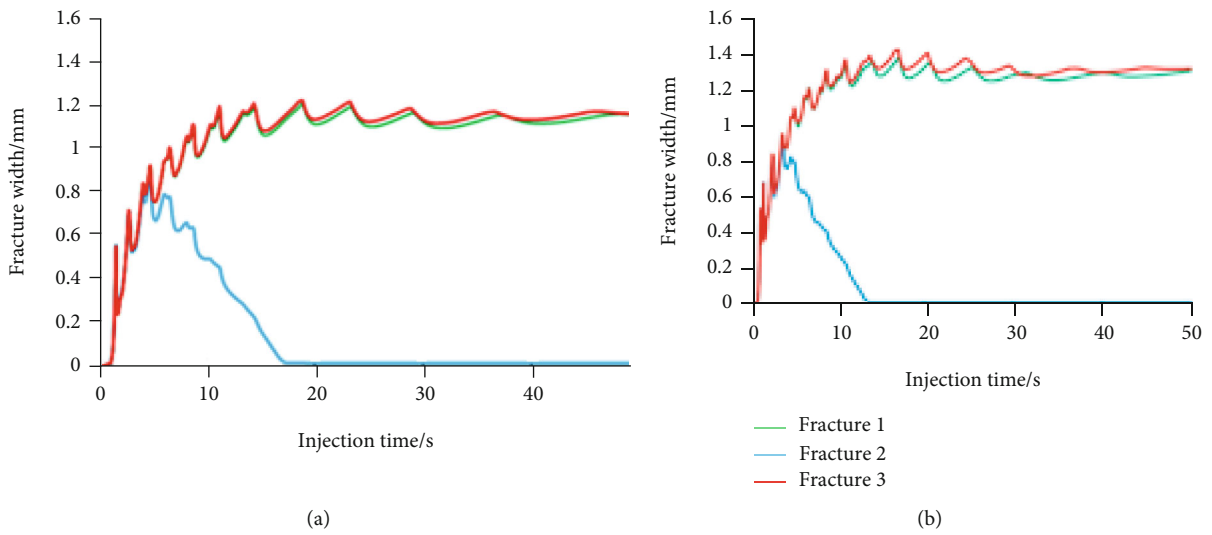


FIGURE 7: The maximum fracture width of each cluster as a function of time for different flow rates: (a) case 1 ( $6 \text{ m}^3/\text{min}$ ); (b) case 2 ( $10 \text{ m}^3/\text{min}$ ).

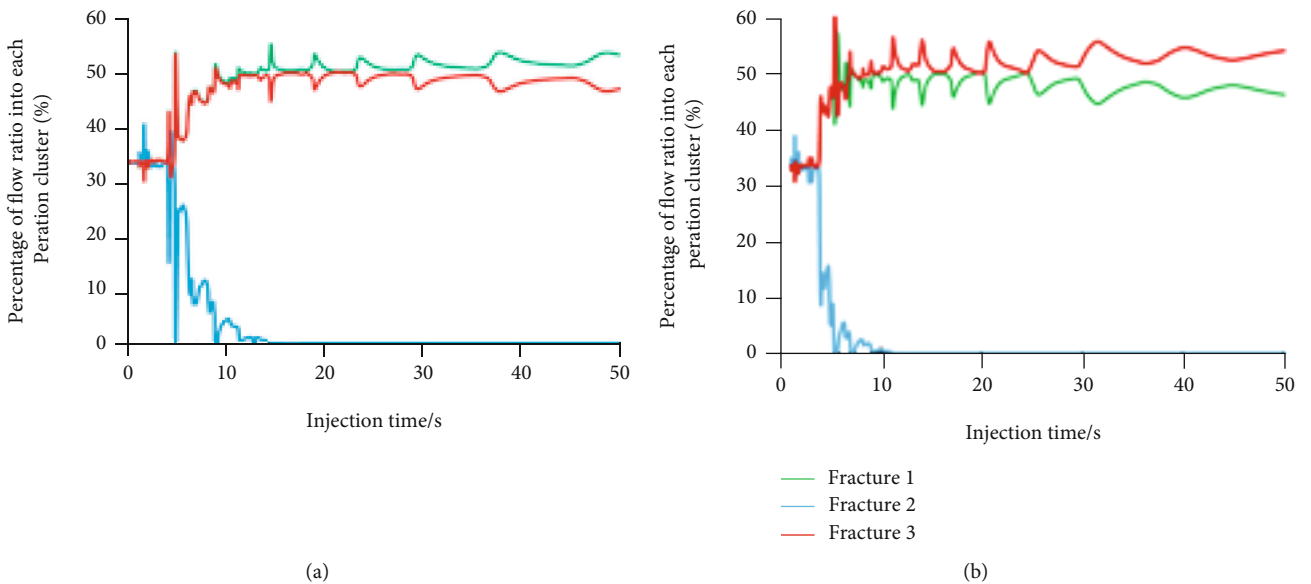


FIGURE 8: Percentage of flow into each cluster as a function of time for different flow rates: (a) case 1 ( $6 \text{ m}^3/\text{min}$ ); (b) case 2 ( $10 \text{ m}^3/\text{min}$ ).

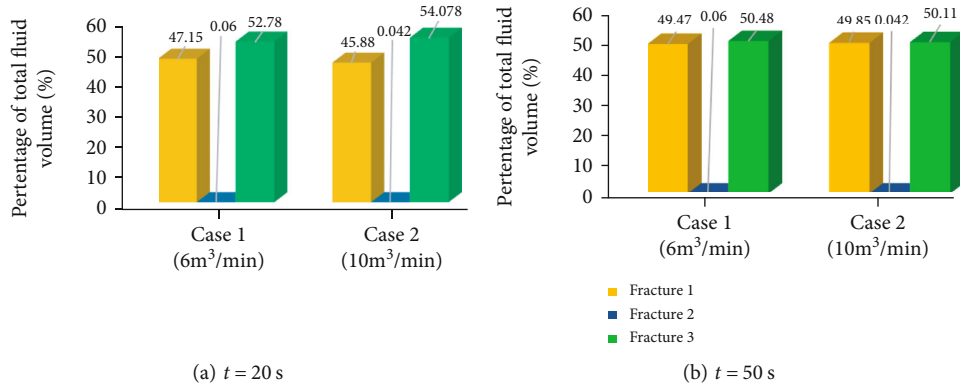


FIGURE 9: The total fluid volume distribution of each cluster after pumping for 20 s and 50 s for two different flow rates.

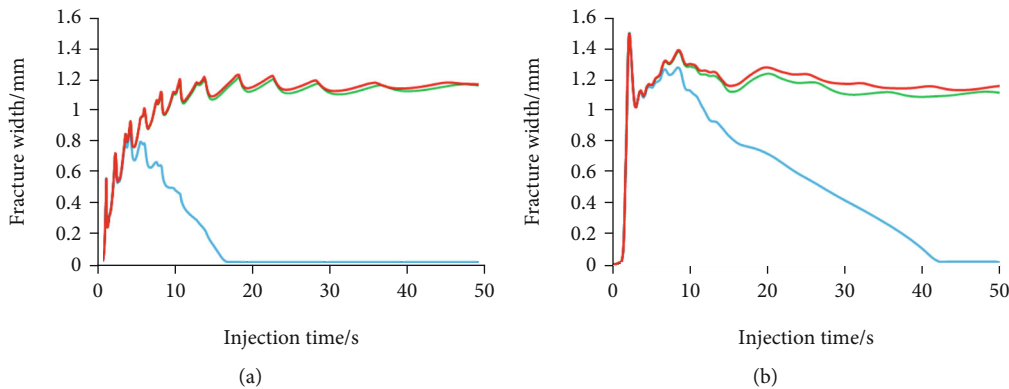


FIGURE 10: The maximum fracture width of each cluster as a function of time for different fracturing 484 fluid viscosities: (a) case 1 (1 cp); (b) case 3 (100 cp).

viscosities are considered, namely, 1 cp and 100 cp. The fracture geometry injected with fluid in case 1 is shown in Figure 5, and that injected with fluid in case 3 is shown in Figure 6.

A plot of the change in the maximum fracture width along the direction of fracture propagation is shown in Figure 10. As shown in Figure 10(a), the width of the fracture increases rapidly with the initiation of the fracture, and the width of the middle fracture decreases continuously until it approaches 0 mm. The fractures on both sides continue to fluctuate and rise, and the widths of the three fractures remain stable after a period of fluid injection. The difference is that as shown in Figure 10(b), in case 3 (with higher fracturing fluid viscosity), the middle fracture propagates for a longer time, and the overall width of the three fractures is larger than that in case 1. According to Figure 10(a), the maximum fracture widths of fractures 1, 2, and 3 are 1.2 mm, 0.895 mm, and 1.23 mm, respectively. The maximum width of fracture 2 is almost zero after 17 s. According to Figure 10(b), the maximum fracture widths of fractures 1, 2, and 3 are 1.47 mm, 1.47 mm, and 1.47 mm, respectively. The maximum width of fracture 2 is almost zero after 42 s. Combined with Figures 11 and 10, it can be seen that with the increase in fracturing fluid viscosity, the middle fracture continues to propagate after 20 s of pumping, but the area of its propagation is much smaller than that of fracture propagation on both sides. After pump-

ing for 50 s, the middle fracture is closed, the fractures on both sides continue to propagate, and the overall width of the fractures increases. Compared to fracture 1, fracture 3 is closer to the pumping point. As shown in Figure 11, when the viscosity increases from 1 cp to 100 cp, the range of large fracture width of fracture 3 (represented as yellow and red area) is greater than that of fracture 1. It means that as the fracturing fluid viscosity increases, the flow friction becomes higher and the effect of wellbore friction becomes relatively more pronounced.

The dynamic percentage of the flow rate into each cluster is illustrated in Figure 12. In Figure 12(a), the percentage of flow into fracture 2 is almost 0 after 14 s. The percentages of flow into fracture 1 and fracture 3 are almost identical. The percentages of flow into fracture 1 and fracture 3 are almost the same at first, but as more fracturing fluid is pumped, the flow percentage into fracture 1 is gradually higher than that entering fracture 3, and this trend slowly increases. However, Figure 12(b) shows that the percentage of flow into fracture 2 is almost zero after 33 s. The flow percentages into fracture 1 and fracture 3 rapidly diverge as the percentage of flow into fracture 2 decreases. Moreover, with the increase of injection time, the difference of the flow percentages into fracture 1 and fracture 3 becomes further greater. Combined with Figures 10 and 12, it can be seen that as the fracturing fluid is pumped, the three fractures initiate simultaneously and divide the injected fracturing fluid

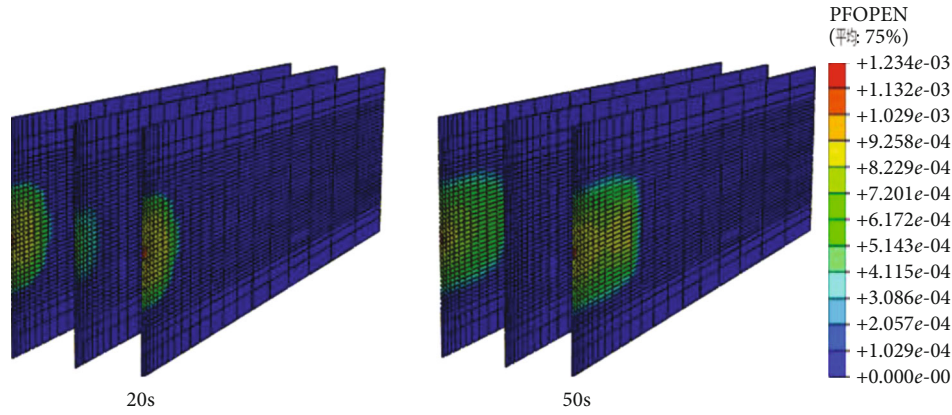


FIGURE 11: Fracture geometry after pumping for 20 s and 50 s in case 3.

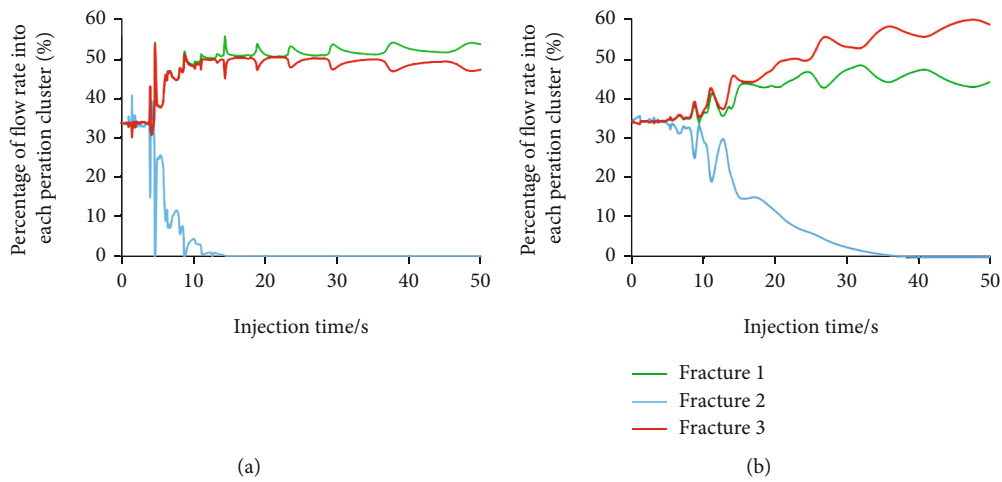


FIGURE 12: Percentage of flow into each cluster as a function of time for different fracturing fluid viscosities: (a) case 1 (1 cp); (b) case 3 (100 cp).

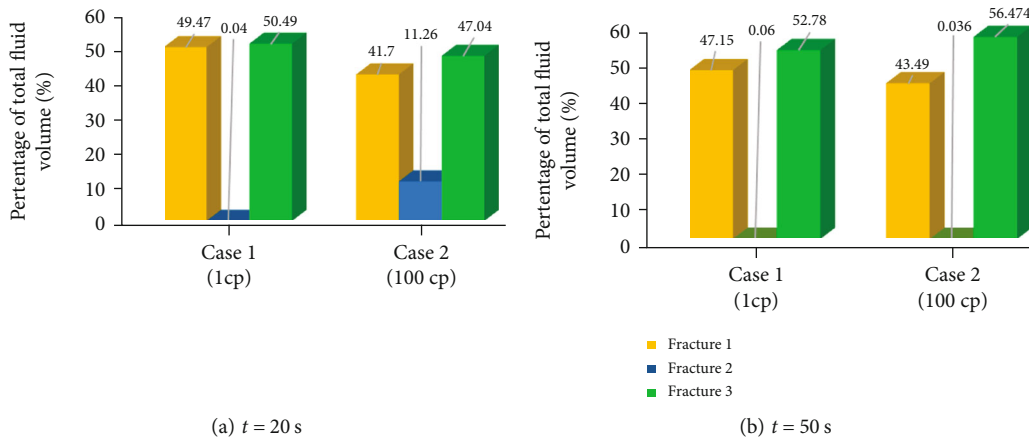


FIGURE 13: The total fluid volume distribution of each cluster after pumping for 20 s and 50 s for two different fracturing fluid viscosities.

equally. However, with the increase of pump injection time, the fracturing fluid of middle fracture gradually decreases. With the decrease of the middle fracture's fracturing fluid proportion, the difference of the fracturing fluid proportion of fractures on both sides gradually increased, suggesting

that when fracturing fluid viscosity is bigger, it can reduce the effect of stress shadow to some extent and amplify the effect of wellbore friction.

After pumping for 20 s and 50 s, the percentage of flow into each cluster is presented in Figure 13. The percentage

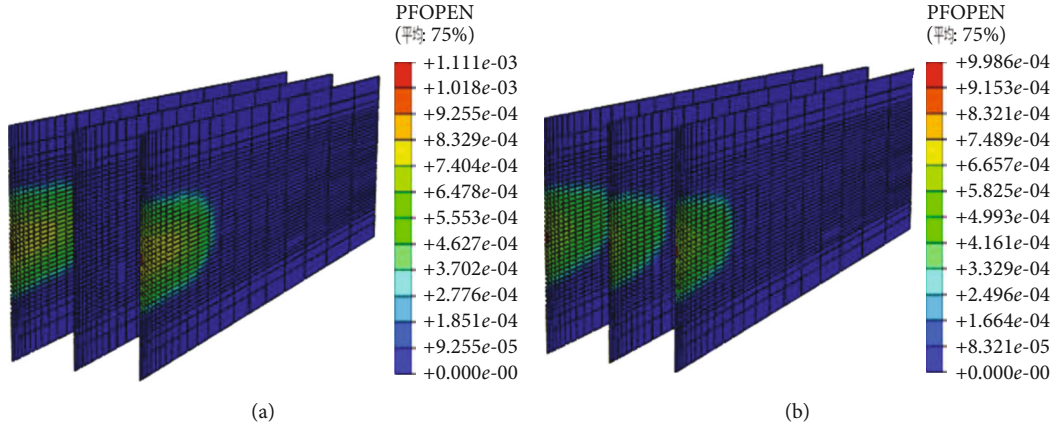


FIGURE 14: Fracture geometry after pumping for 50 s for different perforation frictions: (a) case 4; (b) case 5.

of flow into fracture 2 is minimal and is much smaller than the percentage of flow into the fractures on either side. The percentage of flow into fracture 3 is more than the percentage of flow into fracture 1 because of the effect of wellbore fluid friction. When the fracturing fluid viscosity ranges from 1 cp to 100 cp, however, due to the stress shadow effect, fracture 2 still cannot be fully developed. However, after pumping for 20 s, in case 2, the percentage of the total fluid volume of the middle fracture is 11.26%, which is much larger than that of the middle fracture in case 1, which is 0.04%. After pumping for 50 s, the flow rate uniformity into the two sides of the fracture worsens because of the higher fracturing fluid viscosity, from a 5.63% to 12.984% difference. Therefore, we believe that fracturing fluid viscosity is conducive to the uniform development of fractures when perforation friction is not considered and that increasing fracturing fluid viscosity can improve fracture width. However, when fracture 2 is no longer developed, the flow into fracture 2 cannot be evenly distributed between the other two fractures.

In engineering, when perforating friction is small, simply increasing the fracturing fluid viscosity can help multiple fractures develop to a certain extent. Unfortunately, the development of each fracture will be reduced to a certain extent.

**6.4. The Effect of Perforation Friction (Case 1, Case 4, and Case 5).** In this section, the influence of perforation friction is studied. In multicluster fracturing, a change in the number of perforations in each perforation cluster or perforation diameter directly leads to a change in perforation friction. Therefore, the effect of perforation friction on the simultaneous propagation of multiple fractures in multicluster fracturing is investigated in three cases: in addition to case 1, one with eight perforations per cluster and a perforation diameter of 15 mm (case 4) and the second with 32 perforations per cluster and a perforation diameter of 5 mm (case 5). Equation (6) shows that with the change in the number of perforations or perforation diameter, the perforation friction changes, thus changing the initiation and propagation of multiple fractures. In this section, according to the perforation parameters set in different cases, the value of perfora-

tion friction is case 5 > case 4 > case 1. The fracture geometry injected with fluid in case 1 is shown in Figure 5, the fracture geometry injected with fluid in case 4 is shown in Figure 14(a), and that injected with fluid in case 5 is shown in Figure 14(b).

The change curve image of the maximum fracture width along the direction of fracture propagation is shown in Figure 15. As shown in Figures 1(a) and 15(b), with the initiation of the fractures, the width of the fractures increases rapidly, and the width of the middle fracture decreases continuously until it is close to 0 mm. The fractures on both sides continued to fluctuate, and the widths of the three fractures remained stable after a period of fluid injection. The difference, as shown in Figure 15(c), is that in case 5 (with high perforation friction), the development continued after pumping for 50 s, and the widths of the three fractures remained stable after a period of injection, with the widths of the middle fractures being slightly smaller than those of the sides when stable.

The dynamic percentage of the flow rate into each cluster is illustrated in Figure 16. Figure 16(a) shows that the percentage of flow into fracture 2 is almost 0 after 17 s. The percentage of flow into fracture 1 and fracture 3 is almost identical. The percentage of flow into fracture 1 and fracture 3 is almost the same at first, but as more fracturing fluid is pumped, the flow percentage into fracture 1 is gradually higher than that entering fracture 3, and this trend slowly increases. In Figure 16(b), the percentage of flow into fracture 2 is almost 0 after 28 s. The percentage of flow into fracture 1 and fracture 3 is almost identical. However, as you can see from Figure 16(c), although the percentage of flow into fracture 2 is slightly smaller than that into the other two fractures, it still propagates until 50 s. In combination with Figures 14 and 16, it can be seen that when the perforation friction increases by a certain amount, the fracture propagation has the same trend; that is, the three fractures begin to evenly divide the injected fracturing fluid and initiate. After a period of propagation, the middle fracture is closed, and the fractures on both sides continue to propagate.

However, in combination with Figures 14 and 17, it can be seen that when the perforation friction increases to a



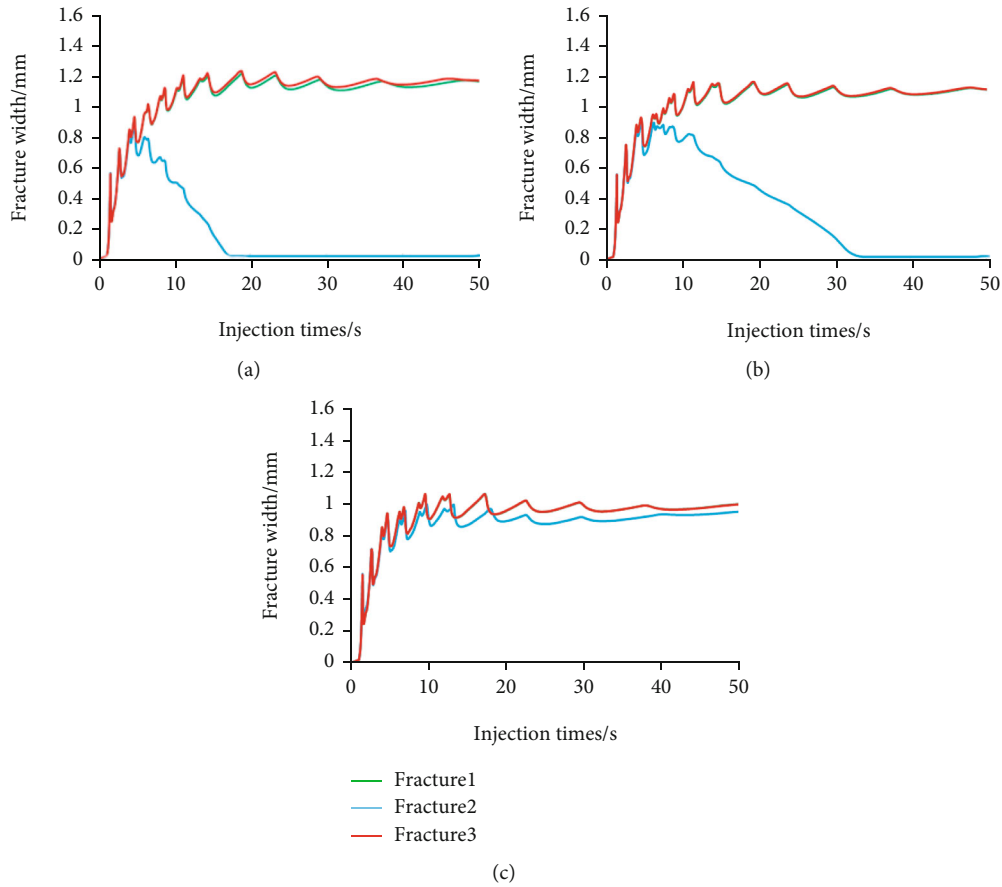


FIGURE 15: The maximum fracture width of each cluster as a function of time for different perforation design parameters: (a) case 1; (b) case 4; (c) case 5.

certain extent, the middle fracture does not close during pumping for 50 s. The three fractures first divide fracturing fluid evenly and initiate and then propagate together. There is a small decrease in the proportion of fracturing fluid in the middle fracture.

After pumping for 20 s and 50 s, the total fluid volume distribution of each cluster is presented in Figure 18. Case 1 and case 4 show that the percentage of flow into fracture 2 is the minimum and is much smaller than the percentage of flow into the fractures on either side due to the impact of stress shadow effect which causes the pressure of fracture 2 to be too large to allow fracturing fluid to enter. The percentage of flow into fracture 3 is more than the percentage of flow into fracture 1 due to the presence of wellbore friction. The difference between the percentage of flow into fracture 1 and fracture 2 was reduced from 5.63% to 0.69% ( $t = 50$  s) due to the change in perforation friction. The influence of perforating friction is much greater than that of wellbore friction. With the increase of perforation friction, the compressive stress field applied by the two sides of the fractures to the middle fracture will be improved, and the influence of stress shadow effect can be effectively suppressed. Therefore, in case 5, all three fractures are initiated and fully developed simultaneously, the percentage of flow into 2 is 5.53% lower than the percentage of flow into fracture 1, the percentage of flow into fracture1 and fracture 3 is nearly

the same, and the percentage of flow into fracture 2 exhibits a small decrease.

The increase in perforation friction (e.g., the decrease in the number of perforations or the diameter of perforations) contributes to the uniform propagation of multiple fractures. However, with the increase in perforating friction, the bottomhole pressure increases greatly, and the pressure at the fracture mouth is not similar to the bottomhole pressure but far less than the bottomhole pressure. To quantitatively study the influence of perforation friction on the bottomhole pressure and pressure at the fracture mouth, the bottomhole pressure and pressure at the three fracture mouths are compared in Figure 17 when the fracturing continues for 50 s. The bottomhole pressure is almost identical to the pressure at every fracture mouth when the perforating friction is not considered. However, when perforating friction is considered, the pressure at the fracture mouth and the bottomhole pressure increase. In case 4, the pressure at the middle fracture mouth is close to the bottomhole pressure, while the pressure at the lateral fracture is small. In case 5, compared with the bottomhole pressure, the pressure at the fracture mouth of the three fractures decreases significantly, and the middle fracture (50.4 MPa) is slightly higher than the two sides (49.2 MPa). This is due to the greater perforation friction in case 5 and more equal distribution of fracturing fluid to the three fractures, all of which are affected by the

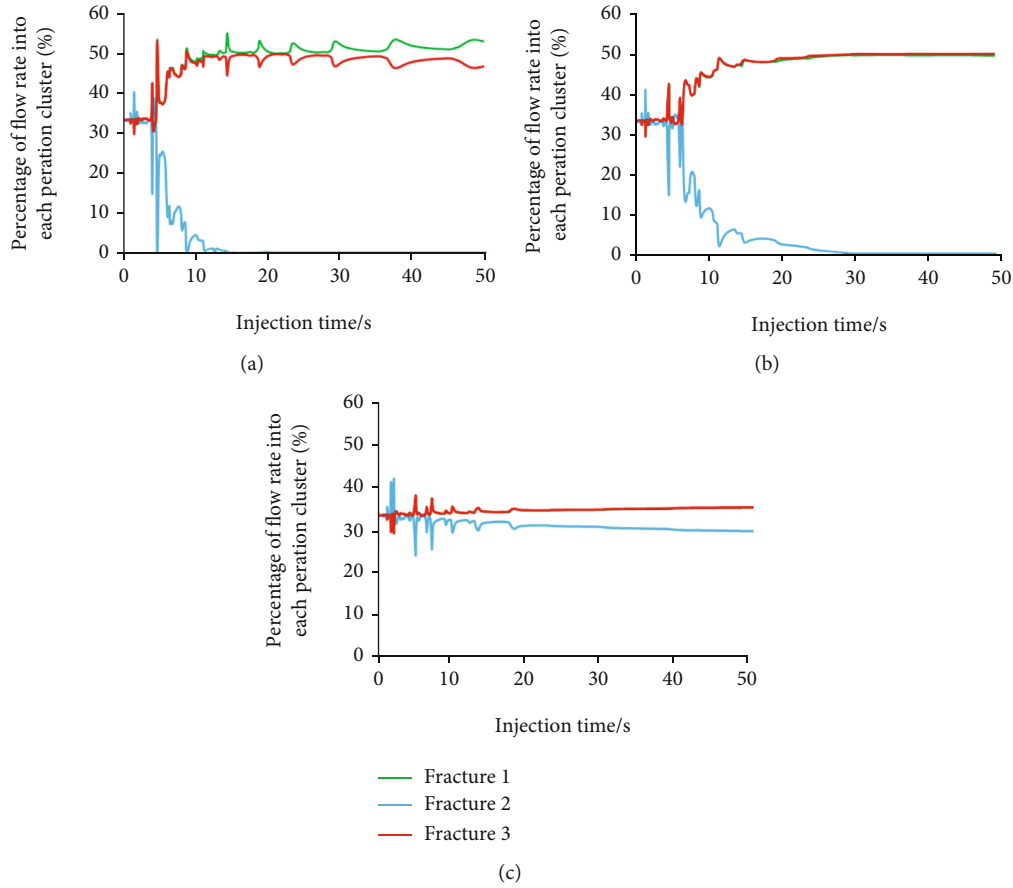


FIGURE 16: Percentage of flow into each cluster as a function of time for different perforation design parameters: (a) case 1; (b) case 4; (c) case 5.

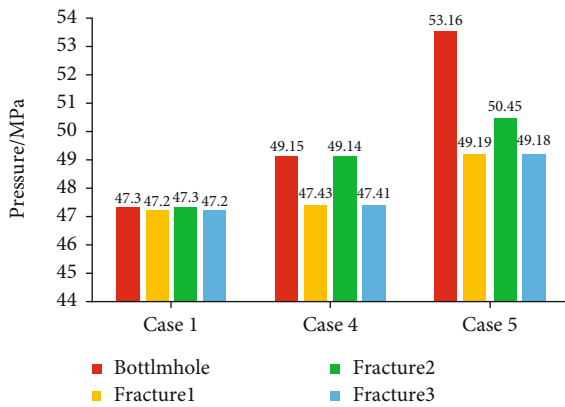


FIGURE 17: Bottomhole pressure and pressure at various fracture mouths when fracturing for 50 s for three different perforation design parameters.

perforation friction as they propagate. Through the analysis, it is believed that perforation friction can reduce the impact of stress shadows due to the uniform development of multiple fractures, but increasing perforation friction leads to an increase in the bottomhole pressure, so engineering equipment is more demanding.

In engineering, increasing perforation friction can effectively help multiple fractures develop. However, as the perfo-

rating friction increases, higher engineering pressure is required for fracture propagation. Therefore, it is necessary to find an appropriate perforation design.

6.5. *The Effect of the Injection Rate when the Value of Perforation Friction Is Large (Case 5, Case 6, and Case 7).* In this section, the influence of the flow rate on multicluster fracturing is studied with the existence of perforation friction. Three flow rates are considered:  $6 \text{ m}^3/\text{min}$  (case 5),  $8 \text{ m}^3/\text{min}$  (case 6), and  $10 \text{ m}^3/\text{min}$  (case 7).

The change curve image of the maximum fracture width along the direction of fracture propagation is shown in Figure 19. For different flow rates, the curves show similar characteristics. A higher flow rate leads to a larger fracture width. As a higher percentage of the fluid flows into the second fracture when the flow rate increases from  $6 \text{ m}^3/\text{s}$  to  $10 \text{ m}^3/\text{s}$  (see Figure 19), a high flow rate is more beneficial to the propagation of the middle fracture. For example, up to 50 s, the maximum fracture widths of fractures 1, 2, and 3 are 1 mm, 0.95 mm, and 1 mm, respectively, and the maximum fracture width of the middle fracture is slightly smaller than the maximum fracture width of the fractures on both sides. In addition, as the injection rate increases, the maximum widths of the three fractures tend to be the same after injection for 50 s. Combined with Figures 14, 19, and 20, it can be seen that as the flow rate increases,

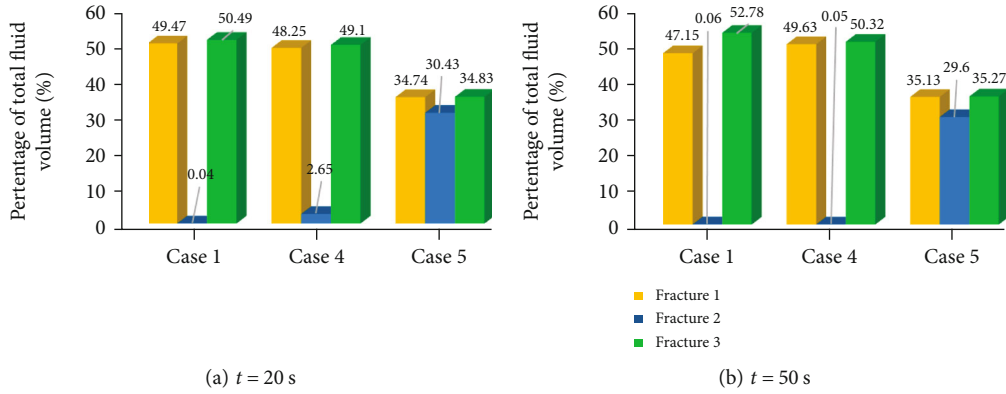


FIGURE 18: The total fluid volume distribution of each cluster after pumping for 20 s and 50 s for three different perforation design parameters.

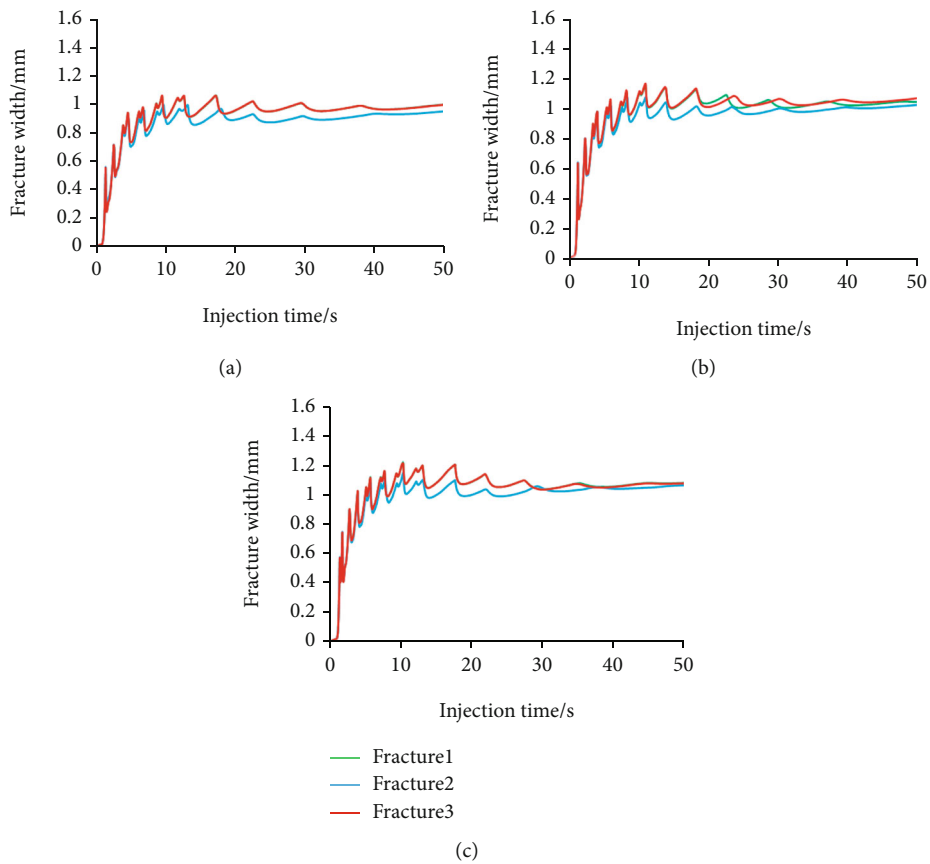


FIGURE 19: The maximum fracture width of each cluster as a function of time for different flow rates: (a) case 5 (6 m<sup>3</sup>/min); (b) case 6 (8 m<sup>3</sup>/min); (c) case 7 (10 m<sup>3</sup>/min).

the three fractures have a similar tendency to propagate such that the three fractures initially divide the pumped fracturing fluid equally and initiate at the same time. As fracturing fluid is pumped in, three fractures continue to propagate. In addition, the fracture length increases with the injection rate.

When the fracturing time is 50 s, the comparison of the bottomhole pressure and the fracture width pressure is shown in Figure 21. With increasing injection rate, the bottomhole pressure increases faster, but the pressure at the

fracture mouth increases less, and the difference between the two increases. The difference between the bottomhole pressure and the pressure at the fracture mouth is most remarkable when the injection rate is 10 m<sup>3</sup>/min. In each case, the pressure at the fracture mouth of the middle fracture is slightly greater than that at the two sides.

Because perforation friction weakens the stress shadow effect, the effect of the total flow rate on multicluster fracturing becomes evident and is conducive to the uniform

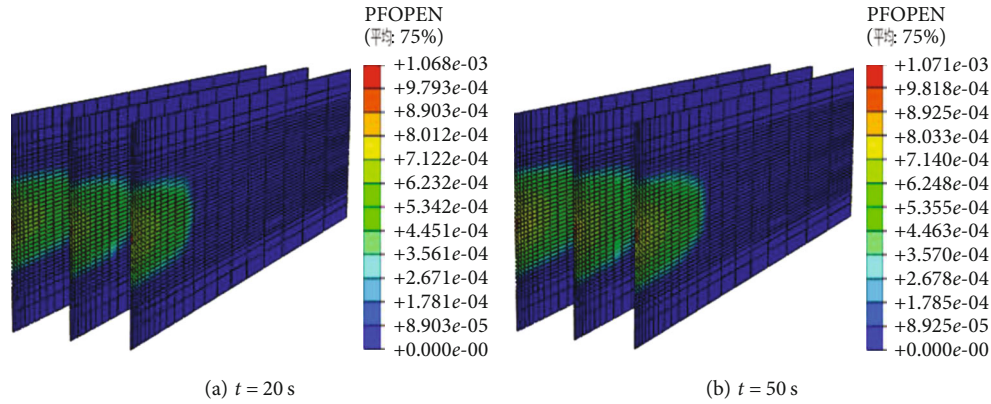


FIGURE 20: Fracture geometry after pumping for 50 s for different injection rates: (a) case 6 ( $8\text{ m}^3/\text{min}$ ); (b) case 7 ( $10\text{ m}^3/\text{min}$ ).

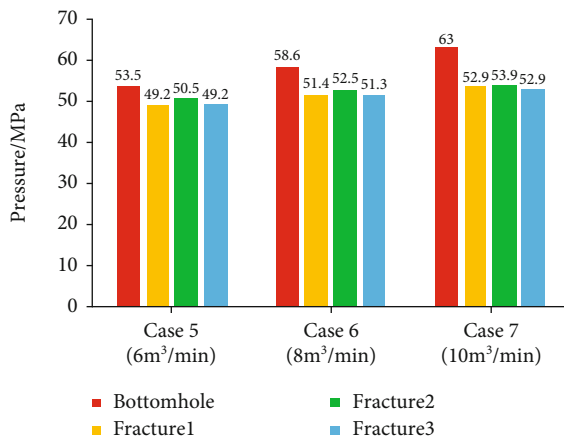


FIGURE 21: Bottomhole pressure and pressure at various fracture mouths when fracturing for 50 s for three different flow rates.

propagation of multiple fractures. As the flow rate increases, the bottomhole pressure gradually increases. At this time, the influence of the perforation friction will be enhanced, leading to a greater drop in bottomhole pressure at the fracture mouth and a greater difference between the pressure at fracture mouth and the bottomhole pressure. As the total flow rate increases, the fracture length of each fracture increases after pumping for 50 s, but increasing the total flow rate also increases the engineering pressure and has little effect on the fracture width.

In engineering, when perforation friction is high, increasing the injection rate is favourable for multiple fracture propagation. However, as the injection rate increases, high engineering pressure is required for each fracture propagation, and higher requirements on the field equipment is also a challenge.

*6.6. The Effect of Fracturing Fluid Viscosity when the Value of Perforation Friction Is Large (Case 5, Case 8, and Case 9).* In this part, the influence of the flow rate on multicluster fracturing is considered based on perforation friction. Each cluster has 32 perforations, the perforation diameter is 5 mm, the total flow rate is  $6\text{ m}^3/\text{min}$ , and the fracture fluid viscosity is

set to 10 cp and 100 cp. Based on the reference model in case 5, different fracturing fluid viscosities are considered, namely, 10 cp and 100 cp. The fracture geometry injected with fluid in case 5 is shown in Figure 2, the fracture geometry injected with fluid in case 8 is shown in Figure 22(a), and that injected with fluid in case 9 is shown in Figure 22(b).

The change curve image of the maximum fracture width along the direction of fracture propagation is shown in Figure 23. As shown in Figures 23(a) and 23(b), with the initiation of fractures, the width of fractures increases rapidly, and the three fractures continue to fluctuate and remain stable after a period of fluid injection. In case 5, the maximum fracture width of fracture 2 is slightly lower than fracture 1 and fracture 3, while in case 8, the maximum fracture width of three fractures is nearly equal. As shown in Figure 23(c), the difference is that in case 9 (higher fracturing fluid viscosity), the width of the three fractures increases sharply as the fracture is initiated and gradually decreases as the fracturing fluid is pumped in. After some time, the widths of the three fractures remain stable as the fluid is pumped in. According to Figures 23(a) and 23(b), the maximum fracture widths in both cases are almost the same, approximately 1.1 mm. However, according to Figure 23(c), the maximum fracture widths of fracture 1, 2, and 3 are 1.506 mm, 1.506 mm, and 1.506 mm, respectively. Compared with the previous two cases, the maximum fracture widths increased by 0.4 mm. As seen from Figure 23, with the increase of fracturing fluid viscosity, after injecting the 50 s, the maximum widths of the three fractures tend to be the same when the fracturing fluid is 10 cp. When the fracturing fluid viscosity is 100 cp, the maximum widths of fractures 1, 2, and 3 are 1 mm, 0.97 mm, and 1 mm, respectively. Combined with Figures 5, 22, and 23, it can be seen that as the flow rate increases, the three fractures have a similar tendency to propagate such that the three fractures initially divide the pumped fracturing fluid equally and initiate at the same time. As fracturing fluid is pumped in, three fractures continue to propagate. However, as the fracturing fluid viscosity increased, the fracture width increased, but the length and height of all three fractures decreased, especially the middle fracture.

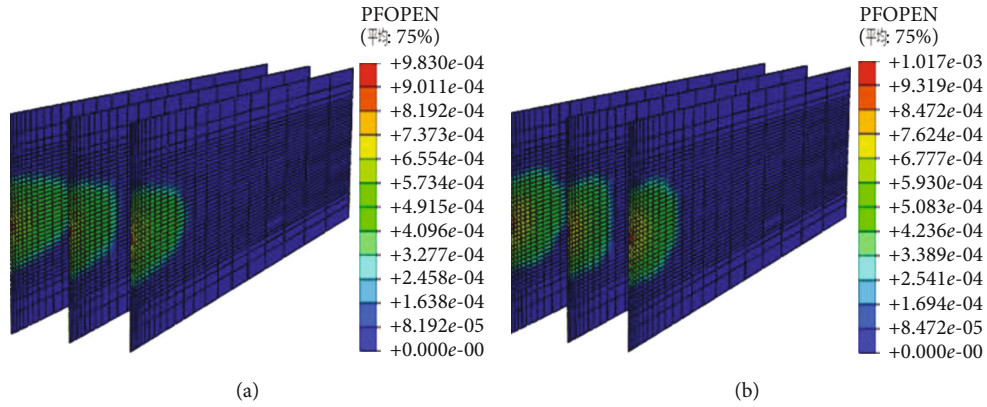


FIGURE 22: Fracture geometry after pumping for 50 s for different fracturing fluid viscosities: (a) case 8 (10 cp); (b) case 9 (100 cp).

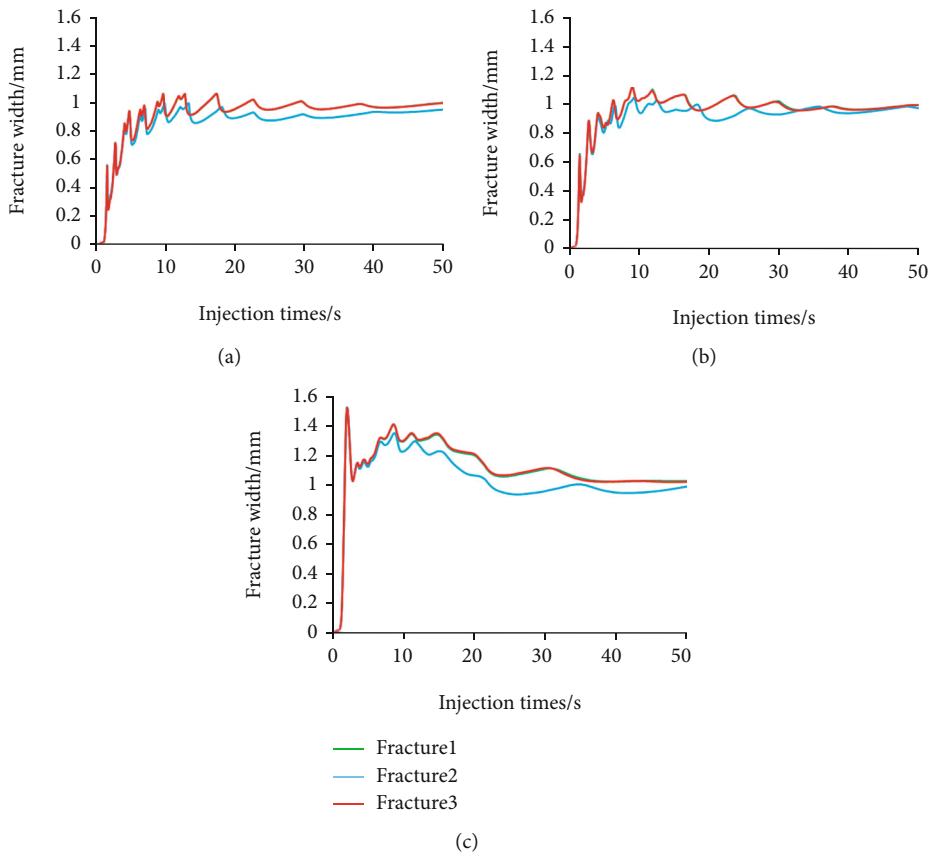


FIGURE 23: Maximum fracture width of each cluster as a function of time for different fracturing fluid viscosities: (a) case 5 (1 cp); (b) case 8 (10 cp); (c) case 9 (100 cp).

When the fracturing time is 50 s, the comparison of the bottomhole pressure and the fracture width pressure is shown in Figure 24. With the increase in fracturing fluid viscosity, the bottomhole pressure and the pressure at the fracture mouth show almost no change in the three kinds of cases. When fracturing fluid viscosity increases, higher fluid pressure in the fractures leads to greater fracture width. However, the bottomhole pressure and the pressure at the fracture mouth have no obvious change. It suggests that for engineering pressure, the effect of the injection rate is

more obvious. With regard to the fracturing fluid viscosity, only the morphology of fracture is affected. There is no significant effect on the bottomhole pressure and the pressure at the fracture mouth.

As perforation friction weakens the stress shadow effect, the effect of fracturing fluid viscosity on multicluster fracturing is mainly reflected in the increase in fracture width and the decrease in fracture length and fracture height, and the effect on the uniform propagation of multiple fractures is not as obvious as when the stress shadow effect plays a dominant role.

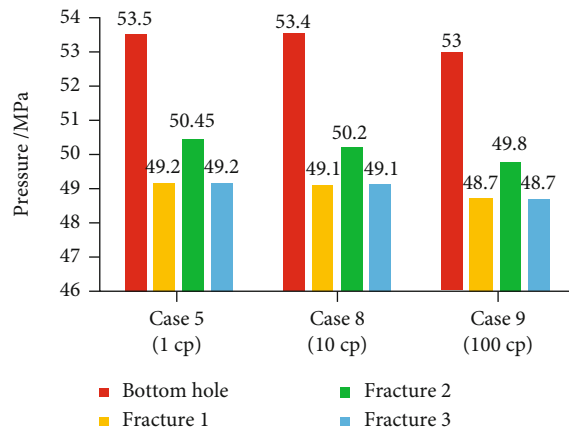


FIGURE 24: Bottomhole pressure and pressure at various fracture mouths when fracturing for 50 s for three different fracturing fluid viscosities.

In engineering, when the perforating friction is large, to the effect of high viscosity on the uniform development of multiple fractures can be ignored.

## 7. Conclusions

In this study, based on the CZM model and Bernoulli equation, we established a three-dimensional multicluster fracturing model with multiple clusters of fractures simultaneously initiating and propagating considering perforation friction and explored how engineering parameters affect the uniform development of multiple fractures through this model. Some key conclusions are as follows:

- (1) Increasing perforation friction by reducing the number of perforations in each perforation cluster or the diameter of perforation can effectively reduce the influence of the stress shadow effect and make the development of each fracture more uniform
- (2) Increasing the viscosity of the fracturing fluid under the influence of stress shadows can increase the fracture width and effectively improve the problem that middle cluster fractures cannot develop
- (3) When the stress shadow effect is weakened by perforating friction and dynamic partitioning of the flow rate is dominant, increasing the injection rate can promote the development of multiple fractures more evenly. In this case, the fracturing fluid viscosity has little effect on the uniform development of fractures and can only increase the width of fractures to a certain extent
- (4) To promote the uniform development of multiple fractures by increasing perforation friction and the injection rate increase in the engineering pressure, it is necessary to comprehensively consider the setting of engineering parameters according to the actual engineering capacity

## Data Availability

The chart data used to support the findings of this study are included within the article.

## Conflicts of Interest

The authors declare that there are no conflicts of interest regarding the publication of this paper.

## References

- [1] Q. Zhang, X.-P. Zhang, and W. Sun, "A review of laboratory studies and theoretical analysis for the interaction mode between induced hydraulic fractures and pre-existing fractures," *Journal of Natural Gas Science and Engineering*, vol. 86, p. 103719, 2021.
- [2] K. H. S. M. Sampath, M. S. A. Perera, and P. G. Ranjith, "Theoretical overview of hydraulic fracturing break-down pressure," *Journal of Natural Gas Science and Engineering*, vol. 58, pp. 251–265, 2018.
- [3] N. P. Roussel, "Implications of fracturing pressure data recorded during a horizontal completion on stage spacing design," in *Society of Petroleum Engineers-SPE Hydraulic Fracturing Technology Conference*, pp. 794–807, 2012.
- [4] A. P. P. Bungler, R. G. G. Jeffrey, and X. Zhang, "Constraints on simultaneous growth of hydraulic fractures from multiple perforation clusters in horizontal wells," *SPE Journal (Society of Petroleum Engineers (U.S.) : 1996)*, vol. 19, no. 4, pp. 608–620, 2014.
- [5] X. L. Wang, C. Liu, H. Wang, H. Liu, and H. A. Wu, "Comparison of consecutive and alternate hydraulic fracturing in horizontal wells using XFEM-based cohesive zone method," *Journal of Petroleum Science & Engineering*, vol. 143, pp. 14–25, 2016.
- [6] H. Y. Wang, "Numerical investigation of fracture spacing and sequencing effects on multiple hydraulic fracture interference and coalescence in brittle and ductile reservoir rocks," *Engineering Fracture Mechanics*, vol. 157, pp. 107–124, 2016.
- [7] B. Wang, F. Zhou, Y. Zou et al., "Effects of previously created fracture on the initiation and growth of subsequent fracture during TPMSF," *Engineering Fracture Mechanics*, vol. 200, pp. 312–326, 2018.
- [8] J. Zhu, "Cluster spacing and well spacing optimization using multi-well simulation for the Lower Spraberry Shale in Midland Basin," in *Society of Petroleum Engineers - SPE Liquids - Rich Basins Conference - North America 2017*, 2017.
- [9] C. Miller, "Evaluation of production log data from horizontal wells drilled in organic shales," in *Society of Petroleum Engineers-SPE Americas Unconventional Gas Conference 2011*, pp. 623–645, UGC 2011, 2011.
- [10] D. R. Spain, "Geo-engineered completion optimization: an integrated, multi-disciplinary approach to improve stimulation efficiency in unconventional shale reservoirs," in *Society of Petroleum Engineers-SPE Middle East Unconventional Resources Conference and Exhibition 2015- The Journey of Unconventional Resources: From Exploration to Successful Development*, pp. 88–99, 2015.
- [11] W. El Rabaa, "Experimental study of hydraulic fracture geometry initiated from horizontal wells," *SPE Reprint Series*, vol. 47, pp. 166–173, 1998.

- [12] H. Zhu, J. Deng, X. Jin, L. Hu, and B. Luo, "Hydraulic fracture initiation and propagation from wellbore with oriented perforation," *Rock Mechanics and Rock Engineering*, vol. 48, no. 2, pp. 585–601, 2015.
- [13] Y. Feng and K. E. Gray, "Parameters controlling pressure and fracture behaviors in field injectivity tests: a numerical investigation using coupled flow and geomechanics model," *Computers and Geotechnics*, vol. 87, pp. 49–61, 2017.
- [14] J. E. Olson, *Multi-Fracture Propagation Modeling: Applications to Hydraulic Fracturing in Shales and Tight Gas Sands*, 42nd U.S. Rock Mechanics -2nd U.S.-Canada Rock Mechanics Symposium, 2008.
- [15] Y. Cheng, "Impacts of the number of perforation clusters and cluster spacing on production performance of horizontal shale-gas wells," *SPE Reservoir Evaluation & Engineering*, vol. 15, no. 1, pp. 31–40, 2012.
- [16] S. Salimzadeh, T. Usui, A. Paluszny, and R. W. Zimmerman, "Finite element simulations of interactions between multiple hydraulic fractures in a poroelastic rock," *International Journal of Rock Mechanics and Mining Sciences (Oxford, England: 1997)*, vol. 99, pp. 9–20, 2017.
- [17] D. H. Shin and M. M. Sharma, "Factors controlling the simultaneous propagation of multiple competing fractures in a horizontal well," in *Society of Petroleum Engineers-SPE Hydraulic Fracturing Technology Conference 2014*, pp. 269–288, 2014.
- [18] M. Haddad and K. Sepehrnoori, "XFEM-based CZM for the simulation of 3D multiple-cluster hydraulic fracturing in quasi-brittle shale formations," *Rock Mechanics and Rock Engineering*, vol. 49, no. 12, pp. 4731–4748, 2016.
- [19] P. Zhao, L. Xie, Q. Ge, Y. Zhang, J. Liu, and B. He, "Numerical study of the effect of natural fractures on shale hydraulic fracturing based on the continuum approach," *Journal of Petroleum Science & Engineering*, vol. 189, p. 107038, 2020.
- [20] K. Wu, J. Olson, M. T. Balhoff, and W. Yu, "Numerical analysis for promoting uniform development of simultaneous multiple-fracture propagation in horizontal wells," *SPE Production & Operations*, vol. 32, no. 1, pp. 41–50, 2017.
- [21] K. Wu and J. E. Olson, "Mechanisms of simultaneous hydraulic-fracture propagation from multiple perforation clusters in horizontal wells," *SPE Journal (Society of Petroleum Engineers (U.S.) : 1996)*, vol. 21, no. 3, pp. 1000–1008, 2016.
- [22] J. Guo, Q. Lu, H. Zhu, Y. Wang, and L. Ma, "Perforating cluster space optimization method of horizontal well multi-stage fracturing in extremely thick unconventional gas reservoir," *Journal of Natural Gas Science and Engineering*, vol. 26, pp. 1648–1662, 2015.
- [23] Z.-Z. Yang, L.-P. Yi, X.-G. Li, and W. He, "Pseudo-three-dimensional numerical model and investigation of multi-cluster fracturing within a stage in a horizontal well," *Journal of Petroleum Science & Engineering*, vol. 162, pp. 190–213, 2018.
- [24] Q. Wang, Y. Hu, J. Zhao, S. Chen, C. Fu, and C. Zhao, "Numerical simulation of fracture initiation, propagation and fracture complexity in the presence of multiple perforations," *Journal of Natural Gas Science and Engineering*, vol. 83, p. 103486, 2020.
- [25] J. Zhao, X. Chen, Y. Li, B. Fu, and W. Xu, "Numerical simulation of multi-stage fracturing and optimization of perforation in a horizontal well," *Petroleum Exploration and Development*, vol. 44, no. 1, pp. 119–126, 2017.
- [26] D. Chuprakov, O. Melchaeva, and R. Prioul, "Injection-sensitive mechanics of hydraulic fracture interaction with discontinuities," *Rock Mechanics and Rock Engineering*, vol. 47, no. 5, pp. 1625–1640, 2014.
- [27] W. Xu, J. Zhao, S. S. Rahman, Y. Li, and Y. Yuan, "A comprehensive model of a hydraulic fracture interacting with a natural fracture: analytical and numerical solution," *Rock Mechanics and Rock Engineering*, vol. 52, no. 4, pp. 1095–1113, 2019.
- [28] E. Eberhardt, D. Stead, B. Stimpson, and E. Z. Lajtai, "The effect of neighbouring cracks on elliptical crack initiation and propagation in uniaxial and triaxial stress fields," *Engineering Fracture Mechanics*, vol. 59, no. 2, pp. 103–115, 1998.
- [29] A. P. P. Bungler, X. Zhang, and R. G. G. Jeffrey, "Parameters affecting the interaction among closely spaced hydraulic fractures," *SPE Journal (Society of Petroleum Engineers (U.S.) : 1996)*, vol. 17, no. 1, pp. 292–306, 2012.
- [30] Y. Cheng, "Boundary element analysis of the stress distribution around multiple fractures: implications for the spacing of perforation clusters of hydraulically fractured horizontal wells," *SPE Eastern Regional Meeting*, pp. 267–281, 2009.
- [31] B. Wheaton, "Integration of distributed temperature and distributed acoustic survey results with hydraulic fracture modeling: a case study in the Woodford shale," in *Society of Petroleum Engineers - SPE/AAPG/SEG Unconventional Resources Technology Conference*, 2016.
- [32] B. Lecampion and J. Desroches, "Simultaneous initiation and growth of multiple radial hydraulic fractures from a horizontal wellbore," *Journal of the Mechanics and Physics of Solids*, vol. 82, pp. 235–258, 2015.
- [33] A. P. Peirce and A. P. Bungler, "Interference fracturing: non-uniform distributions of perforation clusters that promote simultaneous growth of multiple hydraulic fractures," *SPE Journal (Society of Petroleum Engineers (U.S.) : 1996)*, vol. 20, no. 2, pp. 384–395, 2015.
- [34] X.-G. Li, L.-P. Yi, and Z.-Z. Yang, "Numerical model and investigation of simultaneous multiple-fracture propagation within a stage in horizontal well," *Environmental Earth Sciences*, vol. 76, no. 7, 2017.
- [35] Y. Li, J. G. Deng, W. Liu, and Y. Feng, "Modeling hydraulic fracture propagation using cohesive zone model equipped with frictional contact capability," *Computers and Geotechnics*, vol. 91, pp. 58–70, 2017.
- [36] J. B. Crump, "Effects of perforation-entry friction on bottom-hole treating analysis," *Journal of Petroleum Technology*, vol. 40, no. 8, pp. 1041–1048, 1988.
- [37] N. Modeland, "Statistical analysis of the effect of completion methodology on production in the Haynesville shale," in *Society of Petroleum Engineers-SPE Americas Unconventional Gas Conference 2011*, pp. 447–461, UGC 2011, 2011.
- [38] C. G. Dávila, "Mixed-mode decohesion elements for analyses of progressive delamination," in *Collection of Technical Papers-AIAA/ASME/ASCE/AHS/ASC Structures, Structural Dynamics and Materials Conference*, vol. 3, pp. 2277–2288, 2001.
- [39] M. L. Benzeggagh and M. Kenane, "Measurement of mixed-mode delamination fracture toughness of unidirectional glass/epoxy composites with mixed-mode bending apparatus," *Composites Science and Technology*, vol. 56, no. 4, pp. 439–449, 1996.

## Research Article

# Nanopore Confinement Effect on the Phase Behavior of CO<sub>2</sub>/Hydrocarbons in Tight Oil Reservoirs considering Capillary Pressure, Fluid-Wall Interaction, and Molecule Adsorption

Zhixue Zheng <sup>1,2</sup>, Yuan Di <sup>1,2</sup> and Yu-Shu Wu<sup>3</sup>

<sup>1</sup>College of Engineering, Peking University, Beijing 100871, China

<sup>2</sup>Institute of Energy, Peking University, Beijing 100871, China

<sup>3</sup>Department of Petroleum Engineering, Colorado School of Mines, Golden CO 80401, USA

Correspondence should be addressed to Yuan Di; [diyuan@mech.pku.edu.cn](mailto:diyuan@mech.pku.edu.cn)

Received 8 July 2021; Revised 25 July 2021; Accepted 9 August 2021; Published 21 August 2021

Academic Editor: Steffen Berg

Copyright © 2021 Zhixue Zheng et al. This is an open access article distributed under the Creative Commons Attribution License, which permits unrestricted use, distribution, and reproduction in any medium, provided the original work is properly cited.

The pore sizes in tight reservoirs are nanopores, where the phase behavior deviates significantly from that of bulk fluids in conventional reservoirs. The phase behavior for fluids in tight reservoirs is essential for a better understanding of the mechanics of fluid flow. A novel methodology is proposed to investigate the phase behavior of carbon dioxide (CO<sub>2</sub>)/hydrocarbons systems considering nanopore confinement. The phase equilibrium calculation is modified by coupling the Peng-Robinson equation of state (PR-EOS) with capillary pressure, fluid-wall interaction, and molecule adsorption. The proposed model has been validated with CMG-Winprop and experimental results with bulk and confined fluids. Subsequently, one case study for the Bakken tight oil reservoir was performed, and the results show that the reduction in the nanopore size causes noticeable difference in the phase envelope and the bubble point pressure is depressed due to nanopore confinement, which is conducive to enhance oil recovery with a higher possibility of achieving miscibility in miscible gas injection. As the pore size decreases, the interfacial tension (IFT) decreases whereas the capillary pressure increases obviously. Finally, the recovery mechanisms for CO<sub>2</sub> injection are investigated in terms of minimum miscibility pressure (MMP), solution gas-oil ratio, oil volume expansion, viscosity reduction, extraction of lighter hydrocarbons, and molecular diffusion. Results indicate that nanopore confinement effect contributes to decrease MMP, which suppresses to 650 psi (65.9% smaller) as the pore size decreases to 2 nm, resulting in the suppression of the resistance of fluid transport. With the nanopore confinement effect, the CO<sub>2</sub> solution gas-oil ratio and the oil formation volume factor of the oil increase with the decrease of pore size. In turn, the oil viscosity reduces as the pore size decreases. It indicates that considering the nanopore confinement effect, the amount of gas dissolved into crude oil increases, which will lead to the increase of the oil volume expansion and the decrease of the viscosity of crude oil. Besides, considering nanopore confinement effect seems to have a slightly reduced effect on extraction of lighter hydrocarbons. On the contrary, it causes an increase in the CO<sub>2</sub> diffusion coefficient for liquid phase. Generally, the nanopore confinement appears to have a positive effect on the recovery mechanisms for CO<sub>2</sub> injection in tight oil reservoirs. The developed novel model could provide a better understanding of confinement effect on the phase behavior of nanoscale porous media in tight reservoirs. The findings of this study can also help for better understanding of a flow mechanism of tight oil reservoirs especially in the case of CO<sub>2</sub> injection for enhancing oil recovery.

## 1. Introduction

According to the predictions, global energy demand is projected to grow by about a third by 2040, particularly in India, China, and across Asia [1]. Tight oil reservoirs have been increasingly concerned due to its abundant reserves, huge

development, and utilization potential. As illustrated in EIA's crude oil production forecast graph from 2020 annual report, tight oil in the United States is predicted to increase the total amount of crude oil production by 160% from 2010 to 2050. Tight oil production will more than double from 2015 to 2040 as shown in Figure 1 [2]. To meet oil



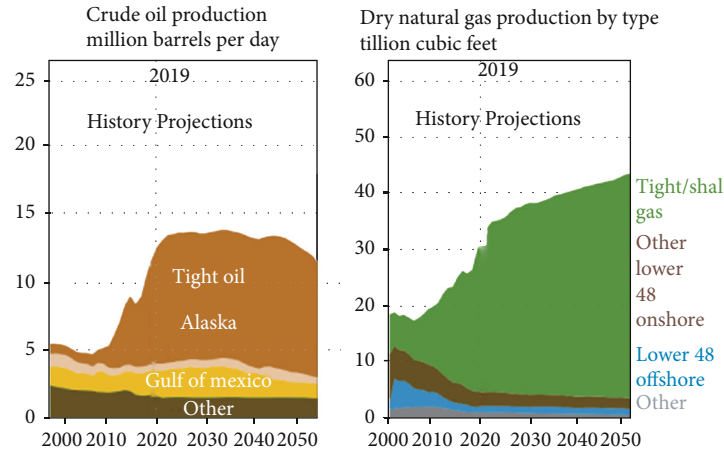


FIGURE 1: Historical and projected sources of crude oil and natural gas in the US (EIA, 2020).

demand, substantial ongoing investment in tight oil reservoir development will be required.

Despite horizontal drilling and multistage hydraulic fracturing technologies achieving tremendous success for economic development of tight oil reservoirs, the oil industry still faces challenges such as low oil recovery and rapidly declining production rate due to unknown fluid phase behavior and recovery mechanisms in tight oil reservoirs accurately [3–6]. Therefore, understanding the phase behavior for fluids in nanopores is essential for a better developing tight oil reservoirs and predicting well performance.

The pore sizes in tight reservoirs are nanopores, where the phase behavior deviates significantly from that of bulk fluids in conventional reservoirs [7–9]. Wang et al. [10] conducted nanofluidic device experiments with pure alkane and showed that the vaporization of the liquid phase in nanochannels is obviously suppressed compared to that in microchannels. Nojabaei et al. [11] found that the PVT properties of crude oil were significantly different under the two conditions comparing the PVT properties of crude oil in a PVT cylinder with those in nanoscale porous media. Luo et al. [12, 13] studied nanopore confinement effect using differential scanning calorimetry (DSC) and found that the bubble point alteration is significant when the pore size under 4.1 nm. Pinho et al. [14] introduced a novel technique to conduct a microfluidic multicomponent phase behavior and showed that multicomponent P-T diagrams are altered under nanopore confinement effect. Other experimental techniques including temperature-programmed desorption (TPD) [15], neutron diffraction [16], volumetric measurement [17], X-ray diffraction [18], scanning electron microscope (SEM) [19], and micro-CT scanning [20] also have found similar phenomena in nanopores. All these experiments showed that nanoscale interaction had a remarkable effect on the gas-liquid equilibrium of hydrocarbon components, but the results were influenced by experimental materials, and there were few experimental studies on the phase behavior in nanopores with a radius smaller than 50 nm was present in the literature due to the unconventional characteristics of tight oil reservoirs and the limitations of laboratory equipment. Molecular simulation is also widely used

to investigate the fluid phase behavior under nanopore confinement. Wang et al. [21] presented Monte Carlo simulation (MC) to investigate the adsorption behavior of pentane, heptane, and their mixtures in slit-nanopores and found that multiple adsorption layers properties depend on pore size and fluid compositions. Jin and Firoozabadi [22] analyzed the effect of pore size distribution by gauge-GCMC simulation and revealed that fluids in tiny pores condense before that in large pores, and the shift of the phase diagram would increase with the proportion of small pores. Despite these simulation studies providing details of the behavior of confined fluids, it is not applicable to employ the molecular simulation method to analyze the nanopore confinement effect on the phase behavior at an engineering scale due to their high computation costs. Therefore, researchers have focused on developing thermodynamics models to characterize the fluid phase behavior of confined tight oil reservoirs.

The equation of state (EOS) is one of the most used approaches in thermodynamics models, and it has accomplished a huge success in modeling bulk phase behavior. Recently, experimental and theoretical studies have shown the existence of capillary pressure effect in nanopores. In an effort to consider the nanopore confinement effect on the phase behavior in tight oil reservoirs, Zhang et al. [23] modified flash calculation with capillary pressure and performed the studies of the phase behavior of CO<sub>2</sub>/hydrocarbons systems in Bakken formations, and the results indicated that the capillary pressure effect cannot be neglected in nanopores. MMP of CO<sub>2</sub> injection decreases with the capillary pressure effect, resulting in the suppression of the resistance of fluid transport. Li and Sheng [24] performed the phase equilibrium of Wolfcamp shale reservoir by coupling Peng-Robinson equation of state (PR-EOS) with capillary pressure and shifted critical properties, and results presented that nanopore confinement narrowed the two-phase region and decreased the interfacial tension. The confined space in tight oil reservoirs causes the molecular radius to be comparable to the pore size, and the interaction between the fluid molecular and pore wall strengthens to a point that cannot be ignored. Yang et al. [25] recently

revealed the size effect of the solid-liquid interface energy and found that the mechanical action of the solid-liquid interface plays an important role in capillary condensation under nanometer or subnanometer scale, rather than the gas-liquid interface, which is generally believed to play a dominant role. In order to consider the influence of the interaction between the fluid and pore wall on the phase equilibrium, Travalloni et al. [26] proposed a modified PR-EOS considering both molecule–molecule and molecule-wall interaction and claimed that the molecule-wall interaction cannot be negligible. Yang et al. [27] extended PR-EOS by introducing a new term representing the molecule-wall interaction and showed that the molecule-wall interaction causes a significant alteration of the two-phase region. Adsorption has been an important factor in studying the fluid phase behavior under nanopore confinement. Dong et al. [28] coupled the multicomponent potential theory of adsorption with PR-EOS to investigate the fluid phase behavior of pure hydrocarbons and their mixtures in organic slit-like and cylindrical nanopores and showed that adsorption played an important role in the fluid phase behavior. Cui et al. [29] improved PR-EOS by reducing mole number of fluids caused by adsorption. Sandoval et al. [30] explored the adsorption effect on the fluid phase behavior in nanopores and incorporated the adsorption film thickness into the calculation of the effective capillary radius. Song et al. [31] introduced a novel method for describing fluid adsorption in nanopores by modifying the molar volume term in PR-EOS and showed that adsorption induced critical shifts of confined fluids in nanopores.

As mentioned above, nanopore confinement effects including capillary pressure, fluid-wall interaction, and molecule adsorption cannot be ignored in porous media with pore diameters less than 50 nm and greater than 2 nm [32–34]. Although numerous models have been proposed to explore the phase behavior in nanopores, they focused on one or both aspects of nanoscale confinement [23–31], and there still lack an accurate model that takes into account capillary pressure, fluid-wall interaction, and adsorption effect simultaneously. Additionally, despite methods being there to investigate nanopore confinement effect, only a few of them have studies the influence of nanopore confinement effect on CO<sub>2</sub> injection recovery mechanisms in tight oil reservoirs. Motivated by these points, a modified PR-EOS model is established to study the fluid phase behavior and recovery mechanisms in tight oil reservoirs for CO<sub>2</sub> injection.

The rest of the paper is organized as follows. In Section 2, the methodology section illustrates the procedures of model development by coupling fluid-wall interaction and adsorption effect in the EOS and capillary pressure in the flash calculation. Subsequently, the proposed model is validated with CMG-Winprop and experimental results with bulk and confined fluids, and then, we performed to analyze one case study from the Bakken tight oil reservoir at various pore sizes in Section 3. In Section 4, based on the investigation of the phase behavior of tight oil with CO<sub>2</sub> injection under different scenarios, the recovery mechanisms affected by minimum miscible pressure (MMP), solution gas-oil

ratio, oil volume expansion, viscosity reduction, extraction of lighter hydrocarbons, and molecular diffusion are studied with respect to the confinement effect. At the end, summary and conclusions are provided in Section 5 to give some suggestions. The developed novel model provides a better understanding of confinement effect on the phase behavior in tight reservoirs and even nanoscale porous media. The findings of this study can also help for better understanding of the flow mechanism of tight oil reservoirs especially in the case of CO<sub>2</sub> injection for enhancing oil recovery.

## 2. Materials and Methods

The fluid phase behavior in tight oil reservoirs is governed by the interactions of fluid-fluid and fluid-wall interactions within the confining geometry [11]. In the pore networks, fluid molecules are usually adsorbed onto the pore wall [35–37]. At large pore sizes, the number of molecules adsorbed is negligible compared to the volume of the liquid. When the pore size decreases further (<10 nm), the interaction between molecules and pore walls of porous media is significant [32]. Adsorption will be significant and greatly reduces the number of fluid molecules in the free state which then will affect the molecular molar volume. In the nanopores, the larger capillary pressure, van der Waals forces, fluid-wall interaction, and adsorption effect lead to the deviation of physical properties in the bulk fluid.

In this section, the methodology is introduced to describe the nanopore confinement effect on the phase behavior, and the PR-EOS and Rachford-Rice flash calculation are modified considering capillary pressure, fluid-wall interaction, and adsorption effect.

*2.1. Fluid-Wall Interaction.* The original PR-EOS consists of a repulsion pressure  $P_R$  and an attraction pressure  $P_A$  as follows [38]:

$$P = P_R + P_A = \frac{RT}{V_m - b} - \frac{a}{V_m(V_m + b) + b(V_m - b)}, \quad (1)$$

$$P_R = \frac{RT}{V_m - b}, \quad (2)$$

$$P_A = -\frac{a}{V_m(V_m + b) + b(V_m - b)}, \quad (3)$$

where  $P$  is the system pressure,  $R$  is the gas constant,  $T$  is the system temperature,  $V_m$  is the molar volume,  $a$  represents “attraction” parameter, and  $b$  is the van der Waals co-volume, which represent “repulsion” parameter.

In nanopores, in order to consider fluid-wall interaction effect, we introduce a molecule-wall interaction pressure term  $P_{FW}$  which plays a role of diminishing the attractive component [25] into Equation (1) as follows:

$$P = \frac{RT}{V_m - b} - \frac{a}{V_m(V_m + b) + b(V_m - b)} + \frac{c}{V_m(V_m + b) + b(V_m - b)},$$

$$P_{FW} = \frac{c}{V_m(V_m + b) + b(V_m - b)}, \quad (4)$$

where  $c$  is the fluid-wall interaction effect coefficient.

**2.2. Adsorption Effect.** There are many models describing the adsorption effect, such as ideal adsorbed solution theory, multicomponent potential theory of adsorption, and Langmuir isothermal adsorption model [39–41]. For the sake of incorporating the adsorption effect on nanopore confinement conveniently, in this paper, the fluid molecules adsorbed in the organic matters and pore walls are assumed stationary, and adsorption leads to the reduction number of movable fluid molecules, which in turn increases the effective mole volume of fluid molecules in the bulk phase [29]. An adsorption effect coefficient  $\alpha$  is introduced into Equation (1) as follows:

$$P = \frac{RT}{\alpha V_m - b} - \frac{a}{\alpha V_m(\alpha V_m + b) + b(\alpha V_m - b)}. \quad (5)$$

**2.3. The Modified PR-EOS.** The original PR-EOS could be modified by two parameters representing separately fluid-wall interaction and adsorption effect. Then, the PR-EOS is modified as follows:

$$P = \frac{RT}{\alpha V_m - b} - \frac{a - c}{\alpha V_m(\alpha V_m + b) + b(\alpha V_m - b)}. \quad (6)$$

From Equation (6), it can be seen that when  $\alpha = 1$  and  $c = 0$ , that is to say, fluid-wall interaction and adsorption effect are not taken into account, the modified PR-EOS can be reduced to original PR-EOS.

For the PR-EOS, the isotherm merely has a horizontal tangent and inflection point at the critical point in the typical pressure-volume diagram [42]. This can be expressed mathematically that the first and second derivatives of pressure with respect to volume at a constant temperature are equal to 0.

$$\left(\frac{\partial P}{\partial V}\right)_{T=T_c} = \left(\frac{\partial^2 P}{\partial V^2}\right)_{T=T_c} = 0, \quad (7)$$

where  $T_c$  represents the critical temperature.

Imposing Equation (7) on Equation (6) and parameters  $a - c$  and  $b$  yields could be expressed by

$$a - c = 0.45724 \frac{R^2 T_c^2}{P_c}, \quad (8)$$

$$b = 0.07780 \frac{RT_c}{\alpha P_c}. \quad (9)$$

The details of “ $a - c$ ” and “ $b$ ” calculations are specified in the Appendix. From Equations (6)–(9), the expressions

of critical pressure and critical temperature can be obtained as follows:

$$P_{CC} = 0.01324 \frac{a - c}{\alpha^2 b^2},$$

$$T_{CC} = 0.17015 \frac{a - c}{\alpha b R}, \quad (10)$$

where  $P_{CC}$  and  $T_{CC}$  are the critical pressure and critical temperature determined by the modified PR-EOS.

The dimensionless shifts of critical pressure  $\Delta P$  and critical temperature  $\Delta T$  are defined as follows:

$$\Delta P = \frac{P_c - P_{CC}}{P_c} = \frac{a\alpha^2 - a + c}{a\alpha^2}, \quad (11)$$

$$\Delta T = \frac{T_c - T_{CC}}{T_c} = \frac{a\alpha - a + c}{a\alpha}. \quad (12)$$

**2.4. Correlation for Critical Pressure and Critical Temperature.** Equations (11) and (12) exhibit that fluid-wall interaction and adsorption effect influence the critical pressure and critical temperature in nanopores. It has been reported that the pore size  $r_p$  and collision diameter  $\sigma_{LJ}$  (Lennard-Jones molecular size parameter) are the important factors on shifts of critical pressure and critical temperature [27, 31]. The confined fluid critical pressure shift and critical temperature shift for different components ( $\text{CO}_2$ ,  $\text{CH}_4$ ,  $\text{C}_2\text{H}_4$ ,  $\text{C}_2\text{H}_6$ ,  $\text{C}_4\text{H}_{10}$ ,  $\text{C}_8\text{H}_{18}$ , and  $\text{C}_{10}\text{H}_{22}$ ) are collected from references [43–51]. Then, the correlations between the shifts of critical properties and the dimensionless pore size ( $r_p/\sigma_{LJ}$ ) can be obtained and demonstrated in Figures 2(a) and 2(b).

As described in Figures 2(a) and 2(b), the correlations of shifts of critical pressure and critical temperature with dimensionless pore size are

$$\Delta P = 0.9793 \left(\frac{r_p}{\sigma_{LJ}}\right)^{-0.6366},$$

$$\Delta T = 0.7597 \left(\frac{r_p}{\sigma_{LJ}}\right)^{-0.7708}, \quad (13)$$

where  $r_p$  is the radius of pore throat and  $\sigma_{LJ}$  is the Lennard-Jones molecular size parameter.

From Equations (11) and (12), both fluid-wall interaction effect coefficient  $\alpha$  and adsorption effect coefficient  $c$  can be calculated by shifts of critical pressure and temperature.

$$\alpha = \frac{1 - \Delta T}{1 - \Delta P} = \frac{1 - 0.7597(r_p/\sigma_{LJ})^{-0.7708}}{1 - 0.9793(r_p/\sigma_{LJ})^{-0.6366}},$$

$$c = (1 - \alpha(1 - \Delta T))a = \left(1 - \frac{(1 - 0.7597(r_p/\sigma_{LJ})^{-0.7708})^2}{1 - 0.9793(r_p/\sigma_{LJ})^{-0.6366}}\right)a. \quad (14)$$

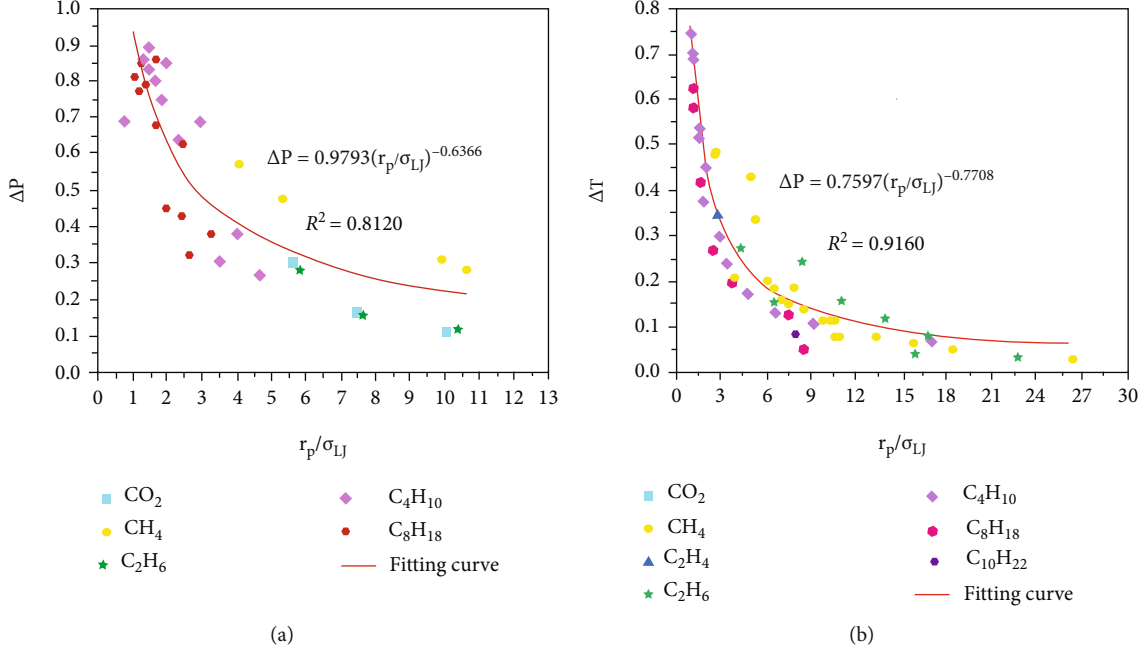


FIGURE 2: (a) Correlation of shift of critical pressure and (b) correlation of shift of critical temperature with the dimensionless pore size.

**2.5. Phase Equilibrium Calculation considering Capillary Pressure, Fluid-Wall Interaction, and Molecule Adsorption.** According to the thermodynamic theory, for a system containing  $N_c$  components, the thermodynamic condition for the phase equilibrium state is that when the temperature and pressure of each phase are equal, the chemical potential or fugacity of each component is equal.

$$\begin{aligned}
 f_i^L(T, P_L, x_i) &= f_i^V(T, P_V, y_i) \quad i = 1, 2, \dots, N_c, \\
 f_i^L &= x_i \varphi_i^L P_L, \\
 f_i^V &= y_i \varphi_i^V P_V,
 \end{aligned} \quad (15)$$

where  $f_i^L$  and  $f_i^V$  are fugacity of component  $i$  in the liquid and vapor phases, respectively.  $x_i$  and  $y_i$  are the mole fraction of component  $i$  in the liquid and vapor phases, respectively.  $P_L$  and  $P_V$  are the liquid and vapor pressures, respectively.  $\varphi_i^L$  and  $\varphi_i^V$  are the fugacity coefficient of component  $i$  in the liquid and vapor phases.  $N_c$  is the number of components.

According to the mass balance equation, Rachford and Rice [52] proposed an isothermal flash calculation method to determine the equilibrium phase composition and mole fraction of the component in the liquid and gas phases. The mass balance equation and Rachford-Rice equation are presented in

$$\sum_{i=1}^{N_c} x_i = \sum_{i=1}^{N_c} y_i = 1 \quad i = 1, 2, \dots, N_c, \quad (16)$$

$$z_i = (1 - n_V)x_i + n_V y_i, \quad (17)$$

$$\sum_{i=1}^{N_c} \frac{(K_i - 1)z_i}{1 + n_V(K_i - 1)} = 0 \quad i = 1, 2, \dots, N_c, \quad (18)$$

where  $z_i$  is the overall mole fraction of component  $i$ .  $n_V$  is overall number of moles in vapor phase.  $K_i$  is phase equilibrium ratio of component  $i$ .

The difference between liquid pressure and vapor pressure is defined as capillary pressure  $P_{\text{cap}}$ , which is calculated by the Young-Laplace equation [53]:

$$P_{\text{cap}} = P_V - P_L = \frac{2\sigma \cos \theta}{r_p}, \quad (19)$$

where  $\theta$  is the contact angle.  $r_p$  is the radius of pore throat.  $\sigma$  is the interfacial tension which can be calculated by Macleod-Sugden correlation [54] as follows:

$$\sigma = \left[ \sum_{i=1}^{N_c} (\rho_L x_i [P]_i - \rho_V y_i [P]_i) \right]^4, \quad (20)$$

where  $\rho_L$  and  $\rho_V$  are the densities of liquid phase and vapor phase, respectively.  $[P]_i$  is the parachor of component  $i$  in the liquid or vapor phase.

The formula of the compressibility factor in nanopores is presented as follows:

$$Z = \frac{\alpha P V_m}{RT}, \quad (21)$$

where  $Z$  is the compressibility factor.

Hence, rearranging Equation (6) into the compressibility factor form rewrites

$$Z^3 - (1 - B)Z^2 + (A - 3B^2 - 2B)Z - (AB - B^2 - B^3) = 0, \quad (22)$$

where

$$\begin{aligned} A &= \frac{(a-c)P}{(RT)^2}, \\ B &= \frac{bP}{\alpha RT}. \end{aligned} \quad (23)$$

Since the pressures of the liquid and vapor phases are not equal, Equation (21) can be separately rewritten for liquid phase with the following:

$$Z_L^3 - (1 - B_L)Z_L^2 + (A_L - 3B_L^2 - 2B_L)Z_L - (A_L B_L - B_L^2 - B_L^3) = 0, \quad (24)$$

where  $Z_L$  is the compressibility factor of the liquid phase.

Similarly, for vapor phase is as follows:

$$Z_V^3 - (1 - B_V)Z_V^2 + (A_V - 3B_V^2 - 2B_V)Z_V - (A_V B_V - B_V^2 - B_V^3) = 0, \quad (25)$$

where  $Z_V$  is the compressibility factor of the vapor phase.

The fugacity coefficient for the liquid and vapor phases are defined by the following expressions:

$$\begin{aligned} \ln \varphi_i^L &= -\ln [Z_L - B_L] + \frac{b_{iL}}{b_L} (Z_L - 1) + \frac{A_L}{2\sqrt{2}B_L} \\ &\quad \cdot \left[ \frac{2\sum_{i=1}^{N_c} x_{iL}(1 - k_{ij})\sqrt{a_{iL}a_{jL}}}{a_L} - \frac{b_{iL}}{b_L} \right] \\ &\quad \cdot \ln \left[ \frac{Z_L + B_L(1 + \sqrt{2})}{Z_L + B_L(1 - \sqrt{2})} \right], \\ \ln \varphi_i^V &= -\ln [Z_V - B_V] + \frac{b_{iV}}{b_V} (Z_V - 1) + \frac{A_V}{2\sqrt{2}B_V} \\ &\quad \cdot \left[ \frac{2\sum_{i=1}^{N_c} x_{iV}(1 - k_{ij})\sqrt{a_{iV}a_{jV}}}{a_V} - \frac{b_{iV}}{b_V} \right] \\ &\quad \cdot \ln \left[ \frac{Z_V + B_V(1 + \sqrt{2})}{Z_V + B_V(1 - \sqrt{2})} \right]. \end{aligned} \quad (26)$$

Hence, the liquid-vapor phase equilibrium accounting for the capillary pressure effect can be obtained using the aforementioned equations. Successive substitution and Newton-Raphson method are applied for solving nonlinear equations. Figure 3 demonstrates the flow chart for the phase equilibrium calculation with the nanopore confinement effect considering capillary pressure, fluid-wall interaction, and molecule adsorption.

### 3. Model Validation and Analysis

**3.1. Model Validation.** To validate the accuracy of modified model considering capillary pressure, fluid-wall interaction, and molecule adsorption effect, in this section, the developed model results are compared with CMG-Winprop results and experimental results. The phase equilibrium ratio ( $K$ -value) of fluid components in Tahe Oilfield in China at  $T = 124.4^\circ\text{C}$  and  $P = 20.78 \text{ MPa}$  is first calculated. The fluid type in Tahe Oilfield is bulk fluids.

The predicted results and CMG-Winprop results are summarized in Table 1. Furthermore, we calculate the phase equilibrium ratio ( $K$ -value) of fluid components at  $T = 344.8 \text{ K}$  and  $P = 61.8 \text{ psi}$ . The data from experimental studies are reported in the literature [10], and the fluid type is confined fluids. The predicted results and experimental results are summarized in Table 2. The compared analysis indicates a good agreement between the developed model data with CMG-Winprop and experimental results. The average deviation between the predicted  $K$ -value and CMG-Winprop results is 2.71%, indicating that the modified model proposed in this study can effectively predict the phase behavior of fluids in bulk. The average deviation between the predicted  $K$ -value and experimental results is 1.02%. Compared with the model only considering capillary pressure whose average deviation is 2.78%, the error is more acceptable.

**3.2. Nanopore Confinement Effect on Phase Behavior of Fluids in Bakken Tight Oil Reservoir.** The Bakken tight oil reservoir is one of the largest tight oil resources in the world, with total daily production exceeding  $19 \times 10^4 \text{ t}$ . In this study, we investigate the nanopore confinement effect on the phase behavior of a typical fluid in Bakken tight oil reservoirs. The composition and physical property parameters of crude oil are taken from Zhang and Yu et al. [32, 55], which are shown in Tables 3 and 4, respectively.

**3.2.1. Phase Envelope.** The modified model is used to determine the phase envelope of the Bakken tight oil reservoir for the pore radius ranging from 5 nm to 50 nm. Figure 4 conducts the sensitivity analyses of pore size on the phase envelope by separately considering capillary pressure, fluid-wall interaction, and adsorption effect. As shown in Figure 4(a) where only capillary pressure is considered, the bubble point curve is lowered as the pore size decreases. After considering capillary pressure, the bubble point pressure is obviously suppressed when the pore size is less than 50 nm. The significant changes caused by the capillary pressure effect on bubble point pressures can reach as high as 630 psi when the pore size reduces to 5 nm. As the system goes above the bubble point pressure, the fluids in the Bakken tight oil reservoir may remain in the single-phase region. When the pressure is lower than the bubble point pressure, the amount of light or medial hydrocarbons tend to be evaporated to the form of gas bubble. Hence, the reduction in the bubble point pressure delays the process of vapor extracts out of the liquid and indicates that the fluids may remain in the liquid phase much longer. Therefore, considering capillary pressure has a positive influence on the tight oil

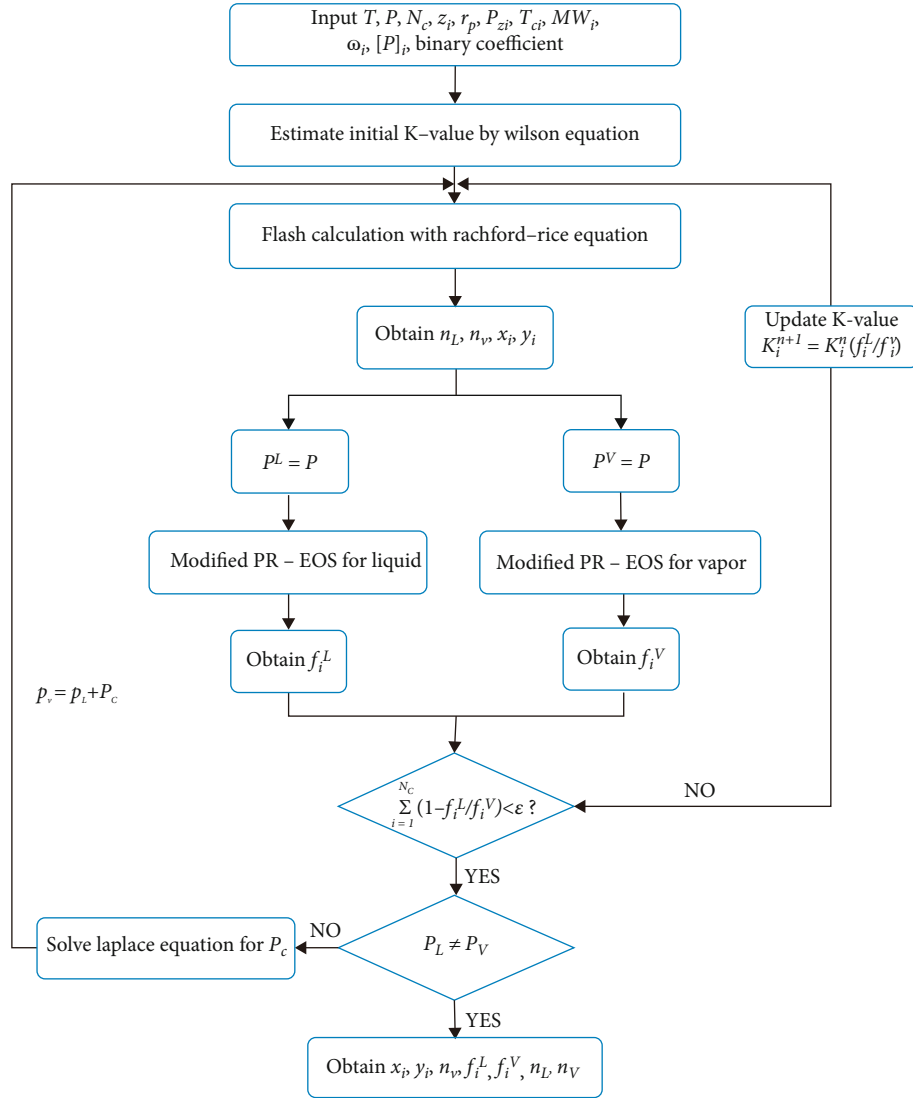


FIGURE 3: Flow char for phase equilibrium calculation with modified PR-EOS.

TABLE 1: Comparison of phase equilibrium ratio between predicted results and CMG-Winprop results.

Fluid types	Components	Molar fraction (%)	CMG-Winprop results	Simulation results	Relative deviation (%)
Bulk fluids	C <sub>1</sub>	43.96	2.3186	2.3798	2.64
	C <sub>2</sub> -C <sub>4</sub>	21.03	1.0071	0.9943	1.27
	C <sub>5</sub> -C <sub>7</sub>	6.81	0.3447	0.3337	2.94
	C <sub>8</sub> -C <sub>9</sub>	7.59	0.1897	0.1823	3.90
	C <sub>10+</sub>	18.71	0.0068	0.0070	3.13
	CO <sub>2</sub>	1.90	1.6850	1.7255	2.40

TABLE 2: Comparison of phase equilibrium ratio between predicted results and experimental or simulation results.

Fluid types	Components	Molar fraction (%)	Experimental data	Simulation results with P <sub>c</sub>	Relative deviation (%)	Simulation results this paper	Relative deviation (%)
Confined fluids	i-C <sub>4</sub>	61.89	2.652	2.816	6.18	2.594	2.19
	n-C <sub>4</sub>	18.11	1.885	1.904	1.01	1.894	0.48
	C <sub>8</sub>	20.00	0.0524	0.053	1.15	0.0522	0.38

TABLE 3: The composition and physical property parameters of crude oil for the Bakken formation.

Components	$T_{ci}$ (K)	$P_{ci}$ (bar)	$V_c$ (L/mol)	$MW_i$ (g/mol)	$\omega_i$	Parachor	$z_i$ (%)
C <sub>1</sub>	190.60	45.40	0.0990	16.04	0.0080	77.0	25.06
C <sub>2</sub> -C <sub>4</sub>	363.30	42.54	0.1970	42.82	0.1432	145.2	22.00
C <sub>5</sub> -C <sub>7</sub>	511.56	33.76	0.3338	83.74	0.2474	250.0	20.00
C <sub>8</sub> -C <sub>9</sub>	579.34	30.91	0.4062	105.91	0.2861	306.0	13.00
C <sub>10+</sub>	788.74	21.58	0.9208	200.00	0.6869	686.3	19.94

TABLE 4: Binary interaction parameters for oil components.

Components	C <sub>1</sub>	C <sub>2</sub> -C <sub>4</sub>	C <sub>5</sub> -C <sub>7</sub>	C <sub>8</sub> -C <sub>9</sub>	C <sub>10+</sub>
C <sub>1</sub>	0	0.0078	0.0242	0.0324	0.0779
C <sub>2</sub> -C <sub>4</sub>	0.0078	0	0.0046	0.0087	0.0384
C <sub>5</sub> -C <sub>7</sub>	0.0242	0.0046	0	0.0006	0.0169
C <sub>8</sub> -C <sub>9</sub>	0.0324	0.0087	0.0006	0	0.0111
C <sub>10+</sub>	0.0779	0.0384	0.0169	0.0111	0

production, as illustrated in Figure 4(b) where only fluid-wall interaction is considered, the entire phase envelope is suppressed as the pore size decreases. Especially, considering fluid-wall interaction also reduces the critical point instead of considering only the capillary pressure. As the pore size decreases, the critical point and bubble point pressure become smaller. The phase envelope at 50 nm is almost the same as that of bulk phase, whereas the critical pressure at 5 nm is suppressed by 8.3%. This is because when the pore size decreases, the interaction between fluid molecules and pore wall increases. As can be seen in Figure 4(c) where only adsorption effect is considered, it's similar to just considering fluid-wall interaction. It can be seen from the Figures 4(a)–4(c) that the effect of capillary pressure, fluid-wall interaction and adsorption effect on the phase behavior in nanopores cannot be ignored.

By considering capillary pressure, fluid-wall interaction, and adsorption effect together, the P-T phase envelope of the Bakken tight oil reservoir at various pore sizes is plotted in Figure 4(d). It is illustrated that the phase envelope tends to move downward with the decrease of pore size. The critical point is reduced and the dew point curve shrinks compared with the phase envelope that only considers capillary pressure. The bubble point curve shrinks further than the phase envelope that considers only fluid-wall interaction or adsorption effect.

**3.2.2. Bubble Point Pressure.** The bubble point pressures at different pore sizes are calculated. Figure 5 describes the bubble point pressure at the reservoir temperature of 230°F and compares the nanopore confinement on bubble point pressure with different pore sizes. As illustrated in Figure 6, the smaller the pore size, the more significant the nanopore confinement effect. When the pore size is smaller than 10 nm, significant changes can be observed. The bubble point pressure reduces to 1542 psi (19.1% smaller) when the pore size is 10 nm, and the bubble point pressure suppresses to 650 psi (65.9% smaller) as the pore size decreases to 2 nm. However, when the pore size is above 100 nm, the bubble

point pressure approaches to the bulk fluids, and the nanopore confinement effect can be neglected.

**3.2.3. Interfacial Tension and Capillary Pressure.** In this section, the interfacial tension (IFT) and capillary pressure ( $P_c$ ) in different radii under different pressures at the reservoir temperature of 230°F are calculated. As shown in Figure 6, as the pressure increases, the interfacial tension decreases. The interfacial tension is significantly affected by the existence of nanopore confinement. The smaller the pore size, the greater the interfacial tension decreases. As described by Figure 7, when the pressure increases, the capillary pressure also decreases. The smaller the pore size, the greater the capillary pressure. When the pressure is 1500 psi, the capillary pressure with pore size of 5 nm is more than 5 times that of the bulk phase. As the pressure is smaller, the multiple increases. Therefore, the nanopore confinement effect will lead to high capillary pressure which cannot be ignored in tight oil reservoirs.

## 4. Recovery Mechanisms of CO<sub>2</sub> Injection

The accepted recovery mechanisms of CO<sub>2</sub>-EOR in conventional reservoirs are as follows: (1) reduction of the vapor and liquid phase interfacial tension towards achieving miscibility with the crude oil, (2) CO<sub>2</sub> dissolves into crude oil, leading to oil volume expansion and crude oil viscosity reduction, (3) CO<sub>2</sub> extraction of lighter hydrocarbons from the liquid phase, (4) CO<sub>2</sub> molecular diffusion, and (5) the sweep efficiency is improved, thereby enhancing the ultimate oil recovery [56, 57]. Because of these recovery mechanisms, CO<sub>2</sub> flooding can greatly improve oil recovery. However, CO<sub>2</sub> injection in unconventional reservoirs such as tight oil reservoirs has not attracted enough attention. A better understanding of the effect of nanopore confinement effect on recovery mechanisms will help to optimize the design strategy for CO<sub>2</sub> injection in tight oil reservoirs.

**4.1. Minimum Miscible Pressure (MMP).** Minimum miscible pressure (MMP) is an important factor to decide miscible flooding. It is defined as the minimum pressure where the injected gas and the oil phase have no obvious interface and then become miscible with each other [58]. A series of PVT and core flooding tests have validated that CO<sub>2</sub> is much easier to become miscible with crude oil than other gases including flue gas, natural gas, and nitrogen [59]. Based on the calculation of phase equilibrium, we obtain the MMP at different CO<sub>2</sub> injection ratios. As observed in Figure 8, the MMP decreases gradually with the increase of CO<sub>2</sub>

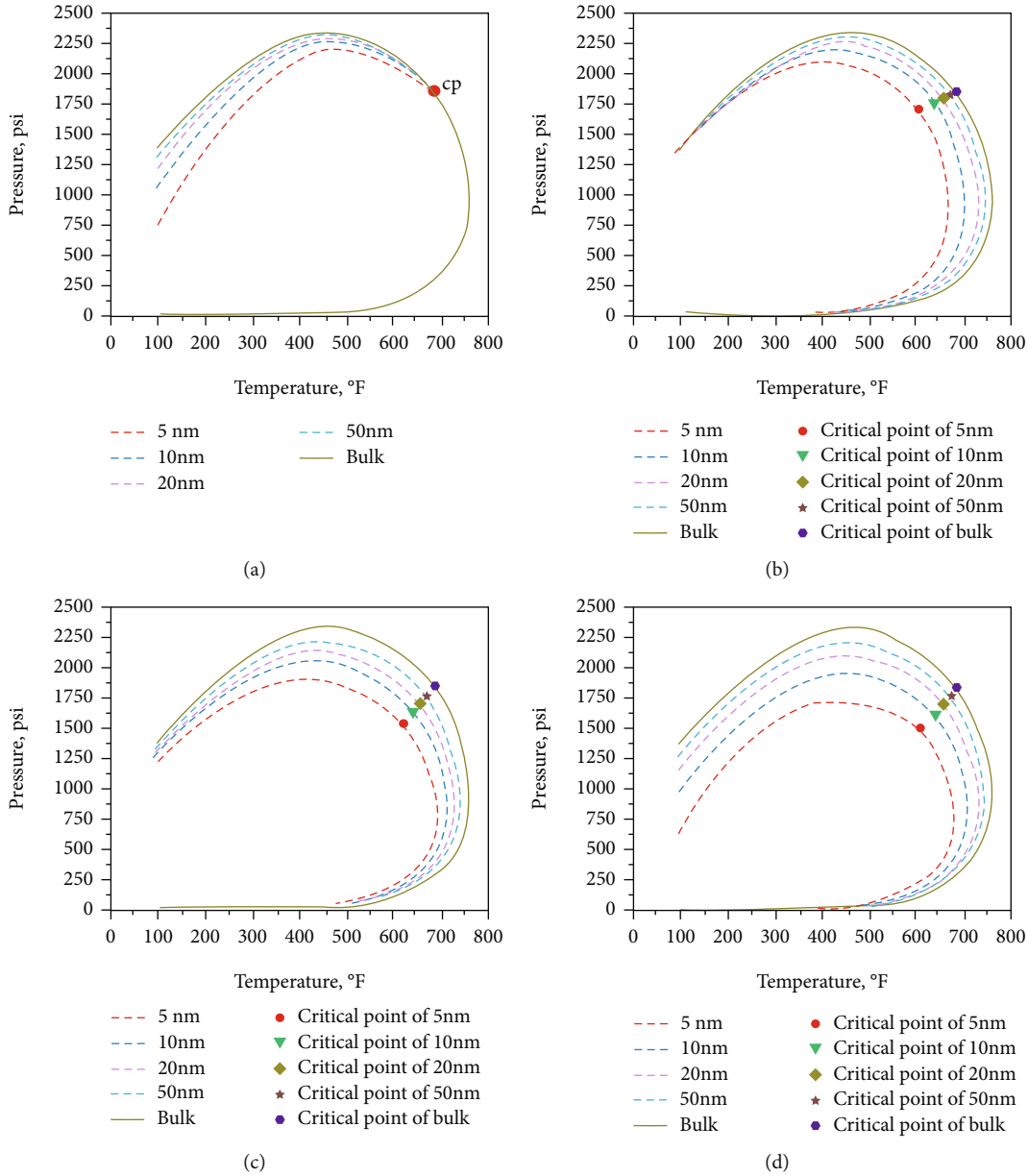


FIGURE 4: P-T phase envelope for Bakken tight oil reservoir at various pore sizes considering (a) capillary pressure, (b) fluid-wall interaction, (c) adsorption effect, and (d) nanopore confinement effect.

injection. When the gas injection ratio is 100%, the MMP decreased by 9.7% compared with the CO<sub>2</sub> injection ratio is 10%. In order to explore the influence of nanopore confinement effect on the MMP in tight oil reservoir, we also evaluated the MMP of 100% CO<sub>2</sub> injection at various pore sizes. As illustrated in Figure 9, the MMP tends to be lowered as the pore size decreases. When the pore size is 5 nm, the MMP decreased by 16.2% compared with the pore size is 100 nm.

4.2. CO<sub>2</sub> Solution Gas-Oil Ratio (GOR). The solution gas-oil ratio (GOR) is defined as the volume of gas at standard condition that evolves from the oil divided by the volume of oil at standard condition. CO<sub>2</sub> could dissolve into crude oil, leading to oil volume expansion and crude oil viscosity

reduction. GOR is an important factor in evaluating the degree of CO<sub>2</sub> dissolution. We calculate the CO<sub>2</sub> solution gas-oil ratio of Bakken tight oil versus pressure at various CO<sub>2</sub> injections at T = 230°F as shown in Figure 10. It is obvious that the CO<sub>2</sub> solution gas-oil ratio increases with the increase of gas injection. When the gas injection ratio is 100%, the CO<sub>2</sub> solution gas-oil ratio is about 3 times that of the gas injection ratio is 30%. In order to explore the influence of nanopore confinement effect on the CO<sub>2</sub> solution gas-oil ratio in tight oil reservoir, we also evaluated the CO<sub>2</sub> solution gas-oil ratio of 100% CO<sub>2</sub> injection at various pore sizes. As illustrated in Figure 11, before CO<sub>2</sub> is completely dissolved into crude oil, the CO<sub>2</sub> solution gas-oil ratio increases with the decrease of pore size. It indicates that considering the influence of nanopore confinement



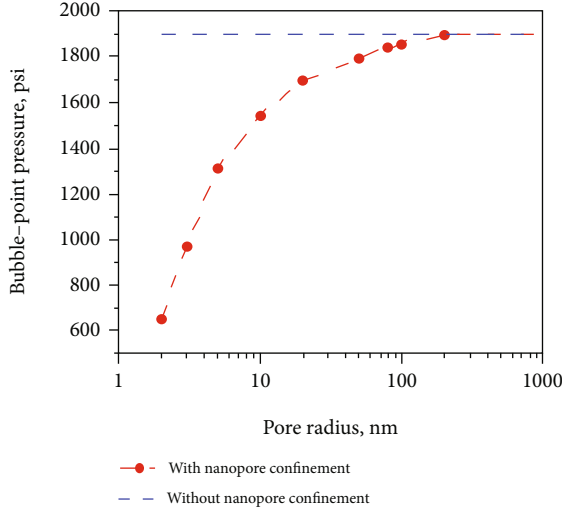


FIGURE 5: Bubble point pressure of the Bakken tight oil at various pore radii at  $T = 230^\circ\text{F}$ .

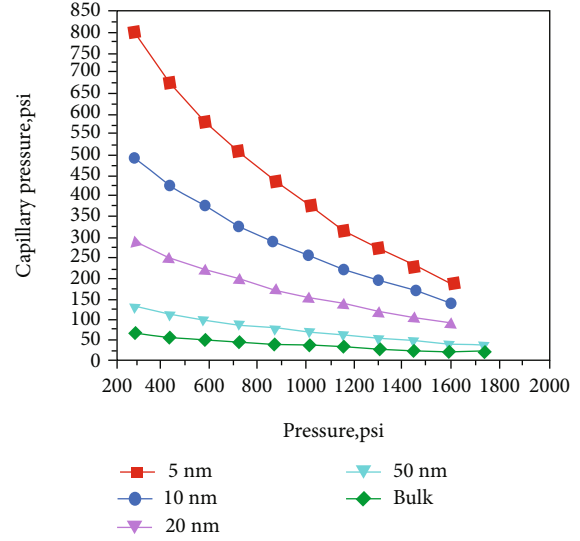


FIGURE 7: Capillary pressure of the Bakken tight oil versus pressure at various pore radii at  $T = 230^\circ\text{F}$ .

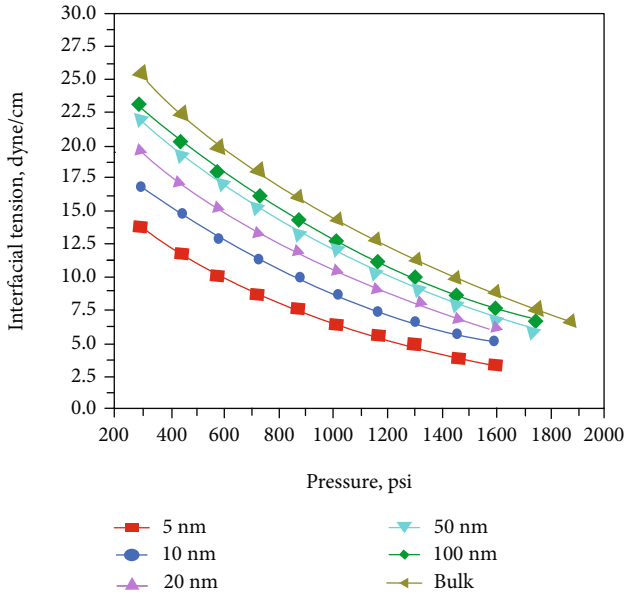


FIGURE 6: Interfacial tension of the Bakken tight oil versus pressure at various pore radii at  $T = 230^\circ\text{F}$ .

effect, the amount of gas dissolved into crude oil increases, which will lead to the increase of the oil volume expansion and the decrease of the viscosity of crude oil, as shown in the following two sections. When the reservoir pressure is higher than the bubble point pressure, all the gas will be dissolved into the crude oil without free gas, and the value of solution gas-oil ratio will remain unchanged.

**4.3. Oil Volume Expansion.**  $\text{CO}_2$  dissolves into the oil phase that causes the oil volume increase. The volumetric expansion capacity of crude oil can be characterized by the oil formation volume factor. The oil formation volume factor defines as the oil volume at reservoir condition divided by the oil volume at standard condition.

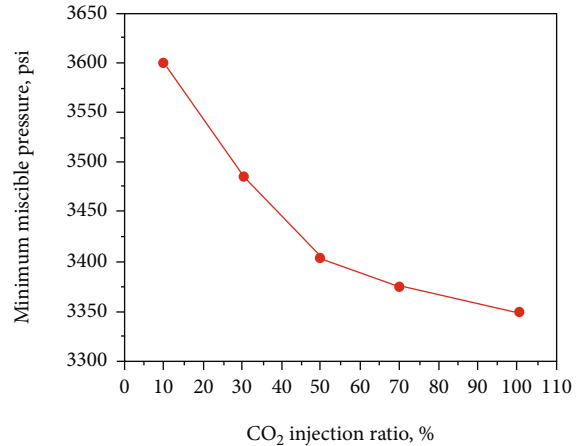


FIGURE 8: Minimum miscible pressure of the Bakken tight oil versus  $\text{CO}_2$  injection.

$$B_o = \frac{(n_L(V_m)_L)_{RC}}{(n_L(V_m)_L)_{STD}} \quad (27)$$

where  $n_L$  represents liquid phase mole fraction,  $(V_m)_L$  represents liquid phase molar volume, RC represents reservoir condition, and STD represents standard condition.

Based on the phase equilibrium calculation, we calculate the oil formation volume factor of Bakken tight oil versus pressure at various  $\text{CO}_2$  injections at  $T = 230^\circ\text{F}$ . As shown in Figure 12, it is obvious that the oil formation volume factor increases with the increase of gas injection. When the  $\text{CO}_2$  injection ratio is 100%, the oil formation volume factor increased by 31.9% compared with that without  $\text{CO}_2$  injection at pressure 4351.2 psi. This can be also explained by the variation trend of  $\text{CO}_2$  solution gas-oil ratio in the upper section. In order to explore the influence of nanopore confinement effect on the oil formation volume in tight oil

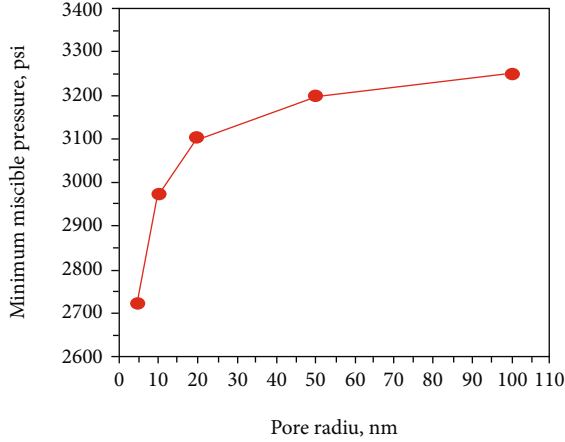


FIGURE 9: Minimum miscible pressure of the Bakken tight oil versus pore size.

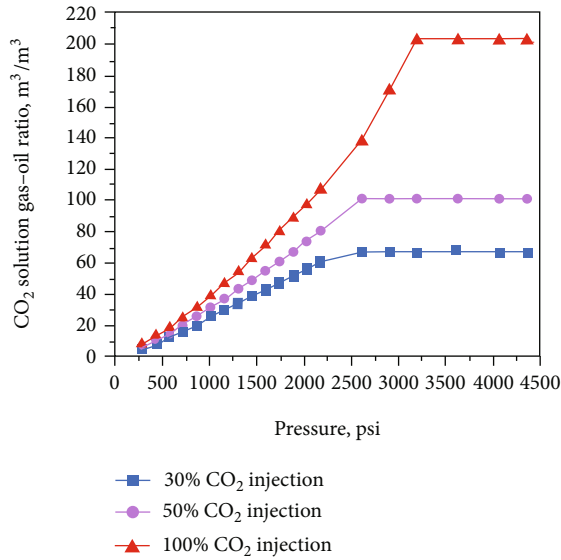


FIGURE 10: CO<sub>2</sub> solution gas-oil ratio of the Bakken tight oil versus pressure at various CO<sub>2</sub> injections at  $T = 230^\circ\text{F}$ .

reservoir, we also evaluate the oil formation volume factor of Bakken tight oil versus pressure at various pore radii at  $T = 230^\circ\text{F}$ . As illustrated in Figure 13, the oil formation volume factor of the oil increases as the pore size decreases. When the pore size decreases from infinity to 50 nm, 20 nm, 10 nm, and 5 nm, the increment of oil formation volume factor at pressure 4351.2 psi is almost 1.5%, 5.9%, 9.2%, and 14.7%.

4.4. *Viscosity reduction.* The oil viscosity is calculated by the Jossi-Stiel-Thodos (JST) model [60, 61].

$$[(\mu - \mu^*) + 10^{-4}]^{1/4} = a_0 + a_1\rho_r + a_2\rho_r^2 + a_3\rho_r^3 + a_4\rho_r^4, \quad (28)$$

where  $\mu$  is the viscosity of crude oil under formation conditions, and the values of  $a_0$ ,  $a_1$ ,  $a_2$ ,  $a_3$ , and  $a_4$  are 0.1023, 0.023364, 0.058533, -0.040758, and 0.0093324, respectively.

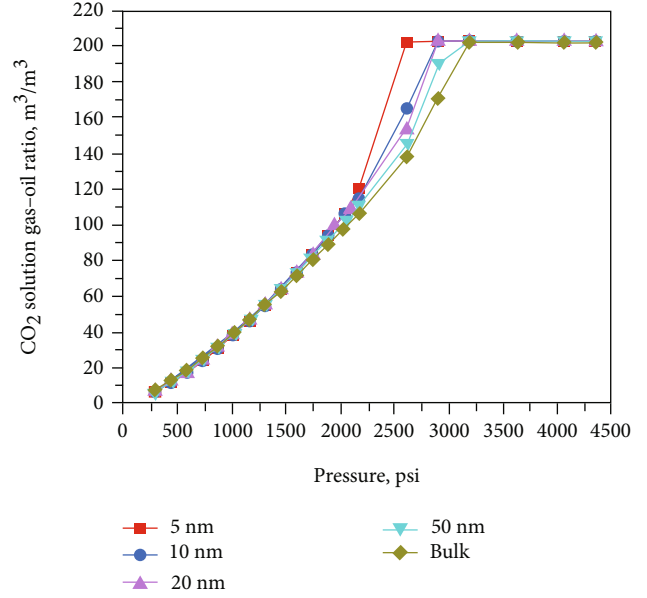


FIGURE 11: CO<sub>2</sub> solution gas-oil ratio of the Bakken tight oil versus pressure at various pore radii at  $T = 230^\circ\text{F}$ .

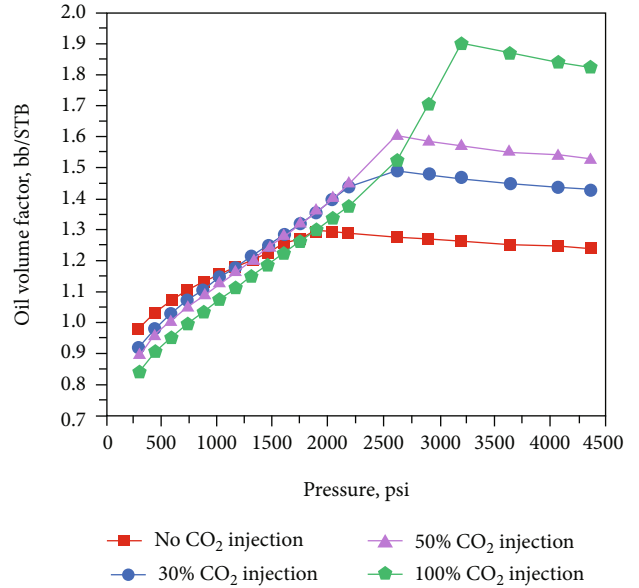


FIGURE 12: Oil volume factor of the Bakken tight oil versus pressure at various CO<sub>2</sub> injections at  $T = 230^\circ\text{F}$ .

$\rho_r$  is defined as

$$\rho_r = \rho_L \left[ \sum_{i=1}^{N_c} x_i V_{ci} \right]^{1/\alpha}, \quad (29)$$

where  $V_{ci}$  is a critical volume of component  $i$ , and the value of  $\alpha$  is 1.

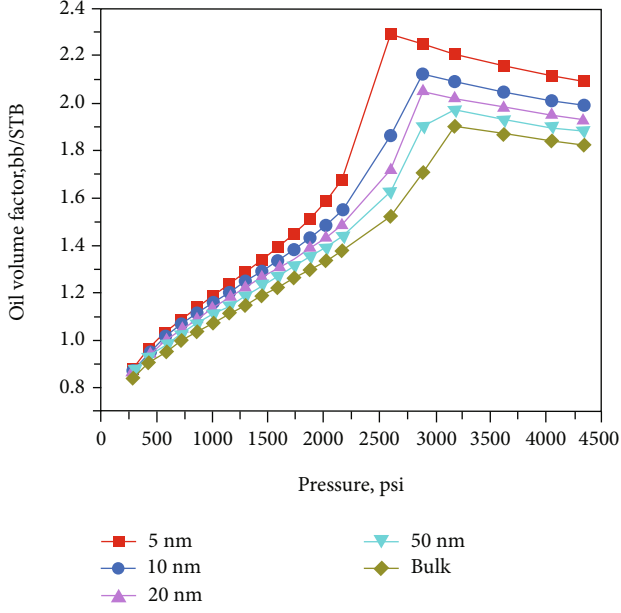


FIGURE 13: Oil volume factor of the Bakken tight oil versus pressure at various pore radii at  $T = 230^\circ\text{F}$ .

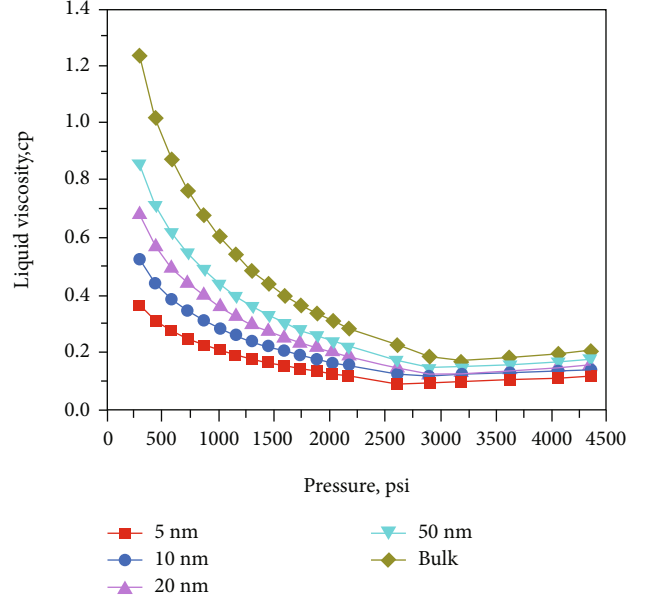


FIGURE 15: Oil viscosity of the Bakken tight oil versus pressure at various pore radii at  $T = 230^\circ\text{F}$ .

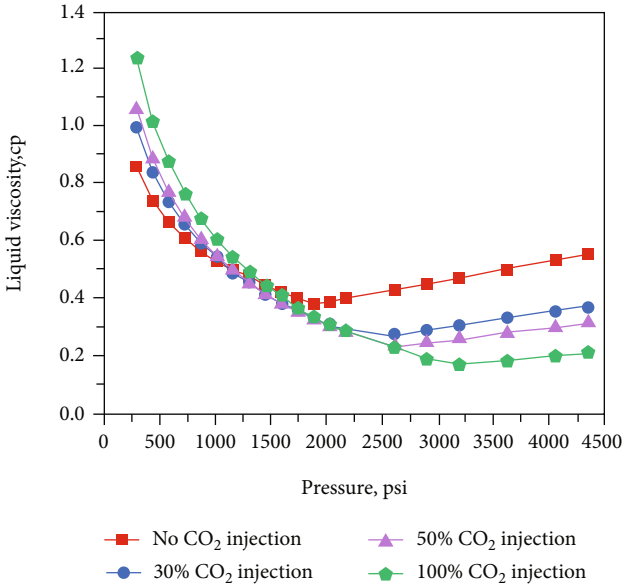


FIGURE 14: Oil viscosity of the Bakken tight oil versus pressure at various  $\text{CO}_2$  injections at  $T = 230^\circ\text{F}$ .

The viscosity parameters of the mixture  $\xi$  are calculated by the following formula:

$$\xi = \left( \sum_{i=1}^{N_c} x_i T_{ci} \right)^{1/6} \left( \sum_{i=1}^{N_c} x_i M_i \right)^{-1/2} \left( \sum_{i=1}^{N_c} x_i P_{ci} \right)^{-2/3} \quad (30)$$

$\mu^*$  is defined as

$$\mu^* = \frac{\sum_{i=1}^{N_c} (x_i \mu_i^* M_i^{1/2})}{\sum_{i=1}^{N_c} (x_i M_i^{1/2})} \quad (31)$$

$\mu_i^*$  can be calculated by the Stiel-Thodos formula:

$$\mu_i^* \xi_i = \left[ \frac{4.610 T_{ri}^{0.618} - 2.04 e^{-0.449 T_{ri}}}{+1.94 e^{-4.058 T_{ri}} + 0.1} \right] \times 10^{-4}, \quad (32)$$

where  $\xi_i = T_{ci}^{1/6} M_i^{1/2} P_{ci}^{2/3}$ ,  $T_{ri} = T/T_{ci}$ .

Based on the phase equilibrium calculation, we calculate oil viscosity of the Bakken tight oil versus pressure at various  $\text{CO}_2$  injections at  $T = 230^\circ\text{F}$ . As shown in Figure 14, it is obvious that the viscosity decreases with the increase of gas injection. When the  $\text{CO}_2$  injection ratio is 100%, the oil viscosity decreased by 62.4% compared with that without  $\text{CO}_2$  injection at pressure 4351.2 psi. This can be explained by the variation trend of  $\text{CO}_2$  solution gas-oil ratio in the upper section. Hence,  $\text{CO}_2$  has obvious viscosity reduction effect. In order to explore the influence of nanopore confinement effect on the oil viscosity in tight oil reservoir, we also evaluate the oil viscosity of Bakken tight oil versus pressure at various pore radius at  $T = 230^\circ\text{F}$ . As illustrated in Figure 15, the viscosity of the oil reduces as the pore size decreases. When the pore size decreases from infinity to 50 nm, 20 nm, 10 nm, and 5 nm, the suppression of oil viscosity at corresponding bubble point pressure are almost 13.4%, 24.8%, 33.8%, and 42.8%. It indicates that considering the influence of nanopore confinement effect, the oil mobility could be increased.

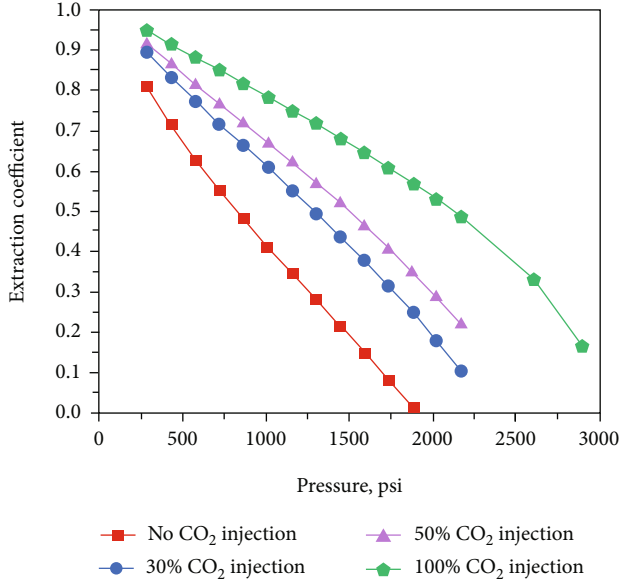


FIGURE 16: Extraction coefficient of lighter hydrocarbons for the Bakken tight oil versus pressure at various CO<sub>2</sub> injections at T = 230°F.

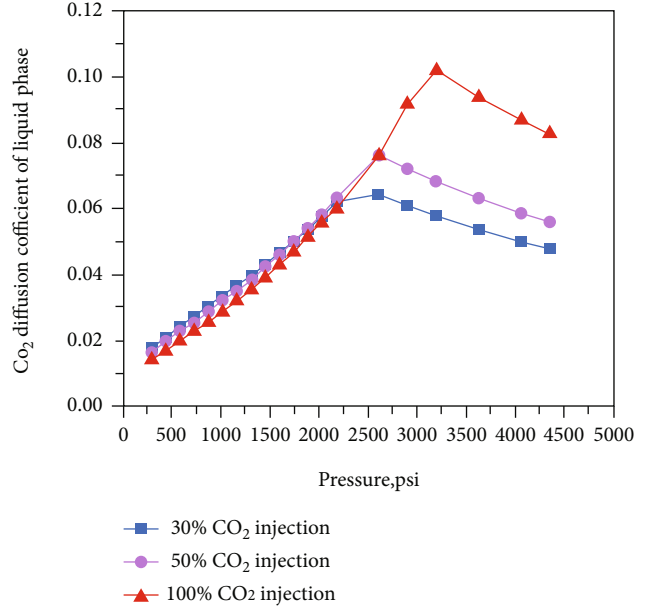


FIGURE 18: CO<sub>2</sub> diffusion coefficient of liquid phase for the Bakken tight oil versus pressure at various CO<sub>2</sub> injection at T = 230°F.

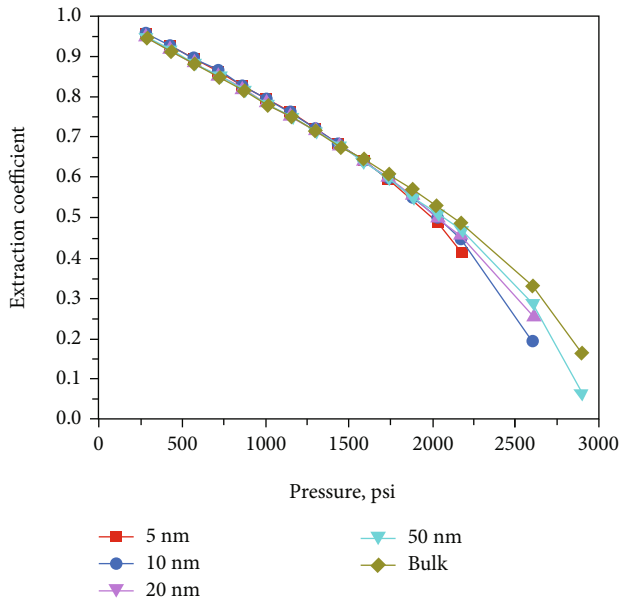


FIGURE 17: Extraction coefficient of lighter hydrocarbons for the Bakken tight oil versus pressure at various pore radii at T = 230°F.

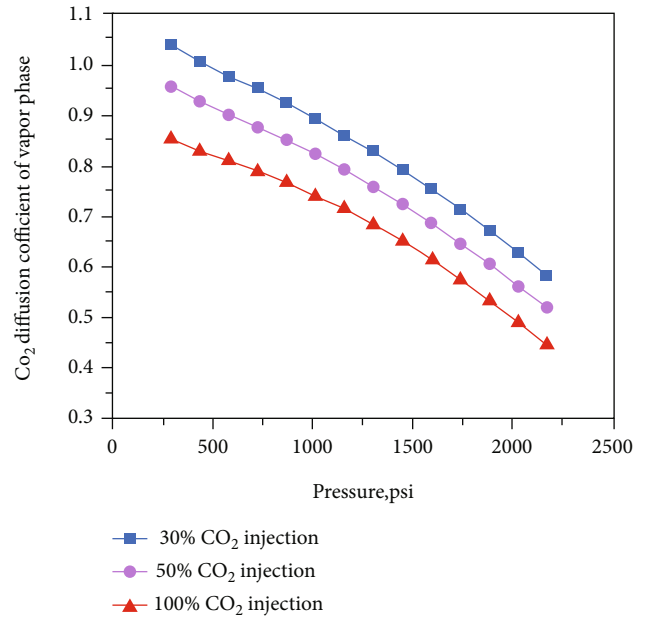


FIGURE 19: CO<sub>2</sub> diffusion coefficient of vapor phase for the Bakken tight oil versus pressure at various CO<sub>2</sub> injections at T = 230°F.

4.5. *Extraction of Lighter Hydrocarbons.* Many experiments and simulations have shown that the content of light components in the oil produced after CO<sub>2</sub> injection increases while the content of heavy components decreases. The mass transfer between CO<sub>2</sub> and formation crude oil results in substantial physical changes of the system.

The extraction coefficient  $\beta_e$  of lighter hydrocarbon is defined as

$$\beta_e = \frac{n_V y_i}{z_i} \tag{33}$$

Based on the phase equilibrium calculation, we calculate the extraction coefficient of lighter hydrocarbon of the Bakken tight oil versus pressure at various CO<sub>2</sub> injections at T = 230°F. As shown in Figure 16, it is obvious that the extraction coefficient of lighter hydrocarbon increases with the increase of gas injection. This can be explained by the following mechanisms: Carbon dioxide dissolves and the liquid phase is relatively light, which contributes to the evaporation of light components and the enrichment of gas phase. Because the gas phase is enriched and the liquid phase is relatively light, the difference of components in the gas and

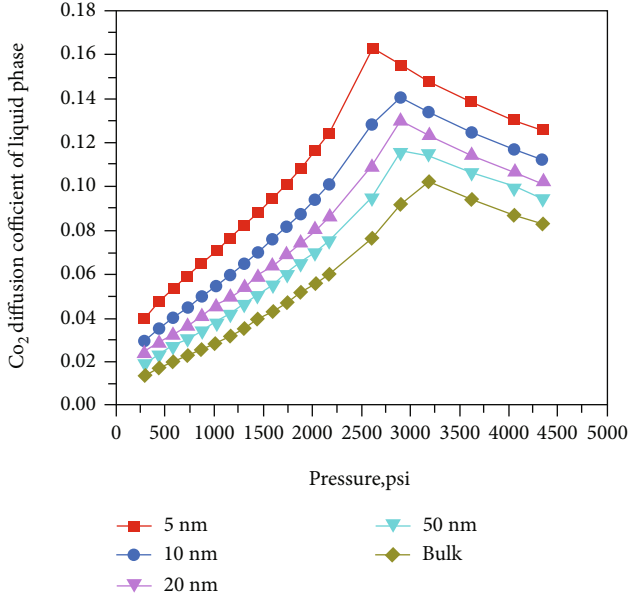


FIGURE 20: CO<sub>2</sub> diffusion coefficient of liquid phase for Bakken tight oil versus pressure at various pore radii at  $T = 230^\circ\text{F}$ .

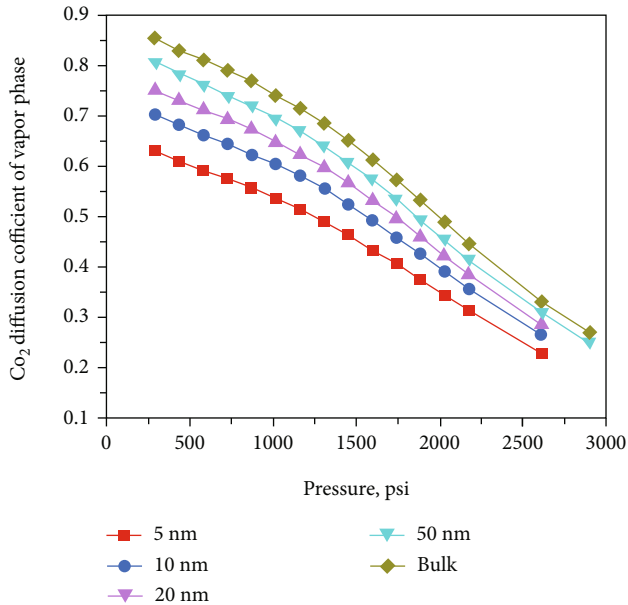


FIGURE 21: CO<sub>2</sub> diffusion coefficient of vapor phase for Bakken tight oil versus pressure at various pore radii at  $T = 230^\circ\text{F}$ .

liquid phase is relatively small. According to the similar compatibility principle, the mass transfer capacity of gas-liquid system is enhanced, and the result is that the enriched gas further extracts the light hydrocarbon and the intermediate hydrocarbon components of crude oil to form the rich hydrocarbon phase. Therefore, the CO<sub>2</sub> extraction of lighter hydrocarbons is conducive to improving the properties of crude oil and enhancing oil recovery.

In order to explore the influence of nanopore confinement effect on the oil formation volume in tight oil reservoir, we also evaluate the extraction coefficient of lighter hydro-

carbon of the Bakken tight oil versus pressure at various pore radii at  $T = 230^\circ\text{F}$ . As illustrated in Figure 17, the extraction coefficient of lighter hydrocarbon slightly reduces as the pore size decreases. It indicates that considering nanopore confinement effect seems to have a slightly reduced effect on extraction of lighter hydrocarbons.

**4.6. Molecular Diffusion.** Molecular diffusion is one of favorable mechanism factors for oil recovery, especially for tight oil reservoirs. The flow velocity is low in tight oil reservoirs with low matrix permeability that the relative contribution of molecular diffusion becomes more significant compared with molecular diffusion in conventional reservoirs. Two empirical correlations frequently applied are by the Wilke-Chang correlation [62] and the Sigmund correlation [63]. In this study, we employed Wilke-Chang equation to estimate the CO<sub>2</sub> diffusion coefficient as

$$D_{ik} = \frac{7.4 \times 10^8 (\phi M_i)^{1/2} T}{\mu_k V_{kb}^{0.6}}, \quad (34)$$

where  $D_{ik}$  represents the diffusion coefficient of component  $i$  in phase  $k$ ,  $M_{\text{CO}_2}$  is the molar mass of component  $i$ ,  $T$  is the temperature of system,  $\mu_k$  is viscosity of phase  $k$ ,  $V_{kb}$  is the critical volume of phase  $k$  under the bubble point, and  $\phi$  is association factor, which depends on the properties of the solvent itself. If ethanol is the solvent, it has a value of 1.5. However, the calculation error is larger for nonassociative systems, and Sun and Chen [64] deduced the relationship between the association factor and temperature through the free volume theory as follows:

$$\phi(T) = 3.97 - 3.92 \times 10^{-3} T. \quad (35)$$

Based on the phase equilibrium calculation, we evaluate the CO<sub>2</sub> diffusion coefficient for the liquid and vapor phases at various CO<sub>2</sub> injections at  $T = 230^\circ\text{F}$ . As shown in Figures 18 and 19, CO<sub>2</sub> diffusion coefficient of the liquid phase increases with the increase of gas injection while.

CO<sub>2</sub> diffusion coefficient of vapor phase decreases with the increase of gas injection. In order to explore the influence of nanopore confinement effect on the CO<sub>2</sub> diffusion coefficient in tight oil reservoir, we also evaluate the CO<sub>2</sub> diffusion coefficient of Bakken tight oil versus pressure at various pore radii at  $T = 230^\circ\text{F}$ . As illustrated in Figures 20 and 21, the CO<sub>2</sub> diffusion coefficient is also different for the liquid phase and vapor phase under nanopore confinement effect. CO<sub>2</sub> diffusion coefficient for the liquid phase is larger in smaller pores whereas CO<sub>2</sub> diffusion coefficient for the vapor phase is smaller.

## 5. Summary and Conclusions

- (1) An efficient model is proposed to calculate phase behavior in tight oil reservoir with capillary pressure, fluid-wall interaction and adsorption effect in this work. Fluid-wall interaction and adsorption effect are introduced to modify the PR-EOS, and capillary

pressure is used to modify the flash calculation for phase equilibrium calculation. The model has been verified against commercial software (CMG-Winprop) and experimental data with bulk fluids and confined fluids. The results show that the nanopore confinement effects including capillary pressure, fluid-wall interaction, and adsorption effect are significant when the pore radius reduces to the orders of nanometers

- (2) For the Bakken tight oil reservoir, nanopore confinement effects impose an overall shrinkage to the  $P$ - $T$  phase envelope. Capillary pressure lowers bubble point curve as the pore size decreases. Fluid-wall interaction and adsorption effect suppress the entire phase envelope as the pore size decreases. Especially, they reduce the critical point instead of capillary pressure. The bubble point pressure of Bakken oil is suppressed by 19.1% when the pore size is 10 nm under nanopore confinement effect compared with the counterpart case without pore proximity. It is reduced by 65.9% when the pore size is 2 nm. As the pore size decreases, the IFT decreases whereas the capillary pressure increases obviously
- (3) The recovery mechanisms for  $\text{CO}_2$  injection are also investigated in the Bakken tight oil reservoir from different respects. Results show that the MMP decreases gradually with the increase of  $\text{CO}_2$  injection. When the gas injection ratio is 100%, the MMP decreased by 9.7% compared with the  $\text{CO}_2$  injection ratio is 10%. On this basis, the effect of nanopore confinement on the MMP for  $\text{CO}_2$  injection is also calculated. Results indicate that under the nanopore confinement effect, the MMP will decrease, resulting in the suppression of the resistance of fluid transport. Hence, it will be easier to reach miscibility and improve the well performance. Besides, as the increase of  $\text{CO}_2$  injection, the  $\text{CO}_2$  solubility will increase, the volume of crude oil expands, and the oil viscosity will decrease. With the nanopore confinement effect, the  $\text{CO}_2$  solution gas-oil ratio and the oil formation volume factor of the oil increase with the decrease of pore size. In turn, the oil viscosity reduces as the pore size decreases. Furthermore, the extraction coefficient of lighter hydrocarbon increases with the increase of gas injection. With the nanopore confinement effect, the extraction coefficient of lighter hydrocarbon slightly reduces as the pore size decreases. It indicates that considering nanopore confinement effect seems to have a slightly reduced effect on extraction of lighter hydrocarbons. The  $\text{CO}_2$  diffusion coefficients for liquid phase and vapor phase are different in that  $\text{CO}_2$  diffusion coefficients for liquid phase increase with the increase of gas injection while  $\text{CO}_2$  diffusion coefficient of vapor phase decreases. On this basis, we also evaluate the effect of nanopore confinement on the  $\text{CO}_2$  diffusion. Results show that  $\text{CO}_2$  diffusion coefficient are also different for liquid

phase and vapor phase under nanopore confinement effect.  $\text{CO}_2$  diffusion coefficient for liquid phase is larger in smaller pores whereas  $\text{CO}_2$  diffusion coefficient for vapor phase is smaller

- (4) An efficient model is proposed to calculate phase behavior in tight oil reservoir with capillary pressure, fluid-wall interaction, and adsorption effect simultaneously. However, the model does not take the effect of water on phase behavior into account, and the pore size distribution is also not considered. Further extensive research on these will continue to investigate

## Appendix

The modified PR-EOS is given as follows:

$$P = \frac{RT}{V'_m - b} - \frac{a - c}{V'_m(V'_m + b) + b(V'_m - b)}. \quad (\text{A.1})$$

The first and second derivatives of pressure with respect to volume at critical point are yielded:

$$\left(\frac{\partial P}{\partial V}\right)_{T=T_c} = -\frac{\alpha RT_c}{(\alpha V_c - b)^2} + \frac{2\alpha(a - c)(\alpha V_c + b)}{[\alpha V_c(\alpha V_c + b) + b(\alpha V_c - b)]^2} = 0, \quad (\text{A.2})$$

$$\begin{aligned} \left(\frac{\partial^2 P}{\partial V^2}\right)_{T=T_c} &= \frac{2\alpha^2 RT_c}{(\alpha V_c - b)^3} \\ &+ \frac{2\alpha^2(a - c)[b(\alpha V_c - b) - (\alpha V_c + b)(3\alpha V_c + 4b)]}{[\alpha V_c(\alpha V_c + b) + b(\alpha V_c - b)]^3} = 0. \end{aligned} \quad (\text{A.3})$$

From Equation (A.2), it is given as

$$\frac{RT_c}{(\alpha V_c - b)^3} = \frac{2(a - c)(\alpha V_c + b)}{[\alpha V_c(\alpha V_c + b) + b(\alpha V_c - b)]^2(\alpha V_c - b)}. \quad (\text{A.4})$$

Imposing Equation (A.4) on Equation (A.3), it is yielded as

$$\frac{2(\alpha V_c + b)}{\alpha V_c - b} = \frac{(\alpha V_c + b)(3\alpha V_c + 4b) - b(\alpha V_c - b)}{(\alpha V_c(\alpha V_c + b) + b(\alpha V_c - b))}. \quad (\text{A.5})$$

It can be rewritten as

$$-(\alpha V_c + b)(\alpha V_c - b)(3\alpha V_c + 2b) + 2\alpha V_c(\alpha V_c + b)^2 + b(\alpha V_c - b)^2 = 0. \quad (\text{A.6})$$

We assume  $b = k\alpha V_c$ , and Equation (A.6) can be rewritten as

$$3k^3 + 3k^2 + 3k - 1 = 0. \quad (\text{A.7})$$

Solving for  $k$  could obtain  $k = 0.25308$ .

$$b = 0.25308\alpha V_c. \quad (\text{A.8})$$

Imposing Equation (A.8) on Equation (A.2), it is written as

$$-\frac{RT_c}{(1-k)^2} + \frac{2(a-c)(1+k)}{(\alpha V_c)[(1+k) + k(1-k)]^2} = 0. \quad (\text{A.9})$$

Thus,

$$a - c = \frac{RT_c(\alpha V_c)[(1+k) + k(1-k)]^2}{2(1+k)(1-k)^2} = 1.48742\alpha RT_c V_c. \quad (\text{A.10})$$

Applying Equation (A.1) to the critical point and substituting Equations (A.8) and (A.10) into Equation (A.1), it is obtained as

$$\frac{P_c V_c}{RT_c} = \frac{0.30740}{\alpha}. \quad (\text{A.11})$$

$b$  is the van der Waals covolume, and the relationship between  $b$  and  $V_c$  should be obtained from the traditional PR-EOS,

$$b = 0.25308V_c. \quad (\text{A.12})$$

From Equations (A.10), (A.11), and (A.12)), the parameters  $a$  and  $b$  are given as follows:

$$a - c = 0.45724 \frac{R^2 T_c^2}{P_c}, \quad (\text{A.13})$$

$$b = 0.07780 \frac{RT_c}{\alpha P_c}.$$

## Nomenclature

$P$ :	System pressure
$T$ :	System temperature
$R$ :	Gas constant
$V_m$ :	Molar volume
$a$ :	“Attraction” parameter
$b$ :	“Repulsion” parameter
$c$ :	Fluid-wall interaction effect coefficient
$\alpha$ :	Adsorption effect coefficient
$P_{CC}$ :	The critical pressure determined by the modified PR-EOS
$T_{CC}$ :	The critical temperature determined by the modified PR-EOS
$\Delta P$ :	The dimensionless shifts of critical pressure
$\Delta T$ :	The dimensionless shifts of critical temperature
$r_p$ :	Pore size
$\sigma_{LJ}$ :	Lennard-Jones molecular size parameter
$N_c$ :	The number of components
$f_i^L$ :	Fugacity of component $i$ in the liquid phase

$f_i^V$ :	Fugacity of component $i$ in the vapor phase
$x_i$ :	Mole fraction of component $i$ in the liquid phase
$y_i$ :	Mole fraction of component $i$ in the vapor phase
$z_i$ :	Overall mole fraction of component $i$
$\phi_i^L$ :	Fugacity coefficient of component $i$ in the liquid phase
$\phi_i^V$ :	Fugacity coefficient of component $i$ in the vapor phase
$n_L$ :	Overall number of moles in liquid phase
$n_V$ :	Overall number of moles in vapor phase
$K_i$ :	Phase equilibrium ratio of component $i$
$P_{cap}$ :	Capillary pressure
$\sigma$ :	Interfacial tension
$\theta$ :	Contact angle
$\rho_L$ :	Density of liquid phase
$\rho_V$ :	Density of vapor phase
$[P]_i$ :	The parachor of component $i$
$Z$ :	The compressibility factor
$B_o$ :	Oil formation volume factor
$\mu$ :	Viscosity of crude oil
$V_{ci}$ :	Critical volume of component $i$
$\beta_e$ :	The extraction coefficient
$D_{ik}$ :	The diffusion coefficient of component $i$ in phase $k$
RC:	Reservoir condition
STD:	Standard condition.

## Data Availability

All the data supporting this study can be found in the manuscript.

## Conflicts of Interest

The authors declare that there is no conflict of interest regarding the publication of this paper.

## Acknowledgments

This work was supported by the National Nature Science Foundation of China (51674010). We would like to acknowledge Computer Modeling Group Ltd. for providing the CMG software for this study of example validation.

## References

- [1] BP, *BP Energy Outlook*, BP, 2019.
- [2] EIA, “US energy information administration,” 2019, <https://www.eia.gov/>.
- [3] L. Wang, E. Parsa, Y. Gao, J. T. Ok, K. Neeves, and X. Yin, “Experimental study and modeling of the effect of nanoconfinement on hydrocarbon phase behavior in un-conventional reservoirs,” in *Presented at the SPE western North American and rocky mountain joint regional meeting*, pp. 1–8, Denver, CO, USA, 2014.
- [4] S. Salahshoor, M. Fahes, and C. Teodoriu, “A review on the effect of confinement on phase behavior in tight formations,” *Journal of Natural Gas Science and Engineering*, vol. 51, pp. 89–103, 2018.
- [5] Q. Feng, S. Xu, X. Xing, W. Zhang, and S. Wang, “Advances and challenges in shale oil development: a critical review,”

- Advances in Geo-Energy Research*, vol. 4, no. 4, pp. 406–418, 2020.
- [6] S. Sun and T. Zhang, “A 6M digital twin for modelling and simulation for subsurface reservoirs,” *Advances in Geo-Energy Research*, vol. 4, pp. 349–351, 2020.
- [7] S. Roy, R. Raju, H. Chuang, B. Cruden, and M. Meyyappan, “Modeling gas flow through microchannels and nanopores,” *Journal of Applied Physics*, vol. 93, no. 8, pp. 4870–4879, 2003.
- [8] P. H. Nelson, “Pore-throat sizes in sandstones, tight sandstones, and shales,” *AAPG Bulletin*, vol. 93, no. 3, pp. 329–340, 2009.
- [9] J. Wang, S. Wu, Q. Li, J. Zhang, and Q. Guo, “Characterization of the pore-throat size of tight oil reservoirs and its control on reservoir physical properties: a case study of the Triassic tight sandstone of the sediment gravity flow in the Ordos Basin, China,” *Journal of Petroleum Science and Engineering*, vol. 186, article 106701, 2019.
- [10] Y. Wang, B. Yan, and J. Killough, “Compositional modeling of tight oil using dynamic nanopore properties,” in *Paper SPE 166267 presented at SPE Annual Technical Conference and Exhibition*, pp. 1–13, New Orleans, LA, USA, 2013.
- [11] B. Nojabaei, R. T. Johns, and L. Chu, “Effect of capillary pressure on phase behavior in tight rocks and shales,” in *Paper SPE 159258 presented at the SPE Annual Technical Conference and Exhibition*, pp. 281–289, San Antonio, TX, USA, 2012.
- [12] S. Luo, H. Nasrabadi, and J. L. Lutkenhaus, “Effect of confinement on the bubble points of hydrocarbons in nanoporous media,” *AIChE Journal*, vol. 62, no. 5, pp. 1772–1780, 2016.
- [13] S. Luo, J. L. Lutkenhaus, and H. Nasrabadi, “Experimental study of pore size distribution effect on phase transitions of hydrocarbons in nanoporous media,” *Fluid Phase Equilibria*, vol. 487, p. 8015, 2019.
- [14] B. Pinho, S. Girardon, F. Bazer-Bachi, G. Bergeot, S. Marre, and C. Aymonier, “A microfluidic approach for investigating multicomponent system thermodynamics at high pressures and temperatures,” *Lab on a Chip*, vol. 14, no. 19, pp. 3843–3849, 2014.
- [15] V. R. Choudhary and K. Mantri, “Temperature-programmed desorption of benzene on mesoporous Si-MCM-41, Na-ALSi-MCM-41, and H-ALSi-MCM-41,” *Langmuir*, vol. 16, pp. 8024–8030, 2020.
- [16] H. Xu, “Probing nanopore structure and confined fluid behavior in shale matrix: a review on small-angle neutron scattering studies,” *International Journal of Coal Geology*, vol. 217, article 103325, 2020.
- [17] H. Cho, M. H. Bartl, and M. Deo, “Bubble point measurements of hydrocarbon mixtures in mesoporous media,” *Energy Fuels*, vol. 31, no. 4, pp. 3436–3444, 2017.
- [18] G. Günther, J. Prass, O. Paris, and M. Schoen, “Novel insights into nanopore deformation caused by capillary condensation,” *Physical Review Letters*, vol. 101, no. 8, article 086104, 2008.
- [19] J. Zhong, S. Talebi, Y. Xu, Y. Pang, F. Mostowfi, and D. Sinton, “Fluorescence in sub-10 nm channels with an optical enhancement layer,” *Lab on a Chip*, vol. 18, no. 4, pp. 568–573, 2018.
- [20] Y. Liu, X. Dong, Z. Chen, Y. Hou, Q. Luo, and Y. Chen, “A novel experimental investigation on the occurrence state of fluids in microscale pores of tight reservoirs,” *Journal of Petroleum Science and Engineering*, vol. 196, article 107656, 2020.
- [21] S. Wang, Q. Feng, M. Zha et al., “Molecular dynamics simulation of liquid alkane occurrence state in pores and slits of shale organic matter,” *Petroleum Exploration and Development*, vol. 42, no. 6, pp. 844–851, 2015.
- [22] Z. Jin and A. Firoozabadi, “Thermodynamic modeling of phase behavior in shale media,” *SPE Journal*, vol. 21, no. 1, pp. 190–207, 2016.
- [23] Y. Zhang, W. Yu, K. Sepehrnoori, and Y. Di, “Investigation of nanopore confinement on fluid flow in tight reservoirs,” *Journal of Petroleum Science and Engineering*, vol. 150, pp. 265–271, 2017.
- [24] L. Li and J. J. Sheng, “Nanopore confinement effects on phase behavior and capillary pressure in a Wolfcamp shale reservoir,” *Journal of Taiwan Institute of Chemical Engineers*, vol. 78, pp. 317–328, 2017.
- [25] Q. Yang, P. Sun, L. Fumagalli et al., “Capillary condensation under atomic-scale confinement,” *Nature*, vol. 588, no. 7837, pp. 250–253, 2020.
- [26] L. Travalloni, M. Castier, F. W. Tavares, and S. I. Sandler, “Thermodynamic modeling of confined fluids using an extension of the generalized van der Waals theory,” *Chemical Engineering Science*, vol. 65, no. 10, pp. 3088–3099, 2010.
- [27] G. Yang, Z. Fan, and X. Li, “Determination of confined fluid phase behavior using extended Peng-Robinson equation of state,” *Chemical Engineering Journal*, vol. 378, pp. 122–132, 2019.
- [28] X. Dong, H. Liu, K. Wu et al., “Confined behavior of CO<sub>2</sub>/hydrocarbon system in nanopores of tight and shale rocks,” in *Unconventional Resources Technology Conference. Society of Exploration Geophysicists*, pp. 1–14, Denver, Colorado, USA, 2019.
- [29] X. Cui, E. Yang, K. Song, and J. Huang, “Phase equilibrium of hydrocarbons confined in nanopores from a modified Peng-Robinson equation of state,” in *SPE Annual Technical Conference and Exhibition, Society of Petroleum Engineers*, pp. 1–21, Dallas, Texas, USA, 2018.
- [30] D. R. Sandoval, W. Yan, M. L. Michelsen, and E. H. Stenby, “Influence of adsorption and capillary pressure on phase equilibria inside shale reservoirs,” *Energy & Fuels*, vol. 32, no. 3, pp. 2819–2833, 2018.
- [31] Z. Song, Y. Song, J. Guo, Z. Zhang, and J. Hou, “Adsorption induced critical shifts of confined fluids in shale nanopores,” *Chemical Engineering Journal*, vol. 385, article 123837, 2020.
- [32] Y. Zhang, H. Lashgari, Y. di, and K. Sepehrnoori, “Capillary pressure effect on phase behavior of CO<sub>2</sub>/hydrocarbons in unconventional reservoirs,” *Fuel*, vol. 197, pp. 575–582, 2017.
- [33] X. Zhang and W. Wang, “Square-well fluids in confined space with discretely attractive wall-fluid potentials: critical point shift,” *Physical Review E*, vol. 74, no. 6, article 062601, 2006.
- [34] K. Wu, Z. Chen, X. Li, and X. Dong, “Methane storage in nanoporous material at supercritical temperature over a wide range of pressures,” *Scientific Reports*, vol. 6, no. 1, article 33461, 2016.
- [35] Z. Jiang, L. Zhao, and D. Zhang, “Study of adsorption behavior in shale reservoirs under high pressure,” *Journal of Natural Gas Science and Engineering*, vol. 49, pp. 275–285, 2018.
- [36] K. Zhang, N. Jia, and L. Liu, “Adsorption thicknesses of confined pure and mixing fluids in nanopores,” *Langmuir*, vol. 34, no. 43, pp. 12815–12826, 2018.
- [37] A. Taghaviyeh, M. Sharifi, E. Heidaryan, K. Liu, and M. Ostadhassan, “Flow modeling in shale gas reservoirs: a comprehensive review,” *Journal of Natural Gas Science and Engineering*, vol. 83, article 103535, 2020.



- [38] D. Y. Peng and D. B. Robinson, "A new two-constant equation of state," *Industrial and Engineering Chemistry Fundamentals*, vol. 15, no. 1, pp. 59–64, 1976.
- [39] M. Fechtner and A. Kienle, "Efficient simulation and equilibrium theory for adsorption processes with implicit adsorption isotherms - ideal adsorbed solution theory," *Chemical Engineering Science*, vol. 177, pp. 284–292, 2018.
- [40] A. A. Shapiro and E. H. Stenby, "Potential theory of multicomponent adsorption," *Journal of Colloid and Interface Science*, vol. 201, no. 2, pp. 146–157, 1998.
- [41] R. S. Myong, "Gaseous slip models based on the Langmuir adsorption isotherm," *Physics of Fluids*, vol. 16, no. 1, pp. 104–117, 2004.
- [42] A. Tarek, *Equation of State and PVT Analysis: Application for Improved Reservoir Modeling*, Gulf Publishing Company, 2nd edition, 2016.
- [43] C. G. Burgess, D. H. Everett, and S. Nuttall, "Adsorption of carbon dioxide and xenon by porous glass over a wide range of temperature and pressure-applicability of the Langmuir case VI equation," *Langmuir*, vol. 6, no. 12, pp. 1734–1738, 1990.
- [44] A. Vishnyakov, E. M. Piotrovskaya, E. N. Brodskaya, E. V. Votyakov, and Y. K. Tovbin, "Critical properties of Lennard-Jones fluids in narrow slit-shaped pores," *Langmuir*, vol. 17, no. 14, pp. 4451–4458, 2001.
- [45] B. R. Didar and I. Y. Akkutlu, "Pore-size dependence of fluid phase behavior and properties in organic-rich shale reservoirs," in *SPE International Symposium on Oilfield Chemistry. Society of Petroleum Engineers*, pp. 1–19, Woodlands, Texas, USA, 2013.
- [46] T. Pitakbunkate, P. Balbuena, G. J. Moridis, and T. A. Blasingame, "Effect of confinement on PVT properties of hydrocarbons in shale reservoirs," in *SPE Annual Technical Conference and Exhibition. Society of Petroleum Engineers*, pp. 1–16, Amsterdam, Netherlands, 2014.
- [47] B. Jin and H. Nasrabadi, "Phase behavior of multi-component hydrocarbon systems in nano-pores using gauge-GCMC molecular simulation," *Fluid Phase Equilibria*, vol. 425, pp. 324–334, 2016.
- [48] S. Luo, J. L. Lutkenhaus, and H. Nasrabadi, "Use of differential scanning calorimetry to study phase behavior of hydrocarbon mixtures in nano-scale porous media," *Journal of Petroleum Science and Engineering*, vol. 163, pp. 731–738, 2018.
- [49] S. K. Singh, A. Sinha, G. Deo, and J. K. Singh, "Vapor-liquid phase coexistence, critical properties, and surface tension of confined alkanes," *Journal of Physical Chemistry C*, vol. 113, no. 17, pp. 7170–7180, 2009.
- [50] S. P. Tan, X. Qiu, M. Dejam, and H. Adidharma, "Critical point of fluid confined in nanopores: experimental detection and measurement," *Journal of Physical Chemistry C*, vol. 123, no. 15, pp. 9824–9830, 2019.
- [51] A. W. Islam, T. W. Patzek, and A. Y. Sun, "Thermodynamics phase changes of nanopore fluids," *Journal of Natural Gas Science and Engineering*, vol. 25, pp. 134–139, 2015.
- [52] H. H. Rachford and J. D. Rice, "Procedure for use of electronic digital computers in calculating flash vaporization hydrocarbon equilibrium," *Journal of Petroleum Technology*, vol. 4, no. 10, pp. 19–30, 1952.
- [53] A. W. Adamson, *Physical Chemistry of Surfaces*, John Wiley & Sons, 5th edition, 1990.
- [54] K. S. Pedersen and P. L. Christensen, *Phase Behavior of Petroleum Reservoir Fluids*, CRC Press, 2007.
- [55] W. Yu, H. R. Lashgari, K. Wu, and K. Sepehrnoori, "CO<sub>2</sub> injection for enhanced oil recovery in Bakken tight oil reservoirs," *Fuel*, vol. 159, pp. 354–363, 2015.
- [56] B. Jia, J. S. Tsau, and R. Barati, "A review of the current progress of CO<sub>2</sub> injection EOR and carbon storage in shale oil reservoirs," *Fuel*, vol. 236, pp. 404–427, 2019.
- [57] Z. Song, Y. Song, Y. Li, B. Bai, K. Song, and J. Hou, "A critical review of CO<sub>2</sub> enhanced oil recovery in tight oil reservoirs of North America and China," *Fuel*, vol. 276, article 118006, 2020.
- [58] O. O. Adekunle and B. T. Hoffman, "Minimum miscibility pressure studies in the Bakken," in *Paper SPE 169077 presented at the SPE Improved Oil Recovery Symposium*, pp. 1–16, Tulsa, OK, USA, 2014.
- [59] S. Wu, Z. Li, and H. K. Sarma, "Influence of confinement effect on recovery mechanisms of CO<sub>2</sub>-enhanced tight-oil recovery process considering critical properties shift, capillarity and adsorption," *Fuel*, vol. 262, article 116569, 2020.
- [60] P. Yoonm and G. Thodos, "Viscosity of nonpolar gaseous mixtures at normal pressures," *AICHE Journal*, vol. 16, no. 2, pp. 300–304, 1970.
- [61] D. K. Fong and L. X. Nghiem, "A viscosity model for reservoir fluid," *Computer Modeling Group Research Report*, 1980.
- [62] C. R. Wilke and P. Chang, "Correlation of diffusion coefficients in dilute solutions," *AICHE Journal*, vol. 1, no. 2, pp. 264–270, 1955.
- [63] P. M. Sigmund, "Prediction of molecular diffusion at reservoir conditions. Part 1-measurement and prediction of binary dense gas diffusion coefficients," *Journal of Canadian Petroleum Technology*, vol. 15, pp. 48–57, 1976.
- [64] C. K. J. Sun and S. H. Chen, "Tracer diffusion in dense ethanol: a generalized correlation for nonpolar and hydrogen-bonded solvents," *AICHE Journal*, vol. 32, no. 8, pp. 1367–1371, 1986.

## Research Article

# High-Precision Numerical Simulation on the Cyclic High-Pressure Water Slug Injection in a Low-Permeability Reservoir

Jie Zhan <sup>1,2</sup>, Chao Fan <sup>1,2</sup>, Xianlin Ma <sup>1,2</sup>, Zigang Zheng <sup>3</sup>, Zezhong Su <sup>1,2</sup>  
and Zhihao Niu <sup>1,2</sup>

<sup>1</sup>School of Petroleum Engineering, Xi'an Shiyou University, Xi'an 710065, China

<sup>2</sup>Engineering Research Center of Development and Management for Low to Ultra-Low Permeability Oil & Gas Reservoirs in West China, Ministry of Education, Xi'an Shiyou University, Xi'an 710065, China

<sup>3</sup>Petroleum Exploration and Development Research Institute, PetroChina Changqing Oilfield Company, Xi'an 710018, China

Correspondence should be addressed to Jie Zhan; zhanjie@xsyu.edu.cn and Xianlin Ma; xianlinm@126.com

Received 8 May 2021; Accepted 12 July 2021; Published 30 July 2021

Academic Editor: Jianchao Cai

Copyright © 2021 Jie Zhan et al. This is an open access article distributed under the Creative Commons Attribution License, which permits unrestricted use, distribution, and reproduction in any medium, provided the original work is properly cited.

The paper presents a novel waterflooding technique, coupling cyclic high-pressure water slug injection with an asynchronous injection and production procedure, to address the inefficient development of low-permeability oil reservoir in Shengli Oilfield, a pilot test with 5-spot well pattern. Based on the first-hand data from the pilot test, the reservoir model is established. With an in-depth understanding of the mechanism of the novel waterflooding technique, different simulation schemes are employed to screen the best scheme to finely investigate the historical performance of the pilot test. The production characteristics of the pilot test are both qualitatively and quantitatively investigated. It is found that the novel waterflooding technique can provide pressure support within a short period. And the formation around the injector is significantly activated and deformed. Once passing the short stage of the small elastic deformation, the reservoir immediately goes through the dilation deformation accompanied with the opening of microfractures so that the reservoir properties are significantly improved, which leads to better reservoir performance. With the multicyclic dilation-recompaction geomechanical model, the impact of pressure cyclic evolution on the reservoir properties and performance under the novel waterflooding mode of cyclic high-pressure water slug injection is taken into consideration. The historical data of the pilot test is well matched. In the study, a high-precision simulation scheme for the novel waterflooding technique in low-permeability reservoirs is proposed, which provides significant technical support for further optimization of the pilot test and large-scale application of the novel waterflooding technique.

## 1. Introduction

About 38% of the global and 46% of China's oil and gas resources are of low quality mainly in low-permeability reservoirs, which need to be effectively developed to ensure sustainable development worldwide [1–4]. In recent years, with the exploration and development of unconventional oil and gas, numerous studies on the efficient development of low-permeability reservoirs have been done by many researchers [5–11]. With the application of horizontal well, multistage hydraulic fracturing and acidizing, synchronous/asynchronous water injection, advanced water injection, lay-

ered water injection, and other techniques, the low-permeability reservoir is commercially and sustainably developed [12–21]. At present, water injection is still the primary method for the development of low-permeability reservoirs. But the effectiveness of water injection varies according to the formation characteristics. As to the reservoir with the development of fracture, the injected water tends to transport along the fracture, leading to water channeling and ineffective water injection. As to the low-permeability reservoir without fracture development, the poor reservoir properties with high start-up pressure gradient have a negative impact on the injectivity, such as Block A of Shengli Oilfield.

Therefore, according to different reservoir characteristics, an effective pressure-driven system between the injector and producer needs to be established to optimize the water injection. Based on traditional water injection mode and technology, it is urgent to develop an effective water injection mode and corresponding supporting technology to improve the reservoir performance, where many researchers have conducted extensive research. Wu et al. proposed a development scheme for ultra-low-permeability reservoirs, combining cyclic water injection, volumetric stimulation, and asynchronous injection-production into a novel recovery technique [22]. A feasibility study of water injection pressure close to failure pressure for a low-permeability reservoir was conducted by Liang et al. [23]. Inspired by the idea of hydraulic fracturing in shale gas reservoirs, Liu et al. proposed a development method for fractured-vuggy reservoirs, increasing the injection pressure to the failure pressure so that the connection between the well and the cavity is established to enhance reservoir performance [24]. Based on the extensive investigation and evaluation, Shengli Oilfield proposes an innovative waterflooding technique, coupling cyclic high-pressure water slug injection with an asynchronous injection and production procedure. And a pilot test is carried out with 5-spot well pattern. Various techniques, combined into a novel waterflooding mode, have been implemented to efficiently develop Block A, such as high-pressure water injection with multi-cycle, large injection volume, and asynchronous injection-production.

The paper presents a high-precision numerical simulation method for the novel waterflooding technique applied in Shengli Oilfield, including the primary mechanisms of the process. Taking the pilot test in Block A of Shengli Oilfield as an example, the reservoir model, which employs a multicycle dilation-recompaction geomechanical model to finely history-match the pilot test data, is established to quantify the evolution of reservoir properties and reservoir performance during high-pressure water slug injection. With this methodology presented in the study, not only the pilot test can be further optimized, leading to a more efficient and sustainable development, but also the feasibility of high-pressure water slug injection applied to other low-permeability reservoirs can be quantitatively analyzed and evaluated, which promotes the development and application of high-pressure water slug injection technology in China and worldwide.

## 2. Reservoir Model and Simulation Schemes

**2.1. Overview of Block A.** The development of the block has started since 2014. The target formation is the third member of Shahejie Formation in the Dongying Depression, which is low-permeability lithologic reservoir with average pore throat radius of  $0.39 \mu\text{m}$ . The average porosity of the reservoir is 20%. And the average permeability is 5 md. Before the pilot test of high-pressure water slug injection, the pilot site is depleted for several years with the cumulative oil production of  $0.63 \times 10^4 \text{ t}$ , the cumulative water production of  $0.39 \times 10^4 \text{ m}^3$ , and cumulative water injection of  $0.27 \times 10^4 \text{ m}^3$ . The reservoir is depleted without any energy supplement

for years, leading to a rapid decline in productivity. Before the pilot test of high-pressure water slug injection, only one well is producing with an average daily liquid production of 1.3 t, daily oil production of 1.0 t, and water cut of 21.2%. With the high-pressure water slug injection for about two months, the cumulative injection water of four slugs is  $6.0 \times 10^4 \text{ m}^3$ . The cumulative oil/water production of the pilot test is 373.7 t and  $322 \text{ m}^3$ , respectively. The pilot test performs as expected. But there is an urgent need to clarify the mechanism of the process and establish a systematic understanding of the novel technique. Meanwhile, the corresponding simulation technology for the novel waterflooding mode needs to be developed to promote the efficient development of low-permeability reservoirs with the high-pressure water slug injection.

**2.2. High-Pressure Water Slug Injection.** The low-permeability reservoir with poor reservoir properties results in relatively high seepage resistance and start-up pressure. High-pressure water injection not only reduces the negative impact arising from high seepage resistance and start-up pressure, leading to the increase of the injectivity, but also overcomes the additional resistance induced by capillary force and improves the recovery, which effectively overcomes the related problems on low water injectivity and oil recovery and comprehensively improves the low-permeability reservoir performance from both injection and production sides. With the depletion of the reservoir, the reservoir pressure decreased rapidly. Compared with the traditional water injection mode, the high-pressure water slug injection with a large injection volume can provide the formation with tremendous energy within a short period. With the high-pressure water slug injection in low-permeability reservoirs, the BHP of the injector is close to the failure pressure. And the formation around the injector is effectively activated with dilation. With the opening of microfractures around the injector, the reservoir properties (permeability and porosity) are significantly improved, which leads to better reservoir performance.

**2.3. Dilation-Recompaction Model.** The application of high-pressure water slug injection leads to high water injectivity within a short period. The conventional numerical reservoir model has several limitations to deal with the novel waterflooding mode. Firstly, high-pressure injection with large injection volume results in the rapid BHP build-up (BHP higher than failure pressure), which does not align with the actual situation (BHP close to failure pressure). Meanwhile, the rapid pressure build-up will lead to poor numerical stability of the model. Secondly, the conventional simulation method cannot objectively represent the piecewise and path-dependent evolution of reservoir properties with the pore pressure. In a word, the conventional way cannot objectively simulate activated and significantly deformed formation due to the high-pressure water slug injection.

In this study, the multicyclic dilation-recompaction geomechanical model is introduced to make up for the limitations of the conventional simulation method and establish the simulation technique for the high-pressure water slug

injection, finely simulating the pilot test. The multicyclic dilation-recompaction geomechanical model, also referred as the Beattie-Boberg model, was proposed by Beattie et al. for the first time to depict the cyclic deformation of rock with pressure under cyclic steam stimulation (CSS). The model quantitatively characterizes the piecewise and path-dependent evolution of porosity with reservoir pressure, as shown in Figure 1 [25–29].

With the injection of huge amounts of fluids, the pore pressure increases from the initial reservoir pressure, and the effective stress decreases. The rock behaves elastically, and the porosity changes slightly with the pressure (from point  $a$  to point  $b$  in Figure 1). If the pressure decreases from a point on the elastic curve at a certain moment, porosity follows a reversible elastic compaction curve to the initial reservoir porosity (from point  $b$  to point  $a$  in Figure 1). As pressure continues to increase to exceed the dilation pressure ( $P_D$ ), dilation of the reservoir occurs. Then, porosity follows the irreversible dilation curve until either pressure declines or the maximum porosity ( $\phi_{\max}$ ) is reached (from point  $b$  to point  $c$  in Figure 1). In the model, the maximum porosity ( $\phi_{\max}$ ) is related to the  $r_{\text{at}}$ , which is the maximum allowed proportional increase in porosity. The minimum allowed value of  $r_{\text{at}}$  is 1. The maximum recommended value of  $r_{\text{at}}$  is 1.3, which is the upper limit for  $r_{\text{at}}$ . Porosity increases rapidly with the increase of pressure during dilation. If pressure decreases from a point on the dilation curve, there are two stages of compaction: one is elastic compaction, and the other one is recompaction. Once the pressure begins to decline, before it reaches the recompaction pressure ( $P_R$ ), porosity follows a reversible elastic compaction path (from point  $c$  to point  $d$  in Figure 1). As pressure decreases further till the pressure is less than the recompaction pressure ( $P_R$ ), recompaction occurs. This process is irreversible (from point  $d$  to point  $e$  in Figure 1). The residual dilation fraction ( $f_r$ ) is defined as the fraction of the total dilation that is permanent and unrecoverable. For instance,  $f_r = 0$  means that the pore volume that increased from dilation could be diminished completely and  $f_r = 1$  indicates that the dilation of the block is maintained definitely.

With the multicyclic injection, the rock follows the same rule but with cyclic dilation-recompaction evolution, as shown in Figure 2. When the pressure increases from a point on the recompaction curve, the reservoir follows an elastic compaction path until reaching the dilation curve. Then, the dilation occurs again, as shown in Cycle 1. If the pressure begins to decrease before the dilation pressure is reached, the reservoir undergoes reversible elastic deformation. With the decrease of the pressure, the reservoir undergoes elastic compaction or even recompaction, as shown in Cycle 2. The multicyclic dilation-recompaction geomechanical model essentially reflects that the rock property evolution follows a piecewise and path-dependent rule. In this model, the analytical relation between the porosity and pore pressure is expressed by the following equation:

$$\phi = \phi_r e^{[c(p-p_r)]}, \quad (1)$$

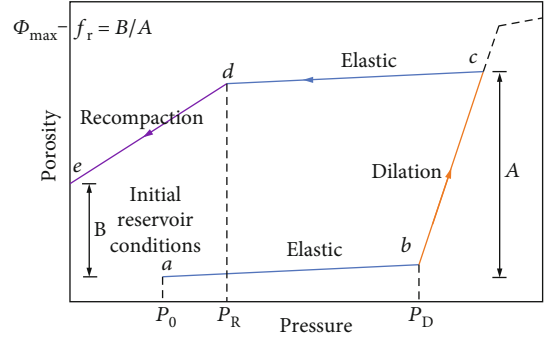


FIGURE 1: Dilation-recompaction model (modified from ref. [29]).

where  $c$  is the compressibility;  $p_r$  is reference pressure; and  $\phi_r$  is the porosity at the reference pressure.

Due to the stress sensitivity of a low-permeability reservoir, the reservoir permeability also evolves with the pressure. The analytical correlation is that the permeability evolves with the porosity which is a function of reservoir pressure [30–35]. We model the permeability change with the following analytical dilation-recompaction permeability model. The permeability is a function of fluid porosity via a permeability multiplier. Based on the equation, the change of permeability with porosity is more significant if a bigger multiplier is applied.

$$K = K_0 e^{[K_{\text{MUL}}(\phi - \phi_0)/(1 - \phi_0)]}, \quad (2)$$

where  $K_0$  is the original permeability;  $K_{\text{MUL}}$  is a user-defined permeability multiplier; and  $\phi_0$  is the original porosity.

With the large amounts of water being injected, the pore space is greatly expanded along with the storage of the elastic energy, so that the pore pressure increases with the decrease of the effective stress, leading to enhanced reservoir properties and better reservoir performance. The key geomechanical parameter dominating each deformation stage is the piecewise rock compressibility, to which different values are assigned based on the range of pore pressure and the direction of the pore pressure change.

**2.4. Reservoir Model.** Based on the CMG, a homogeneous 3D reservoir model of high-pressure water slug injection is established. The dimensions of the numerical model are 1500 m  $\times$  1950 m  $\times$  4.5 m, corresponding to the length, width, and thickness of the reservoir, respectively. One vertical injector and four vertical producers, which are perforated from top to the bottom of the reservoir, are simulated in the model for a 5-spot well pattern, as shown in Figures 3 and 4.  $6.0 \times 10^4 \text{ m}^3$  of water is injected by four slugs for the pilot test in two months, as shown in Figure 5. The specific parameters employed in the numerical model are listed in Table 1. The specific parameters used in the dilation-recompaction model are listed in Table 2.

### 3. Numerical Simulation

Based on the numerical model established above, the high-precision simulation method suitable for the novel high-

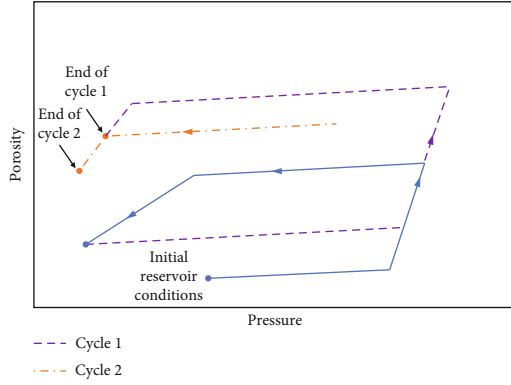


FIGURE 2: Multicycle process of dilation-recompaction (modified from the ref. [29]).

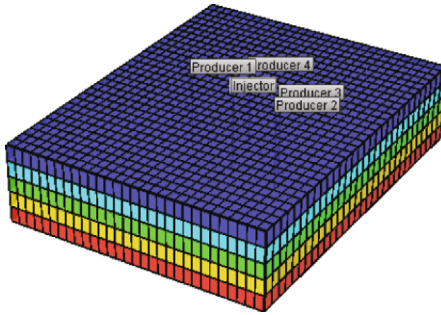


FIGURE 3: Three-dimensional reservoir model.

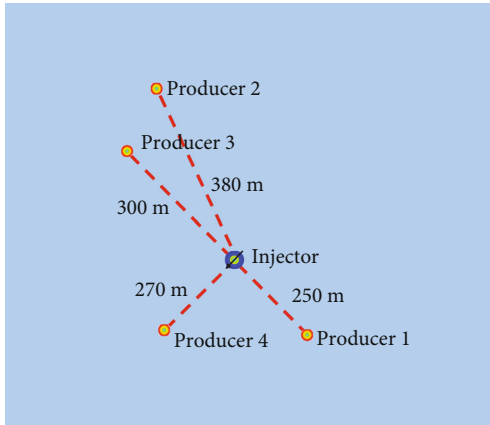


FIGURE 4: Display of the pilot well group.

pressure water slug injection is investigated. Then, the historical performance of the pilot test can be examined and the relevant mechanisms of the high-pressure-driven water-flooding can be quantified, which provides scientific guidance for the large-scale application of this technique.

**3.1. Numerical Simulation without Dilation-Recompaction Model.** Based on the reservoir engineering method, the compressibility coefficient of reservoir rock is inverted as  $\sim 5.0 \times 10^{-3} \text{ Mpa}^{-1}$  with the collected pressure data from producer 4, which indicates that the rock is highly compressible. It provides storage space for the fluid injected by the high-

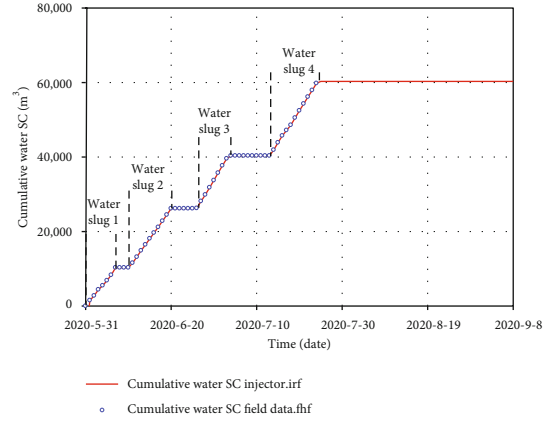


FIGURE 5: Cumulative water injection.

TABLE 1: List of model parameters.

Model dimensions (m)	1500 × 1950 × 4.5
Thickness (m)	4.5
Depth (m)	3200
Porosity	20%
Permeability (md)	5
Initial reservoir pressure (MPa)	28
Reservoir temperature (°C)	123

TABLE 2: Parameters used in the dilation-recompaction model.

Initial reservoir pressure ( $P_0$ ) (MPa)	28
Dilation pressure ( $P_D$ ) (MPa)	50
Recompaction pressure ( $P_R$ ) (MPa)	30
Compressibility coefficient ( $c_{ab}$ ) (1/kPa)	8.5E-6
Dilation compressibility coefficient ( $c_{bc}$ ) (1/kPa)	3.0E-4
Residual dilation fraction ( $f_r$ )	0.1
Maximum allowed proportional increase in porosity ( $r_{at}$ )	1.3
Permeability multipliers ( $IJJ/K$ ) ( $K_{MUL}$ )	50

pressure injection scheme. Combined with the calibration of reservoir permeability and other simulation techniques, we try to match historical data. Figure 6 illustrates that oil/water production data can be well matched by this method. But the pressure cannot be matched. The results of history matching on pressure are shown in Figure 7(a), where the error cannot be ignored. The simulated pressure is much larger than the actual data. The compressibility coefficient is adjusted to reduce the gap between the simulated data and real data. The history matching on pressure tends to be better, but the results are still not good enough, as shown in Figure 7(b).

**3.2. Numerical Simulation with Dilation-Recompaction Model.** With an in-depth understanding of the mechanism of high-pressure water slug injection, it is recognized that

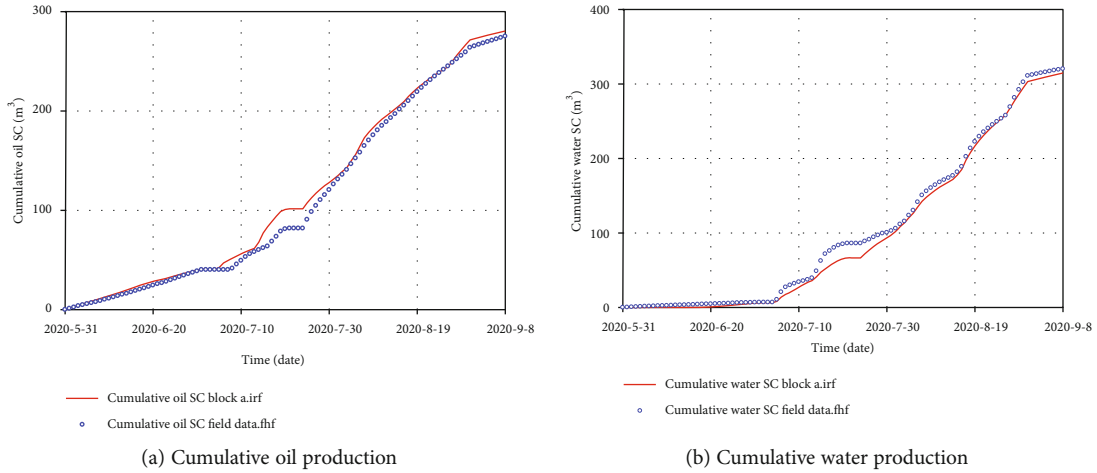


FIGURE 6: History match of production data.

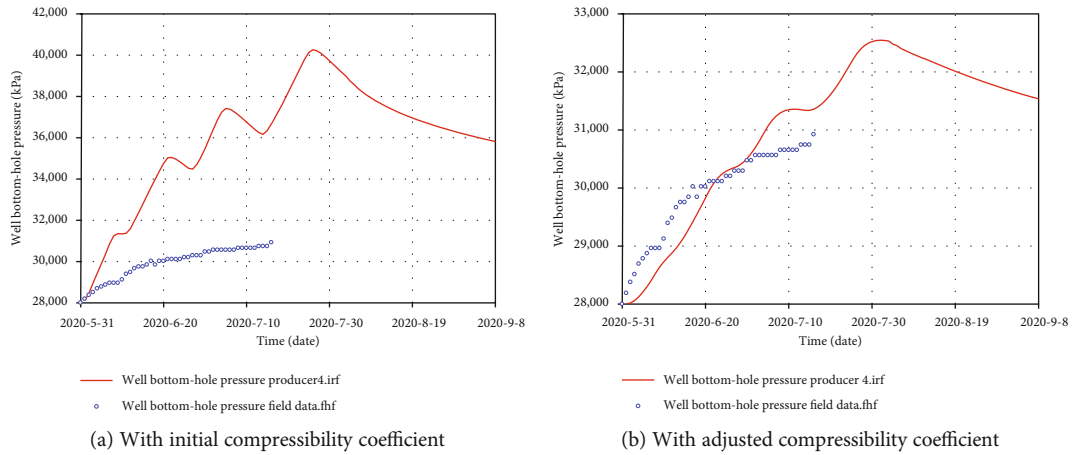


FIGURE 7: History match of pressure: BHP of producer 4.

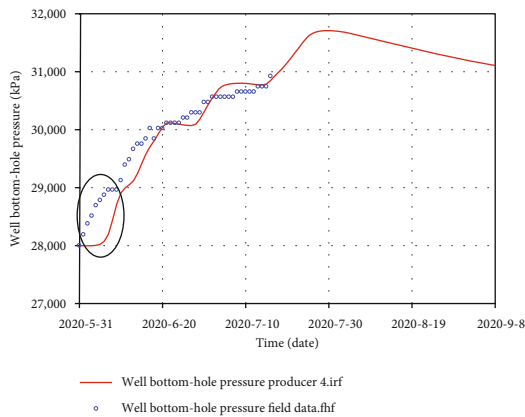


FIGURE 8: Simulation results with the dilation-recompaction model: permeability multiplier of 50.

the reservoir properties around the injector are effectively and dynamically improved. The reservoir around the injector undergoes significant dynamic deformation. The compression coefficient of the conventional rock model is static, and it cannot represent piecewise and path-dependent change

of the reservoir properties with the cyclic evolution of pressure. In other words, the conventional simulation scheme is impossible to precisely reproduce the physical process of high-pressure water slug injection, where the rock properties evolve with cyclic pressure from the elastic stage with small deformation to the dilation with large deformation. Therefore, based on the previous simulation scheme, coupled with the dilation-recompaction geomechanical model, the BHP of producer 4 can be further matched, as shown in Figure 8. Based on the simulation method coupled with dilation-recompaction geomechanical model, historical data can be well matched, but the early part of the simulation for the pressure response is still poor.

In the system of multiphase flow in porous media, the efficiency of energy transfer is positively related to permeability. Based on the dilation-recompaction geomechanical model, three submodels are established to analyze the sensitivity of the permeability multiplier to further match the pressure. The simulation results suggest that scheme 2 is the best case to match the pressure compared with other schemes, as shown in Figure 9. The parameters of sensitivity analysis are listed in Table 3.

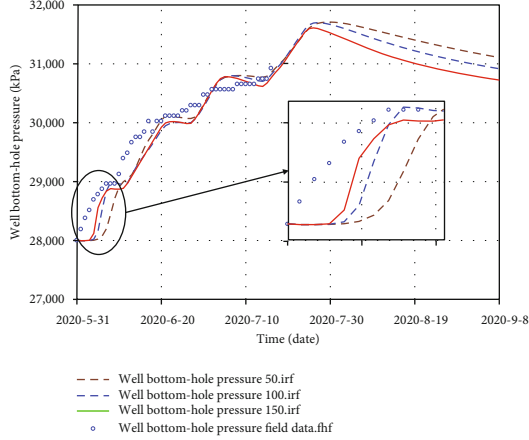


FIGURE 9: Simulation results of schemes 1-3.

**3.3. Evolution of Pressure and Reservoir Properties.** Based on the best case, the dynamic evolution of reservoir properties (porosity and permeability) and transient pressure behavior are finely studied.

**3.3.1. The BHP Evolution of the Injector.** The dynamic evolution of BHP of the injector is further studied based on the above cases. The simulation presented in Section 3.1 shows that the BHP of the injector increases continuously and periodically, as shown in Figure 10(a). This is because the conventional simulation scheme cannot objectively reflect the dynamic evolution of reservoir properties (porosity and permeability) during the high-pressure water slug injection. This simulation method, without taking the dilation-recompaction model into consideration, only characterizes the gradual reversible elastic small deformation. It cannot characterize piecewise and path-dependent deformation. With the pressure close to the failure pressure, the large deformation actually occurs and microfractures near the wellbore are activated. Due to the limitation of this simulation scheme, with the large volume of injected fluid, the elastic energy cannot spread out in time. Therefore, the pressure will continue to increase in each cycle of water slug injection, resulting in the “cyclic and continuous pressure build-up” behavior.

The simulation method presented in Section 3.2 considers the geomechanical factors and the dilation-recompaction model. It can be observed that during the high-pressure water slug injection, the BHP is relatively stable, which is kept basically around 50 MPa. Such response of BHP tends to align with the actual situation, stable and close to failure pressure. The formation energy is efficiently replenished due to the large volume of injected water within a short time. Meanwhile, the reservoir rocks are efficiently deformed. The dilation with large deformation occurs immediately after a short elastic stage with small deformation. The reservoir near the injector is effectively activated with the improved reservoir properties, providing storage space for the injected water and facilitating the diffusion of elastic energy to the producer from the injection spot. Because the pressure is easily diffused outwards from the injection spot,

TABLE 3: Sensitivity analysis.

Scheme	Permeability multiplier
Scheme 1	50
Scheme 2	100
Scheme 3	150

the pressure does not build up around the injector, facilitating the water injection. This is also the reason why  $6.0 \times 10^4 \text{ m}^3$  of water can be effectively injected within a short time ( $\sim 2$  months). The large pressure fluctuation in Figure 10(b) occurs at the moment of restarting injection after the soaking. During the soaking stage, the pressure continues to diffuse outwards from the injection spot and decreases, triggering the compaction of reservoir rocks and leading to relatively poor reservoir properties at that moment. At the beginning of the next water slug injection cycle, the pressure cannot be diffused immediately, resulting in a pressure peak. Meanwhile, at the pressure peak (like the “breakdown pressure” of minifraccking), due to the opening of microfractures around the injector, the reservoir properties have also been significantly improved, along with immediate spread out of peak pressure. Then, the pressure goes back to stable and smooth status. The BHP evolution without the dilation-compaction model illustrates a continuous “pressure build-up” behavior, while the BHP evolution with the dilation-compaction model clearly demonstrates a stable pressure response, accompanied by the instantaneous “breakdown pressure” response.

**3.3.2. The Porosity Evolution.** For the pilot test, the initial reservoir property is poor. With the injected fluid, the elastic energy cannot spread out in time, resulting in the “pressure build-up” around the injector. Due to the significant change of pressure, the dilation-recompaction model is activated. The rapid rise of pressure leads to the reservoir rock only undergoing a short elastic stage with small deformation, as shown by the highlighted segment **ab** in Figure 11(a). Then the dilation with large deformation is triggered by the pressure build-up, which is illustrated by the highlighted segment **bc** in Figure 11(a). With the dilation of reservoir rock, the porosity increases rapidly. So does the permeability. The dynamic change of porosity is shown in Figure 11. The porosity evolution of the grid block, where the injector is perforated, is consistent with the BHP evolution. With the injector undergoing a short stage of pressure rapid rise (corresponding to the short stage of elastic small deformation), the BHP is kept basically around 50 MPa during the whole process. The rock is dilated with large deformation since the BHP reached  $\sim 50$  MPa. In the soaking and asynchronous production stages, the BHP of the injector decreases. The reservoir rock is elastically compacted demonstrated by the highlighted segment **cd**. But the pressure does not decrease to  $P_R$ , which does not trigger the recompaction. With the next cycle of water injection, the reservoir rocks undergo the next cycle of dilation-recompaction till the whole process is completed.

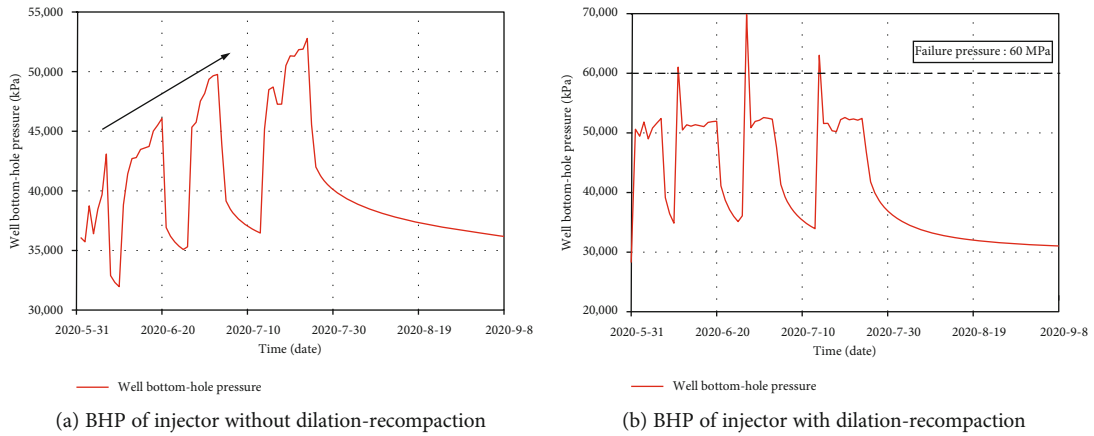


FIGURE 10: The BHP evolution of injector.

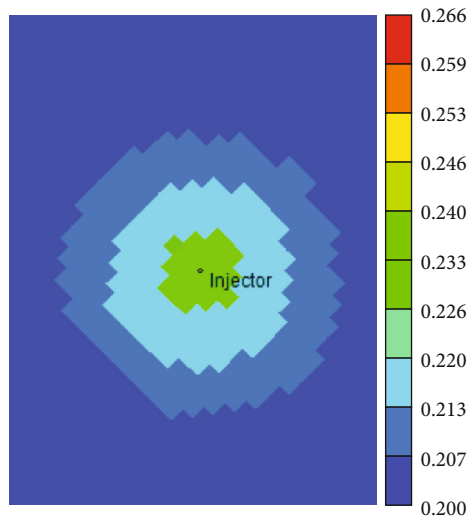
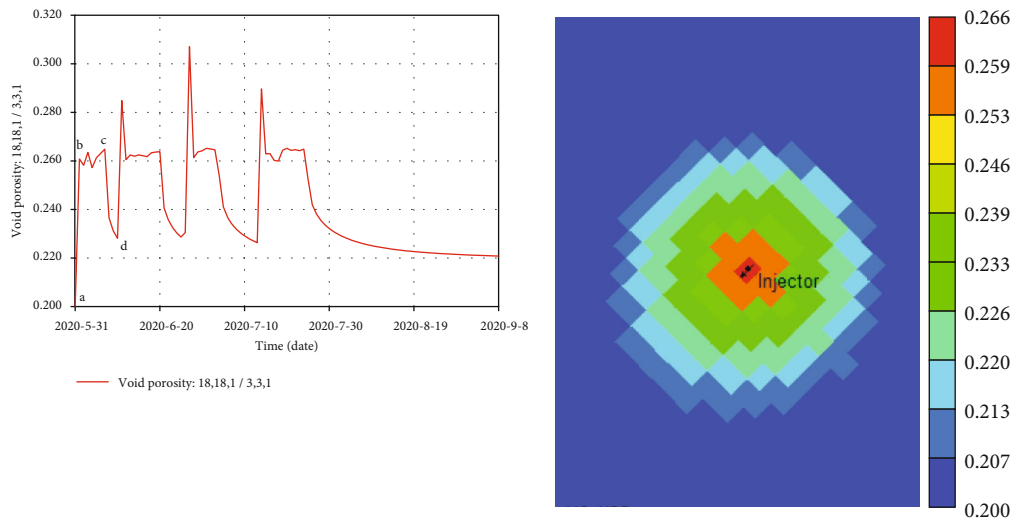


FIGURE 11: Porosity evolution.



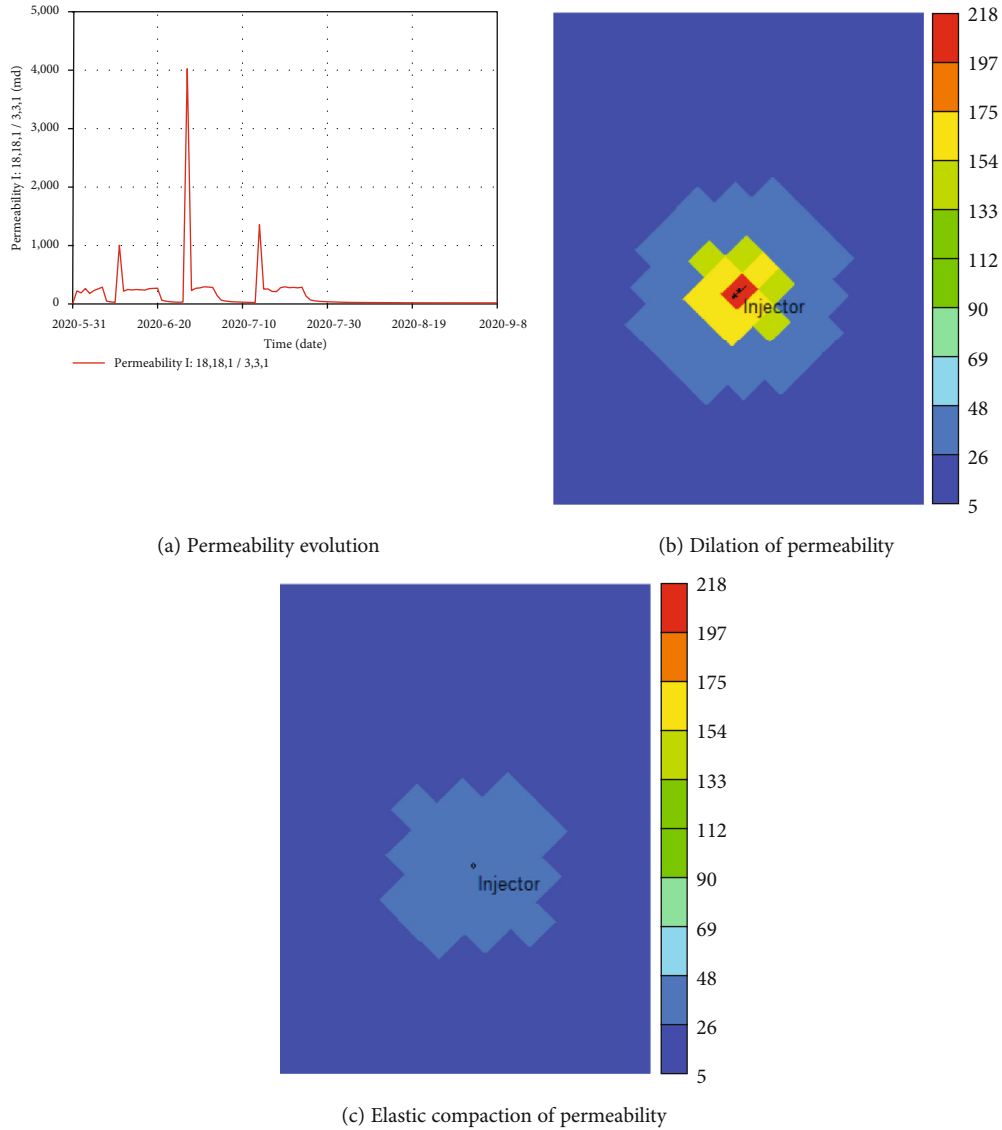


FIGURE 12: Permeability evolution.

**3.3.3. The Permeability Evolution.** According to the analytical relation between porosity and permeability, permeability changes directly with porosity. The permeability evolution is closely related to the porosity evolution. The dilation and compaction stages are consistent with the corresponding evolution stages of porosity, as shown in Figure 12. The change of permeability is also consistent with pressure change. Based on the pressure evolution, it can be observed that the microfractures tend to be activated at the peak pressure, where the permeability fluctuates significantly.

## 4. Conclusion

In this paper, with the data from the pilot test, a high-precision simulation method, coupled with multicyclic dilation-recompaction geomechanical model, for the novel waterflooding technique is proposed. Meanwhile, the dynamic evolution is further studied to provide scientific

guidance for the large-scale application of this technology. Based on the above research, the following conclusions are obtained:

- (1) A novel waterflooding technique, coupling cyclic high-pressure water slug injection with an asynchronous injection and production procedure, for the efficient development of low-permeability reservoirs is developed.
- (2) Compared with the conventional simulation method, the primary mechanism of high-pressure water slug injection can be effectively depicted with the proposed simulation method. Based on the method, the historical performance of the pilot test is reproduced. The BHP of the injector evolves into a relatively stable status with the instantaneous “breakdown pressure” response. The reservoir properties around the injector deform significantly, immediately entering

the dilation stage with large deformation accompanied with the opening of microfractures after a short elastic small deformation.

## Data Availability

Data is available upon request.

## Conflicts of Interest

The authors declare no conflict of interest.

## Acknowledgments

School of Petroleum Engineering in Xi'an Shiyou University is highly appreciated. This research is funded by the General Project of National Natural Science Foundation of China (Grant No. 51974253), the Youth Project of National Natural Science Foundation of China (Grant No. 52004219), the Scientific Research Program Funded by Education Department of Shaanxi Province (Grant No. 20JS117), the Natural Science Basic Research Program of Shaanxi (Grant Nos. 2020JQ-781 and 221717005), and the Graduate Student Innovation and Practical Ability Training Program of Xi'an Shiyou University (Grant Nos. YCS21113089 and YCS21111002).

## References

- [1] H. Wang, F. Ma, X. Tong et al., "Assessment of global unconventional oil and gas resources," *Petroleum Exploration and Development*, vol. 43, no. 6, pp. 925–940, 2016.
- [2] W. Hu, Y. Wei, and J. Bao, "Development of the theory and technology for low permeability reservoirs in China," *Petroleum Exploration and Development*, vol. 45, no. 4, pp. 685–697, 2018.
- [3] Q. Wang and X. Song, "Forecasting China's oil consumption: a comparison of novel nonlinear-dynamic grey model (GM), linear GM, nonlinear GM and metabolism GM," *Energy*, vol. 183, pp. 160–171, 2019.
- [4] F. Song, L. Bo, S. Zhang, and Y. Sun, "Nonlinear flow in low permeability reservoirs: modelling and experimental verification," *Advances in Geo-Energy Research*, vol. 3, no. 1, pp. 76–81, 2019.
- [5] Q. Lei, W. Xiong, J. Yuan, S. Gao, and Y. Wu, "Behavior of flow through low-permeability reservoirs," in *Europe/EAGE Conference and Exhibition*, OnePetro, June, 2008.
- [6] S. A. Holditch, "Unconventional oil and gas resource development—let's do it right," *Journal of Unconventional Oil and Gas Resources*, vol. 1, pp. 2–8, 2013.
- [7] W. Wang, D. Zheng, G. Sheng, Q. Zhang, and Y. Su, "A review of stimulated reservoir volume characterization for multiple fractured horizontal well in unconventional reservoirs," *Advances in Geo-Energy Research*, vol. 1, no. 1, pp. 54–63, 2017.
- [8] J. Cai and X. Hu, *Petrophysical Characterization and Fluids Transport in Unconventional Reservoirs*, Elsevier, 2019.
- [9] X. Yin, S. Jiang, Y. Li et al., "Impact of pore structure and clay content on the water-gas relative permeability curve within tight sandstones: a case study from the LS block, eastern Ordos Basin, China," *Journal of Natural Gas Science and Engineering*, vol. 81, p. 103418, 2020.
- [10] Y. Cao, M. Tang, Q. Zhang, J. Tang, and S. Lu, "Dynamic capillary pressure analysis of tight sandstone based on digital rock model," *Capillarity*, vol. 3, no. 2, pp. 28–35, 2020.
- [11] Y. Tian, O. Uzun, Y. Shen et al., "Feasibility study of gas injection in low permeability reservoirs of Changqing oilfield," *Fuel*, vol. 274, p. 117831, 2020.
- [12] S. D. Joshi, "A review of horizontal well and drainhole technology," in *SPE annual technical conference and exhibition*, OnePetro, September 1987.
- [13] F. Ma, J. Hu, J. Zhuang, Q. Shi, and Q. Wu, "Advanced water injection in low permeability reservoir of block Xin119," *Special Oil & Gas Reservoirs*, vol. 3, 2005.
- [14] S. Morsy, J. J. Sheng, and M. Y. Soliman, "Improving hydraulic fracturing of shale formations by acidizing," in *SPE Eastern Regional Meeting*, OnePetro, August 2013.
- [15] C. Liu, H. Liu, Y. Zhang, D. Deng, and H. Wu, "Optimal spacing of staged fracturing in horizontal shale-gas well," *Journal of Petroleum Science and Engineering*, vol. 132, pp. 86–93, 2015.
- [16] S. Mu and M. Hb, "Sandstone matrix acidizing knowledge and future development," *Journal of Petroleum Exploration and Production Technology*, vol. 7, no. 4, pp. 1205–1216, 2017.
- [17] Y. He, Z. Chai, J. Huang, P. Li, S. Cheng, and J. Killough, "Simulation of inter-fracture injection and production in tight reservoirs based on compartmental embedded discrete fracture model," in *SPE Reservoir Simulation Conference*, OnePetro, March 2019.
- [18] O. SalahEldin Hussien, K. A. Elraies, A. Almansour, H. Husin, A. Belhaj, and L. Ern, "Experimental study on the use of surfactant as a fracking fluid additive for improving shale gas productivity," *Journal of Petroleum Science and Engineering*, vol. 183, p. 106426, 2019.
- [19] F. Zhang, B. Damjanac, and S. Maxwell, "Investigating hydraulic fracturing complexity in naturally fractured rock masses using fully coupled multiscale numerical modeling," *Rock Mechanics and Rock Engineering*, vol. 52, no. 12, pp. 5137–5160, 2019.
- [20] C. Wang, Z. Huang, and Y. Wu, "Coupled numerical approach combining X-FEM and the embedded discrete fracture method for the fluid-driven fracture propagation process in porous media," *International Journal of Rock Mechanics and Mining Sciences*, vol. 130, p. 104315, 2020.
- [21] H. Feng, "Feasibility study on reservoir layered injection in Sabei Development Zone," *IOP Conference Series: Earth and Environmental Science*, vol. 558, no. 2, p. 22074, 2020.
- [22] Z. Wu, L. Li, and Y. Yan, "The new development mode of volume fracturing and imbibition in ultra-low permeability reservoirs," *Fault block oil and gas fields*, vol. 26, no. 4, pp. 491–494, 2019.
- [23] C. Liang, W. Liu, and Y. Shi, "Feasibility of near-fracture pressure water injection in low permeability reservoirs - taking Beishiliu reservoir in Beisantai oilfield as an example," *Xinjiang petroleum geology*, vol. 32, no. 2, pp. 153–156, 2011.
- [24] P. Liu, C. Li, and L. Jiang, "Research and application of water injection by imitating bottom water and fracturing in fault-karst carbonate reservoirs," *Reservoir Evaluation and Development*, vol. 10, no. 2, pp. 54–59, 2020.
- [25] A. Settari and J. M. Raisbeck, "Analysis and numerical modeling of hydraulic fracturing during cyclic steam stimulation in oil sands," *Journal of Petroleum Technology*, vol. 33, no. 11, pp. 2201–2212, 1981.

- [26] Y. Ito, "The introduction of the microchanneling phenomenon to cyclic steam stimulation and its application to the numerical simulator (sand deformation concept)," *SPE Journal*, vol. 24, no. 4, pp. 417–430, 1984.
- [27] J. K. Dietrich, "Cyclic steaming of tar sands through hydraulically induced fractures," *SPE Reservoir Evaluation & Engineering*, vol. 1, no. 3, pp. 217–229, 1986.
- [28] W. D. Pethrick, E. S. Sennhauser, and T. G. Harding, "Numerical modelling of cyclic steam stimulation in Cold Lake oil sands," *Journal of Canadian Petroleum Technology*, vol. 27, no. 6, 1988.
- [29] C. I. Beattie, T. C. Boberg, and G. S. McNab, "Reservoir simulation of cyclic steam stimulation in the Cold Lake oil sands," in *SPE California Regional Meeting*, OnePetro, April 1989.
- [30] N. H. Kilmer, N. R. Morrow, and J. K. Pitman, "Pressure sensitivity of low permeability sandstones," *Journal of Petroleum Science and Engineering*, vol. 1, no. 1, pp. 65–81, 1987.
- [31] R. A. Farquhar, B. G. D. Smart, A. C. Todd, D. E. Tompkins, and A. J. Tweedie, "Stress sensitivity of low-permeability sandstones from the Rotliegendes sandstone," in *SPE annual technical conference and exhibition*, OnePetro, October 1993.
- [32] X. Huang, *Application of dilation-recompaction model in hydraulic fracturing simulation [M.S thesis]*, University of Calgary, Calgary, 2015.
- [33] X. Huang, J. Wang, S. Chen, and I. D. Gates, "A simple dilation-recompaction model for hydraulic fracturing," *Journal of Unconventional Oil and Gas Resources*, vol. 16, pp. 62–75, 2016.
- [34] R. Gao, X. Wang, Z. Yang et al., "Application of dilation-recompaction model in fracturing optimisation in tight oil reservoir," in *International Petroleum Technology Conference*, OnePetro, March 2019.
- [35] B. Y. Jamaloei, "Impact of formation dilation–recompaction on cyclic steam stimulation," *SPE Reservoir Evaluation & Engineering*, vol. 24, no. 1, pp. 98–126, 2021.

## Research Article

# Study on the Water Invasion and Its Effect on the Production from Multilayer Unconsolidated Sandstone Gas Reservoirs

**Yong Hu,<sup>1,2</sup> Xizhe Li ,<sup>1,2</sup> Weijun Shen ,<sup>3,4</sup> Changmin Guo,<sup>1,2</sup> Chunyan Jiao,<sup>1,2</sup> Xuan Xu,<sup>1,2</sup> and Yuze Jia<sup>5</sup>**

<sup>1</sup>Research Institute of Petroleum Exploration & Development, PetroChina, Beijing 100083, China

<sup>2</sup>Key Laboratory of Gas Reservoir Formation and Development, CNPC, LangFang 065007, China

<sup>3</sup>Key Laboratory for Mechanics in Fluid Solid Coupling Systems, Institute of Mechanics, Chinese Academy of Sciences, Beijing 100190, China

<sup>4</sup>School of Engineering Science, University of Chinese Academy of Sciences, Beijing 100049, China

<sup>5</sup>College of Earth and Planetary Sciences, University of Chinese Academy of Sciences, Beijing 100049, China

Correspondence should be addressed to Xizhe Li; [lxz69@petrochina.com.cn](mailto:lxz69@petrochina.com.cn) and Weijun Shen; [wjshen763@imech.ac.cn](mailto:wjshen763@imech.ac.cn)

Received 10 April 2021; Revised 3 June 2021; Accepted 14 June 2021; Published 26 July 2021

Academic Editor: Steffen Berg

Copyright © 2021 Yong Hu et al. This is an open access article distributed under the Creative Commons Attribution License, which permits unrestricted use, distribution, and reproduction in any medium, provided the original work is properly cited.

Water invasion is a common occurrence in multilayer unconsolidated gas reservoirs, which results in excessive water production and reduces the economic life of gas wells. However, due to multiple layers, active edge water, and strong heterogeneity, the mechanism of water invasion and its effect in the unconsolidated sandstone gas reservoir require understanding in order to improve efficiency and minimize economic cost. In this study, an experimental study on edge water invasion of the multilayer commingled production in unconsolidated sandstone gas reservoirs was conducted to understand the water invasion process along with different permeability layers. The results show that the edge water invasion in the commingling production is mainly affected by two major factors including reservoir permeability and gas production rate, which jointly control the encroaching water advance path and speed. The nonuniform invade of edge water may occur easily and water prefers to invade toward the gas well along with high permeability layers when the commingling production is in the condition of large permeability gradient and high production rate. The bypass flow will occur when there are high permeability channels between the layers, which causes water blocking to low-permeability layers and periphery reservoirs far away from gas wells. The findings of this study can help for a better understanding of water invasion and the effects of reservoir properties so as to optimize extraction conditions and predict gas productivity in unconsolidated sandstone gas reservoirs.

## 1. Introduction

As a clean and efficient low-carbon energy, natural gas has been attracting greatly wide concerns from governments around the world, which exhibits an increasingly broad development prospect [1]. The natural gas resources in China are rather abundant, and the gas reserves and production are increasing rapidly. According to the statistics from PetroChina Company Limited, China's natural gas geological resources have exceeded 220 trillion cubic meters in 2015, and the recoverable gas resources were about 31% of total

resources, and the annual production increased from 17.4 billion cubic meters in 1995 to 135 billion cubic meters in 2015 with an average annual growth rate of 11% [2–4]. The Quaternary unconsolidated sandstone gas reservoir in the Qaidam Basin, Northwest China, is an important strategic successor gas source for the West-East Gas Pipeline project, which belongs to a rare biogenetic gas reservoir [5, 6]. Geologically, the gas reservoir is characterized by long interval, multiple layers, and active edge water, which is based on the multilayer commingled production, and there exist lots of difficult problems to solve in the production and

development [7]. Therefore, it is very important to develop the gas reservoir effectively and guarantee a stable gas supply in the sustainable development of the national economy.

Most of the gas reservoirs in China belong to water-drive gas reservoirs surrounded by aquifers, in which there are about 40 to 50 percent of gas reservoirs with active edge-and-bottom water [8, 9]. Due to the existence of edge-and-bottom water in gas reservoirs, the reservoir pressure will gradually decrease with the exploitation of gas reservoirs, which results in the invasion of the edge-and-bottom water into the gas pay zones. The gas-water two-phase flow occurs in gas reservoirs with the edge-and-bottom water drive, and the gas phase permeability will be decreased, which consequently interferes with gas production and impacts on the recovery factor of gas reservoirs [10–12]. In addition, water invasion can also block a large amount of gas through snapping, bypassing and water locking in gas reservoirs, which will greatly reduce the gas production of a single well [13–15]. Thus, understanding the questions such as water invasion in gas reservoirs and its effects on gas production is significant for predicting gas productivity and improving recovery rate during the development of gas reservoirs.

The problem of water invasion in gas reservoirs has always been one of the major concerns in terms of productivity, increased operating costs, and environmental effects, and there have been many studies carried out on water invasion in gas reservoirs and its effects on gas productivity in the past years. Persoff and Pruess [16] and Zhou et al. [17] used a transparent microphysical model of a water-driven gas experiment to analyze the water invasion, and they considered that water would trap the gas in the matrix block by means of circumfluence, cut off phenomenon, and water locking. Tokunaga and Wan [18, 19] conducted water films flow on fracture surfaces under near-zero-matrix potentials and examines the possibility of fast unsaturated flow along the macroscopic rock fracture surface. Saad et al. [20] and Bahrami et al. [21] analyzed the problem of water coning in naturally fractured reservoirs with the experiment and field data, respectively. Perez et al. [22] applied a coning radial model to analyze the occurrence of coning in naturally fractured reservoirs. Hu et al. [23] conducted the water invasion mechanism of gas reservoirs under horizontal fracture conditions and analyzed the changes of water saturation of reservoirs at different locations from the bottom of the well during gas reservoir depletion. Azim [24] developed a fully coupled poroelastic multiphase fluid flow model to evaluate the water invasion in naturally fractured reservoir under the effects of fluid properties. Shen et al. [25] and Fang et al. [26] used full-diameter core experiments to analyze the effects of different influencing factors on water invasion in pore gas reservoirs. Based on the material balance equation, Kabir et al. [27] and Patachini [28] analyzed and predicted the water invasion intensity and speed combined with the production data. Although there were a lot of studies conducted on the water invasion of gas reservoirs, the above studies focused on naturally fractured gas reservoirs. And water invasion in the multilayer unconsolidated sandstone gas reservoir was somewhat lacking. The unconsolidated sandstone gas reservoir in the Qaidam Basin is characterized

by multiple layers and strong heterogeneity, and there exist many uncertainties in the gas production. Hence, there is an extreme necessity to understand the mechanism of generating edge water nonuniform water invasion and evaluate the effects on different edge water so as to predict gas production and optimize the producing method in the unconsolidated sandstone gas reservoir.

In this study, the physical experiment of edge water invasion in the commingling production was established to understand the water invasion process along with the reservoirs with different permeability layers, based on the geological characteristics of unconsolidated sandstone gas reservoirs. Then, the edge water invasion characteristics and mechanism of the multilayer production were analyzed. Furthermore, the effects of edge water invasion on the development of gas reservoirs such as gas phase seepage capability, recovery rate, and residual gas storage were determined. The results can provide the theoretical guidance for establishing a reasonable gas recovery rate and water control development in unconsolidated sandstone gas reservoirs.

## 2. Gas Reservoir Geological Characteristics and Experimental Method

*2.1. Gas Reservoir Geological Characteristics.* The Quaternary unconsolidated sandstone gas reservoir of the Sebei gas field is located in the Qaidam Basin, Northwest China, which is mainly a structural gas reservoir [6]. The internal structures of the gas reservoir are intact without any faults developed and their lithological changes are small. The gas reservoir has many gas layers in structural high positions with large thickness while there are few gas layers in structural low positions with small thickness, which is surrounded by edge water. There exists a set of lacustrine facies beach-bar sandstone with sedimentary subfacies including shore swamp, shore lake, shallow lake and semideep lake subfacies, and sedimentary microfacies including sand bank, beach sand, sand sheet, mud bank, and marsh mud microfacies in the gas reservoir.

*2.2. Experimental Method.* Based on the geological multilayer characteristics of the unconsolidated sandstone gas reservoir in the Qaidam Basin, Northwest China, the characteristics of reservoir heterogeneity and edge water invasion are considered, and a set of physical simulation experimental methods on edge water invasion during the commingling production is established to understand the edge water invasion in the unconsolidated sandstone gas reservoirs. The experimental apparatus for physical simulation of water invasion in multilayer commingled production of gas reservoirs are shown in Figure 1, which is mainly composed of the confining pressure, water body, gas source, experimental model, gas rate control, and gas-water separation measurement system. The experiment features four basic characteristics as follows: (1) four sets of cores with different magnitudes of permeability are selected to assembly connect so as to reproduce the longitudinal multigas layer geological model, and the maximum permeability difference is 12.6; (2) high-precision back pressure and confining pressure control systems are used to

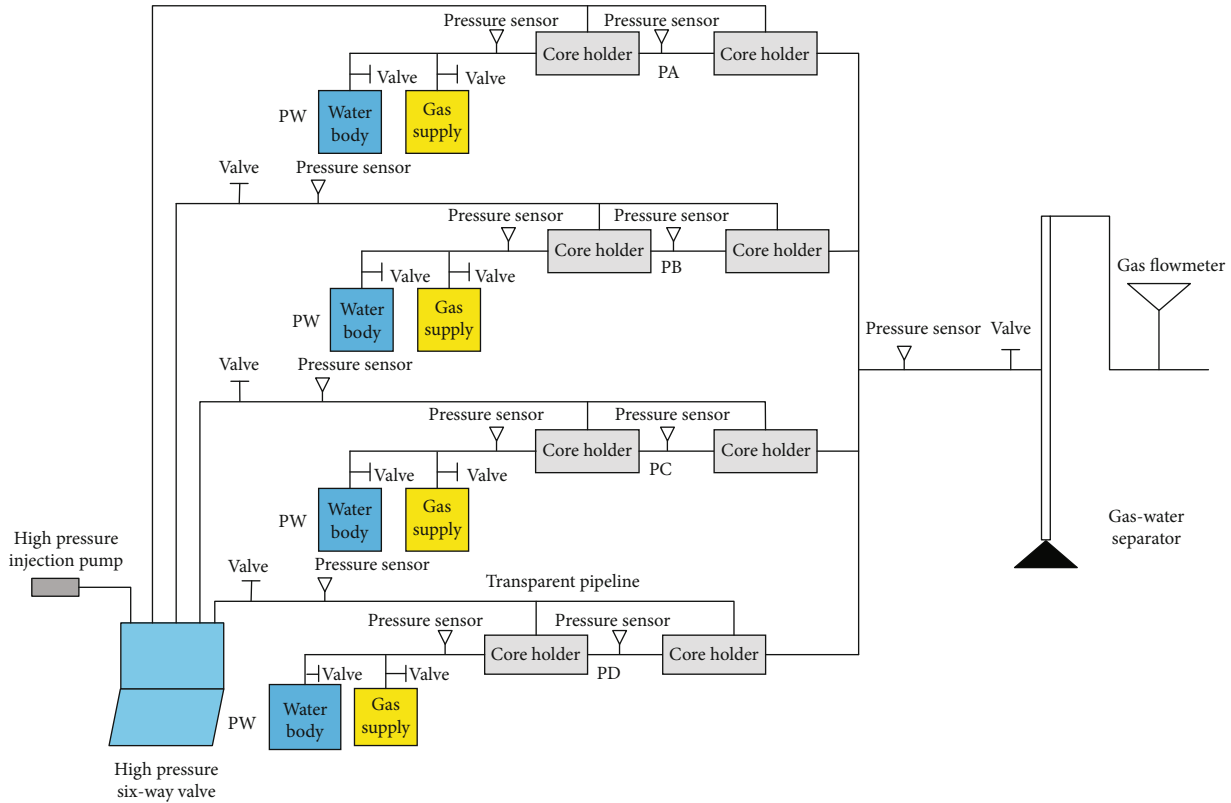


FIGURE 1: Experimental apparatus for physical simulation of water invasion in multilayer commingled production of gas reservoirs.

achieve the gas well exploitation, which can be simulated under any production rates or any production pressure difference; (3) the high-pressure transparent pipelines are connected in series between the two core holders of each group to visualize observation of the water invasion progress process as illustrated in Figure 2; (4) the encroaching water advance speed can be calculated in the experiment. When the edge water can be pushed to the transparent pipeline, it can be calculated according to the length of the core and the time for making it into the transparent pipeline. When it cannot be pushed into the transparent pipeline, the core is removed at the end of the experiment, and the advanced speed can be calculated based on the length of the core with water invasion and the time.

To understand the mechanism of edge water invasion and its effects during the multilayer commingled production in unconsolidated sandstone gas reservoir, the following experimental schemes are designed in this study: (1) four sets of cores with different permeability are used to simulate the commingled production with the vertical four gas layers, as shown in Table 1; (2) the encroaching water advance process in different permeability layers can be observed by the series connection experiment flow of high-pressure transparent pipeline; (3) different production rates (20 mL/min, 50 mL/min, 80 mL/min, 100 mL/min, 150 mL/min) are adopted in the experiment to simulate the gas well exploitation process and study the effects of production rate on the water invasion; (4) the core is saturated with gas until the pore pressure is at around 4 MPa, and the outside of the gas layer is connected to a water body with a constant pressure as shown

in Figure 2; (5) in the experimental process, the parameters such as experimental time, reservoir pressure, water invasion path, and gas production rate are recorded to analyze the encroaching water advance speed and the effects of edge water invasion on the gas phase seepage capacity and recovery rate as well as the residual gas storage.

### 3. Results and Discussion

#### 3.1. Edge Water Invasion Characteristics of the Multilayer Production

**3.1.1. Characteristics of the Encroaching Water Advance Path.** In this study, the characteristics of the encroaching water advance path in the gas reservoir multilayer production are recorded through the visualized experimental process, which is illustrated in Figure 1. According to the analysis results, the characteristics diagram of the encroaching water advance path is shown in Figure 2. From the result of Figure 2, it can be observed that the encroaching water advance path is mainly influenced by reservoir permeability and distribution and gas production rate. The commingled production in gas reservoirs with four layers of different permeability is conducted in the experiment; due to the permeability difference in the gas layers, the edge water exhibits the nonuniform advancement characteristics. The water invasion preferentially advances into the gas well along with two layers with the permeability of 24.4 mD and 9.34 mD, while the water invasion in the layers with the permeability of 5.37 mD and 1.93 mD is weak. The results imply that the reservoir

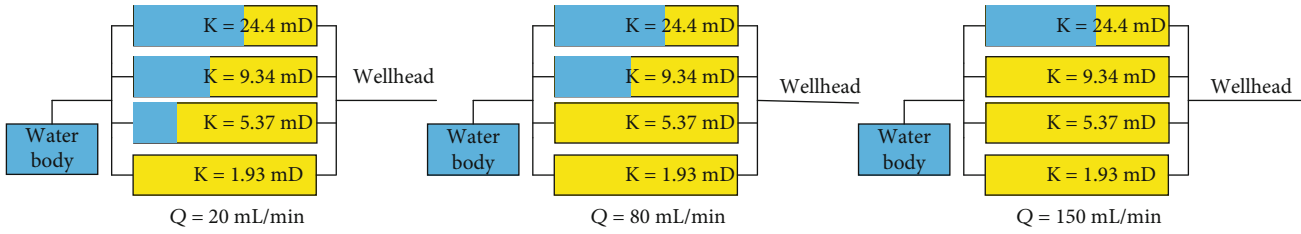


FIGURE 2: Characteristics diagram of the encroaching water advance path.

permeability and distribution are the dominant factors of the water invasion path. When the reservoir permeability exceeds 10 mD, it will be the key channel for water invasion. Besides, the gas production rate is also an important factor on the water invasion path. When the gas production rate is 20 mL/min, the edge water is uniformly pushed along three layers with the permeability of 24.4 mD, 9.34 mD, and 5.37 mD, respectively. Once the gas production rate reaches 150 mL/min, the edge water rushes along the single direction in the reservoir with the permeability of 24.4 mD, which implies that the gas production rate is a key factor affecting water invasion advance path. In addition, when the reservoir is characterized by strong heterogeneous, a larger gas production rate will result in nonuniform water invasion easily.

**3.1.2. Characteristics of the Encroaching Water Advance Speed.** According to the encroaching water advance path and experimental time, the calculation of the encroaching water advance speed can be expressed as follows:

$$v = L/t, \quad (1)$$

where  $v$  is the encroaching water advance speed, cm/min;  $L$  is the encroaching water advance path, cm; and  $t$  is the experimental time, min.

Based on the experimental results, the effects and comparisons of production rate on different encroaching water advance speeds are illustrated in Figure 3 and Table 2 (no water invasion is abbreviated as NWI). From the results of Figure 2 and Table 2, it can be seen that the encroaching water advance speed is also influenced by both reservoir permeability and production rate. When the production rate is low, the edge water is relatively uniformly pushed along the multiple layers, and the encroaching water advance speed is slower. For instance, when the production rate is 20 mL/min in the experiment, the edge water is uniformly pushed along three gas layers with the permeability of 24.4 mD, 9.34 mD, and 5.37 mD, and the advance speeds are 0.64 cm/min, 0.60 cm/min, and 0.34 cm/min, respectively; when the production rate is 50 mL/min, 80 mL/min, or 100 mL/min, and the edge water permeability is 24.4 mD and 9.34 mD, it is pushed nonuniformly in both gas layers and the advance speed is obviously increased between 0.92 cm/min and 1.71 cm/min. When the production rate reaches 150 mL/min, it will rush unidirectional advance along with the gas layer with the permeability of 24.4 mD, and the encroaching water advance speed is 2.19 cm/min.

As previously mentioned, the rule of edge water invasion during the commingling production in gas reservoirs is

mainly affected by the reservoir permeability and distribution and gas production rate. The two influencing factors jointly control the encroaching water advance path and speed. When the commingling production development is under the conditions with large permeability contrast and high production rate, the edge water is prone to nonuniform rush. The water invasion preferentially advances along with the high permeability layers into gas wells, and the encroaching water advance speed is fast. If the gas production rate is properly reduced, the edge water is pushed relatively uniformly along multiple layers, and the advance speed will be much slower than that in a single high permeability layer.

### 3.2. Edge Water Invasion Mechanism of the Multilayer Production

**3.2.1. Nonuniform Rush of Edge Water along with High Permeability Layers.** Permeability is an important property of the reservoir rock that measures the capacity of the formation to transmit fluid, and there exist a few preferred pathways that water flow through the high permeability reservoir [29–31]. In this study, the threshold pressure of gas-water seepage flows in an unconsolidated sandstone reservoir is illustrated in Figure 4. Threshold pressure is the minimum pressure at which the fluid begins to flow in the low permeability reservoir. From the result of Figure 4, as can be seen, there are obvious differences in the threshold pressure of gas-water seepage flow in different permeability reservoirs. For unconsolidated sandstone reservoir with the permeability greater than 10 mD, the threshold pressure of gas flooding is generally less than 1.0 MPa. When the permeability of the unconsolidated sandstone reservoirs is no more than 10 mD, the threshold pressure of gas-water seepage flow is generally greater than 1.0 MPa. The lower the reservoir permeability is, and the higher the threshold pressure of gas-water seepage flow is. Thus, when the commingling production is in multiple gas layers with different magnitudes of reservoir permeability, gas and water will be prone to choosing preferential a seepage path along with high permeability layers under the same displacement pressure. As the displacement pressure increases, i.e., the production pressure difference is increased, gas and water can be able to form seepage flows along with the relatively low permeability reservoirs. This is the primary reason why the edge water will choose to rush along high permeability layers during commingling production in gas reservoirs.

**3.2.2. Effect of Gas Production Rate on Nonuniform Advancement of Water Invasion.** The gas production rate is

TABLE 1: Some properties of unconsolidated sandstone core samples used in this study.

Group	Sample	Well	Permeability (mD)	Porosity (%)	Length (cm)	Diameter (cm)
Group I, series	1-2-7	Tai4-31	1.93	29.4	5.495	2.355
	1-2-8	Tai4-31	2.11	29.4	5.645	2.386
Group II, series	5-3-2	Tai4-31	9.34	29.5	4.398	3.693
	6-5-1	Tai4-31	10.2	27.0	5.625	3.707
Group III, series	1-3-5	Tai4-31	5.37	33.6	5.346	2.394
	1-4-1	Tai4-31	5.71	32.2	5.394	2.306
Group IV, series	1-5-3	Tai4-31	24.4	36.7	4.535	2.419
	2-2-3	Tai4-31	22.1	37.2	4.438	2.480

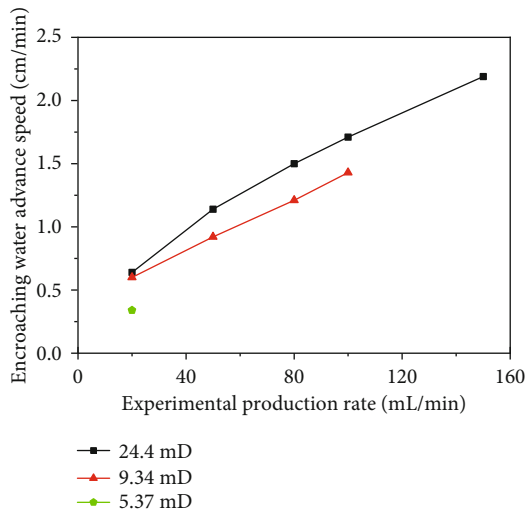


FIGURE 3: Effects of production rate on different encroaching water advance speeds.

TABLE 2: Comparison of the different encroaching water advance speeds.

Permeability (mD)	Encroaching water advance speeds under different production rates (cm/min)				
	20	50	80	100	150
24.4	0.64	1.14	1.5	1.71	2.19
9.34	0.60	0.92	1.21	1.43	NWI
5.37	0.34	NWI	NWI	NWI	NWI
1.93	NWI	NWI	NWI	NWI	NWI

a significant parameter during the gas reservoir exploitation, which affects water invasion and ultimate recovery of gas reservoirs [8, 32]. In order to understand the effect of gas production rate on nonuniform water invasion, the pressure difference between water bodies and different permeability reservoirs is measured by conducting water invasion physical simulation experiments on different production rates. Figure 5 shows the pressure difference between water bodies and different permeability reservoirs on different production rates. From the result of Figure 5, as can be seen, water invasion is influenced by gas production rates, when the pressure

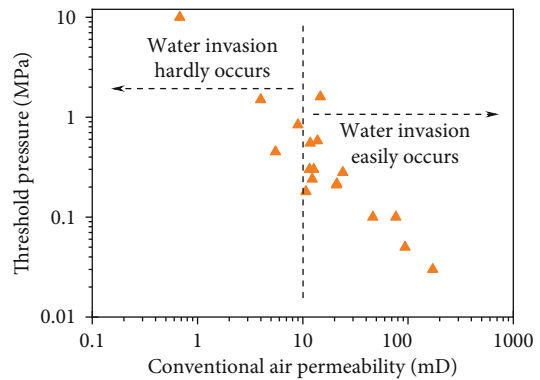


FIGURE 4: Threshold pressure of gas-water seepage flow in unconsolidated sandstone reservoirs.

difference between water bodies and different permeability reservoirs is large. The gas supply is mainly from the high permeability layers when the gas production rate is more than 100 mL/min, and the pressure difference between the water body and high permeability layers is much larger than that between the water body and low-permeability layers. Due to the pressure difference between the water body and the reservoir layers, when the pressure difference is 3.99 MPa ( $PW - PA = 4.11$  MPa,  $PW - PD = 0.12$  MPa), the water body is pushed forward along the high permeability layers. When the gas production rate is 20 mL/min, the pressure difference between the water body and the reservoir with each scale of permeability will be reduced. For example, when the pressure difference is 2.80 MPa ( $PW - PA = 3.0$  MPa,  $PW - PD = 0.2$  MPa) in the experiment, which implies that if the production rate is properly controlled, the pressure differences between the edge water and the reservoir with different scales of permeability reservoir are close, and the water invasion is more easily pushed uniformly along the permeability reservoirs. When the gas production rate is high, the gas supply capacity of the high permeability layer is much larger than that of the low permeability layer, and the high permeability layer will be produced faster than the low permeability layer, which results in the pressure difference between the water body and the high permeability layers greater than that between the water body and the low permeability layers. Consequently, the water body will



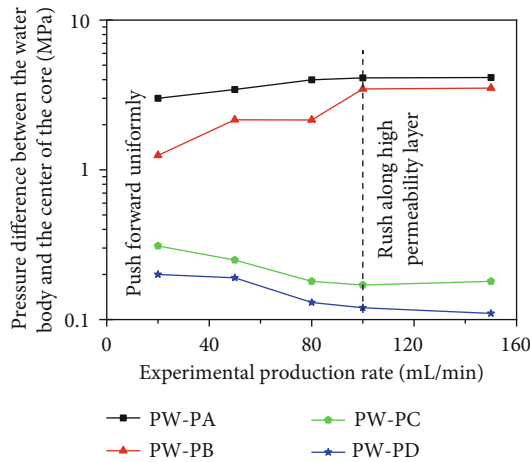


FIGURE 5: Pressure difference between water body and different permeability reservoirs on different production rates.

preferentially rush advance along with the high permeability layers under high production rate conditions.

#### 4. Effects of the Edge Water Invasion

**4.1. Effect on the Gas Phase Seepage Capability.** The water production from gas-producing well is a common occurrence observed in gas reservoirs, which results in the water-gas two-phase filtration and reduces gas phase seepage capability [33–35]. In this study, the gas permeability measurement under residual water saturation is conducted on the unconsolidated sandstone cores with different permeabilities. The relationship between conventional permeability and gas permeability under the residual water saturation is shown in Figure 6. From the result of Figure 6, it can be observed that there are significant differences in the effect of residual water saturation on the gas phase seepage capacity of different permeability sandstone reservoirs. Compared with the permeability of dry cores, there is a great effect on the gas phase seepage capacity of the reservoirs with the permeability less than 5 mD, and the gas phase permeability under residual water saturation decreases by nearly 100%. For the cores with the permeability of 5 ~ 50 mD, the gas phase permeability under residual water saturation drops of more than 90%, and the gas phase permeability under residual water saturation declines by more than 80% when the permeability exceeds 50 mD. Hence, the water will have a great influence on the gas flow seepage capacity of the reservoirs with the permeability less than 5 mD, and water invasion rushing along the high permeability layers should be avoided so as not to form water blocking during the development in the low permeability gas reservoir.

**4.2. Effect on the Recovery Rate.** Due to the existence of edge-and-bottom water in gas reservoirs, the edge and bottom water will invade the gas pay zones with the gas reservoir exploitation, which leads to the lower recovery rate of gas reservoirs, and some previous studies have indicated the recovery rate of water-driven gas reservoirs was significantly lower than that of dry gas reservoirs [36–38]. In the study, three

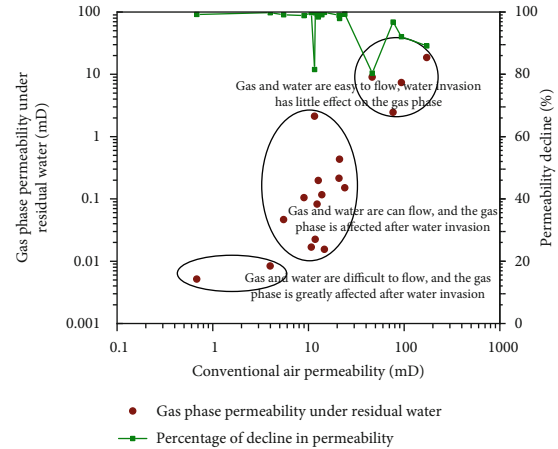


FIGURE 6: Relationship between conventional permeability and gas permeability under residual water saturation.

physical models, including no water invasion, water invasion without bypass flow, and water invasion with bypass flow, are designed to analyze the effect on the recovery rate during the production. Figure 7 illustrates the recovery rate comparison of gas reservoirs with and without water invasion. From the result of Figure 7, it can be seen that the recovery rates of the two water invasion models are significantly lower compared with the recovery rate of the no water invasion model, which indicates that it will have a major influence on gas reservoir recovery rate when the water invasion occurs in the gas reservoir development. The water invasion with bypass flow has the lowest recovery rate, which is about 30% lower than that of the no water invasion. While the recovery rate of water invasion without bypass flow ranges between 80% and 90%, which is about 10% lower than that of the no water invasion model. Although this is an experimental result, it can still reflect the changing trend, which is used as a reference during the gas reservoir development evaluation. However, the results seem to be optimistic in terms of the recovery rate itself, and it is difficult to reflect the overall gas recovery, and the simulation results can be regarded as the recovery rate of the near well areas.

**4.3. Effect on the Residual Gas Storage.** The gas recovery under water drive in gas reservoirs appears to depend on an important way on the residual gas saturation, and some studies have indicated that gas recovery may be as low as 45 percent of the initial gas in place due to the water invasion [39, 40]. In order to understand the effect on the residual gas storage, the residual gas ratio of each group of cores is analyzed at the end of the physical simulation experiment in this study, and the residual gas ratio is defined as the ratio between residual gas and the reserves. The experimental results of the residual gas ratio in different permeability cores are shown in Table 3. From the result of Table 3, as can be seen, there is a certain amount of residual gas that can hardly be recovered during the multilayers commingled production in gas reservoir. The ratio of residual gas to the reserves is in the range between 31% and 36%, and the residual gas is mainly distributed in the low-permeability layers. For

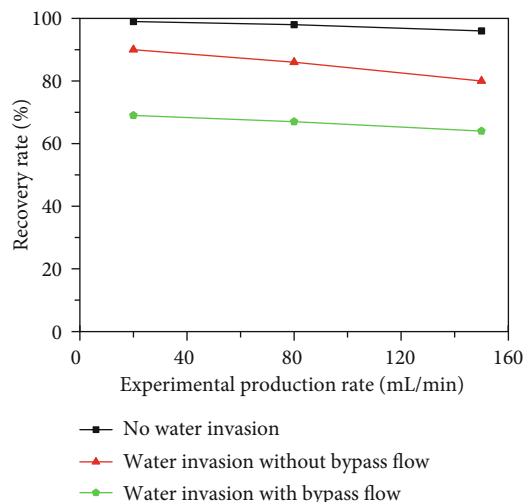


FIGURE 7: Recovery rate comparison of gas reservoirs with and without water invasion.

TABLE 3: Results of the residual gas ratio in core samples of different permeabilities.

Permeability mD	Residual gas ratio (%)		
	20 mL/min	80 mL/min	150 mL/min
156.0	29	30	29
57.5	29	30	32
11.7	32	34	34
3.6	35	37	50
Average value	31	33	36

instance, the ratio of residual gas in the gas layer with the permeability of 3.6 mD is apparently higher than that in other gas layers. The gas production rate has a certain effect on the residual gas, especially in the low-permeability layers. The larger the gas production is, and the more the residual gas is. The overall ratio of residual gas in the gas layers is 31% when the gas production rate is 20 mL/min, while the overall residual gas ratio is 36% when the production rate is 150 mL/min.

## 5. Summary and Conclusions

In this study, based on the geological characteristics of an unconsolidated sandstone gas reservoir, the physical experiment of edge water invasion was conducted to understand the mechanism of water invasion and its effect on the development phase during the commingling production. Then, the edge water invasion characteristics and mechanism of the multilayer production were discussed, and the effects such as gas phase seepage capability, recovery rate, and residual gas storage on the edge water invasion were analyzed. According to the above results, the conclusions from this study are summarized as follows: (1) During the commingled production phase, the edge water invasion is mainly affected by reservoir permeability and gas production rate, and the two influencing factors jointly control the encroaching water

advance path and speed. When the gas reservoir is characterized by strong heterogeneity, a larger gas production rate will cause easily nonuniform water invasion. (2) When the commingling production is in large permeability gradation and high production rate, the nonuniform rush of edge water along the high permeability layers will occur. While there exists interflow in the high-permeability channel, the bypass flow will emerge, and water block will be formed in the low-permeability layers and the peripheral reservoirs, which results in a significant decline in productive capacity and recovery rate. (3) The residual water saturation is a great influence on the gas phase seepage capacity of the reservoir less than 5 mD. Compared with no water invasion, the recovery rates of water invasion with and without bypass flow decrease by 30% and 10%, respectively, and there exists a certain amount of residual gas that can hardly be recovered during the commingling production, which is mainly distributed in the low-permeability layer.

## Data Availability

The data used to support the findings of this study are included within the article.

## Conflicts of Interest

The authors declare that they have no conflicts of interest.

## Acknowledgments

This work was supported by the National Natural Science Foundation of China (NO. U1762216 and NO. 11802312) and by the Open Fund (PLN201810) of State Key Laboratory of Oil and Gas Reservoir Geology and Exploitation (Southwest Petroleum University). We also thank the support from the Youth Foundation of Key Laboratory for Mechanics in Fluid Solid Coupling Systems, Chinese Academy of Sciences.

## References

- [1] J. Y. Liu, S. X. Wang, N. Wei, X. Chen, H. Y. Xie, and J. Wang, "Natural gas consumption forecasting: a discussion on forecasting history and future challenges," *Journal of Natural Gas Science and Engineering*, vol. 90, article 103930, 2021.
- [2] Y. F. Ma and Y. L. Li, "Analysis of the supply-demand status of China's natural gas to 2020," *Petroleum Science*, vol. 7, no. 1, pp. 132–135, 2010.
- [3] W. J. Shen, X. Z. Li, T. R. Ma, J. C. Cai, X. B. Lu, and S. W. Zhou, "High-pressure methane adsorption behavior on deep shales: experiments and modeling," *Physics of Fluids*, vol. 33, no. 6, article 063103, 2021.
- [4] X. Li, Z. Guo, Y. Hu et al., "Efficient development strategies for large ultra-deep structural gas fields in China," *Petroleum Exploration and Development*, vol. 45, no. 1, pp. 118–126, 2018.
- [5] Y. Q. Dang, W. Z. Zhao, A. G. Su et al., "Biogenic gas systems in eastern Qaidam Basin," *Marine and Petroleum Geology*, vol. 25, no. 4-5, pp. 344–356, 2008.

- [6] S. C. Zhang, Y. H. Shuai, L. Huang et al., "Timing of biogenic gas formation in the eastern Qaidam Basin, NW China," *Chemical Geology*, vol. 352, no. 1, pp. 70–80, 2013.
- [7] S. Huang, Y. Wu, X. Meng, L. Liu, and W. Ji, "Recent advances on microscopic pore characteristics of low permeability sandstone reservoirs," *Advances in Geo-Energy Research*, vol. 2, no. 2, pp. 122–134, 2018.
- [8] F. F. Fang, W. J. Shen, S. S. Gao, H. X. Liu, Q. F. Wang, and Y. Li, "Experimental study on the physical simulation of water invasion in carbonate gas reservoirs," *Applied Sciences*, vol. 7, no. 7, p. 697, 2017.
- [9] C. Li, X. Li, S. Gao et al., "Experiment on gas-water two-phase seepage and inflow performance curves of gas wells in carbonate reservoirs: a case study of Longwangmiao Formation and Dengying Formation in Gaoshiti-Moxi block, Sichuan Basin, SW China," *Petroleum Exploration and Development*, vol. 44, no. 6, pp. 983–992, 2017.
- [10] W. J. Shen, X. H. Liu, X. Z. Li, and J. L. Lu, "Water coning mechanism in Tarim fractured sandstone gas reservoirs," *Journal of Central South University (English Edition)*, vol. 22, no. 1, pp. 344–349, 2015.
- [11] W. J. Shen, F. Q. Song, X. Hu, G. M. Zhu, and W. Y. Zhu, "Experimental study on flow characteristics of gas transport in micro- and nanoscale pores," *Scientific Reports*, vol. 9, no. 1, article 10196, 2019.
- [12] A. Movahhed, M. N. Bidhendi, M. Masihi, and A. Emamzadeh, "Introducing a method for calculating water saturation in a carbonate gas reservoir," *Journal of Natural Gas Science and Engineering*, vol. 70, no. 102942, article 102942, 2019.
- [13] V. Suicmez, M. Piri, and M. Blunt, "Effects of wettability and pore-level displacement on hydrocarbon trapping," *Advances in Water Resources*, vol. 31, no. 3, pp. 503–512, 2008.
- [14] S. Zendehboudi, A. Elkamel, I. Chatzis, M. A. Ahmadi, A. Bahadori, and A. Lohi, "Estimation of breakthrough time for water coning in fractured systems: experimental study and connectionist modeling," *AIChE Journal*, vol. 60, no. 5, pp. 1905–1919, 2014.
- [15] K. Singh, H. Menke, M. Andrew et al., "Dynamics of snap-off and pore-filling events during two-phase fluid flow in permeable media," *Scientific Reports*, vol. 7, no. 1, pp. 1–13, 2017.
- [16] P. Persoff and K. Pruess, "Two-phase flow visualization and relative permeability measurement in natural rough-walled rock fractures," *Water Resources Research*, vol. 31, no. 5, pp. 1175–1186, 1995.
- [17] K. M. Zhou, N. Li, Q. X. Zhang, and X. G. Tang, "Experimental research on gas-water two phase flow and confined gas formation mechanism," *Natural Gas Industry*, vol. 22, no. S1, pp. 122–125, 2002.
- [18] T. K. Tokunaga and J. M. Wan, "Water film flow along fracture surfaces of porous rock," *Water Resources Research*, vol. 33, no. 6, pp. 1287–1295, 1998.
- [19] T. K. Tokunaga, J. M. Wan, and S. R. Sutton, "Transient film flow on rough fracture surfaces," *Water Resources Research*, vol. 36, no. 7, pp. 1737–1746, 2000.
- [20] E. Saad, T. Darwich, and Y. Asaad, *Water coning in fractured basement reservoirs*, Society of Petroleum Engineers, 1995.
- [21] H. Bahrami, S. Shadizadeh, and I. Goodarzniya, "Numerical simulation of coning phenomena in naturally fractured reservoirs," in *9th Iranian Chemical of Engineering Congress*, Iran, November, 2004.
- [22] E. Perez, F. Garza, and F. Samaniego-Verduzco, *Water coning in naturally fractured carbonate heavy oil reservoir—a simulation study*, Society of Petroleum Engineers, 2012.
- [23] Y. Hu, X. Z. Li, X. G. Lu et al., "Varying law of water saturation in the depletion-drive development of sandstone gas reservoirs," *Petroleum Exploration and Development*, vol. 41, no. 6, pp. 790–793, 2014.
- [24] R. Abdel Azim, "Evaluation of water coning phenomenon in naturally fractured oil reservoirs," *Journal of Petroleum Exploration and Production Technology*, vol. 6, no. 2, pp. 279–291, 2016.
- [25] W. J. Shen, X. Z. Li, X. H. Liu, J. L. Lu, and C. Y. Jiao, "Physical simulation of water influx mechanism in fractured gas reservoirs," *Journal of Central South University (Science and Technology)*, vol. 45, no. 9, pp. 3283–3287, 2014.
- [26] F. F. Fang, W. J. Shen, X. Z. Li, S. S. Gao, H. X. Liu, and J. Li, "Experimental study on water invasion mechanism of fractured carbonate gas reservoirs in Longwangmiao Formation, Moxi block, Sichuan Basin," *Environmental Earth Sciences*, vol. 78, no. 10, pp. 1–11, 2019.
- [27] C. Kabir, B. Parekh, and M. Mustafa, "Material-balance analysis of gas and gas-condensate reservoirs with diverse drive mechanisms," *Journal of Natural Gas Science and Engineering*, vol. 32, no. 1, pp. 158–173, 2016.
- [28] L. Patacchini, "Peripheral water injection efficiency for material balance applications," *Journal of Petroleum Science & Engineering*, vol. 149, no. 1, pp. 720–739, 2017.
- [29] C. F. Tsang and I. Neretnieks, "Flow channeling in heterogeneous fractured rocks," *Reviews of Geophysics*, vol. 36, no. 2, pp. 275–298, 1998.
- [30] C. L. Cheng, E. Perfect, B. Donnelly et al., "Rapid imbibition of water in fractures within unsaturated sedimentary rock," *Advances in Water Resources*, vol. 77, no. 1, pp. 82–89, 2015.
- [31] X. H. Tan, J. Y. Liu, X. P. Li, L. H. Zhang, and J. C. Cai, "A simulation method for permeability of porous media based on multiple fractal model," *International Journal of Engineering Science*, vol. 95, no. 1, pp. 76–84, 2015.
- [32] L. A. Høyland, P. Papatzacos, and S. M. Skjæveland, "Critical rate for water coning: correlation and analytical solution," *SPE Reservoir Engineering*, vol. 4, no. 4, pp. 495–502, 1989.
- [33] M. Li, W. J. Yang, Q. Y. Xiao, S. C. Liu, J. Zhang, and G. M. Peng, *Determination of the Aquifer Activity Level and the Recovery of Water Drive Gas Reservoirs*, Society of Petroleum Engineers, 2010.
- [34] M. Rezaee, B. Rostami, M. Zadeh, and M. Mojarrad, *Experimental Determination of Optimized Production Rate and Its Upscaling Analysis in Strong Water Drive Gas Reservoirs*, Society of Petroleum Engineers, 2013.
- [35] M. R. Mohammadi, H. Bahmaninia, S. Ansari et al., "Evaluation of asphaltene adsorption on minerals of dolomite and sandstone formations in two and three-phase systems," *Advances in Geo-Energy Research*, vol. 5, no. 1, pp. 39–52, 2021.
- [36] R. G. Agarwal, R. al-Hussainy, and H. J. Ramey, "The importance of water influx in gas reservoirs," *Journal of Petroleum Technology*, vol. 17, no. 11, pp. 1336–1342, 1965.
- [37] Y. Cheng, L. Mu, E. Zhu et al., "Water producing mechanisms of carbonate reservoirs gas wells: a case study of the Right Bank Field of Amu Darya, Turkmenistan," *Petroleum Exploration and Development*, vol. 44, no. 1, pp. 89–96, 2017.

- [38] X. Z. Li, Z. H. Guo, Y. J. Wan et al., "Geological characteristics and development strategies for Cambrian Longwangmiao Formation gas reservoir in Anyue gas field, Sichuan Basin, SW China," *Petroleum Exploration and Development*, vol. 44, no. 3, pp. 428–436, 2017.
- [39] M. Li, T. Li, J. Q. Jiang, H. Yang, and S. C. Liu, "The gas recovery of water-drive gas reservoirs," *Journal of Hydrodynamics*, vol. 27, no. 4, pp. 530–541, 2015.
- [40] C. Y. Xu, P. C. Li, and D. T. Lu, "Production performance of horizontal wells with dendritic-like hydraulic fractures in tight gas reservoirs," *Journal of Petroleum Science & Engineering*, vol. 148, no. 1, pp. 64–72, 2017.

## Research Article

# Expansion Velocity Model of Steam-Assisted Gravity Drainage considering Thermal Convection

Dian-Fa Du,<sup>1</sup> Yao-Zu Zhang ,<sup>1</sup> Li-Na Zhang,<sup>2</sup> Meng-Ran Xu,<sup>1</sup> and Xin Liu<sup>2</sup>

<sup>1</sup>College of Petroleum Engineering, China University of Petroleum, Qingdao, China

<sup>2</sup>Research Institute of Petroleum Exploration & Development, East China Company, SINOPEC, Nanjing, China

Correspondence should be addressed to Yao-Zu Zhang; 2650527785@qq.com

Received 9 March 2021; Revised 27 May 2021; Accepted 5 June 2021; Published 22 June 2021

Academic Editor: Chenhao Sun

Copyright © 2021 Dian-Fa Du et al. This is an open access article distributed under the Creative Commons Attribution License, which permits unrestricted use, distribution, and reproduction in any medium, provided the original work is properly cited.

Steam-assisted gravity drainage (SAGD) is an important method used in the development of heavy oil. A heat transfer model in the SAGD production process is established based on the heat transfer effect caused by the temperature difference at the front edge of the steam chamber and the heat convection effect caused by the pressure difference. The observation well temperature method is used in this model to calculate the horizontal expansion speed of the steam chamber. In this manner, an expansion speed model considering heat convection and heat conduction is established for a steam chamber with a steam-assisted gravity drainage system. By comparing this with the production data extracted from the Fengcheng Oilfield target block, it is verified that the model can be effectively applied for actual field development. Simultaneously, by using the derived model, the temperature distribution at the edge of the steam chamber and production forecast can be predicted. Sensitivity analysis of the expansion rate of the steam chamber demonstrates that the larger the thermal conductivity, the faster is the steam chamber horizontal expansion speed, and the two are positively correlated; the larger the reservoir heat capacity, the slower is the steam chamber horizontal expansion speed. A larger heat capacity of the convective liquid indicates that there are more water components in the convective liquid, the viscosity of the convective liquid is low, and the expansion speed of the steam chamber increases accordingly. This research closely integrates theory with actual field production and provides theoretical support for the development of heavy oil reservoirs.

## 1. Introduction

Steam-assisted gravity drainage (SAGD) is one of the most important methods currently used for the development of heavy oil. It is characterised by a high recovery rate, a high degree of steam cavity formation, and it takes effect quickly and has a low pollution rate. For SAGD production, the degree to which the steam chamber is developed directly determines the developmental effect of the steam-assisted gravity drainage system as well as the efficiency of the oil displacement and its recovery factor. The steam, which is at a high temperature, heats the oil sands and heavy oil, which are at a low temperature, and the viscosity of the liquid then rapidly drops to form a cavity. The production mechanism is illustrated in Figure 1. Gravity pulls the condensate and heavy oil down from the drain zone to the edge, and down to the production well, while the heat exchange is predominantly produced by heat conduction and convection at the

edge of the steam cavity. The heat transfer and expansion speed models of the steam chamber are the key factors determining the degree of steam cavity development. Therefore, studying the heat transfer and velocity models in the SAGD oil recovery process is the primary task, and it is an extremely important step in evaluating the developmental effects and guiding actual production.

In the 1980s, Butler [1, 2] analysed salt water injection well technology and applied it to the development of the heavy oil industry. When the steam cavity in a homogeneous oil reservoir only underwent heat conduction, he considered the establishment of a heat transfer model and a macroscopic gravity drainage heat transfer mathematical model. This oil drainage equation sets a precedent for the theoretical production of SAGD.

In the following years, Reis, Edmuds, Aukhaev, Azad, and others continued to improve upon this basic model, but they have not yet considered the influence of steam cavity thermal

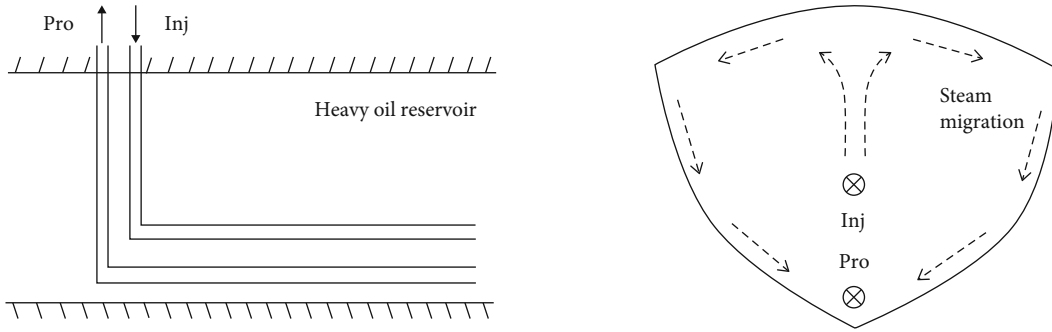


FIGURE 1: SAGD production mechanism diagram for double horizontal wells.

convection [3]. Sharma and Gates [4] assumed that the condensate velocity normal to the interface was the steam chamber interface velocity multiplied by the fluid mobility ratio. Although it is an assumption, the resultant equation provides an understanding of the role of convection. In 2013, Irani and Ghannadi [5] conducted a certain degree of research on the convection caused by the water phase, and they established a steam-assisted gravity drainage heat transfer model that considered thermal convection. Irani believed in the heat transfer method of thermal convection, but their research on thermal convection was only carried out under ideal conditions, while actual reservoir conditions are far from ideal and can, of course, deviate considerably. Qing and Zhang [6] used a constant heat flow boundary condition to verify the widely used constant-temperature boundary condition at the edge of the steam chamber. Our study confirmed the accuracy of the study by Irani et al. He offered a simple formula to demonstrate the connection between the condensate velocities normal to the chamber interface and the movement velocity of the chamber interface, which is helpful for studying the expansion speed of the steam cavity and heat convection. Yang et al. [7] and Fan and Li [8] also proposed that heat conduction and heat convection exist simultaneously during SAGD production. Furthermore, they believe that heat convection, when in the vicinity of the steam cavity, is the main mechanism by which heat is transferred. This study confirmed that thermal convection occurs during SAGD production. It also considered the heterogeneity of the reservoir and established a relatively complete heat transfer model. However, the study argues that thermal convection is only generated by the water phase and that the steam cavity expansion rate is a fixed value. Therefore, the research results deviate from the actual reservoir conditions.

Professor Gates et al. [9] studied the influence of steam quality on  $\Delta Ra$  temperature; if the steam quality was equal to 50%, the supplied temperature exceeded  $178.31^{\circ}\text{C}$ , which is unstable. The steam quality should be as high as possible at the edge of the chamber to enhance the instability for achieving maximum bitumen production from the reservoir. Given that the chamber is under saturation conditions, its temperature is constant; however, there exists a quality gradient throughout the chamber that is the highest at the injection well and decreases moving away from the injection well. In 2015, Gotawala and Gates [10] used linear stability analysis to check the stability of the edge of the steam cham-

ber, as it will exist in the steam-assisted gravity drainage process. He observed that the densities and viscosities of the steam/water and bitumen are strong functions of temperature, and thus the energy content contributes to the stability criterion. If the difference in the energy-weighted Darcy-Rayleigh numbers of the steam/water phases and oil phase is negative, then the system is unstable and perturbations of the edge grow. We herein observe that the higher the steam quality and steam injection temperature, the greater is the instability of the edge of the chamber, which is more conducive to the horizontal expansion of the steam chamber.

The convection phase during the actual production process comprised a mixed phase of condensed water and crude oil. Taking this into consideration, Liu et al. [11] discovered a heat conduction effect caused by the temperature difference at the front edge of the steam chamber, as well as a convection effect caused by the pressure difference. This steam chamber heat transfer model is more in line with the actual conditions. Although it improves upon the heat transfer model used in the SAGD production process by making it more complete, it only idealises the steam chamber expansion speed parameter as a fixed value and has not yet offered a suitable calculation method. Therefore, when the expansion speed of the steam chamber changes, the results deviate.

Based on Butler's basic heat transfer model, Zhou et al. [12] proposed the theory that the expansion speed of the steam chamber is variable. The steam chamber expansion speed was obtained through both the observation well temperature method and the drain zone temperature distribution method. The newly changed steam chamber expansion speed in this study takes into account the influencing factors when the steam cavity expands but again idealises the reservoir conditions while ignoring the heat convection phenomenon caused by the pressure difference. This steam cavity expansion model is based only on the heat transfer that considers heat conduction. However, during the actual production process, thermal convection is the main mechanism by which steam transfers heat at the drain zone, and it is also a key factor affecting the expansion speed of the steam chamber. Therefore, the results show a large deviation from the actual production situation.

In 2020, Zargar et al. [13] established a comprehensive constant heat injection (CCHI) model by studying the relation between steam injection parameters and oil production. This model considers the expansion speed of the steam

chamber as the production time increases; it decreases owing to the relation between energy and mass balances. Zargar's study has considered that the steam chamber expansion rate is a variable during the SAGD production process, and it has thus calculated it using the CCHI model to obtain the best steam injection parameters. However, this study only confirmed that the expansion speed of the steam chamber was variable, and the horizontal expansion speed of the steam chamber could not be obtained through the CCHI model. There is no explanation for the influence of the changing steam chamber expansion rate on the steam chamber expansion law. Simultaneously, the changing steam chamber expansion speed has not been studied, and the steam chamber horizontal expansion speed model has not been obtained, so predicting the steam chamber migration law is impossible. There is an urgent need for a complete and accurate steam chamber expansion speed model for SAGD production.

Therefore, in this study, considering that the convective liquid is composed of a mixed phase of condensate and crude oil, introducing the thermal convection velocity which includes the relative permeability, viscosity, pressure, and other parameters of the two phases, the thermal convection velocity is considered in the SAGD steam cavity heat transfer model. In addition, as the steam cavity's heat transfer model considers both heat conduction and heat convection, the observation well temperature method is used to establish the expansion velocity model of the steam cavity. This is used to calculate the horizontal expansion velocity of the drain zone and predict the temperature distribution in both the drain zone and in SAGD production. We herein provide a tool for rapid field-scale optimisation and performance predictions, as opposed to the use of extremely time-consuming thermal numerical simulators.

## 2. Steam Chamber Expansion Research

**2.1. Model Assumptions.** The entire production process for steam-assisted gravity drainage can be divided into three main stages—the rising stage of the steam chamber, lateral expansion stage, and decay stage [14–16]. The production characteristics of each stage are different. The key stage for oil production is the horizontal expansion stage of the steam chamber. This stage comprises the peak oil drainage period during SAGD production, and it is the core stage required to study the expansion speed of the steam chamber.

However, we herein selected the steam cavity's lateral expansion stage as the research target. To facilitate our research, the following assumptions were made for when the steam cavity moved laterally along the top of the reservoir:

- (1) The oil reservoir is a homogeneous reservoir
- (2) The steam chamber reached the top of the reservoir and began to expand laterally on both sides
- (3) The thermal conductivity of the reservoir was constant

- (4) Both heat conduction and convection occur in the reservoir
- (5) Heat transfer only moves in a direction perpendicular to the outer edge of the steam chamber; that is, there is a one-dimensional heat transfer process
- (6) At a certain moment, the system is in a quasisteady state process; that is, at a certain moment, the steam chamber advances at a fixed speed along the edge in a normal direction
- (7) We ignored the heat loss during the flow of heavy oil

**2.2. Heat Transfer Model.** According to Butler's research [1, 2], the heat transfer process at the front interface of steam-assisted gravity drainage of the steam cavity is a pseudosteady-state process. Figure 2 is a schematic of the expansion of the steam chamber, and it shows that the basic heat transfer differential equation can be obtained according to the conservation of energy:

$$K\nabla^2 T - \rho_c c_{pc}(\mathbf{v} \cdot \nabla T) = \rho_r c_{pr} \dot{T}. \quad (1)$$

The first term on the left side of the equation represents the heat conduction of the steam chamber, and the second term on the left side represents the heat convection that runs perpendicular to the direction of the steam chamber:

$$\begin{aligned} K \left( \frac{\partial^2 T}{\partial x^2} + \frac{\partial^2 T}{\partial y^2} + \frac{\partial^2 T}{\partial z^2} \right) - \rho_c c_{pc} \left( V \frac{\partial T}{\partial x} + V \frac{\partial T}{\partial y} + V \frac{\partial T}{\partial z} \right) \\ = \rho_r c_{pr} \left( \frac{\partial T}{\partial t} \right), \end{aligned} \quad (2)$$

where  $K$  is the reservoir thermal conductivity,  $V$  is the convective velocity,  $\rho_c$  is the convective phase density,  $\rho_r$  is the reservoir density,  $c_{pc}$  is the specific heat capacity of the convective liquid,  $c_{pr}$  is the specific heat capacity of the reservoir,  $x$  is the normal direction of the steam cavity interface,  $y$  is the tangent direction of the steam chamber interface, and  $z$  is parallel to the horizontal well axis.

As the oil reservoir is a homogeneous reservoir, the temperature gradient in the  $x$  and  $y$  directions can be ignored, and Equation (2) can be converted as follows:

$$K \left( \frac{\partial^2 T}{\partial x^2} \right) - \rho_c c_{pc} \left( V \frac{\partial T}{\partial x} \right) = \rho_r c_{pr} \left( \frac{\partial T}{\partial t} \right). \quad (3)$$

Introducing the variable  $\xi$  (apparent distance) [17], we deduce according to the assumptions that the expansion speed  $U_\xi$  of the steam chamber for a certain period of time is a fixed value.

$$\xi = x - \int_0^t U_\xi dt = x - U_\xi t. \quad (4)$$

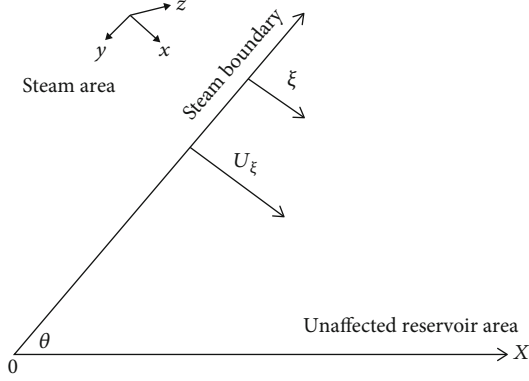


FIGURE 2: Steam chamber expansion diagram.

In the equation, the partial differential of  $x$  is replaced by  $\xi$ :

$$\frac{\partial^2 T}{\partial x^2} = \frac{\partial^2 T}{\partial \xi^2}, \quad (5)$$

$$\frac{\partial T}{\partial t} = -U_\xi \frac{\partial T}{\partial \xi}. \quad (6)$$

Substituting Equations (5) and (6) into Equation (3), we obtain

$$K \left( \frac{\partial^2 T}{\partial \xi^2} \right) - (\rho_c c_{pc} V - \rho_r c_{pr} U_\xi) \left( \frac{\partial T}{\partial \xi} \right) = \rho_r c_{pr} \left( \frac{\partial T}{\partial t} \right). \quad (7)$$

When the heat transfer at the front edge of the steam chamber is stable, and the temperature distribution does not change with time, Equation (7) becomes Equation (8).

$$K \left( \frac{\partial^2 T}{\partial \xi^2} \right) - (\rho_c c_{pc} V - \rho_r c_{pr} U_\xi) \left( \frac{\partial T}{\partial \xi} \right) = 0. \quad (8)$$

The above equation is the SAGD heat transfer model that considers both heat conduction and heat convection.

**2.3. Temperature Distribution at the Edge of Steam Chamber.** Based on the SAGD heat transfer model, with the following boundary conditions:

$$\begin{cases} T(\infty) = T_r, \\ T(0) = T_s. \end{cases} \quad (9)$$

We can obtain

$$\begin{aligned} T &= T_r + (T_s - T_r) \times e^{\rho_c c_{pc} V - \rho_r c_{pr} U_\xi / K \times \xi}, \\ \xi &= \frac{K}{U_\xi \rho_r c_{pr} - V \rho_c c_{pc}} \ln \frac{T_s - T_r}{T - T_r}. \end{aligned} \quad (10)$$

The viscosity distribution in crude oil is an important factor in determining temperature distribution. As the viscosity distribution in crude oil has a certain power function relation

with temperature [18], the relation between the two can be approximately expressed as

$$\frac{\mu_s}{\mu_o} = \left( \frac{T - T_r}{T_s - T_r} \right)^m, \quad (11)$$

where  $\mu_s$  is the oil viscosity when at the injected steam temperature,  $\mu_o$  is the oil viscosity,  $T$  is the temperature at a certain point on the edge of the steam chamber,  $T_r$  is the original reservoir temperature,  $T_s$  is the temperature of the injected steam, and  $m$  denotes the temperature–viscosity factor.

Irani and Ghannadi studied the convection caused by the water phase in the SAGD process and observed that the pressure distribution at the front edge of the steam chamber is also in the form of a power function. Figure 3 was obtained through the calculation of Irani's model. According to the comparison, the temperature and pressure distribution trends at the front edge of the steam chamber were similar. Therefore, according to Equation (11), the pressure distribution at the edge of the steam chamber is in a power function relation with the viscosity distribution of crude oil [11]:

$$\frac{\mu_s}{\mu_o} = \left( \frac{P - P_r}{P_s - P_r} \right)^n, \quad (12)$$

where  $P$  is the pressure at a certain point on the edge of the steam chamber,  $P_r$  is the original reservoir pressure,  $P_s$  is the injection pressure, and  $n$  is the pressure–viscosity factor.

By combining the above two equations, the relation between the temperature and pressure distributions can be obtained.

$$\frac{P - P_r}{P_s - P_r} = \left( \frac{T - T_r}{T_s - T_r} \right)^{m/n}. \quad (13)$$

According to Equation (13), the derivative of  $\xi$  can be obtained:

$$\frac{1}{P_s - P_r} \frac{\partial P}{\partial \xi} = \frac{1}{(T_s - T_r)^{m/n}} \frac{m}{n} (T - T_r)^{m/n-1} \frac{\partial T}{\partial \xi}, \quad (14)$$

because the thermal convection velocity in the steam cavity is

$$V = - \left( \frac{kk_{ro}}{\mu_o} + \frac{kk_{rw}}{\mu_w} \right) \frac{\partial P}{\partial \xi}. \quad (15)$$

According to Sharma and Gate's research [4], the relative permeability of the oil and water phases is as follows:

$$\begin{cases} \frac{kk_{ro}}{\mu_o} = \frac{kk_{rocv}}{\mu_s} (S_{oD})^a (1 - T^*)^a (T^*)^m, \\ \frac{kk_{rw}}{\mu_w} = \frac{kk_{rwrw}}{\mu_w} [1 - S_{oD}(1 - T^*)]^b, \end{cases} \quad (16)$$

where  $k_{ro}$  is the relative permeability of the oil phase,  $k_{rocv}$  is the relative permeability of the oil phase when under an irreducible water saturation,  $k_{rwrw}$  is the relative permeability of



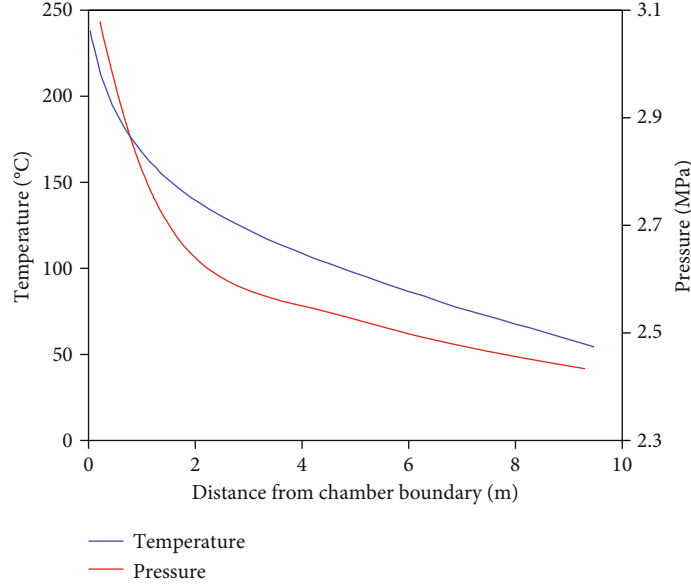


FIGURE 3: Temperature distribution and pressure distribution calculated from Irani and Ghannadi's model.

the water phase,  $k_{rwo}$  is the relative permeability of the water phase under the residual oil saturation,  $ab$  is the Corey coefficient, and  $\alpha$  is the thermal diffusivity.

where  $S_{oD} = S_{io} - S_{or}/1 - S_{wc} - S_{or}$ ,  $T^* = T - T_r/T_s - T_r = e^{-U\xi/\alpha}$ .

Then, the fluidity of the edge of the steam chamber is

$$\lambda = \frac{kk_{rocw}}{\mu_s} (S_{oD})^a (1 - T^*)^a (T^*)^m + \frac{kk_{rwo}}{\mu_w} [1 - S_{oD}(1 - T^*)]^b. \quad (17)$$

Substituting Equations (14) and (17) into Equation (15), we can obtain

$$V = \frac{mU\xi\lambda(P_s - P_r)}{n\alpha} (T^*)^{m/n}. \quad (18)$$

The above equation shows that the convection velocity is a function of  $\xi$ . When the thermal convection velocity is introduced into the edge temperature distribution function of the steam cavity, the edge temperature distribution function of the steam cavity can be considered for both heat conduction and thermal convection:

$$\xi = \frac{n\alpha K}{n\alpha\rho_r c_{pr} - \rho_c c_{pc} \left[ m\lambda(P_s - P_r)(T^*)^{m/n} \right]} \frac{1}{U\xi} \ln \frac{T_s - T_r}{T - T_r}. \quad (19)$$

**2.4. Steam Chamber Expansion Speed Model.** To better describe the development and expansion of the steam cavity during the SAGD production process, we herein use the observation well temperature measurement method to obtain the expansion speed of the steam cavity under the conditions of the known observation well position, steam cavity temperature, and oil reservoir temperature. This is car-

ried out to further obtain the horizontal movement speed of the steam outlet cavity and its edge position, thereby providing a theoretical basis for field development.

In the same monitoring well, the temperature at two different depths in the high-temperature section can be measured separately, as shown in Figure 4.

The relation between the distance from the oil drain interface and the temperature at these two depths, when measured simultaneously, is as follows [12].

$$\begin{cases} \xi_1 = \frac{K}{U\xi\rho_r c_{pr} - V_1\rho_c c_{pc}} \ln \frac{T_s - T_r}{T_1 - T_r}, \\ \xi_2 = \frac{K}{U\xi\rho_r c_{pr} - V_2\rho_c c_{pc}} \ln \frac{T_s - T_r}{T_2 - T_r}, \end{cases} \quad (20)$$

where  $V_1$  is the convective velocity at observation point 1,  $V_2$  is the convective velocity at observation point 2,  $T_1$  is the temperature at observation point 1, and  $T_2$  is the temperature at observation point 2.

$\xi$  can also be expressed as a function describing depth:

$$\begin{cases} \xi_1 = (h_1 - h_o) \cos \theta, \\ \xi_2 = (h_2 - h_o) \cos \theta. \end{cases} \quad (21)$$

$\xi_2$  minus  $\xi_1$ , and simplified to

$$\begin{aligned} & (h_2 - h_1) \cos \theta \frac{n\alpha K}{\rho_r c_{pr} n\alpha - \rho_c c_{pc} (T_1 - T_r/T_s - T_r)} \frac{1}{U\xi} \ln \frac{T_1 - T_r}{T_2 - T_r} \\ & - \left[ \frac{n\alpha K}{\rho_r c_{pr} n\alpha - \rho_c c_{pc} (T_2 - T_r/T_s - T_r)} \right. \\ & \left. - \frac{n\alpha K}{\rho_r c_{pr} n\alpha - \rho_c c_{pc} (T_1 - T_r/T_s - T_r)} \right] \frac{1}{U\xi} \ln \frac{T_2 - T_r}{T_s - T_r}. \end{aligned} \quad (22)$$

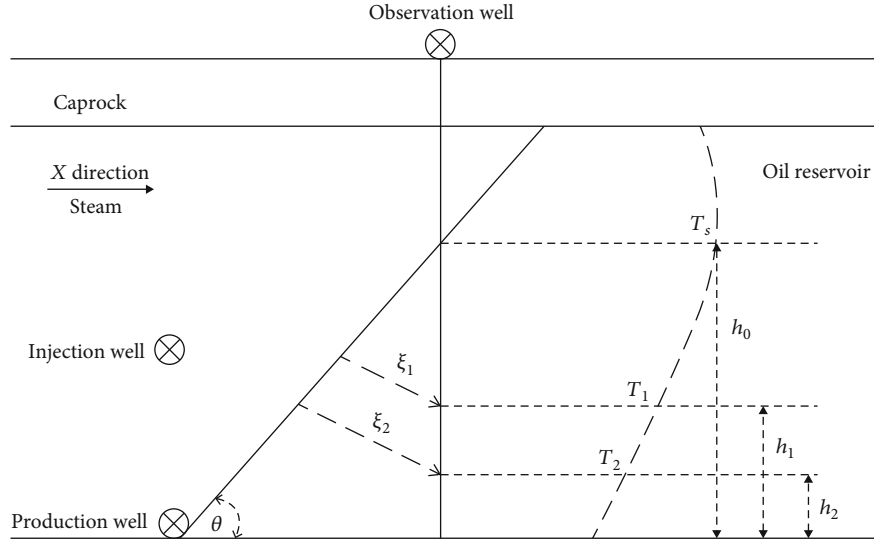


FIGURE 4: Schematic of the observation well temperature measurement method.

We can obtain

$$U_{\xi} = \frac{n\alpha K}{(h_2 - h_1) \cos \theta \{n\alpha \rho_r c_{pr} - \rho_c c_{pc} [m\lambda(P_{st} - P_r)] \times (T_1 - T_r/T_s - T_r)^{m/n}\}} \ln \left[ \frac{T_1 - T_r}{T_2 - T_r} + \left[ \frac{n\alpha K}{\rho_r c_{pr} n\alpha - \rho_c c_{pc} (T_2 - T_r/T_s - T_r)} \right] \frac{1}{(h_2 - h_1) \cos \theta} \ln \frac{T_2 - T_r}{T_s - T_r} \right] - \frac{n\alpha K}{\rho_r c_{pr} n\alpha - \rho_c c_{pc} (T_1 - T_r/T_s - T_r)} \frac{1}{(h_2 - h_1) \cos \theta} \ln \frac{T_2 - T_r}{T_s - T_r} \quad (23)$$

After simplification, the expansion velocity equation of the steam cavity interface, considering heat conduction and heat convection, is obtained as

$$U_{\xi} = \frac{\varphi}{(h_2 - h_1) \cos \theta} \ln \frac{T_1 - T_r}{T_2 - T_r} + \frac{\gamma}{(h_2 - h_1) \cos \theta} \ln \frac{T_1 - T_r}{T_s - T_r}, \quad (24)$$

where  $\varphi = n\alpha K / [n\alpha \rho_r c_{pr} - \rho_c c_{pc} [m\lambda(P_{st} - P_r)] \times (T_1 - T_r/T_s - T_r)^{m/n}]$ ,  $\gamma = n\alpha K / [\rho_r c_{pr} n\alpha - \rho_c c_{pc} (T_2 - T_r/T_s - T_r)] - n\alpha K / [\rho_r c_{pr} n\alpha - \rho_c c_{pc} (T_1 - T_r/T_s - T_r)]$ .

The horizontal expansion speed of the steam chamber is

$$U_X = \frac{U_{\xi}}{\sin \theta} = \frac{2\varphi}{(h_2 - h_1) \sin 2\theta} \ln \frac{T_1 - T_r}{T_2 - T_r} + \frac{2\gamma}{(h_2 - h_1) \sin 2\theta} \ln \frac{T_1 - T_r}{T_s - T_r}. \quad (25)$$

Under the condition that the position and temperature of the oil layer are measured, according to Equation (25), the horizontal expansion speed of the steam chamber at the corresponding time can be obtained.

### 3. Model Validation

The model can be solved using a mathematical iterative method. To verify the accuracy of the desired steam chamber expansion speed model, Irani's model was compared with the new model, and the temperature change curves of the steam chamber at different depths of the two models were calculated by using MATLAB software; the parameters are listed in Table 1. In addition, the two models were compared with the production monitoring data of Well Z in the SAGD production test area of Xinjiang Fengcheng Oilfield. In the actual field, to observe the development and expansion of the steam cavity during the SAGD production process, an observation well was set between two horizontal wells. In addition, in the early stages of SAGD production, steam stimulation is usually required to ensure better development of the steam chamber. Therefore, the horizontal expansion stages of the steam chamber in the first and second years were excluded, so the third year of SAGD production was selected as the target year for our comparison.

Figure 5 shows the temperature change curves from the observation wells at different production times. Whether it is looking at the new model, the Irani and Ghannadi model, or the data from the actual field, you can see an obvious steam cavity development shape, and you can also see a temperature peak zone in the middle of the steam chamber [19–22]. Furthermore, the peak area was approximately 50 m. As the depth of the steam chamber increased, the temperature gradually decreased from 220°C to 70°C. The temperature curve of the entire steam chamber remains at 150°C–230°C, which agrees well with previous research. As the thermal convection considered by the Irani and Ghannadi models is only a simplified case under ideal conditions and they have not yet considered the change in the expansion speed of the steam chamber, they are too idealistic compared to the new model derived in this study, so the peak temperature of the steam chamber and the steam chamber temperature at the same depth are much higher than those

TABLE 1: Model verification parameter table.

Item	Value	Item	Value
Porosity	0.3	Steam temperature	240°C
Permeability	$7.5 \times 10^{-12}$ k/m <sup>2</sup>	Steam chamber angle	45°
Reservoir thickness	20 m	Chamber temperature	280°C
Caprock thickness	15 m	Reservoir temperature	30°C
Well spacing	100 m	Reservoir density	2500 kg·m <sup>-3</sup>
Horizontal well length	350 m	Convective phase density	1500 kg·m <sup>-3</sup>
Reservoir pressure	1.2 MPa	Moving speed of steam	$2.5 \times 10^{-2}$ m/d
Oil viscosity	$2.4 \times 10^5$ mPa·s	Thermal diffusivity	$7.5 \times 10^{-7}$ m <sup>2</sup> /s
Water specific heat capacity	4200 J/(kg·K)	Original oil saturation	0.85
Oil specific heat capacity	1800 J/(kg·K)	Connate-water saturation	0.15
Thermal conductivity	1.5 W/(m·°C)	Relative permeability of bound water oil phase	0.85
Injection pressure	1.80 MPa	Absolute reservoir permeability	$6 \times 10^{-12}$
Pressure–viscosity factor	2		
Temperature–viscosity factor	3	Relative permeability of water phase under residual oil	0.03

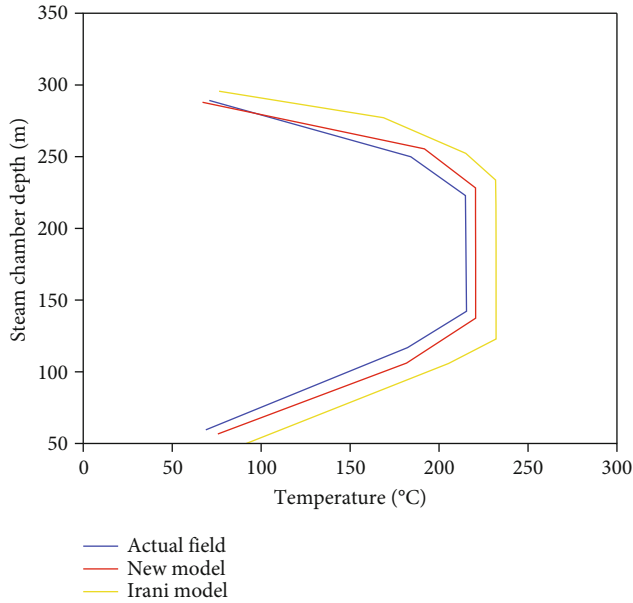


FIGURE 5: Schematic of temperature change curves of different steam chambers.

of the new model and actual mine data. In particular, in the interval where the depth of the steam chamber is 150–200 m, the new model is closest to the actual field data, which shows the new steam cavity expansion speed model for steam-assisted gravity drainage is correct.

The edge position of the steam chamber can be calculated when the edge of the steam chamber passes through the observation well. MATLAB was used to calculate and simulate the edge position of the steam chamber at different times. Figure 6 shows that in 2018, the predicted edge of the steam chamber moved 22.51 m in the X direction, and the steam chamber migration speed at this time was  $2 \times 10^{-2}$  m/day. The edge position of the steam chamber was 22.83 m, which was obtained via four-dimensional seismic data detection.

The two data were very consistent, verifying the accuracy of the new model established herein.

## 4. Application

*4.1. Temperature Distribution at the Edge of the Steam Chamber.* Although thermal convection is considered in existing heat transfer equations for the production process of steam-assisted gravity drainage, only the water phase is considered as the convection phase in the model, and this ignores the role of heavy oil in the thermal convection process. Thus, the new model deviates slightly from the actual situation. Therefore, we herein comprehensively consider the oil–water two-phase flow and the mixed relative flow velocity, establish the SAGD heat transfer model, including heat conduction and heat convection, and calculate the temperature distribution at the edge of the air cavity.

Through the establishment of this temperature distribution, when the steam chamber drain zone reaches a certain observation position, the position of the steam chamber's front edge and its temperature can be obtained in real-time to predict the width of the drain zone and the movement speed of the steam chamber [2, 23–25]. Furthermore, by incorporating the geological parameters of Well Z into the temperature equation at the edge of the steam chamber, a temperature distribution map of the oil drainage zone can be obtained. As shown in Figure 7, as the production time for steam-assisted gravity drainage increases, the horizontal expansion speed of the steam chamber gradually decreases, as does the temperature of the front edge of the steam chamber. The shape of the drain zone gradually flattens, but the temperature of the steam chamber remains stable. This indicates that as the production years increase, the output gradually stabilises, which is in line with the actual situation. By studying the temperature changes at the edge of the steam chamber, the temperature distribution of the front edge of the steam chamber can be quantitatively characterised, thereby providing theoretical support for actual production.

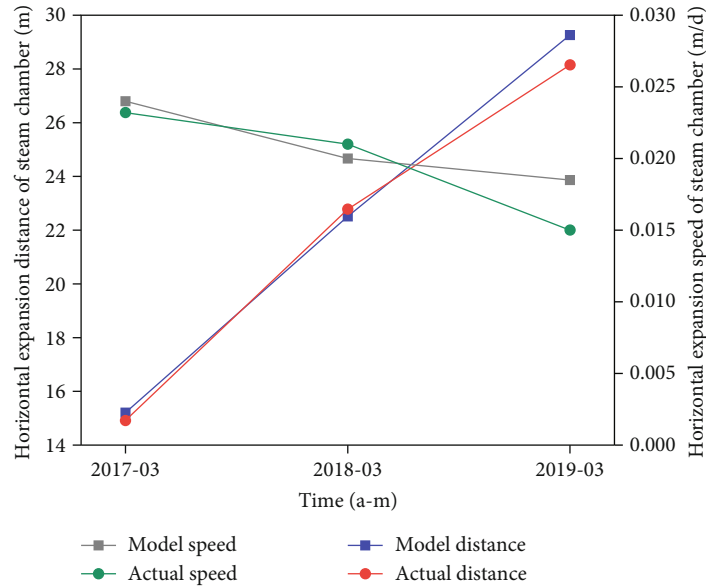


FIGURE 6: Schematic of the edge and velocity distribution of the steam chamber at different times.

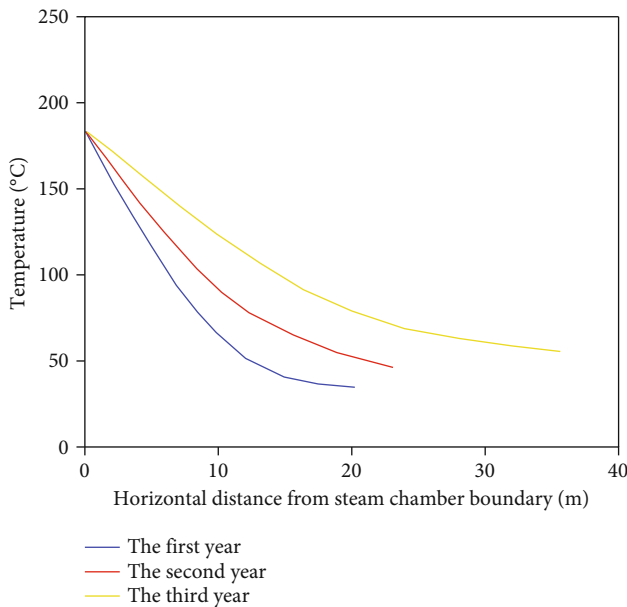


FIGURE 7: Schematic of temperature distribution at the edge of the steam chamber.

**4.2. Sensitivity Analysis of Steam Chamber Expansion Speed.** To help the field better understand the influencing factor of the steam chamber's horizontal expansion speed during the SAGD generation process, sensitivity analysis is performed to maintain the shape of the gas chamber and improve the recovery factor. Under the condition of measuring the position and temperature of the oil layer, in accordance with Equation (25), we can obtain the expansion speed of the steam chamber under different production times, and a sensitivity analysis of the expansion speed of the steam chamber can be carried out to analyse the influence of different influencing factors on the expansion speed of the steam chamber. The data used in the sensitivity analysis are listed in Table 2.

#### (1) Analysis of the influence of thermal conductivity

Figure 8 shows that the horizontal expansion speed of the steam chamber is directly proportional to thermal conductivity. The larger the thermal conductivity of the steam chamber, the faster is the horizontal expansion speed, and the larger is the moving distance [26–28]. On the contrary, when the thermal conductivity is small, the heat transfer of the steam will slow. Although thermal convection will still occur when it is small, the time the heavy oil in the reservoir has to be affected by the steam will be considerably reduced, which directly leads to the horizontal expansion speed of the steam cavity. If it slows down, the horizontal extension distance will also slow; this will eventually lead to a decrease in the SAGD oil displacement effect and a decrease in oil recovery.

#### (2) Analysis of the influence of the reservoir heat capacity

Heat capacity generally refers to the specific heat capacity, i.e., the energy required for the oil phase material to increase the temperature. Under the condition of controlling other unchanged values, the heat capacity of the reservoir is increased from  $1 \times 10^6 \text{ J}/(\text{m}^3 \cdot \text{K})$  to  $3 \times 10^6 \text{ J}/(\text{m}^3 \cdot \text{K})$ . As shown in Figure 9, as the specific heat capacity of the reservoir continued to increase, the horizontal expansion rate of the steam cavity decreased. This indicates that a larger specific heat capacity in the reservoir hinders the development of the steam cavity and reduces the SAGD and horizontal expansion speed of the steam chamber during production. This is because the higher the viscosity and density of the heavy oil, the higher is the specific heat capacity of the crude oil [29–33]. However, more energy is consumed in the process of reducing the viscosity of heavy oil. In the case of limited thermal steam energy, the greater the specific heat capacity of the heavy oil, the lower is the transmission efficiency, and the lower is the horizontal expansion speed of

TABLE 2: Sensitivity analysis parameter table.

Item	Value
Reservoir temperature	30°C
Thermal diffusivity	$7.5 \times 10^{-7} \text{ m}^2/\text{s}$
Oil specific heat capacity	1800 J/(kg·K)
Reservoir density	$2500 \text{ kg}\cdot\text{m}^{-3}$
Convective phase density	$1500 \text{ kg}\cdot\text{m}^{-3}$
Steam chamber angle	45°
Pressure-viscosity factor	2
Temperature-viscosity factor	3

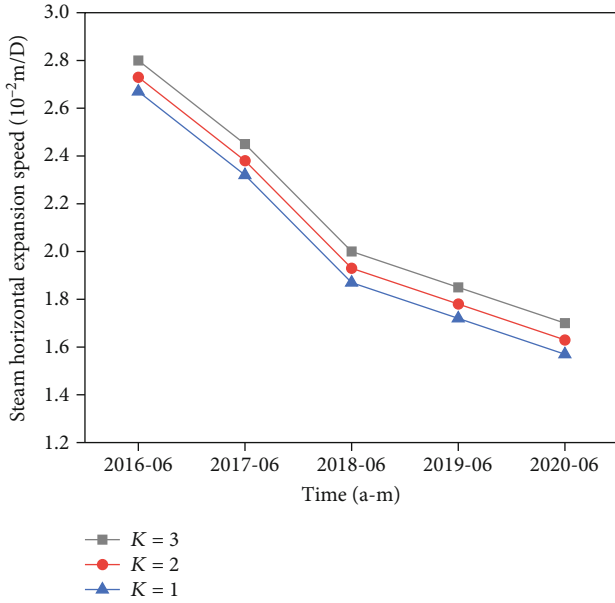


FIGURE 8: Schematic of the lateral expansion speed of the steam chamber under different thermal conductivities.

the steam chamber, which is not conducive to the development of the steam chamber and results in a decrease in oil recovery.

(3) Analysis of influence of convective liquid heat capacity

Although several studies have considered the influence of thermal convection, there are deviations in the understanding of the components of the convection fluid. This indicates that the research results are inaccurate and cannot accurately describe the thermal convection during the development and expansion of the steam cavity. In this study, the components of the convective liquid were regarded as the mixed phase of the water and oil phases. Therefore, to analyse its influence on the horizontal expansion speed of the steam chamber, the control variable method was used to explore the influence of the mixed-phase convective liquid on the horizontal expansion speed.

Figure 10 shows that as the specific heat capacity of the convective liquid continues to increase, so does the steam

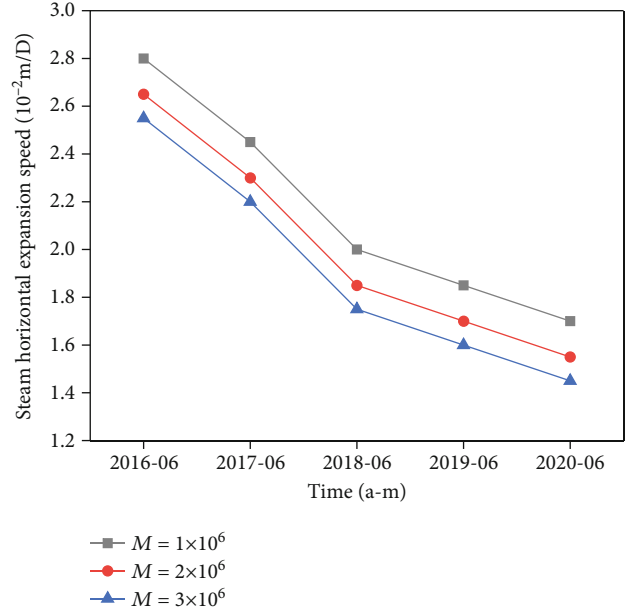


FIGURE 9: Schematic of the lateral expansion speed of steam cavity under different reservoir heat capacities.

chamber’s horizontal expansion speed and that the two are shown to be in a proportional relation. As the convection liquid is composed of two miscible phases—a water phase and an oil phase—when the specific heat capacity of the convection liquid increases, the water phase in the miscible phase accounts for a larger proportion. In addition, the speed with which the steam spreads will increase, while the steam’s energy from the heat will slowly decrease. Therefore, the chamber’s horizontal expansion speed is also at a maximum.

When the specific heat capacity of the convective liquid decreases, the proportion of the oil phase increases, the crude oil in the area affected by the thermal energy of the steam thickens, the viscosity of the convective liquid increases, and the chamber’s horizontal expansion speed decreases. This conclusion allows for a better understanding of the influence of the specific heat capacity of the convection liquid on the horizontal expansion speed of the steam chamber during the steam diffusion stage, thus, providing a theoretical basis for actual field development.

4.3. Production Calculation Based on Expansion Speed of Steam Chamber. During the SAGD production process, there are often differences in the interface speed of the steam chamber at different times owing to the different production systems. However, most existing production studies are based on Butler’s traditional equation that ignores the heat convection as well as the influence of the steam chamber’s varying expansion speeds at different times on the output. Therefore, according to the existing production equations [1, 34], we obtain

$$q = \frac{M_p K g L \sin \theta}{m \mu_s U_\xi \rho_r c_{pr}}, \quad (26)$$

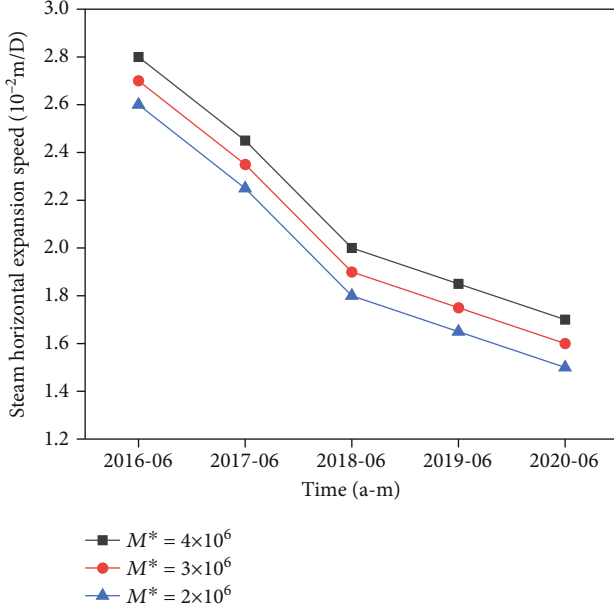


FIGURE 10: Schematic of the lateral expansion speed of the steam chamber under different convective liquid heat capacities.

TABLE 3: Basic parameter table for yield calculation.

Item	Value
Viscosity-temperature constant	2
Acceleration of gravity	9.8 m <sup>2</sup> /s
Thermal diffusivity	9.5 × 10 <sup>-2</sup> m <sup>2</sup> /d
Oil kinematic viscosity	5 × 10 <sup>-6</sup> m <sup>2</sup> /s
Effective permeability of the oil phase	0.45 × 10 <sup>-12</sup> m <sup>2</sup>
Horizontal section length	350 m

where  $M_p$  is the effective permeability of the oil phase and  $L$  is the length of the horizontal section.

On incorporating Equation (25) into Equation (26), we get

$$q = \frac{M_p g \alpha L}{m \mu_s U_x}. \quad (27)$$

The above equation becomes a production equation (oil production) that considers the horizontal expansion speed of the steam chamber. This equation can be used to perform actual field fitting and production predictions to guide field development.

According to the expansion speed of the steam chamber across different time periods, the SAGD production at different times can be obtained. To facilitate the popularisation and application of this method, the actual production at different time nodes is used to fit Equation (27), and the basic parameter list is shown in Table 3. By inputting the data from the table into the production model, the average daily oil production in the model during the third year is observed to be 59.32 m<sup>3</sup>/day, and the actual average daily production from

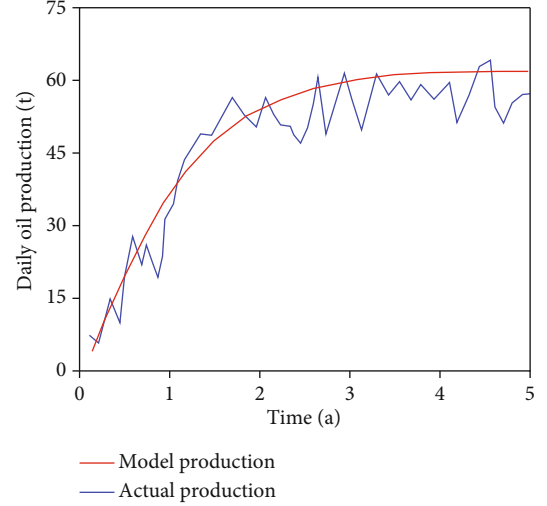


FIGURE 11: Comparison chart of the actual production and calculated production.

Well Z is 55.67 m<sup>3</sup>/day, when ignoring the effect that heat loss has. The following two data points are close, verifying that the model can meet production forecast requirements. In addition, the steam chamber's varying expansion speeds when at different production times is brought into the output equation, and once the curve is smoothed, a comparison chart showing the actual output and model calculated output is obtained (as shown in Figure 11).

Through the actual output and the calculated output comparison chart, the calculated output and the actual output have the same curve trend, but the model's output enters the stable production period earlier than the actual output, and the cumulative oil production is slightly higher than in the actual field. This is because the calculated production model ignores the heat lost during movement in the steam chamber and simplifies the steam chamber into an inverted triangle. In addition, owing to other influencing factors such as operations in the actual field, the calculated output will be slightly higher than the actual output, and thus it enters the stable production period sooner.

## 5. Conclusions

The development and expansion of the steam cavity are decisive factors for steam-assisted gravity drainage to ensure its recovery factor. We herein established the steam cavity's heat transfer and expansion speed models by considering various influencing factors and then validated the model. The study of the mechanism model yielded the following conclusions.

- (1) During the horizontal expansion stage of the steam cavity interface toward the reservoir, heat conduction and thermal convection occur simultaneously, and heat flows perpendicular to the steam cavity's interface under the action of the pressure difference. The convective liquid here is a combination of the water and oil phases, with the oil phase being an important part of the convective liquid

- (2) According to the actual well field, the observation well data obtained, and the analysis of the steam chamber expansion speed model, the steam chamber expansion speed was the largest in the early stages of SAGD production. With the increase in production time, the expansion speed of the steam chamber will decrease, and at this time, it needs to be changed. This can be achieved by changing the production system or changing the production method to add energy to the injection well, thereby maintaining high efficiency and stable production
- (3) After studying the sensitivity of the steam chamber expansion speed model, under the condition of other factors being constant, the greater the thermal conductivity of the reservoir, the faster is the steam chamber expansion speed. In this case, the heat capacity of the oil reservoir will require more heat energy to reduce viscosity, and the expansion speed of the steam chamber will also decrease. This is because as the convective liquid is miscible, the greater the heat capacity, the greater is the water phase ratio, indicating that the convective liquid will have low viscosity and the steam chamber will expand quickly
- (4) The established SAGD heat transfer model was used to derive the temperature distribution function at the edge of the steam chamber. This predicts the expansion shape of the steam chamber and the edge temperature change and provides a theoretical basis for the subsequent dynamic control of production. Based on Butler's classic production equation, a production equation that considers the expansion speed of the steam chamber is established. Finally, by looking at the change in expansion speeds of the steam chamber (due to the working system) at different time periods, oil production can be accurately calculated at different times. This will help advance field development

## Nomenclature

$K$ :	Reservoir thermal conductivity, W/m $\cdot$ °C
$\alpha$ :	Thermal diffusivity, m <sup>2</sup> /s
$\rho_c$ :	Convective phase density, kg $\cdot$ m <sup>-3</sup>
$\rho_r$ :	Reservoir density, kg $\cdot$ m <sup>-3</sup>
$c_{pc}$ :	Specific heat capacity of the convective liquid, J/(kg $\cdot$ K)
$c_{pr}$ :	Specific heat capacity of the reservoir, J/(kg $\cdot$ K)
$\mu_s$ :	Oil phase viscosity when at the injected steam temperature, mPa $\cdot$ s
$\mu_o$ :	Oil viscosity, mPa $\cdot$ s
$T$ :	Temperature at a certain point on the edge of the steam chamber, °C
$T_r$ :	Original reservoir temperature, °C
$T_s$ :	Temperature of the injected steam, °C
$m$ :	Temperature-viscosity factor, dimensionless
$n$ :	Pressure-viscosity factor, dimensionless
$P$ :	Pressure at a certain point on the edge of the steam chamber, MPa

$P_r$ :	Original reservoir pressure, MPa
$P_s$ :	Steam injection pressure, MPa
$k_{ro}$ :	Relative permeability of the oil phase, dimensionless
$k_{roCW}$ :	Relative permeability of the oil phase when under an irreducible water saturation, dimensionless
$k_{rw}$ :	Relative permeability of the water phase, dimensionless
$k_{rwro}$ :	Relative permeability of the water phase under the residual oil saturation, dimensionless
$S_{io}$ :	Initial oil saturation, dimensionless
$S_{or}$ :	Residual oil saturation, dimensionless
$S_{oD}$ :	Normalized oil saturation, dimensionless
$S_{wc}$ :	Connate-water saturation, dimensionless
$a$ :	Corey coefficient, which sets the curvature of the oil relative permeability curve, dimensionless
$b$ :	Corey coefficient, which sets the curvature of the water relative permeability curve, dimensionless
$\theta$ :	Angle of steam chamber and horizontal line, °
$M_p$ :	Effective permeability of the oil phase, m <sup>2</sup>
$L$ :	Length of the horizontal section, m.

## Data Availability

No data were used to support this study.

## Conflicts of Interest

The authors declare that there is no conflict of interest regarding the publication of this paper.

## Acknowledgments

This article is especially grateful to Professor Wen-Dong Wang from China University of Petroleum (East China) for his great support and help in writing. The project was funded by Sinopec Shengli Oilfield Exploration and Development Research Institute, and the funded subject was "Research on the Expansion Law and Dynamic Control Technology of Heavy Oil Steam Drive Cavity".

## References



- [1] R. M. Butler, "A new approach to the modelling of steam-assisted gravity drainage," *Journal of Canadian Petroleum Technology*, vol. 24, no. 3, pp. 42–51, 1985.
- [2] R. M. Butler, G. S. McNab, and H. Y. Lo, "Theoretical studies on the gravity drainage of heavy oil during in-situ steam heating," *The Canadian journal of chemical engineering*, vol. 59, no. 4, pp. 455–460, 1981.
- [3] M. Nukhaev, V. P. Pimenov, A. Shandrygin, and V. V. Ter-tychnyi, "A new analytical model for the SAGD production phase," in *SPE annual technical conference and exhibition*, San Antonio, TX, USA, 2006.
- [4] J. Sharma and I. D. Gates, "Multiphase flow at the edge of a steam chamber," *Canadian Journal of Chemical Engineering*, vol. 88, no. 3, pp. 312–321, 2010.
- [5] M. Irani and S. Ghannadi, "Understanding the heat-transfer mechanism in the steam-assisted-gravity-drainage (SAGD) process and comparing the conduction and convection flux

- in bitumen reservoirs,” *SPE Journal*, vol. 18, no. 1, pp. 134–145, 2013.
- [6] L. Qing and X. C. Zhang, “A new analysis on the convective heat transfer at the edge of the SAGD chamber,” in *SPE Annual Technical Conference and Exhibition*, Houston, TX, USA, 2015.
- [7] R. Yang, J. Zhang, L. Yang, H. Chen, and S. Tang, “Performance and calculation method of steam chamber overcoming high water saturation intervals during SAGD process,” in *Paper IPTC-18747-MS presented at the International Petroleum Technology Conference*, Bangkok, Thailand, 2016.
- [8] J. Fan and X. F. Li, “Research on the heat transfer model of the front edge of the steam cavity for steam-assisted gravity drainage,” *Science Technology and Engineering*, vol. 16, no. 3, pp. 42–47, 2016.
- [9] I. D. Gates, J. Kenny, I. L. Hernandez-Hdez, and G. L. Bunio, “Steam injection strategy and energetics of steam-assisted gravity drainage,” *SPE Reservoir Evaluation and Engineering*, vol. 10, no. 1, pp. 19–34, 2007.
- [10] D. R. Gotawala and I. D. Gates, “Stability of the edge of a SAGD steam chamber in a bitumen reservoir,” *Chemical Engineering Science*, vol. 66, no. 8, pp. 1802–1809, 2011.
- [11] Z. X. Zhang, H. Q. Liu, X. H. Dong, P. Qi, H. L. Jiang, and Y. Yang, “Research on a new model of steam-assisted gravity drainage,” *Energy and Environmental Protection*, vol. 39, no. 11, pp. 9–13, 2017, 19.
- [12] Y. Zhou, T. Lu, S. Y. Wu, L. X. Shi, X. Du, and J. L. Wang, “Calculation model and application of steam cavity expansion velocity of dual horizontal well steam assisted gravity drainage,” *Petroleum Exploration and Development*, vol. 46, no. 2, pp. 334–341, 2019.
- [13] Z. Zeinab, S. M. Razavi, and S. M. F. Ali, “Analytical model of steam-assisted gravity drainage (SAGD) process in relation to constant injection rate,” *Fuel*, vol. 265, p. 116772, 2020.
- [14] X. X. Liu, Y. W. Jiang, Y. B. Wu, and J. Wang, “Mathematical model and index prediction of constant temperature electric preheating with steam assisted gravity drainage for dual horizontal wells,” *Petroleum Exploration and Development*, vol. 45, no. 5, pp. 839–846, 2018.
- [15] B. L. Liu, “Study on SAGD physical simulation of thickened oil in thin bed,” *Chemical Engineer*, vol. 179, no. 8, pp. 16–20, 2010.
- [16] C. F. Wang, G. H. Wu, T. Wei, and Y. H. Sun, “Physical simulation experiment of nitrogen gas and dissolve solvent aided SAGD for thin formation and extra-super heavy oil reservoir,” *Petroleum Geology and Recovery Efficiency*, vol. 24, no. 1, pp. 81–85, 2017.
- [17] R. M. Butler and D. J. Stephens, “The gravity drainage of steam-heated heavy oil to parallel horizontal wells (in English) PETSOC-81-02-07,” *Journal of Canadian Petroleum Technology*, vol. 20, no. 2, pp. 90–96, 1981.
- [18] M. C. Mazdairani, “Discussion on the effects of temperature on thermal properties in the steam-assisted-gravity-drainage (SAGD) process,” *Part 1: Thermal conductivity. SPE 170064-MS*, 2014.
- [19] W. Shaolei, C. Linsong, H. Wenjun, H. Shijun, and L. Shuai, “Prediction for steam chamber development and production performance in SAGD process,” *Journal of Natural Gas Science & Engineering*, vol. 19, no. 7, pp. 303–310, 2014.
- [20] D. S. Ma, J. Guo, and C. Zan, “Physical simulation of steam-assisted gravity drainage to improve the uniformity of steam cavity development,” *Petroleum Exploration and Development*, vol. 40, no. 2, pp. 188–193, 2013.
- [21] X. Chen, Y. L. Jia, L. X. Sang, and M. Qing, “A new method to determine the development speed and range of the steam cavity front of steam gravity recovery (SAGD),” *Reservoir Evaluation and Development*, vol. 6, no. 1, pp. 36–39, 2016.
- [22] J. Tian, H. Q. Liu, Z. X. Pang, W. Zhao, Z. N. Gao, and S. X. Bing, “SAGD three-dimensional physical simulation experiment of double-horizontal well in high pressure environment,” *Acta Petrolei Sinica*, vol. 38, no. 4, pp. 453–460, 2017.
- [23] S. Chen, B. Ding, L. Gong, Z. Huang, B. Yu, and S. Sun, “Comparison of multi-field coupling numerical simulation in hot dry rock thermal exploitation of enhanced geothermal systems,” *Advances in Geo-Energy Research*, vol. 3, no. 4, pp. 396–409, 2019.
- [24] S. Huang, H. Xiong, and M. A. Kuiqian, “SAGD production capacity prediction model considering non-uniform steam absorption along the way,” *Journal of China University of Petroleum (Edition of Natural Science)*, vol. 41, no. 4, pp. 107–115, 2017.
- [25] X. Sun, B. Xu, G. Qian, and B. Li, “The application of geometrical SAGD dilation startup in a Xinjiang oil field heavy-oil reservoir,” *Journal of Petroleum Science and Engineering*, vol. 196, pp. 7–75, 2021.
- [26] K. Sasaki, A. Satoshi, N. Yazawa, and F. Kaneko, “Microscopic visualization with high resolution optical-fiber scope at steam chamber interface on initial stage of SAGD process,” in *Presented at the SPE/DOE Improved Oil Recovery Symposium*, Society of Petroleum Engineers, 2002.
- [27] F. Xu, Q. Chen, M. Ma, Y. Wang, F. Yu, and J. Li, “Displacement mechanism of polymeric surfactant in chemical cold flooding for heavy oil based on microscopic visualization experiments,” *Advances in Geo-Energy Research*, vol. 4, no. 1, pp. 77–85, 2020.
- [28] H. Dehghanpour, M. Murtaza, and Z. He, “Modeling three-phase flow during steam chamber rise-impact of water drainage on oil production rate,” in *Presented at the SPE Heavy Oil Conference-Canada*, Calgary, Alberta, Canada, 2013.
- [29] C. Harden, “Discount rate development in oil and gas valuation,” in *SPE hydrocarbon economics and evaluation symposium*, Houston, Texas, USA, 2014.
- [30] A. Honarvar, J. Rozhon, and D. Millington, *Economic Impact of New Oil Sands Projects in Alberta (2010-2015)*, 2011, ISBN 1-896091-99-7.
- [31] J. Vogel, “Simplified heat calculations for steamfloods,” *Journal of petroleum technology*, vol. 36, no. 7, 1984.
- [32] Y. Ito, T. Hirata, and M. Ichikawa, “The growth of the steam chamber during the early period of the UTF phase B and hangingstone phase I projects,” *Journal of Canadian Petroleum Technology*, vol. 40, no. 9, 2001.
- [33] J. J. Ijeje, Q. Gan, and J. Cai, “Influence of permeability anisotropy on heat transfer and permeability evolution in geothermal reservoir,” *Advances in Geo-Energy Research*, vol. 3, no. 1, pp. 43–51, 2019.
- [34] F. L. Zhang, L. P. Zhang, J. G. Bao, and H. Zhang, “The steam-assisted heavy-duty oil drainage technology is in super thick application in oil development,” *Special Oil and Gas Reservoir*, vol. 14, no. 2, pp. 70–72, 2007.



## Research Article

# Geochemical Characteristics and Oil Source Correlation of Minfeng Area, Dongying Depression, China

Dongmei Bo,<sup>1</sup> Lin Jiang ,<sup>1</sup> Wen Zhao ,<sup>1,2</sup> Youlu Jiang,<sup>3</sup> Hua Liu,<sup>3</sup> and Haowen Ou<sup>4</sup>

<sup>1</sup>Research Institute of Petroleum Exploration and Development, PetroChina, Beijing 100083, China

<sup>2</sup>College of Geosciences, China University of Petroleum (Beijing), Beijing 102249, China

<sup>3</sup>College of Geosciences, China University of Petroleum (East China), Qingdao 266580, China

<sup>4</sup>Dongxin Geological Department, Shengli Oilfield Company, Sinopec, Dongying 100083, China

Correspondence should be addressed to Lin Jiang; [jianglin01@petrochina.com.cn](mailto:jianglin01@petrochina.com.cn) and Wen Zhao; [zhaow625@126.com](mailto:zhaow625@126.com)

Received 26 March 2021; Revised 13 May 2021; Accepted 19 May 2021; Published 1 June 2021

Academic Editor: Chenhao Sun

Copyright © 2021 Dongmei Bo et al. This is an open access article distributed under the Creative Commons Attribution License, which permits unrestricted use, distribution, and reproduction in any medium, provided the original work is properly cited.

The identification of the oil-source correlation plays a significant role in petroleum exploration and development. In this study, we identify the oil-source correlation by a hierarchical cluster analysis method combined with traditional methods. The results shed light on the oil-source correlation in Minfeng area and revealed the oil migration and accumulation process. The crude oil in different structural belts and different horizons has different geochemical characteristics. According to the four types of crude oil and their planner distribution, it was considered that the crude oil mainly migrates along with favorable sand bodies and unconformity surfaces in the lateral direction and then charged and accumulated in the glutenite of Sha3 and Sha4 members since the area from sag to Yan Jia Oil and the gas field was lacking of oil source faults. Further analysis shows that the traps of fault blocks in Yong'anzen are formed in the same phase, while the crude oil generated in the early stage is charged and accumulated in the fault block of the near source. Along with increasing of the buried depth of source rocks, the overlying source rocks gradually entered into the hydrocarbon generation phase, when crude oil started to charge in the fault blocks farther away.

## 1. Introduction

Identifying the source of discovered oil (also called oil-source correlation) is of vital significance for oil petroleum exploration and development [1]. Therefore, the oil-source correlation is conducted at each confidence level for reservoir exploration and development in all sedimentary basins [2, 3]. Along with the continuous discoveries of oil and gas in the Minfeng area in recent years, the oil-source relationship has attracted researchers' attention gradually.

Although the physical and chemical properties of hydrocarbon from the same set of source rocks change slightly in the process of hydrocarbon migration, they still show certain regularity [4]. Therefore, the establishment of the connection between source rocks and reservoir can effectively guide the exploration and development of oil and gas. Oil source corre-

lation is to clarify the migration path of oil and gas by studying this law [5]. At present, oil source correlation is mainly studied by carbon isotope characteristics and biomarkers.

When using carbon isotopes to make oil source correlation, the carbon isotopic values of kerogen or extractable organic matter are mainly compared with those of hydrocarbon [6]. If the difference between the two results is small, it indicates that they are correlated. Since biomarkers are basically not affected by hydrocarbon secondary processes, they can provide more information about the origin of source rocks, sedimentary environment, and thermal maturity and play an important role in oil-source correlation. The n-alkane components can reflect the type of organic matter, the nature of sedimentary environment, and the degree of thermal evolution. Previous studies on saturated hydrocarbon chromatogram showed that different peak values of

carbon number could be used to determine the origin of hydrocarbon. The low-carbon number group was mainly the combination of low aquatic organisms, while the later peak high-carbon number group was mainly the product of the biochemical interaction between aquatic and terrestrial plants. In isoprenoids, the Pr/Ph ratio is usually used to characterize the sedimentary environment. Generally, when Pr/Ph is greater than 3, it indicates the oxidation environment and organic matter comes from terrestrial higher plants. When Pr/Ph is less than 0.8, it indicates the reduction environment and the Pr/Ph ratio of marine crude oil is usually small. Steranes are mainly derived from phytosterols in plankton, among which the distribution of  $C_{27}$ - $C_{28}$ - $C_{29}$  sterol homologs can be used to indicate different sedimentary environments and are widely used in oil-source correlation.

There are many methods during the treatment process of geochemical data in oil-source correlation, such as the direct inspection of chromatograms [7], the homologous series distribution pattern [8], 2D/3D ternary plots, or cross-plots of biomarkers ratio [9]. The above standard methods are widely adopted in the oil-source correlation process. However, these methods also have disadvantages. Although the characters of large numbers of samples can be described with the cross/ternary plot method, it has limitations when working with multiple parameters [10]. Multiple biomarkers can be well considered with the methods of chromatograms or homologous series distribution patterns. Since only a few samples can be tested, the geochemical characteristics of the oil system cannot be well considered, which will improve the uncertainties in oil-source correlation and cannot meet the accuracy needed in oil-source correlation [11, 12]. To overcome the above limitations, researchers adopt multivariate statistical analysis methods in the oil-source correlation, which can process multiple geochemical parameters and large numbers of samples simultaneously [13, 14]. Multivariate statistical methods have become the focus in the oil-source correlation process [15, 16]. As a typical multivariate statistical method, hierarchical cluster analysis (HCA) (also called hierarchical cluster) is considered to be a helpful method in oil-source correlation [17, 18]. It is an algorithm that groups similar objects into groups called clusters. The endpoint is a set of clusters, where each cluster is distinct from the other cluster and the items within each cluster are broadly similar to each other. In this work, to investigate the oil-source correlation directly and comprehensively, HCA combined with standard treatment methods (fingerprinting comparison, sterane and terpane fingerprint comparison, and scatter diagram method) are adopted.

The rest of this paper is organized as follows. In Section 2, the geological background of the Minfeng area will be introduced. The geochemical characteristics of crude oil from 25 samples are tested; four crude oil types are divided in Section 3. In Section 4, we use common treatments combined with HAC to investigate the oil-source correlation. The oil-source relationship is well correlated through the systematic collection and analysis of crude oil and oil sand samples, and the hydrocarbon migration and accumulation process are revealed in the Minfeng area.

## 2. Geological Background

Minfeng area is located in the northeast of the central uplift of Dongying Depression in the Bohai Bay Basin, China, with about 460 km<sup>2</sup>. It is bordering on Chenjiazhuang uplift to the north, central uplift belt to the south, Qingtouzi uplift to the east, and Shengtuo Oilfield to the west (Figure 1). During the deep rift period, under the control of paleoclimate and water body variation, three sets of effective source rock measures with different lithological combinations and stratigraphic development features are formed in Mingfeng subsag (upper Sha4 submember, lower Sha3 submember, and middle Sha3 submember) [19]. The primary production zone of the Yonganzhen oil and gas field is the glutenite reservoirs of Paleogene Sha2 member (Es2) and upper Sha4 submember (Es4s), while the significant production zone of the Yanjia oil and gas field is the glutenite reservoir of Sha3 member (Es3) and Sha4 member (Es4).

## 3. Geochemical Characteristics

The crude oil's biomarker characteristics in different oil and gas fields in the study area are different. According to the gas chromatographic characteristics and steroid terpane characteristics of the saturated hydrocarbon in the samples, the crude oil of the study area could be divided into four types (as shown in Table 1.).

- (1) Type A is featured by smooth distribution curves of n-alkanes when the bimodal OEP value is generally less than 1.1, which means that there is no distinct odd-even predominance; the  $\sum C_{21}^- / \sum C_{22}^+$  value is more significant than 0.7,  $C_{21} + C_{22} / (C_{28} + C_{29})$  is greater than 1.3, and the Pr/Ph ratio is larger than 0.5; the gammacerane index is greater than 0.2; the  $C_{27}$  sterane content is low,  $\alpha\alpha\alpha RC_{27} / (C_{27} + C_{28} + C_{29})$  is generally less than 0.3, and  $\alpha\beta\beta S / \alpha\alpha\alpha R$  is usually less than 0.3, while  $\alpha\alpha\alpha 20S / (20R + 20S)$  of  $C_{29}$  sterane is greater than 0.4, indicating a high thermal evolution degree. The typical crude oil of type A is that in upper Sha4 submember of Well Yong 921-X19 in the Yanjia oil and gas field, which mainly distributes in the glutenite interval of Sha3 and Sha4 members in the Yanjia oil and gas field as well as the sandstone interval of Sha2 member in Yong3 Block of the Yonganzhen oil and gas field
- (2) Type B shows an obvious bimodal postpeak in the n-alkane distribution curve, where odd number carbon is taken predominance and CPI is greater than 1.1; the  $\sum C_{21}^- / \sum C_{22}^+$  value is about 0.5, the  $C_{21} + C_{22} / (C_{28} + C_{29})$  value is about 0.9, and the Pr/Ph ratio is generally less than 0.5; the gammacerane content is high and the gammacerane index is greater than 0.2, the Ts/(Ts + Tm) value is less than 0.4;  $\alpha\alpha\alpha R C_{27} / (C_{27} + C_{28} + C_{29})$  had a value of 0.3–0.4,  $C_{29} \alpha\alpha\alpha 20S / (20R + 20S)$  has a value of 0.37–0.48, and  $\alpha\beta\beta S C_{27} / \alpha\alpha\alpha R C_{27}$  had a value of 0.3 to 0.5. Type B's typical crude oil is that of Sha2 member of well Ce77 in

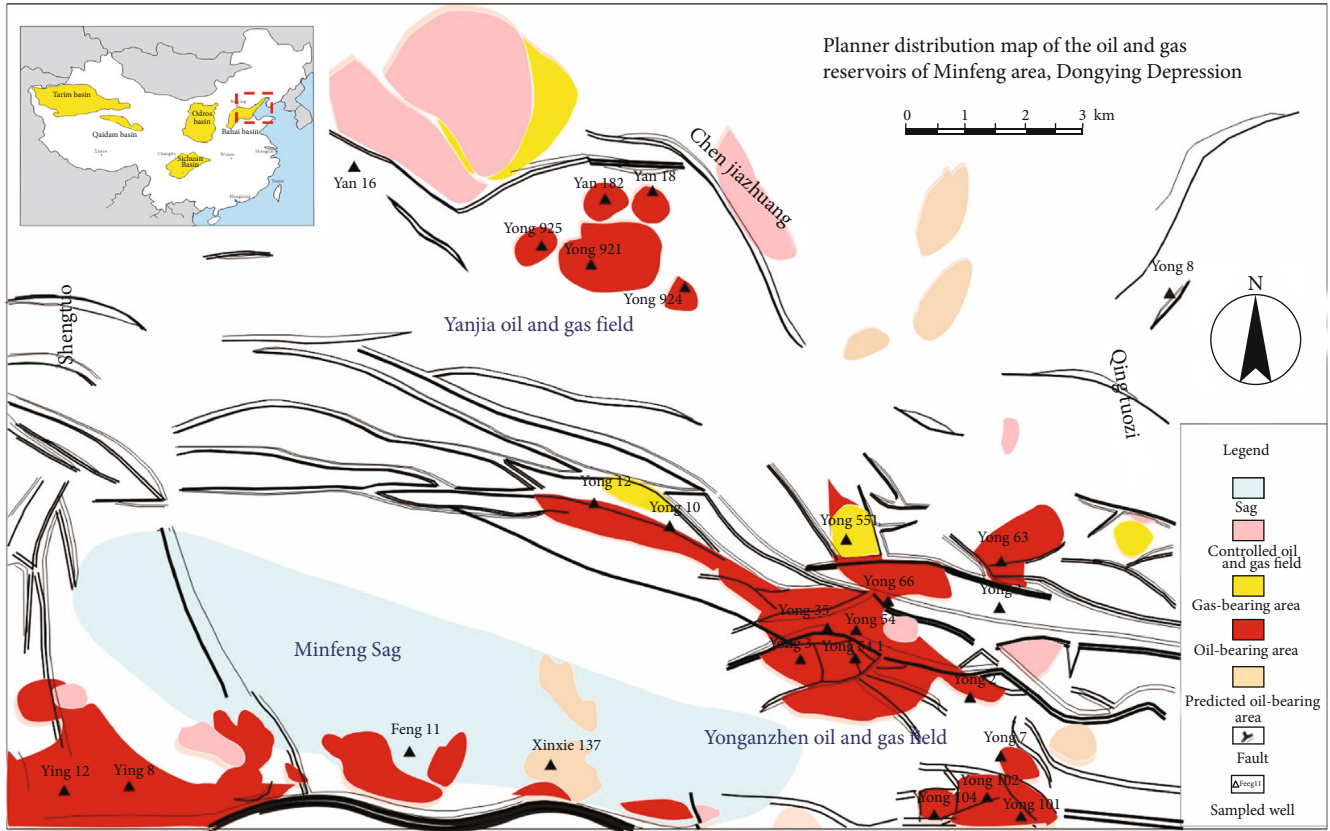


FIGURE 1: Map of the main sedimentary basins of China and hydrocarbon distribution in Minfeng area, Dongying Depression. On the upper map, the yellow is the sedimentary basin. In the lower map, the grey is the subsag; red represents the oil-bearing area and yellow represents the gas-bearing area.

TABLE 1: Crude oil geochemical characteristics of four types.

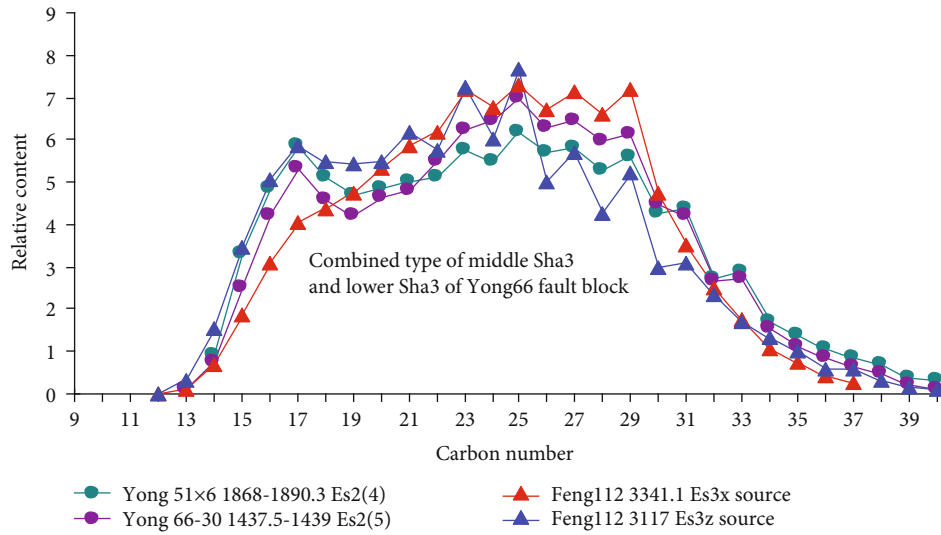
Type	A	B	C	D
OEP	<1.1	>1.1	<1.1	>1.1
$\sum C_{21}^- / \sum C_{22}^+$	>0.7	0.5	>1.3	0.5
$C_{21} + C_{22} / (C_{28} + C_{29})$	>1.3	0.9	>1.3	0.9
Pr/Ph	>0.5	<0.5	<0.5	<0.5
Gammacerane index	>0.2	>0.2	>0.3	0.1–0.3
$\alpha\alpha\alpha RC_{27} / (C_{27} + C_{28} + C_{29})$	<0.3	0.3–0.4	>0.38	0.3–0.4
$\alpha\alpha\alpha 20S / (20R + 20S)$ of $C_{29}$	>0.4	0.37–0.48	<0.35	0.38–0.5
Ts/(Ts + Tm)	<0.35	<0.4	<0.35	0.26–0.4
$\alpha\beta\beta S C_{27} / \alpha\alpha\alpha R C_{27}$	<0.3	0.3–0.5	<0.3	0.4–0.5
$C_{29}\beta\beta / (\beta\beta + \alpha\alpha)$	<0.32	0.35–0.42	<0.32	0.35–0.42

Yong3 Blocks, which mainly distributes in the Yong2, Yong3, Yong12, and Yong66 Blocks in Yonganzhen area

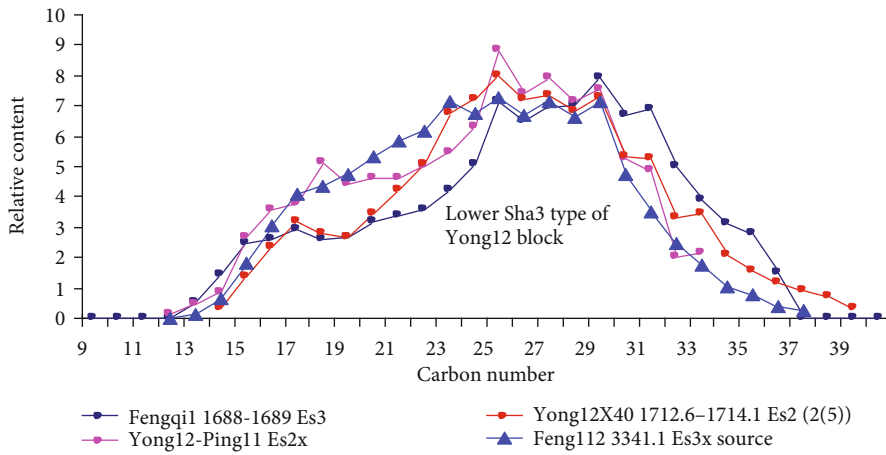
- (3) Type C is characterized by the typical bimodal pre-peak type of the n-alkane distribution curve with the carbon number of  $C_{17}$  in the main peak, OEP and CPI values are generally less than 1.1, the  $C_{21} + C_{22} / (C_{28} + C_{29})$  value is generally greater than

1.3,  $\sum C_{21}^- / \sum C_{22}^+$  is greater than 1.3, and the Pr/Ph ratio is less than 0.5. The gammacerane content is high and the gammacerane index is greater than 0.3, the Ts/(Ts + Tm) value is less than 0.35; the  $\alpha\alpha\alpha RC_{27} / (C_{27} + C_{28} + C_{29})$  value is greater than 0.38, the  $C_{29}\alpha\alpha\alpha 20S / (20R + 20S)$  value is less than 0.35, the  $C_{29}\beta\beta / (\beta\beta + \alpha\alpha)$  value is less than 0.32, and the  $\alpha\beta\beta S / \alpha\alpha\alpha R C_{27}$  value is less than 0.3. The typical crude oil of type C is mainly produced from Sha3 member of Yong63-13 Block, which distributes in the reservoirs of middle Sha3 submember in Yong63 Block and Yong2 Block of the Yonganzhen oil field and Minfeng subsag

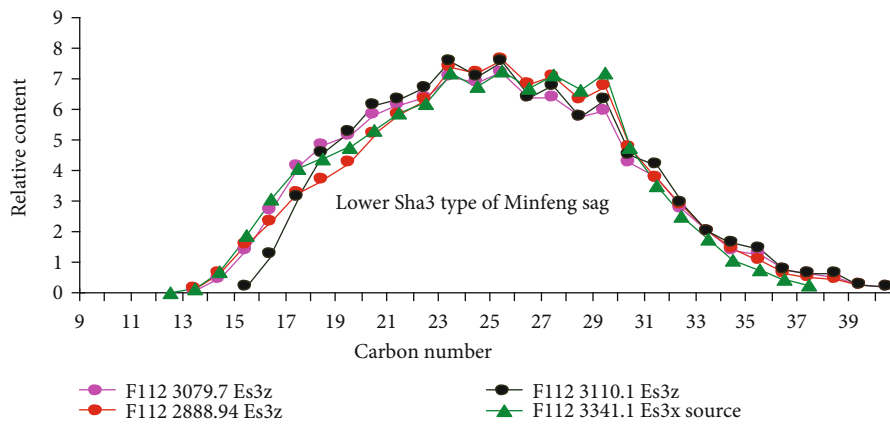
- (4) Type D shows a single peak in the n-alkane distribution curve. The OEP is greater than 1.1, the  $\sum C_{21}^- / \sum C_{22}^+$  value is around 0.5, and the Pr/Ph ratio is generally less than 0.5. The gammacerane content is high and the gammacerane index is between 0.1 and 0.3; Ts/(Ts + Tm) has a value of 0.26–0.40;  $\alpha\alpha\alpha RC_{27} / (C_{27} + C_{28} + C_{29})$  has a value of 0.3 to 0.4,  $C_{29}\alpha\alpha\alpha 20S / (20R + 20S)$  has a value of 0.38–0.5,  $C_{29}\beta\beta / (\beta\beta + \alpha\alpha)$  has a value of 0.35 to 0.42, and  $\alpha\beta\beta S C_{27} / \alpha\alpha\alpha R C_{27}$  has a value of 0.4 to 0.5. This kind is produced from well 112 in middle Sha3 submember, which mainly distributes in the Minfeng Sag



(a)

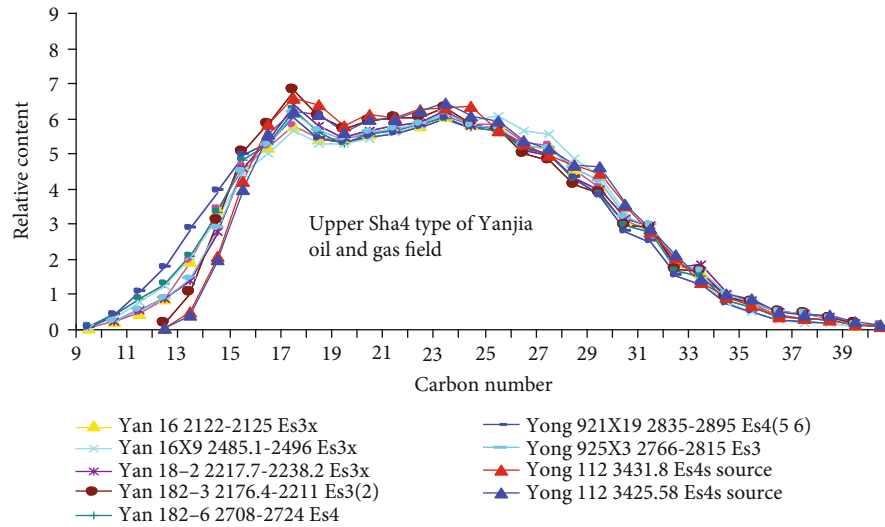


(b)

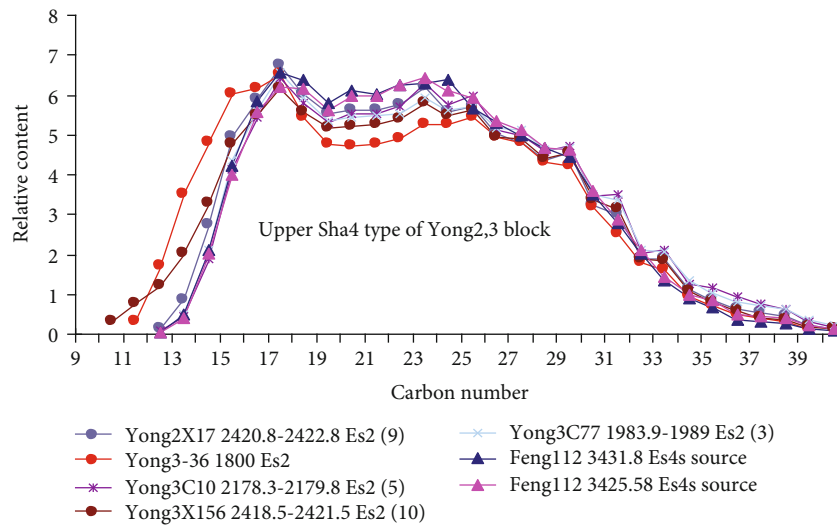


(c)

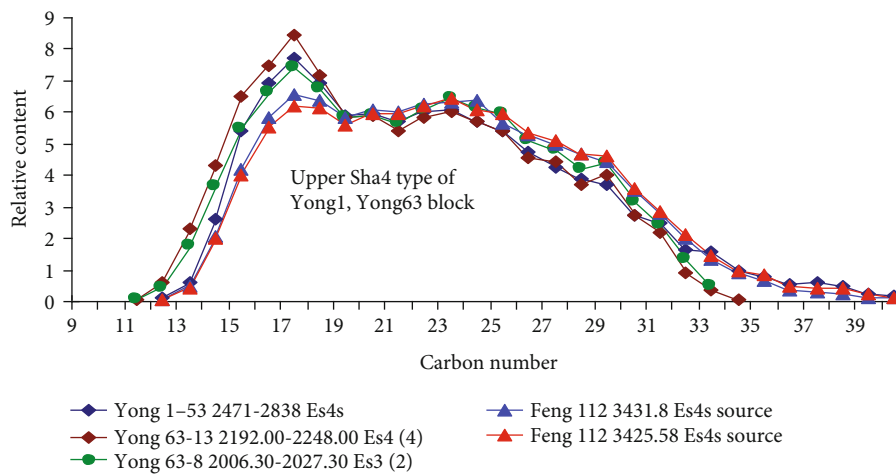
FIGURE 2: Continued.



(d)



(e)



(f)

FIGURE 2: Comparison diagram of carbon number distributions in some crude oil and hydrocarbon source rocks in the study area of n-alkanes.

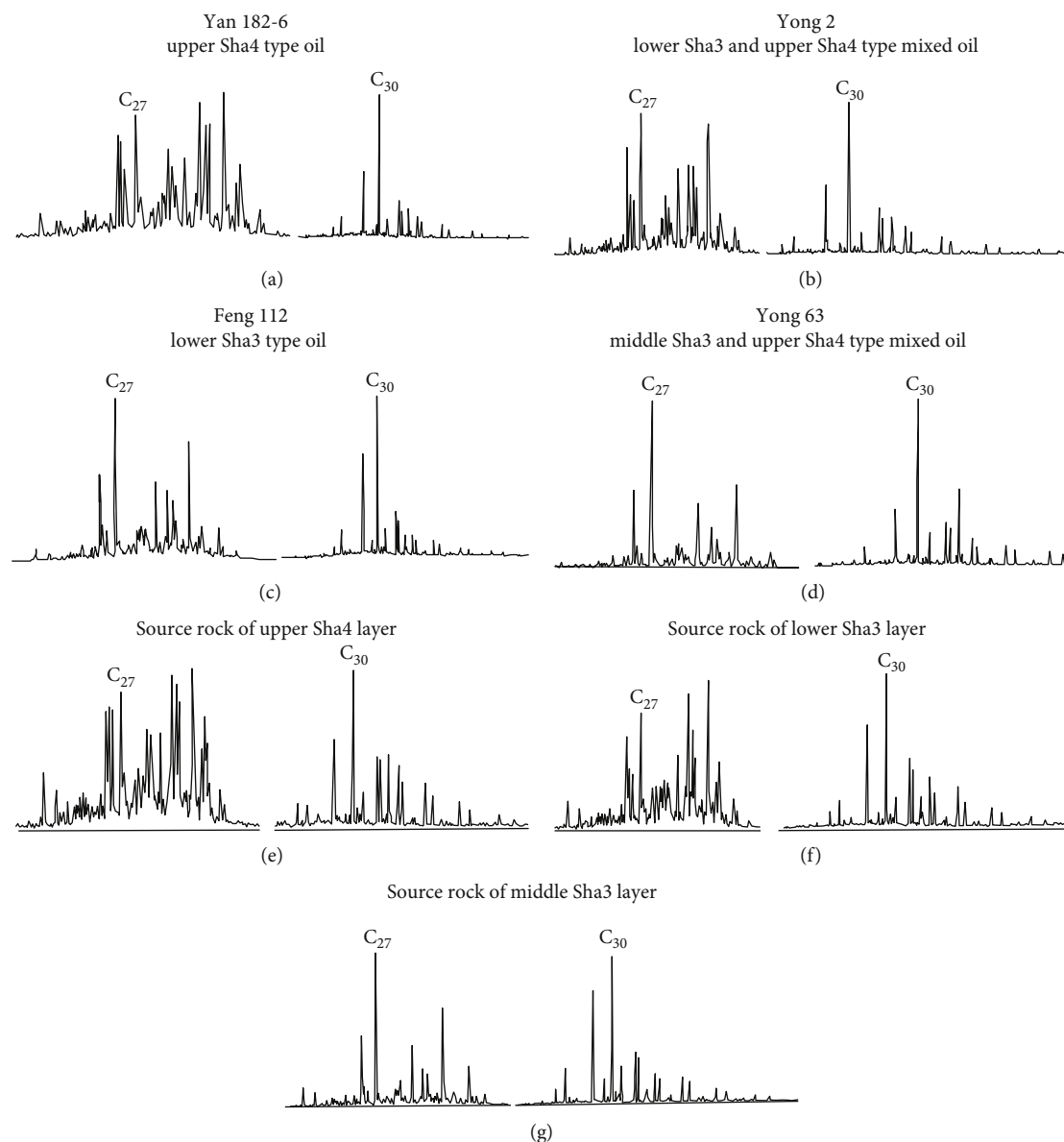


FIGURE 3: Sterane and terpane fingerprint comparison diagram of the source rocks and crude oil in the study area. (a–d) Are diagrams for crude oil and (e–g) are diagrams for source rock.

#### 4. Oil-Source Correlation

In this section, we will investigate the oil-source correlation with the HCA method combined with standard procedures. The traditional oil-source correlation involves various methods, such as the fingerprinting method, parameter comparison method, scatter diagram method, carbon isotope distribution curve method, and other conventional methods [20, 21]. Since a single method often has limitations and multiple solutions, HCA will be applied to verify further the oil-source relationship in this paper based on the conventional methods.

**4.1. Fingerprinting Comparison of Carbon Number Distribution in *n*-Alkanes.** The composition and distribution characteristics of *n*-alkanes are affected by multiple factors

such as parent material types and organic matter evolution degree, which can be used to identify oil-source relations. The fingerprint contains 25 crude oil samples and 13 source rock samples, including the shape of the *n*-alkane distribution curve, odd number carbon advantages, and the degree of curve smoothness. Results indicate that the crude oil produced in the Yanjia oil and gas field, Yong2, Yong3, Yong12, and Yong63 Blocks of Yonganzhen has the features of the upper Sha4 type, while the crude oil produced in Yong66 Block has the characteristics of the combined type of middle Sha3 and lower Sha3; the crude oil produced in Minfeng Sag has the attributes of the lower Sha3 type (Figure 2).

**4.2. Sterane and Terpane Fingerprint Comparison.** Steranes and terpane are two kinds of essential biomarker compounds, recording shreds of evidence of evolution from the

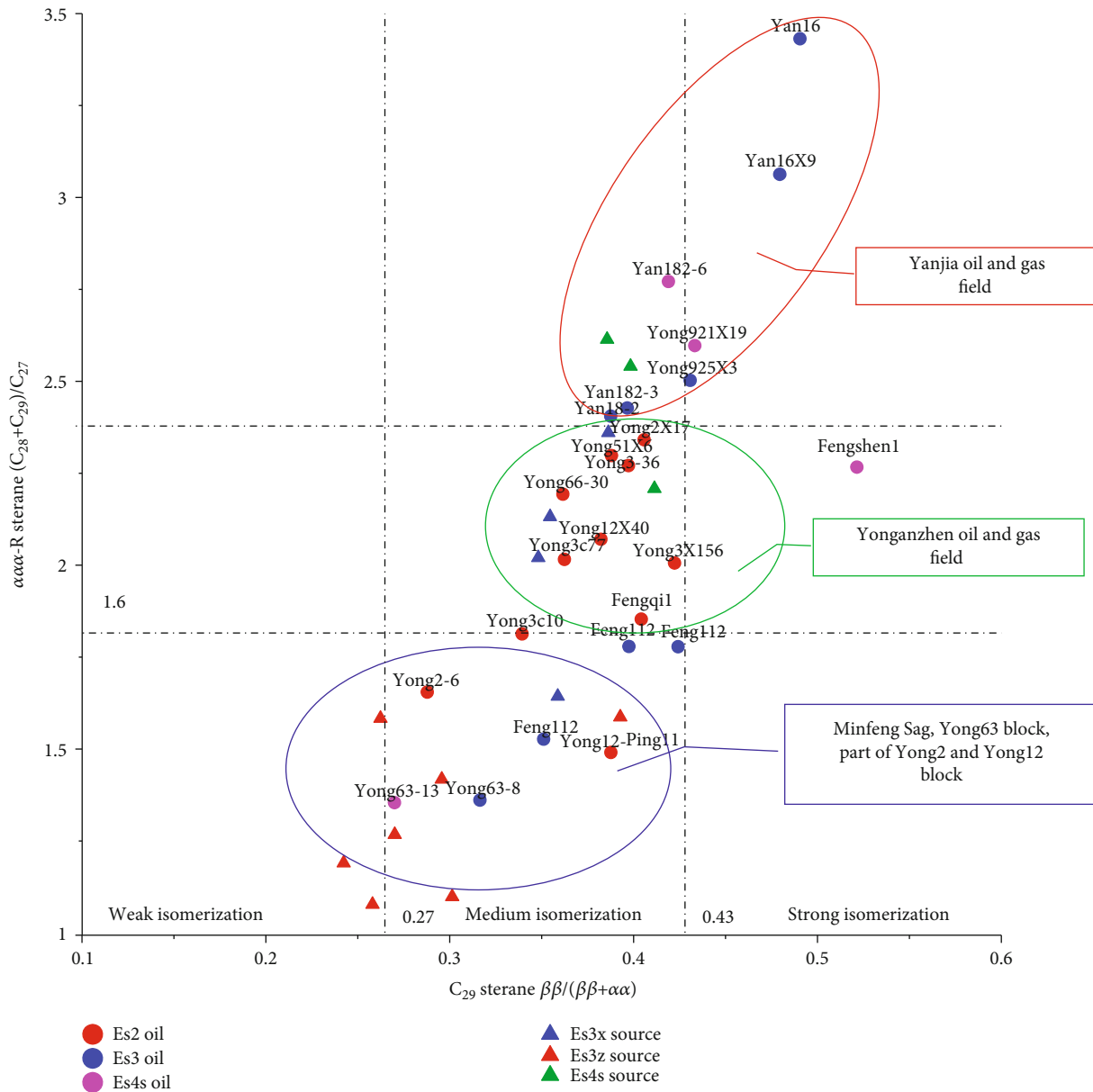


FIGURE 4: Correlation map between  $\alpha\alpha\alpha$ R sterane  $C_{28} + C_{29}/C_{27}$  and  $C_{29}$  sterane  $\beta\beta/(\beta\beta + \alpha\alpha)$ .

biological organic matter to sedimentary organic matter, which can reflect the depositional environment of source rocks and organic matter input [22]. Although the crude oil is generated in the same set of source rock beds, after secondary migration and accumulation, their chemical compositions will change significantly, since a series of geochemical changes would occur due to the changes of geological-geochemical conditions, such as the biodegradation and hydrolysis of crude oil in the reservoir, thermal alteration, and fluid-rock interaction and fractionation during the process of oil and gas migration [23]. However, part of the sterane and terpane biomarkers in the crude oil will represent a relatively stable distribution because biodegradation of a light-medium degree, migration effect, and maturity have no apparent impact on them [24].

According to the characteristics of sterane and terpane fingerprints, the  $C_{27}$ - $C_{28}$ - $C_{29}$  sterane of source rock and crude oil in the study area distributed as a “V” shape, among which the source rocks of upper Sha4 and lower Sha3 submember have a relatively high content of  $C_{29}$  sterane and high gammacerane index. In contrast, the source rocks of middle Sha3 submember have a relatively high content of  $C_{27}$  sterane and low gammacerane index (Figure 3). Correlation results showed that the crude oil of the Yanjia oil and gas field is the upper Sha4 type; the crude oil of Minfeng Sag is the lower Sha3 type; the crude oil of the Yonganzhen oil field is mixed with various types, which is a combined type of upper Sha4 and lower Sha3 in Yong2, Yong3, Yong12, and Yong66 fault blocks; the crude oil of Yong63 Block is the middle Sha3 type, but its gammacerane content is high in

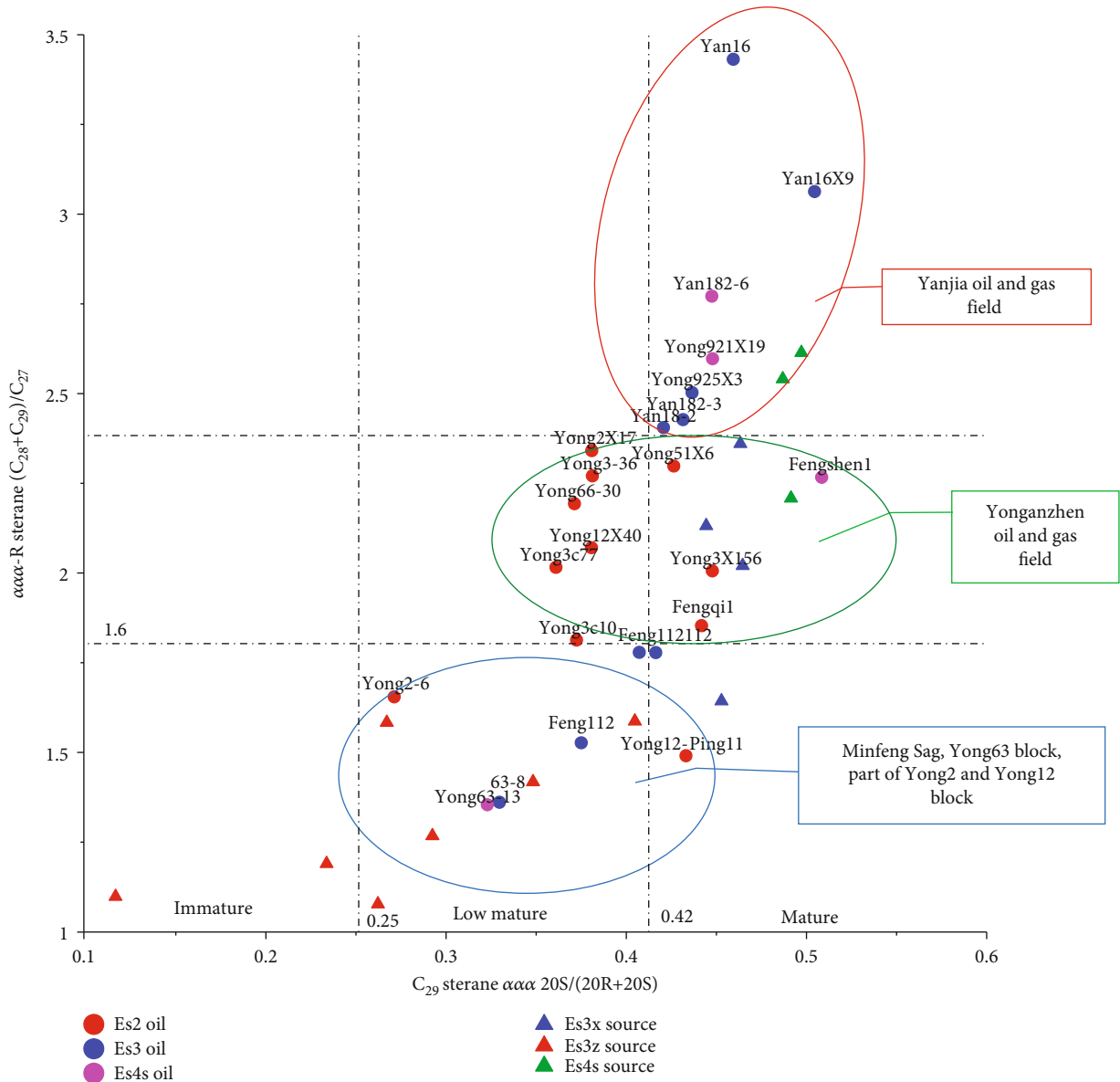


FIGURE 5: Correlation map between  $\alpha\alpha R$  sterane  $(C_{28} + C_{29})/C_{27}$  and  $C_{29}$  sterane  $\alpha\alpha 20S/(20R + 20S)$ .

terpane. Therefore, it also showed the characteristics of the upper Sha4 type (Figure 4), which needed to be further confirmed combining with maturity indicators.

**4.3. Scatter Diagram Method.** The parameters used for the scatter diagram methodology this time are parent source and maturity, among which the parent source parameter is the  $C_{29}$  sterane isomerization parameter (includes two types: epimerism and ring isomerism), and the parent source parameter is  $(C_{28} + C_{29})/C_{27}$  of normal sterane  $\alpha\alpha R$  biological configuration.

The scatter plot (Figures 5 and 4) reveals that three types of crude oil and source rocks with a different parent material and maturity exist in the study area, distributed in three point groups, which indicates the affinities of oil sources intuitively: the first is the sample points of the crude oil of the Yanjia oil and gas field as well as the source rock of lower Sha4 sub-

member; the second is the sample points of the source rocks from the lower Sha3 submember and part upper Sha3 submember as well as the crude oil from Yong3 Block (upthrown wall), Yong66 Block, Yong3 Block (7–9 sand groups), Yong 51 Block, and part of Yong 12 Block of the Yonganzhen oil field; the third is the sample points of the crude oil from Yong63 Block, part of Yong2 Block and Yong12 Block, Minfeng Sag, and the source rock of middle Sha3 submember.

**4.4. Clustering Method.** To avoid multiple solutions, cluster analysis is further adopted with mathematical statistics for the 24 crude oil samples and 14 source rock samples of the study area using 17 geochemical parameters. The clustering method is the correlation coefficient group-averaging method, whose parameters are the gammacerane index,  $Ts/(Ts + Tm)$ , gammacerane content,  $C_{29}$  sterane  $\alpha\alpha 20S/(20R + 20S)$ ,  $C_{29}$  sterane  $\beta\beta/(\beta\beta + \alpha\alpha)$ ,  $C_{27}$  sterane  $\alpha\beta\beta S/\alpha\alpha R$ ,



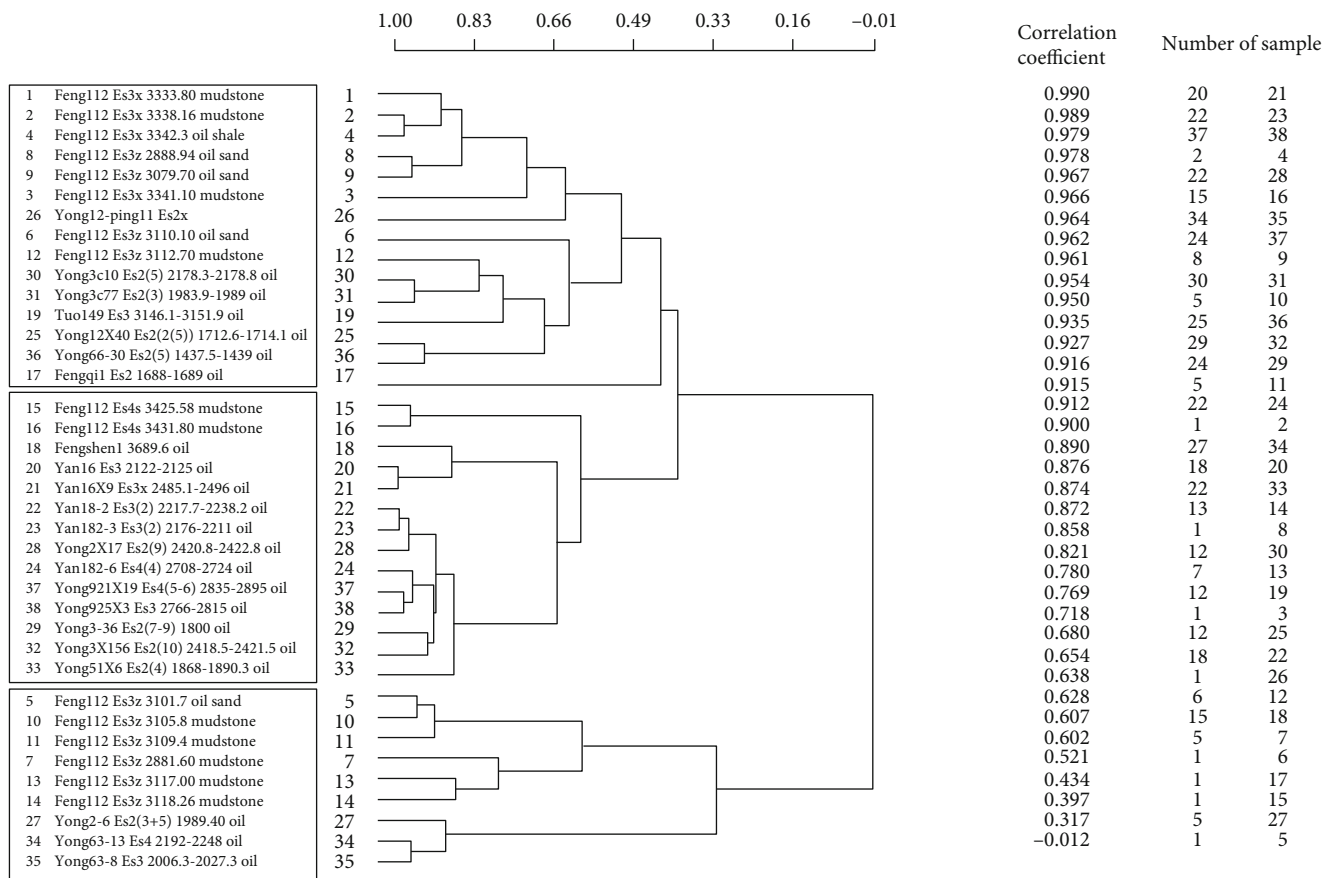


FIGURE 6: Clustering hierarchical diagram by correlation coefficient group averaging method.

$C_{27}$  steranes  $\alpha\alpha\alpha R$ ,  $C_{28}$  steranes  $\alpha\alpha\alpha R$ ,  $\alpha\alpha\alpha RC_{27} + C_{28} + C_{29}$  sterane,  $\alpha\alpha\alpha RC_{27}/(C_{27} + C_{28} + C_{29})$  steranes,  $\alpha\alpha\alpha RC_{29}/(C_{27} + C_{28} + C_{29})$  steranes, OEP, CPI,  $\sum C_{21}^- / \sum C_{22}^+$ , pristane/phytane, and  $C_{17} / \sum C_7^+$ .

The clustering hierarchical diagram (Figure 6) indicates that the samples of source rocks and crude oil could be divided into three groups: the first group is the crude oil of middle Sha3 submember in Minfeng Sag, the crude oil of Sha2 Member no.3 and no.5 sand groups in Yong3 Block, the crude oil of Yong66 Block, the crude oil of Yong12 Block, and the source rocks of lower Sha3 submember and part of middle Sha3 submember, among which the crude oil of middle Sha3 submember and the source rocks of lower Sha3 submember developed in the sag are well correlated with each other whose correlation coefficient reached up to 0.858, while the correlation coefficient between the crude oil of Sha2 member no.3 and no.5 sand groups in Yong3 Block, the crude oil of Yong66 Block, the crude oil of Yong12 Block, and the source rocks of middle Sha3 submember is 0.68. The population correlation coefficient reaches 0.521.

The second group is the source rock of upper Sha4 member and the crude oil of the Yanjia oil and gas field and the crude oil of Yong3 Block and Yong 51 Block, among which the correlation coefficient between the crude oil of the Yanjia oil and gas field and the crude oil of Yong3 Block and Yong 51 Block reaches 0.989, while the population correlation coefficient reaches 0.521.

The third group is the source rock of middle Sha3 submember and the crude oil of middle Sha3 submember in Minfeng Sag and the crude oil of Yong2 and Yong63 Blocks, among which the crude oil in the sag and the source rocks of middle Sha3 submember are highly correlated with each other, whose maximum correlation coefficient is 0.95. In contrast, the crude oil of Yong63 Block and Yong2 Block is poorly associated with each other, whose correlation coefficient is less than 0.317.

Combined with the comparison results of the three methods above, the maturity of the oil-source, and provenance, the oil-source relationship was confirmed: the crude oil of Sha2 member (no.7 ~ 10 sand groups) of Yong3 Block, Sha2 member (no.4 sand group) of Yong51 Block, and the Yan Jia oil and gas field is the upper Sha4 type; the crude oil of the middle Sha3 type and lower Sha3 type was confirmed as the self-generation and self-preservation type that is developed in Minfeng Sag. Besides, the crude oil of the lower Sha3 type is developed in middle Sha3 submember; the crude oil of Sha2 member (no. 3 and no. 5 sand groups) of Yong3 Block, Yong66 Block, Yong12 Block, and Yong51 Block is the combined type of upper Sha4 and lower Sha3; the crude oil of Yong2 Block (no. 3 and no. 5 sand groups) and Yong63 Block is the middle Sha3 type. The results of oil source correlation on the plane show that only the crude oil of upper Sha4 type is developed in the Yanjia oil and gas field; the crude oil of various types is developed in the

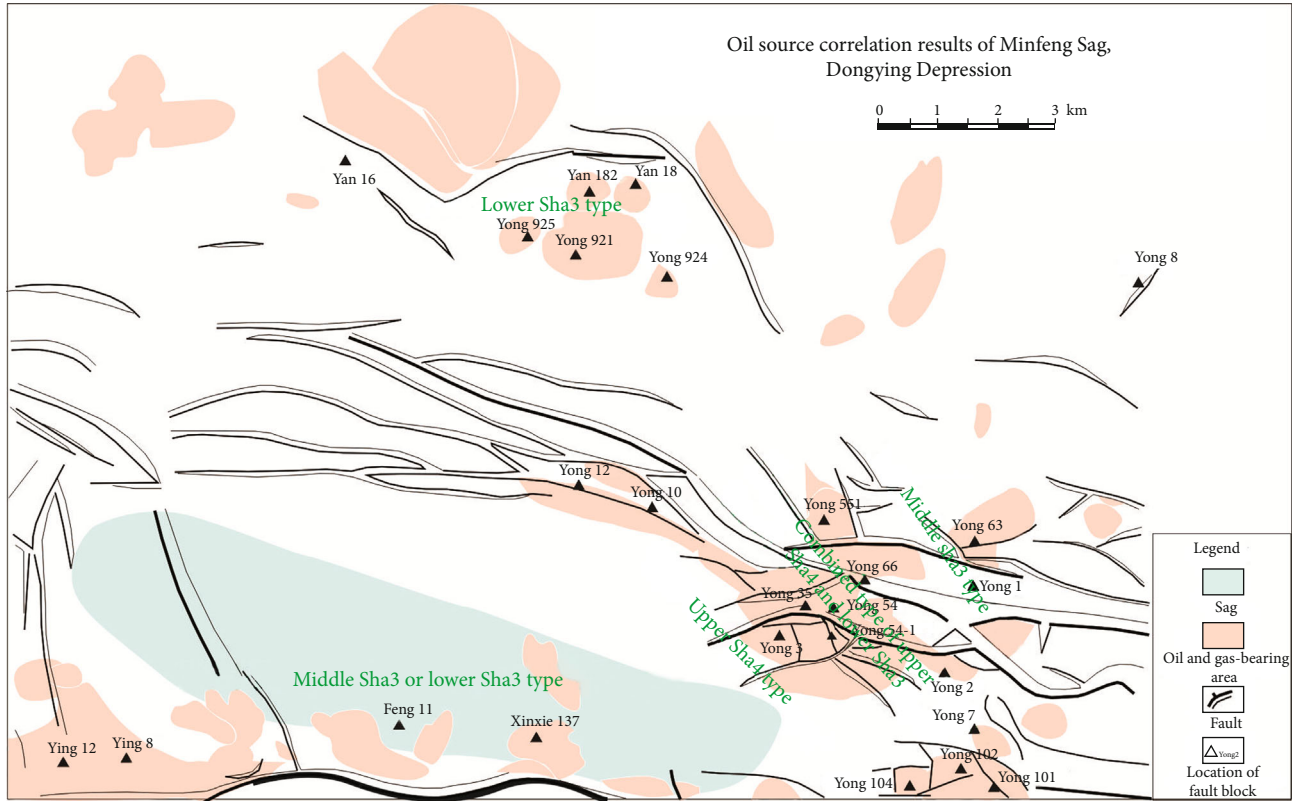


FIGURE 7: Oil source correlation results and hydrocarbon migration direction of the Minfeng Sag, Dongying Depression.

Yonganzhen oil and gas field, which represents a regular variation from the sag to the Qingtuozi uplift; the crude oil is the upper Sha4 type in the area near the sag, combined type of upper Sha4 and lower Sha3 eastward, and middle Sha3 type far away (Figure 7). It is considered that the traps of the fault blocks in Yonganzhen were formed in the same phase, while the crude oil generated in the early phase charged and accumulated in the fault block of the near source. Along with the increasing of the buried depth of source rock, the overlying source rocks gradually entered into the hydrocarbon generation phase, when crude oil started to charge into the fault blocks farther away.

## 5. Conclusions

(1) There are four types of crude oil with different biomarkers developed in Minfeng area: type A mainly distributes in Sha2 member of Yong3 Block, Sha2 member of Yong51 Block in the Yong Anzhen oil field and Yan Jia oil and gas field. Type B distributes in Sha2 member of Yong3 Block, Yong66 Block, Yong12 Block, and Yong51 Block of Yong Anzhen gas field. Type C distributes in middle Sha3 submember of Minfeng Sag and Yong2 Block, and Yong63 Block of the Yong Anzhen oil and gas field. Type D distributes in middle Sha3 submember and lower Sha3 submember of Minfeng Sags

- (2) Results shed light on the oil-source correlation: the crude oil of Sha2 member of Yong3 Block, Sha2 member of Yong51 Block, and Yan Jia oil and gas field is the upper Sha4 type; the crude oil of the middle Sha3 type and lower Sha3 type is confirmed as self-generation and self-preservation that is developed in Minfeng Sag. In addition, the crude oil of the lower Sha3 type is developed in middle Sha3 submember; the crude oil of Sha2 member of Yong3 Block, Yong66 Block, Yong12 Block, and Yong51 Block is the combined type of upper Sha4 and lower Sha3; the crude oil of Yong2 Block and Yong63 Block is the middle Sha3 type
- (3) The migration and accumulation process is revealed. The crude oil mainly migrated along favorable sand bodies and unconformity surfaces in the lateral direction and then charged and accumulated in the glauconite of Sha3 and Sha4 members since the area from sag to the Yan Jia oil and gas field lacks oil source faults. From Minfeng Sag to Yonganzhen Oilfield and Qing Tuozi uplift, the crude oil represented various types with regular variation, which showed the upper Sha4 type in the fault block of the near source
- (4) The traps of the fault block in Yonganzhen were formed in the same phase; the crude oil generated in the early phase charged and accumulated in the fault block of the near source, along with the

increasing of the buried depth of source rocks and the overlying source rocks gradually entering into the hydrocarbon generation phase, when the crude oil started to charge into the fault blocks farther away

## Data Availability

All data used can be found in our manuscript.

## Conflicts of Interest

The authors declare that they have no conflicts of interest.

## References

- [1] J. A. Curiale, "Oil-source rock correlations - Limitations and recommendations," *Organic Geochemistry*, vol. 39, no. 8, pp. 1150–1161, 2008.
- [2] P. K. Mukhopadhyay, J. A. Wade, and M. A. Kruger, "Organic facies and maturation of Jurassic/Cretaceous rocks, and possible oil-source rock correlation based on pyrolysis of asphaltene, Scotian Basin, Canada," *Organic Geochemistry*, vol. 22, no. 1, pp. 85–104, 1995.
- [3] W. Zhao, C. Jia, L. Jiang et al., "Fluid charging and hydrocarbon accumulation in the sweet spot, Ordos Basin, China," *Journal of Petroleum Science and Engineering*, vol. 200, p. 108391, 2021.
- [4] L. Liu, Z. Zhang, C. Li et al., "Hydrate growth in quartzitic sands and implication of pore fractal characteristics to hydraulic, mechanical, and electrical properties of hydrate-bearing sediments," *Journal of Natural Gas Science and Engineering*, vol. 75, p. 103109, 2020.
- [5] G. Wang, X. Qin, J. Zhou, F. Han, and J. Cai, "Simulation of coal microstructure characteristics under temperature-pressure coupling based on micro-computer tomography," *Journal of Natural Gas Science and Engineering*, vol. 91, p. 103906, 2021.
- [6] C. Wang and G. Shi, "Redox condition and organic carbon accumulation mechanism in the Cryogenian Nanhua Basin, South China: insights from iron chemistry and sulfur, carbon, oxygen isotopes of the Datangpo Formation," *Advances in Geo-Energy Research*, vol. 3, no. 1, pp. 67–75, 2019.
- [7] Z. S. Mashhadi and A. R. Rabbani, "Organic geochemistry of crude oils and Cretaceous source rocks in the Iranian sector of the Persian Gulf: An oil-oil and oil-source rock correlation study," *International Journal of Coal Geology*, vol. 146, pp. 118–144, 2015.
- [8] Z. Chen, T. G. Wang, M. Li, F. Yang, and B. Cheng, "Biomarker geochemistry of crude oils and Lower Paleozoic source rocks in the Tarim Basin, Western China: an oil-source rock correlation study," *Marine and Petroleum Geology*, vol. 96, pp. 94–112, 2018.
- [9] W. Zhao, C. Jia, T. Zhang et al., "Effects of nanopore geometry on confined water flow: a view of lattice Boltzmann simulation," *Chemical Engineering Science*, vol. 230, article 116183, 2021.
- [10] P. F. Greenwood, L. Mohammed, K. Grice, M. McCulloch, and L. Schwark, "The application of compound-specific sulfur isotopes to the oil-source rock correlation of Kurdistan petroleum," *Organic Geochemistry*, vol. 117, pp. 22–30, 2018.
- [11] L. Zhang, G. Bai, X. Zhao et al., "Oil-source correlation in the slope of the Qikou Depression in the Bohai Bay Basin with discriminant analysis," *Marine and Petroleum Geology*, vol. 109, pp. 641–657, 2019.
- [12] W. Zhao, T. Zhang, C. Jia, X. Li, K. Wu, and M. He, "Numerical simulation on natural gas migration and accumulation in sweet spots of tight reservoir," *Journal of Natural Gas Science and Engineering*, vol. 81, p. 103454, 2020.
- [13] H. Huang, S. Zhang, and J. Su, "Palaeozoic oil-source correlation in the Tarim Basin, NW China: a review," *Organic Geochemistry*, vol. 94, pp. 32–46, 2016.
- [14] H. Yang, W. Zhang, K. Wu, S. Li, and Y. Qin, "Uranium enrichment in lacustrine oil source rocks of the Chang 7 member of the Yanchang Formation, Erdos Basin, China," *Journal of Asian Earth Sciences*, vol. 39, no. 4, pp. 285–293, 2010.
- [15] S. Fu, Z. Liu, Y. M. Zhang et al., "Source rocks geochemistry and oil-source correlation in the Aershan and first member of Tengge'er formations of the Wulan-Hua Sag in south of Erlian Basin, Northeastern China," *Journal of Petroleum Science and Engineering*, vol. 182, p. 106334, 2019.
- [16] K. E. Peters, L. S. Ramos, J. E. Zumberge, Z. C. Valin, C. R. Scotese, and D. L. Gautier, "Circum-Arctic petroleum systems identified using decision-tree chemometrics," *AAPG Bulletin*, vol. 91, no. 6, pp. 877–913, 2007.
- [17] D. A. Wood and A. Choubineh, "Reliable predictions of oil formation volume factor based on transparent and auditable machine learning approaches," *Advances in Geo-Energy Research*, vol. 3, no. 3, pp. 225–241, 2019.
- [18] I. M. Mohialdeen, M. H. Hakimi, and F. M. Al-Beyati, "Biomarker characteristics of certain crude oils and the oil-source rock correlation for the Kurdistan oilfields, Northern Iraq," *Arabian Journal of Geosciences*, vol. 8, no. 1, pp. 507–523, 2015.
- [19] J. Li, K. Yan, H. Ren, and Z. Sun, "Detailed quantitative description of fluvial reservoirs: a case study of L6-3 layer of sandgroup 6 in the second member of Shahejie Formation, Shengtuo Oilfield, China," *Advances in Geo-Energy Research*, vol. 4, no. 1, pp. 43–53, 2020.
- [20] P. A. Mello, J. S. Pereira, M. F. Mesko, J. S. Barin, and E. M. Flores, "Sample preparation methods for subsequent determination of metals and non-metals in crude oil—a review," *Analytica Chimica Acta*, vol. 746, pp. 15–36, 2012.
- [21] Z. Wang, C. Yang, Z. Yang, C. E. Brown, B. P. Hollebone, and S. A. Stout, *Petroleum Biomarker Fingerprinting for Oil Spill Characterization and Source Identification*, In standard handbook oil spill environmental forensics, Academic press, 2016.
- [22] F. Wang, L. Jiao, J. Zhao, and J. Cai, "A more generalized model for relative permeability prediction in unsaturated fractal porous media," *Journal of Natural Gas Science and Engineering*, vol. 67, pp. 82–92, 2019.
- [23] J. A. Miles, "Secondary migration routes in the Brent sandstones of the Viking Graben and East Shetland Basin: evidence from oil residues and subsurface pressure data," *AAPG Bulletin*, vol. 74, no. 11, pp. 1718–1735, 1990.
- [24] Z. Wang, M. Fingas, C. Yang, and J. H. Christensen, *Crude Oil and Refined Product Fingerprinting: Principles*, In environmental forensics, Academic press, 1964.